INTERNATIONAL EDITION

Aerodynamics for Engineers

SIXTH EDITION

John J. Bertin • Russell M. Cummings

ALWAYS LEARNING

PEARSON

AERODYNAMICS FOR ENGINEERS

Sixth Edition

JOHN J. BERTIN
Late Professor Emeritus, United States Air Force Academy

and

RUSSELL M. CUMMINGS
Professor Emeritus, California Polytechnic State University

International Edition contributions by

P VENKATA REDDY
Rajiv Gandhi University of Knowledge Technologies, Andhra Pradesh

PEARSON

Boston Columbus Indianapolis New York San Francisco Upper Saddle River
Amsterdam Cape Town Dubai London Madrid Milan Munich Paris Montréal Toronto
Delhi Mexico City São Paulo Sydney Hong Kong Seoul Singapore Taipei Tokyo

This edition of Aerodynamics for Engineers is dedicated to the memory of John J. Bertin

Vice President and Editorial Director, ECS: *Marcia J. Horton*
Executive Editor: *Norrin Dias*
Editorial Assistant: *Sandra Rodriguez*
Executive Marketing Manager: *Tim Galligan*
Marketing Assistant: *Jon Bryant*
Permissions Project Manager: *Karen Sanatar*
Senior Managing Editor: *Scott Disanno*
Production Project Manager /Editorial Production Manager: *Greg Dulles*
Publisher, International Edition: *Angshuman Chakraborty*
Publishing Administrator and Business Analyst, International Edition: *Shokhi Shah Khandelwal*
Associate Print and Media Editor, International Edition: *Anuprova Dey Chowdhuri*
Acquisitions Editor, International Edition: *Sandhya Ghoshal*
Publishing Administrator, International Edition: *Hema Mehta*
Project Editor, International Edition: *Karthik Subramanian*
Senior Manufacturing Controller, Production, International Edition: *Trudy Kimber*
Creative Director: *Jayne Conte*
Cover Designer: *Bruce Kenselaar*
Cover Image: *EmiliaUngur/Shutterstock*
Production and Manufacturing: *Pat Brown*
Full-Service Project Management: *Jogender Taneja, Aptara®, Inc.*
Cover Printer: *Courier Westford*

Pearson Education Limited
Edinburgh Gate
Harlow
Essex CM20 2JE
England

and Associated Companies throughout the world

Visit us on the World Wide Web at:
www.pearsoninternationaleditions.com

ISBN 10: 0-273-79327-6
ISBN 13: 978-0-273-79327-4

British Library Cataloguing-in-Publication Data
A catalogue record for this book is available from the British Library

10 9 8 7 6 5 4 3 2 1
14 13 12 11 10

Typeset in TimesTen Roman by Aptara®, Inc.

Printed and bound by Courier Westford in The United States of America
The publisher's policy is to use paper manufactured from sustainable forests.

Contents

Preface

A great deal has happened since the preface to the fifth edition of *Aerodynamics for Engineers* was written early in 2008. During the spring and early summer of 2008, John Bertin and I were busy checking chapter proofs for "The Book" (as he liked to call it). John was at home in Houston and teaching at his beloved Rice University (you may have noticed that covers of the various editions of *Aerodynamics for Engineers* were usually blue and light gray, the colors of Rice University). I was a visiting researcher at the Institute of Aerodynamics and Flow Technology at The German Aerospace Center (DLR) in Braunschweig. John had two major struggles in his life at the time: he was working through the last stages of the illness that would take his wife, Ruth, from him. He had also been diagnosed with pancreatic cancer, and was dealing with doctors, treatments, and hospitals. We spoke on the phone often about the various challenges he was facing, both with his wife's and his own health. Through the support of his family, as well as his desire to finish the fifth edition, he made it through the summer of 2008 in reasonably good shape. Copies of the book were shipped to us in July 2008, and he was very glad that we had finished the undertaking we had started so many years earlier.

Unfortunately, John's pancreatic cancer took a turn for the worse in late summer of 2008, and he passed away on October 11, 2008. A large number of former co-workers from NASA and various universities, as well as his family and friends, attended his funeral later that month, and we all knew that a very special person had passed from our ranks.

One of the things that John and I talked about during his last months of life was his desire for *Aerodynamics for Engineers* to continue to grow and evolve, even if he was not around to help with that task. I cannot help but think that he asked me to be his co-author for the fifth edition for this purpose. So, in spite of the fact that John is no longer with us, his spirit and excitement for learning will continue to live.

So, there were many goals for writing the sixth edition of *Aerodynamics for Engineers*: (1) to continue the legacy of Professor Bertin; (2) to rewrite many of the sections that provide readers with a motivation for studying aerodynamics in a more casual, enjoyable, and readable manner; (3) to update the technical innovations and advancements that have taken place in aerodynamics since the writing of the previous edition; and (4) to add aerodynamics concept boxes throughout the book to enhance the interest of readers.

To help achieve these goals, I provided readers with new sections, listed under What's New to This Edition on the next page. In addition, there are numerous new figures containing updated information, as well as numerous, additional up-to-date references throughout the book. Finally, numerous new example problems have been added throughout the book to enhance the learning of aerodynamics by the reader, and answers to selected problems have been added to help students know when they have done the problems correctly. Users of the fifth edition of the book will find that all material included in that edition is still included in the sixth edition, with the new material added throughout the book to bring a real-world flavor to the concepts being developed. I hope that readers will find the inclusion of all of this additional material helpful and informative.

Finally, no major revision of a book like *Aerodynamics for Engineers* can take place without the help of many people. I am especially indebted to everyone who aided in collecting new

materials for the sixth edition. I want to especially thank Preston A. Henne and Robert van't Riet of McDonnell Douglas; Eli Reshotko of Case Western Reserve University; David W. Hall of DHC Engineering; Stuart Rogers of NASA Ames Research Center; David McDaniel of the University of Alabama, Birmingham; Hans Hornung of Caltech; Andreas Schütte, Thomas Streit, and Martin Hepperle of DLR; Patrick Champigny of ONERA; Aaron Byerley of the U.S. Air Force Academy; John McMasters of The Boeing Company; and William H. Mason of Virginia Tech. In addition, I am very grateful for the excellent suggestions and comments made by the reviewers of the sixth edition: Roger L. Simpson of Virginia Tech, Tej R. Gupta of Embry-Riddle Aeronautical University, Serhat Hosder of Missouri University of Science and Technology, and Lisa Grega of The College of New Jersey. The editorial and production staff at Pearson has been outstanding in their support of this new edition: I greatly appreciate their efforts. I am also extremely grateful to the many students at the U.S. Air Force Academy who have pointed out errors that they found in the previous edition. I hope that everyone who reads this book will find it useful and educational.

The publishers would like to thank Ramesh Kolluru of BMS College of Engineering, Bangalore for reviewing the content of the International Edition.

WHAT'S NEW TO THIS EDITION?

- Aerodynamics concept boxes added throughout the book to bring real-world examples and applications to light as new material is being learned
- Chapter objectives to give readers a better understanding of the goal of each chapter and what concepts they should understand after reading through the chapter
- Significant re-writing of material and derivations from previous editions to improve clarity and usefulness
- Extra example problems to improve understanding of how to apply concepts to useful applications
- Significant new sections added on the topics of: importance of aerodynamics to aircraft performance, a description of the airplane, the irrotational flow condition, applications of potential flow theory to aerodynamics, expanded description of airfoil geometry and nomenclature, high lift military airfoils, the effect of taper ratio on wing efficiency, induced drag estimation, converging-diverging nozzles, shock/shock interactions, subsonic compressible transformations, additional compressibility corrections, critical Mach number, drag divergence Mach number, base drag, and the distinguishing characteristics of hypersonic flow
- Updated figures and photographs to help readers see concepts from real examples and on real aircraft
- Answers to selected problems

Enjoy your study of aerodynamics!

INSTRUCTORS RESOURCES

Resources to accompany the text are located on the Instructor Resource Center website at www.pearsoninternationaleditions.com/cummings. If you are in need of a login and password for this site, please contact your local Pearson representative. Resources include; Instructor Solutions Manual, Matlab files for several example problems and lecture slides for most chapters.

RUSSELL M. CUMMINGS
Larkspur, Colorado

1 WHY STUDY AERODYNAMICS?

Chapter Objectives

- Learn why aerodynamics is important in determining the performance characteristics of airplanes
- Develop a basic understanding of fluid properties such as density, temperature, pressure, and viscosity and know how to calculate these properties for a perfect gas
- Learn about the atmosphere and why we use a "standard atmosphere" model to perform aerodynamic calculations; learn how to perform calculations of fluid properties in the atmosphere
- Learn the basic components of an airplane and what they are used for

The study of aerodynamics is a challenging and rewarding discipline within aeronautics since the ability of an airplane to perform (how high, how fast, and how far an airplane will fly, such as the F-15E shown in Fig. 1.1) is determined largely by the aerodynamics of the vehicle. However, determining the aerodynamics of a vehicle (finding the lift and drag) is one of the most difficult things you will ever do in engineering, requiring complex theories, experiments in wind tunnels, and simulations using modern high-speed computers. Doing any of these things is a challenge, but a challenge well worth the effort for those wanting to better understand aircraft flight.

Figure 1.1 Aerodynamics is required for all components of the F-15E in flight, including the wing, fuselage, horizontal and vertical tails, stores, and how they interact with each other (U.S. Air Force photo by Staff Sgt. Samuel Rogers).

In order to prepare you for the challenge of learning about aerodynamics, we will first look at some interesting aspects of aircraft performance, and how we could determine if one airplane will outperform another airplane in a dog fight. Hopefully this will lead us to the point where we realize that aerodynamics is one of the prime characteristics of an airplane, which will determine the performance of the vehicle.

Of course, aerodynamics also requires that we understand some basic information about fluid dynamics, since physical materials known as fluids are made up of both liquids and gasses, and air is a gas. So some basic concepts about fluid properties and how we can describe a fluid will also be necessary. Since airplanes fly in the atmosphere, we will also develop a standard way to describe the properties of air in the atmosphere. And finally, we will discuss some of the basic geometry of an airplane, so we will have a common nomenclature for discussing how airplanes fly and for the aerodynamics of the various parts of an airplane. All of these pieces of background information will help us get started on the path to understanding aerodynamics, which is the goal of this book.

1.1 AERODYNAMICS AND THE ENERGY-MANEUVERABILITY TECHNIQUE

Early in the First World War, fighter pilots (at least those good enough to survive their first engagement with the enemy) quickly developed tactics that were to serve them throughout the years. German aces, such as Oswald Boelcke and Max Immelman,

realized that if they initiated combat starting from an altitude that was greater than that of their adversary, they could dive upon their foe, trading potential energy (height) for kinetic energy (velocity). Using the greater speed of his airplane to close from the rear (i.e., from the target aircraft's "six o'clock position"), the pilot of the attacking aircraft could dictate the conditions of the initial phase of the air-to-air combat. Starting from a superior altitude and converting potential energy to kinetic energy, the attacker might be able to destroy his opponent on the first pass. These tactics were refined, as the successful fighter aces gained a better understanding of the nuances of air combat by building an empirical database through successful air-to-air battles. A language grew up to codify these tactics: "Check your six."

This data base of tactics learned from successful combat provided an empirical understanding of factors that are important to aerial combat. Clearly, the sum of the potential energy plus the kinetic energy (i.e., the total energy) of the aircraft is one of the factors.

EXAMPLE 1.1: The total energy

Compare the total energy of a B-52 (shown in Fig. 1.2a) that weighs 450,000 pounds and that is cruising at a true air speed of 250 knots at an altitude of 20,000 ft with the total energy of an F-5 (shown in Fig. 1.2b) that weighs 12,000 pounds and that is cruising at a true air speed of 250 knots at an altitude of 20,000 ft. The equation for the total energy is

$$E = \frac{1}{2}mV^2 + mgh \tag{1.1}$$

Solution: To have consistent units, the units for velocity should be feet per second rather than knots. A knot is a nautical mile per hour and is equal to 1.69 ft per second, so 250 knots is equal to 422.5 ft/s. The mass is given by the equation:

$$m = \frac{W}{g} \tag{1.2}$$

(a) B-52H (b) F-5E

Figure 1.2 Aircraft used in energy-maneuverability comparison (U.S. Air Force photos; B-52H photo by Mike Cassidy).

Note that the units of mass could be grams, kilograms, lbm, slugs, or $\text{lbf} \cdot \text{s}^2/\text{ft}$. The choice of units often will reflect how mass appears in the application. The mass of the "Buff" (i.e., the B-52) is 13,986 $\text{lbf} \cdot \text{s}^2/\text{ft}$ or 13,986 slugs, while the mass for the F-5 is 373 slugs. The total energy for the B-52 is:

$$E = \frac{1}{2}\left(13{,}986\frac{\text{lbf}\cdot\text{s}^2}{\text{ft}}\right)\left(422.5\frac{\text{ft}}{\text{s}}\right)^2 + (450{,}000\ \text{lbf})(20{,}000\ \text{ft})$$

$$E = 1.0248 \times 10^{10}\ \text{ft}\cdot\text{lbf}$$

Similarly, the total energy of the F-5 fighter is

$$E = \frac{1}{2}\left(373\frac{\text{lbf}\cdot\text{s}^2}{\text{ft}}\right)\left(422.5\frac{\text{ft}}{\text{s}}\right)^2 + (12{,}000\ \text{lbf})(20{,}000\ \text{ft})$$

$$E = 2.7329 \times 10^{8}\ \text{ft}\cdot\text{lbf}$$

The total energy of the B-52 is 37.5 times the total energy of the F-5. Even though the total energy of the B-52 is so very much greater than that for the F-5, it just doesn't seem likely that a B-52 would have a significant advantage in air-to-air combat with an F-5. Notice that the two aircraft are cruising at the same flight conditions (velocity/altitude combination). So in this case the difference in total energy is in direct proportion to the difference in the weights of the two aircraft. Perhaps the specific energy (i.e., the energy per unit weight) is a more realistic parameter when trying to predict which aircraft would have an edge in air-to-air combat.

EXAMPLE 1.2: The energy height

Since the weight specific energy also has units of height, it will be given the symbol H_e and is called the energy height. Dividing the terms in equation (1.1) by the weight of the aircraft ($W = m\,g$)

$$H_e = \frac{E}{W} = \frac{V^2}{2\,g} + h \qquad \textbf{(1.3)}$$

Compare the energy height of a B-52 flying at 250 knots at an altitude of 20,000 ft with that of an F-5 cruising at the same altitude and at the same velocity.

Solution: The energy height of the B-52 is

$$H_e = \frac{1}{2}\frac{\left(422.5\frac{\text{ft}}{\text{s}}\right)^2}{32.174\frac{\text{ft}}{\text{s}^2}} + 20000\ \text{ft}$$

$$H_e = 22774\ \text{ft}$$

Since the F-5 is cruising at the same altitude and at the same true air speed as the B-52, it has the same energy height (i.e., the same weight specific energy).

If we consider only this weight specific energy, the B-52 and the F-5 are equivalent. This is obviously an improvement over the factor of 37.5 that the "Buff" had over the F-5, when the comparison was made based on the total energy. However, the fact that the energy height is the same for these two aircraft indicates that further effort is needed to provide a more realistic comparison for air-to-air combat.

Based on these examples, there must be some additional parameters that are relevant when comparing the one-on-one capabilities of two aircraft in air-to-air combat. Captain Oswald Boelcke developed a series of rules based on his combat experience as a forty-victory ace by October 19, 1916. Boelcke specified seven rules, or "dicta" [Werner (2005)]. The first five, which deal with tactics, are

1. Always try to secure an advantageous position before attacking. Climb before and during the approach in order to surprise the enemy from above, and dive on him swiftly from the rear when the moment to attack is at hand.
2. Try to place yourself between the sun and the enemy. This puts the glare of the sun in the enemy's eyes and makes it difficult to see you and impossible to shoot with any accuracy.
3. Do not fire the machine guns until the enemy is within range and you have him squarely within your sights.
4. Attack when the enemy least expects it or when he is preoccupied with other duties, such as observation, photography, or bombing.
5. Never turn your back and try to run away from an enemy fighter. If you are surprised by an attack on your tail, turn and face the enemy with your guns.

Although Boelcke's dicta were to guide fighter pilots for decades to come, they were experienced-based empirical rules. The first dictum deals with your total energy, the sum of the potential energy plus the kinetic energy. We learned from the first two example calculations that predicting the probable victor in one-on-one air-to-air combat is not based on energy alone.

Note that the fifth dictum deals with maneuverability. ***Energy AND Maneuverability!*** The governing equations should include maneuverability as well as the specific energy.

It wasn't until almost half a century later that a Captain in the U.S. Air Force brought the needed complement of talents to bear on the problem [Coram (2002)]. Captain John R. Boyd was an aggressive and talented fighter pilot who had an insatiable intellectual curiosity for understanding the scientific equations that had to be the basis of the "Boelcke dicta." John R. Boyd was driven to understand the physics that was the foundation of the tactics that, until that time, had been learned by experience for the fighter pilot lucky enough to survive his early air-to-air encounters with an enemy. In his role as Director of Academics at the U.S. Air Force Fighter Weapons School, it became not only his passion, but his job.

Air combat is a dynamic ballet of move and countermove that occurs over a continuum of time. Therefore, Boyd postulated that perhaps the time derivatives of

the energy height are more relevant than the energy height itself. How fast can we, in the target aircraft, with an enemy on our "six." quickly dump energy and allow the foe to pass? Once the enemy has passed, how quickly can we increase our energy height and take the offensive? John R. Boyd taught these tactics in the Fighter Weapons School. Now he became obsessed with the challenge of developing the science of fighter tactics.

1.1.1 Specific Excess Power

If the pilot of the 12,000 lbf F-5 that is flying at a velocity of 250 knots (422.5 ft/s) and at an altitude of 20,000 ft is to gain the upper hand in air-to-air combat, his aircraft must have sufficient power either to out-accelerate or to outclimb his adversary. Consider the case where the F-5 is flying at a constant altitude. If the engine is capable of generating more thrust than the drag acting on the aircraft, the acceleration of the aircraft can be calculated using Newton's Law:

$$\sum F = m\,a$$

which for an aircraft accelerating at a constant altitude becomes

$$T - D = \frac{W}{g}\frac{dV}{dt} \tag{1.4}$$

Multiplying both sides of equation (1.4) by V and dividing by W gives

$$\frac{(T - D)V}{W} = \frac{V}{g}\frac{dV}{dt} \tag{1.5}$$

which is the specific excess power, P_s.

EXAMPLE 1.3: The specific excess power and acceleration

The left-hand side of equation (1.5) is excess power per unit weight, or specific excess power, P_s. Use equation (1.5) to calculate the maximum acceleration for a 12,000-lbf F-5 that is flying at 250 knots (422.5 ft/s) at 20,000 ft.

Solution: Performance charts for an F-5 that is flying at these conditions indicate that it is capable of generating 3550 lbf thrust (T) with the afterburner lit, while the total drag (D) acting on the aircraft is 1750 lbf. Thus, the specific excess power is

$$P_s = \frac{(T - D)V}{W} = \frac{[\,(3550 - 1750)\ \text{lbf}\,]\ 422.5\ \text{ft/s}}{12000\ \text{lbf}} = 63.38\ \text{ft/s}$$

Rearranging equation (1.5) to solve for the acceleration gives

$$\frac{dV}{dt} = P_s\frac{g}{V} = (63.38\ \text{ft/s})\frac{32.174\ \text{ft/s}^2}{422.5\ \text{ft/s}} = 4.83\ \text{ft/s}^2$$

1.1.2 Using Specific Excess Power to Change the Energy Height

Taking the derivative with respect to time of the two terms in equation (1.3), we obtain:

$$\frac{dH_e}{dt} = \frac{V}{g}\frac{dV}{dt} + \frac{dh}{dt} \tag{1.6}$$

The first term on the right-hand side of equation (1.6) represents the rate of change of kinetic energy (per unit weight). It is a function of the rate of change of the velocity as seen by the pilot $\left(\frac{dV}{dt}\right)$. The significance of the second term is even less cosmic. It is the rate of change of the potential energy (per unit weight). Note also that $\left(\frac{dh}{dt}\right)$ is the vertical component of the velocity [i.e., the rate of climb (ROC)] as seen by the pilot on his altimeter. Air speed and altitude—these are parameters that fighter pilots can take to heart.

Combining the logic that led us to equations (1.5) and (1.6) leads us to the conclusion that the specific excess power is equal to the time-rate-of-change of the energy height. So,

$$P_s = \frac{(T - D)V}{W} = \frac{dH_e}{dt} = \frac{V}{g}\frac{dV}{dt} + \frac{dh}{dt} \tag{1.7}$$

Given the specific excess power calculated in Example 1.3, we could use equation (1.7) to calculate the maximum rate-of-climb (for a constant velocity) for the 12,000 lbf F-5 as it passes through 20,000 ft at 250 knots.

$$\frac{dh}{dt} = P_s = 63.38 \text{ ft/s} = 3802.8 \text{ ft/min}$$

Clearly, to be able to generate positive values for the terms in equation (1.7), we need an aircraft with excess power (i.e., one for which the thrust exceeds the drag). Weight is another important factor, since the lighter the aircraft, the greater the benefits of the available excess power.

"Boyd, as a combat pilot in Korea and as a tactics instructor at Nellis AFB in the Nevada desert, observed, analyzed, and assimilated the relative energy states of his aircraft and those of his opponent's during air combat engagements. . . . He also noted that, when in a position of advantage, his energy was higher than that of his opponent and that he lost that advantage when he allowed his energy to decay to less than that of his opponent."

"He knew that, when turning from a steady-state flight condition, the airplane under a given power setting would either slow down, lose altitude, or both. The result meant he was losing energy (the drag exceeded the thrust available from the engine). From these observations, he concluded that maneuvering for position was basically an energy problem. Winning required the proper management of energy available at the conditions existing at any point during a combat engagement" [Hillaker (1997)].

In the mid-1960s, Boyd had gathered energy-maneuverability data on all of the fighter aircraft in the U.S. Air Force inventory and on their adversaries. He sought to understand the intricacies of maneuvering flight. What was it about the airplane that would limit or prevent him from making it to do what he wanted it to do?

1.1.3 John R. Boyd Meet Harry Hillaker

The relation between John R. Boyd and Harry Hillaker "dated from an evening in the mid-1960s when a General Dynamics (GD) engineer named Harry Hillaker was sitting in the Officer's Club at Eglin AFB, Florida, having an after dinner drink. Hillaker's host introduced him to a tall, blustery pilot named John R. Boyd, who immediately launched a frontal attack on GD's F-111 fighter. Hillaker was annoyed but bantered back" [Grier (2004)]. Hillaker countered that the F-111 was designated a fighter-bomber.

"A few days later, he (Hillaker) received a call—Boyd had been impressed by Hillaker's grasp of aircraft conceptual design and wanted to know if Hillaker was interested in more organized meetings."

"Thus was born a group that others in the Air Force dubbed the 'fighter mafia.' Their basic belief was that fighters did not need to overwhelm opponents with speed and size. Experience in Vietnam against nimble Soviet-built MiGs had convinced them that technology had not yet turned air-to-air combat into a long-range shoot-out." [Grier (2004)]

The fighter mafia knew that a small aircraft could enjoy a high thrust-to-weight ratio: small aircraft have less drag. "The original F-16 design had about one-third the drag of an F-4 in level flight and one-fifteenth the drag of an F-4 at a high angle-of-attack" [Grier (2004)].

1.1.4 The Importance of Aerodynamics to Aircraft Performance

The importance of the previous discussion is that aircraft performance is largely determined by the aerodynamic characteristics of the airplane (as well as the mass properties and thrust of the airplane). Parameters like lift and drag determine aircraft performance such as energy height. Lift and drag also determine more easy-to-understand parameters like range, rate of climb, and glide ratio (which is exactly the lift/drag ratio of the airplane). Without knowing the aerodynamics of the airplane (as well as the mass properties and thrust), we will not be able to determine how well an airplane will perform. This requires knowing the flow field around the airplane so that the pressures, shear stress, and heating on the surface of the airplane can be determined. That is why the study of aerodynamics is an essential stepping stone to gaining a fuller understanding of how an airplane will perform, and how to improve that performance to achieve flight requirements.

1.2 SOLVING FOR THE AEROTHERMODYNAMIC PARAMETERS

The fundamental problem facing the aerodynamicist is to predict the aerodynamic forces and moments and the heat-transfer rates acting on a vehicle in flight. In order to predict these aerodynamic forces and moments with suitable accuracy, it is necessary

to be able to describe the pattern of flow around the vehicle. The resultant flow pattern depends on the geometry of the vehicle, its orientation with respect to the undisturbed free stream, and the altitude and speed at which the vehicle is traveling. In analyzing the various flows that an aerodynamicist may encounter, assumptions about the fluid properties may be introduced. In some applications, the temperature variations are so small that they do not affect the velocity field. In addition, for those applications where the temperature variations have a negligible effect on the flow field, it is often assumed that the density is essentially constant. However, in analyzing high-speed flows, the density variations cannot be neglected. Since density is a function of pressure and temperature, it may be expressed in terms of these two parameters. In fact, for a gas in thermodynamic equilibrium, any thermodynamic property may be expressed as a function of two other independent, thermodynamic properties. Thus, it is possible to formulate the governing equations using the enthalpy and the entropy as the flow properties instead of the pressure and the temperature.

1.2.1 Concept of a Fluid

From the point of view of fluid mechanics, matter can be in one of two states—either solid or fluid. The technical distinction between these two states lies in their response to an applied shear, or tangential, stress. A solid can resist a shear stress by a static deformation; a fluid cannot. A *fluid* is a substance that deforms continuously under the action of shearing forces. An important corollary of this definition is that there can be no shear stresses acting on fluid particles if there is no relative motion within the fluid; that is, such fluid particles are not deformed. Thus, if the fluid particles are at rest or if they are all moving at the same velocity, there are no shear stresses in the fluid. This zero shear stress condition is known as the *hydrostatic stress condition*.

A fluid can be either a liquid or a gas. A liquid is composed of relatively closely packed molecules with strong cohesive forces. As a result, a given mass of liquid will occupy a definite volume of space. If a liquid is poured into a container, it assumes the shape of the container up to the volume it occupies and will form a free surface in a gravitational field if unconfined from above. The upper (or free) surface is planar and perpendicular to the direction of gravity. Gas molecules are widely spaced with relatively small cohesive forces. Therefore, if a gas is placed in a closed container, it will expand until it fills the entire volume of the container. A gas has no definite volume. Thus, if it is unconfined, it forms an atmosphere that is essentially hydrostatic.

1.2.2 Fluid as a Continuum

There are two basic ways to develop equations that describe the motion of a system of fluid particles: we can either define the motion of each and every molecule or define the average behavior of the molecules within a given elemental volume. Our primary concern for problems in this text will not be with the motion of individual molecules, but with the general behavior of the fluid. We are concerned with describing the fluid motion in physical spaces that are very large compared to molecular dimensions (the size of molecules), so our elemental volume will contain

a large number of molecules. The fluid in these problems may be considered to be a continuous material whose properties can be determined from a statistical average for the particles in the volume: a macroscopic representation. The assumption of a continuous fluid is valid when the smallest volume of fluid that is of interest contains so many molecules that statistical averages are meaningful. In addition, we will assume that the number of molecules within the volume will remain essentially constant even though there is a continuous flux of molecules through the boundaries. If the elemental volume is too large (as large as the vehicle or body being considered), there could be a noticeable variation in the fluid properties determined statistically at various points in the volume.

For example, the number of molecules in a cubic meter of air at room temperature and at sea-level pressure is approximately 2.5×10^{25}. So, there are 2.5×10^{10} molecules in a cube 0.01 mm on a side. The mean free path of the molecules (the average distance a molecule travels between impacts with other molecules) at sea level is 6.6×10^{-8}m. There are sufficient molecules in this volume for the fluid to be considered a continuum, and the fluid properties can be determined from statistical averages. In contrast, at a very high altitude of 130 km there are only 1.6×10^{17} molecules in a cube 1 m on a side; the mean free path at this altitude is 10.2 m. Therefore, at this altitude the fluid cannot be considered a continuum (this is known as low density of rarefied flow).

A parameter that is commonly used to identify the onset of low-density effects is the Knudsen number, which is the ratio of the mean free path to a characteristic dimension of the body. Although there is no definitive criterion, the continuum flow model starts to break down when the Knudsen number is roughly of the order of 0.1. Because rarefied flows describe a fluid that is not a continuum, different equations would have to be derived than those for a continuum. This book will concentrate, however, on the development of equations for flow in a continuum.

1.2.3 Fluid Properties

By employing the concept of a continuum, we can describe the gross behavior of the fluid motion using certain observable, macroscopic properties. Properties used to describe a general fluid motion include the temperature, the pressure, the density, the viscosity, and the speed of sound.

Temperature. We are all familiar with *temperature* in qualitative terms: an object feels hot (or cold) to the touch. However, because of the difficulty in quantitatively defining the temperature, we typically define situations where there is an equality of temperature. Two bodies have equality of temperature when no change in any observable property occurs when they are in thermal contact. Furthermore, two bodies respectively equal in temperature to a third body must be equal in temperature to each other. Because of this observation, an arbitrary scale of temperature can be defined in terms of a convenient temperature for a standard body (e.g., the freezing point of water).

Pressure. Individual molecules of a fluid continually strike a surface that is placed in the fluid because of the random motion of the molecules due to their thermal

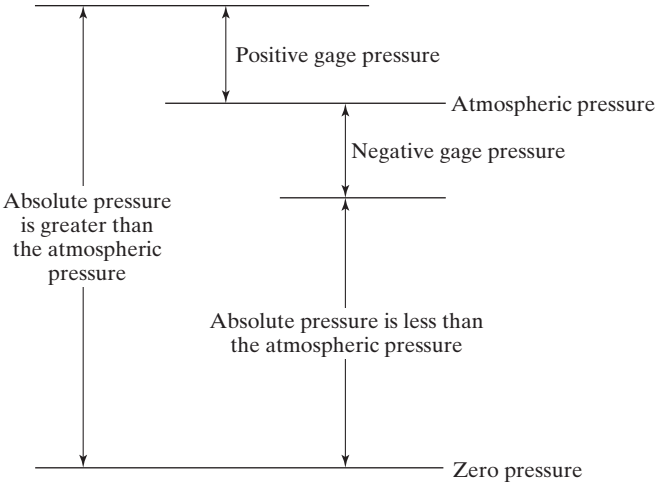

Figure 1.3 Terms used in pressure measurements.

energy. These collisions occur even though the surface is at rest relative to the fluid. By Newton's second law, a force is exerted on the surface equal to the time rate of change of the momentum of the rebounding molecules. *Pressure* is the magnitude of this force per unit area of surface and has units of (force)/(length)^2. Since a fluid that is at rest cannot sustain tangential forces, the pressure on the surface must act in the direction perpendicular to that surface. Furthermore, the pressure acting at a point in a fluid at rest is the same in all directions.

Standard atmospheric pressure at sea level is defined as the pressure that can support a column of mercury 760 mm in length when the density of the mercury is 13.5951 g/cm^3 and the acceleration due to gravity is the standard sea level value. The standard atmospheric pressure at sea level in SI (System International) units is 1.01325×10^5 N/m^2. In English units, the standard atmospheric pressure at sea level is 14.696 lbf/in^2 or 2116.22 lbf/ft^2.

In many aerodynamic applications, we are interested in the difference between the absolute value of the local pressure and the atmospheric pressure. Many pressure gages indicate the difference between the absolute pressure and the atmospheric pressure existing at the gage. This difference, which is referred to as *gage pressure*, is illustrated in Fig. 1.3.

Aerodynamics Concept Box: Consistent Units

Performing calculations with the correct units can be one of the most challenging aspects of aerodynamics (or any field of engineering for that matter). The fact that aerodynamics is often done in both SI and English units can make the challenge even greater. Performing calculations in consistent units can greatly reduce the chance of making errors and greatly increase the ease of getting results.

Consistent units are the units of length, time, force, and mass that make Newton's second law balance for unit values of each term:

$$F = ma$$

$$1 \text{ force unit} = 1 \text{ mass unit} \times 1 \text{ acceleration unit}$$

For calculations in the SI system, the consistent units are Newtons (force), kilograms (mass), and m/s^2 (acceleration), or in other words:

$$1 \text{ Newton} = 1 \text{ kilogram} \times 1 \text{ m/s}^2$$

Using these units in calculations will ensure that units cancel correctly. If any other units appear in a problem, they should immediately be converted to these consistent units prior to performing calculations (grams should be converted to kilograms, centimeters should be converted to meters, hours should be converted to seconds, etc.).

For calculations in the English system, the consistent units are pounds force (often just called pounds), slugs, feet, and seconds:

$$1 \text{ lbf (or lb)} = 1 \text{ slug} \times 1 \text{ ft/s}^2$$

Any other units appearing in problems are most easily dealt with by converting to these consistent units (pounds mass [lbm] should be converted to slugs, miles should be converted to feet, hours should be converted to seconds, etc.). Using consistent units consistently will save a great deal of pain and suffering while performing calculations!

Density. The *density* of a fluid at a point in space is the mass of the fluid per unit volume surrounding the point. As is the case when evaluating the other fluid properties, the incremental volume must be large compared to molecular dimensions yet very small relative to the dimensions of the vehicle whose flow field we seek to analyze. Provided that the fluid may be assumed to be a continuum, the density at a point is defined as

$$\rho = \lim_{\delta(\text{vol}) \to 0} \frac{\delta(\text{mass})}{\delta(\text{vol})} \tag{1.8}$$

where δ represents a change rather than a differential. The dimensions of density are $(\text{mass})/(\text{length})^3$.

In general, the density of a gas is a function of the composition of the gas, its temperature, and its pressure. The relation

$$\rho(\text{composition}, T, p) \tag{1.9}$$

is known as an *equation of state*. For a thermally perfect gas, the equation of state is

$$\rho = \frac{p}{RT} \tag{1.10}$$

The gas constant R has a particular value for each substance. The gas constant for air has the value $287.05 \text{ N} \cdot \text{m/kg} \cdot \text{K}$ in SI units and $53.34 \text{ ft} \cdot \text{lbf/lbm} \cdot {}^\circ\text{R}$ or $1716.16 \text{ ft}^2/\text{s}^2 \cdot {}^\circ\text{R}$ in English units. The temperature in equation (1.10) should be in absolute units. Thus, the temperature is either in K or in °R, but never in °C or in °F. The density of air at standard day sea level conditions is 1.2250 kg/m^3 or $0.002377 \text{ slug/ft}^3$.

EXAMPLE 1.4: Density in SI units

Calculate the density of air when the pressure is 1.01325×10^5 N/m^2 and the temperature is 288.15 K. Since air at this pressure and temperature behaves as a perfect gas, we can use equation (1.10).

Solution:

$$\rho = \frac{1.01325 \times 10^5 \text{ N/m}^2}{(287.05 \text{ N} \cdot \text{m/kg} \cdot \text{K})(288.15 \text{ K})}$$
$$= 1.2250 \text{ kg/m}^3$$

EXAMPLE 1.5: Density in English units

Calculate the density of air when the pressure is 2116.22 lbf/ft^2 and the temperature is 518.67°R. Since air at this pressure and temperature behaves as a perfect gas, we can use equation (1.10). Note that throughout the remainder of this book, air will be assumed to behave as a perfect gas unless specifically stated otherwise.

Solution:

$$\rho = \frac{2116.22 \dfrac{\text{lbf}}{\text{ft}^2}}{\left(53.34 \dfrac{\text{ft} \cdot \text{lbf}}{\text{lbm} \cdot {}^\circ\text{R}}\right)(518.67{}^\circ\text{R})} = 0.07649 \frac{\text{lbm}}{\text{ft}^3}$$

Alternatively,

$$\rho = \frac{2116.22 \dfrac{\text{lbf}}{\text{ft}^2}}{\left(1716.16 \dfrac{\text{ft}^2}{\text{s}^2 \cdot {}^\circ\text{R}}\right)(518.67{}^\circ\text{R})} = 0.002377 \frac{\text{lbf} \cdot \text{s}^2}{\text{ft}^4}$$

The unit lbf · s^2/ft^4 is often written as slugs/ft^3, where slugs are alternative units of mass in the English system. One slug is the equivalent of 32.174 lbm.

For vehicles that are flying at approximately 100 m/s (330 ft/s), or less, the density of the air flowing past the vehicle is assumed constant when obtaining a solution for the flow field. Rigorous application of equation (1.10) would require that the pressure and the temperature remain constant (or change proportionally) in order for the density to remain constant throughout the flow field. We know that the pressure around the vehicle is not constant, since the aerodynamic forces and moments in which we are interested are the result of pressure variations associated with the flow pattern. However, the assumption of constant density for velocities below 100 m/s is a valid approximation because the pressure changes that occur from one point to another in the flow field are small relative to the absolute value of the pressure.

Viscosity. In all real fluids, a shearing deformation is accompanied by a shearing stress. The fluids of interest in this text are *Newtonian* in nature; that is, the shearing stress is proportional to the rate of shearing deformation. The constant of proportionality is called the *coefficient of viscosity*, μ. Therefore,

$$\text{shear stress} = \mu \times \text{transverse gradient of velocity} \tag{1.11}$$

There are many problems of interest for which the effects of viscosity can be neglected. In such problems, the magnitude of the coefficient of viscosity of the fluid and of the velocity gradients in the flow field are such that their product is negligible relative to the inertia of the fluid particles and to the pressure forces acting on them. We will use the term *inviscid flow* in these cases to emphasize the fact that it is the character both of the flow field and of the fluid that allows us to neglect viscous effects. No real fluid has a zero coefficient of viscosity, but there are times when the effects of viscosity are negligible.

The viscosity of a fluid relates to the transport of momentum in the direction of the velocity gradient (but opposite in sense). Therefore, viscosity is a transport property. In general, the coefficient of viscosity is a function of the composition of the gas, its temperature, and its pressure. The viscosity of air is independent of pressure for temperatures below 3000 K (5400°R). In this temperature range, we could use Sutherland's equation to calculate the coefficient of viscosity:

$$\mu = C_1 \frac{T^{1.5}}{T + C_2} \tag{1.12}$$

For SI units where temperature, T, is in units of K and μ is in units of kg/s · m use $C_1 = 1.458 \times 10^{-6}$ and $C_2 = 110.4$. For English units where temperature, T, is in units of °R and μ is in units of lbf · s/ft^2, use $C_1 = 2.27 \times 10^{-8}$ and $C_2 = 198.6$.

EXAMPLE 1.6: Viscosity in SI units

Calculate the viscosity of air when the temperature is 288.15 K.

Solution:

$$\mu = 1.458 \times 10^{-6} \frac{(288.15)^{1.5}}{288.15 + 110.4}$$
$$= 1.7894 \times 10^{-5}\ \text{kg/s} \cdot \text{m}$$

EXAMPLE 1.7: Viscosity in English units

Calculate the viscosity of air when the temperature is 59.0°F.

Solution: First, convert the temperature to the absolute scale for English units, °R, 59.0°F + 459.67 = 518.67°R.

$$\mu = 2.27 \times 10^{-8} \frac{(518.67)^{1.5}}{518.67 + 198.6}$$
$$= 3.7383 \times 10^{-7} \frac{\text{lbf} \cdot \text{s}}{\text{ft}^2}$$

Equations used to calculate the coefficient of viscosity depend on the model used to describe the intermolecular forces of the gas molecules, so that it is necessary to define the potential energy of the interaction of the colliding molecules. Svehla (1962) noted that the potential energy for the Sutherland model is described physically as a rigid, impenetrable sphere, surrounded by an inverse-power attractive force. This model is qualitatively correct in that the molecules attract one another when they are far apart and exert strong repulsive forces upon one another when they are close together.

Chapman and Cowling (1960) note that equation (1.12) closely represents the variation of μ with temperature over a "fairly" wide range of temperatures. They caution, however, that the success of Sutherland's equation in representing the variation of μ with temperature for several gases does not establish the validity of Sutherland's molecular model for those gases. "In general it is not adequate to represent the core of a molecule as a rigid sphere, or to take molecular attractions into account to a first order only. The greater rapidity of the experimental increase of μ with T, as compared with that for nonattracting rigid spheres, has to be explained as due partly to the 'softness' of the repulsive field at small distances, and partly to attractive forces which have more than a first-order effect. The chief value of Sutherland's formula seems to be as a simple interpolation formula over restricted ranges of temperature" [Chapman and Cowling (1960)].

The Lennard-Jones model for the potential energy of an interaction, which takes into account both the softness of the molecules and their mutual attraction at large distances, has been used by Svehla (1962) to calculate the viscosity and the thermal conductivity of gases at high temperatures. The coefficients of viscosity for air as tabulated by Svehla are compared with the values calculated using equation (1.12) in Table 1.1. These comments are made to emphasize the fact that even the basic fluid properties may involve approximate models that have a limited range of applicability.

Kinematic Viscosity. The aerodynamicist may encounter many applications where the ratio μ/ρ has been replaced by a single parameter. Because this ratio appears frequently, it has been given a special name, the kinematic viscosity. The symbol used to represent the kinematic viscosity is ν, where:

$$\nu = \frac{\mu}{\rho} \tag{1.13}$$

In this ratio, the force units (or, equivalently, the mass units) cancel. Therefore, ν has the dimensions of $(\text{length})^2/(\text{time})$ (e.g., square meters per second or square feet per second).

TABLE 1.1 Comparison of the Coefficient of Viscosity for Air as Tabulated by Svehla (1962) and as Calculated Using Sutherland's Equation [Equation (1.12)]

T (K)	$\mu \times 10^5$ (kg/m·s)*	$\mu \times 10^5$ (kg/m·s)†
200	1.360	1.329
400	2.272	2.285
600	2.992	3.016
800	3.614	3.624
1000	4.171	4.152
1200	4.695	4.625
1400	5.197	5.057
1600	5.670	5.456
1800	6.121	5.828
2000	6.553	6.179
2200	6.970	6.512
2400	7.373	6.829
2600	7.765	7.132
2800	8.145	7.422
3000	8.516	7.702
3200	8.878	7.973
3400	9.232	8.234
3600	9.579	8.488
3800	9.918	8.734
4000	10.252	8.974
4200	10.580	9.207
4400	10.902	9.435
4600	11.219	9.657
4800	11.531	9.874
5000	11.838	10.087

* From Svehla (1962)

† Calculated using equation (1.12)

EXAMPLE 1.8: Kinematic Viscosity in English units

Using the results of Examples 1.5 and 1.7, calculate the kinematic viscosity of air when the temperature is 518.67°R and the pressure is 2116.22 lbf/ft^2.

Solution: From Example 1.5, $\rho = 0.07649\,\text{lbm/ft}^3 = 0.002377\,\text{lbf}\cdot\text{s}^2/\text{ft}^4$; while from Example 1.7, $\mu = 3.7383 \times 10^{-7}\,\text{lbf}\cdot\text{s/ft}^2$. Therefore,

$$\nu = \frac{\mu}{\rho} = \frac{3.7383 \times 10^{-7}\dfrac{\text{lbf}\cdot\text{s}}{\text{ft}^2}}{0.002377\dfrac{\text{lbf}\cdot\text{s}^2}{\text{ft}^4}} = 1.573 \times 10^{-4}\frac{\text{ft}^2}{\text{s}}$$

If we use the alternative units for the density, we must employ the factor g_c, which is equal to $32.174\,\text{ft}\cdot\text{lbm/lbf}\cdot\text{s}^2$, to arrive at the appropriate units.

$$\nu = \frac{\mu}{\rho} = \frac{3.7383 \times 10^{-7}\dfrac{\text{lbf}\cdot\text{s}}{\text{ft}^2}}{0.07649\dfrac{\text{lbm}}{\text{ft}^3}}\left(32.174\frac{\text{ft}\cdot\text{lbm}}{\text{lbf}\cdot\text{s}^2}\right)$$
$$= 1.573 \times 10^{-4}\,\text{ft}^2/\text{s}$$

Speed of Sound. The speed at which a disturbance of infinitesimal proportions propagates through a fluid that is at rest is known as the *speed of sound*, which is designated in this book as a (the acoustic speed). The speed of sound is established by the properties of the fluid. For a perfect gas $a = \sqrt{\gamma RT}$, where γ is the ratio of specific heats (see Chapter 8) and R is the gas constant. For the range of temperature over which air behaves as a perfect gas, $\gamma = 1.4$ and the speed of sound is given by

$$a = 20.047\sqrt{T} \qquad \textbf{(1.14a)}$$

where T is the temperature in K and the units for the speed of sound are m/s. In English units

$$a = 49.02\sqrt{T} \qquad \textbf{(1.14b)}$$

where T is the temperature in °R and the units for the speed of sound are ft/s.

1.2.4 Pressure Variation in a Static Fluid Medium

In order to compute the forces and moments or the heat-transfer rates acting on a vehicle, or to determine the flight path (i.e., the trajectory) of the vehicle, we will often need an analytic model of the atmosphere instead of using a table, such as Table 1.2. To do this, we will develop the equations describing the pressure variation in a static fluid medium. If fluid particles, when viewed as a continuum, are either all at rest or all moving with the same velocity, the fluid is said to be a *static medium*. Thus, the term *static fluid properties* may be applied to situations in which the elements of the fluid are moving, provided that there is no relative motion between fluid elements. Since there is no relative motion between adjacent layers of the fluid, there are no shear forces. So, with no relative motion between fluid elements, the viscosity of the fluid is of no concern. For these inviscid flows, the only forces acting on the surface of the fluid element are pressure forces.

TABLE 1.2A U.S. Standard Atmosphere, 1976 SI Units

Geometric Altitude (*km*)	*Pressure* (N/m^2)	*Temperature* (*K*)	*Density* (kg/m^3)	*Viscosity* ($kg/m \cdot s$)	*Speed of Sound* (m/s)
0	1.0133 *E* + 05	288.150	1.2250 *E* + 00	1.7894 *E* − 05	340.29
1	8.9875 *E* + 04	281.651	1.1117 *E* + 00	1.7579 *E* − 05	336.43
2	7.9501 *E* + 04	275.154	1.0066 *E* + 00	1.7260 *E* − 05	332.53
3	7.0121 *E* + 04	268.659	9.0926 *E* − 01	1.6938 *E* − 05	328.58
4	6.1669 *E* + 04	262.166	8.1934 *E* − 01	1.6612 *E* − 05	324.59
5	5.4048 *E* + 04	255.676	7.3643 *E* − 01	1.7885 *E* − 05	320.55
6	4.7217 *E* + 04	249.187	6.6012 *E* − 01	1.5949 *E* − 05	316.45
7	4.1105 *E* + 04	242.700	5.9002 *E* − 01	1.5612 *E* − 05	312.31
8	3.5651 *E* + 04	236.215	5.2578 *E* − 01	1.5271 *E* − 05	308.11
9	3.0800 *E* + 04	229.733	4.6707 *E* − 01	1.4926 *E* − 05	303.85
10	2.6500 *E* + 04	223.252	4.1351 *E* − 01	1.4577 *E* − 05	299.53
11	2.2700 *E* + 04	216.774	3.6481 *E* − 01	1.4223 *E* − 05	295.15
12	1.9399 *E* + 04	216.650	3.1193 *E* − 01	1.4216 *E* − 05	295.07
13	1.6579 *E* + 04	216.650	2.6660 *E* − 01	1.4216 *E* − 05	295.07
14	1.4170 *E* + 04	216.650	2.2786 *E* − 01	1.4216 *E* − 05	295.07
15	1.2111 *E* + 04	216.650	1.9475 *E* − 01	1.4216 *E* − 05	295.07
16	1.0352 *E* + 04	216.650	1.6647 *E* − 01	1.4216 *E* − 05	295.07
17	8.8497 *E* + 03	216.650	1.4230 *E* − 01	1.4216 *E* − 05	295.07
18	7.5652 *E* + 03	216.650	1.2165 *E* − 01	1.4216 *E* − 05	295.07
19	6.4675 *E* + 03	216.650	1.0400 *E* − 01	1.4216 *E* − 05	295.07
20	5.5293 *E* + 03	216.650	8.8911 *E* − 02	1.4216 *E* − 05	295.07
21	4.7289 *E* + 03	217.581	7.5715 *E* − 02	1.4267 *E* − 05	295.70
22	4.0474 *E* + 03	218.574	6.4510 *E* − 02	1.4322 *E* − 05	296.38
23	3.4668 *E* + 03	219.567	5.5006 *E* − 02	1.4376 *E* − 05	297.05
24	2.9717 *E* + 03	220.560	4.6938 *E* − 02	1.4430 *E* − 05	297.72
25	2.5491 *E* + 03	221.552	4.0084 *E* − 02	1.4484 *E* − 05	298.39
26	2.1883 *E* + 03	222.544	3.4257 *E* − 02	1.4538 *E* − 05	299.06
27	1.8799 *E* + 03	223.536	2.9298 *E* − 02	1.4592 *E* − 05	299.72
28	1.6161 *E* + 03	224.527	2.5076 *E* − 02	1.4646 *E* − 05	300.39
29	1.3904 *E* + 03	225.518	2.1478 *E* − 02	1.4699 *E* − 05	301.05
30	1.1970 *E* + 03	226.509	1.8411 *E* − 02	1.4753 *E* − 05	301.71

TABLE 1.2B U.S. Standard Atmosphere, 1976 English Units

Geometric Altitude (*kft*)	*Pressure* (lbf/ft^2)	*Temperature* (°*R*)	*Density* ($slug/ft^3$)	*Viscosity* ($slug/ft \cdot s$)	*Speed of Sound* (ft/s)
0	2.1162 *E* + 03	518.67	2.3769 *E* − 03	3.7383 *E* − 07	1116.44
2	1.9677 *E* + 03	511.54	2.2409 *E* − 03	3.6982 *E* − 07	1108.76
4	1.8277 *E* + 03	504.41	2.1109 *E* − 03	3.6579 *E* − 07	1100.98
6	1.6960 *E* + 03	497.28	1.9869 *E* − 03	3.6173 *E* − 07	1093.18
8	1.5721 *E* + 03	490.15	1.8685 *E* − 03	3.4764 *E* − 07	1085.33
10	1.4556 *E* + 03	483.02	1.7556 *E* − 03	3.5353 *E* − 07	1077.40
12	1.3462 *E* + 03	475.90	1.6479 *E* − 03	3.4939 *E* − 07	1069.42
14	1.2436 *E* + 03	468.78	1.5455 *E* − 03	3.4522 *E* − 07	1061.38
16	1.1473 *E* + 03	461.66	1.4480 *E* − 03	3.4102 *E* − 07	1053.31
18	1.0575 *E* + 03	454.53	1.3553 *E* − 03	3.3679 *E* − 07	1045.14
20	9.7733 *E* + 02	447.42	1.2673 *E* − 03	3.3253 *E* − 07	1036.94
22	8.9459 *E* + 02	440.30	1.1836 *E* − 03	3.2825 *E* − 07	1028.64
24	8.2116 *E* + 02	433.18	1.1044 *E* − 03	3.2392 *E* − 07	1020.31
26	7.5270 *E* + 02	426.07	1.0292 *E* − 03	3.1958 *E* − 07	1011.88
28	6.8896 *E* + 02	418.95	9.5801 *E* − 04	3.1519 *E* − 07	1003.41
30	6.2966 *E* + 02	411.84	8.9070 *E* − 04	3.1078 *E* − 07	994.85
32	5.7457 *E* + 02	404.73	8.2704 *E* − 04	3.0633 *E* − 07	986.22
34	5.2347 *E* + 02	397.62	7.6695 *E* − 04	3.0185 *E* − 07	977.53
36	4.7611 *E* + 02	390.51	7.1029 *E* − 04	2.9734 *E* − 07	968.73
38	4.3262 *E* + 02	389.97	6.4640 *E* − 04	2.9700 *E* − 07	968.08
40	3.9311 *E* + 02	389.97	5.8728 *E* − 04	2.9700 *E* − 07	968.08
42	3.5722 *E* + 02	389.97	5.3366 *E* − 04	2.9700 *E* − 07	968.08
44	3.2477 *E* + 02	389.97	4.8494 *E* − 04	2.9700 *E* − 07	968.08
46	2.9477 *E* + 02	389.97	4.4068 *E* − 04	2.9700 *E* − 07	968.08
48	2.6806 *E* + 02	389.97	4.0046 *E* − 04	2.9700 *E* − 07	968.08
50	2.4360 *E* + 02	389.97	3.6393 *E* − 04	2.9700 *E* − 07	968.08
52	2.2138 *E* + 02	389.97	3.3072 *E* − 04	2.9700 *E* − 07	968.08
54	2.0119 *E* + 02	389.97	3.0056 *E* − 04	2.9700 *E* − 07	968.08
56	1.8288 *E* + 02	389.97	2.7315 *E* − 04	2.9700 *E* − 07	968.08
58	1.6618 *E* + 02	389.97	2.4824 *E* − 04	2.9700 *E* − 07	968.08
60	1.5103 *E* + 02	389.97	2.2561 *E* − 04	2.9700 *E* − 07	968.08
62	1.3726 *E* + 02	389.97	2.0505 *E* − 04	2.9700 *E* − 07	968.08
64	1.2475 *E* + 02	389.97	1.8637 *E* − 04	2.9700 *E* − 07	968.08
66	1.1339 *E* + 02	390.07	1.6934 *E* − 04	2.9706 *E* − 07	968.21
68	1.0307 *E* + 02	391.16	1.5351 *E* − 04	2.9775 *E* − 07	969.55
70	9.3725 *E* + 01	392.25	1.3920 *E* − 04	2.9845 *E* − 07	970.90

(*continues on next page*)

TABLE 1.2B U.S. Standard Atmosphere, 1976 English Units (continued)

Geometric Altitude (kft)	*Pressure (lbf/ft^2)*	*Temperature (°R)*	*Density ($slug/ft^3$)*	*Viscosity ($slug/ft \cdot s$)*	*Speed of Sound (ft/s)*
72	8.5250 *E* + 01	393.34	1.2626 *E* − 04	2.9914 *E* − 07	972.24
74	7.7572 *E* + 01	394.43	1.1456 *E* − 04	2.9983 *E* − 07	973.59
76	7.0587 *E* + 01	395.52	1.0397 *E* − 04	3.0052 *E* − 07	974.93
78	6.4257 *E* + 01	396.60	9.4387 *E* − 05	3.0121 *E* − 07	976.28
80	5.8511 *E* + 01	397.69	8.5711 *E* − 05	3.0190 *E* − 07	977.62
82	5.3293 *E* + 01	398.78	7.7855 *E* − 05	3.0259 *E* − 07	978.94
84	4.8552 *E* + 01	399.87	7.0739 *E* − 05	3.0328 *E* − 07	980.28
86	4.4248 *E* + 01	400.96	6.4290 *E* − 05	3.0396 *E* − 07	981.63
88	4.0335 *E* + 01	402.05	5.8446 *E* − 05	3.0465 *E* − 07	982.94
90	3.6778 *E* + 01	403.14	5.3147 *E* − 05	3.0533 *E* − 07	984.28
92	3.3542 *E* + 01	404.22	4.8344 *E* − 05	3.0602 *E* − 07	985.60
94	3.0601 *E* + 01	405.31	4.3985 *E* − 05	3.0670 *E* − 07	986.94
96	2.7924 *E* + 01	406.40	4.0029 *E* − 05	3.0738 *E* − 07	988.25
98	2.5488 *E* + 01	407.49	3.6440 *E* − 05	3.0806 *E* − 07	989.57
100	2.3272 *E* + 01	408.57	3.3182 *E* − 05	3.0874 *E* − 07	990.91

Take a look at the small fluid element whose center is defined by the coordinates x, y, z in Fig. 1.4. A first-order Taylor's series expansion is used to evaluate the pressure at each face. The pressure at the back face of the element is $p - (\partial p/\partial x)(\Delta x/2)$, and the pressure at the front face is $p + (\partial p/\partial x)(\Delta x/2)$. If the fluid is not accelerating, the element must be in equilibrium. For equilibrium, the sum of the forces in any direction must be zero. Therefore,

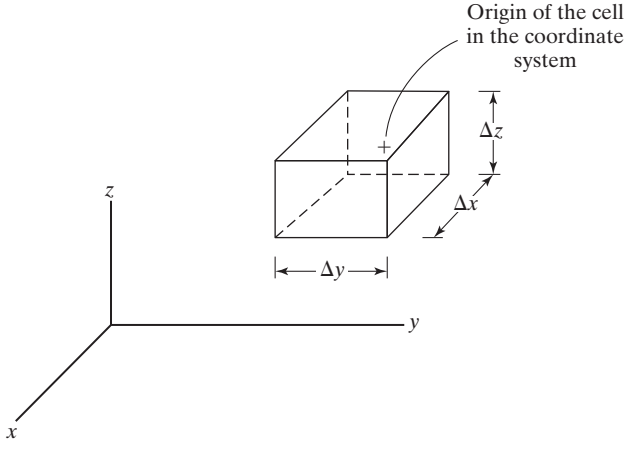

Figure 1.4 Small fluid element used in the derivation of equations (1.15) through (1.17).

$$-\left(p + \frac{\partial p}{\partial x}\frac{\Delta x}{2}\right)\Delta y\,\Delta z + \left(p - \frac{\partial p}{\partial x}\frac{\Delta x}{2}\right)\Delta y\,\Delta z = 0 \qquad \textbf{(1.15a)}$$

$$-\left(p + \frac{\partial p}{\partial y}\frac{\Delta y}{2}\right)\Delta x\,\Delta z + \left(p - \frac{\partial p}{\partial y}\frac{\Delta y}{2}\right)\Delta x\,\Delta z = 0 \qquad \textbf{(1.15b)}$$

$$-\left(p + \frac{\partial p}{\partial z}\frac{\Delta z}{2}\right)\Delta x\,\Delta y + \left(p - \frac{\partial p}{\partial z}\frac{\Delta z}{2}\right)\Delta x\,\Delta y - \rho g\,\Delta x\,\Delta y\,\Delta z = 0 \qquad \textbf{(1.15c)}$$

Note that the coordinate system has been chosen such that gravity acts in the negative z direction. Combining terms and dividing by $\Delta x\,\Delta y\,\Delta z$ gives us

$$\frac{\partial p}{\partial x} = 0 \qquad \textbf{(1.16a)}$$

$$\frac{\partial p}{\partial y} = 0 \qquad \textbf{(1.16b)}$$

$$\frac{\partial p}{\partial z} = -\rho g \qquad \textbf{(1.16c)}$$

The three equations can be written as one using vector notation as:

$$\nabla p = \rho\vec{f} = -\rho g\hat{k} \qquad \textbf{(1.17)}$$

where $\vec{f}$ represents the body force per unit mass and ∇ is the gradient operator. For the cases of interest in this book, the body force is gravity.

These equations illustrate two important principles for a nonaccelerating, hydrostatic, or shear-free, flow: (1) There is no pressure variation in the horizontal direction; that is, the pressure is constant in a plane perpendicular to the direction of gravity; and (2) the vertical pressure variation is proportional to gravity, density, and change in depth. Furthermore, as the element shrinks to zero volume (i.e., as $\Delta z \rightarrow 0$), it can be seen that the pressure is the same on all faces. That is, pressure at a point in a static fluid is independent of orientation.

Since the pressure varies only with z, that is, it is not a function of x or y, an ordinary derivative may be used and equation (1.16c) may be written

$$\frac{dp}{dz} = -\rho g \qquad \textbf{(1.18)}$$

Now assume that the air behaves as a perfect gas. The expression for density given by equation (1.10) can be substituted into equation (1.18) to give

$$\frac{dp}{dz} = -\rho g = -\frac{pg}{RT} \qquad \textbf{(1.19)}$$

In those regions where the temperature can be assumed to constant (an iso-thermal region), separating the variables and integrating between two points yields

$$\int\frac{dp}{p} = \ln\frac{p_2}{p_1} = -\frac{g}{RT}\int dz = -\frac{g}{RT}(z_2 - z_1)$$

where the integration reflects the fact that the temperature has been assumed constant. Rearranging yields

$$p_2 = p_1 \exp\left[\frac{g(z_1 - z_2)}{RT}\right] \tag{1.20}$$

The pressure variation described by equation (1.20) is a reasonable approximation of that in the atmosphere near the earth's surface, or in any iso-thermal region.

An improved correlation for pressure variation in the earth's atmosphere can be obtained if we account for the temperature variation with altitude (which is known as a gradient region). The earth's mean atmospheric temperature decreases almost linearly with z up to an altitude of nearly 11,000 m. That is,

$$T = T_0 - Bz \tag{1.21}$$

where T_0 is the sea-level temperature (absolute) and B is the lapse rate, both of which vary from day to day. The following standard values will be assumed to apply from 0 to 11,000 m:

$$T_0 = 288.15\,\text{K} \qquad \text{and} \qquad B = 0.0065\,\text{K/m}$$

Substituting equation (1.21) into the relation

$$\int \frac{dp}{p} = -\int \frac{g\,dz}{RT}$$

and integrating, we obtain

$$p = p_0\left(1 - \frac{Bz}{T_0}\right)^{g/RB} \tag{1.22}$$

The exponent g/RB, which is dimensionless, is equal to 5.26 for air.

1.2.5 The Standard Atmosphere

In order to correlate flight-test data with wind-tunnel data acquired at different times at different conditions, or to compute flow fields, it is important to have agreed-upon standards of atmospheric properties as a function of altitude. Since the earliest days of aeronautical research, "standard" atmospheres have been developed based on the knowledge of the atmosphere at the time. The one used in this text is the 1976 U.S. Standard Atmosphere, which represents the mid-latitude values of an "average" day for the atmosphere. The atmospheric properties most commonly used in the analysis and design of flight vehicles, as taken from the U.S. Standard Atmosphere (1976), are reproduced in Table 1.2. These are the properties used in the examples in this text.

The basis for establishing a standard atmosphere is a defined variation of temperature with altitude. This atmospheric temperature profile is developed from measurements obtained from balloons, from sounding rockets, and from aircraft at a variety of locations at various times of the year and represents a mean expression of these measurements. A reasonable approximation is that the temperature varies linearly with altitude in some regions and is constant in other altitude regions. Given the temperature

profile, the hydrostatic equation [equation (1.17)] and the perfect-gas equation of state [equation (1.10)] are used to derive the pressure and the density as functions of altitude. Viscosity and the speed of sound can be determined as functions of altitude from equations such as equation (1.12), Sutherland's equation, and equation (1.14), respectively. In reality, variations would exist from one location on earth to another and over the seasons at a given location. Nevertheless, a standard atmosphere is a valuable tool that provides engineers with a standard when conducting analyses and performance comparisons of different aircraft designs.

Aerodynamics Concept Box: Atmospheric Layers

The atmosphere is made up of alternating temperature layers: first a gradient region, followed by an iso-thermal region, etc., as shown below. Each iso-thermal region marks the beginning of a new layer of the atmosphere, where each layer is given a name: troposphere, stratosphere, mesosphere, etc. For example, the stratosphere begins at approximately 11 km (36,000 ft) where an iso-thermal region begins. If you look at Table 1.2, you will see

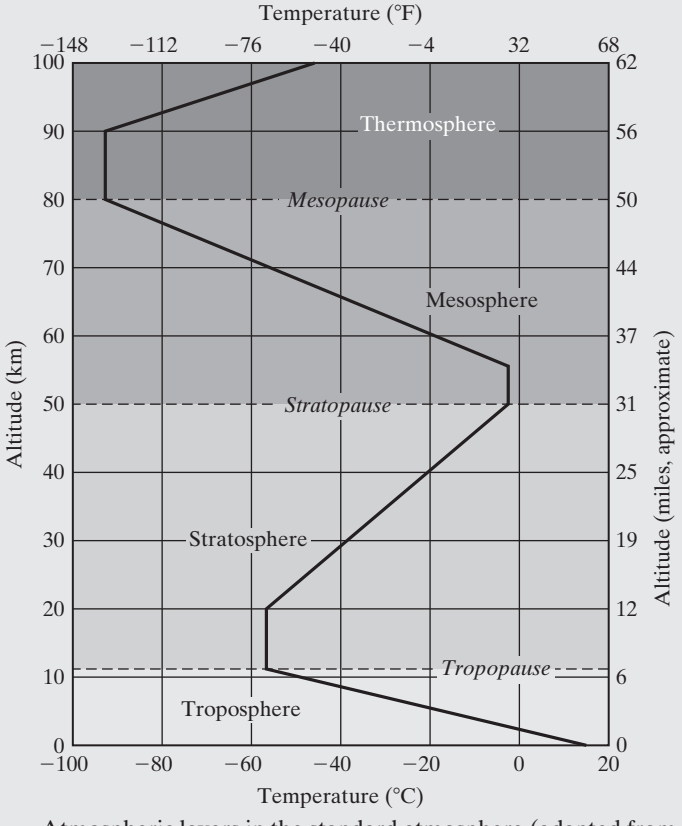

Atmospheric layers in the standard atmosphere (adapted from PhysicalGeography.net)

that the temperature between 11 km and 20 km is constant. This is followed by a gradient region, which ends at 50 km. The dividing line between the troposphere and the stratosphere is called the tropopause, and the dividing line between the stratosphere and the mesosphere is called the stratopause. The standard atmosphere values in Table 1.2 do a very good job of showing these atmospheric layers and the regions that make them.

EXAMPLE 1.9: Properties of the standard atmosphere at 10 km

Using equations (1.21) and (1.22), calculate the temperature and pressure of air at an altitude of 10 km. Compare the tabulated values with those presented in Table 1.2.

Solution: The ambient temperature at 10,000 m is

$$T = T_0 - Bz = 288.15 - 0.0065(10^4) = 223.15\ \text{K}$$

The tabulated value from Table 1.2 is 223.252 K. The calculated value for the ambient pressure is

$$\begin{aligned} p &= p_0\left(1 - \frac{Bz}{T_0}\right)^{g/RB} \\ &= 1.01325 \times 10^5\left[1 - \frac{0.0065(10^4)}{288.15}\right]^{5.26} \\ &= 1.01325 \times 10^5(0.26063) = 2.641 \times 10^4\ \text{N/m}^2 \end{aligned}$$

The comparable value in Table 1.2 is $2.650 \times 10^4\ \text{N/m}^2$.

EXAMPLE 1.10: Properties of the standard atmosphere in English units

Develop equations for the pressure and for the density as a function of altitude from 0 to 65,000 ft. The analytical model of the atmosphere should make use of the hydrostatic equations [i.e., equation (1.18)], for which the density is eliminated through the use of the equation of state for a thermally perfect gas. Assume that the temperature of air from 0 to 36,100 ft is given by

$$T = 518.67 - 0.003565z$$

and that the temperature from 36,100 to 65,000 ft is constant at 389.97°R.

Solution: From 0 to 36,000 ft, the temperature varies linearly as described in general by equation (1.21). Specifically,

$$T = 518.67 - 0.003565z$$

Therefore, $T_0 = 518.67°\text{R}$ and $B = 0.003565°\text{R/ft}$. Using English unit terms in equation (1.22) gives us

$$p = p_0\left(1 - \frac{Bz}{T_0}\right)^{g/RB}$$
$$= 2116.22(1.0 - 6.873 \times 10^{-6}\, z)^{5.26}$$

For a thermally perfect gas, the density is

$$\rho = \frac{p}{RT} = \frac{2116.22(1.0 - 6.873 \times 10^{-6}\, z)^{5.26}}{53.34(518.67 - 0.003565z)}$$

Dividing by ρ_0, the value of the density at standard sea-level conditions,

$$\rho_0 = \frac{p_0}{RT_0} = \frac{2116.22}{(53.34)(518.67)}$$

we obtain the nondimensionalized density:

$$\frac{\rho}{\rho_0} = (1.0 - 6.873 \times 10^{-6}\, z)^{4.26}$$

Since the temperature is constant from 36,100 to 65,000 ft, equation (1.20) can be used to express the pressure, with the values at 36,100 ft serving as the reference values p_1 and z_1:

$$p_{36,100} = 2116.22(1.0 - 6.873 \times 10^{-6}\, z)^{5.26} = 472.19\,\text{lbf/ft}^2$$

Thus,

$$p = 472.9 \exp\left[\frac{g(36{,}100 - z)}{RT}\right]$$

In English units,

$$\frac{g}{RT} = \frac{32.174\dfrac{\text{ft}}{\text{s}^2}}{\left(53.34\dfrac{\text{ft}\cdot\text{lbf}}{\text{lbm}\cdot°\text{R}}\right)(389.97°\text{R})}$$

However, to have the correct units, multiply by $(1/g_c)$, so that

$$\frac{g}{RT} = \frac{32.174\dfrac{\text{ft}}{s^2}}{\left(53.34\dfrac{\text{ft}\cdot\text{lbf}}{\text{lbm}\cdot°\text{R}}\right)(389.97°\text{R})\left(32.174\dfrac{\text{ft}\cdot\text{lbm}}{\text{lbf}\cdot\text{s}^2}\right)} = 4.8075 \times 10^{-5}/\text{ft}$$

Thus,

$$\frac{p}{p_0} = 0.2231 \exp(1.7355 - 4.8075 \times 10^{-5}\, z)$$

The nondimensionalized density is:

$$\frac{\rho}{\rho_0} = \frac{p}{p_0}\frac{T_0}{T}$$

Since $T = 389.97°\text{R} = 0.7519T_0$,

$$\frac{\rho}{\rho_0} = 0.2967 \exp\left(1.7355 - 4.8075 \times 10^{-5} z\right)$$

1.3 DESCRIPTION OF AN AIRPLANE

Vince Lombardi, the celebrated coach of the Green Bay Packers in the 1960s, used to start training camp each year by standing in front of the team, holding up a football, and saying: "Gentlemen, this is a football." Why did he do that? He was trying to make a point, every year, that no matter how long you had been doing something, it was always good to get back to basics. Besides, no matter how many people in the room knew everything he was going to tell them, some people in the room might not know what he was about to say, so everyone learned (yet again) what a football looked like.

How does this relate to airplanes? Airplanes have become incredibly commonplace in the modern world, with people flying millions of miles over the course of their life. But no matter how commonplace airplanes are, there are aspects of airplanes that many of us are not aware of. Even an experienced pilot or passenger may not know all of the names and definitions for various parts of an airplane, so in the spirit of "getting back to basics," we will spend a little time going over the major parts of an airplane.

A typical commercial airliner (often called a "transport") is shown in Fig. 1.5. The components have been broken down into three categories: lifting surfaces or devices, control surfaces, and miscellaneous components. For the category of lifting surfaces, the most important component is the wing, which is the surface that produces the majority of lift on

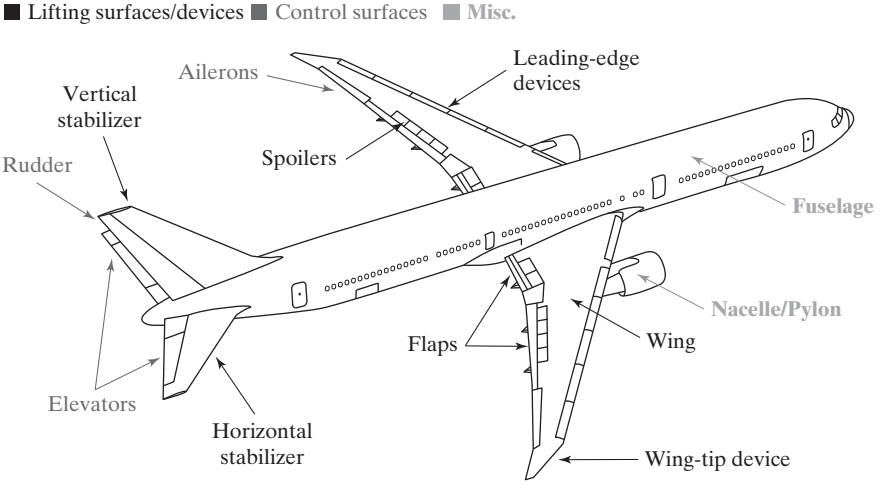

Figure 1.5 Major components of a modern commercial airliner.

the airplane and allows the airplane to fly. Also on the wing are various subcomponents, including the flaps that create additional lift for taking off and landing, spoilers that "spoil" the flow of air over the wing by causing flow separation and creating drag (sometimes called speed brakes), and leading-edge devices used for creating additional lift at low speeds. Many modern wings also have wing-tip devices, which aid in the reduction of induced drag.

Other important lifting surfaces are found on many aircraft in the tail section of the airplane; the tail section is also referred to as the empennage. Typically, tail sections include a horizontal and vertical stabilizer, which keeps the airplane flying with the nose in front and the tail section in the back (much as feathers on an arrow).

Also included on the wings and empennage are three control surfaces. Since an airplane can maneuver in three dimensions, three sets of control surfaces are typically required for creating the moments that cause the airplane to roll, pitch, and yaw. These surfaces are known as the ailerons (which create roll motions where one wing goes up while the other wing goes down), the elevators (which create pitch motions where the nose goes up while the tail goes down), and the rudder (which creates yaw motion where the nose goes left while the tail goes right).

Finally, there are various portions of the airplane that are not there for creating aerodynamic lift. These components are there for holding important parts of the airplane within protective, drag-reducing coverings. An example is the passenger or cargo section, which is known as the fuselage, which accounts for a large percentage of the volume of the airplane. Finally, there is the attachment point for the jet engines, where the wing-like surface holding the engine to the airplane is called a pylon, and the covering around the engine is called a nacelle.

While there are many smaller components on a typical airplane, the parts mentioned above constitute the most important, and largest, components. Knowing the names and purposes of these airplane components is an important part of being an aerodynamicist. Understanding how each of these components works, and learning how to estimate the lift and drag for each component, can be quite challenging. But having a firm grasp of the names and purposes of each component is a good start. The purpose of the rest of the book is to begin to learn about each of these airplane aerodynamic devices and how they work.

1.4 SUMMARY

Aerodynamics is all about estimating the pressures, shear stresses, heat, lift, drag, and moments created by various airplane components. We do this so that we can estimate the performance and flying characteristics of airplanes, and hopefully design better airplanes than have existed in the past. Achieving this goal will require having basic knowledge about fluid properties (e.g., viscosity, density, and speed of sound) that have been presented in this chapter. The reader should note that it may be necessary under certain conditions to use alternative relations for calculating fluid properties. For instance, for the relatively high temperatures associated with hypersonic flight, it may be necessary to account for real-gas effects (e.g., dissociation). Numerous references present the thermodynamic properties and transport properties of gases at high temperatures and pressures [e.g., Moeckel and Weston (1958), Hansen (1957), and Yos (1963)], but in this book we will concentrate on speeds and altitudes where this will not be necessary. Also, we have looked at how the atmosphere can be modeled in order to perform consistent

calculations for the aerodynamics of airplanes. Finally, we reviewed the major components of airplanes so that we can have a consistent language and definitions as we dive deeper into aerodynamics. Hopefully the contents of this first chapter have wetted your appetite and will cause you to learn more about aerodynamics in the chapters that follow.

PROBLEMS

Problems 1.1 through 1.5 deal with the Energy-Maneuverability Technique for a T-38A that is powered by two J85-GE-5A engines. Presented in Fig. P1.1 are the thrust available and the thrust required for the T-38A that is cruising at 20,000 ft. The thrust available is presented as a function of Mach number for the engines operating at military power ("Mil") or operating with the afterburner ("Max"). With the aircraft cruising at a constant altitude (of 20,000 ft), the speed of sound is constant for Fig. P1.1 and the Mach number ($M = U/a$) could be replaced by the velocity, that is by the true air speed.

When the vehicle is cruising at a constant altitude and at a constant attitude, the total drag is equal to the thrust required and the lift balances the weight. As will be discussed in

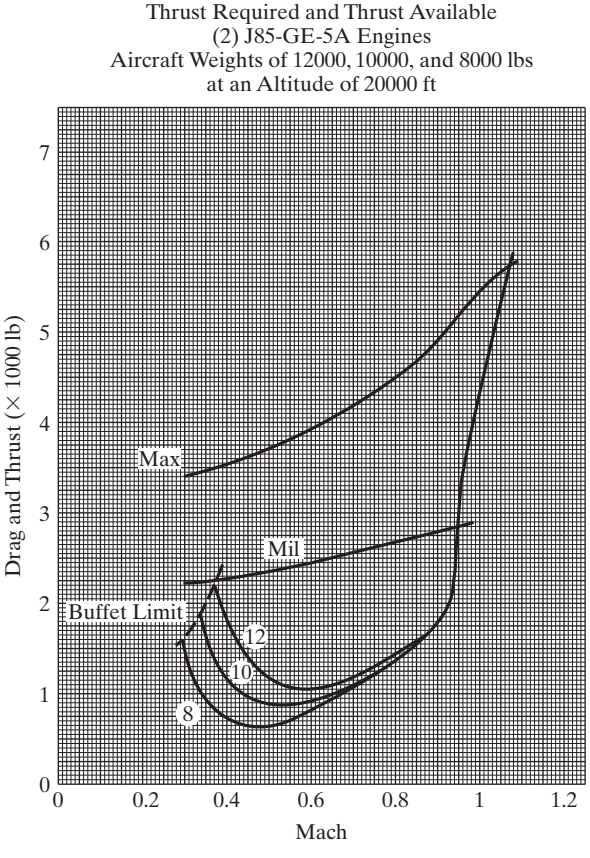

Figure P1.1

Chapter 5, the total drag is the sum of the induced drag, the parasite drag, and the wave drag. Therefore, when the drag (or thrust required) curves are presented for aircraft weights of 8,000 lbf, 10,000 lbf, and 12,000 lbf, they reflect the fact that the induced drag depends on the lift. But the lift is equal to the weight. Thus, at the lower velocities, where the induced drag dominates, the drag is a function of the weight of the aircraft.

1.1. The maximum velocity at which an aircraft can cruise occurs when the thrust available with the engines operating with the afterburner lit ("Max") equals the thrust required, which are represented by the bucket shaped curves. What is the maximum cruise velocity that a 5,000-lbf T-38A can sustain at 26,000 feet?

As the vehicle slows down, the drag acting on the vehicle (which is equal to the thrust required to cruise at constant velocity and altitude) reaches a minimum (D_{min}). The lift-to-drag ratio is, therefore, a maximum $[(L/D)_{max}]$. What is the maximum value of the lift-to-drag ratio $[(L/D)_{max}]$ for our 5,000-lbf T-38A cruising at 26,000 ft? What is the velocity at which the vehicle cruises, when the lift-to-drag ratio is a maximum? As the vehicle slows to speeds below that for $[(L/D)_{min}]$, which is equal to $[(L/D)_{max}]$, it actually requires more thrust (i. e., more power) to fly slower. You are operating the aircraft in the region of reverse command. More thrust is required to cruise at a slower speed. Eventually, one of two things happens: either the aircraft stalls (which is designated by the term "Buffet Limit" in Fig. P1.1) or the drag acting on the aircraft exceeds the thrust available. What is the minimum velocity at which a 5,000-lbf T-38A can cruise at 26,000 ft? Is this minimum velocity due to stall or is it due to the lack of sufficient power?

1.2. What are the total energy, the energy height, and the specific excess power, if our 10,000-lbf T-38A is using "Mil" thrust to cruise at a Mach number of 0.65 at 20,000 ft?

1.3. What is the maximum acceleration that our 10,000-lbf T-38A can achieve using "Mil" thrust, while passing through Mach 0.65 at a constant altitude of 20,000 ft? What is the maximum rate-of-climb that our 10,000-lbf T-38A can achieve at a constant velocity (specifically, at a Mach number of 0.65), when using "Mil" thrust while climbing through 20,000 ft?

1.4. Compare the values of $(L/D)_{max}$ for aircraft weights of 8,000 lbf, 10,000 lbf, and 12,000 lbf, when our T-38A aircraft cruises at 20,000 ft. Compare the velocity that is required to cruise at $(L/D)_{max}$ for each of the three aircraft weights.

1.5. Compare the specific excess power for a 10,000-lbf T-38A cruising at the Mach number required for $(L/D)_{max}$ while operating at "Mil" thrust with that for the aircraft cruising at a Mach number of 0.35 and with that for the aircraft cruising at a Mach number of 0.70.

1.6. Nitrogen is often used in wind tunnels as the test gas substitute for air. Compare the value of the kinematic viscosity

$$\nu = \frac{\mu}{\rho} \tag{1.6}$$

for nitrogen at a temperature of 350°F and at a pressure of 150 psia with that for air at the same conditions.

The constants for Sutherland's equation to calculate the coefficient of viscosity, that is equation 1.12, are:

$$C_1 = 2.27 \times 10^{-8} \frac{\text{lbf} \cdot \text{s}}{\text{ft}^2 \cdot °\text{R}^{0.5}} \text{ and } C_2 = 198.6°\text{R}$$

for air. Similarly,

$$C_1 = 2.16 \times 10^{-8} \frac{\text{lbf} \cdot \text{s}}{\text{ft}^2 \cdot °\text{R}^{0.5}} \text{ and } C_2 = 183.6°\text{R}$$

for nitrogen. The gas constant, which is used in the calculation of the density for a thermally perfect gas,

$$\rho = \frac{p}{RT} \tag{1.10}$$

is equal to $53.34 \frac{\text{ft} \cdot \text{lbf}}{\text{lbm} \cdot {}^\circ\text{R}}$ for air and to $55.15 \frac{\text{ft} \cdot \text{lbf}}{\text{lbm} \cdot {}^\circ\text{R}}$ for nitrogen.

1.7. Compare the value of the kinematic viscosity for nitrogen in a wind-tunnel test, where the free-stream static pressure is 586 N/m^2 and the free-stream static temperature is 54.3 K, with the value for air at the same conditions.

The constants for Sutherland's equation to calculate the coefficient of viscosity (i.e., equation 1.12) are:

$$C_1 = 1.458 \times 10^{-6} \frac{\text{kg}}{\text{s} \cdot \text{m} \cdot \text{K}^{0.5}} \text{ and } C_2 = 110.4\text{K}$$

for air. Similarly,

$$C_1 = 1.39 \times 10^{-6} \frac{\text{kg}}{\text{s} \cdot \text{m} \cdot \text{K}^{0.5}} \text{ and } C_2 = 102\text{K}$$

for nitrogen. The gas constant, which is used in the calculation of the density for a thermally perfect gas,

$$\rho = \frac{p}{RT} \tag{1.10}$$

is equal to $287.05 \frac{\text{N} \cdot \text{m}}{\text{kg} \cdot \text{K}}$ for air and to $297 \frac{\text{N} \cdot \text{m}}{\text{kg} \cdot \text{K}}$ for nitrogen. What would be the advantage(s) of using nitrogen as the test gas instead of air?

1.8. A gas is compressed from atmospheric pressure to a pressure of 4 atm. Temperature changes from 300K to 400K. Find the density after compression. Assume perfect gas behavior for gas with initial density of 1.176 kg/m^3.

1.9. The isentropic expansion of perfect air takes place such that p/ρ^γ is a constant, where $\gamma = 1.4$ for air. If the pressure decreases to one-third of its original value, what happens to the density? If the initial density is 1.176 kg/m^3, what is the final density?

1.10. Using the values for the pressure and for the temperature given in Table 1.2, calculate the density [use the equation for density (1.10) for a thermally perfect gas] and the dynamic viscosity [using Sutherland's equation (1.12a) for dynamic viscosity] at an altitude 15 km.

1.11. Using the dynamic viscosity, density, temperature values for problem 1.10 at an altitude 15 km, what is the kinematic viscosity at this altitude [use the relation between dynamic viscosity and kinematic viscosity from the equation (1.13)] and speed of sound for a thermally perfect gas?

1.12. The pilot announces that you are flying at an altitude of 10 km where stagnation temperature is measured to be 625 K, find the speed of aircraft. Use Table 1.2 to obtain the values for the temperature and speed of the sound.

1.13. The air in Tunnel B is expanded through a convergent/divergent nozzle to the test section, where the Mach number is 7, the free-stream static pressure is $586\,N/mm^2$ and the free-stream temperature is 54.3 K. Using the perfect-gas relations, what are the corresponding values for the test-section density, viscosity, and velocity? Note that $U_\infty = M_\infty a_\infty$.

1.14. The conditions in the reservoir (or stagnation chamber) of Aero-thermal Tunnel C at the Arnold Engineering Development Center (AEDC) are that the pressure (p_{t1}) is 170×10^3 N/m^2 and the temperature (T_t) is 923.15 K. Using the perfect-gas relations, what are the density and the viscosity in the reservoir?

1.15. The air in Tunnel C accelerates through a convergent/divergent nozzle until the Mach number is 4 in the test section. The corresponding values for the free-stream pressure and the free-stream temperature in the test section are 1100 N/m^2 abs. and 219.15 K respectively. What are the corresponding values for the free-stream density, viscosity, and velocity in the test section? Note that $M_\infty = U_\infty / a_\infty$. Using the values for the static pressure given in Table 1.2, what is the pressure altitude simulated in the wind tunnel by this test condition?

1.16. If you are flying at Mach number 0.8 at a height of 10 km, what is the speed of aircraft in m/s, ft/s and knots? Use Table 1.2 to obtain the value of the speed of sound.

1.17. Using equations (1.21) and (1.22), calculate the temperature and pressure of the atmosphere at 9000 m. Compare the tabulated values with those presented in Table 1.2.

1.18. Using an approach similar to that used in Example 1.7, develop metric-unit expressions for the pressure, the temperature, and the density of the atmosphere from 11,000 to 20,000 m. The temperature is constant and equal to 216.650 K over this range of altitude.

1.19. Using the expressions developed in Problem 1.18, what are the pressure, the density, the viscosity, and the speed of sound for the ambient atmospheric air at 18 km? Compare these values with the corresponding values tabulated in Table 1.2.

1.20. Using the expressions developed in Example 1.7, calculate the pressure, the temperature, and the density for the ambient atmospheric air at 10,000, 30,000, and 65,000 ft. Compare these values with the corresponding values presented in Table 1.2.

Problems 1.21 and 1.22 deal with standard atmosphere usage. The properties of the standard atmosphere are frequently used as the free-stream reference conditions for aircraft performance predictions. It is common to refer to the free-stream properties by the altitude in the atmospheric model at which those conditions occur. For instance, if the density of the free-stream flow is 0.00199 slugs/ft^3, then the density altitude (h_ρ) would be 6000 ft.

1.21. One of the design requirements for a multirole jet fighter is that it can survive a maximum sustained load factor of 9g at 20,000 *ft* MSL (mean sea level). What are the atmospheric values of the pressure, of the temperature, and of the density, that define the free-stream properties that you would use in the calculations that determine if a proposed design can meet this requirement?

1.22. An aircraft flying at geometric altitude of 20,000 ft has instrument readings of $p = 1195.57\ lbf/ft^2$ and $T = 475.90°R$.

(a) Find the values for the pressure altitude h_p the temperature altitude h_T and the density altitude h_ρ to the nearest 500 ft.

(b) If the aircraft were flying in a standard atmosphere, what would be the relationship among h_p, h_T and h_ρ.

1.23. A U-tube manometer is used to measure the pressure in water pipeline "A". One side of the manometer is connected to the water pipe line and other side is open to atmosphere. If there is a difference of 50 cm in the mercury levels in the two tubes, what is the pressure in the pipe line "A" ? Neglect the frictional losses. Take specific gravity is 13.6 and $p_{atm} = 101325$ N/m^2.

1.24. A U-tube manometer is used to measure the pressure at the stagnation point of a model in a wind tunnel. One side of the manometer goes to an orifice at the stagnation point; the other side is open to the atmosphere (Fig. P1.24). If there is a difference of 3.0 cm in the mercury levels in the two tubes, what is the pressure difference in N/m^2.

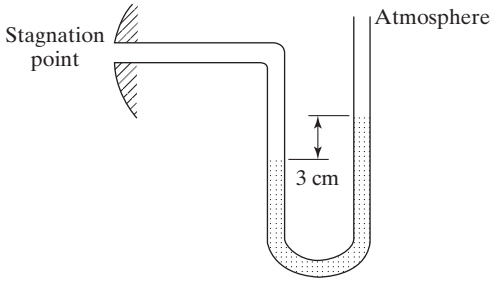

Figure P1.24

1.25. Consult a reference that contains thermodynamic charts for the properties of air, e.g., Hansen (1957), and delineate the temperature and pressure ranges for which air behaves:

(1) as a thermally perfect gas, i.e., $\frac{p}{\rho RT} = 1$ and

(2) as a calorically perfect gas, i.e., h $= c_p T$, where c_p is a constant.

1.26. A fairing for an optically perfect window for an airborne telescope is being tested in a wind tunnel. A manometer is connected to two pressure ports, one on the inner side of the window and the other port on the outside. The manometer fluid is water. During the testing at the maximum design airspeed, the column of water in the tube that is connected to the outside pressure port is 40 cm higher that the column of water in the tube that is connected to the inside port.

(a) What is the difference between the pressure that is acting on the inner surface of the window relative to the pressure acting on the outer surface of the window?

(b) If the window has a total area of 0.8 m^2, what is the total force acting on the window due to the pressure difference?

REFERENCES

Chapman S, Cowling TG. 1960. *The Mathematical Theory of Non-uniform Gases*. Cambridge: Cambridge University Press

Coram R. 2002. *Boyd, The Fighter Pilot Who Changed the Art of War*. Boston: Little Brown

Grier P. 2004. The Viper revolution. *Air Force Magazine* 87(1):64–69

Hansen CF. 1957. Approximations for the thermodynamic properties of air in chemical equilibrium. *NACA Tech. Report R-50*

Hillaker H. 1997. Tribute to John R. Boyd. *Code One Magazine* 12(3)

Moeckel WE, Weston KC. 1958. Composition and thermodynamic properties of air in chemical equilibrium. *NACA Tech. Note 4265*

Svehla RA. 1962. Estimated viscosities and thermal conductivities of gases at high temperatures. *NASA Tech.Report R-132*

1976. *U.S. Standard Atmosphere.* Washington, DC: U.S. Government Printing Office

Werner J. 2005. *Knight of Germany: Oswald Boelcke – German Ace*. Mechanicsburg: Stackpole Books

Yos JM. 1963. Transport properties of nitrogen, hydrogen, oxygen, and air to 30,000 K. *AVCO Corp. RAD-TM-63-7*

2 FUNDAMENTALS OF FLUID MECHANICS

Chapter Objectives

- Understand the physical laws that form the basis of the fluid equations of motion
- Learn how to obtain the equations of fluid motion in both derivative and integral form
- Be able to apply the equations of motion to calculate properties of fluid flows
- Understand dynamic similarity and how to calculate Mach number and Reynolds number
- Understand the various Mach and Reynolds number regimes and their distinguishing characteristics

As we discussed in Chapter 1, to accurately predict the aerodynamic forces and moments that act on a vehicle in flight, we will need to be able to describe the pattern of flow around the configuration. The resultant flow pattern depends on the geometry of the vehicle, the orientation of the vehicle with respect to the undisturbed free-stream flow, and the altitude and speed at which the vehicle is traveling. This will require us to solve the fundamental equations of fluid dynamics, in one way or another.

The fundamental physical laws used to solve for the fluid motion in a general problem are:

1. Conservation of mass (or the continuity equation)
2. Conservation of linear momentum (or Newton's second law of motion)
3. Conservation of energy (or the first law of thermodynamics)

Because the flow patterns are often very complex, it may be necessary to also use experimental investigations, theoretical analysis, and/or computational simulations to aid in describing the resultant flow. The theoretical and computational descriptions may utilize simplifying approximations in order to obtain any solution at all, depending on the complexity of the flow field. The validity of the simplifying approximations for a particular application should always be verified experimentally. That is why it is important to understand the fundamental laws that govern the fluid motion so that we can relate the theoretical solutions obtained using approximate flow models with experimental results, which usually involve scale models.

2.1 INTRODUCTION TO FLUID DYNAMICS

To calculate the aerodynamic forces acting on an airplane, it is necessary to solve the equations governing the flow field about the vehicle. The flow-field solution can be formulated from the point of view of an observer on the ground or from the point of view of the pilot. Provided that the two observers apply the appropriate boundary conditions to the governing equations, both observers will obtain the same values for the aerodynamic forces acting on the airplane.

To an observer on the ground, the airplane is flying into a mass of air substantially at rest (assuming there is no wind). The neighboring air particles are accelerated and decelerated by the airplane and the reaction of the particles to the acceleration results in a force on the airplane. The motion of a typical air particle is shown in Fig. 2.1. The particle, which is initially at rest well ahead of the airplane, is accelerated by the passing airplane. The description of the flow field in the ground-observer-fixed coordinate system must represent the time-dependent motion (i.e., a nonsteady flow).

As viewed by the pilot, the air is flowing past the airplane and moves in response to the geometry of the vehicle. If the airplane is flying at constant altitude and constant velocity, the terms of the flow-field equations that contain partial derivatives with respect to time are zero in the vehicle-fixed coordinate system. Thus, as shown in Fig. 2.2, the velocity and the flow properties of the air particles that pass through a specific location relative to the vehicle are independent of time. The flow field is steady relative to a set of axes fixed to the vehicle (or pilot). Therefore, the equations are usually easier to solve in the vehicle (or pilot)-fixed coordinate system rather than in the ground-observer-fixed coordinate system. Because of the resulting simplification of the mathematics through the Galilean transformation from the ground-fixed-reference coordinate system to the vehicle-fixed-reference coordinate system, many problems in aerodynamics are formulated as the flow of a stream of fluid past a body at rest. Note that the subsequent locations of the air

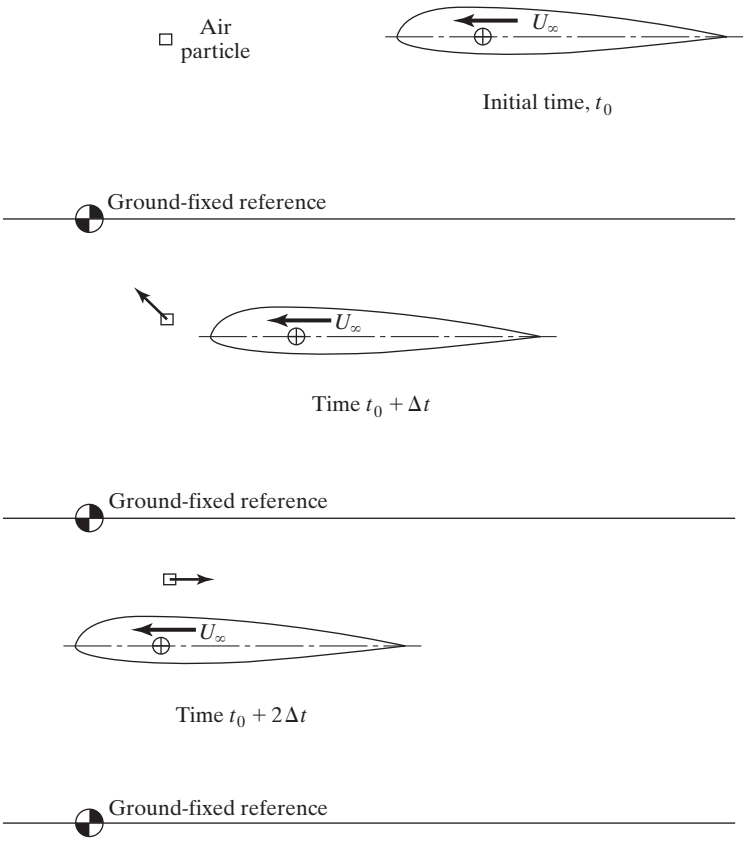

Figure 2.1 (Nonsteady) airflow around a wing in the ground-fixed coordinate system.

particle that passed through our control volume at time t_0 are included for comparison with Fig. 2.2.

In this text, we will use the vehicle (or pilot)-fixed coordinate system. Instead of describing the fluid motion around a vehicle flying through the air, we will examine air flowing around a fixed vehicle. At points far from the vehicle (i.e., the undisturbed free stream), the fluid particles are moving toward the vehicle with the velocity U_∞ (see Fig. 2.2), which is in reality the speed of the vehicle (see Fig. 2.1). The subscript ∞ or 1 will be used to denote the undisturbed (or free-stream) flow conditions (i.e., those conditions far from the vehicle). Since all the fluid particles in the free stream are moving with the same velocity, there is no relative motion between them, and, hence, there are no shearing stresses in the free-stream flow. When there is no relative motion between the fluid particles, the fluid is termed a *static medium* (as discussed in Section 1.2.4). The values of the static fluid properties (e.g., pressure and temperature) are the same for either coordinate system.

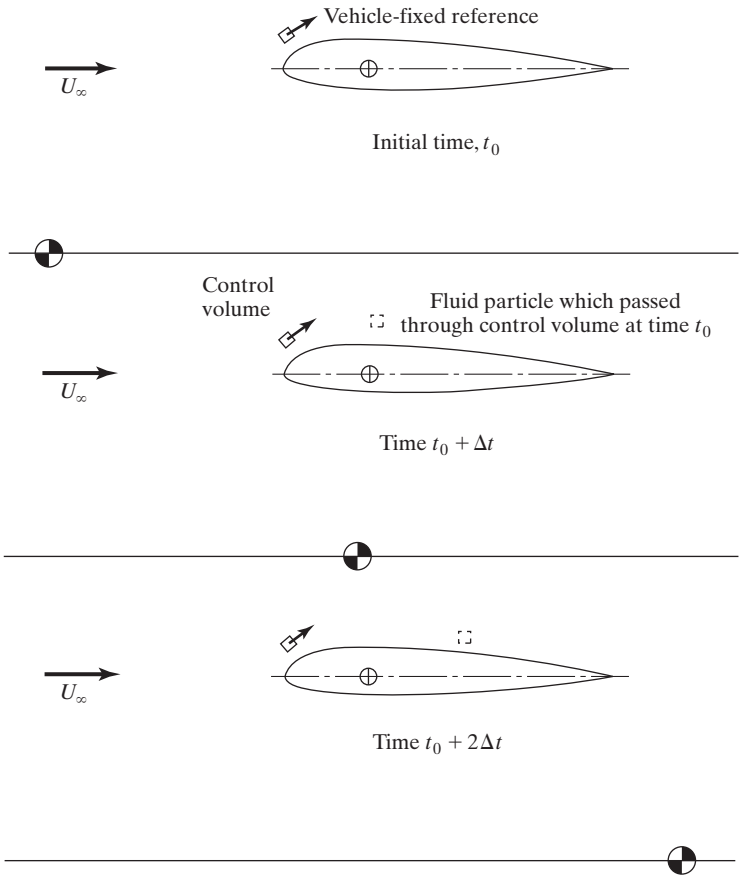

Figure 2.2 (Steady) airflow around a wing in a vehicle-fixed coordinate system.

2.2 CONSERVATION OF MASS

The conservation of mass is one of the most important and useful equations in fluid dynamics. It allows us to determine if a given flow field conserves mass, and is therefore physically possible. If mass is not conserved, then we are wasting our time analyzing the details of the flow, since it cannot occur physically.

First, we will apply the principle of conservation of mass to a small volume of space (a control volume) through which the fluid can move freely. It is important to understand that the "walls" of the control volume are fictitious and do not interfere with the flow. For convenience, we will use a Cartesian coordinate system (x, y, z), as shown in Fig. 2.3. Furthermore, in the interest of simplicity, we will look at a two-dimensional flow, that is, one in which there is no flow along the z axis; flow patterns are the same for any xy plane. As indicated in the sketch of Fig. 2.3, the component of the fluid velocity in the x direction will be designated by u, and that in the y direction by v. The net outflow of mass through the surface surrounding the volume must be equal to the decrease of mass within

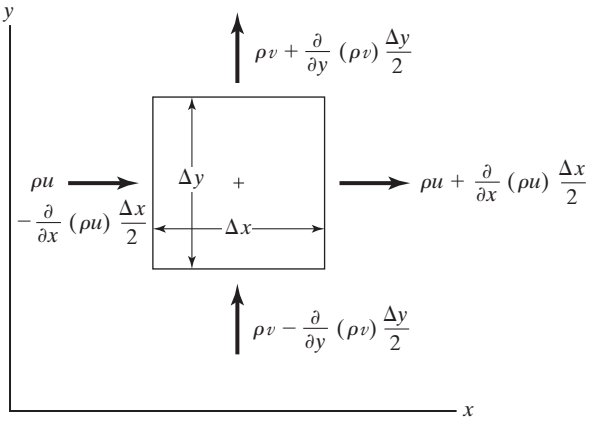

Figure 2.3 Velocities and densities for the mass-flow balance through a fixed volume element in two dimensions.

the volume (this is the statement required for mass to be conserved). The mass-flow rate through a surface bounding the element is equal to the product of the density, the velocity component normal to the surface, and the area of that surface (flow out of the volume is considered positive). A first-order Taylor's series expansion is used to evaluate the flow properties at the faces of the element, since the properties are a function of position. We could use many terms in the series (including second-order and third-order terms), but they would vanish when we assumed that the control volume was small. Referring to Fig. 2.3, the net outflow of mass per unit time per unit depth (into the paper) is

$$\left[\rho u + \frac{\partial(\rho u)}{\partial x}\frac{\Delta x}{2}\right]\Delta y + \left[\rho v + \frac{\partial(\rho v)}{\partial y}\frac{\Delta y}{2}\right]\Delta x$$
$$-\left[\rho u - \frac{\partial(\rho u)}{\partial x}\frac{\Delta x}{2}\right]\Delta y - \left[\rho v - \frac{\partial(\rho v)}{\partial y}\frac{\Delta y}{2}\right]\Delta x$$

which must equal the rate at which the mass contained within the element decreases:

$$-\frac{\partial \rho}{\partial t}\Delta x\,\Delta y$$

Equating the two expressions, combining terms, and dividing by $\Delta x\,\Delta y$, we obtain

$$\frac{\partial \rho}{\partial t} + \frac{\partial}{\partial x}(\rho u) + \frac{\partial}{\partial y}(\rho v) = 0$$

The fact that the size of the control volume, $\Delta x\,\Delta y$, vanished at this point means that our choice of volume was arbitrary (as long as it was larger than a microscopic scale and smaller than the scale of the airplane).

If the approach had been extended to include flow in the z direction, we would obtain the general differential form of the continuity equation:

$$\frac{\partial \rho}{\partial t} + \frac{\partial}{\partial x}(\rho u) + \frac{\partial}{\partial y}(\rho v) + \frac{\partial}{\partial z}(\rho w) = 0 \qquad \textbf{(2.1)}$$

In vector form, the equation is

$$\frac{\partial \rho}{\partial t} + \nabla \cdot (\rho \vec{V}) = 0 \tag{2.2}$$

As has been discussed, the pressure variations that occur in relatively low-speed flows are sufficiently small so that the density is essentially constant. For these incompressible flows, the continuity equation simplifies to:

$$\frac{\partial u}{\partial x} + \frac{\partial v}{\partial y} + \frac{\partial w}{\partial z} = 0 \tag{2.3}$$

In vector form, the incompressible continuity equation is:

$$\nabla \cdot \vec{V} = 0 \tag{2.4}$$

Using appropriate boundary conditions, such as the requirement that there is no flow through a solid surface (i.e., the normal component of the velocity is zero at a solid surface), we can solve equation (2.4) for the velocity field. By doing this, we obtain a detailed picture of the fluid velocity as a function of position throughout the flow field, which is one of our goals in aerodynamics.

EXAMPLE 2.1: A basic flow where mass is conserved

Determine whether the steady, two-dimensional, incompressible flow given by

$$u = 2x \qquad v = -2y$$

satisfies the conservation of mass.

Solution: The incompressible conservation of mass is given by equation (2.3). Simplifying for two-dimensional flow yields:

$$\frac{\partial u}{\partial x} + \frac{\partial v}{\partial y} = 0$$

The required derivatives are: $\partial u/\partial x = 2$ and $\partial v/\partial y = -2$. Substituting these derivatives into the continuity equation results in:

$$\frac{\partial u}{\partial x} + \frac{\partial v}{\partial y} = 2 - 2 = 0$$

Therefore, mass is conserved for this flow field. We will examine this flow field in more detail in Chapter 3.

EXAMPLE 2.2: Incompressible boundary layer

Consider the case where a steady, incompressible, uniform flow whose velocity is U_∞ (i.e., a free-stream flow) approaches a flat plate. In the viscous region near the surface, which is called the boundary layer and is

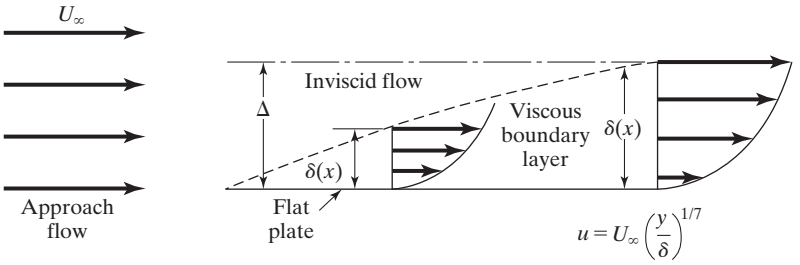

Figure 2.4 Incompressible boundary layer; flow diagram for Example 2.2.

discussed at length in Chapter 4, the streamwise component of velocity is given by

$$u = U_\infty \left(\frac{y}{\delta}\right)^{1/7}$$

where δ, the boundary-layer thickness at a given station, is a function of x. Is a horizontal line parallel to the plate and a distance Δ from the plate (where Δ is equal to δ at the downstream station) a streamline? (See Fig. 2.4.)

Solution: By continuity for this steady, two-dimensional, incompressible flow,

$$\frac{\partial u}{\partial x} + \frac{\partial v}{\partial y} = 0$$

Since $u = U_\infty (y/\delta)^{1/7}$ and $\delta = \delta(x)$

$$\frac{\partial v}{\partial y} = -\frac{\partial u}{\partial x} = \frac{U_\infty}{7} \frac{y^{1/7}}{\delta^{8/7}} \frac{d\delta}{dx}$$

Integrating with respect to y yields

$$v = \frac{U_\infty}{8} \frac{y^{8/7}}{\delta^{8/7}} \frac{d\delta}{dx} + C$$

where C, the constant of integration, can be set equal to zero since $v = 0$ when $y = 0$ (i.e., there is no flow through the wall). Thus, when $y = \Delta$,

$$v_e = \frac{U_\infty}{8} \left(\frac{\Delta}{\delta}\right)^{8/7} \frac{d\delta}{dx}$$

Since v is not equal to zero, there is flow across the horizontal line which is Δ above the surface, and this line is not a streamline.

If the details of the flow are not of concern, the mass conservation principle can be applied directly to the entire region. Integrating equation (2.2) over a fixed finite volume in our fluid space (see Fig. 2.5) yields

$$\iiint_{\text{vol}} \frac{\partial \rho}{\partial t} d(\text{vol}) + \iiint_{\text{vol}} \nabla \cdot (\rho \vec{V}) d(\text{vol}) = 0$$

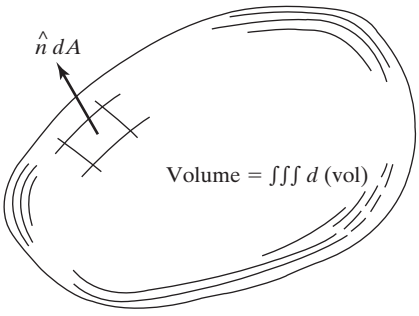

Figure 2.5 Nomenclature for the integral form of the continuity equation.

The second volume integral can be transformed into a surface integral using Gauss's theorem (also known as the divergence theorem), which relates the volume integral of a vector (in this case ρV) to the surface integral of the same vector as:

$$\iiint_{\text{vol}} \nabla \cdot (\rho \vec{V}) d(\text{vol}) = \oiint_{A} \hat{n} \cdot \rho \vec{V}\, dA$$

where $\hat{n}\,dA$ is a vector normal to the surface dA which is positive when pointing outward from the enclosed volume and which is equal in magnitude to the surface area. The circle through the integral sign for the area indicates that the integration is to be performed over the entire surface bounding the volume. Since the control volume is fixed in space (and the limits of integration are also fixed), the time derivative can be moved outside the integral. The resultant equation is the general integral expression for the conservation of mass:

$$\frac{\partial}{\partial t} \iiint_{\text{vol}} \rho d(\text{vol}) + \oiint_{A} \rho \vec{V} \cdot \hat{n}\, dA = 0 \qquad \textbf{(2.5)}$$

In words, the time rate of change of the mass within the volume plus the net efflux (outflow) of mass through the surface bounding the volume must be zero.

The volumetric flux Q is the flow rate through a particular surface and is equal to $\iint \vec{V} \cdot \hat{n}\, dA$, which we will use in Chapter 3. For a sample problem using the integral form of the continuity equation, see Example 2.4.

2.3 CONSERVATION OF LINEAR MOMENTUM

The equation for the conservation of linear momentum is obtained by applying Newton's second law: the net force acting on a fluid particle is equal to the time rate of change of the linear momentum of the fluid particle. As the fluid element moves in space, its velocity, density, shape, and volume may change, but its mass is conserved. Thus, using a coordinate system that is neither accelerating nor rotating, which is called an *inertial coordinate system*, we may write

$$\vec{F} = m\frac{d\vec{V}}{dt} \qquad \textbf{(2.6)}$$

The velocity $\vec{V}$ of a fluid particle is, in general, an explicit function of time t as well as of its position x, y, z. Furthermore, the position coordinates x, y, z of the fluid particle are themselves a function of time. Since the time differentiation of equation (2.6) follows a given particle in its motion, the derivative is frequently termed the *particle, total*, or *substantial derivative* of $\vec{V}$. Since $\vec{V}(x, y, z, t)$ and $x(t)$, $y(t)$, and $z(t)$,

$$\frac{d\vec{V}}{dt} = \frac{\partial \vec{V}}{\partial x}\frac{dx}{dt} + \frac{\partial \vec{V}}{\partial y}\frac{dy}{dt} + \frac{\partial \vec{V}}{\partial z}\frac{dz}{dt} + \frac{\partial \vec{V}}{\partial t} \tag{2.7}$$

(The reader should note that some authors use *D/Dt* instead of *d/dt* to represent the substantial derivative.) However,

$$\frac{dx}{dt} = u \qquad \frac{dy}{dt} = v \qquad \frac{dz}{dt} = w$$

Therefore, the acceleration of a fluid particle is

$$\frac{d\vec{V}}{dt} = \frac{\partial \vec{V}}{\partial t} + u\frac{\partial \vec{V}}{\partial x} + v\frac{\partial \vec{V}}{\partial y} + w\frac{\partial \vec{V}}{\partial z} \tag{2.8}$$

or

$$\frac{d\vec{V}}{dt} = \frac{\partial \vec{V}}{\partial t} + (\vec{V}\cdot\nabla)\vec{V}\left(= \frac{D\vec{V}}{Dt}\right) \tag{2.9}$$

Thus, the substantial derivative is the sum of the local, time-dependent changes that occur at a point in the flow field and of the changes that occur because the fluid particle moves around in space. Problems where the local, time-dependent changes are zero,

$$\frac{\partial \vec{V}}{\partial t} = 0$$

are known as *steady-state flows*. Note that even for a steady-state flow where $\partial\vec{V}/\partial t$ is equal to zero, fluid particles can accelerate due to the unbalanced forces acting on them. This is the case for an air particle that accelerates as it moves from the stagnation region to the low-pressure region above the airfoil. The convective acceleration of a fluid particle as it moves to different points in space is represented by the second term in equation (2.9). An unsteady flow is a flow where the velocity varies as a function of time at a point in the flow field, not necessarily a flow where velocity varies from one point to another.

The principal forces with which we are concerned are those that act directly on the mass of the fluid element, the *body forces*, and those that act on its surface, the *pressure forces* and *shear forces*. The stress system acting on an element of the surface is illustrated in Fig. 2.6. The stress components τ acting on the surface of a small cube are assigned subscripts. The first subscript indicates the direction of the normal to the surface on which the stress acts and the second indicates the direction in which the stress acts. Thus, τ_{xy} denotes a stress acting in the y direction on the surface whose normal points in the x direction. Similarly, τ_{xx} denotes a normal stress acting on that surface. The stresses are described in terms of a right-hand

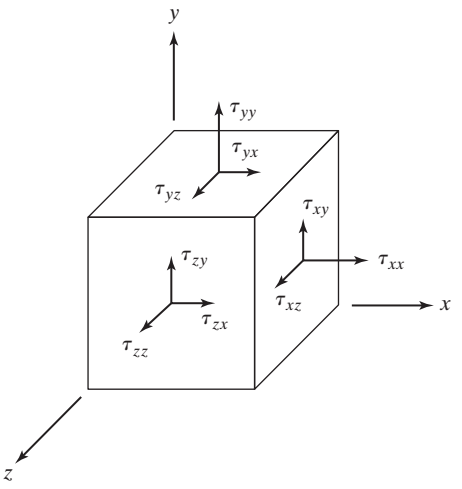

Figure 2.6 Nomenclature for the normal stresses and the shear stresses acting on a fluid element.

coordinate system in which the outwardly directed surface normal indicates the positive direction.

The properties of most fluids have no preferred direction in space, which is called an *isotropic property*. As a result of the isotropic nature of many fluids,

$$\tau_{xy} = \tau_{yx} \qquad \tau_{yz} = \tau_{zy} \qquad \tau_{zx} = \tau_{xz} \tag{2.10}$$

as shown in Schlichting and Gersten (2000).

In general, the various stresses change from point to point. Thus, they produce net forces on the fluid particle, which cause it to accelerate. The forces acting on each surface are obtained by taking into account the variations of stress with position by using the center of the element as a reference point. To simplify the illustration of the force balance on the fluid particle, we will again consider a two-dimensional flow, as shown in Fig. 2.7. The force in the x direction (for a unit depth in the z direction) is:

$$\begin{aligned}\rho f_x \Delta x \Delta y &+ \left[\tau_{xx} + \frac{\partial}{\partial x}(\tau_{xx})\frac{\Delta x}{2}\right]\Delta y - \left[\tau_{xx} - \frac{\partial}{\partial x}(\tau_{xx})\frac{\Delta x}{2}\right]\Delta y \\ &\left[\tau_{yx} + \frac{\partial}{\partial y}(\tau_{yx})\frac{\Delta y}{2}\right]\Delta x - \left[\tau_{yx} - \frac{\partial}{\partial y}(\tau_{yx})\frac{\Delta y}{2}\right]\Delta x \\ &= \rho f_x \Delta x \Delta y + \frac{\partial}{\partial x}(\tau_{xx})\Delta x \Delta y + \frac{\partial}{\partial y}(\tau_{yx})\Delta x \Delta y\end{aligned}$$

where f_x is the body force per unit mass in the x direction. The body force for the flow fields of interest in this text is gravity, but other body forces could exist (such as electromagnetic forces).

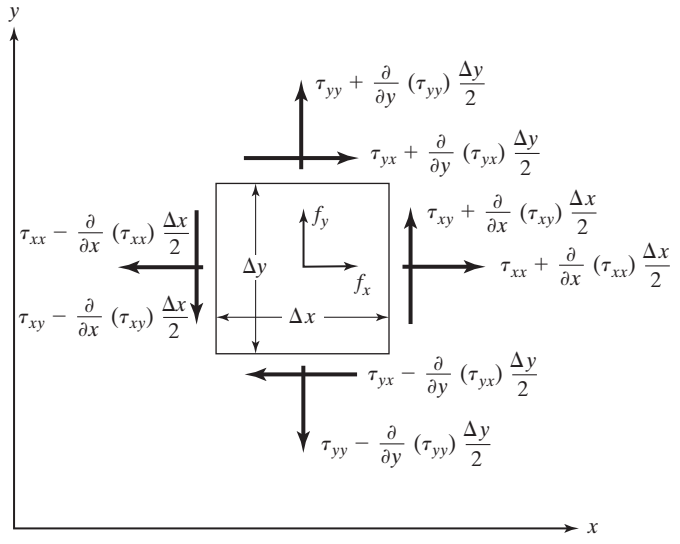

Figure 2.7 Stresses acting on a two-dimensional element of fluid.

Including flow in the z direction, the resultant force in the x direction is

$$F_x = \rho f_x \,\Delta x\,\Delta y\,\Delta z + \frac{\partial}{\partial x}(\tau_{xx})\,\Delta x\,\Delta y\,\Delta z + \frac{\partial}{\partial y}(\tau_{yx})\,\Delta y\,\Delta x\,\Delta z + \frac{\partial}{\partial z}(\tau_{zx})\,\Delta z\,\Delta y\,\Delta x$$

which, by equation (2.6), is equal to

$$ma_x = \rho\,\Delta x\,\Delta y\,\Delta z\frac{du}{dt} = \rho\,\Delta x\,\Delta y\,\Delta z\left[\frac{\partial u}{\partial t} + (\vec{V}\cdot\nabla)u\right]$$

Equating the two and dividing by the volume of the fluid particle $\Delta x\,\Delta y\,\Delta z$ yields the linear momentum equation for the x direction:

$$\rho\frac{du}{dt} = \rho f_x + \frac{\partial}{\partial x}\tau_{xx} + \frac{\partial}{\partial y}\tau_{yx} + \frac{\partial}{\partial z}\tau_{zx} \tag{2.11a}$$

Similarly, we obtain the equation of motion for the y direction:

$$\rho\frac{dv}{dt} = \rho f_y + \frac{\partial}{\partial x}\tau_{xy} + \frac{\partial}{\partial y}\tau_{yy} + \frac{\partial}{\partial z}\tau_{zy} \tag{2.11b}$$

and for the z direction:

$$\rho\frac{dw}{dt} = \rho f_z + \frac{\partial}{\partial x}\tau_{xz} + \frac{\partial}{\partial y}\tau_{yz} + \frac{\partial}{\partial z}\tau_{zz} \tag{2.11c}$$

Next, we need to relate the stresses to the motion of the fluid. For a fluid at rest or for a flow for which all the fluid particles are moving at the same velocity, there is no shearing

stress, and the normal stress is in the nature of a pressure. For fluid particles, the stress is related to the rate of strain by a physical law based on the following assumptions:

1. Stress components may be expressed as a linear function of the components of the rate of strain. The friction law for the flow of a Newtonian fluid where $\tau = \mu(\partial u/\partial y)$ is a special case of this linear stress/rate-of-strain relation. The viscosity μ is more precisely called the first viscosity coefficient. In a more rigorous development, we should include the second viscosity coefficient (λ), which would appear in the normal stress terms. The term involving λ disappears completely when the flow is incompressible, since $\nabla \cdot \vec{V} = 0$ by continuity. For other flows, Stokes's hypothesis ($\lambda = -\frac{2}{3}\mu$) is presumed to apply [see Schlichting and Gersten (2000) for more details]. The second viscosity coefficient is of significance in a few specialized problems, such as the analysis of the structure of a shockwave, where extremely large changes in pressure and temperature take place over very short distances.
2. The relations between the stress components and the rate-of-strain components must be invariant to a coordinate transformation consisting of either a rotation or a mirror reflection of axes, since a physical law cannot depend upon the choice of the coordinate system.
3. When all velocity gradients are zero (i.e., the shear stress vanishes), the stress components must reduce to the hydrostatic pressure, p.

For a fluid that satisfies all three of these criteria,

$$\tau_{xx} = -p - \frac{2}{3}\mu\nabla\cdot\vec{V} + 2\mu\frac{\partial u}{\partial x}$$

$$\tau_{yy} = -p - \frac{2}{3}\mu\nabla\cdot\vec{V} + 2\mu\frac{\partial v}{\partial y}$$

$$\tau_{zz} = -p - \frac{2}{3}\mu\nabla\cdot\vec{V} + 2\mu\frac{\partial w}{\partial z}$$

$$\tau_{xy} = \tau_{yx} = \mu\left(\frac{\partial u}{\partial y} + \frac{\partial v}{\partial x}\right)$$

$$\tau_{xz} = \tau_{zx} = \mu\left(\frac{\partial u}{\partial z} + \frac{\partial v}{\partial x}\right)$$

$$\tau_{yz} = \tau_{zy} = \mu\left(\frac{\partial v}{\partial z} + \frac{\partial w}{\partial y}\right)$$

With the appropriate expressions for the surface stresses substituted into equation (2.11), we obtain:

$$\underbrace{\rho\frac{\partial u}{\partial t}}_{\substack{\text{Local}\\ \text{Acceleration}}} + \underbrace{\rho(\vec{V}\cdot\nabla)u}_{\text{Convection}} = \underbrace{\rho f_x}_{\substack{\text{Body}\\ \text{Force}}} - \underbrace{\frac{\partial p}{\partial x}}_{\substack{\text{Pressure}\\ \text{Force}}} + \underbrace{\left(2\mu\frac{\partial u}{\partial x} - \frac{2}{3}\mu\nabla\cdot\vec{V}\right)}_{\text{Stress Force}} + \underbrace{\frac{\partial}{\partial y}\left[\mu\left(\frac{\partial u}{\partial y} + \frac{\partial v}{\partial x}\right)\right]}_{\text{Stress Force}} + \underbrace{\frac{\partial}{\partial z}\left[\mu\left(\frac{\partial w}{\partial x} + \frac{\partial u}{\partial z}\right)\right]}_{\text{Stress Force}} \qquad \textbf{(2.12a)}$$

$$\rho\frac{\partial v}{\partial t} + \rho(\vec{V}\cdot\nabla)v = \rho f_y + \frac{\partial}{\partial x}\left[\mu\left(\frac{\partial u}{\partial y} + \frac{\partial v}{\partial x}\right)\right] - \frac{\partial p}{\partial y} + \frac{\partial}{\partial y}\left(2\mu\frac{\partial v}{\partial y} - \frac{2}{3}\mu\nabla\cdot\vec{V}\right) + \frac{\partial}{\partial z}\left[\mu\left(\frac{\partial w}{\partial y} + \frac{\partial v}{\partial z}\right)\right] \quad \textbf{(2.12b)}$$

$$\rho\frac{\partial w}{\partial t} + \rho(\vec{V}\cdot\nabla)w = \rho f_z + \frac{\partial}{\partial x}\left[\mu\left(\frac{\partial w}{\partial x} + \frac{\partial u}{\partial z}\right)\right] + \frac{\partial}{\partial y}\left[\mu\left(\frac{\partial v}{\partial z} + \frac{\partial w}{\partial y}\right)\right] - \frac{\partial p}{\partial z} + \frac{\partial}{\partial z}\left(2\mu\frac{\partial w}{\partial z} - \frac{2}{3}\mu\nabla\cdot\vec{V}\right) \quad \textbf{(2.12c)}$$

These general, differential equations for the conservation of linear momentum are known as the *Navier-Stokes equations*. Notice that each term in the equation represents either a force or acceleration (with the forces being on the right-hand side and the acceleration terms being on the left-hand side). Equation (2.12a) has the various terms labeled for convenience: local acceleration, convection, body forces, pressure forces, and stress forces. Also notice that the viscosity μ is considered to be dependent on the spatial coordinates. This is done since, for a compressible flow, the changes in velocity and pressure, together with the heat due to friction, bring about considerable temperature variations. The temperature dependence of viscosity in the general case should, therefore, be incorporated into the governing equations [see equation (1.12) for example]. Finally, the units of the equation are force per unit volume, since we divided through by the volume during the derivation.

For a general application, the unknown parameters that appear in the Navier-Stokes equations are the three velocity components (u, v, and w), the pressure (p), the density (ρ), and the viscosity (μ). As we discussed in Chapter 1, for a fluid of known composition that is in equilibrium, the density and the viscosity are unique functions of pressure and temperature [for example using the equation of state and Sutherland's equation, equations (1.10) and (1.12), respectively]. Therefore, we have five primary (or primitive) variables for a general flow problem: the three velocity components, the pressure, and the temperature. However, at present we have only four equations: the continuity equation [equation (2.2)] and the three components of the momentum equation [equations (2.12a) through (2.12c)]. To solve for a general flow involving all five variables, we would need to introduce the energy equation.

Since equations (2.12a) through (2.12c) are the general differential equations for the conservation of linear momentum, the equations for a static medium can be obtained by neglecting the terms relating to the acceleration of the fluid particles and to the viscous forces. Neglecting these terms in equations (2.12a) through (2.12c) and assuming that the body force is gravity and that it acts in the z direction, the reader would obtain equations (1.16a) through (1.16c).

The integral form of the momentum equation can be obtained by returning to Newton's law. The sum of the forces acting on a system of fluid particles is equal to

the rate of change of momentum of the fluid particles. Therefore, the sum of the body forces and of the surface forces equals the time rate of change of momentum within the volume plus the net efflux of momentum through the surface bounding the volume, as shown in Fig. 2.5. In vector form, the Navier-Stokes equations are,

$$\vec{F}_{\text{body}} + \vec{F}_{\text{surface}} = \frac{\partial}{\partial t}\iiint_{\text{vol}} \rho\vec{V}\, d(\text{vol}) + \oiint_{A} \vec{V}(\rho\vec{V}\cdot\hat{n}\, dA) \qquad \textbf{(2.13)}$$

This equation can also be obtained by integrating equation (2.12) over a volume and using Gauss's Theorem.

2.4 APPLICATIONS TO CONSTANT-PROPERTY FLOWS

For many flows, temperature variations are sufficiently small that the density and viscosity may be assumed constant throughout the flow field. Such flows will be termed *constant-property* flows in this text. The terms *low-speed* and/or *incompressible* flows will also be used in the description of these flows. A gas flow is considered incompressible if the Mach number is less than 0.3 to 0.5, depending upon the application. For these flows, there are only four unknowns: the three velocity components (u, v, and w) and the pressure (p). Therefore, we have a system of four independent equations that can be solved for the four unknowns: the energy equation is not needed to obtain the velocity components and the pressure of a constant-property flow.

We will consider two solution methods for constant-property flows, one for which the solution will be obtained using differential equations [equations (2.12)] and one for which the integral equations are used [equation (2.13)]. Each of these methods is useful in different types of applications.

2.4.1 Poiseuille Flow

Poiseuille flow is one of a class of flows that have parallel streamlines and for which the Navier-Stoke equations [equations (2.12)] can be solved analytically. Poiseuille flow is the steady, low-speed flow of a viscous fluid in an infinitely long, two-dimensional channel of height h (as shown in Fig. 2.8). Since the flow is low speed, we will assume that the viscosity and density are constant. Because the channel is infinitely long, the velocity components do not change in the x direction. In fluid dynamics, such a flow is called a

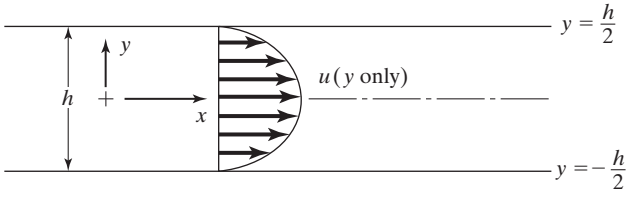

Figure 2.8 Parallel flow between two flat plates.

fully developed flow (see Fig. 2.9). We will also assume that the body forces are negligible since the flow is horizontal and gravity has very little effect. We want to find the velocity profile and the shear-stress distribution for this flow.

For a two-dimensional flow, $w \equiv 0$ and all the derivatives with respect to z are zero. The continuity equation [equation (2.3)] for this steady-state, constant-property flow becomes:

$$\frac{\partial u}{\partial x} + \frac{\partial v}{\partial y} = 0$$

Since the velocity components do not change in the x direction, $\dfrac{\partial u}{\partial x} = 0$ and, hence,

$$\frac{\partial v}{\partial y} = 0$$

Furthermore, since $v = 0$ at both walls (i.e., there is no flow through the walls) and v does not depend on x or z, then $v \equiv 0$ everywhere. Therefore, the flow is parallel to the x axis all along the plate.

Since we know that $v \equiv 0$ and $w = 0$ everywhere, then u is a function of y only, since it does not depend on x, z, or t. Therefore, all the terms in equations (2.12b) and (2.12c) are zero and do not need to be considered further. Now if we expand the acceleration terms of equation (2.12a), we obtain:

$$\begin{aligned}\rho\frac{\partial u}{\partial t} + \rho(\vec{V}\cdot\nabla)u &= \rho\frac{\partial u}{\partial t} + \rho(u\hat{i} + v\hat{j} + w\hat{k})\cdot\left(\frac{\partial u}{\partial x}\hat{i} + \frac{\partial u}{\partial y}\hat{j} + \frac{\partial u}{\partial z}\hat{k}\right)\\ &= \rho\frac{\partial u}{\partial t} + \rho u\frac{\partial u}{\partial x} + \rho v\frac{\partial u}{\partial y} + \rho w\frac{\partial u}{\partial z}\end{aligned}$$

and equation (2.12a) becomes:

$$\begin{aligned}\rho\frac{\partial u}{\partial t} + \rho u\frac{\partial u}{\partial x} + \rho v\frac{\partial u}{\partial y} + \rho w\frac{\partial u}{\partial z} = \rho f_x - \frac{\partial p}{\partial x} + \frac{\partial}{\partial x}\left(2\mu\frac{\partial u}{\partial x} - \frac{2}{3}\mu\nabla\cdot\vec{V}\right)\\ + \frac{\partial}{\partial y}\left[\mu\left(\frac{\partial u}{\partial y} + \frac{\partial v}{\partial x}\right)\right] + \frac{\partial}{\partial z}\left[\mu\left(\frac{\partial u}{\partial z} + \frac{\partial w}{\partial x}\right)\right]\end{aligned} \quad \textbf{(2.14)}$$

Because we are considering low-speed of a simple fluid, μ is constant throughout the flow field. Therefore, we can rewrite the viscous terms of this equation as follows:

$$\begin{aligned}&\frac{\partial}{\partial x}\left(2\mu\frac{\partial u}{\partial x} - \frac{2}{3}\mu\nabla\cdot\vec{V}\right) + \frac{\partial}{\partial y}\left[\mu\left(\frac{\partial u}{\partial y} + \frac{\partial v}{\partial x}\right)\right] + \frac{\partial}{\partial z}\left[\mu\left(\frac{\partial u}{\partial z} + \frac{\partial w}{\partial x}\right)\right]\\ &\quad= \mu\frac{\partial^2 u}{\partial x^2} + \mu\frac{\partial}{\partial x}\left(\frac{\partial u}{\partial x}\right) - \frac{2}{3}\mu\frac{\partial}{\partial x}(\nabla\cdot\vec{V}) + \mu\frac{\partial^2 u}{\partial y^2}\\ &\qquad+\mu\frac{\partial}{\partial x}\left(\frac{\partial v}{\partial y}\right) + \mu\frac{\partial^2 u}{\partial z^2} + \mu\frac{\partial}{\partial x}\left(\frac{\partial w}{\partial z}\right)\\ &\quad= \mu\left(\frac{\partial^2 u}{\partial x^2} + \frac{\partial^2 u}{\partial y^2} + \frac{\partial^2 u}{\partial z^2}\right) + \mu\frac{\partial}{\partial x}\left(\frac{\partial u}{\partial x} + \frac{\partial v}{\partial y} + \frac{\partial w}{\partial z}\right) - \frac{2}{3}\mu\frac{\partial}{\partial x}(\nabla\cdot\vec{V})\end{aligned}$$

We can also show that the divergence of the velocity vector is given by:

$$\frac{\partial u}{\partial x} + \frac{\partial v}{\partial y} + \frac{\partial w}{\partial z} = \nabla \cdot \vec{V}$$

and that $\nabla \cdot \vec{V} = 0$ (since this is a way of writing the continuity equation for a constant density flow). We can write the resulting equation as:

$$\rho\frac{\partial u}{\partial t} + \rho u\frac{\partial u}{\partial x} + \rho v\frac{\partial u}{\partial y} + \rho w\frac{\partial u}{\partial z} = \rho f_x - \frac{\partial p}{\partial x} + \mu\left(\frac{\partial^2 u}{\partial x^2} + \frac{\partial^2 u}{\partial y^2} + \frac{\partial^2 u}{\partial z^2}\right) \qquad \textbf{(2.15)}$$

However, we can further simplify equation (2.15) by eliminating terms whose value is zero:

$$\rho\frac{\partial u}{\partial t} = 0 \qquad \text{because the flow is steady}$$

$$\rho u\frac{\partial u}{\partial x} = 0 \qquad \text{because } u = u(y \text{ only})$$

$$\rho v\frac{\partial u}{\partial y} = 0 \qquad \text{because } v \equiv 0$$

$$\rho w\frac{\partial u}{\partial z} = \mu\frac{\partial^2 u}{\partial x^2} = \mu\frac{\partial^2 u}{\partial z^2} = 0 \qquad \text{because } u = u(y \text{ only})$$

$$\rho f_x = 0 \qquad \text{because body forces are negligible}$$

Neglecting these terms leads us to:

$$0 = -\frac{\partial p}{\partial x} + \mu\frac{\partial^2 u}{\partial y^2}$$

$$0 = -\frac{\partial p}{\partial y}$$

$$0 = -\frac{\partial p}{\partial z}$$

These three equations require that the pressure is a function of x only, but also recall that u is a function of y only. These two statements can be true only if:

$$\mu\frac{d^2 u}{dy^2} = \frac{dp}{dx} = \text{constant}$$

which is the equation that describes Poiseuille flow. We can solve the equation by integrating twice to obtain:

$$u = \frac{1}{2\mu}\frac{dp}{dx}y^2 + C_1 y + C_2$$

To evaluate the constants of integration, we apply the viscous-flow boundary condition that the fluid particles at a solid surface move with the same speed as the surface (i.e., do not slip relative to the surface). This tells us that

$$\text{at } y = -\frac{h}{2} \quad u = 0$$

$$\text{at } y = +\frac{h}{2} \quad u = 0$$

When we apply these conditions, we find that:

$$C_1 = 0$$

$$C_2 = -\frac{1}{2\mu}\frac{dp}{dx}\frac{h^2}{4}$$

which results in a velocity profile given by:

$$u = +\frac{1}{2\mu}\frac{dp}{dx}\left(y^2 - \frac{h^2}{4}\right)$$

The velocity profile is parabolic, with the maximum velocity occurring at the center of the channel, as shown in Fig. 2.8. The shear stress distribution is given by:

$$\tau = \mu\frac{du}{dy} = 2\mu\frac{1}{2\mu}\frac{dp}{dx}y = y\frac{dp}{dx}$$

The lower wall is given by $y = -h/2$ and the upper wall is given by $y = +h/2$. So, using the above equation, the shear stress at the lower wall is:

$$\tau_l = \mu\frac{du}{dy} = -\frac{h}{2}\frac{dp}{dx}$$

and the shear stress at the upper wall is:

$$\tau_u = \mu\frac{du}{dy} = +\frac{h}{2}\frac{dp}{dx}$$

Since the pressure must decrease in the x direction (i.e., dp/dx must be negative) to have a velocity in the direction shown, the shear stress at the lower wall is:

$$\tau_l = +\frac{h}{2}\left|\frac{dp}{dx}\right|$$

and the shear stress at the upper wall is:

$$\tau_u = -\frac{h}{2}\left|\frac{dp}{dx}\right|$$

Since the upper wall shear stress is defined relative to a local wall coordinate system (looking at the flow from the top wall rather than the bottom wall), the shear stress is actually pointing to the right (which is the positive direction in our flow coordinate system). So both the lower and upper walls have a shear stress pointing to the right that creates drag. This solution for Poiseuille flow shows that it is possible to obtain useful solutions to the equations of motion for a fairly basic flow. There are a number of other analytic flow solutions for the governing equations, one of which we will look at now (Couette flow), and another that we will see in Chapter 4 (Blasius flow).

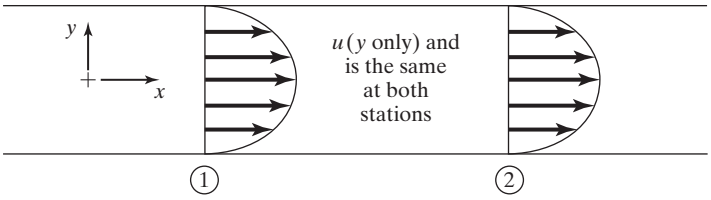

Figure 2.9 Fully developed flow between two flat plates.

2.4.2 Couette Flow

Another solution of the same ordinary differential equation that described Poiseuille flow can be found for parallel flow between two flat plates, where the lower plate is stationary and the upper plate is moving to the right with velocity U. This flow is easier to solve if the coordinate system is moved to the bottom plate, as shown in Fig. 2.10, and the distance between the two plates is h. The governing equation for this flow is:

$$\mu\frac{d^2u}{dy^2} = \frac{dp}{dx} = \text{constant}$$

which is the same as Poiseuille flow, but the boundary conditions are:

$$\text{at } y = 0 \qquad u = 0$$

$$\text{at } y = h \qquad u = U$$

After integrating in the same way as was done previously:

$$u = \frac{1}{2\mu}\frac{dp}{dx}y^2 + C_1 y + C_2$$

Evaluating the boundary condition at $y = 0$ gives $C_2 = 0$. Evaluating the boundary condition at $y = h$ gives that $C_1 = U/h$, and the velocity distribution, as well as the nondimensional velocity distribution, becomes (with some algebraic re-arrangement):

$$u = U\frac{y}{h} - \frac{h^2}{2\mu}\frac{dp}{dx}\frac{y}{h}\left(1 - \frac{y}{h}\right) = U\frac{y}{h} + UP\frac{y}{h}\left(1 - \frac{y}{h}\right)$$

$$\frac{u}{U} = \frac{y}{h} - \frac{h^2}{2\mu U}\frac{dp}{dx}\frac{y}{h}\left(1 - \frac{y}{h}\right) = \frac{y}{h} + P\frac{y}{h}\left(1 - \frac{y}{h}\right)$$

The solution for the flow is shown in Fig. 2.10, where $P = -\dfrac{h^2}{2\mu U}\dfrac{dp}{dx}$ is a dimensionless pressure gradient. When $P > 0$, the pressure gradient is negative (the pressure is decreasing in the x direction, which is a favorable pressure gradient), and the flow is accelerating. When $P < 0$, the pressure gradient is positive (the pressure is increasing in the x direction, which is an adverse pressure gradient), and the flow has reversed direction (back flow). For $P = 0$, there is no pressure gradient and the flow is simply being sheared by the motion of the upper plate in a linear manner.

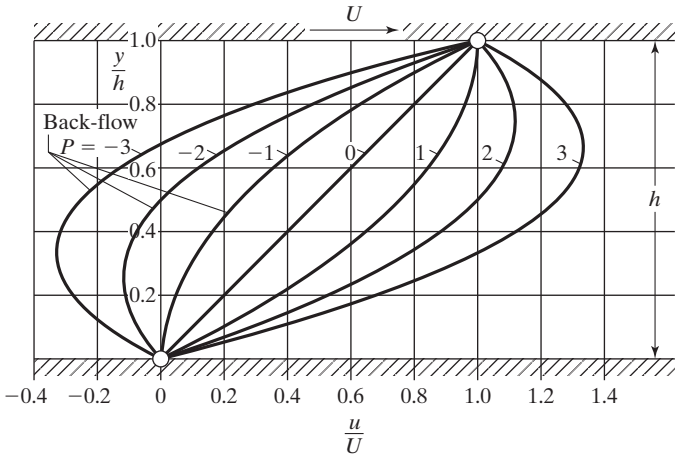

Figure 2.10 Couette flow between two parallel walls [Schlichting and Gersten (2000)].

EXAMPLE 2.3: Couette flow analysis

Find the shear stress distribution, the volumetric flow rate, the average velocity, and the point of maximum velocity for Couette flow of standard day sea-level air as a function of P, the nondimensional pressure gradient. Evaluate the volumetric flow rate, the average velocity, and the point of maximum velocity for $U = 2$ m/s, $h = 0.1$ m, and $P = 1$.

Solution: The velocity profile for Couette flow is given by:

$$\frac{u}{U} = \frac{y}{h} + P\frac{y}{h}\left(1 - \frac{y}{h}\right)$$

and the shear stress distribution is:

$$\tau = \mu\frac{du}{dy} = \mu\frac{U}{h} + \frac{2\mu U}{h}P\left(\frac{1}{2} - \frac{y}{h}\right)$$

The volumetric flow rate is given by $Q = \int_A \vec{V}\cdot dA$, and since the flow is aligned with the x direction, the volumetric flow rate per unit depth, d, into the paper is:

$$\frac{Q}{d} = \int_0^h \left[U\frac{y}{h} + UP\frac{y}{h}\left(1 - \frac{y}{h}\right)\right]dy = \frac{Uh}{2} + \frac{Uh}{6}P = \frac{Uh}{2}\left(1 + \frac{P}{3}\right)$$

The average velocity is found by dividing the volume flow rate by the area:

$$\overline{V} = \frac{Q}{A} = \frac{dQ/d}{hd} = \frac{U}{2}\left(1 + \frac{P}{3}\right)$$

Finally, the point of maximum velocity is found by taking the derivative of the velocity variation and setting it equal to zero, $du/dy = 0$. We found the derivative previously, so:

$$\frac{du}{dy} = \frac{U}{h} + \frac{2U}{h}P\left(\frac{1}{2} - \frac{y}{h}\right) = 0$$

which takes places at:

$$y = \frac{h}{2} - \frac{\mu U/h}{dp/dx} = \frac{h}{2} + \frac{h}{2P} = \frac{h}{2}\left(1 + \frac{1}{P}\right)$$

For the given values $Q/d = \frac{4}{30}\text{m}^2/s, \overline{V} = \frac{4}{3}\text{m/s} = \frac{2}{3}U, y = 0.1\text{ m}$ (look at Fig. 2.10 to see if these results make sense).

2.4.3 Integral Equation Application

Applying the integral equations to a flow problem can also lead to exact solutions. These formulations do not require the integration of an ordinary differential equation, but do require the application of the surface and volume integrals to a flow problem.

As an example of such an application, we can re-look at the Poiseuille flow problem from Section 2.4.1, but this time we analyze the problem with the integral form of the governing equations. Examination of the integral momentum equation (2.13) verifies that a change in pressure must occur to balance the shear forces. We can verify this by using equation (2.13) on the control volume shown in Fig. 2.9. Since the flow is fully developed, the velocity profile at the upstream station (i.e., station 1) is identical to that at the downstream station (i.e., station 2). Therefore, the positive momentum efflux at station 2 is balanced by the negative momentum influx at station 1:

$$\oiint \vec{V}(\rho\vec{V}\cdot\hat{n}\,dA) = 0$$

Therefore, for this steady flow with negligible body forces:

$$\vec{F}_{\text{surface}} = 0$$

or:

$$p_1 h - p_2 h - 2\tau\,\Delta x = 0$$

where the factor of 2 accounts for the existence of shear forces at the upper and lower walls. Finally, as shown in the approach using the differential equation,

$$\tau = -\frac{p_2 - p_1}{\Delta x}\frac{h}{2} = -\frac{dp}{dx}\frac{h}{2}$$

Note, as we discussed previously, that there are subtle implications regarding the signs in these terms. For the velocity profile shown, the shear acts to retard the fluid motion and the pressure must decrease in the x direction (i.e., $dp/dx < 0$).

EXAMPLE 2.4: Drag on a flat-plate airfoil

A steady, uniform ($\vec{V} = U_\infty \hat{i}$), low-speed flow approaches a very thin, flat-plate "airfoil" whose length is c. Because of viscosity, the flow near the plate slows, such that velocity measurements at the trailing edge of the plate indicate that the x component of the velocity (above the plate) varies as:

$$u = U_\infty \left(\frac{y}{\delta}\right)^{1/7}$$

Below the plate, the velocity is a mirror image of this profile. The pressure is uniform over the entire control surface. Neglecting the body forces, what is the drag coefficient for this flow if $\delta = 0.01c$? The drag coefficient is the drag per unit span, d (unit depth into the page), divided by the product of the free-stream dynamic pressure ($\frac{1}{2}\rho_\infty U_\infty^2$) and the reference area per unit span (which is the chord length c):

$$C_d = \frac{d}{\frac{1}{2}\rho_\infty U_\infty^2 c}$$

Solution: We can apply the integral form of the momentum equation [i.e., equation (2.13)] to this flow. Noting that the momentum equation is a vector equation, we can consider the x component only, since that is the direction in which the drag force acts. Furthermore, since the flow is planar symmetric, only the control volume above the plate will be considered (i.e., from $y = 0$ to $y = \delta$). Since the pressure is uniform over the control surface and since the body forces are negligible, the only force acting on the fluid in the control volume is the retarding force of the plate on the fluid, which is $-d/2$.

Because the flow is steady, the first term on the right-hand side of equation (2.13) is zero. Thus,

$$-\frac{d}{2} = \oiint (\rho \vec{V} \cdot \hat{n}\, dA) V_x$$

Noting that $V_x \equiv u$ and using the values that are shown in Fig. 2.11, we can find that

$$-\frac{d}{2} = \underbrace{\int_0^\delta [\rho(U_\infty \hat{i}) \cdot (-\hat{i}\, dy)]\, U_\infty}_{(1)} + \underbrace{\int_0^c [\rho(U_\infty \hat{i} + v_e \hat{j}) \cdot (\hat{j}\, dx)]\, U_\infty}_{(2)}$$

$$+ \underbrace{\int_0^\delta \left\{\rho\left[U_\infty \left(\frac{y}{\delta}\right)^{1/7} \hat{i} + v\hat{j}\right] \cdot (\hat{i}\, dy)\right\} U_\infty \left(\frac{y}{\delta}\right)^{1/7}}_{(3)}$$

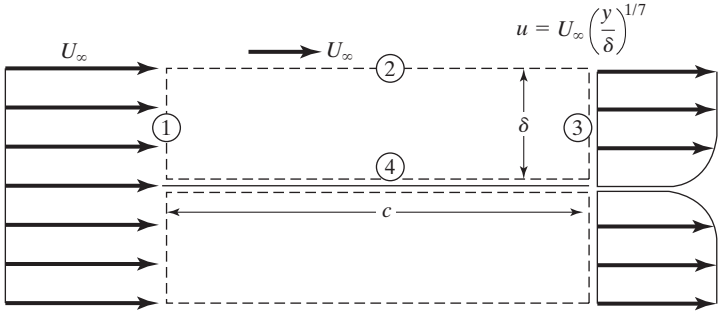

Figure 2.11 Low-speed flow over a thin flat plate; flow diagram for Example 2.4.

Now we can better understand the meaning of each term describing the momentum efflux from each surface of the control volume:

1. Since $\hat{n}\,dA$ is a vector normal to the surface dA which is positive when pointing outward from the enclosed volume, $\hat{n}$ is in the $-x$ direction and dA per unit span is equal to dy.
2. Because viscosity slows the air particles near the plate, line 2 is not a streamline, and the velocity vector along this surface is
$$\vec{V} = U_\infty \hat{i} + v_e \hat{j}$$
The volumetric flow rate (per unit depth) across this surface is $\int_0^c v_e dx$, which will be represented by the symbol Q_2.
3. Because of viscosity, the velocity vector has a y component which is a function of y. However, this y component of velocity does not transport fluid across the area $\hat{i}\,dy$.
4. There is no flow across this surface of the control volume since it is at a solid wall.

Furthermore, because the flow is low speed, the density will be assumed constant, and the momentum equation becomes:

$$-\frac{d}{2} = -\rho U_\infty^2 \delta + \rho U_\infty Q_2 + \frac{7}{9}\rho U_\infty^2 \delta$$

To obtain an expression for Q_2, we can use the integral form of the continuity equation, equation (2.5), for the flow of Fig. 2.11.

$$\oiint \rho \vec{V} \cdot \hat{n}\, dA = \underbrace{\int_0^\delta [\rho(U_\infty \hat{i}) \cdot (-\hat{i}\, dy)]}_{(1)} + \underbrace{\int_0^c [\rho(U_\infty \hat{i} + v_e \hat{j}) \cdot (\hat{j}\, dx)]}_{(2)} + \underbrace{\int_0^\delta \left\{\rho\left[U_\infty \left(\frac{y}{\delta}\right)^{1/7} \hat{i} + v\hat{j}\right] \cdot (\hat{i}\, dy)\right\}}_{(3)} = 0$$

$$-\rho U_\infty \delta + \rho \int_0^c v_e dx + \rho U_\infty \left(\tfrac{7}{8}\delta\right) = 0 \qquad \int_0^c v_e dx = Q_2 = \tfrac{1}{8} U_\infty \delta$$

Now substitute Q_2 into the momentum equation to obtain:

$$-\frac{d}{2} = -\rho U_\infty^2 \delta + \frac{1}{8}\rho U_\infty^2 \delta + \frac{7}{9}\rho U_\infty^2 \delta$$

$$d = \left(2 - \frac{1}{4} - \frac{14}{9}\right)\rho U_\infty^2 \delta = \frac{7}{36}\rho U_\infty^2 \delta$$

and the drag coefficient for $\delta = 0.01c$ is:

$$C_d = \frac{d}{\frac{1}{2}\rho_\infty U_\infty^2 c} = \frac{\frac{7}{36}\rho U_\infty^2 (0.01c)}{\frac{1}{2}\rho_\infty U_\infty^2 c} = 0.00389$$

2.5 REYNOLDS NUMBER AND MACH NUMBER AS SIMILARITY PARAMETERS

Because of the difficulty of obtaining theoretical solutions of the flow field around a vehicle, numerous experimental programs have been conducted to directly measure the parameters that define the flow field. Some of the objectives of such test programs are as follows:

1. To obtain information necessary to develop a flow model that could be used in numerical solutions
2. To investigate the effect of various geometric parameters on the flow field (such as determining the best location for the engines on a supersonic transport)
3. To verify numerical predictions of the aerodynamic characteristics for a particular configuration
4. To directly measure the aerodynamic characteristics of a complete vehicle

Usually, either scale models of the complete vehicle or large-scale simulations of elements of the vehicle (such as the wing section) have been used in these wind-tunnel programs. Furthermore, in many test programs, the free-stream conditions (such as the velocity, the static pressure, etc.) for the wind-tunnel tests were not equal to the values for the flight condition that was being simulated.

The question every aerodynamicist has to ask about wind tunnel testing is "Are the results obtained meaningful for the full-scale aircraft configuration of interest?" Part of the difficulty in answering that question is the large number of modeling issues for wind tunnel testing, having to do with differences between the wind tunnel test environment and the actual aircraft being evaluated. The importance of these differences and the impact they can make on wind tunnel data accuracy were discussed at length by Bushnell (2006). Bushnell created a list of issues for wind tunnel testing that includes (among other items): wind tunnel walls and how to correct for their presence; aeroelastic distortion differences due to different structure and material for the wind tunnel model; Reynolds number scaling that is especially critical for transonic flows, longitudinal vortices, and large transitional flow influences; free-stream disturbance fields, especially their influence on transition, model mounting influences due to stings, struts, wires, etc.; free-stream gross

unsteadiness, which is of special concern for wing buffet; installed propulsion influences, or the lack thereof; geometric fidelity since there can be critical differences in results for even "minor" differences in the model. Accounting for these differences between wind tunnel, flight, or computations can be a major issue in aerodynamics.

Aerodynamics Concept Box: Wind Tunnel Validation Studies

A classic example of a wind tunnel test that was conducted in order to create data for comparisons with computational or theoretical predictions is the ONERA M6 Wing. This semi-span wing was tested at transonic speeds in the ONERA S2MA wind tunnel (the wing installed in the wind tunnel is shown below).

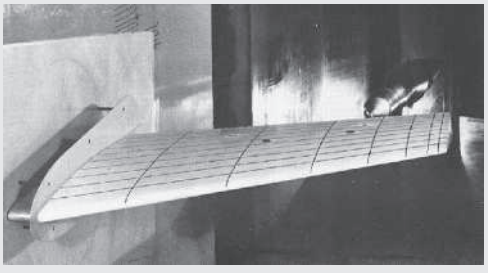

M6 wing in ONERA S2MA wind tunnel
[Schmitt and Charpin (1979); photo courtesy of ONERA]

The wing was tested at several transonic Mach numbers ($M = 0.7, 0.84, 0.88, 0.92$) and various angles of attack up to 6 degrees. The Reynolds number was approximately 12×10^6 based on the mean aerodynamic chord. The wing had a span of 1.1963 m, a mean aerodynamic chord of 0.64607 m, an aspect ratio of 3.8, a taper ratio of 0.562, and a leading-edge sweep of 30.0 degrees. Detailed pressures were measured at six spanwise stations along the wing, which provided data (including locations of shock waves) for comparisons with other predictions.

What if the wind tunnel test were trying to simulate flow over a wing for a full-scale airplane, rather than for computational validation purposes? What if the full-scale airplane had a cruise velocity and altitude that equated to a Reynolds number of 30×10^6? Would the aerodynamic characteristics of the wing be the same? Understanding the differences will require more information about lift, drag, shock waves, flow separation, and boundary layer transition, which will come in later chapters.

It is important, then, to determine under what conditions the experimental results obtained for one flow are applicable to another flow that is confined by boundaries that are geometrically similar (but of different size). To do this, consider the x-momentum equation as applied to the two flows of Fig. 2.12. For simplicity, we will limit ourselves to constant-property flows, but keep in mind that real flows in real wind tunnels may not

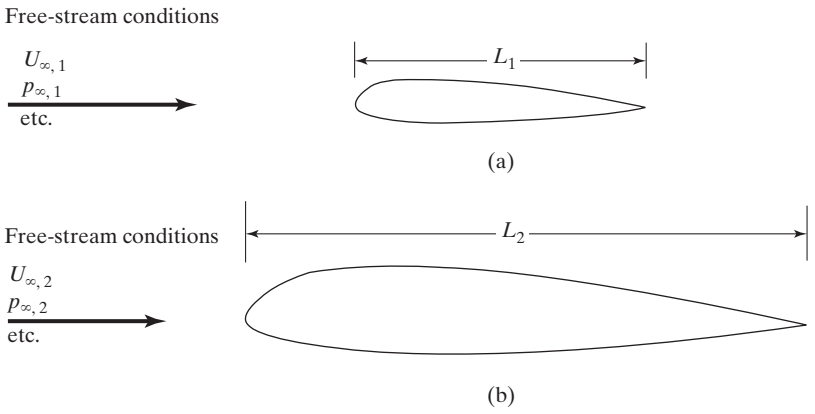

Figure 2.12 Flow around geometrically similar (but different size) configurations: (a) first flow; (b) second flow.

be constant. Since the body-force term is usually negligible in aerodynamic problems, equation (2.15) can be written

$$\rho\frac{\partial u}{\partial t} + \rho u\frac{\partial u}{\partial x} + \rho v\frac{\partial u}{\partial y} + \rho w\frac{\partial u}{\partial z} = -\frac{\partial p}{\partial x} + \mu\frac{\partial^2 u}{\partial x^2} + \mu\frac{\partial^2 u}{\partial y^2} + \mu\frac{\partial^2 u}{\partial z^2} \qquad \textbf{(2.16)}$$

Now divide each of the thermodynamic properties by the value of that property at a point far from the vehicle (i.e., the free-stream value of the property) for each of the two flows. So, for the first flow:

$$p_1^* = \frac{p}{p_{\infty,1}} \qquad \rho_1^* = \frac{\rho}{\rho_{\infty,1}} \qquad \mu_1^* = \frac{\mu}{\mu_{\infty,1}}$$

and for the second flow:

$$p_2^* = \frac{p}{p_{\infty,2}} \qquad \rho_2^* = \frac{\rho}{\rho_{\infty,2}} \qquad \mu_2^* = \frac{\mu}{\mu_{\infty,2}}$$

Note that the free-stream values for all three nondimensionalized (*) thermodynamic properties are unity for both cases. Similarly, we can divide the velocity components by the free-stream velocity to obtain for the first flow:

$$u_1^* = \frac{u}{U_{\infty,1}} \qquad v_1^* = \frac{v}{U_{\infty,1}} \qquad w_1^* = \frac{w}{U_{\infty,1}}$$

and for the second flow:

$$u_2^* = \frac{u}{U_{\infty,2}} \qquad v_2^* = \frac{v}{U_{\infty,2}} \qquad w_2^* = \frac{w}{U_{\infty,2}}$$

With the velocity components now nondimensionalized, the free-stream boundary conditions are the same for both flows—that is, at points far from the vehicle

$$u_1^* = u_2^* = 1 \quad \text{and} \quad v_1^* = v_2^* = w_1^* = w_2^* = 0$$

A characteristic dimension L is used to nondimensionalize the independent variables. For example, all lengths can be divided by L and all times can be divided by L/U_∞, which is a characteristic time.

$$x_1^* = \frac{x}{L_1} \quad y_1^* = \frac{y}{L_1} \quad z_1^* = \frac{z}{L_1} \quad t_1^* = \frac{tU_{\infty,1}}{L_1}$$

and

$$x_2^* = \frac{x}{L_2} \quad y_2^* = \frac{y}{L_2} \quad z_2^* = \frac{z}{L_2} \quad t_2^* = \frac{tU_{\infty,2}}{L_2}$$

In terms of these dimensionless parameters, the x-momentum equation (2.16) for the first flow becomes:

$$\rho_1^*\frac{\partial u_1^*}{\partial t_1^*} + \rho_1^* u_1^*\frac{\partial u_1^*}{\partial x_1^*} + \rho_1^* v_1^*\frac{\partial u_1^*}{\partial y_1^*} + \rho_1^* w_1^*\frac{\partial u_1^*}{\partial z_1^*} = -\left(\frac{p_{\infty,1}}{\rho_{\infty,1}U_{\infty,1}^2}\right)\frac{\partial p_1^*}{\partial x_1^*} + \left(\frac{\mu_{\infty,1}}{\rho_{\infty,1}U_{\infty,1}L_1}\right)\left(\mu_1^*\frac{\partial^2 u_1^*}{\partial x_1^{*2}} + \mu_1^*\frac{\partial^2 u_1^*}{\partial y_1^{*2}} + \mu_1^*\frac{\partial^2 u_1^*}{\partial z_1^{*2}}\right) \quad \textbf{(2.17a)}$$

Likewise, for the second flow equation (2.16) becomes:

$$\rho_2^*\frac{\partial u_2^*}{\partial t_2^*} + \rho_2^* u_2^*\frac{\partial u_2^*}{\partial x_2^*} + \rho_2^* v_2^*\frac{\partial u_2^*}{\partial y_2^*} + \rho_2^* w_2^*\frac{\partial u_2^*}{\partial z_2^*} = -\left(\frac{p_{\infty,2}}{\rho_{\infty,2}U_{\infty,2}^2}\right)\frac{\partial p_2^*}{\partial x_2^*} + \left(\frac{\mu_{\infty,2}}{\rho_{\infty,2}U_{\infty,2}L_2}\right)\left(\mu_2^*\frac{\partial^2 u_2^*}{\partial x_2^{*2}} + \mu_2^*\frac{\partial^2 u_2^*}{\partial y_2^{*2}} + \mu_2^*\frac{\partial^2 u_2^*}{\partial z_2^{*2}}\right) \quad \textbf{(2.17b)}$$

Both the dependent variables and the independent variables have been nondimensionalized, as indicated by the * quantities. The dimensionless *boundary-condition values* for the dependent variables are the same for the two flows around geometrically similar configurations. As a consequence, the solutions of the two problems in terms of the dimensionless variables will be identical provided that the differential equations [equations (2.17a) and (2.17b)] are identical. The differential equations will be identical if the parameters in the parentheses have the same values for both problems. In this case, the flows are said to be *dynamically similar* as well as geometrically similar.

Now we can find the conditions to make the two flows dynamically similar. The first similarity parameter from equation (2.17) is:

$$\frac{p_\infty}{\rho_\infty U_\infty^2} \quad \textbf{(2.18)}$$

Recall that for a perfect gas, the equation of state is

$$p_\infty = \rho_\infty R T_\infty$$

and the free-stream speed of sound is given by

$$a_\infty = \sqrt{\gamma R T_\infty}$$

Substituting these relations into equation (2.18) yields

$$\frac{p_\infty}{\rho_\infty U_\infty^2} = \frac{RT_\infty}{U_\infty^2} = \frac{a_\infty^2}{\gamma U_\infty^2} = \frac{1}{\gamma M_\infty^2} \quad \textbf{(2.19)}$$

since we define the *Mach number* to be $M_\infty = U_\infty / a_\infty$. Therefore, the first dimensionless similarity parameter can be interpreted in terms of the free-stream Mach number.

The inverse of the second similarity parameter is written as:

$$\mathrm{Re}_{\infty, L} = \frac{\rho_\infty U_\infty L}{\mu_\infty} \tag{2.20}$$

which is the *Reynolds number*, a measure of the ratio of inertia effects to viscous effects. So the two flows in Fig. 2.12 will be dynamically similar if $M_1 = M_2$ and $Re_1 = Re_2$. Matching the Mach and Reynolds numbers becomes an important consideration when testing scale modes of airfoils, wings, or airplanes in a wind tunnel.

As has been discussed in Chapter 1, the free-stream values of the fluid properties, such as the static pressure and the static temperature, are a function of altitude. So, once the velocity, the altitude, and the characteristic dimension of the vehicle are defined, the free-stream Mach number and the free-stream Reynolds number can be calculated as a function of velocity and altitude. This has been done in Fig. 2.13 using the values

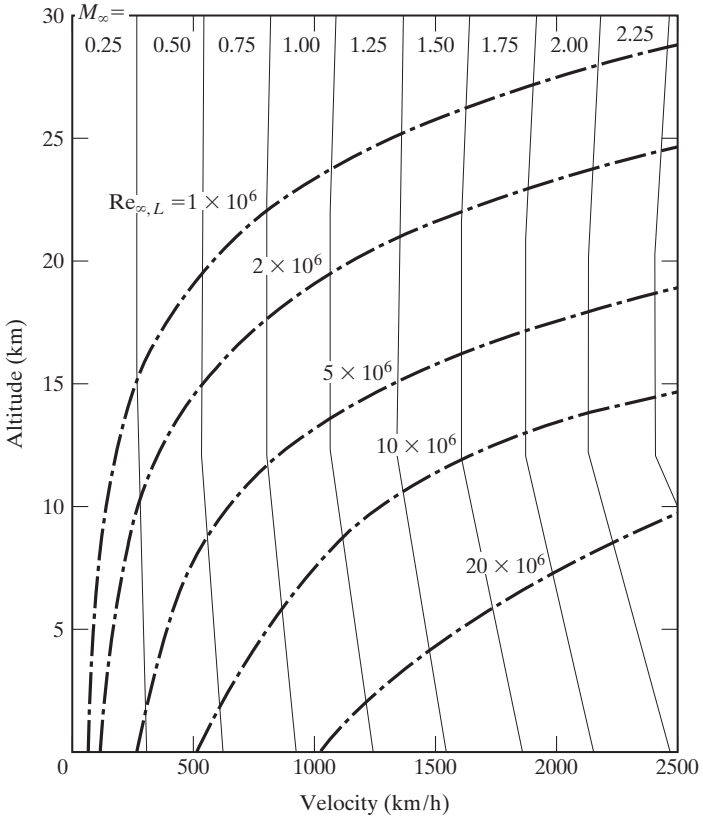

Figure 2.13 Reynolds number/Mach number correlations as a function of velocity and altitude for U.S. Standard Atmosphere.

presented in Table 1.2. The free-stream Reynolds number is defined by equation (2.20) with the characteristic length L (e.g., the chord of the wing or the diameter of the missile) chosen to be 1.0 m for the correlations shown. The correlations represent altitudes up to 30 km (9.84×10^4 ft) and velocities up to 2500 km/h (1554 mi/h or 1350 knots). Note that 1 knot $\equiv$ 1 nautical mile per hour.

EXAMPLE 2.5: Calculating the Mach number

An airplane is flying at a velocity of 472 m/s at an altitude of 14 km. What Mach number is the airplane flying at? What would the Mach number be if the airplane were flying at the same velocity at an altitude of 19 km?

Solution: From Table 1.2A, the speed of sound at 14 km on a standard day is 295.07 m/s. So the Mach number of the airplane is:

$$M_\infty = \frac{U_\infty}{a_\infty} = \frac{472 \text{ m/s}}{295.07 \text{ m/s}} \approx 1.6$$

If the airplane were flying at 19 km, the speed of sound would be the same, so the Mach number would be the same. This is because the temperature is constant between approximately 11 km and 21 km since this portion of the atmosphere is an isothermal layer.

EXAMPLE 2.6: Calculating the Reynolds number

An airplane is flying at a Mach number of 2 at an altitude of 40,000 ft. If the characteristic length for the aircraft is 14 ft, what is the velocity in miles/hour, and what is the Reynolds number for this flight condition?

Solution: The density, the viscosity, and the speed of sound of the free-stream flow at 40,000 ft can be found in Table 1.2.

$$\mu_\infty = 0.79447\mu_{SL} = 2.9713 \times 10^{-7} \frac{\text{lbf} \cdot \text{s}}{\text{ft}^2}$$

$$\rho_\infty = 0.2471\rho_{SL} = 5.8711 \times 10^{-4} \frac{\text{slug}}{\text{ft}^3}$$

$$a_\infty = 968.08 \text{ ft/s}$$

Since the Mach number is 2.0,

$$U_\infty = M_\infty a_\infty = 2.0\left(968.08 \frac{\text{ft}}{\text{s}}\right) = 1936.16 \frac{\text{ft}}{\text{s}} \left(\frac{3600 \frac{\text{s}}{\text{h}}}{5280 \frac{\text{ft}}{\text{mi}}} \right) = 1320.11 \frac{\text{mi}}{\text{h}}$$

The corresponding Reynolds number is

$$\mathrm{Re}_{\infty,L} = \frac{\rho_\infty U_\infty L}{\mu_\infty} = \frac{\left(5.8711 \times 10^{-4} \frac{\text{lbf} \cdot \text{s}^2}{\text{ft}^4}\right)\left(1936.16 \frac{\text{ft}}{\text{s}}\right)(14\ \text{ft})}{2.9713 \times 10^{-7} \frac{\text{lbf} \cdot \text{s}}{\text{ft}^2}}$$

$$= 5.3560 \times 10^7$$

In addition to matching Reynolds and Mach numbers as similarity parameters, we need to also consider the various flow regimes that these parameters represent. For example, if the Mach number of a particular flow is $M = 0.2$, then it may not be significant for the Mach number to exactly match, but rather for the Mach number to fall within the same speed regime (for the case of this example, the incompressible speed regime). Likewise, if the Reynolds number of a desired flow is 5×10^7, then it may not be necessary to exactly match that Reynolds number, since the flow characteristics of boundary layer separation and skin friction may be well matched as long as the Reynolds number is relatively close.

While we will learn more about the various Mach and Reynolds regimes as we progress through the study of aerodynamics, Tables 2.1 and 2.2 will give some initial concepts that will help you understand the differences. For example, subsonic compressible Mach numbers can be easily related to each other using compressibility corrections. Also, once the Reynolds number gets very high, there may be insignificant differences between slightly different values. These are concepts that experienced aerodynamicists need to understand, so start trying to absorb the material in these two tables.

TABLE 2.1 Mach Number Regimes and Characteristics for an Airfoil

Mach regime	*Mach number range*	*Characteristics*
Incompressible Subsonic	$0 < M < \approx 0.3$	Classical low speed aerodynamics
Compressible Subsonic	$\approx 0.3 < M < \approx 0.8$	Compressibility effects, no shocks
Transonic	$\approx 0.8 < M < \approx 1.6$	Normal shocks, shock/boundary layer interactions, etc.
Supersonic	$\approx 1.6 < M < \approx 5.0$	Oblique shocks, expansion waves, linear characteristics
Hypersonic	$M > \approx 5.0$	Bow shocks, thin shock layers, high temperature effects, shock/shock interactions, low density flows, etc.

TABLE 2.2 Reynolds Number Regimes and Characteristics for an Airfoil

Reynolds number regime	*Reynolds number range*	*Characteristics*
Creep	$0 < Re_L < \approx 10^2$	Viscous effects dominate, drag inversely proportional to Re_L
Low Re_L laminar	$\approx 10^2 < Re_L < \approx 10^4$	Vortex shedding, separation bubbles, reduced lift, drag proportional to Re_L
Laminar	$\approx 10^4 < Re_L < \approx 10^5$	Separation bubbles, decreased skin friction, earlier separation, earlier stall
Transitional	$\approx 10^5 < Re_L < \approx 10^6$	Both laminar and turbulent boundary layers with characteristics of both
Turbulent	$Re_L > \approx 10^6$	Inertial effects dominate, increased skin friction, delayed separation, delayed stall

Aerodynamics Concept Box: An Innovative Approach to Aircraft Testing

As we mentioned previously, most aircraft development programs use wind tunnel testing to determine aerodynamic characteristics. In modern aircraft development programs, wind tunnel testing is supplemented with computational simulations as well. Most of the wind tunnels

F/A-18 mounted in NASA Ames 80 ft × 120 ft wind tunnel (photo courtesy of NASA)

available for large aircraft development (such as commercial airliners) are capable of matching the Mach number, but cannot match the Reynolds number due to model size restrictions and tunnel operational conditions (pressure and temperature limitations). In order to increase the Reynolds number in the wind tunnel, the tunnels would have to increase in size, but the power required to run these larger tunnels also goes up with the size of the models.

For example, the wind tunnel with the largest test section is the NASA Ames Research Center 80 ft $\times$ 120 ft low speed wind tunnel, shown below with a full-sized F/A-18 mounted on supports for testing. This wind tunnel requires six 40-ft diameter fans to operate, and each fan uses an 18,000 horsepower motor. The power requirements for using this wind tunnel are very large, and in many cases prohibitive, and the maximum velocity is only about 100 knots.

A new option for testing aircraft affordably was put forth by John McMasters of The Boeing Company [McMasters (2007)]. Using Fig. 2.12, we can estimate that a full-size 767 flying at 12,000 m altitude at M = 0.95 would have a chord-based Reynolds number of approximately 36×10^6 (the mean aerodynamic chord of the 767 is approximately 6 m). A ¼-scale model of the aircraft flying at the same Mach number and lift coefficient but at low altitudes would have a Reynolds number of nearly 30×10^6, which is over 80% of the full-scale Reynolds number. Since the ¼-scale model could be radio controlled, it would be much more affordable than wind tunnel testing while still achieving dynamic similarity for aerodynamic purposes.

2.6 CONCEPT OF THE BOUNDARY LAYER

For many high-Reynolds-number flows (such as those of interest to the aerodynamicist), the flow field may be divided into two regions: (1) a viscous *boundary layer* adjacent to the surface of the vehicle and (2) the essentially inviscid flow outside the boundary layer. The velocity of the fluid particles increases from a value of zero (in a vehicle-fixed coordinate system) at the wall to the value that corresponds to the external "frictionless" flow outside the boundary layer, whose edge is represented by the solid lines in Fig. 2.14. Because of the resultant velocity gradients, the shear forces are relatively large in the boundary layer. Outside the boundary layer, the velocity gradients become so small that the shear stresses acting on a fluid element are negligible. Therefore, the effect of the viscous terms may generally be ignored in the solution for the flow field external to the boundary layer. To generate a solution for the inviscid portion of the flow field, we require that the velocity of the fluid particles at the surface be parallel to the surface (but not necessarily of zero magnitude). This represents the physical boundary condition requirement that there is no flow through a solid surface. The analyst may approximate the effects of the boundary layer on the inviscid solution by defining the geometry of the surface to be that of the actual surface plus a displacement due to the presence of the boundary layer. The "effective" inviscid body (the actual configuration plus the displacement thickness) is represented by the shaded area of Fig. 2.14. The solution of the boundary-layer equations and the subsequent determination of a corresponding displacement thickness are dependent on the velocity at the edge of the boundary layer (which is, in effect, the velocity at the surface that corresponds to the inviscid solution). The process of determining the interaction of the solutions provided by the inviscid-flow equations with those for the boundary-layer equations requires a thorough understanding of the problem [e.g., refer to Brune et al. (1974)].

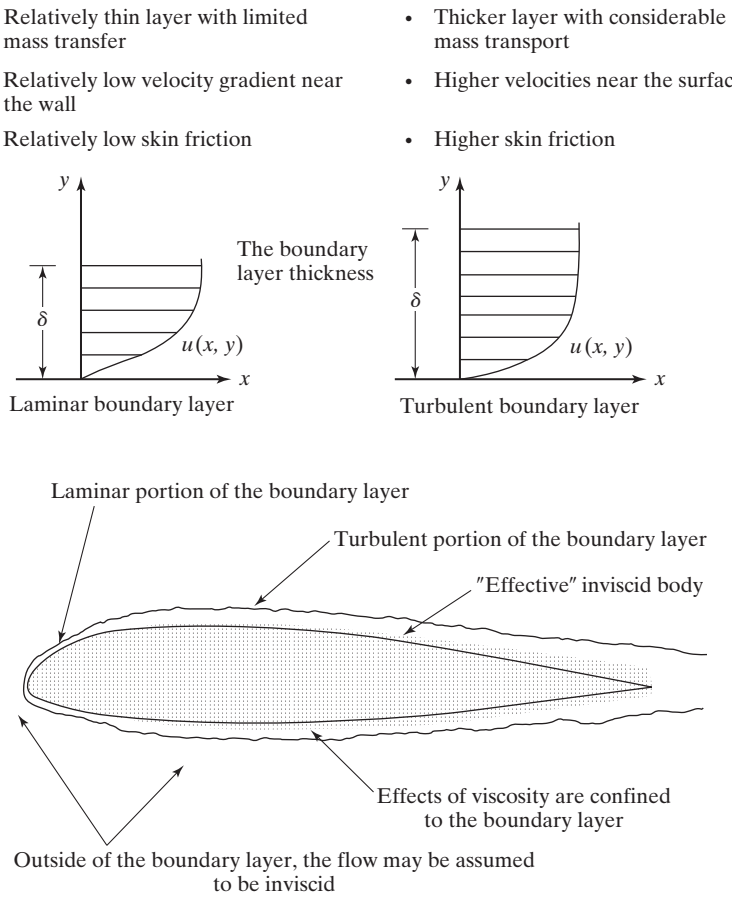

Figure 2.14 Viscous boundary layer on an airfoil.

For many problems involving flow past streamlined shapes such as airfoils and wings (at low angles of attack), the presence of the boundary layer causes the actual pressure distribution to be only negligibly different from the inviscid pressure distribution. We can consider this statement further by studying the x and y components of equation (2.12) for a two-dimensional incompressible flow. The resultant equations, which define the flow in the boundary layer shown in Fig. 2.14, are

$$\rho\frac{\partial u}{\partial t} + \rho u\frac{\partial u}{\partial x} + \rho v\frac{\partial u}{\partial y} = -\frac{\partial p}{\partial x} + \mu\frac{\partial^2 u}{\partial x^2} + \mu\frac{\partial^2 u}{\partial y^2}$$

and

$$\rho\frac{\partial v}{\partial t} + \rho u\frac{\partial v}{\partial x} + \rho v\frac{\partial v}{\partial y} = -\frac{\partial p}{\partial y} + \mu\frac{\partial^2 v}{\partial x^2} + \mu\frac{\partial^2 v}{\partial y^2}$$

where the x coordinate is measured parallel to the airfoil surface and the y coordinate is measured perpendicular to it. Solving for the pressure gradients gives us:

$$-\frac{\partial p}{\partial x} = \left(\rho\frac{\partial}{\partial t} + \rho u\frac{\partial}{\partial x} + \rho v\frac{\partial}{\partial y} - \mu\frac{\partial^2}{\partial x^2} - \mu\frac{\partial^2}{\partial y^2}\right)u$$

$$-\frac{\partial p}{\partial y} = \left(\rho\frac{\partial}{\partial t} + \rho u\frac{\partial}{\partial x} + \rho v\frac{\partial}{\partial y} - \mu\frac{\partial^2}{\partial x^2} - \mu\frac{\partial^2}{\partial y^2}\right)v$$

Providing that the boundary layer near the solid surface is thin, the normal component of velocity is usually much less than the streamwise component of velocity (i.e., $v < u$). Thus, the terms on the right-hand side of the equation in the second line are typically smaller than the corresponding terms in the first line. We can conclude that:

$$\frac{\partial p}{\partial y} < \frac{\partial p}{\partial x}$$

As a result, the pressure gradient normal to the surface is typically assumed to be negligible:

$$\frac{\partial p}{\partial y} \approx 0$$

which is verified by experiments for flow over a flat plate. Since the static pressure variation across the boundary layer is usually negligible, the pressure distribution around the airfoil is essentially that of the inviscid flow (accounting for the displacement effect of the boundary layer).

The assumption that the static pressure variation across the boundary layer is negligible breaks down for turbulent boundary layers at very high Mach numbers. Bushnell et al. (1977) cites data for which the wall pressure is significantly greater than the edge value for turbulent boundary layers where the edge Mach number is approximately 20. But in general the inviscid pressure distribution is a good approximation for an airfoil. The characteristics distinguishing laminar and turbulent boundary layers were briefly touched on in Table 2.2, and will be further discussed in Chapter 4.

When the combined action of an adverse pressure gradient and the viscous forces causes the boundary layer to separate from the vehicle surface (which may occur for blunt bodies or for streamlined shapes at high angles of attack), the flow field is very sensitive to the Reynolds number. The Reynolds number, therefore, also serves as an indicator of how much of the flow can be accurately described by the inviscid-flow equations. For detailed discussions of the viscous portion of the flow field, you should refer to Chapter 4 and to the books by Schlichting and Gersten (2000), White (2005), Schetz and Bowersox (2011), and/or Wilcox (1998).

2.7 CONSERVATION OF ENERGY

There are many flows that involve sufficient temperature variations so that convective heat transfer is important, but for which the constant-property assumption is reasonable. An example is flow in a heat exchanger. For these flows, the temperature field is obtained by solving the energy equation after the velocity field has been determined by solving the continuity equation and the momentum equation. This is because, for

this case, the continuity equation and the momentum equation are independent of the energy equation, but not vice versa.

We must also include the energy equation in the solution algorithm for compressible flows. Compressible flows are those in which the pressure and temperature variations are sufficiently large that we must account for changes in the other fluid properties (e.g., density and viscosity). For compressible flows, the continuity equation, the momentum equation, and the energy equation must be solved simultaneously. Recall the discussion relating to the momentum equations (2.12a) through (2.12c) for the number of unknown variables and the number of equations available. We will need the energy equation to form a complete set of equations to describe compressible flow. In the remainder of this chapter, we will derive the energy equation and discuss its application to various flows.

2.8 FIRST LAW OF THERMODYNAMICS

To develop the energy equation, we will again consider a system of fluid particles. Everything outside the group of particles is called the *surroundings* of the system. The *first law of thermodynamics* results from the fundamental experiments of James Joule, who found that, for a cyclic process (one in which the initial state and the final state of the fluid are identical), the following relation held:

$$\oint \delta q - \oint \delta w = 0 \tag{2.21}$$

Joule showed that the heat transferred from the surroundings to the system, less the work done by the system on its surroundings, during a cyclic process is zero. In equation (2.21), we have adopted the convention that heat transfer to the system is positive and that work done by the system is positive, which accounts for the heat term in equation (2.21) being positive and the work term being negative. The use of lower case symbols to represent the parameters means that we are considering the magnitude of the parameter per unit mass of the fluid, which are usually referred to as *specific* properties. We use the symbols δq and δw to designate that the incremental heat transfer to the system and the incremental work done by the system are not exact differentials, but depend on the process used in going from state 1 to state 2. In addition, q and w are not properties of the fluid (like density or temperature). Equation (2.21) is true for any and all cyclic processes. Therefore, if we apply equation (2.21) to a process that takes place between any two states (1 and 2), then we obtain:

$$\delta q - \delta w = de = e_2 - e_1 \tag{2.22}$$

where e is the total energy per unit mass of the fluid, or the specific total energy. Note that de is an exact differential and the energy is, therefore, a property of the fluid. The energy is usually divided into three components: (1) kinetic energy, (2) potential energy, and (3) all other energy. The internal energy of the fluid is part of the third component. In this book, we will be concerned only with kinetic, potential, and internal energies. Chemical, nuclear, and other forms of energy are normally not relevant to the study of aerodynamics. Since we are normally only concerned with changes in energy rather than its absolute value, an arbitrary zero energy (or datum) state can usually be assigned.

In terms of the three energy components discussed above, equation (2.22) becomes

$$\delta q - \delta w = dke + dpe + du_e \tag{2.23}$$

Note that u_e is the symbol used for specific internal energy (i.e., the internal energy per unit mass).

Some comments on work: In mechanics, work is usually defined as the effect that is produced by a system on its surroundings when the system moves the surroundings in the direction of the force exerted by the system on its surroundings. The magnitude of the effect is measured by the product of the displacement times the component of the force in the direction of the motion (force times distance). Thermodynamics deals with phenomena considerably more complex than covered by this definition from mechanics. Thus, we may say that work is done by a system on its surroundings if we can postulate a process in which the system passes through the same series of states as in the original process, but in which the sole effect on the surroundings is the raising of a weight.

In an inviscid flow, the only forces acting on a fluid system (providing we neglect gravity) are the pressure forces. Consider a small element of the surface dA of a fluid system, as shown in Fig. 2.15. The force acting on dA due to the fluid in the system is $p\,dA$. If this force displaces the surface a differential distance ds in the direction of the force, the work done is $p\,dA\,ds$. Differential displacements are assumed so that the process is reversible, which means there are no dissipative factors such as friction and/or heat transfer. But the product of dA times ds is just d(vol), the change in volume of the system. Thus, the work per unit mass is

$$\delta w = +p\,dv \tag{2.24a}$$

where v is the volume per unit mass (or specific volume), which is the reciprocal of the density ($v = 1/\rho$). Be very careful not to confuse the symbol v with the y component of velocity! Equivalently, equation (2.24a) can be written between state 1 and state 2 as:

$$w = +\int_1^2 p\,dv \tag{2.24b}$$

where the work done by the system on its surroundings [a finite process, as given by equation (2.24b)], is positive when dv represents an increase in volume.

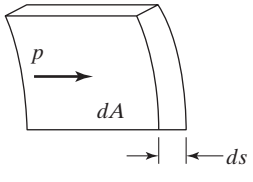

Figure 2.15 Incremental work done by the pressure force, which acts normal to the surface.

2.9 DERIVATION OF THE ENERGY EQUATION

Having discussed the first law and its implications, we are now ready to derive the differential form of the energy equation for a viscous, heat-conducting compressible flow. Consider the fluid particles shown in Fig. 2.16. Writing equation (2.23) in rate form, we can describe the energy balance on the particle as it moves along in the flow as:

$$\rho\dot{q} - \rho\dot{w} = \rho\frac{d}{dt}(e) = \rho\frac{d}{dt}(ke) + \rho\frac{d}{dt}(pe) + \rho\frac{d}{dt}(u_e) \qquad \textbf{(2.25)}$$

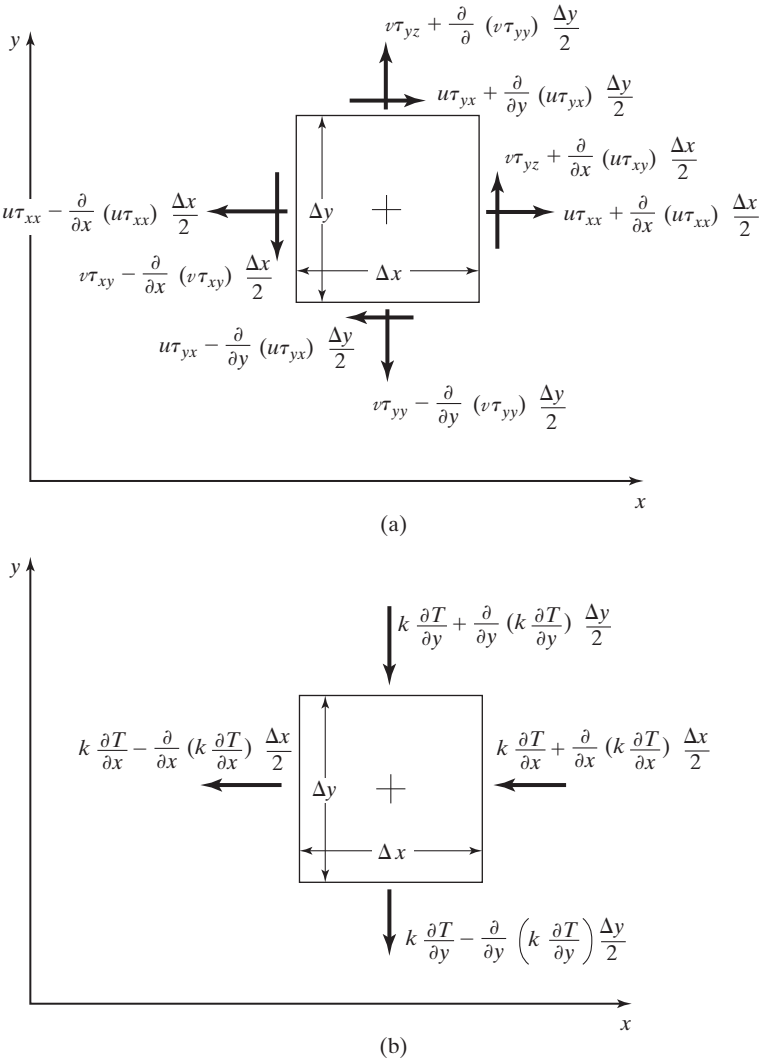

Figure 2.16 Heat-transfer and flow-work terms for the energy equation for a two-dimensional fluid element: (a) work done by stresses acting on a two-dimensional element; (b) heat transfer to a two-dimensional element.

where the overdot notation denotes differentiation with respect to time. Recall that the substantial (or total) derivative is

$$\frac{d}{dt} = \frac{\partial}{\partial t} + \vec{V} \cdot \nabla$$

and therefore represents the local, time-dependent changes, as well as those due to convection through space.

To simplify the illustration of the energy balance on the fluid particle, we will again consider a two-dimensional flow, as shown in Fig. 2.16. The rate at which work is done by the system on its surrounding is equal to the negative of the product of the forces acting on a boundary surface times the flow velocity (i.e., the displacement per unit time) at that surface. The work done by the body forces is not included in this term, but rather is accounted for in the potential energy term, equation (2.27). Now, using the nomenclature of Fig. 2.16a, we can evaluate the rate at which work is done by the system (per unit depth):

$$-\dot{W} = \frac{\partial}{\partial x}(u\tau_{xx})\,\Delta x\,\Delta y + \frac{\partial}{\partial x}(v\tau_{xy})\,\Delta x\,\Delta y + \frac{\partial}{\partial y}(u\tau_{yx})\,\Delta y\Delta x + \frac{\partial}{\partial y}(v\tau_{yy})\,\Delta y\,\Delta x$$

Using the constitutive relations for τ_{xx}, τ_{xy}, τ_{yx}, and τ_{yy} given in Section 2.3, and dividing by $\Delta x\,\Delta y$, we obtain

$$\begin{aligned} -\rho\dot{w} = {} & 2\mu\left[\left(\frac{\partial u}{\partial x}\right)^2 + \left(\frac{\partial v}{\partial y}\right)^2\right] - p\left(\frac{\partial u}{\partial x} + \frac{\partial v}{\partial y}\right) - \frac{2}{3}\mu(\nabla \cdot \vec{V})^2 \\ & + \mu\left[\left(\frac{\partial u}{\partial y} + \frac{\partial v}{\partial x}\right)^2\right] + u\frac{\partial \tau_{xx}}{\partial x} + v\frac{\partial \tau_{yy}}{\partial y} + v\frac{\partial \tau_{xy}}{\partial x} + u\frac{\partial \tau_{yx}}{\partial y} \end{aligned} \qquad \textbf{(2.26a)}$$

From the linear momentum equations (2.11), multiplied by the velocity in each direction, we obtain:

$$u\frac{\partial \tau_{xx}}{\partial x} + u\frac{\partial \tau_{yx}}{\partial y} = u\rho\frac{du}{dt} - u\rho f_x \qquad \textbf{(2.26b)}$$

$$v\frac{\partial \tau_{xy}}{\partial x} + v\frac{\partial \tau_{yy}}{\partial y} = v\rho\frac{dv}{dt} - v\rho f_y \qquad \textbf{(2.26c)}$$

We will also need a relation for the heat change, which we obtain from Fourier's law of heat conduction,

$$\dot{Q} = -k\hat{n}A \cdot \nabla T$$

We can now evaluate the rate at which heat is added to the system (per unit depth). Note that the symbol T will be used to denote temperature, the symbol t, time, and $\dot{Q}$, the total heat flux rate. Referring to Fig. 2.16b and noting that, if the temperature is increasing in the outward direction, heat is added to the particle (which is positive by our convention),

$$\dot{Q} = +\frac{\partial}{\partial x}\left(k\frac{\partial T}{\partial x}\right)\Delta x\,\Delta y + \frac{\partial}{\partial y}\left(k\frac{\partial T}{\partial y}\right)\Delta y\,\Delta x$$

Therefore,

$$\rho\dot{q} = \frac{\partial}{\partial x}\left(k\frac{\partial T}{\partial x}\right) + \frac{\partial}{\partial y}\left(k\frac{\partial T}{\partial y}\right) \qquad \textbf{(2.26d)}$$

Substituting equations (2.26) into equation (2.25), we obtain

$$\frac{\partial}{\partial x}\left(k\frac{\partial T}{\partial x}\right) + \frac{\partial}{\partial y}\left(k\frac{\partial T}{\partial y}\right) + 2\mu\left[\left(\frac{\partial u}{\partial x}\right)^2 + \left(\frac{\partial v}{\partial y}\right)^2\right] - p\nabla\cdot\vec{V}$$
$$-\frac{2}{3}\mu(\nabla\cdot\vec{V})^2 + \mu\left[\left(\frac{\partial u}{\partial y} + \frac{\partial v}{\partial x}\right)^2\right] + \rho u\frac{du}{dt} - \rho u f_x + \rho v\frac{dv}{dt} - \rho v f_x$$
$$= \rho\frac{d[(u^2 + v^2)/2]}{dt} + \rho\frac{d(pe)}{dt} + \rho\frac{d(u_e)}{dt} \tag{2.27}$$

From the continuity equation,

$$\nabla\cdot\vec{V} = -\frac{1}{\rho}\frac{d\rho}{dt}$$

and from the definition

$$\rho\frac{d(p/\rho)}{dt} = \frac{dp}{dt} - \frac{p}{\rho}\frac{d\rho}{dt}$$

we can write the continuity equation in the form:

$$-p\nabla\cdot\vec{V} = -\rho\frac{d(p/\rho)}{dt} + \frac{dp}{dt} \tag{2.28a}$$

Also, for a conservative force field,

$$\rho\frac{d(pe)}{dt} = \rho\vec{V}\cdot\nabla F = -\rho u f_x - \rho v f_y \tag{2.28b}$$

where F is the body-force potential and $\nabla F = -\bar{f}$, as will be introduced in equation (3.3).

Substituting equations (2.28a and 2.28b) into equation (2.27), we obtain:

$$\frac{\partial}{\partial x}\left(k\frac{\partial T}{\partial x}\right) + \frac{\partial}{\partial y}\left(k\frac{\partial T}{\partial y}\right) + 2\mu\left[\left(\frac{\partial u}{\partial x}\right)^2 + \left(\frac{\partial v}{\partial y}\right)^2\right] - \frac{2}{3}\mu(\nabla\cdot\vec{V})^2$$
$$+\mu\left[\left(\frac{\partial u}{\partial y} + \frac{\partial v}{\partial x}\right)^2\right] - \rho\frac{d(p/\rho)}{dt} + \frac{dp}{dt} + \rho u\frac{du}{dt} + \rho v\frac{dv}{dt} - \rho u f_x - \rho v f_y$$
$$= \rho u\frac{du}{dt} + \rho v\frac{dv}{dt} - \rho u f_x - \rho v f_y + \rho\frac{d(u_e)}{dt} \tag{2.29}$$

Since the terms u_e and p/ρ appear as a sum in many flow applications, it is convenient to introduce a symbol for this sum. We will introduce the definition:

$$h \equiv u_e + \frac{p}{\rho} \tag{2.30}$$

where h is the specific enthalpy. Using equation (2.30) and combining terms, we can write equation (2.29) as

$$\frac{\partial}{\partial x}\left(k\frac{\partial T}{\partial x}\right) + \frac{\partial}{\partial y}\left(k\frac{\partial T}{\partial y}\right) + 2\mu\left[\left(\frac{\partial u}{\partial x}\right)^2 + \left(\frac{\partial v}{\partial y}\right)^2\right] - \frac{2}{3}\mu(\nabla \cdot \vec{V})^2 + \mu\left[\left(\frac{\partial u}{\partial y} + \frac{\partial v}{\partial x}\right)^2\right] = \rho\frac{dh}{dt} - \frac{dp}{dt} \tag{2.31}$$

This is the energy equation for a general, compressible flow in two dimensions. The process can be extended to a three-dimensional flow field to yield

$$\rho\frac{dh}{dt} - \frac{dp}{dt} = \nabla \cdot (k\nabla T) + \phi \tag{2.32a}$$

where

$$\phi = -\frac{2}{3}\mu(\nabla \cdot \vec{V})^2 + 2\mu\left[\left(\frac{\partial u}{\partial x}\right)^2 + \left(\frac{\partial v}{\partial y}\right)^2 + \left(\frac{\partial w}{\partial z}\right)^2\right] + \mu\left[\left(\frac{\partial u}{\partial y} + \frac{\partial v}{\partial x}\right)^2 + \left(\frac{\partial v}{\partial z} + \frac{\partial w}{\partial y}\right)^2 + \left(\frac{\partial w}{\partial x} + \frac{\partial u}{\partial z}\right)^2\right] \tag{2.32b}$$

Equation (2.32b) defines the dissipation function ϕ, which represents the rate at which work is done by the viscous forces per unit volume.

2.9.1 Integral Form of the Energy Equation

The integral form of the energy equation is

$$\dot{Q} - \dot{W} = \iiint \frac{\partial}{\partial t}(\rho e)d(\text{vol}) + \oiint e\rho\vec{V} \cdot \hat{n}\, dA \tag{2.33}$$

That is, the net rate heat added to the system less the net rate work done by the system is equal to the time rate of change of energy within the control volume plus the net efflux of energy across the system boundary. Remember that the heat added to the system and the work done by the system are positive. Conversely, heat transferred from the system or work done on the system is negative by this convention.

2.9.2 Energy of the System

As we discussed in Section 2.8, the energy of the system can take a variety of forms. Typically we group energy forms as follows:

1. ***Kinetic energy (ke):*** energy associated with the directed motion of the mass
2. ***Potential energy (pe):*** energy associated with the position of the mass in the external field
3. ***Internal energy (u_e):*** energy associated with the internal fields and the random motion of the molecules

So, the energy of the system may be written simply as:

$$e = ke + pe + u_e \tag{2.34a}$$

Now we can further examine the terms that comprise the energy of the system. The kinetic energy per unit mass is given by

$$ke = \frac{V^2}{2} \tag{2.34b}$$

Note that the change in kinetic energy during a process clearly depends only on the initial velocity and final velocity of the system of fluid particles. Assuming that the external force field is that of gravity, the potential energy per unit mass is given by

$$pe = gz \tag{2.34c}$$

Note that the change in the potential energy depends only on the initial and final elevations. Finally, the change in internal energy is also a function of the values at the endpoints only.

Substituting equations (2.34) into equation (2.33), we obtain

$$\dot{Q} - \dot{W} = \frac{\partial}{\partial t}\iiint \rho\left(\frac{V^2}{2} + gz + u_e\right)d(\text{vol}) + \oiint \rho\left(\frac{V^2}{2} + gz + u_e\right)\vec{V}\cdot\hat{n}\,dA \tag{2.35}$$

You should notice that, while the changes in the energy components are a function of the states, the amount of heat transferred and the amount of work done during a process are path dependent. That is, the changes depend not only on the initial and final states but on the process that takes place between these states.

Now we can further consider the term for the rate at which work is done, $\dot{W}$. For convenience, the total work rate is divided into flow work rate ($\dot{W}_f$), viscous work rate ($\dot{W}_v$), and shaft work rate ($\dot{W}_s$), which will be discussed in more detail below.

2.9.3 Flow Work

Flow work is the work done by the pressure forces on the surroundings as the fluid moves through space. Consider flow through the streamtube shown in Fig. 2.17. The pressure p_2 acts over the differential area $\hat{n}_2\,dA_2$ at the right end (i.e., the downstream end) of the control volume. Remember that the pressure is a compressive force acting on the system of particles. Thus, the force acting on the right end surface is $-p_2\hat{n}_2\,dA_2$. In moving the surrounding fluid through the distance $\vec{V}_2\,\Delta t$ for the velocity shown in Fig. 2.17, the system does work on the surroundings (which is positive by our sign convention). Thus, the work done is the dot product of the force times the distance:

$$p_2\hat{n}_2\,dA_2\cdot\vec{V}_2\,\Delta t$$

$$\dot{W}_{f,2} = p_2\vec{V}_2\cdot\hat{n}_2\,dA_2 = \frac{p_2}{\rho_2}\rho_2\vec{V}_2\cdot\hat{n}_2\,dA_2 \tag{2.36a}$$

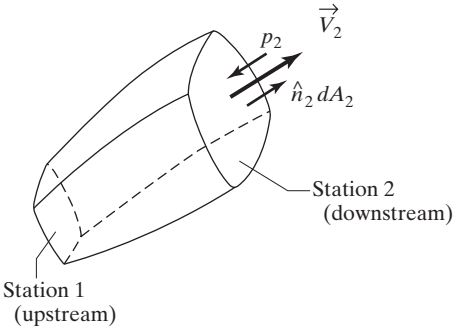

Figure 2.17 Streamtube for derivation of equation (2.36).

The positive sign is consistent with the assumed directions of Fig. 2.17 (i.e., the velocity and the area vectors are in the same direction). Therefore, the dot product is consistent with the convention that work done by the system on the surroundings is positive.

In a similar manner, we can show that the flow work done on the surrounding fluid at the upstream end (station 1) is:

$$\dot{W}_{f,1} = -\frac{p_1}{\rho_1}\rho_1 \vec{V}_1 \cdot \hat{n}_1\, dA_1 \qquad \textbf{(2.36b)}$$

The negative sign results because the pressure force is compressive (acts on the system of particles), and the assumed velocity represents movement of the fluid particles in that direction. Therefore, since work is done by the surroundings on the system at the upstream end, it is negative by our sign convention.

2.9.4 Viscous Work

Viscous work is similar to flow work in that it is the result of a force acting on the surface bounding the fluid system. In the case of viscous work, however, the pressure is replaced by the viscous shear. The rate at which viscous work is done by the system over some incremental area of the system surface (dA) is

$$\dot{W}_v = -\bar{\tau} \cdot \vec{V}\, dA \qquad \textbf{(2.36c)}$$

2.9.5 Shaft Work

Shaft work is defined as any other work done by the system other than the flow work and the viscous work. This usually enters or leaves the system through the action of a shaft (from which the term originates), which either takes energy out of or puts energy into the system. Since a turbine extracts energy from the system, the system does work on the surroundings and $\dot{W}_s$ is positive. In the case where the "shaft" is a pump, the surroundings are doing work on the system and $\dot{W}_s$ is negative.

2.9.6 Application of the Integral Form of the Energy Equation

Based on the preceding definitions, the energy equation can be written as:

$$\dot{Q} - \dot{W}_v - \dot{W}_s = \frac{\partial}{\partial t}\iiint \rho\left(\frac{V^2}{2} + gz + u_e\right)d(\text{vol}) + \oiint \rho\left(\frac{V^2}{2} + gz + u_e + \frac{p}{\rho}\right)\vec{V}\cdot\hat{n}\,dA \qquad \textbf{(2.37)}$$

Notice that the flow work, as represented by equation (2.36), has been incorporated into the second integral of the right-hand side of equation (2.37).

For a steady, adiabatic flow ($\dot{Q} = 0$) with no shaft work ($\dot{W}_s = 0$) and with no viscous work ($\dot{W}_v = 0$), equation (2.37) can be written as:

$$\oiint \rho\left(\frac{V^2}{2} + gz + h\right)\vec{V}\cdot\hat{n}\,dA = 0 \qquad \textbf{(2.38)}$$

where the definition for enthalpy has been used.

EXAMPLE 2.7: A flow where the energy equation is Bernoulli's equation

Consider the steady, inviscid, one-dimensional flow of water in the curved pipe shown in Fig. 2.18. If water drains to the atmosphere at station 2 at the rate of 0.001π m^3/s, what is the static pressure at station 1? There is no shaft work or heat transfer, and there are no perceptible changes in the internal energy.

Solution: We will apply equation (2.37) to the control volume that encloses the fluid in the pipe between stations 1 and 2. Applying the conditions and assumptions in the problem statement,

$$\text{No heat transfer } \dot{Q} = 0$$
$$\text{No shaft work } \dot{W}_s = 0$$
$$\text{No viscous work } \dot{W}_v = 0$$
$$\text{Steady flow } \frac{\partial}{\partial t} = 0$$

Therefore,

$$\oiint \left(\frac{V^2}{2} + gz + u_e + \frac{p}{\rho}\right)\rho\vec{V}\cdot\hat{n}\,dA = 0$$

Since the properties for the inviscid, one-dimensional flow are uniform over the plane of each station, and since the velocities are perpendicular to the cross-sectional area, the integral can readily be evaluated as:

$$\left(\frac{V_1^2}{2} + gz_1 + u_{e1} + \frac{p_1}{\rho_1}\right)\rho_1 V_1 A_1 = \left(\frac{V_2^2}{2} + gz_2 + u_{e2} + \frac{p_2}{\rho_2}\right)\rho_2 V_2 A_2$$

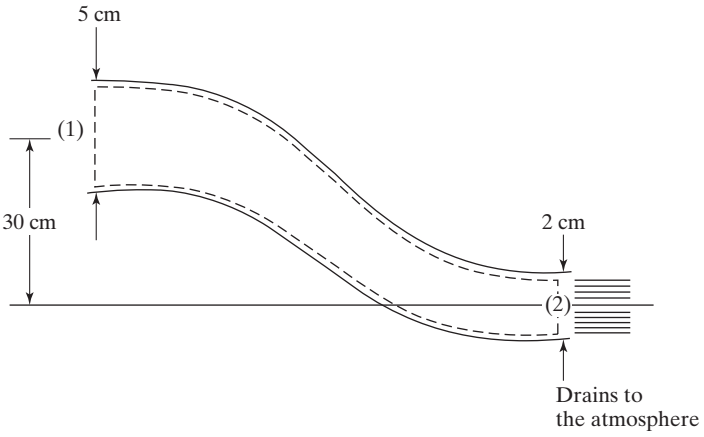

Figure 2.18 Pipe flow for Example 2.7.

Due to the conservation of mass, $\rho_1 V_1 A_1 = \rho_2 V_2 A_2$, and since water is incompressible, $\rho_1 = \rho_2 = 1000\ \text{kg/m}^3$. Furthermore, we were told that there are no perceptible changes in the internal energy (i.e., $u_{e1} = u_{e2}$), so the energy equation becomes:

$$\frac{V_1^2}{2} + gz_1 + \frac{p_1}{\rho} = \frac{V_2^2}{2} + gz_2 + \frac{p_2}{\rho}$$

You should notice that the resultant form of the energy equation for this flow is Bernoulli's equation.

Therefore, for an incompressible, steady, nondissipative flow, we have a mechanical energy equation that simply equates the flow work with the sum of the changes in potential energy and in kinetic energy.

$$V_2 = \frac{Q}{A_2} = \frac{0.001\pi\ \text{m}^3/s}{\pi(0.02\ \text{m})^2/4} = 10\ \text{m/s}$$

Since $V_1 A_1 = V_2 A_2$

$$V_1 = \frac{\pi D_2^2/4}{\pi D_1^2/4} V_2 = \left(\frac{D_2}{D_1}\right)^2 V_2 = 0.16(10\ \text{m/s}) = 1.6\ \text{m/s}$$

Thus,

$$\frac{(1.6\ \text{m/s})^2}{2} + (9.8066\ \text{m/s}^2)(0.3\ \text{m}) + \frac{p_1}{1000\ \text{kg/m}^3} = \frac{(10\ \text{m/s})^2}{2} + \frac{p_{\text{atm}}}{1000\ \text{kg/m}^3}$$

$$p_1 = p_{\text{atm}} + (50 - 1.28 - 2.94)\ \text{m}^2/\text{s}^2(1000\ \text{kg/m}^3)$$
$$= 4.58 \times 10^4\ \text{N/m}^2, \text{gage}$$

2.10 SUMMARY

Both the differential and integral forms of the equations of motion for a compressible, viscous flow have been developed in this chapter. Presented were the continuity equation, equation (2.2) or (2.5); the momentum equation, equation (2.12) or (2.13); and the energy equation, equation (2.32) or (2.33). The dependent variables, or unknowns, in these equations include pressure, temperature, velocity, density, viscosity, thermal conductivity, internal energy, and enthalpy. For many applications, simplifying assumptions can be introduced to eliminate one or more of the dependent variables. For example, a common assumption is that the variation in the fluid properties as the fluid moves through the flow field is very small when the Mach number is less than 0.3. Therefore, assuming that the density, the viscosity, and the thermal conductivity are constant, we can eliminate them as variables and still obtain solutions of suitable accuracy. Examples of constant-property flows will be worked out in subsequent chapters.

PROBLEMS

2.1. Derive the continuity equation in cylindrical coordinates, starting with the general vector form

$$\frac{\partial \rho}{\partial t} + \nabla \cdot (\rho \vec{V}) = 0$$

where

$$\nabla = \hat{e}_r \frac{\partial}{\partial r} + \frac{\hat{e}_\theta}{r} \frac{\partial}{\partial \theta} + \hat{e}_z \frac{\partial}{\partial z}$$

in cylindrical coordinates. Note also that $\frac{\partial \hat{e}_r}{\partial \theta}$ and $\frac{\partial \hat{e}_\theta}{\partial \theta}$ are not zero.

$$\frac{1}{r} \frac{\partial (\rho r v_r)}{\partial r} + \frac{1}{r} \frac{\partial (\rho v_\theta)}{\partial \theta} + \frac{\partial (\rho v_z)}{\partial z} = 0$$

2.2. Which of the following flows are physically possible, that is, satisfy the continuity equation? Substitute the expressions for density and for the velocity field into the continuity equation to substantiate your answer.

(a) Water, which has a density of 1.0 g/cm^3, is flowing radially outward from a source in a plane such that $\vec{V} = (K/2\pi r)\hat{e}_r$. Note that $v_\theta = v_z = 0$. Note also that, in cylindrical coordinates,

$$\nabla = \hat{e}_r \frac{\partial}{\partial r} + \frac{\hat{e}_\theta}{r} \frac{\partial}{\partial \theta} + \hat{e}_z \frac{\partial}{\partial z}$$

(b) A gas is flowing at relatively low speeds (so that its density may be assumed constant) where

$$u = -\frac{2xyz}{(x^2 + y^2)^2} U_\infty L$$

$$v = \frac{(x^2 - y^2)z}{(x^2 + y^2)^2} U_\infty L$$

$$w = \frac{y}{x^2 + y^2} U_\infty L$$

Here U_∞ and L are a reference velocity and a reference length, respectively.

2.3. Two of the three velocity components for an incompressible flow are:

$$u = x^3 + 3xz \qquad v = y^3 + 3yz$$

What is the general form of the velocity component $w(x,y,z)$ that satisfies the continuity equation?

2.4. A two-dimensional velocity field is given by

$$u = -\frac{Ky}{x^2 + y^2} \qquad v = +\frac{Kx}{x^2 + y^2}$$

where K is a constant. Does this velocity field satisfy the continuity equation for incompressible flow? Transform these velocity components into the polar components v_r and v_θ in terms of r and θ. What type of flow might this velocity field represent?

2.5. The velocity components for a two-dimensional flow are

$$u = \frac{C(y^2 - x^2)}{(x^2 + y^2)^2} \qquad v = \frac{-2Cxy}{(x^2 + y^2)^2}$$

where C is a constant. Does this flow satisfy the continuity equation?

2.6. For the two-dimensional flow of incompressible air near the surface of a flat plate, the steamwise (or x) component of the velocity may be approximated by the relation

$$u = a_1\frac{y}{\sqrt{x}} - a_2\frac{y^3}{x^{1.5}}$$

Using the continuity equation, what is the velocity component v in the y direction? Evaluate the constant of integration by noting that $v = 0$ at $y = 0$.

2.7. Consider a one-dimensional steady flow along a streamtube. Differentiate the resultant integral continuity equation to show that

$$\frac{d\rho}{\rho} + \frac{dA}{A} + \frac{dV}{V} = 0$$

For a low-speed, constant-density flow, what is the relation between the change in area and the change in velocity?

2.8. Water flows through a circular pipe, as shown in Fig. P2.8, at a constant volumetric flow rate of 0.5 m^3/s. Assuming that the velocities at stations 1, 2, and 3 are uniform across the cross section (i.e., the flow is one dimensional), use the integral form of the continuity equation to calculate the velocities, V_1, V_2, and V_3. The corresponding diameters are $d_1 = 0.4$ m, $d_2 = 0.2$ m, and $d_3 = 0.6$ m.

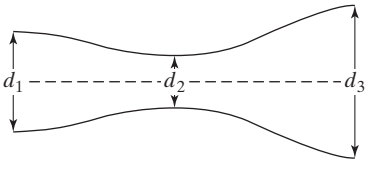

Figure P2.8

2.9. A long pipe (with a reducer section) is attached to a large tank, as shown in Fig. P2.9. The diameter of the tank is 5.0 m; the diameter to the pipe is 20 cm at station 1 and 10 cm at station 2. The effects of viscosity are such that the velocity (u) may be considered constant across the cross section at the surface (s) and at station 1, but varies with the radius at station 2 such that

$$u = U_0\left(1 - \frac{r^2}{R_2^2}\right)$$

where U_0 is the velocity at the centerline, R_2 the radius of the pipe at station 2, and r the radial coordinate. If the density is 0.85 g/cm^3 and the mass flow rate is 10 kg/s, what are the velocities at s and 1, and what is the value of U_0 ?

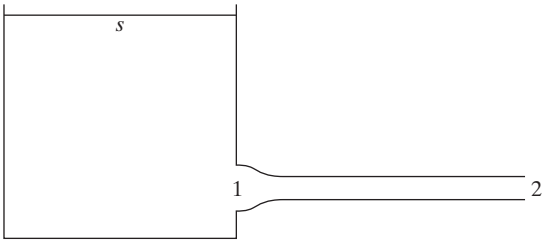

Figure P2.9

A note for Problems 2.10 through 2.13 and 2.27 through 2.31. The drag force acting on an airfoil can be calculated by determining the change in the momentum of the fluid as it flows past the airfoil. As part of this exercise, one measures the velocity distribution well upstream of the airfoil and well downstream of the airfoil. The integral equations of motion can be applied to either a rectangular control volume or a control volume bounded by streamlines.

2.10. Velocity profiles are measured at the upstream end (surface 1) and at the downstream end (surface 2) of a rectangular control volume, as shown in Fig. P2.10. If the flow is incompressible, two dimensional, and steady, what is the total volumetric flow rate ($\iint \vec{V} \cdot \hat{n}\, dA$) across the horizontal surfaces (surfaces 3 and 4)?

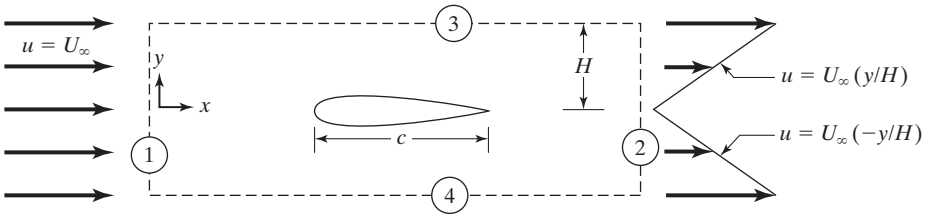

Figure P2.10

2.11. Velocity profiles are measured at the upstream end (surface 1) and at the downstream end (surface 2) of the control volume shown in Fig. P2.11. The flow is incompressible, two dimensional, and steady. If surfaces 3 and 4 are streamlines, what is the vertical dimension of the upstream station (H_U)?

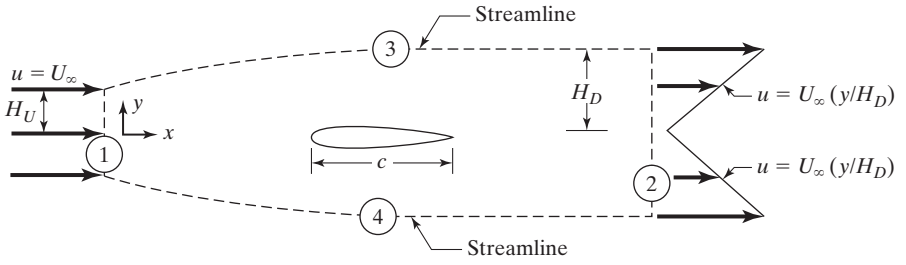

Figure P2.11

2.12. Velocity profiles are measured at the upstream end (surface 1) and at the downstream end (surface 2) of a rectangular control volume, as shown in Fig. P2.12. If the flow is incompressible, two dimensional, and steady, what is the total volumetric flow rate ($\iint \vec{V} \cdot \hat{n}\, dA$) across the horizontal surfaces (surfaces 3 and 4)?

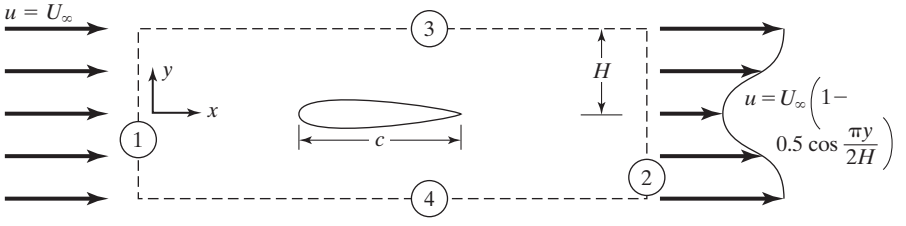

Figure P2.12

2.13. Velocity profiles are measured at the upstream end (surface 1) and at the downstream end (surface 2) of the control volume shown in Fig. P2.13. The flow is incompressible, two dimensional, and steady. If surfaces 3 and 4 are streamlines, what is the vertical dimension of the upstream station (H_U)?

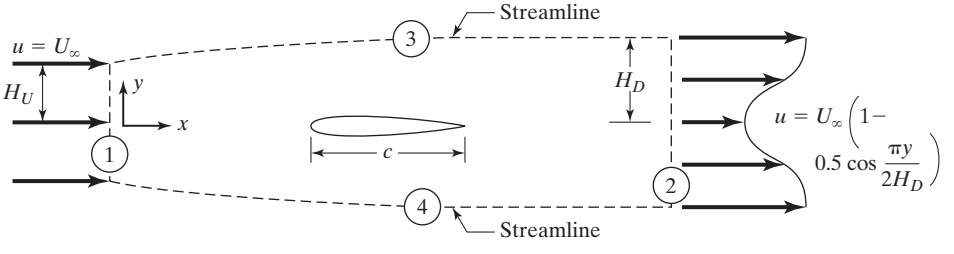

Figure P2.13

2.14. One cubic meter per second of water enters a rectangular duct as shown in Fig. P2.14. Two of the surfaces of the duct are porous. Water is added through the upper surface at a rate shown by the parabolic curve, while it leaves through the front face at a rate that decreases linearly with the distance from the entrance. The maximum values of both flow rates, shown in the sketch, are given in cubic meters per second per unit length along the duct. What is the average velocity of water leaving the duct if it is 1.0 m long and has a cross section of 0.1 m^2?

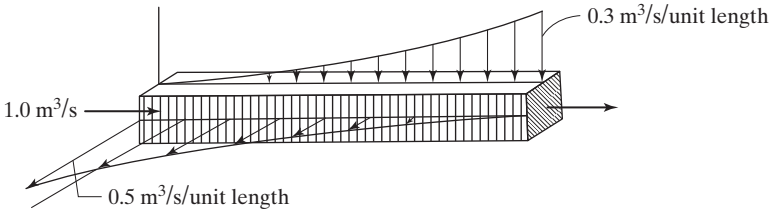

Figure P2.14

2.15. For the conditions of Problem 2.14, determine the position along the duct where the average velocity of flow is a minimum. What is the average velocity at this station?

2.16. As shown in Fig. P2.16, 1.5 m^3/s of water leaves a rectangular duct. Two of the surfaces of the duct are porous. Water leaves through the upper surface at a rate shown by the parabolic curve, while it enters the front face at a rate that decreases linearly with distance from the entrance. The maximum values of both flow rates, shown in the sketch, are given in cubic meters per second per unit length along the duct. What is the average velocity of the water entering the duct if it is 1.0 m long and has a cross section of 0.1 m^2?

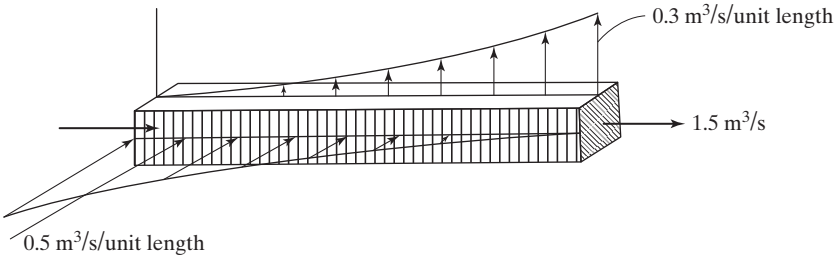

Figure P2.16

2.17. Consider the velocity field

$$\vec{V} = -\frac{x}{2t}\hat{i}$$

in a compressible flow where $\rho = \rho_0 xt$. Using equation (2.8), what is the total acceleration of a particle at (1, 1, 1) at time $t = 10$?

2.18. Given the velocity field

$$\vec{V} = (6 + 2xy + t^2)\hat{i} - (xy^2 + 10t)\hat{j} + 25\hat{k}$$

what is the acceleration of a particle at (3, 0, 2) at time $t = 1$?

2.19. Consider steady two-dimensional flow about a cylinder of radius R (Fig. P2.19). Using cylindrical coordinates, we can express the velocity field for steady, inviscid, incompressible flow around the cylinder as

$$\vec{V}(r, \theta) = U_\infty\left(1 - \frac{R^2}{r^2}\right)\cos\theta\,\hat{e}_r - U_\infty\left(1 + \frac{R^2}{r^2}\right)\sin\theta\,\hat{e}_\theta$$

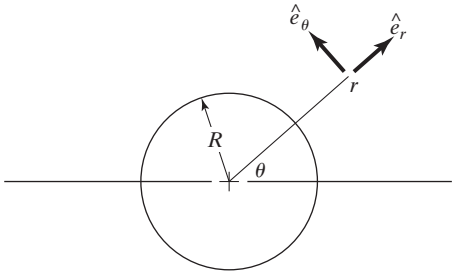

Figure P2.19

where U_∞ is the velocity of the undisturbed stream (and is, therefore, a constant). Derive the expression for the acceleration of a fluid particle at the surface of the cylinder (i.e., at points where $r = R$). Use equation (2.8) and the definition that

$$\nabla = \hat{e}_r \frac{\partial}{\partial r} + \frac{\hat{e}_\theta}{r} \frac{\partial}{\partial \theta} + \hat{e}_z \frac{\partial}{\partial z}$$

and

$$\vec{V} = v_r \hat{e}_r + v_\theta \hat{e}_\theta + v_z \hat{e}_z$$

2.20. Consider the one-dimensional motion of a fluid particle moving on the centerline of the converging channel, as shown in Fig. P2.20. The vertical dimension of the channel (and, thus, the area per unit depth) varies as

$$2y = 2h - h \sin\left(\frac{\pi}{2} \frac{x}{L}\right)$$

Assume that the flow is steady and incompressible. Use the integral form of the continuity equation to describe the velocity along the channel centerline. Also determine the corresponding axial acceleration. If u at $x = 0$ is 2 m/s, h is 1 m, and $L = 1$ m, calculate the acceleration when $x = 0$ and when $x = 0.5L$.

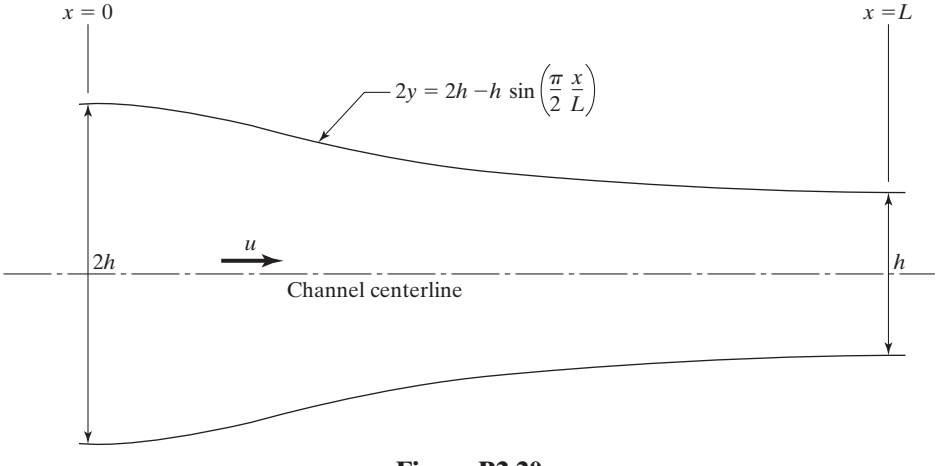

Figure P2.20

2.21. You are relaxing on an international flight when a terrorist leaps up and tries to take over the airplane. The crew refuses the demands of the terrorist and he fires his pistol, shooting a small hole in the airplane. Panic strikes the crew and other passengers. But you leap up and shout, "Do not worry! I am an engineering student and I know that it will take _____ seconds for the cabin pressure to drop from 0.5×10^5 N/m^2 to 0.25×10^5 N/m^2." Calculate how long it will take the cabin pressure to drop. Make the following assumptions:

(i) The air in the cabin behaves as a perfect gas: $\rho_c = \dfrac{p_c}{RT_c}$ where the subscript c stands for the cabin. $R = 287.05\ N \cdot \text{m/kg} \cdot \text{K}$. Furthermore, $T_c = 22°\text{C}$ and is constant for the whole time.

(ii) The volume of air in the cabin is 71.0 m^3. The bullet hole is 0.75 cm in diameter.

(iii) Air escapes through the bullet hole according to the equation: $\dot{m}_c = -0.040415 \dfrac{p_c}{\sqrt{T_c}}[A_{hole}]$ where p_c is in N/m^2, T_c is in K, A_{hole} is in m^2, and $\dot{m}_c$ is in kg/s.

2.22. The crew refuses the demands of a terrorist and he fires the pistol, shooting a small hole in the airplane. Panic strikes the crew and other passengers. But you leap up and shout, "Do not worry! I am an engineering student and I know that it will take _____ seconds for the cabin pressure to drop by a factor of two from 50×10^3 N/m^2 to 25×10^3 N/m^2." Calculate how long it will take the cabin pressure to drop. Make the following assumptions:

(i) The air in the cabin behaves as a perfect gas: $\rho_c = \dfrac{p_c}{RT_c}$ where the subscript c stands for the cabin. R = 287.05 N-m/kg-K for air Furthermore, $T_c = 300$ K and is constant for the whole time.

(ii) The volume of air in the cabin is 70 m^3. The bullet hole is 1.0 cm. diameter.

(iii) Air escapes through the bullet hole according to the equation: $\dot{m}_c = -0.02307 \dfrac{p_c}{\sqrt{T_c}}[A_{hole}]$ where p_c is in N/m^2, T_c is in K, A_{hole} is in m^2 and is in $\dot{m}_c$ kg/s.

2.23. Oxygen leaks slowly through a small orifice from an oxygen bottle. The volume of the bottle is 0.1 mm and the diameter of the orifice is 0.1 mm. Assume that the temperature in the tank remains constant at 18°C and that the oxygen behaves as a perfect gas. The mass flow rate is given by

$$\dot{m}_{O_2} = -0.6847 \frac{p_{O_2}}{\sqrt{R_{O_2} T_{O_2}}}[A_{hole}]$$

(The units are those of Prob. 2.21.) How long does it take for the pressure in the tank to decrease from 10 to 5 MPa?

2.24. Consider steady, low-speed flow of a viscous fluid in an infinitely long, two-dimensional channel of height h (i.e., the flow is fully developed; Fig. P2.24). Since this is a low-speed flow, we will assume that the viscosity and the density are constant. Assume the body forces

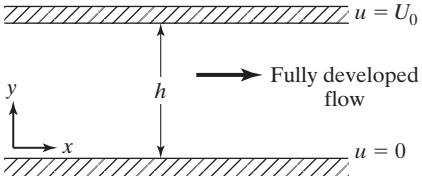

Figure P2.24

to be negligible. The upper plate (which is at $y = h$) moves in the x direction at the speed V_0, while the lower plate (which is at $y = 0$) is stationary.

(a) Develop expressions for u, v, and w (which satisfy the boundary conditions) as functions of U_0, h, μ, dp/dx, and y.

(b) Write the expression for dp/dx in terms of μ, U_0, and h, if $u = 0$ at $y = h/2$.

2.25. Consider steady, laminar, incompressible flow between two parallel plates, as shown in Fig. P2.25. The upper plate moves at velocity U_0 to the right and the lower plate is stationary. The pressure gradient is zero. The lower half of the region between the plates (i.e., $0 \le y \le h/2$) is filled with fluid of density ρ_1 and viscosity μ_1, and the upper half ($h/2 \le y \le h$) is filled with fluid of density ρ_2 and viscosity μ_2.

(a) State the condition that the shear stress must satisfy for $0 < y < h$.

(b) State the conditions that must be satisfied by the fluid velocity at the walls and at the interface of the two fluids.

(c) Obtain the velocity profile in each of the two regions and sketch the result for $\mu_1 > \mu_2$.

(d) Calculate the shear stress at the lower wall.

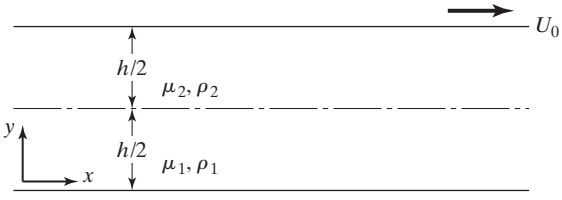

Figure P2.25

2.26. Consider the fully developed flow in a circular pipe, as shown in Fig. P2.26. The velocity u is a function of the radial coordinate only:

$$u = U_{\text{C.L.}}\left(1 - \frac{r^2}{R^2}\right)$$

where $U_{\text{C.L.}}$ is the magnitude of the velocity at the centerline (or axis) of the pipe. Use the integral form of the momentum equation [i.e., equation (2.13)] to show how the pressure drop per unit length dp/dx changes if the radius of the pipe were to be doubled while the mass flux through the pipe is held constant at the value m. Neglect the weight of the fluid in the control volume and assume that the fluid properties are constant.

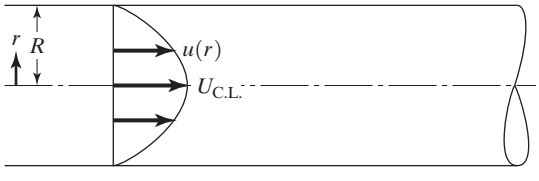

Figure P2.26

2.27. Velocity profiles are measured at the upstream end (surface 1) and at the downstream end (surface 2) of a rectangular control volume, as shown in Fig. P2.27. If the flow is incompressible, two dimensional, and steady, what is the drag coefficient for the airfoil? The vertical dimension H is *0.025c* and

$$C_d = \frac{d}{\frac{1}{2}\rho_\infty U_\infty^2 c}$$

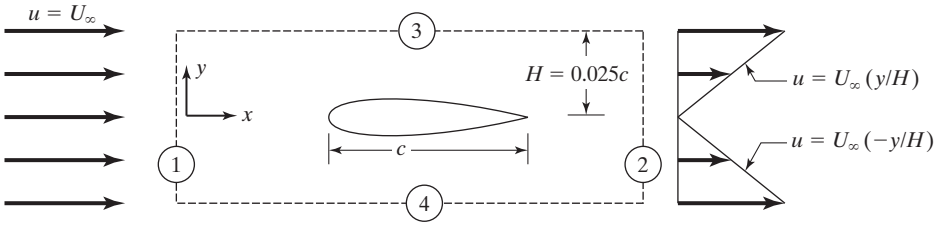

Figure P2.27

The pressure is p_∞ (a constant) over the entire surface of the control volume. (This problem is an extension of Problem 2.10.)

2.28. Velocity profiles are measured at the upstream end (surface 1) and at the downstream end (surface 2) of the control volume shown in Fig. P2.28. Surfaces 3 and 4 are streamlines. If the flow is incompressible, two dimensional, and steady, what is the drag coefficient for the airfoil? The vertical dimension H_D is $0.025c$. You will need to calculate the vertical dimension of the upstream station (H_U). The pressure is p_∞ (a constant) over the entire surface of the control volume. (This problem is an extension of Problem 2.11.)

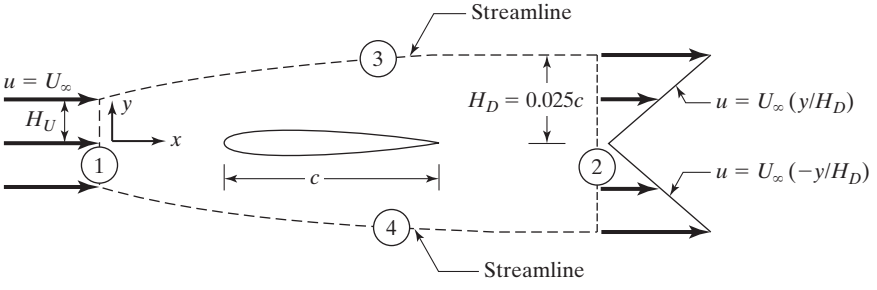

Figure P2.28

2.29. Velocity profiles are measured at the upstream end (surface 1) and at the downstream end (surface 2) of a rectangular control volume, as shown in Fig. P2.29. If the flow is incompressible, two dimensional, and steady, what is the drag coefficient? The vertical dimension $H = 0.025c$. The pressure is p_∞ (a constant) over the entire surface of the control volume. (This problem is a variation of Problem 2.27.) At the upstream end (surface 1), $\vec{V} = U_\infty \hat{i}$. At the downstream end of the control volume (surface 2),

$$0 \le y \le H \quad \vec{V} = \frac{U_\infty y}{H}\hat{i} + v\hat{j}$$

$$H \le y \le 2H \quad \vec{V} = U_\infty \hat{i} + v_0\hat{j}$$

$$-H \le y \le 0 \quad \vec{V} = -\frac{U_\infty y}{H}\hat{i} - v\hat{j}$$

$$-2H \le y \le -H \quad \vec{V} = U_\infty \hat{i} - v_0\hat{j}$$

where $v(x, y)$ and $v_0(x)$ are y components of the velocity, which are not measured.

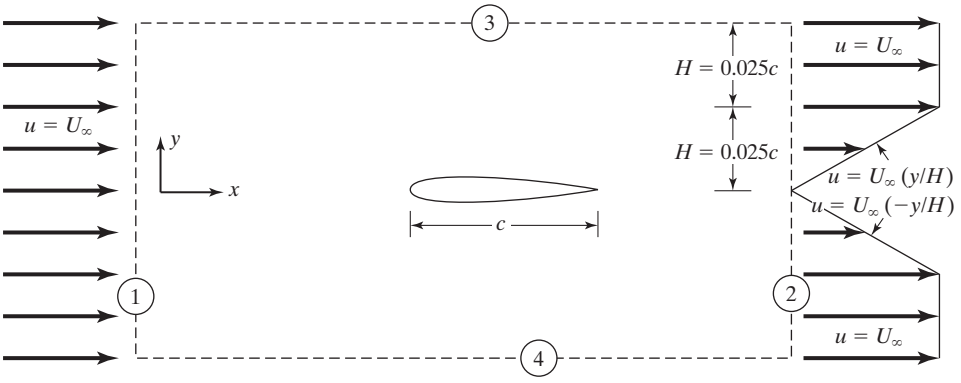

Figure P2.29

2.30. Velocity profiles are measured at the upstream end (surface 1) and at the downstream end (surface 2) of a rectangular control volume, as shown in Fig. P2.30. If the flow is incompressible, two dimensional, and steady, what is the drag coefficient for the airfoil? The vertical dimension H is $0.025c$. The pressure is p_∞ (a constant) over the entire surface of the control volume. (This problem is an extension of Problem 2.12.)

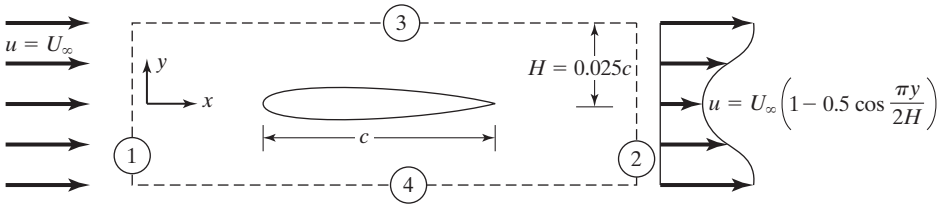

Figure P2.30

2.31. Velocity profiles are measured at the upstream end (surface 1) and at the downstream end (surface 2) of the control volume shown in Fig. P2.31. Surfaces 3 and 4 are streamlines. If the flow is incompressible, two dimensional, and steady, what is the drag coefficient for the airfoil? The vertical dimension at the downstream station (station 2) is $H_D = 0.025c$. The pressure is p_∞ (a constant) over the entire surface of the control volume. (This problem is an extension of Problem 2.13.)

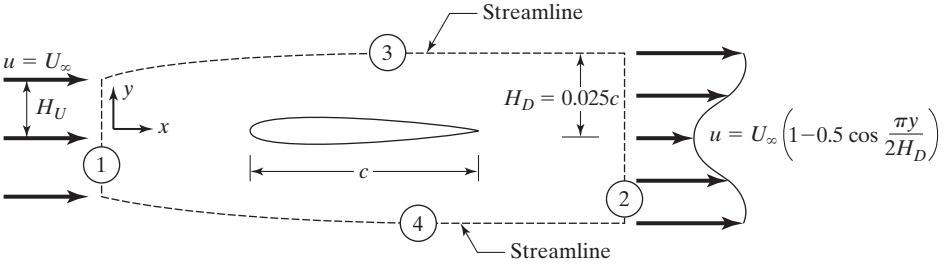

Figure P2.31

2.32. What are the free-stream Reynolds number [as given by equation (2.20)] and the free-stream Mach number [as given by equation (2.19)] for the following flows?

(a) A golf ball, whose characteristic length (i.e., its diameter) is 4.5 cm, moves through the standard sea level atmosphere at 60 m/s.

(b) Boeing 747 whose characteristic length is 70.6 m flies at an altitude of 10 km. with a speed of 250 m/s.

2.33. **(a)** An airplane has a characteristic chord length of 10.4 m. What is the free-stream Reynolds number for the Mach 3 flight at an altitude of 20 km?

(b) What is the characteristic free-stream Reynolds number of an airplane flying 160 mi/h in a standard sea-level environment? The characteristic chord length is 4.0 ft.

2.34. To illustrate the point that the two integrals in equation (2.21) are path dependent, consider a system consisting of air contained in a piston/cylinder arrangement (Fig. P2.34). The system of air particles is made to undergo two cyclic processes. Note that all properties (p, T, ρ, etc.) return to their original value (i.e., undergo a net change of zero), since the processes are cyclic.

(a) Assume that both cycles are reversible and determine (1) $\oint \delta q$ and (2) $\oint \delta w$ for each cycle.

(b) Describe what occurs physically with the piston/cylinder/air configuration during each leg of each cycle.

(c) Using the answers to part (a), what is the value of ($\oint \delta q - \oint \delta w$) for each cycle?

(d) Is the first law satisfied for this system of air particles?

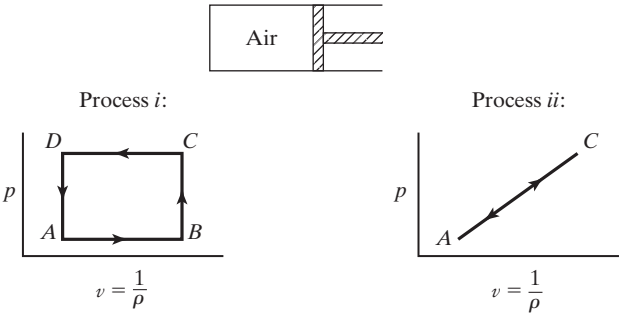

Figure P2.34

2.35. In Problem 2.25, the entropy change in going from A to C directly (i.e., following process *ii*) is

$$s_C - s_A$$

Going via B (i.e., following process *i*), the entropy change is

$$s_C - s_A = (s_C - s_B) + (s_B - s_A)$$

(a) Is the net entropy change ($s_C - s_A$) the same for both paths?

(b) Processes AC and ABC were specified to be reversible. What is $s_C - s_A$ if the processes are irreversible? Does $s_C - s_A$ depend on the path if the process is irreversible?

2.36. What assumptions were made in deriving equation (2.32)?

2.37. Show that for an adiabatic, inviscid flow, equation (2.32a) can be written as $ds/dt = 0$.

2.38. Consider the wing-leading edge of a Cessna 172 flying at 60 m/s through the standard atmosphere at 3 km altitude. Use the Mach number and total temperature relationship

$$\frac{T_t}{T_\infty} = 1 + \frac{\gamma - 1}{2} M_\infty^2$$

For air $\gamma = 1.4$, M_∞ is the free stream Mach number, T_∞ is the free stream temperature and T_t is the total temperature.

Mach number M_∞ is defined as

$$M_\infty = \frac{u_\infty}{a_\infty}$$

where a_∞ is the speed of sound, which is given as $\sqrt{\gamma RT_\infty}$. Find the total temperature and compare with the free-stream static temperature for this flow. Is convective heating likely to be a problem for this aircraft?

2.39. Consider the wing-leading edge of an SR-71 flying at Mach Number 2.0 at 25 km altitude. Using the Mach number and total temperature relationship

$$\frac{T_t}{T_\infty} = 1 + \frac{\gamma - 1}{2} M_\infty^2$$

For air $\gamma = 1.4$, M_∞ is the free stream Mach number, T_∞ is the free stream temperature and T_t is the total temperature.

Mach number M_∞ is defined as

$$M_\infty = \frac{u_\infty}{a_\infty}$$

where a_∞ is the speed of sound, which is given as $\sqrt{\gamma RT_\infty}$. Find the total temperature and compare with the free-stream static temperature for this flow. Is convective heating likely to be a problem for this aircraft? Find the total temperature and compare with the free-stream static temperature for this flow. Is convective heating likely to be a problem for this aircraft?

2.40. Start with the integral form of the energy equation for a one-dimensional, steady, adiabatic flow:

$$H_t = h + \tfrac{1}{2}U^2$$

and the equation for the entropy change for a perfect gas:

$$s - s_t = c_p \ln\frac{T}{T_t} - R \ln\frac{p}{p_t}$$

and develop the expression relating the local pressure to the stagnation pressure:

$$\frac{p}{p_{t1}} = \left(1 + \frac{\gamma - 1}{2} M^2\right)^{-\gamma(\gamma-1)}$$

Carefully note the assumptions made at each step of the derivation. Under what conditions is this valid?

REFERENCES

Brune GW, Rubbert PW, Nark TC. 1974. *A new approach to inviscid flow/boundary layer matching*. Presented at Fluid and Plasma Dynamics Conf., 7th, AIAA Pap. 74-601, Palo Alto, CA

Bushnell DM, Cary AM, Harris JE. 1977. Calculation methods for compressible turbulent boundary layers. *NASA SP-422*

Bushnell DM. 2006. Scaling: Wind tunnel to flight. *Annual Review of Fluid Mechanics*. 38:111–128

McMasters JH. 2007. Innovative approaches to testing and validation. AIAA Distinguished Lecture Series.

Schetz JA, Bowersox RDW. 2011. *Boundary Layer Analysis*. 2nd Ed. Reston, VA: AIAA

Schlichting H, Gersten K. 2000. *Boundary Layer Theory*. 8th Ed. Berlin: Springer

Schmitt V, Charpin F. 1979. Pressure distributions on the ONERA-M6-Wing at transonic Mach numbers, *AGARD AR* 138

White FM. 2005. *Viscous Fluid Flow*. 3rd Ed. New York: McGraw-Hill

Wilcox DC. 1998. *Turbulence Modeling for CFD*. 2nd Ed. La Cañada, CA: DCW Industries

3 DYNAMICS OF AN INCOMPRESSIBLE, INVISCID FLOW FIELD

Chapter Objectives

- Understand what is meant by inviscid flow, and why it is useful in aerodynamics
- Learn how to use Bernoulli's equation and how static and dynamic pressure relate to each other for incompressible flow
- Know the basic process in measuring (and correcting) air speed in an airplane
- Have a physical understanding of circulation and how it relates to aerodynamics
- Learn the assumptions required for potential flow
- Be able to use potential flow functions to analyze the velocities and pressures for various flow fields
- Understand how potential flow theory can be applied to an airplane

For many applications of aerodynamics (such as preliminary design of aircraft at cruise conditions), solutions of the inviscid flow field can provide important information (see Chapters 2 and 14 for more details). Furthermore, once the inviscid flow field has been defined, it can be used as boundary conditions for a thin, viscous boundary layer adjacent to the surface, which gives some additional assessment of viscous effects. For these reasons, the inviscid flow field is an important aspect in modern aerodynamics, even

though we have experimental and computational capabilities that can give us viscous results. Because of this, the analysis of the flow field done in this text will make use of a two-region flow model (one region in which the viscous forces are negligible, i.e., the inviscid region, and one region in which viscous forces cannot be neglected, i.e., the viscous boundary layer near the surface). This approach will allow us to gain a great deal of understanding of the aerodynamics of an airplane without having to conduct expensive or time-consuming experimental or computational projects.

3.1 INVISCID FLOWS

As we learned in Chapter 2, the shearing stresses for a fluid may be expressed as the product of the viscosity μ times the shearing stress velocity gradient (i.e., $\tau = \mu du/dy$). There are no real fluids for which the viscosity is zero; however, there are many situations where the product of the viscosity times the shearing velocity gradient is sufficiently small that the shear-stress terms may be neglected when compared to the other terms in the governing equations. We will use the term *inviscid flow* to describe the flow in those regions of the flow field where the viscous shear stresses are negligibly small. By using the term *inviscid flow* instead of *inviscid fluid*, we emphasize that the viscous shear stresses are small because the combined product of viscosity and the shearing velocity gradients has a small effect on the flow field and not that the fluid viscosity is zero. In fact, once the solution for the inviscid flow field is obtained, you may want to solve the boundary-layer equations and calculate the skin-friction drag on the configuration, as we will learn to do in Chapters 4 and 5.

In regions of the flow field where the viscous shear stresses are negligibly small (i.e., in regions where the flow is *inviscid*), equation (2.12) becomes

$$\rho\frac{du}{dt} = \rho\frac{\partial u}{\partial t} + \rho(\vec{V}\cdot\nabla)u = \rho f_x - \frac{\partial p}{\partial x} \tag{3.1a}$$

$$\rho\frac{dv}{dt} = \rho\frac{\partial v}{\partial t} + \rho(\vec{V}\cdot\nabla)v = \rho f_y - \frac{\partial p}{\partial y} \tag{3.1b}$$

$$\rho\frac{dw}{dt} = \rho\frac{\partial w}{\partial t} + \rho(\vec{V}\cdot\nabla)w = \rho f_z - \frac{\partial p}{\partial z} \tag{3.1c}$$

In vector form, the equation can be written as:

$$\frac{\overrightarrow{dV}}{dt} = \frac{\overrightarrow{\partial V}}{\partial t} + (\vec{V}\cdot\nabla)\vec{V} = \vec{f} - \frac{1}{\rho}\nabla p \tag{3.2}$$

No assumption has been made about density up to now, so these equations apply to a compressible flow as well as to an incompressible one. These equations, derived in 1755 by Leonhard Euler, are called the *Euler equations*.

In this chapter, we will develop the fundamental concepts for describing the flow around configurations in a low-speed stream. We will assume that the viscous boundary layer is thin and therefore has a negligible influence on the inviscid flow field (the effect of violating this assumption will be discussed when we compare theoretical results with data; flow separation is one example of a situation that would violate this assumption).

Then we will derive equations that will allow us to find the solution for the inviscid portion of the flow field (i.e., the flow outside the boundary layer).

3.2 BERNOULLI'S EQUATION

As we discussed in Chapters 1 and 2, the density is essentially constant when the gas particles in the flow field move at relatively low speeds, or when the fluid is a liquid. Typically, compressibility effects are negligible when the Mach number is less than $M_\infty \approx 0.3$. We will also only consider body forces that are conservative (such as is the case for gravity), which means the force vector can be written as the gradient of a scalar fields as:

$$\vec{f} = -\nabla F \tag{3.3}$$

Finally, we will limit ourselves to flows that are steady (or steady state), so that:

$$\frac{\overrightarrow{\partial V}}{\partial t} = 0$$

We can change our equations into a more useful form by using the vector identity:

$$(\vec{V} \cdot \nabla)\vec{V} = \nabla\left(\frac{U^2}{2}\right) - \vec{V} \times (\nabla \times \vec{V})$$

and then equation (3.2) (for the assumptions made above) becomes:

$$\nabla\left(\frac{U^2}{2}\right) + \nabla F + \frac{1}{\rho}\nabla p - \vec{V} \times (\nabla \times \vec{V}) = 0 \tag{3.4}$$

In these equations U is the scalar magnitude of the velocity, that is $U = |\vec{V}|$ (the subsequent applications leads us to use U rather than V for the velocity magnitude).

We can calculate the change in the magnitude of each of the terms in equation (3.4) along an arbitrary path whose length and direction are defined by the vector $\overrightarrow{ds}$. To do this, we take the dot product of each term in equation (3.4) and the vector $\overrightarrow{ds}$. The result is:

$$d\left(\frac{U^2}{2}\right) + dF + \frac{dp}{\rho} - \vec{V} \times (\nabla \times \vec{V}) \cdot \overrightarrow{ds} = 0 \tag{3.5}$$

Note that, since $\vec{V} \times (\nabla \times \vec{V})$ is a vector perpendicular to $\vec{V}$ (since by definition the cross product of two vectors is a vector perpendicular to the plane containing those two vectors), the last term is zero: (1) for any displacement $\overrightarrow{ds}$ if the flow is irrotational (i.e., where $\nabla \times \vec{V} = 0$), or (2) for a displacement along a streamline if the flow is rotational. Therefore, for a flow that is:

1. Inviscid,
2. Incompressible,
3. Steady,
4. Irrotational (or, if the flow is rotational, we consider only displacements along a streamline), and for which
5. The body forces are conservative,

the first integral of Euler's equation is

$$\int d\left(\frac{U^2}{2}\right) + \int dF + \int \frac{dp}{\rho} = \text{constant} \tag{3.6}$$

Since each term involves an exact differential, equation (3.6) becomes:

$$\frac{U^2}{2} + F + \frac{p}{\rho} = \text{constant} \tag{3.7}$$

As we mentioned in Chapter 2, the force potential most often encountered in aerodynamics is that due to gravity. We will take the z axis to be positive when pointing upward and normal to the surface of the earth; the force per unit mass due to gravity is directed downward and is of magnitude g. Therefore, referring to equation (3.3),

$$\vec{f} = -\frac{\partial F}{\partial z}\hat{k} = -g\hat{k}$$

so for gravity:

$$F = gz \tag{3.8}$$

Finally, inserting equation (3.8) into equation (3.7), the momentum equation becomes:

$$\frac{U^2}{2} + gz + \frac{p}{\rho} = \text{constant} \tag{3.9}$$

Equation (3.9) is known as *Bernoulli's equation*, which we previously discussed in Example 2.7. Bernoulli's equation shows that, for a flow which is inviscid, incompressible, steady, and irrotational with conservative body forces, the conservation of momentum equation reduces to this useful form, which is valid anywhere in the flow field. If the flow is rotational, then Bernoulli's equation is only valid along a streamline.

Because the density has been assumed constant, it is not necessary to include the energy equation in the procedure to solve for the velocity and pressure fields. In fact, equation (3.9), which is a form of the momentum equation, can be derived from equation (2.37) which is the integral form of the energy equation. As indicated in Example 2.7, there is an interrelation between the total energy of the flow and the flow work. In deriving equation (3.9), we assumed that dissipative mechanisms do not significantly affect the flow. As a corollary, Bernoulli's equation is valid only for flows where there is no mechanism for dissipation, such as viscosity. In thermodynamics, the flow process would be called *reversible*.

Notice that, if the acceleration is zero throughout the entire flow field, the pressure variation in a static fluid as given by equation (3.9) is identical to that given by equation (1.17). This is as it should be, since the five conditions required for Bernoulli's equation are valid for a static fluid.

For aerodynamic problems, the changes in potential energy are typically negligible. Neglecting the change in potential energy, equation (3.9) may be simplified as:

$$p + \tfrac{1}{2}\rho U^2 = \text{constant} \tag{3.10}$$

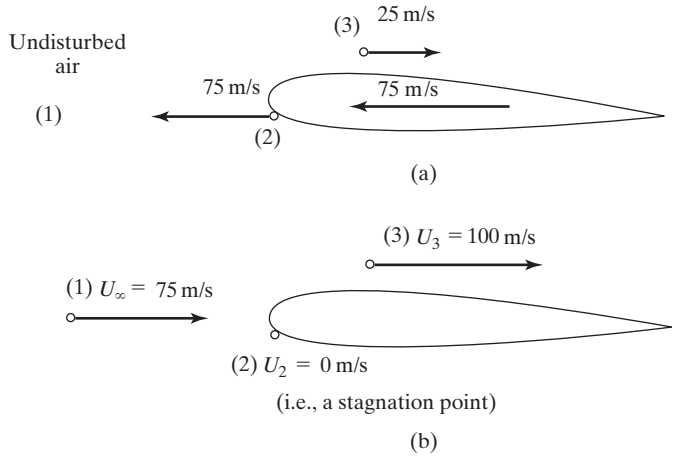

Figure 3.1 Velocity field around an airfoil: (a) ground-fixed coordinate system; (b) vehicle-fixed coordinate system.

This equation establishes a direct relation between the static pressure and the velocity. Thus, if either parameter is known, the other can be uniquely determined provided that the flow does not violate the assumptions listed above. Bernoulli's equation can be used to relate the flow at various points around the vehicle, including: (1) a point far from the vehicle (i.e., the free stream), (2) a point where the velocity relative to the vehicle is zero (i.e., a stagnation point), and (3) a general point just outside the boundary layer. The nomenclature for these points in the flow is illustrated in Fig. 3.1.

Recall from the discussion associated with Fig. 2.1 that the flow around a wing in a ground-fixed coordinate system is unsteady. Thus, we cannot apply Bernoulli's equation to the flow depicted in Fig. 3.1a. However, the flow can be made steady through the Gallilean transformation to the vehicle-fixed coordinate system of Fig. 2.2. In the vehicle-fixed coordinate system of Fig. 3.1b, we can apply Bernoulli's equation to points (1), (2), and (3) as:

$$p_\infty + \tfrac{1}{2}\rho_\infty U_\infty^2 = p_t = p_3 + \tfrac{1}{2}\rho_\infty U_3^2 \qquad \textbf{(3.11)}$$

Note that at point (2), the static pressure is equal to the total pressure since the velocity at this point is zero. The *stagnation* (or total) *pressure*, which is the constant of equation (3.10), is the sum of the free-stream static pressure (p_∞) and the free-stream *dynamic pressure* ($\frac{1}{2}\rho_\infty U_\infty^2$), which is designated by the symbol q_∞. Remember, however, that this statement is not true if the flow is compressible. Bernoulli's equation is telling us that there is a balance between static and dynamic pressure, with their sum always adding up to the total pressure. If a flow speeds up, then the dynamic pressure increases and the static pressure decreases. Conversely, if the flow slows down, then the dynamic pressure decreases and the static pressure increases.

EXAMPLE 3.1: Calculations made using Bernoulli's equation

The airfoil of Fig. 3.1a moves through the air at 75 m/s at an altitude of 2 km. The fluid at point 3 moves downstream at 25 m/s relative to the ground-fixed coordinate system. What are the values of the static pressure at points (1), (2), and (3)?

Solution: To solve this problem, we can superimpose a velocity of 75 m/s to the right so that the airfoil is at rest in the transformed coordinate system. In this vehicle-fixed coordinate system, the fluid "moves" past the airfoil, as shown in Fig. 3.1b. The velocity at point 3 is 100 m/s relative to the stationary airfoil, and the resultant flow is steady. p_∞ can be found directly in Table 1.2 using the static pressure for the standard day atmosphere:

$$\text{Point 1: } p_\infty = 79{,}501 \text{ N/m}^2$$

$$\text{Point 2: } p_t = p_\infty + \tfrac{1}{2}\rho_\infty U_\infty^2$$
$$= 79{,}501 \text{ N/m}^2 + \tfrac{1}{2}(1.0066 \text{ kg/m}^3)(75 \text{ m/s})^2$$
$$= 82{,}332 \text{ N/m}^2$$

$$\text{Point 3: } p_3 + \tfrac{1}{2}\rho_\infty U_3^2 = p_\infty + \tfrac{1}{2}\rho_\infty U_\infty^2$$
$$p_3 = 82{,}332 \text{ N/m}^2 - \tfrac{1}{2}(1.0066 \text{ kg/m}^3)(100 \text{ m/s})^2$$
$$= 77{,}299 \text{ N/m}^2$$

3.3 USE OF BERNOULLI'S EQUATION TO DETERMINE AIRSPEED

Equation (3.11) indicates that a Pitot-static probe (as shown in Fig. 3.2) can be used to measure a vehicle's airspeed. The Pitot head has no internal flow velocity, and the pressure in the Pitot tube is equal to the total pressure of the airstream (p_t). The purpose of the static ports is to sense the true static pressure of the free stream (p_∞). When the aircraft is operated through a large angle of attack range, the surface pressure may vary markedly. As a result, the pressure sensed at the static port may be significantly different from the free-stream static pressure, depending on the orientation of the aircraft. The total-pressure and the static-pressure lines can be attached to a differential pressure gage in order to determine the airspeed using the value of the free-stream density for the altitude at which the vehicle is flying:

$$U_\infty = \sqrt{\frac{2(p_t - p_\infty)}{\rho_\infty}}$$

As indicated in Fig. 3.2, the measurements of the local static pressure are often made using an orifice flush-mounted at the vehicle's surface. Although the orifice opening is located on the surface beneath the viscous boundary layer, the static pressure measurement is used to calculate the velocity at the (outside) edge of the

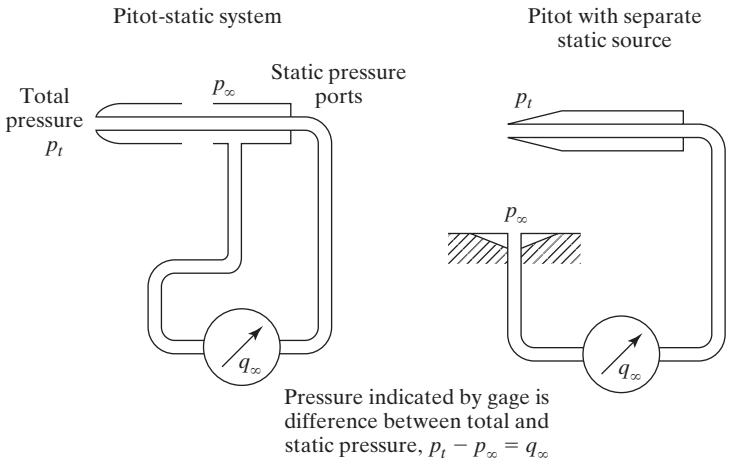

Figure 3.2 Pitot-static probes that can be used to "measure" air speed.

boundary layer (i.e., the velocity of the inviscid stream). Nevertheless, the use of Bernoulli's equation (which is valid only for an inviscid, incompressible flow) is appropriate because (as we discussed in Chapter 2) the analysis of the y-momentum equation reveals that the static pressure is essentially constant across a thin boundary layer. As a result, the value of the static pressure measured at the wall is essentially equal to the value of the static pressure in the inviscid stream (immediately outside the boundary layer).

There can be many conditions of flight where the airspeed indicator may not reflect the actual velocity of the vehicle relative to the air (one example is the aircraft orientation which was mentioned previously). These deviations in the measured velocity when compared with the actual velocity are corrected in a series of calculations, each defining a new airspeed definition. The definitions for the various terms associated with airspeed are as follows:

1. ***Indicated airspeed (IAS).*** Indicated airspeed is equal to the Pitot-static airspeed indicator reading as installed in the airplane without correction for airspeed indicator system errors but including the sea-level standard adiabatic compressible flow correction. (The latter correction is included in the calibration of the airspeed instrument dials.)
2. ***Calibrated airspeed (CAS).*** CAS is the result of correcting IAS for errors of the instrument and errors due to position or location of the pitot-static installation. The instrument error may be small by design of the equipment and is usually negligible in equipment that is properly maintained and cared for. The position error of the installation must be small in the range of airspeed involving critical performance conditions. Position errors are most usually confined to the static source in that the actual static pressure sensed at the static port may be different from the free airstream static pressure.

3. ***Equivalent airspeed (EAS).*** Equivalent airspeed is equal to the airspeed indicator reading corrected for position error, instrument error, and for adiabatic compressible flow for the particular altitude. The equivalent airspeed (EAS) is the flight speed in the standard day sea-level air mass that would produce the same free-stream dynamic pressure as flight at the true airspeed at the correct density altitude.
4. ***True airspeed (TAS).*** The true airspeed results when the EAS is corrected for density altitude. Since the airspeed indicator is calibrated for the dynamic pressures corresponding to air speeds at standard day sea-level conditions, we must account for variations in air density away from the standard day values. To relate EAS and TAS requires consideration that the EAS coupled with standard day sea-level density produces the same dynamic pressure as the TAS coupled with the actual air density of the flight condition. From this reasoning, the TAS can be calculated from:

$$\text{TAS} = \text{EAS}\sqrt{\frac{\rho_{\text{SL}}}{\rho}}$$

where

$$\begin{aligned} \text{TAS} &= \text{true airspeed} \\ \text{EAS} &= \text{equivalent airspeed} \\ \rho &= \text{actual air density} \\ \rho_{\text{SL}} &= \text{standard day sea-level air density.} \end{aligned}$$

The result shows that the EAS is a function of TAS and density altitude. Table 3.1 presents the EAS and the dynamic pressure as a function of TAS and altitude. The free-stream properties are those of the U.S. Standard Atmosphere (1976).

TABLE 3.1 Dynamic Pressure and EAS as a Function of Altitude and TAS

	Altitude					
	Sea level ($\rho = 1.0000\rho_{\text{SL}}$)		*10,000 m* ($\rho = 0.3376\rho_{\text{SL}}$)		*20,000 m* ($\rho = 0.0726\rho_{\text{SL}}$)	
TAS (km/h)	q_∞ (N/m^2)	*EAS* (km/h)	q_∞ (N/m^2)	*EAS* (km/h)	q_∞ (N/m^2)	*EAS* (km/h)
200	1.89×10^3	200	6.38×10^2	116.2	1.37×10^2	53.9
400	7.56×10^3	400	2.55×10^3	232.4	5.49×10^2	107.8
600	1.70×10^4	600	5.74×10^3	348.6	1.23×10^3	161.6
800	3.02×10^4	800	1.02×10^4	464.8	2.20×10^3	215.5
1000	4.73×10^4	1000	1.59×10^3	581.0	3.43×10^3	269.4

3.4 THE PRESSURE COEFFICIENT

Engineers often use experimental data or theoretical solutions for one flow condition to gain insight into the flow field that exists at another flow condition. Wind-tunnel data, where scale models are exposed to flow conditions that simulate the design flight environment, are used to gain insight to describe the full-scale flow field at other flow conditions. Therefore, it is desirable to present (experimental or theoretical) correlations in terms of dimensionless coefficients that depend only on the configuration geometry and the angle of attack. One such dimensionless coefficient is the *pressure coefficient*, which is defined as

$$C_p = \frac{p - p_\infty}{\frac{1}{2}\rho_\infty U_\infty^2} = \frac{p - p_\infty}{q_\infty} \tag{3.12}$$

In flight tests and wind-tunnel tests, pressure orifices, which are located flush mounted in the surface, sense the local static pressure at the wall [p in equation (3.12)]. These experimentally determined static pressures, which are located beneath the viscous boundary layer, can be presented as the dimensionless pressure coefficient using equation (3.12).

If we consider those flows for which Bernoulli's equation applies, we can express the pressure coefficient in terms of the nondimensionalized local velocity. Rearranging equation (3.11),

$$p_3 - p_\infty = \tfrac{1}{2}\rho_\infty U_\infty^2 \left[1 - \frac{U_3^2}{U_\infty^2} \right]$$

Treating point 3 as a general point in the flow field, we can write the pressure coefficient as

$$C_p = \frac{p - p_\infty}{\frac{1}{2}\rho_\infty U_\infty^2} = 1 - \frac{U^2}{U_\infty^2} \tag{3.13}$$

Now we can evaluate the pressure coefficient at the stagnation point, where the local velocity is zero, $C_p = C_{p,t} = 1.0$ for an incompressible flow. Notice that the stagnation-point value is independent of the free-stream flow conditions or the configuration geometry. The pressure coefficient has values that relate it to free stream pressure and velocity (for incompressible flow) according to Table 3.2, which is well worth remembering when working with pressure coefficients.

TABLE 3.2 Variation of Pressure Coefficient with Velocity and Static Pressure

Velocity	*Static Pressure*	*Pressure Coefficient*
$U < U_\infty$	$p > p_\infty$	$C_p > 0$
$U = U_\infty$	$p = p_\infty$	$C_p = 0$
$U > U_\infty$	$p < p_\infty$	$C_p < 0$

EXAMPLE 3.2: Flow in an open test-section wind tunnel

Consider flow in a subsonic wind tunnel with an open test section, which is a tunnel where the model is located in a section open to the room in which the tunnel is located. Thus, as shown in Fig. 3.3, the air accelerates from a reservoir (or stagnation chamber) where the velocity is essentially zero, through a converging nozzle, exhausting into the room (i.e., the test section) in a uniform, parallel stream of velocity U_∞. Using a barometer located on the wall in the room where the tunnel is located, we know that the barometric pressure in the room is 29.5 in Hg.

The model is a cylinder of infinite span (i.e., the dimension normal to the paper is infinite), which is simulated in a wind tunnel by having a cylinder that extends beyond the sides of the tunnel (or if the test section has walls, the cylinder would extend to the walls). There are two pressure orifices flush with the wind-tunnel walls and two orifices flush with the model surface, as shown in Fig. 3.3. The pressure sensed at orifice 3, which is at the stagnation point of the cylindrical model, is +2.0 in of water, gage. Furthermore, we know that the pressure coefficient for point 4 is −1.2.

What is the pressure sensed by orifice 1 in the stagnation chamber? What is the pressure sensed by orifice 2, located in the exit plane of the wind-tunnel nozzle? What is the free-stream velocity, U_∞? What is the static pressure at point 4? What is the velocity of an air particle just outside the boundary layer at point 4?

In working this example, we will assume that the variation in the static pressure across the boundary layer is negligible. Thus, as will be discussed in Section 4.1, the static pressure at the wall is approximately equal to the static pressure at the edge of the boundary layer.

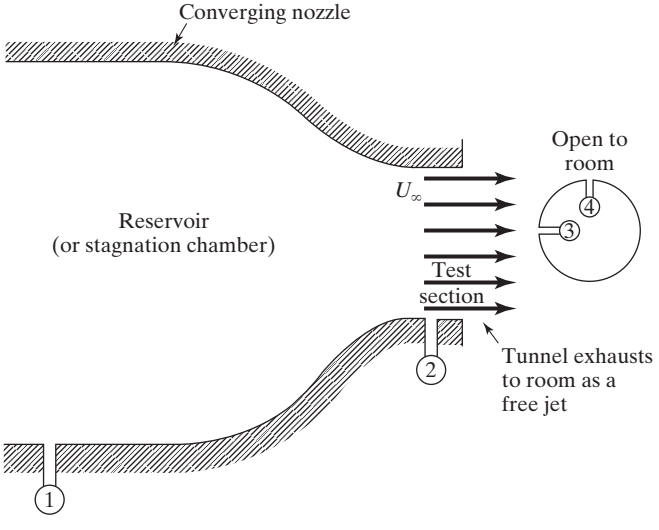

Figure 3.3 Open test-section wind tunnel used in Example 3.2.

Solution: As discussed in Chapter 1, the standard atmospheric pressure at sea level is defined as that pressure which can support a column of mercury 760 mm high (also equal to 2116.22 lbf/ft^2). Therefore, an equivalency statement may be written:

$$760 \text{ mm Hg} = 29.92 \text{ in Hg} = 2116.22 \text{ lbf/ft}^2$$

Since the barometric pressure is 29.5 in Hg, the pressure in the room is

$$p_{\text{room}} = 29.5 \text{ in Hg}\left(\frac{2116.22 \text{ lbf/ft}^2/\text{atm}}{29.92 \text{ in Hg/atm}}\right) = 2086.51 \text{ lbf/ft}^2$$

Furthermore, since the nozzle exhausts into the room at subsonic speeds and since the streamlines are essentially straight (so that there is no pressure variation normal to the streamlines), the pressure in the room is equal to the free-stream static pressure for the test section (p_∞) and is equal to the static pressure in the exit plane of the nozzle (p_2).

$$p_{\text{room}} = p_\infty = p_2 = 2086.51 \text{ lbf/ft}^2$$

We will assume that the temperature changes are negligible and, therefore, the free-stream density is reduced proportionally from the standard atmosphere's sea-level value:

$$\rho_\infty = (2086.51 \text{ lbf/ft}^2)\left(\frac{0.002376 \text{ slug/ft}^3}{2116.22 \text{ lbf/ft}^2}\right) = 0.00234 \text{ slug/ft}^3$$

Since the pressure measurement sensed by orifice 3 is given as a gage pressure, it is the difference between the stagnation pressure and the free-stream pressure, that is,

$$\begin{aligned} p_3 - p_\infty &= 2 \text{ in } H_2O, \text{ gage}\left(\frac{2116.22 \text{ lbf/ft}^2/\text{atm}}{407.481 \text{ in } H_2O/\text{atm}}\right) \\ &= 10.387 \text{ lbf/ft}^2, \text{ gage} \end{aligned}$$

where 407.481 in H_2O is the column of water equivalent to 760 mm Hg if the density of water is 1.937 slugs/ft^3. But since $p_3 = p_t$, we can rearrange Bernoulli's equation:

$$p_3 - p_\infty = p_t - p_\infty = \tfrac{1}{2}\rho_\infty U_\infty^2$$

Equating these expressions and solving for U_∞,

$$U_\infty = \sqrt{\frac{2(10.387 \text{ lbf/ft}^2)}{0.00234 \text{ lbf} \cdot \text{s}^2/\text{ft}^4}} = 94.22 \text{ ft/s}$$

Since $\frac{1}{2}\rho_\infty U_\infty^2$ is the dynamic pressure, we can rearrange the definition for the pressure coefficient to find the static pressure at point 4:

$$\begin{aligned} p_4 &= p_\infty + C_{p4} q_\infty = 2086.51 + (-1.2)(10.387) \\ &= 2074.05 \text{ lbf/ft}^2 \end{aligned}$$

Since we want to know the velocity of the air particles just outside the boundary layer above orifice 4, Bernoulli's equation is applicable, and we can use equation (3.13):

$$\frac{U_4^2}{U_\infty^2} = 1 - C_{p4} = 2.2$$

Therefore, $U_4 = 139.75$ ft/s.

3.5 CIRCULATION

One of the most important concepts we will use in describing aerodynamic flow is circulation. *Circulation* is defined as the line integral of the velocity around any closed curve. Referring to the closed curve C of Fig. 3.4, the circulation is given by:

$$-\Gamma = \oint_C \vec{V} \cdot \overrightarrow{ds} \tag{3.14}$$

where $\vec{V} \cdot \overrightarrow{ds}$ is the scalar product of the velocity vector and the differential vector length along the path of integration. As indicated by the circle through the integral sign, the integration is carried out for the complete closed path. The path of the integration is counterclockwise, so the area enclosed by the curve C is always on the left. A negative sign is used in equation (3.14) for convenience in the subsequent application to lifting-surface aerodynamics.

Consider the circulation around a small, square element in the xy plane, as shown in Fig. 3.5a. Integrating the velocity components along each of the sides and proceeding counterclockwise (i.e., keeping the area on the left of the path),

$$-\Delta\Gamma = u\,\Delta x + \left(v + \frac{\partial v}{\partial x}\Delta x\right)\Delta y - \left(u + \frac{\partial u}{\partial y}\Delta y\right)\Delta x - v\,\Delta y$$

Simplifying yields

$$-\Delta\Gamma = \left(\frac{\partial v}{\partial x} - \frac{\partial u}{\partial y}\right)\Delta x\,\Delta y$$

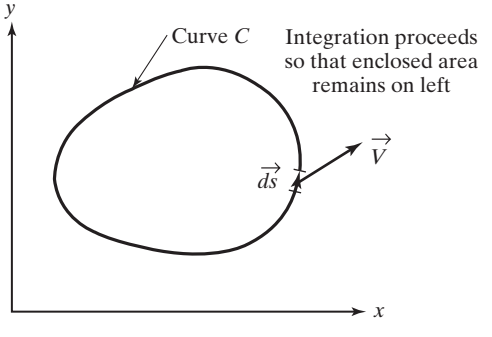

Figure 3.4 Concept of circulation.

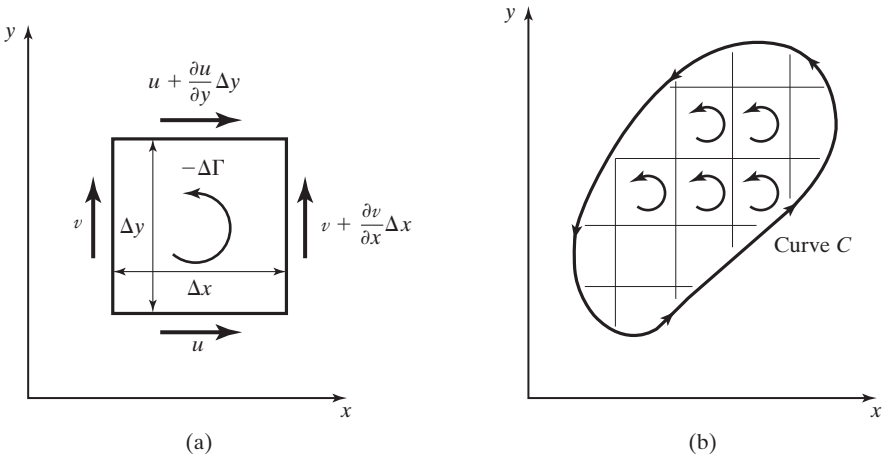

Figure 3.5 Circulation for elementary closed curves: (a) rectangular element; (b) general curve *C*.

This procedure can be extended to calculate the circulation around a general curve *C* in the *xy* plane, such as that of Fig. 3.5b. The result for this general curve in the *xy* plane is

$$-\Gamma = \oint_C (u\,dx + v\,dy) = \iint_A \left(\frac{\partial v}{\partial x} - \frac{\partial u}{\partial y}\right) dx\,dy \tag{3.15}$$

Equation (3.15) represents *Green's lemma* for the transformation from a line integral to a surface integral in two-dimensional space. The transformation from a line integral to a surface integral in three-dimensional space is governed by *Stokes's theorem*:

$$\oint_C \vec{V} \cdot \overrightarrow{ds} = \iint_A (\nabla \times \vec{V}) \cdot \hat{n}\,dA \tag{3.16}$$

where $\hat{n}\,dA$ is a vector normal to the surface, positive when pointing outward from the enclosed volume, and equal in magnitude to the incremental surface area (see Fig. 3.6). Note that equation (3.15) is a planar simplification of the more general vector equation, which is given in equation (3.16). In words, the integral of the normal component of the curl of the velocity vector over any surface *A* is equal to the line integral of the tangential component of the velocity around the curve *C* which bounds *A*. Stokes's

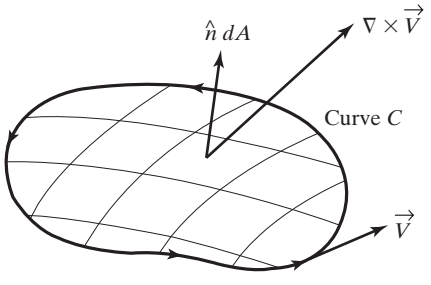

Figure 3.6 Nomenclature for Stokes's theorem.

theorem is valid when A represents a simply connected region in which $\vec{V}$ is continuously differentiable. (A simply connected region is one where any closed curve can be shrunk to a point without leaving the simply connected region.) Thus, equation (3.16) is not valid if the area A contains regions where the velocity is infinite.

Aerodynamics Concept Box: What Does Circulation Mean?

Circulation as defined in equation (3.14) can be a little difficult to understand, so we will take a short break from the derivation to see if we can develop a physical understanding of circulation. If we look at the integral that defines circulation, we see:

$$-\Gamma = \oint_C \vec{V} \cdot \overrightarrow{ds}$$

which is a line integral around a contour C (see below), with a differential length along the contour, $\overrightarrow{ds}$, a velocity vector on the contour, $\vec{V}$, and in equation (3.16) there is the area inside C, which is A. Remember that the contour is fictitious (it does not really exist in the flow)!

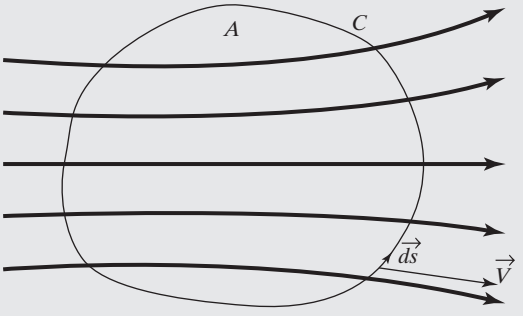

So, what is the integral asking us to do? First, there is a scalar (dot) product operation to perform, $\vec{V} \cdot \overrightarrow{ds}$. A scalar product can be found by $\vec{V} \cdot \overrightarrow{ds} = |\vec{V}||\overrightarrow{ds}|\cos\theta$, where θ is the angle between the two vectors. When will the scalar product contribute the most to the integral? Since the magnitudes are multiplied by the $\cos\theta$, the maximum contribution occurs when the two vectors are aligned ($\theta = 0$) and the minimum contribution occurs when the two vectors are perpendicular to each other ($\theta = \pi/2$). So, circulation happens when the velocity vector is along the path of integration, C, and it doesn't happen when the velocity vector is perpendicular to C.

If we look at the streamlines shown above (which are parallel and to the right as they approach the contour but spread out as they leave the contour), there would be very little circulation created at the left and right portions of C since the velocity is nearly normal to the contour. There would be circulation created at the top and bottom of the contour, however, but since the vectors are aligned at the bottom ($\theta = 0$ and $\cos\theta = 1$), but opposite to each other at the top ($\theta = \pi$ and $\cos\theta = -1$), it is possible that the top and bottom contributions could easily cancel each other out. So, when would there be a non-zero circulation? This can only happen if the flow has some net curvature within the contour C. Or, in other words, circulation can only exist if the flow is turned. Therefore, the physical meaning of circulation is that there is some net turning of the flow in the region of the contour of integration. This can happen in aerodynamics when there is flow over an airfoil at angle of attack or with camber (or both), which we will discuss in greater detail in Chapter 6. Another situation when the flow is turned is when flaps are deflected, which will be discussed in Chapters 7 and 13.

3.6 IRROTATIONAL FLOW

By using Stokes's theorem, equation (3.16), we can see that if the curl of $\vec{V}$ (i.e., $\nabla \times \vec{V}$) is zero at all points in the region bounded by C, then the line integral of $\vec{V} \cdot \overrightarrow{ds}$ around the closed path is also zero. That is, if:

$$\nabla \times \vec{V} = \begin{vmatrix} \hat{i} & \hat{j} & \hat{k} \\ \frac{\partial}{\partial x} & \frac{\partial}{\partial y} & \frac{\partial}{\partial z} \\ u & v & w \end{vmatrix} = \left(\frac{\partial w}{\partial y} - \frac{\partial v}{\partial z}\right)\hat{i} - \left(\frac{\partial w}{\partial x} - \frac{\partial u}{\partial z}\right)\hat{j} + \left(\frac{\partial v}{\partial x} - \frac{\partial u}{\partial y}\right)\hat{k} = 0 \quad \textbf{(3.17)}$$

and the flow contains no singularities, the flow is said to be *irrotational*. The definition of circulation and Stokes's theorem [equations (3.14) and (3.16), respectively] lead us to the conclusion that an irrotational flow cannot have any circulation:

$$-\Gamma = \oint_C \vec{V} \cdot \overrightarrow{ds} = \underbrace{\iint_A (\nabla \times \vec{V}) \cdot \hat{n} dA}_{=0 \text{ for irrotational flow}} = 0$$

For this irrotational velocity field, the line integral

$$\int \vec{V} \cdot \overrightarrow{ds}$$

is independent of path. A necessary and sufficient condition that the integral be independent of path is that the curl of $\vec{V}$ is everywhere zero. Therefore, the value of the integral only depends on its limits. However, a line integral can be independent of the path of integration only if the integrand is an exact differential, such as:

$$\vec{V} \cdot \overrightarrow{ds} = d\phi \quad \textbf{(3.18)}$$

where $d\phi$ is an exact differential. Expanding equation (3.18) in Cartesian coordinates gives us:

$$u\,dx + v\,dy + w\,dz = \frac{\partial \phi}{\partial x}dx + \frac{\partial \phi}{\partial y}dy + \frac{\partial \phi}{\partial z}dz$$

We have now shown that:

$$\vec{V} = \nabla \phi \quad \textbf{(3.19)}$$

So, a *velocity potential* $\phi(x, y, z)$ exists for this flow such that the partial derivative of ϕ in any direction is the velocity component in that direction. That equation (3.19) is a valid representation of the velocity field for an irrotational flow can be seen by noting that:

$$\nabla \times \nabla\phi = \begin{vmatrix} \hat{i} & \hat{j} & \hat{k} \\ \frac{\partial}{\partial x} & \frac{\partial}{\partial y} & \frac{\partial}{\partial z} \\ \frac{\partial \phi}{\partial x} & \frac{\partial \phi}{\partial y} & \frac{\partial \phi}{\partial z} \end{vmatrix} = \left(\frac{\partial}{\partial y}\frac{\partial \phi}{\partial z} - \frac{\partial}{\partial z}\frac{\partial \phi}{\partial y}\right)\hat{i} - \left(\frac{\partial}{\partial x}\frac{\partial \phi}{\partial z} - \frac{\partial}{\partial z}\frac{\partial \phi}{\partial x}\right)\hat{j} + \left(\frac{\partial}{\partial x}\frac{\partial \phi}{\partial y} - \frac{\partial}{\partial y}\frac{\partial \phi}{\partial x}\right)\hat{k} = 0 \quad \textbf{(3.20)}$$

As long as ϕ and its first derivatives are continuous, then the derivative order does not matter. That is, the curl of any gradient is necessarily zero. That is why an irrotational flow is also called a *potential flow*.

3.7 KELVIN'S THEOREM

Having defined the necessary and sufficient condition for the existence of a flow that has no circulation, we can examine a theorem first demonstrated by Lord Kelvin in 1869. For an inviscid, barotropic flow with conservative body forces, the circulation around a closed fluid line remains constant with respect to time. A barotropic flow (sometimes called a homogeneous flow) is one in which the density depends only on the pressure, $\rho = \rho(p)$.

The time derivative of the circulation along a closed fluid line (i.e., a fluid line that is composed of the same fluid particles) is found from equation (3.14) as:

$$-\frac{d\Gamma}{dt} = \frac{d}{dt}\left(\oint_C \vec{V}\cdot\overrightarrow{ds}\right) = \oint_C \frac{\overrightarrow{dV}}{dt}\cdot \mathrm{n}\,\overrightarrow{ds} + \oint_C \vec{V}\cdot\frac{d}{dt}\left(\overrightarrow{ds}\right) \tag{3.21}$$

Euler's equation, equation (3.2), which is the momentum equation for an inviscid flow, is given by:

$$\frac{\overrightarrow{dV}}{dt} = \vec{f} - \frac{1}{\rho}\nabla p$$

Using the constraint that the body forces are conservative (as is true for gravity, the body force of most interest in aerodynamics), we have:

$$\vec{f} = -\nabla F$$

and

$$\frac{\overrightarrow{dV}}{dt} = -\nabla F - \frac{1}{\rho}\nabla p \tag{3.22}$$

where F is the body-force potential. Since we are following a particular fluid particle, the order of time and space differentiation does not matter, which gives us:

$$\frac{d}{dt}\left(\overrightarrow{ds}\right) = d\left(\frac{\overrightarrow{ds}}{dt}\right) = \overrightarrow{dV} \tag{3.23}$$

Substituting equations (3.22) and (3.23) into equation (3.21) yields

$$\frac{d}{dt}\oint_C \vec{V}\cdot\overrightarrow{ds} = -\oint_C dF - \oint_C \frac{dp}{\rho} + \oint_C \vec{V}\cdot\overrightarrow{dV} \tag{3.24}$$

Since the density is a function of the pressure only, all the terms on the right-hand side involve exact differentials. The integral of an exact differential around a closed curve is zero, so equation (3.24) reduces to:

$$\frac{d}{dt}\left(\oint_C \vec{V}\cdot\overrightarrow{ds}\right) = 0 \tag{3.25}$$

Or, as given in the statement of Kelvin's theorem, the circulation remains constant along the closed fluid line for a flow with conservative body forces.

3.7.1 Implication of Kelvin's Theorem

If the fluid starts from rest, or if the velocity of the fluid in some region is uniform and parallel, the rotation in this region is zero. Kelvin's theorem leads to the important conclusion that the entire flow remains irrotational in the absence of viscous forces and of discontinuities provided that the flow is barotropic and the body forces can be described by a potential function.

In many flow problems (including most of those of interest in aerodynamics), the undisturbed, free-stream flow is a uniform parallel flow in which there are no shear stresses. Kelvin's theorem implies that although the fluid particles in the subsequent flow patterns may follow curved paths, the flow remains irrotational except in those regions where the dissipative viscous forces are an important factor. This concept is important for developing airfoil theory, and will be discussed further in Chapter 6.

3.8 INCOMPRESSIBLE, IRROTATIONAL FLOW AND THE VELOCITY POTENTIAL

Kelvin's theorem states that for an inviscid flow having a conservative force field, the circulation must be constant around a path that moves so as always to touch the same particles and which contains no singularities. Thus, since the free-stream flow is irrotational, a barotropic flow around the vehicle will remain irrotational provided that viscous effects are not important. For an irrotational flow, the velocity may be expressed in terms of a potential function in two dimensions as:

$$\vec{V} = u\hat{i} + v\hat{j} = \nabla\phi = \frac{\partial\phi}{\partial x}\hat{i} + \frac{\partial\phi}{\partial y}\hat{j} \tag{3.19}$$

Equating the two vectors yields important relationships between the velocity components and the velocity potential: $u = \partial\phi/\partial x$ and $v = \partial\phi/\partial y$. For relatively low-speed flows (i.e., incompressible flows), the continuity equation is

$$\nabla \cdot \vec{V} = 0 \tag{2.4}$$

Notice that equation (2.4) is valid for a three-dimensional flow, as well as a two-dimensional flow, but in two dimensions it can be written as:

$$\frac{\partial u}{\partial x} + \frac{\partial v}{\partial y} = 0$$

Combining equations (2.4) and (3.19), we find that for an incompressible, irrotational flow,

$$\frac{\partial u}{\partial x} + \frac{\partial v}{\partial y} = \frac{\partial}{\partial x}\left(\frac{\partial\phi}{\partial x}\right) + \frac{\partial}{\partial y}\left(\frac{\partial\phi}{\partial y}\right) = \frac{\partial^2\phi}{\partial x^2} + \frac{\partial^2\phi}{\partial y^2} = \nabla^2\phi = 0 \tag{3.26}$$

Therefore, the governing equation, which is known as *Laplace's equation*, is a linear, second-order partial differential equation of the elliptic type.

3.8.1 Irrotational Condition

Now that we have found that the velocity potential used in the continuity equation for incompressible flow yields Laplace's equation, we will also see what happens when we use the velocity potential in the irrotational flow condition. The irrotational flow condition [equation (3.17)] states that the curl of the velocity vector must be zero. Using the definition of the curl operator, vorticity can be calculated and set to zero to obtain the irrotational flow condition:

$$\nabla \times \vec{V} = \begin{vmatrix} \hat{i} & \hat{j} & \hat{k} \\ \dfrac{\partial}{\partial x} & \dfrac{\partial}{\partial y} & \dfrac{\partial}{\partial z} \\ u & v & w \end{vmatrix} = \left(\frac{\partial w}{\partial y} - \frac{\partial v}{\partial z}\right)\hat{i} - \left(\frac{\partial w}{\partial x} - \frac{\partial u}{\partial z}\right)\hat{j} + \left(\frac{\partial v}{\partial x} - \frac{\partial u}{\partial y}\right)\hat{k}$$

$$= \xi_x \hat{i} + \xi_y \hat{j} + \xi_z \hat{k} = \vec{\xi} = 0$$

where ξ_x, ξ_y, and ξ_z are the vorticity components and $\vec{\xi}$ is the vorticity vector. In two dimensions, all z derivatives and w velocities are zero, resulting in a straight-forward relationship for irrotational flow:

$$\frac{\partial v}{\partial x} - \frac{\partial u}{\partial y} = 0$$

Substituting the velocity potential relations into the irrotational flow condition results in:

$$\frac{\partial v}{\partial x} - \frac{\partial u}{\partial y} = \frac{\partial}{\partial x}\left(\frac{\partial \phi}{\partial y}\right) - \frac{\partial}{\partial y}\left(\frac{\partial \phi}{\partial x}\right) = 0$$

as long as the velocity potential and its first derivatives are continuous functions. Since the irrotational condition is identically satisfied by the velocity potential, the velocity potential must represent an irrotational flow, something which will be very important in the development of potential flow theory. In fact, the velocity potential was originally defined in order to identically satisfy the irrotational flow condition so that Laplace's equation would be the governing equation for two-dimensional, incompressible, irrotational flow.

3.8.2 Boundary Conditions

Within certain constraints on geometric slope continuity, a bounded, simply connected velocity field is uniquely determined by the distribution on the flow boundaries either of the normal component of the total velocity $\nabla\phi \cdot \hat{n}$ or of the total potential ϕ. These boundary-value problems are respectively designated Neumann or Dirichlet problems. For applications in this book, the Neumann formulation will be used since most practical cases involve prescribed normal velocity boundary conditions. Specifically, the flow tangency requirement associated with inviscid flow past a solid body is expressed mathematically as

$$\nabla\phi \cdot \hat{n} = 0$$

because the velocity component normal to the surface is zero at a solid surface.

Aerodynamics Concept Box: What Is Vorticity?

Just as circulation is a difficult concept to understand, so is the concept of vorticity. If we look at the partial derivative terms in the vorticity equation [equation (3.17)], we will start to understand the physical meaning of vorticity. If we just consider two-dimensional flow, the vorticity is given by

$$\vec{\xi} = \nabla \times \vec{V} = \left(\frac{\partial v}{\partial x} - \frac{\partial u}{\partial y} \right) \hat{k}$$

The terms that are important are $\partial v/\partial x$ and $\partial u/\partial y$, which represent the change in velocity acting on the edges of a fluid element, as shown below. If there are net changes in velocity in both x and y directions, then the fluid element will typically rotate (physically), which is represented by a non-zero term in the vorticity equation (mathematically, as long as we remember the minus sign).

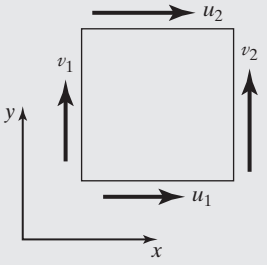

In other words, the vorticity, ξ, is directly related to the fluid element rotational velocity—in fact, the vorticity turns out to be twice the rotational velocity of the fluid element, $\xi = 2\omega$. If the flow field does not have any vorticity (which means that the fluid elements are not rotating), then the flow is called irrotational (shown below). If the flow field does have vorticity, then the flow is called rotational. It is very important at this point not to confuse rotation of a fluid element with curvature (or turning) of the flow—these are two separate (although related) concepts. It is theoretically possible for a turning flow to be irrotational, just as it is possible for a flow following a straight path to be rotational.

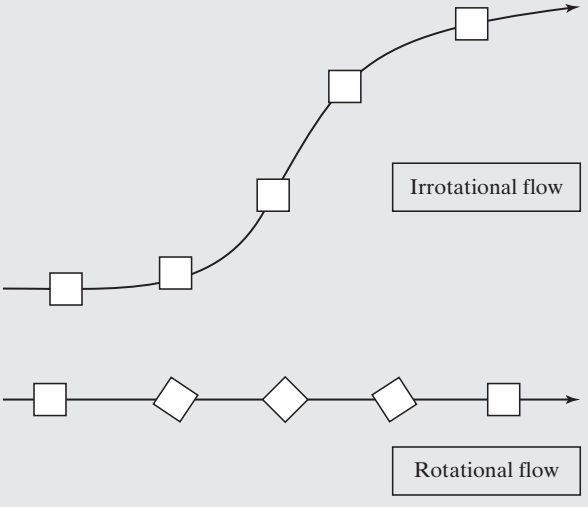

3.9 STREAM FUNCTION IN A TWO-DIMENSIONAL, INCOMPRESSIBLE FLOW

Just as the condition of irrotationality is the necessary and sufficient condition for the existence of a velocity potential, so the equation of continuity for an incompressible, two-dimensional flow is the necessary and sufficient condition for the existence of a stream function. The flow needs to be two dimensional only in the sense that it requires only two spatial coordinates to describe the motion. Therefore, stream functions exist both for plane flow and for axially symmetric flow. You should keep in mind that stream functions can exist for compressible, two-dimensional flows if they are steady, although we will not be using stream functions for those purposes. Stream functions can also exist for rotational flows, which makes them useful in describing laminar boundary layer flows.

Examining the continuity equation for an incompressible, two-dimensional flow in Cartesian coordinates [equation (2.4)],

$$\nabla \cdot \vec{V} = \frac{\partial u}{\partial x} + \frac{\partial v}{\partial y} = 0$$

A stream function, ψ, is defined with velocity components given by:

$$u = \frac{\partial \psi}{\partial y} \tag{3.27a}$$

$$v = -\frac{\partial \psi}{\partial x} \tag{3.27b}$$

We can easily show that the stream function identically satisfies continuity since:

$$\frac{\partial u}{\partial x} + \frac{\partial v}{\partial y} = \frac{\partial}{\partial x}\left(\frac{\partial \psi}{\partial y}\right) + \frac{\partial}{\partial y}\left(-\frac{\partial \psi}{\partial x}\right) = 0$$

as long as the stream function and its first derivatives are continuous. A corollary to this observation is that the existence of a stream function is a necessary condition for a physically possible flow (i.e., one that satisfies the continuity equation).

Since ψ is a point function where $\psi = \psi(x,y)$, the differential of ψ is:

$$d\psi = \frac{\partial \psi}{\partial x} dx + \frac{\partial \psi}{\partial y} dy$$

Substituting equation (3.27) into this differential yields:

$$d\psi = -v\, dx + u\, dy \tag{3.28a}$$

Since a streamline is a curve whose tangent at every point coincides with the direction of the velocity vector (or the slope of the curve must equal the local velocity component ratio), the definition of a streamline in a two-dimensional flow is

$$\frac{dy}{dx} = \frac{v}{u}$$

therefore, we know that:

$$\frac{dx}{u} = \frac{dy}{v}$$

Rearranging, we can see that:

$$u\,dy - v\,dx = 0 \tag{3.28b}$$

along a streamline. Equating equations (3.28a) and (3.28b), we find that:

$$d\psi = udy - vdx = 0$$

along a streamline. Therefore, the change in ψ is zero along a streamline or, equivalently, ψ is constant along a streamline. A corollary statement is that lines of constant ψ are streamlines of the flow.

Referring to Fig. 3.7, it is clear that the product $v(-dx)$ represents the volumetric flow rate per unit depth across AO and the product $u\,dy$ represents the volumetric flow rate per unit depth across OB. By continuity, the fluid crossing lines AO and OB must cross the curve AB. Therefore, $d\psi$ is a measure of the volumetric flow rate per unit depth across AB. A line can be passed through A for which $\psi = \psi_A$ (a constant), while a line can be passed through B for which $\psi = \psi_B = \psi_A + d\psi$ (a different constant). The difference $d\psi$ is the volumetric flow rate (per unit depth) between the two streamlines. It follows, then, that the volumetric flow rate (per unit depth) between any two points in the flow is the difference between the values of the stream function at the two points of interest, $Q = d\psi$.

The fact that the flow is always tangent to a streamline and has no component of velocity normal to it has an important consequence. Any streamline in an inviscid flow can be replaced by a solid boundary of the same shape without affecting the remainder of the flow pattern. We will make good use of this observation in our applications of potential flow.

The velocity components for a two-dimensional flow in cylindrical coordinates can also be calculated using a stream function as:

$$v_r = \frac{1}{r}\frac{\partial \psi}{\partial \theta} \qquad v_\theta = -\frac{\partial \psi}{\partial r} \tag{3.29}$$

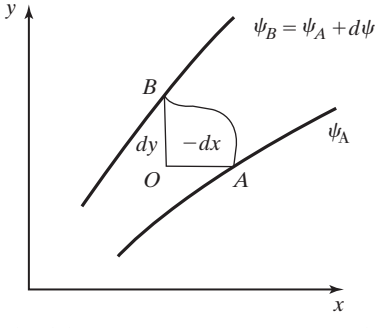

Figure 3.7 The significance of the stream function.

If a two-dimensional flow is irrotational, we know:

$$\nabla \times \vec{V} = \frac{\partial v}{\partial x} - \frac{\partial u}{\partial y} = 0$$

Then writing the velocity components in terms of the stream function, as defined in equation (3.27), we find that:

$$\frac{\partial v}{\partial x} - \frac{\partial u}{\partial y} = \frac{\partial}{\partial x}\left(-\frac{\partial \psi}{\partial x}\right) - \frac{\partial}{\partial y}\left(\frac{\partial \psi}{\partial y}\right) = 0 \text{ and } \nabla^2 \psi = 0 \tag{3.30}$$

Therefore, for an irrotational, two-dimensional, incompressible flow, the stream function is also governed by Laplace's equation. Note, however, that the stream function was physically possible without being irrotational, so a stream function can represent a rotational or irrotational flow. For our developments in the following sections, however, we will assume that the flows are irrotational and the stream function must satisfy Laplace's equation.

3.10 RELATION BETWEEN STREAMLINES AND EQUIPOTENTIAL LINES

If a flow is incompressible, irrotational, and two dimensional, the velocity field may be calculated using either a potential function or a stream function. Using the potential function, the velocity components in Cartesian coordinates are

$$u = \frac{\partial \phi}{\partial x} \qquad v = \frac{\partial \phi}{\partial y}$$

For a potential function in two dimensions, $\phi = \phi(x,y)$, and the differential is given by:

$$d\phi = \frac{\partial \phi}{\partial x} dx + \frac{\partial \phi}{\partial y} dy = u\, dx + v\, dy$$

Therefore, for lines of constant potential ($d\phi = 0$), which are called equipotential lines:

$$\left(\frac{dy}{dx}\right)_{\phi = C} = -\frac{u}{v} \tag{3.31}$$

Since a streamline is everywhere tangent to the local velocity, the slope of a streamline, which is a line of constant ψ, is

$$\left(\frac{dy}{dx}\right)_{\psi = C} = \frac{v}{u} \tag{3.32}$$

which we discussed in association with equation (3.28a).

Comparing equations (3.31) and (3.32) yields:

$$\left(\frac{dy}{dx}\right)_{\phi = C} = -\frac{1}{(dy/dx)_{\psi = C}} \tag{3.33}$$

The slope of an equipotential line is the negative reciprocal of the slope of a streamline. Therefore, streamlines (ψ = constant) are everywhere orthogonal (perpendicular) to

equipotential lines (ϕ = constant). This observation is not true, however, at stagnation points, where the components vanish simultaneously.

EXAMPLE 3.3: Equipotential lines and streamlines for a corner flow

Consider the incompressible, irrotational, two-dimensional flow, where the stream function is given by:

$$\psi = 2xy$$

(a) What is the velocity at $x = 1, y = 1$? At $x = 2, y = \frac{1}{2}$? Note that both points are on the same streamline, since $\psi = 2$ for both points.

(b) Sketch the streamline pattern and discuss the significance of the spacing between the streamlines.

(c) What is the velocity potential for this flow?

(d) Sketch the lines of constant potential. How do the lines of equipotential relate to the streamlines?

Solution:

(a) The stream function can be used to calculate the velocity components:

$$u = \frac{\partial \psi}{\partial y} = 2x \qquad v = -\frac{\partial \psi}{\partial x} = -2y$$

This was the same flow discussed in Example 2.1. Now we can find the velocity magnitudes using:

$$\vec{V} = 2x\hat{i} - 2y\hat{j}$$

At $x = 1, y = 1, \vec{V} = 2\hat{i} - 2\hat{j}$, and the magnitude of the velocity is

$$U = |\vec{V}| = \sqrt{(2)^2 + (-2)^2} = \sqrt{8} = 2.8284$$

At $x = 2, y = \frac{1}{2}, \vec{V} = 4\hat{i} - \hat{j}$, and the magnitude of the velocity is

$$U = |\vec{V}| = \sqrt{(4)^2 + (-1)^2} = \sqrt{17} = 4.1231$$

(b) A sketch of the streamline pattern is presented in Fig. 3.8. Results are presented only for the first quadrant (x positive, y positive). Mirror-image patterns would exist in the other quadrants. Note that the $x = 0$ and the $y = 0$ axes represent the $\psi = 0$ "streamline." These axes, therefore, could be thought of as solid surfaces, and the first quadrant flow field would represent flow in a 90 degree corner.

Since the flow is incompressible and steady, the integral form of the continuity equation (2.5) indicates that the product of the velocity times the distance between the streamlines is a constant. That is, since ρ = constant,

$$\oiint \vec{V} \cdot \hat{n}\, dA = 0$$

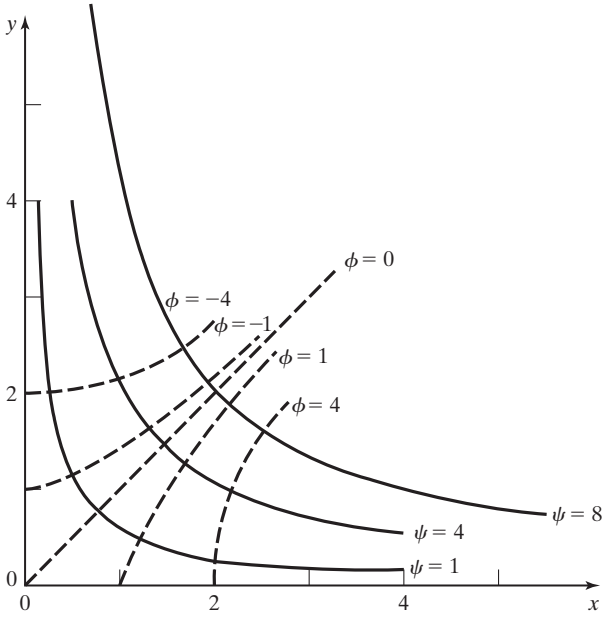

Figure 3.8 Equipotential lines and streamlines for Example 3.3.

Therefore, the distance between the streamlines decreases as the magnitude of the velocity increases.

(c) Since $u = \partial\phi/\partial x$ and $v = \partial\phi/\partial y$, we can integrate both equations to obtain:

$$\int \frac{\partial \phi}{\partial x} dx = \phi = \int u dx = \int 2x dx = x^2 + g(y)$$

Likewise:

$$\int \frac{\partial \phi}{\partial y} dy = \phi = \int u dy = \int (-2y) dy = -y^2 + f(x)$$

The functions $f(x)$ and $g(y)$ appear (rather than constants of integration) because we are integrating partial derivatives. The potential function that satisfies both of these equations, since $g(y) = -y^2$ and $f(x) = x^2$, is:

$$\phi = x^2 - y^2 + C$$

where C is an arbitrary constant.

(d) The equipotential lines are included in Fig. 3.8, where C, the arbitrary constant, has been set equal to zero. The lines of equipotential are everywhere perpendicular to the streamlines.

3.11 SUPERPOSITION OF FLOWS

Laplace's equation, either equation (3.26) for the potential function or equation (3.30) for the stream function, is a linear partial differential equation whose solutions may be added together (called superposition) to describe a desired, more complicated flow. Superposition is the concept that one solution to Laplace's equation can be added to another solution to create a third solution. The difficulty is in finding solutions that might describe realistic flows that will be useful for analysis.

In fact, finding solutions to Laplace's equation is quite easy. Since both terms of the equation have second derivatives, constants or functions of x or y to the first power are automatically solutions. For example, we can start with $\phi = 5x$, then $\phi_x = \partial\phi/\partial x = 5$ and $\phi_{xx} = \partial^2\phi/\partial x^2 = 0$ (and since there is no function of y in this velocity potential, $\phi_{yy} = 0$). So $\phi = 5x$ is a solution to Laplace's equation. Likewise, $\phi = 2y$ will also be a solution. Due to superposition, therefore, $\phi = 5x + 2y$ will also be a solution. Note that any of these velocity potentials could have a constant added, which will not change the results at all; that is, $\phi = 5x + 2y + 3$ is also a solution. But we do not just want to find solutions to Laplace's equation, we want to find solutions that represent interesting and realistic flow patterns. But before we do that, we will need to define the boundary conditions that will apply to our flow fields.

There are two main boundary conditions for these flows: (1) the resultant velocity is equal to the free-stream value at points far from the solid surface and (2) the component of the velocity normal to a solid surface is zero (i.e., the surface is a streamline). There are two ways to solve the equations: either by choosing functions and applying the boundary conditions to see what flow is created, or by finding a flow of interest and determining the function that would create it (which is known as an "inverse" method). There are numerous two-dimensional and axisymmetric solutions available through inverse methods. These inverse methods do not begin with a prescribed boundary surface and directly solve for the potential flow, but instead assume a set of known singularities in the presence of an onset flow. The total potential function (or stream function) for the singularities and the onset flow are then used to determine the streamlines, any one of which may be considered to be a "boundary surface." If the resultant boundary surface corresponds to the shape of interest, the desired solution has been obtained. The singularities most often used in such approaches, which were suggested by Rankine in 1871, include a uniform flow, a source, a sink, a doublet, and a vortex.

For a constant-density potential flow, the velocity field can be determined using only the continuity equation and the condition of irrotationality. Thus, the equation of motion is not used, and the velocity may be determined independently of the pressure. Once the velocity field has been determined, Bernoulli's equation can be used to calculate the corresponding pressure field. It is important to remember that pressures of the component flows cannot be superimposed (or added together), since they are nonlinear functions of the velocity. Referring to equation (3.10), you can see that the pressure is a quadratic function of the velocity. However, velocities may be superimposed (just like velocity potentials or stream functions), which greatly aids in developing physical understanding while working with more complicated flows.

3.12 ELEMENTARY FLOWS

Before we determine our elementary flow functions, we should remember that all functions must be solutions to Laplace's equation. While we could spend a great deal of time deriving many interesting flow types, experience has shown that the four basic elementary functions suggested by Rankine are enough to create almost any aerodynamic flow of interest through the use of superposition. Therefore, we will concentrate on these four elementary flow functions: uniform flow, source or sink flow, doublet flow, and vortex flow.

3.12.1 Uniform Flow

The simplest flow is a *uniform stream* moving in a fixed direction at a constant speed. For this uniform flow, the streamlines are straight and parallel to each other everywhere in the flow field (as shown in Fig. 3.9). Using a cylindrical coordinate system, the potential function for a uniform flow moving parallel to the x axis is:

$$\phi = U_\infty r \cos\theta + C \tag{3.34}$$

where U_∞ is the velocity of the fluid particles. Using a Cartesian coordinate system, the potential function for the uniform stream of Fig. 3.9 is:

$$\phi = U_\infty x + C \tag{3.35a}$$

where we have included an arbitrary constant, C, in the velocity potential. While there can always be such a constant, we will usually leave it out of our flow functions for simplicity. We can see that equation (3.35a) represents a uniform flow in the x direction by using equation (3.19):

$$u = \frac{\partial \phi}{\partial x} = U_\infty \qquad v = \frac{\partial \phi}{\partial y} = 0$$

which is a uniform flow in the x direction as we intended.

The stream function for a uniform flow in the x direction could also be used to determine the flow field:

$$\psi = U_\infty y$$

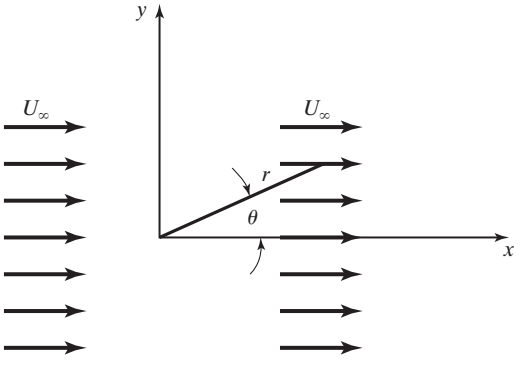

Figure 3.9 Streamlines for a uniform flow parallel to the x axis.

Recall that a streamline is a line where the stream function is set equal to a constant, so setting the stream function for a uniform flow equal to a constant yields:

$$\psi = U_\infty y = C$$

which gives us the equation $y = C/U_\infty =$ constant, which is the equation for straight, horizontal lines, with each line being determined by a unique value for C. These are the uniform flow streamlines shown in Fig. 3.9. We could also find the velocity components from:

$$u = \frac{\partial \psi}{\partial y} = U_\infty \qquad v = -\frac{\partial \psi}{\partial x} = 0$$

Notice that we could also equate the velocity components for the velocity potential and the stream function to obtain:

$$u = \frac{\partial \phi}{\partial x} = \frac{\partial \psi}{\partial y} \qquad v = \frac{\partial \phi}{\partial y} = -\frac{\partial \psi}{\partial x}$$

which are the Cauchy-Riemann equations for Cartesian coordinates [Churchill and Brown (1984)].

For a uniform stream inclined relative to the x axis by the angle α, the potential function is:

$$\phi = U_\infty (x \cos \alpha + y \sin \alpha) \tag{3.35b}$$

We can also show that this function results in the flow we intended by applying equation (3.19):

$$u = \frac{\partial \phi}{\partial x} = U_\infty \cos \alpha \qquad v = \frac{\partial \phi}{\partial y} = U_\infty \sin \alpha$$

which is a uniform flow inclined at an angle α to the horizontal.

3.12.2 Source or Sink

A *source* is defined as a point from which fluid issues and flows radially outward (as shown in Fig. 3.10). The continuity equation is satisfied everywhere but at the singularity that exists at the source's center, since mass is being introduced at this point. The potential function for a two-dimensional (planar) source centered at the origin is:

$$\phi = \frac{K}{2\pi} \ln r \tag{3.36}$$

where r is the radial coordinate from the origin of the source and K is the source strength. This two-dimensional source is sometimes referred to as a line source, because its center extends infinitely far out of, and far into, the page. The resultant velocity field in cylindrical coordinates (which is used because the flow follows a radial path from the origin) is:

$$\vec{V} = \nabla \phi = \hat{e}_r \frac{\partial \phi}{\partial r} + \frac{\hat{e}_\theta}{r} \frac{\partial \phi}{\partial \theta} \tag{3.37}$$

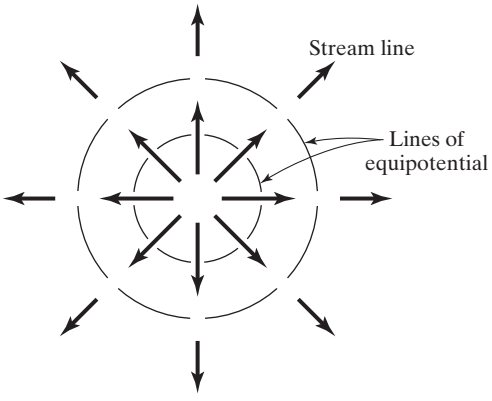

Figure 3.10 Equipotential lines and streamlines for flow from a two-dimensional source.

since

$$\vec{V} = \hat{e}_r v_r + \hat{e}_\theta v_\theta$$

$$v_r = \frac{\partial \phi}{\partial r} = \frac{K}{2\pi r} \qquad v_\theta = \frac{1}{r}\frac{\partial \phi}{\partial \theta} = 0$$

Note that the resultant velocity only has a radial component, and that this component varies inversely with the radial distance from the source.

Another related flow function is a sink, which is just a source in reverse; that is, fluid flows into a sink along radial streamlines, where fluid flows out of a source. Thus, for a sink of strength K centered at the origin:

$$\phi = -\frac{K}{2\pi}\ln r \tag{3.38a}$$

Note that the dimensions of K are $(\text{length})^2/(\text{time})$.

The stream function for a source flow is given by:

$$\psi = \frac{K\theta}{2\pi} \tag{3.38b}$$

which will yield the same velocity components as the velocity potential, since:

$$v_r = \frac{1}{r}\frac{\partial \psi}{\partial \theta} = \frac{K}{2\pi r} \qquad v_\theta = -\frac{\partial \psi}{\partial r} = 0$$

Notice that we can equate the velocity components from the velocity potential and the stream function for cylindrical coordinates to find:

$$v_r = \frac{\partial \phi}{\partial r} = \frac{1}{r}\frac{\partial \psi}{\partial \theta} \qquad v_\theta = \frac{1}{r}\frac{\partial \phi}{\partial \theta} = -\frac{\partial \psi}{\partial r}$$

which are the Cauchy-Riemann equations for cylindrical coordinates.

EXAMPLE 3.4: Flow rate for a two-dimensional source

Show that the flow rate passing through a circle of radius r is proportional to K, the strength of the two-dimensional source, and is independent of the radius.

Solution:

$$\begin{aligned}\dot{m} &= \iint \rho \vec{V} \cdot \hat{n}\, dA \\ &= \int_0^{2\pi} \rho\left(\frac{K}{2\pi r}\right) r\, d\theta \\ &= K\rho\end{aligned}$$

3.12.3 Doublet

A *doublet* is perhaps the most difficult to understand of our elementary flow functions. Interestingly, a doublet (and all of potential flow theory) has an analogous function in electro-magnetic theory, where an electric field and a magnetic field were described with a similar potential field theory by James Maxwell in the early 1860s. These fields are everywhere orthogonal (just like our velocity potential and stream function) and can be analyzed using Maxwell's theory. One of the concepts Maxwell was trying to model was a magnet, and he developed the concept of a dipole for his model. A dipole is a magnet with the "north" and "south" ends brought very close together. A dipole is essentially the same thing as a doublet, which is a source and a sink brought very close together, as shown in Fig. 3.11.

There is one problem with doing this, however. If we add a source and a sink with the same strengths and located at the same location, we get:

$$\phi = \underbrace{+\frac{K}{2\pi}\ln r}_{\text{source}} \underbrace{-\frac{K}{2\pi}\ln r}_{\text{sink}} = 0$$

which is no flow field at all. So, in order to create a source and a sink very close to each other, we will have to bring them together very carefully and in a very special way. Therefore, a doublet is defined as a source and a sink of equal strength which are brought together so that the product of their strengths (K) and their distance apart (a) remains constant at a preselected finite value: $\lim_{a\to 0}(Ka) = 2\pi B$, where B is the strength of the doublet. The line along which the approach is made (the x axis in Fig. 3.11) is called the *axis of the doublet*. The potential for a two-dimensional (line) doublet for which the flow proceeds out from the origin in the negative x direction (see Fig. 3.11) is:

$$\phi = \frac{B}{r}\cos\theta \qquad \textbf{(3.39a)}$$

where B is the doublet strength. The velocity components for a doublet may be found the same way we found them for the source:

$$v_r = \frac{\partial \phi}{\partial r} = -\frac{B\cos\theta}{2\pi r^2} \qquad v_\theta = \frac{1}{r}\frac{\partial \phi}{\partial \theta} = -\frac{B\sin\theta}{2\pi r^2}$$

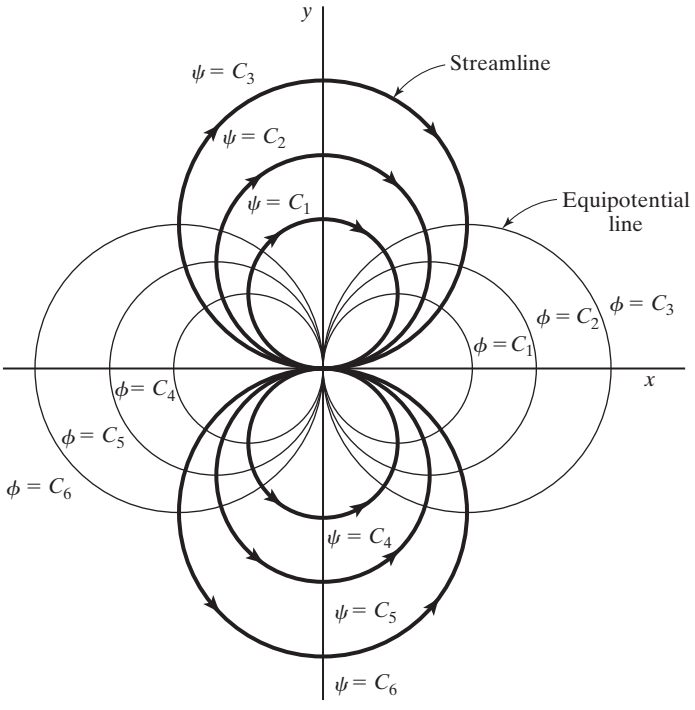

Figure 3.11 Equipotential lines and streamlines for a doublet (flow proceeds out from the origin in the negative x direction).

The stream function for a doublet is given by:

$$\psi = -\frac{B}{r}\sin\theta \tag{3.39b}$$

which will result in the same velocity field as we found from the velocity potential.

In general, the potential function of a line doublet whose axis is at an angle α relative to the positive x axis is

$$\phi = -\frac{B}{r}\cos\alpha\cos\theta \tag{3.39c}$$

3.12.4 Potential Vortex

A *potential vortex* is defined as a singularity about which fluid flows with concentric streamlines (as shown in Fig. 3.12). The velocity potential for a vortex centered at the origin is

$$\phi = -\frac{\Gamma\theta}{2\pi} \tag{3.40}$$

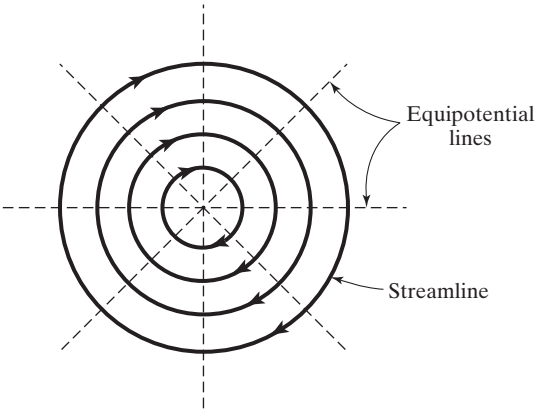

Figure 3.12 Equipotential lines and streamlines for a potential vortex.

where Γ is the strength of the vortex. We have used a minus sign to represent a vortex with clockwise circulation. Vortex flow, in many ways, is the "inverse" of source flow. Simply interchanging the velocity potential and stream function lines of a source gives the lines for a vortex (radial lines and circles become circles and radial lines); compare the velocity potential and stream function for these two flows in Table 3.3 to see this more clearly.

Differentiating the potential function, we can find the velocity distribution about an isolated vortex to be

$$v_r = \frac{\partial \phi}{\partial r} = 0$$

$$v_\theta = \frac{1}{r}\frac{\partial \phi}{\partial \theta} = -\frac{\Gamma}{2\pi r}$$

TABLE 3.3 Stream Functions and Potential Functions for Elementary Flows

Flow	ψ	ϕ
Uniform flow in x direction	$U_\infty r \sin\theta$, $U_\infty y$	$U_\infty r \cos\theta$, $U_\infty x$
Uniform flow at angle α	$U_\infty(y\cos\alpha - x\sin\alpha)$	$U_\infty(x\cos\alpha + y\sin\alpha)$
Source	$\frac{K\theta}{2\pi}$	$\frac{K}{2\pi}\ln r$
Doublet	$-\frac{B}{r}\sin\theta$	$\frac{B}{r}\cos\theta$
Vortex (with clockwise circulation)	$\frac{\Gamma}{2\pi}\ln r$	$-\frac{\Gamma\theta}{2\pi}$
90° corner flow	Axy	$\frac{1}{2}A(x^2 - y^2)$
Solid-body rotation	$\frac{1}{2}\omega r^2$	Does not exist since flow is rotational

So, there is no radial velocity component and the circumferential component varies with the reciprocal of the radial distance from the vortex. Note that the dimensions of Γ are $(\text{length})^2/(\text{time})$. A potential vortex is also known as a *free vortex*.

The curl of the velocity vector for the potential vortex can be found using the definition for the curl of $\vec{V}$ in cylindrical coordinates

$$\nabla \times \vec{V} = \frac{1}{r}\begin{vmatrix} \hat{e}_r & r\hat{e}_\theta & \hat{e}_z \\ \dfrac{\partial}{\partial r} & \dfrac{\partial}{\partial \theta} & \dfrac{\partial}{\partial z} \\ v_r & rv_\theta & v_z \end{vmatrix} = \frac{1}{r}\left\{\left(\frac{\partial v_z}{\partial \theta} - \frac{\partial r v_\theta}{\partial z}\right)\hat{e}_r - \left(\frac{\partial v_z}{\partial r} - \frac{\partial v_r}{\partial z}\right)r\hat{e}_\theta + \left(\frac{\partial r v_\theta}{\partial r} - \frac{\partial v_r}{\partial \theta}\right)\hat{e}_z\right\}$$

which simplifies in two dimensions to:

$$\frac{1}{r}\left(\frac{\partial (rv_\theta)}{\partial r} - \frac{\partial v_r}{\partial \theta}\right) = \frac{1}{r}\left(\frac{\partial}{\partial r}\left(-\frac{\Gamma}{2\pi}\right) - \frac{\partial}{\partial \theta}(0)\right) = 0$$

Although the flow is irrotational, we must remember that the velocity is infinite at the origin (i.e., when $r = 0$). In fact, the flow field at the origin is rotational and vorticity exists there.

We will now calculate the circulation around a closed curve C_1 which encloses the origin. We can choose a circle of radius r_1, as shown in Fig. 3.13a. Using equation (3.14), the circulation is

$$-\Gamma_{C_1} = \oint_{C_1} \vec{V} \cdot \overrightarrow{ds} = \int_0^{2\pi} \left(-\frac{\Gamma}{2\pi r_1}\hat{e}_\theta\right) \cdot r_1\, d\theta\, \hat{e}_\theta$$
$$= \int_0^{2\pi} (-)\frac{\Gamma}{2\pi} d\theta = -\Gamma$$

Recall that Stokes's theorem, equation (3.16), is not valid if the region contains points where the velocity is infinite, which is true for vortex flow at the origin.

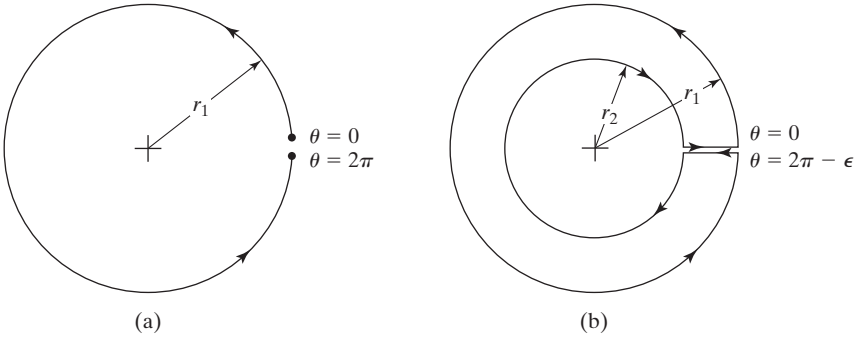

Figure 3.13 Paths for the calculation of the circulation for a potential vortex: (a) closed curve C_1, which encloses origin; (b) closed curve C_2, which does not enclose the origin.

However, if we calculate the circulation around a closed curve C_2, which does not enclose the origin, such as that shown in Fig. 3.13b, we find that

$$-\Gamma_{C_2} = \vec{V} \cdot \overrightarrow{ds} = \int_0^{2\pi-\varepsilon} (-)\frac{\Gamma}{2\pi r_1} r_1 \, d\theta + \int_{2\pi-\varepsilon}^{0} (-)\frac{\Gamma}{2\pi r_2} r_2 \, d\theta$$

or

$$-\Gamma_{C_2} = 0$$

Therefore, the circulation around a closed curve not containing the origin is zero. This means that circulation requires vorticity to exist, as we found when viewing the circulation definition in equation (3.16). This is a very important concept to remember when we start talking about airfoils and wings in Chapters 6 and 7.

You may already be familiar with the rotation of a two-dimensional, solid body about its axis, such as the rotation of a wheel. For solid-body rotation,

$$v_r = 0$$
$$v_\theta = r\omega$$

where ω is the angular velocity. Substituting these velocity components into the definition of vorticity in cylindrical coordinates in two dimensions:

$$\nabla \times \vec{V} = \frac{1}{r}\left(\frac{\partial(rv_\theta)}{\partial r} - \frac{\partial v_r}{\partial \theta}\right)\hat{e}_z$$

we find that

$$\nabla \times \vec{V} = 2\omega\hat{e}_z \neq 0$$

We see that the velocity field which describes two-dimensional solid-body rotation is not irrotational and, therefore, cannot be defined using a potential function. This type of vortex is known as a *forced vortex*.

3.12.5 The Vortex Theorems of Helmholtz

Vortex lines (or filaments) will have an important role in the study of the flow around wings in Chapter 7, so we will present some important theorems about them now. Therefore, we will summarize the vortex theorems of Hermann von Helmholtz, who was the first person to determine these "rules" for using a vortex filament, which he did in 1858. For a barotropic (homogeneous) inviscid flow acted upon by conservative body forces, the following statements about vortex filaments are true:

1. The circulation around a given vortex line (i.e., the strength of the vortex filament) is constant along its length.
2. A vortex filament cannot end in a fluid. It must form a closed path, end at a boundary, or go to infinity. Examples of these three kinds of behavior are a smoke ring, a vortex bound to a two-dimensional airfoil that spans from one wall to the other in a wind tunnel (see Chapter 6), and the downstream ends of the horseshoe vortices representing the loading on a three-dimensional wing (see Chapter 7).

Figure 3.14 Ground vortices between engine intake and ground for YC-14 research aircraft during static tests [US Air Force photo from Campbell and Chambers (1994)].

3. No fluid particle can have rotation if it did not originally rotate. Or, equivalently, in the absence of rotational external forces, a fluid that is initially irrotational remains irrotational. In general, we can conclude that vortices are preserved as time passes. Only through the action of viscosity (or some other dissipative mechanism) will they decay or disappear.

A vortex created by the rotational motion of a jet engine can be seen in the photograph of Fig. 3.14, which is taken from Campbell and Chambers (1994). The vortex can be seen entering the left engine. Because a vortex filament cannot end in a fluid, the vortex axis turns sharply and the vortex quickly goes to the ground.

Aerodynamics Concept Box: A Real Vortex

We saw earlier that there were two kinds of theoretical vortices: a potential vortex and a forced vortex (due to solid body rotation). The potential vortex creates a circumferential velocity component, $v_\theta = -\Gamma/2\pi r$, and creates a velocity distribution as shown below. This simulates a **free vortex** (or irrotational vortex), but has a singularity at the center of the vortex where velocities become infinite. A "real" vortex does have a free vortex outer portion, but the inner portion is actually better modeled as a **forced vortex** (a rotational vortex) where

$v_\theta = r\omega$, which is solid body rotation. An actual vortex contains a forced core, with a free outer section, which is the combination of the two vortex types.

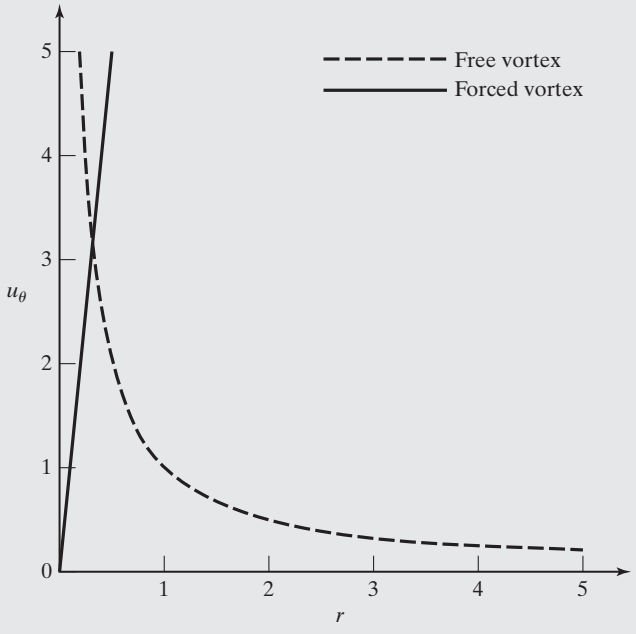

An example of a real vortex is a tornado (shown below), where the velocities near the core can be very high, sometimes in excess of 500 km/hr (depending on the pressure difference in the tornado).

Tornado in Central Oklahoma in 1999 (photo courtesy of U.S. National Oceanic and Atmospheric Administration)

Airplanes also create a vortex in the vicinity of their wing tips, as shown for a Boeing 727 below. These vortices also have high rotational velocities, and can be very dangerous

to following aircraft, which is one reason aircraft separation during landing is critical for safety.

Wing-tip vortices behind a Boeing 727 (photo courtesy of NASA Dryden Flight Research Center)

3.12.6 Summary of Stream Functions and of Potential Functions

Table 3.3 summarizes the potential functions and the stream functions for the elementary flows discussed previously.

EXAMPLE 3.5: Flow field formed from uniform flow and a source

Find the flow field created by adding together uniform flow and a source located at the origin.

Solution: In order to find the flow field created by adding together these two flows, simply add the velocity potential or stream function for each flow. Since we want to determine the streamlines of the flow, we will use the stream function in cylindrical coordinates and set the function equal to a constant (since lines of constant ψ are streamlines):

$$\psi = \underbrace{U_\infty r \sin\theta}_{\text{uniform flow}} + \underbrace{\frac{K\theta}{2\pi}}_{\text{source}} = C$$

The flow will be easier to understand if we find the velocity field, which is given by:

$$v_r = \frac{1}{r}\frac{\partial \psi}{\partial \theta} = U_\infty \cos\theta + \frac{K}{2\pi r}$$

$$v_\theta = -\frac{\partial \psi}{\partial r} = -U_\infty \sin\theta$$

Notice that the velocity field is also just the superposition of the velocity fields for uniform flow and a source, so we could have found these relations directly from the velocity fields determined previously. The stagnation points of the flow can now be found by setting the velocity components to zero (a stagnation point is a point in the flow where the fluid has been brought to rest without any losses).

$$v_r = U_\infty \cos\theta + \frac{K}{2\pi r} = 0$$

$$v_\theta = -U_\infty \sin\theta = 0$$

From the circumferential velocity component, stagnation points can exist at $\theta = 0,\pi$. Putting these values into the radial velocity equation and solving for r gives us a stagnation point located at $(r,\theta) = (K/2\pi U_\infty,\pi)$, or to the left of the source at $x = -K/2\pi U_\infty$. This is because, to the left of the origin, the source has a velocity to its left of $K/2\pi Ur$, and the uniform flow has a velocity to the right of U_∞, and the two velocity components cancel each other at some point. But what happens to the fluid that enters this stagnation point both from the left and the right? It cannot just disappear, so to satisfy the conservation of mass it must go up and down out of the stagnation point. Once the flow leaves the stagnation point, it begins to turn to the right due to the contribution of the free-stream velocity. The resulting streamline is shown below (these types of graphs are actually quite easy to make on computer algebra or programming systems).

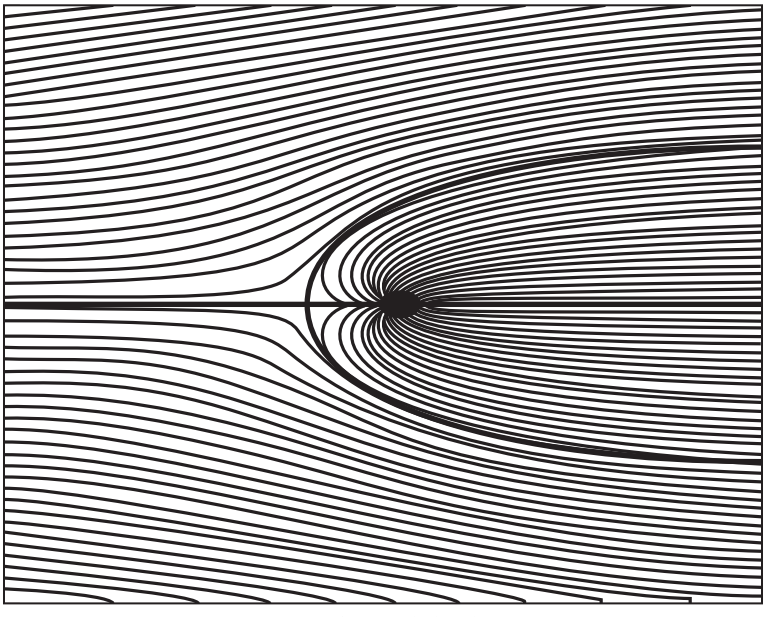

Rankine half body

Since any streamline in a potential flow can also simulate a solid surface, we can consider the streamline going through the stagnation point as a solid surface. This creates a half body with flow around it which is known as a Rankine body. We also can see the flow inside the body, but that is not typically of interest in aerodynamics. Since we now know the velocity field everywhere, we can find the velocities along the surface of the body, and from Bernoulli's equation we could find the pressures there as well.

EXAMPLE 3.6: Flow field formed from uniform flow, a source, and a sink

Find the flow field created by adding together uniform flow, a source located at $x = -a$, and a sink located at $x = +a$.

Solution: If we add uniform flow, a source at $x = -a$, and a sink at $x = +a$, we would have the following stream function:

$$\psi = \underbrace{U_\infty r \sin\theta}_{\text{uniform flow}} + \underbrace{\frac{K\theta_1}{2\pi}}_{\text{source}} - \underbrace{\frac{K\theta_2}{2\pi}}_{\text{sink}} = U_\infty r \sin\theta + \frac{K}{2\pi}(\theta_1 - \theta_2) = C$$

where θ_1 and θ_2 will have to be determined based on the positions of the source and sink. The values for the angles can be determined from their position in the figure shown below:

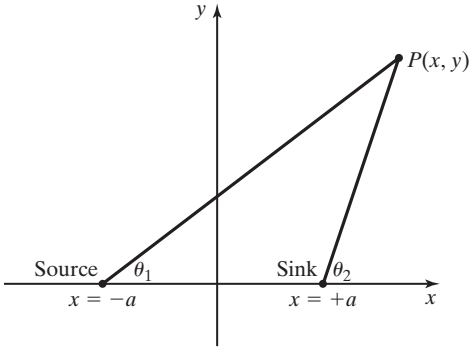

$$\theta_1 = \tan^{-1}\left(\frac{y}{x + a}\right) \quad \theta_2 = \tan^{-1}\left(\frac{y}{x - a}\right)$$

Once again, the streamlines can be easily drawn using a computer algebra or programming system, yielding a flow as shown below. As in Example 3.5, any streamline can be thought of as a solid surface, and in this case the stagnation streamlines form a body in the shape of an oval, which is known as a Rankine oval. The width and height of the oval is determined by the free-stream velocity and the strengths of the source and sink.

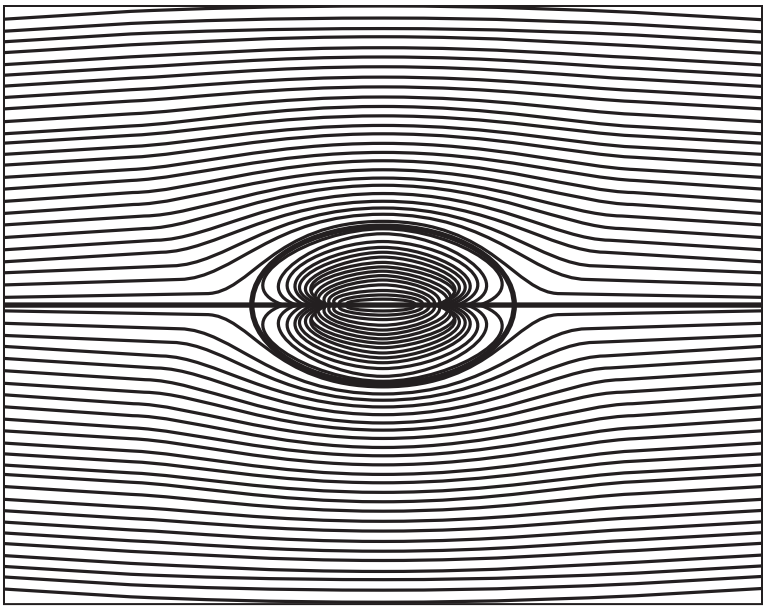

Rankine oval

In fact, as long as the source and sink have equal but opposite strengths, an infinite number of body shapes can be found from this stream function. In addition, if more sources and sinks were placed along the x axis, non-oval shapes would be created, and as long as the total source strength was equal and opposite to the total sink strength, the body would close at the rear.

3.13 ADDING ELEMENTARY FLOWS TO DESCRIBE FLOW AROUND A CYLINDER

3.13.1 Velocity Field

Now we will consider the case where a uniform flow is superimposed on a doublet whose axis is parallel to the direction of the uniform flow, and is oriented so that the direction of the efflux opposes the uniform flow (as shown in Fig. 3.15). Substituting the velocity potential for a uniform flow [equation (3.34)] and that for the doublet [equation (3.39a) into the expression for the velocity field [equation (3.37)], we find that:

$$v_\theta = \frac{1}{r}\frac{\partial \phi}{\partial \theta} = -U_\infty \sin\theta - \frac{B}{r^2}\sin\theta$$

and

$$v_r = \frac{\partial \phi}{\partial r} = U_\infty \cos\theta - \frac{B}{r^2}\cos\theta$$

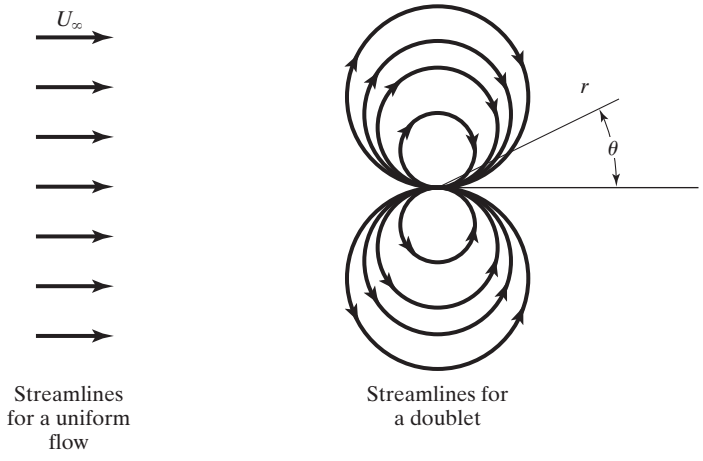

Figure 3.15 Streamlines for the two elementary flows which, when superimposed, describe the flow around a cylinder.

Note that $v_r = 0$ at every point where $r = \sqrt{B/U_\infty}$ which is a constant. Since the velocity is always tangent to a streamline, the fact that there is no velocity component (v_r) perpendicular to the circle of radius $r = R = \sqrt{B/U_\infty}$ means that the circle may be considered as a streamline of the flow field. Replacing B by $R^2 U_\infty$ allows us to write the velocity components as

$$v_\theta = -U_\infty \sin\theta\left(1 + \frac{R^2}{r^2}\right) \tag{3.41a}$$

$$v_r = U_\infty \cos\theta\left(1 - \frac{R^2}{r^2}\right) \tag{3.41b}$$

The velocity field not only satisfies the surface boundary condition that an inviscid flow is tangent to a solid wall, but the velocity at points far from the cylinder is equal to the undisturbed free-stream velocity U_∞. Streamlines for the resultant inviscid flow field are illustrated in Fig. 3.16. The resultant two-dimensional, irrotational (inviscid), incompressible flow is that around a cylinder of radius R whose axis is perpendicular to the free-stream direction.

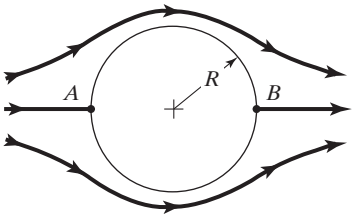

Figure 3.16 Two-dimensional, inviscid flow around a cylinder with zero circulation.

Setting $r = R$, we see that the velocity on the surface of the cylinder is equal to

$$v_\theta = -2U_\infty \sin\theta \tag{3.42}$$

Of course, as we noticed earlier, $v_r = 0$ on the surface of the cylinder. Since the solution is for the inviscid model of the flow field, it is consistent that the fluid particles next to the surface move relative to the surface (i.e., violate the no-slip requirement). When $\theta = 0$ or π (points B and A, respectively, of Fig. 3.16) the fluid is at rest with respect to the cylinder [i.e., $(v_r = v_\theta = 0)$]. These points are called *stagnation points*, as we found in Examples 3.5 and 3.6.

3.13.2 Pressure Distribution on the Cylinder

Because the velocity at the surface of the cylinder is a function of θ, as seen in equation (3.42), the local static pressure will also be a function of θ. Once the pressure distribution has been defined, it can be used to determine the forces and the moments acting on the configuration. Using Bernoulli's equation [equation (3.10)] for $\rho = \rho_\infty$ and $U = v_\theta = -2U_\infty \sin\theta$, we can obtain the expression for the θ-distribution of the static pressure using dimensional parameters:

$$\begin{aligned} p &= p_\infty + \tfrac{1}{2}\rho_\infty(U_\infty^2 - U^2) = p_\infty + \tfrac{1}{2}\rho_\infty(U_\infty^2 - 4U_\infty^2\sin^2\theta) \\ &= p_\infty + \tfrac{1}{2}\rho_\infty U_\infty^2(1 - 4\sin^2\theta) \end{aligned} \tag{3.43}$$

Expressing the pressure in terms of the dimensionless pressure coefficient, which is presented in equation (3.13), we have:

$$C_p = 1 - \frac{U^2}{U_\infty^2} = 1 - \frac{4U_\infty^2\sin^2\theta}{U_\infty^2} = 1 - 4\sin^2\theta \tag{3.44}$$

The resulting pressure coefficient variation is shown in Fig. 3.17 as a function of θ. Recall that, for cylindrical coordinates, $\theta = 180°$ corresponds to the plane of symmetry for the windward surface or forebody (i.e., the surface facing the free stream). Starting with the undisturbed free-stream flow and following the streamline that "wets" the surface, the flow is decelerated from the free-stream velocity to zero velocity at the (windward) stagnation point in the plane of symmetry. The flow then accelerates along the surface of the cylinder, reaching a maximum velocity equal in magnitude to twice the free-stream velocity, which occurs at $\theta = 90°$ and at 270°. From these velocity maxima, the flow tangent to the leeward surface decelerates to a stagnation point at the surface in the leeward plane of symmetry (at $\theta = 0°$).

In spite of the fact that viscosity of air is relatively small, the actual flow field around the cylinder is radically different from the inviscid solution described in the previous paragraphs (as shown in Figs. 3.17 and 3.18). When the air particles in the boundary layer, which have already been slowed by the action of viscosity, encounter the relatively large adverse pressure gradient associated with the deceleration of the leeward flow for this blunt configuration, boundary-layer separation occurs.

Experimental pressure distributions are presented in Fig. 3.17 for the cases where the forebody boundary layer is laminar (a subcritical Reynolds number) and where the

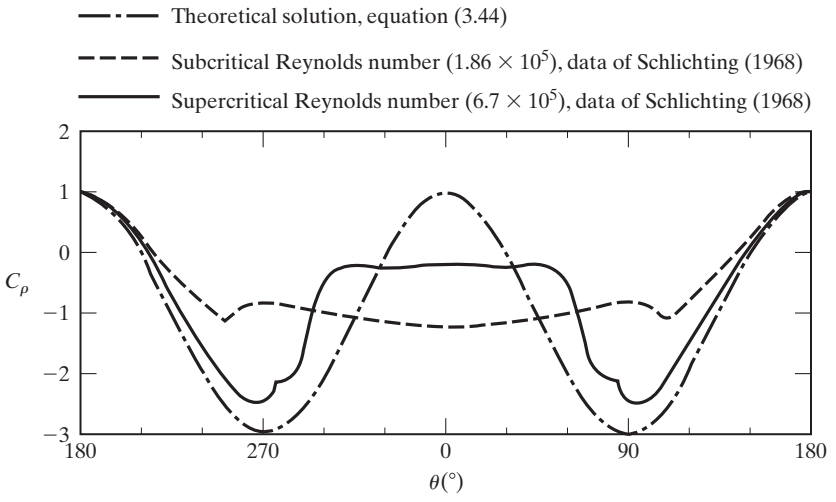

Figure 3.17 Theoretical pressure distribution around a circular cylinder, compared with data for a subcritical Reynolds number and that for a supercritical Reynolds number [data from Boundary Layer Theory by H. Schlichting (1968)].

forebody boundary layer is turbulent (a supercritical Reynolds number). The subcritical pressure-coefficient distribution is essentially unchanged over a wide range of Reynolds numbers below the critical Reynolds numbers. Similarly, the supercritical pressure-coefficient distribution is independent of Reynolds numbers over a wide range of Reynolds numbers above the critical Reynolds number. For the flow upstream of the separation location, the boundary layer is thin, and the pressure-coefficient distribution

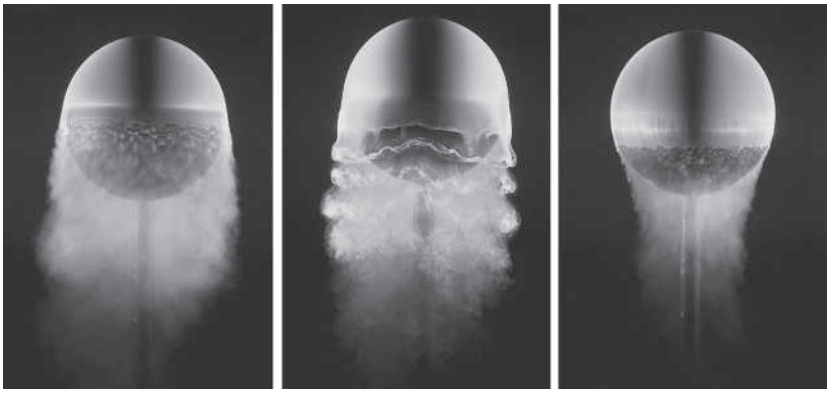

(a) Subcritical (b) Transitional (c) Supercritical

Figure 3.18 Water tunnel visualizations of flow patterns around a sphere for three Reynolds number flows: (a) subcritical (b) transitional, and (c) supercritical (photographs by H. Werlé, courtesy of ONERA).

is essentially independent of the character of the boundary layer for the cylinder. However, because the character of the attached boundary layer affects the separation location, it affects the pressure in the separated region. If the attached boundary layer is turbulent, separation is delayed and the pressure in the separated region is higher and closer to the inviscid level.

The photograph of the water tunnel patterns for flow around a sphere presented in Fig. 3.18 clearly illustrates the flow separation at subcritical (Fig. 3.18a), transitional (Fig. 3.18b), and supercritical Reynolds numbers (Fig. 3.18c). Recall that separation occurs when the fluid particles in the boundary layer (already slowed by viscosity) encounter an adverse pressure gradient that they cannot overcome. However, not all boundary layers separate when they encounter an adverse pressure gradient. There is a relation between the characteristics of the boundary layer and the magnitude of the adverse pressure gradient that is required to produce separation. A turbulent boundary layer (Fig. 3.18c), which has relatively fast-moving particles near the wall, remains attached longer than a laminar boundary layer (Figs. 3.18a and 3.18b), which has slower-moving particles near the wall for the same value of the edge velocity (boundary layers are discussed in more detail in Chapter 4). Therefore, the separation location, the size of the wake, and the surface pressure in the wake region depend on the character of the forebody boundary layer.

The experimentally determined separation locations for a circular cylinder as reported by Achenbach (1968) are presented as a function of Reynolds number in Fig. 3.19. As we discussed in Chapter 2, the Reynolds number is a dimensionless parameter (in this case, $\mathrm{Re}_d = \rho_\infty U_\infty d/\mu_\infty$) that relates to the viscous characteristics of the flow. At subcritical Reynolds numbers (i.e., less than approximately 3×10^5), the boundary layer on the windward surface (or forebody) is laminar and separation occurs for $\theta \sim 100°$, that is, 80° from the windward stagnation point. Note that the occurrence of separation so alters the flow that separation actually occurs on the windward surface, where the inviscid solution, as given by equation (3.44) and presented in Fig. 3.17, indicates that there still should be a favorable pressure gradient (i.e., one for which the static pressure decreases in the streamwise direction). Separation would not occur if the pressure were actually decreasing in the streamwise direction. Therefore, the occurrence of separation alters the pressure distribution on the forebody (windward surface) of the cylinder. Above the critical Reynolds number, the forebody boundary layer is turbulent. Due to the higher levels of energy for the fluid particles near the surface in a turbulent boundary layer, the flow is able to run longer against the adverse pressure gradient. In the critical region, Achenbach observed an intermediate "separation bubble" with final separation not occurring until $\theta = 40°$ (i.e., 140° from the stagnation point). For $\mathrm{Re}_d > 1.5 \times 10^6$, the separation bubble no longer occurs, indicating that the supercritical state of flow has been reached. For supercritical Reynolds numbers, separation occurs in the range $60° < \theta < 70°$ (you should keep in mind that the critical Reynolds number is sensitive both to the turbulence level in the free stream and to the surface roughness).

3.13.3 Lift and Drag

Our original goal for studying aerodynamics was to determine the forces and moments acting on a vehicle moving through the air. The most important forces for creating flight are lift and drag, which we will now define and quantify for a cylinder.

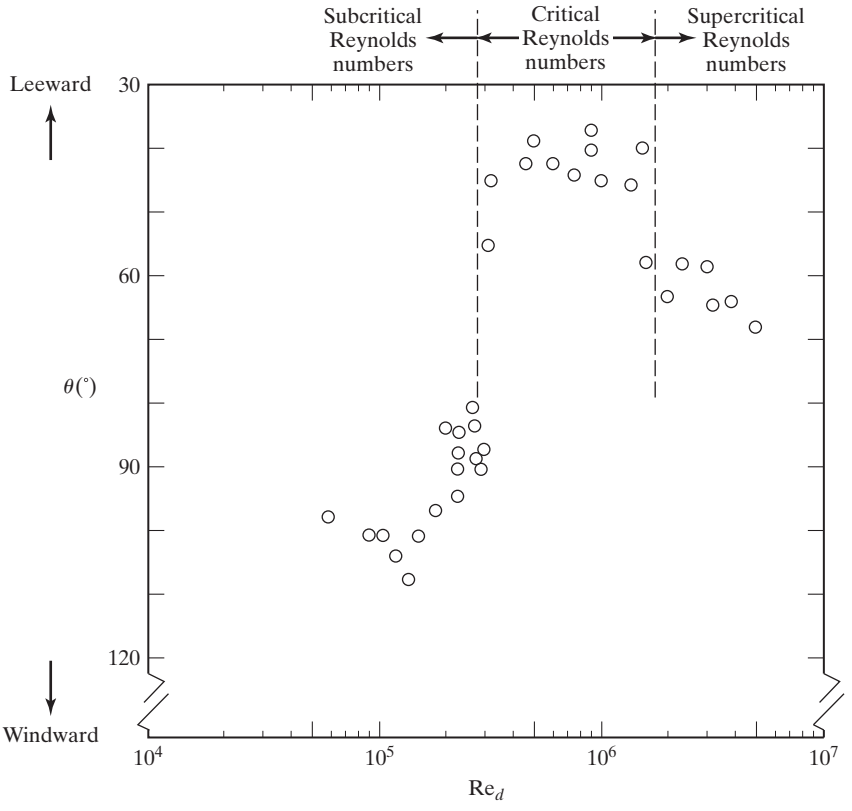

Figure 3.19 Location of the separation points on a circular cylinder as a function of the Reynolds number [data from Achenbach (1968)].

The motion of the air particles around the cylinder produces forces that may be viewed as a normal (or pressure) component and a tangential (or shear) component. It is conventional to resolve the resultant force on the cylinder into a component perpendicular to the free-stream velocity direction (called the *lift*) and a component parallel to the free-stream velocity direction (called the *drag*); the nomenclature is illustrated in Fig. 3.20.

Since the expressions for the velocity distribution [equation (3.42)] and for the pressure distribution [equations (3.43) or (3.44)] were obtained for an inviscid flow, we will consider only the contribution of the pressure to the lift and to the drag (since there is no shear predicted by inviscid theory). As shown in Fig. 3.20, the lift per unit span of the cylinder for the pressure defined in equation (3.43) is:

$$l = -\int_0^{2\pi} p \sin\theta \, R d\theta = -\int_0^{2\pi} [\, p_\infty + \tfrac{1}{2}\rho_\infty U_\infty^2 (1 - 4\sin^2\theta)\,] \sin\theta \, R d\theta \qquad \textbf{(3.45)}$$

Since the free-stream pressure is a constant, it does not contribute to the lift integral, leaving only integrals of the form: $\int_0^{2\pi} \sin\theta \, d\theta = 0$ and $\int_0^{2\pi} \sin^3\theta \, d\theta = 0$, which results in:

$$l = 0 \qquad \textbf{(3.46)}$$

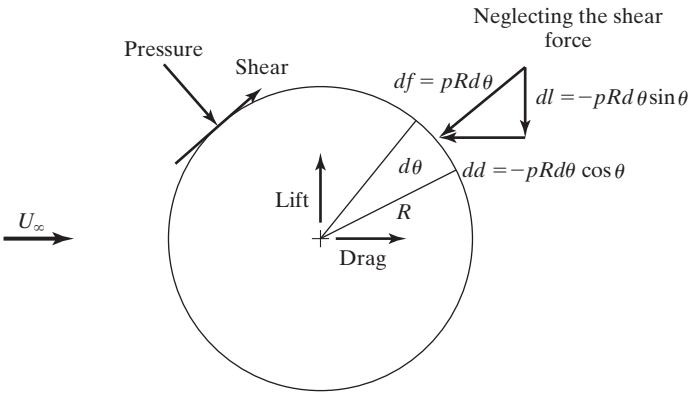

Figure 3.20 Forces acting on a cylinder whose axis is perpendicular to the free-stream flow.

It is not surprising that there is zero lift per unit span of the cylinder, since the pressure distribution is symmetric on the upper and lower surfaces of the cylinder.

Instead of using equation (3.43), which is the expression for the static pressure, the aerodynamicist more commonly would use equation (3.44), which is the expression for the dimensionless pressure coefficient. To do this, note that the net force in any direction due to a constant pressure acting on a closed surface is zero. As a result,

$$\int_0^{2\pi} p_\infty \sin\theta \, R \, d\theta = 0 \tag{3.47}$$

Adding equations (3.45) and (3.47) gives:

$$l = -\int_0^{2\pi} (p - p_\infty) \sin\theta \, R \, d\theta$$

Dividing both sides of this equation by the product $q_\infty 2R$, which is (dynamic pressure) $\times$ (area per unit span in the x plane), gives:

$$\frac{l}{q_\infty 2R} = -\tfrac{1}{2}\int_0^{2\pi} C_p \sin\theta \, d\theta \tag{3.48}$$

Both sides of equation (3.48) are dimensionless. The expression of the left-hand side is known as the *section lift coefficient* for a cylinder:

$$C_l = \frac{l}{q_\infty 2R} \tag{3.49}$$

Using equation (3.44) to define C_p as a function of θ,

$$C_l = -\tfrac{1}{2}\int_0^{2\pi} C_p \sin\theta \, d\theta = -\tfrac{1}{2}\int_0^{2\pi} (1 - 4\sin^2\theta)\sin\theta \, d\theta = 0$$

which, of course, is the same result as was obtained by integrating the pressure directly.

Referring to Fig. 3.20 and following a similar procedure, we can calculate the drag per unit span for the cylinder in an inviscid flow. Thus, the drag per unit span is

$$d = -\int_0^{2\pi} p \cos\theta \, R \, d\theta \tag{3.50}$$

Substituting equation (3.43) for the local pressure,

$$d = -\int_0^{2\pi} p \sin\theta \, R d\theta = -\int_0^{2\pi} [p_\infty + \tfrac{1}{2}\rho_\infty U_\infty^2 (1 - 4\sin^2\theta)] \cos\theta \, R d\theta$$

we find that

$$d = 0 \tag{3.51}$$

A drag of zero is an obvious contradiction to our experience, since we all know that bodies moving through air experience drag. This unusual result is known as *d'Alembert's paradox*, since Jean le Rond d'Alembert first arrived at this result in 1752. In fact, this result created a rift between the more practical side of fluid dynamics (the experimentalists) and the more theoretical side (the theoreticians). This rift would not be repaired until Ludwig Prantdl developed the concept of the boundary layer in the early twentieth century, which helped to explain that viscous effects cause flow separation.

Note that the actual pressure in the separated wake region near the leeward plane of symmetry (in the vicinity of $\theta = 0$ in Fig. 3.17) is much less than the theoretical value. It is the resultant difference between the high pressure acting near the windward plane of symmetry (in the vicinity of $\theta = 180°$, i.e., the stagnation point) and the relatively low pressures acting near the leeward plane of symmetry that produces the large drag component.

A drag force that represents the streamwise component of the pressure force integrated over the entire configuration is termed *pressure* (or *form*) *drag*. The drag force that is obtained by integrating the streamwise component of the shear force over the vehicle is termed *skin-friction drag*. Note that in the case of real flow past a cylinder, the skin-friction drag is small. However, significant form drag results because of the action of viscosity, which causes the boundary layer to separate and therefore radically alters the pressure field. The pressure near the leeward plane of symmetry is higher (and closer to the inviscid values) when the forebody boundary layer is turbulent. Thus, the difference between the pressure acting on the foreward surface and that acting on the leeward surface is less in the turbulent case. As a result, the form drag for a turbulent boundary layer is markedly less than the corresponding value for a laminar (forebody) boundary layer.

The *drag coefficient* per unit span for a cylinder is given by:

$$C_d = \frac{d}{q_\infty 2R} = -\tfrac{1}{2}\int_0^{2\pi} C_p \cos\theta \, d\theta \tag{3.52}$$

Experimental drag coefficients for a smooth circular cylinder in a low-speed stream [Schlichting (1968)] are presented as a function of Reynolds number in Fig. 3.21.

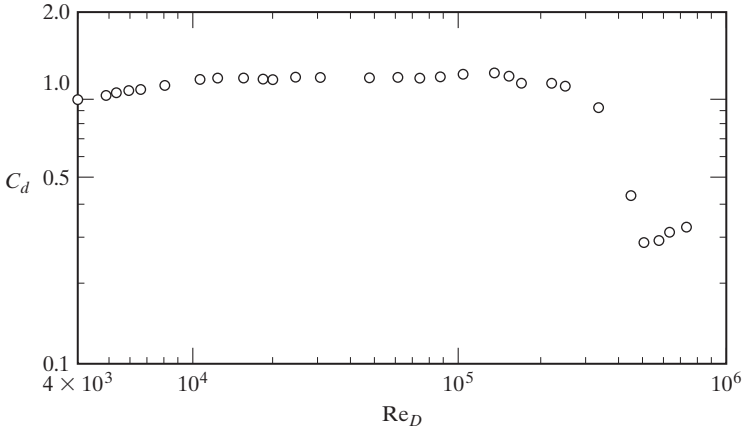

Figure 3.21 Drag coefficient for a smooth circular cylinder as a function of the Reynolds number [data from *Boundary Layer Theory* by H. Schlichting (1968)].

For Reynolds numbers below 300,000 the drag coefficient is essentially constant (approximately 1.2), and independent of Reynolds number. Recall that when we were discussing the experimental values of C_p presented in Fig. 3.17, we noted that the subcritical pressure-coefficient distribution is essentially unchanged over a wide range of Reynolds number. For blunt bodies, the pressure (or form) drag is the dominant drag component. Since the pressure coefficient distribution for a circular cylinder is essentially independent of Reynolds number below the critical Reynolds number, it follows that the drag coefficient would be essentially independent of the Reynolds number. (For streamlined bodies at small angles of attack, the dominant component of drag is skin friction, which is Reynolds-number dependent). Above the critical Reynolds number (when the forebody boundary layer is turbulent), the drag coefficient is significantly lower. Reviewing the supercritical pressure distribution, we recall that the pressure in the separated region is closer to the inviscid level. In a situation where the Reynolds number is subcritical, it may be desirable to induce boundary-layer transition by roughening the surface. Examples of such transition-promoting roughness elements are the dimples on a golf ball or the seams on a baseball. The dimples on a golf ball are intended to reduce drag by reducing the form (or pressure) drag with only a slight increase in the friction drag.

3.14 LIFT AND DRAG COEFFICIENTS AS DIMENSIONLESS FLOW-FIELD PARAMETERS

Aerodynamic coefficients are typically used so that we can compare an aircraft of a certain size with a certain velocity to a scale model of the aircraft flying at a different velocity (see Section 2.5 for more details). This led us to the nondimensional similarity

parameters of Mach and Reynolds number, but it also leads us to the use of nondimensional force and moment coefficients.

The formulas for the section drag coefficient [equation (3.52)] and for the section lift coefficient for a cylinder [equation (3.49)] have the same elements. So, we will define a *force coefficient* as:

$$C_F = \frac{\text{force}}{\underbrace{\frac{1}{2}\rho_\infty U_\infty^2}_{\substack{\text{dynamic}\\ \text{pressure}}} \underbrace{S}_{\substack{\text{reference}\\ \text{area}}}} \tag{3.53}$$

Notice that, for a configuration of infinite span, a force per unit span would be divided by the reference area per unit span; the resulting value is called a section coefficient [see equations (3.49) and (3.52)]. Ideally, the force coefficient would be independent of size and would be a function of configuration geometry and of attitude only. However, the effects of viscosity and compressibility cause variations in the force coefficients. These effects can be correlated in terms of parameters such as the Reynolds number and the Mach number. Such variations are especially evident in the drag coefficient measurements presented in this chapter.

From equation (3.53), we can see that an aerodynamic force is proportional to the square of the free-stream velocity, to the free-stream density, to the size of the object, and to the force coefficient. An indication of the effect of configuration geometry on the total drag and on the drag coefficient is shown in Figs. 3.22 and 3.23, which are taken from Talay (1975). The actual drag for several incompressible, flow condition/configuration geometry combinations is presented in Fig. 3.22. Compare the results for configurations (a), (b), and (c), which are configurations having the same width and exposed to the same Reynolds number free stream. Streamlining produces dramatic reductions in the pressure (or form) drag with only a slight increase in skin-friction drag at this Reynolds number. Thus, streamlining reduces the drag coefficient.

You should notice that the diameter of the small cylinder is one-tenth that of the other configurations. Therefore, in the same free-stream flow as configuration (b), the small cylinder operates at a Reynolds number of 10^4. Because the size is reduced, the drag forces for (d) are an order of magnitude less than for (b). However, over this range of Reynolds number, the drag coefficients are essentially equal (as shown in Fig. 3.21). Also, the total drag of the small cylinder is equal to that of the much thicker streamlined shape. You can readily imagine how much additional drag was produced by the wire bracing of a biplane during World War I.

When the Reynolds number of the large cylinder is increased to 10^7 (corresponding to the supercritical flow of Fig. 3.21), the pressure drag is very large. However, the drag coefficient for this condition is only 0.6, which is less than the drag coefficient for the subcritical flow (b), even though the pressure drag is significantly greater. Note that since the cylinder diameter is the same for both (b) and (e), the two order of magnitude increase in Reynolds number is accomplished by increasing the free-stream density and the free-stream velocity. Therefore, the denominator of equation (3.52) increases more than the numerator. As a result, even though the dimensional force is increased, the nondimensionalized force coefficient is decreased.

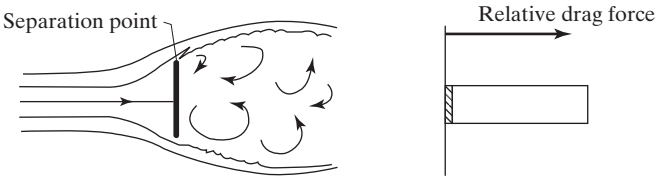

(a) Flat plate broadside to the flow (height = d), $\mathrm{Re}_d = 10^5$

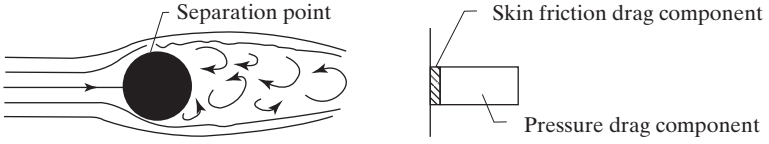

(b) Large cylinder with subcritical flow (diameter = d), $\mathrm{Re}_d = 10^5$

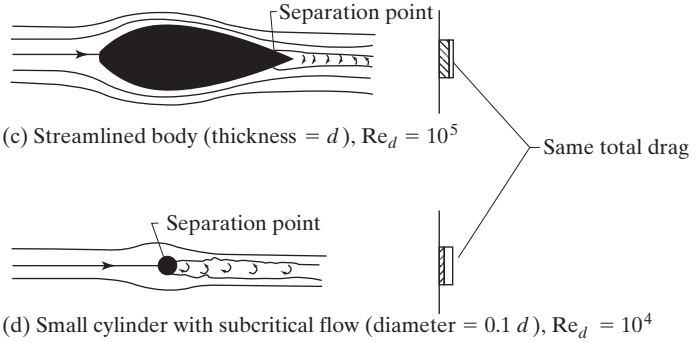

(c) Streamlined body (thickness = d), $\mathrm{Re}_d = 10^5$

(d) Small cylinder with subcritical flow (diameter = 0.1 d), $\mathrm{Re}_d = 10^4$

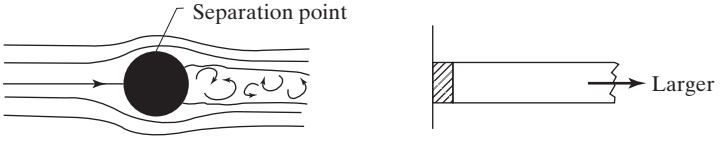

(e) Large cylinder with supercritical flow (diameter = d), $\mathrm{Re}_d = 10^7$

Figure 3.22 Comparison of the drag components for various shapes and flows [from Talay (1975)].

There are a variety of sources of interesting aerodynamic data. However, *Fluid Dynamic Drag* by Hoerner (1958) and *Fluid Dynamic Lift* by Hoerner and Borst (1975) offer the reader unique and entertaining collections of data. In these volumes, you will find aerodynamic coefficients for flags, World War II airplanes, and vintage automobiles as well as more classical configurations. These books are valuable resources for the aerodynamicist.

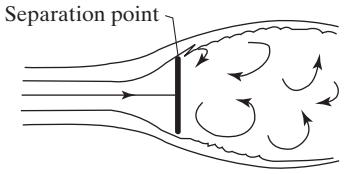

(a) Flat plate broadside to the flow (height $= d$), $\text{Re}_d = 10^5$

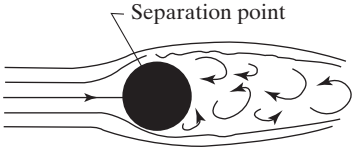

(b) Large cylinder with subcritical flow (diameter $= d$), $\text{Re}_d = 10^5$

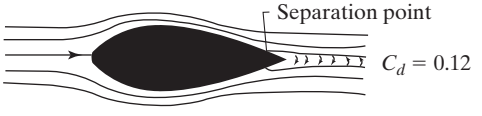

(c) Streamlined body (thickness $= d$), $\text{Re}_d = 10^5$

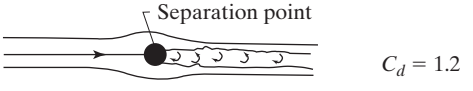

(d) Small cylinder with subcritical flow (diameter $= 0.1d$), $\text{Re}_d = 10^4$

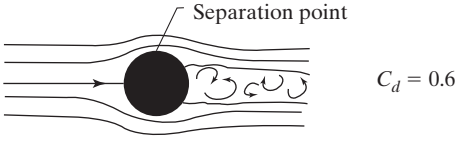

(e) Large cylinder with supercritical flow (diameter $= d$), $\text{Re}_d = 10^7$

Figure 3.23 Comparison of section drag coefficients for various shapes and flows [from Talay (1975)].

EXAMPLE 3.7: Forces on a (semi-cylinder) quonset hut

You are to design a quonset hut to serve as temporary housing near the seashore. The quonset hut may be considered to be a closed (no leaks) semicylinder, whose radius is 5 m, mounted on tie-down blocks, as shown in Fig. 3.24. Neglect viscous effects and assume that the flow field over the top of the hut is identical to the flow over the cylinder for $0 \leq \theta \leq \pi$. When calculating the flow over the upper surface of the hut, neglect the presence

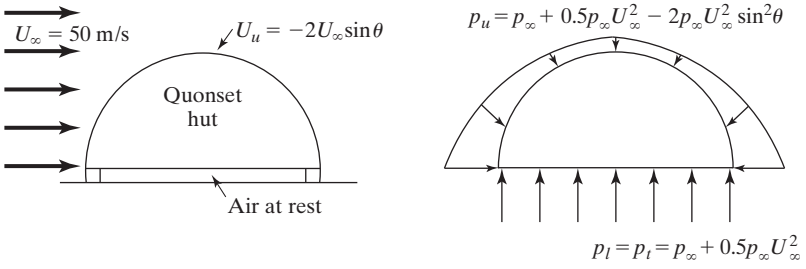

Figure 3.24 Inviscid flow model for quonset hut of Example 3.5.

of the air space under the hut. The air under the hut is at rest and the pressure is equal to the stagnation pressure, p_t.

What is the net lift force acting on the quonset hut? The wind speed is 50 m/s and the static free-stream properties are those for standard day sea-level conditions.

Solution: Since we will assume that the flow over the upper surface of the quonset hut is identical to an inviscid flow over a cylinder, the velocity on the surface is given by equation (3.42):

$$U_u = v_\theta = -2U_\infty \sin\theta$$

and the pressure is given by equation (3.43):

$$p_u = p_\infty + \tfrac{1}{2}\rho_\infty U_\infty^2 - 2\rho_\infty U_\infty^2 \sin^2\theta$$

The pressure on the lower surface (under the hut) is

$$p_l = p_t = p_\infty + \tfrac{1}{2}\rho_\infty U_\infty^2$$

Equation (3.45) and Fig. 3.20 can be used to calculate the lifting contribution of the upper surface but not the lower surface, since it is a "flat plate" rather than a circular arc. The lift per unit depth of the quonset hut is

$$\begin{aligned} l &= -\int_0^\pi p_u \sin\theta\, R\, d\theta + p_t(2R) \\ &= -R\int_0^\pi (p_\infty \sin\theta + \tfrac{1}{2}\rho_\infty U_\infty^2 \sin\theta - 2\rho_\infty U_\infty^2 \sin^3\theta)\, d\theta \\ &\quad + p_\infty 2R + \tfrac{1}{2}\rho_\infty U_\infty^2 2R \\ &= +p_\infty R\cos\theta\Big|_0^\pi + \tfrac{1}{2}\rho_\infty U_\infty^2 R\cos\theta\Big|_0^\pi + 2\rho_\infty U_\infty^2 R(-\cos\theta + \tfrac{1}{3}\cos^3\theta)\Big|_0^\pi \\ &\quad + p_\infty 2R + \tfrac{1}{2}\rho_\infty U_\infty^2 2R \\ &= \tfrac{8}{3}\rho_\infty U_\infty^2 R \end{aligned}$$

The lift coefficient is found from:

$$C_l = \frac{l}{\frac{1}{2}\rho_\infty U_\infty^2 (2R)} = \frac{\frac{8}{2}\rho_\infty U_\infty^2 R}{\rho_\infty U_\infty^2 R} = \frac{8}{3}$$

Since we have assumed that the flow is inviscid and incompressible, the lift coefficient is independent of the Mach number and Reynolds number.

The actual lift force is:

$$l = \frac{8}{3}\left(1.225\frac{\text{kg}}{\text{m}^3}\right)\left(50\frac{\text{m}}{\text{s}}\right)^2(5\text{ m}) = 40{,}833\text{ N/m}$$

By symmetry, the drag is zero, which reflects the fact that we neglected the effects of viscosity.

3.15 FLOW AROUND A CYLINDER WITH CIRCULATION

We will now take the solution for flow over a cylinder one step further by adding a vortex to the flow field. The power of superposition can be seen in the development, since we can simply add the vortex to the previous results for flow over a cylinder.

3.15.1 Velocity Field

Consider the flow field that results if a vortex with clockwise circulation is superimposed on the doublet/uniform-flow combination we just discussed. The resultant velocity potential function is:

$$\phi = U_\infty r\cos\theta + \frac{B}{r}\cos\theta - \frac{\Gamma\theta}{2\pi} \tag{3.54}$$

which gives velocity components of:

$$v_r = \frac{\partial\phi}{\partial r} = U_\infty\cos\theta - \frac{B\cos\theta}{r^2} \tag{3.55a}$$

$$v_\theta = \frac{1}{r}\frac{\partial\phi}{\partial\theta} = \frac{1}{r}\left(-U_\infty r\sin\theta - \frac{B}{r}\sin\theta - \frac{\Gamma}{2\pi}\right) = -U_\infty\sin\theta - \frac{B}{r^2}\sin\theta - \frac{\Gamma}{2\pi r} \tag{3.55b}$$

As was true for flow over a cylinder, $v_r = 0$ at every point where $r = \sqrt{B/U_\infty}$, which is a constant and will be designated as R (the radius of the cylinder). Since the velocity is always tangent to a streamline, the fact that there is no velocity component (v_r) perpendicular to the circle of radius R means that the circle may be considered as a streamline of the flow field. Thus, the resultant potential function also represents flow around a cylinder. For this flow, however, the streamline pattern away from the surface is not symmetric about the horizontal plane. The velocity at the surface of the cylinder is equal to

$$v_\theta = -U_\infty\sin\theta - \frac{B}{r^2}\sin\theta - \frac{\Gamma}{2\pi r} = -U_\infty\sin\theta - \frac{B}{\sqrt{B/U_\infty}^2}\sin\theta - \frac{\Gamma}{2\pi R} = -2U_\infty\sin\theta - \frac{\Gamma}{2\pi R} \tag{3.56}$$

The resulting irrotational flow about the cylinder is uniquely determined once the magnitude of the circulation around the body is specified. Using the definition for the pressure coefficient [equation (3.13)], we can obtain:

$$\begin{aligned} C_p &= 1 - \frac{U^2}{U_\infty^2} = 1 - \frac{1}{U_\infty^2}\left[-2U_\infty \sin\theta - \frac{\Gamma}{2\pi R}\right]^2 \\ &= 1 - \frac{1}{U_\infty^2}\left[4U_\infty^2 \sin^2\theta + \frac{2\Gamma U_\infty \sin\theta}{\pi R} + \left(\frac{\Gamma}{2\pi R}\right)^2\right] \\ &= 1 - \left[4\sin^2\theta + \frac{2\Gamma \sin\theta}{\pi R U_\infty} + \left(\frac{\Gamma}{2\pi R U_\infty}\right)^2\right] \end{aligned} \tag{3.57}$$

Notice that two of the three terms inside the square brackets are functions of Γ, meaning that these terms are due to the addition of the vortex. Also notice that if $\Gamma = 0$, equation (3.57) simplifies to equation (3.44), which is the pressure coefficient for flow over a cylinder without circulation. Any differences in our results for the rotating cylinder will have to be due to the terms containing the vortex strength, which is again due to the linear nature of the solutions.

3.15.2 Lift and Drag

If the pressure distribution from equation (3.57) is substituted into the expression for the drag force per unit span of the cylinder, equation (3.50), we obtain:

$$d = -\int_0^{2\pi} p \cos\theta \, R \, d\theta = 0$$

This is true since all of the integrals that result are one of the following three types:

$$\int_0^{2\pi} \sin^2\theta \cos\theta \, d\theta = \int_0^{2\pi} \sin\theta \cos\theta \, d\theta = \int_0^{2\pi} \cos\theta \, d\theta = 0$$

The prediction of zero drag may be generalized to apply to any general, two-dimensional body in an irrotational, steady, incompressible flow. In any real two-dimensional flow, a drag force does exist. For incompressible flow, drag is due to viscous effects, which produce the shear force at the surface and which may also produce significant changes in the pressure field (causing form drag) due to flow separation.

Integrating the pressure distribution to determine the lift force per unit span for the cylinder, equation (3.45), we can obtain:

$$l = -\int_0^{2\pi} p \sin\theta \, R \, d\theta = \rho_\infty U_\infty \Gamma \tag{3.58}$$

This is true since the integrals that result are one of the following three types:

$$\int_0^{2\pi} \sin^3\theta \, d\theta = \int_0^{2\pi} \sin\theta \, d\theta = 0 \qquad \int_0^{2\pi} \sin\theta^2 d\theta = \pi$$

The only non-zero integral is associated with one of the terms containing circulation in equation (3.5):

$$C_p = -\frac{2\Gamma \sin\theta}{\pi R U_\infty} \quad \text{or} \quad p - p_\infty = \left(\frac{1}{2}\rho_\infty U_\infty^2\right)\frac{-2\Gamma \sin\theta}{\pi R U_\infty}$$

and

$$l = -\int_0^{2\pi} \frac{-\rho_\infty U_\infty \Gamma}{\pi} \sin^2\theta \, d\theta = \rho_\infty U_\infty \Gamma$$

Therefore, the lift per unit span is directly related to the circulation about the cylinder. This result, which is known as the *Kutta-Joukowski theorem*, applies to the potential flow about closed cylinders of arbitrary cross section. To see this, consider the circulating flow field around the closed configuration to be represented by the superposition of a uniform flow and a unique set of sources, sinks, and vortices within the body. For a closed body, continuity requires that the sum of the source strengths be equal to the sum of the sink strengths. If we look at the flow field from a point far from the surface of the body, the distance between the sources and sinks becomes negligible and the flow field appears to be that generated by a single doublet with circulation equal to the sum of the vortex strengths within the body. Therefore, in the limit, the forces acting are independent of the shape of the body and:

$$l = \rho_\infty U_\infty \Gamma$$

The locations of the stagnation points (as shown in Fig. 3.25) also depend on the circulation. To locate the stagnation points, we need to find where:

$$v_r = v_\theta = 0$$

Since $v_r = 0$ at every point on the cylinder, the stagnation points occur when $v_\theta = 0$:

$$-2U_\infty \sin\theta - \frac{\Gamma}{2\pi R} = 0$$

or

$$\theta = \sin^{-1}\left(-\frac{\Gamma}{4\pi R U_\infty}\right) \tag{3.59}$$

If $\Gamma < 4\pi R U_\infty$, there are two stagnation points on the surface of the cylinder which are symmetrically located about the y axis (see Fig. 3.25). If $\Gamma = 4\pi U_\infty R$, only one stagnation point exists on the cylinder at $\theta = 270°$. For this magnitude of the circulation, the lift per unit span is

$$l = \rho_\infty U_\infty \Gamma = \rho_\infty U_\infty^2 R 4\pi \tag{3.60}$$

The lift coefficient per unit span of the cylinder is:

$$C_l = \frac{\rho_\infty U_\infty^2 R 4\pi}{\frac{1}{2}\rho_\infty U_\infty^2 2R} = 4\pi \tag{3.61}$$

The value 4π represents the maximum lift coefficient that can be generated for a circulating flow around a cylinder unless the circulation is so strong that no stagnation point

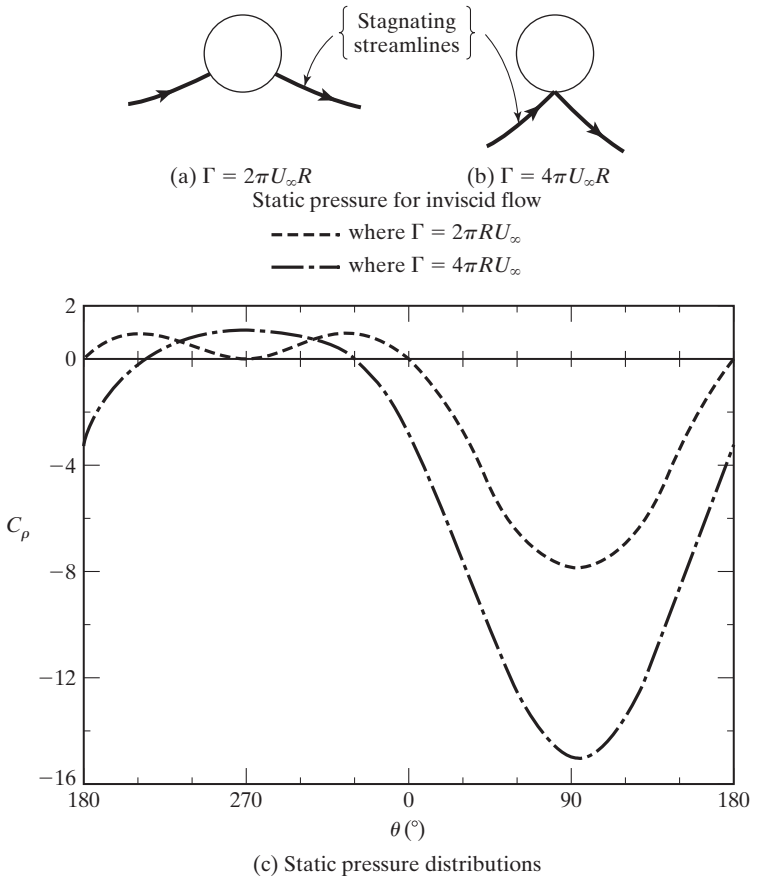

(c) Static pressure distributions

Figure 3.25 Stagnating streamlines and the static pressure distribution for a two-dimensional circulating flow around a cylinder. (a) $\Gamma = 2\pi U_\infty R$; (b) $\Gamma = 4\pi U_\infty R$.

exists on the body. This result is an important "upper limit" for airfoil aerodynamics, which will be important to understand in Chapter 6.

3.15.3 Applications of Potential Flow to Aerodynamics

At this point in our development of potential flow theory, we have only seen a few direct applications of our results to practical aerodynamic shapes. In fact, there are a number of ways to proceed with potential flow theory in order to obtain flow over practical aerodynamic shapes, such as airfoils. These approaches include: conformal mapping, panel methods, and thin airfoil theory. We will briefly describe conformal mapping here, show an example of a panel method in the next section, and develop thin airfoil theory in Chapter 6.

Traditionally, potential flow theory was used to obtain the flow over airfoil shapes using conformal transformations from complex variable theory [Churchill and Brown (1984)]. In this approach, we take the already completed solutions for flow over the cylinder (with or without circulation) and transform that flow into the flow over an airfoil. Although the potential flow around a cylinder is not an accurate model, when transformed into a streamlined shape like an airfoil it actually works very well. One of the more common transformations used is the Joukowski transformation (shown in Fig. 3.26), which produces a family of airfoils with interesting and informative results about the effects of thickness, camber, and angle of attack on airfoil aerodynamics [Karamcheti (1980)].

Once the airfoil shape is mapped using the transformation function, the flow field for the cylinder can be mapped to the airfoil flow. In addition, the pressures acting on the cylinder can be mapped, leading to a fairly straightforward method for obtaining the lift on the airfoil. Interested readers should refer to Karamcheti (1980) for more details about conformal transformations since they lend themselves to computational solutions which are easily accomplished on personal computers.

The other two methods commonly used to find the flow over airfoils are the panel method and thin airfoil theory. Both of these methods require the use of the potential flow singularities described in this chapter to create airfoils and wings by distributing sources, vortices, and doublets to create appropriate flowfields. The panel method is a computational method (described in Section 3.16) that simulates the airfoil surface

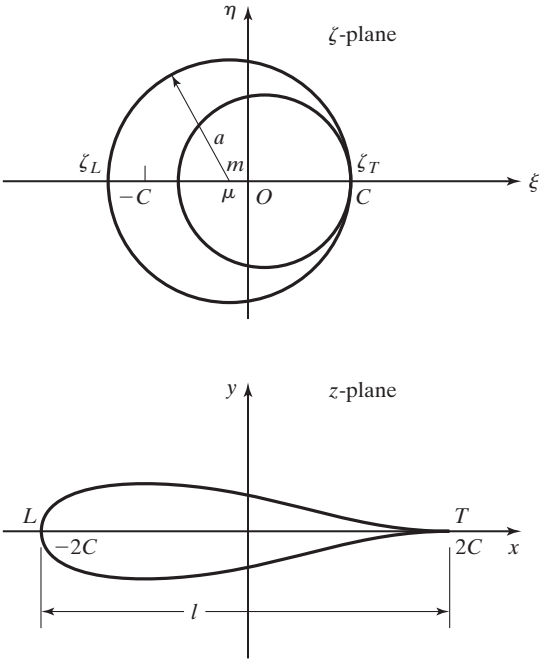

Figure 3.26 Conformal transformation of a circle into a Joukowski airfoil [from Karamcheti (1980)].

with potential flow functions and then determines the velocity and pressure fields due to those functions. The panel method has shown itself to be very useful since it is able to predict the flow over a variety of shapes, including full aircraft configurations. Thin-airfoil theory accomplishes the simulation analytically using vortices to represent the mean camber line of the airfoil, and therefore the results are limited to thin airfoils. We will derive thin-airfoil theory in detail in Chapter 6.

3.16 SOURCE DENSITY DISTRIBUTION ON THE BODY SURFACE

Thus far, we have studied fundamental fluid phenomena, such as the Kutta-Joukowski theorem, using the inverse method. Flow fields for other elementary configurations, such as axisymmetric shapes in a uniform stream parallel to the axis of symmetry, can be represented by a source distribution along the axis of symmetry. An "exact" solution for the flow around an arbitrary configuration can be approached using a direct method in a variety of ways, all of which must finally become numerical and make use of a computing machine. The reader is referred to Hess and Smith (1966) for an extensive review of the problem.

Consider a two-dimensional configuration in a uniform stream, such as shown in Fig. 3.27. The coordinate system used in this section (i.e., x in the chordwise direction and y in the spanwise direction) will be used in subsequent chapters on wing and airfoil aerodynamics. The configuration is represented by a finite number (M) of linear segments, or panels. The effect of the jth panel on the flow field is characterized by a distributed source whose strength is uniform over the surface of the panel. Referring to equation (3.36), a source distribution on the jth panel causes an induced velocity whose potential at a point (x, z) is given by

$$\phi(x, z) = \int \frac{k_j \, ds_j}{2\pi} \ln r \tag{3.62}$$

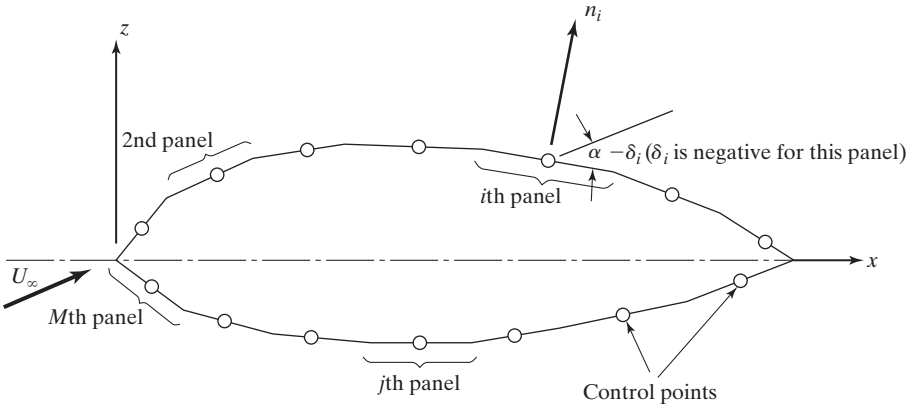

Figure 3.27 Source density distribution of the body surface.

where k_j is defined as the volume of fluid discharged per unit area of the panel and the integration is carried out over the length of the panel ds_j. Note also that

$$r = \sqrt{(x - x_j)^2 + (z - z_j)^2} \tag{3.63}$$

Since the flow is two dimensional, all calculations are for a unit length along the y axis, or span.

Each of the M panels can be represented by similar sources. To determine the strengths of the various sources k_j, we need to satisfy the physical requirement that the surface must be a streamline. Thus, we require that the sum of the source-induced velocities and the free-stream velocity is zero in the direction normal to the surface of the panel at the surface of each of the M panels. The points at which the requirement that the resultant flow is tangent to the surface will be numerically satisfied are called the *control points*. The control points are chosen to be the midpoints of the panels, as shown in Fig. 3.27.

At the control point of the ith panel, the velocity potential for the flow resulting from the superposition of the M source panels and the free-stream flow is

$$\phi(x_i, z_i) = U_\infty x_i \cos\alpha + U_\infty z_i \sin\alpha + \sum_{j=1}^{M} \frac{k_j}{2\pi} \int \ln r_{ij}\, ds_j \tag{3.64}$$

where r_{ij} is the distance from the control point of the ith panel to a point on the jth panel.

$$r_{ij} = \sqrt{(x_i - x_j)^2 + (z_i - z_j)^2} \tag{3.65}$$

Note that the source strength k_j has been taken out of the integral, since it is constant over the jth panel. Each term in the summation represents the contribution of the jth panel (integrated over the length of the panel) to the potential at the control point of the ith panel.

The boundary conditions require that the resultant velocity normal to the surface be zero at each of the control points. Thus,

$$\frac{\partial}{\partial n_i} \phi_i(x_i, z_i) = 0 \tag{3.66}$$

must be satisfied at each and every control point. Care is required in evaluating the spatial derivatives of equation (3.64), because the derivatives become singular when the contribution of the ith panel is evaluated. Referring to equation (3.65), we have

$$r_{ij} = 0$$

where $j = i$. A rigorous development of the limiting process is given by Kellogg (1953). Although the details will not be repeated here, the resultant differentiation indicated in equation (3.66) yields

$$\frac{k_i}{2} + \sum_{\substack{j=1 \\ (j \neq i)}}^{M} \frac{k_j}{2\pi} \int \frac{\partial}{\partial n_i} (\ln r_{ij}) ds_j = -U_\infty \sin(\alpha - \delta_i) \tag{3.67}$$

where δ_i is the slope of the ith panel relative to the x axis. Note that the summation is carried out for all values of j except $j = i$. The two terms of the left side of equation (3.67)

have a simple interpretation. The first term is the contribution of the source density of the ith panel to the outward normal velocity at the point (x_i, z_i), that is, the control point of the ith panel. The second term represents the contribution of the remainder of the boundary surface to the outward normal velocity at the control point of the ith panel.

Evaluating the terms of equation (3.67) for a particular ith control point yields a linear equation in terms of the unknown source strengths k_j (for $j = 1$ to M, including $j = i$). Evaluating the equation for all values of i (i.e., for each of the M control points) yields a set of M simultaneous equations which can be solved for the source strengths. Once the panel source strengths have been determined, the velocity can be determined at any point in the flow field using equations (3.64) and (3.65). With the velocity known, Bernoulli's equation can be used to calculate the pressure field.

Lift can be introduced by including vortex or doublet distributions and by introducing the Kutta condition, as we will discuss in Chapters 6 and 7.

EXAMPLE 3.8: Application of the source density distribution

We can apply the surface source density distribution to describe the flow around a cylinder in a uniform stream, where the free-stream velocity is U_∞. For simplicity, we will assume the radius of the cylinder is unity. The cylinder is represented by eight equal-length linear segments, as shown in Fig. 3.28. The panels are arranged such that panel 1 is perpendicular to the undisturbed stream.

Solution: We can calculate the contribution of the source distribution on panel 2 to the normal velocity at the control point of panel 3. A detailed sketch of the two panels involved in this sample calculation is presented in Fig. 3.29. Referring to equation (3.67), we are to evaluate the integral:

$$\int \frac{\partial}{\partial n_i}(\ln r_{ij})\, ds_j$$

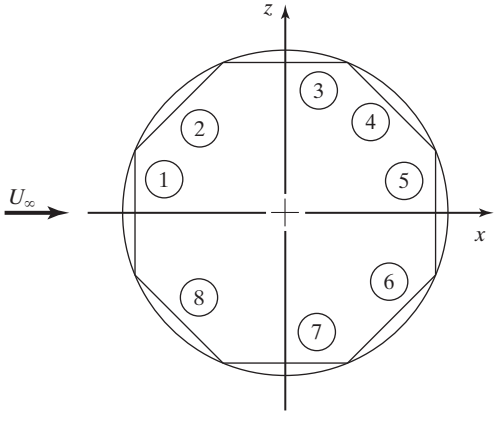

Figure 3.28 Representation of flow around a cylinder of unit radius by eight surface source panels.

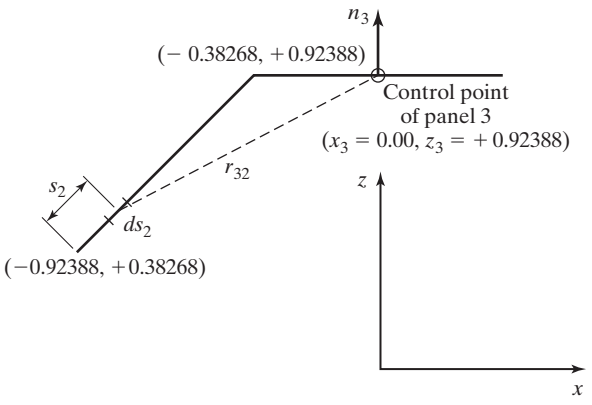

Figure 3.29 Detailed sketch for calculation of the contribution of the source distribution on panel 2 to the normal velocity at the control point of panel 3.

where $i = 3$ and $j = 2$. We will call this integral I_{32}. Note that

$$\frac{\partial}{\partial n_3}(\ln r_{32}) = \frac{1}{r_{32}}\frac{\partial r_{32}}{\partial n_3}$$
$$= \frac{(x_3 - x_2)\dfrac{\partial x_3}{\partial n_3} + (z_3 - z_2)\dfrac{\partial z_3}{\partial n_3}}{(x_3 - x_2)^2 + (z_3 - z_2)^2} \tag{3.68}$$

where $x_3 = 0.00$ and $z_3 = 0.92388$ are the coordinates of the control point of panel 3. Note also that

$$\frac{\partial x_3}{\partial n_3} = 0.00, \qquad \frac{\partial z_3}{\partial n_3} = 1.00$$

Furthermore, for the source line represented by panel 2 we know:

$$x_2 = -0.92388 + 0.70711 s_2$$
$$z_2 = +0.38268 + 0.70711 s_2$$

and the length of the panel is:

$$l_2 = 0.76537$$

Combining these expressions, we can obtain:

$$I_{32} = \int_0^{0.76537} \frac{(0.92388 - 0.38268 - 0.70711 s_2)\,ds_2}{(0.92388 - 0.70711 s_2)^2 + (0.92388 - 0.38268 - 0.70711 s_2)^2}$$

This equation can be rewritten as:

$$I_{32} = 0.54120 \int_0^{0.76537} \frac{ds_2}{1.14645 - 2.07195s_2 + 1.00002s_2^2}$$
$$-0.70711 \int_0^{0.76537} \frac{s_2 ds_2}{1.14645 - 2.07195s_2 + 1.00002s_2^2}$$

Using the integral tables to evaluate these expressions, we can now obtain:

$$I_{32} = -0.70711\left[\tfrac{1}{2}\ln(s_2^2 - 2.07195s_2 + 1.14645)\right]_{s_2=0}^{s_2=0.76537}$$
$$-0.70711\left[\tan^{-1}\left(\frac{2s_2 - 2.07195}{\sqrt{0.29291}}\right)\right]_{s_2=0}^{s_2=0.76537}$$

Therefore:

$$I_{32} = 0.3528$$

In a similar manner, we could calculate the contributions of source panels 1, 4, 5, 6, 7, and 8 to the normal velocity at the control point of panel 3. Substituting the values of these integrals into equation (3.67), we obtain a linear equation of the form:

$$I_{31}k_1 + I_{32}k_2 + \pi k_3 + I_{34}k_4 + I_{35}k_5 + I_{36}k_6 + I_{37}k_7 + I_{38}k_8 = 0.00 \quad \textbf{(3.69)}$$

The right-hand side is zero since $\alpha = 0$ and $\delta_3 = 0$.

Repeating the process for all eight control points, we would obtain a set of eight linear equations involving the eight unknown source strengths. Solving the system of equations, we would find that:

$$k_1 = 2\pi U_\infty(+0.3765)$$
$$k_2 = 2\pi U_\infty(+0.2662)$$
$$k_3 = 0.00$$
$$k_4 = 2\pi U_\infty(-0.2662)$$
$$k_5 = 2\pi U_\infty(-0.3765)$$
$$k_6 = 2\pi U_\infty(-0.2662)$$
$$k_7 = 0.00$$
$$k_8 = 2\pi U_\infty(+0.2662)$$

Note there is a symmetrical pattern in the source distribution, as should be expected due to the symmetrical flow pattern. Also,

$$\sum k_i = 0 \quad \textbf{(3.70)}$$

as must be true since the sum of the strengths of the sources and sinks (negative sources) must be zero if we are to have a closed configuration.

3.17 INCOMPRESSIBLE, AXISYMMETRIC FLOW

The irrotational flows discussed thus far have been planar (two dimensional). That is, the flow field that exists in the plane of the paper will exist in any and every plane parallel to the plane of the paper. Although sketches of the flow field defined by equations (3.41) through (3.61) depict the flow around a circle of radius R, in reality they represent the flow around a circular cylinder whose axis is perpendicular to the plane of the paper. For these flows, $w \equiv 0$ and $\partial/\partial z \equiv 0$.

We will now consider another type of "two-dimensional" flow: an axisymmetric flow. The coordinate system for axisymmetric flow is illustrated in Fig. 3.30. There are no circumferential variations in an axisymmetric flow, which means:

$$v_\theta \equiv 0 \quad \text{and} \quad \frac{\partial}{\partial \theta} \equiv 0$$

Thus, the incompressible, continuity equation becomes

$$\nabla \cdot \vec{V} = \frac{\partial v_r}{\partial r} + \frac{v_r}{r} + \frac{\partial v_z}{\partial z} = 0$$

Notice that r and z are the independent coordinates (i.e., variables), we can rewrite this expression as

$$\frac{\partial}{\partial r}(rv_r) + \frac{\partial}{\partial z}(rv_z) = 0 \tag{3.71}$$

As we discussed before, a stream function can exist for an incompressible, two-dimensional flow. The flow need be two dimensional only in the sense that it requires only two spatial coordinates to describe the motion. The stream function that identically satisfies equation (3.71) is

$$\frac{\partial \psi}{\partial z} = rv_r \quad \text{and} \quad \frac{\partial \psi}{\partial r} = -rv_z$$

Therefore, in the coordinate system of Fig. 3.30,

$$v_r = \frac{1}{r}\frac{\partial \psi}{\partial z} \quad \text{and} \quad v_z = -\frac{1}{r}\frac{\partial \psi}{\partial r} \tag{3.72}$$

Note that $\psi =$ constant defines a stream surface.

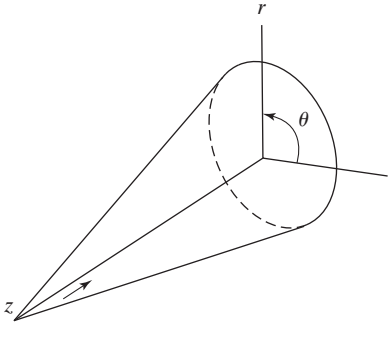

Figure 3.30 Coordinate system for an axisymmetric flow.

3.17.1 Flow around a Sphere

To describe a steady, inviscid, incompressible flow around a sphere, we will add the axisymmetric potential functions for a uniform flow and for a point doublet. We will first introduce the necessary relations in spherical coordinates. For a spherical coordinate system,

$$v_r = \frac{\partial \phi}{\partial r} \qquad v_\omega = \frac{1}{r}\frac{\partial \phi}{\partial \omega} \qquad v_\theta = \frac{1}{r \sin \omega}\frac{\partial \phi}{\partial \theta} \tag{3.73}$$

for an irrotational flow where $\vec{V} = \nabla\phi$. In equation (3.73), ϕ represents the potential function, and r, θ, and ω represent the independent coordinates. By symmetry,

$$v_\theta = 0 \quad \text{and} \quad \frac{\partial}{\partial \theta} = 0$$

The velocity potential for an axisymmetric doublet is

$$\phi = +\frac{B}{4\pi r^2}\cos \omega$$

where the doublet is so oriented that the source is placed upstream and the doublet axis is parallel to the uniform flow. The potential function for a uniform flow is

$$\phi = U_\infty r \cos \omega$$

Thus, the sum of the potential functions is

$$\phi = U_\infty r \cos \omega + \frac{B}{4\pi r^2}\cos \omega \tag{3.74}$$

The velocity components for this potential function are

$$v_r = \frac{\partial \phi}{r} = U_\infty \cos \omega - \frac{B}{2\pi r^3}\cos \omega \tag{3.75a}$$

and

$$v_\omega = \frac{1}{r}\frac{\partial \phi}{\partial \omega} = -U_\infty \sin \omega - \frac{B}{4\pi r^3}\sin \omega \tag{3.75b}$$

As we did when modeling the inviscid flow around a cylinder, we note that

$$v_r = 0$$

when

$$r^3 = \frac{B}{2\pi U_\infty} = \text{constant} = R^3$$

Thus, if $B = 2\pi U_\infty R^3$, we can use the potential function described by equation (3.74) to describe steady, inviscid, incompressible flow around a sphere of radius R. For this flow,

$$v_r = U_\infty\left(1 - \frac{R^3}{r^3}\right)\cos \omega \tag{3.76a}$$

and

$$v_\omega = -U_\infty\left(1 + \frac{R^3}{2r^3}\right)\sin\omega \tag{3.76b}$$

On the surface of the sphere (i.e., for $r = R$), the resultant velocity is given by

$$U = |\vec{V}| = v_\omega = -\tfrac{3}{2}U_\infty \sin\omega \tag{3.77}$$

The static pressure acting at any point on the sphere can be calculated using equation (3.77) to represent the local velocity in Bernoulli's equation:

$$p = p_\infty + \tfrac{1}{2}\rho_\infty U_\infty^2 - \tfrac{1}{2}\rho_\infty U_\infty^2(\tfrac{9}{4}\sin^2\omega) \tag{3.78}$$

Rearranging the terms, we obtain the expression for the pressure coefficient for steady, inviscid, incompressible flow around a sphere:

$$C_p = 1 - \tfrac{9}{4}\sin^2\omega \tag{3.79}$$

Compare this expression with equation (3.44) for flow around a cylinder of infinite span whose axis is perpendicular to the free-stream flow:

$$C_p = 1 - 4\sin^2\theta$$

Note that both θ and ω represent the angular coordinate relative to the axis, one for the two-dimensional flow, the other for axisymmetric flow. Thus, although the configurations have the same cross section in the plane of the paper (a circle) and both are described in terms of two coordinates, the flows are significantly different.

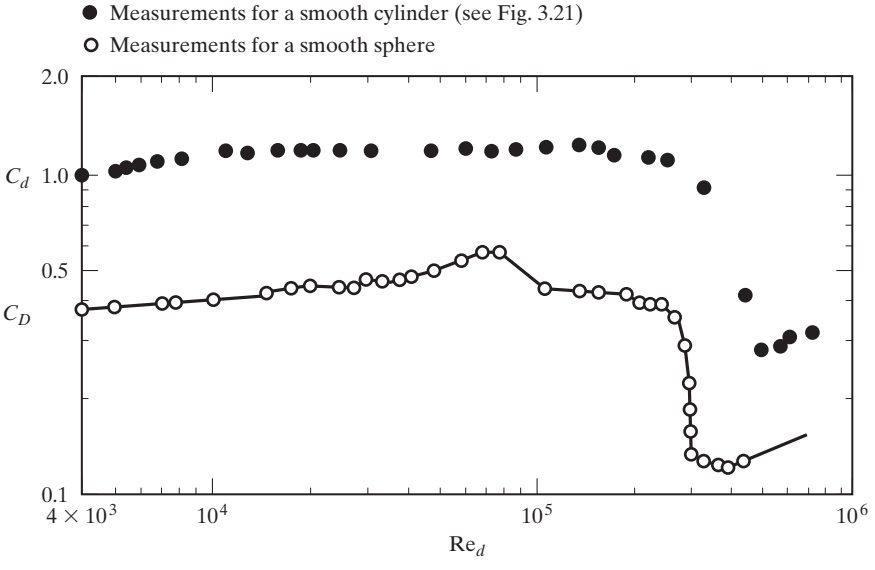

Figure 3.31 Drag coefficient for a sphere as a function of the Reynolds number [data from Schlichting, *Boundary Layer Theory* (1968)].

The drag coefficients for a sphere, as reported in Schlichting (1968), are presented as a function of the Reynolds number in Fig. 3.31. The drag coefficient for a sphere is defined as

$$C_D = \frac{\text{drag}}{q_\infty(\pi d^2/4)} \tag{3.80}$$

The Reynolds number dependence of the drag coefficient for a smooth sphere is similar to that for a smooth cylinder. Again, a significant reduction in drag occurs as the critical Reynolds number is exceeded and the windward boundary layer becomes turbulent.

3.18 SUMMARY

In most flow fields of interest to the aerodynamicist, there are regions where the product of the viscosity times the shearing velocity gradient is sufficiently small that we may neglect the shear stress terms in our analysis. The momentum equation for these inviscid flows is known as Euler's equation. From Kelvin's theorem, we know that a flow remains irrotational in the absence of viscous forces and discontinuities provided that the flow is barotropic and the body forces are conservative. Potential functions can be used to describe the velocity field for such flows. If we assume further that the flow is incompressible (i.e., low speed), we can linearly add potential functions to obtain the velocity field for complex configurations and use Bernoulli's equation to determine the corresponding pressure distribution. The inviscid flow field solutions form the outer (edge) boundary conditions for the thin viscous boundary layer adjacent to the wall. The characteristics of the boundary layer and techniques for analyzing it are described in the next chapter.

PROBLEMS

3.1. A truck carries an open tank, that is 6 m long, 2 m wide, and 3 m deep. Assuming that the driver will not accelerate or decelerate the truck at a rate greater than 2 m/s^2, what is the maximum depth to which the tank may be filled so that the water will not be spilled?

3.2. The wind reaches at a speed of 50 m/s in a storm. Calculate the force acting on the window of Cross-section area 2 sq.m facing the storm. The window is in a high-rise building, so the speed is not reduced due to ground effects. Let the density of the air $\rho = 1.27$ kg/m^3.

3.3. A Pitot tube is mounted on the nose of an aircraft to measure the pressure. If the aircraft is flying at an altitude of 4500 m and the reading of Pitot tube is 60000 N/m^2 (abs). What is the airspeed?

3.4. Water fills the circular tank (which is 20.0 ft in diameter) shown in Fig. P3.4. Water flows out of a hole which is 1.0 in. in diameter and which is located in the side of the tank, 15.0 ft from the top and 15.0 ft from the bottom. Consider the water to be inviscid. $\rho_{H_2O} = 1.940$ slug/ft^3.

(a) Calculate the static pressure and the velocity at points 1, 2, and 3. For these calculations, you can assume that the fluid velocities are negligible at points more than 10.0 ft from the opening.

(b) Having calculated U_3 in part (a), what is the velocity U_1? Was the assumption of part (a) valid?

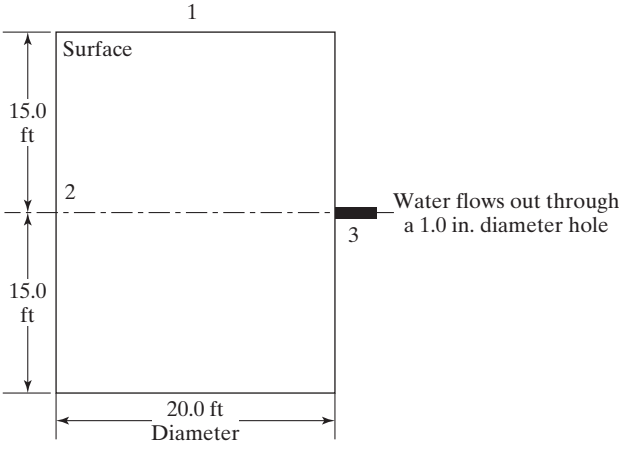

Figure P3.4

3.5. Consider a low-speed, steady flow around the thin airfoil shown in Fig. P3.5. We know the velocity and altitude at which the vehicle is flying. Thus, we know p_∞ (i.e., p_1) and U_∞. We have obtained experimental values of the local static pressure at points 2 through 6. At which of these points can we use Bernoulli's equation to determine the local velocity? If we cannot, why not?

Point 2: at the stagnation point of airfoil

Point 3: at a point in the inviscid region just outside the laminar boundary layer

Point 4: at a point in the laminar boundary layer

Point 5: at a point in the turbulent boundary layer

Point 6: at a point in the inviscid region just outside the turbulent boundary layer

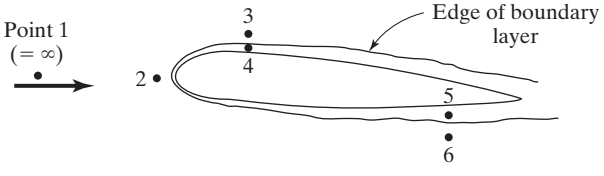

Figure P3.5

3.6. Assume that the airfoil of problem 3.5 is moving at 300 km/h at an altitude of 3 km. The experimentally determined pressure coefficients are

Point	2	3	4	5	6
C_p	1.00	−3.00	−3.00	+0.16	+0.16

(a) What is the Mach number and the Reynolds number for this configuration? Assume that the characteristic dimension for the airfoil is 1.5 m.

(b) Calculate the local pressure in N/m^2 and in $lbf/in.^2$ at all five points. What is the percentage change in the pressure relative to the free-stream value? That is, what is $(p_{local} - p_\infty)/p_\infty$? Was it reasonable to assume that the pressure changes are sufficiently small that the density is approximately constant?

(c) Why are the pressures at points 3 and 4 equal and at points 5 and 6 equal?
(d) At those points where Bernoulli's equation can be used validly, calculate the local velocity.

3.7. A Pitot-static probe is used to determine the airspeed of an airplane that is flying at an altitude of 5000 m. If the stagnation pressure is 5.7540×10^4 N/m^2 what is the airspeed? What is the pressure recorded by a gage that measures the difference between the stagnation pressure and the static pressure (such as that shown in Fig. 3.2)? How fast would an airplane have to fly at sea level to produce the same reading on this gage?

3.8. The pressure far from an irrotational vortex in the atmosphere is zero gage. If the velocity of the air V_1 is 20 m/s at a distance $r_1 = 20$ m, then estimate the velocity of the air V_2 and the pressure P_2 at a distance $r_2 = 1.0$ m. Let density of the air $\rho = 1.2$ kg/m^3.

3.9. A high-rise office building located in a city at sea level is exposed to a wind of 75 km/h. What is the static pressure of the airstream away from the influence of the building? What is the maximum pressure acting on the building? Pressure measurements indicate that a value of $C_p = -4$ occurs near the corner of the wall parallel to the wind direction. If the internal pressure equals to the free-stream static pressure, what is the total force on the pane of glass 1 m $\times$ 3 m located in this region?

3.10. You are working as a flight-test engineer at the Dryden Flight Research Center. During the low-speed phase of the test program for the X-37, you know that the plane is flying at an altitude of 8 km. The pressure at gage 1 is 1550 N/m^2, gage; the pressure at gage 2 is -3875 N/m^2, gage.

(a) If gage 1 is known to be at the stagnation point, what is the velocity of the airplane? What is its Mach number?
(b) What is the free-stream dynamic pressure for this test condition?
(c) What is the velocity of the air at the edge of the boundary layer at the second point relative to the airplane? What is the velocity relative to the ground? What is C_p for this gage?

3.11. Air flows through a converging pipe section, as shown in Fig. P3.11. Since the centerline of the duct is horizontal, the change in potential energy is zero. The Pitot probe at the upstream station provides a measure of the total pressure (or stagnation pressure). The downstream end of the U-tube provides a measure of the static pressure at the second station. Assuming the density of air to be 0.002367 slug/ft^3 and neglecting the effects of viscosity, compute the volumetric flow rate in ft^3/s. The fluid in the manometer is unity weight oil ($\rho_{oil} = 1.94033$ slug/ft^3).

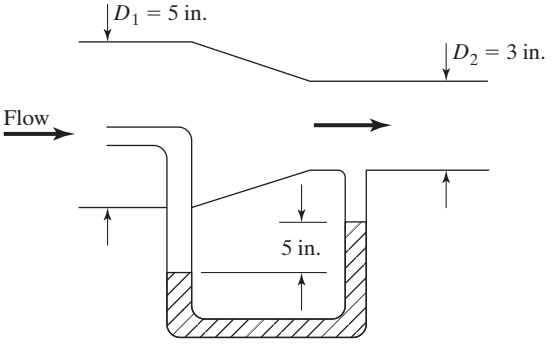

Figure P3.11

3.12. An in-draft wind tunnel (Fig. P3.12) takes air from the quiescent atmosphere (outside the tunnel) and accelerates it in the converging section, so that the velocity of the air at a point in the test section but far from the model is 60 m/s. What is the static pressure at this point? What is the pressure at the stagnation point on a model in the test section? Use Table 1.2 to obtain the properties of the ambient air, assuming that the conditions are those for the standard atmosphere at sea level.

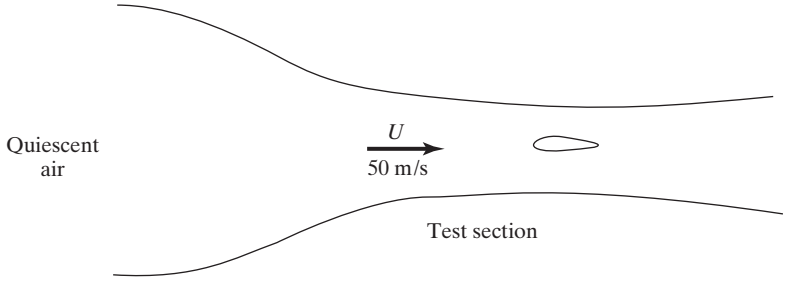

Figure P3.12

3.13. A venturi meter is a device that is inserted into a pipeline to measure incompressible flow rates. As shown in Fig. P3.13, it consists of a convergent section that reduces the diameter to between one-half and one-fourth of the pipe diameter. This is followed by a divergent section through which the flow is returned to the original diameter. The pressure difference between a location just before the venturi and one at the throat of the venturi is used to determine the volumetric flow rate (Q). Show that

$$Q = C_d\left[\frac{A_2}{\sqrt{1 - (A_2/A_1)^2}}\sqrt{\frac{2g(p_1 - p_2)}{\gamma}}\right]$$

where C_d is the coefficient of discharge, which takes into account the frictional effects and is determined experimentally or from handbook tabulations.

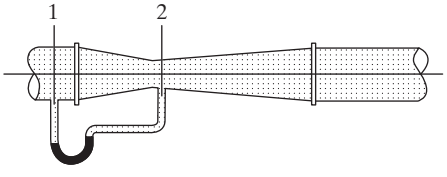

Figure P3.13

3.14. You are in charge of the pumping unit used to pressurize a large water tank on a fire truck. The fire that you are to extinguish is on the sixth floor of a building, 70 ft higher than the truck hose level, as shown in Fig. P3.14.

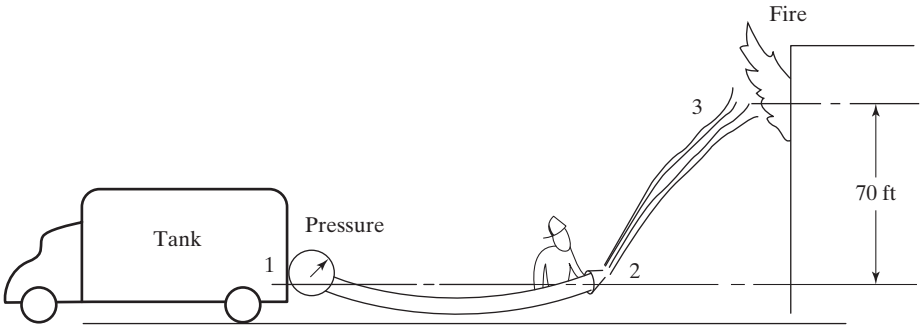

Figure P3.14

(a) What is the minimum pressure in the large tank for the water to reach the fire? Neglect pressure losses in the hose.

(b) What is the velocity of the water as it exits the hose? The diameter of the nozzle is 3.0 in. What is the flow rate in gallons per minute? Note that 1 gal/min equals 0.002228 ft^3/s.

3.15. A free jet of water leaves the tank horizontally, as shown in Fig. P3.15. Assuming that the tank is large and the losses are negligible, derive an expression for the distance X (from the tank to the point where the jet strikes the floor) as a function of h and H? What is X, if the liquid involved was gasoline for which $\sigma = 0.70$?

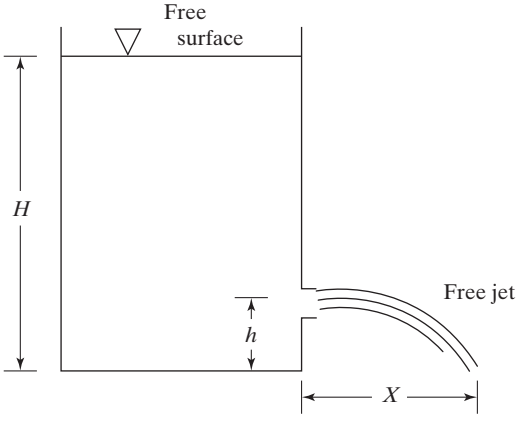

Figure P3.15

3.16. **(a)** What conditions are necessary before you can use a stream function to solve for the flow field?

(b) What conditions are necessary before you can use a potential function to solve for the flow field?

(c) What conditions are necessary before you can apply Bernoulli's equation to relate two points in a flow field?

(d) Under what conditions does the circulation around a closed fluid line remain constant with respect to time?

3.17. What is the circulation around a circle of constant radius R_1 for the velocity field given as

$$\vec{V} = \frac{\Gamma}{2\pi r}\hat{e}_\theta$$

3.18. The velocity field for the fully developed viscous flow discussed in Example 2.2 is

$$u = 0$$
$$v = 0$$
$$w = \frac{1}{\mu}\frac{dp}{dx}\left(y - \frac{h}{2}\right)$$

Is the flow rotational or irrotational? Why?

3.19. Find the integral along the path $\vec{s}$ between the points $(0, 0)$ and $(1, 2)$ of the component of $\vec{V}$ in the direction of $\vec{s}$ for the following three cases:

(a) $\vec{s}$ a straight line.
(b) $\vec{s}$ a parabola with vertex at the origin and opening to the right.
(c) $\vec{s}$ a portion of the x axis and a straight line perpendicular to it.

The components of $\vec{V}$ are given by the expressions

$$u = x^2 + y^2$$
$$v = 2xy^2$$

3.20. Consider the velocity field given in Problem 3.12:

$$\vec{V} = (x^2 + y^2)\hat{i} + 2xy^2\hat{j}$$

Is the flow rotational or irrotational? Calculate the circulation around the right triangle shown in Fig. P3.20.

$$\oint \vec{V} \cdot \overrightarrow{ds} = ?$$

What is the integral of the component of the curl $\vec{V}$ over the surface of the triangle? That is,

$$\iint (\nabla \times \vec{V}) \cdot \hat{n}\, \overrightarrow{dA} = ?$$

Are the results consistent with Stokes's theorem?

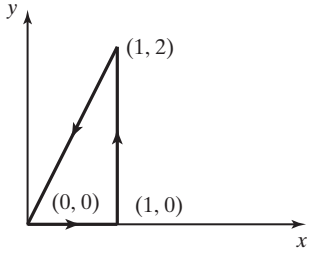

Figure P3.20

3.21. The absolute value of velocity and the equation of the potential function lines in a two-dimensional velocity field (Fig. P3.21) are given by the expressions

$$|\vec{V}| = \sqrt{4x^2 + 4y^2}$$
$$\phi = x^2 - y^2 + C$$

Evaluate both the left-hand side and the right-hand side of equation (3.16) to demonstrate the validity of Stokes's theorem of this irrotational flow.

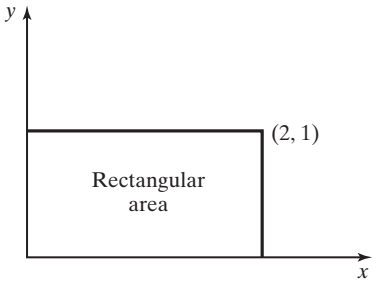

Figure P3.21

3.22. Consider the incompressible, irrotational two-dimensional flow where the potential function is

$$\phi = K \ln \sqrt{x^2 + y^2}$$

where K is an arbitrary constant.

(a) What is the velocity field for this flow? Verify that the flow is irrotational. What is the magnitude and direction of the velocity at $(2, 0)$, at $(\sqrt{2}, \sqrt{2})$, and at $(0, 2)$?
(b) What is the stream function for this flow? Sketch the streamline pattern.
(c) Sketch the lines of constant potential. How do the lines of equipotential relate to the streamlines?

3.23. The stream function of a two-dimensional, incompressible flow is given by

$$\psi = \frac{\Gamma}{2\pi} \ln r$$

(a) Graph the streamlines.
(b) What is the velocity field represented by this stream function? Does the resultant velocity field satisfy the continuity equation?
(c) Find the circulation about a path enclosing the origin. For the path of integration, use a circle of radius 3 with a center at the origin. How does the circulation depend on the radius?

3.24. The absolute value of the velocity and the equation of the streamlines in a velocity field are given by

$$|\vec{V}| = \sqrt{2y^2 + x^2 + 2xy}$$
$$\psi = y^2 + 2xy = \text{constant}$$

Find u and v.

3.25. The absolute value of the velocity and the equation of the streamlines in a two-dimensional velocity field (Fig. P3.25) are given by the expressions

$$|\vec{V}| = \sqrt{5y^2 + x^2 + 4xy}$$
$$\psi = xy + y^2 = C$$

Find the integral over the surface shown of the normal component of curl $\vec{V}$ by two methods.

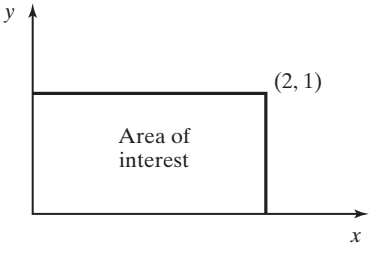

Figure P3.25

3.26. Given an incompressible, steady flow, where the velocity is

$$\vec{V} = (x^2y - xy^2)\,\hat{i} + \left(\frac{y^3}{3} - xy^2\right)\hat{j}$$

(a) Does the velocity field satisfy the continuity equation? Does a stream function exist? If a stream function exists, what is it?
(b) Does a potential function exist? If a potential function exists, what is it?
(c) For the region shown in Fig. P3.26, evaluate

$$\iint (\nabla \times \vec{V}) \cdot \hat{n}\, \overrightarrow{dA} = ?$$

and

$$\oint \vec{V} \cdot \overrightarrow{ds} = ?$$

to demonstrate that Stokes's theorem is valid.

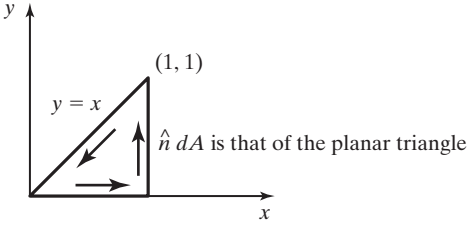

Circulation around the triangle

Figure P3.26

3.27. Consider the superposition of a uniform flow and a source of strength K. If the distance from the source to the stagnation point is R, calculate the strength of the source in terms of U_∞ and R.

(a) Determine the equation of the streamline that passes through the stagnation point. Let this streamline represent the surface of the configuration of interest.

(b) Noting that

$$v_r = \frac{1}{r}\frac{\partial \psi}{\partial \theta} \qquad v_\theta = -\frac{\partial \psi}{\partial r}$$

complete the following table for the surface of the configuration.

θ	$\frac{r}{R}$	$\frac{U}{U_\infty}$	C_p
30°			
45°			
90°			
135°			
150°			
180°			

3.28. A two-dimensional free vortex is located near an infinite plane at a distance h above the plane (Fig. P3.28). The pressure at infinity is p_∞ and the velocity at infinity is U_∞ parallel to the plane. Find the total force (per unit depth normal to the paper) on the plane if the pressure on the underside of the plane is p_∞. The strength of the vortex is Γ. The fluid is incompressible and perfect. To what expression does the force simplify if h becomes very large?

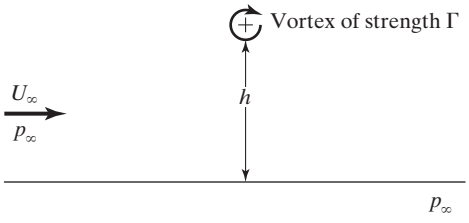

Figure P3.28

3.29. A perfect, incompressible irrotational fluid is flowing past a wall with a sink of strength K per unit length at the origin (Fig. P3.29). At infinity the flow is parallel and of uniform velocity U_∞. Determine the location of the stagnation point x_0 in terms of U_∞ and K. Find the pressure distribution along the wall as a function of x. Taking the free-stream static pressure at infinity to be p_∞, express the pressure coefficient as a function of x/x_0. Sketch the resulting pressure distribution.

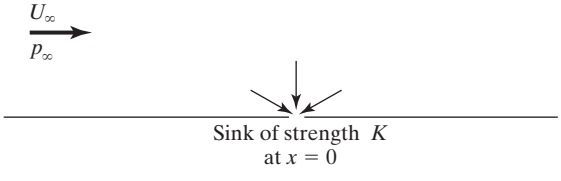

Figure P3.29

3.30. What is the stream function that represents the potential flow about a cylinder whose radius is 2 m and which is located in an air stream where the free-stream velocity is 30 m/s? What is the change in pressure from the free-stream value to the value at the top of the cylinder (i.e., $\theta = 90°$)? What is the change in pressure from the free-stream value to that at the stagnation point (i.e., $\theta = 180°$)? Assume that the free-stream conditions are those of the standard atmosphere at sea level.

3.31. Consider the flow formed by a uniform flow superimposed on a doublet whose axis is parallel to the direction of the uniform flow and is so oriented that the direction of the efflux opposes the uniform flow. This is the flow field of Section 3.13.1. Using the stream functions for these two elementary flows, show that a circle of radius R, where

$$R = \sqrt{\frac{B}{U_\infty}}$$

is a streamline in the flow field.

3.32. Consider the flow field that results when a vortex with clockwise circulation is superimposed on the doublet/uniform-flow combination discussed in Problem 3.31. This is the flow field of Section 3.15.1. Using the stream functions for these three elementary flows, show that a circle of radius R, where

$$R = \sqrt{\frac{B}{U_\infty}}$$

is a streamline in the flow field.

3.33. A cylindrical tube with three radially drilled orifices, as shown in Fig. P3.33, can be used as a flow-direction indicator. Whenever the pressure on the two side holes is equal, the pressure at the center hole is the stagnation pressure. The instrument is called a *direction-finding Pitot tube*, or a *cylindrical yaw probe*.

(a) If the orifices of a direction-finding Pitot tube were to be used to measure the free-stream static pressure, where would they have to be located if we use our solution for flow around a cylinder?

(b) For a direction-finding Pitot tube with orifices located as calculated in part (a), what is the sensitivity? Let the sensitivity be defined as the pressure change per unit angular change (i.e., $\partial p/\partial\theta$).

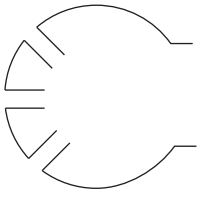

Figure P3.33

3.34. An infinite-span cylinder (two-dimensional) serves as a plug between the two airstreams, as shown in Fig. P3.34. Both air flows may be considered to be steady, inviscid, and incompressible. Neglecting the body forces in the air and the weight of the cylinder, in which direction does the plug move (i.e., due to the airflow)?

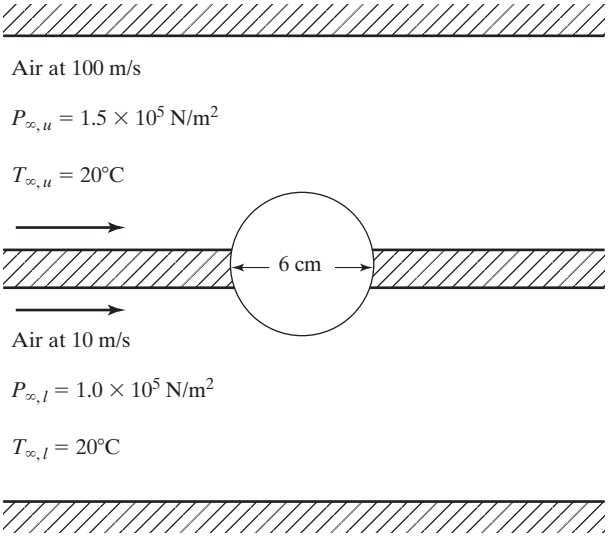

Figure P3.34

3.35. Using the data of Fig. 3.30, calculate the force and the overturning moment exerted by a 4 m/s wind on a cylindrical smokestack that has a diameter of 3 m and a height of 50 m. Neglect variations in the velocity of the wind over the height of the smokestack. The temperature of the air is 30°C; its pressure is 99 kPa. What is the Reynolds number for this flow?

3.36. Calculate the force and the overturning moment exerted by a 20 m/s wind on a cylindrical flagpole that has a diameter of 15 cm. and a height of 4.5 m. Neglect variations in the velocity of the wind over the height of the flagpole. The temperature of the air is 303.15°C; its pressure is 99000 N/m^2. What is the Reynolds number of this flow?

3.37. A cylinder 0.9 m in diameter is placed in a stream of air at temperature 293.15 K where the free-stream velocity is 36 m/s. What is the vortex strength required in order to place the stagnation points at $\theta = 30°$ and $\theta = 150°$? If the free-stream pressure is 95000 N/m^2, what is the pressure at the stagnation points? What will be the velocity and the static pressure at $\theta = 90°$? at $\theta = 270°$? What will be the theoretical value of the lift per span wise meter of the cylinder?

3.38. Consider the flow around the quonset hut shown in Fig. P3.38 to be represented by superimposing a uniform flow and a doublet. Assume steady, incompressible, potential flow. The ground plane is represented by the plane of symmetry and the hut by the upper half of the cylinder. The free-stream velocity is 175 km/h; the radius R_0 of the hut is 6 m. The door is not well sealed, and the static pressure inside the hut is equal to that on the outer surface of the hut, where the door is located.

(a) If the door to the hut is located at ground level (i.e., at the stagnation point), what is the net lift acting on the hut? What is the lift coefficient?

(b) Where should the door be located (i.e., at what angle θ_0 relative to the ground) so that the net force on the hut will vanish?

For both parts of the problem, the opening is very small compared to the radius R_0. Thus, the pressure on the door is essentially constant and equal to the value of the angle θ_0 at which the door is located. Assume that the wall is negligibly thin.

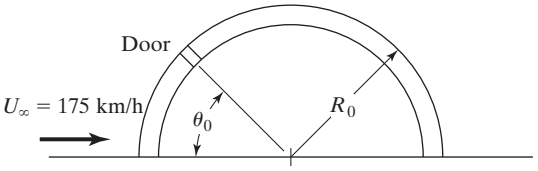

Figure P3.38

3.39. Consider an incompressible flow around a semicylinder, as shown in Fig. P3.39. Assume that velocity distribution for the windward surface of the cylinder is given by the inviscid solution

$$\vec{V} = -2U_\infty \sin\theta\, \hat{e}_\theta$$

Calculate the lift and drag coefficients if the base pressure (i.e., the pressure on the flat, or leeward, surface) is equal to the pressure at the separation point, p_{corner}.

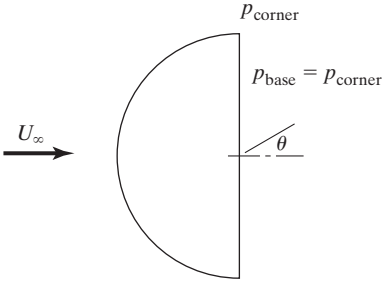

Figure P3.39

3.40. A fully loaded aircraft weighing 900 kN has a wing area of 230m^2. If the wing has the characteristics of a NACA 23012 airfoil and during takeoff operates at a 6^0 angle of attack, what is the required takeoff speed at sea level? What is the takeoff speed at an elevation of 2000 m? Let $C_L = 0.79$.

3.41. You are to design quonset huts for a military base in the mideast. The design wind speed is 100 ft/s. The static free-stream properties are those for standard sea-level conditions. The quonset hut may be considered to be a closed (no leaks) semicylinder, whose radius is 15 ft, mounted on tie-down blocks, as shown in Example 3.5. The flow is such that the velocity distribution and, thus, the pressure distribution over the top of the hut (the semicircle of the sketch) are represented by the potential function

$$\phi = U_\infty r\cos\theta + \frac{B}{r}\cos\theta$$

When calculating the flow over the hut, neglect the presence of the air space under the hut. The air under the hut is at rest and the pressure is equal to stagnation pressure, $p_t (= p_\infty + \frac{1}{2}\rho_\infty U_\infty^2)$.

(a) What is the value of B for the 15-ft-radius (R) quonset hut?
(b) What is the net lift force acting on the quonset hut?
(c) What is the net drag force acting on the quonset hut?

3.42. Using equation (3.56) to define the surface velocity distribution for inviscid flow around a cylinder with circulation, derive the expression for the local static pressure as a function of θ. Substitute the pressure distribution into the expression for the lift to verify that equation (3.58) gives the lift force per unit span. Using the definition that

$$C_l = \frac{l}{q_\infty 2R}$$

(where l is the lift per unit span), what is the section lift coefficient?

3.43. Combining equations (3.45) and (3.49), it has been shown that the section lift coefficient for inviscid flow around a cylinder is

$$C_l = -\tfrac{1}{2}\int_0^{2\pi} C_p \sin\theta \, d\theta \tag{3.48}$$

Using equation (3.57) to define the pressure coefficient distribution for inviscid flow with circulation, calculate the section lift coefficient for this flow.

3.44. There were early attempts in the development of the airplane to use rotating cylinders as airfoils. Consider such a cylinder having a diameter of 0.5 m and a length of 5 m. If this cylinder is rotated at 200 rpm while the plane moves at a speed of 50 km/h through the air at 1 km standard atmosphere, estimate the maximum lift that could be developed, disregarding end effects?

3.45. Using the procedures illustrated in Example 3.6, calculate the contribution of the source distribution on panel 3 to the normal velocity at the control point of panel 4. The configuration geometry is illustrated in Fig. 3.27.

3.46. Consider the pressure distribution shown in Fig. P3.46 for the windward and leeward surfaces of a thick disk whose axis is parallel to the free-stream flow. What is the corresponding drag coefficient?

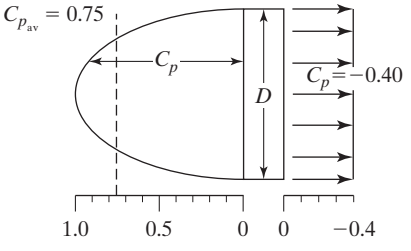

Figure P3.46

3.47. Consider an incompressible flow around a hemisphere, as shown in Fig. P3.39. Assume that the velocity distribution for the windward surface of the cylinder is given by the inviscid solution

$$V = -\tfrac{3}{2}U_\infty \sin\omega \tag{3.77}$$

Calculate the lift and drag coefficients if the base pressure (i.e., the pressure on the flat, or leeward surface) is equal to the pressure at the separation point, p_{comer}. How does the drag coefficient for a hemisphere compare with that for a hemicylinder (i.e., Problem 3.47.)

3.48. A hemisphere, as shown in Fig. P3.48, is submerged in an airstream where $\rho_\infty = 0.00266\ slug/ft^3$ and $U_\infty = 100\ ft/s$ The radius is 1.0 ft. What are the lift and drag forces on the hemisphere using the equations developed in Problem 3.47.)

3.49. Consider air flowing past a hemisphere resting on a flat surface, as shown in Fig. P3.49. Neglecting the effects of viscosity, if the internal pressure is p_i, find an expression for the pressure force on the hemisphere. At what angular location should a hole be cut in the surface of the hemisphere so that the net pressure force will be zero?

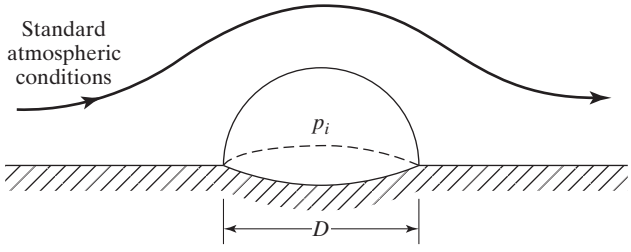

Figure P3.49

3.50. A two-dimensional flow field is given by $V = 2x^3i - 6x^2yj$. Check whether the flow is rotational or irrotational? If rotational, determine the angular velocity, vorticity, shear strain, and dilatency. Also find the circulation about the circle $x^2 + y^2 - 2ry = 0$.

3.51. Derive the stream functions for the elementary flows of Table 3.3.

3.52. What condition(s) must prevail in order for a velocity potential to exist? For a stream function to exist?

REFERENCES

Achenbach E. 1968. Distributions of local pressure and skin friction around a circular cylinder in cross flow up to Re $= 5 \times 10^6$. *J. Fluid Mechanics* 34:625–639

Campbell J, Chambers JR. 1994. Patterns in the sky: Natural visualization of aircraft flow fields. *NASA SP-514*

Churchill RV, Brown JW. 1984. *Complex Variables and Applications*. New York: McGraw-Hill

Hess JL, Smith AMO. 1966. Calculations of potential flow about arbitrary bodies. *Progr. Aeronaut. Sci*. 8:1–138

Hoerner SF. 1958. *Fluid Dynamic Drag*. Midland Park, NJ: published by the author

Hoerner SF, Borst HV. 1975. *Fluid Dynamic Lift*. Midland Park, NJ: published by the authors

Karamcheti K. 1980. *Principles of Ideal-Fluid Aerodynamics*. Malabar: Krieger Publishing Company

Kellogg OD. 1953. *Fundamentals of Potential Theory*. New York: Dover

Schlichting H. 1968. *Boundary Layer Theory*. 6th Ed. New York: McGraw-Hill

Talay TA. 1975. Introduction to the aerodynamics of flight. *NASA SP-367*

1976. *U.S. Standard Atmosphere.* Washington, DC: U.S. Government Printing Office

4 VISCOUS BOUNDARY LAYERS

Chapter Objectives

- Develop a basic understanding of boundary layers and their impact on aerodynamic flows
- Be able to obtain solutions for basic laminar flows and use the results to estimate properties, such as boundary layer thickness, shear stress, and skin friction
- Describe the characteristics of turbulent boundary layers, and how they compare to laminar boundary layers
- Understand how drag is impacted by laminar and turbulent boundary layers, including friction and separation
- Be able to estimate turbulent boundary layer properties, such as boundary layer thickness, shear stress, and skin friction
- Be able to complete a control volume analysis of a boundary layer flow
- Describe why turbulence models are important and how they are used
- Learn how to calculate the heat transfer and heat-transfer rate for a constant-property flow

The equation for the conservation of linear momentum was developed in Chapter 2 by applying Newton's law, which states that the net force acting on a fluid particle is equal to the time rate of change of the linear momentum of the fluid particle. The principal

forces considered were those that act directly on the mass of the fluid element (i.e., the body forces) and those that act on the surface (i.e., the pressure forces and shear forces). The resulting equations are known as the Navier-Stokes equations. Even today, there are no general solutions for the complete Navier-Stokes equations. Nevertheless, reasonable approximations can be introduced to describe the motion of a viscous fluid if the viscosity is either very large or very small. The latter case is of special interest to us, since two important fluids, water and air, have very small viscosities. Not only is the viscosity of these fluids very small, but the velocity for many of the practical applications relevant to aerodynamics is such that the Reynolds number is very large.

Even in the limiting case where the Reynolds number is large, a reasonable approach for estimating aerodynamics has to be found that does not require the solution of the Navier-Stokes equations for specific boundary conditions. One common approach is to divide the flow field into two regions: (1) a viscous boundary layer adjacent to the surface of the vehicle and (2) the essentially inviscid flow outside the boundary layer. The velocity of the fluid particles increases from a value of zero (in a vehicle-fixed coordinate system) at the wall to the value that corresponds to the external "frictionless" flow outside the boundary layer. Outside the boundary layer, the transverse velocity gradients become so small that the shear stresses acting on a fluid element are negligibly small. Thus, the effect of the viscous terms may be ignored when solving for the flow field external to the boundary layer.

When using the two-region flow model to solve for the flow field, the first step is to solve for the inviscid portion of the flow field. The solution for the inviscid portion of the flow field must satisfy the boundary conditions: (1) that the velocity of the fluid particles far from the body be equal to the free-stream value and (2) that the velocity of the fluid particles adjacent to the body be parallel to the "surface." The second boundary condition represents the physical requirement that there is no flow through a solid surface. However, since the flow is inviscid, the velocity component parallel to the surface does not have to be zero. Having solved for the inviscid flow field, the second step is to calculate the boundary layer using the inviscid flow as the outer boundary condition.

If the boundary layer is relatively thick, it may be necessary to use an iterative process for calculating the flow field. To start the second iteration, the inviscid flow field is recalculated, replacing the actual configuration by the "effective" configuration, which is determined by adding the displacement thickness of the boundary layer from the first iteration to the surface coordinate of the actual configuration, as shown in Fig. 2.13. The boundary layer is recalculated using the second-iterate inviscid flow as the boundary condition. As discussed in DeJarnette and Ratcliffe (1996), the iterative procedure required to converge to a solution requires an understanding of each region of the flow field and their interactions.

In Chapter 3, we generated solutions for the inviscid flow field for a variety of configurations. In this chapter, we will examine the viscous region in detail, assuming that the inviscid flow field is already known.

4.1 EQUATIONS GOVERNING THE BOUNDARY LAYER FOR A STEADY, TWO-DIMENSIONAL, INCOMPRESSIBLE FLOW

In order to obtain engineering solutions for viscous flow, we will discuss techniques for the boundary layer when it is either laminar or turbulent. The transition process through which the boundary layer "changes" from a laminar state to a turbulent state is

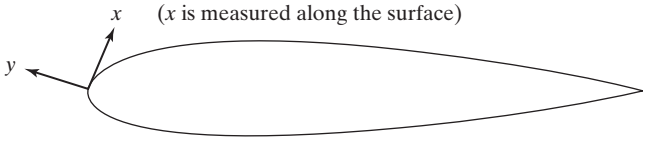

Figure 4.1 Coordinate system for the boundary-layer equations.

quite complex and depends on many parameters (e.g., surface roughness, surface temperature, pressure gradient, and Mach number). A brief summary of the factors affecting transition is presented later in this chapter, and some straightforward engineering approximations for transition will be discussed. For a more detailed discussion of the parameters that affect transition, you are encouraged to read Schlichting and Gersten (2000) and White (2005).

To simplify the development of the solution techniques, we will consider the flow to be steady, two-dimensional, and constant property (or, equivalently, incompressible for a gas flow). By restricting ourselves to such flows, we can concentrate on the development of the solution techniques themselves. As shown in Fig. 4.1, the coordinate system is fixed to the surface of the body, where the x coordinate is measured in the streamwise direction along the surface of the configuration. The stagnation point (or the leading edge if the configuration is a sharp object) is at $x = 0$. The y coordinate is perpendicular to the surface. This coordinate system is used throughout the developments in this chapter.

Referring to equation (2.3), the differential form of the continuity equation for an incompressible flow in two dimensions is:

$$\frac{\partial u}{\partial x} + \frac{\partial v}{\partial y} = 0 \tag{4.1}$$

Referring to equation (2.16) and neglecting body forces, the x component of momentum for this steady, two-dimensional flow is:

$$\rho u\frac{\partial u}{\partial x} + \rho v\frac{\partial u}{\partial y} = -\frac{\partial p}{\partial x} + \mu\frac{\partial^2 u}{\partial x^2} + \mu\frac{\partial^2 u}{\partial y^2} \tag{4.2}$$

Similarly, the y component of momentum is:

$$\rho u\frac{\partial v}{\partial x} + \rho v\frac{\partial v}{\partial y} = -\frac{\partial p}{\partial y} + \mu\frac{\partial^2 v}{\partial x^2} + \mu\frac{\partial^2 v}{\partial y^2} \tag{4.3}$$

If the boundary layer is thin and the streamlines are not highly curved, then we will assume that $u \gg v$, which will typically be true as long as we are not too close to the stagnation point. This observation allows us to compare each term in equation (4.3) with the corresponding term in equation (4.2) and make the following conclusions:

$$\rho u\frac{\partial u}{\partial x} > \rho u\frac{\partial v}{\partial x} \quad \rho v\frac{\partial u}{\partial y} > \rho v\frac{\partial v}{\partial y} \quad \mu\frac{\partial^2 u}{\partial x^2} > \mu\frac{\partial^2 v}{\partial x^2} \quad \mu\frac{\partial^2 u}{\partial y^2} > \mu\frac{\partial^2 v}{\partial y^2}$$

Therefore, as we discussed in Chapter 2, we can conclude that:

$$\frac{\partial p}{\partial x} > \frac{\partial p}{\partial y}$$

The essential information supplied by the y component of the momentum equation is that the static pressure variation in the y direction may be neglected for most boundary layer flows. This is true whether the boundary layer is laminar, transitional, or turbulent. It is not true in wake flows, that is, separated regions in the lee side of blunt bodies such as those behind cylinders, which were discussed in Chapter 3. The assumption that the static pressure variation across a thin boundary layer is negligible only breaks down for turbulent boundary layers at very high Mach numbers. The common assumption for thin boundary layers also may be written as:

$$\frac{\partial p}{\partial y} \approx 0 \tag{4.4}$$

which is true since we are not in regions with high streamline curvature. Therefore, the local static pressure is a function of x only and is determined from the solution of the inviscid portion of the flow field. As a result, Euler's equation for a steady flow with negligible body forces, equation (3.1), which relates the streamwise pressure gradient to the velocity gradient for the inviscid flow, can be used to evaluate the pressure gradient in the viscous region as:

$$-\frac{\partial p}{\partial x} = -\frac{dp_e}{dx} = \rho_e u_e \frac{du_e}{dx} \tag{4.5}$$

where the subscript e represents the conditions at the edge of the boundary layer, where we could know the solution for the inviscid flow field. Substituting equation (4.5) into equation (4.2), and noting that $\mu(\partial^2 u/\partial x^2) < \mu(\partial^2 u/\partial y^2)$, we obtain

$$\rho u \frac{\partial u}{\partial x} + \rho v \frac{\partial u}{\partial y} = \rho_e u_e \frac{du_e}{dx} + \mu \frac{\partial^2 u}{\partial y^2} \tag{4.6}$$

Now we can examine equations (4.1) and (4.6) together. The assumption that the flow is constant property (or incompressible) implies that fluid properties, such as density ρ and viscosity μ, are constants. For low-speed flows of gases, the changes in pressure and temperature through the flow field are sufficiently small that the corresponding changes in ρ and μ have a negligible effect on the flow field. By limiting ourselves to incompressible flows, it is not necessary to include the energy equation in the formulation of our solution. For compressible (or high-speed) flows, the temperature changes in the flow field are sufficiently large that the temperature dependence of the viscosity and of the density must be included. As a result, the analysis of a compressible boundary layer involves the simultaneous solution of the continuity equation, the x momentum equation, and the energy equation. For a detailed treatment of compressible boundary layers, you should consult Chapter 8, as well as Schlichting and Gersten (2000) and Dorrance (1962).

When the boundary layer is laminar, the transverse exchange of momentum (i.e., the momentum transfer in a direction perpendicular to the principal flow direction) takes place on a molecular (or microscopic) scale. As a result of the molecular movement, slower-moving fluid particles from the lower layer (or lamina) of fluid move upward, slowing the particles in the upper layer. Conversely, when the faster-moving fluid particles from the upper layer migrate downward, they tend to accelerate the fluid particles in that layer. This molecular interchange of momentum for a laminar flow is depicted in Fig. 4.2a. Therefore, the shear stress at a point in a Newtonian fluid is given by the constitutive relations preceding equation (2.12).

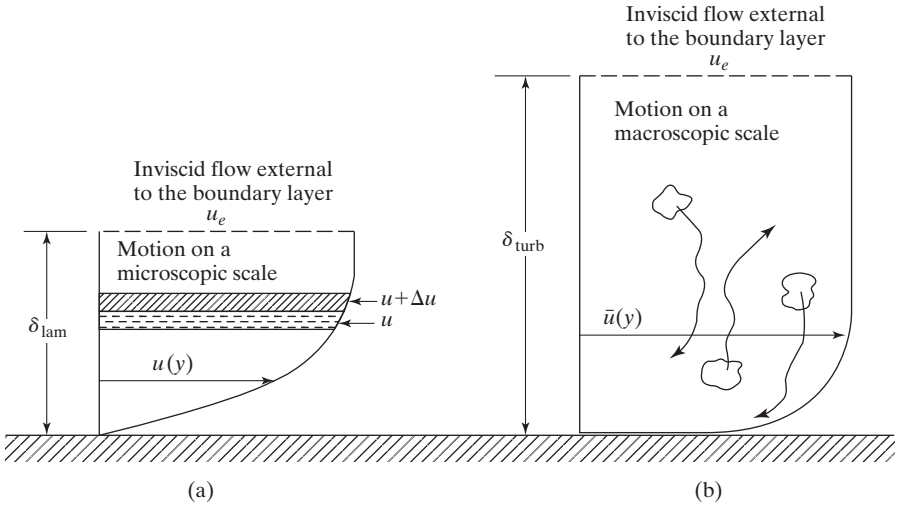

Figure 4.2 Momentum-transport models: (a) laminar boundary layer; (b) turbulent boundary layer.

For a turbulent boundary layer, there is a macroscopic transport of fluid particles, as shown in Fig. 4.2b. In addition to the laminar shear stress described in the preceding paragraph, there is an effective *turbulent shear stress* that is due to the transverse transport of momentum and that is very large. Because slower-moving fluid particles near the wall are transported far upward, the turbulent boundary layer is relatively thick when compared with a laminar boundary layer. Because faster-moving fluid particles (which are normally located near the edge of the boundary layer) are transported toward the wall, they produce relatively high velocities for the fluid particles near the surface. Thus, the shear stress at the wall for a turbulent boundary layer is larger than that for a laminar boundary layer. Because the macroscopic transport of fluid introduces large localized variations in the flow at any instant, the values of the fluid properties and the velocity components are (in general) the sum of the "average" value and a fluctuating component.

We could introduce the fluctuating characteristics of turbulent flow at this point and treat both laminar and turbulent boundary layers in a unified fashion. For a laminar boundary layer, the fluctuating components of the flow would be zero. However, to simplify the discussion, we will first discuss laminar flows and their analysis followed by turbulent boundary layers and their analysis.

4.2 BOUNDARY CONDITIONS

Now that we have simplified the equations for incompressible viscous flow, we can consider the boundary conditions that we must apply in order to obtain solutions. Since we are considering that portion of the flow field where the viscous forces are important, the condition of no slip on the solid boundaries must be satisfied. That is, at $y = 0$,

$$u(x, 0) = 0 \qquad \textbf{(4.7a)}$$

At a solid wall, the normal component of velocity must also be zero:

$$v(x, 0) = 0 \tag{4.7b}$$

The velocity boundary conditions for porous walls through which fluid can flow are treated in the problems at the end of the chapter.

Furthermore, at points far from the wall (i.e., at large values of y), we reach the edge of the boundary layer where the streamwise component of the velocity equals that given by the inviscid solution. In equation form, this can be expressed as:

$$u(x, y \text{ large}) = u_e(x) \tag{4.8}$$

4.3 INCOMPRESSIBLE, LAMINAR BOUNDARY LAYER

In this section, we will analyze the boundary layer in the region from the stagnation point (or from the leading edge of a sharp object) to the onset of transition (i.e., that "point" at which the boundary layer becomes turbulent). You should realize that, in reality, the boundary layer does not go from a laminar state to a turbulent state at a point but that the transition process takes place over a finite distance. In fact, the length of the transition zone may be as long as the laminar region. Typical velocity profiles for the laminar boundary layer are presented in Fig. 4.3. The streamwise (or x) compo-

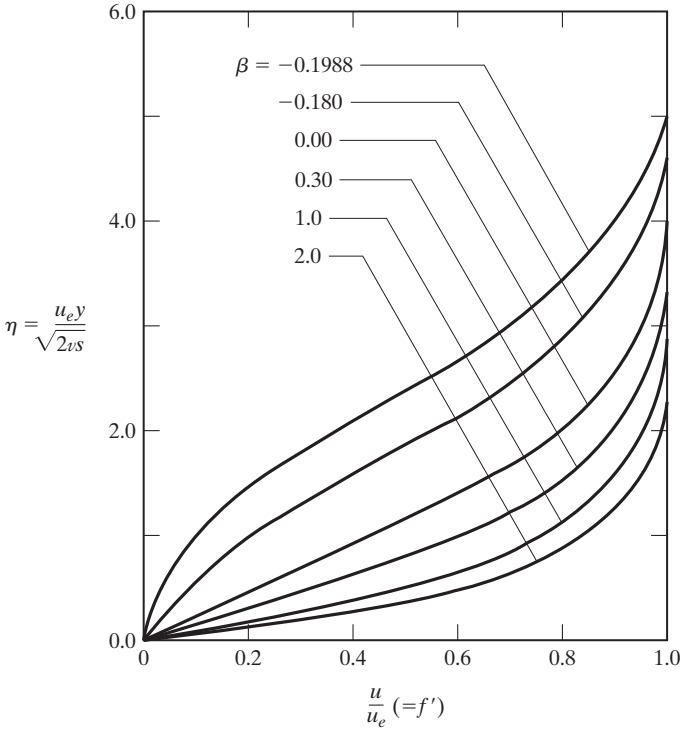

Figure 4.3 Solutions for the dimensionless streamwise velocity for the Falkner-Skan, laminar, similarity flows.

nent of velocity is presented as a function of distance from the wall (the y coordinate). Instead of presenting the dimensional parameter u, which is a function both of x and y, we will use a dimensionless velocity parameter that can be written as a function of a single variable. Notice that, at each station, the velocity varies from zero at $y = 0$ (i.e., at the wall) to u_e for the inviscid flow outside of the boundary layer. The local velocity at the edge of the boundary layer u_e is a function of x only; therefore, a logical dimensionless velocity parameter is u/u_e.

Instead of using the dimensional y coordinate, we will use a dimensionless coordinate η, which is proportional to y/δ for these incompressible, laminar boundary layers. The boundary-layer thickness δ at any x station depends not only on the magnitude of x but on the kinematic viscosity, the local velocity at the edge of the boundary layer, and the velocity variation from the origin to the point of interest. So, we will introduce the following coordinate transformation for η:

$$\eta = \frac{u_e y}{\sqrt{2\nu s}} \tag{4.9a}$$

where ν is the kinematic viscosity, as defined in Chapter 1, and where s is the transformed x coordinate:

$$s = \int u_e dx \tag{4.9b}$$

Notice that for flow past a flat plate, u_e is a constant (independent of x) and is equal to the free-stream velocity upstream of the plate U_∞, which results in equation (4.9a) becoming:

$$\eta = \frac{u_e y}{\sqrt{2\nu s}} = \frac{u_e y}{\sqrt{2\nu u_e x}} = y\sqrt{\frac{u_e}{2\nu x}} \tag{4.10}$$

If you are familiar with the transformations used in more complete treatments of boundary layer theory, you will recognize that this definition for η is consistent with that commonly used to transform the incompressible laminar boundary layer on a flat plate [see White (2005)]. The flat-plate solution is the classical Blasius solution. This transformation is also consistent with more general forms used in the analysis of a compressible laminar flow, as is shown in Dorrance (1962). By using this definition of s as the transformed x coordinate, we can account for the effect of the variation in u_e on the streamwise growth of the boundary layer.

Now we have two equations [equations (4.1) and (4.6)] with two unknowns, the velocity components u and v. Since the flow is two dimensional and the density is constant, the necessary and sufficient conditions for the existence of a stream function are satisfied. (*Note*: because of viscosity, the boundary-layer flow cannot be considered as irrotational; therefore, potential functions cannot be used to describe the flow in the boundary layer). We shall define the stream function such that:

$$u = \left(\frac{\partial \psi}{\partial y}\right)_x \text{ and } \nu = -\left(\frac{\partial \psi}{\partial x}\right)_y$$

By introducing the stream function, the continuity equation (4.1) is automatically satisfied (as we showed in Chapter 3). Therefore, we only need to solve one equation, the x component of the momentum equation, in terms of one unknown, the stream function.

This makes it much more likely that we will be able to find solutions for these boundary layer flow fields.

Now we can transform our equations from the x, y coordinate system to the s, η coordinate system. To do this, we use equation (4.9a) and the chain rule to obtain:

$$\left(\frac{\partial}{\partial y}\right)_x = \left(\frac{\partial \eta}{\partial y}\right)_x \left(\frac{\partial}{\partial \eta}\right)_s = \frac{u_e}{\sqrt{2\nu s}} \left(\frac{\partial}{\partial \eta}\right)_s \tag{4.11a}$$

$$\left(\frac{\partial}{\partial x}\right)_y = \left(\frac{\partial s}{\partial x}\right)_y \left[\left(\frac{\partial \eta}{\partial s}\right)_y \left(\frac{\partial}{\partial \eta}\right)_s + \left(\frac{\partial}{\partial s}\right)_\eta\right] \tag{4.11b}$$

Therefore, the streamwise component of velocity may be written in terms of the stream function as:

$$u = \left(\frac{\partial \psi}{\partial y}\right)_x = \frac{u_e}{\sqrt{2\nu s}} \left(\frac{\partial \psi}{\partial \eta}\right)_s \tag{4.12a}$$

Now introduce a transformed stream function f, which we define so that:

$$u = u_e \left(\frac{\partial f}{\partial \eta}\right)_s \tag{4.12b}$$

Comparing equations (4.12a) and (4.12b), we see that:

$$f = \frac{1}{\sqrt{2\nu s}} \psi \tag{4.13}$$

Similarly, we can develop an expression for the transverse component of velocity by using the definition of the stream function, equation (4.11b), and equation (4.13):

$$\begin{aligned} \nu &= -\left(\frac{\partial \psi}{\partial x}\right)_y = -\left(\frac{\partial s}{\partial x}\right)_y \left[\left(\frac{\partial \eta}{\partial s}\right)_y \left(\frac{\partial \psi}{\partial \eta}\right)_s + \left(\frac{\partial \psi}{\partial s}\right)_\eta\right] \\ &= -u_e \left[\sqrt{2\nu s} \left(\frac{\partial \eta}{\partial s}\right)_y \left(\frac{\partial f}{\partial \eta}\right)_s + \left(\frac{\partial (\sqrt{2\nu s} f)}{\partial s}\right)_\eta\right] \\ &= -u_e \sqrt{2\nu s} \left[\left(\frac{\partial \eta}{\partial s}\right)_y \left(\frac{\partial f}{\partial \eta}\right)_s + \left(\frac{\partial f}{\partial s}\right)_\eta + \left(\frac{f}{2s}\right)\right] \end{aligned} \tag{4.14}$$

In equations (4.12b) and (4.14), we have written the two velocity components, which were the unknowns in the original formulation of the problem, in terms of the transformed stream function. We can rewrite equation (4.6) using the differentials of the variables in the s, η coordinate system, equations (4.11a) and (4.11b), where we can obtain terms like:

$$\begin{aligned} \frac{\partial^2 u}{\partial y^2} &= \frac{\partial}{\partial y}\left[\frac{\partial \eta}{\partial y} \frac{\partial (u_e f')}{\partial n}\right] = \left(\frac{\partial \eta}{\partial y}\right)^2 u_e \frac{\partial^2 f'}{\partial \eta^2} \\ &= \frac{u_e^2}{2\nu s} u_e f''' \end{aligned}$$

where the prime ($'$) denotes differentiation with respect to η. Using these substitutions, the momentum equation becomes:

$$f f'' + f''' + [1 - (f')^2] \frac{2s}{u_e} \frac{du_e}{ds} = 2s \left[f' \left(\frac{\partial f'}{\partial s}\right)_y - f'' \left(\frac{\partial f}{\partial s}\right)_y\right] \tag{4.15}$$

As we discussed in Chapter 3, by using a stream function we automatically satisfy the continuity equation. Therefore, we have reduced the formulation for this flow to one equation with one unknown.

For many problems, the parameter $(2s/u_e)(du_e/ds)$, which is represented by the symbol β, is assumed to be constant. The assumption that β is a constant implies that the s derivatives of f and f' are zero. As a result, the transformed stream function and its derivatives are functions of η only, and equation (4.15) becomes the ordinary differential equation:

$$ff'' + f''' + [1 - (f')^2]\beta = 0 \tag{4.16}$$

We have transformed the partial differential equations that describe flow of a two dimensional, incompressible fluid, equations (4.1) through (4.3), into a single ordinary differential equation, which means we are much more likely to be able to find solutions. In addition, because the dimensionless velocity function f' is a function of η only, the velocity profiles at one s station are the same as those at another; therefore, the solutions are called *similar solutions*. Notice that the Reynolds number does not appear as a parameter when the momentum equation is written in the transformed coordinates, but it will appear when our solutions are transformed back into the x, y coordinate system. There are no analytical solutions to this third-order ordinary differential equation, which is known as the *Falkner-Skan equation*. Nevertheless, there are a variety of well-known numerical techniques available to solve equation (4.16).

Now we need to examine the three boundary conditions necessary to solve equation (4.16). Substituting the definition that:

$$f' = \frac{u}{u_e}$$

into the boundary conditions given by equations (4.7) and (4.8), the wall boundary condition becomes:

$$f'(s, 0) = 0 \tag{4.17a}$$

and far from the wall:

$$f'(s, \eta_{\text{large}}) = 1.0 \tag{4.17b}$$

Using equations (4.14) and (4.7), the boundary condition that the transverse velocity be zero at the wall becomes:

$$f(s, 0) = 0 \tag{4.17c}$$

Since f is the transformed stream function, this third boundary condition states that the stream function is constant along the wall (i.e., the surface is a streamline). This is consistent with the requirement that $v(x, 0) = 0$, which results because the component of velocity normal to a streamline is zero.

4.3.1 Numerical Solutions for the Falkner-Skan Problem

Numerical solutions of equation (4.16) that satisfy the boundary conditions represented by equation (4.17) have been generated for $-0.1988 \leq \beta \leq +2.0$; the resultant velocity profiles are presented in Fig. 4.3 and Table 4.1. Since

$$\beta = \frac{2s}{u_e}\frac{du_e}{ds}$$

TABLE 4.1 Numerical Values of the Dimensionless Streamwise Velocity $f'(\eta)$ for the Falkner-Skan, Laminar, Similarity Flows

	β					
η	−0.1988	−0.180	0.000	0.300	1.000	2.000
0.0	0.0000	0.0000	0.0000	0.0000	0.0000	0.0000
0.1	0.0010	0.0138	0.0470	0.0760	0.1183	0.1588
0.2	0.0040	0.0293	0.0939	0.1489	0.2266	0.2979
0.3	0.0089	0.0467	0.1408	0.2188	0.3252	0.4185
0.4	0.0159	0.0658	0.1876	0.2857	0.4145	0.5219
0.5	0.0248	0.0867	0.2342	0.3494	0.4946	0.6096
0.6	0.0358	0.1094	0.2806	0.4099	0.5663	0.6834
0.7	0.0487	0.1337	0.3265	0.4671	0.6299	0.7450
0.8	0.0636	0.1597	0.3720	0.5211	0.6859	0.7959
0.9	0.0804	0.1874	0.4167	0.5717	0.7351	0.8377
1.0	0.0991	0.2165	0.4606	0.6189	0.7779	0.8717
1.2	0.1423	0.2790	0.5452	0.7032	0.8467	0.9214
1.4	0.1927	0.3462	0.6244	0.7742	0.8968	0.9531
1.6	0.2498	0.4169	0.6967	0.8325	0.9323	0.9727
1.8	0.3127	0.4895	0.7611	0.8791	0.9568	0.9845
2.0	0.3802	0.5620	0.8167	0.9151	0.9732	0.9915
2.2	0.4510	0.6327	0.8633	0.9421	0.9839	0.9955
2.4	0.5231	0.6994	0.9011	0.9617	0.9906	
2.6	0.5946	0.7605	0.9306	0.9755	0.9946	
2.8	0.6635	0.8145	0.9529	0.9848		
3.0	0.7277	0.8606	0.9691	0.9909		
3.2	0.7858	0.8985	0.9804	0.9947		
3.4	0.8363	0.9285	0.9880			
3.6	0.8788	0.9514	0.9929			
3.8	0.9131	0.9681	0.9959			
4.0	0.9398	0.9798				
4.2	0.9597	0.9876				
4.4	0.9740	0.9927				
4.6	0.9838	0.9959				
4.8	0.9903					
5.0	0.9944					

these solutions represent a variety of inviscid flow fields and, therefore, represent the flow around different configurations. Note that when $\beta = 0$, $u_e =$ constant, and the solution is for flow past a flat plate (known as the Blasius solution). Negative values of β correspond to cases where the inviscid flow is decelerating, which corresponds to an adverse pressure gradient [i.e., $(dp/dx) > 0$]. Positive values of β correspond to an accelerating inviscid flow, which results from a favorable pressure gradient [i.e., $(dp/dx) < 0$].

As we noted in the discussion of flow around a cylinder in Chapter 3, when the air particles in the boundary layer encounter a relatively large adverse pressure gradient, boundary-layer separation may occur. Separation results because the fluid particles in the viscous layer have been slowed to the point that they cannot overcome the adverse pressure gradient. The effect of an adverse pressure gradient is evident in the velocity

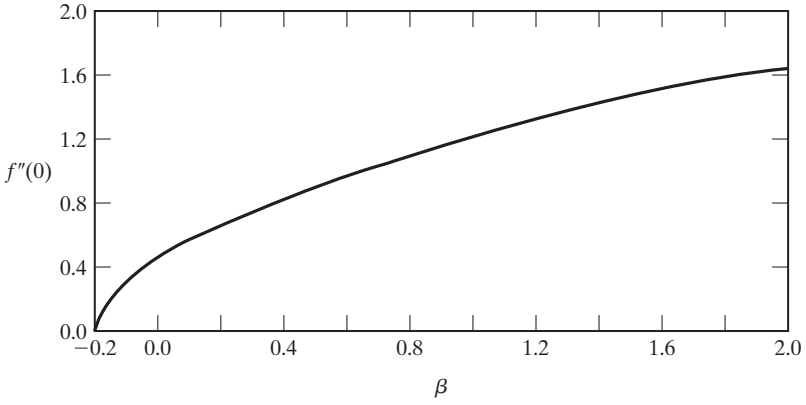

Figure 4.4 Transformed shear function at the wall for laminar boundary layers as a function of β.

profiles presented in Fig. 4.3. When $\beta = -0.1988$, not only is the streamwise velocity zero at the wall, but the velocity gradient $\partial u/\partial y$ is also zero at the wall. If the adverse pressure gradient were any larger, the laminar boundary layer would separate from the surface, and flow reversal would occur.

For the accelerating flows (i.e., positive β), the velocity increases rapidly with distance from the wall, so $\partial u/\partial y$ at the wall is relatively large. Referring to equation (1.11), we would expect that the shear force at the wall would be relatively large. To calculate the shear force at the wall,

$$\tau = \left(\mu \frac{\partial u}{\partial y}\right)_{y=0} \tag{4.18}$$

Now we can introduce the transformation presented in equation (4.11a) and find the shear as:

$$\tau = \frac{\mu u_e^2}{\sqrt{2\nu s}} f''(0) \tag{4.19}$$

Because of its use in equation (4.19), we will call f'' the *transformed shear function*. Theoretical values of $f''(0)$ are presented in Fig. 4.4 and in Table 4.2. Notice that $f''(0)$ is a unique function of β for these incompressible, laminar boundary layers; the value does not depend on the free-stream conditions, such as velocity or Reynolds number.

For laminar flow over a flat plate, $\beta = 0, f''(0) = 0.4696$, and the shear stress is:

$$\tau = 0.332\sqrt{\frac{\rho\mu u_e^3}{x}} \tag{4.20}$$

TABLE 4.2 Theoretical Values of the Transformed Shear Function at the Wall for Laminar Boundary Layers as a Function of β

β	−0.1988	−0.180	0.000	0.300	1.000	2.000
$f''(0)$	0.000	0.1286	0.4696	0.7748	1.2326	1.6872

As we noted earlier, for flow past a flat plate the velocity at the edge of the boundary layer (u_e) is equal to the free-stream value (U_∞). We can now express the shear in terms of the dimensionless skin-friction coefficient, which is defined as:

$$C_f = \frac{\tau}{\frac{1}{2}\rho_\infty U_\infty^2} = \frac{0.664}{\sqrt{\mathrm{Re}_x}} \tag{4.21}$$

where the Reynolds number is

$$\mathrm{Re}_x = \frac{\rho u_e x}{\mu} = \frac{\rho U_\infty x}{\mu} \tag{4.22}$$

Substituting the values of $f''(0)$ presented in Fig. 4.4, we see that the shear is zero when $\beta = -0.1988$. Therefore, this value of β corresponds to the onset of separation. Conversely, when the inviscid flow is accelerating, the shear is greater than that for a zero pressure gradient flow.

The transformed stream function (f), the dimensionless streamwise velocity (f'), and the shear function (f'') are presented as a function of η for a laminar boundary layer on a flat plate in Table 4.3. Note that as η increases (i.e., as y increases) the shear goes to zero and the function f' tends asymptotically to 1.0.

TABLE 4.3 Solution for the Laminar Boundary Layer on a Flat Plate ($\beta = 0$)

η	f	f'	f''
0.0	0.0000	0.0000	0.4696
0.1	0.0023	0.0470	0.4696
0.2	0.0094	0.0939	0.4693
0.3	0.0211	0.1408	0.4686
0.4	0.0375	0.1876	0.4673
0.5	0.0586	0.2342	0.4650
0.6	0.0844	0.2806	0.4617
0.7	0.1147	0.3265	0.4572
0.8	0.1497	0.3720	0.4512
0.9	0.1891	0.4167	0.4436
1.0	0.2330	0.4606	0.4344
1.2	0.3336	0.5452	0.4106
1.4	0.4507	0.6244	0.3797
1.6	0.5829	0.6967	0.3425
1.8	0.7288	0.7610	0.3005
2.0	0.8868	0.8167	0.2557
2.2	1.0549	0.8633	0.2106
2.4	1.2315	0.9010	0.1676
2.6	1.4148	0.9306	0.1286
2.8	1.6032	0.9529	0.0951
3.0	1.7955	0.9691	0.0677
3.2	1.9905	0.9804	0.0464
3.4	2.1874	0.9880	0.0305
3.5	2.2863	0.9907	0.0244
4.0	2.7838	0.9978	0.0069
4.5	3.2832	0.9994	0.0015

Now we will define the boundary layer thickness δ as that distance from the wall for which $u = 0.99u_e$. While this definition is somewhat arbitrary, it is fairly standard and useful. We can now find the value of η corresponding to the boundary layer thickness as:

$$\eta_\delta = 3.5$$

which is independent of the specific flow properties of the free stream. Converting this value to a physical distance, the corresponding boundary layer thickness (δ) is:

$$\delta = y_\delta = \eta_\delta \sqrt{\frac{2\nu x}{u_e}}$$

or

$$\frac{\delta}{x} = \frac{5.0}{\sqrt{\mathrm{Re}_x}} \tag{4.23}$$

Notice that the thickness of a laminar boundary layer is proportional to $\sqrt{x}$ and is inversely proportional to the square root of the Reynolds number. In other words, a high Reynolds number flow will have a relatively thin boundary layer.

Although the transverse component of velocity at the wall is zero, it is not zero at the edge of the boundary layer. Referring to equation (4.14), we can see that at the edge of the boundary layer over a flat plate where $\eta_e = u_e y/\sqrt{2\nu s}$ and $s = u_e x$:

$$\begin{aligned}
\frac{v_e}{u_e} &= -\sqrt{2\nu s}\left[\left(\frac{\partial \eta}{\partial s}\right)_y \left(\frac{\partial f}{\partial \eta}\right)_s + \underbrace{\left(\frac{\partial f}{\partial s}\right)_\eta}_{=0} + \left(\frac{f}{2s}\right)\right] \\
&= -\sqrt{2\nu s}\left[-\frac{1}{2s}\eta_e (f')_e + \left(\frac{f_e}{2s}\right)\right] = -\frac{\sqrt{2\nu s}}{2s}\left[-\eta_e (f')_e + f_e\right] \\
&= \sqrt{\frac{\nu}{2u_e x}}\left[\eta_e (f')_e - f_e\right]
\end{aligned} \tag{4.24}$$

Using the values given in Table 4.3, $\eta_e = 3.5, f_e = 2.2863$, $f'_e = 0.9907$, and the transverse velocity is:

$$\frac{v_e}{u_e} = \frac{0.84}{\sqrt{\mathrm{Re}_x}} \tag{4.25}$$

This means that at the outer edge there is an upward flow, which is due to the fact that the increasing boundary-layer thickness causes the fluid to be displaced from the wall as it flows downstream. Also remember that there is no boundary-layer separation for this flow past a flat plate, since the streamwise pressure gradient is zero.

Since the streamwise component of the velocity in the boundary layer asymptotically approaches the local free-stream value, the magnitude of δ is very sensitive to the ratio of u/u_e, which was chosen as the criterion for the edge of the boundary layer [e.g., 0.99 was the value used to develop equation (4.23)]. A more significant measure of the boundary layer is the displacement thickness δ^*, which is the distance by which the external streamlines are shifted due to the presence of the boundary layer. Referring to Fig. 4.5,

$$\rho_e u_e \delta^* = \int_0^\delta \rho(u_e - u)\,dy$$

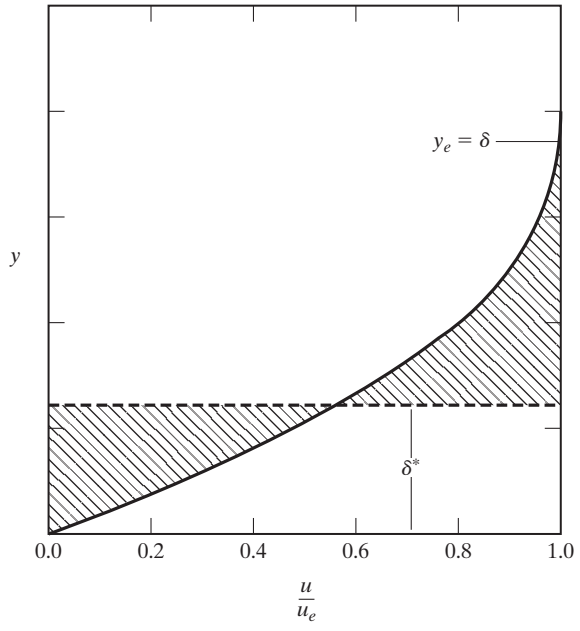

Figure 4.5 Velocity profile for a laminar boundary layer on a flat plate illustrating the boundary-layer thickness δ and the displacement thickness δ^*.

Therefore, for any incompressible boundary layer (where ρ = constant)

$$\delta^* = \int_0^{\delta} \left(1 - \frac{u}{u_e}\right) dy \tag{4.26}$$

Notice that since the integrand is zero for any point beyond δ, the upper limit for the integration does not matter providing it is equal to (or greater than) δ. Substituting the transformation of equation (4.10) for the laminar boundary layer on a flat plate yields:

$$\delta^* = \sqrt{\frac{2\nu x}{u_e}} \int_0^{\infty} (1 - f')\, d\eta$$

Using the values presented in Table 4.3, we obtain:

$$\frac{\delta^*}{x} = \frac{\sqrt{2}(\eta_e - f_e)}{\sqrt{\mathrm{Re}_x}} = \frac{1.72}{\sqrt{\mathrm{Re}_x}} \tag{4.27}$$

Therefore, for a flat plate at zero incidence in a uniform stream, the displacement thickness δ^* is on the order of one-third the boundary-layer thickness δ, which is found by comparing the values from equations (4.23) and (4.27).

The momentum thickness, θ, for an incompressible boundary layer is given by:

$$\theta = \int_0^{\infty} \frac{u}{u_e}\left(1 - \frac{u}{u_e}\right) dy \tag{4.28}$$

The momentum thickness represents the height of the free-stream flow which would be needed to make up the deficiency in momentum flux within the boundary layer due to the shear force at the surface. Following a similar transformation as we performed to obtain equation (4.27), the momentum thickness for an incompressible, laminar boundary layer is:

$$\frac{\theta}{x} = \frac{0.664}{\sqrt{\mathrm{Re}_x}} \tag{4.29}$$

which is approximately 13% of the boundary-layer thickness from equation (4.23) and is the same value as the local skin-friction coefficient from equation (4.21).

Another convenient formulation for skin-friction on a flat plate is found by integrating the "local" skin-friction coefficient, C_f, found in equation (4.21) to obtain a "total" or "average" skin-friction drag coefficient on the flat plate [White (2005)]. The use of the total skin-friction drag coefficient avoids performing the same integration numerous times with different flat-plate lengths accounting for different results. The total skin-friction coefficient is defined as:

$$\overline{C}_f \equiv \frac{D_f}{q_\infty S_{\mathrm{wet}}} \tag{4.30}$$

where D_f is the friction drag on the plate and S_{wet} is the wetted area of the plate (the wetted area is the area of the plate in contact with the fluid—for one side of the plate, $S_{\mathrm{wet}} = Lb$). The total skin-friction coefficient for laminar boundary layers becomes:

$$\begin{aligned}\overline{C}_f &= \frac{1}{q_\infty S_{\mathrm{wet}}} b \int_0^L \tau \, dx = \frac{b}{q_\infty L b} \int_0^L C_f(x) q_\infty dx \\ &= \frac{1}{L} \int_0^L \frac{0.664}{\sqrt{\mathrm{Re}_x}} dx = 2C_f(L) = \frac{2\theta}{L}\end{aligned} \tag{4.31}$$

which is just twice the value of the local skin-friction coefficient evaluated at $x = L$. The total skin-friction coefficient for laminar flow simply becomes:

$$\overline{C}_f = \frac{1.328}{\sqrt{\mathrm{Re}_L}} \tag{4.32}$$

where Re_L is the Reynolds number evaluated at $x = L$, which is the end of the flat plate.

Since drag coefficients are normally nondimensionalized by a reference area rather than a wetted area [see equation (3.53)], the drag coefficient due to skin-friction is obtained from equation (4.30) as:

$$C_D \equiv \frac{D_f}{q_\infty S_{\mathrm{ref}}} = \overline{C}_f \frac{S_{\mathrm{wet}}}{S_{\mathrm{ref}}} \tag{4.33}$$

It can be tempting to add together the total skin-friction coefficients for various flat plates in order to obtain a total skin-friction drag—this must never be done! Since each total skin-friction coefficient is defined with a different wetted area, doing this would result in an incorrect result. In other words,

$$\overline{C}_{f_{\mathrm{total}}} \neq \sum_{i=1}^{N} \overline{C}_{f_i}$$

Always convert total skin-friction coefficients into drag coefficients (based on a single reference area) and then add the drag coefficients to obtain a total skin-friction drag coefficient:

$$C_D = \sum_{i=1}^{N} C_{D_i} \tag{4.34}$$

EXAMPLE 4.1:

A rectangular plate, whose streamwise dimension (or chord c) is 0.2 m and whose width (or span b) is 1.8 m, is mounted in a wind tunnel. The free-stream velocity is 40 m/s. The density of the air is 1.2250 kg/m^3, and the absolute viscosity is 1.7894×10^{-5} kg/m · s. Graph the velocity profiles at $x = 0.0$ m, $x = 0.05$ m, $x = 0.10$ m, and $x = 0.20$ m. Calculate the chordwise distribution of the skin-friction coefficient and the displacement thickness. What is the drag coefficient for the plate?

Solution: Since the span (or width) of the plate is 9.0 times the chord (or streamwise dimension), we will assume that the flow is two dimensional (i.e., it is independent of the spanwise coordinate). The maximum value of the local Reynolds number, which occurs when $x = c$, is

$$\mathrm{Re}_c = \frac{(1.225\ \mathrm{kg/m^3})(40\ \mathrm{m/s})(0.2\ \mathrm{m})}{(1.7894 \times 10^{-5}\ \mathrm{kg/m \cdot s})} = 5.477 \times 10^5$$

This Reynolds number is close enough to the transition criteria for a flat plate that we will assume that the boundary layer is laminar for its entire length. Therefore, we will use the relations developed in this section to calculate the required parameters.

Noting that

$$y = \sqrt{\frac{2\nu x}{u_e}}\eta = 8.546 \times 10^{-4}\sqrt{x}\,\eta$$

we can use the results presented in Table 4.3 to calculate the velocity profiles. The resultant profiles are presented in Fig. 4.6. At the leading edge of the flat plate (i.e., at $x = 0$), the velocity is constant (independent of y). The profiles at the other stations illustrate the growth of the boundary layer with distance from the leading edge. Note that the scale of the y coordinate is greatly expanded relative to that for the x coordinate. Even though the streamwise velocity at the edge of the boundary layer (u_e) is the same at all stations, the velocity within the boundary layer is a function of x and y. However, if the dimensionless velocity (u/u_e) is presented as a function of η, the profile is the same at all stations. Specifically, the profile is that for $\beta = 0.0$ in Fig. 4.3. Since the dimensionless profiles are similar at all x stations, the solutions are termed *similarity solutions*.

The displacement thickness in meters is:

$$\delta^* = \frac{1.72x}{\sqrt{\mathrm{Re}_x}} = 1.0394 \times 10^{-3}\sqrt{x}$$

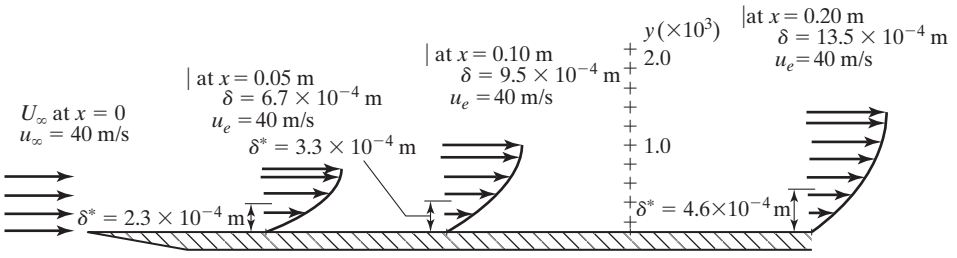

Figure 4.6 Velocity profile for the flat-plate laminar boundary layer $\mathrm{Re}_c = 5.477 \times 10^5$.

The chordwise (or streamwise) distribution of the displacement thickness is presented in Fig. 4.6. These calculations verify the validity of the common assumption that the boundary layer is thin. Therefore, the inviscid solution obtained neglecting the boundary layer altogether and that obtained for the effective geometry (the actual surface plus the displacement thickness) are essentially the same.

The local skin-friction coefficient is given by:

$$C_f = \frac{0.664}{\sqrt{\mathrm{Re}_x}} = \frac{4.013 \times 10^{-4}}{\sqrt{x}}$$

Now we can calculate the drag coefficient for the plate. Obviously, the pressure contributes nothing to the drag since there is no *dy* dimension for an infinitely thin flat plate. Therefore, the drag force acting on the flat plate is due only to skin friction. Using general notation, we see that:

$$D = 2b \int_0^c \tau \, dx \tag{4.35}$$

We need integrate only in the x direction, since by assuming the flow to be two dimensional, we have assumed that there is no spanwise variation in the flow. In equation (4.35), the integral, which represents the drag per unit width (or span) of the plate, is multiplied by b (the span) and by 2 (since friction acts on both the top and bottom surfaces of the plate). Substituting the expression for the laminar shear forces given in equation (4.20),

$$\begin{aligned} D &= 0.664b\sqrt{\rho\mu u_e^3} \int_0^c \frac{dx}{\sqrt{x}} \\ &= 1.328b\sqrt{c\rho\mu u_e^3} \end{aligned} \tag{4.36}$$

Since the edge velocity (u_e) is equal to the free-stream velocity (U_∞), the drag coefficient for the plate is:

$$C_D = \frac{D}{q_\infty cb} = \frac{2.656}{\sqrt{\mathrm{Re}_c}} \tag{4.37}$$

For the present problem, $C_D = 3.589 \times 10^{-3}$.

Alternatively, using the total skin-friction coefficient, equation (4.32), and computing drag on the top and bottom of the plate, we obtain:

$$C_D = \overline{C}_f \frac{S_{wet}}{S_{ref}} = \frac{1.328}{\sqrt{\mathrm{Re}_c}} \frac{2cb}{cb} = \frac{2.656}{\sqrt{5.477 \times 10^5}} = 3.589 \times 10^{-3}$$

EXAMPLE 4.2:

The streamwise velocity component for a laminar boundary layer is sometimes assumed to be roughly approximated by the linear relation

$$u = \frac{y}{\delta} u_e$$

where $\delta = 1.25 \times 10^{-2}\sqrt{x}$. Assume that we are trying to approximate the flow of air at standard sea-level conditions past a flat plate where $u_e = 2.337$ m/s. Calculate the streamwise distribution of the displacement thickness (δ^*), the velocity at the edge of the boundary layer (v_e), and the skin-friction coefficient (C_f). Compare the values obtained assuming a linear velocity profile with the more exact solutions presented in this chapter.

Solution: As given in Table 1.2, the standard day atmospheric conditions at sea level are:

$$\rho_\infty = 1.2250\ \mathrm{kg/m^3} \quad \text{and} \quad \mu_\infty = 1.7894 \times 10^{-5}\ \mathrm{kg/s \cdot m}$$

So, for constant-property flow past a flat plate,

$$\mathrm{Re}_x = \frac{\rho_\infty u_e x}{\mu_\infty} = 1.60 \times 10^5 x$$

Using the definition for the displacement thickness of an incompressible boundary layer, equation (4.26),

$$\delta^* = \int_0^\delta \left(1 - \frac{u}{u_e}\right) dy = \delta \int_0^1 \left(1 - \frac{u}{u_e}\right) d\left(\frac{y}{\delta}\right)$$

Notice that, since we have u/u_e in terms of y/δ, we have changed our independent variable from y to y/δ. We must also change the upper limit on our integral from δ to 1. Therefore, since:

$$\frac{u}{u_e} = \frac{y}{\delta} \text{ and } \delta = 1.25 \times 10^{-2}\sqrt{x}$$

then

$$\delta^* = 1.25 \times 10^{-2}\sqrt{x} \int_0^1 \left(1 - \frac{y}{\delta}\right) d\left(\frac{y}{\delta}\right) = 0.625 \times 10^{-2}\sqrt{x}$$

for the linear profile.

Using the equation for the more exact formulation [equation (4.27)], and noting that $\mathrm{Re}_x = 1.60 \times 10^5 x$, we find that

$$\delta^* = 0.430 \times 10^{-2}\sqrt{x}$$

Using the continuity equation, we would find that the linear approximation gives a value for v_e of:

$$v_e = \frac{3.125 \times 10^{-3}}{\sqrt{x}} u_e$$

Using the more exact formulation of equation (4.25) yields:

$$v_e = \frac{0.84}{\sqrt{\mathrm{Re}_x}} u_e = \frac{2.10 \times 10^{-3}}{\sqrt{x}} u_e$$

Finally, we find that the skin friction for the linear velocity approximation is given by:

$$\tau = \mu \left(\frac{\partial u}{\partial y} \right)_{y=0} = \frac{\mu u_e}{\delta}$$

Therefore, the skin-friction coefficient is:

$$C_f = \frac{\tau}{\frac{1}{2}\rho_\infty u_e^2} = \frac{2\mu_\infty}{\rho_\infty u_e \delta} = \frac{2}{1.60 \times 10^5 (1.25 \times 10^{-2}\sqrt{x})}$$
$$= \frac{1.00 \times 10^{-3}}{\sqrt{x}}$$

For the more exact formulation,

$$C_f = \frac{0.664}{\sqrt{\mathrm{Re}_x}} = \frac{1.66 \times 10^{-3}}{\sqrt{x}}$$

Summarizing these calculations provides the following comparison:

	Linear approximation	More exact solution
δ^*	$0.625 \times 10^{-2}\sqrt{x}$	$0.430 \times 10^{-2}\sqrt{x}$
v_e	$(3.125 \times 10^{-3} u_e)/\sqrt{x}$	$(2.10 \times 10^{-3} u_e)/\sqrt{x}$
C_f	$(1.00 \times 10^{-3})/\sqrt{x}$	$(1.66 \times 10^{-3})/\sqrt{x}$

Comparing the velocity profiles, which are presented in Fig. 4.7, the reader should be able to use physical reasoning to determine that these relationships are intuitively correct. That is, if you use a linear profile the shear would be less than that for the exact solution, where δ^* and v_e would be greater for the linear profile.

In this example, we assumed that the boundary-layer thickness δ was $1.25 \times 10^{-2}\sqrt{x}$ which is the value obtained using the more exact formulation [i.e., equation (4.23)]. However, if we had used the integral approach to determine the value of δ for a linear profile, we would have obtained:

$$\delta = \frac{3.464x}{\sqrt{\mathrm{Re}_x}} = 0.866 \times 10^{-2}\sqrt{x}$$

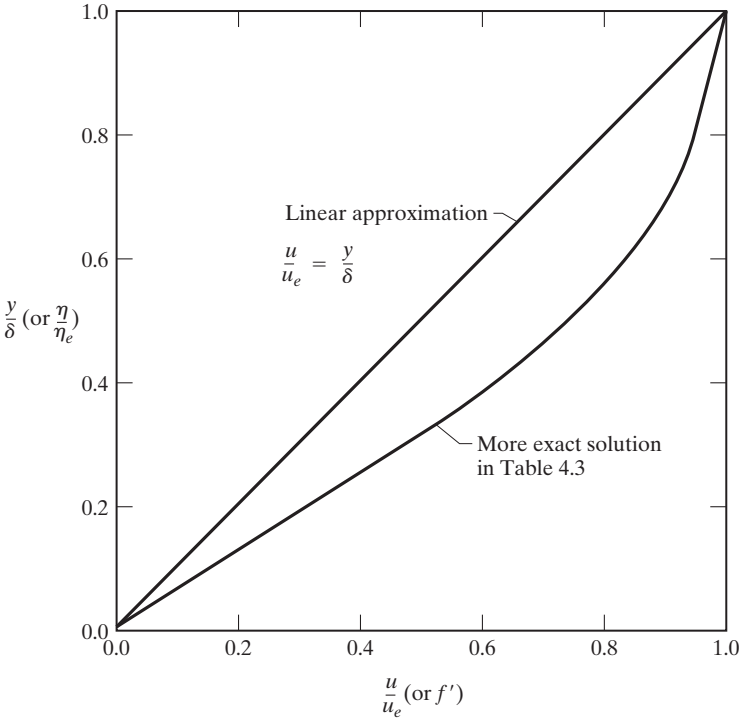

Figure 4.7 Comparison of velocity profiles for a laminar boundary layer on a flat plate.

Although this is considerably less than the assumed (more correct) value, the values of the other parameters (e.g., δ^* and C_f) would be in closer agreement with those given by the more exact solution.

Although the linear profile for the streamwise velocity component is a convenient approximation to use when demonstrating points about the continuity equation or about Kelvin's theorem, it clearly does not provide reasonable values for engineering parameters, such as δ^* and C_f. A more realistic approximation for the streamwise velocity component in a laminar boundary layer is given by:

$$\frac{u}{u_e} = \frac{3}{2}\left(\frac{y}{\delta}\right) - \frac{1}{2}\left(\frac{y}{\delta}\right)^3 \tag{4.38}$$

EXAMPLE 4.3: Calculate the velocity gradient, β

Calculate the velocity gradient parameter β, which appears in the Falkner-Skan form of the momentum equation, equation (4.16), for the NACA 65-006 airfoil. The coordinates of this airfoil section, which are given in Table 4.4, are given in terms of the coordinate system used in Fig. 4.8.

TABLE 4.4 Pressure Distribution for the NACA 65-006

$\tilde{x}(= x/c)$	$\tilde{z}(= z/c)$	C_p
0.000	0.0000	1.000
0.005	0.0048	−0.044
0.025	0.0096	−0.081
0.050	0.0131	−0.100
0.100	0.0182	−0.120
0.150	0.0220	−0.134
0.200	0.0248	−0.143
0.250	0.0270	−0.149
0.300	0.0285	−0.155
0.350	0.0295	−0.159
0.400	0.0300	−0.163
0.450	0.0298	−0.166
0.500	0.0290	−0.165
0.550	0.0274	−0.145
0.600	0.0252	−0.124
0.650	0.0225	−0.100
0.700	0.0194	−0.073
0.750	0.0159	−0.044
0.800	0.0123	−0.013
0.850	0.0087	+0.019
0.900	0.0051	+0.056
0.950	0.0020	+0.098
1.000	0.0000	+0.142

Source: Abbott and von Doenhoff (1949).

Note that the maximum thickness is located relatively far aft in order to maintain a favorable pressure gradient, which tends to delay transition. The β distribution is required as an input to obtain the local similarity solutions for a laminar boundary layer.

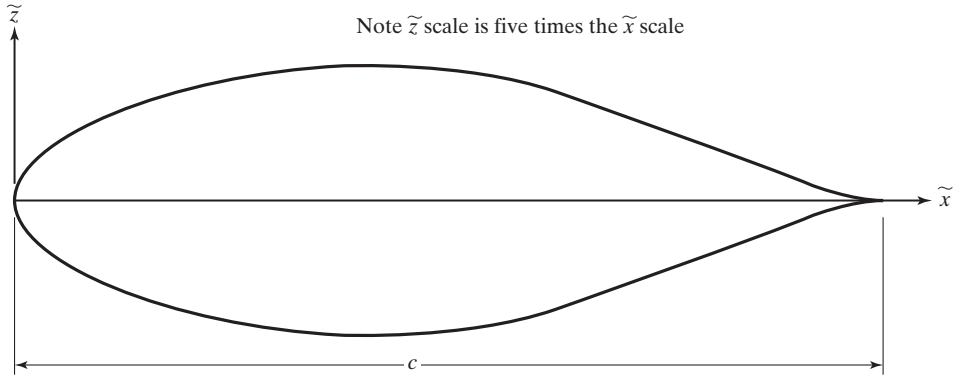

Figure 4.8 Cross section for symmetric NACA 65-006 airfoil of Example 4.3.

Solution: Using the definition for β from Section 4.3.1 and equation (4.9b) gives us

$$\beta = \frac{2s}{u_e}\frac{du_e}{ds} = \frac{2\int u_e\,dx}{u_e}\frac{du_e}{dx}\frac{dx}{ds}$$

But

$$\frac{dx}{ds} = \frac{1}{u_e}$$

$$\frac{u_e}{U_\infty} = (1 - C_p)^{0.5}$$

Therefore, at any chordwise location for a thin airfoil

$$\beta = \frac{\int_0^{\tilde{x}}(1 - C_p)^{0.5}d\tilde{x}}{(1 - C_p)^{1.5}}\frac{dC_p}{d\tilde{x}}$$

where $\tilde{x} = x/c$

The resultant β distribution is presented in Fig. 4.9. Note that a favorable pressure gradient acts over the first half of the airfoil ($\beta > 0$). For $\tilde{x} \geq 0.6$ the negative values of β exceed that required for separation of a similar laminar boundary layer. Because of the large streamwise variations in β, the non-similar character of the boundary layer should be taken into account when establishing a separation criterion. Nevertheless, these

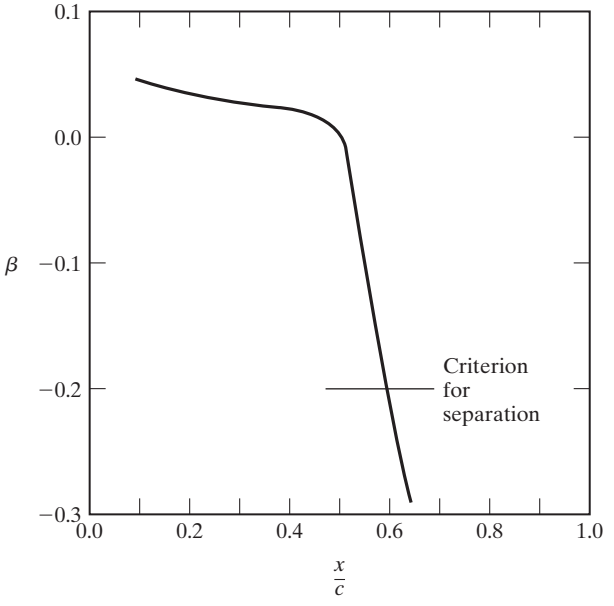

Figure 4.9 Distribution for NACA 65-606 airfoil (assuming that the boundary layer does not separate).

calculations indicate that, if the boundary layer were laminar along its entire length, it would separate, even for this airfoil at zero degrees angle of attack. Boundary-layer separation would result in significant changes in the flow field. However, the experimental measurements of the pressure distribution indicate that the actual flow field corresponds closely to the inviscid flow field. Therefore, boundary-layer separation apparently does not occur at zero degrees angle of attack. The reason that separation does not occur is as follows: at the relatively high Reynolds numbers associated with airplane flight, the boundary layer is turbulent over a considerable portion of the airfoil. As discussed previously, a turbulent boundary layer can overcome an adverse pressure gradient longer, and separation is not as likely to occur.

The fact that a turbulent boundary layer can flow without separation into regions of much steeper adverse pressure gradients than can a laminar boundary layer is illustrated in Fig. 4.10. Incompressible boundary-layer solutions were generated for symmetrical Joukowski airfoils at zero degrees angle of attack. The edge velocity and therefore the corresponding inviscid pressure distributions are shown in Fig. 4.10. At the conditions indicated, boundary-layer separation will occur for any Joukowski airfoil that is thicker than 4.6% if the flow is entirely laminar. However, if the boundary layer is turbulent, separation will not occur until a thickness of about 31% has been

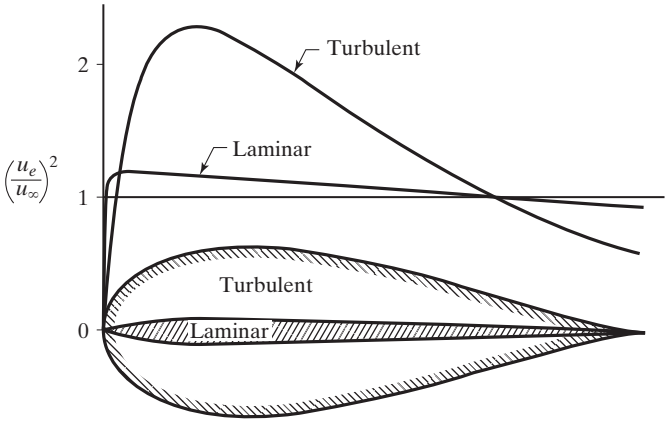

Figure 4.10 Thickest symmetrical Joukowski airfoils capable of supporting fully attached laminar and turbulent flows. The angle of attack is 0°, and the Mach number is 0. For turbulent flow, transition is assumed to occur at the velocity peak. The turbulent case is calculated for $\mathrm{Re}_c = 10^7$. Results for laminar flow are independent of Reynolds number. Maximum thickness for laminar flow is about 4.6%, for turbulent flow, 31%. If displacement-thickness effects on pressure distribution were included, the turbulent airfoil would increase to about 33%. The change in the laminar case would be negligible [from Cebeci and Smith (1974)].

Figure 4.11 Vortex generators, which can be seen in front of the ailerons and near the wing leading edge of an A-4, are an effective, but not necessarily an aerodynamically efficient, way of delaying separation (from Ruth Bertin's collection).

exceeded. The boundary layer effectively thickens the airfoil, especially near the trailing edge, since δ^* increases with distance. This thickening alleviates the adverse pressure gradients, which in turn permits somewhat thicker sections before separation occurs. To ensure that boundary-layer transition occurs and delays or avoids separation altogether, you might use vortex generators or other forms of surface roughness, as shown in Fig. 4.11.

4.4 BOUNDARY-LAYER TRANSITION

As the boundary layer develops in the streamwise direction, it is subjected to numerous disturbances. The disturbances may be due to surface roughness, temperature irregularities, background noise, and so on. For some flows, these disturbances are damped and the flow remains laminar. For other flows, the disturbances amplify and the boundary layer becomes turbulent. The onset of transition from a laminar boundary layer to a turbulent layer (if it occurs at all) can depend on many parameters, such as the following:

1. Pressure gradient
2. Surface roughness
3. Compressibility effects (usually related to the Mach number)

4. Surface temperature
5. Suction or blowing at the surface
6. Free-stream turbulence

Aerodynamics Concept Box: An Amazing Picture of Transition

Boundary layer transition is very difficult to see in real life. If you scour through fluid dynamics or aerodynamics textbooks, you might see pictures of laminar boundary layers and turbulent boundary layers, but rarely will you see transition. That is why the picture below is quite amazing. Researchers at Caltech [Rasheed et al. (2002)] were studying flow on a cone in hypersonic flow, hoping to see and measure transition under these conditions. On the upper surface of the cone, they took a shadowgraph photograph of the smooth surface and found an image of laminar flow developing instabilities, and eventually transitioning to fully turbulent flow (the flow in the picture below is going from left to right). They were also evaluating the effect of surface porosity on transition by placing a porous sheet on the lower surface of the cone, which maintained a laminar boundary layer along the entire length of the region being tested.

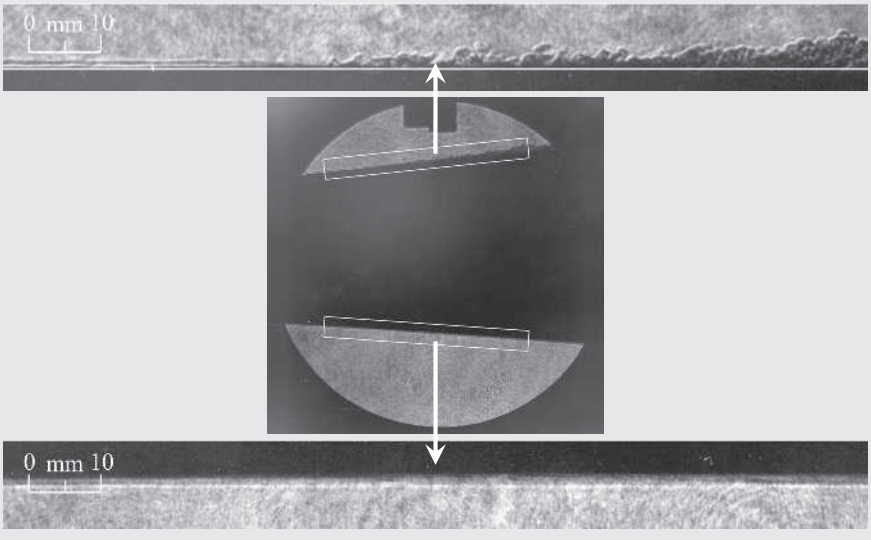

Shadowgraph showing transition on a cone in hypersonic flow; smooth surface on top and porous surface on the bottom (courtesy of Hans Hornung of Caltech)

Notice the boundary layer on the top surface at the far left: it is smooth, steady, and relatively thin. This is a laminar boundary layer. Just a few centimeters downstream, however, you can start to see small oscillations in the flow near the surface, which are the initial instabilities that will eventually grow and cause the boundary layer to transition. Once the oscillations reach a fairly large amplitude, you see the start of turbulent flow about 40 cm from the left side of the picture. The turbulent eddies start to grow in size, thickening the boundary layer, and eventually reaching a fully turbulent state at the right side of the picture. As we will discuss later, the transition process actually takes place over a finite length, especially if you include the region where the instabilities begin.

Obviously, no single criterion for the onset of transition can be applied to a wide variety of flow conditions. However, as a rule of thumb, adverse pressure gradients, surface roughness, blowing at the surface, and free-stream turbulence promote transition, that is, cause it to occur early. Conversely, favorable pressure gradients, increased Mach numbers, suction at the surface, and surface cooling delay transition. Although the parameters used and the correlation formula for the onset of transition depend on the details of the application, transition criteria typically incorporate a Reynolds number. For incompressible flow past a flat plate, a typical transition criterion is

$$\mathrm{Re}_{x,\,\mathrm{tr}} = 500{,}000 \tag{4.39}$$

Therefore, the location for the onset of boundary-layer transition would occur at

$$x_{\mathrm{tr}} = \frac{\mathrm{Re}_{x,\,\mathrm{tr}}}{\rho u_e/\mu} \tag{4.40}$$

Once the critical Reynolds number is exceeded, the flat-plate boundary layer would contain regions with the following characteristics as it transitioned from the laminar state to a fully turbulent flow:

1. Stable, laminar flow near the leading edge
2. Unstable flow containing two-dimensional Tollmien-Schlichting (T-S) waves
3. A region where three-dimensional unstable waves and hairpin eddies develop
4. A region where vortex breakdown produces locally high shear
5. Fluctuating, three-dimensional flow due to cascading vortex breakdown
6. A region where turbulent spots form
7. Fully turbulent flow

A sketch of the idealized transition process is presented in Fig. 4.12.

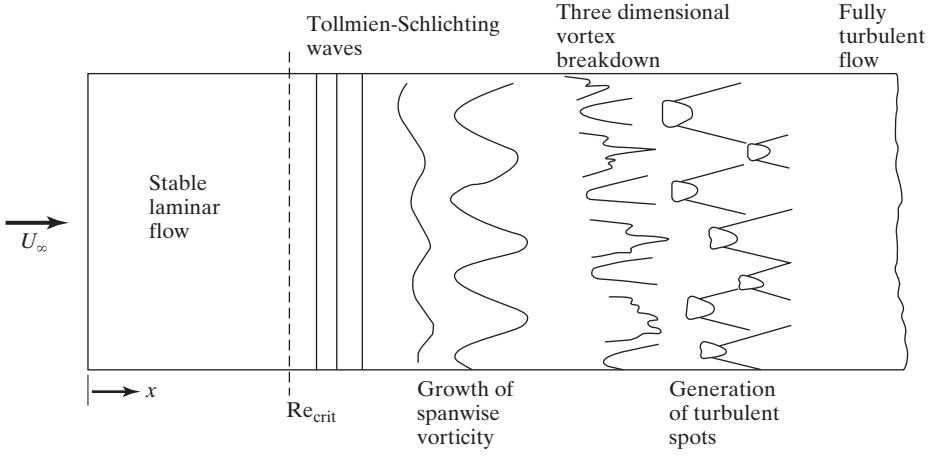

Figure 4.12 Idealized sketch of the transition process on a flat plate (based on the sketch from *Viscous Fluid Flow* by F. M. White).

Figure 4.13 Flow visualization of the transition process on a flat plate (photograph supplied by A. S. W. Thomas, Lockheed Aeronautical Systems Company, Georgia Division).

Stability theory predicts and experiment verifies that the initial instability is in the form of two-dimensional T-S waves that travel in the mean flow direction. Even though the mean flow is two dimensional, three-dimensional unstable waves and hairpin eddies soon develop as the T-S waves begin to show spanwise variations. The experimental verification of the transition process is illustrated in the photograph of Fig. 4.13. A vibrating ribbon perturbs the low-speed flow upstream of the left margin of the photograph. Smoke accumulation in the small recirculation regions associated with the T-S waves can be seen at the left edge of the photograph. The sudden appearance of three dimensionality is associated with the nonlinear growth region of the laminar instability. In the advanced stages of the transition process, intense local fluctuations occur at various times and locations in the viscous layer. From these local intensities, true turbulence bursts forth and grows into a turbulent spot. Downstream of the region where the spots first form, the flow becomes fully turbulent. This shows that transition occurs over a finite length rather than at a single location, as equation (4.39) implies. In spite of this, however, aerodynamicists commonly assume transition takes place at a single location for ease in making calculations and estimates.

Transition-promoting phenomena, such as an adverse pressure gradient and finite surface roughness, may short circuit the transition process, eliminating one or more of the five transitional regions described previously. When one or more of the transitional regions are by-passed, we term the cause (e.g., roughness) a by-pass mechanism.

Additional information about laminar flow airfoils will be discussed in Section 6.6. Also, laminar flow control, an important topic in aerodynamics, will be discussed in Section 13.4.2.

4.5 INCOMPRESSIBLE, TURBULENT BOUNDARY LAYER

Now that we have examined laminar boundary layers and transition, we can look at flows where transition has occurred and the boundary layer is fully turbulent. A turbulent flow is one in which irregular fluctuations (mixing or eddying motions) are superimposed on the mean flow. Because of this, the velocity at any point in a turbulent boundary layer is a function of time. The fluctuations occur in the direction of the mean flow and at right angles to it, and they affect macroscopic "lumps" of fluid, as shown in Fig. 4.2b.

Therefore, even when the inviscid (mean) flow is two dimensional, a turbulent boundary layer will be three dimensional because of the three-dimensional character of the fluctuations. However, whereas momentum transport occurs on a microscopic (or molecular) scale in a laminar boundary layer, it occurs on a macroscopic scale in a turbulent boundary layer. Although the velocity fluctuations may be only several percent of the local streamwise values, they have a decisive effect on the overall motion. The size of these macroscopic lumps determines the scale of turbulence, which will be an important concept to understand when evaluating turbulent boundary layers.

The effects caused by the fluctuations are as if the viscosity were increased by a factor of 10 or more. As a result, the shear forces at the wall and the skin-friction component of the drag are much larger when the boundary layer is turbulent. However, since a turbulent boundary layer can negotiate an adverse pressure gradient for a longer distance, boundary-layer separation may be delayed or even avoided altogether. Delaying (or avoiding) the onset of separation reduces the pressure component of the drag (i.e., the form drag). For a blunt body or for a slender body at angle of attack, the reduction in form drag usually dominates the increase in skin-friction drag.

Aerodynamics Concept Box: Turbulence

Understanding turbulence is difficult, and predicting turbulent flow behavior is even more difficult. Perhaps a fairly simple flow example will help to illustrate this point. The photograph below shows a turbulent boundary layer and provides a good image to describe turbulence. A turbulent flow has several characteristics:

- Chaotic and irregular—fundamentally unsteady and three dimensional
- Enhanced mixing of momentum, heat, and mass
- Large Reynolds numbers
- Three-dimensional vorticity fluctuations

Other important features of turbulence are the length and time scales that are found within turbulent flows. The boundary layer is highly unsteady, with flow quantities (such as velocity, density, pressure, and temperature) fluctuating at high frequencies. In addition to the fluctuations of the flow properties, there are both large- and small-scale structures in turbulent flow.

The large-scale structures are visible, appearing like waves convecting along with the flow, having a length scale on the order of the boundary layer thickness. These are normally called eddies, and are in effect "lumps" of fluid that appear to be rolling along

together in the flow. The large-scale structures are essentially "grabbing" kinetic energy from the free-stream flow and dragging it down into the inner layers of the boundary layer (remember, the photo is an instant in time of the unsteady turbulent flow process occurring in an otherwise steady flow). The large-scale structures also eject low momentum fluid from the inner layer to the outer layer. This mixing effect significantly alters the average velocity profile compared to a laminar boundary layer. Underlying the large-scale turbulence is an isotropic small-scale turbulence, meaning it is essentially the same everywhere within the boundary layer and acts in all directions equally. The small-scale turbulence converts the kinetic energy of the large turbulent structures into other forms of energy, including friction and heat.

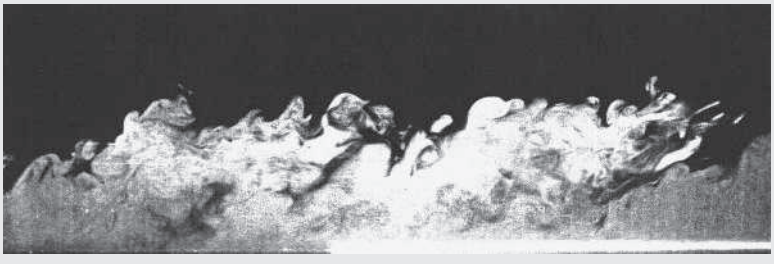

Turbulent boundary layer over a flat plate [Falco (1977)]

When describing a turbulent flow, it is convenient to express the local velocity components as the sum of a mean motion plus a fluctuating, or eddying, motion. For example, as illustrated in Fig. 4.14, we can characterize the time-varying velocity as:

$$u = \overline{u} + u' \tag{4.41}$$

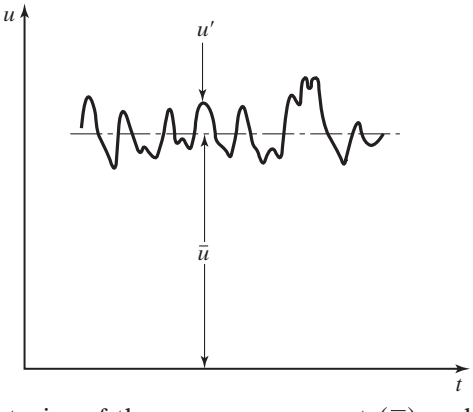

Figure 4.14 Histories of the mean component ($\overline{u}$) and the fluctuating component (u') of the streamwise velocity u for a turbulent boundary layer.

where $\overline{u}$ is the time-averaged value of the u component of velocity, and u' is the time-dependent magnitude of the fluctuating component. The time-averaged value at a given point in space is calculated as

$$\overline{u} = \frac{1}{\Delta t}\int_{t_0}^{t_0+\Delta t} u\, dt \tag{4.42}$$

This approach to turbulence decomposition is known as Reynolds averaging. The integration interval Δt should be much larger than any significant period of the fluctuation velocity u' associated with turbulence, but small compared to the characteristic time for the flow over the vehicle (the time required for a fluid particle to travel the length of the body). As a result, the mean value for a steady flow is independent of time, as it should be. The integration interval depends on the physics and geometry of the problem. Referring to equation (4.42), we see that $\overline{u'} = 0$, by definition; the time average of any fluctuating parameter or its derivative is zero. However, the time average of products of fluctuating parameters and their derivatives is not zero. For example, $\overline{v'} = 0$, $[\,\partial(\overline{v'})\,]/\partial x = 0$; but $\overline{u'v'} \neq 0$. Of fundamental importance to turbulent motion is the way in which the fluctuations u', v', and w' influence the mean motion $\overline{u}$, $\overline{v}$, and $\overline{w}$.

4.5.1 Derivation of the Momentum Equation for Turbulent Boundary Layer

Let us now derive the x (or streamwise) momentum equation for a steady, constant-property, two-dimensional, turbulent boundary layer. Since the density is constant, the continuity equation [equation (2.3)] can be decomposed according to equation (4.41) as:

$$\frac{\partial(\overline{u} + u')}{x} + \frac{\partial(\overline{v} + v')}{y} = 0 \tag{4.43}$$

Expanding the derivative terms yields:

$$\frac{\partial \overline{u}}{\partial x} + \frac{\partial \overline{v}}{\partial y} + \frac{\partial u'}{\partial x} + \frac{\partial v'}{\partial y} = 0 \tag{4.44}$$

Now take the time-averaged value for each of these terms. The first two terms already are time-averaged values, so time averaging leaves them unchanged. As we noted when discussing equation (4.42), the time-averaged value of a fluctuating component is zero, so,

$$\frac{\partial \overline{u'}}{\partial x} = \frac{\partial \overline{v'}}{\partial y} = 0$$

Therefore, for a turbulent flow, we learn from the continuity equation that:

$$\frac{\partial \overline{u}}{\partial x} + \frac{\partial \overline{v}}{\partial y} = 0 \tag{4.45a}$$

and that:

$$\frac{\partial u'}{\partial x} + \frac{\partial v'}{\partial y} = 0 \tag{4.45b}$$

Or in other words, the time-averaged continuity equation (4.45a) has the same form as the original continuity equation (2.3), where time-varying terms have been replaced with time-averaged terms.

Now we can perform the same decomposition for the momentum equation. Substituting the fluctuating descriptions for the velocity components into the x momentum equation (4.6), we have

$$\rho(\overline{u} + u')\frac{\partial(\overline{u} + u')}{\partial x} + \rho(\overline{v} + v')\frac{\partial(\overline{u} + u')}{\partial y} = \rho_e u_e \frac{du_e}{dx} + \mu\frac{\partial^2(\overline{u} + u')}{\partial y^2}$$

Expanding each term gives us:

$$\rho\overline{u}\frac{\partial\overline{u}}{\partial x} + \rho\overline{v}\frac{\partial\overline{u}}{\partial y} + \rho u'\frac{\partial\overline{u}}{\partial x} + \rho v'\frac{\partial u'}{\partial y} + \rho u'\frac{\partial u'}{\partial x} + \rho v'\frac{\partial u'}{\partial y} + \rho\overline{u}\frac{\partial u'}{\partial x} + \rho\overline{v}\frac{\partial u'}{\partial y}$$
$$= \rho_e u_e \frac{du_e}{dx} + \mu\frac{\partial^2\overline{u}}{\partial y^2} + \mu\frac{\partial^2 u'}{\partial y^2}$$

Now take the time average of the terms in this equation, remembering that terms which contain only one fluctuating parameter vanish, since their time-averaged value is zero. However, we must also remember that the time average of terms involving the product of fluctuating terms is not zero. Performing these operations gives:

$$\rho\overline{u}\frac{\partial\overline{u}}{\partial x} + \rho\overline{v}\frac{\partial\overline{u}}{\partial y} + \overline{\rho u'\frac{\partial u'}{\partial x}} + \overline{\rho v'\frac{\partial u'}{\partial y}} = \rho_e u_e \frac{du_e}{dx} + \mu\frac{\partial^2\overline{u}}{\partial y^2} \tag{4.46}$$

Now we can multiply the fluctuating portion of the continuity equation (4.45b) by $\rho(\overline{u} + u')$ to obtain:

$$\rho\overline{u}\frac{\partial u'}{\partial x} + \rho u'\frac{\partial u'}{\partial x} + \rho\overline{u}\frac{\partial v'}{\partial y} + \rho u'\frac{\partial v'}{\partial y} = 0$$

Taking the time average of these terms, we find that:

$$\overline{\rho u'\frac{\partial u'}{\partial x}} + \overline{\rho u'\frac{\partial v'}{\partial y}} = 0 \tag{4.47}$$

Adding equation (4.47) to (4.46) and rearranging the terms gives us:

$$\rho\overline{u}\frac{\partial\overline{u}}{\partial x} + \rho\overline{v}\frac{\partial\overline{u}}{\partial y} = \rho_e u_e \frac{du_e}{dx} + \mu\frac{\partial^2\overline{u}}{\partial y^2} - \rho\frac{\partial}{\partial y}(\overline{u'v'}) - \rho\frac{\partial}{\partial x}\overline{(u')^2} \tag{4.48}$$

We will neglect the streamwise gradient of the time-averaged value of the square of the fluctuating velocity component, that is, $(\partial/\partial x)\overline{(u')^2}$ as compared to the transverse gradient. Now, the momentum equation becomes:

$$\rho\overline{u}\frac{\partial\overline{u}}{\partial x} + \rho\overline{v}\frac{\partial\overline{u}}{\partial y} = \rho_e u_e \frac{du_e}{dx} + \mu\frac{\partial^2\overline{u}}{\partial y^2} - \rho\frac{\partial}{\partial y}(\overline{u'v'}) \tag{4.49}$$

We need to further examine the last two terms in equation (4.49):

$$\frac{\partial}{\partial y}\left(\mu\frac{\partial\overline{u}}{\partial y} - \rho\overline{u'v'}\right) \tag{4.50}$$

Recall that the first term is the laminar shear stress. To evaluate the second term, we can consider a differential area dA such that the normal to dA is parallel to the y axis, and the directions x and z are in the plane of dA. The mass of fluid passing through this area in time dt is given by the product $(\rho v)(dA)(dt)$. The flux of momentum in the x direction is given by the product $(u)(\rho v)(dA)(dt)$. For a constant density flow, the time-averaged flux of momentum per unit time is

$$\overline{\rho u v}\, dA = \rho(\overline{uv} + \overline{u'v'})\, dA$$

Since the flux of momentum per unit time through an area is equivalent to an equal-and-opposite force exerted on the area by the surroundings, we can treat the term $-\rho\overline{u'v'}$ as equivalent to a "turbulent" shear stress. This "apparent," or Reynolds, stress can be added to the stresses associated with the mean flow. So, we can now write the shear stress as:

$$\tau_{xy} = \mu\left(\frac{\partial \overline{u}}{\partial y}\right) - \rho\overline{u'v'} \tag{4.51}$$

Mathematically, the turbulent inertia terms behave as if the total stress on the system were composed of the Newtonian viscous stress plus an apparent turbulent stress.

The term $-\rho\overline{u'v'}$ is the source of considerable difficulties in the analysis of a turbulent boundary layer because its analytical form is not known a priori. It is related not only to physical properties of the fluid but also to the local flow conditions (velocity, geometry, surface roughness, upstream history, etc.). Furthermore, the magnitude of $-\rho\overline{u'v'}$ depends on the distance from the wall within the boundary layer. Because the wall is a streamline, there is no flow through it. Thus, $\overline{v}$ and v' go to zero at the wall, and the flow for $y < 0.02\delta$ is basically laminar.

The term $-\rho\overline{u'v'}$ represents the turbulent transport of momentum and is known as the *turbulent shear stress* or *Reynolds stress*. At points away from the wall, $-\rho\overline{u'v'}$ is the dominant term. The determination of the turbulent shear-stress term is the critical problem in the analysis of turbulent shear flows. However, this new variable can be defined only through an understanding of the detailed turbulent structure. These terms are related not only to physical fluid properties but also to local flow conditions. Since there are no further physical laws available to evaluate these terms, empirically based correlations are introduced to model them. There is a hierarchy of techniques for *closure* (defining the Reynolds stress terms so that the equations can be solved), which have been developed from models of varying degrees of rigor, which are known as turbulence models.

4.5.2 Approaches to Turbulence Modeling

For the flow fields of practical interest in aerodynamics, the boundary layer is usually turbulent. As discussed by Spalart (2000), current approaches to turbulence modeling include direct numerical simulations (DNS), large-eddy simulations (LES), and Reynolds-averaged Navier-Stokes (RANS). The direct numerical simulation approach attempts to resolve all scales of turbulence by allowing the full Navier-Stokes equations to predict turbulence directly. Because DNS must resolve all scales from the largest to the smallest, the grid resolution requirements for numerical simulation are very

stringent and increase dramatically with Reynolds number. In fact, you can show that the grid requirements (and therefore the computer memory requirements) for three-dimensional DNS are proportional to $Re^{9/4}$, making DNS computations only currently practical for low Reynolds number flows. Large-eddy simulations attempt to model the smaller, more homogeneous scales while resolving the larger, energy-containing scales. This makes LES grid requirements less stringent than those for DNS. The RANS approach attempts to solve for the time-averaged flow, such as that described in equation (4.49). This means that all scales of turbulence must be modeled. Recently, hybrid approaches that combine RANS and LES have been proposed in an attempt to combine the best features of these two approaches.

For the RANS approach, flow quantities of interest are time averaged. When this averaging process is applied to the Navier-Stokes equations (such as was done in Section 4.5.1), the result is an equation for the mean quantities, with extra term(s) involving the fluctuating quantities, the Reynolds stress tensor (e.g., $-\rho\overline{u'v'}$). The Reynolds stress tensor takes into account the transfer of momentum by the turbulent fluctuations. Many models assume that the Reynolds stress tensor is proportional to the mean strain-rate tensor [i.e., $\mu_t(\partial\overline{u}/\partial y)$]. This is known as the Boussinesq eddy-viscosity approximation, where μ_t is the unknown turbulent eddy viscosity, and the turbulent eddy viscosity is determined using a turbulence model. The development of correlations in terms of known parameters is usually termed as the *closure problem*. Closure procedures for the turbulent eddy viscosity are generally categorized by the number of partial differential equations that are solved, with zero-equation, one-equation, and two-equation models being the most popular.

Zero-equation models use no differential equations and are commonly known as algebraic models. Zero-equation models are well adapted to simple, attached flows where local turbulence equilibrium exists (i.e., the local production of turbulence is balanced by the local dissipation of turbulence). Smith (1991) noted, "For solutions of external flows around full aircraft configurations, algebraic turbulence models remain the most popular choice due to their simplicity." However, he further noted, "In general, while algebraic turbulence models are computationally simple, they are more difficult for the user to apply. Since algebraic models are accurate for a narrow range of flows, different algebraic models must be applied to the different types of turbulent flows in a single flow problem. The user must define in advance which model applies to which region, or complex logic must be implemented to automate this process . . . . Different results can be obtained with different implementation of the same turbulence model."

By solving one or more differential equations, the transport of turbulence can be included. That is, the effect of flow history on the turbulence can be modeled. One example where modeling the flow history of turbulence is crucial is in the calculation of turbulent flow over a multi-element airfoil. One equation models are perhaps the simplest way to model this effect. Wilcox (1998), when discussing the one-equation model of Spalart-Allmaras (1992), noted that "it is especially attractive for airfoil and wing applications, for which it has been calibrated." As a result, the Spalart-Allmaras model, which solves a single partial differential equation for a variable that is related to the turbulent kinematic eddy viscosity, is one of the most popular turbulence models.

In two-equation models, one transport equation is used for the computation of the specific turbulence kinetic energy (k) and a second transport equation is used to

determine the turbulent length scale (or dissipation length scale). A variety of transport equations have been proposed for determining the turbulent length scale, including k-ε, k-ω, and k-ε/k-ω models. Again, Wilcox (1998) is an excellent resource for detailed discussions of these turbulence models.

Smith (1991) notes, " For a two equation model, the normal Reynolds stress components are assumed to be equal, while for algebraic models the normal stresses are entirely neglected. Experimental results show the streamwise Reynolds stress component to be two to three times larger than the normal component. For shear flows with only gradual variations in the streamwise direction, the Reynolds shear stress is the dominant stress term in the momentum equations and the two equation models are reasonably accurate. For more complex strain fields, the errors can be significant."

Neumann (1989) notes, "Turbulence models employed in computational schemes to specify the character of turbulent flows are just that . . . models, non-physical ways of describing the character of the physical situation of turbulence. The models are the result of generalizing and applying fundamental experimental observations; they are not governed by the physical principles of turbulence and they are not unique."

In evaluating computations for the flow over aircraft at high angles of attack, Smith (1991) notes that "at higher angles of attack, turbulence modeling becomes more of a factor in the accuracy of the solution." The advantage of the RANS models is that they are relatively cheap to compute and can provide accurate solutions to many engineering flows. However, RANS models lack generality. The coefficients in the various models are usually determined by matching the computations to simple building-block experimental flows [e.g., zero-pressure-gradient (flat-plate) boundary layers]. Therefore, when deciding which turbulence model to use, the user should take care to ensure that the selected turbulence model has been calibrated using measurements from relevant flow fields. Furthermore, the model should have sufficient accuracy and suitable numerical efficiency for the intended applications.

Spalart et al. (1997) estimated the cost in terms of the grid size for DNS and LES computations of a full-scale aircraft at flight Reynolds numbers. Their conclusion, assuming that the computer speed growth trend continues to hold, was that DNS computations would not be feasible for full aircraft at flight Reynolds numbers until approximately the year 2080, and that LES computations would not be possible until 2045. This estimate motivated the formulation of a hybrid turbulence model, Detached-Eddy Simulation, which combines the advantages of LES and RANS into one model, and is usable with today's computers. The model uses RANS in the boundary layer, where RANS performs well with much lower grid requirements than LES. LES is then used in separated flow regions where it can resolve large-scale turbulence motion well. The success of DES and the various derivative models it has spawned led Salas to state that "DES and other RANS-LES hybrids appear to have the greatest promise at this time for unsteady separated flows [Salas (2006)]."

4.5.3 Turbulent Boundary Layer for a Flat Plate

Since u_e is a constant for flow over a flat plate, the pressure gradient term is zero. Even with this simplification, there is no exact solution for the turbulent boundary layer.

Very near the wall, the viscous shear dominates and creates a laminar sub-layer. Ludwig Prandtl deduced that the mean velocity in this region must depend on the wall shear stress, the fluid's physical properties, and the distance y from the wall. Therefore, $\overline{u}$ is a function of (τ_w, ρ, μ, y). To first order, the velocity profile in this region is linear, that is, $\overline{u}$ is proportional to y and the shear stress is:

$$\tau_w = \mu \frac{\partial \overline{u}}{\partial y} = \mu \frac{\overline{u}}{y} \tag{4.52}$$

Now we will define a wall velocity as:

$$u^+ = \frac{\overline{u}}{u^*} \tag{4.53a}$$

and the distance from the wall in "wall units" is:

$$y^+ = \frac{y u^*}{\nu} \tag{4.53b}$$

where u^* is called the *wall-friction velocity* and is defined as:

$$u^* = \sqrt{\frac{\tau_w}{\rho}} \tag{4.53c}$$

You should notice that y^+ has the form of a Reynolds number.

Substituting the definitions for y^+ from equation (4.53a) and u^+ from equation (4.53b) into equation (4.52), and recalling that $\nu = \mu/\rho$, we obtain:

$$\tau_w = \mu \frac{u^+ u^*}{(y^+ v)/u^*} = (u^+/y^+)\rho u^{*2}$$

If we introduce the definition of the wall-friction velocity from equation (4.53c), it is clear that:

$$u^+ = y^+ \tag{4.54}$$

for the laminar sublayer. In the laminar sublayer, the velocities are so small that viscous forces dominate and there is no turbulence. The edge of the laminar sublayer corresponds to a y^+ of approximately 5 to 10, as shown in Fig. 4.15.

In 1930, Theodore von Kármán deduced that, in the outer region of a turbulent boundary layer, the mean velocity $\overline{u}$ is reduced below the free-stream value (u_e). This reduction takes place in a manner that is independent of the viscosity, but is dependent on the wall shear stress and the distance y over which the effect has diffused. Therefore, the velocity defect $(u_e - \overline{u})$ for the outer region is a function of $(\tau_w, \rho, y, \delta)$. For the outer region, the velocity-defect law is given by

$$\frac{u_e - \overline{u}}{u^*} = g\left(\frac{y}{\delta}\right) \tag{4.55}$$

The outer region of a turbulent boundary layer contains 80 to 90% of the boundary-layer thickness δ, although in Fig. 4.15 it is shown in wall units for $y^+ > 200$.

In 1933, Prandtl deduced that the mean velocity in the inner region must depend on the wall shear stress, the fluid physical properties, and the distance y from the wall.

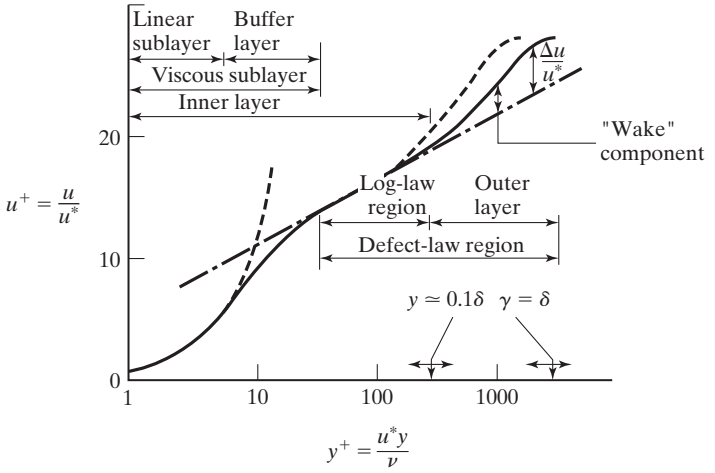

Figure 4.15 Turbulent boundary layer illustrating wall-layer nomenclature.

Therefore, $\overline{u}$ is a function of (τ_w, ρ, μ, y). Specifically, the velocity variation is assumed to have the form:

$$\frac{\overline{u}}{u^*} = f\left[\left(\frac{y}{\delta}\right)\left(\frac{\delta u^*}{\nu}\right)\right] \tag{4.56}$$

for the inner region.

Since the velocities of the inner and outer regions must match at their interface, equations (4.55) and (4.56) are equated as:

$$\frac{\overline{u}}{u^*} = f\left[\left(\frac{y}{\delta}\right)\left(\frac{\delta u^*}{\nu}\right)\right] = \frac{u_e}{u^*} - g\left(\frac{y}{\delta}\right)$$

As a result, the velocity in the inner region is given by

$$\frac{\overline{u}}{u^*} = \frac{1}{\kappa}\ln\frac{yu^*}{\delta} + B \tag{4.57a}$$

or, in terms of u^+, y^+, the equation can be written as

$$u^+ = \frac{1}{\kappa}\ln y^+ + B \tag{4.57b}$$

This velocity correlation is valid only in regions where the laminar shear stress can be neglected in comparison with the turbulent stress. Thus, the flow in this region (i.e., $70 < y^+ < 400$) is fully turbulent.

The velocity in the outer region is given by

$$\frac{u_e - \overline{u}}{u^*} = -\frac{1}{\kappa}\ln\frac{y}{\delta} + A \tag{4.58}$$

where κ A, and B are dimensionless parameters. For incompressible flow past a flat plate,

$$\kappa \simeq 0.40 \quad \text{or} \quad 0.41$$
$$A \simeq 2.35$$
$$B \simeq 5.0 \quad \text{to} \quad 5.5$$

The resultant velocity profile is presented in Fig. 4.15, where all of the various layers and their velocity profiles are shown in wall units.

The computation of the turbulent skin-friction drag for realistic aerodynamic applications presents considerable challenges to the analyst, both because of grid generation considerations and because of the need to develop turbulence models of suitable accuracy for the complex flow-field phenomena that may occur (e.g., viscous/inviscid interactions). In order to accurately determine velocity gradients near the wall, the computational grid should include points in the laminar sublayer. Referring to Fig. 4.15, the computational grid should, therefore, contain points at a y^+ of 5 or less, which is typically very close to the wall. While there are many turbulence models of suitable engineering accuracy available in the literature, you should calibrate the particular model to be used against a relevant data base to ensure that the model provides results of suitable accuracy for the applications of interest.

4.6 EDDY VISCOSITY AND MIXING LENGTH CONCEPTS

In the late nineteenth century, Joseph Boussinesq introduced the concept of eddy viscosity to model the Reynolds shear stress. Boussinesq assumed that the Reynolds stresses act like the laminar shear stresses and are proportional to the transverse gradient of the mean streamwise velocity component. The coefficient of proportionality is called the *eddy viscosity* $\nu_t = \mu_t/\rho$, and the Reynolds stresses were assumed to take the form:

$$-\rho\overline{u'v'} = \rho\nu_t\left(\frac{\partial\overline{u}}{\partial y}\right) \tag{4.59}$$

Having introduced the concept of eddy viscosity, equation (4.51) for the total shear stress may now be written as:

$$\tau = \tau_l + \tau_t = \rho\nu\frac{\partial\overline{u}}{\partial y} + \rho\nu_t\frac{\partial\overline{u}}{\partial y} = \rho(\nu + \nu_t)\frac{\partial\overline{u}}{\partial y} \tag{4.60}$$

Like the kinematic viscosity ν, ν_t has the units of (length)^2/time. However, whereas ν is a property of the fluid and is defined once the pressure and the temperature are known, ν_t is a function of the flow field (including such factors as surface roughness, pressure gradients, etc.). The use of eddy viscosity also allows you to use the laminar equations and obtain turbulent results simply by replacing ν by $\nu + \nu_t$ and then defining ν_t with a turbulence model.

In an attempt to obtain a more generally applicable relation, Prandtl proposed the mixing length concept, whereby the shear stress could be found from:

$$-\rho\overline{u'v'} = \rho l^2\left|\frac{\partial\overline{u}}{\partial y}\right|\frac{\partial\overline{u}}{\partial y} \tag{4.61}$$

where l is the mixing length, which is the distance traveled by lumps of fluid moving up and down within the boundary layer, as shown in Fig. 4.2. Equating the expressions for the Reynolds stress, given by equations (4.59) and (4.61), we can now write a relation between the eddy viscosity and the mixing length:

$$\nu_t = l^2 \left| \frac{\partial \overline{u}}{\partial y} \right| \tag{4.62}$$

From this point on, we will only use the time-averaged (or mean-flow) properties in our formulation, since the Reynolds stresses can be replaced by using equation (4.60). Therefore, we will drop the overbar notation in the subsequent analysis.

The distributions of ν_t and l across the boundary layer are typically obtained from experimental data. Because the eddy viscosity and the mixing length concepts are based on local equilibrium concepts, they provide only rough approximations to the actual flow and often lack generality. However, the eddy viscosity concept is relatively simple to use and provides reasonable values of the shear stress for many engineering applications.

A general conclusion that we can draw from the experimental evidence is that the turbulent boundary layer should be treated as a composite layer consisting of an inner region and an outer region, as shown in Fig. 4.15. For the inner region, the mixing length can be found from:

$$l_i = \kappa y[(1 - \exp(-y/A)] \tag{4.63}$$

where $\kappa = 0.41$ (as discussed in Section 4.5.3) and A, the van Driest damping parameter, is given by:

$$A = \frac{26\nu}{Nu^*} \tag{4.64a}$$

where u^* is the wall friction velocity as defined by equation (4.53c). N is found from:

$$N = (1 - 11.8p^+)^{0.5} \tag{4.64b}$$

and

$$p^+ = \frac{\nu u_e}{(u^*)^3} \frac{du_e}{dx} \tag{4.64c}$$

The eddy viscosity for the inner region can be found from equation (4.62) as:

$$(\nu_t)_i = (\kappa y)^2[1 - \exp(-y/A)]^2 \left| \frac{\partial u}{\partial y} \right| \tag{4.65}$$

For the outer region, the eddy viscosity is given as:

$$(\nu_t)_o = \alpha u_e \delta^* \tag{4.66}$$

where δ^* is the displacement thickness as defined by equation (4.26), and α is found from:

$$\alpha = \frac{0.02604}{1 + \Pi} \tag{4.67a}$$

$$\Pi = 0.55[1 - \exp(-0.243\sqrt{z_1} - 0.298z_1)] \tag{4.67b}$$

and

$$z_1 = \frac{\mathrm{Re}_\theta}{425} - 1 \tag{4.67c}$$

Re_θ is the Reynolds number based on momentum thickness, $\mathrm{Re}_\theta = u_e\theta/\nu$ and the momentum thickness is defined in equation (4.28).

The y coordinate of the interface between the inner region and the outer region is determined by the requirement that the y distribution of the eddy viscosity be continuous. Therefore, the inner region expression [equation (4.65)] is used to calculate the eddy viscosity until its value becomes equal to that given by the outer region expression [equation (4.66)]. The y coordinate is the interface value, y_c, which is where the two expressions for the eddy viscosity are equal [i.e., when $(\nu_t)_i = (\nu_t)_o$]. For $y \geq y_c$, the eddy viscosity is calculated using the outer region expression [equation (4.66)].

Recall that the transition process occurs over a finite length; the boundary layer does not instantaneously change from a laminar state to a fully turbulent profile. For most practical boundary-layer calculations, it is necessary to calculate the boundary layer along its entire length. That is, for a given pressure distribution (inviscid flow field) and for a given transition criterion, the boundary-layer calculation is started at the leading edge or at the forward stagnation point of the body (where the boundary layer is laminar) and proceeds downstream through the transitional flow into the fully turbulent region. To treat the boundary layer in the transition zone, the expressions for the eddy viscosity are multiplied by an intermittency factor, γ_{tr}. The expression for the intermittency factor is given by:

$$\gamma_{\mathrm{tr}} = 1 - \exp\left[-G(x - x_{\mathrm{tr}}) \int_{x_{\mathrm{tr}}}^{x} \frac{dx}{u_e}\right] \tag{4.68a}$$

where x_{tr} is the x coordinate for the onset of transition and G is given by:

$$G = 8.35 \times 10^{-4}\left(\frac{u_e^3}{\nu^2}\right)(\mathrm{Re}_{x,\,\mathrm{tr}})^{-1.34} \tag{4.68b}$$

The intermittency factor varies from 0 (in the laminar region and at the onset of transition) to 1 (at the end of the transition zone and for fully turbulent flow). Therefore, in the transition zone:

$$(\nu_t)_i = (\kappa y)^2[1 - \exp(-y/A)]^2\left|\frac{\partial u}{\partial y}\right|\gamma_{tr} \tag{4.69a}$$

and

$$(\nu_t)_o = \alpha u_e \delta^* \gamma_{tr} \tag{4.69b}$$

Solutions have been obtained using these equations to describe the laminar, transitional, and turbulent boundary layer for flow past a flat plate, with the results presented in Fig. 4.16.

4.7 INTEGRAL EQUATIONS FOR A FLAT-PLATE BOUNDARY LAYER

The eddy viscosity concept or one of the higher-order methods is used in developing turbulent boundary-layer solutions using the differential equations of motion. Although approaches using the differential equations are most common in computational fluid

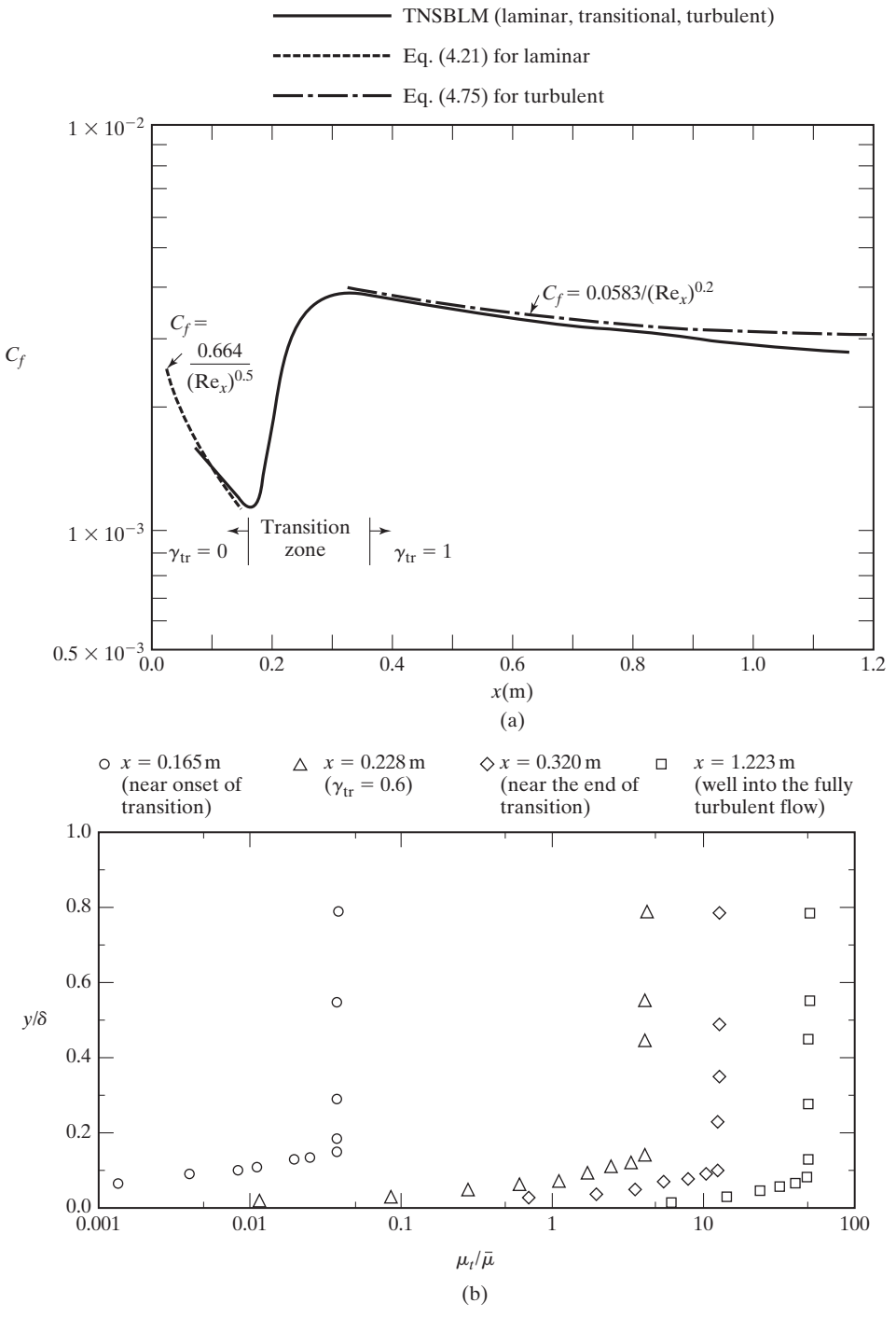

Figure 4.16 Sample of computed boundary layer for incompressible flow past a flat plate, $u_e = 114.1$ ft/s, $T_e = 542°R$, $P_e = 2101.5$ psf, $T_w = 540°R$: (a) skin-friction distribution; (b) turbulent viscosity/thermodynamic viscosity ratio.

dynamics, the integral approach can also be used to obtain approximate solutions for a turbulent boundary layer. Following a suggestion by Prandtl, the turbulent velocity profile can be represented by a power-law approximation, which yields useful and practical results.

We will use the mean-flow properties in the integral form of the equations of motion to develop engineering correlations for the skin-friction coefficient and the boundary-layer thickness for an incompressible, turbulent boundary layer on a flat plate. Since we will use only the time-averaged (or mean-flow) properties in this section, we will drop the overbar notation (as mentioned previously).

Consider the control volume shown in Fig. 4.17 for the boundary layer development along a flat plate. Notice that the free-stream velocity of the flow approaching the plate (U_∞) and the velocity of the flow outside of the boundary layer adjacent to the plate (u_e) are equal and are used interchangeably. The wall is the inner boundary of the control volume. A streamline outside the boundary layer is the outer boundary; any streamline that is outside the boundary layer (and, therefore, has zero shear force acting across it) will do. Because the viscous action retards the flow near the surface, the outer boundary is not parallel to the wall and must be accounted for. Therefore, the streamline is a distance Y_0 away from the wall at the initial station and is a distance Y away from the wall at the downstream station, with $Y > Y_0$. Since $\vec{V} \cdot \hat{n} dA = 0$ for both boundary streamlines, the continuity equation (2.5) only has to take into account the inflow and outflow as:

$$\int_0^Y u(y)dy - u_e Y_0 = 0 \tag{4.70}$$

But we also know that:

$$\int_0^Y u(y)dy = \int_0^Y [\, u_e + (u - u_e)\,]dy$$

$$= u_e Y + \int_0^Y (u - u_e)\, dy \tag{4.71}$$

Combining equations (4.70) and (4.71) and introducing the definition for the displacement thickness from equation (4.26):

$$\delta^* = \int_0^\delta \left(1 - \frac{u}{u_e}\right) dy$$

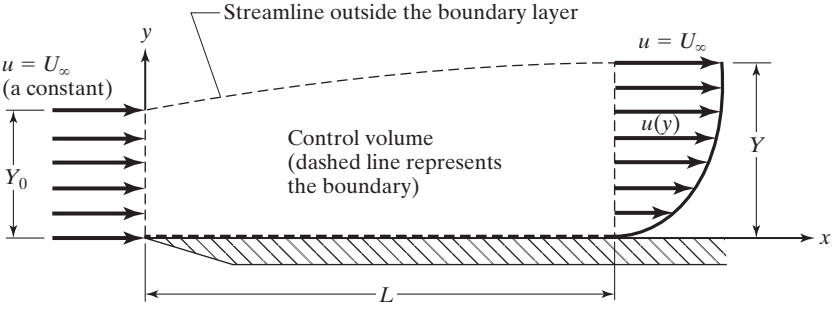

Figure 4.17 Control volume used to analyze the boundary layer on a flat plate.

we find that:

$$Y - Y_0 = \delta^* \tag{4.72}$$

We have now derived the expected result that the outer streamline is deflected by the transverse distance δ^*. In developing this relation, we have used both δ and Y as the upper limit for the integration. Since the integrand in equation (4.71) goes to zero for $y \geq \delta$, the integral is independent of the upper limit of integration, provided that it is at, or beyond, the edge of the boundary layer. This verifies that we could have chosen any streamline outside the boundary layer for our analysis.

Similarly, application of the integral form of the momentum equation (2.13) yields:

$$-d = \int_0^Y u(\rho u\, dy) - \int_0^{Y_0} u_e(\rho u_e\, dy)$$

where d designates the drag per unit span. Now we can evaluate the drag as:

$$d = \rho u_e^2 Y_0 - \int_0^Y (\rho u^2\, dy) \tag{4.73}$$

Using equation (4.70), we find that:

$$d = \rho u_e \int_0^Y u\, dy - \int_0^Y \rho u^2\, dy$$

This equation can be rewritten in terms of the section drag coefficient as

$$\begin{aligned} C_d &= \frac{d}{\frac{1}{2}\rho_\infty U_\infty^2 L} \\ &= \frac{2}{L}\left(\int_0^Y \frac{u}{u_e} dy - \int_0^Y \frac{u^2}{u_e^2} dy \right) \end{aligned} \tag{4.74}$$

Recall that the momentum thickness for an incompressible flow, equation (4.28), can be written as:

$$\theta = \int_0^\delta \frac{u}{u_e}\left(1 - \frac{u}{u_e}\right) dy \tag{4.28}$$

Notice that the result is also independent of the upper limit of integration provided that the upper limit is equal to or greater than the boundary-layer thickness. Therefore, the drag coefficient (for one side of a flat plate of length L) is:

$$C_d = \frac{2\theta}{L} \tag{4.75}$$

The equations developed in this section are valid for incompressible flow past a flat plate whether the boundary layer is laminar or turbulent. The value of the integral technique is that it requires only a "reasonable" approximation for the velocity profile [i.e., *u(y)*] in order to achieve "fairly accurate" drag predictions, because the integration often averages out positive and negative deviations in the assumed velocity function. This makes the results of the next section especially useful in engineering applications, especially for conceptual aircraft design.

4.7.1 Application of the Integral Equations of Motion to a Turbulent, Flat-Plate Boundary Layer

Now that we have the integral equations we can apply them to develop correlations for a turbulent boundary layer on a flat plate. As we discussed earlier, an analytical form for the turbulent shear is not known a priori; therefore, we need some experimental information. Experimental measurements have shown that the time-averaged velocity for a turbulent boundary layer on a flat plate may be represented by the 1/7th power law:

$$\frac{u}{u_e} = \left(\frac{y}{\delta}\right)^{1/7} \tag{4.76}$$

when the local Reynolds number Re_x is in the range 5×10^5 to 1×10^7. However, notice that there is a problem with this profile, since the velocity gradient is:

$$\frac{\partial u}{\partial y} = \frac{u_e}{7}\frac{1}{\delta^{1/7}}\frac{1}{y^{6/7}}$$

which goes to infinity at the wall. So, although the correlation given in equation (4.76) provides a reasonable representation of the actual velocity profile, we need another piece of experimental data: a correlation for the shear acting at the wall. Blasius found that the skin-friction coefficient for a turbulent boundary layer on a flat plate where the local Reynolds number is in the range 5×10^5 to 1×10^7 is given by:

$$C_f = \frac{\tau}{\frac{1}{2}\rho u_e^2} = 0.0456\left(\frac{v}{u_e\delta}\right)^{0.25} \tag{4.77}$$

Now we can differentiate the drag coefficient from equation (4.74), recalling that $C_d = \dfrac{1}{L}\displaystyle\int C_f dx$, so $C_f = L\dfrac{d}{dx}(C_d)$:

$$C_f = -2\frac{d}{dx}\left[\delta \int_0^1 \frac{u}{u_e}\left(\frac{u}{u_e} - 1\right)d\left(\frac{y}{\delta}\right)\right] \tag{4.78}$$

We can now find the boundary layer thickness by substituting equations (4.76) and (4.77) into equation (4.78) to obtain:

$$0.0456\left(\frac{v}{u_e\delta}\right)^{0.25} = -2\frac{d}{dx}\left\{\delta\int_0^1\left[\left(\frac{y}{\delta}\right)^{2/7} - \left(\frac{y}{\delta}\right)^{1/7}\right]d\left(\frac{y}{\delta}\right)\right\}$$

which eventually becomes:

$$\delta^{0.25}d\delta = 0.2345\left(\frac{\nu}{u_e}\right)^{0.25}dx$$

If we assume that the boundary-layer thickness is zero when $x = 0$, we find that

$$\delta = 0.3747\left(\frac{\nu}{u_e}\right)^{0.2}(x)^{0.8}$$

By rearranging, we can find the various thicknesses of a turbulent boundary layer on a flat plate since Schlichting and Gersten (2000) showed that $\delta^* = \delta/(1 + n) = \delta/8$

and $\theta = n\delta/[(1+n)(2+n)] = 7\delta/72$, where $1/n = 1/7$ is the exponent in equation (4.76):

$$\frac{\delta}{x} = \frac{0.3747}{(\mathrm{Re}_x)^{0.2}} \qquad \frac{\delta^*}{x} = \frac{0.0468}{(\mathrm{Re}_x)^{0.2}} \qquad \frac{\theta}{x} = \frac{0.0364}{(\mathrm{Re}_x)^{0.2}} \tag{4.79}$$

Comparing the turbulent correlation given by equation (4.79) with the laminar correlation given by equation (4.23), we see that a turbulent boundary layer grows at a faster rate than a laminar boundary layer subject to the same conditions. Furthermore, at a given x station, a turbulent boundary layer is thicker than a laminar boundary layer for the same free-stream conditions.

Substituting the boundary layer thickness from equation (4.79) into equation (4.77) yields:

$$C_f = \frac{0.0583}{(\mathrm{Re}_x)^{0.2}} \tag{4.80}$$

As with the laminar skin-friction coefficient found in Sec. 4.3.1, a total skin-friction coefficient can be found for turbulent flow by integrating equation (4.80) over the length of a flat plate:

$$\overline{C}_f = \frac{1}{L}\int_0^L C_f(x)\,dx = \frac{1}{L}\int_0^L \frac{0.0583}{(\mathrm{Re}_x)^{0.2}}\,dx$$

$$\overline{C}_f = \frac{0.074}{(\mathrm{Re}_L)^{0.2}} \tag{4.81}$$

This formula, known as the Prandtl formula, is an exact theoretical representation of the turbulent skin-friction drag based on the velocity profile of equation (4.76). However, when compared with experimental data, equation (4.81) is found to be only $\pm 25\%$ accurate. A number of other turbulent skin-friction coefficient relations have been developed, some of which are considerably more accurate than the Prandtl formula [White (2005)]:

Prandtl-Schlichting:

$$\overline{C}_f \equiv \frac{0.455}{(\log_{10}\mathrm{Re}_L)^{2.58}} \quad \pm 3\% \text{ accurate} \tag{4.82}$$

Karman-Schoenherr:

$$\frac{1}{\sqrt{\overline{C}_f}} \equiv 4.13\log_{10}(\mathrm{Re}_L\,\overline{C}_f) \quad \pm 2\% \text{ accurate} \tag{4.83}$$

Schultz-Grunow:

$$\overline{C}_f \equiv \frac{0.427}{(\log_{10}\mathrm{Re}_L - 0.407)^{2.64}} \quad \pm 7\% \text{ accurate} \tag{4.84}$$

While the Karman-Schoenherr relation is the most accurate of these formulations, it requires an iterative solution method to obtain a result, since the drag coefficient is not explicitly represented. Therefore, the most accurate relation which is also straightforward to use is the Prandtl-Schlichting relation, which should usually be used instead of the Prandtl theoretical relation, equation (4.81).

The calculation of the skin-friction drag for a flat plate with transition theoretically would require using the local skin-friction coefficients, equation (4.21) for the laminar portion of the flow and equation (4.80) for the turbulent part of the flow. Taking care to only integrate each relation over the laminar and turbulent lengths, respectively, gives us:

$$C_D = \frac{1}{L}\left\{ \int_0^{x_{tr}} C_{f_{\text{lam}}}\, dx + \int_{x_{tr}}^{L} C_{f_{\text{turb}}}\, dx \right\} \tag{4.85}$$

Another approach is to use the total skin-friction coefficients, which are equation (4.32) for the laminar portion of the flow and equation (4.82) for the turbulent part of the flow. Care must be taken, however, when using the total skin-friction coefficients, since they already represent the integrated skin friction over the entire plate from $x = 0$ to $x = L$. In order to properly simulate a flat plate with transitional flow present, the process shown in Fig. 4.18 should be used. Since you want to simulate the plate with both laminar and turbulent boundary layers present, you start by evaluating the entire plate assuming that the boundary layer is turbulent along the entire length of the plate. Since the distance from the leading edge of the plate to the transition location should be evaluated with laminar flow, that portion of the plate must be evaluated with both the turbulent-flow skin-friction relation and the laminar-flow skin-friction relation by subtracting the turbulent-flow drag from the total plate turbulent results and adding the laminar-flow portion. In equation form, this would be:

$$C_D = \overline{C}_{f_{\text{turb}}} \frac{Lb}{S_{\text{ref}}} - \overline{C}_{f_{\text{turb}}} \frac{x_{\text{tr}} b}{S_{\text{ref}}} + \overline{C}_{f_{\text{lam}}} \frac{x_{\text{tr}} b}{S_{\text{ref}}} \tag{4.86}$$

A more straightforward approach to model transitional flow is to use a correction to the Prandtl-Schlichting turbulent skin-friction relation in equation (4.82) [Dommasch et al. (1967)]:

$$\overline{C}_f \equiv \frac{0.455}{(\log_{10} \text{Re}_L)^{2.58}} - \frac{A}{\text{Re}_L} \tag{4.87}$$

where the correction term reduces the skin friction since laminar boundary layers produce less skin friction than turbulent boundary layers. The experimentally determined

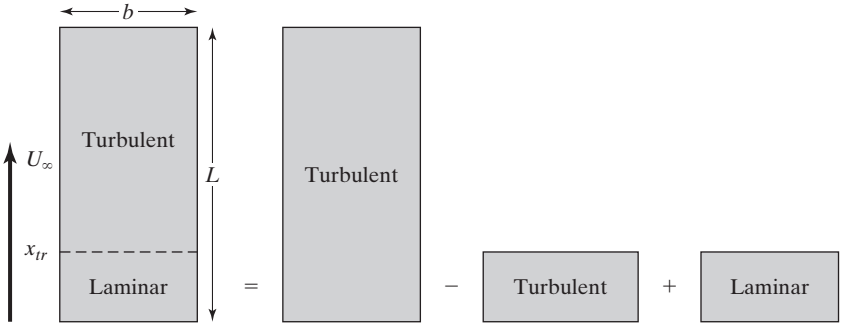

Figure 4.18 Calculation of skin-friction drag coefficient using total skin-friction coefficients.

TABLE 4.5 Empirical Relations for Transition Correction [Schlichting and Gersten (2000)]

$Re_{x,\,tr}$	A
300,000	1050
500,000	1700
1,000,000	3300
3,000,000	8700

constant, A, varies depending on the transition Reynolds number, as shown in Table 4.5. The value $A = 1700$ represents the laminar correction for a transition Reynolds number of $\mathrm{Re}_{x,\,\mathrm{tr}} = 500{,}000$. You can see from this formulation that if the Reynolds number at the end of the plate is very high, then the laminar correction term plays a fairly insignificant role in the total skin-friction drag on the plate. A good rule of thumb is to assume that if transition takes place at less than 10% of the length of the plate, then the laminar correction usually can be ignored, since it is relatively small.

Fig. 4.19 shows how the total skin-friction coefficient varies from the laminar value in equation (4.32), through transition, and finally to the fully turbulent value, in equation (4.82).

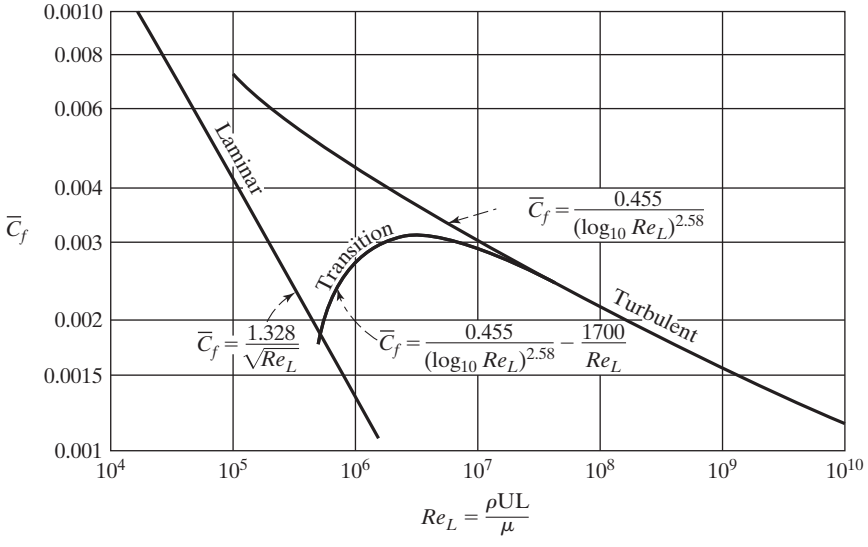

Figure 4.19 Variation of total skin-friction coefficient with Reynolds number for a smooth, flat plate.

EXAMPLE 4.4: Computing the velocity profiles at the "transition point"

Air at standard day sea-level atmospheric pressure and 5°C flows at 200 km/h across a flat plate. Compare the velocity distribution for a laminar boundary layer and for a turbulent boundary layer at the transition point, assuming that the transition process is completed instantaneously at that location.

Solution: For air at atmospheric pressure and 5°C,

$$\rho_\infty = \frac{1.01325 \times 10^5\ \text{N/m}^2}{(287.05\ \text{N}\cdot\text{m/kg}\cdot\text{K})(278.15\ \text{K})} = 1.2691\ \text{kg/m}^3$$

$$\mu_\infty = 1.458 \times 10^{-6}\frac{(278.15)^{1.5}}{278.15 + 110.4} = 1.7404 \times 10^{-5}\ \text{kg/s}\cdot\text{m}$$

and

$$U_\infty = \frac{(200\ \text{km/h})(1000\ \text{m/km})}{3600\ \text{s/h}} = 55.556\ \text{m/s}$$

We will assume that the transition Reynolds number for this incompressible flow past a flat plate is 500,000. Therefore, transition takes place at:

$$x_{\text{tr}} = \frac{\text{Re}_{x,\,\text{tr}}}{\rho u_e/\mu} = 0.12344\ \text{m}$$

The thickness of a laminar boundary layer at this point is

$$\delta_{\text{lam}} = \frac{5.0x}{\sqrt{\text{Re}_x}} = 8.729 \times 10^{-4}\ \text{m}$$

For comparison, we will calculate the thickness of the turbulent boundary layer at this point for this Reynolds number, assuming that the boundary layer is turbulent all the way from the leading edge:

$$\delta_{\text{turb}} = \frac{0.3747x}{(\text{Re}_x)^{0.2}} = 3.353 \times 10^{-3}\ \text{m}$$

which is 3.8 times thicker than the laminar boundary layer.

In reality, the flow is continuous at the transition location and the boundary-layer thickness does not change instantaneously. Furthermore, since we are at the transition location, it is not realistic to use the assumption that the boundary layer is turbulent all the way from the leading edge. (This assumption would be reasonable far downstream of the transition location so that $x \gg x_{\text{tr}}$.) Nevertheless, the object of these calculations is to illustrate the characteristics of the turbulent boundary layer relative to a laminar boundary layer at the same conditions.

The resultant velocity profiles are compared in Table 4.6 and Fig. 4.20. Note that the streamwise velocity component u increases much more rapidly with y near the wall for the turbulent boundary layer. Therefore, the shear at the wall is greater for the turbulent boundary layer even though this layer is much thicker than the laminar boundary layer for the same conditions at a

TABLE 4.6 Velocity Profiles for Example 4.4

$y(m)$	$u_{lam}(m/s)$	$u_{turb}(m/s)$
0.00000	0.00	0.00
0.00017	17.78	36.21
0.00034	33.33	39.98
0.00067	52.50	44.14
0.00101	Inviscid flow	46.78
0.00134	↓	48.74
0.00168		50.32
0.00201		51.64
0.00235		52.79
0.00268		53.81
0.00302		54.71
0.00335		55.56

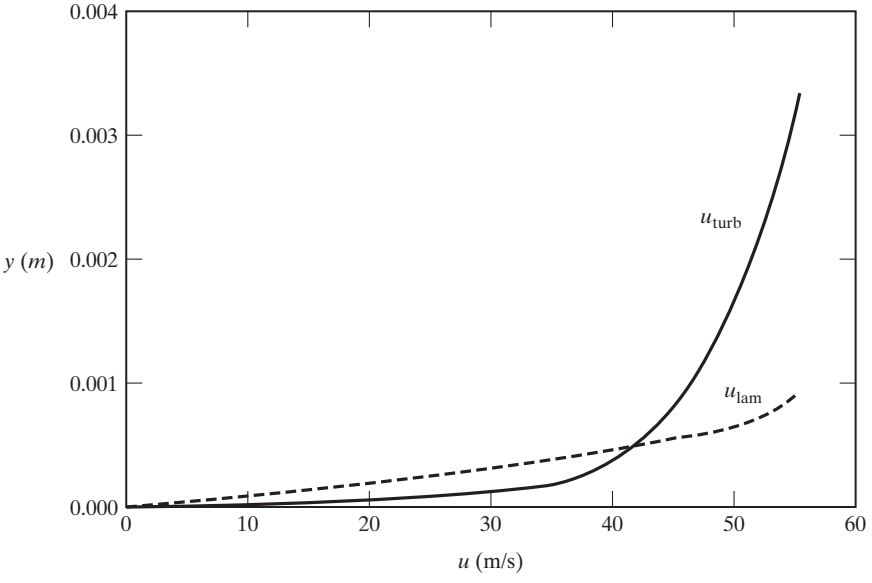

Figure 4.20 Velocity profiles for Example 4.4.

given x station. The macroscopic transport of fluid in the y direction causes both increased shear and increased thickness of the boundary layer.

4.7.2 Integral Solutions for a Turbulent Boundary Layer with a Pressure Gradient

If we apply the integral equations of motion to a flow with a velocity gradient external to the boundary layer, we obtain:

$$\frac{d\theta}{dx} + (2 + H)\frac{\theta}{u_e}\frac{du_e}{dx} = \frac{C_f}{2} \tag{4.88}$$

where θ, the momentum thickness, was defined in equation (4.28). H, the momentum shape factor, is defined as:

$$H = \frac{\delta^*}{\theta} \tag{4.89}$$

where δ^*, the displacement thickness, is defined in equation (4.26). The shape factor has been shown to be a useful way to estimate when a turbulent boundary layer will separate. If you recall from the 1/7th power law velocity distribution for a turbulent boundary layer (see Section 4.7.1), the displacement thickness and momentum thickness could be related to the boundary layer thickness by $\delta^* = \delta/8$ and $\theta = 7\delta/72$, which means the shape factor for this boundary layer is $H = (\delta/8)/(7\delta/72) \approx 1.3$ (or the displacement thickness is approximately 30% larger than the momentum thickness). Kroo (2007) has shown that a fairly reliable value of the shape factor for predicting separation is approximately 2.2, which means the displacement thickness has grown to over twice the size of the momentum thickness. Another method for predicting turbulent boundary layer separation was developed by Stratford (1959).

Equation (4.88) contains three unknown parameters, θ, H, and C_f for a given external velocity distribution. For a turbulent boundary layer, these parameters are interrelated in a complex way. Head (1969) assumed that the rate of entertainment is given by:

$$\frac{d}{dx}(u_e\theta H_1) = u_e F \tag{4.90}$$

where H_1 is defined as:

$$H_1 = \frac{\delta - \delta^*}{\theta} \tag{4.91}$$

Head also assumed that H_1 is a function of the shape factor H, that is, $H_1 = G(H)$. Correlations of several sets of experimental data that were developed by Cebeci and Bradshaw (1979) yielded:

$$F = 0.0306(H_1 - 3.0)^{-0.6169} \tag{4.92}$$

and

$$G = \begin{cases} 0.8234(H - 1.1)^{-1.287} + 3.3 & \text{for } H \le 1.6 \\ 1.5501(H - 0.6778)^{-3.064} + 3.3 & \text{for } H \ge 1.6 \end{cases} \tag{4.93}$$

Equations (4.90) through (4.93) provide a relationship between θ and H. A relation between C_f, θ, and H is needed to complete our system of equations. A curvefit formula given in White (2005) shows that:

$$C_f = \frac{0.3e^{-1.33H}}{(\log \mathrm{Re}_\theta)^{(1.74+0.31H)}} \tag{4.94}$$

where Re_θ is the Reynolds number based on the momentum thickness:

$$\mathrm{Re}_\theta = \frac{\rho u_e \theta}{\mu} \tag{4.95}$$

We can numerically solve this system of equations for a given inviscid flow field. To start the calculations at some initial streamwise station, such as the transition location, values for two of the three parameters, θ, H, and C_f, must be specified at this station. The third parameter is then calculated using equation (4.94). Using this method, the shape factor H can be used as a criterion for separation. Although it is not possible to define an exact value of H corresponding to the separation, the value of H for separation is usually in the range 1.8 to 2.8.

4.8 THERMAL BOUNDARY LAYER FOR CONSTANT-PROPERTY FLOWS

As we discussed earlier, there are many constant-property flows for which we are interested in calculating the convective heat transfer. Thus, the temperature variations in the flow field are sufficiently large that there is heat transfer to or from a body in the flow but are small enough that the corresponding variations in density and viscosity can be neglected. We will look at one such flow, the thermal boundary layer for a steady, low-speed flow past a flat plate. We will consider flows where the boundary layer is laminar. The solution for the velocity field for this flow has been described earlier in this chapter; see equations (4.6) through (4.27).

We will now solve the energy equation (2.32), in order to determine the temperature distribution. For a low-speed, constant-property, laminar boundary layer, the viscous dissipation is negligible (i.e., $\phi = 0$). For flow past a flat plate, $dp/dt = 0$. Therefore, for a calorically perfect gas, which will be defined in Chapter 8, equation (2.32) becomes:

$$\rho u c_p \frac{\partial T}{\partial x} + \rho v c_p \frac{\partial T}{\partial y} = k \frac{\partial^2 T}{\partial y^2} \tag{4.96}$$

Notice that we have already neglected $k(\partial^2 T/\partial x^2)$ since it is small compared to $k(\partial^2 T/\partial y^2)$. We made a similar assumption about the corresponding velocity gradients when working with the momentum equation, equation (4.6).

Now we can change the dependent variable from T to the dimensionless parameter θ, where:

$$\theta = \frac{T - T_w}{T_e - T_w}$$

Note that $\theta = 0$ at the wall (i.e., at $y = 0$), and $\theta = 1$ at the edge of the thermal boundary layer. Using θ as the dependent variable, the energy equation becomes:

$$\rho u \frac{\partial \theta}{\partial x} + \rho v \frac{\partial \theta}{\partial y} = \frac{k}{c_p} \frac{\partial^2 \theta}{\partial y^2} \tag{4.97}$$

Since the pressure is constant along the flat plate, the velocity at the edge of the boundary layer (u_e) is constant, and the momentum equation becomes:

$$\rho u \frac{\partial u}{\partial x} + \rho v \frac{\partial u}{\partial y} = \mu \frac{\partial^2 u}{\partial y^2} \tag{4.98}$$

Now we can replace u in the derivatives by the dimensionless parameter, u^*, where

$$u^* = \frac{u}{u_e}$$

So equation (4.98) becomes:

$$\rho u\frac{\partial u^*}{\partial x} + \rho v\frac{\partial u^*}{\partial y} = \mu\frac{\partial^2 u^*}{\partial y^2} \tag{4.99}$$

Notice that $u^* = 0$ at the wall (i.e., at $y = 0$), and $u^* = 1$ at the edge of the velocity boundary layer.

If we compare equations (4.97) and (4.98), we can see that the equations are identical if $k/c_p = \mu$. Furthermore, the boundary conditions are identical: $\theta = 0$ and $u^* = 0$ at the wall, and $\theta = 1$ and $u^* = 1$ at the edge of the boundary layer. Therefore, if:

$$\frac{\mu c_p}{k} = 1$$

the velocity and the thermal boundary layers are identical. This ratio is called the Prandtl number (Pr) in honor of the German scientist, Ludwig Prandtl:

$$\text{Pr} = \frac{\mu c_p}{k} \tag{4.100}$$

The Prandtl number is an important dimensionless parameter for problems involving convective heat transfer where there is both fluid motion and heat conduction. Typically, however, the Prandtl number for air is less than Pr = 1, with the value typically being around Pr = 0.7. This means that the thermal boundary layer thickness, δ_T, for air is usually larger than the velocity boundary layer, δ, since the ratio of the two layers is $\delta_T/\delta \approx 1/\sqrt{\text{Pr}}$ [Schlichting and Gersten (2000)].

4.8.1 Reynolds Analogy

The shear stress at the wall for a boundary layer is defined as:

$$\tau = \left(\mu\frac{\partial u}{\partial y}\right)_{y=0}$$

Therefore, we can find the skin-friction coefficient for a flat plate using $u^* = u/u_e$ and assuming that u_e = constant:

$$C_f = \frac{\tau}{\frac{1}{2}\rho u_e^2} = \frac{2\mu}{\rho u_e}\frac{\partial u^*}{\partial y} \tag{4.101}$$

The rate at which heat is transferred to the surface ($\dot{q}$) is defined as

$$\dot{q} = \left(k\frac{\partial T}{\partial y}\right)_{y=0} \tag{4.102}$$

The Stanton number (designated by the symbols St or C_h), which is a dimensionless heat-transfer coefficient, is defined as:

$$\text{St} \equiv C_h = \frac{\dot{q}}{\rho u_e c_p(T_e - T_w)} \tag{4.103}$$

Combining these last two expressions with the definition of the dimensionless temperature, $\theta = (T(y) - T_w)/(T_e - T_w)$, we can show that the Stanton number is:

$$\mathrm{St} = \frac{k\dfrac{\partial T}{\partial y}}{\rho u_e c_p (T_e - T_w)} = \frac{k}{\rho u_e c_p}\left[\frac{\partial T/\partial y}{(T_e - T_w)}\right] = \frac{k}{\rho u_e c_p}\frac{\partial \theta}{\partial y} \tag{4.104}$$

Relating the Stanton number, as given by equation (4.104), to the skin-friction coefficient, as defined by equation (4.101), we can obtain the ratio:

$$\frac{C_f}{\mathrm{St}} = \frac{2\mu c_p}{k}\frac{\partial u^*/\partial y}{\partial \theta/\partial y} \tag{4.105}$$

Notice that if $\mu c_p/k \equiv \mathrm{Pr} = 1$, then the thermal boundary layer and the velocity boundary layer are the same:

$$\frac{\partial u^*}{\partial y} = \frac{\partial \theta}{\partial y}$$

Therefore, if the Prandtl number is 1:

$$\mathrm{St} = \frac{C_f}{2} \tag{4.106}$$

This relation between the heat-transfer coefficient and the skin-friction coefficient is known as the Reynolds analogy. This means that if we have a dependable method for estimating the local skin-friction coefficient, then we can also find the local heat-transfer coefficient.

EXAMPLE 4.5: Calculating the thermal properties of air

The thermal conductivity of air can be calculated using the relation

$$k = 4.76 \times 10^{-6}\frac{T^{1.5}}{T + 112}\,\mathrm{cal/cm \cdot s \cdot K} \tag{4.107}$$

over the range of temperatures below those for which oxygen dissociates, which is approximately 2000 K at atmospheric pressure. What is the Prandtl number for air at 15°C (288.15 K)?

Solution: Using the results from Example 1.3, the viscosity is $1.7894 \times 10^{-5}\,\mathrm{kg/s \cdot m}$. The specific heat is $1004.7\,\mathrm{J/kg \cdot K}$. Using the equation to calculate the thermal conductivity:

$$k = 4.76 \times 10^{-6}\frac{(288.15)^{1.5}}{400.15} = 5.819 \times 10^{-5}\,\mathrm{cal/cm \cdot s \cdot K}$$

Noting that there are 4.187 J/cal, the thermal conductivity is:

$$k = 2.436 \times 10^{-2}\,\mathrm{J/m \cdot s \cdot K}$$

Therefore, the Prandtl number is:

$$\mathrm{Pr} = \frac{\mu c_p}{k} = \frac{(1.7894 \times 10^{-5}\,\mathrm{kg/s \cdot m})(1004.7\,\mathrm{J/kg \cdot K})}{2.436 \times 10^{-2}\,\mathrm{J/m \cdot s \cdot K}} = 0.738$$

As we previously discussed, the Prandtl number for air is essentially constant (approximately 0.7) over a wide range of flow conditions.

4.8.2 Thermal Boundary Layer for Pr ≠ 1

To solve for the temperature distribution for the laminar, flat-plate boundary layer, we can introduce the transformation of equation (4.10):

$$\eta = y\sqrt{\frac{u_e}{2\nu x}}$$

Using the transformed stream function f, as defined by equation (4.13), equation (4.85) becomes:

$$\theta'' + (\mathrm{Pr})f\theta' = 0 \tag{4.108a}$$

where the $'$ denotes differentiation with respect to η. But we have already obtained the solution for the stream function. Referring to equation (4.16) for a flat plate (i.e., $\beta = 0$), we have:

$$f = -\frac{f'''}{f''} \tag{4.108b}$$

Combining equations (4.108a) and (4.108b) and rearranging, we can obtain:

$$\frac{\theta''}{\theta'} = (\mathrm{Pr})\frac{f'''}{f''}$$

Integrating this relation twice yields:

$$\theta = C\int_0^\eta (f'')^{\mathrm{Pr}}d\eta + \theta_0 \tag{4.109}$$

where C and θ_0 are constants of integration. They can be evaluated by applying the boundary conditions (1) at $\eta = 0, \theta = 0$, and (2) for $\eta \to$ large, $\theta = 1$.

$$\theta = \frac{T - T_w}{T_e - T_w} = 1 - \frac{\int_\eta^\infty (f'')^{\mathrm{Pr}}d\eta}{\int_\eta^\infty (f'')^{\mathrm{Pr}}d\eta} \tag{4.110}$$

The rate at which heat is transferred to the wall ($\dot{q}$) can be calculated using

$$\dot{q} = \left(k\frac{\partial T}{\partial y}\right)_{y=0} = k(T_e - T_w)\frac{\partial \eta}{\partial y}\left(\frac{\partial \theta}{\partial \eta}\right)_{\eta=0}$$

Using the values of Pohlhausen, we find that:

$$\left(\frac{\partial \theta}{\partial \eta}\right)_{\eta=0} = 0.4696(\mathrm{Pr})^{0.333}$$

Combining these two relations, the rate at which heat is transferred from a laminar boundary layer to the wall is given by the relation

$$\dot{q} = 0.332k(T_e - T_w)(\mathrm{Pr})^{0.333}\sqrt{\frac{u_e}{\nu x}} \tag{4.111}$$

The heat transfer can be expressed in terms of the Stanton number using equation (4.103) as:

$$\mathrm{St} = 0.332\frac{k}{\mu c_p}\sqrt{\frac{\mu}{\rho u_e x}}(\mathrm{Pr})^{0.333}$$

Using the definitions for the Reynolds number and Prandtl number, the Stanton number for laminar flow over a flat plate becomes:

$$\mathrm{St} = \frac{0.332}{(\mathrm{Pr})^{0.667}(\mathrm{Re}_x)^{0.5}} \tag{4.112}$$

Another popular dimensionless heat-transfer parameter is the Nusselt number. The Nusselt number is defined as:

$$\mathrm{Nu}_x = \frac{hx}{k} \tag{4.113a}$$

In this equation, h is the local heat-transfer coefficient, which is defined as:

$$h = \frac{\dot{q}}{T_e - T_w} \tag{4.113b}$$

Combining this definition with equation (4.111) and (4.113a) gives us:

$$\mathrm{Nu}_x = 0.332(\mathrm{Re}_x)^{0.5}(\mathrm{Pr})^{0.333} \tag{4.114}$$

By dividing the expression for the Stanton number, equation (4.112), by that for the skin-friction coefficient, equation (4.21), we obtain

$$\mathrm{St} = \frac{C_f}{2(\mathrm{Pr})^{0.667}} \tag{4.115}$$

Because of the similarity between this equation and equation (4.106), we will call this the *modified Reynolds analogy.*

EXAMPLE 4.6: Calculating the heat-transfer rate for a turbulent boundary layer on a flat plate

Using the modified Reynolds analogy, develop relations for the dimensionless heat-transfer parameters, St and Nu_x for a turbulent flat-plate boundary layer.

Solution: Referring to the discussion of turbulent boundary layers, we recall that the local skin-friction coefficient is:

$$C_f = \frac{0.0583}{(\mathrm{Re}_x)^{0.2}} \tag{4.80}$$

Now, using equation (4.115) for the modified Reynolds analogy, we can approximate the Stanton number as:

$$\mathrm{St} = \frac{0.0292}{(\mathrm{Re}_x)^{0.2}(\mathrm{Pr})^{0.667}} \tag{4.116}$$

Comparing equations (4.112) and (4.114), we see that the Nu_x is given as:

$$\mathrm{Nu}_x = (\mathrm{St})(\mathrm{Pr})(\mathrm{Re}_x)$$

Therefore, the Nusselt number for turbulent flow past a flat plate can be approximated as:

$$\mathrm{Nu}_x = 0.0292(\mathrm{Re}_x)^{0.8}(\mathrm{Pr})^{0.333} \qquad \textbf{(4.117)}$$

EXAMPLE 4.7: Calculating the heat transfer

The radiator systems on many of the early racing aircraft were flush mounted on the external surface of the airplane. We will assume that the local heat-transfer rate can be estimated using the flat-plate relations. What is the local heating rate for $x = 3.0$ m when the airplane is flying at 468 km/h at an altitude of 3 km? The surface temperature is 330 K.

Solution: Use Table 1.2 to find the free-stream flow properties:

$$p_\infty = 7.012 \times 10^4\ \mathrm{N/m^2} \quad T_\infty = 268.659\ \mathrm{K}$$
$$\rho_\infty = 0.9092\ \mathrm{kg/m^3} \qquad \mu_\infty = 1.6938 \times 10^{-5}\ \mathrm{kg/s \cdot m}$$

Since we have assumed that the flow corresponds to that for a flat plate, these values are also the local properties at the edge of the boundary layer at $x = 3.0$ m, and we can find the velocity as:

$$u_e = U_\infty = 468\ \mathrm{km/h} = 130\ \mathrm{m/s}$$

To determine whether the boundary layer is laminar or turbulent, we will calculate the local Reynolds number:

$$\mathrm{Re}_x = \frac{\rho_e u_e x}{\mu_e} = \frac{(0.9092\ \mathrm{kg/m^3})(130\ \mathrm{m/s})(3.0\ \mathrm{m})}{1.6938 \times 10^{-5}\ \mathrm{kg/s \cdot m}} = 2.093 \times 10^7$$

This is well above the transition value. In fact, if the transition Reynolds number is assumed to be 500,000, transition would occur at the point:

$$x_{\mathrm{tr}} = \frac{500{,}000}{(\rho_e u_e)/\mu_e} = 0.072\ \mathrm{m}$$

from the leading edge, which is an extremely short distance. Therefore, the calculation of the heating will be based on the assumption that the boundary layer is turbulent over the entire length of the flat plate.

Combining equations (4.113a) and (4.113b),

$$\dot{q} = \frac{\mathrm{Nu}_x k(T_e - T_w)}{x}$$

where the Nu_x is given by equation (4.117). Therefore,

$$\dot{q} = \frac{0.0292(\mathrm{Re}_x)^{0.8}(\mathrm{Pr})^{0.333} k(T_e - T_w)}{x}$$

To calculate the thermal conductivity for air, we will use the relation from Example 4.5:

$$k = 4.76 \times 10^{-6} \frac{T^{1.5}}{T + 112} = 5.506 \times 10^{-5}\,\text{cal/cm} \cdot \text{s} \cdot \text{K}$$
$$= 2.306 \times 10^{-2}\,\text{J/m} \cdot \text{s} \cdot \text{K}$$

Since $1\,\text{W} = 1\,\text{J/s}$,

$$k = 2.306 \times 10^{-2}\,\text{W/m} \cdot \text{K}$$

Furthermore, the Prandtl number is:

$$\text{Pr} = \frac{\mu c_p}{k} = 0.738$$

Therefore,

$$\dot{q} = \frac{(0.0292)(2.093 \times 10^7)^{0.8}(0.738)^{0.333}(2.306 \times 10^{-2}\,\text{W/m} \cdot \text{K})(268.659 - 330)\,\text{K}}{3.0\,\text{m}}$$
$$= -8.944 \times 10^3\,\text{W/m}^2 = -8.944\,\text{kW/m}^2$$

The minus sign indicates that heat is transferred from the surface to the air flowing past the aircraft. This is as it should be, since the surface is hotter than the adjacent air. Furthermore, since the problem discusses a radiator, proper performance would produce cooling. Since there are 1.341 hp/kW, the heat-transfer rate is equivalent to $1.114\,\text{hp/ft}^2$.

4.9 SUMMARY

In this chapter, we have developed techniques by which we can obtain solutions for a thin, viscous boundary layer near the surface. Techniques have been developed both for a laminar and for a turbulent boundary layer using both integral and differential approaches. We now have reviewed the basic concepts of fluid mechanics in Chapters 1 through 4 and are ready to apply them specifically to aerodynamic problems.

PROBLEMS

4.1. A very thin, "flat-plate" wing of a model airplane moves through the air at standard sea-level conditions at a velocity of 10 m/s. The dimensions of the plate are such that its chord (stream wise dimension) is 0.25 m and its span (length perpendicular to the flow direction) is 4 m. What is the Reynolds number at the trailing edge ($x = 0.25$ m)? Assume that the boundary layer is laminar in answering the remaining questions. What are the boundary-layer thickness and the displacement thickness at the trailing edge? What are the local shear at the wall and the skin-friction coefficient at $x = 0.25$ m. Calculate the total drag on the wing (both sides). Prepare a graph of u_x as a function of y, where u_x designates the x component of velocity relative to a point on the ground, at $x = 0.25$.

4.2. Assume that the inviscid external flow over a configuration is given by

$$u_e = \text{A}x^2$$

Thus, the stagnation point occurs at the leading edge of the configuration (i.e., at $x = 0$). Obtain the expression for β. Using Fig. 4.4 and assuming that the boundary layer is laminar, determine the value of $f''(0)$, that is, the value of the shear function at the wall. What is the relation between the shear at a given value of x for this flow and that for a flat plate?

4.3. Consider two-dimensional, incompressible flow over a cylinder. For ease of use with the nomenclature of the current chapter, we will assume that the windward plane of symmetry (i.e., the stagnation point) is $\theta = 0$ and that θ increases in the stream wise direction. Thus,

$$u_e = 2U_\infty \sin\theta \quad \text{and} \quad x = R\theta$$

Determine the values of β at $\theta = 10^\circ$ at $\theta = 60^\circ$ and at $\theta = 85^\circ$.

4.4. Assume that the wall is porous so that there can be flow through the wall; that is, $v(x, 0) = v_w \neq 0$. Using equation (4.14), show that

$$\frac{v_w}{u_e} = -\frac{f(0)}{\sqrt{2\mathrm{Re}_x}}$$

in order to have similarity solutions; that is, $(\partial f/\partial \mathrm{s})_\eta = 0$ for steady, incompressible flow past a flat plate.

4.5. We plan to use suction through a porous wall as a means of boundary-layer control. Using the equation developed in Problem 4.4, determine $f(0)$ if $v_w = -0.002u_e$ for steady flow past a flat plate where $u_e = 3m/s$ at standard sea-level conditions. What are the remaining two boundary conditions?

4.6. Transpiration (or injecting gas through a porous wall into the boundary layer) is to be used to reduce the skin-friction drag for steady, laminar flow past a flat plate. Using the equation developed in Problem 4.4, determine v_w if $f(0) = -0.5$. The inviscid velocity (u_e) is 25 ft/s with standard atmospheric conditions.

4.7. When we derived the integral equations for a flat-plate boundary layer, the outer boundary of our control volume was a streamline outside the boundary layer (see Fig. 4.17). Let us now apply the integral equations to a rectangular control volume to calculate the sectional drag coefficient for incompressible flow past a flat plate of length L. Thus, as shown in Fig. P4.7, the outer boundary is a line parallel to the wall and outside the boundary layer at all x stations. Owing to the growth of the boundary layer, fluid flows through the upper boundary with a velocity v_e which is a function of x. How does the resultant expression compare with equation (4.70)?

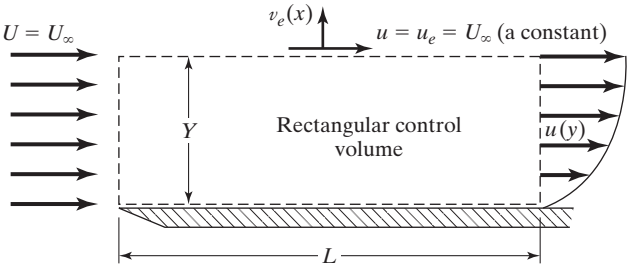

Figure P4.7

4.8. Use the integral momentum analysis and the assumed velocity profile for a laminar boundary layer:

$$\frac{u}{u_e} = \frac{3}{2}\left(\frac{y}{\delta}\right) - \frac{1}{2}\left(\frac{y}{\delta}\right)^3$$

where δ is the boundary-layer thickness, to describe the incompressible flow past a flat plate. For this profile, compute: (a) $(\delta/x)\sqrt{\mathrm{Re}_x}$, (b) $(\delta^*/x)\sqrt{\mathrm{Re}_x}$, (c) $(v_e/u_e)\sqrt{\mathrm{Re}_x}$,

(d) $C_f\sqrt{\mathrm{Re}_x}$, and (e) $C_d\sqrt{\mathrm{Re}_x}$. Compare these values with those presented in the text, which were obtained using the more exact differential technique [e.g., $(\delta/x)\sqrt{\mathrm{Re}_x} = 5.0$]. Prepare a graph comparing this approximate velocity profile and that given in Table 4.3. For the differential solution, use $\eta = 3.5$ to define δ when calculating y/δ.

4.9. Use the integral momentum analysis and a linear velocity profile for a laminar boundary layer

$$\frac{u}{u_e} = \frac{y}{\delta}$$

where δ is the boundary layer thickness. If the viscous flow is incompressible, calculate $(\delta/x)\sqrt{\mathrm{Re}_x}$ $(\delta^*/x)\sqrt{\mathrm{Re}_x}$, and $C_f\sqrt{\mathrm{Re}_x}$. Compare these values with those presented in the chapter that were obtained using the more exact differential technique [e.g., $(\delta/x)\sqrt{\mathrm{Re}_x} = 5.0$].

4.10. Let us represent the wing of an airplane by a flat plate. The airplane is flying at standard sea-level conditions at 100 mph. The dimensions of the wing are chord 5 ft. and span 30 ft. What is the total friction drag acting on the wing? What is the drag coefficient?

4.11. A flat plate at zero angle of attack is mounted in a wind tunnel where

$$p_\infty = 1.01325 \times 10^5\ \mathrm{N/m^2} \qquad \mathrm{U}_\infty = 100\ \mathrm{m/s}$$
$$\mu_\infty = 1.7894 \times 10^{-5}\ \mathrm{kg/m \cdot s} \qquad \mathrm{p}_\infty = 1.2250\ \mathrm{kg/m^3}$$

A Pitot probe is to be used to determine the velocity profile at a station 1.0 m from the leading edge (Fig. P4.11).

(a) Using a transition criterion that $\mathrm{Re}_{x,\,\mathrm{tr}} = 500,000$, where does transition occur?

(b) Use equation (4.79) to calculate the thickness of the turbulent boundary layer at a point 1.00 m from the leading edge.

(c) If the streamwise velocity varies as the $\frac{1}{7}$ th power law [i.e., $u/u_e = (y/\delta)^{1/7}$], calculate the pressure you should expect to measure with the Pitot probe $p_t(y)$ as a function of y. Present the predicted values as

(1) The difference between that sensed by the Pitot probe and that sensed by the static port in the wall [i.e., y versus $p_t(y) - p_{\mathrm{static}}$]

(2) The pressure coefficient

$$y \text{ versus } C_p(y) = \frac{p_t(y) - p_\infty}{\frac{1}{2}\rho_\infty U_\infty^2}$$

Note that for part (c) we can use Bernoulli's equation to relate the static pressure and the velocity on the streamline just ahead of the probe and the stagnation pressure sensed by the probe. Even though this is in the boundary layer, we can use Bernoulli's equation, since we relate properties on a streamline and since we calculate these properties at "point." Thus, the flow slows down isentropically to zero velocity over a very short distance at the mouth of the probe.

(d) Is the flow described by this velocity function rotational or irrotational?

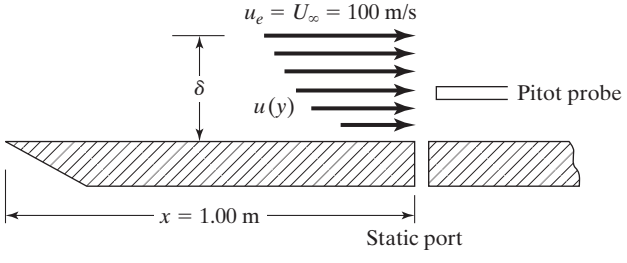

Figure P4.11

4.12. Air at atmospheric pressure and 100°C flows at 100 km/h across a flat plate. Compare the streamwise velocity as a function of y for a laminar boundary layer and for a turbulent boundary layer at the transition point, assuming that the transition process is completed instantaneously at that location. Use Table 4.3 to define the laminar profile and the one-seventh power law to describe the turbulent profile.

4.13. A thin symmetric airfoil section is mounted at zero angle of attack in a low-speed wind tunnel. A Pitot probe is used to determine the velocity profile in the viscous region downstream of the airfoil, as shown in Fig. P4.13. The resultant velocity distribution in the region $-w \leq z \leq +w$

$$u(z) = U_\infty - \frac{U_\infty}{2}\cos\frac{\pi z}{2w}$$

If we apply the integral form of the momentum equation [equation (2.13)] to the flow between the two streamlines bounding this wake, we can calculate the drag force acting on the airfoil section. The integral continuity equation [equation (2.5)] can be used to relate the spacing between the streamlines in the undisturbed flow ($2h$) to their spacing ($2w$) at the x location where the Pitot profile was obtained. If $w = 0.009c$, what is the section drag coefficient C_d?

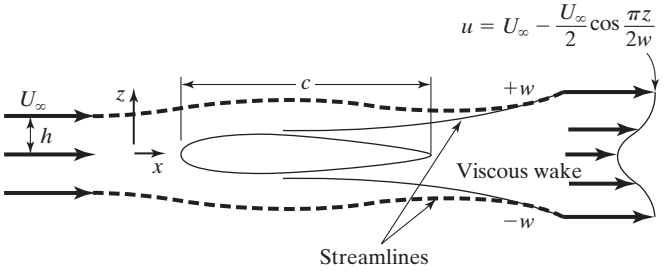

Figure P4.13

4.14. For the wing dimensions and flow properties of Problem 4.1, find the total skin-friction coefficient and the total drag on the wing (both sides) using the method of equation (4.86) and the Prandtl-Schlichting turbulent skin-friction relation. Perform the estimation again using the approximate method of equation (4.87). Comment on the difference between the two approaches and the accuracy of the approximate method.

4.15. Assume the flow over the flat plate of Problem 4.11 is at $U_\infty = 100\ m/s$ (all other conditions are the same). Find the total skin friction drag of the flat plate (both sides) using the Prandtl-Schlichting relation (initially assume that the flow is completely turbulent along the length of the plate). Now find the skin friction drag for the plate using the approximate formula of equation (4.87) which takes into account transition effects. How accurate was the initial assumption of fully turbulent flow?

4.16. Derive equation (4.86) to find the total drag coefficient for the flat plate shown in Fig. 4.18. Convert the resulting relation into a drag relation for the flat plate and simplify the results.

4.17. Using equation (4.95), calculate the thermal conductivity of air at 1500 K. What is the Prandtl number of perfect air at this temperature?

4.18. The boundary conditions that were used in developing the equation for the laminar thermal boundary layer were that the temperature is known at the two limits (1) $\theta = 0$ at $\eta = 0$ and (2) $\theta = 1$ at $\eta \rightarrow$ large. What would be the temperature distribution if the boundary conditions were (1) an adiabatic wall (i.e., $\theta' = 0$ at $\eta = 0$), and (2) $\theta = 1$ at $\eta \rightarrow$ large? *Hint*: From equation (4.97),

$$\theta' = C(f'')^{\mathrm{Pr}}$$

4.19. Represent the wing of an airplane by a flat plate. The airplane is flying at standard sea-level conditions at 150 mi/h. The dimensions of the wing are chord = 5 ft and span = 30 ft What is the total heat transferred to the wing if the temperature of the wing is 50°F?

4.20. A wind tunnel has a 1-m^2, 6-m-long test section in which air at standard sea-level conditions moves at 50 m/s. It is planned to let the walls diverge slightly (slant outward) to compensate for the growth in boundary-layer displacement thickness, and thus maintain a constant area for the inviscid flow. This allows the free-stream velocity to remain constant. At what angle should the walls diverge to maintain a constant velocity between $x = 0.5$ m and $x = 5$ m?

REFERENCES

Abbott IH, von Doenhoff AE. 1949. *Theory of Wing Sections*. New York: Dover

Cebeci T, Bradshaw P. 1979. *Momentum Transfer in Boundary Layers*. New York: McGraw-Hill

Cebeci T, Smith AMO. 1974. *Analysis of Turbulent Boundary Layers*. Orlando: Academic Press

DeJarnette FR, Ratcliffe RA. 1996. Matching inviscid/boundary layer flowfields. *AIAA J*. 34:35–42

Dommasch DO, Sherby SS, Connolly TF. 1967. *Airplane Aerodynamics*. 4th Ed. New York: Pitman

Dorrance WH. 1962. *Viscous Hypersonic Flow*. New York: McGraw-Hill

Falco RE. 1977. Coherent motions in the outer region of turbulent boundary layers. *Physics of Fluids* 20:S124–S132

Head MR. 1969. Cambridge work on entrainment. In *Proceedings, Computation of Turbulent Boundary Layers—1968 AFOSR-IFP-Stanford Conference*, Vol. 1. Stanford: Stanford University Press

Kroo IM. 2007. *Applied Aerodynamics: A Digital Textbook*. Stanford: Desktop Aeronautics

Neumann RD. 1989. Defining the aerothermodynamic environment. In *Hypersonics, Vol I: Defining the Hypersonic Environment*, Ed. Bertin JJ, Glowinski R, Periaux J. Boston: Birkhauser Boston

Rasheed A, Hornung HG, Fedorov AV, Malmuth ND. 2002. Experiments on passive hypervelocity boundary-layer control using an ultrasonically absorptive surface. *AIAA J*. 40:481–489

Salas MD. 2006. Digital Flight: The Last CFD Aeronautical Grand Challenge. *J. Scientific Computing*. 28:479–505

Schlichting H, Gersten K. 2000. *Boundary Layer Theory*. 8th Ed. Berlin: Springer

Smith BR. 1991. *Application of turbulence modeling to the design of military aircraft*. Presented at AIAA Aerosp. Sci. Meet., 29th, AIAA Pap. 91-0513, Reno, NV

Spalart PR, Allmaras SR. 1992. *A one-equation turbulence model for aerodynamic flows*. Presented at AIAA Aerosp. Sci. Meet., 30th, AIAA Pap. 92-0439, Reno, NV

Spalart PR. 2000. *Trends in turbulence treatments*. Presented at Fluids 2000 Conf., AIAA Pap. 2000–2306, Denver, CO

Spalart PR, Jou W-H, Strelets M, Allmaras SR. 1997. Comments on the feasibility of LES for wings, and on a hybrid RANS/LES approach. Advances in DNS/LES, 1st AFOSR International Conference on DNS/LES, Greyden Press, Columbus OH, Aug. 4–8, 1997.

Stratford BS. 1959. The prediction of separation of the turbulent boundary layer. *J. Fluid Mech*. 5:1–16

White FM. 2005. *Viscous Fluid Flow*. 3rd Ed. New York: McGraw-Hill

Wilcox DC. 1998. *Turbulence Modeling for CFD*. 2nd Ed. LaCañada, CA: DCW Industries

5 CHARACTERISTIC PARAMETERS FOR AIRFOIL AND WING AERODYNAMICS

Chapter Objectives

- Understand the basic geometric parameters that define airfoil and wing shapes
- Know the basic aerodynamic forces and moments and be able to define their nondimensional coefficients for airfoils and wings
- Have a general understanding of the impact of airfoil geometry on the resulting aerodynamics, including the effects of camber and thickness
- Know how flow around a wing is different from flow around an airfoil and be able to estimate the impact of wing geometry on lift and drag
- Know the contributing factors to airplane drag and be able to estimate the zero-lift drag coefficient of an airplane

Modern aircraft wings are complex shapes which are required to fulfill multiple, often competing, requirements, as is the case for the C-17 shown in Fig. 5.1. Besides providing lift during cruise for the C-17, the wing must also be able to greatly increase its lift for landing slowly on short, unimproved runways. In addition, the wing aids in drag reduction through the use of wing-tip devices and allows the airplane to fly at higher subsonic Mach numbers through the use of supercritical airfoil sections. Finally, the wing requires a complex and lightweight structure, with the ability to integrate and control

Figure 5.1 The wing of the C-17 (which includes supercritical airfoil sections, leading-edge devices, blown flaps, and wing-tip devices) represents the complexity of a modern airplane wing system (U.S. Air Force photo by Tech Sgt. Keith Brown).

the propulsion system, and since fuel is stored in the wing, all of this is done with an eye on maximizing the internal volume. Defining the airfoil sections and wing planform (shape), while keeping all of the other diverse requirements in mind, is a difficult and challenging task. Hopefully you will learn enough in this chapter to begin to understand how to analyze and design such a complex system.

5.1 CHARACTERIZATION OF AERODYNAMIC FORCES AND MOMENTS

5.1.1 General Comments

The motion of air around the vehicle produces pressure and velocity variations through the flow field. Although viscosity is a fluid property and acts throughout the flow field, the viscous forces acting on the vehicle depend on the velocity gradients near the surface as well as the viscosity itself. The normal (pressure) forces and the tangential (shear) forces which act on the surface due to the motion of air around the vehicle are shown in Fig. 5.2. The pressures and the shear forces can be integrated over the surface on which they act in order to yield the resultant aerodynamic force (R), which acts at the center of pressure (cp) of the vehicle, as shown in Fig. 5.3.

For convenience, the total force vector is usually resolved into components. Body-oriented force components are used when the application is primarily concerned with

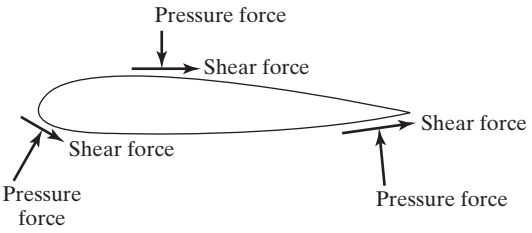

Figure 5.2 Normal (or pressure) and tangential (or shear) forces on an airfoil surface.

the vehicle response (e.g., the aerodynamics or the structural dynamics). We will first consider the forces and moments in the plane of symmetry (i.e., the pitch plane). For the pitch-plane forces depicted in Fig. 5.3, the body-oriented components are the axial force, which is the force parallel to the vehicle axis (A), and the normal force, which is the force perpendicular to the vehicle axis (N).

For applications such as trajectory analysis, the resultant force is divided into components taken relative to the velocity vector (i.e., the flight path). Therefore, for these applications the resultant force is divided into a component parallel to the flight path (parallel to U_∞), which is the drag (D), and a component perpendicular to the flight path (perpendicular to U_∞), which is the lift (L), as shown in Fig. 5.3. The body forces can be related to the wind-axis forces through resolving components of the resultant vector as:

$$L = N\cos\alpha - A\sin\alpha$$
$$D = N\sin\alpha + A\cos\alpha$$

As the airplane moves through the earth's atmosphere, its motion is determined by its weight, the thrust produced by the engine, and the aerodynamic forces acting on the vehicle. Consider the case of steady, level, unaccelerated flight (abbreviated as SLUF) in the horizontal plane. This condition requires: (1) that the sum of the forces along the flight path is zero, and (2) that the sum of the forces perpendicular to the flight path is zero. For now we will only consider cases where the angles are small (e.g., the component of the thrust parallel to the free-stream velocity vector is only slightly less than the thrust itself). Summing the forces along the flight path (parallel to the free-stream velocity), the equilibrium condition requires that the thrust must equal the drag acting on the airplane. Summing the forces perpendicular to the flight path leads to the conclusion that the weight of the aircraft is balanced by the lift. In equation form, this is: $L = W$ and $T = D$.

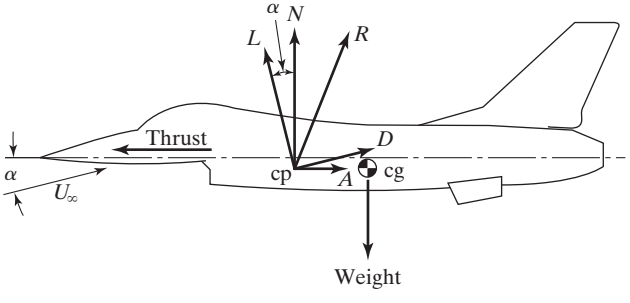

Figure 5.3 Nomenclature for aerodynamic forces in the pitch plane.

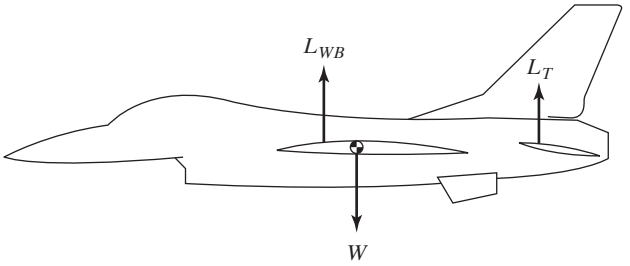

Figure 5.4 Moment balance to trim an aircraft.

Consider the case where the lift generated by the wing/body configuration acts ahead of the center of gravity, as shown in Fig. 5.4. Because the lift force generated by the wing/body configuration, L_{WB}, acts ahead of the center of gravity, it will produce a nose-up (positive) pitch moment about the center of gravity (*cg*). The aircraft is said to be trimmed when the sum of the moments about the *cg* is zero:

$$\sum M_{cg} = 0$$

Therefore, a force from a control surface located aft of the *cg* (e.g., a tail surface) is needed to produce a nose-down (negative) pitch moment about the *cg* which could balance the moment produced by the wing/body lift. The tail-generated lift force, L_T, is indicated in Fig. 5.4. The orientation of the tail surface which produces the lift force depicted in Fig. 5.4 also produces a drag force, which is known as the trim drag. Typically, the trim drag may vary from 0.5% to 5% of the total cruise drag for the airplane. You should remember that the trim drag is associated with the lift generated to trim the vehicle, but does not include the tail profile drag (which is included in the total drag of the aircraft at zero lift conditions).

In addition to the force components which act in the pitch plane (i.e., the lift, which acts upward perpendicular to the undisturbed free-stream velocity, and the drag, which acts in the same direction as the free-stream velocity), there is a side force, *Y*. The side force is the component of force in a direction perpendicular to the geometric plane containing the lift and drag. The side force is positive when acting toward the starboard wing (i.e., the pilot's right).

As we noted earlier, the resulting aerodynamic force usually will not typically act through the origin of the airplane's axis system (i.e., the center of gravity, *cg*). The moment due to the resultant force acting at a distance from the *cg* may be divided into three components, referring to the airplane's reference axes, as shown in Fig. 5.5. The three moment components are the pitch moment, the roll moment, and the yaw moment.

- ***Pitch moment, M.*** The moment about the lateral axis (the *y* axis of the airplane-fixed coordinate system) is the pitch moment. The pitch moment is the result of the lift and the drag forces acting on the vehicle at a point other than the *cg*. A positive pitch moment is in the nose-up direction.
- ***Roll moment, $\mathscr{L}$.*** The moment about the longitudinal axis of the airplane (the *x* axis) is the roll moment. A roll moment is often created by a differential lift on one wing when compared to the other, generated by some type of aileron or spoiler. A positive roll moment causes the right, or starboard, wingtip to move downward.

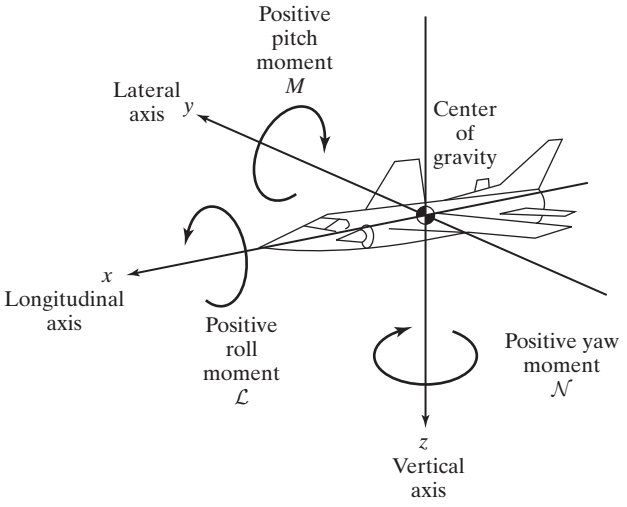

Figure 5.5 Reference axes of the airplane and the corresponding aerodynamic moments.

- ***Yaw moment, 𝒩.*** The moment about the vertical axis of the airplane (the z axis) is the yaw moment. A positive yaw moment tends to rotate the nose to the pilot's right.

Generally an aerodynamicist would have to define all three forces (L, D, and Y) and all three moments ($\mathscr{L}$, M, and $\mathcal{N}$) for an aircraft throughout the flight envelope (at every combination of altitude, Mach number, and Reynolds number). However, in the following chapters we will concentrate on the longitudinal forces and moments, L, D, and M.

5.1.2 Parameters That Govern Aerodynamic Forces

The magnitude of the forces and of the moments that act on an airplane depend on the combined effects of many different variables. Personal observations of the aerodynamic forces acting on an arm extended from a car window or on a ball in flight demonstrate the effect of velocity and of configuration. Pilot manuals advise that a longer length of runway is required if the ambient temperature is relatively high or if the airport elevation is high (i.e., the ambient density is relatively low). Also, airplanes flying at supersonic speeds have very different characteristics than when flying at subsonic speeds. The parameters that govern the magnitude of aerodynamic forces and moments include the following:

- Configuration geometry
- Angle of attack (i.e., vehicle attitude in the pitch plane relative to the flight direction)
- Vehicle size or model scale
- Free-stream velocity
- Density of the undisturbed air
- Reynolds number (as it relates to viscous effects)
- Mach number (as it relates to compressibility effects)

The calculation of the aerodynamic forces and moments acting on a vehicle often requires that the engineer be able to relate data obtained at other flow conditions to the conditions of interest. Therefore, the aerodynamicist often uses data from the wind tunnel, where scale models are exposed to flow conditions that simulate the design environment or data from flight tests at other flow conditions. So that we can correlate the data for various free-stream conditions and configuration scales, the measurements are usually presented in dimensionless form. Ideally, once in dimensionless form, the results would be independent of all but the first two parameters listed, configuration geometry and angle of attack. In practice, flow phenomena such as boundary-layer separation, shock-wave/boundary-layer interactions, and compressibility effects limit the range of flow conditions over which the dimensionless force and moment coefficients remain constant. For these cases, parameters such as the Reynolds number and the Mach number appear in the correlations for the force and moment coefficients.

5.2 AIRFOIL GEOMETRY PARAMETERS

If a horizontal wing is cut by a vertical plane parallel to the centerline of the vehicle, the resultant section is called the *airfoil section*. The generated lift and stall characteristics of the wing depend strongly on the geometry of the airfoil sections that make up the wing. Geometric parameters that have an important effect on the aerodynamic characteristics of an airfoil section include (1) the leading-edge radius, (2) the mean camber line, (3) the maximum thickness and the thickness distribution of the profile, and (4) the trailing-edge angle. The effect of these geometric parameters, which are illustrated in Fig. 5.6, will be discussed after an introduction to airfoil-section nomenclature. Some of the basic parameters used to describe the airfoil geometry are:

- Leading edge—the forward most point on the airfoil (typically placed at the origin for convenience)

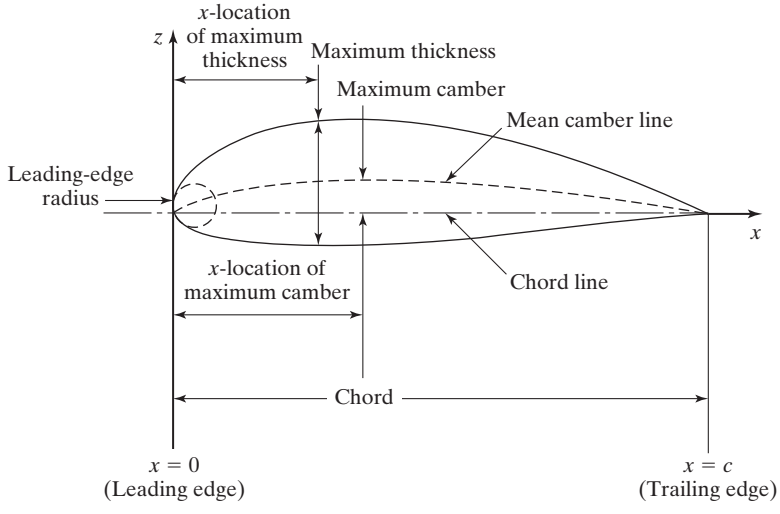

Figure 5.6 Airfoil-section geometry and its nomenclature.

- Trailing edge—the aft most point on the airfoil (typically placed on the x axis for convenience)
- Chord line—a straight line between the leading and trailing edges (the x axis for our convention)
- Mean camber line—a line midway between the upper and lower surfaces at each chordwise position
- Maximum camber—the largest value of the distance between the mean camber line and the chord line, which quantifies the camber of an airfoil
- Maximum thickness—the largest value of the distance between the upper and lower surfaces, which quantifies the thickness of the airfoil
- Leading-edge radius—the radius of a circle that fits the leading-edge curvature

These geometric parameters are used to determine certain aerodynamic characteristics of an airfoil, as we will discuss in the next sections.

5.2.1 Airfoil-Section Nomenclature

Airfoils play an integral role in determining the aerodynamics of wings. Having a basic understanding of how they work and how to estimate their lift, drag, and pitch moment is critical to aerodynamics. Early researchers realized this as the first airfoils were being designed (even the Wright brothers tested various basic airfoil shapes for their flyer). Once airplanes became practical, the National Advisory Committee for Aeronautics (N.A.C.A., which will be written NACA from now on) began to systematically test airfoils in increasingly complex families of shapes. Many of these groundbreaking wind-tunnel experiments were conducted by a group of researchers, and were summarized in the famous airfoil book *Theory of Wing Sections* by Abbott and von Doenhoff (1949).

Abbott and von Doenhoff (1949) summarized the work on airfoil development this way:

> The gradual development of wing theory tended to isolate the wing-section problems from the effects of planform and led to a more systematic experimental approach. The tests made at Göttingen during World War I contributed much to the development of modern types of wing sections. Up to about World War II, most wing sections in common use were derived from more or less direct extensions of the work at Göttingen. During this period, many families of wing sections were tested in the laboratories of various countries, but the work of the NACA was outstanding. The NACA investigations were further systematized by separation of the effects of camber and thickness distribution, and the experimental work was performed at higher Reynolds number than were generally obtained elsewhere.

As a result, the geometry of many airfoil sections is uniquely defined by the NACA designation for the airfoil. There are a variety of NACA airfoil classifications, including NACA four-digit wing sections, NACA five-digit wing sections, and NACA six-series wing sections, among others. As an example, consider the NACA four-digit wing sections, which are designate as:

NACA XYZZ

The first integer, X, indicates the maximum value of the mean camber-line ordinate (see Fig. 5.6) in percent of chord. The second integer, Y, indicates the distance from the leading edge to the maximum camber location in tenths of chord. The last two integers, ZZ, indicate the maximum section thickness in percent of chord. Therefore, the NACA 0010 is a symmetric airfoil section whose maximum thickness is 10% of the chord (the two leading "0" digits indicate that there is no camber, so the airfoil is symmetric about the x axis). The NACA 4412 airfoil section is a 12% thick airfoil which has a 4% maximum camber located at 4/10ths (40%) of the chord.

A series of "standard" modifications to the airfoils were designated by the NACA using a suffix consisting of a dash followed by two digits. These modifications consist essentially of: (1) changes of the leading-edge radius from the normal value, and (2) changes of the position of maximum thickness from the normal position (which is at 0.3c).

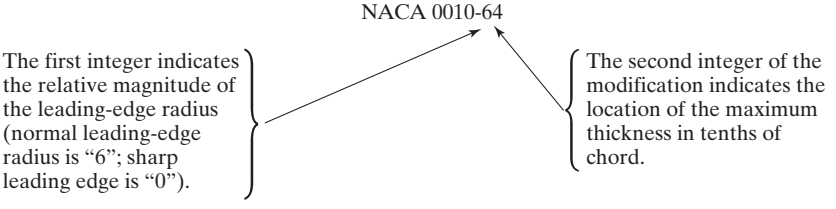

After the NACA four-digit airfoils were tested and the results were tabulated, a second set of wind-tunnel tests was planned with the more advanced NACA five-digit airfoils. The NACA five-digit airfoil family allowed for camber and thickness levels that were not represented as integers, and therefore advanced the level of detail from the NACA four-digit tests. The NACA six-series airfoils were, in general, designed to maximize the amount of laminar flow on the section, and were not designed purely as a geometric family. Other series of airfoil sections were tested by the NACA, and details for them may also be found in Abbott and von Doenhoff (1949).

Because of more recent improvements in design methodology, and because of the broad use of sophisticated numerical codes, there are many airfoil sections being developed that are not described by the standard NACA geometry nomenclature [see the University of Illinois Airfoil Data Site, Selig (2012), for example].

5.2.2 Leading-Edge Radius and Chord Line

The *chord line*, as discussed earlier, is defined as the straight line connecting the leading and trailing edges. The leading edge of airfoils used in subsonic applications is rounded, with a radius that is on the order of 1% of the chord length. The leading-edge radius of the airfoil section is the radius of a circle centered on a line tangent to the leading-edge camber connecting tangency points of the upper and the lower surfaces with the leading edge. The center of the leading-edge radius is located so that the cambered section projects slightly forward of the leading-edge point. The magnitude of the leading-edge

radius has a significant effect on the stall (or boundary-layer separation) characteristics of the airfoil section. Specifically, if the leading-edge radius is too small, the flow will have a tendency to separate near the leading edge, causing fairly abrupt stall characteristics for the airfoil.

The geometric angle of attack is the angle between the chord line and the direction of the undisturbed, "free stream" flow. For many airplanes the chord lines of the airfoil sections are inclined relative to the vehicle axis, which is called *incidence*. Incidence is used to create lift while the airplane is on the runway, which decreases take-off distance, among other benefits.

5.2.3 Mean Camber Line

The locus of the points midway between the upper surface and the lower surface, as measured perpendicular to the chord line, defines the *mean camber line*. The shape of the mean camber line is very important in determining the aerodynamic characteristics of an airfoil section. As we will see in the theoretical solutions and in the experimental data that will be presented in Chapter 6, cambered airfoils in a subsonic flow generate lift even when the section angle of attack is zero. Therefore, an effect of camber is a change in the zero-lift angle of attack, α_{0l}. While symmetric airfoil sections have zero lift at zero degrees angle of attack, zero lift occurs for sections with positive camber when they are at negative angles of attack.

Furthermore, camber has a beneficial effect on the maximum value of the section lift coefficient, $C_{l_{\max}}$. If the maximum lift coefficient is high, the stall speed will be low, all other factors being the same. You should notice, however, that the high thickness and camber necessary for high maximum values of the section lift coefficient produce low critical Mach numbers (as we will discuss in Chapter 9) and high twisting moments at high speeds. We always need to consider the trade-offs in selecting a design value for a particular parameter in aerodynamics.

5.2.4 Maximum Thickness and Thickness Distribution

The maximum thickness and the thickness distribution strongly influence the aerodynamic characteristics of the airfoil section as well. The maximum local velocity to which a fluid particle accelerates as it flows around an airfoil section increases as the maximum thickness increases (see the discussion associated with Fig. 4.10). Therefore, the minimum pressure value is smallest for the thickest airfoil. As a result, the adverse pressure gradient associated with the deceleration of the flow from the location of this pressure minimum to the trailing edge is greatest for the thickest airfoil. As the adverse pressure gradient becomes larger, the boundary layer becomes thicker (and is more likely to separate producing relatively large values for the form drag). Because of this, the beneficial effects of increasing the maximum thickness are limited.

Consider the maximum section lift coefficients for several different thickness-ratio airfoils presented in this table. The values are taken from experimental data presented in Abbott and von Doenhoff (1949). The data show that a low-speed airfoil has an optimum thickness for maximizing the lift of the airfoil. In the case of the data shown below, the optimum thickness to maximize $C_{l_{\max}}$ is approximately 12%.

Airfoil Section	$C_{l_{max}}$
NACA 2408	1.5
NACA 2410	1.65
NACA 2412	1.7
NACA 2415	1.63
NACA 2418	1.48
NACA 2424	1.3

For a very thin airfoil section (which has a relatively small leading-edge radius), boundary-layer separation occurs early, not far from the leading edge of the upper (leeward) surface. As a result, the maximum section lift coefficient for a very thin airfoil section is relatively small. The maximum section lift coefficient increases as the thickness ratio increases from 8% of the chord to 12% of the chord. The separation phenomenon described in the previous paragraph causes the maximum section-lift coefficients for the relatively thick airfoil sections (i.e., those with a thickness ratio of 18% of the chord and of 24% of the chord) to be less than those for medium thickness airfoil sections.

The thickness distribution for an airfoil affects the pressure distribution and the character of the boundary layer. As the location of the maximum thickness moves aft, the velocity gradient (and hence the pressure gradient) in the mid-chord region decreases. The resultant favorable pressure gradient in the mid-chord region promotes boundary-layer stability and increases the possibility that the boundary layer remains laminar. Laminar boundary layers produce less skin-friction drag than turbulent boundary layers but are also more likely to separate under the influence of an adverse pressure gradient. This will be discussed in more detail later in this chapter, as well as in Section 6.6. In addition, the thicker airfoils benefit more from the use of high lift devices but have a lower critical Mach number, which will be discussed in Chapter 9.

5.2.5 Trailing-Edge Angle

The trailing-edge angle affects the location of the aerodynamic center (which will be defined later in this chapter). The aerodynamic center of thin airfoil sections in a subsonic stream is theoretically located at the quarter-chord ($c/4$), but can vary depending on the geometry of the airfoil.

Aerodynamics Concept Box: Airfoil Characteristics

In general, subsonic airfoils have a number of important characteristics, as discussed in Eppler (1990). First of all, increasing the angle of attack generally gives higher upper surface velocities when compared with the lower surface velocities, as can be seen for the NACA 2412 airfoil below. You can see that ΔV (the difference between the velocity on the upper and lower surfaces at one chordwise location) is higher near the leading edge, and decreases to very small values near the trailing edge. Since the lift of the airfoil is proportional to the difference in

velocity $l \propto \int_0^c \Delta V dx$, ΔV is a very important parameter for determining how well an airfoil works. The peak in velocity near the leading edge is known as the "suction peak," which creates an adverse pressure gradient immediately downstream of the suction peak.

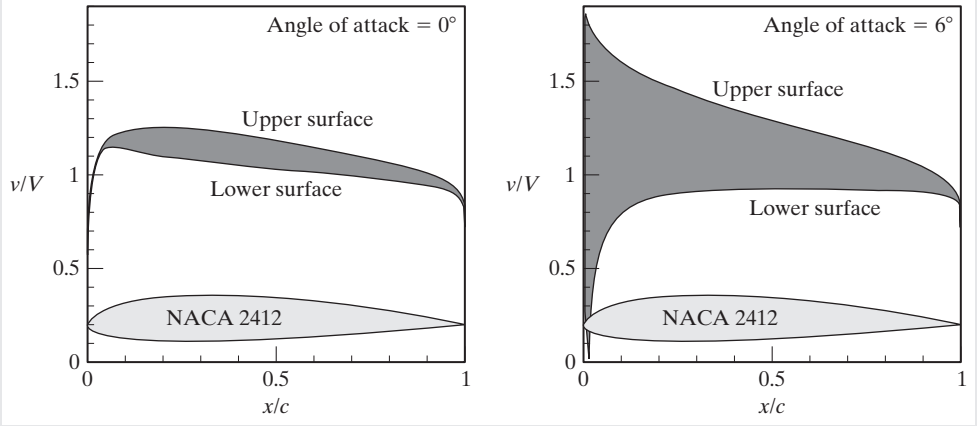

NACA 2412 airfoil surface velocity distributions [from Eppler (1990)]

Boundary-layer separation is strongly affected by the pressure gradient, dp/dx (a favorable pressure gradient means $dp/dx < 0$ and $dV/dx > 0$ and an adverse pressure gradient means $dp/dx > 0$ and $dV/dx < 0$). A strong adverse pressure gradient usually occurs near the trailing edge of the airfoil due to the stagnation point that exists there, so flow typically first experiences separation in this region. A milder adverse pressure gradient usually exists over the upper surface of the airfoil, but if the suction peak is too large due to the leading-edge curvature, the adverse pressure gradient that follows can cause separation to take place here, which is undesirable. In general, thicker airfoils have higher maximum velocities and stronger adverse pressure gradients, which means they will not attain the same levels of lift as somewhat thinner airfoils.

5.3 WING-GEOMETRY PARAMETERS

A wing is a three-dimensional shape made up of two-dimensional airfoil sections. By placing the airfoil sections in various spanwise combinations, wings, horizontal tails, vertical tails, canards, and/or other lifting surfaces are formed. When the parameters that characterize the wing planform are introduced, attention must be directed to the existence of flow components in the spanwise direction (three-dimensional flow). In other words, airfoil section properties deal with flow in two dimensions, while wing planform properties relate to the resultant flow in three dimensions.

Several terms are typically used to fully describe the planform (or projected shape) of a wing. The terms that are pertinent to defining the aerodynamic characteristics of a wing are illustrated in Fig. 5.7, and include:

- The *wing area*, S, is simply the planform area (or projected area) of the wing. Although a portion of the area may be covered by a fuselage or nacelles, the pressure carryover on these surfaces allows legitimate consideration of the entire planform area.

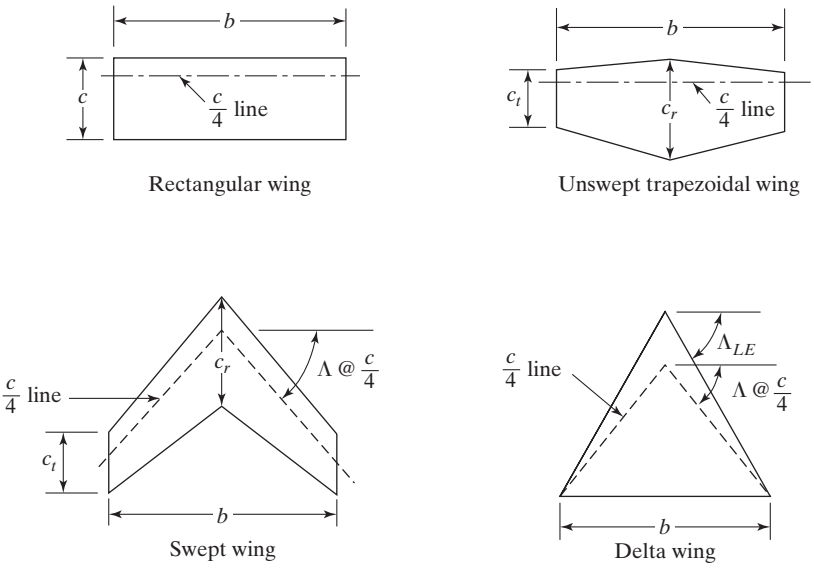

Figure 5.7 Geometric characteristics of the wing planform.

- The *wing span*, b, is the straight-line distance measured from wing tip to wing tip.
- The *average chord*, $\bar{c}$, is determined so that the product of the span and the average chord is the wing area ($b \times \bar{c} = S$).
- The *aspect ratio*, AR, is the ratio of the span and the average chord.

  For a general wing, the aspect ratio is defined as:

$$AR = \frac{b^2}{S}$$

  For a rectangular wing, the aspect ratio is simply:

$$AR = \frac{b}{c}$$

  The aspect ratio is a fineness ratio of the wing and is useful in determining aerodynamic characteristics and structural weight. Typical aspect ratios vary from 35 for a high-performance sailplane to 2 for a supersonic jet fighter.
- The *root chord*, c_r, is the chord at the wing centerline, and the *tip chord*, c_t, is the chord at the wing tip.
- Considering the wing planform to have straight lines for the leading and trailing edges (half the wing will have the shape of a trapezoid), the *taper ratio*, λ, is the ratio of the tip chord to the root chord:

$$\lambda = \frac{c_t}{c_r}$$

The taper ratio affects the lift distribution and the structural weight of the wing. A rectangular wing has a taper ratio of 1.0, while a pointed tip delta wing has a taper ratio of 0.0.

- The *sweep angle*, Λ, is usually measured as the angle between the line of 25% chord and a perpendicular to the root chord. Sweep angles of the leading edge or of the trailing edge are also used often, since they are of interest for many applications. The sweep of a wing causes definite changes in the maximum lift, in the stall characteristics, and in the effects of compressibility.
- The *mean aerodynamic chord*, *mac*, is used together with S to nondimensionalize the pitch moment. Therefore, the mean aerodynamic chord represents another average chord which, when multiplied by the product of the average section moment coefficient, the dynamic pressure, and the wing area, gives the moment for the entire wing. The *mac* is also used to estimate the Reynolds number of the wing for skin-friction calculations. The mean aerodynamic chord is defined by:

$$mac = \frac{1}{S}\int_{-b/2}^{+b/2} [c(y)]^2 dy$$

- The *dihedral angle* is the angle between a horizontal plane containing the root chord and a plane midway between the upper and lower surfaces of the wing. If the wing lies below the horizontal plane, it is termed as the *anhedral angle*. The dihedral angle affects the lateral stability characteristics of the airplane.
- *Geometric twist* defines the situation where the chord lines for the spanwise distribution of airfoil sections do not all lie in the same plane. Therefore, there is a spanwise variation in the geometric angle of incidence for the sections. The chord of the root section of the wing shown in the sketch of Fig. 5.8 is inclined 4° relative to the vehicle axis, which is known as the *incidence angle*. The chord of the tip section, however, is parallel to the longitudinal axis of the vehicle. In this case, where the incidence of the airfoil sections relative to the vehicle axis decreases toward the tip, the wing has "wash out." The wings of numerous subsonic aircraft have wash out to control the spanwise lift distribution and, hence, the boundary-layer separation (i.e., stall) characteristics. If the angle of incidence increases toward the tip, the wing has "wash in." The incidence angle is especially important for take-off characteristics (like runway length required for take-off).

The airfoil section distribution, the aspect ratio, the taper ratio, the twist, and the sweep of a planform are the principal factors that determine the aerodynamic characteristics of a wing and have an important bearing on its stall properties. In addition, dihedral and incidence are important factors for aircraft stability and take-off performance, respectively. These same quantities also have a definite influence on the structural weight and stiffness of a wing, the amount of fuel the aircraft can carry, the propulsion system integration, and access to the aircraft on the ground, which shows why aerodynamic design is a complex, multi-disciplinary field (see the discussion of Fig. 5.1 for example). Values of these parameters for a variety of aircraft have been taken from *Jane's All the World's Aircraft* [Taylor (1973, 1966, 1984) and

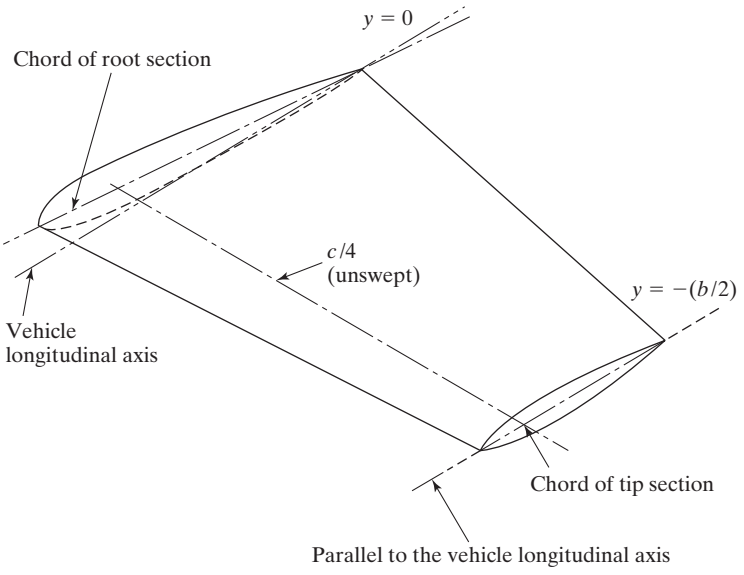

Figure 5.8 Unswept, tapered wing with geometric twist (wash out).

Jackson (2011)], and are summarized in Table 5.1. Data are presented for four-place single-engine aircraft, commercial jetliners and transports, and high-speed military aircraft. Note how the values of these parameters vary from one group of aircraft to another.

The data presented in Table 5.1 indicate that similar designs result for similar applications, regardless of the national origin of the specific design. For example, the aspect ratio for the four-seat, single-engine civil aviation designs is approximately 7, whereas the aspect ratio for the supersonic military aircraft is between 1.7 and 3.8. In fact, as noted in Stuart (1978), which was a case study in aircraft design for the Northrop F-5, "the selection of wing aspect ratio represents an interplay between a large value for low drag-due-to-lift and a small value for reduced wing weight."

There are other trends exhibited in parameters relating to aircraft performance. Notice the grouping by generic classes of aircraft for the correlation between the power-to-weight ratio and the wing loading that is presented in Fig. 5.9. There is a tendency for airplanes to get larger, heavier, and more complex with technological improvements. The trend toward larger, heavier aircraft is evident in this figure. Note that a fully loaded B-17G Flying Fortess, a heavy bomber of World War II, weighed 29,700 kg (65,500 lb) with a wing span of 31.62 m (103.75 ft), whereas the F-15, a modern fighter aircraft, has a maximum takeoff weight of 30,845 kg (68,000 lb) with a wing span of 13.05 m (42.81 ft). However, the successful human-powered aircraft fall in the lower left corner of Fig. 5.9, with wing loadings (the ratio of take-off gross weight to wing area) less than 1 lbf/ft^2. It is in this same region that Lockheed's solar high-altitude powered platform (Solar HAPP) operates.

TABLE 5.1 Wing-Geometry Parameters

Type (Original and Current Manufacturer Names Are Given)	*Wing Span* [m(ft)]	*Aspect Ratio, AR*	*Sweep Angle*	*Dihedral*	*Airfoil Section*	*Speed* [km/h (mi/h)]
a. Four-Place Single-Engine Aircraft						
Socata Rallye (France)	9.61 (31.52)	7.57	None	7°	63A414(mod), 63A416, inc. 4°	173–245 (108–152)
Ambrosini NF 15 (Italy)	9.90 (32.5)	7.37	None	6°	64–215, inc. 4°	325 (202)
Beechcraft Bonanza V35B	10.20 (33.46)	6.30	None	6°	23016.5 at root, 23012 at tip, inc. 4° at root, 1° at tip	298–322 (185–200)
Beechcraft Sierra	9.98 (32.75)	7.35	None	6°30′	63_2 A415, inc. 3° at root, 1° at tip	211–281 (131–162)
Cessna 172	10.92 (35.83)	7.32	None	1°44′	NACA 2412, inc. 1°30′ at root, −1°30′ at tip	211 (131)
Piper Commanche	10.97 (36.0)	7.28	2°30′ forward	5°	64_2A215, inc. 2°	298 (185)
Bellanca, Model 25	10.67 (35.0)	6.70	None	2°	NACA $63_2 - 215$, inc. 2°	458–499 (285–310)
Piper Warrior II	10.67 (35.0)	7.24	None	7°	NACA $65_2 - 415$, inc. 2° at root, −1° at tip	191–235 (119–146)
b. Commercial Jetliners and Transports						
Caravelle 210 (France)	34.3 (112.5)	8.02	20° at $c/4$	3°	NACA 65_1212	790 (490)
BAC 111 (UK)	26.97 (88.5)	8.00	20° at $c/4$	2°	NACA cambered section (mod.), $t/c = 0.125$ at root, 0.11 at tip, inc. 2°30′	815 (507)
Tupolev 204 (Russia)	41.84 (137.3)	9.10	28° at $c/4$	—	$t/c = 0.14$ (inboard) to 0.09 (outboard), inc. twist	850 (528)
Boeing 737	28.35 (93.0)	8.83	25° at $c/4$	6°	$t/c = 0.129$ (av.)	848 (527)
Boeing 747	59.64 (195.7)	6.95	37°30′ at $c/4$	7°	$t/c = 0.134$ (inboard), 0.078 (midspan), 0.080 (outboard), inc. 2°	958 (595)

Type (Original and Current Manufacturer Names Are Given)	*Wing Span* [m(ft)]	*Aspect Ratio, AR*	*Sweep Angle*	*Dihedral*	*Airfoil Section*	*Speed* [km/h (mi/h)]
Boeing 777	64.80 (212.6)	8.68	25° at $c/4$			Mach 0.77
Lockheed C-5A	67.88 (222.8)	7.75	25° at $c/4$	Anhedral 5°30′	NACA 0011 (mod.) near midspan, inc. 3°30′	815 (507)
McDonnell Douglas (Boeing) C-17	50.29 (165)	7.2	25° at $c/4$	Anhedral 3°30′	$t/c = 0.153$ (inboard), 0.122 (outboard)	Mach 0.74–0.77
Airbus A310 (International)	43.89 (144.0)	8.8	28° at $c/4$	11°8′ (inboard at the trailing edge)	$t/c = 0.152$ at root, $t/c = 0.108$ at tip, inc. 5°3′ at root	667–895 (414–556)
Airbus A380 (International)	79.80 (261.8)	7.5	35° at $c/4$ (average)	5.5° (outboard)		945 (587)
			c. High-Speed Military Aircraft			
SAAB-35 Draken (Sweden)	9.40 (30.8)	1.77	Central: leading edge 80° outer: leading edge 57°	—	$t/c = 0.05$	Mach 1.4–2.0
Dassault Mirage III (France)	8.22 (27.0)	1.94	Leading edge 60°34′	Anhedral 1°	$t/c = 0.045$–0.035	Mach 2.2
Northrop F-5E	8.13 (26.67)	3.82	24° at $c/4$	None	65A004.8 (mod.), $t/c = 0.048$	Mach 1.23
McDonnell-Douglas F-4	11.70 (38.4)	2.78	45°	Outer panel 12°	$t/c = 0.051$ (av.)	Over Mach 2.0
LTV F-8	10.81 (35.7)	3.39	35°	Anhedral 5°	Thin, laminar flow section	Nearly Mach 2
LTV A-7	11.80 (38.75)	4.0	35° at $c/4$	Anhedral 5°	65A007, inc. −1°	1123 (698)
Mitsubishi T2 (Japan)	7.88 (25.85)	2.93	35°47′ at $c/4$	Anhedral 9°	NACA 65 series (mod.), $t/c = 0.0466$	Mach 1.6
General Dynamics (Lockheed Martin) F-16	9.14 (30.0)	3.0	40° on leading edges	—	NACA 64A-204	Mach 2.0 +
Lockheed Martin F-22	13.56 (44.5)	2.4	42° on leading edges	Anhedral 3.25°	$t/c = 0.0592$ (inboard) and 0.0429 (outboard); −3.1° at tip	Mach 2.0 +
Eurofighter (International)	11.09 (35.35)	2.5	53° on leading edges	1°	NACA 66 (mod.)	Mach 2.0
Sukhoi Su-27 (Russia)	14.70 (48.2)	3.5	37° at $c/4$	0°	$t/c = 0.05$	Mach 2.35

Source: Data from *Jane's All the World's Aircraft* (1973, 1966, 1984, and 2011).

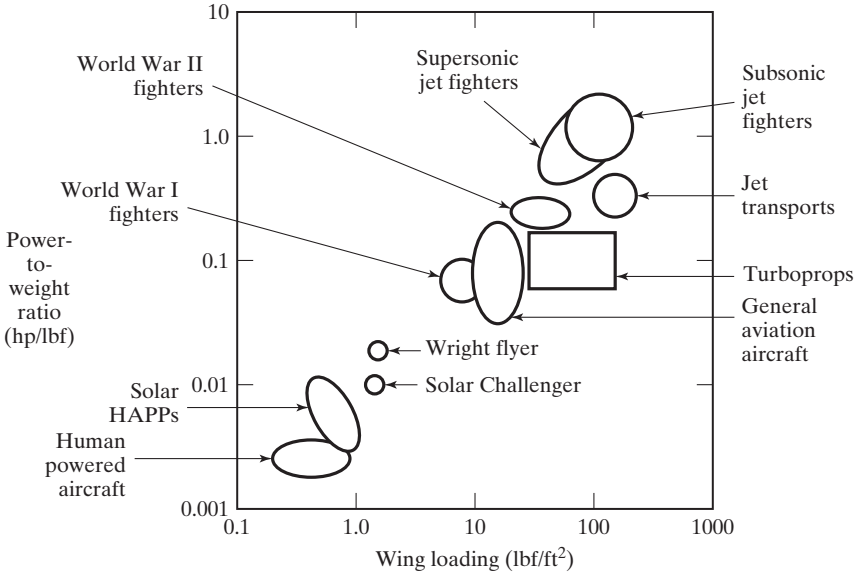

Figure 5.9 Historical ranges of power loading and wing loading [from Hall (1985)].

EXAMPLE 5.1: Aspect ratio of a delta wing

Develop an expression for the aspect ratio of a delta wing in terms of the leading-edge sweep angle (Λ_{LE}).

Solution: Referring to the sketch of the delta wing in Fig. 5.7, the wing area is

$$S = \frac{bc_r}{2}$$

and the $\tan \Lambda_{LE}$ is given by

$$\tan \Lambda_{LE} = \frac{c_r}{(b/2)}$$

Solving this second expression for c_r and substituting it into the expression for the wing area, we obtain:

$$S = \frac{b^2}{4} \tan \Lambda_{LE}$$

Substituting this expression for the wing area into the expression for the aspect ratio gives:

$$AR = \frac{b^2}{S} = \frac{4}{\tan \Lambda_{LE}} \qquad \textbf{(5.1)}$$

EXAMPLE 5.2: Calculate the wing-geometry parameters for the Space Shuttle Orbiter

To calculate the wing-geometry parameters for the Space Shuttle *Orbiter*, the complex shape of the actual wing is replaced by a swept, trapezoidal wing, as shown in Fig. 5.10. For the reference wing of the *Orbiter*, the root chord c_r is 57.44 ft, the tip chord c_t is 11.48 ft, and the span b is 78.056 ft. Using these values which define the reference wing, calculate (a) the wing area S, (b) the aspect ratio AR, (c) the taper ratio λ, and (d) the mean aerodynamic chord *mac*.

Solution:

(a) The area for the trapezoidal reference wing is:

$$S = \left(\frac{c_t + c_r}{2}\right)\frac{b}{2}2 = 2690 \text{ ft}^2$$

(b) The aspect ratio for this swept, trapezoidal wing is:

$$AR = \frac{b^2}{S} = \frac{(78.056 \text{ ft})^2}{2690 \text{ ft}^2} = 2.265$$

(c) The taper ratio is found from:

$$\lambda = \frac{c_t}{c_r} = \frac{11.48 \text{ ft}}{57.44 \text{ ft}} = 0.20$$

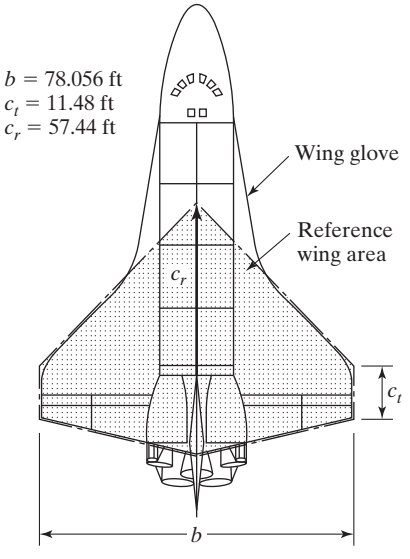

Figure 5.10 Sketch of Space Shuttle *Orbiter* geometry for Example 5.2.

(d) To calculate the mean aerodynamic chord, we will first need an expression for the chord as a function of the distance from the plane of symmetry [i.e., $c(y)$]. The required expression is:

$$c(y) = c_r + \frac{11.48 - 57.44}{39.028} y = 57.44 - 1.1776y$$

Substituting this expression for the chord as a function of y into the equation for the mean aerodynamic chord yields:

$$mac = \frac{2}{S}\int_0^{b/2} [c(y)]^2 dy = \frac{2}{2690}\int_0^{39.028} (57.44 - 1.1776y)^2 dy$$

Integrating this expression, we obtain:

$$mac = 39.57 \text{ ft}$$

5.4 AERODYNAMIC FORCE AND MOMENT COEFFICIENTS

Aerodynamicists have long used force and moment coefficients to describe the aerodynamics of airplanes. Coefficients are nondimensional values which represent the forces and moments without including the effects of altitude (density), velocity, and size. As we discussed in Section 3.14, however, not all flow characteristics can be taken into account when nondimensionalizing forces and moments. That is why certain flight characteristics (such as drag) are still functions of Reynolds number and Mach number, even when considered in coefficient form.

5.4.1 Lift Coefficient

We will now develop the equation for the normal force coefficient to illustrate the physical significance of a dimensionless force coefficient. We choose the normal (or z) component of the resultant force since it is relatively simple to calculate and it has the same relation to the pressure and the shear forces as does the lift. For a relatively thin airfoil section at a relatively low angle of attack, it is clear from Fig. 5.2 that the lift (and similarly the normal force) results primarily from the action of the pressure forces. The shear forces act primarily in the chordwise direction (i.e., contribute primarily to the drag). Therefore, to calculate the force in the z direction, we only need to consider the pressure contribution, which is illustrated in Fig. 5.11. The pressure force acting on a differential area of the vehicle surface is $dF = p\, ds\, dy$, as shown in Fig. 5.12. The elemental surface area is the product of ds, the wetted length of the element in the plane of the cross section, times dy, the element's length in the direction perpendicular to the plane of the cross section (or spanwise direction). Since the pressure force acts normal to the surface, the force component in the z direction is the product of the pressure times the projected planform area:

$$dF_z = p\, dx\, dy \qquad \textbf{(5.2)}$$

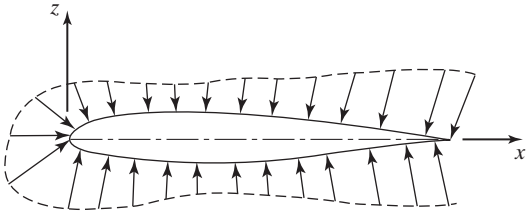

Figure 5.11 Pressure distribution for a lifting airfoil section.

Integrating the pressure over the entire wing surface (including the upper and the lower surfaces) results in the net force in the z direction given by:

$$F_z = \oiint p\, dx\, dy \tag{5.3}$$

Notice that the resultant force in any direction due to a constant pressure over a closed surface is zero. Therefore, the force in the z direction due to a uniform pressure, p_∞, acting over the entire wing area is zero, or:

$$\oiint p_\infty dx\, dy = 0 \tag{5.4}$$

Combining equations (5.3) and (5.4), the resultant force component is:

$$F_z = \oiint (p - p_\infty) dx\, dy \tag{5.5}$$

To nondimensionalize the factors on the right-hand side of equation (5.5), divide by the product $q_\infty cb$, which has the units of force, and represents the characteristic flow and geometry parameters for the wing.

$$\frac{F_z}{q_\infty cb} = \oiint \frac{p - p_\infty}{q_\infty} d\left(\frac{x}{c}\right) d\left(\frac{y}{b}\right)$$

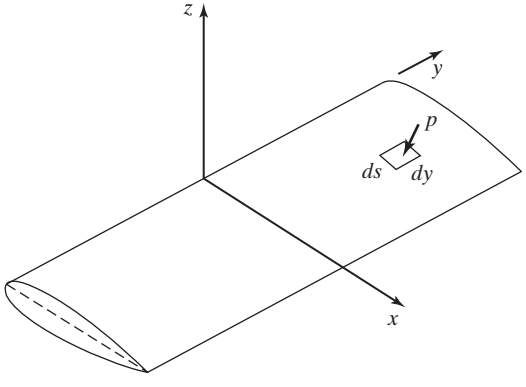

Figure 5.12 Pressure acting on an elemental surface area.

Since the pressure coefficient was defined in equation (3.13) as $C_p = (p - p_\infty)/q_\infty$, and the product cb represents the planform area S of the rectangular wing of Fig. 5.12, we can write the integral as:

$$\frac{F_z}{q_\infty S} = \oint\!\!\oint C_p d\left(\frac{x}{c}\right) d\left(\frac{y}{b}\right) \tag{5.6}$$

When the boundary layer is thin, the pressure distribution around the airfoil is essentially that of an inviscid flow, as we discussed in Chapter 3. Therefore, the pressure distribution is independent of Reynolds number and does not depend on whether the boundary layer is laminar or turbulent. When the boundary layer is thin, the pressure coefficient at a particular location on the surface given by the dimensionless coordinates $(x/c, y/b)$ is independent of vehicle scale and of the flow conditions. Over the range of flow conditions for which the pressure coefficient is a unique function of the dimensionless coordinates $(x/c, y/b)$, the value of the integral in equation (5.6) depends only on the configuration geometry and on the angle of attack, rather than all of the variables discussed in Section 5.1.2. Therefore, the resulting dimensionless force parameter, or force coefficient (in this case, the normal force coefficient), is independent of model scale and of flow conditions. A similar analysis can be used to calculate the lift coefficient, which is defined as:

$$C_L = \frac{L}{q_\infty S} \tag{5.7}$$

Data are presented in Fig. 5.13 for a NACA 23012 airfoil which were obtained from a wind-tunnel model that spanned from one tunnel wall to the other in order to represent a wing of infinite span. The lift acting on a wing of infinite span does not vary in the y direction. For this two-dimensional flow, we are interested in determining the lift acting on a unit width of the wing [i.e., the lift per unit span (l)]. Therefore, the lift measurements are presented in terms of the section lift coefficient C_l. The section lift coefficient is the lift per unit span (l) divided by the product of the dynamic pressure times the planform area per unit span, which is the chord length (c):

$$C_l = \frac{l}{q_\infty c} \tag{5.8}$$

The data from Abbott and von Doenhoff (1949) were obtained in a wind tunnel that could be operated at pressures up to 10 atm. As a result, the Reynolds number ranged from 3×10^6 to 9×10^6 at Mach numbers less than 0.17. In addition to the measurements obtained with a smooth model, data are presented for a model that had "standard" surface roughness applied near the leading edge. Additional comments will be made about surface roughness later in this chapter.

The experimental section lift coefficient is independent of Reynolds number and is a linear function of the angle of attack from approximately $-10°$ to $+10°$. The slope of this linear portion of the curve is called the *two-dimensional lift-curve slope*. Using the experimental data for this airfoil, we can find that:

$$\frac{dC_l}{d\alpha} = C_{l_\alpha} = a_0 = 0.104 \text{ per degree}$$

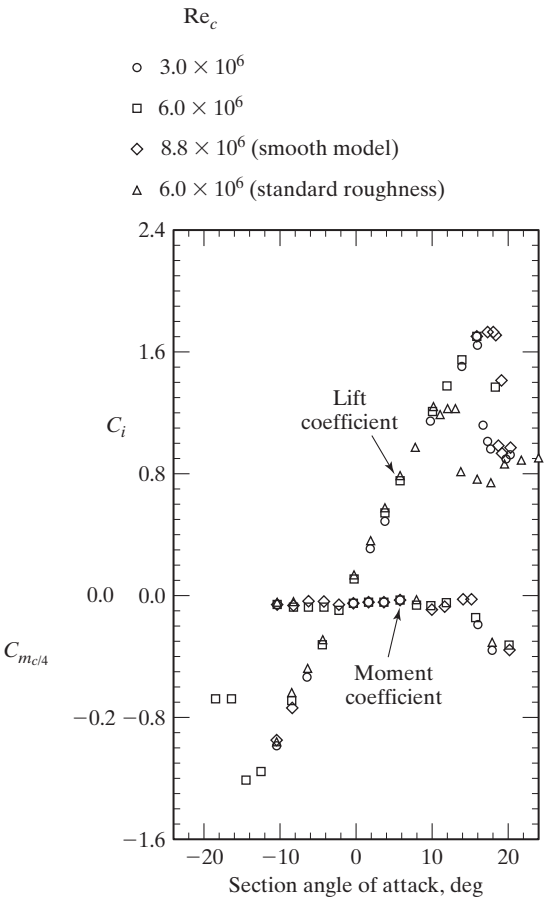

Figure 5.13 Section lift coefficient and section moment coefficient (with respect to *c*/4) for an NACA 23012 airfoil [data from Abbott and von Doenhoff (1949)].

Equations that we will develop in Chapter 6 show that the theoretical value for the two-dimensional lift-curve slope is 2π per radian (0.1097 per degree).

Since the NACA 23012 airfoil section is cambered (the maximum camber is approximately 2% of the chord length), lift is generated at zero degrees angle of attack. In fact, zero lift is obtained at −1.2°, which is designated α_{0l} or the section angle of attack for zero lift. The variation of the lift coefficient with angle of attack in the linear region is given by:

$$C_l = C_{l_\alpha}(\alpha - \alpha_{0l}) \tag{5.9}$$

which is the equation for a straight line (the slope is C_{l_α} and the x intercept is α_{0l}). As the angle of attack is increased above 10°, the section lift coefficient continues to increase

(but is no longer linear with angle of attack) until a maximum value, $C_{l_{max}}$, is reached. Referring to Fig. 5.13, $C_{l_{max}}$ is 1.79 and occurs at an angle of attack of 18°, which is called the stall angle of attack. Partly because of this relatively high value of $C_{l_{max}}$ the NACA 23012 section has been used on many aircraft (e.g., the Beechcraft Bonanza from Table 5.1 and the Brewster Buffalo).

At angles of attack in excess of 10°, the section lift coefficients exhibit a Reynolds-number dependence. Recall from Chapter 4 that the adverse pressure gradient (which the air particles encounter as they move toward the trailing edge of the upper surface) increases as the angle of attack increases. At these higher angles of attack, the air particles which have been slowed by the viscous forces cannot overcome the relatively large adverse pressure gradient, and the boundary layer separates. The separation location depends on the character (laminar or turbulent) of the boundary layer and its thickness, and therefore on the Reynolds number, which is why the stall characteristics vary with Reynolds number. As we will discuss later, boundary-layer separation has a profound effect on the drag acting on the airfoil.

The study of airfoil lift as a function of incidence has shown that, in many instances, the presence of a separation bubble near the leading edge of the airfoil results in laminar section stall. Experimental data on two-dimensional "peaky" airfoil sections indicate that $C_{l_{max}}$ as limited by laminar stall, is strongly dependent on the leading-edge shape and on the Reynolds number. If the laminar boundary layer, which develops near the leading edge of the upper surface of the airfoil, is subjected to a relatively high adverse pressure gradient, it will separate because the relatively low kinetic energy level of the air particles near the wall is insufficient to surmount the "pressure hill" of the adverse pressure gradient. The separated shear layer that is formed may curve back onto the surface within a very short distance. This is known as *short bubble separation*. The separated viscous layer near the pressure peak may not reattach to the surface at all, or it may reattach within 0.3 chord length or more downstream. This extended separation region is known as *long bubble separation*. Once the flow reattaches after a bubble separation, it often has transitioned to a turbulent boundary layer and the original laminar characteristics of the airfoil are lost. More details about separation bubbles will be discussed in Section 6.6.

The separation bubble may not appear at all on relatively thick, strongly cambered profiles operating at high Reynolds numbers. The reason for this is that the Reynolds number is then large enough for a natural transition to a turbulent boundary layer to occur upstream of the strong pressure rise. The relatively high kinetic energy of the air particles in a turbulent boundary layer permits them to climb the "pressure hill," and boundary-layer separation occurs only a short distance upstream of the trailing edge (trailing-edge stall). The separation point moves upstream continuously with increasing angle of attack, and the lift does not drop abruptly after $C_{l_{max}}$ but decreases gradually. Hopefully you can see that the stall characteristics of an airfoil can be very different at different Reynolds numbers, with leading-edge separation taking place at low Reynolds numbers (or for a very small leading-edge radius) and trailing-edge separation taking place at higher Reynolds numbers (or for a relatively large leading-edge radius).

EXAMPLE 5.3: Calculate the lift per unit span on a NACA 23012 airfoil section

Consider tests of an unswept wing that spans the wind tunnel and whose airfoil section is NACA 23012. Since the wing model spans the test section, we will assume that the flow is two dimensional. The chord of the model is 1.3 m. The test section conditions simulate a density altitude of 3 km. The velocity in the test section is 360 km/h.

What is the lift per unit span (in N/m) that you would expect to measure when the angle of attack is 4°? What would be the corresponding section lift coefficient?

Solution: First, we need to calculate the section lift coefficient. We will assume that the lift is a linear function of the angle of attack and that it is independent of the Reynolds number (i.e., the viscous effects are negligible) at these test conditions. These are reasonable assumptions as can be seen by referring to Fig. 5.13. Therefore, the section lift coefficient from equation (5.9) is:

$$C_l = C_{l_\alpha}(\alpha - \alpha_{0l})$$

Using the values presented in the discussion associated with Fig. 5.13,

$$C_l = (0.1041/\text{deg})(4.0^\circ - (-1.2^\circ)) = 0.541$$

At an angle of attack of 4°, the experimental values of the section lift coefficient for an NACA 23012 airfoil section range from 0.50 to 0.57, as shown in Fig. 5.13.

To calculate the corresponding lift force per unit span, we rearrange equation (5.8) to obtain

$$l = C_l q_\infty c$$

To calculate the dynamic pressure (q_∞), we need the velocity in m/s and the density in kg/m^3 in order for the units to be consistent:

$$U_\infty = 360\frac{\text{km}}{\text{h}}\frac{1000\,\text{m}}{\text{km}}\frac{\text{h}}{3600\,\text{s}} = 100\frac{\text{m}}{\text{s}}$$

Given the density altitude is 3 km, we can refer to Appendix B to find that:

$$\rho = 0.9093\,\text{kg/m}^3$$

(*Note:* The fact that we are given the density altitude as 3 km does not provide specific information either about the temperature or pressure.)

So now the lift per unit span is:

$$l = (0.541)\left[\frac{1}{2}\left(0.9093\frac{\text{kg}}{\text{m}^3}\right)\left(100\frac{\text{m}}{\text{s}}\right)^2\right](1.3\,\text{m})$$

$$l = (0.541)\left[4546.5\frac{\text{N}}{\text{m}^2}\right](1.3\,\text{m}) = 3197.6\frac{\text{N}}{\text{m}}$$

5.4.2 Moment Coefficient

The moment created by the aerodynamic forces acting on a wing (or airfoil) is determined about a particular reference axis (also called the moment reference center). The reference axis could be the leading edge, the quarter-chord location, the aerodynamic center, and so on. The significance of these reference axes in relation to the coefficients for thin airfoils will be discussed in Chapter 6.

The procedure used to nondimensionalize the moments created by the aerodynamic forces is similar to that used to nondimensionalize the lift. To demonstrate this nondimensionalization, the pitch moment about the leading edge due to the pressures acting on the surface will first be calculated (refer again to Fig. 5.12). The contribution of the chordwise component of the pressure force and of the skin-friction force to the pitch moment is small and is neglected. Therefore, the pitch moment about the leading edge due to the pressure force acting on the surface element whose area is *ds* times *dy* and which is located at a distance *x* from the leading edge is:

$$dM_0 = \underbrace{p dx dy}_{\text{Force}} \underbrace{x}_{\substack{\text{Lever}\\ \text{Arm}}} \tag{5.10}$$

where *dx dy* is the projected area. Integrating over the entire wing surface, the net pitch moment is given by

$$M_0 = \iint_{\mathcal{S}} p x \, dx \, dy \tag{5.11}$$

As we saw before, when a uniform pressure acts on any closed surface, the resultant pitch moment due to this constant pressure is zero, so:

$$\iint_{\mathcal{S}} p_\infty x \, dx \, dy = 0 \tag{5.12}$$

Combining equations (5.11) and (5.12), the resulting pitch moment about the leading edge is:

$$M_0 = \iint_{\mathcal{S}} (p - p_\infty) x \, dx \, dy \tag{5.13}$$

To nondimensionalize the factors on the right-hand side of equation (5.13), divide by $q_\infty c^2 b$, which has the units of force times length:

$$\frac{M_0}{q_\infty c^2 b} = \iint_{\mathcal{S}} \frac{p - p_\infty}{q_\infty} \frac{x}{c} d\left(\frac{x}{c}\right) d\left(\frac{y}{b}\right)$$

Since the product of *cb* represents the planform area of the rectangular wing *S*, we can write the previous equation as:

$$\frac{M_0}{q_\infty S c} = \iint_{\mathcal{S}} C_p \frac{x}{c} d\left(\frac{x}{c}\right) d\left(\frac{y}{b}\right) \tag{5.14}$$

Now, the dimensionless moment coefficient is defined as:

$$C_{M_0} = \frac{M_0}{q_\infty S c} \tag{5.15}$$

Since the derivation of equation (5.15) was for the rectangular wing of Fig. 5.12, the chord c is used. However, as noted previously in this chapter, the mean aerodynamic chord is used together with S to nondimensionalize the pitch moment for a general wing.

The section moment coefficient is used to represent the dimensionless moment per unit span (m_0):

$$C_{m_0} = \frac{m_0}{q_\infty cc} \tag{5.16}$$

since the surface area per unit span is the chord length c. In general, the section pitch moment coefficient depends on the camber and on the thickness ratio. Section pitch moment coefficients for a NACA 23012 airfoil section with respect to the quarter chord and with respect to the aerodynamic center are presented in Figs. 5.13 and 5.14, respectively. The *aerodynamic center* is that point about which the section moment coefficient is independent of the angle of attack. Therefore, the aerodynamic center is that point along the chord where all changes in lift effectively take place. Since the moment about the

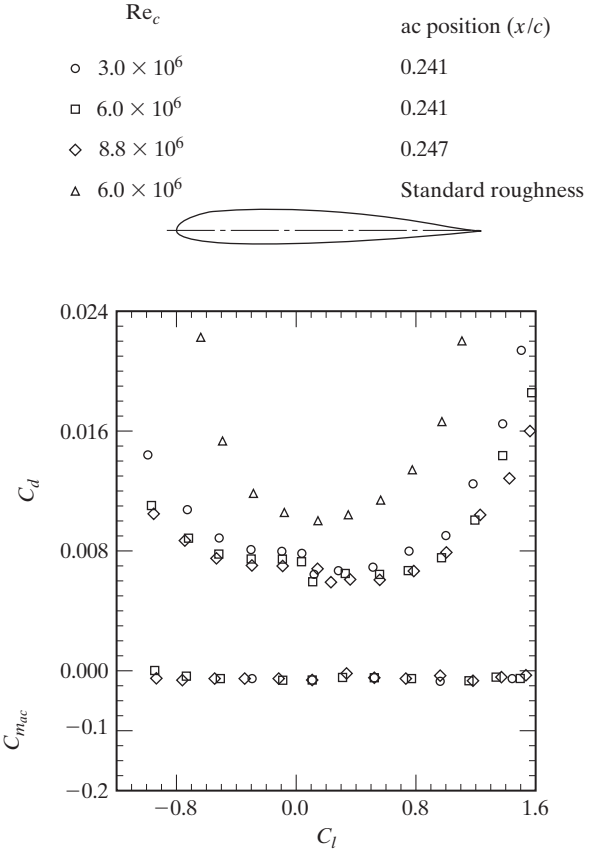

Figure 5.14 Section drag coefficient and section moment coefficient (with respect to the *ac*) for a NACA 23012 airfoil [data from Abbott and von Doenhoff (1949)].

aerodynamic center is the product of a force (the lift that acts at the center of pressure) and a lever arm (the distance from the aerodynamic center to the center of pressure), the center of pressure must move toward the aerodynamic center as the lift increases. The quarter-chord location is significant, since it is the theoretical aerodynamic center for incompressible flow about a two-dimensional airfoil (we will prove this in Chapter 6).

Notice in Figs. 5.13 and 5.14 that the pitch moment coefficient is independent of the Reynolds number (for those angles of attack where the lift coefficient is independent of the Reynolds number), since the pressure coefficient depends only on the dimensionless space coordinates $(x/c, y/b)$ [see equation (5.14)]. One of the nice features of the NACA 23012 airfoil section is a relatively high $C_{l_{max}}$ with only a small $C_{m_{ac}}$.

The characteristic length (or moment arm) for the roll moment and yaw moment is the wing span b (instead of the chord), since the span is the characteristic length in the lateral direction. Therefore, the roll moment coefficient is:

$$C_{\mathscr{L}} = \frac{\mathscr{L}}{q_\infty S b} \tag{5.17}$$

and the yaw moment coefficient is:

$$C_{\mathscr{N}} = \frac{\mathscr{N}}{q_\infty S b} \tag{5.18}$$

5.4.3 Drag Coefficient

The drag force on a wing is due in part to skin friction and in part to the integrated effect of pressure. If $\vec{t}$ denotes the tangential shear stress at a point on the body surface, p the static pressure, and $\hat{n}$ the outward-facing normal to the element of surface dS, the drag can be formally expressed as

$$D = \iint_{\text{body}} \vec{t} \cdot \hat{e}_\infty dS - \iint_{\text{body}} p\hat{n} \cdot \hat{e}_\infty dS \tag{5.19}$$

where $\hat{e}_\infty$ is a unit vector parallel to the free stream and the integration takes place over the entire wetted surface. The first integral represents the friction component and the second integral represents the pressure drag.

The most straightforward approach to calculating the pressure drag is to perform the numerical integration indicated by the second term in equation (5.19). This approach is known as the near-field method of drag computation. Unfortunately, this can be a relatively inaccurate procedure for streamlined configurations at small angles of attack. The inaccuracy results because the pressure drag integral is the difference between the integration on forward-facing and rearward-facing surface elements, this difference being a second-order (and therefore small) quantity for slender bodies. Furthermore, the reader should realize that subtle differences between the computed pressure distribution and the actual pressure distribution can have a significant effect on the validity of the drag estimates, depending where the differences occur. If the pressure difference is near the middle of the aerodynamic configuration, where the local slope is roughly parallel to the free-stream direction, it will have a relatively small effect on the validity of the estimated drag. However, if the pressure difference is near the front or aft end of the configuration (for instance, at the nose or on a nozzle boattail), even

a small difference between the computed pressure and the actual pressure can have a significant effect on the accuracy of the predicted drag.

In Chapter 3 we learned that zero drag results for irrotational, steady, incompressible flow past a two-dimensional body. For an airfoil section (i.e., a two-dimensional geometry) which is at a relatively low angle of attack so that the boundary layer is thin and does not separate, the pressure distribution is essentially that for an inviscid flow. Therefore, skin friction is a major component of the chordwise force per unit span (f_x). Referring to Figs. 5.2 and 5.11, sf_x can be approximated as:

$$sf_x \approx \oint \tau \, dx \tag{5.20}$$

where sf_x is the chordwise force per unit span due to skin friction. Dividing both sides of equation (5.20) by the product $q_\infty c$ gives us an expression for the dimensionless force coefficient:

$$\frac{sf_x}{q_\infty c} \approx \oint C_f d\left(\frac{x}{c}\right) \tag{5.21}$$

where C_f, the skin-friction coefficient, was defined in equation (4.21) as:

$$C_f = \frac{\tau}{\frac{1}{2}\rho_\infty U_\infty^2} \tag{5.22}$$

As we stated in the general discussion of the boundary-layer characteristics in Chapter 4 (see Fig. 4.19), skin friction for a turbulent boundary layer is much greater than that for a laminar boundary layer for given flow conditions. Equations for calculating the skin-friction coefficient were developed in Chapter 4. However, we can introduce the correlations for the skin-friction coefficient for incompressible flow past a flat plate to gain insight into the force coefficient of equation (5.21). Of course, the results for a flat plate only approximate those for an airfoil, but they will help us understand the basic nature of what is happening. The potential function given by equation (3.35a) shows that the velocity at the edge of the boundary layer and, therefore, the local static pressure, is constant along the plate. Such is not the case for an airfoil section, for which the flow accelerates from a forward stagnation point to a maximum velocity, then decelerates to the trailing edge. Nevertheless, the analysis will provide useful insights into the section drag coefficient,

$$C_d = \frac{d}{q_\infty c} \tag{5.23}$$

for an airfoil at relatively low angles of attack.

Referring to Chapter 4, when the boundary layer is laminar the local skin friction coefficient is:

$$C_f = \frac{0.664}{(\mathrm{Re}_x)^{0.5}} \tag{5.24}$$

and for a turbulent boundary layer:

$$C_f = \frac{0.0583}{(\mathrm{Re}_x)^{0.2}} \tag{5.25}$$

For equations (5.24) and (5.25), the local Reynolds number is defined as:

$$\mathrm{Re}_x = \frac{\rho_\infty U_\infty x}{\mu_\infty} \tag{5.26}$$

Also, as was shown in Chapter 4, total skin-friction coefficients can be defined and used as well. The total skin-friction coefficient for laminar flow is given by:

$$\overline{C}_f = \frac{1.328}{\sqrt{\mathrm{Re}_L}} \tag{5.27}$$

and the total skin-friction coefficient for turbulent flow is

$$\overline{C}_f = \frac{0.074}{(\mathrm{Re}_L)^{0.2}} \tag{5.28}$$

which is the Prandtl formulation, although the Prandtl-Schlichting formulation was shown to be more accurate:

$$\overline{C}_f \equiv \frac{0.455}{(\log_{10}\mathrm{Re}_L)^{2.58}} \tag{5.29}$$

These total skin-friction coefficients use the length-based Reynolds number given by:

$$\mathrm{Re}_L = \frac{\rho_\infty U_\infty L}{\mu_\infty} \tag{5.30}$$

where L is the length of a flat plate.

EXAMPLE 5.4: Calculate the local skin friction

Calculate the local skin friction at a point 0.5 m from the leading edge of a flat-plate airfoil flying at 60 m/s at an altitude of 6 km.

Solution: Refer to Table 1.2 to obtain the static properties of undisturbed air at 6 km:

$$\rho_\infty = 0.6601\ \mathrm{kg/m^3}$$
$$\mu_\infty = 1.5949 \times 10^{-5}\ \mathrm{kg/s \cdot m}$$

Now, using equation (5.26),

$$\mathrm{Re}_x = \frac{(0.6601\ \mathrm{kg/m^3})(60\ \mathrm{m/s})(0.5\ \mathrm{m})}{1.5949 \times 10^{-5}\ \mathrm{kg/s \cdot m}}$$
$$= 1.242 \times 10^6$$

If the boundary layer is laminar,

$$C_f = \frac{0.664}{(\mathrm{Re}_x)^{0.5}} = 5.959 \times 10^{-4}$$
$$\tau = C_f\left(\tfrac{1}{2}\rho_\infty U_\infty^2\right) = 0.708\ \mathrm{N/m^2}$$

and if the boundary layer is turbulent,

$$C_f = \frac{0.0583}{(\mathrm{Re}_x)^{0.2}} = 3.522 \times 10^{-3}$$
$$\tau = C_f\left(\tfrac{1}{2}\rho_\infty U_\infty^2\right) = 4.185\ \mathrm{N/m^2}$$

Notice that the local shear stress for the turbulent boundary layer is nearly six times larger than that for the laminar boundary layer.

As we discussed in the text of Chapter 2 and in the homework problems of Chapters 2 and 4, the integral form of the momentum equation can be used to determine the drag acting on an airfoil section. This approach is known as the far-field method of drag determination. Wing-section profile-drag measurements have been made for the Boeing 727 in flight using the Boeing Airborne Traversing Probe, examples of which are presented in Fig. 5.15. The probe consists of four main components: (1) flow sensors, (2) a rotating arm, (3) the drive unit, and (4) the mounting base. As reported by Bowes (1974),

> The measured minimum section profile drag at $M = .73$ was about 15 percent higher than predicted from wind-tunnel test data for a smooth airfoil. The wind-tunnel data used in this correlation were also from wake surveys on the 727 wing. The data were adjusted to fully turbulent flow and extrapolated to flight Reynolds numbers. This quite sizeable difference between the measured and extrapolated values of $C_{d,\,\mathrm{min}}$ has been attributed to surface roughness and excrescences on the airplane wing, although the 15-percent increase in wing-section profile drag is larger than traditionally allotted in airplane drag estimates. The wing section where this

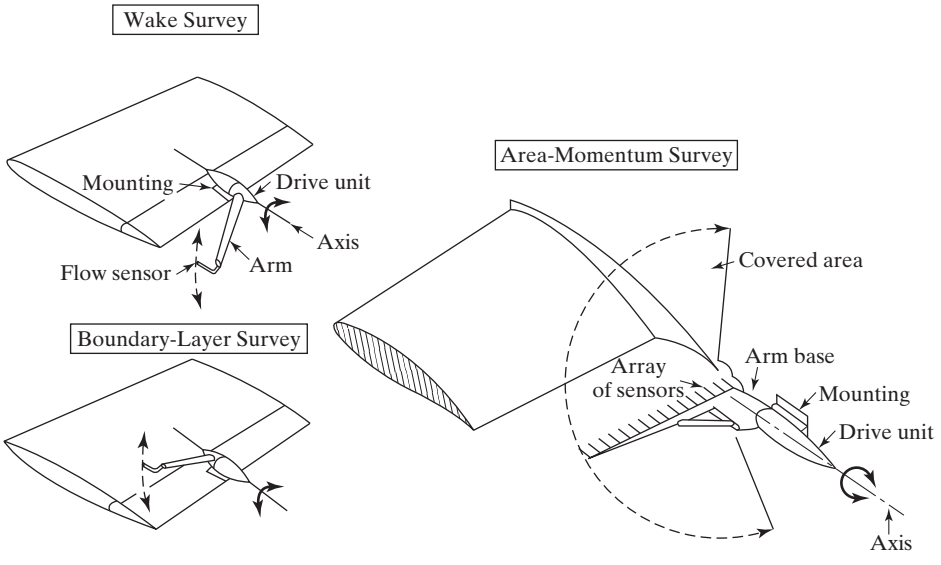

Figure 5.15 Airborne traversing probe concept and configurations [from Bowes (1974)].

survey was performed was inspected and had numerous steps and bumps due to control devices and manufacturing tolerances which would account for this local level of excrescence drag. This is not representative of the entire wing surface.

5.4.4 Boundary-Layer Transition

We talked about transition in Chapter 4, but now we need to find a practical way to make engineering estimations for the impact of transition on aerodynamic forces, especially drag. It is obvious that the force coefficient of equation (5.21) depends on the Reynolds number. The Reynolds number not only affects the magnitude of C_f, but it is also used as an indicator of whether the boundary layer is laminar or turbulent. Since the calculation of the force coefficient requires integration of C_f over the chord length, we must know at what point, if any, the boundary layer becomes turbulent (i.e., where transition occurs).

Near the forward stagnation point on an airfoil, or on a wing, or near the leading edge of a flat plate, the boundary layer is initially laminar. As the flow proceeds downstream, the boundary layer thickens and the viscous forces continue to dissipate the energy of the airstream. Disturbances to the flow in the growing viscous layer may be caused by surface roughness, a temperature variation in the surface, pressure pulses, and so on. If the Reynolds number is low, the disturbances will be damped by viscosity and the boundary layer will remain laminar, but at higher Reynolds numbers the disturbances may grow. In such cases, the boundary layer may become unstable and, eventually, turbulent (i.e., transition will occur). The details of the transition process are quite complex and depend on many parameters, as we discussed in Chapter 4.

The engineer who must develop a transition criterion for design purposes usually uses the Reynolds number. For instance, if the surface of a flat plate is smooth and if the external airstream has no turbulence, transition often is assumed to "occur" at a Reynolds number (Re_x) of approximately 500,000. However, experience has shown that the Reynolds number at which the disturbances will grow and the length over which the transition process takes place depends on the magnitude of the free-stream disturbances and on the flow field. Specifically, the criterion that low-speed transition takes place at a Reynolds number of 500,000 was based on wind-tunnel tests with fairly high levels of free-stream turbulence. That is, the air approaching the flat plate had relatively large fluctuations in velocity, sometimes on the order of 2% to 3% of the free-stream velocity. More recent experiments with low levels of free-stream disturbances have shown that the transition Reynolds number can be much higher than this [Eli Reshotko, personal communication (2012)]. Experiments in the Schubauer-Skramstad wind tunnel (1948) had a transition Reynolds number of 2,800,000 with free-stream turbulence levels less than 0.07%. That wind tunnel, however, was limited by acoustic disturbances. The Klebanoff tunnel at Arizona State University measured transition Reynolds numbers of 3,400,000 according to Saric (1992). There are wind tunnels in Japan, Russia, and Sweden which have measured transition Reynolds numbers above 3,000,000. Estimating the impact of transition Reynolds number on skin friction can be achieved fairly easily by using the appropriate transition correction in Table 4.5 with the total skin-friction relation in equation (4.87). A quick examination of the impact of varying the transition location should be conducted to ensure that a particular result is not highly dependent on an incorrect assumption about transition.

In order to have a fuller understanding of transition, we will briefly consider the effects of surface roughness, surface temperature, pressure gradients in inviscid flow, and local Mach number on transition.

- ***Surface roughness.*** Since transition is the amplification of disturbances to the flow, the presence of surface roughness significantly promotes transition (i.e., causes transition to occur at relatively low Reynolds numbers).
- ***Surface temperature.*** The boundary-layer thickness decreases as the surface temperature is decreased; cooling the surface usually delays transition. However, for supersonic flows, there is a complex relationship between boundary-layer transition and surface cooling.
- ***Pressure gradient.*** A favorable pressure gradient (i.e., the static pressure decreases in the streamwise direction or, equivalently, the inviscid flow is accelerating) delays transition. Conversely, an adverse pressure gradient promotes transition.
- ***Mach number.*** The transition Reynolds number is usually higher (sometimes significantly higher) when the flow is compressible (i.e., as the Mach number is increased). See Section 12.8 for more details.

Stability theory [e.g., see Mack (1984)] can be an important tool that provides insights into the importance of individual parameters without introducing spurious effects that might be due to flow disturbances peculiar to a test facility (e.g., "noise" in a wind tunnel). For a more detailed discussion of transition, you should refer to good reference sources for boundary-layer theory [e.g., Schlichting (1979)].

If the skin friction is the dominant component of the drag, transition should be delayed as long as possible to obtain a low-drag section. To delay transition on a low-speed airfoil section, the point of maximum thickness could be moved aft so that the boundary layer is subjected to a favorable pressure gradient over a longer run. Consider the NACA 0009 section and the NACA 66–009 section; both are symmetric, having a maximum thickness of $0.09c$. The maximum thickness for the NACA 66–009 section is at $0.45c$, while that for the NACA 0009 section is at $0.3c$ (see Fig. 5.16). As a result, the minimum pressure coefficient occurs at $x = 0.6c$ for the NACA 66–009 and a favorable pressure gradient acts to stabilize the boundary layer up to this point. For the NACA 0009, the minimum pressure occurs near $x = 0.1c$, which promotes early transition. The lower local velocities near the leading edge and the extended region of favorable pressure gradient cause transition to be farther aft on the NACA 66–009. Since the drag for a streamlined airfoil at low angles of attack is primarily due to skin friction, use of equation (5.21) would indicate that the drag is lower for the NACA 66–009. This is verified by the data from Abbott and von Doenhoff (1949) which are reproduced in Fig. 5.17. The subsequent reduction in the friction drag due to laminar flow creates a *drag bucket* for the NACA 66–009 section (the term "drag bucket" comes from the narrow region of drag reduction for the laminar airfoil near zero lift). Note that the section drag curve varies only slightly with C_l for moderate excursions in angle of attack, since the skin-friction coefficient varies little with angle of attack. At the very high Reynolds numbers that occur at some flight conditions, it is difficult to maintain a long run of a laminar boundary layer, especially if surface roughnesses develop during the flight operations. However, a *laminar-flow section*, such as the NACA 66–009, offers additional benefits. Comparing the cross sections presented in Fig. 5.16, the

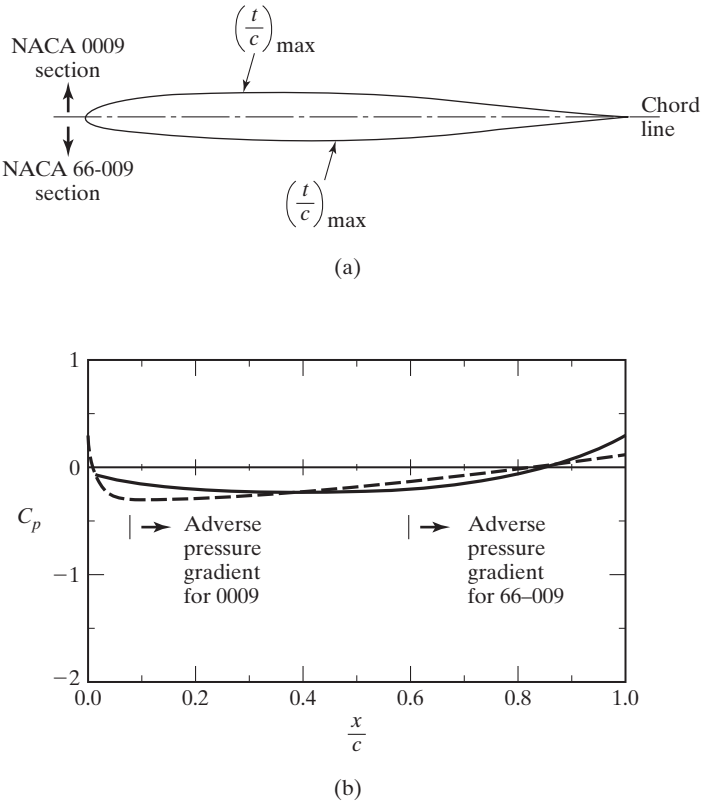

Figure 5.16 Comparison of geometries and resultant pressure distributions for a "standard" airfoil section (NACA 0009) and for a laminar airfoil section (NACA 66–009): (a) comparison of cross section for an NACA 0009 airfoil with that for an NACA 66–009 airfoil; (b) static pressure distribution.

cross section of the NACA 66–009 airfoil provides more flexibility for carrying fuel and for accommodating the load-carrying structure, which are important multidisciplinary aspects of wing design, as discussed at the beginning of the chapter.

For larger angles of attack, the section drag coefficient depends both on Reynolds number and on angle of attack. As the angle of attack and the section lift coefficient increase, the minimum pressure coefficient also decreases, and the adverse pressure gradient that results as the flow decelerates toward the trailing edge increases. When the air particles in the boundary layer, already slowed by viscous action, encounter the relatively strong adverse pressure gradient, the boundary layer thickens and separates. Because the thickening boundary layer and its separation from the surface cause the pressure distribution to be significantly different from the inviscid model at the higher angles of attack, form drag dominates. Notice that at the higher angles of attack (where form drag is important), the drag coefficient for the NACA 66–009 is greater than that for the NACA 0009, as shown in Fig. 5.17. The preceding description points to the great challenge of airfoil design: in order to obtain lift, there must be an increased pressure difference between the

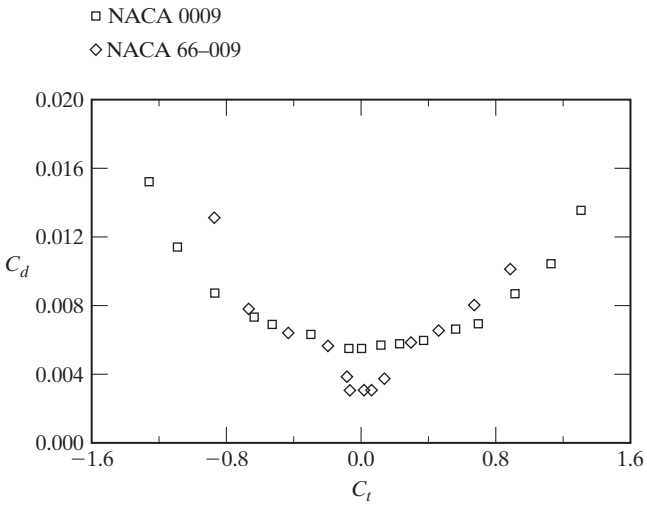

Figure 5.17 Section drag coefficients for NACA 0009 airfoil and for NACA 66–009 airfoil, $\mathrm{Re}_c = 6 \times 10^6$. [data from Abbott and von Doenhoff (1949)].

upper and lower surfaces of the airfoil. The lower upper surface pressures, however, can easily lead to flow separation, which decreases lift and increases drag.

When the viscous effects are secondary, we see that the lift coefficient and the moment coefficient depend only on the vehicle geometry and angle of attack for low-speed flows. However, the drag coefficient exhibits a Reynolds number dependence both at the low angles of attack, where the boundary layer is thin (and the transition location is important), and at high angles of attack, where extensive regions of separated flow exist.

The section drag coefficient for a NACA 23012 airfoil is presented as a function of the section lift coefficient in Fig. 5.14. The data illustrate the dependence on Reynolds number and on angle of attack, which has already been discussed. Notice that the measurements, which are taken from Abbott and von Doenhoff (1949), include data for a *standard roughness*, which will be discussed next.

5.4.5 Effect of Surface Roughness on the Aerodynamic Forces

As discussed in Chapter 2, the Reynolds number is an important parameter when comparing the viscous character of two fields. If we want to reproduce the Reynolds number for a flight test condition in the wind tunnel, then

$$\left(\frac{\rho_\infty U_\infty c}{\mu_\infty}\right)_{\text{wt}} = \left(\frac{\rho_\infty U_\infty c}{\mu_\infty}\right)_{\text{ft}} \tag{5.31}$$

where the subscripts wt and ft designate wind-tunnel and flight conditions, respectively. In many low-speed wind tunnels, the free-stream values for density and for viscosity are roughly equal to the atmospheric values. Therefore,

$$(U_\infty c)_{\text{wt}} \simeq (U_\infty c)_{\text{ft}} \tag{5.32}$$

If the wind-tunnel model is 0.2 scale, the wind-tunnel value for the free-stream velocity would have to be five times the flight value. As a result, the tunnel flow would be transonic or supersonic, which obviously would not be a reasonable simulation since the Mach number would be significantly different. Therefore, since the maximum Reynolds number for this "equal density" subsonic wind-tunnel simulation is much less than the flight value, controlled surface roughness is often added to the model to "fix" boundary-layer transition at the location at which it would occur naturally in flight, or at a known location that would allow for adjustment to flight Reynolds numbers.

Abbott and von Doenhoff (1949) present data on the effect of surface condition on the aerodynamic forces. "The standard leading-edge roughness selected by the NACA for 24-in chord models consisted of 0.011-in carborundum grains applied to the surface of the model at the leading edge over a surface length of $0.08c$ measured from the leading edge on both surfaces. The grains were thinly spread to cover 5 to 10% of the area. This standard roughness is considerably more severe than that caused by the usual manufacturing irregularities or deterioration in service, but it is considerably less severe than that likely to be encountered in service as a result of accumulation of ice, mud, or damage in military combat." The data for the NACA 23012 airfoil (Fig. 5.13) indicate that the angle of zero lift and the lift-curve slope are practically unaffected by the standard leading-edge roughness. However, the maximum lift coefficient is affected by surface roughness. This is further illustrated by the data presented in Fig. 5.18.

When there is no appreciable separation of the flow, the drag on the airfoil is caused primarily by skin friction. Thus, the value of the drag coefficient depends on the relative extent of the laminar boundary layer. A sharp increase in the drag coefficient results when transition is suddenly shifted forward. If the wing surface is sufficiently rough to cause transition near the wing leading edge, large increases in drag are observed, as is evident in the data of Fig. 5.14 for the NACA 23012 airfoil section. In other test results presented in Abbott and von Doenhoff (1949), the location of the roughness strip was systematically varied. The minimum drag increased progressively with forward movement of the roughness strip.

Scaling effects between model simulations and flight applications (as they relate to the viscous parameters) are especially important when the flow field includes an interaction between a shock wave and the boundary layer. The transonic flow field for an airfoil may include a shock-induced separation, a subsequent reattachment to the airfoil surface, and another boundary-layer separation near the trailing edge. According to Pearcey et al. (1968), the prime requirements for correct simulation of these transonic shock/boundary-layer interactions include that the boundary layer is turbulent at the point of interaction and that the thickness of the turbulent boundary layer for the model flow is not so large in relation to the full-scale flow that a rear separation would occur in the simulation that would not occur in the full-scale flow.

Braslow et al. (1966) provide some general guidelines for the use of grit-type boundary-layer transition trips. Whereas it is possible to fix boundary-layer transition far forward on wind-tunnel models at subsonic speeds using grit-type transition trips having little or no grit drag, the roughness configurations that are required to fix transition in a supersonic flow often cause grit drag. Fixing transition on wind-tunnel models becomes increasingly difficult as the Mach number is increased. Since roughness heights several times larger than the boundary-layer thickness can be required to fix transition in a hypersonic flow, the required roughness often produces undesirable distortions of the flow. Sterret et al. (1966)

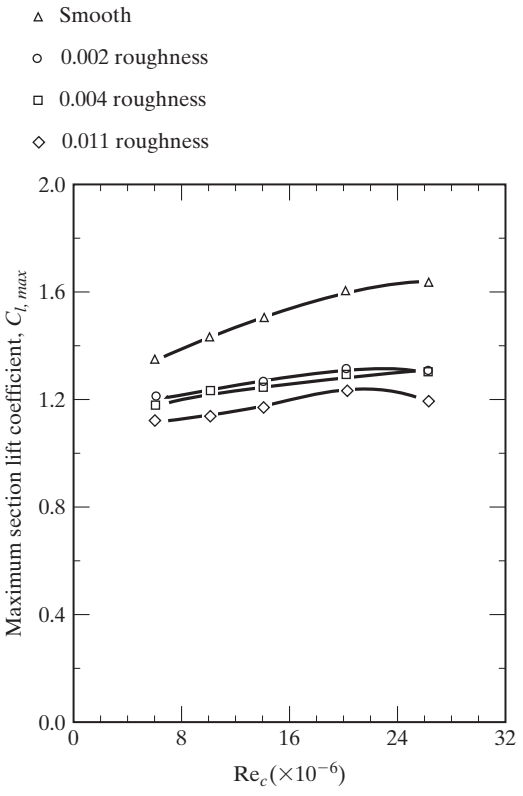

Figure 5.18 Effect of roughness near the leading edge on the maximum section lift for the NACA, 63(420)-422 airfoil [data from Abbott and von Doenhoff (1949)].

provide some general guidelines for the use of boundary-layer trips for hypersonic flows. Data are presented to illustrate problems that can arise from poor trip designs.

The comments regarding the effects of surface roughness were presented for two reasons. (1) The reader should note that, since it is impossible to match the Reynolds number in many scale-model simulations, surface roughness (in the form of boundary-layer trips) is often used to fix transition and therefore the relative extent of the laminar boundary layer. (2) When surface roughness is used, considerable care should be taken to properly size and locate the roughness elements in order to properly simulate the desired flow.

The previous discussion has focused on the effects of roughness elements that have been intentionally placed on the surface to fix artificially the location of transition. As discussed, the use of boundary-layer trips is intended to compensate for the inability to simulate the Reynolds number in ground-test facilities. However, surface roughness produced by environmental "contamination" may have a significant (and unexpected) effect on the transition location. As noted by van Dam and Holmes (1986), loss of laminar flow can be caused by surface contamination such as insect debris, ice crystals, moisture due to mist or rain, surface damage, and "innocent" modifications such as the addition of a spanwise paint stripe.

As noted by van Dam and Holmes (1986), "The surface roughness caused by such contamination can lead to early transition near the leading edge. A turbulent boundary layer which originates near the leading edge of an airfoil, substantially ahead of the point of minimum pressure, will produce a thicker boundary layer at the onset of the pressure recovery as compared to the conditions produced by a turbulent boundary layer which originates further downstream. With sufficiently steep pressure gradients in the recovery region, a change in the turbulent boundary layer conditions . . . can lead to premature turbulent separation . . . , thus affecting the aerodynamic characteristics and the effectiveness of trailing-edge control surfaces. . . . Also, forward movement of transition location and turbulent separation produce a large increase in section drag."

Aerodynamics Concept Box: Boundary-layer Transition Effects on Wind-Tunnel Testing

One of the biggest issues facing researchers conducting wind-tunnel tests on aircraft geometries is transition. Not knowing where transition takes place during a test means a long list of questions will exist about the test, including: was the boundary layer laminar or turbulent?; was transition at the front of the model or halfway back, or did it happen at all?; what impact did transition have on the results (lift, drag, separation, etc.)? To avoid these questions, especially if the results will be used for numerical prediction comparisons, wind-tunnel engineers typically force transition to take place at a known location by using some sort of surface roughness. The pictures below show such a test on a generic UCAV geometry, and the impact of transition was examined at the very beginning of the test [Schütte and Cummings (2011)].

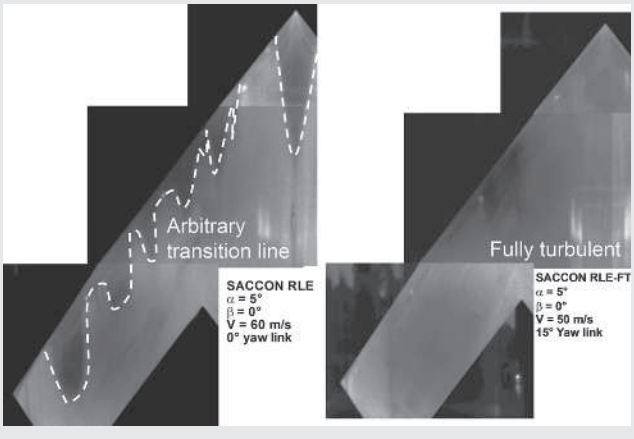

Upper surface infrared thermography pictures of a UCAV configuration. Left: clean leading edge. Right: with carborundum grit trip [Schütte and Cummings (2011)].

Because the precise knowledge of the flow conditions is of paramount importance for tests which are used for computational validation, the wind-tunnel entry was begun with boundary layer transition observations using infrared thermography. In case the model surface and the passing air have different temperatures, the transition line can be observed with an infrared

camera of suitable sensitivity because of the different heat transfer properties of laminar and turbulent boundary layers. The picture on the left shows the UCAV in the tunnel with a smooth leading-edge surface. The dashed line shows the transition front along the wing leading edge, which is quite irregular (as we discussed in Section 4.4). When a strip of carborundum grit was added to the leading edge, the thermography showed the boundary layer to be fully turbulent, answering many of the questions that could be raised later. Knowing the location of transition is essential for good wind-tunnel testing.

5.4.6 Method for Predicting Aircraft Parasite Drag

As you can imagine, total aircraft parasite drag is a complex combination of aircraft configuration, skin friction, pressure distribution, interference among aircraft components, and flight conditions, among other things. Accurately predicting parasite drag would seem an almost impossible task, especially compared with predicting lift. To make the situation even more challenging, there are a variety of terms associated with drag, all of which add confusion about drag and predicting drag. Some of the common terms used to describe drag are [McCormick (1979)]:

- *Induced* (or *vortex*) *drag*—drag due to the trailing vortex system
- *Skin-friction drag*—due to viscous stress acting on the surface of the body
- *Form* (or *pressure*) *drag*—due to the integrated pressure acting on the body, caused by flow separation
- *Interference drag*—due to the proximity of two (or more) bodies (e.g., wing and fuselage)
- *Trim drag*—due to aerodynamic forces required to trim the airplane about the center of gravity
- *Profile drag*—the sum of skin-friction and pressure drag for an airfoil section
- *Parasite drag*—the sum of skin-friction and pressure drag for an aircraft
- *Base drag*—the pressure drag due to a blunt base or afterbody
- *Wave drag*—due to shock wave energy losses

In spite of these complexities, numerous straightforward estimation methods exist for predicting the parasite drag of aircraft, most of which use a combination of theoretical and empirical (called semi-empirical) approaches.

While the building block methods for predicting skin-friction drag have been presented in Sections 4.7.1 and 5.4.3, there are a variety of methods for applying skin-friction prediction methods to determine total aircraft drag. Every aerodynamics group at each aircraft manufacturer has different methods for estimating subsonic aircraft drag. The basic approaches, however, are probably quite similar:

1. Estimate an equivalent flat-plate skin-friction coefficient for each component of the aircraft (wing, fuselage, stabilizers, etc.)
2. Correct the skin-friction coefficient for surface roughness
3. Apply a form factor correction to each component's skin-friction coefficient to take into account supervelocities (velocities greater than free stream around the

component) as well as pressure drag due to flow separation to obtain a parasite-drag coefficient

4. Convert each corrected skin-friction coefficient into an aircraft drag coefficient for that component
5. Sum all aircraft parasite-drag coefficients to obtain a total aircraft drag coefficient

Of course, this approach does not take into account a variety of sources of aircraft drag, including:

- Interference drag (the drag of one component because it is in the vicinity of another component, like a wing attached to a fuselage)
- Excrescence drag (the drag due to various small drag-producing protuberances, including rivets, bolts, wires, etc.)
- Engine installation drag
- Drag due to control surface gaps
- Drag due to fuselage upsweep
- Landing gear drag

The total aircraft drag coefficient is defined as:

$$C_D \equiv \frac{D}{q_\infty S_{\text{ref}}} \tag{5.33}$$

where S_{ref} is usually the wing planform area for an airplane. When the airplane drag coefficient is defined in this way, the term "drag count" refers to a drag coefficient of $C_D = 0.0001$ (e.g., a drag coefficient of $C_D = 0.0100$ would be 100 drag counts); many aerodynamicists refer to drag counts rather than the drag coefficient.

The following approach to determining subsonic aircraft parasite drag is due to Shevell (1989) and also is presented in Schaufele (2000). This approach assumes that each component of the aircraft contributes to the total drag without interfering with each other. While this is not true, the approach provides a good starting point for the estimation of drag. The zero-lift drag coefficient for subsonic flow is obtained by:

$$C_{D_0} = \sum_{i=1}^{N} \frac{K_i \overline{C}_{f_i} S_{\text{wet}_i}}{S_{\text{ref}}} \tag{5.34}$$

where N is the total number of aircraft components making up the aircraft (wing, fuselage, stabilizers, nacelles, pylons, etc.), K_i is the form factor for each component, $\overline{C}_{f_i}$ is the total skin-friction coefficient for each component, S_{wet_i} is the wetted area of each component, and S_{ref} is the aircraft reference area (there is only one reference area for the entire aircraft, which is usually the wing planform area).

Most aircraft components fall into one of two geometric categories: (1) wing-like shapes and (2) body-like shapes. Because of this, there are two basic ways to find the equivalent flat-plate skin-friction coefficient for the various aircraft components.

Wing Method. A wing with a trapezoidal planform (as shown in Fig. 5.19) can be defined by a root chord c_r, a tip chord c_t, a leading-edge sweep Λ, and a semi-span $b/2$. The difficulty comes in applying the flat-plate skin-friction analysis to a wing

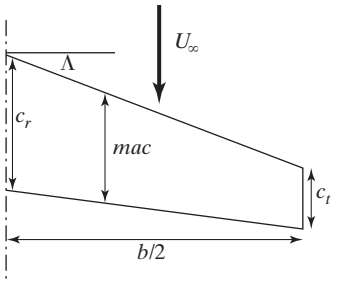

Figure 5.19 Geometry of a wing with a trapezoidal planform.

with variable chord lengths along the span. Since the total skin-friction coefficient is a function of the Reynolds number at the "end of the plate", each spanwise station would have a different Reynolds number, and hence, a different total skin-friction coefficient.

It would be possible to perform a double integration along the chord and span of the wing to obtain a total skin-friction coefficient for the wing; however, an easier approach is to find an equivalent rectangular flat plate using the mean aerodynamic chord (mac) of the wing as the appropriate flat-plate length. The mean aerodynamic chord, defined in Section 5.3, can be calculated using the following formulation which is valid for a trapezoidal wing:

$$mac = \frac{2}{3}\left(c_r + c_t - \frac{c_r c_t}{c_r + c_t}\right) = \frac{2}{3}c_r\left(\frac{\lambda^2 + \lambda + 1}{\lambda + 1}\right) \tag{5.35}$$

where $\lambda = c_t/c_r$ is the taper ratio of the wing. The mean aerodynamic chord can then be used to define a "mean" Reynolds number for the wing:

$$\mathrm{Re}_L = \frac{\rho_\infty U_\infty mac}{\mu_\infty} \tag{5.36}$$

It is important to remember that if a portion of the "theoretical" wing is submerged in the fuselage of the aircraft, then that portion of the wing should not be included in the calculation—the mean aerodynamic chord should be calculated using the root chord at the side of the fuselage!

Now the total skin-friction coefficient for the wing can be found using the Prandtl-Schlichting formula, including the correction for laminar flow (assuming transition takes place at $\mathrm{Re}_{x,\,tr} = 500{,}000$), from equation (4.87):

$$\overline{C}_f = \frac{0.455}{(\log_{10}\mathrm{Re}_L)^{2.58}} - \frac{1700}{\mathrm{Re}_L} \tag{5.37}$$

Before proceeding any farther, the skin-friction coefficient should be corrected for surface roughness and imperfections. Various approaches exist for making this correction, some of which include small imperfections in the wing surface, such as rivets, seams, and gaps. In general, there is no straightforward method for correcting for surface roughness, so an empirical correction is often used, based on the actual flight test data of aircraft compared with the drag prediction using the approach outlined in this section. Most subsonic aircraft have a 6% to 9% increase in drag due to surface roughness, rivets, etc. [Kroo (2003)]. However, Kroo reports that, "carefully built laminar flow, composite aircraft may achieve a lower drag associated with roughness, perhaps as low as 2 to 3%."

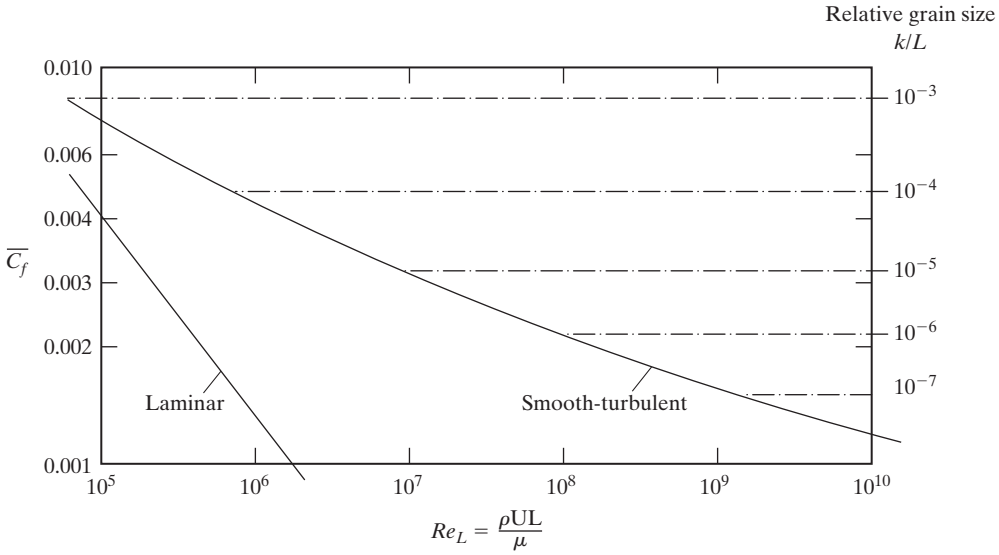

Figure 5.20 Effect of surface roughness on skin-friction drag [roughness curves from Gollos (1953)].

The key factor in correcting for surface roughness is the relative height of the imperfections in the surface compared with the size of the laminar (or viscous) sublayer of the boundary layer (see Fig. 4.15 for details about the laminar sublayer). The laminar sublayer usually is contained within a distance from the wall of $y^+ \approx 10$, so if the equivalent "sand" grain roughness of the surface is contained within the laminar sublayer, than the surface is aerodynamically "smooth." As the sand grain roughness, k, increases in size, the skin friction will increase accordingly, as shown in Fig. 5.20, and eventually remains at a constant value with increasing Reynolds number. Since the thickness of the laminar sublayer actually decreases with Reynolds number, the impact of surface roughness is increased at higher Reynolds numbers, since the roughness will emerge from the sublayer and begin to impact the characteristics of the turbulent boundary layer, as discussed in Hoerner (1965). Notice that as the relative grain size increases, the skin-friction coefficient can deviate from the smooth turbulent value by factors as high as 300%. Keeping aerodynamic surfaces as smooth as possible is essential to reducing skin-friction drag! Equivalent sand grain roughness for different surfaces varies from approximately $k = 0.06 \times 10^{-3}$ in. for a polished metal surface, to $k = 2 \times 10^{-3}$ in. for mass production spray paint, and to $k = 6 \times 10^{-3}$ in. for galvanized metal [Blake (1998)].

Now that the skin-friction coefficient has been found (including a roughness correction), the form factor for the wing can be found from Fig. 5.21. This figure is based on empirical information and shows the correction to the skin-friction coefficient to take into account supervelocities (flow acceleration over the wing which alters the boundary layer properties which are assumed to be based on free-stream levels) and pressure drag due to flow separation. Thicker wings have higher form factors and hence higher drag, while thinner wings have lower form factors and lower drag. An increase in wing sweep also tends to reduce the form factor and the drag coefficient.

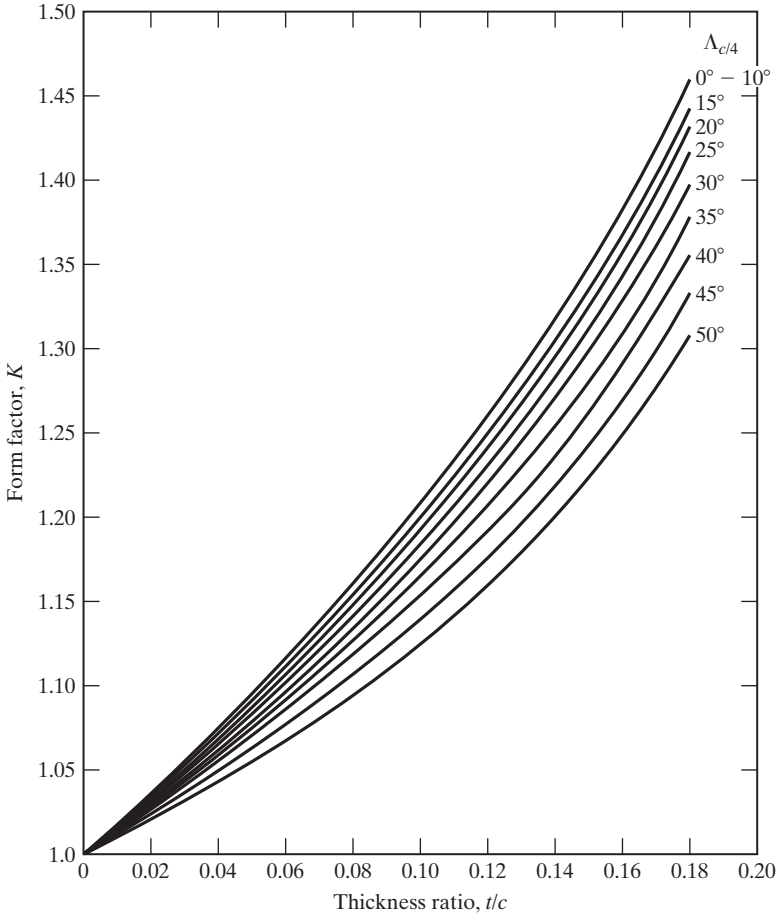

Figure 5.21 Wing form factor as a function of wing thickness ratio and quarter-chord sweep angle [from Shevell (1989)].

Finally, the wetted area of the wing can be calculated using the following relationship from Kroo (2003):

$$S_{\text{wet}} \approx 2.0(1 + 0.2t/c)S_{\text{exposed}} \tag{5.38}$$

where S_{exposed} is the portion of the wing planform that is not buried within the fuselage. The thickness factor in the previous equation takes into account the slight increase in flat-plate area due to the fact that the wing thickness increases the arc length of the wing chord. The exposed area is doubled to take into account the top and bottom of the wing.

The wing parasite-drag coefficient now can be calculated from equation (5.34) as:

$$C_{D_0} = K\overline{C}_f S_{\text{wet}}/S_{\text{ref}} \tag{5.34}$$

Fuselage Method. Since the fuselage has a single length (as shown in Fig. 5.22), the calculation of the skin-friction coefficient is simpler than for a wing. First, find the

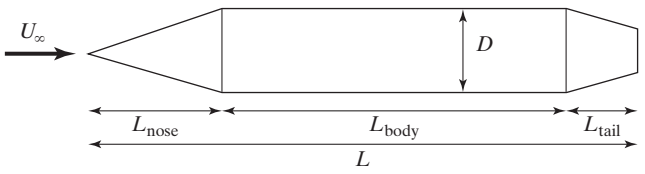

Figure 5.22 Geometry of a fuselage with circular cross sections.

Reynolds number at the end of the fuselage as:

$$\text{Re}_L = \frac{\rho_\infty U_\infty L}{\mu_\infty} \tag{5.30}$$

and calculate the total skin-friction coefficient using equation (5.37). The skin-friction coefficient also can be corrected for surface roughness using the same approximation as discussed for the wing.

The fuselage form factor is a function of the fineness ratio of the body, which is defined as the length of the fuselage divided by the maximum diameter of the fuselage, L/D (not to be confused with the lift-to-drag ratio). The form factor can be found in Fig. 5.23

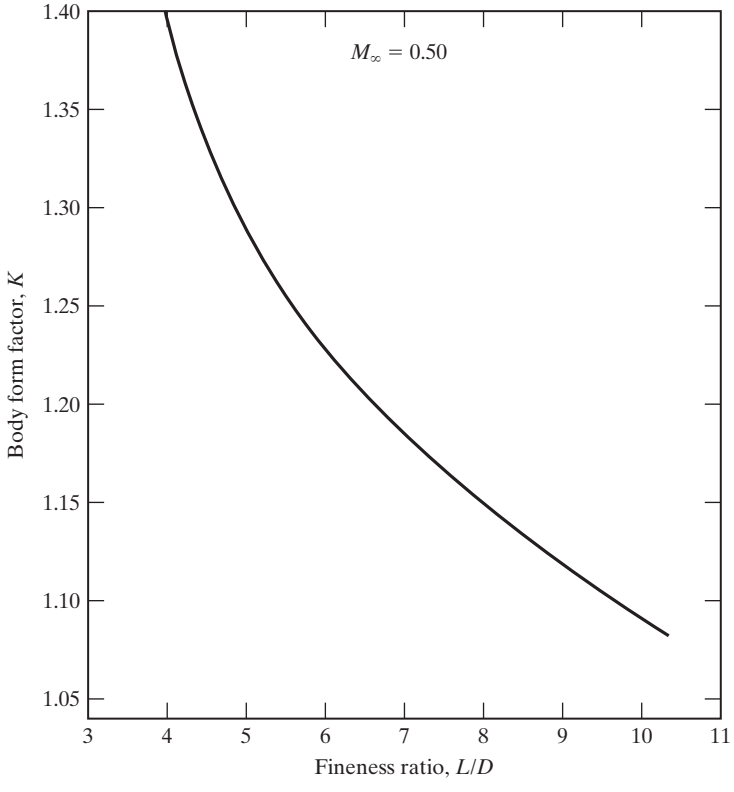

Figure 5.23 Body form factor as a function of fuselage fineness ratio [from Shevell (1989)].

and shows that the more long and slender the fuselage, the smaller the form factor, and the smaller the drag coefficient increment due to separation. Conversely, a short, bluff body would have a high form factor due to large amounts of supervelocities and flow separation, and hence a higher drag coefficient.

The total wetted area of the fuselage can be calculated as:

$$S_{\text{wet}} \approx S_{\text{wet}_{\text{nose}}} + S_{\text{wet}_{\text{body}}} + S_{\text{wet}_{\text{tail}}} \tag{5.39}$$

where the wetted areas can be found assuming that the various portions of the fuselage can be approximated as cones, cylinders, and conical sections [from Kroo (2003)]:

$$\begin{aligned} S_{\text{wet}_{\text{nose}}} &= 0.75\pi DL_{\text{nose}} \\ S_{\text{wet}_{\text{body}}} &= \pi DL_{\text{body}} \\ S_{\text{wet}_{\text{tail}}} &= 0.72\pi DL_{\text{tail}} \end{aligned} \tag{5.40}$$

These formulas do not double the exposed area of the fuselage, since air only flows over one side of the fuselage (namely, hopefully, the outside of the fuselage!).

Total Aircraft Parasite Drag. Now that the drag coefficient for the wing and fuselage have been calculated, the remaining components of the aircraft must be included, as shown in Fig. 5.24. Most of the remaining components can be approximated

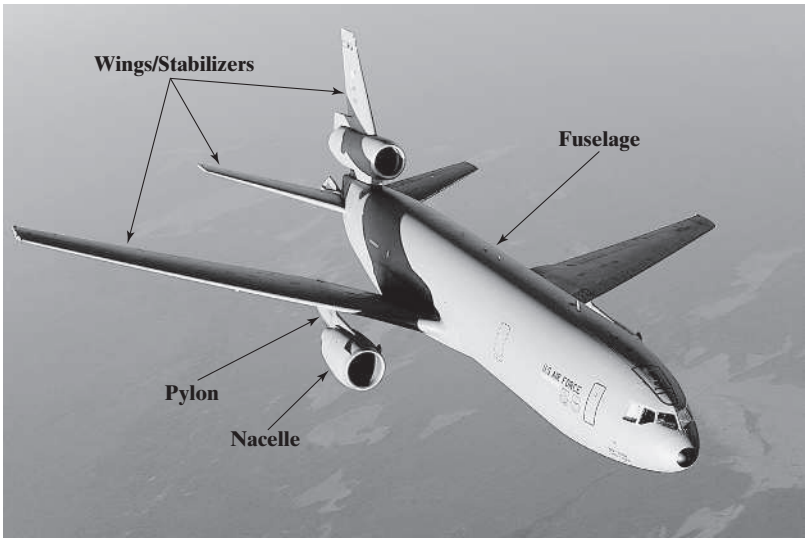

Figure 5.24 Aircraft showing the major components that contribute to drag (U.S. Air Force photo by Staff Sgt Aaron Allmon).

as either wing-like surfaces or fuselage-like surfaces, using the same methods as have been described previously. For example:

- *Vertical* and *horizontal stabilizers*—use wing method
- *Engine pylons*—use wing method
- *Engines nacelles*—use fuselage method
- *Blade antenna*—use wing method

This approach can be continued for the vast majority of the aircraft. Now the total aircraft zero-lift drag coefficient can be found by using equation (5.34) as:

$$C_{D_0} = \sum_{i=1}^{N} \frac{K_i \overline{C}_{f_i} S_{\text{wet}_i}}{S_{\text{ref}}}$$

The remaining drag components are due to smaller affects, such as excrescence drag, base drag, and interference drag. Some of these drag components would be extremely difficult (and time consuming) to calculate. In spite of this, semi-empirical and empirical methods for estimating the drag of rivets, bolts, flap gaps, and other small protuberances can be found in Hoerner's book on drag [Hoerner (1965)]. It is probably more expedient to use an empirical correction for the remainder of the drag, which is often done at aircraft manufacturers based on historical data from previous aircraft [Shevell (1989)].

EXAMPLE 5.5: Estimate the subsonic parasite-drag coefficient

This example will show how the subsonic parasite-drag coefficient for the F-16 can be estimated at a specific altitude. It is important to note that, unlike other aerodynamic coefficients, the subsonic drag coefficient is a function of altitude and Mach number, since the Reynolds number over the surfaces of the aircraft will vary with altitude and Mach. This example will assume that the aircraft is flying at an altitude of 30,000 ft and has a Mach number of 0.4 (to match available flight test data). The theoretical wing area of the F-16 is 300 ft^2, which will serve as the reference area for the aircraft: $S_{\text{ref}} = 300\ ft^2$.

Solution: The first task is to estimate the wetted area of the various surfaces of the aircraft. A good estimate of these areas has been completed in Brandt et al. (2004) and is reproduced here in Fig. 5.25 and Tables 5.2 and 5.3. The aircraft

TABLE 5.2 F-16 Wing-Like Surface Wetted Area Estimations [data from Brandt et al. (2004)]

Surface	*Span,* ft	c_r, ft	c_t, ft	*t/c*	S_{wet}, ft^2
Wing (1 and 2)	12	14	3.5	0.04	419.4
Horizontal tail (3 and 4)	6	7.8	2	0.04	117.5
Strake (5 and 6)	2	9.6	0	0.06	38.6
Inboard vertical tail (7)	1.4	12.5	6	0.10	26.3
Outboard vertical tail (8)	7	8	3	0.06	77.3
Dorsal fins (9 and 10)*	1.5	5	3	0.03	23.9

*not shown in Fig. 5.25

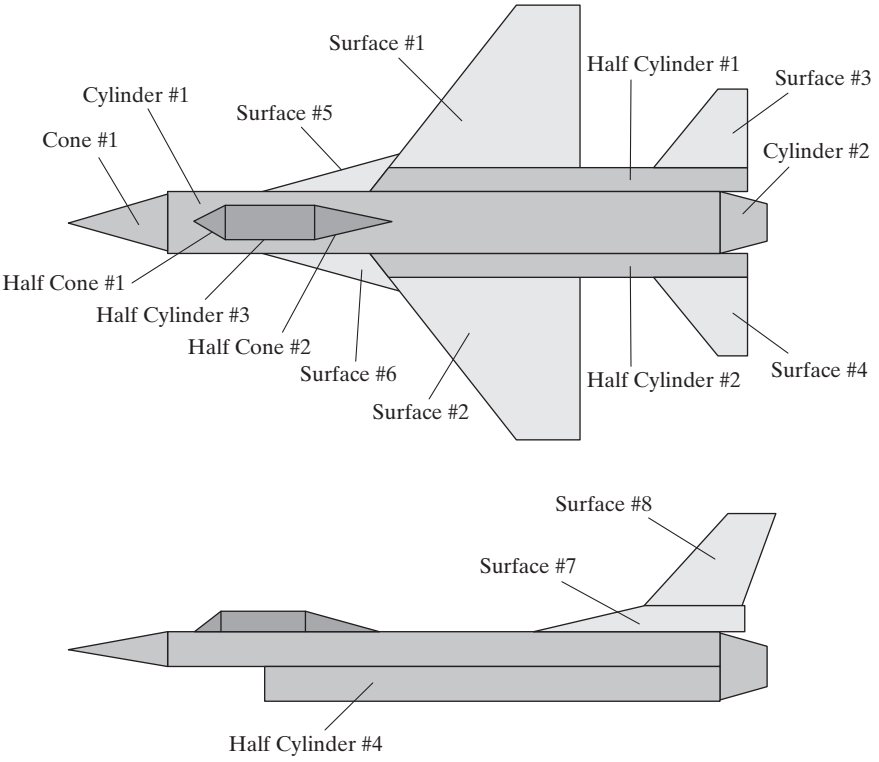

Figure 5.25 F-16 geometry approximated by simple shapes [from Brandt et al. (2004)].

is approximated with a series of wing-like and fuselage-like shapes, as shown in Fig. 5.25. The wetted area for these simplified geometric surfaces is approximated using equations (5.38) and (5.40).

This simplified approximation yields a total wetted area of 1418 ft^2, which is very close to the actual wetted area of the F-16, which is 1495 ft^2

TABLE 5.3 F-16 Fuselage-Like Surface Wetted Area Estimations [data from Brandt et al. (2004)]

Surface	*Length,* ft	*Height,* ft	*Width,* ft	S_{wet}, ft^2	*Net* S_{wet}, ft^2
Fuselage (cylinder 1)	39	2.5	5	551.3	551.3
Nose (cone 1)	6	2.5	5	42.4	42.4
Boattail (cylinder 2)	4	6	6	62.8	62.8
Side (half cylinder 1 and 2)	24	0.8	1	67.9	29.5
Canopy (half cylinder 3)	5	2	2	15.7	5.7
Engine (half cylinder 4)	30	2.5	5	180	32.1
Canopy front (half cone 1)	2	2	2	3.1	1.1
Canopy rear (half cone 2)	4	2	2	6.3	2.3

[Brandt et al. (2004)]. Now that these wetted areas have been obtained, the parasite-drag coefficient for each surface can be estimated.

Wing. First, estimate the mean aerodynamic chord of the wing as:

$$mac = \frac{2}{3}\left(c_r + c_t - \frac{c_r c_t}{c_r + c_t}\right) = \frac{2}{3}\left(14\text{ ft} + 3.5\text{ ft} - \frac{(14\text{ ft})(3.5\text{ ft})}{(14 + 3.5)\text{ ft}}\right) = 9.800\text{ ft}$$

and use the *mac* to calculate the Reynolds number for the equivalent rectangular wing as

$$\text{Re}_L = \frac{\rho_\infty U_\infty mac}{\mu_\infty} = \frac{(0.000891\text{ slug/ft}^3)(397.92\text{ ft/s})(9.800\text{ ft})}{3.107 \times 10^{-7}\text{ lb} - \text{s/ft}^2} = 11.18 \times 10^6$$

Finally, the total skin-friction coefficient for the wing is calculated as:

$$\overline{C}_f = \frac{0.455}{(\log_{10}\text{Re}_L)^{2.58}} - \frac{1700}{\text{Re}_L} = \frac{0.455}{(\log_{10} 11.18 \times 10^6)^{2.58}} - \frac{1700}{11.18 \times 10^6} = 0.00280$$

Assume for the sake of this example that the wing is aerodynamically smooth, so no roughness correction will be applied. However, a form factor correction should be performed. From Fig. 5.21 for a leading-edge sweep of 40° and a thickness ratio of 0.04, $K = 1.06$ and the parasite drag coefficient is:

$$C_{D_0} = \frac{K\overline{C}_f S_{\text{wet}}}{S_{\text{ref}}} = \frac{(1.06)(0.00280)(419.4\text{ ft}^2)}{300\text{ ft}^2} = 0.00415$$

The other wing-like components of the F-16 have had similar analysis performed, resulting in the zero-lift drag predictions presented in Table 5.4.

Fuselage.

$$L = L_{\text{nose}} + L_{\text{fuselage}} + L_{\text{boattail}} = 6 + 39 + 4 = 49.0\text{ ft}$$

$$\text{Re}_L = \frac{(0.000891\text{ slug/ft}^3)(397.92\text{ ft/s})(49.0\text{ ft})}{3.107 \times 10^{-7}\text{ lb} - \text{s/ft}^2} = 55.91 \times 10^6$$

$$\overline{C}_f = \frac{0.455}{(\log_{10} 55.91 \times 10^6)^{2.58}} - \frac{1700}{55.91 \times 10^6} = 0.00228$$

TABLE 5.4 F-16 Wing-Like Surface Zero-Lift Drag Estimations

Surface	*mac, ft*	$Re_L(\times 10^{-6})$	$\overline{C}_f$	*K*	C_{D_0}
Wing (1 and 2)	9.800	11.18	0.00280	1.06	0.00415
Horizontal tail (3 and 4)	5.472	6.568	0.00296	1.06	0.00123
Strake (5 and 6)	6.400	7.303	0.00293	1.04	0.00039
Inboard vertical tail (7)	9.631	10.99	0.00280	1.04	0.00026
Outboard vertical tail (8)	5.879	6.708	0.00295	1.08	0.00082
Dorsal Fins (9 and 10)	4.083	4.660	0.00304	1.04	0.00025
Total					0.00710

TABLE 5.5 F-16 Fuselage-Like Surface Zero-Lift Drag Estimations

Surface	*Length, ft*	$Re_L(\times 10^{-6})$	$\overline{C}_f$	*K*	C_{D_0}
Fuselage + nose + boattail	49.0	55.91	0.00228	1.05	0.00524
Side (half cylinder 1 and 2)	24.0	27.39	0.00251	1.01	0.00025
Canopy (front + center + rear)	11.0	12.55	0.00276	1.25	0.00011
Engine (half cylinder 4)	30.0	34.23	0.00244	1.15	0.00030
Total					0.00590

From Fig. 5.23, for a fineness ratio of $L/D = 49.0\,\text{ft}/[0.5*(2.5 + 5.0)\text{ft}] = 13.067$, $K = 1.05$ (requires some extrapolation from the graph) and the parasite drag coefficient is:

$$C_{D_0} = \frac{K\overline{C}_f S_{\text{wet}}}{S_{\text{ref}}} = \frac{(1.05)(0.00228)(656.5\,\text{ft}^2)}{300\,\text{ft}^2} = 0.00524$$

The other fuselage-like components of the F-16 have had similar analysis performed, resulting in the zero-lift drag predictions presented in Table 5.5.

The total aircraft zero-lift drag coefficient (assuming aerodynamically smooth surfaces) is:

$$C_{D_0} = C_{D_{0(\text{Wings})}} + C_{D_{0(\text{Fuselages})}} = 0.00710 + 0.00590 = 0.01300$$

Since the total wetted area estimate from this analysis was 5.4% lower than the actual wetted area of the F-16 (something which could be improved with a better representation of the aircraft surfaces, such as from a CAD geometry), it would be reasonable to increase the zero-lift drag value by 5.4% to take into account the simplicity of the geometry model. This would result in a zero-lift drag coefficient of $C_{D_0} = 0.01370$.

Again, this result assumes that the surfaces are aerodynamically smooth, that there are no drag increments due to excrescence or base drag, and that there is no interference among the various components of the aircraft. If we assume that the other components of drag account for an additional 10%, then our final estimate for the zero-lift drag coefficient would be $C_{D_0} = 0.0151$; a 15% increase over $C_{D_0} = 0.0137$ would increase the estimate to $C_{D_0} = 0.0158$. Initial flight test data for the F-16 showed that the subsonic zero-lift drag coefficient varied between $C_{D_0} = 0.0160$ and $C_{D_0} = 0.0190$ after correcting for engine effects and the presence of missiles in the flight test data [Webb et al. (1977)]. These results should be considered quite good for a fairly straightforward method that can be used easily on a spreadsheet.

5.5 WINGS OF FINITE SPAN

At this point, we need to determine the aerodynamics of a wing (a three-dimensional shape) based on our knowledge of airfoils (a two-dimensional shape). Unfortunately, there are a number of non-two-dimensional aspects of the flow around wings which

lead to different aerodynamic characteristics than airfoil aerodynamics. For a wing of finite span that is generating lift, the pressure differential between the lower surface and the upper surface causes a spanwise flow. As we will discuss in Chapter 7, the spanwise variation of lift for the resultant three-dimensional flow field produces a corresponding distribution of streamwise vortices. These streamwise vortices in turn create a downwash, which has the effect of "tilting" the undisturbed air, reducing the effective angle of attack. In other words, the airfoils making up the wing are not flying at the angle of attack that the wing seems to be flying at. As a result of the induced downwash velocity, the lift generated by the airfoil section of a finite-span wing which is at the geometric angle of attack α is less than that for the same airfoil section of an infinite-span airfoil configuration at the same angle of attack. Furthermore, the trailing vortex system produces an additional component of drag, known as the *vortex drag* (or the *induced drag*).

5.5.1 Lift

The typical lift curve for a three-dimensional wing composed of a given airfoil section is compared in Fig. 5.26 with that for a two-dimensional airfoil having the same airfoil section. Notice that the lift-curve slope for the three-dimensional wing (which is represented by the symbol C_{L_α}) is considerably less than the lift-curve slope for an unswept, two-dimensional airfoil (which is represented by the symbol C_{l_α}). Recall that a lift-curve slope of approximately 0.1097 per degree is typical for an unswept two-dimensional airfoil, as discussed in Section 5.4.1. As we will find out in Chapter 7, the lift-curve slope for an ideal three-dimensional unswept wing (C_{L_α}) is:

$$C_{L_\alpha} = a = \frac{C_{l_\alpha}}{1 + \dfrac{C_{l_\alpha}}{\pi AR}} = \frac{a_0}{1 + \dfrac{a_0}{\pi AR}} \tag{5.41}$$

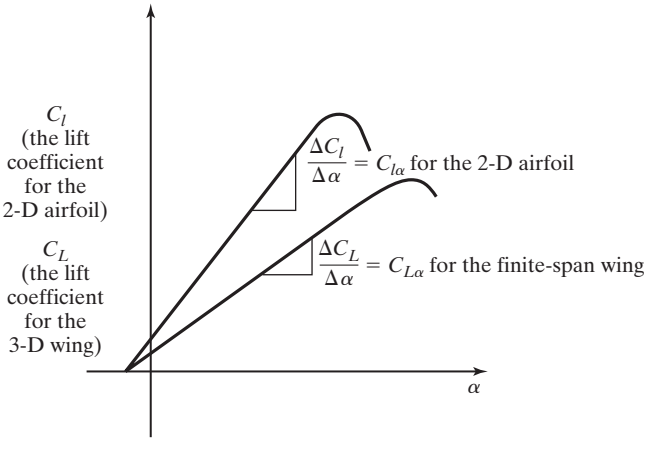

Figure 5.26 Comparison of the lift-curve slope of a two-dimensional airfoil with that for a finite-span wing.

where a is the lift-curve slope of the wing and a_0 is the lift-curve slope of the airfoil (typically $a_0 = 2\pi/\text{rad}$), and the units for the lift-curve slope is 1/rad. In order to find the lift-curve slope in units of 1/deg, either convert the 1/rad result from equation (5.41) or use the formulation $a = \dfrac{a_0}{1 + 57.3a_0/\pi AR}$ and input the airfoil lift-curve slopes in units of 1/deg. Notice that the wing lift-curve slope approaches the airfoil lift-curve slope, $C_{L_\alpha} \rightarrow C_{l_\alpha}$, as the aspect ratio increases, $AR \rightarrow \infty$. In other words, a low-speed wing is most efficient with high aspect ratios. Typically, however, wings are limited in aspect ratio by structural constraints. You can see from Table 5.1 that four-place single engine aircraft, which fly at relatively low speeds, have aspect ratios in the range $6.3 < AR < 7.6$, which is a very small variation. Commercial jetliners and transports have slightly higher aspect ratios, $6.9 < AR < 8.9$, even though they fly at high subsonic speeds. In contrast, high-speed aircraft, which fly supersonically, have very low aspect ratios, $1.7 < AR < 4.0$, for reasons we will discuss in Chapter 11.

Aerodynamics Concept Box: The Design of the C-17 Wing

While the C-17 wing was designed using state-of-the-art aerodynamic prediction tools available at the time (the wing was designed in the early 1980s), there were numerous constraints on the design for non-aerodynamic reasons. This is true of almost any aerodynamic design, as

C-17 with wing flaps and leading-edge devices extended and winglets visible (U.S. Air Force photo by Abner Guzman)

we discussed at the beginning of the chapter. Sometimes the constraints are defined by the "customer" or regulations (in the case of the C-17 the customer was the U.S. Air Force, but for commercial aircraft the customer is the airlines, as constrained by governmental regulations), and sometimes they are determined as part of the design process. Taking a look at some of the design issues related to the wing of the C-17 will help you understand these difficulties.

The C-17 wing was constrained in wing span because the U.S. Air Force did not want the C-17 to have a longer span than the C-141 (due to limitations of aircraft parking space on tarmacs; commercial airliners have a similar constraint due to the size of gates at most airports). Once the span limit was defined and the wing area requirements were determined by the C_{Lmax} performance at low speeds with the externally blown flap (EBF) technology (the landing C_{Lmax} with externally blown flaps was approximately 4.0), then the aspect ratio was determined to be 7.2 (a value which falls in the low end of the range for commercial jetliners and transports, as can be seen in Table 5.1). The maximum lift coefficient for an EBF system could have been higher if high-extension Fowler flaps had been used, but in order to save on weight, cost, and maintenance a hinged flap was used (similar to the flaps on the DC-9 and DC-10). The C_{Lmax} of the flaps without EBF was approximately 2.8 with 43 degrees of flap setting, but this level of maximum lift coefficient would not have allowed the C-17 to take off and land within the required runway length of less than 3000 feet [Van't Riet (1989)].

Other constraints on the aerodynamic design included the requirement that winglets could only be used above the wing so that service trucks would not be able to hit any parts of the winglet while driving under the wing. This led to the winglet design as shown above and in Fig. 5.1, but limited the type and efficiency of wing-tip devices that could be used (see Fig. 13.27 for examples of other wing-tip devices). Also, at the time the wing was being designed, inverse transonic potential flow numerical predictions (computer codes that find the geometry for a given pressure distribution) were limited to two-dimensional airfoils; three-dimensional transonic predictions could only be done for a specified geometry (a "direct" approach). The C-17 uses aft-loaded supercritical airfoils to reduce wave drag at high subsonic Mach numbers (which increases the critical Mach number, as we will discuss in Chapter 11). Most of the airfoil sections were designed in two dimensions using the inverse approach, and then the three-dimensional wing was computationally assembled and analyzed using the "direct" potential flow approach. Iterations of the wing geometry (especially the inboard sections) were done to obtain swept isobars of pressure, but there was a constraint on the curvature allowed for the wing sections [Pres Henne, personal communication (2012)]. During manufacturing, the wing skins were "draped" by performing machining while the sheets were flat (not pre-shaped by shot peening or forming) which greatly reduced the manufacturing cost of the wing. However, the draped wings had a spanwise radius of curvature limit of 5000 inches, which meant that not all possible shapes could be manufactured with this method. Therefore, if the numerical predictions led to wing with a low local radius of curvature, the design was limited by the manufacturing process.

Add into these requirements the integration of propulsion, fuel, electrical, and hydraulic systems, and you have quite a delicate balancing act. If all of this seems complicated . . . . it is! Designing a modern airplane is a complex balancing act between many constraints, and finding a wing that can attain all requirements necessarily means that the wing will not be fully optimized for aerodynamics purposes.

EXAMPLE 5.6: An F-16C in steady, level, unaccelerated flight

The pilot of an F-16 wants to maintain a constant altitude of 30,000 ft flying at idle power. Remember from the discussion at the start of the chapter, for flight in a horizontal plane (i.e., constant altitude), where the angles are small, the lift must balance the weight of the aircraft, which is 23,750 pounds. Therefore, as the vehicle slows down, the pilot must increase the angle of attack of the aircraft in order to increase the lift coefficient to compensate for the decreasing velocity (and dynamic pressure). Use the lift curves for the F-16 aircraft, which were provided by the General Dynamics Staff (1976) and are presented in Fig. 5.27 for several Mach numbers. Assume that the lift curve for $M = 0.2$ is typical of that for incompressible flow, which for the purposes of this problem will be Mach numbers of 0.35, or less. Prepare a graph of the angle of attack as a function of the air speed in knots (nautical miles per hour) as the aircraft decelerates from a Mach number of 1.2 until it reaches its minimum flight speed. The minimum flight speed (i.e., the stall speed) is the velocity at which the vehicle must fly at its limit angle of attack in order to generate sufficient lift to balance the aircraft's weight. The wing reference area S is 300 ft^2.

Solution: We can first calculate the lower limit for the speed range specified, that is the stall velocity. Since the aircraft is flying in a horizontal plane (constant altitude), the lift is equal to the weight, and:

$$W = L = C_L q_\infty S = C_L(\tfrac{1}{2}\rho_\infty U_\infty^2)S \qquad \textbf{(5.42a)}$$

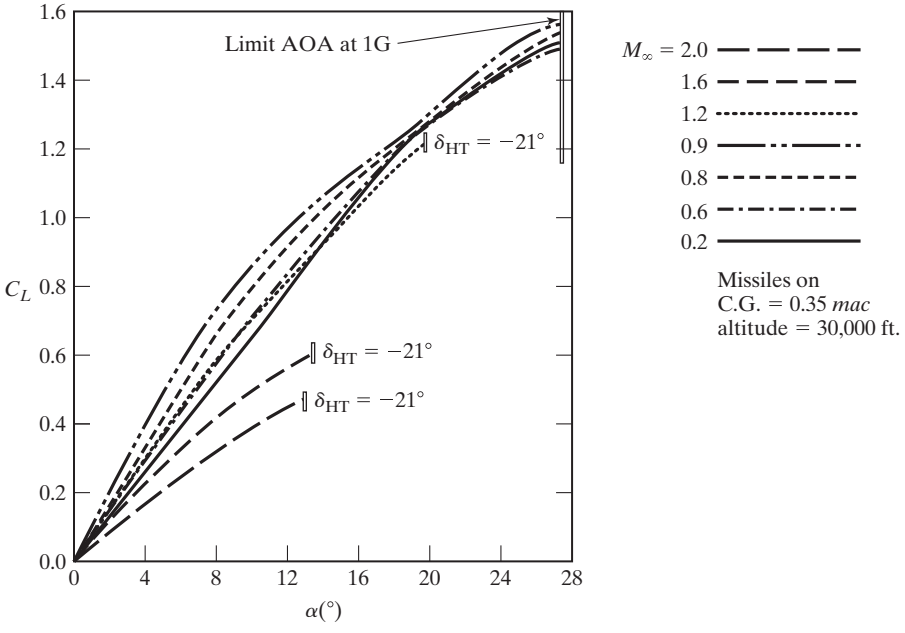

Figure 5.27 Trimmed lift coefficient as a function of the angle of attack for the F-16C. δ_{HT} is deflection of the horizontal tail [provided by the General Dynamics Staff (1976)].

In order to compensate for the low dynamic pressure that occurs when flying at the stall speed (U_{stall}), the lift coefficient must be the maximum attainable value, $C_{L_{\max}}$. Therefore:

$$W = L = C_{L_{\max}} q_\infty S = C_{L_{\max}} (\tfrac{1}{2}\rho_\infty U_{\text{stall}}^2) S$$

Solving for U_{stall}:

$$U_{\text{stall}} = \sqrt{\frac{2W}{\rho_\infty C_{L_{\max}} S}}$$

Referring to Fig. 5.27, the maximum value of the lift coefficient (assuming it occurs at an incompressible flow condition) is 1.57, which corresponds to the stall angle of attack. From Table 1.2b, the free-stream density at 30,000 ft is 0.0008907 slugs/ft^3, or 0.0008907 lbf s^2/ft^4, and:

$$U_{\text{stall}} = \sqrt{\frac{2(23750\ \text{lbf})}{(0.0008907\ \text{lbf s}^2/\text{ft}^4)(1.57)(300\ \text{ft}^2)}}$$

$$U_{\text{stall}} = 336.5\ \text{ft/s} = 199.2\ \text{knots}$$

Therefore, the minimum velocity at which the weight of the F-16 is balanced by the lift at 30,000 ft is 199.2 knots with the aircraft at an angle of attack of 27.5°. The corresponding Mach number is:

$$M_{\text{stall}} = \frac{U_{\text{stall}}}{a} = \frac{336.5\ \text{ft/s}}{994.85\ \text{ft/s}} = 0.338$$

To calculate the lift coefficient as a function of Mach number from $M_\infty = 1.2$ down to the stall value for the Mach number, we need to find the lift coefficient:

$$C_L = \frac{2W}{\rho_\infty (M_\infty a_\infty)^2 S} \qquad \textbf{(5.42b)}$$

and the velocity in knots is given by:

$$U_\infty = M_\infty a_\infty (\text{ft/s}) \left(\frac{0.59209\ \text{knots}}{\text{ft/s}} \right)$$

where U_∞ has units of knots if a_∞ has units of ft/s. The values obtained using these equations and using the lift curves presented in Fig. 5.27 to determine the angle of attack required to produce the required lift coefficient at a given Mach number are presented in the following table.

M_∞ (—)	C_L (—)	α (°)	U_∞ (ft/s)	U_∞ (knots)
1.2	0.125	1.9	1193.82	706.8
0.9	0.222	2.4	895.37	530.1
0.8	0.281	3.5	795.88	471.2
0.6	0.499	6.2	596.91	353.4
0.338	1.57	27.5	336.50	199.2

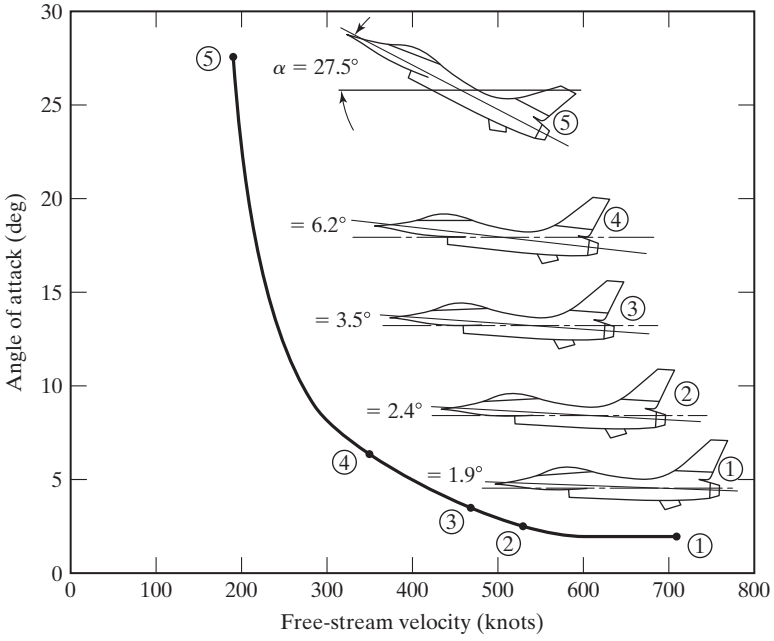

Figure 5.28 Correlation between the angle of attack and the velocity to maintain an F-16C in steady, level, unaccelerated flight.

The correlation between the angle of attack and the velocity (in knots), as determined in this example and as presented in the table, is presented in Fig. 5.28. Notice how rapidly the angle of attack increases toward the stall angle attack in order to generate a lift coefficient sufficient to maintain the altitude as the speed of the F-16 decreases toward the stall velocity. The angle of attack varies much more slowly with velocity at transonic Mach numbers.

5.5.2 Drag

As noted at the start of this section, the three-dimensional flow past a finite-span wing produces an additional component of drag associated with the trailing vortex system. This drag component is proportional to the square of the lift coefficient. In fact, a general expression for the drag acting on a finite-span wing (for which the flow is three dimensional) or on a complete aircraft is given by:

$$C_D = C_{D,\min} + k' C_L^2 + k''(C_L - C_{L,\min})^2 \qquad \textbf{(5.43)}$$

In equation (5.43), k' is a coefficient for the inviscid drag due to lift (which is also known as the induced drag or as the vortex drag). Similarly, k'' is a coefficient for the viscous drag due to lift (which includes the skin-friction drag and the pressure drag associated with the viscous-induced changes to the pressure distribution, such as those due to separation).

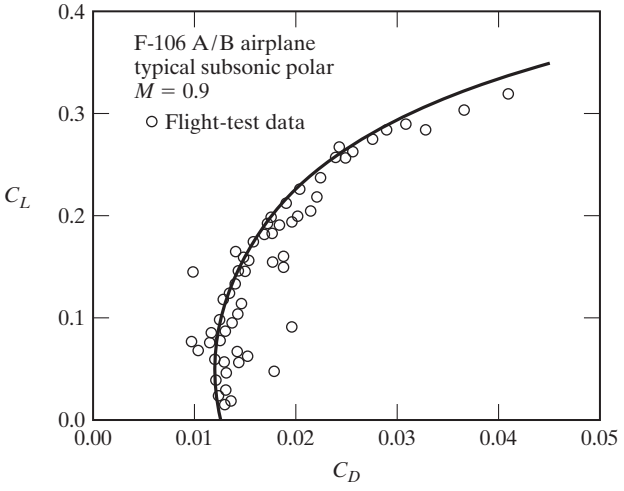

Figure 5.29 Flight data for a drag polar for F-106A/B aircraft at a Mach number of 0.9 [taken from Piszkin et al. (1961)].

Data for a subsonic drag polar are presented in Fig. 5.29 for the F-106A/B aircraft at a Mach number of 0.9. Equation (5.43) correlates these data (the solid line in the figure), which are taken from Piszkin et al. (1961). Note that the minimum drag occurs when C_L is approximately 0.07, so $C_{L,\min}$ is approximately 0.07. Also, $C_{D,\min} \approx 0.012$, which is only slightly lower than C_{D_0}.

Expanding the terms in equation (5.43), we obtain:

$$C_D = (k' + k'')C_L^2 - (2k''C_{L,\min})C_L + (C_{D,\min} + k''C_{L,\min}^2) \tag{5.44}$$

We can rewrite equation (5.44) in the form:

$$C_D = k_1 C_L^2 + k_2 C_L + C_{D_0} \tag{5.45}$$

where:

$$k_1 = k' + k''$$
$$k_2 = -2k''C_{L,\min}$$

and

$$C_{D_0} = C_{D,\min} + k''C_{L,\min}^2$$

Referring to equation (5.45), C_{D_0} is the drag coefficient when the lift is zero, which is also known as the parasite drag coefficient. As noted when discussing Fig. 5.29, $C_{L,\min}$ is relatively small, and k_2 is often neglected. In such cases, we could also assume:

$$C_{D_0} \cong C_{D,\min}$$

which was also noted in Fig. 5.29. Incorporating these observations into equation (5.45), we can rewrite the drag coefficient as:

$$C_D = C_{D_0} + kC_L^2 \tag{5.46}$$

You should note that k_1 has been replaced by k since there is only one constant left. How we account for both the inviscid and the viscous contributions to the lift-related drag will be discussed shortly [(see equation (5.48)].

We can also introduce an additional term to account for the contributions of the compressibility effects to the drag, ΔC_{D_M}. So we finally obtain the expression for the total drag coefficient acting on an airplane:

$$C_D = C_{D_0} + kC_L^2 + \Delta C_{D_M} \tag{5.47}$$

which is valid for our assumptions of $C_{L,\min} \approx 0, k_2 \approx 0$, and $C_{D,\min} \approx C_{D_0}$. In the case where these assumptions are not true, you may need to return to equation (5.45) for modeling drag.

Thus, the total drag for an airplane may be written as the sum of: (1) parasite drag, which is independent of the lift coefficient and therefore exists when the configuration generates zero lift (C_{D_0} or ΔC_{D_p}), (2) the drag associated with lift (kC_L^2), and (3) the compressibility-related effects that are correlated in terms of the Mach number and are known as wave drag (ΔC_{D_M}).

Although the relative importance of the different drag sources depends on the aircraft type and the mission to be flown, approximate breakdowns (by category) for large, subsonic transports are presented in Figs. 5.30 and 5.31. According to Thomas (1985), the greatest contribution arises from turbulent skin-friction drag. The next most significant contribution arises from lift-induced drag, which, when added to skin-friction drag, accounts for about 85% of the total drag of a typical transport aircraft (see Fig. 5.30). Thomas cited the pressure drag due to open separation in the afterbody and other regions, interference effects between aerodynamic components, wave drag due to the compressibility effect at near-sonic flight conditions, and miscellaneous effects, such as roughness effects and leakage, as constituting the remaining 15% (as discussed in Section 5.4.6).

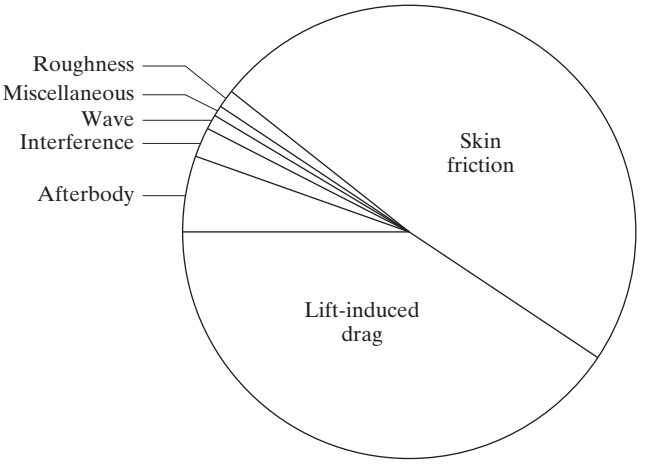

Figure 5.30 Contributions of different drag sources for a typical transport aircraft [from Thomas (1985)].

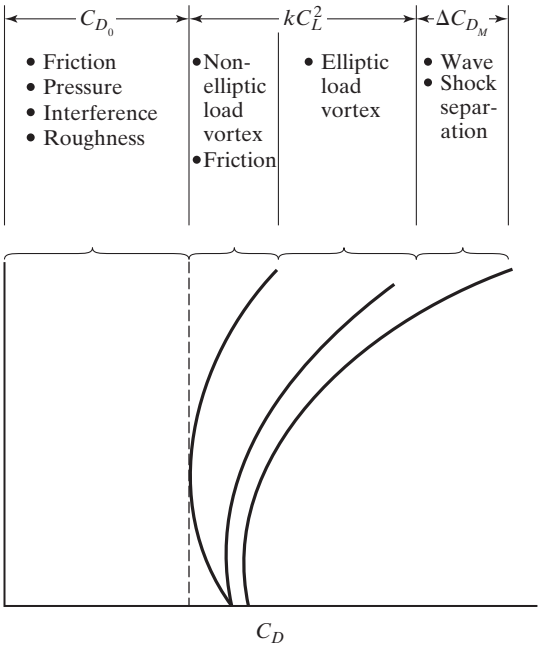

Figure 5.31 Lift/drag polar for a large, subsonic transport [from Bowes (1974); the original version of this material was first published by the Advisory Group for Aerospace Research and Development, North Atlantic Treaty Organization (AGARD, NATO) in Lecture Series 67, May 1974].

Using a slightly different division of the drag-contribution sources, Bowes (1974) presented the lift/drag polar which is reproduced in Fig. 5.31. The majority of the lift-related drag is the vortex drag for an elliptic load distribution at subcritical speeds (i.e., the entire flow is subsonic). Bowes notes that a good wing design should approach an elliptic loading at the design condition, which we will discuss further in Chapter 7.

- ***Zero-lift drag.*** Skin friction and form drag components can be calculated for the wing, tail, fuselage, nacelles, and so on, as discussed in Section 5.4.6. When evaluating the zero-lift drag, you should consider interactions (interference), such as how the growth of the boundary layer on the fuselage reduces the boundary-layer velocities on the wing-root surface, or how the pressure field around the wing changes the flow around the fuselage. Because of the interaction, the wing-root boundary layer is more easily separated in the presence of an adverse pressure gradient. Since the upper wing surface has the more critical pressure gradients, a low wing position on a circular fuselage would be sensitive to this interaction. Adequate filleting and control of the local pressure gradients can minimize the interference effects. Many other interference effects could be considered, but as we said previously, these are typically established from historical trends.

A representative value of C_{D_0} for a complete airplane might be 0.020, of which the wings may account for 50%, the fuselage and the nacelles 40%, and the tail 10%. Since the wing constitutes such a large fraction of the drag, reducing the wing area would reduce C_{D_0} if all other factors are unchanged. Although other factors must be considered, the reasoning implies that an optimum airplane configuration would have a minimum wing surface area and, therefore, highest practical wing loading (W/S).

- ***Drag due to lift.*** The drag due to lift may be represented as:

$$kC_L^2 = \frac{C_L^2}{\pi eAR} \tag{5.48}$$

where e is the airplane efficiency factor (also known as the Oswald efficiency factor). Typical values of the airplane efficiency factor range from 0.6 to 0.95, and are lower than the span efficiency factor we will discuss in Chapter 7. At high lift coefficients (near $C_{L_{\max}}$), e should be changed to account for increased form drag. The deviation of the actual airplane drag from the quadratic correlation, where e is a constant, is significant for airplanes with low aspect ratios and sweepback.

- ***Wave drag.*** Another important drag factor to consider is the effect of compressibility. When the free-stream Mach number is sufficiently large so that regions of supersonic flow exist in the flow field (e.g., free-stream Mach numbers of approximately 0.7, or greater), compressibility-related effects produce an additional drag component, known as wave drag. The correlation of equation (5.47) includes wave drag (i.e., the compressibility effects) as the third term, ΔC_{D_M}. The aerodynamic characteristics of the F-16, which will be incorporated into Example 5.7, illustrate how the drag coefficient increases rapidly with Mach number in the transonic region. As we will discuss in Chapter 9, a designer can delay and/or reduce the compressibility drag rise by using low aspect ratio wings, by sweeping the wings, by using thin airfoils, and/or by using the area rule. This helps to explain why the aircraft in Table 5.1 which fly at compressible Mach numbers have lower aspect ratios and thinner airfoils.

5.5.3 Lift/Drag Ratio

The type of configuration an airplane has, as well as the application of an airplane, is closely related to the lift/drag ratio. Many important items of airplane performance are obtained in flight at $(L/D)_{\max}$. Performance conditions that occur at $(L/D)_{\max}$ include:

- Maximum range of propeller-driven airplanes
- Maximum climb angle for jet-powered airplanes
- Maximum power-off glide ratio (for jet-powered or for propeller-driven airplanes)
- Maximum endurance for jet-powered airplanes.

Representative values of the maximum lift/drag ratios for subsonic flight speeds are as follows:

Type of airplane	$(L/D)_{max}$
High-performance sailplane	25–40
Commercial transport	12–20
Supersonic fighter	4–12
Hypersonic vehicles	1–4

EXAMPLE 5.7: Compute the drag components for an F-16 in steady, level, unaccelerated flight

The pilot of an F-16 wants to maintain steady, level (i.e., in a constant altitude, horizontal plane) unaccelerated flight. Recall from the discussion at the start of this chapter, for flight in a horizontal plane, where the angles are small, the lift must balance the weight and the thrust supplied by the engine must be sufficient to balance the total drag acting on the aircraft. For this exercise, we will assume that the total drag coefficient for this aircraft is given by equation (5.46):

$$C_D = C_{D_0} + kC_L^2$$

Consider the following aerodynamic characteristics for the F-16:

M_∞ (—)	C_{D_0} (—)	k (—)
0.10	0.0208	0.1168
0.84	0.0208	0.1168
1.05	0.0527	0.1667
1.50	0.0479	0.3285
1.80	0.0465	0.4211

Notice that, since we are using equation (5.46) to represent the drag polar, the tabulated values of C_{D_0} include both the profile drag and the compressibility effects. Therefore, the values of C_{D_0} presented in the preceding table include the two components of the drag not related to the lift. If we used equation (5.47), the table would include individual values for the profile drag [the first term in equation (5.47)] and for the compressibility effects [the third term in equation (5.47)]. The parasite drag can be calculated as:

$$D_p = C_{D_0}(\tfrac{1}{2}\rho_\infty U_\infty^2)S$$

The induced drag can be calculated as:

$$D_i = C_{D_i}(\tfrac{1}{2}\rho_\infty U_\infty^2)S$$

where the induced-drag coefficient is given by:

$$C_{D_i} = kC_L^2$$

In order for the aircraft to maintain steady, level, unaccelerated flight, the lift must balance the weight, as represented by equation (5.42a). Therefore, we can solve equation (5.42b) for the lift coefficient as a function of the Mach number. Referring to equation (5.46), the total drag is the sum of the parasite drag and the induced drag. Additional aerodynamic characteristics for the F-16 are:

$$\begin{aligned} \text{Aspect ratio } (AR) &= 3.0 \\ \text{Wing (reference) area} (S) &= 300 \text{ ft}^2 \\ \text{Airplane efficiency factor} (e) &= 0.9084 \end{aligned}$$

Consider an F-16 that weighs 23,750 pounds in steady, level, unaccelerated flight at an altitude of 20,000 ft (standard day atmospheric conditions). Calculate the parasite drag, the induced drag, the total drag, and the lift-to-drag ratio as a function of Mach number in Mach-number increments of 0.1. Use linear fits of the tabulated values to obtain values of C_{D_0} and of k at Mach numbers other than those presented in the table.

Solution: The first step is to use straight lines to generate values of C_{D_0} and of k in Mach-number increments of 0.1. The results are presented in the first three columns of the accompanying table. Note, as mentioned in the problem statement, the values of C_{D_0} for Mach numbers greater than 0.84 include a significant contribution of the wave drag ΔC_{D_M} to the components of drag not related to the lift. The inclusion of the wave drag causes the drag coefficient C_{D_0} to peak at a transonic Mach number of 1.05. Note also that the value of k for a Mach number of 0.10 is consistent with equation (5.48). That is,

$$k = \frac{1}{\pi eAR} = \frac{1}{\pi(0.9084)(3)} = 0.1168$$

The other tabulated values of k incorporate the effects of compressibility.

The free-stream density (0.001267 slugs/ft^3) and the free-stream speed of sound (1036.94 ft/s) for standard atmospheric conditions at 20,000 ft are taken from Table 1.2b.

The computed values of the parasite drag, of the induced drag, and of the total drag are presented in the table and in Fig. 5.32. Notice that when the total drag is a minimum (which occurs at a Mach number of approximately 0.52), the parasite drag is equal to the induced drag, which is also the velocity for $(L/D)_{\max}$.

Since the lift is equal to the weight, the lift-to-drag ratio is given by:

$$\frac{L}{D} = \frac{\text{Weight}}{\text{Total Drag}} = \frac{C_L}{C_{D_0} + C_{D_i}} \qquad \textbf{(5.49)}$$

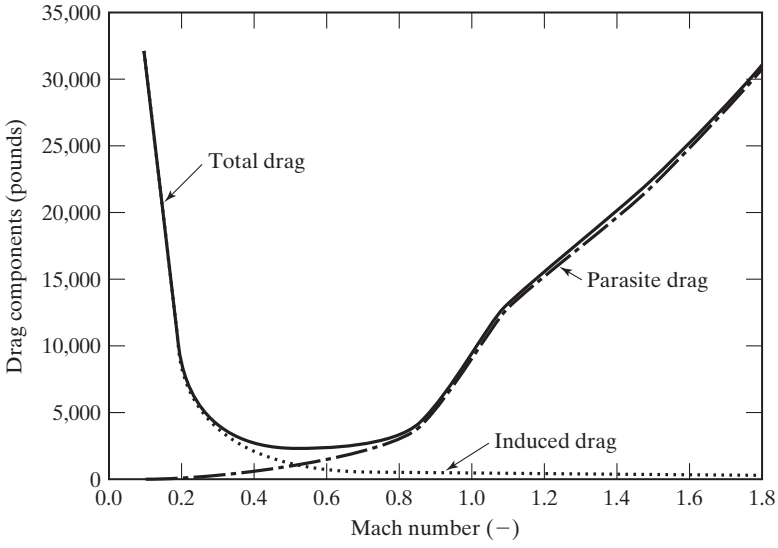

Figure 5.32 Drag components for an F-16C flying in steady, level, unaccelerated flight at 20,000 ft.

The computed values for the lift-to-drag ratio are presented in the table and in Fig. 5.33. Since the weight of the aircraft is fixed, the maximum value of the lift-to-drag ratio occurs when the total drag is a minimum. The fact that the induced drag and the parasite drag are equal at this condition is an underlying principle to the solution of Problem 5.3, and an important concept for aircraft performance.

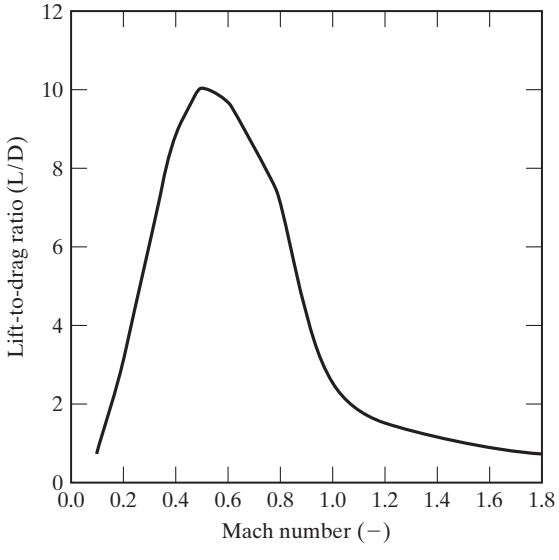

Figure 5.33 L/D ratio as a function of the Mach number for an F-16C flying at 20,000 ft.

Aircraft	*F-16C*										
S (sq ft)	*300*										
span (ft)	*30*										
AR	*3*										
e	*0.9084*										
				a (ft/s)	*ρ*		W(lb)				
				1036.94	*(slug/ft^3)*		*23750*				
	Mach	C_{D_0}	*k*	*Vel*	*0.001267*		*CL*	C_{D_i}			*L/D*
	(—)	*(—)*	*(—)*	(ft/s)	*q*(lb/ft^2)	D_p(lb)	*(—)*	*(—)*	D_i(lb)	*D* (lb)	*(—)*
	0.10	0.0208	0.1168	103.69	6.81	42.50	11.6222	15.7768	32239.99	32282.50	0.7357
	0.20	0.0208	0.1168	207.39	27.25	170.02	2.9056	0.9861	8060.00	8230.02	2.8858
	0.30	0.0208	0.1168	311.08	61.31	382.54	1.2914	0.1948	3582.22	3964.77	5.9903
	0.40	0.0208	0.1168	414.78	108.99	680.08	0.7264	0.0616	2015.00	2695.08	8.8124
	0.50	0.0208	0.1168	518.47	170.29	1062.62	0.4649	0.0252	1289.60	2352.22	10.0968
	0.60	0.0208	0.1168	622.16	245.22	1530.17	0.3228	0.0122	895.56	2425.73	9.7909
	0.70	0.0208	0.1168	725.86	333.77	2082.74	0.2372	0.0066	657.96	2740.70	8.6657
	0.80	0.0208	0.1168	829.55	435.95	2720.31	0.1816	0.0039	503.75	3224.06	7.3665
	0.90	0.0300	0.1312	933.25	551.75	4965.71	0.1435	0.0027	447.10	5412.81	4.3877
	1.00	0.0447	0.1542	1036.94	681.17	9134.46	0.1162	0.0021	425.63	9560.09	2.4843
	1.10	0.0522	0.1832	1140.63	824.21	12907.17	0.0961	0.0017	417.92	13325.09	1.7824
	1.20	0.0511	0.2195	1244.33	980.88	15036.91	0.0807	0.0014	420.75	15457.66	1.5365
	1.30	0.0501	0.2558	1348.02	1151.17	17302.13	0.0688	0.0012	417.80	17719.93	1.3403
	1.40	0.0490	0.2922	1451.72	1335.09	19625.80	0.0593	0.0010	411.51	20037.30	1.1853
	1.50	0.0479	0.3285	1555.41	1532.63	22023.85	0.0517	0.0009	403.00	22426.85	1.0590
	1.60	0.0474	0.3594	1659.10	1743.79	24796.67	0.0454	0.0007	387.52	25184.19	0.9431
	1.70	0.0470	0.3902	1762.80	1968.57	27756.89	0.0402	0.0006	372.68	28129.58	0.8443
	1.80	0.0465	0.4211	1866.49	2206.98	30787.41	0.0359	0.0005	358.75	31146.16	0.7625

PROBLEMS

5.1. For the delta wing of the F-106, the reference area (S) is 50 m^2 and the leading-edge sweep angle is 45°. What are the corresponding values of the aspect ratio and of the wing span?

5.2. In Example 5.1, an expression for the aspect ratio of a delta wing was developed in terms of the leading-edge sweep angle (Λ_{LE}). For this problem, develop an expression for the aspect ratio in terms of the sweep angle of the quarter chord ($\Lambda_{c/4}$).

5.3. Using equation (5.46) and treating C_{D_0} and k as constants, show that the lift coefficient for maximum lift/drag ratio and the maximum lift/drag ratio for an incompressible flow are given by

$$C_{L(L/D)\max} = \sqrt{\frac{C_{D_0}}{k}}$$

$$\left(\frac{L}{D}\right)_{\max} = \frac{1}{2\sqrt{kC_{D_0}}}$$

5.4. A Cessna 172 is cruising at 10,000 ft on a standard day ($\rho_\infty = 0.001756$ slug/ft^3) at 80 mi/h. If the airplane weighs 1500 lb, what C_L is required to maintain level flight?

5.5. Assume that the lift coefficient is a linear function for its operating range. Assume further that the wing has a positive camber so that its zero-lift angle of attack (α_{0L}) is negative, and that the slope of the straight-line portion of the C_L versus α curve is $C_{L,\alpha}$. Using the results of Problem 5.3, derive an expression for $\alpha_{(L/D)\max}$.

5.6. Using the results of Problem 5.3, what is the drag coefficient (C_D) when the lift-to-drag ratio is a maximum? That is, what is $C_{D(L/D)\max}$?

5.7. Consider a flat plate at zero angle of attack in a uniform flow where $U_\infty = 35$ m/s in the standard sea-level atmosphere (Fig. P5.7). Assume that $\mathrm{Re}_{x,\mathrm{tr}} = 500{,}000$ defines the transition point. Determine the section drag coefficient, C_d. Neglect plate edge effects (i.e., assume two-dimensional flow). What error would be incurred if it is assumed that the boundary layer is turbulent along the entire length of the plate?

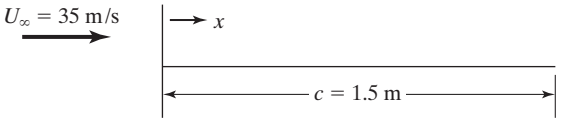

Figure P5.7

5.8. An airplane that weighs 50,000 N and has a wing area of 21.5 m^2 is landing at an airport.

(a) Graph C_L as a function of the true airspeed over the airspeed range 300 to 180 km/h, if the airport is at sea level.

(b) Repeat the problem for an airport that is at an altitude of 1600 m. For the purposes of this problem, assume that the airplane is in steady, level flight to calculate the required lift coefficients.

5.9. The lift/drag ratio of a sailplane is 60. The sailplane has a wing area of 10.0 m^2 and weighs 3150 N. What is C_D when the aircraft is in steady level flight at 340 km/h at an altitude of 1.0 km?

Problems (5.10) through (5.13) make use of pressure measurements taken from Pinkerton (1936) for NACA 4412 airfoil section. The measurements were taken from the centerplane of a rectangular planform wing, having a span of 30 inches and a chord of 5 inches. The test conditions

included an average pressure (standard atmospheres): 21; average Reynolds number: 3,100,000. Pinkerton (1936) spent considerable effort defining the reliability of the pressure measurements. "In order to have true section characteristics (two-dimensional) for comparison with theoretical calculations, a determination must be made of the effective angle of attack, i.e., the angle that the chord of the model makes with the direction of the flow in the region of the midspan of the model." Thus, the experimentally determined pressure distributions, which are presented in Table 5.6, are presented both for the physical angle of attack (α) and the effective angle of attack (α_{eff}). However, "The determination of the effective angle of attack of the midspan section entails certain assumptions that are subject to considerable uncertainty." Nevertheless, the data allow us to develop some interesting graphs.

5.10. Pressure distribution measurements from Pinkerton (1936) are presented in Table 5.6 for the midspan section of a 76.2 cm by 12.7 cm model which had a NACA 4412 airfoil section. Graph C_p as a function of x/c for these three angles of attack. Comment on the movement of the stagnation point. Comment on changes in the magnitude of the adverse pressure gradient toward the trailing edge of the upper surface. How does this relate to possible boundary-layer separation (or stall)?

5.11. Re-arrange equation (3.13) and obtain,

$$\frac{U}{U_\infty} = \sqrt{1 - C_p}$$

to calculate the maximum value of the local velocity at the edge of the boundary layer both on the upper surface and on the lower surface for all three angles of attack. If these velocities are representative of the changes with angle of attack, how does the circulation (or lift) change with the angle of attack?

TABLE 5.6 Experimental Pressure Distributions for an NACA 4412 Airfoil [Abbott and von Doenhoff (1949)].[a]

Orifice location				
x-Station (percent c from the leading edge)	*z-Ordinate (percent c above chord)*	*Values of the pressure coefficient, C_p*		
		$\alpha = -4°$ ($\alpha_{eff} = -4°$)	$\alpha = +2°$ ($\alpha_{\text{eff}} = 1.2°$)	$\alpha = +16°$ ($\alpha_{\text{eff}} = 13.5°$)
100.00	0	0.204	0.181	0.010
97.92	−0.10	0.178	0.164	0.121
94.86	−0.16	0.151	0.154	0.179
89.90	−0.22	0.128	0.152	0.231
84.94	−0.28	0.082	0.148	0.257
74.92	−0.52	0.068	0.136	0.322
64.94	−0.84	0.028	0.120	0.374
54.48	−1.24	−0.024	0.100	0.414
49.98	−1.44	−0.053	0.091	0.426
44.90	−1.64	−0.075	0.088	0.459
39.98	−1.86	−0.105	0.071	0.485
34.90	−2.10	−0.146	0.066	0.516
29.96	−2.30	−0.190	0.048	0.551
24.90	−2.54	−0.266	0.025	0.589

(*continued*)

TABLE 5.6 (Continued)

Orifice location		*Values of the pressure coefficient, C_p*		
x-Station (percent c from the leading edge)	*z-Ordinate (percent c above chord)*	$\alpha = -4°$ ($\alpha_{eff} = -4°$)	$\alpha = +2°$ ($\alpha_{eff} = 1.2°$)	$\alpha = +16°$ ($\alpha_{eff} = 13.5°$)
19.98	−2.76	−0.365	−0.011	0.627
14.94	−2.90	−0.502	−0.053	0.713
9.96	−2.86	−0.716	−0.111	0.818
7.38	−2.72	−0.867	−0.131	0.896
4.94	−2.46	−1.106	−0.150	0.980
2.92	−2.06	−1.380	−0.098	0.993
1.66	−1.60	−1.709	0.028	0.791
0.92	−1.20	−1.812	0.254	0.264
0.36	−0.70	−1.559	0.639	−1.379
0	0	−0.296	0.989	−3.648
0	0.68	0.681	0.854	−6.230
0.44	1.56	0.994	0.336	−5.961
0.94	2.16	0.939	0.055	−5.210
1.70	2.78	0.782	−0.148	−4.478
2.94	3.64	0.559	−0.336	−3.765
4.90	4.68	0.333	−0.485	−3.190
7.50	5.74	0.139	−0.568	−2.709
9.96	6.56	0.017	−0.623	−2.440
12.58	7.34	−0.091	−0.676	−2.240
14.92	7.88	−0.152	−0.700	−2.149
17.44	8.40	−0.210	−0.721	−1.952
19.96	8.80	−0.262	−0.740	−1.841
22.44	9.16	−0.322	−0.769	−1.758
24.92	9.52	−0.322	−0.746	−1.640
27.44	9.62	−0.355	−0.742	−1.535
29.88	9.76	−0.364	−0.722	−1.438
34.95	9.90	−0.381	−0.693	−1.269
39.90	9.84	−0.370	−0.635	−1.099
44.80	9.64	−0.371	−0.609	−0.961
49.92	9.22	−0.329	−0.525	−0.786
54.92	8.76	−0.303	−0.471	−0.649
59.94	8.16	−0.298	−0.438	−0.551
64.90	7.54	−0.264	−0.378	−0.414
69.86	6.76	−0.225	−0.319	−0.316
74.90	5.88	−0.183	−0.252	−0.212
79.92	4.92	−0.144	−0.191	−0.147
84.88	3.88	−0.091	−0.116	−0.082
89.88	2.74	−0.019	−0.026	−0.043
94.90	1.48	−0.069	−0.076	−0.016
98.00	0.68	0.139	−0.143	−0.004

[a] *Source*: Pinkerton (1936).

5.12. Using the small-angle approximations for the local surface inclinations, integrate the experimental chordwise pressure distributions of Table 5.6 to obtain values of the section lift coefficient for $\alpha = -4°$ and $\alpha = +2°$. Assuming that the section lift coefficient is a linear function of α (in this range of α), calculate

$$C_{l_\alpha} = \frac{dC_l}{d\alpha}$$

Does the section lift coefficient calculated using the pressure measurements for an angle of attack of 16° fall on the line? If not, why not?

5.13. Using the small-angle approximations for the local surface inclinations, integrate the experimental chordwise pressure distributions of Table 5.6 to obtain values of the section pitching moment coefficient relative to the quarter chord for each of the three angles of attack. Thus, in equation $dM_0 = p\,dx\,dy\,x$, x is replaced by $(x - 0.25c)$. Recall that a positive pitching moment is in the nose-up direction.

5.14. If one seeks to maintain steady, level unaccelerated flight (SLUF), the thrust supplied by the aircraft's engine must balance the total drag acting on the aircraft. Thus, the total drag acting on the aircraft is equal to the thrust required from the power plant. As calculated in Example 5.7, the total drag of an F-16 flying at a constant altitude of 10,000 ft exhibits a minimum total drag at a Mach number of 0.52. If one wishes to fly at speeds above a Mach number of 0.52, the pilot must advance the throttle to obtain more thrust from the engine. Similarly, if one wishes to fly at speeds below a Mach number of 0.52, the pilot must initially retard the throttle to begin slowing down and then advance the throttle to obtain more thrust from the engine than would be required to cruise at a Mach number of 0.52 in order to sustain the new, slower velocity. This Mach number range is the region known as "reverse command." If the engine of the F-16 generates 5,000 pounds of thrust when flying at 10,000 ft, what is the maximum Mach number at which the F-16 can sustain SLUF? Use the results of the table and of the figures in Example 5.7. What is the minimum Mach number at which the F-16 can sustain SLUF at 10,000 ft, based on an available thrust of 5,000 pounds? If the maximum lift coefficient is 1.57 (see Fig. 5.26), at what Mach number will the aircraft stall? Use the lift coefficients presented in the table of Example 5.7.

5.15. Consider a MiG-29 in steady, level, unaccelerated flight (SLUF) at an altitude of 30,000 ft (standard atmospheric conditions). Calculate the parasite drag, the induced drag, the total drag, and the lift-to-drag ratio as a function of the Mach number in Mach-number increments of 0.1, from a Mach number of 0.1 to a Mach number of 1.8. For the MiG-29, assume the following:

Mach No. (—)	C_{D_0} (—)	k (—)
0.1000	0.0207	0.1279
0.8500	0.0207	0.1279
1.0700	0.0472	0.1773
1.5000	0.0425	0.3317
1.8000	0.0408	0.4240

Other parameters for the MiG-29 include $S = 409$ ft^2; $b = 37.3$ ft; and $e = 0.75$. The weight of the aircraft is 31,000 pounds.

5.16. Consider the Eurofighter 2000 in steady, level, unaccelerated flight (SLUF) at an altitude of 5 km (standard atmospheric conditions). Calculate the parasite drag, the induced drag,

the total drag, and the lift-to-drag ratio as a function of the Mach number in Mach-number increments of 0.1, from a Mach number of 0.1 to a Mach number of 1.8. For the Eurofighter 2000, assume the following:

Mach No. (—)	C_{D_0} (—)	k (—)
0.1000	0.0131	0.1725
0.8600	0.0131	0.1725
1.1100	0.0321	0.2292
1.5000	0.0289	0.3515
1.8000	0.0277	0.4417

Other parameters for the Eurofighter 2000 include $S = 50\ \text{m}^2$; $b = 10.5$ m; and $e = 0.84$. The weight of the aircraft is 17,500 kg.

5.17. A finless missile is flying at sea-level at 225 mph. Estimate the parasite drag (excluding base drag) on the missile. The body has a length of 10.0 ft. and a diameter of 1.2 ft. The reference area for the missile is given by $S_{ref} = \pi d^2/4$ (the cross-sectional area of the missile). Explain why you would not need to correct your results for laminar flow.

5.18. A flying wing has a planform area of 3700 ft^2, a root chord at the airplane centerline of 34 ft, an overall taper ratio of 0.275, and a span of 170 ft. The average weighted airfoil thickness ratio is 10.2% and the wing has 36° of sweepback at the 25% chordline. The airplane is cruising at a pressure altitude of 17,000 ft on a standard day with a wing loading of 105 lb/ft^2. The cruise Mach number is 0.23. Determine the following:

(a) skin-friction drag coefficient (assume a spray-painted surface)
(b) pressure drag coefficient
(c) induced drag coefficient
(d) total drag coefficient
(e) total drag in pounds

REFERENCES

Abbott IH, von Doenhoff AE. 1949. *Theory of Wing Sections*. New York: Dover

Blake WB. 1998. *Missile DATCOM*. AFRL TR-1998-3009

Bowes GM. 1974. *Aircraft lift and drag prediction and measurement*, AGARD Lecture Series 67, 4-1 to 4-41

Brandt SA, Stiles RJ, Bertin JJ, Whitford R. 2004. *Introduction to Aeronautics: A Design Perspective*. 2nd Ed. Reston, VA: AIAA

Braslow AL, Hicks RM, Harris RV. 1966. Use of grit-type boundary-layer transition trips on wind-tunnel models. *NASA Tech. Note D-3579*

Eppler R. 1990. *Airfoil Design and Data*. Berlin: Springer-Verlag

General Dynamics Staff. 1979. *F-16 Air Combat Fighter*. General Dynamics Report F-16-060

Gollos, WW. 1953. Boundary layer drag for non-smooth surfaces. RAND RM-1129

Hall DW. 1985. To fly on the wings of the sun. *Lockheed Horizons*. 18:60–68

Hoerner SR. 1965. *Fluid-Dynamic Drag*. Midland Park, NJ: published by the author

Jackson P, ed. 2011. *Jane's All the World's Aircraft, 2011–2012*. London: Jane's Information Group

Kroo I. 2003. *Applied Aerodynamics: A Digital Textbook*. Stanford: Desktop Aeronautics

Mack LM. 1984. Boundary-layer linear stability theory. In *Special Course on Stability and Transition of Laminar Flow*, Ed. Michel R, AGARD Report 709, pp. 3–1 to 3–81

McCormick BW. 1979. *Aerodynamics, Aeronautics, and Flight Mechanics*. New York: John Wiley and Sons

Pearcey HH, Osborne J, Haines AB. 1968. The interaction between local effects at the shock and rear separation—a source of significant scale effects in wind-tunnel tests on aerofoils and wings. In *Transonic Aerodynamics*, AGARD Conference Proceedings, Vol. 35, Paper 1

Pinkerton RM. 1936. Calculated and measured pressure distributions over the midspan section of the NACA 4412 airfoil. *NACA Report 563*

Piszkin F, Walacavage R, LeClare G. 1961. *Analysis and comparison of Air Force flight test performance data with predicted and generalized flight test performance data for the F-106A and B airplanes*. Convair Technical Report AD-8-163

Saric WS. 1992. The ASU Transition Research Facility. Presented at AIAA Aerospace Ground Testing Conf. 17th, Nashville, TN, AIAA Pap. 1992-3910

Schaufele RD. 2000. *The Elements of Aircraft Preliminary Design*. Santa Ana, CA: Aries Publications

Schlichting H. 1979. *Boundary Layer Theory*. 7th Ed. New York: McGraw-Hill

Schütte A, Cummings RM, 2011. *Introduction to the AVT-161 air facet: An integrated computational/experimental approach to UCAV stability & control estimation*. NATO RTO-TR-AVT-161, pp. 1-1 to 1-20.

Selig M. 2012. UIUC Airfoil Data Site, http://www.ae.illinois.edu/m-selig/ads.html

Shevell RS. 1989. *Fundamentals of Flight*. 2nd Ed. Englewood Cliffs, NJ: Prentice Hall

Sterret JR, Morrisette EL, Whitehead AH, Hicks RM. 1966. Transition fixing for hypersonic flow. *NASA Tech. Note D-4129*

Stuart WG. 1978. *Northrop F-5 Case Study in Aircraft Design*. Washington, DC: AIAA

Taylor JWR, ed. 1973. *Jane's All the World's Aircraft*, *1973–1974*. London: Jane's Yearbooks

Taylor JWR, ed. 1966. *Jane's All the World's Aircraft*, *1966–1967*. London: Jane's Yearbooks

Taylor JWR, ed. 1984. *Jane's All the World's Aircraft*, *1984–1985*. London: Jane's Yearbooks

Thomas ASW. 1985. Aircraft viscous drag reduction technology. *Lockheed Horizons* 19:22–32

Van Dam CP, Holmes BJ. 1986. Boundary-layer transition effects on airplane stability and control. Presented at Atmospheric Flight Mech. Conf., AIAA Pap. 86-2229, Williamsburg, VA

Van't Riet, R. 1989. *C-17 Technical Description*, SAE Aerospace Control Guidance Systems Meeting, Albuquerque, New Mexico

Webb TS, Kent DR, Webb JB. 1977. Correlation of F-16 aerodynamics and performance predictions with early flight test results. In *Performance Prediction Methods*, AGARD Conference Proceeding, Vol. 242, Paper 19

6 INCOMPRESSIBLE FLOWS AROUND AIRFOILS OF INFINITE SPAN

Chapter Objectives

- Understand and be able to use the physical and mathematical concepts of circulation and lift
- Be able to explain how potential flow theory is used to model flow for airfoils
- Understand the physical meaning and use of the Kutta condition
- Be able to estimate the lift and moment acting on an airfoil using thin-airfoil theory
- Understand the usefulness and limitations of thin-airfoil theory
- Know ways potential flow theory can be used to model airfoils other than thin-airfoil theory
- Be able to explain why laminar flow airfoils have different geometries than airfoils used at higher Reynolds numbers
- Have a basic understanding of high-lift systems on aircraft, and how they create lift depending on where they are placed on a wing

Now that we have a basic understanding of airfoil and wing aerodynamics, we need to develop models and theories that will help us predict the lift, drag, and moment for these aerodynamic shapes. The theories will be based on potential flow concepts from Chapter 3, and as with all theories, there will be assumptions and simplifications.

However, we will compare the predictions from the theories with experimental data to see how limiting the assumptions were. In general, we will find airfoil aerodynamics can be fairly well predicted with theoretical models.

6.1 GENERAL COMMENTS

Theoretical relations that describe an inviscid, low-speed flow around a thin airfoil will be developed in this chapter. To obtain the appropriate governing equations, we will assume that the airfoil extends to infinity in both directions from the plane of symmetry (i.e., the airfoil is a wing of infinite aspect ratio). Therefore, the flow field around the airfoil is the same for any cross section perpendicular to the wing span and the flow is two dimensional.

As we discussed in Chapter 5, the term *airfoil* will be used for the two-dimensional flow field that exists when identical airfoil sections are placed side by side so that the spanwise dimension of the resultant configuration is infinite. But the term *airfoil* will also be used when a finite-span model with identical cross sections spans a wind tunnel from wall-to-wall and is perpendicular to the free-stream flow. In this situation, neglecting interactions with the tunnel-wall boundary layer, the flow around the model does not vary in the spanwise direction. For many applications (as we will see in Chapter 7), these two-dimensional airfoil flow fields will be applied to a slice of a three-dimensional wing flow field. That is, they approximate the flow per unit width (or per unit span) around the airfoil sections that make up a finite-span wing. Also, as we mentioned in Chapter 5, the term *wing* will be used when the configuration has a finite span.

The flow around a two-dimensional airfoil can be idealized by superimposing a translational flow past the airfoil section (the free-stream flow), a distortion of the stream that is due to the airfoil thickness, and a circulatory flow that is related to the lifting characteristics of the airfoil. Since it is a two-dimensional configuration, an airfoil in an incompressible free stream experiences no drag force, if we neglect the effects of viscosity, as explained in Section 3.15.2. However, as discussed in Chapters 4 and 5, the viscous forces produce a velocity gradient near the surface of the airfoil and, hence, drag due to skin friction. Furthermore, the presence of the viscous flow near the surface modifies the inviscid flow field and may produce a significant drag force due to the integrated effect of the pressure field (i.e., form drag). To generate high lift, we must either place the airfoil at high angles of attack or employ leading-edge and/or trailing-edge devices. Either way, the interaction between large pressure gradients and the viscous boundary layer produces a complex, Reynolds-number–dependent flow field.

The analytical values of aerodynamic parameters for incompressible flow around thin airfoils will be calculated in Sections 6.3 through 6.5 using classical formulations from the early twentieth century. Although these formulations have long since been replaced by more rigorous numerical models (see Chapter 14), they do provide valuable information about the aerodynamic characteristics for airfoils in incompressible air streams. The comparison of the analytical values of the aerodynamic parameters with the corresponding experimental values will indicate the limits of the applicability of the analytical models. The desired characteristics and the resultant flow fields for high-lift airfoil sections will be discussed in Sections 6.6 through 6.8.

6.2 CIRCULATION AND THE GENERATION OF LIFT

For a lifting airfoil, the pressure on the lower surface of the airfoil is, on the average, greater than the pressure on the upper surface. Bernoulli's equation for steady, incompressible flow leads to the conclusion that the velocity over the upper surface is, on the average, greater than the velocity past the lower surface. Therefore, the flow around the airfoil can be represented by the combination of a translational flow from left to right and a circulating flow in a clockwise direction, as shown in Fig. 6.1. This flow model assumes that the airfoil is sufficiently thin so that thickness effects may be neglected (thickness effects can be treated using the source panel technique, as we discussed in Chapter 3).

If the fluid is initially at rest, the line integral of the velocity around any curve completely surrounding the airfoil is zero, because the velocity is zero for all fluid particles. Therefore, the circulation around the contour in Fig. 6.2a is zero. According to Kelvin's theorem for a frictionless flow (see Section 3.7), the circulation around this line of fluid particles remains zero if the fluid is suddenly given a uniform velocity with respect to the airfoil (which is called an "impulsive" start). Therefore, in Figs. 6.2b and c, the circulation around the contour which encloses the lifting airfoil and which contains the same fluid particles as the contour of Fig. 6.2a should still be zero. However, circulation is necessary to produce lift. Therefore, as explained in the following paragraphs, the circulation around each of the component curves of Figs. 6.2b and c is not zero but equal in magnitude and opposite in sign to the circulation around the other component curve.

6.2.1 Starting Vortex

When an airfoil is accelerated from rest, the circulation around it and, therefore, the lift are not produced instantaneously. At the instant of starting, the flow is a potential flow without circulation, and the streamlines are as shown in Figs. 6.3a, with a stagnation point occurring on the rear upper surface. At the sharp trailing edge, the air is required to change direction suddenly. However, because of viscosity, the large velocity gradients produce large viscous forces, and the air is unable to flow around the sharp trailing edge. Instead, a surface of discontinuity emanating from the sharp trailing edge is rolled up into a vortex, which is called the *starting vortex*. The stagnation point moves toward the trailing edge as the circulation around the airfoil and, therefore, the lift increase progressively. The circulation around the airfoil increases in intensity until the flows from the upper surface and the lower surface join smoothly at the trailing edge, as shown in Fig. 6.3b. So, the generation of circulation around the wing and the resultant lift are necessarily accompanied by a starting vortex, which results because of the effect of viscosity.

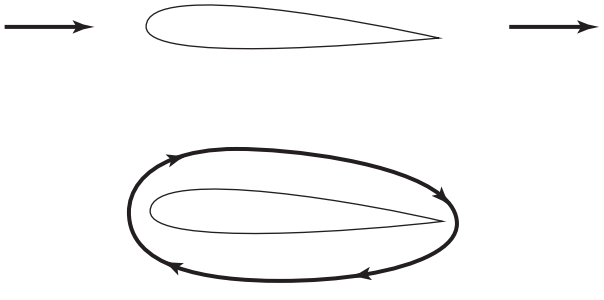

Figure 6.1 Flow around the lifting airfoil section, as represented by two elementary flows.

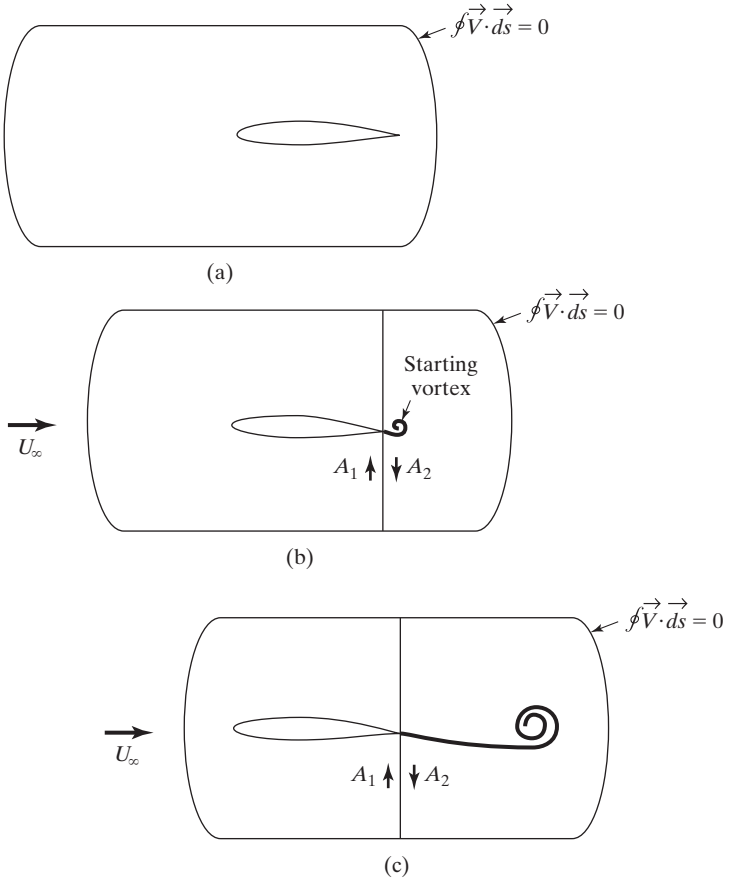

Figure 6.2 Circulation around a fluid line containing the airfoil remains zero: (a) fluid at rest; (b) fluid at time t; (c) fluid at time $t + \Delta t$.

A contour which encloses both the airfoil and the starting vortex and which always contains the same fluid particles is shown in Fig. 6.2. The total circulation around this line remains zero, since the circulation around the airfoil is equal in strength but opposite in direction to that of the starting vortex. Therefore, the existence of circulation is not in contradiction to Kelvin's theorem. Referring to Fig. 6.2, the line integral of the tangential component of the velocity around the curve that encloses area A_1 must be equal and opposite to the corresponding integral for area A_2.

If either the free-stream velocity or the angle of attack of the airfoil is increased, another vortex is shed which has the same direction as the starting vortex. However, if the velocity or the angle of attack is decreased, a vortex is shed which has the opposite direction of rotation relative to the initial vortex.

A simple experiment that can be used to visualize the starting vortex requires only a pan of water and a small, thin board. Place the board upright in the water so that it cuts the surface. If the board is accelerated suddenly at moderate incidence, the starting

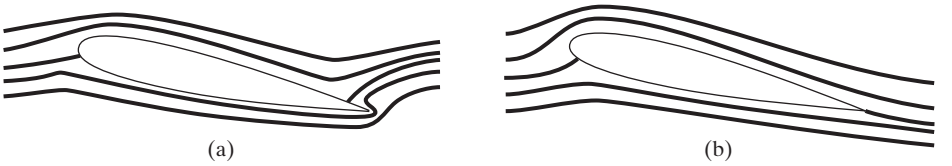

Figure 6.3 Streamlines around the airfoil section: (a) zero circulation, stagnation point on the rear upper surface; (b) full circulation, stagnation point on the trailing edge.

vortex will be seen leaving the trailing edge of the "airfoil." If the board is stopped suddenly, another vortex of equal strength but of opposite rotation is generated.

6.3 GENERAL THIN-AIRFOIL THEORY

It may seem strange that we will model the viscous flow around an airfoil with an inviscid theory, but potential flow theory coupled with some essential viscous observations can produce very good predictions of airfoil aerodynamics. In fact, one of the most important viscous concepts is that a fluid flowing over a surface will tend to stay attached to the surface unless a "large enough" adverse pressure gradient is present. This viscous observation is mimicked quite well by the potential flow result that solid surfaces are streamlines and flow stays attached unless forced to separate. So while the inviscid assumptions will lead to shortcomings for airfoil theory, it will also produce very good results.

The essential assumptions of thin-airfoil theory are: (1) that the lifting characteristics of an airfoil below stall are negligibly affected by the presence of the boundary layer, (2) that the airfoil is operating at a small angle of attack, and (3) that the resultant of the pressure forces (magnitude, direction, and line of action) is only slightly influenced by the airfoil thickness, since the maximum mean camber is small and the ratio of maximum thickness to chord is small.

Notice that we assume there is sufficient viscosity to produce the circulation that results in the flow depicted in Fig. 6.3b. However, we neglect the effect of viscosity as it relates to the boundary layer. The boundary layer is assumed to be thin and, therefore, does not significantly alter the static pressures from the values that correspond to those for the inviscid flow model. Furthermore, the boundary layer does not cause the flow to separate when it encounters an adverse pressure gradient. Typically, airfoil sections have a maximum thickness of approximately 12% of the chord and a maximum mean camber of approximately 2% of the chord. For thin-airfoil theory, the airfoil will be represented by its mean camber line in order to calculate the section aerodynamic characteristics, which means we will be neglecting the effects of thickness.

A velocity difference across the infinitely thin profile which represents the airfoil section is required to produce the lift-generating pressure difference. This results directly from the concept of circulation in Chapter 3, which stated that unless there is a local curvature to the flow there cannot be circulation and lift. The only way for the flow to turn is for the fluid above the airfoil to travel faster than the fluid below the airfoil. A vortex sheet coincident with the mean camber line produces a velocity distribution that exhibits the required velocity jump (which is the difference in velocity between the

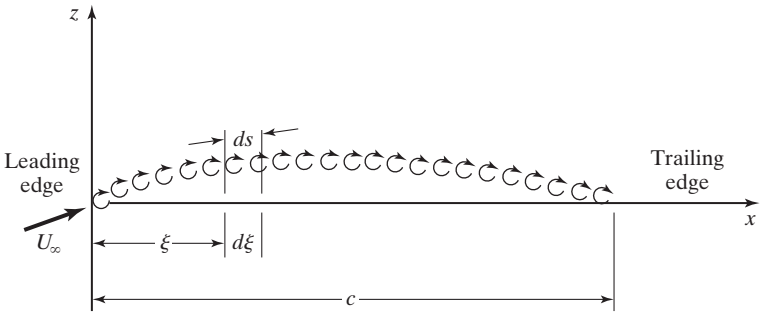

Figure 6.4 Representation of the mean camber line by a vortex sheet whose filaments are of variable strength $\gamma(s)$.

upper and lower surfaces of the mean camber line). Therefore, the desired flow will be obtained by superimposing on a uniform flow a field induced by an infinite series of line vortices of infinitesimal strength which are located along the camber line, as shown in Fig. 6.4. The total circulation is the sum of the circulations of the vortex filaments

$$\Gamma = \int_0^c \gamma(s)\, ds \tag{6.1}$$

where $\gamma(s)$ is the distribution of vorticity (or vortex strength) for the line vortices. The length of an arbitrary element of the camber line is *ds* and positive circulation is in the clockwise direction.

The velocity field around the sheet is the sum of the free-stream velocity and the velocity induced by all the vortex filaments that make up the vortex sheet since potential flow satisfies Laplace's equation (see Chapter 3). For the vortex sheet to be a streamline of the flow, it is necessary that the resultant velocity be tangent to the mean camber line at each point (the mean camber line is a streamline). Therefore, the sum of the components normal to the surface for these two velocities must be zero. In addition, the condition that the flows from the upper surface and the lower surface join smoothly at the trailing edge (i.e., the Kutta condition) requires that $\gamma = 0$ at the trailing edge. Ideally (i.e., for an inviscid potential flow), the circulation that forms places the rear stagnation point exactly on the sharp trailing edge. When the effects of friction are included, there is a reduction in circulation relative to the value determined for an "inviscid flow." Therefore, the Kutta condition places a constraint on the vorticity distribution that is consistent with the effects of the boundary layer—in other words, the Kutta condition is a viscous boundary condition based on physical observation which we will use with our inviscid theoretical development.

The portion of the vortex sheet designated *ds* in Fig. 6.5 produces a velocity at point *P* which is perpendicular to the line whose length is *r* and which joins the element *ds* and the point *P*. The induced velocity component normal to the camber line at *P* due to the vortex element *ds* is:

$$dV_{s,n} = -\frac{\gamma\, ds \cos \delta_3}{2\pi r}$$

where the negative sign results because the circulation induces a clockwise velocity and the normal to the upper surface is positive outward, and the magnitude is determined

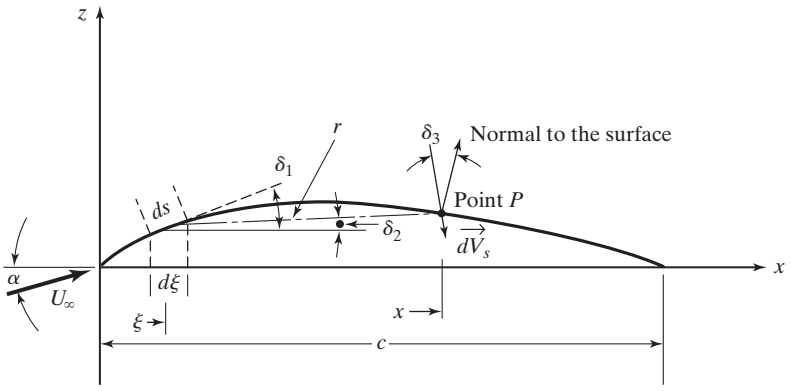

Figure 6.5 Thin-airfoil geometry parameters.

by the velocity field created by a vortex (see Chapter 3). To calculate the resultant vortex-induced velocity at a particular point P, we must integrate over all the vortex filaments from the leading edge to the trailing edge. The chordwise location of the point of interest P will be designated in terms of its x coordinate. The chordwise location of a given element of vortex sheet ds will be given in terms of its ξ coordinate. Therefore, to calculate the cumulative effect of all the vortex elements, it is necessary to integrate over the ξ coordinate from the leading edge ($\xi = 0$) to the trailing edge ($\xi = c$). Noting that

$$\cos \delta_2 = \frac{x - \xi}{r} \quad \text{and} \quad ds = \frac{d\xi}{\cos \delta_1}$$

the resultant vortex-induced velocity at any point P (which has the chordwise location x) is given by:

$$V_{s,n}(x) = -\frac{1}{2\pi} \int_0^c \frac{\gamma(\xi) \cos \delta_2 \cos \delta_3 \, d\xi}{(x - \xi) \cos \delta_1} \tag{6.2}$$

Likewise, the component of the free-stream velocity normal to the mean camber line at P is given by:

$$U_{\infty,n}(x) = U_\infty \sin(\alpha - \delta_P)$$

where α is the angle of attack and δ_P is the slope of the camber line at the point of interest P:

$$\delta_P = \tan^{-1} \frac{dz}{dx}$$

where $z(x)$ is the function that describes the mean camber line. As a result,

$$U_{\infty,n}(x) = U_\infty \sin\left(\alpha - \tan^{-1} \frac{dz}{dx}\right) \tag{6.3}$$

Since the sum of the velocity components normal to the surface must be zero at all points along the vortex sheet, the velocity induced by the vortex sheet

(equation 6.2) must be equal and opposite to the component due to the free-stream flow (equation 6.3).

$$\frac{1}{2\pi}\int_0^c \frac{\gamma(\xi)\cos\delta_2\cos\delta_3\,d\xi}{(x-\xi)\cos\delta_1} = U_\infty \sin\left(\alpha - \tan^{-1}\frac{dz}{dx}\right) \tag{6.4}$$

The vorticity distribution $\gamma(\xi)$ that satisfies this integral equation makes the vortex sheet (and, therefore, the mean camber line) a streamline of the flow. The desired vorticity distribution must also satisfy the Kutta condition that $\gamma(c) = 0$.

Within the assumptions of thin-airfoil theory, the angles δ_1, δ_2, δ_3, and α are small. Using the approximate trigonometric relations for small angles, equation (6.4) becomes

$$\frac{1}{2\pi}\int_0^c \frac{\gamma(\xi)d\xi}{x-\xi} = U_\infty\left(\alpha - \frac{dz}{dx}\right) \tag{6.5}$$

This is the fundamental equation of thin airfoil theory, which is simply the boundary condition requiring that no flow crosses the mean camber line. We will solve this relation for two cases of interest: symmetric airfoils and cambered airfoils.

6.4 THIN, FLAT-PLATE AIRFOIL (SYMMETRIC AIRFOIL)

First we will solve the fundamental equation of thin airfoil theory, equation (6.5), for the case of a symmetric airfoil. For this case, the mean camber line is coincident with the chord line, and the geometry is just a thin flat plate. For subsonic flow past a flat plate even at small angles of attack, a region of dead air (or stalled flow) will exist over the upper surface. For the actual airfoil, the rounded nose allows the flow to accelerate from the stagnation point onto the upper surface without separation. Of course, when the angle of attack is sufficiently large (the value depends on the cross-section geometry), stall will occur for the actual profile. The approximate theoretical solution for a thin airfoil with two sharp edges represents an irrotational flow with finite velocity at the trailing edge but with infinite velocity at the leading edge. Because it does not account for the thickness distribution nor for the viscous effects, the approximate solution does not describe the chordwise variation of the flow around the actual airfoil. However, as will be discussed, the theoretical values of the lift coefficient (obtained by integrating the circulation distribution along the airfoil) are in reasonable agreement with the experimental values.

For the camber line of the symmetric airfoil, dz/dx is everywhere zero, and equation (6.5) becomes:

$$\frac{1}{2\pi}\int_0^c \frac{\gamma(\xi)}{x-\xi}\,d\xi = U_\infty\alpha \tag{6.6}$$

It is convenient for the purposes of integration to introduce the coordinate transformation:

$$\xi = \frac{c}{2}(1-\cos\theta) \quad \text{and} \quad d\xi = \frac{c}{2}\sin\theta\,d\theta \tag{6.7}$$

Similarly, the x coordinate transforms to θ_0 using:

$$x = \frac{c}{2}(1-\cos\theta_0)$$

The corresponding limits of integration become:

$$\xi = 0 \quad \text{at} \quad \theta = 0 \quad \text{and} \quad \xi = c \quad \text{at} \quad \theta = \pi$$

and equation (6.6) becomes:

$$\frac{1}{2\pi}\int_0^\pi \frac{\gamma(\theta)\frac{c}{2}\sin\theta\, d\theta}{\frac{c}{2}(1-\cos\theta_0)-\frac{c}{2}(1-\cos\theta)} = \frac{1}{2\pi}\int_0^\pi \frac{\gamma(\theta)\sin\theta\, d\theta}{(\cos\theta-\cos\theta_0)} = U_\infty\alpha \qquad \textbf{(6.8)}$$

The required vorticity distribution, $\gamma(\theta)$, must not only satisfy this integral equation, but must also satisfy the Kutta condition, namely that $\gamma(\pi) = 0$. The solution requires performing an integral of an unknown function, $\gamma(\theta)$, to determine a known result, $U_\infty\alpha$. This is very different than the type of integration typical in Calculus, where you usually integrate known functions to find unknown results (e.g., $\int_0^1 x\, dx = \frac{1}{2}$). However, using the concept of the anti-derivative we can obtain:

$$\gamma(\theta) = 2\alpha U_\infty \frac{1+\cos\theta}{\sin\theta} \qquad \textbf{(6.9)}$$

This is a valid solution, as can be seen by substituting the expression for $\gamma(\theta)$ given by equation (6.9) into equation (6.8). The resulting equation,

$$\frac{\alpha U_\infty}{\pi}\int_0^\pi \frac{(1+\cos\theta)\, d\theta}{\cos\theta-\cos\theta_0} = U_\infty\alpha$$

can be reduced to an identity using the relation:

$$\int_0^\pi \frac{\cos n\theta\, d\theta}{\cos\theta-\cos\theta_0} = \frac{\pi\sin n\theta_0}{\sin\theta_0} \qquad \textbf{(6.10)}$$

where n assumes only integer values. Using l'Hospital's rule, we can show that the expression for $\gamma(\theta)$ also satisfies the Kutta condition, since:

$$\gamma(\pi) = 2\alpha U_\infty \frac{1+\cos\pi}{\sin\pi} = \frac{0}{0}$$

which is undefined. So, taking the derivative of the numerator and denominator yields:

$$\gamma(\pi) = 2\alpha U_\infty \frac{-\sin\pi}{\cos\pi} = 0$$

which is the Kutta condition.

Now that we have determined that the Kutta condition is satisfied, we can find the total circulation around the airfoil as $\Gamma = \int_0^c \gamma(\xi)d\xi = \int_0^\pi \gamma(\theta)d\theta$. The Kutta-Joukowski theorem for steady flow about a two-dimensional body of any cross section shows that the force per unit span is equal to $\rho_\infty\, U_\infty\, \Gamma$ and acts perpendicular to U_∞. Therefore, for two-dimensional inviscid flow, an airfoil has no drag (remember d'Alembert's paradox in Chapter 3) but experiences a lift per unit span equal to the product of the free-stream density, the free-stream velocity, and the total circulation. The lift per unit span is therefore:

$$l = \int_0^c \rho_\infty U_\infty \gamma(\xi)\, d\xi \qquad \textbf{(6.11)}$$

Using the circulation distribution of equation (6.9) and the coordinate transformation of equation (6.7), the lift per unit span is

$$l = \rho_\infty U_\infty^2 \, \alpha c \int_0^\pi (1 + \cos\theta) \, d\theta$$

$$l = \pi \rho_\infty U_\infty^2 \, \alpha c \tag{6.12}$$

To determine the section lift coefficient of the airfoil, notice that the reference area per unit span is the chord, and the section lift coefficient is:

$$C_l = \frac{l}{\frac{1}{2}\rho_\infty U_\infty^2 c} = \frac{\pi \rho_\infty U_\infty^2 \alpha c}{\frac{1}{2}\rho_\infty U_\infty^2 c} = 2\pi\alpha \tag{6.13}$$

where α is the angle of attack in radians. If we take the derivative of the lift coefficient with respect to the angle of attack, we can find the lift-curve slope as $C_{l_\alpha} = 2\pi$ 1/rad $= 0.1097$ 1/deg, which is the value we discussed in Chapter 5. Therefore, thin-airfoil theory yields a section lift coefficient for a symmetric airfoil that is directly proportional to the geometric angle of attack. The geometric angle of attack is the angle between the free-stream velocity and the chord line of the airfoil. The theoretical relation is independent of the airfoil thickness. However, because the airfoil thickness distribution and the boundary layer affect the flow field, the actual two-dimensional lift curve slope will typically be less than 2π per radian (see the discussion in Section 5.4.1). In fact, most airfoils have a lift-curve slope very close to 2π per radian.

It may seem strange that the net force for an inviscid flow past a symmetric airfoil is perpendicular to the free-stream flow rather than perpendicular to the airfoil (i.e., the resultant force has only a lift component and not both a lift and a drag component). As we saw in Section 3.15.2, the prediction of zero drag for potential flow applications may be generalized to any general, two-dimensional body in an irrotational, steady, incompressible flow. Consider an incompressible, inviscid flow about a symmetric airfoil at a small angle of attack. There is a stagnation point on the lower surface of the airfoil just downstream of the leading edge. From this stagnation point, flow accelerates around the leading edge to the upper surface. Referring to the first paragraph in this section, the approximate theoretical solution for a thin, symmetric airfoil with two sharp edges yields an infinite velocity at the leading edge. The high velocities for flow over the leading edge result in low pressures in this region, producing a component of force along the leading edge, known as the *leading-edge suction force*, which exactly cancels the streamwise component of the pressure distribution acting on the rest of the airfoil, resulting in zero drag.

As noted by Carlson and Mack (1980), "Linearized theory places no bounds on the magnitude of the peak suction pressure, which, therefore, can become much greater than practically realizable values." However, "limitations imposed by practically realizable pressures may have a relatively insignificant effect on the normal force but could, at the same time, severely limit the attainment of the thrust force."

The pressure distribution also produces a pitch moment about the leading edge (per unit span), which can be found by multiplying the lift in equation (6.11) by a moment arm, ξ, to obtain:

$$m_0 = -\int_0^c \rho_\infty U_\infty \gamma(\xi)\xi \, d\xi \tag{6.14}$$

The lift-generating circulation of an element $d\xi$ produces an upward force that acts a distance ξ downstream of the leading edge. The lift force, therefore, produces a nose-down pitching moment about the leading edge. Therefore, a negative sign is used in equation (6.14) because nose-up pitch moments are considered positive. Again, using the coordinate transformation [equation (6.7)] and the circulation distribution [equation (6.9)], the pitch moment (per unit span) about the leading edge is:

$$\begin{aligned} m_0 &= -\frac{1}{2}\rho_\infty U_\infty^2 \alpha c^2 \int_0^\pi (1 - \cos^2\theta)\, d\theta \\ &= -\frac{\pi}{4}\rho_\infty U_\infty^2 \alpha c^2 \end{aligned} \tag{6.15}$$

The section moment coefficient is defined as:

$$C_{m_0} = \frac{m_0}{\frac{1}{2}\rho_\infty U_\infty^2 c c} \tag{6.16}$$

Notice that the reference area per unit span for the airfoil is the chord and the reference length for the pitch moment is also the chord. So, for the symmetric airfoil:

$$C_{m_0} = -\frac{\pi}{2}\alpha = -\frac{C_l}{4} \tag{6.17}$$

The pitch moment coefficient transferred to $c/4$ is $C_{m_{c/4}} = 0$, or in other words the quarter chord is the aerodynamic center.

The center of pressure x_{cp} is the x coordinate where the resultant lift force could be placed to produce the pitch moment m_0. Equating the moment about the leading edge [equation (6.15)] to the product of the lift [equation (6.12)] and the center of pressure gives us:

$$-\frac{\pi}{4}\rho_\infty U_\infty^2 \alpha c^2 = -\pi\rho_\infty U_\infty^2 \alpha c x_{\text{cp}}$$

Solving for x_{cp}, we obtain:

$$x_{\text{cp}} = \frac{c}{4} \tag{6.18}$$

which is also the quarter chord of the airfoil. The result is independent of the angle of attack and is therefore independent of the section lift coefficient. As with the lift-curve slope, the center of pressure of airfoils with thickness typically is somewhat different than $c/4$, but the quarter chord is a good assumption for the center of pressure location. The center of pressure being at the quarter chord implies that the distribution of pressure on the airfoil (see Fig. 5.10) is not symmetric between the leading edge and trailing edge, but rather the pressure difference is higher near the leading edge. In other words, more lift is produced near the leading edge of the airfoil than near the trailing edge (see the airfoil concept box in Chapter 5 to understand why).

EXAMPLE 6.1: Theoretical aerodynamic coefficients for a symmetric airfoil

The theoretical aerodynamic coefficients calculated using the thin-airfoil relations are compared with the data of Abbott and von Doenhoff (1949) in Fig. 6.6. Data are presented for two different airfoil sections. One, the NACA 0009 airfoil, has a maximum thickness which is 9% of the chord and is located at $x = 0.3c$. The theoretical lift coefficient calculated using equation (6.13) is in excellent agreement with the data for the NACA 0009 airfoil up to an angle of attack of 12°. At higher angles of attack, the viscous effects significantly alter the flow field and hence the experimental lift coefficients. That is why the theoretical values would not be expected to agree with the data at high angles of attack in the stall region. Since the theory presumes that viscous effects are small, it is valid only for angles of attack below stall. According to thin-airfoil theory, the moment about the quarter chord is zero. The measured moments for the NACA 0009 are also in excellent agreement with thin-airfoil theory prior to stall. The correlation between the theoretical values and the experimental values is not as good for the NACA 0012-64 airfoil section, although

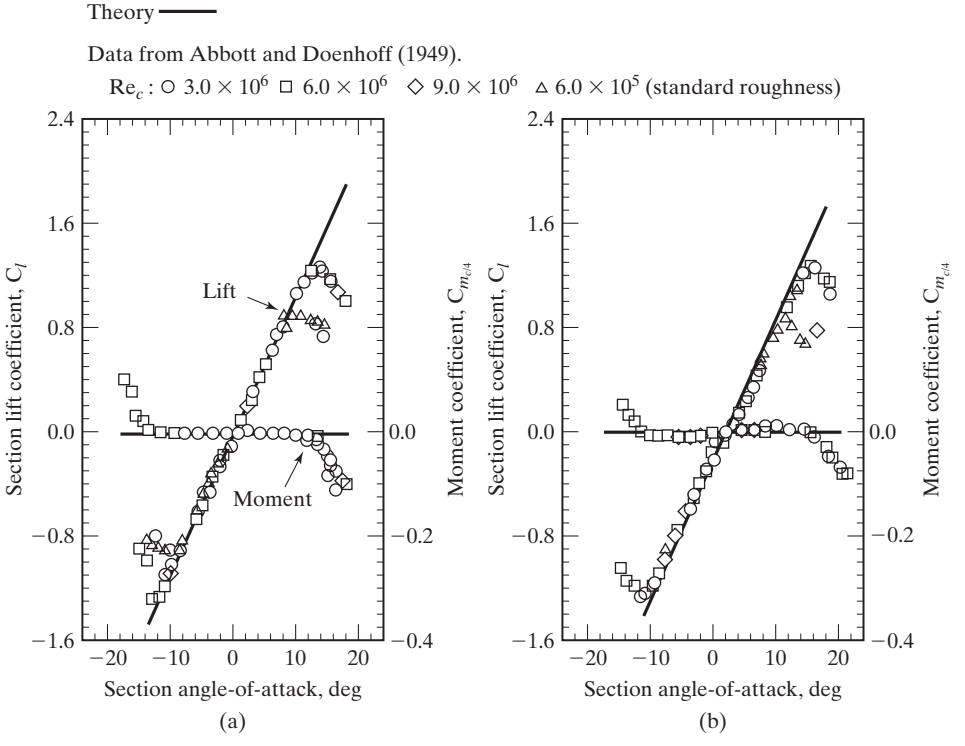

Figure 6.6 Comparison of the aerodynamic coefficients calculated using thin-airfoil theory for symmetric airfoils: (a) NACA 0009 wing section; (b) NACA 0012-64 wing section [data from Abbott and von Doenhoff (1949)].

the theory is very close to the data. The difference in the correlation between theory and data for these two airfoil sections is attributed to viscous effects since the maximum thickness of the NACA 0012-64 is greater and located farther aft. Therefore, the adverse pressure gradients that cause separation of the viscous boundary layer and thereby alter the flow field would be greater for the NACA 0012-64 airfoil. In both cases, thin-airfoil theory does a very good job of predicting the lift and moment coefficients of the airfoils.

6.5 THIN, CAMBERED AIRFOIL

The method of determining the aerodynamic characteristics for a cambered airfoil is similar to that followed for the symmetric airfoil. A vorticity distribution, $\gamma(\theta)$, is sought which satisfies both the condition that the mean camber line is a streamline [equation (6.5)] and the Kutta condition. However, because of camber, the actual computations are more involved. Again, we will use the coordinate transformation:

$$\xi = \frac{c}{2}(1 - \cos\theta) \tag{6.7}$$

and the fundamental equation of thin-airfoil theory, equation (6.5), becomes:

$$\frac{1}{2\pi}\int_0^{\pi} \frac{\gamma(\theta)\sin\theta\, d\theta}{\cos\theta - \cos\theta_0} = U_\infty\left(\alpha - \frac{dz}{dx}\right) \tag{6.19}$$

Notice that the expression is only different from equation (6.8) by the inclusion of the dz/dx term. Recall that this integral equation expresses the requirement that the resultant velocity for the inviscid flow is parallel to the mean camber line (which represents the airfoil). The vorticity distribution $\gamma(\theta)$ that satisfies the integral equation makes the vortex sheet (which is coincident with the mean camber line) a streamline of the flow. However, when we solved the symmetric airfoil case, equation (6.8), we were solving an integral of an unknown function, $\gamma(\theta)$, to find a known *constant*, $U_\infty\alpha$. In the case of a cambered airfoil, we are solving the integral of an unknown function to find a known *function*, $U_\infty(\alpha - dz/dx)$. This is a much more difficult integration to perform and will require the use of Fourier analysis.

6.5.1 Vorticity Distribution

The desired vorticity distribution, which satisfies equation (6.19) and the Kutta condition, may be represented by a series involving:

- A term of the form for the vorticity distribution for a symmetric airfoil from equation (6.9),

$$2U_\infty A_0 \frac{1 + \cos\theta}{\sin\theta}$$

- A Fourier sine series whose terms automatically satisfy the Kutta condition,

$$2U_\infty \sum_{n=1}^{\infty} A_n \sin n\theta$$

The coefficients A_n of the Fourier series depend on the shape of the mean camber line. Putting these two requirements together gives us:

$$\gamma(\theta) = 2U_\infty\left(A_0\frac{1+\cos\theta}{\sin\theta} + \sum_{n=1}^{\infty}A_n\sin n\theta\right) \tag{6.20}$$

Since each term is zero when $\theta = \pi$, the Kutta condition is satisfied [i.e., $\gamma(\pi) = 0$].

Substituting the vorticity distribution [equation (6.20)] into equation (6.19) yields

$$\frac{1}{\pi}\int_0^\pi \frac{A_0(1+\cos\theta)\,d\theta}{\cos\theta-\cos\theta_0} + \frac{1}{\pi}\int_0^\pi \sum_{n=1}^{\infty}\frac{A_n\sin n\theta\sin\theta\,d\theta}{\cos\theta-\cos\theta_0} = \alpha - \frac{dz}{dx} \tag{6.21}$$

This integral equation can be used to evaluate the coefficients $A_0, A_1, A_2, \ldots, A_n$ in terms of the angle of attack and the mean camber-line slope, which is known for a given airfoil section. The first integral on the left-hand side of equation (6.21) can be readily evaluated using equation (6.10). To evaluate the series of integrals represented by the second term, we must use equation (6.10) and the trigonometric identity:

$$(\sin n\theta)(\sin\theta) = \frac{1}{2}[\cos\{(n-1)\theta\} - \cos\{(n+1)\theta\}]$$

Using this approach, equation (6.21) becomes:

$$\frac{dz}{dx} = \alpha - A_0 + \sum_{n=1}^{\infty}A_n\cos n\theta \tag{6.22}$$

which applies to any chordwise station. Since we are evaluating both dz/dx and $\cos n\theta_0$ at the general point θ_0 (i.e., x), we have dropped the subscript 0 from equation (6.22) and from all subsequent equations. Therefore, the coefficients $A_0, A_1, A_2, \ldots, A_n$ must satisfy equation (6.22) if equation (6.20) is to represent the vorticity distribution which satisfies the condition that the mean camber line is a streamline. Since the geometry of the mean camber line would be known for the airfoil of interest, the slope is a known function of θ, so we can determine the values of the coefficients.

To evaluate A_0, notice that:

$$\int_0^\pi A_n\cos n\theta\,d\theta = 0$$

for any value of n. Therefore, by algebraic manipulation of equation (6.22) we can find:

$$A_0 = \alpha - \frac{1}{\pi}\int_0^\pi \frac{dz}{dx}d\theta \tag{6.23}$$

Multiplying both sides of equation (6.22) by $\cos m\theta$, where m is an unspecified integer, and integrating from 0 to π, we obtain:

$$\int_0^\pi \frac{dz}{dx}\cos m\theta\,d\theta = \int_0^\pi(\alpha - A_0)\cos m\theta\,d\theta + \int_0^\pi\sum_{n=1}^{\infty}A_n\cos n\theta\cos m\theta\,d\theta$$

The first term on the right-hand side is zero for any value of m since $\alpha - A_0 = \alpha_{0l}$ is a known constant. Also notice that:

$$\int_0^\pi A_n\cos n\theta\cos m\theta\,d\theta = 0 \qquad \text{when } n \neq m$$

but

$$\int_0^{\pi} A_n \cos n\theta \cos m\theta \, d\theta = \frac{\pi}{2} A_n \qquad \text{when } n = m$$

Therefore,

$$A_n = \frac{2}{\pi} \int_0^{\pi} \frac{dz}{dx} \cos n\theta \, d\theta \tag{6.24}$$

Using equations (6.23) and (6.24) to define the coefficients, equation (6.20) can be used to evaluate the vorticity distribution for a cambered airfoil in terms of the geometric angle of attack and the shape of the mean camber line. Notice that, for a symmetric airfoil, $A_0 = \alpha, A_1 = A_2 = \cdots = A_n = 0$, and the vorticity distribution for a symmetric airfoil, as we found using equation (6.20), is:

$$\gamma(\theta) = 2\alpha U_\infty \frac{1 + \cos\theta}{\sin\theta}$$

which is identical to equation (6.9). Therefore, the general expression for the cambered airfoil includes the symmetric airfoil as a special case. Now that we know the vorticity distribution for the airfoil, we can find the aerodynamic coefficients.

6.5.2 Aerodynamic Coefficients for a Cambered Airfoil

The lift and the moment coefficients for a cambered airfoil are found using the same approach as for the symmetric airfoil. The section lift coefficient is given by

$$C_l = \frac{l}{\frac{1}{2}\rho_\infty U_\infty^2 c} = \int_0^c \rho_\infty U_\infty \gamma(\xi) \, d\xi$$

Using the coordinate transformation [equation (6.7)] and the expression for γ [equation (6.20)], we obtain:

$$C_l = 2\left[\int_0^{\pi} A_0(1 + \cos\theta) \, d\theta + \int_0^{\pi} \sum_{n=1}^{\infty} A_n \sin n\theta \sin\theta \, d\theta \right]$$

Notice that $\int_0^{\pi} A_n \sin n\theta \sin\theta \, d\theta = 0$ for any value of n other than unity. Therefore, after integration we obtain:

$$\begin{aligned} C_l &= 2\pi\left(A_0 + \frac{A_1}{2} \right) = 2\pi\left[\alpha - \frac{1}{\pi}\int_0^{\pi} \frac{dz}{dx} d\theta + \frac{1}{\pi}\int_0^{\pi} \frac{dz}{dx} \cos\theta \, d\theta \right] \\ &= 2\pi\left[\alpha + \frac{1}{\pi}\int_0^{\pi} \frac{dz}{dx}(\cos\theta - 1) d\theta \right] = 2\pi(\alpha - \alpha_{0l}) \end{aligned} \tag{6.25}$$

From these derivations, we can quickly see two important things. First, we now have a way to find α_{0l} by comparing terms in the previous equation:

$$C_l = 2\pi\left[\alpha + \frac{1}{\pi}\int_0^{\pi} \frac{dz}{dx}(\cos\theta - 1) d\theta \right] = 2\pi(\alpha - \alpha_{0l})$$

so

$$\alpha_{0l} = -\frac{1}{\pi}\int_0^{\pi}\frac{dz}{dx}(\cos\theta - 1)\,d\theta$$

Second, the slope of the lift curve is:

$$C_{l_\alpha} = \frac{\partial C_l}{\partial \alpha} = 2\pi \text{ 1/rad}$$

which was the same result that we found for the symmetric airfoil. In other words, according to thin-airfoil theory, the lift-curve slope is always the same, 2π 1/rad. So how did adding camber impact the lift of the airfoil? The camber did not change the slope of the lift curve, but it did change the intercept, α_{0l}, which means at a given angle of attack a cambered airfoil will produce more lift than a symmetric airfoil.

The section moment coefficient for the pitching moment about the leading edge is given by

$$C_{m_0} = -\frac{\int_0^c \rho_\infty U_\infty \gamma(\xi)\xi\,d\xi}{\frac{1}{2}\rho_\infty U_\infty^2 c^2}$$

Again, using the coordinate transformation and the vorticity distribution, we can integrate and obtain:

$$C_{m_0} = -\frac{\pi}{2}\left(A_0 + A_1 - \frac{A_2}{2}\right) \tag{6.26}$$

In other words, in spite of the fact that $\gamma(\theta)$ in equation (6.20) is represented by an infinite series, the lift and pitch moment coefficients are only functions of A_0, A_1, and A_2.

The center of pressure relative to the leading edge is again found by dividing the moment about the leading edge (per unit span) by the lift per unit span.

$$x_{\text{cp}} = -\frac{m_0}{l}$$

The negative sign is used since a positive lift force with a positive moment arm x_{cp} results in a nose-down, or negative moment, as shown in the sketch of Fig. 6.7. Therefore, the center of pressure is:

$$x_{\text{cp}} = \frac{c}{4}\left(\frac{2A_0 + 2A_1 - A_2}{2A_0 + A_1}\right)$$

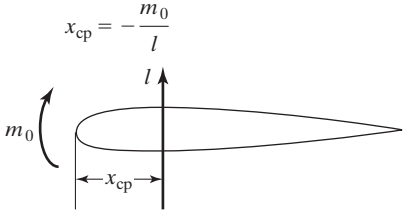

Figure 6.7 Center of pressure for a thin, cambered airfoil.

Noting that $C_l = \pi(2A_0 + A_1)$, the expression for the center of pressure simplifies to:

$$x_{\text{cp}} = \frac{c}{4}\left[1 + \frac{\pi}{C_l}(A_1 - A_2)\right] \tag{6.27}$$

So, for the cambered airfoil, the position of the center of pressure depends on the lift coefficient and therefore the angle of attack. The line of action for the lift, as well as the magnitude, must be specified for each angle of attack.

If the pitch moment per unit span produced by the pressure distribution is referred to a point $c/4$ downstream of the leading edge (i.e., the quarter chord), then the moment is given by:

$$m_{c/4} = \int_0^{c/4} \rho_\infty U_\infty \gamma(\xi)\left(\frac{c}{4} - \xi\right) d\xi - \int_{c/4}^{c} \rho_\infty U_\infty \gamma(\xi)\left(\xi - \frac{c}{4}\right) d\xi$$

Again, the signs are chosen so that a nose-up moment is positive. Rearranging the relation above gives us:

$$m_{c/4} = \frac{c}{4}\int_0^c \rho_\infty U_\infty \gamma(\xi)\, d\xi - \int_0^c \rho_\infty U_\infty \gamma(\xi)\xi\, d\xi$$

The first integral on the right-hand side of this equation represents the lift per unit span, while the second integral represents the moment per unit span about the leading edge. Therefore,

$$m_{c/4} = \frac{c}{4} l + m_0 \tag{6.28}$$

The section moment coefficient about the quarter-chord point is given by:

$$C_{m_{c/4}} = \frac{C_l}{4} + C_{m_0} = \frac{\pi}{4}(A_2 - A_1) \tag{6.29}$$

Since A_1 and A_2 depend on the camber only, the section moment coefficient about the quarter-chord point is independent of the angle of attack. The point about which the section moment coefficient is independent of the angle of attack is called the *aerodynamic center of the section*. Therefore, according to the theoretical relations for a thin-airfoil section, the aerodynamic center is at the quarter-chord. This is true for cambered airfoils as well as symmetric airfoils, since the results for symmetric airfoils are just a special case of equation (6.29). The primary difference in the pitch moment for a cambered airfoil is that $C_{m_{c/4}}$ will be negative, and for a symmetric airfoil $C_{m_{c/4}} = 0$ (camber creates a nose-down pitch moment).

In order for the section pitch moment to remain constant as the angle of attack is increased, the product of the moment arm (relative to the aerodynamic center) and C_l must remain constant. This means that the moment arm (relative to the aerodynamic center) decreases as the lift increases. This is evident in the expression for the center of pressure, which is given in equation (6.27). Alternatively, the aerodynamic center is the point at which all changes in lift effectively take place. Because of these factors, the center of gravity of an airplane is usually located near the aerodynamic center.

If we include the effects of viscosity on the flow around the airfoil, the lift due to angle of attack would not necessarily be concentrated at the exact quarter-chord point. However, for angles of attack below the onset of stall, the actual location of the aerodynamic center for the various sections is usually between the 23% chord point and the 27% chord point. Therefore, the moment coefficient about the aerodynamic center, which is given the symbol $C_{m_{ac}}$, is also given by equation (6.29). If equation (6.24) is used to define A_1 and A_2, then $C_{m_{ac}}$ becomes:

$$C_{m_{ac}} = \frac{1}{2}\int_0^{\pi} \frac{dz}{dx}(\cos 2\theta - \cos\theta)\, d\theta \tag{6.30}$$

As we discussed when comparing theory with data in the preceding section, the $C_{m_{ac}}$ is zero for a symmetric airfoil.

EXAMPLE 6.2: Theoretical aerodynamic coefficients for a cambered airfoil

The relations developed in this section will now be used to calculate the aerodynamic coefficients for a representative cambered airfoil section. The airfoil section selected for use in this sample problem is the NACA 2412 airfoil. As discussed in Abbott and Doenhoff (1949) the first digit defines the maximum camber in percent of chord, the second digit defines the location of the maximum camber in tenths of chord, and the last two digits represent the thickness ratio (i.e., the maximum thickness in percent of chord). The equation for the mean camber line is defined in terms of the maximum camber and its location, which for this airfoil is $0.4c$. Forward of the maximum camber position ($0 \le x/c \le 0.4$), the equation of the mean camber line is

$$\left(\frac{z}{c}\right)_{\text{fore}} = 0.125\left[0.8\left(\frac{x}{c}\right) - \left(\frac{x}{c}\right)^2\right]$$

and aft of the maximum camber position ($0.4 \le x/c \le 1.0$),

$$\left(\frac{z}{c}\right)_{\text{aft}} = 0.0555\left[0.2 + 0.8\left(\frac{x}{c}\right) - \left(\frac{x}{c}\right)^2\right]$$

Solution: To calculate the section lift coefficient and the section moment coefficient, it is only necessary to evaluate the coefficients A_0, A_1, and A_2. To evaluate these coefficients, we need to integrate the slope of the mean camber line. Therefore, the slope of the mean camber line will be expressed in terms of the θ coordinate, which is given in equation (6.7). Forward of the maximum camber location the slope is given by:

$$\left(\frac{dz}{dx}\right)_{\text{fore}} = 0.1 - 0.25\frac{x}{c} = 0.125\cos\theta - 0.025$$

Aft of the maximum camber location, the slope is given by

$$\left(\frac{dz}{dx}\right)_{\text{aft}} = 0.0444 - 0.1110\frac{x}{c} = 0.0555\cos\theta - 0.0111$$

Since the maximum camber location serves as a limit for the integrals, it is necessary to convert the x coordinate, which is $0.4c$, to the corresponding θ coordinate. To do this, we use the transformation given by equation (6.7):

$$\frac{c}{2}(1 - \cos\theta) = 0.4c$$

The resulting location of the maximum camber is $\theta = 78.463° = 1.3694$ rad. Referring to equations (6.23) and (6.24), the necessary coefficients are:

$$A_0 = \alpha - \frac{1}{\pi}\left[\int_0^{1.3694} (0.125\cos\theta - 0.025)\, d\theta + \int_{1.3694}^{\pi} (0.0555\cos\theta - 0.0111)\, d\theta\right]$$

$$= \alpha - 0.004517$$

$$A_1 = \frac{2}{\pi}\left[\int_0^{1.3694} (0.125\cos^2\theta - 0.025\cos\theta)\, d\theta + \int_{1.3694}^{\pi} (0.0555\cos^2\theta - 0.0111\cos\theta)\, d\theta\right]$$

$$= 0.08146$$

$$A_2 = \frac{2}{\pi}\left[\int_0^{1.3694} (0.125\cos\theta\cos 2\theta - 0.025\cos 2\theta)\, d\theta + \int_{1.3694}^{\pi} (0.0555\cos\theta\cos 2\theta - 0.0111\cos 2\theta)\, d\theta\right]$$

$$= 0.01387$$

The section lift coefficient can now be found from equation (6.25):

$$C_l = 2\pi\left(A_0 + \frac{A_1}{2}\right) = 2\pi\alpha + 0.2297$$

Solving for the angle of attack for zero lift, we obtain:

$$\alpha_{0l} = -\frac{0.2297}{2\pi}\,\text{rad} = -2.095°$$

According to thin-airfoil theory, the aerodynamic center is at the quarter-chord location. So, the section moment coefficient about the quarter chord is equal to that about the aerodynamic center. The two coefficients are given by

$$C_{m_{ac}} = C_{m_{c/4}} = \frac{\pi}{4}(A_2 - A_1) = -0.05309$$

The theoretical values of the section lift coefficient and of the section moment coefficients are compared with the measured values from Abbott and Doenhoff (1949) in Figs. 6.8 and 6.9, respectively. Since the theoretical coefficients do not depend on the airfoil

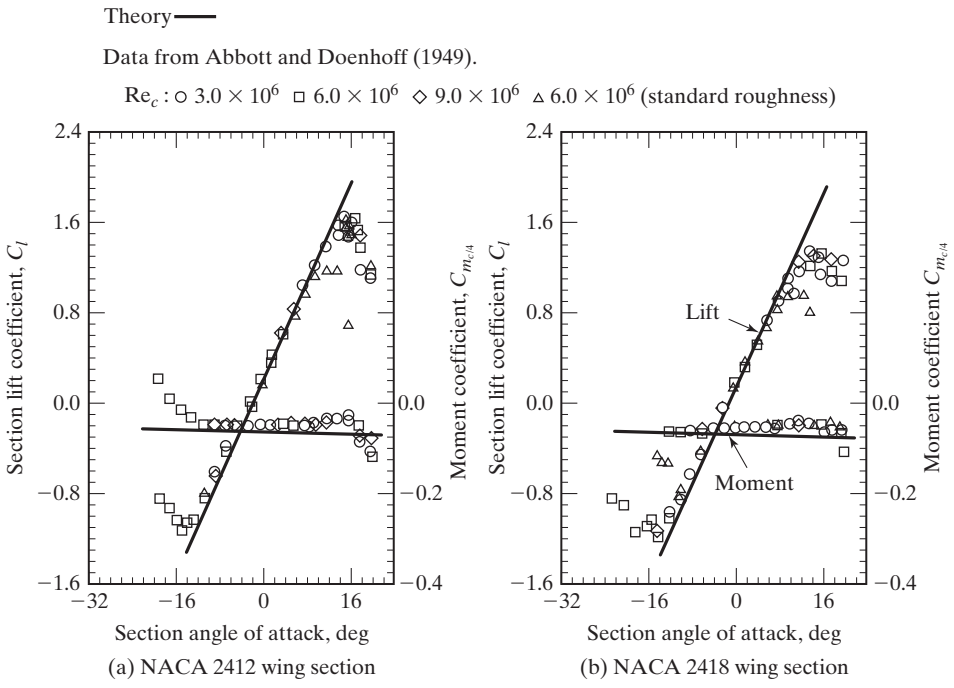

Figure 6.8 Comparison of the aerodynamic coefficients calculated using thin airfoil theory for cambered airfoils: (a) NACA 2412 wing section; (b) NACA 2418 wing section [data from Abbott and von Doenhoff (1949)].

section thickness, they will be compared with data from Abbott and Doenhoff (1949) for a NACA 2418 airfoil as well as for a NACA 2412 airfoil. For both airfoil sections, the maximum camber is 2% of the chord length and is located at $x = 0.4c$. The maximum thickness is 12% of chord for the NACA 2412 airfoil section and is 18% of the chord for the NACA 2418 airfoil section. While an 18% thick airfoil is not considered "thin," it will be informative to see how well thin-airfoil theory does at predicting the aerodynamics of this airfoil.

The correlation between the theoretical and the experimental values of lift coefficient is satisfactory for both airfoils (Fig. 6.8) until the angle of attack becomes so large that viscous phenomena significantly affect the flow field. The theoretical value for the zero lift angle of attack agrees very well with the measured values for the two airfoils. The theoretical value of C_{l_α} is 2π per radian. Based on the measured lift coefficients for angles of attack for 0° to 10°, the experimental value of $C_{l,\alpha}$ is approximately 6.0 per radian for the NACA 2412 airfoil and approximately 5.9 per radian for the NACA 2418 airfoil, which are 4.5% and 6.1% below 2π, respectively.

The experimental values of the moment coefficient referred to the aerodynamic center (approximately -0.045 for the NACA 2412 airfoil and -0.050 for the NACA 2418 airfoil) compare favorably with the theoretical value of -0.053, as shown in Fig. 6.9. The correlation between the experimental values of the moment coefficient referred to the quarter chord, which vary with the angle of attack, and the theoretical value is

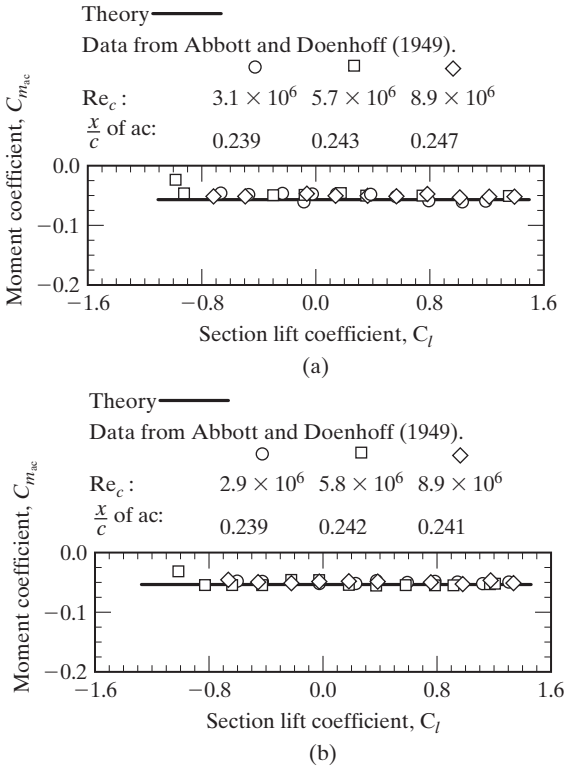

Figure 6.9 Comparison of the theoretical and the experimental section moment coefficient (about the aerodynamic center) for two cambered airfoils: (a) NACA 2412 wing section; (b) NACA 2418 wing section [data from Abbott and von Doenhoff (1949)].

not as good (see Fig. 6.8). Note also that the experimentally determined location of the aerodynamic center for these two airfoils is between 0.239c and 0.247c. As we saw previously, the location is normally between 0.23c and 0.27c for a real fluid flow, as compared with the value of $c/4$ calculated using thin-airfoil theory.

Although the thickness ratio of the airfoil section does not enter into the theory, except as an implied limit to its applicability, the data of Figs. 6.8 and 6.9 show thickness-related variations. Notice that the maximum value of the experimental lift coefficient is consistently greater for the NACA 2412 airfoil and that it occurs at a higher angle of attack. Also notice that as the angle of attack increases beyond the maximum lift value, the measured lift coefficients decrease more sharply for the NACA 2412. So, the thickness ratio influences the interaction between the adverse pressure gradient and the viscous boundary layer, as we discussed in Chapter 4. The interaction, in turn, affects the aerodynamic coefficients. $C_{l_{\max}}$ is presented as a function of the thickness ratio for the NACA 24XX series airfoils in Fig. 6.10. The data of Abbott and von Doenhoff (1949) and the results of McCormick (1967) are presented. McCormick notes that below a thickness ratio of approximately 12%, $C_{l_{\max}}$ decreases rapidly with decreasing thickness. Above a thickness ratio of 12%, the variation in $C_{l_{\max}}$ is less pronounced, but also

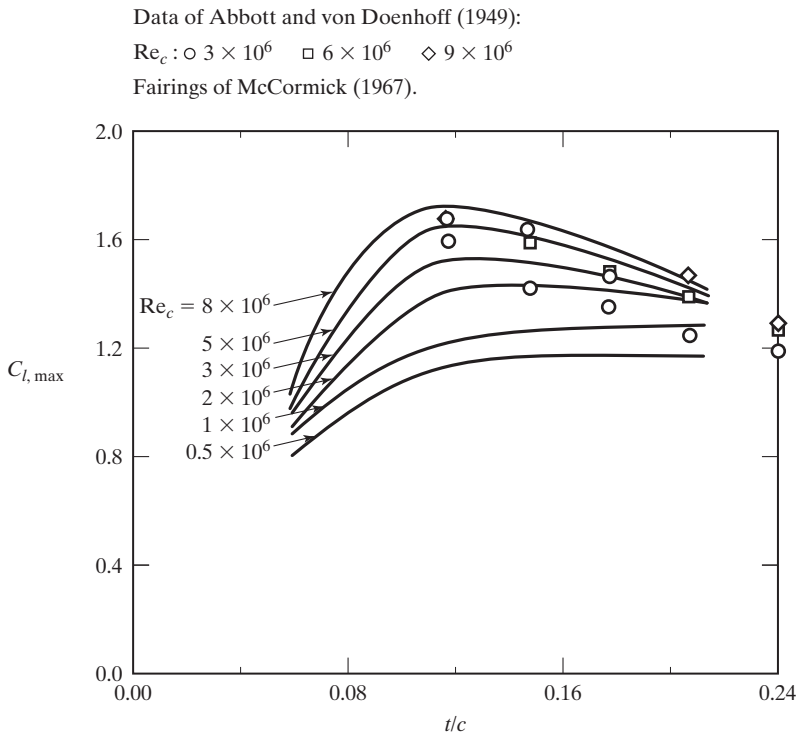

Figure 6.10 Effect of the thickness ratio on the maximum lift coefficient, NACA 24XX series airfoil sections.

decreases. Therefore, an airfoil of approximately 12% thickness obtains a maximum value of $C_{l_{\max}}$ in low-speed flow.

The correlations presented in Figs. 6.6 and 6.8 indicate that, at low angles of attack, the theoretical lift coefficients based on thin-airfoil theory are in good agreement with the measured values from Abbott and von Doenhoff (1949). However, to compute the airfoil lift and pitching moment coefficients for various configurations exposed to a wide range of flow environments, especially if knowledge of the maximum section lift coefficient $C_{l_{\max}}$ is important, it is necessary to include the effects of the boundary layer and of the separated wake. Using repeated application of a panel method (see Chapters 3 and 7) to solve for the separated wake displacement surface, Henderson (1978) discussed the relative importance of separation effects, which are illustrated in Fig. 6.11. The lift coefficient calculated using potential flow analysis with no attempt to account for the affects either of the boundary layer or of separation is compared with wind-tunnel data in Fig. 6.11a. At low angles of attack where the boundary layer is thin and there is little, if any, separation, potential flow analysis of the surface alone is a fair approximation to the data; as the angle of attack is increased, the correlation degrades, due to the increased importance of viscous effects.

Henderson (1978) notes, "Rarely will the boundary layers be thin enough that potential flow analysis of the bare geometry will be sufficiently accurate." By including the effect of the boundary layer but not the separated wake in the computational flow model, the agreement between the theoretical lift coefficients and the wind-tunnel values is good at low angles of attack, as shown in Fig. 6.11b. When the angle of attack

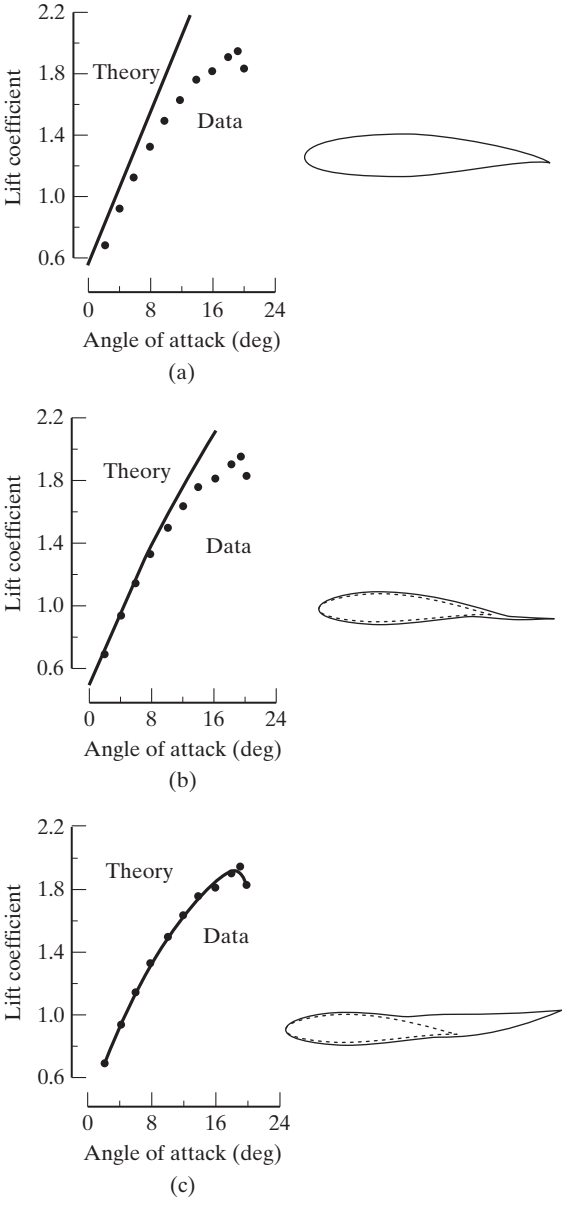

Figure 6.11 Relative importance of separation effects: (a) analysis of geometry alone; (b) analysis with boundary layer modeled; (c) analysis with boundary layer and separated wake modeled [from Henderson (1978)].

is increased and separation becomes important, the predicted and the measured lift coefficients again begin to diverge.

Separation effects must be modeled in order to predict the maximum lift coefficient. As shown in Fig. 6.11c, when we account for the boundary layer and the separated wake, there is good agreement between theoretical values and experimental values through $C_{l_{\max}}$. This will be the case for any gradually separating section, such as the GAW-1, used in the example of Fig. 6.11, but will not always give such good results for all airfoils.

6.6 LAMINAR-FLOW AIRFOILS

Airplane designers have long sought the drag reduction that would be attained if the boundary layer over an airfoil were largely laminar rather than turbulent (see Section 5.4.4 for details about boundary-layer transition and its impact on drag). Aerodynamicists since the 1930s have developed airfoils that could reduce drag by maintaining laminar flow, culminating in the NACA developing laminar-flow airfoils for use on full-scale aircraft, which are the 6-series airfoils discussed in Section 5.2.1 [Jacobs (1939)]. Comparing equations (4.25) and (4.81) shows that there is a fairly significant reduction in skin-friction drag (at reasonably high Reynolds numbers) if the boundary layers are laminar rather than turbulent. The Blasius laminar skin-friction relation is:

$$\overline{C}_f = \frac{1.328}{\sqrt{\mathrm{Re}_L}} \tag{4.25}$$

And the Prandtl turbulent skin-friction relation is:

$$\overline{C}_f = \frac{0.074}{(\mathrm{Re}_L)^{0.2}} \tag{4.81}$$

Early attempts at designing laminar-flow airfoils centered around modifications to the airfoil geometry that would maintain a favorable pressure gradient over a majority of the airfoil surface, as shown in Fig. 6.12. This was accomplished primarily by moving the maximum thickness location of the airfoil further aft, preferably to the mid-chord or beyond, as is evidenced by the NACA 63_1-412 airfoil, and even more pronounced for the NACA 66_1-212 airfoil, especially when compared with the NACA 23012 airfoil.

An entire series of these airfoils were designed and tested, and many of the resulting shapes can be found in *Theory of Wing Sections* by Abbott and von Doenhoff (1949) as the 6-digit airfoil series. These airfoil sections long have been used on general aviation aircraft, including airplanes like the Piper Archer. In the wind tunnel, these airfoils initially showed very promising drag reduction at cruise angles of attack, as shown in

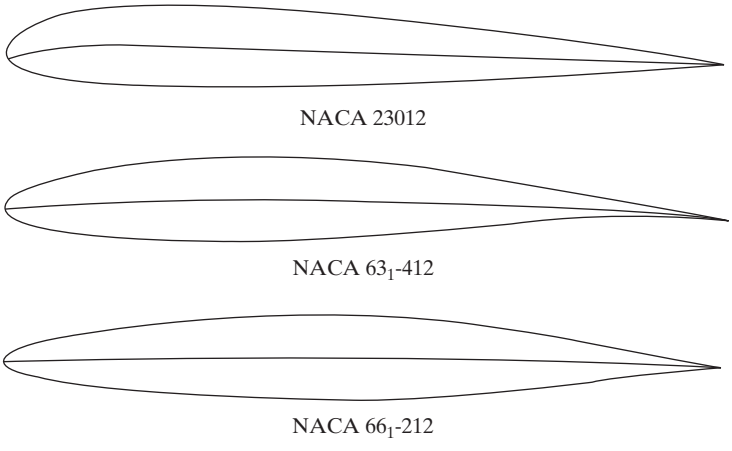

Figure 6.12 Shapes of two NACA laminar-flow airfoil sections compared with the NACA 23012 airfoil section [from Loftin (1985)].

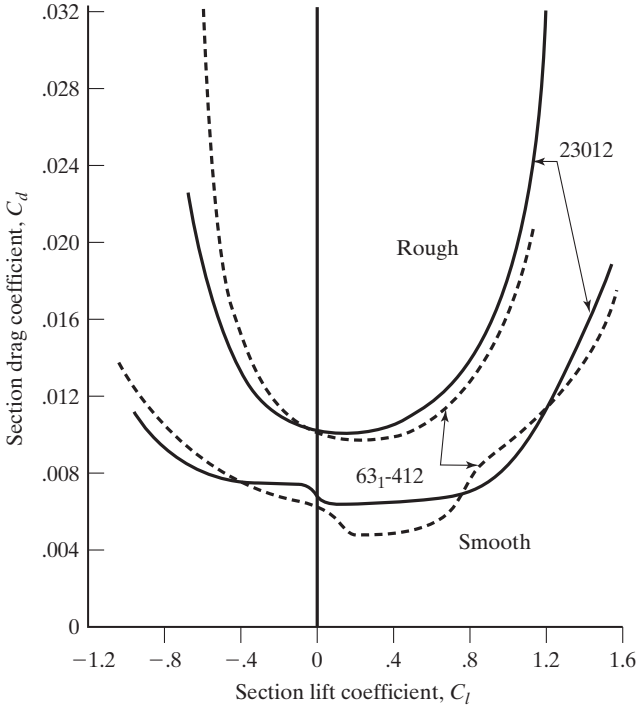

Figure 6.13 Drag characteristics of NACA laminar flow and conventional airfoils sections with both smooth and rough leading edges [from Loftin (1985)].

Fig. 6.13. The "bucket" in the drag curve for the laminar-flow airfoil occurs at angles of attack that normally might be required for cruise, and show a potential drag reduction of up to 25% over the conventional airfoil. Notice, however, that when the wind-tunnel model had typical surface roughness, the flow transitioned to turbulent, and the laminar flow benefits were greatly reduced, even eliminated.

The P-51 was the first production aircraft to utilize these laminar flow airfoils in an attempt to improve range by increasing the wing size and fuel volume for the same amount of drag as a turbulent-flow airfoil (see Fig. 6.14). Unfortunately, laminar-flow airfoils do not function properly if the boundary layer transitions to turbulent, which can happen easily if the wing surface is not smooth. Keeping an airfoil smooth is something that is relatively easy to achieve with wind-tunnel models but rarely takes place with production aircraft due to the use of rivets and bolts, as well as the dents that may take place around the leading edge (or even from insects that become stuck to the leading edge of the wing). "As a consequence, the use of NACA laminar-flow airfoil sections has never resulted in any significant reduction in drag as a result of the achievement of laminar flow" [Loftin (1985)]. This has led to a variety of flow-control devices being used to actively maintain laminar flow, but most of these devices require additional power sources (such as boundary-layer suction or blowing, as discussed in Section 13.4.2), which usually does not make them practical as a drag-reduction concept.

Figure 6.14 Restored NACA P-51 with laminar flow airfoil sections [courtesy of NASA Dryden Flight Research Center].

The relatively high Reynolds numbers of full-scale aircraft flying at common flight altitudes made the realization of lower drag using laminar flow impractical, but new applications have revived interest in laminar flow airfoils, including micro UAVs [Grasmeyer and Keennon (2001)] and high-altitude aircraft (see both concepts in Fig. 6.15). These aircraft have vastly different configurations, ranging from very low aspect-ratio "flying discs" to very high aspect-ratio aircraft. The difference in design is dictated by the difference in application, with the micro UAV flying at such low Reynolds numbers that typical design thinking about aspect ratio no longer holds. Heavier aircraft often have higher aspect ratios, because induced drag is so much larger than skin-friction drag at higher Reynolds numbers. As the size of the vehicle decreases (and as weight and Reynolds number also decreases), aspect ratio no longer is the dominant factor in creating drag—skin-friction drag becomes more important, hence the low aspect-ratio design common for micro UAVs [Drela et al. (2003)]. The high-altitude aircraft (such as Helios shown in Fig. 6.15) also fly at low Reynolds numbers but require fairly heavy weights in order to carry the solar panels and batteries required for propulsion—the high aspect-ratio aircraft once again becomes more efficient.

The most important fluid dynamic characteristic for the design of laminar airfoils are laminar separation bubbles and transition. Laminar flow separates easier than

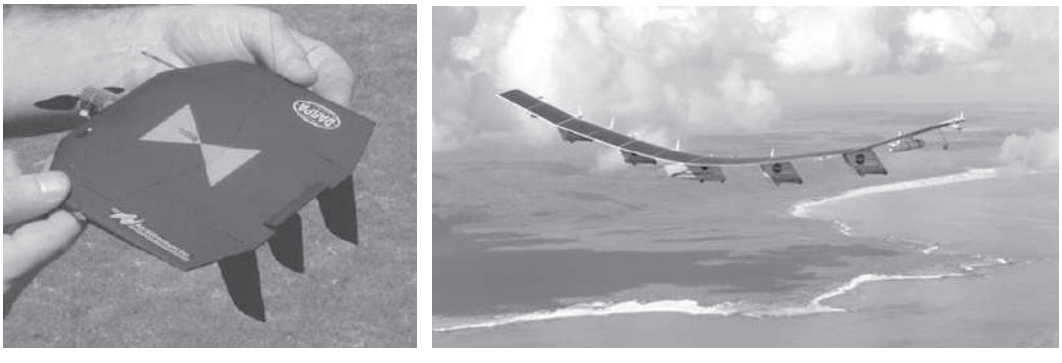

Figure 6.15 Candidate laminar-flow airfoil aircraft: Black Widow Micro UAV (left) and Helios high-altitude solar-powered aircraft (right) [Black Widow from Grasmeyer and Keennon (2001), courtesy of AeroVironment, Inc.; Helios courtesy of NASA Dryden Flight Research Center].

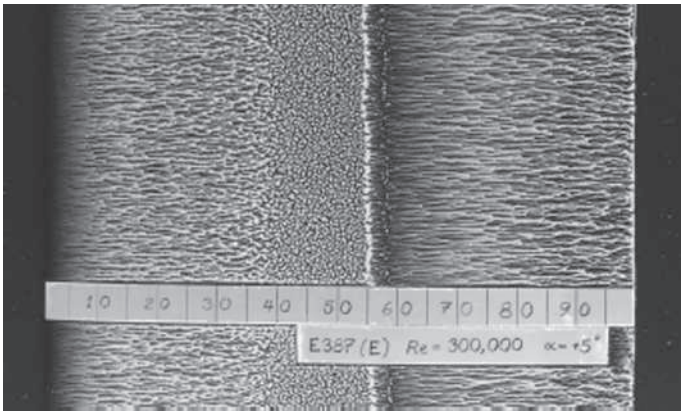

Figure 6.16 Laminar separation bubble on an airfoil shown by surface oil flow where separation and reattachment are visible [from Selig (2003)].

turbulent flow and often leads to separation bubbles, as shown in Fig. 6.16. These separated flow regions reattach, but the boundary layer usually transitions to turbulent through the separation process, leading to higher drag due to the bubble and turbulent flow after the bubble. Methods to overcome the laminar separation bubble include the tailoring of the airfoil geometry ahead of the bubble formation to control the adverse pressure gradient, or by using transition trips. While transition trips do increase the skin-friction drag, if used properly they also can lead to a net reduction in drag due to the elimination of the separation bubble [Gopalarathnam et al. (2001)].

The fact that the uses for laminar airfoils vary a great deal (ranging from UAVs to gliders and to high-altitude aircraft) means that there is no single optimum airfoil: each application requires a different wing and airfoil design in order to optimize performance [Torres and Mueller (2004)]. This led many researchers to begin wind-tunnel testing laminar-flow airfoils so that designers could choose optimum airfoil sections depending on their requirements [Selig et al. (1989 and 2001)]. A good overview of the type of airfoils that work for various uses is presented by Selig (2003), including wind turbines, airfoils with low pitching moments, high-lift airfoils, and radio-controlled sailplanes (candidate airfoils are shown in Fig. 6.17). Another approach is to use various numerical prediction methods which have been developed over the years, including Eppler's code

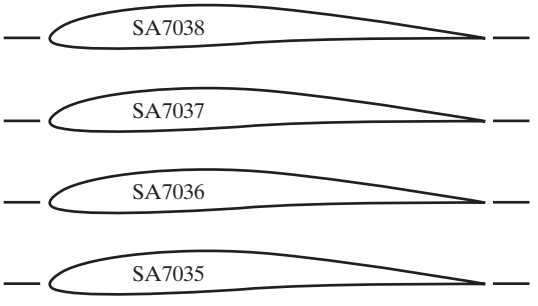

Figure 6.17 Candidate airfoils for radio controlled sailplanes [from Selig (2003)].

[Eppler and Somers (1980), Eppler (1990)], XFOIL [Drela (1989)], and inverse design methods such as PROFOIL [Selig and Maughmer (1992)] and its applications [Jepson and Gopalarathnam (2004)]. These codes partially rely on semi-empirical or theoretical methods for predicting laminar separation bubbles, transition, and separation, and have been found to produce reasonable results for typical airfoils.

6.7 HIGH-LIFT AIRFOIL SECTIONS

Since stall occurs on airfoils at relatively low angles of attack (between 10 and 20 degrees depending on the airfoil geometry and Reynolds number), it would be convenient if there was another way to increase lift without increasing the angle of attack. As noted by Smith (1975), "The problem of obtaining high lift is that of developing the lift in the presence of boundary layers—getting all the lift possible without causing separation. Provided that boundary-layer control is not used, our only means of obtaining higher lift is to modify the geometry of the airfoil. For a one-piece airfoil, there are several possible means for improvement—changed leading-edge radius, a flap, changed camber, a nose flap, a variable-camber leading edge, and changes in detail shape of a pressure distribution."

So, if more lift is to be generated, the circulation around the airfoil section must be increased, or, equivalently, the velocity over the upper surface must be increased relative to the velocity over the lower surface. However, once the effect of the boundary layer is included, the Kutta condition at the trailing edge requires that the upper-surface and the lower-surface velocities assume a value slightly less than the free-stream velocity. Hence, when the higher velocities over the upper surface of the airfoil are produced in order to get more lift, larger adverse pressure gradients are required to decelerate the flow from the maximum velocity to the trailing-edge velocity. Again, referring to Smith (1975), "The process of deceleration is critical, for if it is too severe, separation develops. The science of developing high lift, therefore, has two components: (1) analysis of the boundary layer, prediction of separation, and determination of the kinds of flows that are most favorable with respect to separation; and (2) analysis of the inviscid flow about a given shape with the purpose of finding shapes that put the least stress on a boundary layer."

Stratford (1959) has developed a formula for predicting the point of separation in an arbitrary decelerating flow. The resultant Stratford pressure distribution, which recovers a given pressure distribution in the shortest distance, has been used in the work of Liebeck (1973). To develop a class of high-lift airfoil sections, Liebeck used a velocity distribution that satisfied "three criteria: (1) the boundary layer does not separate; (2) the corresponding airfoil shape is practical and realistic; and (3) maximum possible C_l is obtained." The optimized form of the airfoil velocity distribution is markedly different than that for a typical airfoil section (which is shown in Fig. 6.18). The velocity distribution is presented as a function of s, the distance along the airfoil surface, where s begins at the lower-surface trailing edge and proceeds clockwise around the airfoil surface to the upper-surface trailing edge. In the s-coordinate system, the velocities are negative on the lower surface and positive on the upper surface. The "optimum" velocity distribution, modified to obtain a realistic airfoil, is presented in Fig. 6.19. The lower-surface velocity is as low as possible in the interest of obtaining the maximum lift and increases continuously from the leading-edge stagnation point to the trailing-edge velocity. The upper-surface acceleration region is shaped to provide good off-design

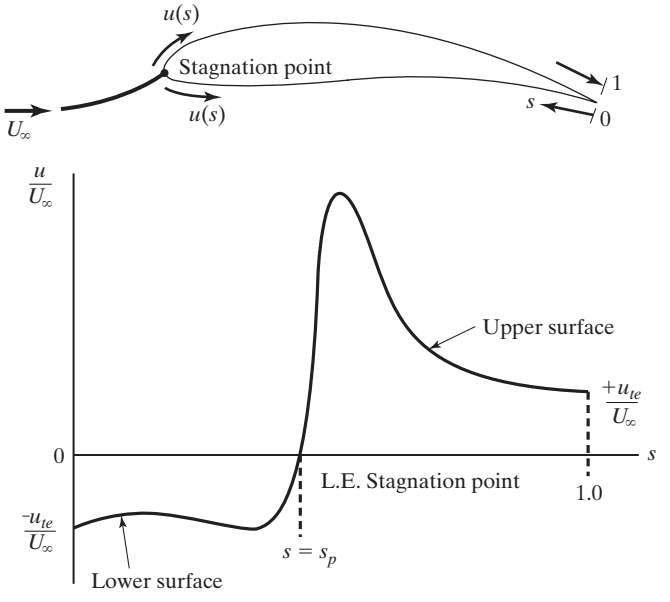

Figure 6.18 General form of the velocity distribution around a typical airfoil [from Liebeck (1973)].

performance. A short boundary-layer transition ramp (the region where the flow decelerates, since an adverse pressure gradient promotes transition) is used to ease the boundary layer's introduction to the severe initial Stratford gradient.

Once the desired airfoil velocity distribution has been defined, there are two options available for calculating the potential flow. One method uses conformal mapping of the flow to a unit circle domain to generate the airfoil, as was discussed in Chapter 3 [e.g., Eppler and Somers (1980) and Liebeck (1976)]. A second approach uses the panel method for the airfoil analysis, which was also shown in Chapter 3, with an extended discussion in Chapter 7 [e.g., Stevens et al. (1971)]. Olson et al. (1978) note that, in the potential flow analysis, the airfoil section is represented by a closed polygon of planar

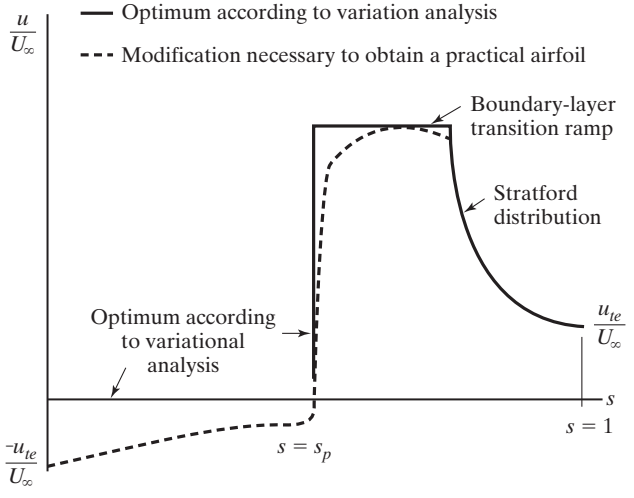

Figure 6.19 "Optimized" velocity distribution for a high-lift, single-element airfoil section [from Liebeck (1973)].

panels connecting the input coordinate pairs. The boundary condition for the inviscid flow—that there be no flow through the airfoil surface—is applied at each of the panel centers. An additional equation, used to close the system, specifies that the upper- and lower-surface velocities have a common limit at the trailing edge (i.e., the Kutta condition). The effect of boundary-layer displacement is simulated by piecewise linear source distributions on the panels describing the airfoil contour. Instead of modifying the airfoil geometry by an appropriate displacement thickness to account for the boundary layer, the boundary condition is modified by introducing surface transpiration. Miranda (1984) notes, "The latter approach is more satisfactory because the surface geometry and the computational grid are not affected by the boundary layer. This means that, for panel methods, the aerodynamic influence coefficients and, for finite difference methods, the computational grid do not have to be recomputed at each iteration." The boundary condition on the surface panels requires that the velocity normal to the surface equals the strength of the known source distribution.

Liebeck has developed airfoil sections which, although they "do not appear to be very useful" [the quotes are from Liebeck (1973)], develop an l/d of 600 (typical low-speed airfoils have lift-to-drag ratios of approximately 100). The airfoil section, theoretical pressure distribution, the experimental lift curve and drag polar, and the experimental pressure distributions for a more practical, high-lift section are presented in Figs. 6.20 through 6.22. The pressure distributions indicate that the flow remains

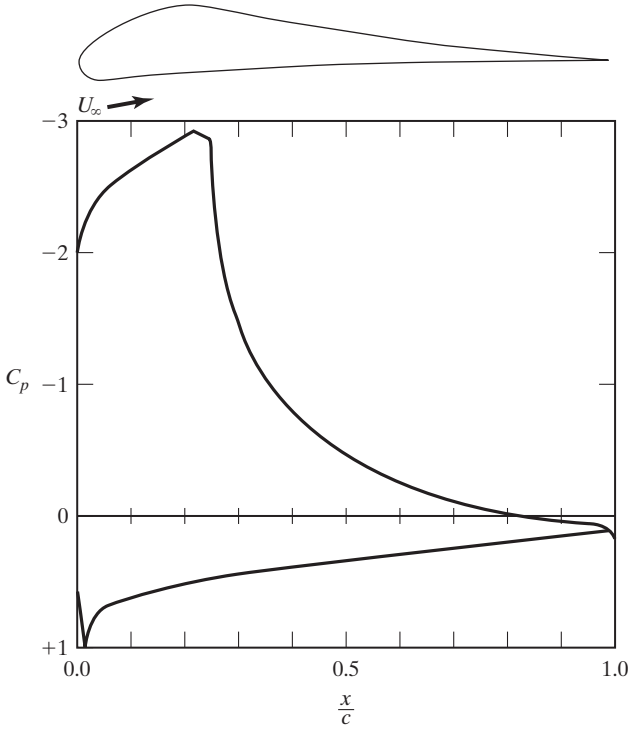

Figure 6.20 Theoretical pressure distribution for high-lift, single-element airfoil, $\mathrm{Re}_c = 3 \times 10^6, t_{\max} = 0.125c, C_l = 1.35$ [from Liebeck (1973)].

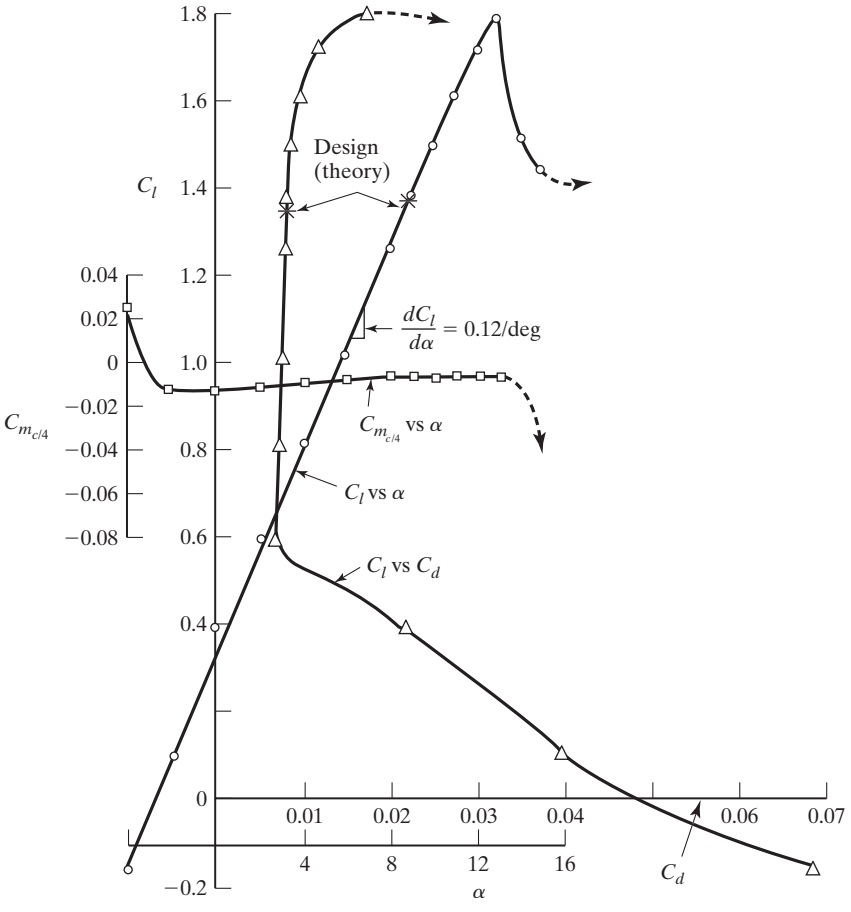

Figure 6.21 Experimental lift coefficient curve, drag polar, and pitch coefficient curve for a high-lift, single-element airfoil, $\text{Re}_c = 3 \times 10^6$ [from Liebeck (1973)].

attached all the way to the trailing edge. The flow remains completely attached until the stalling angle is reached, at which point the entire recovery region separates instantaneously. Reducing the angle of attack less than 0.5° results in an instantaneous and complete reattachment, indicating a total lack of hysteresis effect on stall recovery.

Improvements of a less spectacular nature have been obtained for airfoil sections being developed by NASA for light airplanes. One such airfoil section is the General Aviation (Whitcomb) number 1 airfoil, GA(W)-1, which is 17% thick with a blunt nose and a cusped lower surface near the trailing edge. The geometry of the GA(W)-1 section is similar to that of the supercritical airfoil, which will be discussed in Chapter 9. Experimentally determined lift coefficients, drag coefficients, and pitch moment coefficients, which are taken from McGhee and Beasley (1973), are presented in Fig. 6.23. Included for comparison are the corresponding correlations for the NACA 65_2-415 and the NACA 65_3-418 airfoil sections. Both the GA(W)-1 and the NACA

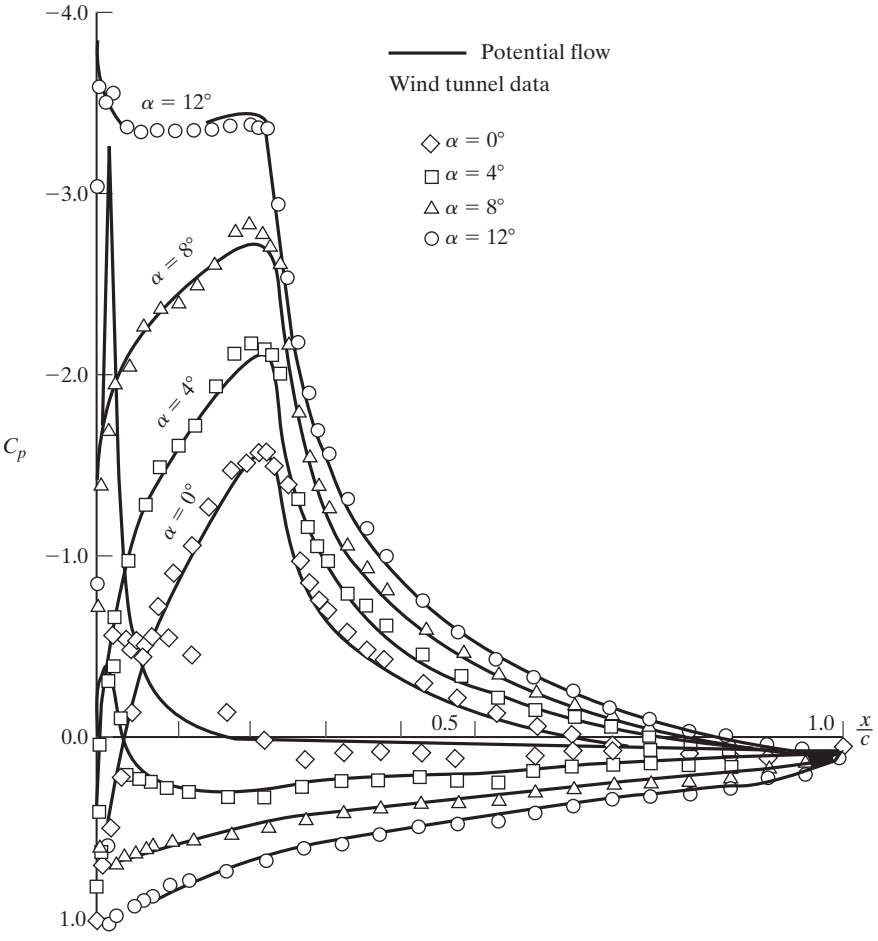

Figure 6.22 Comparison of the theoretical potential-flow and the experimental pressure distribution of a high-lift, single-element airfoil, $\mathrm{Re}_c = 3 \times 10^6$ [from Liebeck (1973)].

65_3-418 airfoils have the same design lift coefficient (0.40), and both have roughly the same mean thickness distribution in the region of the structural box (typical aircraft have a leading-edge spar at about 0.15c and a trailing edge spar at around 0.60c). However, the experimental value of the maximum section lift coefficient for the GA(W)-1 was approximately 30% greater than for the NACA 65 series airfoil for a Reynolds number of 6×10^6. Since the section drag coefficient remains approximately constant to higher lift coefficients for the GA(W)-1, significant increases in the lift/drag ratio are obtained. At a lift coefficient of 0.90, the lift/drag ratio for the GA(W)-1 was approximately 70, which is 50% greater than that for the NACA 65_3-418 section. This is of particular importance from a safety standpoint for light general aviation airplanes, where large values of section lift/drag ratio at high lift coefficients result in improved climb performance.

Aerodynamics Concept Box: How to Create High Lift

According to thin airfoil theory, the way to increase lift is to change α_{0l} by adding camber to the airfoil. The development of the theory for cambered airfoils in Section 6.5.2 showed that the zero-lift angle of attack is defined by:

$$\alpha_{0l} = -\frac{1}{\pi}\int_0^{\pi}\frac{dz}{dx}(\cos\theta - 1)\,d\theta$$

Examining the integral we see that camber changes, dz/dx, are multiplied by the term $(\cos\theta - 1)$. Recall that $\theta = 0$ corresponds to the leading edge of the airfoil and $\theta = \pi$ corresponds to the trailing edge of the airfoil. So changes in camber at the leading edge are multiplied by $(\cos(0) - 1) = 0$. In other words, there is no contribution to the integral at $\theta = 0$, no matter how large dz/dx happens to be. Of course, there would be a small contribution to the integral at points near the leading edge, but camber changes in this region would still have very small impact on changing α_{0l}. Now we can look at changing the camber at the trailing edge: dz/dx at the trailing edge is multiplied by $(\cos(\pi) - 1) = -2$. In other words, camber changes at the trailing edge have a large impact on α_{0l}. So, thin airfoil theory, which is an inviscid theory, tells us to create more lift by increasing camber in the region of the trailing edge of the airfoil. That is why aircraft have large high-lift devices along the trailing edge of the wing, as seen below for the Boeing 747 triple-slotted flap system.

Triple-slotted flap and Krueger flap systems on the Boeing 747 [public domain photo by Adrian Arpingstone]

The picture also shows that there are devices along the leading edge of the wing, which seems to be in contradiction to the results of thin airfoil theory. Remember, though, that thin airfoil theory is an inviscid theory. We will find out that leading edge high-lift devices, like those seen on the 747 above, are viscous flow control devices: they are placed along the leading edge in order to control flow separation and delay stall, which will be discussed in the next section and in Chapter 13. Remember from our earlier discussions about airfoils—creating lift also makes flow separation more likely, so we must always be mindful of the delicate balance between lift and flow separation.

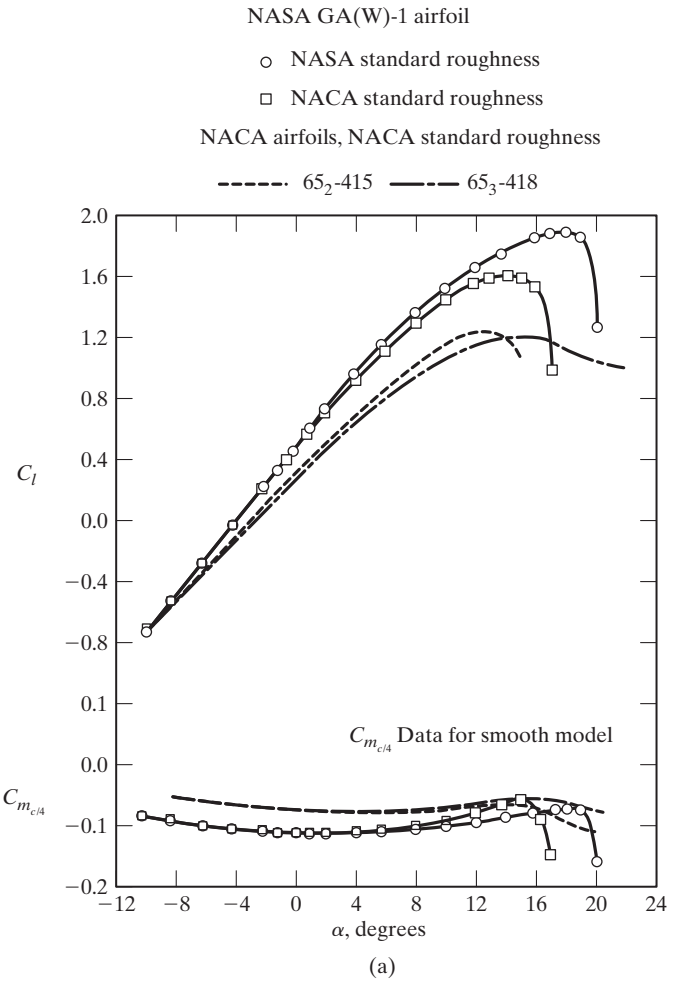

Figure 6.23a Aerodynamic coefficients for a NASA GA(W)-1 airfoil, for a NACA 65_2-415 airfoil, and for a NACA 65_3-418 airfoil; $M_\infty = 0.20, \mathrm{Re}_c = 6 \times 10^6$: (a) lift coefficient and pitch moment coefficient curves; (b) drag polars [data from McGhee and Beasley (1973)].

6.8 MULTIELEMENT AIRFOIL SECTIONS FOR GENERATING HIGH LIFT

Since single element airfoils that produce high lift, as discussed in the previous section, require unusual shaping, it is more common to use multi-element airfoil sections to produce higher levels of lift. As noted by Meredith (1993), "High-lift systems are used on commercial jet transports to provide adequate low-speed performance in terms of take-off and landing field lengths, approach speed, and community noise. The importance of the high-lift system is illustrated by the following trade factors derived for a generic large twin engine transport:

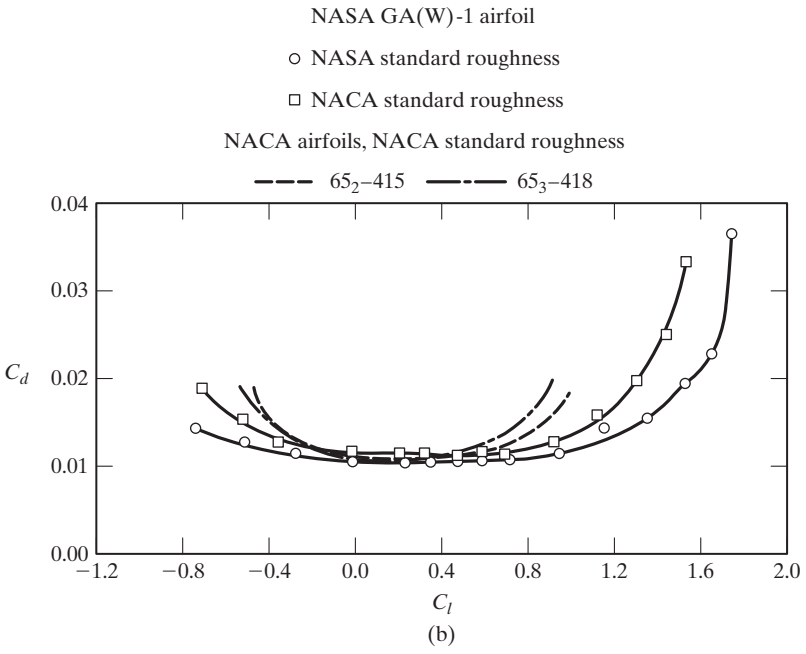

(b)

Figure 6.23b (*continued*)

- A 0.10 increase in lift coefficient at constant angle of attack is equivalent to reducing the approach attitude by about one degree. For a given aft body-to-ground clearance angle, the landing gear may be shortened resulting in a weight savings of 1400 lb.
- A 1.5% increase in the maximum lift coefficient is equivalent to a 6600 lb increase in payload at a fixed approach speed.
- A 1% increase in take-off *L/D* is equivalent to a 2800 lb increase in payload or a 150 nm increase in range.

While necessary, high-lift systems increase the airplane weight, cost, and complexity significantly. Therefore, the goal of the high-lift system designer is to design a high-lift system which minimizes these penalties while providing the required airplane take-off and landing performance."

Jasper et al. (1993) noted, "Traditionally (and for the foreseeable future) high-lift systems incorporate multi-element geometries in which a number of highly-loaded elements interact in close proximity to each other." Fig. 6.24 shows a sketch depicting the cross section of a typical configuration incorporating four elements: a leading-edge slat, the main-element airfoil, a flap vane, and trailing-edge flap. Jasper et al. (1993) continued, "Such configurations generate very complex flowfields containing regions of separated flow, vortical flow, and confluent boundary layers. Laminar, turbulent, transitional, and re-laminarizing boundary layers may exist. Although high lift systems are typically deployed at low freestream Mach numbers, they still exhibit compressibility effects due to the large pressure gradients generated. . . . It should be noted that many of the flowfield phenomena (e.g., separation, transition, turbulence, etc.) are areas of

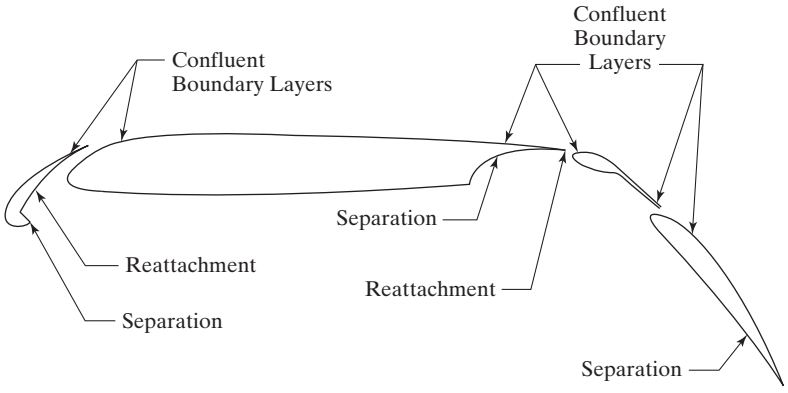

Figure 6.24 Sketch of the cross section of a typical high-lift multielement airfoil section [from Jasper et al. (1993)].

intense research in the computational community and are not yet fully amenable to computational analysis."

As noted by Yip et al. (1993), "Two-dimensional multi-element flow issues include the following:

- compressibility effects including shock/boundary-layer interaction on the slat;
- laminar separation-induced transition along the upper surfaces;
- confluent turbulent boundary layer(s)—the merging and interacting of wakes from upstream elements with the boundary layers of downstream elements;
- cove separation and reattachment; and
- massive flow separation on the wing/flap upper surfaces."

The cove is the region vacated by the flap system when it deploys, as seen in Fig. 6.24.

The complex flowfields for high-lift multielement airfoils are very sensitive to Reynolds number-related phenomena and to Mach number-related phenomena. As we mentioned in the previous paragraph, many of the relevant flow-field issues (e.g., separation, transition, and turbulence) are difficult to model numerically, and also pose challenges to simulate in wind tunnels.

The airfoil configuration that is chosen based on cruise requirements determines a lot of important parameters for the high-lift devices, such as the chord and the thickness distribution. Only the type of the high-lift devices, the shape, the spanwise extensions, and the settings can be chosen by the designer of the high-lift system. Even then, the designer is limited by several constraints. As noted by Flaig and Hilbig (1993), "Usually the chordwise extension of the high-lift devices is limited by the location of the front spar and rear spar respectively, which can not be changed due to considerations of wing stiffness (twist, bending) and internal fuel volume." These constraints are depicted in the sketches of Fig. 6.25, where F/S depicts the front spar and R/S depicts the rear spar.

Flaig and Hilbig (1993) note further, "Especially the required fuel capacity for a long-range aircraft can be of particular significance in the wing sizing. Moreover, the inner wing flap chord of a typical low set wing aircraft is limited by the required storage space for the retracted main undercarriage.

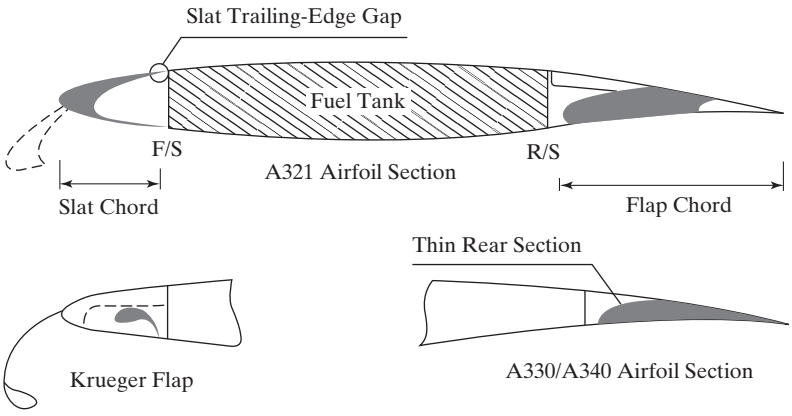

Figure 6.25 General constraints on the design of high-lift multielement airfoil sections [from Flaig and Hilbig (1993)].

After the chordwise extension of the leading edge and trailing edge devices has been fixed, the next design item is the optimization of their shapes.

The typical leading-edge devices of today's transport aircraft are slats and Krueger flaps. In the case of a slat, the profile of upper and lower surface is defined by the cruise wing nose shape. Therefore, only the shape of the slat inner side and the nose of the fixed-wing can be optimized.

A Krueger flap with a folded nose or flexible shape, as an example, generally offers greater design freedom to achieve an ideal upper surface shape, and thus gains a little in L/D and $CL_{\max}$. But, trade-off studies carried out in the past for A320 and A340 have shown that this advantage for the Krueger flap is compromised by a more complex and heavier support structure than required for a slat."

The required maximum lift capability for the landing configuration determines the complexity of the high-lift system. In particular, the number of slots (or elements) of trailing-edge devices has a significant effect on $C_{L_{\max}}$. The degrading effect of wing sweep on the maximum lift coefficient necessitates an increase in the complexity of the high-lift system.

The general trend of the maximum lift efficiency is presented as a function of the system complexity in Fig. 6.26, which is taken from Flaig and Hilbig (1993). Note that the maximum value for the coefficient of lift for unpowered high-lift systems is approximately 3 (on an aircraft with typical 25° wing sweep). Powered high-lift systems with additional active boundary-layer control may achieve maximum values of the lift coefficient up to 7, as shown on the right side of Fig. 6.26.

The problem of computing the aerodynamic characteristics of multielement airfoils can be subdivided into the following broad topical areas, each requiring models for the computer program [Stevens et al. (1971)]:

- Geometry definition
- Solution for the inviscid, potential flow
- Solution for the conventional boundary layer

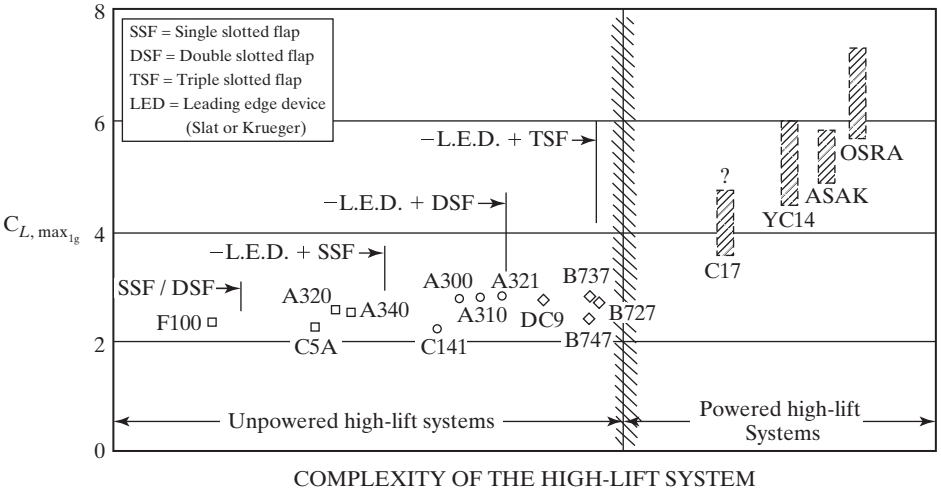

Figure 6.26 The maximum lift coefficient as a function of the complexity of the high-lift system [from Flaig and Hilbig (1993)].

- Solution for the viscous wakes and slot-flow characteristics
- Combined inviscid/viscous solution

Stevens et al. (1971) note that the geometric modeling of the complete airfoil, including slots, slats, vanes, and flaps, requires a highly flexible indexing system to ensure that conventional arrangements of these components can be readily adapted to the code. This level of detailed geometric modeling is also difficult in subscale wind-tunnel testing, where the component parts would be too small to adequately manufacture (depending on the size of the wind tunnel and the model).

To compute the inviscid, potential flow, Stevens et al. (1971) and Olson et al. (1978) use distributed vortex singularities as the fundamental solution to the Laplace equation. Olson et al. (1978) note that viscous calculations can be separated into three types of flows: conventional boundary layers, turbulent wakes, and confluent boundary layers (i.e., wakes merging with conventional boundary layers), which are illustrated in Fig. 6.27. To obtain a complete viscous calculation, the conventional boundary layers on the upper and lower surfaces of the main airfoil are first analyzed. These calculations provide the initial conditions to start the turbulent-wake analysis at the trailing edge of the principal airfoil. The calculations proceed downstream until the wake merges with the outer edge of the boundary layer on the upper surface of the flap, as shown in Fig. 6.28. The wake from the principal airfoil and the boundary layer of the flap combine into a single viscous layer at this point, a so-called confluent boundary layer. The calculation procedure continues stepwise downstream to the flap trailing edge. At the flap trailing edge, this confluent boundary-layer solution merges with the boundary layer from the lower surface of the flap. The calculation then continues downstream into the wake along a potential-flow streamline.

Although the techniques used to calculate the viscous effects differ from those described in the preceding paragraph, the importance of including the viscous effects is illustrated in Fig. 6.29. Using repeated application of a panel method to solve for the

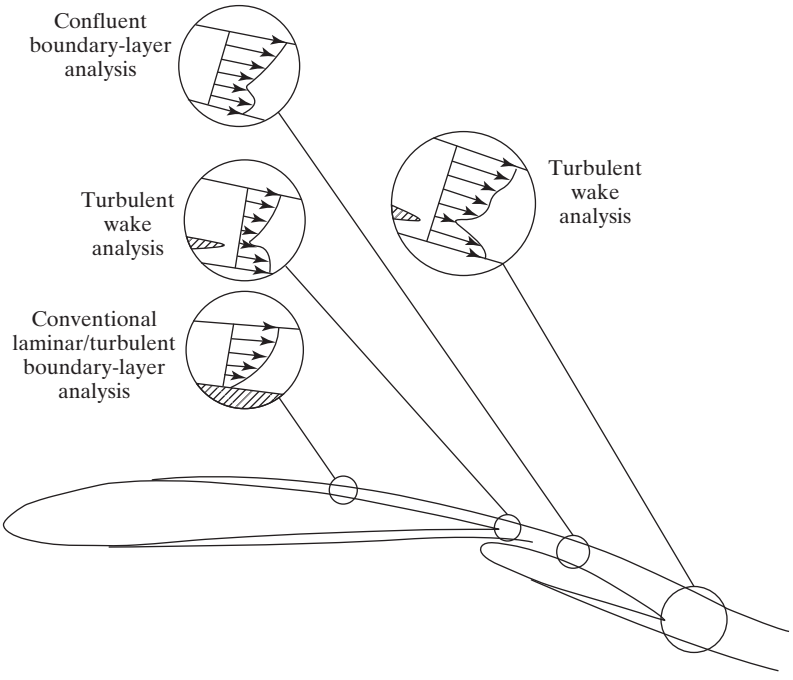

Figure 6.27 Theoretical flow models for the various viscous regions [from Olson et al. (1978)].

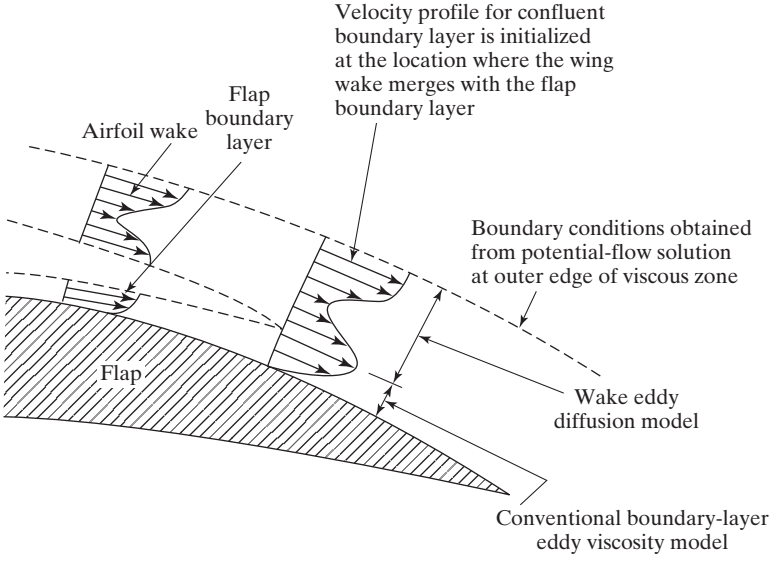

Figure 6.28 Flow model for merging of the wake from the principal airfoil with the boundary layer on the flap to form the confluent boundary layer on the upper surface of the flap [from Olson et al. (1978)].

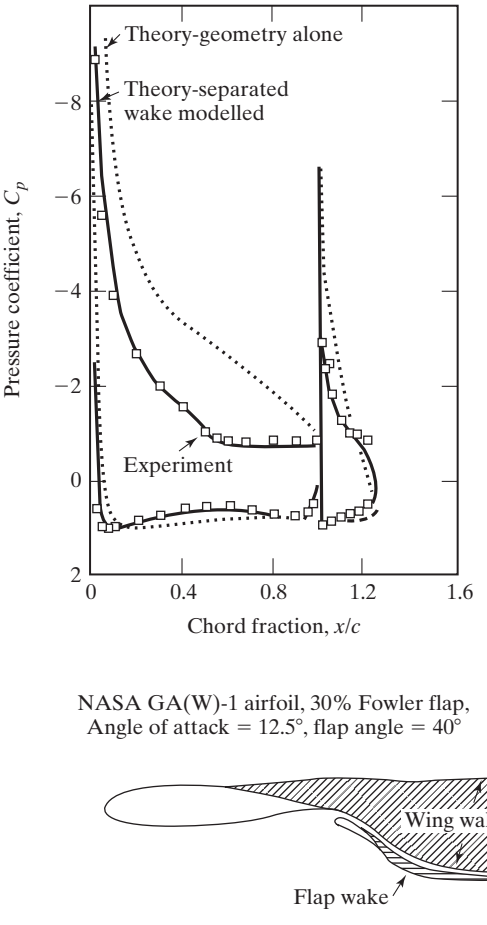

Figure 6.29 Comparison of experimental and calculated pressure distributions on a two-element airfoil with separation from both surfaces [from Henderson (1978)].

separated wake displacement surface, Henderson (1978) found a significant effect on the pressure distributions both on the principal airfoil and the flap for the GA(W)-1 airfoil for which α was 12.5° and the flap angle was 40°. Although a separation wake occurred for both models, the agreement between the calculated pressures and the experimental values was quite good.

As aircraft become more and more complex, and as computational and experimental tools improve, the high-lift design process has matured a great deal. As was stated earlier, including viscous effects in high-lift design is important, but even with modern computer systems a high-lift design still may require a combination of viscous and inviscid numerical predictions. The Boeing 777 high-lift system was designed with various codes at different phases of the design process: a three-dimensional lifting surface code was used during preliminary design, two-dimensional viscous-inviscid coupled codes were used to design the multielement airfoil sections, and three-dimensional panel codes were used to evaluate flow interactions. Navier-Stokes and Euler codes were not used during the design process, according to Brune and McMasters (1990) and Nield (1995). This approach allowed for a reduction in wind-tunnel testing and

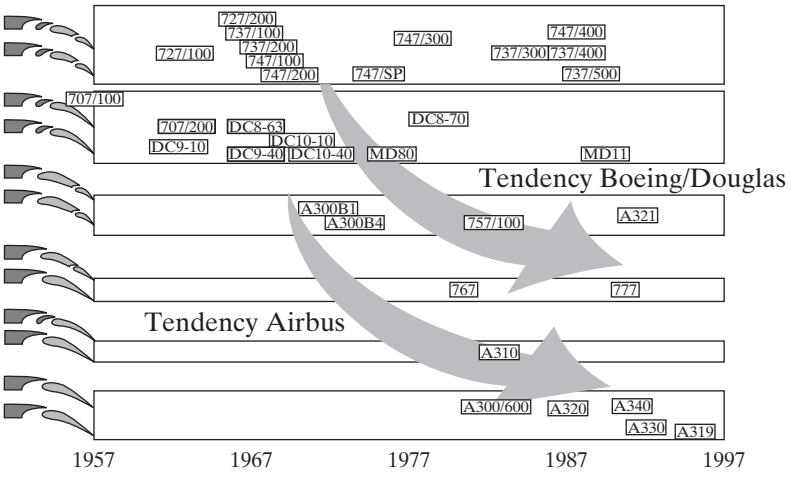

Figure 6.30 Design evolution of high-lift trailing edge systems [from Reckzeh (2003)].

resulted in a double-slotted flap that was more efficient than the triple-slotted flaps used on previous Boeing aircraft.

In fact, as the design process for high-lift systems has matured, the systems have become less complex, more affordable, more dependable, and more efficient. Fig. 6.30 shows how high-lift airfoils designed by both Boeing/Douglas and Airbus have improved since the 1960s. The improvement has been brought about by the increased use of numerical predictions, including the addition of Navier-Stokes and Euler methods to the predictions of high-lift airfoils [Rogers et al. (2001) and van Dam (2002)]. The evolution has been from triple-slotted flaps (such as on the Boeing 737), to double-slotted flaps (such as on the Boeing 777), and now to single-slotted flaps (such as on the Airbus A380 and Boeing 787). However, numerical predictions still require further improvement, including the addition of unsteady effects and improved turbulence models, before high-lift design will be as evolved as one might hope [Rumsey and Ying (2002) and Cummings et al. (2004)]. Additional details about various high-lift systems used in aircraft design may be found in Section 13.1. Many of these concepts have found their way onto various aircraft, but some of the concepts remain to be applied.

6.9 HIGH-LIFT MILITARY AIRFOILS

Military aircraft, especially fighters, have to be highly agile and maneuverable. Over the past decades, this requirement has led to the addition of strakes (also called leading-edge extensions), as well as various leading-edge devices. Fig. 6.31 shows the F-18 HARV (High Angle of Attack Research Vehicle) flying at $\alpha = 30^\circ$ with smoke visualizing the leading-edge extension vortex and tufts aiding in the visualization of the near-surface flow patterns. Notice that the leading-edge flaps are extended significantly in addition to a mild extension of the trailing-edge flaps. These high-lift devices are automatically controlled by the flight control computer, so the pilot does not have to be concerned

Figure 6.31 F-18 HARV at $\alpha = 30^{\circ}$ with smoke and tuft visualization (courtesy of NASA Dryden Flight Research Center).

with high-lift settings during flight. The smoke shows vortex breakdown just prior to the wing, and the outboard section of the wing is stalled, as shown by the tufts.

As noted by Kern (1996), "There are two major geometric differences that distinguish modern high performance multi-role strike/fighter military airfoils from commercial configurations: (1) leading-edge shape and (2) airfoil thickness. Integration of stealth requirements typically dictates sharp leading edges and transonic and supersonic efficiency dictates thin airfoils on the order of 5 to 8% chord. . . . The Navy also depends on low-speed high-lift aerodynamics, since it enables high performance multi-role strike aircraft to operate from a carrier deck." To obtain high lift at low speeds, the advanced fighter wing sections are configured with a plain leading-edge flap and a slotted trailing-edge flap. The schematic diagram presented in Fig. 6.32 indicates some of the features of the complex flow field. The sharp leading edge causes the flow to separate, resulting in a shear layer that convects either above or below the airfoil surface. Depending on the angle of attack, the shear layer may or may not reattach to the surface of the airfoil. The flow field also contains cove flow, slot flow, merging shear layers, main element wake mixing, and trailing-edge flap separation.

Hobbs et al. (1996) presented the results of an experimental investigation using a 5.75% thick airfoil, which has a 14.07% chord plain leading-edge (L.E.) flap, a single slotted 30% chord trailing-edge (T.E.) flap, and a 8.78% chord shroud. Reproduced in Fig. 6.33 are the experimentally determined lift coefficients for the airfoil with δ_n (the leading-edge flap deflection angle) equal to 34°, with δ_f (the trailing-edge flap deflection angle) equal to 35°, and with δ_s (the shroud deflection angle) equal to 22.94°. This configuration provides the aircraft with the maximum lift required for catapult and approach configurations. Because of the leading-edge flow separation bubble, the lift curve displays no "linear" dependence on the angle of attack. The maximum lift coefficient of approximately 2.2 occurs at an angle of attack of 2°. The airfoil then gradually stalls, until total separation occurs at an angle of attack of 10°, with a rapid decrease in

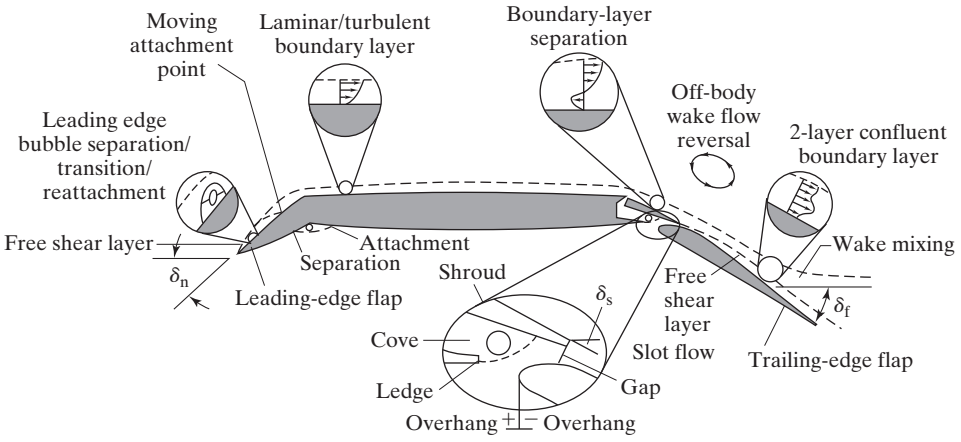

Figure 6.32 Sketch of the flow field for a military airfoil in a high-lift configuration [a composite developed from information presented in Kern (1996) and Hobbs et al. (1996)].

the section lift coefficient. As noted by Kern (1996), "This behavior seems less surprising when considering split-flap NACA 6% thick airfoils which all stall around $\alpha = 4°$."

Because the flow field includes trailing viscous wakes, confluent boundary layers, separated flows, and different transition regions, the Reynolds number is an important parameter in modeling the resultant flow field. The maximum values of the measured lift coefficients are presented as a function of the Reynolds number in Fig. 6.34. The data, which were obtained at a Mach number of 0.2, indicate that the maximum lift coefficient is essentially constant for Reynolds numbers above 9×10^6. These results (for a two-dimensional flow) suggest that airfoils should be tested at a Reynolds number of 9×10^6, or more, in order to simulate maximum lift performance at full-scale flight conditions. Conversely, testing at a Reynolds number of 9×10^6 is sufficient to simulate full-scale maximum lift performance for this flow.

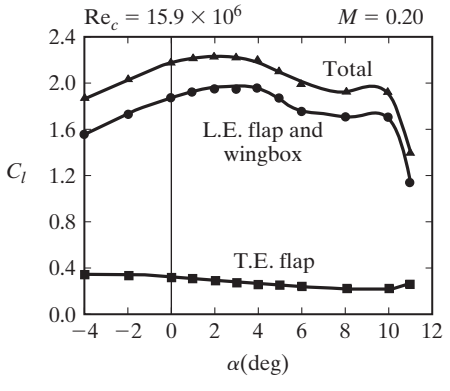

Figure 6.33 Total and component lift curves, $\delta_n = 34°$, $\delta_f = 35°$, $\delta_s = 22.94°$ [from Hobbs et al. (1996)].

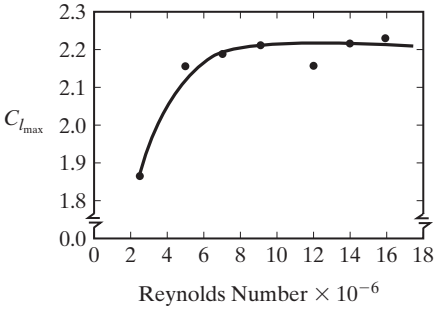

Figure 6.34 The effect of Reynolds number on $C_{l_{max}}$, $\delta_n = 34°$,$\delta_f = 35°$, $\delta_s = 22.94°$ [from Hobbs (1996)].

6.10 SUMMARY

We have seen that potential flow theory, as applied in thin-airfoil theory, can accurately model the flow around real airfoils within the limitations of the theory. Specifically, thin-airfoil theory does a very good job predicting the lift and pitch moment coefficients for relatively thin airfoils until viscous effects become important at higher angles of attack. Thin-airfoil theory also leads us to adding high-lift devices to airfoils in order to increase lift without increasing the angle of attack. Thin-airfoil theory also gives us a practical feeling for how airfoils behave, which is perhaps as valuable as the quantitative predictions it provides.

PROBLEMS

6.1. Using the identity given in equation (6.10), show that the vorticity distribution

$$\gamma(\theta) = 2\alpha U_\infty \frac{1 + \cos\theta}{\sin\theta}$$

satisfies the condition that flow is parallel to the surface [i.e., equation (6.8)]. Show that the Kutta condition is satisfied. Sketch the $2\gamma/U_\infty$ distribution as a function of x/c for a section lift coefficient of 0.5. What is the physical significance of $2\gamma/U_\infty$? What angle of attack is required for a symmetric airfoil to develop a section lift coefficient of 0.5?

Using the vorticity distribution, calculate the section pitching moment about a point 0.75 chord from the leading edge. Verify your answer, using the fact that the center of pressure (x_{cp}) is at the quarter chord for all angles of attack and the definition for lift.

6.2. Calculate C_l and $C_{m_{c/4}}$ for a NACA 0009 airfoil that has a plain flap whose length is $0.2c$ and which is deflected 25°. When the geometric angle of attack is 4°, what is the section lift coefficient? Where is the center of pressure?

6.3. The mean camber line of an airfoil is formed by a segment of a circular arc (having a constant radius of curvature). The maximum mean camber (which occurs at midchord) is equal to kc, where k is a constant and c is a chord length. Develop an expression for the γ distribution in terms of the free-stream velocity U_∞ and the angle of attack α. Since kc is small, you can neglect the higher-order terms in kc in order to simplify the mathematics. What is the angle of attack for zero lift (α_{0l}) for this airfoil section? What is the section moment coefficient about the aerodynamic center ($C_{m_{ac}}$)?

6.4. The numbering system for wing sections of the NACA five-digit series is based on a combination of theoretical aerodynamic characteristics and geometric characteristics. The first integer indicates the amount of camber in terms of the relative magnitude of the design lift coefficient; the design lift coefficient in tenths is three halves of the first integer. The second and third integers together indicate the distance from the leading edge to the location of the maximum camber; this distance in percent of the chord is one-half the number represented by these integers. The last two integers indicate the section thickness in percent of the chord. The NACA 23012 wing section thus has a design lift coefficient of 0.3, has its maximum camber at 15% of the chord, and has a maximum thickness of $0.12c$. The equation for the mean camber line is

$$\frac{z}{c} = 2.6595\left[\left(\frac{x}{c}\right)^3 - 0.6075\left(\frac{x}{c}\right)^2 + 0.11471\left(\frac{x}{c}\right)\right]$$

for the region $0.0c \leq x \leq 0.2025c$ and

$$\frac{z}{c} = 0.022083\left(1 - \frac{x}{c}\right)$$

for the region $0.2025c \leq x \leq 1.000c$.

Calculate the A_0, A_1, and A_2 for this airfoil section. What is the section lift coefficient, C_l? What is the angle of attack for zero lift, α_{0l}? What angle of attack is required to develop the design lift coefficient of 0.3? Calculate the section moment coefficient about the theoretical aerodynamic center. Compare your theoretical values with the experimental values in Fig. P6.4 that are reproduced from the work of Abbott and von Doenhoff (1949). When the geometric angle of attack is 3°, what is the section lift coefficient? What is the x/c location of the center of pressure?

6.5. Look at the three airfoil geometries shown in Fig. 6.12. Discuss the geometric modifications to the laminar flow airfoils that make them distinct from the typical airfoil (NACA 23012). Include in your description airfoil geometric parameters such as camber, thickness, location of maximum camber, location of maximum thickness, leading-edge radius, and trailing edge shape. Why were these modifications successful in creating a laminar flow airfoil?

6.6. What is a laminar separation bubble? What impact does it have on airfoil aerodynamics? What airfoil design features could be changed to eliminate (or largely reduce) the separation bubble?

6.7. What has enabled the evolution of commercial aircraft high-lift systems from triple-slotted to double- or even single-slotted geometries (see Fig. 6.30)? What are the advantages of these changes to aircraft design?

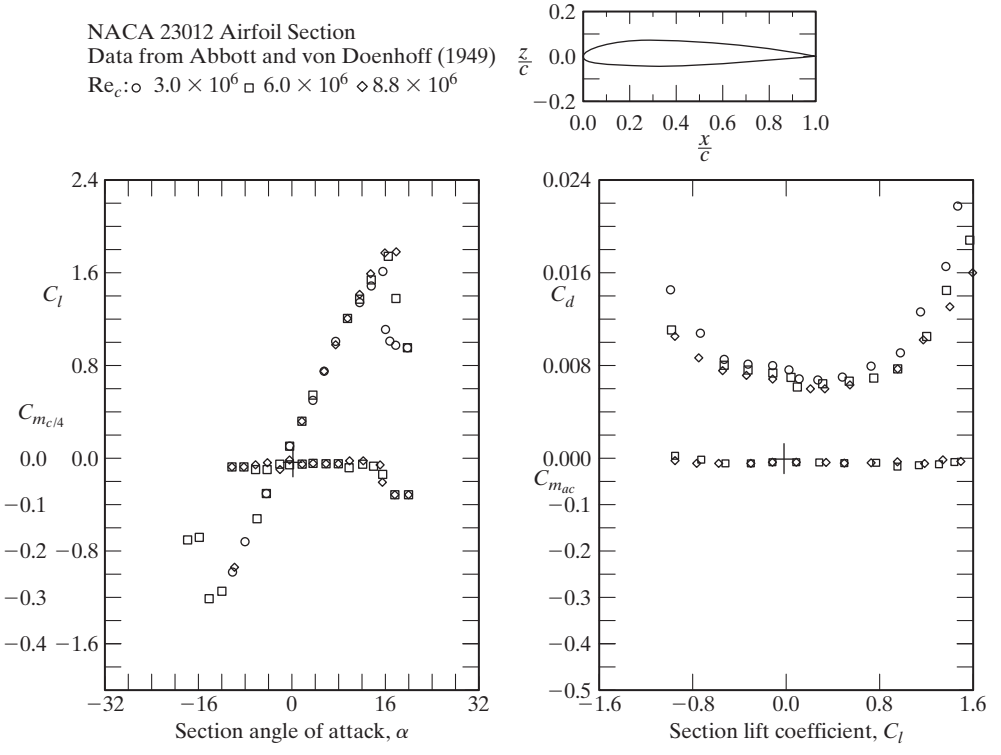

Figure P6.4

REFERENCES

Abbott IH, von Doenhoff AE. 1949. *Theory of Wing Sections*. New York: Dover

Brune GW, McMasters JH. 1990. Computational aerodynamics applied to high-lift systems. In *Computational Aerodynamics*, Ed. Henne PA. Washington, DC: AIAA

Carlson HW, Mack RJ. 1980. Studies of leading-edge thrust phenomena. *J. Aircraft* 17:890–897

Cummings RM, Morton SA, Forsythe JR. 2004. *Detached-eddy simulation of slat and flap aerodynamics for a high-lift wing*. Presented at AIAA Aerosp. Sci. Meet., 42nd, AIAA Pap. 2004–1233, Reno, NV

Drela M. 1989. XFOIL: An analysis and design system for low Reynolds number airfoils. In *Low Reynolds Number Aerodynamics*, Ed. Mueller TJ. New York: Springer-Verlag

Drela M, Protz JM, Epstein AH. 2003. *The role of size in the future of aeronautics*. Presented at Intl. Air and Space Symp., AIAA Pap. 2003–2902, Dayton, OH

Eppler R, Somers DM. 1980. A computer program for the design and analysis of low-speed airfoils. *NASA Tech. Mem. 80210*

Eppler R. 1990. *Airfoil Design and Data*. New York: Springer-Verlag

Flaig A, Hilbig R. 1993. High-lift design for large civil aircraft. In *High-Lift System Aerodynamics, AGARD CP 515*

Gopalarathnam A, Broughton BA, McGranahan BD, Selig MS. 2001. *Design of low Reynolds number airfoils with trips*. Presented at Appl. Aerodyn. Conf., 19th, AIAA Pap. 2001–2463, Anaheim, CA

Grasmeyer JM, Keennon MT. 2001. *Development of the Black Widow micro air vehicle*. Presented at AIAA Aerosp. Sci. Meet., 39th, AIAA Pap. 2001–0127, Reno, NV

Henderson ML. 1978. *A solution to the 2-D separated wake modeling problem and its use to predict C_{Lmax} of arbitrary airfoil sections*. Presented at AIAA Aerosp. Sci. Meet., 16th, AIAA Pap. 78–156, Huntsville, AL

Hobbs CR, Spaid FW, Ely WL, Goodman WL. 1996. *High lift research program for a fighter-type, multi-element airfoil at high Reynolds numbers*. Presented at AIAA Aerosp. Sci. Meet., 34th, AIAA Pap. 96–0057, Reno, NV

Jacobs EN. 1939. Preliminary report on laminar-flow airfoils and new methods adopted for airfoil and boundary-layer investigation. *NACA WR L–345*

Jasper DW, Agrawal S, Robinson BA. 1993. Navier-Stokes calculations on multi-element airfoils using a chimera-based solver. In *High-Lift System Aerodynamics, AGARD CP 515*

Jepson JK, Gopalarathnam A. 2004. *Inverse design of adaptive airfoils with aircraft performance consideration*. Presented at AIAA Aerosp. Sci. Meet., 42nd, AIAA Pap. 2004–0028, Reno, NV

Kern S. 1996. *Evaluation of turbulence models for high lift military airfoil flowfields*. Presented at AIAA Aerosp. Sci. Meet., 34th, AIAA Pap. 96–0057, Reno, NV

Liebeck RH. 1973. A class of airfoils designed for high lift in incompressible flows. *J. Aircraft* 10:610–617

Liebeck RH. 1976. On *the design of subsonic airfoils for high lift*. Presented at Fluid and Plasma Dyn. Conf., 9th, AIAA Pap. 76–406, San Diego, CA

Loftin LK. 1985. Quest for performance: the evolution of modern aircraft. *NASA SP-468*

McCormick BW. 1967. *Aerodynamics of V/STOL Flight*. New York: Academic Press

McGhee RJ, Beasley WD. 1973. Low-speed aerodynamic characteristics of a 17-percent-thick section designed for general aviation applications. *NASA Tech. Note D-7428*

Meredith PT. 1993. Viscous phenomena affecting high-lift systems and suggestions for future CFD development. In *High-Lift System Aerodynamics, AGARD CP 515*

Miranda LR. 1984. Application of computational aerodynamics to airplane design. *J. Aircraft* 21:355–369

Nield BN. 1995. An overview of the Boeing 777 high lift aerodynamic design. *The Aeronaut. J*. 99:361–371

Olson LE, James WD, McGowan PR. 1978. *Theoretical and experimental study of the drag of multielement airfoils*. Presented at Fluid and Plasma Dyn. Conf., 11th, AIAA Pap. 78–1223, Seattle, WA

Reckzeh D. 2003. Aerodynamic design of the high-lift wing for a megaliner aircraft. *Aerosp. Sci. Tech*. 7:107–119

Rogers SE, Roth K, Cao HV, Slotnick JP, Whitlock M, Nash SM, Baker D. 2001. Computation of viscous flow for a Boeing 777 aircraft in landing configuration. *J. Aircraft* 38: 1060–1068

Rumsey CL, Ying SX. 2002. Prediction of high lift: review of present CFD capability. *Progr. Aerosp. Sci*. 38:145–180

Selig MS, Donovan JF, Fraser DB. 1989. *Airfoils at Low Speeds*. Virginia Beach, VA: HA Stokely

Selig MS, Maughmer MD. 1992. A multi-point inverse airfoil design method based on conformal mapping. *AIAA J*. 30:1162–1170

Selig MS, Gopalaratham A, Giguére P, Lyon CA. 2001. Systematic airfoil design studies at low Reynolds number. In *Fixed and Flapping Wing Aerodynamics for Micro Air Vehicle Applications*, Ed. Mueller TJ. New York: AIAA, pp. 143–167

Selig MS. 2003. Low Reynolds number airfoil design. In *Low Reynolds Number Aerodynamics of Aircraft*, VKI Lecture Series

Smith AMO. 1975. High-lift aerodynamics. *J. Aircraft* 12:501–530

Stevens WA, Goradia SH, Braden JA. 1971. Mathematical model for two-dimensional multi-component airfoils in viscous flow. *NASA CR 1843*

Stratford BS. 1959. The prediction of separation of the turbulent boundary layer. *J. Fluid Mech*. 5:1–16

Torres GE, Mueller TJ. 2004. Low-aspect ratio wing aerodynamics at low Reynolds number. *AIAA J*. 42:865–873

van Dam CP. 2002. The aerodynamic design of multi-element high-lift systems for transport airplanes. *Progr. Aerosp. Sci*. 38:101–144

Yip LP, Vijgen PMHW, Hardin JD, van Dam CP. 1993. In-flight pressure distributions and skin-friction measurements on a subsonic transport high-lift wing section. In *High-Lift System Aerodynamics, AGARD CP 515*

7 INCOMPRESSIBLE FLOW ABOUT WINGS OF FINITE SPAN

Chapter Objectives

- Understand the difference between airfoils and wings and know the physical processes that cause those differences
- Be able to describe the impact of wing-tip vortices on the flow around the airfoil sections that make up a wing
- Understand the concepts behind Lifting-Line theory and be able to use the results to predict the lift and induced drag of a wing
- Understand the basic approach and usefulness of panel methods and vortex lattice methods
- Understand how delta wing aerodynamics differ from traditional wing aerodynamics, and be able to compute the aerodynamic forces acting on a delta wing
- Be able to explain why some tactical aircraft use leading-edge extensions (strakes) and how they work
- Describe the asymmetric flow patterns that can take place around an aircraft flying at high angles of attack, and know the physical processes that cause the flow

Understanding how a wing works and being able to predict the lift, drag, and pitch moment of a wing are important concepts in aerodynamics. While we have fairly thoroughly discussed the basic concepts for airfoil aerodynamics, making a useful wing out

of airfoil sections is not a straight-forward task. The goal of this chapter is to give you enough physical understanding and theoretical tools to be able to start the process of designing a useful wing.

7.1 GENERAL COMMENTS

We have already discussed the aerodynamic characteristics for subsonic flow about an unswept *airfoil* in Chapters 5 and 6. Since the span of an *airfoil* is infinite, the flow is identical for each spanwise station (i.e., the flow is two dimensional). The lift produced by the pressure differences between the lower surface and the upper surface of the airfoil section, and therefore the circulation (integrated along the chord length of the section), does not vary along the span.

Since incompressible flow passes pressure information in all directions equally, pressure variations can be sensed between the upper and lower surfaces of a wing. The low-pressure region over the wing causes fluid from the high-pressure region below the wing to flow around the wing tip, creating a vortex in the region of the wing tip. As a consequence of the tendency of the pressures acting on the top surface near the tip of the wing to equalize with those on the bottom surface, the lift force per unit span decreases toward the wing tips. A sketch of a representative aerodynamic load distribution is presented in Fig. 7.1. As indicated in Fig. 7.1a, there is a chordwise variation in the pressure differential between the lower surface and the upper surface. The resultant lift force acting on a section (i.e., a unit span) is obtained by integrating the pressure distribution over the chord length. A procedure that can be used to determine the sectional lift coefficient has already been discussed in Chapter 6.

As indicated in the sketch of Fig. 7.1b, there is a spanwise variation in the lift force. As a result of the spanwise pressure variation, the air on the upper surface flows inboard toward the root. Similarly, on the lower surface, air will tend to flow outward toward the wing tips. The resultant flow around a wing of finite span is three dimensional, having both chordwise and spanwise velocity components. Where the flows from the upper surface and the lower surface join at the trailing edge, the difference in spanwise velocity components will cause the air to roll up into a number of streamwise vortices, distributed along the span. These small vortices roll up into two large vortices just inboard of the wing tips (as shown in Fig. 7.2). The formation of a wing-tip vortex is illustrated in the sketch of Fig. 7.2c and in the filaments of smoke in the photograph taken in the U.S. Air Force Academy's Smoke Tunnel (Fig. 7.2d). Very high velocities and low pressures exist at the core of the wing-tip vortices. In many instances, water vapor condenses as the air is drawn into the low-pressure flow field of the tip vortices. Condensation clearly defines the tip vortices (just inboard of the wing tips) of the Shuttle Orbiter *Columbia* on approach to a landing at Kennedy Space Center (see Fig. 7.3), where the vortices are very evident due to the high water vapor content of the air at this geographic location. The alleviation of the impact of wing-tip vortices through the use of wing-tip devices will be discussed in Section 13.4.3.

In order to model the flow of air around the wing mathematically, we customarily assume: (1) that the vortex wake, which is of finite thickness, may be replaced by an infinitesimally thin surface of discontinuity, designated the trailing vortex sheet,

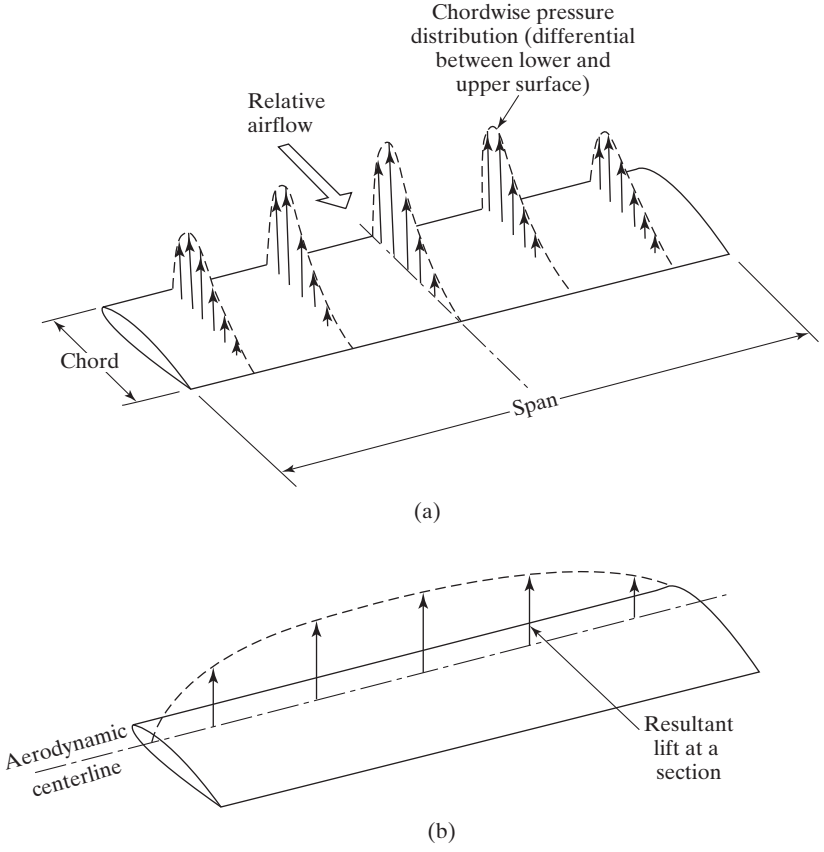

Figure 7.1 Aerodynamic load distribution for a rectangular wing in subsonic airstream: (a) differential pressure distribution along the chord for several spanwise stations; (b) spanwise lift distribution.

and (2) that the trailing vortex sheet remains flat as it extends downstream from the wing. Spreiter and Sacks (1951) note that "it has been firmly established that these assumptions are sufficiently valid for the prediction of the forces and moments on finite-span wings."

An important difference in the three-dimensional flow field around a wing (as compared with the two-dimensional flow around an airfoil) is the spanwise variation in lift. Since the lift force acting on the wing section at a given spanwise location is related to the strength of the circulation, there is also a corresponding spanwise variation in circulation, such that the circulation at the wing tip is zero (since the lift at the wing tip is zero). Procedures that can be used to determine the vortex-strength distribution produced by the flow field around a three-dimensional lifting wing will be discussed next.

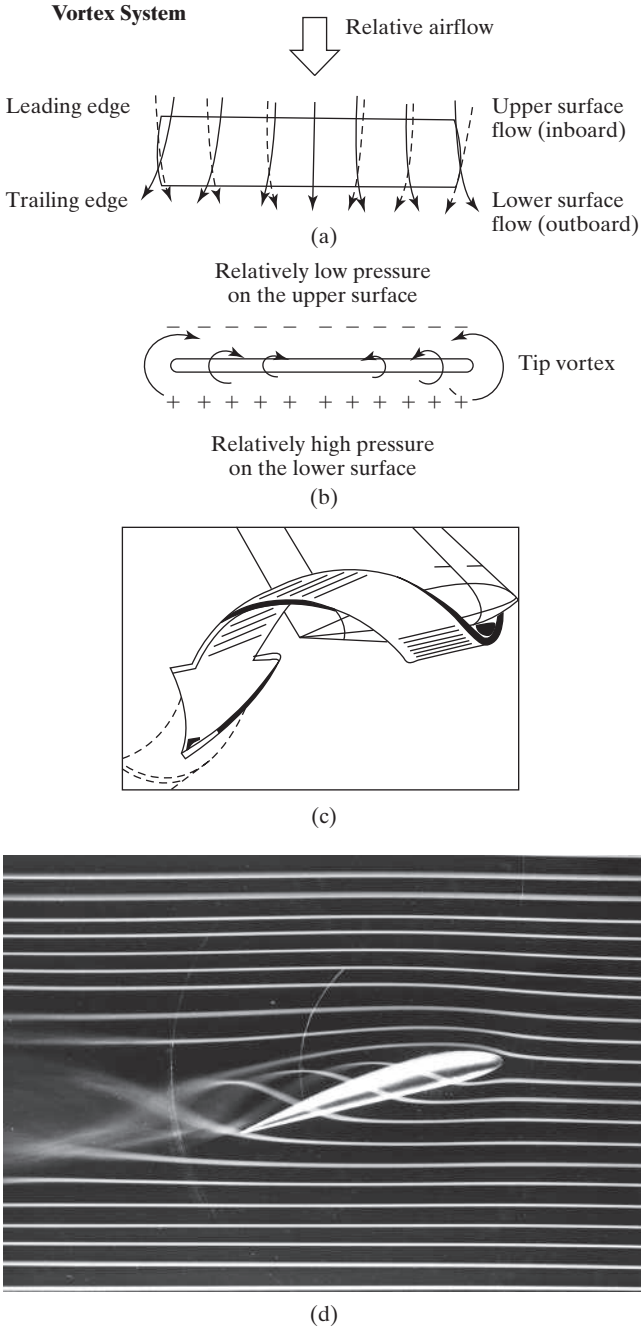

Figure 7.2 Generation of the trailing vortices due to the spanwise load distribution: (a) view from bottom; (b) view from trailing edge; (c) formation of the tip vortex; (d) smoke-flow pattern showing tip vortex (photograph courtesy U.S. Air Force Academy).

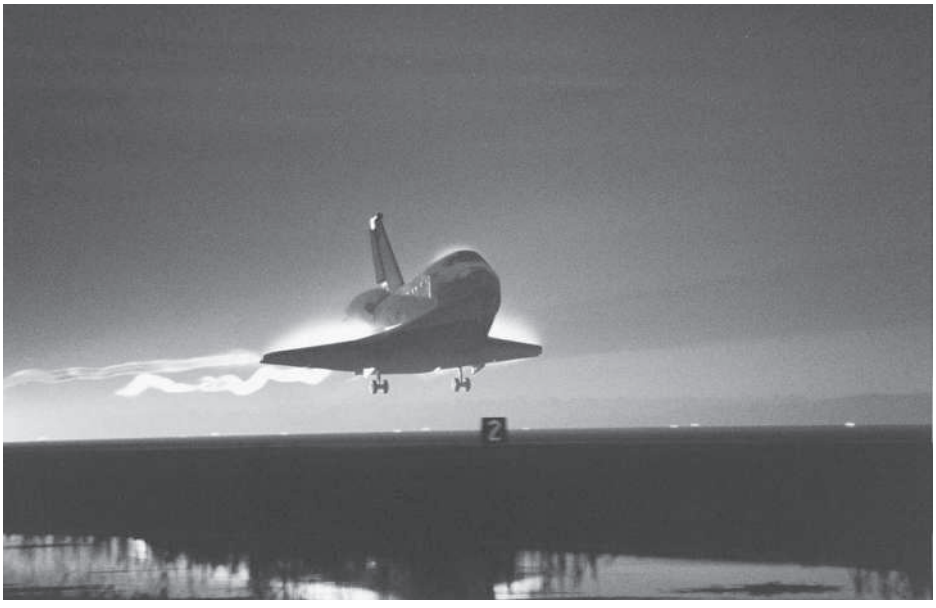

Figure 7.3 Condensation marks the wing-tip vortices of the Space Shuttle Orbiter *Columbia* (photo courtesy NASA).

7.2 VORTEX SYSTEM

We want to find a model of the flow for the vortex system produced by a lifting wing. A suitable distribution of vortices would represent the physical wing in every way except that of thickness. This mathematical description was first accomplished by Ludwig Prandtl in Germany and Frederick Lanchester in England in the early years of the twentieth century. While the approaches of these researchers were quite different, it is customary today to follow the model of Prandtl. In Prandtl's approach, the vortex system consists of:

- the bound vortex system
- the trailing vortex system
- the "starting" vortex

We saw in Chapter 6 that the "starting" vortex is associated with a change in circulation and would, therefore, relate to changes in lift that might occur as the wing begins moving or as the angle of attack changes during flight.

The representation of the wing by a bound vortex system is not to be interpreted as a rigorous flow model. However, the idea allows a relation to be established between:

- the physical load distribution for the wing (which depends on the wing geometry and on the aerodynamic characteristics of the wing sections)
- the trailing vortex system

This relation then allows us to quantify the impact of the trailing vortex system on the lift and drag of the wing, which will show us how much different the wing airfoil sections behave compared with the infinite-span airfoil sections.

7.3 LIFTING-LINE THEORY FOR UNSWEPT WINGS

We are interested in developing a model that can be used to estimate the aerodynamic characteristics of a wing which is unswept (or is only slightly swept) and which has an aspect ratio of 4.0 or greater. The spanwise variation in lift, $l(y)$, is similar to that depicted in Fig. 7.1b. Prandtl and Tietjens (1957) hypothesized that each airfoil section of the wing acts as though it is an isolated two-dimensional section, provided that the spanwise flow is not too great. Therefore, each section of the finite-span wing generates a section lift equivalent to that acting on a similar section of an infinite-span wing having the same section circulation. We will assume that the lift acting on an incremental spanwise element of the wing is related to the local circulation through the Kutta-Joukowski theorem (see Section 3.15.2). That is,

$$l(y) = \rho_\infty U_\infty \Gamma(y) \tag{7.1}$$

Orloff (1980) showed that the spanwise lift distribution could be obtained from flow field velocity surveys made behind an airfoil section of the wing only and related to the circulation around a loop containing that airfoil section. The velocity surveys employed the integral form of the momentum equation in a manner similar to that used to estimate the drag in Problems 2.10 through 2.13 and Problems 2.27 through 2.31.

In Prandtl's approach, the spanwise lift distribution is represented by a system of vortex filaments, the axis of which is normal to the plane of symmetry and which passes through the aerodynamic center of the lifting surface, as shown in Fig. 7.4. Since the theoretical relations developed in Chapter 6 for inviscid flow past a thin airfoil showed that the aerodynamic center is at the quarter chord, we will place the bound-vortex system at the quarter-chord line. The strength of the bound-vortex system at any spanwise location $\Gamma(y)$ is proportional to the local lift acting at that location $l(y)$. However, as discussed in Section 3.12.4, the vortex theorems of Helmholtz state that a vortex filament has constant strength along its length. Therefore, we will model the lifting character of the wing by a large number of vortex filaments (i.e., a large bundle of infinitesimal-strength filaments) that lie along the quarter chord of the wing. This is the bound-vortex system, which represents the spanwise loading distribution, as shown in Fig. 7.4 (a), and is known as the *lifting line*. At any spanwise location y, the sum of the strengths of all of the vortex filaments in the bundle at that station is $\Gamma(y)$. When the lift changes at some spanwise location [i.e., $\Delta l(y)$], the total strength of the bound-vortex system changes proportionally [i.e., $\Delta\Gamma(y)$]. But Helmholtz also stated that vortex filaments cannot end in the fluid. Therefore, the change $\Delta\Gamma(y)$ is represented in our model by having some of the filaments from our bundle of filaments turn 90° and continue in the streamwise direction (i.e., in the x direction). The strength of the trailing vortex at any y location is equal to the change in the strength of the bound-vortex system. The strength of the vortex filaments continuing in the bound-vortex system depends on the spanwise variation in lift and, therefore, depends upon geometric parameters such as the wing planform, the airfoil sections that make up the wing, the geometric twist of the wing, etc. Therefore, as shown in Fig. 7.4a, if the strength of the vortex filaments in the bundle making up the bound-vortex system change by the amount $\Delta\Gamma$, a trailing vortex of strength $\Delta\Gamma$ must be shed in the x direction.

The vortex filaments that make up the bound-vortex system do not end in the fluid when the lift changes, but turn backward at each end to form a pair of vortices in the

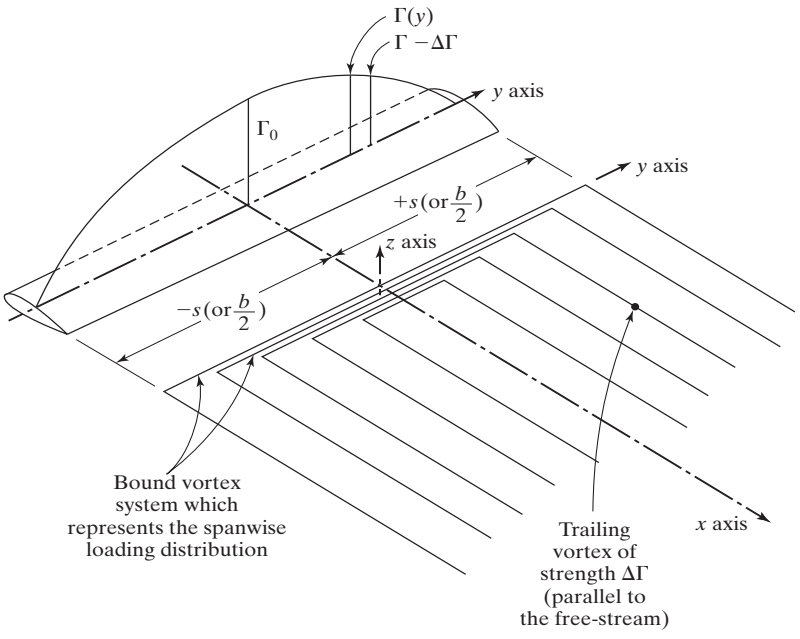

Figure 7.4 (a) Schematic trailing-vortex system.

trailing-vortex system. For steady flight conditions, the *starting* vortex is left far behind, so that the trailing-vortex pair effectively stretches to infinity. The three-sided vortex, which is termed a *horseshoe vortex*, is presented in Fig. 7.4a. For practical purposes, the system consists of the bound-vortex system and the related system of trailing vortices. Also included in Fig. 7.4a is a sketch of a symmetrical lift distribution (the variation is the same on each half of the wing), which the vortex system represents.

A number of vortices are made visible by using a smoke generation system for the flow over a Boeing 747 wing shown in Fig. 7.4b. Flow from the wing tip region and two other locations can be seen leaving the trailing edge on each wing and then rolling up into two counter-rotating vortice (one for each wing). This shows why it is important to include shed vorticity from along the entire span when creating a mathematical model of a wing. These streamwise vorticity filaments correspond to the trailing vortices shed by the spanwise variation in vorticity across the wing that is depicted in the schematic of Fig. 7.4a.

Conventional Prandtl lifting-line theory (PLLT) provides reasonable estimates of the lift and induced drag until boundary-layer effects become important (when flow separation takes place). Therefore, there will be reasonable agreement between the calculations and the experimental values for a single lifting surface having no sweep, no dihedral, and an aspect ratio of 4.0 or greater, operating at relatively low angles of attack. Of course, the skin-friction component of drag will not be represented in the PLLT calculations at any angle of attack, but could be added separately using the methods of Section 5.4.6.

Because improvements continue to be made in calculation procedures [e.g., Rasmussen and Smith (1999) and Phillips and Snyder (2000)] and in ways of accounting for the nonlinear behavior of the aerodynamic coefficients [e.g., Anderson et al. (1980)], lifting-line theory is still widely used today.

Figure 7.4 (*Continued*) (b) Streamwise vorticity shedding along the trailing edge of a Boeing 747 rolling up into wing-tip vortices (courtesy of NASA Dryden Flight Research Center).

7.3.1 Trailing Vortices and Downwash

A consequence of the vortex theorems of Helmholtz is that a bound-vortex system does not change strength between two sections unless a vortex filament equal in strength to the change joins or leaves the vortex bundle (see Fig. 7.4a). If $\Gamma(y)$ denotes the strength of the circulation along the y axis (the spanwise coordinate), a semi-infinite vortex of strength $\Delta\Gamma$ trails from the segment Δy, as shown in Fig. 7.5. The strength of the trailing vortex is given by:

$$\Delta\Gamma = \frac{d\Gamma}{dy}\Delta y$$

We will assume that each spanwise strip of the wing (Δy) behaves as if the flow were locally two dimensional, which is why the model cannot be applied to cases with large amounts of spanwise flow. To calculate the influence of a trailing vortex filament located at y, consider the semi-infinite vortex line, parallel to the x axis (which is parallel to the free-stream flow) and extending downstream to infinity from the line through the aerodynamic center of the wing (i.e., the y axis). The vortex at y induces a velocity at a general point y_1 on the aerodynamic centerline which is one-half the velocity that would be induced by an infinitely long vortex filament of the same strength:

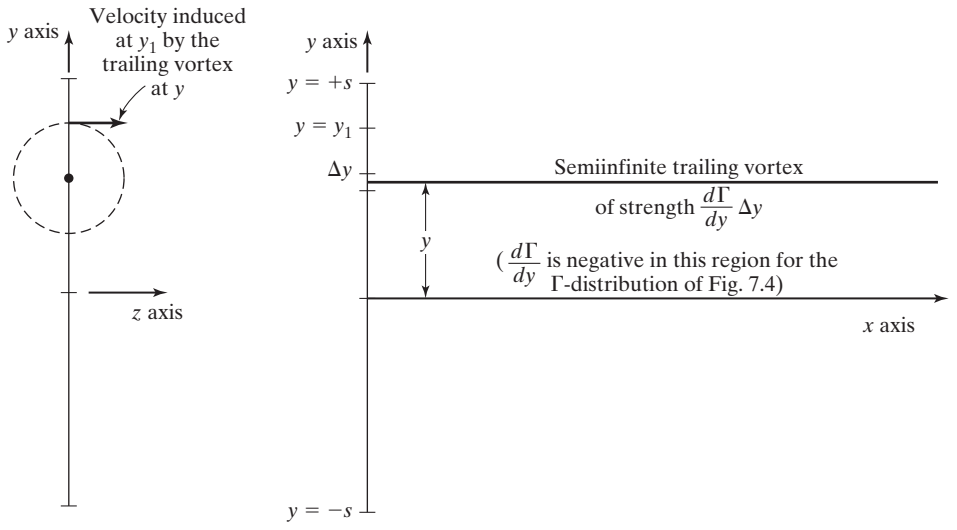

Figure 7.5 Geometry for the calculation of the induced velocity at $y = y_1$.

$$\delta w_{y1} = \frac{1}{2}\left[+\frac{d\Gamma}{dy}dy\frac{1}{2\pi(y - y_1)}\right]$$

The positive sign results because, when both $(y - y_1)$ and $d\Gamma/dy$ are negative, the trailing vortex at y induces an upward component of velocity, as shown in Fig. 7.5, which is in the positive z direction.

To calculate the resultant induced velocity at any point y_1 due to the cumulative effect of all the trailing vortices, the preceding expression is integrated with respect to y from the left wing tip $(-s)$ to the right wing tip $(+s)$:

$$w_{y1} = +\frac{1}{4\pi}\int_{-s}^{+s}\frac{d\Gamma/dy}{y - y_1}dy \tag{7.2}$$

where s is the wing semi-span ($s = b/2$). The resultant induced velocity at y_1 is, in general, in a downward direction (i.e., negative, since the majority of filaments are rotating in that direction) and is called the *downwash*. As shown in the sketch of Fig. 7.6, the downwash angle is

$$\varepsilon = \tan^{-1}\left(-\frac{w_{y1}}{U_\infty}\right) \approx -\frac{w_{y1}}{U_\infty} \tag{7.3}$$

where the small angle assumption has been made ($\tan\theta \approx \theta$). The downwash velocity component has the effect of "tilting" the undisturbed air, so the effective angle of attack of the airfoil at the aerodynamic center (i.e., the quarter chord, as shown in Fig. 7.6) is:

$$\alpha_e = \alpha - \varepsilon \tag{7.4}$$

The significance of this reduction in the effective angle of attack, as we will see shortly, is that the airfoil section produces less left and has a new component of drag. Notice that if the wing has a geometric twist, both the angle of attack (α) and the downwash angle

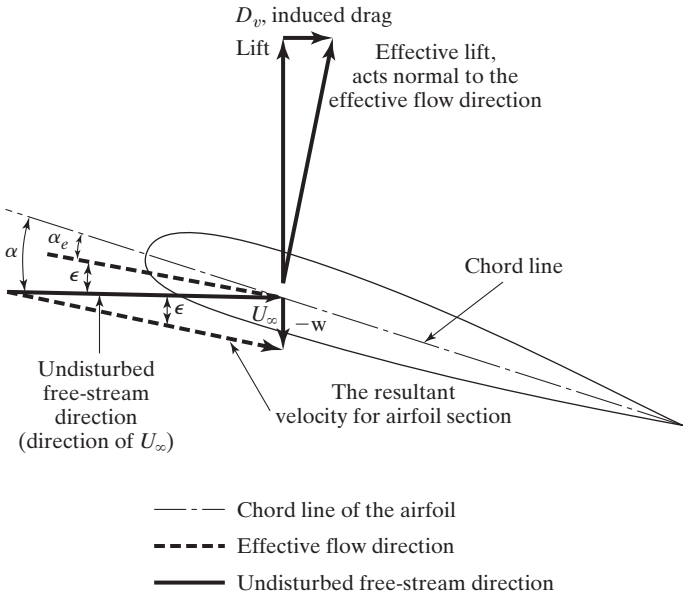

Figure 7.6 Induced flow.

(ε) would be a function of the spanwise position. Since the direction of the resultant velocity at the aerodynamic center is inclined downward relative to the direction of the undisturbed free-stream air, the effective lift of the section of interest is inclined aft by the same amount. Therefore, the effective lift on the wing has a component of force parallel to the undisturbed free-stream air (as shown in Fig. 7.6), which is defined as a drag force. This drag force is a consequence of the lift developed by a finite wing and is termed *vortex drag* (or the *induced drag* or the *drag-due-to-lift*). For subsonic flow past a finite-span wing, in addition to the skin-friction drag and the form (or pressure) drag, there is a drag component due to lift. As a result of the induced downwash velocity, the lift generated by a finite-span wing composed of a given airfoil section, which is at the geometric angle of attack α_e, is less than that for an infinite-span airfoil composed of the same airfoil section and which is at the same angle of attack α, as was shown in Fig. 5.25. Therefore, at a given α, the three-dimensional flow over a finite-span wing generates less lift than the two-dimensional flow over an infinite-span airfoil; we will quantify the change in lift shortly.

Based on the Kutta-Joukowski theorem from Section 3.15.2, the lift on an elemental airfoil section of the wing is:

$$l(y) = \rho_\infty U_\infty \Gamma(y) \tag{7.1}$$

while the vortex drag is just a component of the lift. The drag is given using the small angle assumption and $l(y)\tan(-w(y)/U_\infty) \approx -l(y)w(y)/U_\infty$ as:

$$d_v(y) = -\rho_\infty w(y)\Gamma(y) \tag{7.5}$$

The minus sign results because a downward (or negative) value of w produces a positive drag force. Integrating over the entire span of the wing, the total lift is given by

$$L = \int_{-s}^{+s} \rho_\infty U_\infty \Gamma(y)\, dy \tag{7.6}$$

and the total vortex drag is given by:

$$D_v = -\int_{-s}^{+s} \rho_\infty w(y)\Gamma(y)\, dy \tag{7.7}$$

Notice that for the two-dimensional airfoil (i.e., a wing of infinite span), the circulation strength Γ is constant across the span (i.e., it is independent of y) and the induced downwash velocity is zero at all points since there are no trailing vortices. Therefore, $D_v = 0$ for a two-dimensional airfoil as we discussed in Chapter 6. As a consequence of the trailing vortex system, the aerodynamic characteristics are modified significantly from those of a two-dimensional airfoil of the same section, which we will now quantify.

7.3.2 Case of Elliptic Spanwise Circulation Distribution

An especially simple circulation distribution, which also has significant practical implications, is given by the elliptic circulation distribution (as shown in Fig. 7.7):

$$\Gamma(y) = \Gamma_0 \sqrt{1 - \left(\frac{y}{s}\right)^2} \tag{7.8}$$

Since the lift is a function only of the free-stream density, the free-stream velocity, and the circulation ($L = \rho_\infty U_\infty \Gamma$), an elliptic distribution of circulation also produces an elliptic distribution of lift. However, to calculate the section lift coefficient, the section lift force is divided by the product of q_∞ and the local chord length at the section of interest. Therefore, only when the wing has a rectangular planform (and c is constant) is the spanwise section lift coefficient distribution (C_l) elliptic when the spanwise lift distribution is elliptic.

For the elliptic spanwise circulation distribution of equation (7.8), the induced downwash velocity is found from equation (7.2):

$$w_{y1} = +\frac{1}{4\pi}\int_{-s}^{+s} \frac{d\Gamma/dy}{y - y_1}\, dy = -\frac{\Gamma_0}{4\pi s}\int_{-s}^{+s} \frac{y}{\sqrt{s^2 - y^2}(y - y_1)}\, dy$$

which can be rewritten as

$$w_{y1} = -\frac{\Gamma_0}{4\pi s}\left[\int_{-s}^{+s} \frac{(y - y_1)\, dy}{\sqrt{s^2 - y^2}(y - y_1)} + \int_{-s}^{+s} \frac{y_1\, dy}{\sqrt{s^2 - y^2}(y - y_1)}\right]$$

Now we can integrate this expression to obtain:

$$w_{y1} = -\frac{\Gamma_0}{4\pi s}(\pi + y_1 I) \tag{7.9}$$

where

$$I = \int_{-s}^{+s} \frac{dy}{\sqrt{s^2 - y^2}(y - y_1)}$$

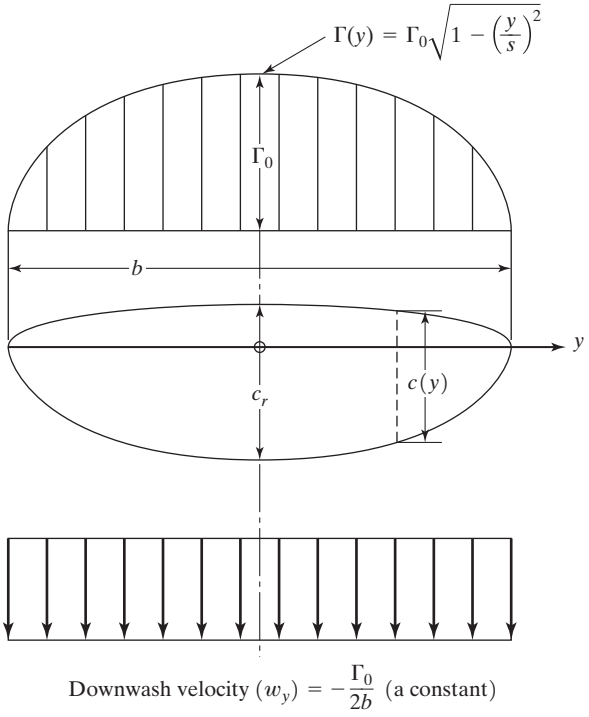

Figure 7.7 Elliptic-circulation distribution and the resultant downwash velocity.

Since the elliptic loading is symmetric about the pitch plane of the vehicle (i.e., $y = 0$), the velocity induced at a point $y_1 = +a$ should be equal to the velocity at a point $y_1 = -a$. Referring to equation (7.9), this can only be true if $I = 0$. Therefore, for the elliptic circulation distribution the downwash is:

$$w_{y1} = w(y) = -\frac{\Gamma_0}{4s} \tag{7.10}$$

which is the very interesting result that the induced velocity is independent of the spanwise position on the wing.

The total lift for the wing is given by the Kutta-Joukowski theorem as:

$$L = \int_{-s}^{+s} \rho_\infty U_\infty \Gamma_0 \sqrt{1 - \left(\frac{y}{s}\right)^2}\, dy$$

The lift equation can be made easier to integrate by using the coordinate transformation:

$$y = -s\cos\phi \qquad dy = s\sin\phi\, d\phi$$

where the left wing tip corresponds to $\phi = 0$ and the right wing tip corresponds to $\phi = \pi$, resulting in:

$$L = \int_0^\pi \rho_\infty U_\infty \Gamma_0 \sqrt{1 - \left(\frac{-s\cos\phi}{s}\right)^2}\, s\sin\phi\, d\phi = \int_0^\pi \rho_\infty U_\infty \Gamma_0 \sqrt{1 - \cos^2\phi}\, s\sin\phi\, d\phi$$

This expression can now be integrated to find:

$$L = \rho_\infty U_\infty \Gamma_0 \, s \, \frac{\pi}{2} = \frac{\pi}{4} b \rho_\infty U_\infty \Gamma_0 \tag{7.11}$$

and the lift coefficient for the wing is:

$$C_L = \frac{L}{\frac{1}{2}\rho_\infty U_\infty^2 S} = \frac{\pi b \Gamma_0}{2 U_\infty S} \tag{7.12}$$

From this equation, we can find the mid-span circulation as:

$$\Gamma_0 = \frac{2 C_L U_\infty S}{\pi b} \tag{7.13}$$

From equation (7.10), we can also find the downwash angle since:

$$\varepsilon = -\frac{w}{U_\infty} = +\frac{\Gamma_0}{4 U_\infty s} = \frac{\Gamma_0}{4 U_\infty \frac{b}{2}}$$

Combining the previous two equations shows that the downwash angle is:

$$\varepsilon = \frac{\Gamma_0}{4 U_\infty \frac{b}{2}} = \frac{2 C_L U_\infty S}{4 U_\infty \frac{b}{2} \pi b} = \frac{C_L}{\pi AR} \tag{7.14}$$

since the aspect ratio is defined as $AR = b^2/S$. Notice that the downwash angle is constant along the span of the wing for the elliptic lift distribution.

Similarly, we can calculate the total vortex (or induced) drag for the wing.

$$D_v = \int_{-s}^{+s} \frac{\rho_\infty \Gamma_0}{4s} \Gamma_0 \sqrt{1 - \left(\frac{y}{s}\right)^2} \, dy$$

Introducing the coordinate transformation again, we obtain:

$$\begin{aligned} D_v &= \frac{\rho_\infty \Gamma_0^2}{4s} \int_0^\pi \sqrt{1 - \cos^2\phi} \, s \sin\phi \, d\phi \\ &= \frac{\pi}{8} \rho_\infty \Gamma_0^2 \end{aligned} \tag{7.15}$$

and the drag coefficient for the induced component is

$$C_{Dv} = \frac{D_v}{\frac{1}{2}\rho_\infty U_\infty^2 S} = \frac{\pi \Gamma_0^2}{4 U_\infty^2 S} \tag{7.16}$$

Using the relation for Γ_0 from equation (7.13), the vortex drag coefficient becomes:

$$C_{Dv} = \frac{\pi}{4 U_\infty^2 S} \left(\frac{2 C_L U_\infty S}{\pi b} \right)^2$$

or

$$C_{Dv} = \frac{C_L^2}{\pi} \left(\frac{S}{b^2} \right)$$

Again using the definition of the aspect ratio, the vortex drag coefficient becomes:

$$C_{Dv} = \frac{C_L^2}{\pi AR} \tag{7.17}$$

We again see that the induced drag is zero for a two-dimensional airfoil (i.e., a wing with an aspect ratio of infinity), since the effect of the vortices is diminished as the aspect ratio goes to infinity. Note also that the trailing vortex drag for an inviscid flow around a wing is not zero but is proportional to C_L^2.

The induced drag coefficient given by equation (7.17) and the measurements for a wing whose aspect ratio is 5 are compared in Fig. 7.8. The experimental values of the induced drag coefficient, which were presented by Schlichting and Truckenbrodt (1969), closely follow the theoretical values up to an angle of attack of 20°. The relatively constant difference between the measured values and the theoretical values is due to the influence of skin friction, which was not included in the development of equation (7.17). Therefore, as noted in Chapter 5, the drag coefficient for an incompressible flow is typically written as:

$$C_D = C_{D_0} + kC_L^2 \tag{7.18}$$

where C_{D_0} is the drag coefficient at zero lift and kC_L^2 is the lift-dependent drag coefficient. The lift-dependent drag coefficient includes that part of the viscous drag and of the form drag, which results as the angle of attack changes from α_{0l}.

These relations describing the influence of the aspect ratio on the lift and the drag have been verified experimentally by Prandtl and Betz. If we compare the drag polars for two wings which have aspect ratios of AR_1 and AR_2, respectively, then for a given value of the lift coefficient,

$$C_{D,2} = C_{D,1} + \frac{C_L^2}{\pi}\left(\frac{1}{AR_2} - \frac{1}{AR_1}\right) \tag{7.19}$$

where $C_{D_{0,1}}$ has been assumed to be equal to $C_{D_{0,2}}$. The data from Prandtl (1921) for a series of rectangular wings are reproduced in Fig. 7.9. The experimentally determined drag polars are presented in Fig. 7.9a. Equation (7.19) has been used to convert the drag polars for the different aspect ratio wings to the equivalent drag polar for a wing whose aspect ratio is 5 (i.e., $AR_2 = 5$). These converted drag polars, which are presented in Fig. 7.9b, collapse quite well to a single curve. Therefore, the correlation of the measurements confirms the validity of equation (7.19).

We can also determine the effect of the aspect ratio on the correlation between the lift coefficient and the geometric angle of attack. To calculate the geometric angle of attack α_2 required to generate a particular lift coefficient for a wing of AR_2 if a wing with an aspect ratio of AR_1 generates the same lift coefficient at α_1, we use the equation

$$\alpha_2 = \alpha_1 + \frac{C_L}{\pi}\left(\frac{1}{AR_2} - \frac{1}{AR_1}\right) \tag{7.20}$$

Experimentally determined lift coefficients [from Prandtl (1921)] are presented in Fig. 7.10. The data presented in Fig. 7.10a are for the same rectangular wings of Fig. 7.9. The results of converting the coefficient-of-lift measurements using equation (7.20) in

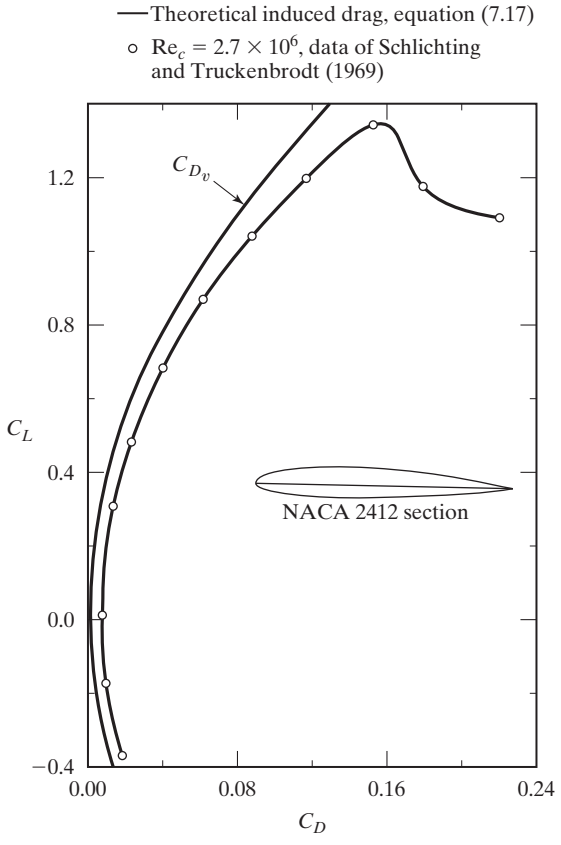

Figure 7.8 Experimental drag polar for a wing with an aspect ratio of 5 compared with the theoretical induced drag.

terms of a wing whose aspect ratio is 5 (i.e., $AR_2 = 5$) are presented in Fig. 7.10b. Again, the converted curves collapse into a single correlation. So, the validity of equation (7.20) is experimentally verified.

EXAMPLE 7.1: Lift and vortex drag coefficients for a wing with an elliptic lift distribution

The Cessna 172 aircraft has a wing geometry described in Table 5.1, a wing area of 174 ft^2, and a gross weight of 2450 pounds. If the airplane is flying at 100 miles per hour on a standard day at sea level, find the lift and vortex drag coefficients assuming the wing has an elliptic lift distribution and all of the lift is generated by the wing.

Solution: The velocity of the airplane is given in miles per hour and needs to be converted to feet per second in order to use consistent units.

$$U_\infty = (100\ \text{mile/h})(5280\ \text{ft/mile})/(3600\ \text{s/h}) = 146.7\ \text{ft/s}$$

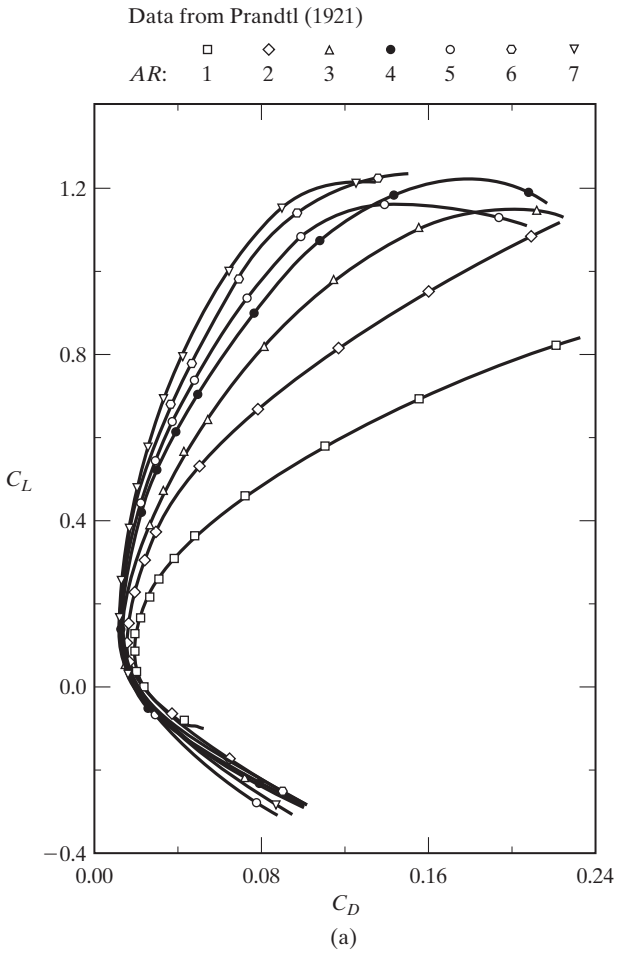

Figure 7.9 Effect of the aspect ratio on the drag polar for rectangular wings (AR from 1 to 7): (a) measured drag polars.

The lift coefficient is found assuming the aircraft is flying in SLUF conditions where $L = W$. The lift coefficient can then be found from:

$$C_L = \frac{L}{\frac{1}{2}\rho_\infty U_\infty^2 S} = \frac{W}{\frac{1}{2}\rho_\infty U_\infty^2 S} = \frac{2450\,\text{lb}}{\frac{1}{2}(0.002377\,\text{slug/ft}^3)(146.7\,\text{ft/s})^2(174\,\text{ft}^2)} = 0.551$$

From Table 5.1 the aspect ratio of the Cessna 172 is given as 7.32. Using equation (7.17) the vortex drag coefficient for an elliptic lift distribution is:

$$C_{Dv} = \frac{C_L^2}{\pi AR} = \frac{(0.551)^2}{7.32\pi} = 0.0132$$

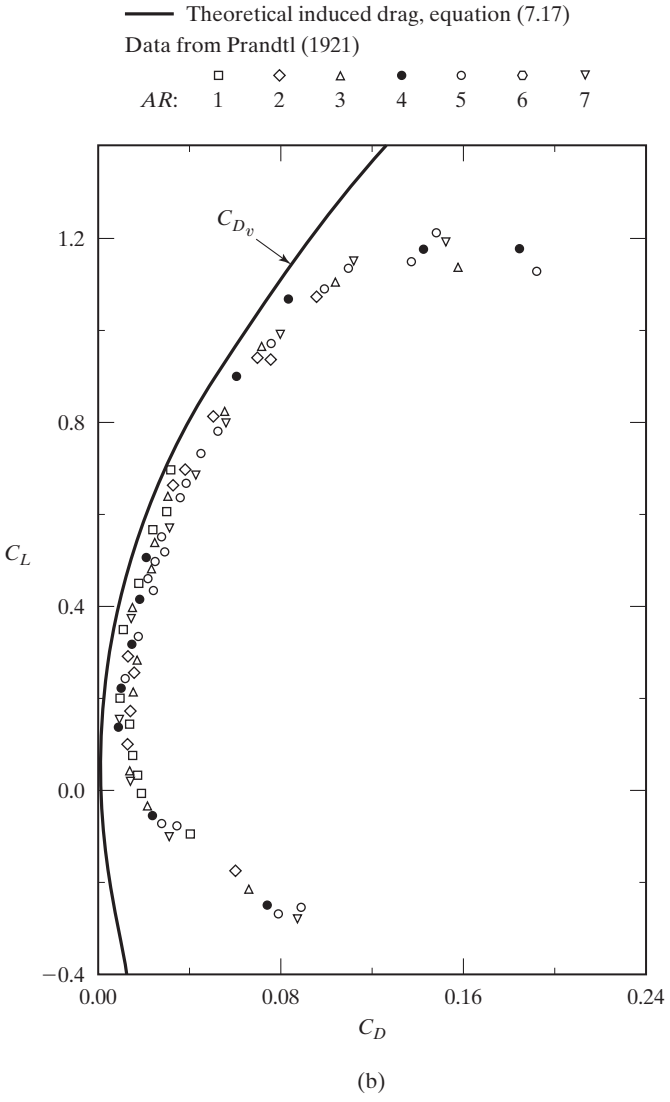

(b)

Figure 7.9 (b) drag polars converted to $AR = 5$.

7.3.3 Technique for General Spanwise Circulation Distribution

Consider a spanwise circulation distribution that can be represented by a Fourier sine series consisting of N terms:

$$\Gamma(\phi) = 4sU_\infty \sum_{1}^{N} A_n \sin n\phi \tag{7.21}$$

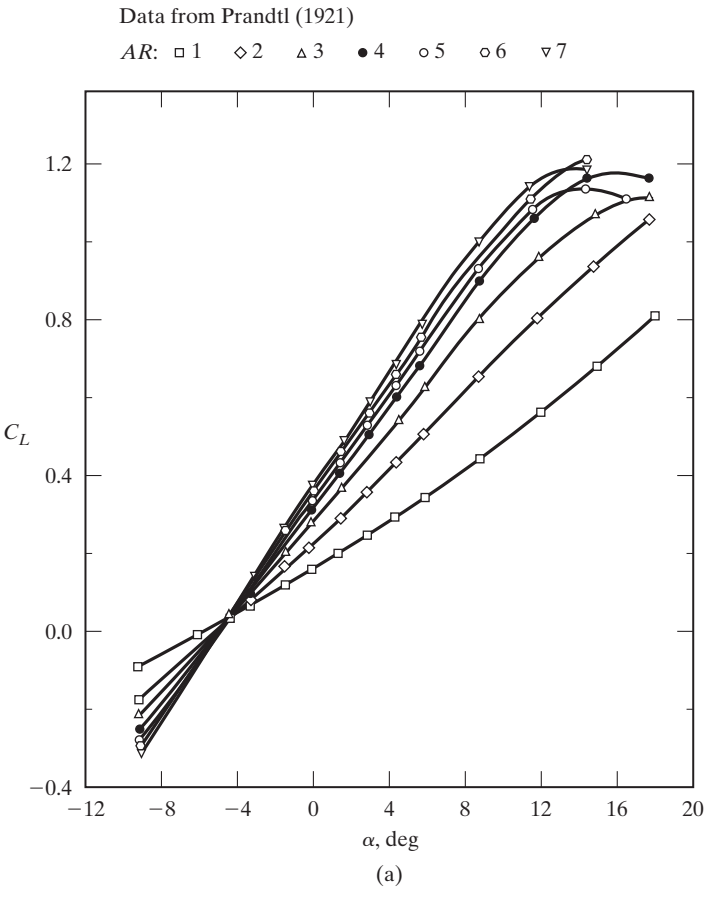

Figure 7.10 Effect of aspect ratio on the lift coefficient for rectangular wings (AR from 1 to 7): (a) measured lift coefficients.

As was done previously, the physical spanwise coordinate (y) has been replaced by the ϕ coordinate:

$$\frac{y}{s} = -\cos\phi$$

A sketch of one such Fourier series is presented in Fig. 7.11. Since the spanwise lift distribution represented by the circulation of Fig. 7.11 is symmetrical, only the odd terms remain.

The section lift force [i.e., the lift acting on that spanwise section for which the circulation is $\Gamma(\phi)$] is found by applying the Kutta-Joukowski theorem to equation (7.21):

$$l(\phi) = \rho_\infty U_\infty \Gamma(\phi) = 4\rho_\infty U_\infty^2 s \sum_1^N A_n \sin n\phi \qquad \textbf{(7.22)}$$

To evaluate the coefficients $A_1, A_2, A_3, \ldots, A_N$, it is necessary to determine the circulation at N spanwise locations. Once this is done, the N-resultant linear equations can be solved for the A_n coefficients. Typically, the series is truncated to a finite series and

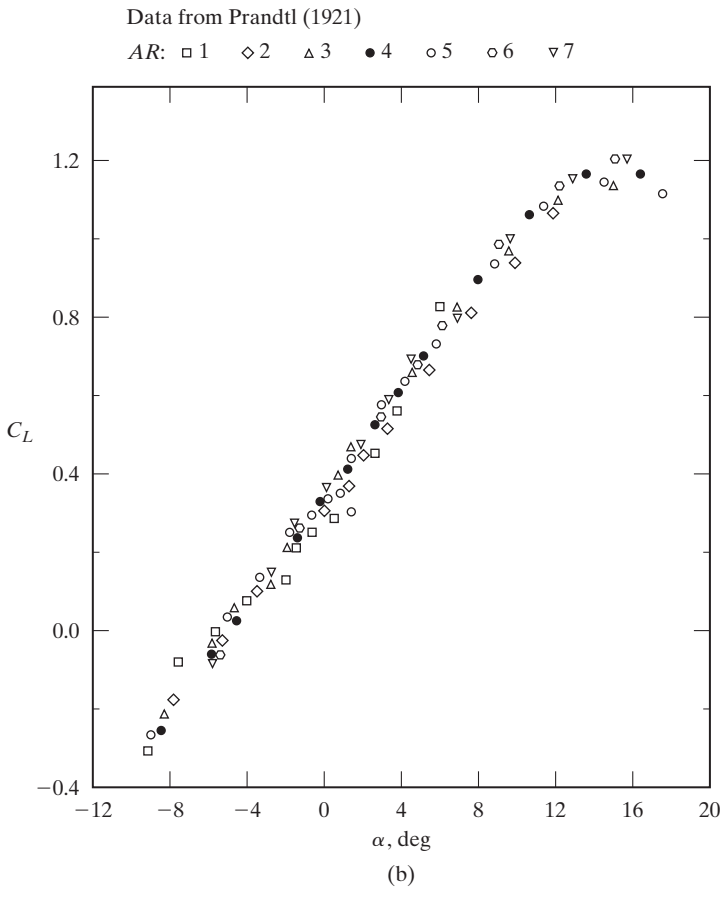

Figure 7.10 (b) Lift correlations converted to $AR = 5$.

the coefficients in the finite series are evaluated by requiring the lifting-line equation to be satisfied at a number of spanwise locations equal to the number of terms in the series. This method, known as the collocation method, will be developed in this section.

Recall that the section lift coefficient is defined as

$$C_l(\phi) = \frac{\text{lift per unit span}}{\frac{1}{2}\rho_\infty U_\infty^2 c}$$

Using the local circulation to determine the local lift per unit span, we obtain

$$C_l(\phi) = \frac{\rho_\infty U_\infty \Gamma(\phi)}{\frac{1}{2}\rho_\infty U_\infty^2 c} = \frac{2\Gamma(\phi)}{U_\infty c} \tag{7.23}$$

It is also possible to evaluate the section lift coefficient by using the linear correlation between the lift and the angle of attack for the equivalent two-dimensional flow. Referring to Fig. 7.12 for the nomenclature, we obtain:

$$C_l = \left(\frac{dC_l}{d\alpha}\right)_0 (\alpha_e - \alpha_{0l}) \tag{7.24}$$

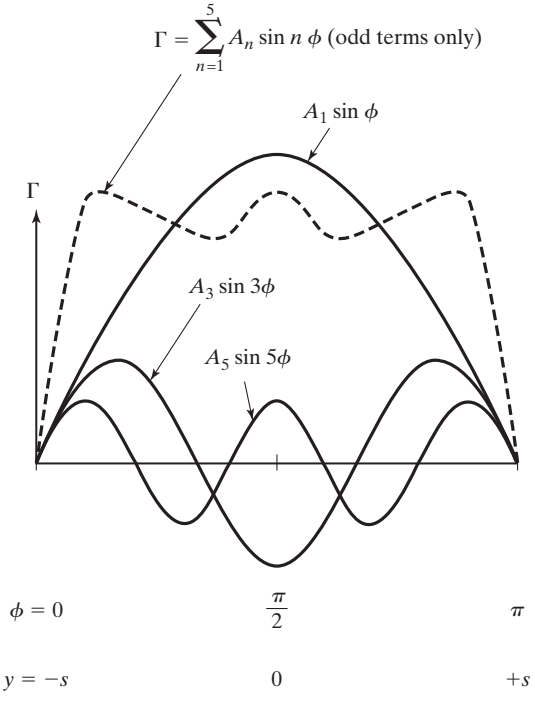

Figure 7.11 Symmetric spanwise lift distribution as represented by a sine series.

We now have two expressions for calculating the section lift coefficient at a particular spanwise location ϕ. We can set the expression in equation (7.23) equal to that in equation (7.24) to form an important equation for lifting-line theory.

Let the equivalent lift-curve slope $(dC_l/d\alpha)_0$ be designated by the symbol a_0. Notice that since $\alpha_e = \alpha - \varepsilon$, equations (7.23) and (7.24) can be combined to yield the relation:

$$\frac{2\Gamma(\phi)}{c(\phi)a_0} = U_\infty[\alpha(\phi) - \alpha_{0l}(\phi)] - U_\infty\varepsilon(\phi) \qquad \textbf{(7.25)}$$

For the present analysis, five parameters in equation (7.25) may depend on the spanwise location ϕ (or, equivalently, y) at which we will evaluate the terms. The five parameters are: (1) Γ, the local circulation; (2) ε, the downwash angle, which depends on the circulation distribution; (3) c, the chord length, which varies with ϕ for a tapered wing planform; (4) α, the local geometric angle of attack, which varies with ϕ when the wing is twisted (i.e., geometric twist, which is illustrated in Fig. 5.7); and (5) α_{0l}, the zero lift angle of attack, which varies with ϕ when the airfoil section varies in the spanwise direction (which is known as *aerodynamic twist*). Using equation (7.3), we can find the induced angle of attack in terms of the downwash velocity as:

$$U_\infty\varepsilon = -w = -\frac{1}{4\pi}\int_{-s}^{+s} \frac{d\Gamma/dy}{y - y_1}\,dy$$

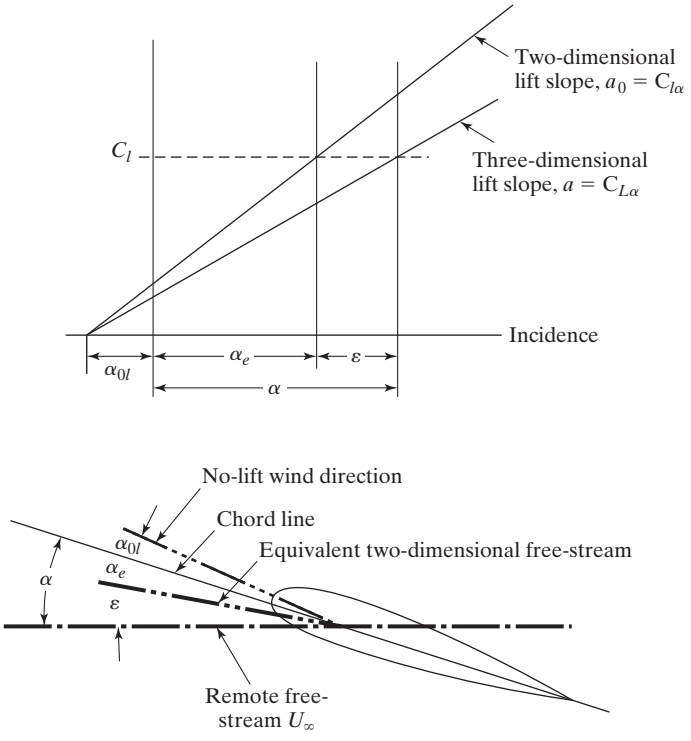

Figure 7.12 Nomenclature for wing/airfoil lift.

Using the Fourier series representation for Γ and the coordinate transformation, we obtain:

$$-w = U_\infty \varepsilon = U_\infty \underbrace{\frac{\sum nA_n \sin n\phi}{\sin \phi}}_{\varepsilon}$$

$$\varepsilon = -\frac{w}{U_\infty} = \frac{\sum nA_n \sin n\phi}{\sin \phi}$$

Equation (7.25) can now be rewritten using the above relation:

$$\frac{2\Gamma}{ca_0} = U_\infty(\alpha - \alpha_{0l}) - U_\infty \frac{\sum nA_n \sin n\phi}{\sin \phi}$$

Since $\Gamma = 4sU_\infty \sum A_n \sin n\phi$, the equation becomes:

$$\frac{8s}{ca_0} \sum A_n \sin n\phi = (\alpha - \alpha_{0l}) - \frac{\sum nA_n \sin n\phi}{\sin \phi}$$

Defining $\mu = ca_0/8s$, the resultant governing equation is:

$$\mu(\alpha - \alpha_{0l}) \sin \phi = \sum A_n \sin n\phi (\mu n + \sin \phi) \qquad \textbf{(7.26)}$$

which is known as the *monoplane equation*. If we consider only symmetrical loading distributions, only the odd terms of the series need to be considered. That is, as shown in the sketch of Fig. 7.11,

$$\Gamma(\phi) = 4sU_\infty(A_1 \sin\phi + A_3 \sin 3\phi + A_5 \sin 5\phi + \cdots)$$

7.3.4 Lift on the Wing

The lift on the wing can now be found using equation (7.22):

$$L = \int_{-s}^{+s} \rho_\infty U_\infty \Gamma(y)\, dy = \int_0^\pi \rho_\infty U_\infty s \Gamma(\phi) \sin\phi\, d\phi$$

Using the Fourier series for $\Gamma(\phi)$ we find that:

$$L = 4\rho_\infty U_\infty^2 s^2 \int_0^\pi \sum A_n \sin n\phi \sin\phi\, d\phi$$

Noting that $\sin A \sin B = \frac{1}{2}\cos(A - B) - \frac{1}{2}\cos(A + B)$, the integration yields

$$L = 4\rho_\infty U_\infty^2 s^2 \left\{ A_1 \left[\frac{\phi}{2} + \frac{\sin 2\phi}{4} \right] \Bigg|_0^\pi + \sum_3^N \frac{1}{2} A_n \left[\frac{\sin(n-1)\phi}{n-1} - \frac{\sin(n+1)\phi}{n+1} \right] \Bigg|_0^\pi \right\}$$

The summation represented by the second term on the right-hand side of the equation is zero, since each of the terms is zero for $n \neq 1$. Therefore, the integral expression for the lift becomes:

$$L = (4s^2)\left(\tfrac{1}{2}\rho_\infty U_\infty^2\right) A_1 \pi = C_L \left(\tfrac{1}{2}\rho_\infty U_\infty^2\right)(S)$$

and the wing lift coefficient is:

$$C_L = A_1\, \pi\, AR \qquad \textbf{(7.27)}$$

You can see that the lift depends only on the magnitude of the first coefficient, no matter how many terms may be present in the series describing the distribution.

7.3.5 Vortex-Induced Drag

Now that we have found the lift coefficient for the wing, the vortex-induced drag can also be found using equation (7.5).

$$\begin{aligned} D_v &= -\int_{-s}^{+s} \rho_\infty w \Gamma\, dy \\ &= \rho_\infty \int_0^\pi \underbrace{\frac{U_\infty \sum n A_n \sin n\phi}{\sin\phi}}_{-w} \underbrace{4sU_\infty \sum A_n \sin n\phi}_{\Gamma} s \underbrace{\sin\phi\, d\phi}_{dy} \\ &= 4\rho_\infty s^2 U_\infty^2 \int_0^\pi \sum n A_n \sin n\phi \sum A_n \sin n\phi\, d\phi \end{aligned}$$

The integral can be evaluated as:

$$\int_0^{\pi} \sum nA_n \sin n\phi \sum A_n \sin n\phi \, d\phi = \frac{\pi}{2} \sum nA_n^2$$

So, the coefficient for the vortex-induced drag is:

$$C_{Dv} = \pi \cdot AR \sum nA_n^2 \tag{7.28}$$

Since $A_1 = C_L/(\pi \cdot AR)$, we can re-write equation (7.28) as:

$$C_{Dv} = \frac{C_L^2}{\pi \cdot AR} \sum n \left(\frac{A_n}{A_1} \right)^2$$

where only the odd terms in the series are considered for a symmetric lift distribution ($n = 1, 3, 5, \ldots$).

$$C_{Dv} = \frac{C_L^2}{\pi \cdot AR} \left[1 + \left(\frac{3A_3^2}{A_1^2} + \frac{5A_5^2}{A_1^2} + \frac{7A_7^2}{A_1^2} + \cdots \right) \right]$$

or

$$C_{Dv} = \frac{C_L^2}{\pi AR}(1 + \delta) = \frac{C_L^2}{\pi eAR} \tag{7.29}$$

where e is the span efficiency factor of the wing and $e = 1/(1 + \delta)$. Typical values for the span efficiency factor range between 0.6 and 0.95, with $e = 1$ being the value for an elliptic lift distribution. In general, values of the span efficiency factor should be as close to $e = 1$ as possible to improve the aerodynamic efficiency of the wing. The induced drag factor δ is given by:

$$\delta = \frac{3A_3^2}{A_1^2} + \frac{5A_5^2}{A_1^2} + \frac{7A_7^2}{A_1^2} + \cdots$$

Since $\delta \geq 0$, the induced drag is minimum when $\delta = 0$ ($e = 1$). In this case, the only term in the series representing the circulation distribution is the first term:

$$\Gamma(\phi) = 4sU_\infty A_1 \sin\phi$$

which is the elliptic distribution, as we discussed in Section 7.3.2.

The effect of the taper ratio on the spanwise variation of the lift coefficient is illustrated in Fig. 7.13. Theoretical solutions are presented for untwisted wings having taper ratios from 0 to 1. The wings, which were composed of NACA 2412 airfoil sections, all had an aspect ratio of 7.28. Again, the local lift coefficient has been divided by the overall lift coefficient for the wings according to:

$$\frac{C_l(\phi)}{C_L} = \frac{2(1 + \lambda)}{\pi A_1} \frac{c_r}{c(\phi)} \sum \{ A_{2n-1} \sin[(2n - 1)\phi] \}$$

The values of the local (or section) lift coefficient near the tip of the highly tapered wings are significantly greater than the overall lift coefficient for that planform. As discussed earlier, this result is important relative to the separation (or stall) of the boundary layer for a particular planform when it is operating at a relatively high angle of attack, since a highly loaded tip will stall first, placing any ailerons in the unsteady flow field downstream of the stall region.

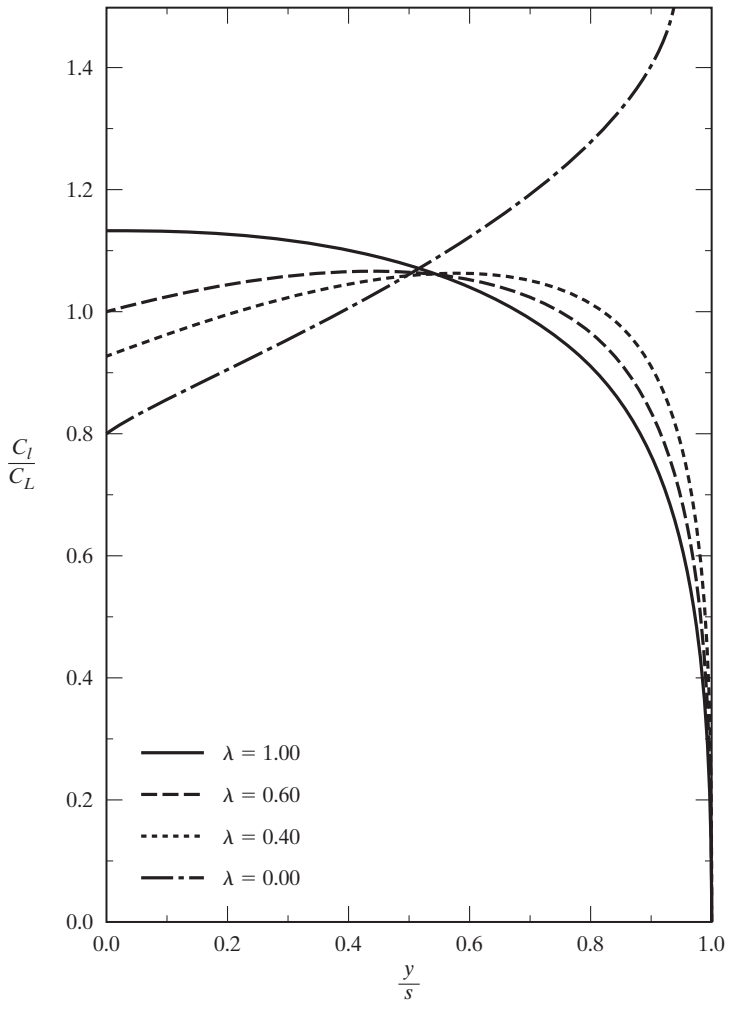

Figure 7.13 Effect of taper ratio on the spanwise variation of the lift coefficient for an untwisted wing.

Lifting-line theory can also predict the change in the wing lift-curve slope, as we mentioned in Chapter 5. Specifically, since each airfoil section is "seeing" an effective angle of attack which is less than the geometric angle of attack (see Fig. 7.12), the lift of the wing is reduced. Specifically the geometric angle of attack is given by $\alpha = \alpha_e + \varepsilon$, and from equation (7.19) the downwash angle for an elliptic lift distribution is $\varepsilon = C_L/\pi AR$, then the geometric angle of attack for an elliptic lift distribution is:

$$\alpha = \alpha_e + \frac{C_L}{\pi AR}$$

Taking the derivative of this equation with respect to the lift coefficient gives us [Glauert (1948)]:

$$\frac{1}{a} = \frac{1}{a_0} + \frac{1}{\pi AR}$$

which can be re-arranged to obtain:

$$a = C_{L_\alpha} = \frac{a_0}{1 + \dfrac{a_0}{\pi AR}} = \frac{C_{l_\alpha}}{1 + \dfrac{C_{l_\alpha}}{\pi AR}}$$

which is equation (5.41). This is the lift-curve slope for a wing with an elliptic lift distribution, which can be extended to a general lift distribution in a similar fashion to the induced drag in equation (7.29) by the addition of a lift-curve slope parameter, τ:

$$a = \frac{a_0}{1 + \dfrac{a_0}{\pi AR}(1 + \tau)} \tag{7.30}$$

The slope parameter can be obtained from the Fourier coefficients in a similar fashion to δ, but it is common to show the parameter graphically. Fig. 7.14a shows the induced drag parameter, δ, for planar wings with non-elliptic lift distributions as a function of taper ratio and aspect ratio, and Fig. 7.14b shows the slope parameter, τ [Bridges (2005)]. Notice that both parameters have high values at low taper ratios (pointed wing tips) as well as fairly high values at high taper ratios (rectangular wings). Each parameter is minimized (and the impact of the wing on induced drag and lift-curve slope reduction is minimized) when the taper ratio is $\lambda \approx 0.3 - 0.4$. A trapezoidal wing with this taper ratio approximates an elliptic planform shape and gives the best results for lift and drag.

Once the local lift coefficient reaches the stall angle of attack of the airfoil section, the local airfoil will be stalled, creating a region of flow separation in that vicinity. As the angle of attack is further increased, stall patterns will form on the wing, depending on the local lift coefficient variation along the span. Sketches of stall patterns are presented in Fig. 7.15. The desirable stall pattern for a wing is a stall which begins at the root sections so that the ailerons remain effective at high angles of attack. The spanwise load distribution for a rectangular wing indicates stall will begin at the root and proceed outward, which is a favorable stall pattern. The spanwise load distribution for a wing with a moderate taper ratio ($\lambda = 0.4$) approximates that of an elliptical wing (i.e., the local lift coefficient is roughly constant across the span). As a result, all sections will reach stall at essentially the same angle of attack.

Tapering of the wing also reduces the wing-root bending moments, since the inboard portion of the wing carries more of the wing's lift than the tip. Furthermore, the longer wing-root chord makes it possible to increase the actual thickness of the wing while maintaining a low thickness ratio, which is needed if the airplane is to operate at high speeds also. While taper reduces the actual loads carried outboard, the lift coefficients near the tip are higher than those near the root for a tapered wing. Therefore, there is a strong tendency to stall near (or at) the tip for highly tapered (or pointed) wings.

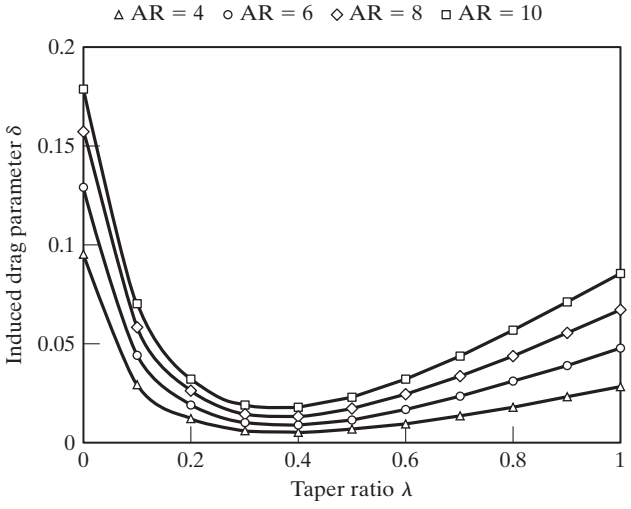

(a) induced drag parameter

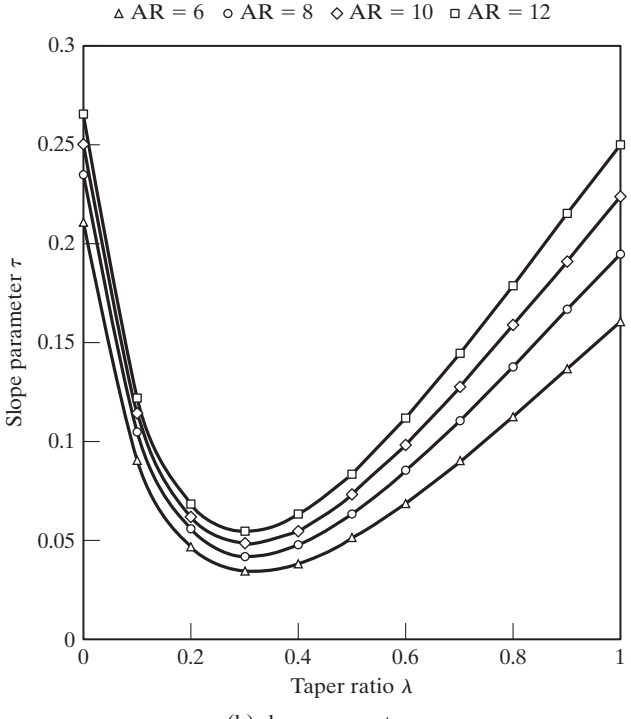

(b) slope parameter

Figure 7.14 Effect of aspect ratio and taper ratio on: (a) induced drag parameter and (b) lift-curve slope parameter. Airfoil lift-curve slope is assumed to be 2π/rad [from Bridges (2005)].

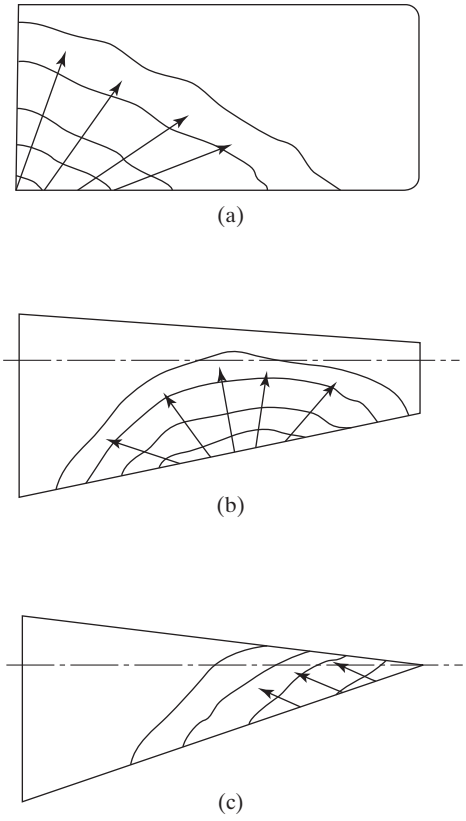

Figure 7.15 Typical stall patterns: (a) rectangular wing, $\lambda = 1.0$; (b) moderately tapered wing, $\lambda = 0.4$; (c) pointed wing, $\lambda = 0.0$.

In order to prevent the stall pattern from beginning in the region of the ailerons, the wing may be given a geometric twist, or washout, to decrease the local angles of attack at the tip (see examples in Table 5.1). The addition of leading-edge slots or slats toward the tip increases the stall angle of attack and is useful in avoiding tip stall and the loss of aileron effectiveness.

EXAMPLE 7.2: Use the monoplane equation to compute the aerodynamic coefficients for a wing

The monoplane equation [i.e., equation (7.26)] will be used to compute the aerodynamic coefficients of a wing for which aerodynamic data are available. The geometry of the wing to be studied is illustrated in Fig. 7.16. The wing, which is unswept at the quarter chord, is composed of NACA 65–210 airfoil sections. Referring to the data of Abbott and von Doenhoff (1949), the zero-lift angle of attack (α_{0l}) for this airfoil is approximately $-1.2°$ across the span. Since the wing is untwisted, the geometric angle of

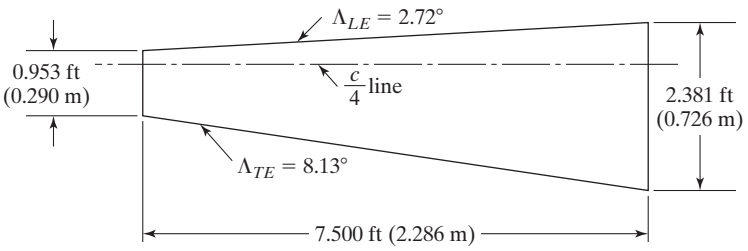

Figure 7.16 Planform for an unswept wing, $AR = 9.00$, $\lambda = 0.40$, airfoil section NACA 65–210.

attack is the same at all spanwise positions. The aspect ratio (AR) of the full wing is 9.00, and the taper ratio λ (c_t/c_r) is 0.40. Since the wing planform is trapezoidal,

$$S = \tfrac{1}{2}(c_r + c_t)b = \tfrac{1}{2}c_r(1 + \lambda)b$$

and

$$AR = \frac{2b}{c_r + c_t}$$

Therefore, the parameter μ in equation (7.26) becomes:

$$\mu = \frac{ca_0}{4b} = \frac{ca_0}{2(AR)\cdot c_r(1 + \lambda)}$$

where c is the local chord, $c(y)$.

Solution: Since the terms are to be evaluated at spanwise stations for $0 \le \phi \le \pi/2$ [i.e., $-s \le y \le 0$ (which corresponds to the port wing or left side of the wing)],

$$\mu = \frac{a_0}{2(1 + \lambda)AR}[1 + (\lambda - 1)\cos\phi]$$
$$= 0.24933(1 - 0.6\cos\phi) \qquad \textbf{(7.31)}$$

where the equivalent lift-curve slope (i.e., for a two-dimensional flow over the airfoil section a_0) has been assumed to be equal to 2π 1/rad. It might be interesting to know that numerical solutions for lift and vortex-drag coefficients were essentially the same for this geometry whether the series representing the spanwise circulation distribution included 4 terms or 10 terms. Therefore, to help the reader perform the required calculations more easily, a four-term series will be used to represent the spanwise loading. Equation (7.26) becomes:

$$\mu(\alpha - \alpha_{0l})\sin\phi = A_1\sin\phi(\mu + \sin\phi) + A_3\sin 3\phi(3\mu + \sin\phi)$$
$$+A_5\sin 5\phi(5\mu + \sin\phi) + A_7\sin 7\phi(7\mu + \sin\phi) \qquad \textbf{(7.32)}$$

TABLE 7.1 Values of the Factors for Equation (7.32)

Station	ϕ	$-\frac{y}{s}$ (= cos ϕ)	sin ϕ	sin 3ϕ	sin 5ϕ	sin 7ϕ	μ
1	22.5°	0.92388	0.38268	0.92388	0.92388	0.38268	0.11112
2	45.0°	0.70711	0.70711	0.70711	−0.70711	−0.70711	0.14355
3	67.5°	0.38268	0.92388	−0.38268	−0.38268	0.92388	0.19208
4	90.0°	0.00000	1.00000	−1.00000	1.00000	−1.00000	0.24933

Since there are four coefficients (i.e., A_1, A_3, A_5, and A_7) to be evaluated, equation (7.32) must be evaluated at four spanwise locations. The resultant values for the factors are summarized in Table 7.1. Notice that since we are considering the left side of the wing, the y coordinate is negative.

For a geometric angle of attack of 4°, equation (7.32) becomes:

$$0.00386 = 0.18897A_1 + 0.66154A_3 + 0.86686A_5 + 0.44411A_7$$

for $\phi = 22.5°$ (i.e., $y = -0.92388s$). For the other stations, the equation becomes:

$$0.00921 = 0.60150A_1 + 0.80451A_3 - 1.00752A_5 - 1.21053A_7$$
$$0.01611 = 1.03101A_1 - 0.57407A_3 - 0.72109A_5 + 2.09577A_7$$
$$0.02263 = 1.24933A_1 - 1.74799A_3 + 2.24665A_5 - 2.74531A_7$$

which is four equations in four unknowns. The solution of this system of linear equations yields:

$$A_1 = 1.6459 \times 10^{-2}$$
$$A_3 = 7.3218 \times 10^{-5}$$
$$A_5 = 8.5787 \times 10^{-4}$$
$$A_7 = -9.6964 \times 10^{-5}$$

Using equation (7.27), the lift coefficient for an angle of attack of 4° is:

$$C_L = A_1 \pi AR = 0.4654$$

The theoretically determined lift coefficients are compared in Fig. 7.17 with data for this wing. In addition to the geometric characteristics already described, the wing has a dihedral angle of 3°, which we are not modeling. The measurements reported by Sivells (1947) were obtained at a Reynolds number of approximately 4.4×10^6 and a Mach number of approximately 0.17, and our theory assumes inviscid, incompressible flow. In spite of these differences, the agreement between the theoretical values and the experimental values is very good.

The spanwise distribution for the local lift coefficient of this wing is presented in Fig. 7.18. As noted by Sivells (1947), the variation of the section

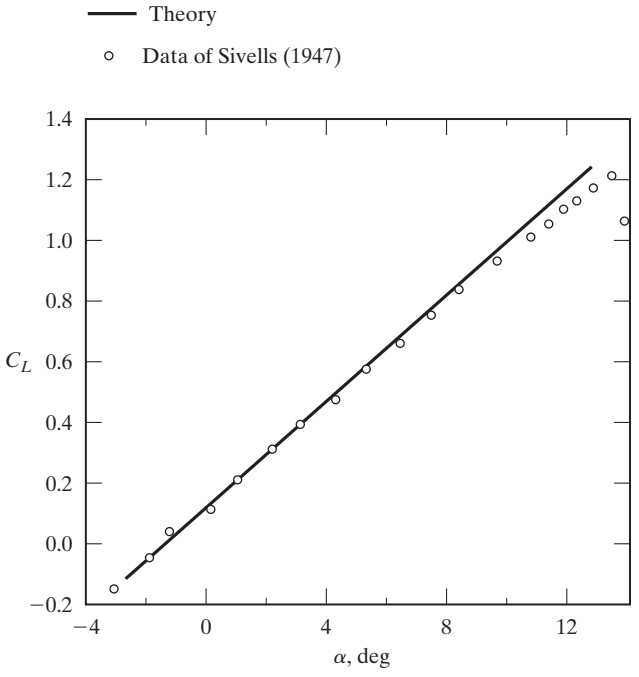

Figure 7.17 Comparison of the theoretical and the experimental lift coefficients for an unswept wing in a subsonic stream (wing is that of Fig. 7.16).

lift coefficient can be used to determine the spanwise position of initial stall. The local lift coefficient is given by:

$$C_l = \frac{\rho_\infty U_\infty \Gamma}{\frac{1}{2}\rho_\infty U_\infty^2 c}$$

where c is the local chord at a given location along the span, $c(y)$. For the trapezoidal wing under consideration is:

$$C_l(\phi) = 2AR(1 + \lambda)\frac{c_r}{c(\phi)}\sum \{A_{2n-1}\sin[(2n - 1)\phi]\} \qquad \textbf{(7.33)}$$

The theoretical value of the induced drag coefficient for an angle of attack of 4°, as determined using equation (7.29), is:

$$C_{Dv} = \frac{C_L^2}{\pi AR}\left(1 + \frac{3A_3^2}{A_1^2} + \frac{5A_5^2}{A_1^2} + \frac{7A_7^2}{A_1^2}\right) = \frac{C_L^2}{\pi AR}(1 + \delta)$$
$$= 0.00766(1.0136) = 0.00776$$

and $\delta = 0.0136$. The theoretically determined induced drag coefficients are compared in Fig. 7.19 with the measured drag coefficients for this wing.

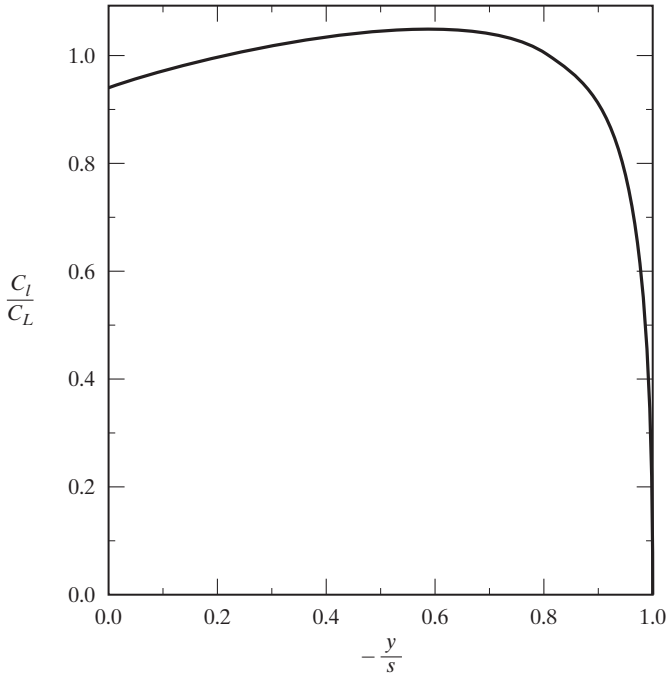

Figure 7.18 Spanwise distribution of the local lift coefficient, $AR = 9, \lambda = 0.4$, untwisted wing composed of NACA 65–210 airfoil sections.

As we noted earlier, the theoretical relations developed in this chapter do not include the effects of skin friction. The relatively constant difference between the measured values and the theoretical values is due to the influence of skin friction.

EXAMPLE 7.3: Use the induced drag factor and lift-curve slope parameter to compute the aerodynamic coefficients for a wing

Using the same wing as shown in Example 7.2, in conjunction with the induced drag factor and slope parameter graphs in Fig. 7.14, we can evaluate the effectiveness of a "short-cut" method for estimating wing aerodynamics.

Solution: Equation (7.30) gives the lift-curve slope for a wing in terms of the slope parameter, τ. If we assume that the airfoil lift-curve slope is 2π 1/rad, and find the slope parameter from Fig. 7.14b as $\tau \approx 0.06$, then the wing lift-curve slope is:

$$C_{L_\alpha} = a = \frac{a_0}{1 + \dfrac{a_0}{\pi AR}(1+\tau)} = \frac{2\pi\ 1/\text{rad}}{1 + \dfrac{2\pi}{9\pi}(1.06)} = 5.085\,1/\text{rad} = 0.0888\,1/\text{deg}$$

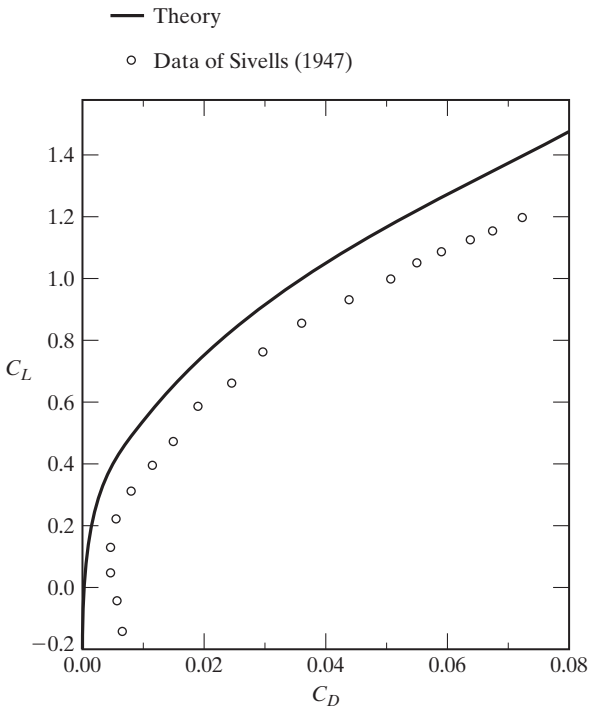

Figure 7.19 Comparison of the theoretical induced drag coefficients and the measured drag coefficients for an unswept wing in a subsonic stream (wing is that of Fig. 7.16).

and the lift curve is defined by:

$$C_L = a(\alpha - \alpha_{0l}) = (0.0888\,1/\text{deg})(\alpha + 1.2^\circ)$$

which gives essentially the same results as those shown in Fig. 7.17. For an angle of attack of 4°, $C_L = 0.4618$, which compare very well with the value from Example 7.2.

The vortex drag coefficient can also be found using equation (7.29) and Fig. 7.14b, which gives a value for the induced drag factor of $\delta \approx 0.015$:

$$C_{Dv} = \frac{C_L^2}{\pi AR}(1 + \delta) = \frac{0.4618^2}{9\pi}(1 + 0.015) = 0.00766$$

which is also very close to the value from Example 7.2. The obvious benefit of the approach from this example is the relative speed of obtaining results compared with the monoplane equation approach of Example 7.2. However, the results come with a level of inaccuracy, since the values of the induced drag factor and slope parameter have to be read from a graph, and the values from the graph are for a parametric set of wings with a trapezoidal planform and an airfoil lift-curve slope of 2π 1/rad. However, if used for conceptual design studies where trends are often the most important result, this approach supplies reasonable results very quickly.

7.3.6 Some Final Comments on Lifting-Line Theory

With continuing improvements, lifting-line theory is still used to provide rapid estimates of the spanwise load distributions and certain aerodynamic coefficients for unswept, or slightly swept, wings. In the Fourier series analysis of Rasmussen and Smith (1999), the planform and the twist distributions for general wing configurations are represented explicitly. The spanwise circulation distribution $\Gamma(y)$ is obtained explicitly in terms of the Fourier coefficients for the chord distribution and the twist distribution.

The method of Rasmussen and Smith (1999) was used to solve for the aerodynamic coefficients for the wing of Example 7.2. The induced drag factor δ, as taken from Rasmussen and Smith (1999), is reproduced in Fig. 7.20. The values of the induced drag factor are presented as a function of the number of terms in the Fourier series. The values of δ are compared with the values computed using the collocation method of Example 7.2. The two methods produce values which are very close, when six, seven, or eight terms are used in the Fourier series. Rasmussen and Smith (1999) claim, "The method converges faster and is more accurate for the same level of truncation than collocation methods."

The *lifting-line theory* of Phillips and Snyder (2000) is in reality the vortex-lattice method applied using only a single lattice element in the chordwise direction for each spanwise subdivision of the wing. So, the method is very much like that used in Example 7.2, except that many more panels are used to provide better resolution of the spanwise loading.

Incorporating empirical information into the modeling, we can extend the range of *applicability* of lifting-line theory. Anderson et al. (1980) noted that "certain leading-edge modifications can favorably tailor the high-lift characteristics of wings for light, single-engine general aviation airplanes so as to inhibit the onset of stall/spins. Since

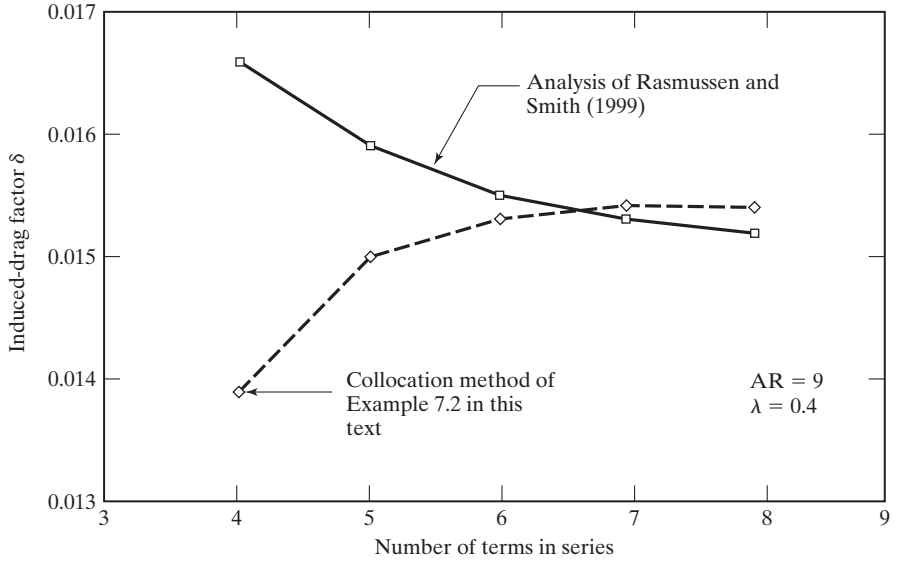

Figure 7.20 Convergence properties of induced drag factor δ for tapered wing, $\lambda = 0.4$ [from Rasmussen and Smith (1999)].

more than 30% of all general aviation accidents are caused by stall/spins, such modifications are clearly of practical importance. A modification of current interest is an abrupt extension and change in shape of the leading edge along a portion of the wing span—a so called 'drooped' leading edge." The concept is shown in Fig. 7.21, where you can see that the chord is extended approximately 10% over a portion of the wing. Anderson et al. (1980) continue: "The net aerodynamic effect of this modification is a smoothing of the normally abrupt drop in lift coefficient C_L at stall, and the generation of a relatively large value of C_L at very high post-stall angles of attack . . . As a result, an airplane with a properly designed drooped leading edge has increased resistance toward stalls/spins."

The post-stall behavior was modeled by introducing the experimentally determined values of the lift-curve slope in place of a_0 [Anderson et al. (1980)]; you should re-read the discussion leading up to equations (7.25) and (7.26). The authors noted that the greatest compromise in using lifting-line theory into the stall angle-of-attack

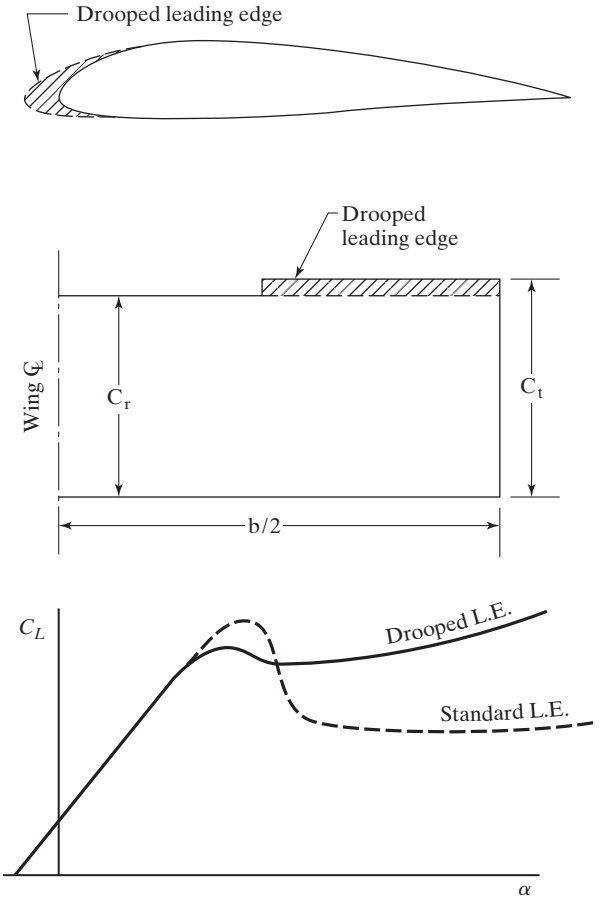

Figure 7.21 Drooped leading-edge characteristic [from Anderson et al. (1980)].

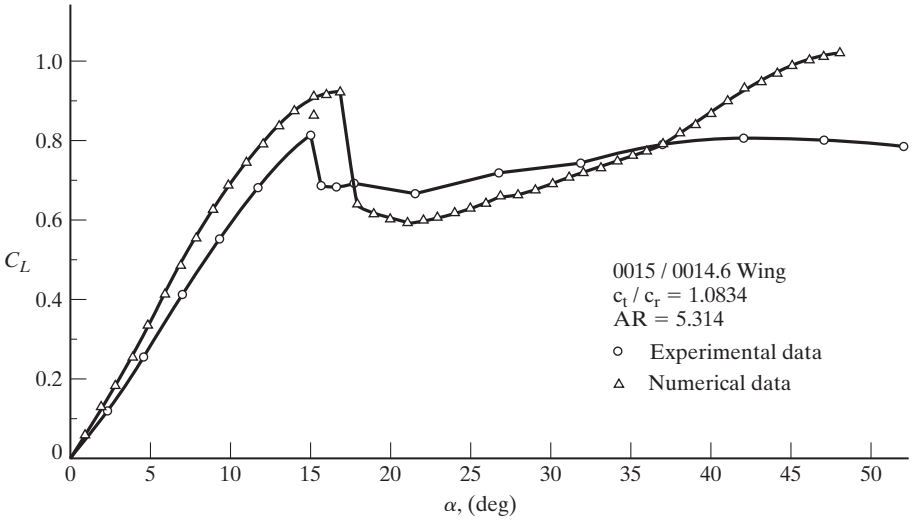

Figure 7.22 Lift coefficient versus angle of attack for a drooped leading-edge wing; comparison between experiment and numerical results [from Anderson et al. (1980)].

range and beyond is the use of data for the *two-dimensional flow around an airfoil*. The actual flow for this configuration is a complex, three-dimensional flow with separation. Nevertheless, with the use of experimental values for the lift-curve slope of the airfoil section, lifting-line theory generates reasonable estimates for C_L, when compared with experimental data, as shown in Fig. 7.22.

7.4 PANEL METHODS

Although lifting-line theory [i.e., the monoplane equation, equation (7.26)] provides a reasonable estimate of the lift and of the induced drag for an unswept, thin wing of relatively high aspect ratio in a subsonic free stream flow, an improved flow model is needed to calculate the lifting flow field about a highly swept wing or a delta wing. Panel methods, among other approaches, have been developed to compute the flow about a thin wing which is operating at a small angle of attack so that the resultant flow may be assumed to be steady, inviscid, irrotational, and incompressible.

The basic concept of panel methods is illustrated in Fig. 7.23. The configuration is modeled by a large number of elementary quadrilateral panels lying either on the actual aircraft surface, or on some mean surface (such as the mean camber line), or a combination of both. For each elementary panel, one or more types of singularity distributions (such as sources, vortices, and doublets) are attached. These singularities are determined by specifying some functional variation across the panel (e.g., constant, linear, quadratic), whose actual value is set by corresponding strength parameters (source strength, vortex strength, etc.). These strength parameters are determined by solving for appropriate boundary condition equations, and once the singularity strengths have been determined, the velocity field and the pressure field can be computed using the same methods we developed in Chapter 3.

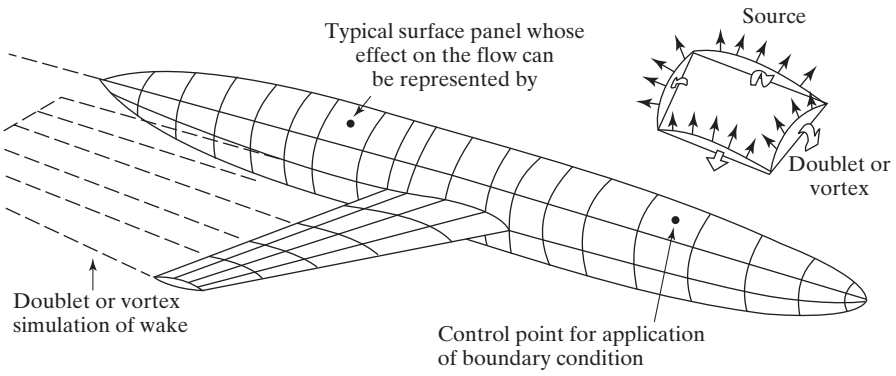

Figure 7.23 Representation of an airplane flowfield by panel (or singularity) methods.

7.4.1 Boundary Conditions

As we just mentioned, the boundary conditions for the flow field determine the singularity strengths for a panel method. This requires some basic background knowledge about boundary-value problems in mathematics. Johnson (1980) noted that, as a general rule, a boundary-value problem associated with Laplace's equation [equation (3.26)] is well posed if either ϕ or $(\partial\phi/\partial n)$ is specified at every point of the surface of the configuration which is being analyzed or designed (where ϕ is the solution variable for the problem of interest, typically the velocity potential for fluid problems). Johnson (1980) also notes, "Fluid flow boundary conditions associated with Laplace's equation are generally of analysis or design type. Analysis conditions are employed on portions of the boundary where the geometry is considered fixed, and resultant pressures are desired. The permeability of the fixed geometry is known; hence, analysis conditions are of the Neumann type (specification of normal velocity). Design boundary conditions are used wherever a geometry perturbation is allowed for the purpose of achieving a specific pressure distribution. Here a perturbation to an existing tangential velocity vector field is made; hence, design conditions are fundamentally of the Dirichlet type (specification of potential). The design problem in addition involves such aspects as stream surface lofting (i.e., integration of streamlines passing through a given curve), and the relationship between a velocity field and its potential."

Neumann boundary conditions (specification of $\partial\phi/\partial n$ at every point on the surface) arise naturally in the analysis of fixed configurations bounded by surfaces of known permeability (which is the amount of fluid allowed to flow through a surface). If the surface of the configuration is impermeable (as is the case for almost every application discussed in aerodynamics), the normal component of the resultant velocity must be zero at every point of the surface ($\partial\phi/\partial n = 0$). Once a solution for ϕ has been found for the boundary-value problem, the pressure coefficient at each point on the surface of the impermeable boundary can be computed using the incompressible pressure coefficient from equation (3.13):

$$C_p = 1 - \frac{U_t^2}{U_\infty^2} \tag{7.34}$$

You should note that the tangential velocity at the "surface" of a configuration in an inviscid flow is represented by the symbols U and U_t in equation (3.13) and equation (7.34), respectively.

Johnson (1980) noted further that Dirichlet boundary conditions (specification of ϕ) arise in connection with the inverse problem (i.e., that of solving for a specified pressure distribution on the surface of the configuration by varying the shape of the surface). The specification of ϕ guarantees a predetermined tangential velocity vector field and, therefore, a predetermined pressure coefficient distribution, as related through equation (7.34). However, the achievement of a desired pressure distribution on the surface is not physically significant without restrictions on the flux through the surface. To achieve both a specified pressure distribution and a normal flow distribution on the surface, the position of the surface must, in general, be perturbed, so that the surface will be a stream surface of the flow field. The total design problem is thus composed of two problems. The first is to find a perturbation potential for the surface that yields the desired distribution for the pressure coefficient and the second is to update the surface geometry so that it is a stream surface of the resultant flow. Johnson (1980) concluded, "The two problems are coupled and, in general, an iterative procedure is required for solution."

7.4.2 Solution Methods

The first step in a panel method is to divide the boundary surface into a number of panels. A finite set of control points (equal in number to the number of singularity parameters) is selected at which the boundary conditions are imposed. The construction of each network requires developments in three areas: (1) the definition of the surface geometry, (2) the definition of the singularity strengths, and (3) the selection of the control points and the specification of the boundary conditions.

Numerous computer codes using panel-method techniques have been developed since the 1960s [e.g., Hess and Smith (1962) or Bristow and Grose (1978)], the variations depending mainly on the choice of type and form of singularity distribution, the geometric layout of the elementary panels, and the type of boundary condition imposed. The choice of these parameters and their combinations is not a trivial matter. Although many different combinations are in principle mathematically equivalent, their numerical implementation may yield significantly different results from the point of view of numerical stability, computational economy, accuracy, and overall code robustness. Bristow and Grose (1978) note that there is an important equivalence between surface doublet distributions and vorticity distributions; a surface doublet distribution can be replaced by an equivalent surface vortex distribution. However, the theoretical equivalency between vorticity distributions and doublet distributions does not imply equivalent simplicity in a numerical formulation.

For each control point (and there is one control point per panel), the velocities induced at that control point by the singularities associated with each of the other panels of the configuration are summed, resulting in a set of linear algebraic equations that express the exact boundary condition of flow tangency on the surface. For many applications, the aerodynamic coefficients computed using panel methods are reasonably accurate. Bristow and Grose (1978) discuss some problems with the source panel class of methods when used on thin, highly loaded surfaces such as the aft portion of a

supercritical airfoil. In such cases, source strengths with strong gradients can degrade the local velocity calculations.

Margason et al. (1985) compare computed aerodynamic coefficients using one vortex lattice method (VLM, which will be discussed in the next section), one source panel method, two low-order surface potential distributions, and two high-order surface potential distributions. The computed values of C_L are presented as a function of α for a 45° swept-back and a 45° swept-forward wing in Figs. 7.24a and b, respectively. The five surface panel methods consistently overpredict the experimental data with little difference between the lift coefficients predicted by the various surface panel methods. As Margason et al. (1985) note, "The VLM predicts the experimental data very well, due to the fact that vortex lattice methods neglect both thickness and viscosity effects. For most cases, the effect of viscosity offsets the effect of thickness, fortuitously yielding good agreement between the VLM and experiment."

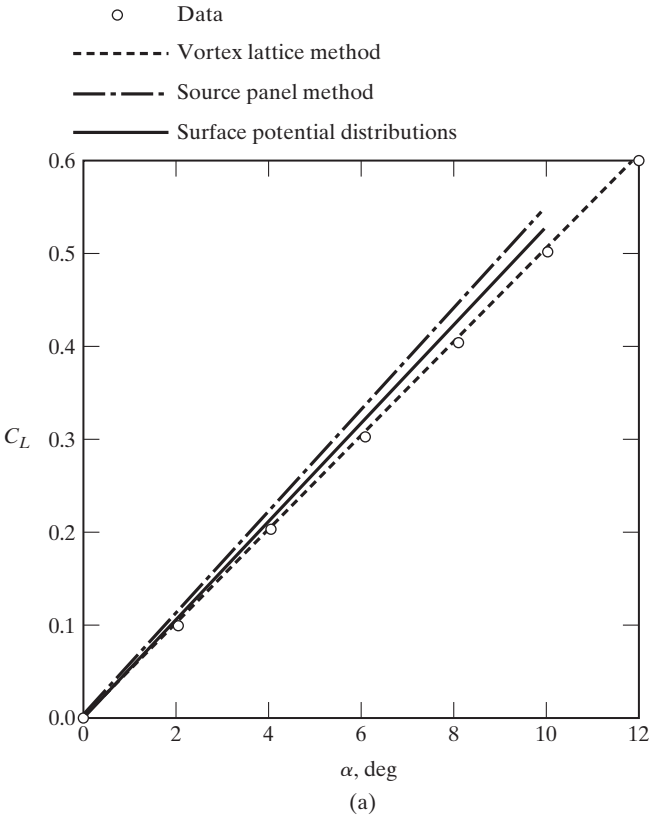

Figure 7.24 Comparison of the lift coefficient as a function of angle of attack: (a) $\Lambda_{c/4} = 45°$, NACA 64A010 section, $AR = 3.0$, $\lambda = 0.5$, aft swept wing [from Margason et al. (1985)].

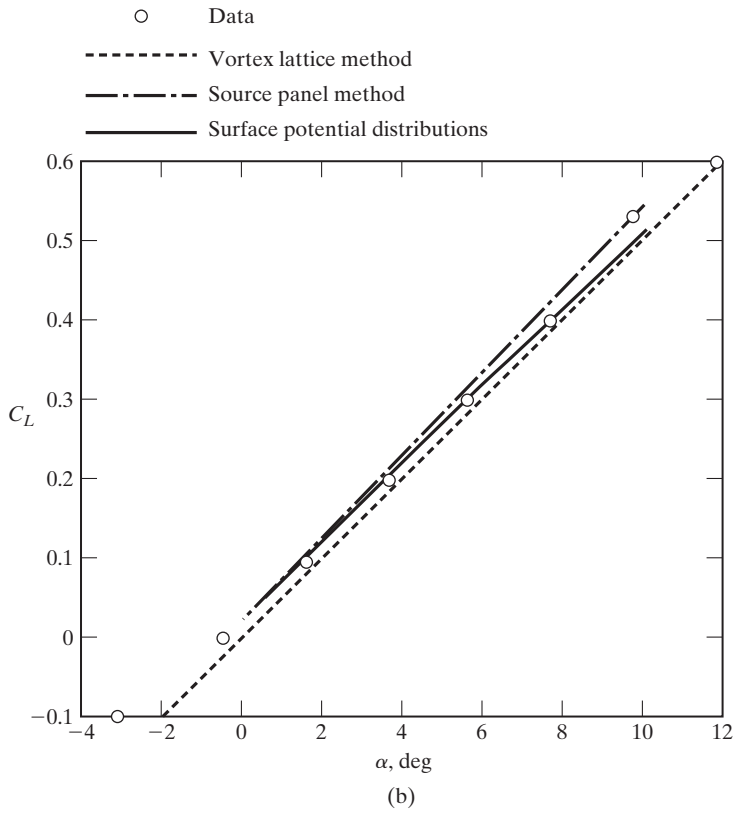

Figure 7.24 (b) $\Lambda_{c/4} = -45°$, NACA 64A112 section, $AR = 3.55$, $\lambda = 0.5$, forward swept wing [from Margason et al. (1985)].

7.5 VORTEX LATTICE METHOD

The vortex lattice method is the simplest of the methods reviewed by Margason et al. (1985). The VLM represents the wing as a surface on which a grid of horseshoe vortices (from lifting-line theory) is superimposed. The velocities induced by each horseshoe vortex at a specified control point are calculated using the Biot-Savart law. A summation is performed for all control points on the wing to produce a set of linear algebraic equations for the horseshoe vortex strengths that satisfy the boundary condition of no flow through the wing. The vortex strengths are related to the wing circulation and the pressure differential between the upper and lower wing surfaces. The pressure differentials are integrated to yield the total forces and moments.

In our approach to solving the governing equation, the continuous distribution of bound vorticity over the wing surface is approximated by a finite number of discrete horseshoe vortices, as shown in Fig. 7.25. The individual horseshoe vortices are placed in trapezoidal panels (also called *finite elements* or *lattices*). This procedure for obtaining a numerical solution to the flow is termed the vortex lattice method.

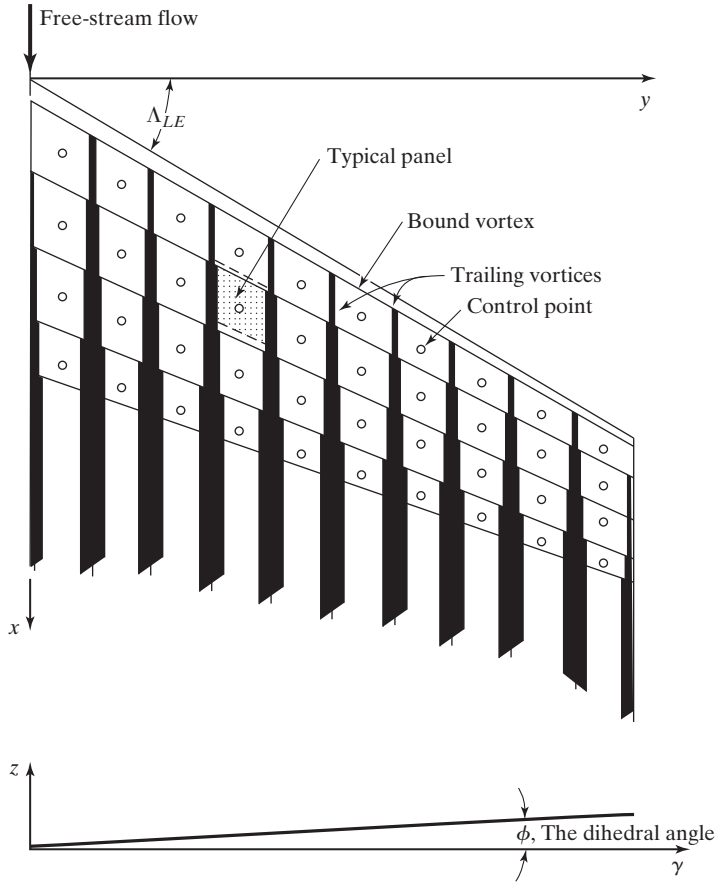

Figure 7.25 Coordinate system, elemental panels, and horseshoe vortices for a typical wing planform in the vortex lattice method.

The bound vortex typically coincides with the quarter-chord line of the panel (or element) and is, therefore, aligned with the local sweepback angle. In a rigorous theoretical analysis, the vortex lattice panels are located on the mean camber surface of the wing and, when the trailing vortices leave the wing, they follow a curved path. However, for many engineering applications, suitable accuracy can be obtained using linearized theory in which straight-line trailing vortices extend downstream to infinity. In the linearized approach, the trailing vortices are aligned either parallel to the free stream or parallel to the vehicle axis. Both orientations provide similar accuracy within the assumptions of linearized theory. We will assume that the trailing vortices are parallel to the axis of the vehicle, as shown in Fig. 7.26. This orientation of the trailing vortices is chosen because the computation of the influences of the various vortices (which we will call the *influence coefficients*) is simpler. Furthermore, these geometric coefficients do not change as the angle of attack is changed. Application of the boundary condition that the flow is tangent to the wing surface at "the" control point of each of

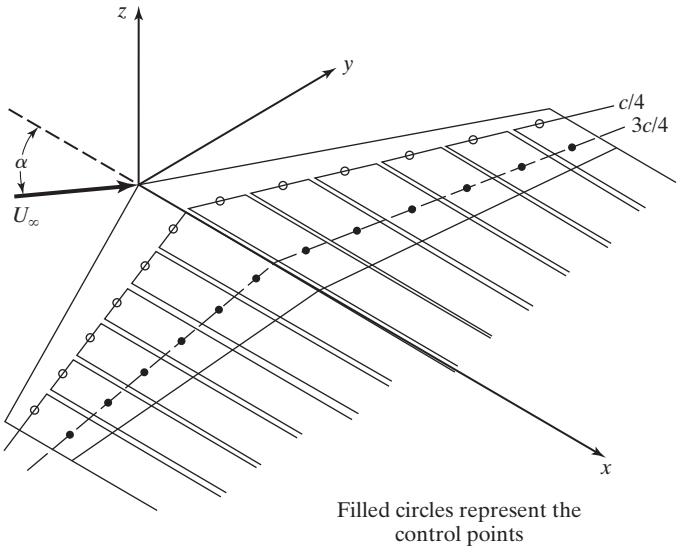

Figure 7.26 Distributed horseshoe vortices representing the lifting flow field over a swept wing.

the $2N$ panels (i.e., there is no flow through the surface) provides a set of simultaneous equations in terms of the unknown vortex circulation strengths. The control point of each panel is centered spanwise on the three-quarter-chord line midway between the trailing-vortex legs.

An indication of why the three-quarter-chord location is used as the control point may be seen by referring to Fig. 7.27. A vortex filament whose strength Γ represents the lifting character of the section is placed at the quarter-chord location. The filament induces a velocity,

$$U = \frac{\Gamma}{2\pi r}$$

at the point c, the control point which is a distance r from the vortex filament. If the flow is to be parallel to the surface at the control point, the incidence of the surface relative to the free stream is given by:

$$\alpha \approx \sin\alpha = \frac{U}{U_\infty} = \frac{\Gamma}{2\pi r U_\infty}$$

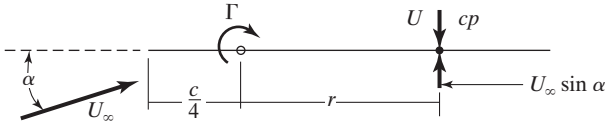

Figure 7.27 Planar airfoil section indicating location of control point where flow is parallel to the surface.

But, as we discussed for equations (6.11) and (6.12),

$$l = \tfrac{1}{2}\rho_\infty U_\infty^2\, c 2\pi\alpha = \rho_\infty U_\infty \Gamma$$

Combining the preceding relations gives us:

$$\pi\rho_\infty U_\infty^2 c \frac{\Gamma}{2\pi r U_\infty} = \rho_\infty U_\infty \Gamma$$

and solving for r yields:

$$r = \frac{c}{2}$$

Therefore, we see that the control point is at the three-quarter-chord location for this two-dimensional geometry. The use of the chordwise slope at the 0.75-chord location to define the effective incidence of a panel in a finite-span wing has long been in use [e.g., Falkner (1943) and Kalman et al. (1971)].

Consider the flow over the swept wing that is shown in Fig. 7.26. Notice that the bound-vortex filaments for the port (or left-hand) wing are not parallel to the bound-vortex filaments for the starboard (or right-hand) wing. Thus, for a lifting swept wing, the bound-vortex system on one side of the wing produces downwash on the other side of the wing. This downwash reduces the net lift and increases the total induced drag produced by the flow over the finite-span wing. The downwash resulting from the bound-vortex system is greatest near the center of the wing, while the downwash resulting from the trailing-vortex system is greatest near the wing tips. So, for a swept wing the lift is reduced both near the center and near the tips of the wing. This will be evident in the spanwise lift distribution presented for the wing of Example 7.4.

7.5.1 Velocity Induced by a General Horseshoe Vortex

The velocity induced by a vortex filament of strength Γ_n and a length of dl is given by the *Biot-Savart law* [see Robinson and Laurmann (1956)]:

$$\vec{dV} = \frac{\Gamma_n(\vec{dl} \times \vec{r})}{4\pi r^3} \tag{7.35}$$

Referring to the sketch of Fig. 7.28, the magnitude of the induced velocity is:

$$dV = \frac{\Gamma_n \sin\theta\, dl}{4\pi r^2} \tag{7.36}$$

Since we are interested in the flow field induced by a horseshoe vortex which consists of three straight segments, we can use equation (7.35) to calculate the effect of each segment separately. Let AB be such a segment, with the vorticity vector directed from A to B. Let C be a point in space whose normal distance from the line AB is r_p. We can integrate between A and B to find the magnitude of the induced velocity:

$$V = \frac{\Gamma_n}{4\pi r_p}\int_{\theta_1}^{\theta_2} \sin\theta\, d\theta = \frac{\Gamma_n}{4\pi r_p}(\cos\theta_1 - \cos\theta_2) \tag{7.37}$$

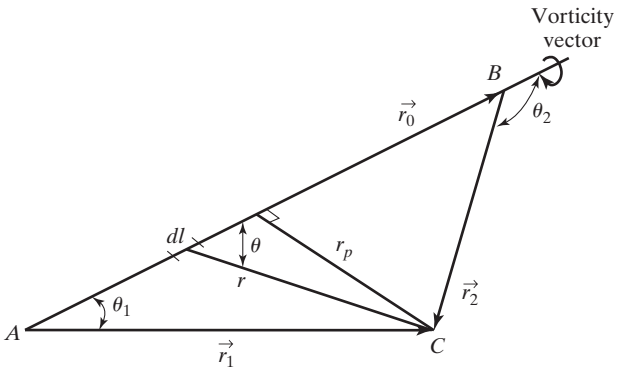

Figure 7.28 Nomenclature for calculating the velocity induced by a finite-length vortex segment.

Notice that, if the vortex filament extends to infinity in both directions, then $\theta_1 = 0$ and $\theta_2 = \pi$, and

$$V = \frac{\Gamma_n}{2\pi r_p}$$

which is the result used in Chapter 6 for the infinite-span airfoils. Let $\vec{r}_0$, $\vec{r}_1$, and $\vec{r}_2$ designate the vectors $\overrightarrow{AB}$, $\overrightarrow{AC}$, and $\overrightarrow{BC}$, respectively, as shown in Fig. 7.28. Then

$$r_p = \frac{|\vec{r}_1 \times \vec{r}_2|}{r_0} \qquad \cos\theta_1 = \frac{\vec{r}_0 \cdot \vec{r}_1}{r_0 r_1} \qquad \cos\theta_2 = \frac{\vec{r}_0 \cdot \vec{r}_2}{r_0 r_2}$$

In these equations, if a vector quantity (such as $\vec{r}_0$) is written without a superscript arrow, the symbol represents the magnitude of the parameter. Thus, r_0 is the magnitude of the vector $\vec{r}_0$. Also note that $|\vec{r}_1 \times \vec{r}_2|$ represents the magnitude of the vector cross product. Substituting these expressions into equation (7.37) and noting that the direction of the induced velocity is given by the unit vector:

$$\frac{\vec{r}_1 \times \vec{r}_2}{|\vec{r}_1 \times \vec{r}_2|}$$

yields

$$\vec{V} = \frac{\Gamma_n}{4\pi} \frac{\vec{r}_1 \times \vec{r}_2}{|\vec{r}_1 \times \vec{r}_2|^2} \left[\vec{r}_0 \cdot \left(\frac{\vec{r}_1}{r_1} - \frac{\vec{r}_2}{r_2} \right) \right] \tag{7.38}$$

This is the basic expression for the calculation of the induced velocity by the horseshoe vortices in the VLM. It can be used regardless of the assumed orientation of the vortices.

We will now use equation (7.38) to calculate the velocity that is induced at a general point in space (x, y, z) by the horseshoe vortex shown in Fig. 7.29. The horseshoe vortex may be assumed to represent a typical wing panel (e.g., the nth panel) in Fig. 7.25. Segment AB represents the bound vortex portion of the horseshoe system and coincides with the quarter-chord line of the panel element and the trailing vortices are parallel to the x axis. The resultant induced velocity vector will be calculated by considering the influence of each of the elements.

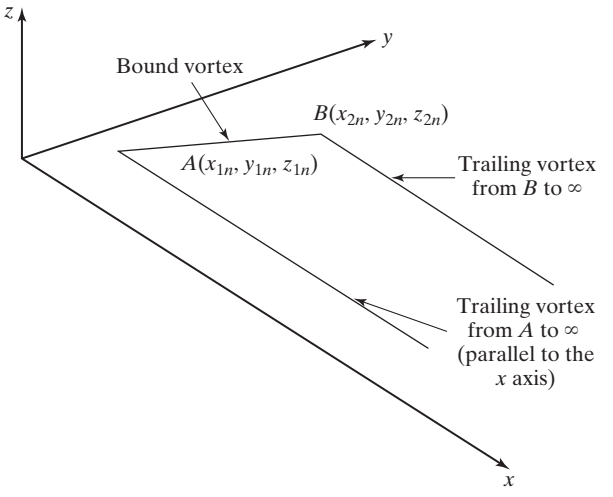

Figure 7.29 "Typical" horseshoe vortex.

For the bound vortex, segment $\overrightarrow{AB}$,

$$\vec{r}_0 = \overrightarrow{AB} = (x_{2n} - x_{1n})\hat{i} + (y_{2n} - y_{1n})\hat{j} + (z_{2n} - z_{1n})\hat{k}$$
$$\hat{r}_1 = (x - x_{1n})\hat{i} + (y - y_{1n})\hat{j} + (z - z_{1n})\hat{k}$$
$$\hat{r}_2 = (x - x_{2n})\hat{i} + (y - y_{2n})\hat{j} + (z - z_{2n})\hat{k}$$

Now, we will use equation (7.38) to calculate the velocity induced at some point $C(x, y, z)$ by the vortex filament AB (shown in Figs. 7.29 and 7.30),

$$\vec{V}_{AB} = \frac{\Gamma_n}{4\pi}\{\text{Fac1}_{AB}\}\{\text{Fac2}_{AB}\} \qquad \textbf{(7.39a)}$$

where

$$\begin{aligned}\{\text{Fac1}_{AB}\} &= \frac{\vec{r}_1 \times \vec{r}_2}{|\vec{r}_1 \times \vec{r}_2|^2} \\ &= \{[(y - y_{1n})(z - z_{2n}) - (y - y_{2n})(z - z_{1n})]\hat{i} \\ &\quad - [(x - x_{1n})(z - z_{2n}) - (x - x_{2n})(z - z_{1n})]\hat{j} \\ &\quad + [(x - x_{1n})(y - y_{2n}) - (x - x_{2n})(y - y_{1n})]\hat{k}\}/ \\ &\quad \{[(y - y_{1n})(z - z_{2n}) - (y - y_{2n})(z - z_{1n})]^2 \\ &\quad + [(x - x_{1n})(z - z_{2n}) - (x - x_{2n})(z - z_{1n})]^2 \\ &\quad + [(x - x_{1n})(y - y_{2n}) - (x - x_{2n})(y - y_{1n})]^2\}\end{aligned}$$

and

$$\begin{aligned}\{\text{Fac2}_{AB}\} &= \left(\vec{r}_0 \cdot \frac{\vec{r}_1}{r_1} - \vec{r}_0 \cdot \frac{\vec{r}_2}{r_2}\right) \\ &= \{[(x_{2n} - x_{1n})(x - x_{1n}) + (y_{2n} - y_{1n})(y - y_{1n}) + (z_{2n} - z_{1n})(z - z_{1n})]/ \\ &\quad \sqrt{(x - x_{1n})^2 + (y - y_{1n})^2 + (z - z_{1n})^2}\end{aligned}$$

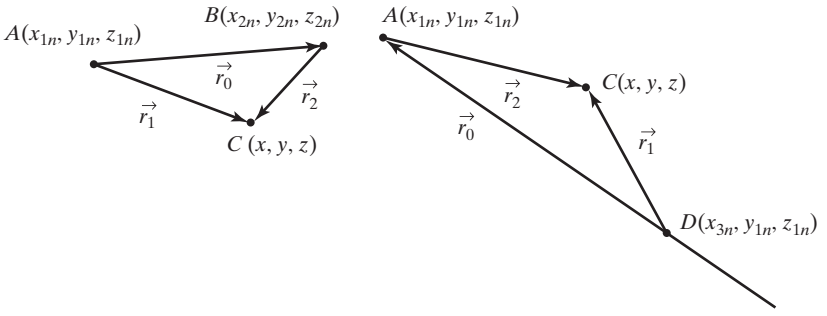

Figure 7.30 Vector elements for the calculation of the induced velocities.

$$-\left[(x_{2n}-x_{1n})(x-x_{2n})+(y_{2n}-y_{1n})(y-y_{2n})+(z_{2n}-z_{1n})(z-z_{2n})\right]/\sqrt{\{(x-x_{2n})^2+(y-y_{2n})^2+(z-z_{2n})^2\}}$$

To calculate the velocity induced by the filament that extends from A to ∞, we will first calculate the velocity induced by the collinear, finite-length filament that extends from A to D. Since $\vec{r}_0$ is in the direction of the vorticity vector,

$$\vec{r}_0 = \overrightarrow{DA} = (x_{1n} - x_{3n})\,\hat{i}$$
$$\vec{r}_1 = (x - x_{3n})\,\hat{i} + (y - y_{1n})\,\hat{j} + (z - z_{1n})\hat{k}$$
$$\vec{r}_2 = (x - x_{1n})\,\hat{i} + (y - y_{1n})\,\hat{j} + (z - z_{1n})\hat{k}$$

as shown in Fig. 7.30. So, the induced velocity is:

$$\overrightarrow{V_{AD}} = \frac{\Gamma_n}{4\pi}\{\mathrm{Fac1}_{AD}\}\,\{\mathrm{Fac2}_{AD}\}$$

where

$$\{\mathrm{Fac1}_{AD}\} = \frac{(z - z_{1n})\,\hat{j} + (y_{1n} - y)\hat{k}}{[\,(z - z_{1n})^2 + (y_{1n} - y)^2\,](x_{3n} - x_{1n})}$$

and

$$\{\mathrm{Fac2}_{AD}\} = (x_{3n} - x_{1n})\left\{\frac{x_{3n} - x}{\sqrt{(x - x_{3n})^2 + (y - y_{1n})^2 + (z - z_{1n})^2}} + \frac{x - x_{1n}}{\sqrt{(x - x_{1n})^2 + (y - y_{1n})^2 + (z - z_{1n})^2}}\right\}$$

Letting x_3 go to ∞, the first term of $\{\mathrm{Fac2}_{AD}\}$ goes to 1.0. Therefore, the velocity induced by the vortex filament which extends from A to ∞ in a positive direction parallel to the x axis is given by:

$$\overrightarrow{V_{A\infty}} = \frac{\Gamma_n}{4\pi}\left\{\frac{(z - z_{1n})\,\hat{j} + (y_{1n} - y)\hat{k}}{[\,(z - z_{1n})^2 + (y_{1n} - y)^2\,]}\right\}\left[1.0 + \frac{x - x_{1n}}{\sqrt{(x - x_{1n})^2 + (y - y_{1n})^2 + (z - z_{1n})^2}}\right] \quad \textbf{(7.39b)}$$

Similarly, the velocity induced by the vortex filament that extends from B to ∞ in a positive direction parallel to the x axis is given by:

$$\overrightarrow{V_{B\infty}} = -\frac{\Gamma_n}{4\pi}\left\{\frac{(z - z_{2n})\hat{j} + (y_{2n} - y)\hat{k}}{[(z - z_{2n})^2 + (y_{2n} - y)^2]}\right\} \left[1.0 + \frac{x - x_{2n}}{\sqrt{(x - x_{2n})^2 + (y - y_{2n})^2 + (z - z_{2n})^2}}\right] \quad \textbf{(7.39c)}$$

The total velocity induced at some point (x, y, z) by the horseshoe vortex representing one of the surface elements (i.e., that for the nth panel) is the sum of the components given in equation (7.39). Let the point (x, y, z) be the control point of the mth panel, which we will designate by the coordinates (x_m, y_m, z_m). The velocity induced at the mth control point by the vortex representing the nth panel will be designated as $\overrightarrow{V_{m,n}}$. Examining equation (7.39), we see that

$$\overrightarrow{V_{m,n}} = \overrightarrow{C_{m,n}}\,\Gamma_n \quad \textbf{(7.40)}$$

where the influence coefficient $\overrightarrow{C_{m,n}}$ depends on the geometry of the nth horseshoe vortex and its distance from the control point of the mth panel. Since the governing equation is linear, the velocities induced by the $2N$ vortices are added together to obtain an expression for the total induced velocity at the mth control point:

$$\overrightarrow{V_m} = \sum_{n=1}^{2N} \overrightarrow{C_{m,n}}\,\Gamma_n \quad \textbf{(7.41)}$$

We will have $2N$ of these equations, one for each of the control points.

7.5.2 Application of the Boundary Conditions

It will be possible to determine the resultant induced velocity at any point in space if the strengths of the $2N$ horseshoe vortices are known. However, their strengths are not known a priori. To compute the strengths of the vortices, Γ_n, which represent the lifting flow field of the wing, we use the boundary condition that the surface is a streamline. That is, the resultant flow is tangent to the wing at each and every control point (which is located at the midspan of the three-quarter-chord line of each elemental panel). If the flow is tangent to the wing, the component of the induced velocity normal to the wing at the control point balances the normal component of the free-stream velocity. To evaluate the induced velocity components, we must introduce at this point our convention that the trailing vortices are parallel to the vehicle axis [i.e., the x axis for equation (7.39) is the vehicle axis]. Referring to Fig. 7.31, the tangency requirement yields the relation

$$-u_m \sin\delta\cos\phi - v_m \cos\delta\sin\phi + w_m \cos\phi\cos\delta + U_\infty \sin(\alpha - \delta)\cos\phi = 0 \quad \textbf{(7.42)}$$

where ϕ is the dihedral angle, as shown in Fig. 7.25, and δ is the slope of the mean camber line at the control point, which is given by

$$\delta = \tan^{-1}\left(\frac{dz}{dx}\right)_m$$

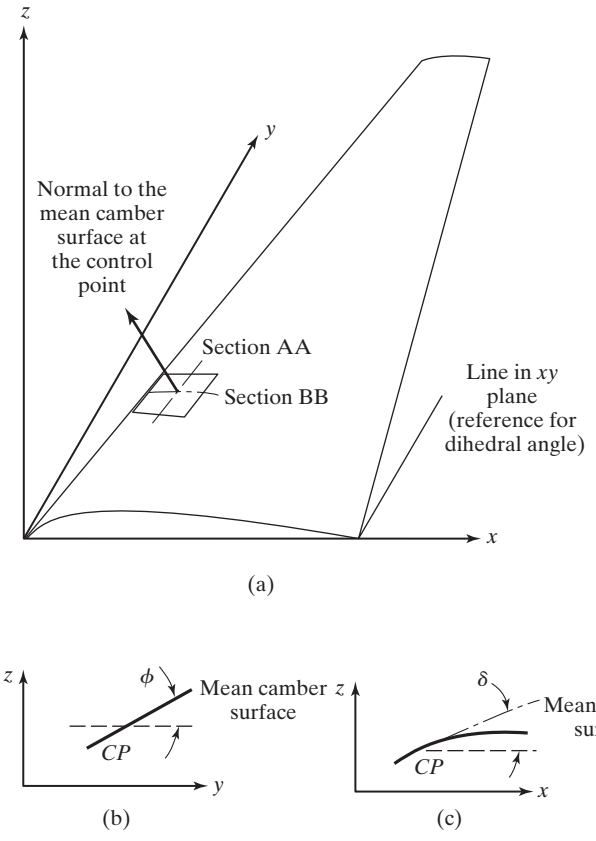

Figure 7.31 Nomenclature for the tangency requirement: (a) normal to element of the mean camber surface; (b) section AA; (c) section BB.

For wings where the slope of the mean camber line is small and which are at small angles of attack, equation (7.42) can be replaced by the approximation:

$$w_m - v_m \tan\phi + U_\infty \left[\alpha - \left(\frac{dz}{dx} \right)_m \right] = 0 \qquad \textbf{(7.43)}$$

This approximation is consistent with the assumptions of linearized theory. The unknown circulation strengths (Γ_n) required to satisfy these tangent flow boundary conditions are determined by solving the system of simultaneous equations represented by equation (7.41). The solution involves the inversion of a matrix.

7.5.3 Relations for a Planar Wing

Relations for the VLM where the trailing vortices are parallel to the x axis are given in equations (7.39) through (7.43), and can be solved to determine the lifting flow for a twisted wing with dihedral. We will apply these equations to a relatively simple geometry, a planar wing (i.e., one that lies in the xy plane), so that we can learn the significance of the various operations using a geometry which we can readily visualize.

For a planar wing, $z_{1n} = z_{2n} = 0$ for all the bound vortices. Furthermore, $z_m = 0$ for all the control points. So, for our planar wing,

$$\overrightarrow{V_{AB}} = \frac{\Gamma_n}{4\pi} \frac{\hat{k}}{(x_m - x_{1n})(y_m - y_{2n}) - (x_m - x_{2n})(y_m - y_{1n})} \left[\frac{(x_{2n} - x_{1n})(x_m - x_{1n}) + (y_{2n} - y_{1n})(y_m - y_{1n})}{\sqrt{(x_m - x_{1n})^2 + (y_m - y_{1n})^2}} - \frac{(x_{2n} - x_{1n})(x_m - x_{2n}) + (y_{2n} - y_{1n})(y_m - y_{2n})}{\sqrt{(x_m - x_{2n})^2 + (y_m - y_{2n})^2}} \right] \tag{7.44a}$$

$$\overrightarrow{V_{A\infty}} = \frac{\Gamma_n}{4\pi} \frac{\hat{k}}{y_{1n} - y_m} \left[1 + \frac{x_m - x_{1n}}{\sqrt{(x_m - x_{1n})^2 + (y_m - y_{1n})^2}} \right] \tag{7.44b}$$

$$\overrightarrow{V_{A\infty}} = \frac{\Gamma_n}{4\pi} \frac{\hat{k}}{y_{2n} - y_m} \left[1 + \frac{x_m - x_{2n}}{\sqrt{(x_m - x_{2n})^2 + (y_m - y_{2n})^2}} \right] \tag{7.44c}$$

Notice that for a planar wing, all three components of the vortex representing the nth panel induce a velocity at the control point of the mth panel which is in the z direction (i.e., a downwash). Therefore, we can simplify equation (7.44) by combining the components into one expression:

$$w_{m,n} = \frac{\Gamma_n}{4\pi} \left\{ \frac{1}{(x_m - x_{1n})(y_m - y_{2n}) - (x_m - x_{2n})(y_m - y_{1n})} \left[\frac{(x_{2n} - x_{1n})(x_m - x_{1n}) + (y_{2n} - y_{1n})(y_m - y_{1n})}{\sqrt{(x_m - x_{1n})^2 + (y_m - y_{1n})^2}} - \frac{(x_{2n} - x_{1n})(x_m - x_{2n}) + (y_{2n} - y_{1n})(y_m - y_{2n})}{\sqrt{(x_m - x_{2n})^2 + (y_m - y_{2n})^2}} \right] + \frac{1}{y_{1n} - y_m} \left[1 + \frac{x_m - x_{1n}}{\sqrt{(x_m - x_{1n})^2 + (y_m - y_{1n})^2}} \right] - \frac{1}{y_{2n} - y_m} \left[1 + \frac{x_m - x_{2n}}{\sqrt{(x_m - x_{2n})^2 + (y_m - y_{2n})^2}} \right] \right\} \tag{7.45}$$

Summing the contributions of all the vortices to the downwash at the control point of the mth panel, we obtain:

$$w_m = \sum_{n=1}^{2N} w_{m,n} \tag{7.46}$$

Now we can apply the tangency requirement defined by equations (7.42) and (7.43). Since we are considering a planar wing in this section, $(dz/dx)_m = 0$ everywhere and $\phi = 0$. The component of the free-stream velocity perpendicular to the wing is $U_\infty \sin\alpha$ at any point on the wing. So, the resultant flow will be tangent to the wing if the total vortex-induced downwash at the control point of the mth panel, which is calculated using equation (7.46) balances the normal component of the free-stream velocity:

$$w_m + U_\infty \sin\alpha = 0 \tag{7.47}$$

For small angles of attack $\sin\alpha \approx \alpha$ in radians, and:

$$w_m = -U_\infty \alpha \tag{7.48}$$

In Example 7.4, we will solve for the aerodynamic coefficients for a wing that has a relatively simple planform and an uncambered section. The vortex lattice method will be applied using only a single lattice element in the chordwise direction for each spanwise subdivision of the wing. Applying the boundary condition that there is no flow through the wing at only one point in the chordwise direction is reasonable for this flat-plate wing. However, it would not be adequate for a wing with cambered sections or a wing with deflected flaps.

EXAMPLE 7.4: Use the vortex lattice method (VLM) to calculate the aerodynamic coefficients for a swept wing

We will use the relations developed in this section to calculate the lift coefficient for a swept wing. So that the calculation procedures can be easily followed, we will consider a wing that has a relatively simple geometry (i.e., that illustrated in Fig. 7.32). The wing has an aspect ratio of 5, a taper ratio of unity (i.e., $c_r = c_t$), and an uncambered section (i.e., it is a flat plate). Since the taper ratio is unity, the leading edge, the quarter-chord line, the three-quarter-chord line, and the trailing edge all have the same sweep, 45°. Since

$$AR = 5 = \frac{b^2}{S}$$

and since for an untapered wing:

$$S = bc$$

we can find the span to be $b = 5c$. Using this relation, it is possible to calculate all of the necessary coordinates in terms of the parameter b. Therefore, the solution does not require that we know the physical dimensions of the configuration, just the planform of the wing.

Solution: The flow field under consideration is symmetric with respect to the $y = 0$ plane (xz plane) since there is no yaw. The lift force acting at a point on the starboard wing $(+y)$ is equal to that at the corresponding point on the port wing $(-y)$. Because of symmetry, we need only to solve for the strengths of the vortices of the starboard wing. Furthermore, we need to apply the tangency condition [i.e., equation (7.48)] only at the control points of the starboard wing. However, we must remember to include the contributions of the horseshoe vortices of the port wing to the velocities induced at these control points (of the starboard wing). So, for this planar symmetric flow, equation (7.46) becomes:

$$w_m = \sum_{n=1}^{N} w_{m,ns} + \sum_{n=1}^{N} w_{m,np}$$

where the symbols s and p represent the starboard and port wings, respectively.

The planform of the starboard wing is divided into four panels, with each panel extending from the leading edge to the trailing edge. By limiting

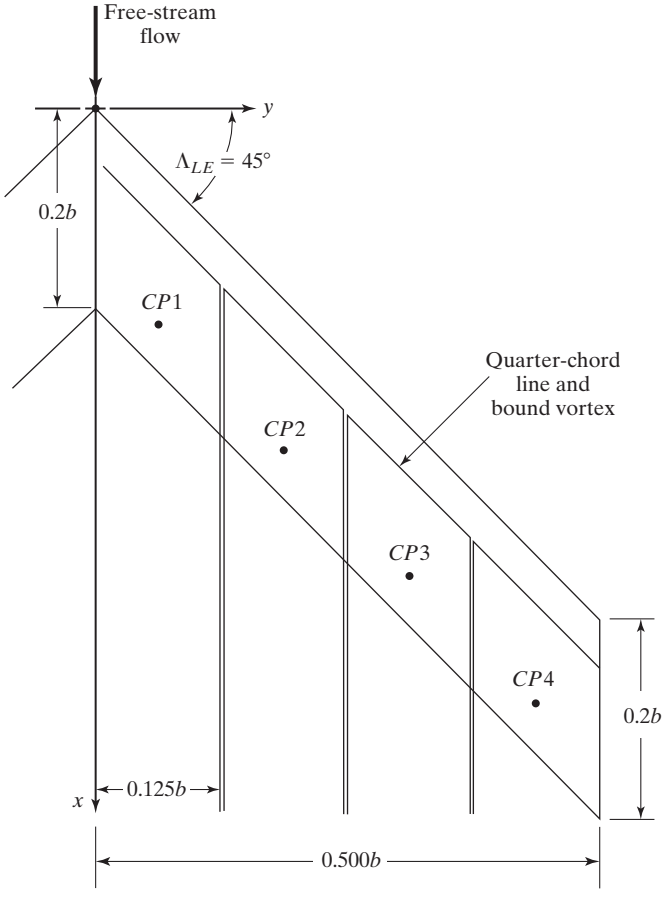

Figure 7.32 Four-panel representation of a swept planar wing, taper ratio of unity, AR = 5, $\Lambda = 45°$.

ourselves to only four spanwise panels, we can calculate the strength of the horseshoe vortices using only a calculator or desktop computer. Therefore, we can more easily see how the terms are to be evaluated. As before, the bound portion of each horseshoe vortex coincides with the quarter-chord line of its panel and the trailing vortices are in the plane of the wing, parallel to the x axis. The control points are designated by the solid symbols in Fig. 7.32. Recall that $(x_m, y_m, 0)$ are the coordinates of a given control point and that $(x_{1n}, y_{1n}, 0)$ and $(x_{2n}, y_{2n}, 0)$ are the coordinates of the "ends" of the bound-vortex filament AB. The coordinates for a 4×1 lattice (four spanwise divisions and one chordwise division) for the starboard (right) wing are summarized in Table 7.2.

Using equation (7.45) to calculate the downwash velocity at the CP of panel 1 (of the starboard wing) induced by the horseshoe vortex of panel 1 of the starboard wing,

$$w_{1,1s} = \frac{\Gamma_1}{4\pi}\left\{\frac{1.0}{(0.1625b)(-0.0625b) - (0.0375b)(0.0625b)}\right.$$
$$\left[\frac{(0.1250b)(0.1625b) + (0.1250b)(0.0625b)}{\sqrt{(0.1625b)^2 + (0.0625b)^2}}\right.$$

$$
\begin{aligned}
&- \frac{(0.1250b)(0.0375b) + (0.1250b)(-0.0625b)}{\sqrt{(0.0375b)^2 + (-0.0625b)^2}}\Bigg] \\
&+ \frac{1.0}{-0.0625b}\left[1.0 + \frac{0.1625b}{\sqrt{(0.1625b)^2 + (0.0625b)^2}}\right] \\
&- \frac{1.0}{0.0625b}\left[1.0 + \frac{0.0375b}{\sqrt{(0.0375b)^2 + (-0.0625b)^2}}\right]\Bigg\} \\
&= \frac{\Gamma_1}{4\pi b}(-16.3533 - 30.9335 - 24.2319)
\end{aligned}
$$

TABLE 7.2 Coordinates of the Bound Vortices and of the Control Points of the Starboard (Right) Wing

Panel	x_m	y_m	x_{1n}	y_{1n}	x_{2n}	y_{2n}
1	0.2125*b*	0.0625*b*	0.0500*b*	0.0000*b*	0.1750*b*	0.1250*b*
2	0.3375*b*	0.1875*b*	0.1750*b*	0.1250*b*	0.3000*b*	0.2500*b*
3	0.4625*b*	0.3125*b*	0.3000*b*	0.2500*b*	0.4250*b*	0.3750*b*
4	0.5875*b*	0.4375*b*	0.4250*b*	0.3750*b*	0.5500*b*	0.5000*b*

Notice that, as you might expect, each of the vortex elements induces a negative (downward) component of velocity at the control point. You should visualize the flow induced by each segment of the horseshoe vortex to verify that a negative value for each of the components is intuitively correct. In addition, the velocity induced by the vortex trailing from A to ∞ is greatest in magnitude. Adding the components together, we find:

$$w_{1,1s} = \frac{\Gamma_1}{4\pi b}(-71.5187)$$

The downwash velocity at the CP of panel 1 (of the starboard wing) induced by the horseshoe vortex of panel 1 of the port wing is:

$$
\begin{aligned}
w_{1,1p} = \frac{\Gamma_1}{4\pi}\Bigg\{&\frac{1.0}{(0.0375b)(0.0625b) - (0.1625b)(0.1875b)} \\
&\left[\frac{(-0.1250b)(0.0375b) + (0.1250b)(0.1875b)}{\sqrt{(0.0375b)^2 + (0.1875b)^2}}\right. \\
&\left. - \frac{(-0.1250b)(0.1625b) + (0.1250b)(0.0625b)}{\sqrt{(0.1625b)^2 + (0.0625b)^2}}\right] \\
&+ \frac{1.0}{-0.1875b}\left[1.0 + \frac{0.0375b}{\sqrt{(0.0375b)^2 + (0.1875b)^2}}\right] \\
&- \frac{1.0}{-0.0625b}\left[1.0 + \frac{0.1625b}{\sqrt{(0.1625b)^2 + (0.0625b)^2}}\right]\Bigg\}
\end{aligned}
$$

$$= \frac{\Gamma_1}{4\pi b}[-6.0392 - 6.3793 + 30.9335]$$

$$= \frac{\Gamma_1}{4\pi b}(18.5150)$$

Similarly, using equation (7.45) to calculate the downwash velocity at the CP of panel 2 induced by the horseshoe vortex of panel 4 of the starboard wing, we obtain

$$w_{2,4s} = \frac{\Gamma_4}{4\pi}\left\{\frac{1.0}{(-0.0875b)(-0.3125b) - (-0.2125b)(-0.1875b)}\right.$$
$$\left[\frac{(0.1250b)(-0.0875b) + (0.1250b)(-0.1875b)}{\sqrt{(-0.0875b)^2 + (-0.1875b)^2}}\right.$$
$$\left.\left. - \frac{(0.1250b)(-0.2125b) + (0.1250b)(-0.3125b)}{\sqrt{(-0.2125b)^2 + (-0.3125b)^2}}\right]\right.$$
$$+ \frac{1.0}{0.1875b}\left[1.0 + \frac{-0.0875b}{\sqrt{(-0.0875b)^2 + (-0.1875b)^2}}\right]$$
$$\left. - \frac{1.0}{0.3125b}\left[1.0 + \frac{-0.2125b}{\sqrt{(-0.2125b)^2 + (-0.3125b)^2}}\right]\right\}$$
$$= \frac{\Gamma_4}{4\pi b}[-0.60167 + 3.07795 - 1.40061]$$

$$= \frac{\Gamma_4}{4\pi b}(1.0757)$$

Again, you should visualize the flow induced by each segment to verify that the signs and the relative magnitudes of the components are individually correct.

Evaluating all of the various components (or influence coefficients), we find that at control point 1 the downwash is:

$$w_1 = \frac{1}{4\pi b}[(-71.5187\Gamma_1 + 11.2933\Gamma_2 + 1.0757\Gamma_3 + 0.3775\Gamma_4)_s$$
$$+ (+18.5150\Gamma_1 + 2.0504\Gamma_2 + 0.5887\Gamma_3 + 0.2659\Gamma_4)_p]$$

At CP 2,

$$w_2 = \frac{1}{4\pi b}[(+20.2174\Gamma_1 - 71.5187\Gamma_2 + 11.2933\Gamma_3 + 1.0757\Gamma_4)_s$$
$$+ (+3.6144\Gamma_1 + 1.1742\Gamma_2 + 0.4903\Gamma_3 + 0.2503\Gamma_4)_p]$$

At CP 3,

$$w_3 = \frac{1}{4\pi b}[(+3.8792\Gamma_1 + 20.2174\Gamma_2 - 71.5187\Gamma_3 + 11.2933\Gamma_4)_s$$
$$+ (+1.5480\Gamma_1 + 0.7227\Gamma_2 + 0.3776\Gamma_3 + 0.2179\Gamma_4)_p]$$

At CP 4,

$$w_4 = \frac{1}{4\pi b}[(+1.6334\Gamma_1 + 3.8792\Gamma_2 + 20.2174\Gamma_3 - 71.5187\Gamma_4)_s + (+0.8609\Gamma_1 + 0.4834\Gamma_2 + 0.2895\Gamma_3 + 0.1836\Gamma_4)_p$$

Since the wing is planar with no dihedral, the no-flow-through condition of equation (7.48) requires that:

$$w_1 = w_2 = w_3 = w_4 = -U_\infty \alpha$$

Therefore:

$$\begin{aligned}
-53.0037\Gamma_1 + 13.3437\Gamma_2 + 1.6644\Gamma_3 + 0.6434\Gamma_4 &= -4\pi b U_\infty \alpha \\
+23.8318\Gamma_1 - 70.3445\Gamma_2 + 11.7836\Gamma_3 + 1.3260\Gamma_4 &= -4\pi b U_\infty \alpha \\
+5.4272\Gamma_1 + 20.9401\Gamma_2 - 71.1411\Gamma_3 + 11.5112\Gamma_4 &= -4\pi b U_\infty \alpha \\
+2.4943\Gamma_1 + 4.3626\Gamma_2 + 20.5069\Gamma_3 - 71.3351\Gamma_4 &= -4\pi b U_\infty \alpha
\end{aligned}$$

which is four equations in four unknowns. Solving for Γ_1, Γ_2, Γ_3, and Γ_4, we find that:

$$\Gamma_1 = +0.0273(4\pi b U_\infty \alpha) \quad \textbf{(7.49a)}$$

$$\Gamma_2 = +0.0287(4\pi b U_\infty \alpha) \quad \textbf{(7.49b)}$$

$$\Gamma_3 = +0.0286(4\pi b U_\infty \alpha) \quad \textbf{(7.49c)}$$

$$\Gamma_4 = +0.0250(4\pi b U_\infty \alpha) \quad \textbf{(7.49d)}$$

Having determined the strength of each of the vortices by satisfying the boundary conditions that the flow is tangent to the surface at each of the control points, the lift of the wing may be calculated. For wings that have no dihedral over any portion of the wing, all the lift is generated by the free-stream velocity crossing the spanwise vortex filament, since there are no sidewash or backwash velocities. Furthermore, since the panels extend from the leading edge to the trailing edge, the lift acting on the nth panel is:

$$l_n = \rho_\infty U_\infty \Gamma_n \quad \textbf{(7.50)}$$

which is also the lift per unit span. Since the flow is symmetric, the total lift for the wing is:

$$L = 2\int_0^{b/2} \rho_\infty U_\infty \Gamma(y)\, dy \quad \textbf{(7.51a)}$$

or, in terms of the finite-element panels,

$$L = 2\rho_\infty U_\infty \sum_{n=1}^{4} \Gamma_n \Delta y_n \quad \textbf{(7.51b)}$$

Since $\Delta y_n = 0.1250b$ for each panel,

$$\begin{aligned}
L &= 2\rho_\infty U_\infty 4\pi b U_\infty \alpha (0.0273 + 0.0287 + 0.0286 + 0.0250) 0.1250b \\
&= \rho_\infty U_\infty^2 b^2 \pi \alpha (0.1096)
\end{aligned}$$

To calculate the lift coefficient, recall that $S = bc$ and $b = 5c$ for this wing, therefore:

$$C_L = \frac{L}{q_\infty S} = 1.096\pi\alpha$$

Furthermore,

$$C_{L_\alpha} = \frac{dC_L}{d\alpha} = 3.443 \text{ per radian} = 0.0601 \text{ per degree}$$

Comparing this value of C_{L_α} with that for an unswept wing (such as the results presented in Fig. 7.17, it is apparent that an effect of sweepback is the reduction in the lift-curve slope.

The theoretical lift curve generated using the VLM is compared in Fig. 7.33 with experimental results reported by Weber and Brebner (1958).

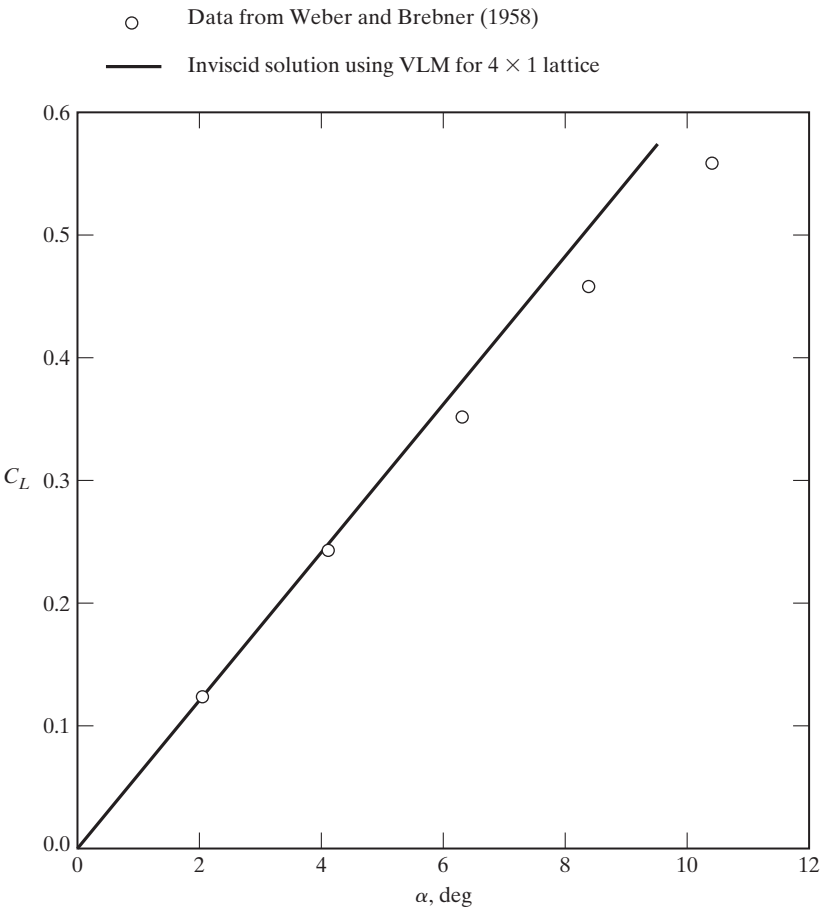

Figure 7.33 Comparison of the theoretical and the experimental lift coefficients for the swept wing of Fig. 7.32 in a subsonic stream.

The experimentally determined values of the lift coefficient are for a wing of constant chord and of constant section, which was swept 45° and which had an aspect ratio of 5. The theoretical lift coefficients are in good agreement with the experimental values.

Since the lift per unit span is given by equation (7.50), the section lift coefficient for the nth panel is:

$$C_{l(n\text{th})} = \frac{l_n}{\frac{1}{2}\rho_\infty U_\infty^2 c_{\text{av}}} = \frac{2\Gamma}{U_\infty c_{\text{av}}} \tag{7.52}$$

When the panels extend from the leading edge to the trailing edge, such as is the case for the 4×1 lattice shown in Fig. 7.32, the value of Γ given in equation (7.49) is used in equation (7.52). When there are a number of discrete panels in the chordwise direction, such as the 10×4 lattice shown in Fig. 7.25 you should sum (from the leading edge to the trailing edge) the values of Γ for those bound-vortex filaments at the spanwise location (i.e., in the chordwise strip) of interest. For a chordwise row:

$$\frac{C_l c}{c_{\text{av}}} = \sum_{j=1}^{J_{\max}} \left(\frac{l}{q_\infty c_{\text{av}}} \right)_j \tag{7.53}$$

where c_{av} is the average chord (and is equal to S/b), c is the local chord, and j is the index for an elemental panel in the chordwise row. The total lift coefficient is obtained by integrating the lift over the span:

$$C_L = \int_0^1 \frac{C_l c}{c_{\text{av}}} d\left(\frac{2y}{b} \right) \tag{7.54}$$

The spanwise variation in the section lift coefficient is presented in Fig. 7.34. The theoretical distribution is compared with the experimentally determined spanwise load distribution for an angle of attack of 4.2°, which was presented by Weber and Brebner (1958). The increased loading of the outer wing sections promotes premature boundary-layer separation at that location. This unfavorable behavior is amplified by the fact that the spanwise velocity component causes the already decelerated fluid particles in the boundary layer to move toward the wing tips. This transverse flow results in a large increase in the boundary-layer thickness near the wing tips. Therefore, at large angles of attack, premature flow separation may occur on the suction side of the wing near the tip. If significant tip stall occurs on the swept wing, there is a loss of effectiveness of the control surfaces and a forward shift in the wing center of pressure that creates an unstable, nose-up increase in the pitch moment.

Boundary-layer fences are often used to break up the spanwise flow on swept wings. The spanwise distribution of the local lift coefficient [taken from Schlichting (1960)] without and with a boundary-layer fence is presented in Fig. 7.35. The essential effect of the boundary-layer fence does not so much consist in the prevention of the transverse flow but, much more important, in that the fence divides each wing into an inner and an outer portion. Both transverse flow and boundary-layer separation may be present, but to a reduced extent. Boundary-layer fences are evident on the swept wings of the Trident shown in Fig. 7.36.

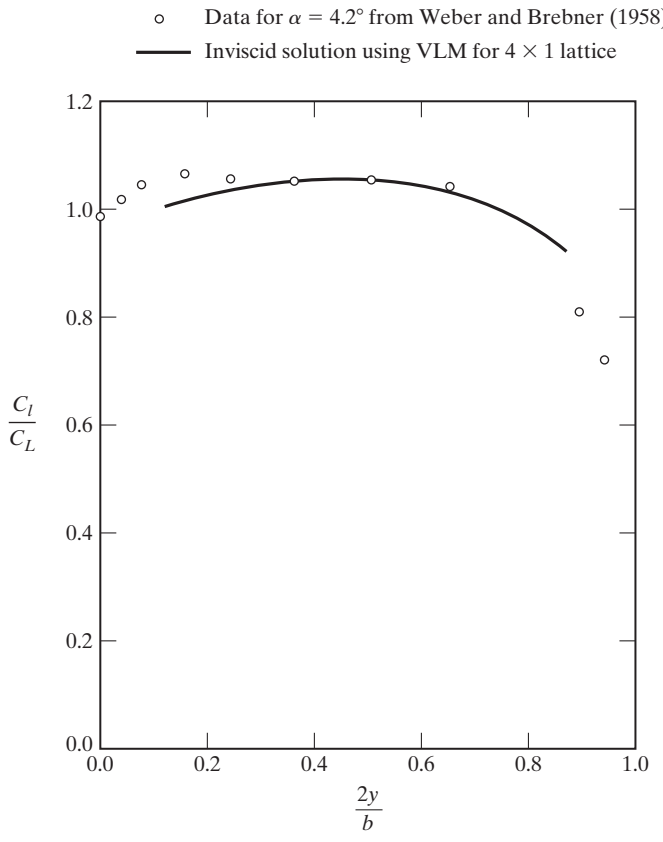

Figure 7.34 Comparison of the theoretical and the experimental spanwise lift distribution for the wing of Fig. 7.32.

Once we have obtained the solution for the section lift coefficient (i.e., that for a chordwise strip of the wing), the induced drag coefficient may be calculated using the relation given by Multhopp (1950), which is just the component of the local lift in the airplane drag direction:

$$C_{Dv} = \frac{1}{S}\int_{-b/2}^{+b/2} C_l\, c\alpha_i\, dy \tag{7.55}$$

where α_i, which is the induced incidence, is given by

$$\alpha_i = -\frac{1}{8\pi}\int_{-b/2}^{+b/2} \frac{C_l c}{(y-\eta)^2}\, d\eta \tag{7.56}$$

For a symmetrical loading, equation (7.56) may be written

$$\alpha_i = -\frac{1}{8\pi}\int_{0}^{b/2}\left[\frac{C_l c}{(y-\eta)^2} + \frac{C_l c}{(y+\eta)^2}\right] d\eta \tag{7.57}$$

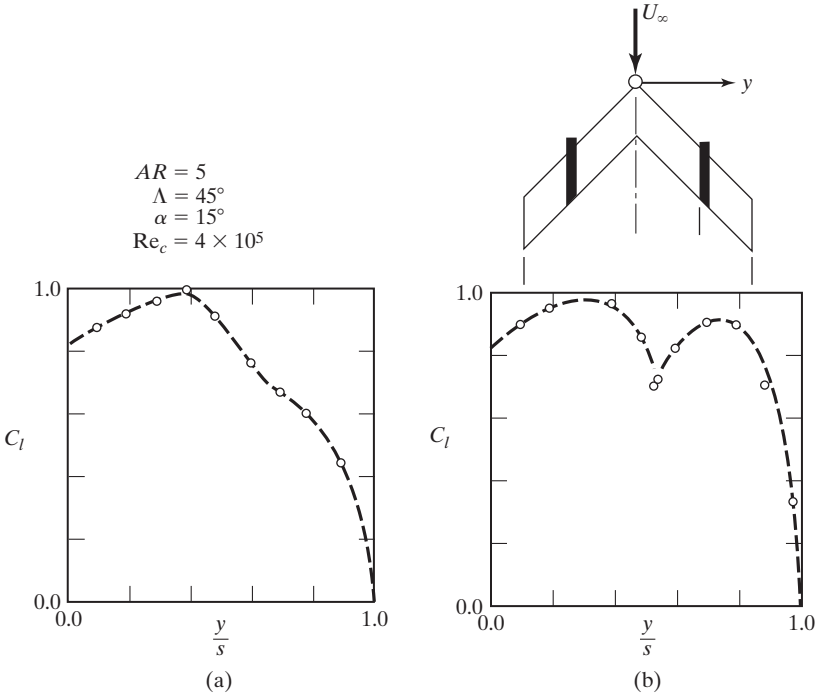

Figure 7.35 Effect of a boundary-layer fence on the spanwise distribution of the local lift coefficient: (a) without fence; (b) with fence [data from Schlichting (1960)].

Figure 7.36 Trident illustrating boundary-layer fences on the wing (courtesy of BAE Systems).

Following the approach of Kalman et al. (1970), we can consider the mth chordwise strip, which has a semiwidth of e_m and whose centerline is located at $\eta = y_m$. Now we can approximate the spanwise lift distribution across the strip by a parabolic function:

$$\left(\frac{C_l c}{C_L \bar{c}}\right)_m = a_m \eta^2 + b_m \eta + c_m \tag{7.58}$$

To solve for the coefficients a_m, b_m, and c_m, note that:

$$y_{m+1} = y_m + (e_m + e_{m+1})$$
$$y_{m-1} = y_m - (e_m + e_{m-1})$$

Thus,

$$c_m = \left(\frac{C_l c}{C_L \bar{c}}\right)_m - a_m \eta_m^2 - b_m \eta_m$$

$$a_m = \frac{1}{d_{mi} d_{mo}(d_{mi} + d_{mo})}\left\{d_{mi}\left(\frac{C_l c}{C_L \bar{c}}\right)_{m+1} - (d_{mi} + d_{mo})\left(\frac{C_l c}{C_L \bar{c}}\right)_m + d_{mo}\left(\frac{C_l c}{C_L \bar{c}}\right)_{m-1}\right\}$$

and

$$b_m = \frac{1}{d_{mi} d_{mo}(d_{mi} + d_{mo})}\left\{d_{mo}(2\eta_m - d_{mo})\left[\left(\frac{C_l c}{C_L \bar{c}}\right)_m - \left(\frac{C_l c}{C_L \bar{c}}\right)_{m-1}\right]\right.$$
$$\left. - d_{mi}(2\eta_m - d_{mi})\left[\left(\frac{C_l c}{C_L \bar{c}}\right)_{m+1} - \left(\frac{C_l c}{C_L \bar{c}}\right)_m\right]\right\}$$

where

$$d_{mi} = e_m + e_{m-1}$$

and

$$d_{mo} = e_m + e_{m+1}$$

For a symmetric load distribution, we let:

$$\left(\frac{C_l c}{C_L \bar{c}}\right)_{m-1} = \left(\frac{C_l c}{C_L \bar{c}}\right)_m$$

and

$$e_{m-1} = e_m$$

at the root. Similarly, we let

$$\left(\frac{C_l c}{C_L \bar{c}}\right)_{m+1} = 0$$

and

$$e_{m+1} = 0$$

at the tip. Substituting these expressions into equations (7.57) and (7.58), we then obtain the numerical form for the induced incidence:

$$\frac{\alpha_i(y)}{C_L c} = -\frac{1}{4\pi}\sum_{m=1}^{N}\left\{\frac{y^2(y_m + e_m)a_m + y^2 b_m + (y_m + e_m)c_m}{y^2 - (y_m + e_m)^2}\right.$$
$$- \frac{y^2(y_m - e_m)a_m + y^2 b_m + (y_m - e_m)c_m}{y^2 - (y_m - e_m)^2}$$
$$+ \frac{1}{2} y a_m \log\left[\frac{(y - e_m)^2 - y_m^2}{(y + e_m)^2 - y_m^2}\right]^2$$
$$\left. + \frac{1}{4} b_m \log\left[\frac{y^2 - (y_m + e_m)^2}{y^2 - (y_m - e_m)^2}\right]^2 + 2e_m a_m\right\} \tag{7.59}$$

We then assume that the product $C_l c\alpha_i$ also has a parabolic variation across the strip.

$$\left[\left(\frac{C_l c}{C_L \bar{c}}\right)\left(\frac{\alpha_i}{C_L \bar{c}}\right)\right]_n = a_n y^2 + b_n y + c_n \tag{7.60}$$

The coefficients a_n, b_n, and c_n can be obtained using an approach identical to that employed to find a_m, b_m, and c_m. The numerical form of equation (7.55) is then a generalization of Simpson's rule:

$$\frac{C_{Dv}}{C_L^2} = \frac{4}{\mathrm{AR}}\sum_{n=1}^{N} e_n\left\{\left[y_n^2 + \left(\frac{1}{3}\right)e_n^2\right]a_n + y_n b_n + c_n\right\} \tag{7.61}$$

The lift developed along the chordwise bound vortices in a chordwise row of horseshoe vortices varies from the leading edge to the trailing edge of the wing because of the longitudinal variation of both the sidewash velocity and the local value of the vortex strength for planforms that have a nonzero dihedral angle. For techniques to compute the lift, the pitch moment, and the roll moment for more general wings, the reader is referred to Margason and Lamar (1971).

Numerous investigators have studied methods for improving the convergence and the rigor of the VLM. Therefore, there is an ever-expanding body of relevant literature with which you should be familiar before attempting to analyze complex flow fields. Furthermore, as noted in the introduction to this section, VLM is only one (and, indeed, a relatively simple one) of the methods used to compute aerodynamic coefficients.

Aerodynamics Concept Box: Birds Flying in Formation

Have you ever wondered why birds fly in formation (as shown in the photograph below)? Migratory birds, such as geese, spend many days flying from their summer to winter homes in the fall (and vice versa in the spring) and need incredible amounts of energy for the trip. We can use lifting-line theory to help us understand the benefits of flying in a formation during these migratory flights.

Migrating birds flying in formation

We can look at just two birds flying in formation as an example, and we will not even have to perform detailed calculations to understand the benefit. Model each bird flying in formation with a single lifting line as shown below. (Note that the horseshoe vortex systems have been staggered slightly for clarity). We will also assume that each wing has the same span and each bird has the same weight (and therefore the same vortex circulation).

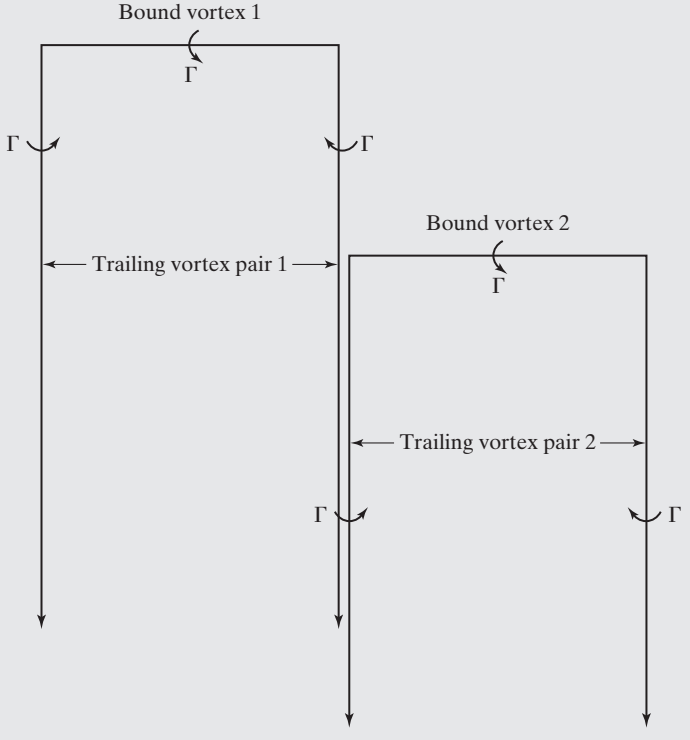

Since we already know what a trailing vortex system does to the wing that creates it (creates downwash and reduces lift while creating induced drag), we will concentrate on the incremental impact of each bird on the other. Consider what the horseshoe vortex system for Bird 1 does to the flow on the wing for Bird 2: the left trailing vortex from Bird 1 will create downwash on the wing of Bird 2, but that vortex filament is farther away than the others, so this impact is small; the right trailing vortex from Bird 1 will create upwash on the wing of Bird 2, which actually improves the aerodynamics of the wing (in fact the right trailing vortex essentially negates the left trailing vortex of Bird 2); the bound vortex of Bird 1 will also increase the downwash on the wing of Bird 2, but this filament is quite short and also fairly far away. The net impact is that there probably is a net reduction of downwash on Bird 2, which will increase the lift and reduce the induced drag of Bird 2. If you perform a similar analysis for the impact of Bird 2 on Bird 1, you will find that the leading bird also is aided, which means both birds benefit from flying in formation.

7.6 FACTORS AFFECTING DRAG DUE-TO-LIFT AT SUBSONIC SPEEDS

The term representing the lift-dependent drag coefficient in equation (7.17) includes those parts of the viscous drag and of the form drag, which result when the angle of attack changes from α_{ol}. For the present analysis, the "effective leading-edge suction" (s) will be used to characterize the drag-due-to-lift. For 100% suction, the drag-due-to-lift coefficient is the potential flow induced vortex drag, which is represented by the symbol C_{Dv}. For an elliptically loaded wing, this value would be $C_L^2/(\pi A\mathrm{R})$ as given in equation (7.17). Zero percent suction corresponds to the condition where the resultant force vector is normal to the chord line, as a result of extensive separation at the wing leading edge.

Aircraft designed to fly efficiently at supersonic speeds often employ thin, highly swept wings. Values of the leading-edge suction reported by Henderson (1966) are reproduced in Fig. 7.37. The data presented in Fig. 7.37 were obtained at the lift coefficient

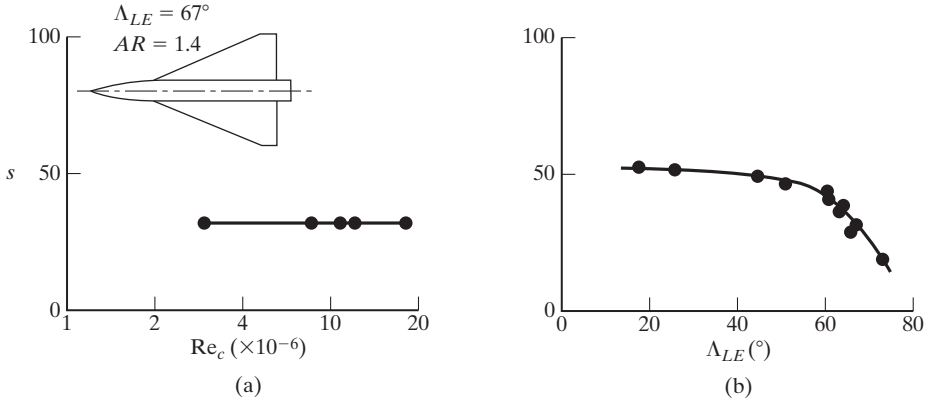

Figure 7.37 The variation of the effective leading-edge suction (s) as (a) a function of the Reynolds number and (b) of the leading-edge sweep angle for a wing with a sharp leading edge, $C_{L,\mathrm{opt}}$ and $M < 0.30$ [from Henderson (1966)].

for which (L/D) is a maximum, designated $C_{L,\text{opt}}$. Values of s are presented as a function of the free-stream Reynolds number based on the chord length for a wing with an aspect ratio of 1.4 and whose sharp leading edge is swept 67° in Fig. 7.37a. The values of s vary only slightly with Reynolds number. Therefore, the suction parameter can be presented as a function of the leading-edge sweep angle (independent of the Reynolds number). Values of s are presented in Fig. 7.37b as a function of the leading-edge sweep angle for several sharp-edge wings. Even for relatively low values for the sweep angle, suction values no higher than about 50% were obtained.

Several features that can increase the effective leading-edge suction can be incorporated into a wing design. The effect of two of the features (leading-edge flaps and wing warp) is illustrated in Fig. 7.38. Values of s are presented as a function of the Reynolds number for a wing swept 74° for $C_{L,\text{opt}}$. The data [again taken from Henderson (1966)] show that both leading-edge flaps and wing warp significantly increase the values of the effective leading-edge suction relative to those for a symmetrical, sharp leading-edge wing.

A third feature that can be used to improve the effective leading-edge suction is the wing leading-edge radius. Data originally presented by Henderson (1966) are reproduced in Fig. 7.39. Values of s are presented as a function of the Reynolds number for a wing with an aspect ratio of 2.0 and whose leading edge is swept 67°. Again, the wing with a sharp leading edge generates relatively low values of s, which are essentially independent of the Reynolds number. The values of s for the wing with a rounded leading

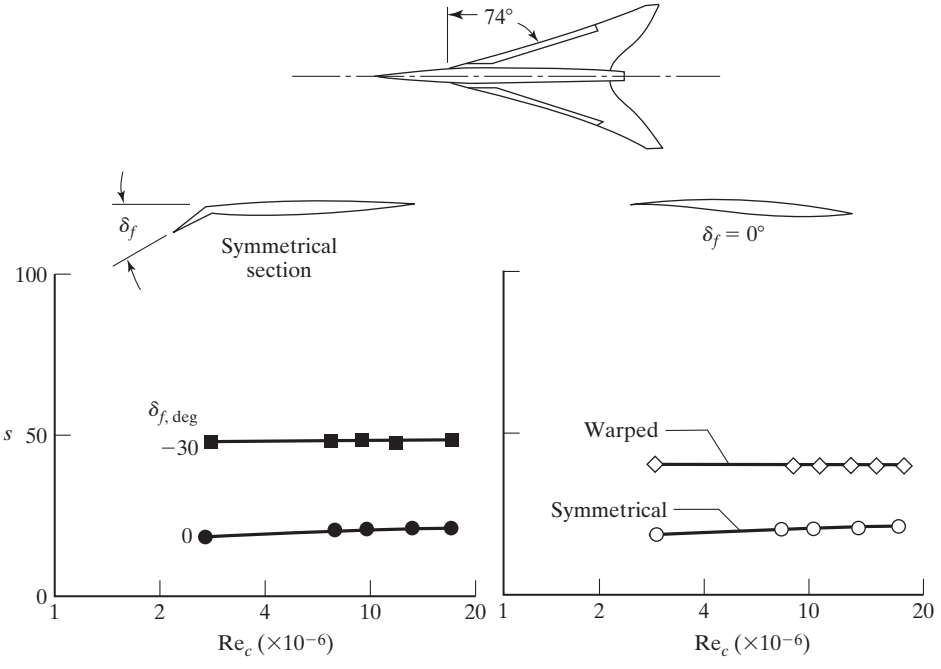

Figure 7.38 The effect of leading-edge flaps and wing warp on the effective leading-edge suction (s) for $C_{L,\text{opt}}$ $M < 0.30$ [from Henderson (1966)].

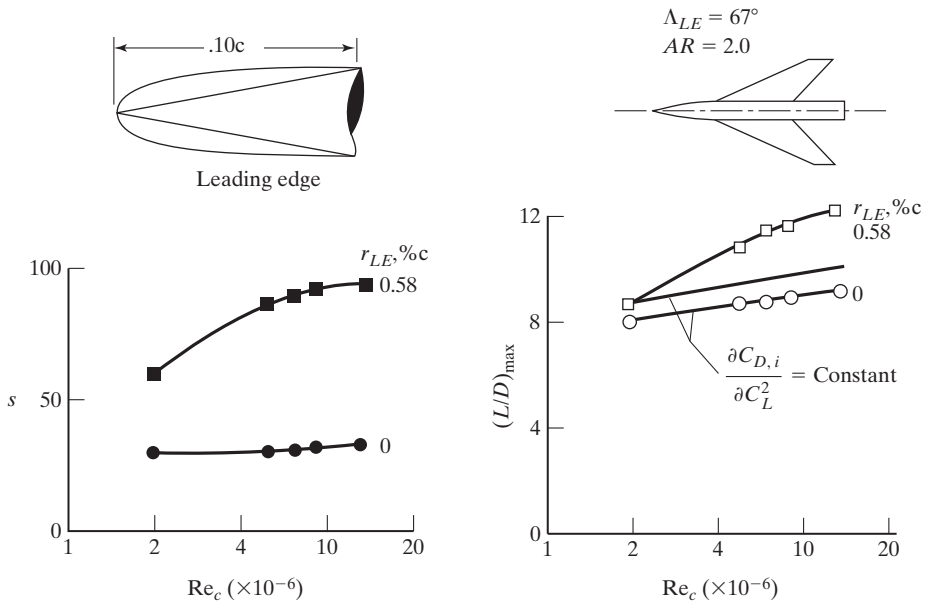

Figure 7.39 The effect of the leading-edge shape, $C_{L,\text{opt}}$ $M < 0.30$ [from Henderson (1966)].

edge ($r_{\text{LE}} = 0.0058\text{c}$) exhibit large increases in s as the Reynolds number increases. As noted by Henderson (1966), the increase in the effective leading-edge suction due to the leading-edge radius accounts for 2/3 of the increase in $(L/D)_{\max}$ from 8 to 12. A reduction in the skin-friction drag accounts for the remaining 1/3 of the increase in $(L/D)_{\max}$.

The total trim drag has two components: (1) the drag directly associated with the tail, and (2) an increment in drag on the wing due to the change in the wing lift coefficient required to offset the tail load. A very important consideration when you study trim drag is the wing efficiency, represented here by the subsonic drag-due-to-lift parameter as shown in Fig. 7.40. McKinney and Dollyhigh (1971) state, "The full leading-edge suction

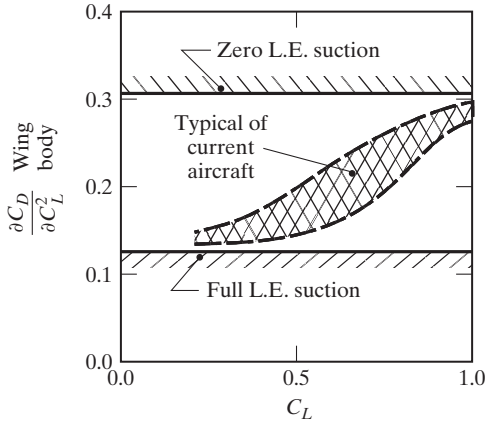

Figure 7.40 Typical variation of drag-due-to-lift parameter; aspect ratio = 2.5; subsonic speeds [from Henderson (1966)].

line and the zero leading-edge suction line are shown for reference. The variation of leading-edge suction with Reynolds number and wing geometry is discussed in a paper by Henderson (1966). The cross-hatched area indicates a typical range of values of the drag-due-to-lift parameter for current aircraft, including the use of both fixed camber and twist or wing flaps for maneuvering. At low lift coefficients ($C_L \approx 0.30$) typical of 1-g flight, drag-due-to-lift values approaching those corresponding to full leading-edge suction are generally obtained. At the high lift coefficient ($C_L \approx 1.0$) which corresponds to the maneuvering case. . . , the drag-due-to-lift typically approaches the zero leading-edge suction line even when current maneuver flap concepts are considered. The need for improving drag-due-to-lift characteristics of wings at the high-lift coefficients by means such as wing warp, improved maneuver devices, and so forth, is recognized."

7.7 DELTA WINGS

As we discussed previously, a major aerodynamic consideration in wing design is the prediction and the control of flow separation. However, as the sweep angle is increased and the section thickness is decreased in order to avoid undesirable compressibility effects, it becomes increasingly more difficult to prevent boundary-layer separation. Although many techniques have been discussed to alleviate these problems, it is often necessary to employ complicated variable-geometry devices in order to satisfy a wide range of conflicting design requirements which result due to the flow-field variations for the flight envelope of high-speed aircraft. Beginning with the delta-wing design of Alexander Lippisch in Germany during World War II, supersonic aircraft designs have often used thin, highly swept wings of low aspect ratio to minimize the wave drag at supersonic cruise conditions. It is interesting to note that during the design of the world's first operational jet fighter, the Me 262, the outer panels of the wing were swept to resolve difficulties arising when increasingly heavier turbojets caused the center of gravity to move. Therefore, the introduction of sweepback in this case did not reflect an attempt to reduce the effects of compressibility [Voight (1976)]. This historical note is included here to remind the reader that many parameters enter into the design of an airplane; aerodynamics is only one of them. The final configuration will always reflect design priorities and trade-offs.

At subsonic speeds, delta-wing planforms have aerodynamic characteristics which are substantially different from those of the relatively straight, high-aspect-ratio wings designed for subsonic flight. Because they operate at relatively high angles of attack, the boundary layer on the lower surface flows outward and separates as it goes over the leading edge, forming a free shear layer. The shear layer curves upward and inboard, eventually rolling up into a core of high vorticity, as shown in Fig. 7.41. There is an appreciable axial component of motion and the fluid spirals around and along the axis. A spanwise outflow is induced on the upper surface, beneath the coiled vortex sheet, and the flow separates again as it approaches the leading edge [Stanbrook and Squire (1964)], creating a secondary vortex under the primary vortex. The size and the strength of the coiled vortex sheets increase with increasing incidence and they become a dominant feature of the flow, which remains steady throughout the range of practical flight attitudes of the wing. The formation of these vortices creates lift (due to low pressure in the vortex core) and is responsible for the nonlinear aerodynamic characteristics that exist over the angle-of-attack range [Hummel (2004)].

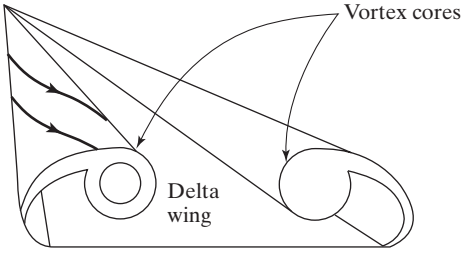

(a)

(b)

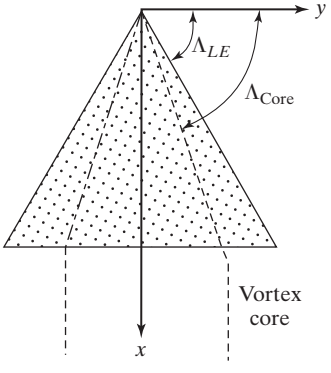

(c)

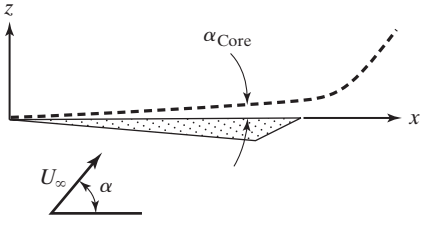

(d)

Figure 7.41 (a) Vortex core that develops for flow over a delta wing. (b) Water vapor condenses due to the pressure drop revealing the vortex core for a F-16 (US Air Force photo by Staff Sgt. Larry E. Reid Jr.) (c) Trajectory of the leading-edge vortex [from Visbal (1995)]. (d) Inclination angle of the vortex trajectory [from Visbal (1995)].

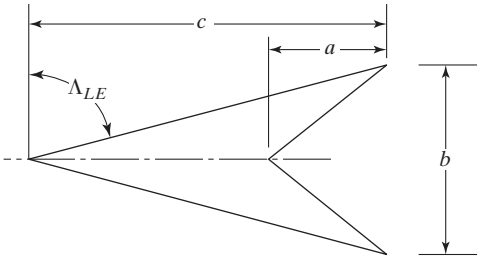

Figure 7.42 Wing geometry nomenclature.

The leading-edge suction analogy developed by Polhamus (1971a, b) can be used to calculate the lift and the drag-due-to-lift characteristics which arise when the separated flow around sharp-edge delta wings reattaches on the upper surface; the correlations apply to thin wings having neither camber nor twist. Furthermore, the method is applicable to wings for which the leading edges are of sufficient sharpness that separation is fixed at the leading edge. Since the vortex flow induces reattachment, and since the Kutta condition must be satisfied at the trailing edge, the total lift coefficient consists of a potential-flow term and a vortex-lift term. The total lift coefficient can be represented by the sum

$$C_L = K_p \sin\alpha \cos^2\alpha + K_v \sin^2\alpha \cos\alpha \qquad \textbf{(7.62)}$$

The constant K_p is simply the normal-force slope calculated using the potential-flow lift-curve slope. The constant K_v can be estimated from the potential flow leading-edge suction calculations. Using the nomenclature for arrow-, delta-, and diamond-planform wings illustrated in Fig. 7.42, K_p and K_v are presented as a function of the planform parameters in Figs. 7.43 and 7.44, respectively.

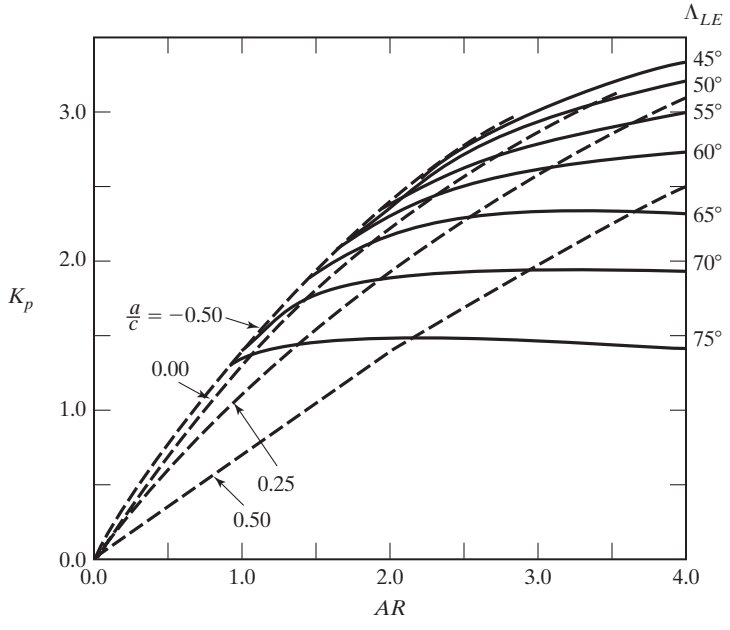

Figure 7.43 Variation of potential-flow lift constant with planform parameters [from Pollhamus (1971b)].

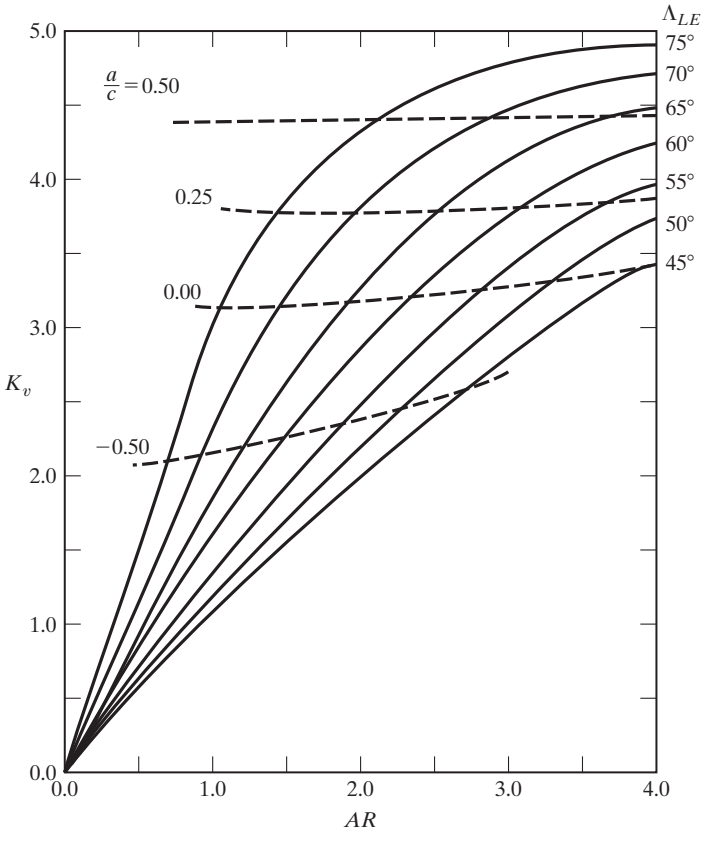

Figure 7.44 Variation of vortex-lift constant with planform parameters [from Pollhamus (1971b)].

Values of the lift coefficient calculated using equation (7.62) are compared in Fig. 7.45 with experimental values for uncambered delta wings that have sharp leading edges. Data are presented for wings of aspect ratio from 1.0 [Peckham (1958)] to 2.0 [Bartlett and Vidal (1955)]. Since the analytical method is based on an analogy with potential-flow leading-edge suction, which requires that flow reattaches on the upper surface inboard of the vortex, the correlation between theory and data breaks down as flow reattachment fails to occur. The lift coefficients calculated using equation (7.62) for $AR = 1.0$ and 1.5 are in good agreement with the measured values up to angles of attack in excess of 20°. However, for a delta wing with an aspect ratio of 2.0, significant deviations between the calculated values and the experimental values exist for angles of attack above 15°.

If the leading edges of the wing are rounded, separation occurs well inboard on the wing's upper surface. The result is that, outboard of the loci of the separation points, the flow pattern is essentially that of potential flow and the peak negative pressures at the section extremity are preserved. However, as noted by Peckham (1958), increasing the thickness causes a reduction in net lift. The combined effect of the thickness ratio and of the shape of the leading edges is illustrated in the experimental lift coefficients

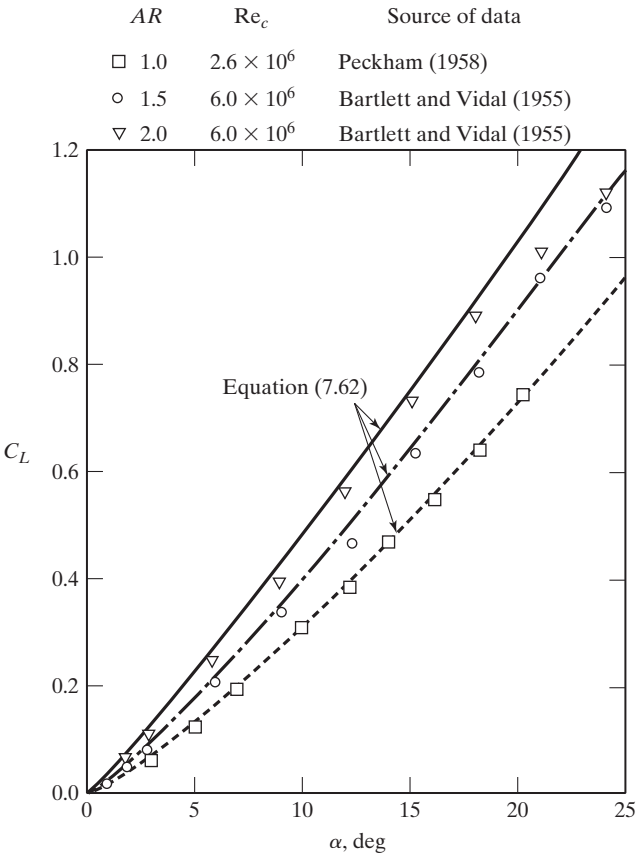

Figure 7.45 Comparison of the calculated and the experimental lift coefficients for thin, flat delta wings with sharp leading edges.

presented in Fig. 7.46, which are taken from Bartlett and Vidal (1955). The lift coefficients are less for the thicker wings, which also have rounded leading edges.

The lift coefficients for a series of delta wings are presented as a function of the angle of attack in Fig. 7.47. The lift-curve slope, $dC_L/d\alpha$, becomes progressively smaller as the aspect ratio decreases. However, for all but the smallest aspect ratio wing, the maximum value of the lift coefficient and the angle of attack at which it occurs increase as the aspect ratio decreases.

For a thin flat-plate model, the resultant force acts normal to the surface. Therefore, the induced drag ΔC_D for a flat-plate wing would be:

$$\Delta C_D = C_D - C_{D_0} = C_L \tan\alpha \tag{7.63}$$

Using equation (7.62) to evaluate C_L, we obtain:

$$C_D = C_{D_0} + K_p \sin^2\alpha \cos\alpha + K_v \sin^3\alpha \tag{7.64}$$

Experimental values of the drag coefficient from Bartlett and Vidal (1955) are compared with the correlation of equation (7.63) in Fig. 7.48. The experimental drag coefficient

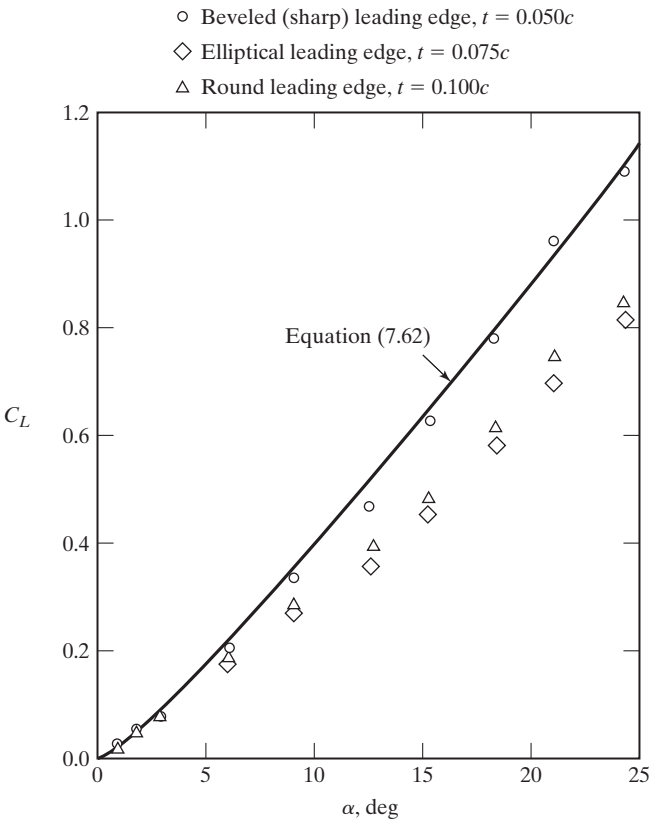

Figure 7.46 Effect of the leading-edge shape on the measured lift coefficient for thin, flat delta wings for which $AR = 1.5$, $\mathrm{Re}_c = 6 \times 10^6$ [data from Bartlett and Vidal (1955)].

increases with angle of attack (as shown in Fig. 7.48); the correlation is best for the higher values of the lift coefficient.

The flow field over a delta wing is such that the resultant pressure distribution produces a large nose-down (negative) pitching moment about the apex, as illustrated by the experimental values from Bartlett and Vidal (1955) presented in Fig. 7.49. The magnitude of the negative pitching moment increases as the angle of attack is increased. The resultant aerodynamic coefficients present a problem relating to the low-speed performance of a delta-wing aircraft which is designed to cruise at supersonic speeds, since the location of the aerodynamic center for subsonic flows differs from that for supersonic flows. At low speeds (and, therefore, at relatively low values of dynamic pressure), delta wings must be operated at relatively high angles of attack in order to generate sufficient lift, since:

$$L = \tfrac{1}{2}\rho_\infty U_\infty^2 S C_L$$

However, if the wing is at an angle of attack that is high enough to produce the desired C_L, a large nose-down pitch moment results. Therefore, the basic delta configuration is

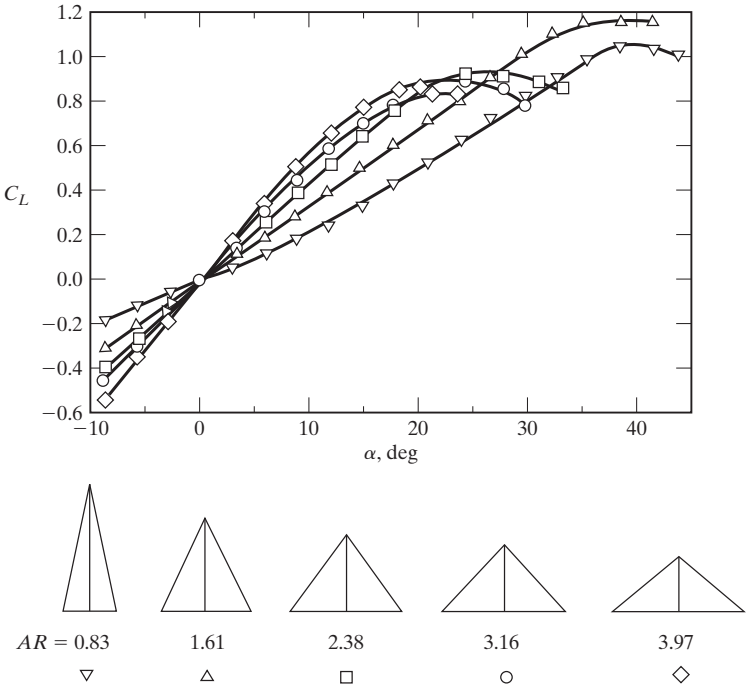

Figure 7.47 Lift coefficients for delta wings of various aspect ratios; $t = 0.12c, \mathrm{Re}_c \approx 7 \times 10^5$ [data from Schlichting and Truckenbrodt (1969)].

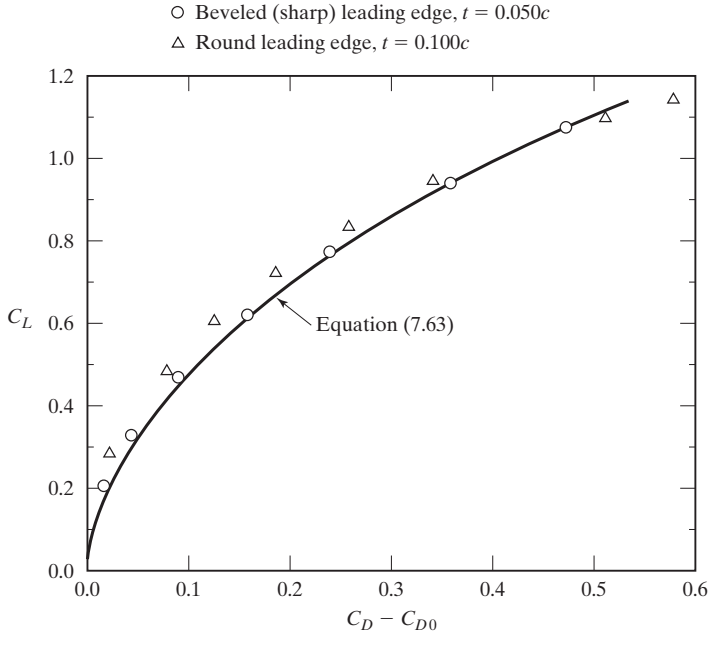

Figure 7.48 Drag correlation for thin, flat delta wings for which $AR = 1.5, \mathrm{Re}_c = 6 \times 10^6$ [data from Bartlett and Vidal (1955)].

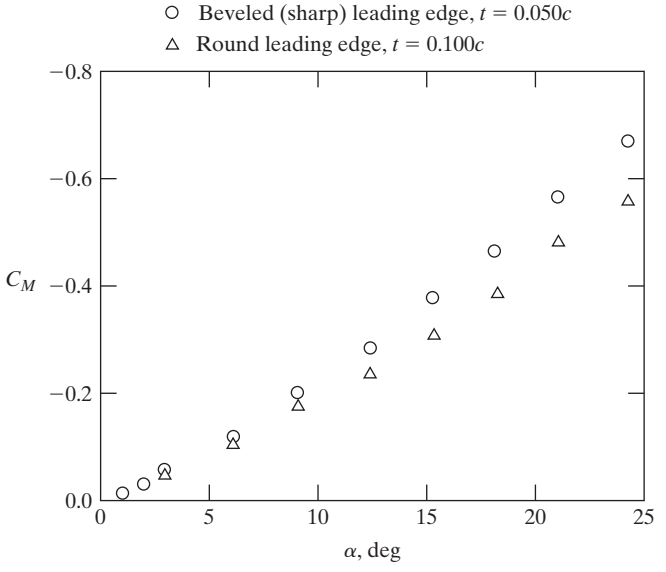

Figure 7.49 Moment coefficient (about the apex) for thin, flat delta wings for which $AR = 1.5$, $\mathrm{Re}_c = 6 \times 10^6$ [data from Bartlett and Vidal (1955)].

often augmented by a lifting surface in the nose region (called a canard), which provides a nose-up trimming moment. The canards may be fixed, such as those shown in Fig. 7.50 on North American's XB-70 Valkyrie, or retractable, such as those on the Dassault Mirage. An alternative design approach, which is used on the Space Shuttle *Orbiter*, uses a reflexed wing trailing edge (i.e., negative camber) to provide the required trimming moment.

Figure 7.50 North American XB-70 illustrating the use of canards (photo courtesy of NASA).

Aerodynamics Concept Box: The X-31 Highly Maneuverable Aircraft

The X-31 was a joint German/U.S. flight test program in the 1990s created to determine enhanced fighter maneuverability through the use of advanced control systems, including thrust vector control. The flight test program, conducted at NASA's Dryden Flight Research Center, provided valuable information for engineers to be able to design the next generation of highly maneuverable fighters.

The X-31 had canards, wing control surfaces, and aft-mounted strakes. The canards were mounted just behind the nose and on a higher level than the wing. The canards could either be free to rotate with the local flow or moved by the flight control system to control the aircraft at high angles of attack. The strakes supplied a nose-down pitch moment to aid in aircraft control at high angles of attack.

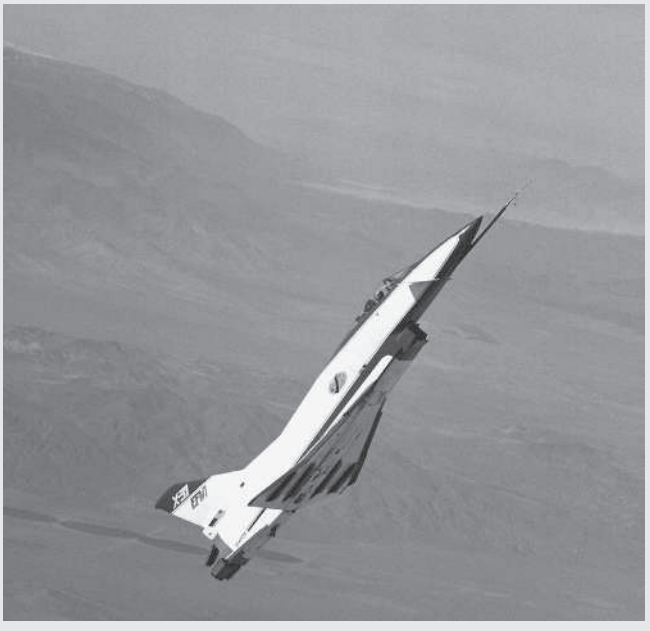

The X-31 performing a maneuver (courtesy of NASA Dryden Flight Research Center)

Because of the highly maneuverable characteristics of the X-31, the airplane was able to perform a variety of unusual maneuvers, including the Herbst Maneuver, which was a 180° turn which took place after the aircraft was already stalled, showing the ability of the multi-mode flight control system to maneuver the aircraft. The demonstration of maneuverability displayed by the X-31 represented an important advancement in aircraft aerodynamics and controllability.

As noted by Gloss and Washburn (1978), "the proper use of canard surfaces on a maneuvering aircraft can offer several attractive features such as potentially higher trimmed-lift capability, improved pitching moment characteristics, and reduced trimmed drag. In addition, the geometric characteristics of close-coupled canard configurations offer a potential for improved longitudinal progression of cross-sectional area which could

result in reduced wave drag at low supersonic speeds and placement of the horizontal control surfaces out of the high wing downwash and jet exhaust." These benefits are primarily associated with the additional lift developed by the canard and with the beneficial interaction between the canard flow field and that of the wing. These benefits may be accompanied by a longitudinal instability (or pitch up) at the higher angles of attack because of the vortex lift developed on the forward canards.

The location of vortices on a delta wing was described by Visbal (1995). For delta wings which are highly swept, the primary separation location is at the sharp leading-edge. The flow separation begins at relatively low angles of attack, and creates a shear layer which develops into a pair of counter-rotating primary vortices, as shown in Fig. 7.41a. The primary vortices have low pressure at their high velocity core, which creates lift to very high angles of attack when compared with wings with low wing sweep. The primary vortex follows a path which is essentially straight with a vortex sweep angle Λ_{core} which varies only slightly with angle of attack, as shown in Fig. 7.41c. The vortex sweep angle is only slightly greater than the wing leading-edge angle, Λ_{LE}. The angle of the vortex path relative to the wing surface α_{Core}, which is shown in Fig. 7.41d, increases linearly with angle of attack, until the vortex reaches the trailing edge when the vortex starts to deflect up toward the free stream.

Visbal (1995) also noted:

> The leading-edge vortices above a delta wing at high angle of attack experience a dramatic form of flow disruption termed "vortex breakdown" or "vortex bursting." This phenomenon is characterized by reverse axial flow and swelling of the vortex core, and is accompanied by marked flow fluctuations downstream. Vortex breakdown poses severe limitations on the performance of agile aircraft due to its sudden effects on the aerodynamic forces and moments and their impact on stability and control. For maneuvering delta wings, the onset of vortex development with its inherent long time scales results in dynamic hysteresis and lags in the vortex development and aerodynamic loads. In addition, the coherent fluctuations within the breakdown region can promote a structural response in aircraft surfaces immersed in the vortex path. An important example is that of "tail buffet" in twin-tailed aircraft where the fluid/structure interaction may result in significant reduction of the service life of structural components.

In a related comment, Visbal (1995) notes, "As the leading-edge sweep and angle of attack increase, the interaction between the counterrotating leading-edge vortices increases and may lead to flow asymmetry. This phenomenon becomes more severe when vortex breakdown is present given the sudden onset and sensitivity and the accompanying swelling of the vortex core."

As noted in the previous paragraphs and as depicted in Fig. 7.41, the flow over a delta wing with sharp leading edges is dominated by vortices inboard of the leading edge. The pressure on the wing's leeward surface beneath these vortices is very low and contributes significantly to the lift. When the aircraft is at moderate to high angles of attack, the axes of the vortices move away from the leeward surface of the wing. With the vortex core away from the surface, the vortex breaks down, or bursts, at some distance from the leading edge. Vortex breakdown, or bursting, is depicted in the water-tunnel

flow of Fig. 7.53. Note that the diameter of the vortex increases suddenly when bursting, or breakdown, occurs. When vortex breakdown occurs, there are large reductions in the peak velocities both in the transverse and in the axial directions.

As the angle of attack increases, the vortex breakdown location moves forward, ahead of the trailing edge toward the apex. The forward movement of the location of vortex breakdown and the attendant increase in the pressure on the leeward surface of the wing beneath the vortices are characteristic of the stall of a delta wing. The location of vortex breakdown during the unsteady pitch-up motion is downstream of its steady-state location, resulting in a lift overshoot. The magnitude of the lift overshoot depends on the leading-edge sweep angle. Defining the positive attributes of a delta wing, Herbst (1980) noted,

> There is a considerable basic aerodynamic potential in terms of lift to drag improvements in delta wings. Theoretical tools are available now to refine the wing planform, profile, and twist distribution. In particular, the leading edge suction can be improved considerably by means of proper leading edge profile, thus improving drag due to lift, the weakness of any highly swept wing . . . . With the help of an electronic digital control system, properly designed with modern aerodynamic tools and suitably equipped with a canard control surface, a delta wing could be designed to maintain its classically good supersonic performance without sacrificing cruise and subsonic performance compared to a more conventional trapezoidal wing.

7.8 LEADING-EDGE EXTENSIONS

The designs of lightweight fighters that can cruise supersonically and maneuver transonically employ additional, highly swept areas ahead of the main wing. These forward areas are called strakes, gloves, fillets, apex regions, and leading-edge extensions (the name used depends on the shape of the modification and the manufacturer of the device). The strake/wing combinations are also known by different names (e.g., ogee and double delta).

Lamar and Frink (1982) note that the mutual benefits derived from strake/wing configurations

> include for the wing: (1) minimal interference at or below the cruise angle of attack, (2) energizing of the upper surface boundary layer with the resulting flow reattachment on the outer wing panel at moderate to high angle of attack due to the strake vortex, and (3) reduced area required for maneuver lift. Benefits for the strake are (1) upwash from the main wing strengthens the strake vortex and (2) the need for only a small area (hence wetted area and comparatively lightweight structure) to generate its significant contribution to the total lift, because the strake provides large amounts of vortex lift. It should be mentioned that these vortex-induced benefits are realized when the strake vortex is stable and maintaining a well-organized vortex system over the wing. Once the angle of attack becomes sufficiently large that strake-vortex breakdown progresses ahead of the wing trailing edge, these favorable effects deteriorate significantly.

A method for estimating the aerodynamic forces and moments for strake/wing/body configurations estimates the vortex flow effects with the suction analogy and the

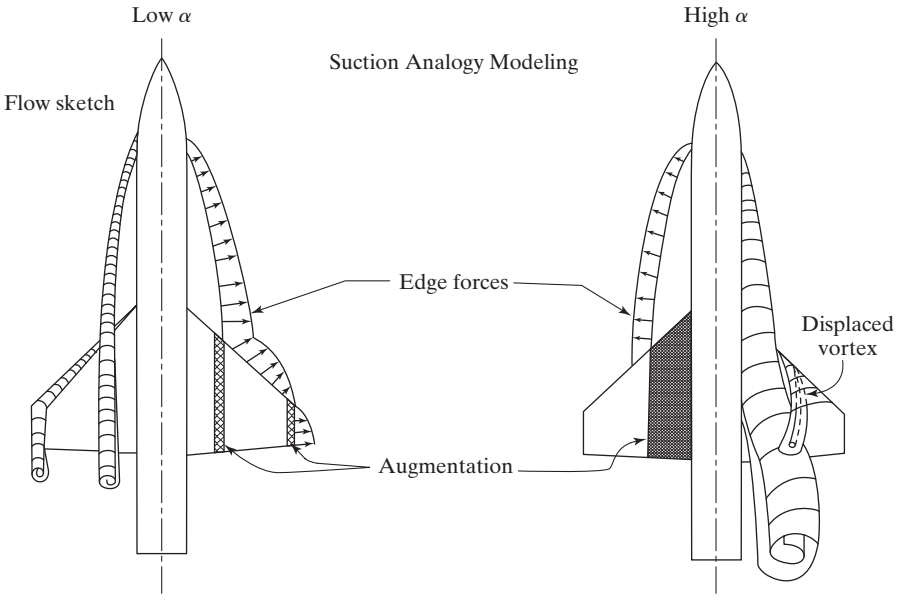

Figure 7.51 Theoretical vortex model for strake/wing configuration [from Lamar and Frink (1982)].

basic potential flow effects with the vortex lattice method [Lamar and Gloss (1975)]. As noted by Lamar and Frink (1982) and illustrated in Fig. 7.51, "at low angle of α, it was concluded that the configuration had attached flow away from the leading and side edges, and downstream from the component tips, vortical flow existed. However, at the higher values of α, the strake vortex becomes much larger and tends to displace the wing-vortex-flow system off the wing, so that this system can no longer cause flow reattachment to occur on the wing. This lack of reattachment causes a large portion of theoretically available aerodynamic effects to be effectively lost to the configuration."

The two theoretical solutions along with a potential flow solution are compared with data [as taken from Lamar and Frink (1982)] in Fig. 7.52. The C_L data are better estimated by the high-α theory. However, there may be an angle-of-attack range below the α for $C_{L_{\max}}$ for which the C_L data are underpredicted. This is most likely associated with the exclusion of any vortex lift from the wing in the high-α theory.

A flow visualization photograph of the vortices shed from the sharp leading edges of slender wings and wing leading-edge extensions (LEXs) or wing-body strakes at high angles of attack is presented in Fig. 7.53; the data were obtained in the Northrop Water Tunnel. Although the Reynolds number was relatively low, the separation point does not vary with Reynolds number, provided that flow separation occurs from a sharp leading edge. Erickson (1982) concluded that "the water tunnel provides a good representation of the wake shed from a wing."

Notice that in the caption of Fig. 7.53 it is stated that the Reynolds number is 10^4 for this test in a water tunnel. The comparisons of the vortex burst locations on the F/A-18 from experiments that spanned the range from 1/48-scale models in water tunnels to actual flight tests of the full-scale aircraft are discussed in Komerath et al.

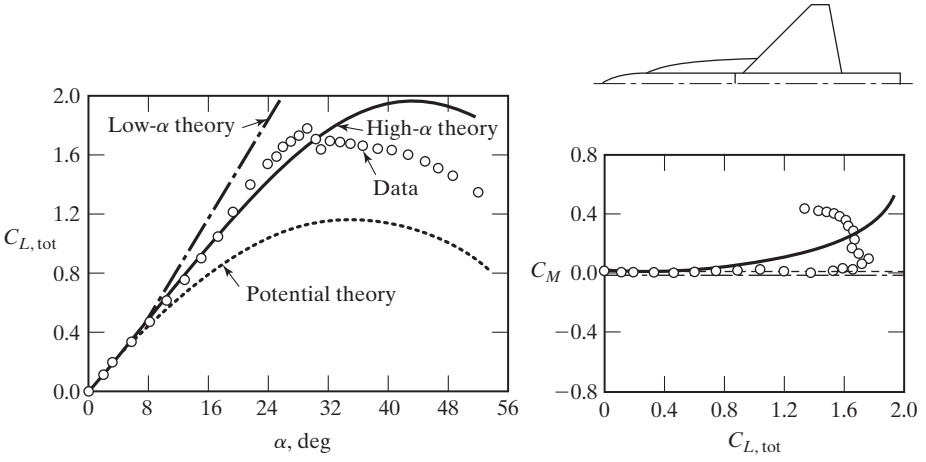

Figure 7.52 Predicted and measured $C_{L,\text{tot}}$ and C_M for strake/wing configuration at $M_\infty = 0.2$ [from Lamar and Frink (1982)].

(1992). While it may seem odd that a water tunnel operating at very low Reynolds numbers could accurately represent the flow around a fighter aircraft like the F/A-18, the comparison between scaled water tunnel tests and flight tests shows remarkable agreement. The good comparison is due to the fact that the leading-edge extension on the F/A-18 has a sharp leading edge, which forces primary separation to take place at

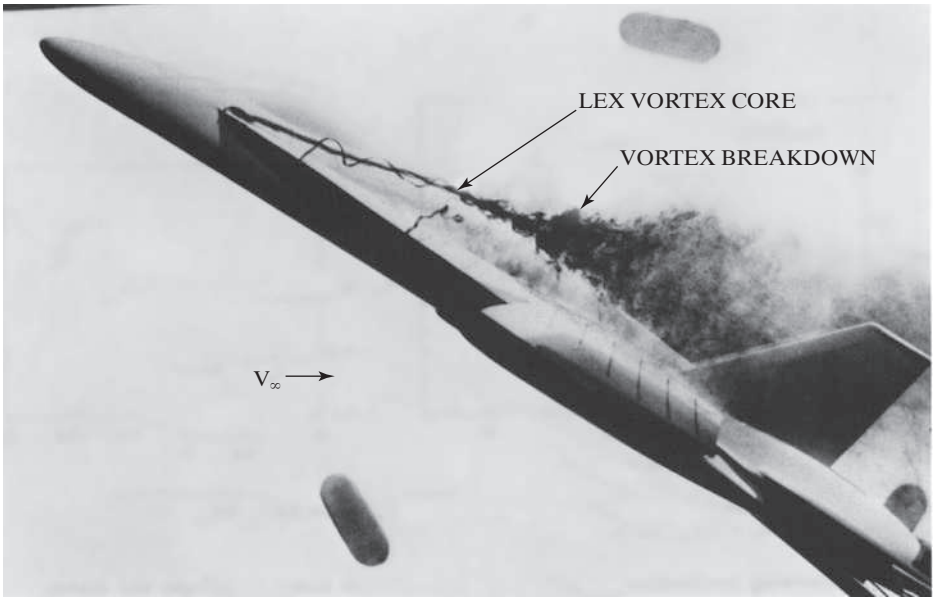

Figure 7.53 Flow visualization of a LEX vortex on a Subscale Advanced Fighter Model; $\alpha = 32°$, $\text{Re} = 10^4$ from the Northrop Water Tunnel [from Erickson (1982), courtesy of Northrop Grumman Corporation].

the leading edge. Therefore, the primary vortex location and strength are comparable between the water tunnel and flight tests. Erickson et al. (1989) show some differences for data at different Reynolds and Mach numbers, which shows the impacts of "surface roughness, freestream turbulence, tunnel wall effects, and model support interference must be considered in each study."

The flow field computed for an F-18C at an angle of attack of 32° is presented in Fig. 7.54 [Wurtzler and Tomaro (1999)]. The free-stream Mach number for this flow is 0.25 and the free-stream Reynolds number (based on the model length) is 15×10^6. The solution was generated using the turbulence model of Spalart and Allmaras (1992) in the Cobalt_{60} code [Strang et al. (1999)]. Notice that the computation of a turbulent separated flow is one of the greatest challenges to the computational fluid dynamicist, nevertheless, the solution exhibits several interesting phenomena.

The surface marking a constant-entropy contour is highlighted in Fig. 7.54, so that you can visualize the vortex core. Notice that vortex breakdown, or bursting, occurs at an x coordinate between the engine inlet and the leading edge of the vertical tail. Also included in Fig. 7.54 are two streamlines of the flow that are affected by the vortex. Near the leading edge of the wing the streamlines form spirals as they are entrained by the vortex. Once the vortex breaks down, the streamlines exhibit chaotic behavior. Despite the differences in the flow conditions and in the geometry, the flow fields of Figs. 7.53 and of 7.54 are qualitatively similar.

As noted in Stuart (1978), the original T-38 wing planform did not include a leading-edge extension (LEX) at the wing root. The effects of the LEX in terms of

Figure 7.54 Flow-field computations for an F-18C at an angle of attack of 32°, $M_\infty = 0.25$, $\text{Re}_L = 15 \times 10^6$ [provided by Wurtzler and Tomaro (1999)].

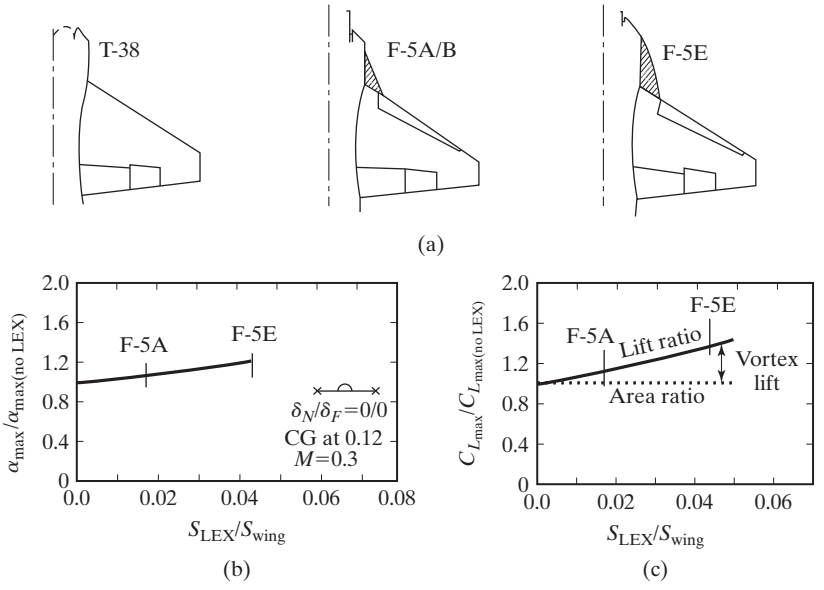

Figure 7.55 Effect of wing leading-edge extensions on the maximum angle of attack and the maximum lift for the F-5 family of aircraft: (a) configurations; (b) maximum angle of attack; (c) maximum lift [from Stuart (1978)].

maximum trimmed angle of attack and trimmed $C_{L\,\max}$ are illustrated in Fig. 7.55. The F-5E LEX with an area increase of 4.4% of the wing reference area provides a $C_{L\,\max}$ increment of 38% of the no-LEX value. Northrop studies suggest a practical LEX upper size limit for any given configuration, and the F-5E LEX is close to this value. The higher trimmed angle of attack capability increases air combat effectiveness. The higher drag associated with the higher angle of attack is very useful in producing overshoots of the attacking aircraft. Although strakes (or leading-edge extensions) produce significant increases in the maximum angle of attack and in the maximum lift coefficient, the load distribution may concurrently produce large nose-up (positive) pitch moments at high angles of attack.

7.9 ASYMMETRIC LOADS ON THE FUSELAGE AT HIGH ANGLES OF ATTACK

Ericsson and Reding (1986) noted that it has long been recognized that asymmetric vortex shedding can occur on bodies of revolution at high angles of attack. Large asymmetric loads can be induced on the body itself, even at zero sideslip. They note that experimental results have shown that the vortex-induced side force can be as high as, or exceed, the normal force.

As a slender body of revolution is pitched through the angle-of-attack range from 0 to 90°, there are four distinct flow patterns that reflect the diminishing influence of the axial flow component. Sketches of these four flow patterns are presented in Fig. 7.56. At low angles of attack ($0° < \alpha < \alpha_{SV}$), the axial-flow component dominates and the flow is

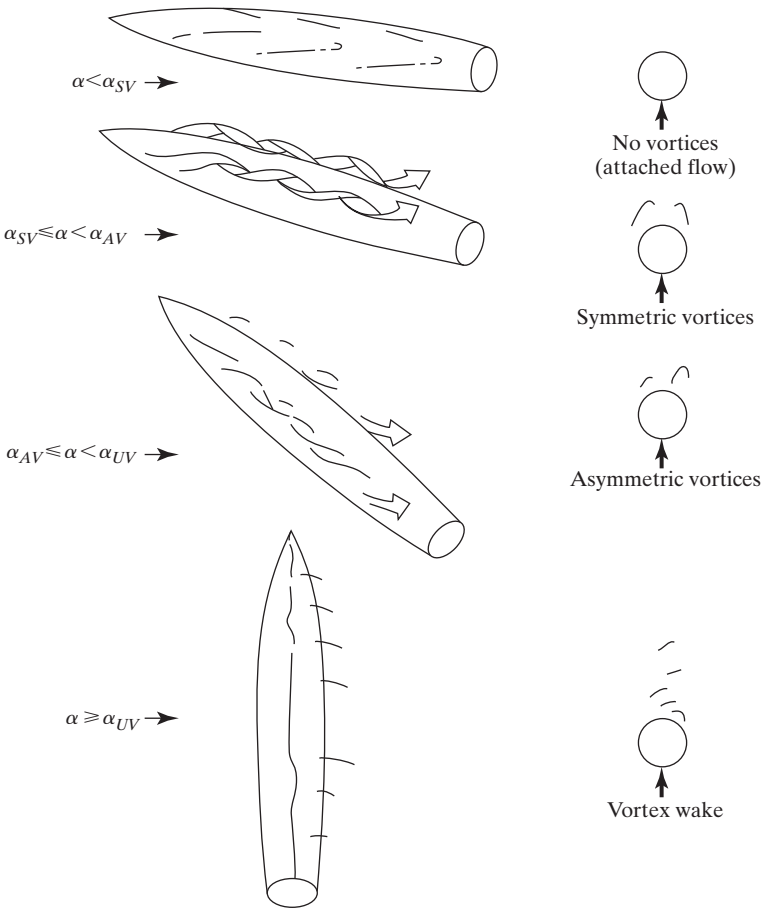

Figure 7.56 Effect of angle of attack on the leeside flowfield [from Ericsson and Reding (1986)].

attached, although the cross-flow effects will generate a thick viscous layer on the leeside. For these vortex-free flows, the normal force is approximately linear with angle of attack, and the side force is zero. At intermediate angles of attack ($\alpha_{\mathrm{SV}} \leq \alpha < \alpha_{\mathrm{AV}}$) [i.e., the angle of attack is equal to or greater than the minimum for the formation of symmetric vortices α_{SV} but less than that for the formation of asymmetric vortices (α_{AV})], the cross flow separates and generates a symmetric pair of vortices. The normal force increases nonlinearly in response to the added *vortex lift*, but there continues to be no side force.

7.9.1 Asymmetric Vortex Shedding

In the angle-of-attack range where vortex shedding is asymmetric ($\alpha_{\mathrm{AV}} \leq \alpha < \alpha_{\mathrm{UV}}$), as shown in third flow pattern shown in Fig. 7.56, the axial flow component is still sufficient to produce steady vortices. However, the vortex pattern is asymmetric, producing a side force and a yawing moment, even at zero sideslip. As observed by Cobleigh

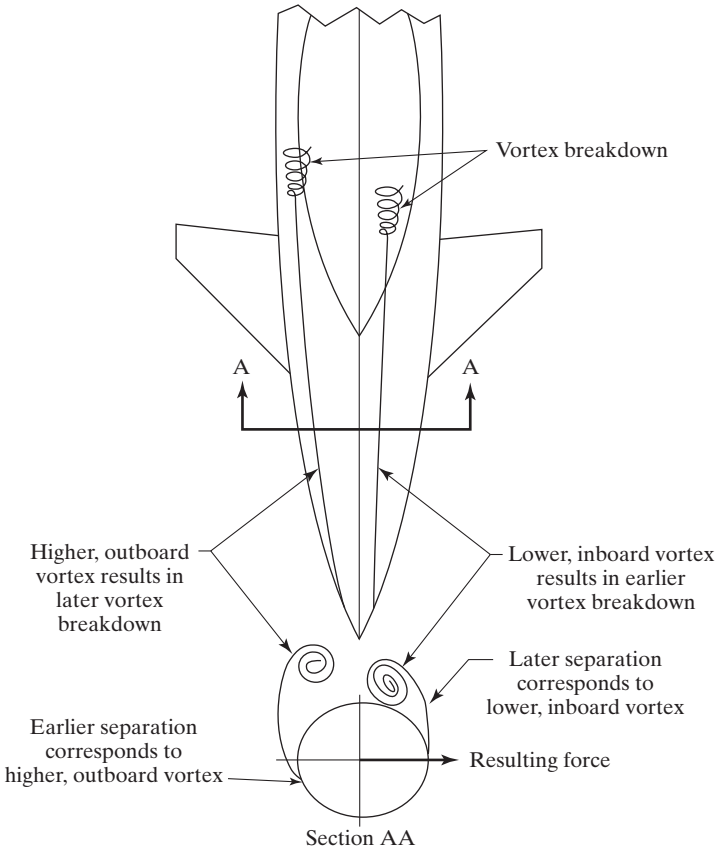

Figure 7.57 Sketch of asymmetric vortices shed from aircraft forebody for $\alpha_{AV} \leq \alpha < \alpha_{UV}$ [from Cobleigh (1994)].

(1994) and shown in Fig. 7.57, "This side force is the result of surface pressure imbalances around the forebody of the aircraft caused by an asymmetric forebody boundary layer and vortex system. In this scenario, the boundary layer on each side of the forebody separates at different locations . . . at separation, corresponding vortex sheets are generated which roll up into an asymmetrically positioned vortex pair. The forces on the forebody are generated primarily by the boundary layer and to a lesser extent by the vortices, depending on their proximity to the forebody surface." Fig. 7.57 shows an asymmetrical vortex pattern, "where the lower, more inboard vortex corresponds to a boundary layer which separates later and, conversely, the higher, more outboard vortex corresponds to the boundary layer which separated earlier. The suction generated by the more persistent boundary layer and the closer vortex combine to create a net force in their direction. Since the center of gravity of the aircraft is well aft of the forebody, a sizeable yawing moment asymmetry develops" [Cobliegh (1994)].

There are a variety of techniques that can be used to modify the asymmetric vortex pattern, including physical surfaces (e.g., strakes) and boundary-layer control (e.g., blowing

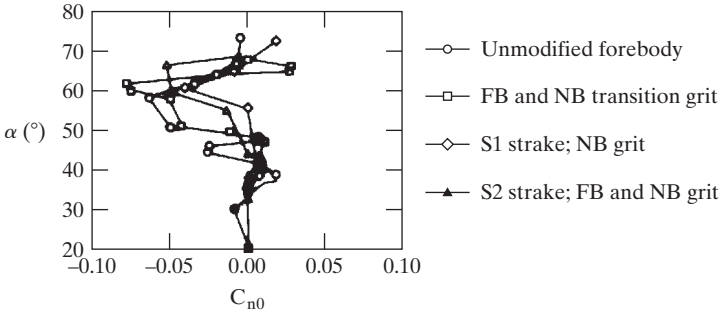

Figure 7.58 Variation of yawing moment asymmetry with angle of attack for an X-31 for a 1-g maneuver [from Cobleigh (1994)].

or suction at the surface). The yawing moment asymmetry for an X-31 during slow decelerations (essentially 1g) to high AOA (angle of attack) conditions, as taken from Cobleigh (1994), is reproduced in Fig. 7.58. For the basic aircraft, the asymmetric forces started to build up, beginning at an angle of attack of 48° reaching a peak value of C_{n_0} (the yawing moment coefficient at zero sideslip) of −0.063 at an angle of attack of approximately 57°. The asymmetric forces decreased rapidly with alpha, becoming relatively small by an angle of attack of 66°. In an attempt to reduce these asymmetries, transition grit strips were installed on both sides of the forebody (FB) and along the sides of the nose boom (NB). The data indicated that the side forces actually increased when grit strips were used. Although the largest asymmetry began to build at the same angle of attack as for the basic aircraft (an AOA of 48°), the peak asymmetry increased to C_{n_0} of −0.078. For the aircraft with these transition strips, the largest asymmetry occurred in the alpha range from 58° to 61°. The use of a strake along with blunting of the nose tip delayed the initiation of the yawing moment asymmetry up to an AOA of 55° (refer to Fig. 7.58). The peak asymmetric yawing moment coefficient C_{n_0} of −0.040 occurred at an angle of attack of 60°, after which the asymmetric yawing moment coefficient decreased. As evident in the data presented in Fig. 7.58, the use of both a strake and boundary-layer transition strips produced significant yawing moments which persisted over a broad angle-of-attack range.

In summary, Cobleigh (1994) reported,

> Several aerodynamic modifications were made to the X-31 forebody with the goal of minimizing the asymmetry. A method for determining the yawing moment asymmetry from flight data was developed and an analysis of the various configuration changes completed. The baseline aircraft were found to have significant asymmetries above 45° angle of attack with the largest asymmetry typically occurring around 60° angle of attack. Applying symmetrical boundary-layer transition strips along the forebody sides increased the magnitude of the asymmetry and widened the angle-of-attack range over which the largest asymmetry acted. Installing longitudinal forebody strakes and rounding the sharp nose of the aircraft caused the yawing moment asymmetry magnitude to be reduced. The transition strips and strakes made the asymmetry characteristic of the aircraft more repeatable than the clean forebody configuration. Although no geometric differences between the aircraft were known, ship 2 consistently had larger yawing moment asymmetries than ship 1.

For axisymmetric bodies with wings or fins, the interaction with the asymmetric vortex pattern can produce rolling moments. Typically, the effectiveness of the vertical tail and rudder to control the yawing moment falls off as the angle of attack increases, because the vertical tail lies in the wake of the wing and of the fuselage.

Ericsson and Reding (1986) note that "the seriousness of the problem is illustrated by the wind-tunnel test results for the F-111, which show the vortex-induced yawing moment to exceed, by an order of magnitude, the available control capability through full rudder deflection. The problem can be cured by use of nose strakes or other types of body reshaping that cause the forebody vortices to be shed symmetrically."

An article by Dornheim (1994) stated:

> The X-31's main problem is directional instability from asymmetric nose vortices around 60 deg. AOA, which caused an unintended departure in flight test. At that 165 knots condition, the yaw moment from the vortices was estimated to be 2.5 times more powerful than the thrust vectoring, and as powerful as the rudder itself would be at 10 deg. AOA. A subtle reshaping of the nose and adding vortex control strakes has tamed the vortices, and the X-31 should be able to fly at least 300 knots, where the 6g structural limit comes into play, before the remaining vortices can overpower the thrust vectoring at high AOA.

7.9.2 Wakelike Flows

Finally, at very high angles of attack ($\alpha_{UV} \leq \alpha < 90°$) the axial-flow component has less and less influence, so that the vortex shedding becomes unsteady, starting on the aft body and progressing toward the nose with increasing angle of attack. In this angle-of-attack range, the leeside flow resembles the wake of a two-dimensional cylinder normal to the flow. The mean side force decreases toward zero in this angle-of-attack range.

7.10 FLOW FIELDS FOR AIRCRAFT AT HIGH ANGLES OF ATTACK

As noted by Mendenhall and Perkins (1996), "Many modern high-performance fighter aircraft have mission requirements which necessitate rapid maneuvers at high angles of attack and large angular rotation rates. Under these flow conditions, the vehicle may operate in a flow regime in which the aerodynamic characteristics are dominated by unsteady nonlinear effects induced by flow separation, vortex shedding, and vortex lag effects (Fig. 7.59). During extreme multiple-axis maneuvering conditions, the dynamic and time-dependent effects of these nonlinear flow characteristics contribute significantly to the behavior and maneuvering capability of aircraft."

Mendenhall and Perkins continue, "The presence of the vortex wake introduces memory into the flow problem, and the nonlinear forces and moments on the vehicle depend on the time history of the motion and the wake development. For example, vorticity shed from the nose of the vehicle will pass downstream to influence the loads on the wing and tail surfaces. The vortex-induced loads depend on the motion of the vehicle and the vortex wake during the time it takes the vorticity to be transported from the nose to the tail."

The vortices associated with flow over highly swept wings (such as delta wings), with the flow over leading-edge extensions (LEXs) and with the flow over the nose region at

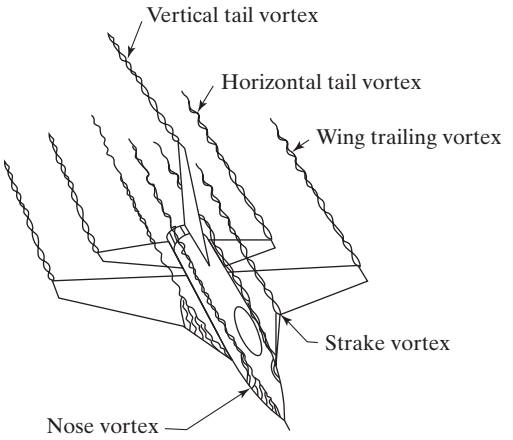

Figure 7.59 Vortex wakes near a maneuvering fighter [from Mendenhall and Perkins (1996)].

high angles of attack, have been discussed individually in the previous sections of this chapter. Numerical predictions [e.g., Cummings et al. (1992)] and in-flight flow-field measurements [e.g., Del Frate and Zuniga (1990)] have been presented for a modified F-18 aircraft called the high-alpha research vehicle (HARV). The HARV was a single-place F-18 aircraft built by McDonnell Douglas and Northrop Aircraft and was powered by two General Electric F404-GE-400 turbofan engines with afterburners. The aircraft featured a mid-wing with leading- and trailing-edge flaps. Leading-edge extensions extend from the wing roots to just forward of the windscreen. A sketch illustrating the location of the forebody vortex core, of the LEX vortex, and of the LEX/forebody vortex interaction, as taken from Del Frate and Zuniga (1990), is reproduced in Fig. 7.60. The pattern is for an angle of attack of 38.7° and for zero sideslip. As noted by Del Frate and Zuniga (1990), "These vortex cores are generated at moderate to high angles of attack by the shape of the forebody and the sharp leading edge of each LEX. The LEX vortex cores are tightly wound and extend downstream until experiencing vortex core breakdown. Visible evidence of the vortex core breakdown is a stagnation of flow in the core with a sudden expansion in the core diameter. Similarly, the forebody vortex cores extend downstream until they interact with the LEX vortices. This interaction results in the forebody vortex cores being pulled beneath the LEX vortices and then redirected outboard."

Lessons learned from comparisons between ground-based tests and flight measurements for the high-angle-of-attack programs on the F-18 High Alpha Research Vehicle (HARV), the X-29 forward-swept wing aircraft, and the X-31 enhanced fighter maneuverability aircraft were presented by Fisher et al. (1998):

> On all three vehicles, Reynolds number effects were evident on the forebodies at high angles of attack. The correlation between flight and wind-tunnel forebody pressure distribution for the F-18 HARV were improved by using twin longitudinal grit strips on the forebody of the wind-tunnel model. Pressure distributions obtained on the X-29 wind-tunnel model at flight Reynolds numbers showed excellent correlation with the flight data up to $\alpha = 50°$, Above $\alpha = 50°$, the pressure

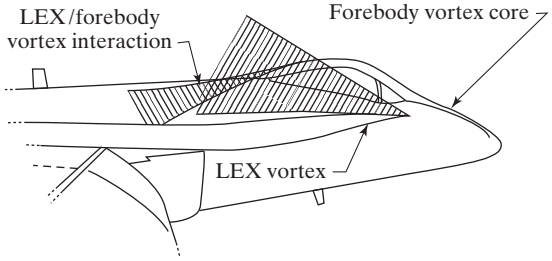

Figure 7.60 Wingtip view of forebody vortex system [from Del Frate and Zuniga (1990)].

distributions for both flight and wind tunnel became asymmetric and showed poorer agreement, possibly because of the different surface finish of the model and aircraft. The detrimental effect of a very sharp nose apex was demonstrated on the X-31 aircraft. Grit strips on the forebody of the X-31 reduced the randomness but increased the magnitude of the asymmetry. Nose strakes were required to reduce the forebody yawing moment asymmetries and the grit strips on the flight test noseboom improved the aircraft handling qualities.

7.11 UNMANNED AIR VEHICLE WINGS

As was mentioned in Chapter 6, unmanned air vehicles (UAV) of various sizes have led to a revolution in airfoil and wing designs in recent years. The tried and true methods for designing wings often can fall short when applied to either very large or very small aircraft, as Reynolds number effects change the basic characteristics of the aerodynamics of these vehicles. In an attempt to classify these vehicles and their resulting aerodynamics, Wood (2002) devised four definitions for the size of unmanned air vehicles (see Table 7.3 and Fig. 7.61). These definitions are used to classify vehicles with similar aerodynamic and technical issues involved in their design.

As was discussed in Chapter 6 for laminar-flow airfoils, as the size of the vehicle decreases (and as weight and Reynolds number also decrease), aspect ratio no longer is the dominant factor in creating drag (see Fig. 7.62)—skin-friction drag becomes more important, hence the low aspect-ratio designs common for micro UAVs [Drela et al. (2003)]. The high-altitude aircraft also fly at low Reynolds numbers but require fairly high weights in order to carry the solar panels and batteries required for propulsion; the high-aspect ratio aircraft once again becomes more efficient. In fact, Drela et al. (2003) found that for each aspect ratio examined there was an aircraft size (weight) that would maximize the range: "this is because, as the aspect ratio increases, the wing is proportionately heavier for a large vehicle than for a smaller vehicle, while at small

TABLE 7.3 Classification of UAVs [Wood (2002)]

UAV Type	*Weight (lbs)*	*Wing Span (ft)*
Micro	<1	<2
Meso	1 to 2,000	2 to 30
Macro	2,000 to 10,000	30 to 150
Mega	$>10{,}000$	>150

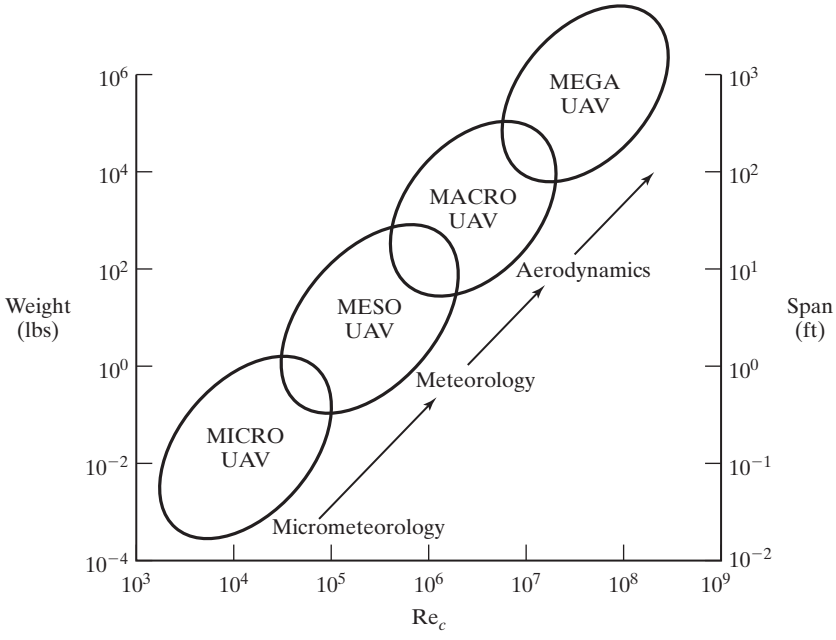

Figure 7.61 Classification of UAVs by weight, span, and Reynolds number [from Wood (2002)].

size, drag is more important so that the increasing friction drag with aspect ratio offsets the reduction in induced drag" [Drela et al. (2003)]. This is related to the well known square-cube law of aircraft design. The weight of the wing varies with the cube of the wing span while the area of the wing varies with the square of the wing span [see for

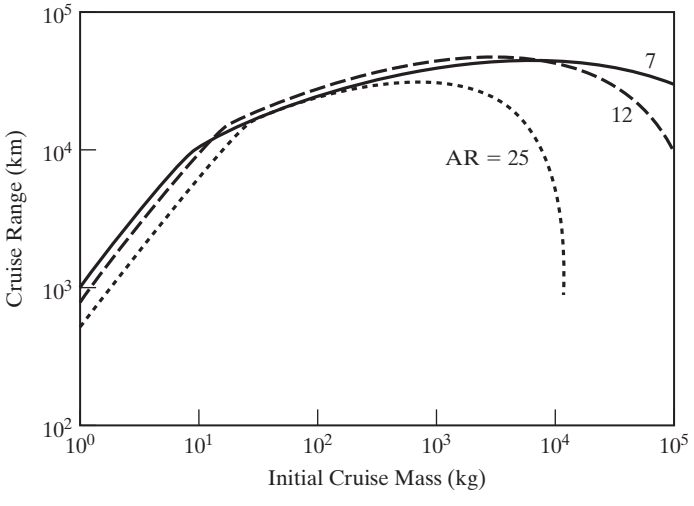

Figure 7.62 The influence of wing aspect ratio on aircraft range as a function of mass (all other factors kept constant) [from Drela et al. (2003)].

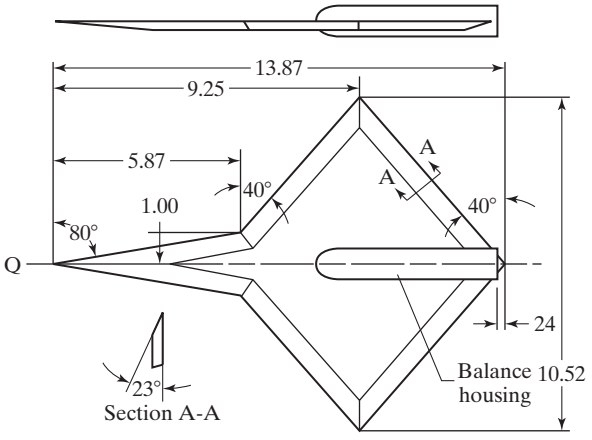

Figure 7.63 Unusual UAV configuration [from Hammons and Thompson (2006)].

example, McMasters (1998)]. This is one of the reasons these wings have such largely different design characteristics. Couple the square-cube law with the various amounts of laminar and turbulent flow the wing can experience, and the resulting wings can be quite unusual when compared with typical aircraft, as shown in Fig. 7.63.

7.12 SUMMARY

The shape of the wing is a dominant parameter in determining the performance and handling characteristics of an airplane. The planform of a wing is defined by the aspect ratio, sweep, and taper ratio. At subsonic speeds, the lift-dependent drag can be reduced by increasing the aspect ratio. A high-aspect-ratio wing produces a high-lift-curve slope, which is useful for takeoff and landing but has a weight penalty since, for a given wing area, more massive root sections are needed to handle the higher bending moments. Furthermore, a swept wing has a greater structural span than a straight wing of the same area and aspect ratio. Thus, the use of sweepback may also lead to a growth in wing weight. As a result, the choice of aspect ratio requires a trade study in which the designer may chose to emphasize one criterion at the expense of another (see the discussion relating to transport aircraft in Chapter 13).

Tapering the wing reduces the wing-root bending moments, since the inboard portion of the wing carries more of the wing's lift than the portion near the tip. While taper reduces the actual loads carried by the outboard sections, the wing-tip sections are subjected to higher lift coefficients and tend to stall first (see Fig. 7.15). Therefore, progressively reducing the incidence of the local section through the use of geometric twist from the root to the tip (i.e., washout) may be used either to reduce local loading or to prevent tip stalling.

PROBLEMS

7.1. Consider an airplane that weighs 13,500 N and cruises in level flight at 250 km/h at an altitude of 2000 m. The wing has a surface area of 15.0 m^2 and an aspect ratio of 5.8. Assume that the lift coefficient is a linear function of the angle of attack and that $\alpha_{0l} = -1.0°$ If the load distribution is elliptic, calculate the value of the circulation in the plane of symmetry

(Γ_0), the downwash velocity (w_{y1}), the induced-drag coefficient (C_{Dv}) the geometric angle of attack ($\propto$), and the effective angle of attack ($\propto_e$).

7.2. Consider the case where the spanwise circulation distribution for a wing is parabolic,

$$\Gamma(y) = \Gamma_0\left(1 - \frac{y}{s}\right)$$

If the total lift generated by the wing with the linear circulation distribution is to be equal to the total lift generated by a wing with an elliptic circulation distribution, what is the relation between the Γ_0 values for the two distributions? What is the relation between the induced downwash velocities at the plane of symmetry for the two configurations?

7.3. When a GA(W)-1 airfoil section (i.e., a wing of infinite span) is at an angle of attack of 5°, the lift coefficient is 0.5. Using equation (7.20), calculate the angle of attack at which a wing whose aspect ratio is 6.5 would have to operate to generate the same lift coefficient. What would the angle of attack have to be to generate this lift coefficient for a wing whose aspect ratio is 5.0?

7.4. Consider a planar wing (i.e., no geometric twist) which has a NACA 0012 section and an aspect ratio of 7.0. Following Example 7.2, use a four-term series to represent the load distribution. Compare the lift coefficient, the induced drag coefficient, and the spanwise lift distribution for taper ratios of **(a)** 0.4, **(b)** 0.5, **(c)** 0.6, and **(d)** 1.0.

7.5. Consider an airplane that weighs 10,000 N and cruises in level flight at 185 km/h at an altitude of 3.0 km. The wing has a surface area of 16.3 m^2, an aspect ratio of 7.52, and a taper ratio of 0.69. Assume that the lift coefficient is a linear function of the angle of attack and the airfoil section is a NACA 2412 (see Chapter 6 for the characteristics of this section). The incidence of the root section is +1.5°; the incidence of the tip section is −1.5°. Thus, there is a geometric twist of −3° (washout). Following Example 7.1, use a four-term series to represent the load distribution and calculate

(a) The lift coefficient (C_L)
(b) The spanwise load distribution ($C_l(y)/C_L$)
(c) The induced drag coefficient (C_{Dv})
(d) The geometric angle of attack (a)

7.6. Use equation (7.38) to calculate the velocity induced at some point $C(x, y, z)$ by the vortex filament AB (shown in Fig. 7.30); that is, derive equation (7.39a).

7.7. Use equation (7.38) to calculate the velocity induced at some point $C(x, y, 0)$ by the vortex filament AB in a planar wing; that is, derive equation (7.44a).

7.8. Calculate the downwash velocity at the CP of panel 1 induced by the horseshoe vortex of panel **4** of the starboard wing for the flow configuration of Example 7.2.

7.9. Following the VLM approach used in Example 7.4, calculate the lift coefficient for a swept wing. The wing has an aspect ratio of 8, a taper ratio of unity (i.e., $c_r = c_t$), and an uncambered section (i.e., it is a flat plate). Since the taper ratio is unity, the leading edge, the quarter-chord line, the three-quarter chord line, and the trailing edge all have the same sweep, 45°. How does the lift coefficient for this aspect ratio (8) compare with that for an aspect ratio of 5 (i.e., that computed in Example 7.4)? Is this consistent with our knowledge of the effect of aspect ratio (e.g., Fig. 7.10)?

7.10. Following the VLM approach used in Example 7.4, calculate the lift coefficient for a swept wing. The wing has an aspect ratio of 5, a taper ratio of 0.5 (i.e., $c_t = 0.5\, c_r$), an uncambered section, and the quarter chord is swept 45°. Since the taper ratio is not unity, the leading edge, the quarter-chord line, the three-quarter-chord line, and the trailing edge have different sweep angles. This should be taken into account when defining the coordinates of the horseshoe vortices and the control points.

7.11. Following the VLM approach used in Example 7.4, calculate the lift coefficient for the forward swept wing of Fig. 7.24b. The quarter chord is swept forward 45°, the aspect ratio is 3.55, and the taper ratio 0.5. The airfoil section (perpendicular to the quarter chord) is a NACA 64A112. For this airfoil section $\alpha_{o2} = -0.94°$ and $C_{l,\alpha} = 6.09$ per radian. For purposes of applying the no-flow boundary condition at the control points, assume that the wing is planar. Prepare a graph of the lift coefficient. How does this compare with that of Fig. 7.24?

7.12. Following the VLM approach used in Example 7.4, calculate the lift coefficient for a delta wing whose aspect ratio is 1.5. What is the sweep angle of the leading edge? The fact that the quarter-chord and the three-quarter-chord lines have different sweeps should be taken into account when defining the coordinates of the horseshoe vortices and the control points. How do the calculated values for the lift coefficient compare with the experimental values presented in Fig. 7.45?

7.13. Use equation (7.61) to calculate the lift coefficient as a function of the angle of attack for a flat delta wing with sharp leading edges. The delta wing has an aspect ratio of 1.0. Compare the solution with the data of Fig. 7.44.

7.14. Use equation (7.62) to calculate the induced drag for a flat delta wing with sharp leading edges. The delta wing has an aspect ratio of 1.0. Compare the solution with the data of Fig. 7.47.

7.15. Assume that the wing area of an airplane is proportional to the square of the wing span and the volume, and thus the weight, is proportional to the cube of the wing span (this is the square-cube law). Find the wing loading of the aircraft as a function of wing span, b. Using these relationships explain why very large aircraft (like the Boeing 747 or the Airbus 380) have to fly with very large wing loadings. If you wanted to re-design an existing aircraft that weighed 82,000 lbs with a wing span of 65 ft, what wing span would you need to add an additional 20% to the weight?

REFERENCES

Abbott IH, von Doenhoff AE. 1949. *Theory of Wing Sections*. New York: Dover

Anderson JD, Corda S, Van Wie DM. 1980. Numerical lifting line theory applied to drooped leading-edge wings below and above stall. *J. Aircraft* 17:898–904

Bartlett GE, Vidal RJ. 1955. Experimental investigations of influence of edge shape on the aerodynamic characteristics of low aspect ratio wings at low speeds. *J. Aeron. Sci.* 22:517–533, 588

Bridges DH. 2005. Finite wing lift-curve slope calculations using lifting-line theory. Presented at Appl. Aerodyn. Conf., 23rd, AIAA Paper 2005-4839, Toronto, Canada

Bristow DR, Grose GG. 1978. Modification of the Douglas Neumann program to improve the efficiency of predicting component and high lift characteristics. *NASA CR 3020*

Cobleigh BR. 1994. High-angle-of-attack yawing moment asymmetry of the X-31 aircraft from flight test. Presented at Appl. Aerodyn. Conf., 12th, AIAA Pap. 94–1803, Colorado Springs, CO

Cummings RM, Rizk YM, Schiff LB, Chaderjian NM. 1992. Navier-Stokes prediction for the F-18 wing and fuselage at large incidence. *J. Aircraft* 29: 565–574

Del Frate JH, Zuniga FA. 1990. In-flight flow field analysis on the NASA F-18 high alpha research vehicle with comparison to the ground facility data. Presented at AIAA Aerosp. Sci. Meet., 28th, AIAA Pap. 90-0231, Reno, NV

Dornheim MA. 1994. X-31, F-16 MATV, F/A-18 HARV explore diverse missions. *Aviat. Week Space Tech.* 140:46–47

Drela M, Protz JM, Epstein AH. 2003. The role of size in the future of aeronautics. Presented at Intl. Air Space Symp., AIAA Pap. 2003–2902, Dayton, OH

Ericsson LE, Reding JP. 1986. Asymmetric vortex shedding from bodies of revolution. In *Tactical Missile Aerodynamics*, Ed. Hemsch MH, Nielsen JN. Washington, DC: AIAA

Erickson GE. 1982. Vortex flow correlation. Presented at Congr. Intl. Coun. Aeron. Sci., 13th, ICAS Pap. 82–6.61, Seattle, WA

Erickson GE, Hall RM, Banks DW, DelFrate JH, Schreiner JA, Hanley RJ, Pulley CT. 1989. Experimental investigation of the F/A-18 vortex flows at subsonic through transonic speeds. Presented at Appl. Aerodyn. Conf., 7th, AIAA Pap. 89–2222, Seattle, WA

Falkner VM. 1943. The calculation of aerodynamic loading on surfaces of any shape. *ARC R&M 1910*

Fisher DF, Cobleigh BR, Banks, DW, Hall RM, Wahls RA. 1998. Reynolds number effects at high angles of attack. Presented at Adv. Meas. Ground Test. Tech. Conf., 20th, AIAA Pap. 98–2879, Albuquerque, NM

Glauert H. 1948. *The Elements of Aerofoil and Airscrew Theory*. Cambridge: Cambridge University Press

Gloss BB, Washburn KE. 1978. Load distribution on a close-coupled wing canard at transonic speeds. *J. Aircraft* 15:234–239

Hammons C, Thompson DS. 2006. A numerical investigation of novel planforms for micro UAVs. Presented at AIAA Aerosp. Sci. Meet., 44th, AIAA Pap. 2006–1265, Reno, NV

Henderson WP. 1966. Studies of various factors affecting drag due to lift at subsonic speeds. *NASA Tech. Note D-3584*

Herbst WB. 1980. Future fighter technologies. *J. Aircraft* 17:561–566

Hess JL, Smith AMO. 1962. Calculation of nonlifting potential flow about arbitrary three-dimensional bodies. Douglas Aircraft Company Report ES40622

Hummel D. 2004. Effects of boundary layer formation on the vortical flow above a delta wing. Presented at NATO RTO Appl. Veh. Tech. Spec. Meet., RTO-MP-AVT-111, Paper 30-1, Prague, Czech Republic.

Johnson FT. 1980. A general panel method for the analysis and design of arbitrary configurations in incompressible flows. *NASA CR 3079*

Kalman TP, Giesing JP, Rodden WP. 1970. Spanwise distribution of induced drag in subsonic flow by the vortex lattice method. *J. Aircraft* 7:574–576

Kalman TP, Rodden WP, Giesing JP. 1971. Application of the doublet-lattice method to nonplanar configurations in subsonic flow. *J. Aircraft* 8:406–413

Komerath NMS, Liou SG, Schwartz RJ, Kim JM. 1992. Flow over a twin-tailed aircraft at angle of attack; part I: spatial characteristic. *J. Aircraft* 29:413–420

Lamar JE, Gloss BB. 1975. Subsonic aerodynamic characteristics of interacting lifting surfaces with separated flow around sharp edges predicted by vortex-lattice method. *NASA Tech. Note D-7921*

Lamar JE, Frink NT. 1982. Aerodynamic features of designed strake-wing configurations. *J. Aircraft* 19:639–646

Margason RJ, Lamar JE. 1971. Vortex-lattice Fortran program for estimating subsonic aerodynamic characteristics of complex planforms. *NASA Tech. Note D-6142*

Margason RJ, Kjelgaard SO, Sellers WL, Morris CEK, Walkey KB, Shields EW. 1985. Subsonic panel methods—a comparison of several production codes. Presented at AIAA Aerosp. Sci. Meet., 23rd, AIAA Pap. 85–0280, Reno, NV

McKinney LW, Dollyhigh SM. 1971. Some trim drag considerations for maneuvering aircraft. *J. Aircraft* 8:623–629

McMasters JH.1998. Advanced configurations for very large transport airplanes. *Aircraft Design* 1:217–242

Mendenhall MR, Perkins SC. 1996. Predicted high-α aerodynamic characteristics of maneuvering aircraft. Presented at Appl. Aerodyn. Conf., 14th, AIAA Pap. 96–2433, New Orleans, LA

Multhopp H. 1950. Method for calculating the lift distribution of wings (subsonic lifting surface theory). *ARC T&M 2884*

Orloff KL. 1980. Spanwise lift distribution on a wing from flowfield velocity surveys. *J. Aircraft* 17:875–882

Peckham DH. 1958. Low-speed wind tunnel tests on a series of uncambered slender pointed wings with sharp edges. *ARC R&M 3186*

Phillips WF, Snyder DO. 2000. Application of lifting-line theory to systems of lifting surfaces. Presented at AIAA Aerosp. Sci. Meet., 38th, AIAA Pap. 2000–0653, Reno, NV

Polhamus ED. 1971a. Predictions of vortex-lift characteristics by a leading-edge suction analogy. *J. Aircraft* 8:193–199

Polhamus ED. 1971b. Charts for predicting the subsonic vortex-lift characteristics of arrow, delta, and diamond wings. *NASA Tech. Note D-6243*

Prandtl L. 1921. Application of modern hydrodynamics to aeronautics. *NACA Report 116*

Prandtl L, Tietjens OG. 1957. *Applied Hydro- and Aeromechanics*. New York: Dover

Rasmussen ML, Smith DE. 1999. Lifting-line theory for arbitrarily shaped wings. *J. Aircraft* 36:340–348

Robinson A, Laurmann JA. 1956. *Wing Theory*. Cambridge: Cambridge University Press

Schlichting H. 1960. Some developments in boundary layer research in the past thirty years. *J. Roy. Aeron. Soc*. 64:64–79

Schlichting H, Truckenbrodt E. 1969. *Aerodynamik des Flugzeuges*. Berlin: Spring-Verlag

Sivells JC. 1947. Experimental and calculated characteristics of three wings of NACA 64-210 and 65-210 airfoil sections with and without washout. *NACA Tech. Note 1422*

Spalart PR, Allmaras R. 1992. A one-equation turbulence model for aerodynamics flows. Presented at AIAA Aerosp. Sci. Meet., 30th, AIAA Pap. 92–0439, Reno, NV

Spreiter JR, Sacks, AH. 1951. The rolling up of the vortex sheet and its effect on the downwash behinds wings. *J. Aeron. Sci*. 18:21–32

Stanbrook A, Squire LC. 1964. Possible types of flow at swept leading edges. *The Aeron. Quart*. 15:72–82

Strang WZ, Tomaro RF, Grismer MJ. 1999. The defining methods of $Cobalt_{60}$: a parallel, implicit, unstructured Euler/Navier-Stokes flow solver. Presented at AIAA Aerosp. Sci. Meet., 37th, AIAA Pap. 99–0786, Reno, NV

Stuart WG. 1978. *Northrop F-5 Case Study in Aircraft Design*. Washington, DC: AIAA

Visbal MR. 1995. Computational and physical aspects of vortex breakdown on delta wings. Presented at AIAA Aerosp. Sci. Meet., 33rd, AIAA Pap. 95–0585, Reno, NV

Voight W. 1976. Gestation of the swallow. *Air Intern*. 10:135–139, 153

Weber J, Brebner GG. 1958. Low-speed tests on 45-deg swept-back wings, part I: pressure measurements on wings of aspect ratio 5. *ARC R&M 2882*

Wood RM. 2002. A discussion of aerodynamic control effectors for unmanned air vehicles. Presented at Tech. Conf. Workshop Unmanned Aerosp. Veh., 1st, AIAA Pap. 2002–3494, Portsmouth, VA

Wurtzler KE, Tomaro RF. 1999. Unsteady aerodynamics of aircraft maneuvering at high angle of attack. Presented at DoD High Perf. Comp. User's Group Meet., Monterey, CA

8 DYNAMICS OF A COMPRESSIBLE FLOW FIELD

Chapter Objectives

- Understand the basic thermodynamic concepts that form the basis of high-speed flow theory
- Develop a basic physical understanding of the second law of thermodynamics
- Be able to use the isentropic flow relationships in analyzing the properties of a flow field
- Develop the ability to analyze flow in a stream tube, and understand how a converging-diverging nozzle works
- Be able to analyze flow fields using shock and expansion calculation methods
- Be able to calculate the local skin-friction coefficient for a compressible boundary layer
- Understand the cause and effect of shock/boundary layer and shock/shock interactions
- Determine how flight vehicles are tested in wind tunnels, and understand why it is difficult to fully model full-scale flight characteristics

So far we have studied the aerodynamic forces for incompressible (constant density) flows past an airplane. At low flight Mach numbers (e.g., below a free-stream Mach number M_∞ of approximately 0.3), Bernoulli's equation [equation (3.10)] provides the

relation between the pressure distribution about an aircraft and the local velocity changes of the air as it flows around the various components of the vehicle. However, as the flight Mach number increases, changes in the local air density also affect the magnitude of the local static pressure. This leads to discrepancies between the actual aerodynamic forces and those predicted by incompressible flow theory. For our purposes, the Mach number is the parameter that determines the extent to which compressibility effects are important. The purpose of this chapter is to introduce those aspects of compressible flows (i.e., flows in which the density is not constant) that have applications to aerodynamics.

Throughout this chapter, air will be assumed to behave as a thermally perfect gas (i.e., the gas obeys the equation of state):

$$p = \rho RT \tag{1.10}$$

We will assume that the gas is also calorically perfect; that is, the specific heats, c_p and c_v, of the gas are constant. These specific heats are discussed further in the next section. The term *perfect gas* will be used to describe a gas that is both thermally and calorically perfect. At extremely high Mach numbers, however, the specific heats may not be constant, leading to difficulties with the perfect gas assumption (see Chapter 12 for more details).

Even though we turn our attention in this and in the subsequent chapters to compressible flows, we may still divide the flow around the vehicle into: (1) the boundary layer near the surface, where the effects of viscosity and heat conduction are important, and (2) the external flow, where the effects of viscosity and heat conduction can be neglected. As has been true in previous chapters, the inviscid flow field is conservative.

8.1 THERMODYNAMIC CONCEPTS

Having reviewed the fundamentals of thermodynamics in Chapter 2 and having derived the energy equation there, we will now turn our attention to the related aerodynamic concepts.

8.1.1 Specific Heats

For simplicity (and without loss of generality), we will consider a system in which there are no changes in the kinetic and the potential energies. For these types of systems, equations (2.23) and (2.24a) become:

$$\delta q - p\, dv = du_e \tag{8.1}$$

As an extension of our discussion of fluid properties in Chapter 1, we should remember that, for any simple substance, the specific internal energy is a function of any other two independent fluid properties. Therefore, the internal energy can be represented as $u_e = u_e(v, T)$. Then, by the chain rule of differentiation,

$$du_e = \left(\frac{\partial u_e}{\partial T}\right)_v dT + \left(\frac{\partial u_e}{\partial v}\right)_T dv \tag{8.2}$$

where the subscript is used to designate which variable is constant during the partial differentiation process.

From the principles of thermodynamics, we may show for a thermally perfect gas (one obeying the perfect gas law),

$$\left(\frac{\partial u_e}{\partial v}\right)_T = 0$$

which is equivalent to saying that the internal energy of a perfect gas does not depend on the specific volume or, equivalently, the density, and therefore depends on the temperature alone. Using this observation, equation (8.2) becomes:

$$du_e = \left(\frac{\partial u_e}{\partial T}\right)_v dT = c_v\, dT \tag{8.3}$$

In equation (8.3), we have introduced the definition that:

$$c_v \equiv \left(\frac{\partial u_e}{\partial T}\right)_v$$

which is the *specific heat at constant volume*. Now we can evaluate the change in the internal energy for a process as:

$$\Delta u_e = u_{e\,2} - u_{e\,1} = \int_1^2 c_v\, dT \tag{8.4}$$

Experimental evidence indicates that for most gases, c_v is constant over a wide range of conditions. Specifically, for air below a temperature of approximately 850 K and over a wide range of pressure, c_v can be treated as a constant; the value for air is:

$$c_v = 717.6\frac{\text{N}\cdot\text{m}}{\text{kg}\cdot\text{K}}\left(\text{or}\ \frac{\text{J}}{\text{kg}\cdot\text{K}}\right) = 0.1717\frac{\text{Btu}}{\text{lbm}\cdot{}^\circ\text{R}} = 4299\frac{\text{ft}\cdot\text{lbf}}{\text{slug}\cdot{}^\circ\text{R}}$$

The assumption that c_v is constant is contained within the more general assumption that the gas is a perfect gas. So, for a perfect gas:

$$\Delta u_e = c_v\, \Delta T \tag{8.5}$$

Since c_v and T are both properties of the fluid, and since the change in a property between any two given states is independent of the process used in going between the two states, equation (8.5) is valid even if the process is not one of constant volume. Therefore, equation (8.5) is valid for any simple substance undergoing any process where c_v can be treated as a constant.

Substituting equation (8.3) into equation (8.1), we can see that c_v is only directly related to the heat transfer if the process is one in which the volume remains constant (i.e., $dv = 0$). However, the name "specific heat" can be misleading. Physically, c_v is the proportionality constant between the amount of heat transferred to a substance and the temperature rise in the substance held at constant volume.

In analyzing many flow problems, the terms u_e and pv appear as a sum, and so it is convenient to define a symbol for this sum:

$$h \equiv u_e + pv \equiv u_e + \frac{p}{\rho} \tag{8.6}$$

where h is called the *specific enthalpy*. Substituting the differential form of equation (8.6) into equation (8.1) and collecting terms yields:

$$\delta q + v\,dp = dh \tag{8.7}$$

which is the first law of thermodynamics expressed in terms of the enthalpy rather than the internal energy.

Since any property of a simple substance can be written as a function of any two other properties, we can also write the enthalpy as a function of pressure and temperature:

$$h = h(p, T) \tag{8.8}$$

Again, using the chain rule:

$$dh = \left(\frac{\partial h}{\partial p}\right)_T dp + \left(\frac{\partial h}{\partial T}\right)_p dT \tag{8.9}$$

From the definition of enthalpy in equation (8.8), we can show that h is also a function of temperature only for a thermally perfect gas, since both u_e and p/ρ are functions of the temperature only. So,

$$\left(\frac{\partial h}{\partial p}\right)_T = 0$$

and equation (8.9) becomes:

$$dh = \left(\frac{\partial h}{\partial T}\right)_p dT = c_p\,dT \tag{8.10}$$

Here we have introduced the definition:

$$c_p \equiv \left(\frac{\partial h}{\partial T}\right)_p \tag{8.11}$$

which is the *specific heat at constant pressure*. In general, c_p depends on the composition of the substance and its pressure and temperature. We can show that:

$$\Delta h = h_2 - h_1 = \int_1^2 c_p\,dT \tag{8.12}$$

Experimental evidence indicates that for most gases c_p is essentially independent of temperature and of pressure over a wide range of conditions. Again, provided that the temperature extremes in a flow field are not too widely separated, c_p can be treated as a constant so that

$$\Delta h = c_p\,\Delta T \tag{8.13}$$

For air below a temperature of approximately 850 K, the value of c_p is:

$$c_p = 1005\,\frac{\mathrm{N\cdot m}}{\mathrm{kg}}\left(\text{or } \frac{\mathrm{J}}{\mathrm{kg\cdot K}}\right) = 0.2404\,\frac{\mathrm{Btu}}{\mathrm{lbm}\cdot{}^\circ R} = 6019\frac{\mathrm{ft\cdot lbf}}{\mathrm{slug}\cdot{}^\circ\mathrm{R}}$$

An argument parallel to that used for c_v shows that equation (8.13) is valid for any simple substance undergoing any process where c_p can be treated as a constant. Again,

we note that the term *specific heat* is somewhat misleading, since c_p is only directly related to the heat transfer if the process is isobaric.

8.1.2 Additional Important Relations

A gas which is thermally and calorically perfect is one that obeys equations (1.10), (8.5), and (8.13). In such a case, there is a simple relation between c_p, c_v, and R. From the definitions of c_p and h, the perfect-gas law, and the knowledge that h depends upon T alone, we can write:

$$c_p \equiv \left(\frac{\partial h}{\partial T}\right)_p = \frac{dh}{dT} = \frac{du_e}{dT} + \frac{d}{dT}\left(\frac{p}{\rho}\right) = c_v + R \tag{8.14}$$

or $R = c_p - c_v$. We can now introduce the definition for the *ratio of specific heats:*

$$\gamma \equiv \frac{c_p}{c_v} \tag{8.15}$$

For the most simple molecular model, the kinetic theory of gases shows that:

$$\gamma = \frac{n + 2}{n}$$

where n is the number of degrees of freedom for the molecule. So, for a monatomic gas, such as helium, $n = 3$ and $\gamma = 1.667$. For a diatomic gas, such as nitrogen, oxygen, or air, $n = 5$ and $\gamma = 1.400$. Extremely complex molecules, such as Freon or tetrafluoromethane, have large values of n and values of γ which approach unity. In many treatments of air at high temperature and high pressure, approximate values of γ (e.g., 1.1 to 1.2) are used to approximate "real-gas" effects.

Combining equations (8.14) and (8.15), we can write:

$$c_p = \frac{\gamma R}{\gamma - 1} \text{ and } c_v = \frac{R}{\gamma - 1} \tag{8.16}$$

which can be very useful when manipulating thermodynamics relations.

8.1.3 Second Law of Thermodynamics and Reversibility

The first law of thermodynamics does not place any constraints regarding what types of processes are physically possible and what types are not, providing that equation (2.22) is satisfied. However, we know from experience and observation that not all processes permitted by the first law actually occur in nature. For instance, when you rub sandpaper across a table, both the sandpaper and the table experience a rise in temperature. The first law is satisfied because the work done on the system by the sander's arm, which is part of the surroundings and which is, therefore, negative work for equation (2.23), is manifested as an increase in the internal energy of the system, which consists of the sandpaper and the table. Therefore, the temperatures of the sandpaper and the table increase. However, we do not expect that we can somehow reverse the process and extract all the work back from the system and have the internal energy (and thus the temperature)

decrease back to its original value, even though the first law would be satisfied. If this could occur, we would say the process was reversible, because the system and its surroundings would be restored to their original states.

The possibility of devising a reversible process, such as the type outlined previously, cannot be settled by a theoretical proof. Experience shows that a truly reversible process has never been devised; this empirical observation is embodied in the *second law of thermodynamics*. For our purposes, an irreversible process is one that involves viscous (friction) effects, shock waves, or heat transfer through a finite temperature gradient. Therefore, in regions outside boundary layers, viscous wakes, and planar shock waves, we can treat the flow as reversible. Notice that the flow behind a curved shock wave can be treated as reversible only along a streamline, which we will see later in this chapter.

The second law of thermodynamics provides a way to quantitatively determine the degree of reversibility (or irreversibility) of a process. Since the effects of irreversibility are dissipative and represent a loss of available energy (e.g., the kinetic energy of an aircraft wake, which is converted to internal energy by viscous stresses, is directly related to the aircraft's drag), the reversible process provides an ideal standard for comparison to real processes. Therefore, the second law is a valuable tool available to the aerodynamicist, since it gives limits to various processes.

There are several logically equivalent statements of the second law. In the remainder of this text, we will usually be considering adiabatic processes, processes in which there is no heat transfer. This is not a restrictive assumption, since heat transfer in aerodynamic problems usually occurs only in the boundary layer and has a negligible effect on the flow in the inviscid region. The most convenient statement of the second law, for our purposes, is:

$$ds \geq 0 \tag{8.17}$$

for an adiabatic process. Therefore, when a system is isolated from all heat exchange with its surroundings, s, the entropy of the system either remains the same (if the process is reversible) or increases (if it is irreversible). It is not possible for a process to occur if the entropy of the system and its surroundings decreases. Just as the first law leads to the definition of internal energy as a property, the second law leads to the definition of entropy as a property.

The entropy change for a reversible process can be written as:

$$\delta q = T\,ds$$

For a reversible process in which the only work done is that done at the moving boundary of the system,

$$T\,ds = du_e + p\,dv \tag{8.18}$$

However, once we have written this equation, we see that it involves only changes in properties and does not involve any path-dependent functions. We conclude, therefore, that this equation is valid for all processes, both reversible and irreversible, and that it applies to the substance undergoing a change of state as the result of flow across the boundary of an open system (i.e., a control volume), as well as to the substance comprising a closed system (i.e., a control mass).

For a perfect gas, we can rewrite equation (8.18) as

$$ds = c_v \frac{dT}{T} + R \frac{dv}{v}$$

This equation can be integrated to give

$$s_2 - s_1 = c_v \ln\left\{\left[\left(\frac{v_2}{v_1}\right)^{\gamma-1}\right]\frac{T_2}{T_1}\right\} \tag{8.19a}$$

Applying the equation of state for a perfect gas to the two states (states 1 and 2) yields:

$$\frac{v_2}{v_1} = \frac{\rho_1}{\rho_2} = \frac{p_1}{p_2}\frac{T_2}{T_1}$$

and equation (8.19a) can be written as:

$$s_2 - s_1 = R \ln\left\{\left[\left(\frac{T_2}{T_1}\right)^{\gamma/(\gamma-1)}\right]\frac{p_1}{p_2}\right\} \tag{8.19b}$$

Equivalently, we can write equation (8.19a) as:

$$s_2 - s_1 = c_v \ln\left\{\left[\left(\frac{\rho_1}{\rho_2}\right)^{\gamma}\right]\frac{p_2}{p_1}\right\} \tag{8.19c}$$

Using the various forms of equation (8.19), we can calculate the entropy change in terms of the properties of the end states [in terms of the specific volume and temperature using equation (8.19a), pressure and temperature using equation (8.19b), or density and pressure using equation (8.19c)].

In many compressible flow problems, the flow external to the boundary layer undergoes processes that are isentropic (i.e., adiabatic and reversible). If the entropy is constant at each step of the process, it follows from equation (8.19) that p, ρ, and T are interrelated since $s_2 - s_1 = 0$. The following equations describe these important relations for isentropic flow:

$$\frac{p}{\rho^{\gamma}} = \text{constant} \tag{8.20a}$$

$$\frac{T^{\gamma/(\gamma-1)}}{p} = \text{constant} \tag{8.20b}$$

and

$$Tv^{(\gamma-1)} = \text{constant} \tag{8.20c}$$

which we will use a great deal in our descriptions of high-speed flow.

Aerodynamics Concept Box: Original Statements of the Second Law

The concept of entropy can be very confusing to most people, especially when it gets lost in mathematics and thermodynamic relations. Perhaps you will agree with an early thermodynamicist, William Gibbs, who said in 1873, "Any method involving the notion of entropy, the very existence of which depends on the second law of thermodynamics, will doubtless seem to many far-fetched, and may repel beginners as obscure and difficult of comprehension." The second law, however, was not originally based on such grandiouse concepts or equations,

but instead it was based on some fairly straightforward observations by scientists like Carnot, Clausius, and Kelvin. Here is what they observed:

> Carnot observation (made by Sadi Carnot in 1824): The natural tendency of the heat is to flow from high temperature reservoir to low temperature reservoir.
>
> Clausius statement (made by Rudolph Clausius in 1850; Clausius was later to introduce the concept of entropy): No process is possible whose sole result is the transfer of heat from a body of lower temperature to a body of higher temperature.
>
> Kelvin statement (made by William Thompson, Lord Kelvin in 1851; also called the Kelvin-Planck statement): No process is possible in which the sole result is the absorption of heat from a reservoir and its complete conversion into work.
>
> Carnot's theorem: All irreversible heat engines between two heat reservoirs are less efficient than a Carnot engine operating between the same reservoirs. All reversible heat engines between two heat reservoirs are equally efficient with a Carnot engine operating between the same reservoirs.

These observations eventually led to our use of entropy and the second law of thermodynamics, which states that for an isolated system,

$$\Delta s \geq 0$$

All of our equations and relationships are simply a way of putting these observations into equation form so that we can calculate entropy changes and determine if a process is possible.

8.1.4 Speed of Sound

From experience, we know that the speed of sound in air is finite. To be specific, the *speed of sound* is defined as the rate at which infinitesimal disturbances are propagated from their source into an undisturbed medium. These disturbances can be thought of as small pressure pulses generated at a point and propagated in all directions. We will learn later that finite disturbances such as shock waves propagate at a greater speed than that of sound waves.

Consider a motionless point source of disturbance in quiescent, homogeneous air (as shown in Fig. 8.1a). Small disturbances generated at the point move outward from the point in a spherically symmetric pattern. The distance between wave fronts is determined by the frequency of the disturbance. Since the disturbances are small, they leave the air behind them in essentially the same state it was before they arrived. The radius of a given wave front is given by:

$$r = at \tag{8.21}$$

where a is the speed of propagation (the speed of sound or the acoustic speed) of the wave front and t is the time since the particular disturbance was generated.

Now, suppose that the point source begins moving from right to left at a constant speed U which is less than the speed of sound a; the wave-front pattern will now appear as shown in Fig. 8.1b. A stationary observer ahead of the source will detect an increase in frequency of the sound, while an observer behind the source will note a decrease in

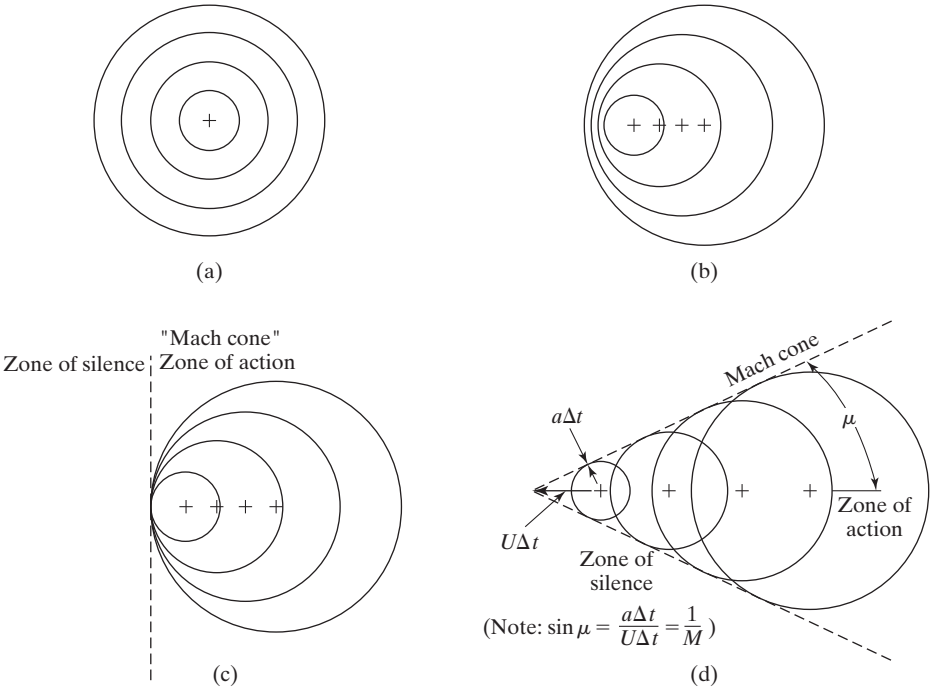

Figure 8.1 Wave pattern generated by pulsating disturbance of infinitesimal strength: (a) disturbance is stationary ($U = 0$); (b) disturbance moves to the left at subsonic speed ($U < a$); (c) disturbance moves to the left at sonic speed ($U = a$); (d) disturbance moves to the left at supersonic speed ($U > a$).

frequency (which is known as the Doppler effect). Still, however, each wave front is separate from its neighbors.

If the speed of the source reaches the speed of sound ($U = a$) in the undisturbed medium, the situation will appear as shown in Fig. 8.1c. We notice that the individual wave fronts are still separate, except at the point where they coalesce at the position of the source.

A further increase in source speed, such that $U > a$, leads to the situation depicted in Fig. 8.1d. The wave fronts now form a conical envelope, which is known as the *Mach cone*, within which the disturbances can be detected. Outside of this "zone of action" is the "zone of silence," where the pressure pulses have not arrived and an observer cannot sense the source.

We see that there is a fundamental difference between subsonic ($U < a$) and supersonic ($U > a$) flow. In subsonic flow, the effect of a disturbance propagates upstream of its location, and the upstream flow is "warned" of the approach of the disturbance. In supersonic flow, however, no such "warning" is possible. Stating it another way, disturbances cannot propagate upstream in a supersonic flow relative to a source-fixed observer. This fundamental difference between the two types of flow has significant consequences on the flow field about an aircraft and its design.

We can see that the half-angle of the Mach cone dividing the zone of silence from the zone of action is given by:

$$\sin \mu = \frac{1}{M} \tag{8.22}$$

where

$$M \equiv \frac{U}{a}$$

is the Mach number, first defined by Ernst Mach in 1877. At $M = 1$ (i.e., when $U = a$), $\mu = 90°$ and as $M \to \infty$, $\mu \to 0$.

To determine the speed of sound a, look at the wave front in Fig. 8.1a propagating into still air. A small portion of the curved wave front can be treated as planar. To an observer attached to the wave, the situation appears as shown in Fig. 8.2, where a control volume is also shown attached to the wave. The boundaries of the volume are selected so that the flow is normal to faces parallel to the wave and tangent to the other faces. We make the key assumption (based on experimental observation) that since the strength of the disturbance is infinitesimal, a fluid particle passing through the wave undergoes a process that is both reversible and adiabatic (i.e., isentropic).

The integral forms of the continuity and the momentum equations for a one-dimensional, steady, inviscid flow, equations (2.5) and (2.13), respectively, applied to the control volume of Fig. 8.2 give:

$$\rho a \, dA = (\rho + d\rho)(a + dU) \, dA \tag{8.23}$$

$$p \, dA - (p + dp) \, dA = [(a + dU) - a] \rho a \, dA \tag{8.24}$$

Simplifying equation (8.24), dividing equations (8.23) and (8.24) by dA, and combining the two relations give:

$$dp = a^2 \, d\rho \tag{8.25}$$

However, since the process we are considering is isentropic,

$$a^2 = \left(\frac{\partial p}{\partial \rho} \right)_s \tag{8.26}$$

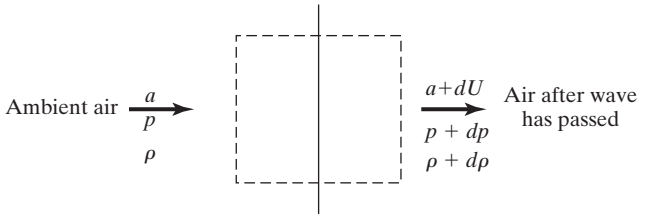

Figure 8.2 Control volume used to determine the speed of sound. (A velocity of equal magnitude and of opposite direction has been superimposed on a wave of Fig. 8.1a so that the sound wave is stationary in this figure.)

where we have indicated that the derivative is taken with entropy fixed, as originally assumed.

For a perfect gas undergoing an isentropic process, equation (8.20a) gives

$$p = c\rho^{\gamma}$$

where c is a constant. Therefore we can write,

$$a^2 = \left(\frac{\partial p}{\partial \rho}\right)_s = \gamma c \rho^{\gamma-1} = \frac{\gamma p}{\rho} \tag{8.27}$$

Using the equation of state for a perfect gas, the speed of sound becomes:

$$a = \sqrt{\frac{\gamma p}{\rho}} = \sqrt{\gamma R T} \tag{8.28}$$

which is the commonly used relation for the acoustic speed, showing that it is only a function of the fluid and the temperature. Be very careful to only use temperatures in equation (8.28) which are absolute (K or $^\circ R$).

8.2 ADIABATIC FLOW IN A VARIABLE-AREA STREAMTUBE

For purposes of derivation, consider the one-dimensional flow of a perfect gas through a variable-area streamtube (as shown in Fig. 8.3). We will apply the integral form of the energy equation [i.e., equation (2.35)] for steady, one-dimensional flow with no change in potential energy. We will also assume that there is no heat transfer through the surface of the control volume (i.e., $\dot{Q} = 0$) and that only flow work (pressure-volume work) is done (as discussed in Section 2.9.3). Work is done on the system by the pressure forces acting at station 1 (which is negative), and work is done by the system at station 2 (which is positive). Therefore, the energy equation applied to the control volume gives:

$$+p_1 U_1 A_1 - p_2 U_2 A_2 = -\left(u_{e1}\rho_1 U_1 A_1 + \frac{U_1^2}{2}\rho_1 U_1 A_1\right) + \left(u_{e\,2}\rho_2 U_2 A_2 + \frac{U_2^2}{2}\rho_2 U_2 A_2\right)$$

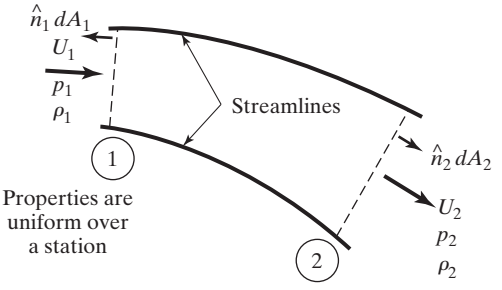

Figure 8.3 One-dimensional flow in a streamtube.

Rearranging and noting that $\rho_1 U_1 A_1 = \rho_2 U_2 A_2$ by continuity, and using the definition for the enthalpy ($h \equiv u_e + pv$), we obtain:

$$H_t = h_1 + \frac{U_1^2}{2} = h_2 + \frac{U_2^2}{2} \tag{8.29}$$

where H_t is the total enthalpy. As is usually the case in aerodynamics problems, changes in potential energy have been neglected. The assumption of one-dimensional flow is valid provided that the streamtube cross-sectional area varies smoothly and gradually in comparison to the axial distance along the streamtube.

For a perfect gas, equation (8.29), in conjunction with equation (8.13), becomes:

$$c_p T_1 + \frac{U_1^2}{2} = c_p T_2 + \frac{U_2^2}{2} \tag{8.30}$$

or

$$T_1 + \frac{U_1^2}{2c_p} = T_2 + \frac{U_2^2}{2c_p} \tag{8.31}$$

which is the conservation of energy for the flow of Fig. 8.3. By definition, the *stagnation temperature* T_t is the temperature reached when the fluid is brought to rest adiabatically. The total temperature from equation (8.31) can be thought of as the sum of the static temperature and the dynamic temperature:

$$T_t = T + \frac{U^2}{2c_p} = T_{static} + T_{dynamic} = \text{constant} \tag{8.32}$$

Since the locations of stations 1 and 2 are arbitrary,

$$T_{t1} = T_{t2} \tag{8.33}$$

That is, the stagnation temperature is a constant for the adiabatic flow of a perfect gas and will be designated simply as T_t. Notice that, whereas it is generally true that the stagnation enthalpy is constant for an adiabatic flow, as indicated by equation (8.29), the stagnation temperature is constant only when c_p is constant (i.e., the gas behaves as a perfect gas).

For any one-dimensional adiabatic flow, equation (8.32) coupled with equation (8.16) can be rewritten as:

$$\frac{T_t}{T} = 1 + \frac{U^2}{2[\gamma R/(\gamma - 1)]T} = 1 + \frac{\gamma - 1}{2} M^2 \tag{8.34}$$

which is the total temperature ratio for the isentropic flow of a perfect gas. Notice that we have used the perfect-gas relations that $c_p = \gamma R/(\gamma - 1)$ and that $a^2 = \gamma RT$.

It is interesting to note that when the flow is isentropic, Euler's equation, equation (3.2), for one-dimensional, steady flow (i.e., the inviscid-flow momentum equation) gives the same result as the energy equation for an adiabatic flow. To see this, we can write equation (3.2) for steady, one-dimensional, inviscid flow:

$$\rho u \frac{du}{ds} = -\frac{dp}{ds} \tag{8.35a}$$

$$\int \frac{dp}{\rho} + \int u\, du = 0 \tag{8.35b}$$

Notice that for a one-dimensional flow $u = U$. For an isentropic process (which is of course adiabatic),

$$p = c\rho^{\gamma}$$

Differentiating, substituting the result into equation (8.35b), and integrating, we obtain

$$\frac{\gamma}{\gamma - 1} c\rho^{\gamma - 1} + \frac{U^2}{2} = \text{constant}$$

Therefore,

$$\frac{1}{\gamma - 1} \frac{\gamma p}{\rho} + \frac{U^2}{2} = \text{constant}$$

Using the perfect-gas equation of state, we obtain

$$h + \frac{U^2}{2} = \text{constant}$$

which is equation (8.29).

EXAMPLE 8.1: An indraft, supersonic wind tunnel

We are designing a supersonic wind tunnel using a large vacuum pump to draw air from the ambient atmosphere into our tunnel, as shown in Fig. 8.4. The air is continuously accelerated as it flows through a convergent/divergent nozzle so that flow in the test section is supersonic. If the ambient air is at the standard sea-level conditions, what is the maximum velocity that we can attain in the test section?

Solution: To calculate this maximum velocity, all we need is the energy equation for a steady, one-dimensional, adiabatic flow. Using equation (8.29), we have

$$h_1 + \tfrac{1}{2}U_1^2 = h_2 + \tfrac{1}{2}U_2^2$$

Since the ambient air (i.e., that which serves as the tunnel's "stagnation chamber" or "reservoir") is at rest, $U_1 = 0$. The maximum velocity in the test section occurs when $h_2 = 0$ (i.e., when the flow expands until the static temperature in the test section is zero).

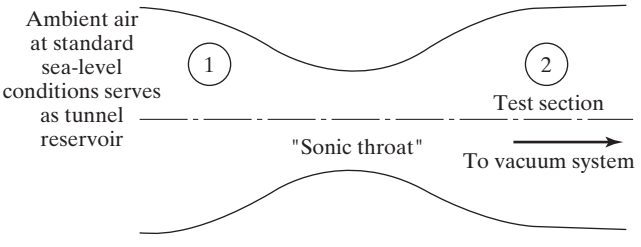

Figure 8.4 Indraft, supersonic wind tunnel.

$$(1004.7)288.15\ \text{J/kg} = \frac{U_2^2}{2}$$

$$U_2 = 760.9\ \text{m/s}$$

Of course, we realize that this limit is physically unattainable, since the water vapor in the air would liquefy first. However, it does represent an upper limit for conceptual considerations.

EXAMPLE 8.2: A simple model for the Shuttle Orbiter flow field

During a nominal reentry trajectory, the Space Shuttle Orbiter flies at 3964 ft/s at an altitude of 100,000 ft. The corresponding conditions at the stagnation point (point 2 in Fig. 8.5) are $p_2 = 490.2\ \text{lbf/ft}^2$ and $T_2 = 1716.0°\text{R}$. The static pressures for two nearby locations (points 3 and 4 of Fig. 8.5) are $p_3 = 259.0\ \text{lbf/ft}^2$ and $p_4 = 147.1\ \text{lbf/ft}^2$. All three points are outside the boundary layer. What are the local static temperature, the local velocity, and the local Mach number at points 3 and 4?

Solution: At these conditions, the air can be assumed to behave approximately as a perfect gas. Furthermore, since all three points are outside the boundary layer and downstream of the bow shock wave, we will assume that the flow expands isentropically from point 2 to point 3 and then to point 4. (Note that because the shock wave is curved, the entropy will vary through the shock layer. For a further discussion of the rotational flow downstream of a curved shock wave, refer to Chapter 12. Thus, validity of the assumption that the expansion is isentropic should be verified for a given application.)

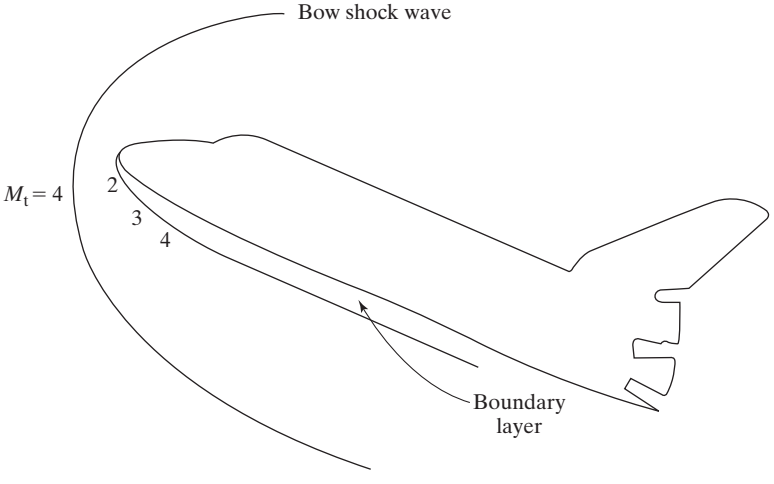

Figure 8.5 Shuttle flow field for Example 8.2.

For an isentropic process, we can use equation (8.20b) to relate the temperature ratio to the pressure ratio between two points:

$$T_3 = T_2\left(\frac{p_3}{p_2}\right)^{(\gamma-1)/\gamma} = (1716.0)(0.83337) = 1430.1°\text{R}$$

Similarly,

$$T_4 = (1716.0)(0.70899) = 1216.6°\text{R}$$

Using the energy equation for the adiabatic flow of a perfect gas [i.e., equation (8.31)], and noting that $U_2 = 0$, since point 2 is a stagnation point,

$$\begin{aligned} U_3 &= [2c_p(T_2 - T_3)]^{0.5} \\ &= \left[2\left(0.2404\frac{\text{Btu}}{\text{Ibm}\cdot°\text{R}}\right)\left(32.174\frac{\text{ft}\cdot\text{Ibm}}{\text{Ibf}\cdot\text{s}^2}\right)\left(778.2\frac{\text{ft}\cdot\text{Ibf}}{\text{Btu}}\right)(285.9°\text{R})\right]^{0.5} \\ &= 1855.2\ \text{ft/s} \end{aligned}$$

Similarly,

$$U_4 = 2451.9\ \text{ft/s}$$

Using equation (1.14b) for the speed of sound in English units,

$$M_3 = \frac{U_3}{a_3} = \frac{1855.2}{49.02(1430.1)^{0.5}} = 1.001$$

$$M_4 = \frac{U_4}{a_4} = \frac{2451.9}{49.02(1216.6)^{0.5}} = 1.434$$

So, the flow accelerates from the stagnation conditions at point 2 to sonic conditions at point 3, and becomes supersonic at point 4.

8.3 ISENTROPIC FLOW IN A VARIABLE-AREA STREAMTUBE

It is particularly useful to study the isentropic flow of a perfect gas in a variable-area streamtube, since it reveals many of the general characteristics of compressible flow. In addition, the assumption of constant entropy is not too restrictive, since the flow outside the boundary layer is essentially isentropic except while crossing linear shock waves or downstream of curved shock waves.

Using equations (8.20) and (8.34), we can write the total property ratios for pressure and density as:

$$\frac{p_{t1}}{p} = \left(1 + \frac{\gamma - 1}{2}M^2\right)^{\gamma/(\gamma-1)} \tag{8.36}$$

$$\frac{\rho_{t1}}{\rho} = \left(1 + \frac{\gamma - 1}{2}M^2\right)^{1/(\gamma-1)} \tag{8.37}$$

where p_{t1} and ρ_{t1} are the *stagnation pressure* and the *stagnation density*, respectively. (Note: the terms *total*, *stagnation*, and *reservoir* all mean the same thing.) Applying these

equations between two streamwise stations shows that if T_t is constant and the flow is isentropic, the stagnation pressure p_{t1} is a constant. The equation of state then requires that ρ_{t1} also is constant.

To get a feeling for the deviation between the pressure values calculated assuming incompressible flow and those calculated using the compressible flow relations, we can expand equation (8.36) in powers of M^2:

$$\frac{p_{t1}}{p} = 1 + \frac{\gamma}{2}M^2 + O(M^4) + \cdots \tag{8.38}$$

Since the flow is essentially incompressible when the Mach number is relatively low, we can neglect higher order terms. Retaining only terms of order M^2 yields

$$\frac{p_{t1}}{p} = 1 + \frac{\gamma}{2}M^2 \tag{8.39}$$

which for a perfect gas becomes

$$\frac{p_{t1}}{p} = 1 + \frac{\gamma}{2}\frac{U^2}{\gamma RT} = 1 + \frac{U^2}{2p/\rho} \tag{8.40}$$

Rearranging, we find the total pressure as:

$$p_{t1} = p + \frac{\rho U^2}{2} \tag{8.41}$$

Therefore, for low Mach numbers the general relation given by equation (8.36) reverts to Bernoulli's equation for incompressible flow. The static pressures predicted by equation (8.36) are compared with those of equation (8.41) in terms of percent error as a function of Mach number in Fig. 8.6. An error of less than 1% results when Bernoulli's equation is used if the local Mach number is less than or equal to 0.5 in air, and an error of less than 0.15% is found for Mach numbers less than 0.3. However, for Mach numbers greater than 0.5, the total pressure cannot be treated as the sum of the static pressure and the dynamic pressure.

In deriving equations (8.34), (8.36), and (8.37), the respective stagnation properties have been used as references to nondimensionalize the static properties. Since the continuity equation for the one-dimensional steady flow requires that ρUA be a constant, the area becomes infinitely large as the velocity goes to zero. We can choose the area where the flow is sonic (i.e., $M = 1$) as the reference area to relate to the streamtube area at a given station. Designating the sonic conditions by a (*) superscript, the continuity equation yields

$$\frac{A^*}{A} = \frac{\rho U}{\rho^* U^*} = \frac{\rho_{t1}(\rho/\rho_{t1})\sqrt{\gamma RT_t}\sqrt{T/T_t}M}{\rho_{t1}(\rho^*/\rho_{t1})\sqrt{\gamma RT_t}\sqrt{T^*/T_t}} \tag{8.42}$$

since $M^* = 1$. Noting that ρ^*/ρ_{t1} and T^*/T_t are to be evaluated at $M = M^* = 1$,

$$\frac{A^*}{A} = M\left[\frac{2}{\gamma+1}\left(1 + \frac{\gamma-1}{2}M^2\right)\right]^{-(\gamma+1)/2(\gamma-1)} \tag{8.43}$$

Given the area, A, and the Mach number, M, at any station, we could compute an A^* for that station from equation (8.43). A^* is the area the streamtube would have to be if the

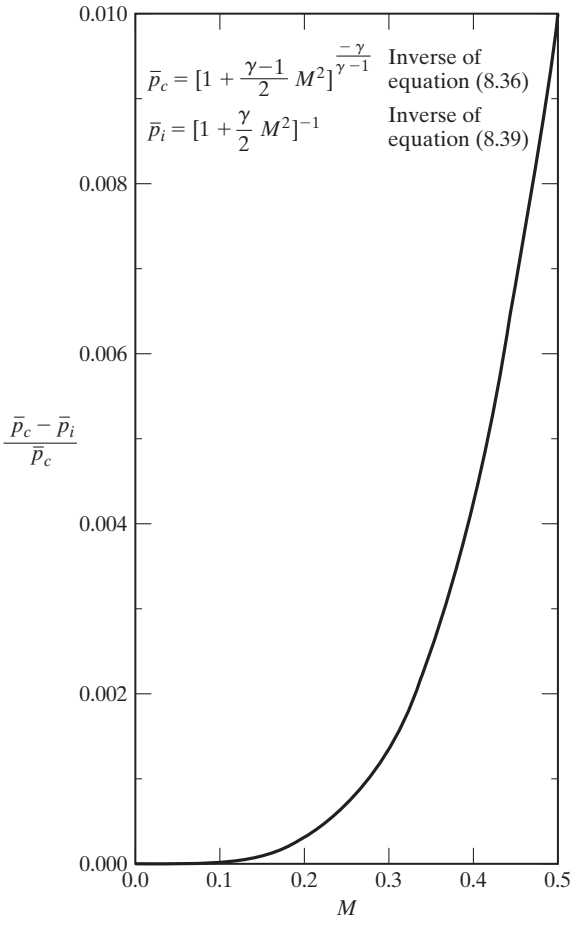

Figure 8.6 Effect of compressibility on the theoretical value for the pressure ratio.

flow were accelerated or decelerated to $M = 1$ isentropically. Equation (8.43) is especially useful in streamtube flows that are isentropic, and therefore where A^* is a constant.

In order to aid in the solution of isentropic flow problems, the temperature ratio [equation (8.34)], the pressure ratio [equation (8.36)], the density ratio [equation (8.37)], and the area ratio [equation (8.43)] are presented as a function of the Mach number in Table 8.1. A more complete tabulation of these data is given in Ames Research Center Staff (1953). The results of Table 8.1 are summarized in Fig. 8.7.

In order to determine the mass-flow rate in the streamtube, we need to find $\dot{m} = \rho UA$:

$$\dot{m} = \rho UA = \rho_{t1}\left(\frac{\rho}{\rho_{t1}}\right) M\sqrt{\gamma R T_t}\sqrt{\frac{T}{T_t}}A$$

$$\frac{\dot{m}}{A} = \sqrt{\frac{\gamma}{R}}\frac{p_{t1}}{\sqrt{T_t}}\frac{M}{\{1 + [(\gamma - 1)/2]M^2\}^{(\gamma+1)/2(\gamma-1)}} \qquad \textbf{(8.44)}$$

TABLE 8.1 Correlations for a One-Dimensional, Isentropic Flow of Perfect Air ($\gamma = 1.4$)

M	$\frac{A}{A^*}$	$\frac{p}{p_{t1}}$	$\frac{\rho}{\rho_{t1}}$	$\frac{T}{T_t}$	$\frac{A}{A^*}\frac{p}{p_{t1}}$
0	∞	1.00000	1.00000	1.00000	∞
0.05	11.592	0.99825	0.99875	0.99950	11.571
0.10	5.8218	0.99303	0.99502	0.99800	5.7812
0.15	3.9103	0.98441	0.98884	0.99552	3.8493
0.20	2.9635	0.97250	0.98027	0.99206	2.8820
0.25	2.4027	0.95745	0.96942	0.98765	2.3005
0.30	2.0351	0.93947	0.95638	0.98232	1.9119
0.35	1.7780	0.91877	0.94128	0.97608	1.6336
0.40	1.5901	0.89562	0.92428	0.96899	1.4241
0.45	1.4487	0.87027	0.90552	0.96108	1.2607
0.50	1.3398	0.84302	0.88517	0.95238	1.12951
0.55	1.2550	0.81416	0.86342	0.94295	1.02174
0.60	1.1882	0.78400	0.84045	0.93284	0.93155
0.65	1.1356	0.75283	0.81644	0.92208	0.85493
0.70	1.09437	0.72092	0.79158	0.91075	0.78896
0.75	1.06242	0.68857	0.76603	0.89888	0.73155
0.80	1.03823	0.65602	0.74000	0.88652	0.68110
0.85	1.02067	0.62351	0.71361	0.87374	0.63640
0.90	1.00886	0.59126	0.68704	0.86058	0.59650
0.95	1.00214	0.55946	0.66044	0.84710	0.56066
1.00	1.00000	0.52828	0.63394	0.83333	0.52828
1.05	1.00202	0.49787	0.60765	0.81933	0.49888
1.10	1.00793	0.46835	0.58169	0.80515	0.47206
1.15	1.01746	0.43983	0.55616	0.79083	0.44751
1.20	1.03044	0.41238	0.53114	0.77640	0.42493
1.25	1.04676	0.38606	0.50670	0.76190	0.40411
1.30	1.06631	0.36092	0.48291	0.74738	0.38484
1.35	1.08904	0.33697	0.45980	0.73287	0.36697
1.40	1.1149	0.31424	0.43742	0.71839	0.35036
1.45	1.1440	0.29272	0.41581	0.70397	0.33486
1.50	1.1762	0.27240	0.39498	0.68965	0.32039
1.55	1.2115	0.25326	0.37496	0.67545	0.30685
1.60	1.2502	0.23527	0.35573	0.66138	0.29414
1.65	1.2922	0.21839	0.33731	0.64746	0.28221
1.70	1.3376	0.20259	0.31969	0.63372	0.27099
1.75	1.3865	0.18782	0.30287	0.62016	0.26042
1.80	1.4390	0.17404	0.28682	0.60680	0.25044
1.85	1.4952	0.16120	0.27153	0.59365	0.24102
1.90	1.5555	0.14924	0.25699	0.58072	0.23211
1.95	1.6193	0.13813	0.24317	0.56802	0.22367
2.00	1.6875	0.12780	0.23005	0.55556	0.21567
2.05	1.7600	0.11823	0.21760	0.54333	0.20808
2.10	1.8369	0.10935	0.20580	0.53135	0.20087
2.15	1.9185	0.10113	0.19463	0.51962	0.19403
2.20	2.0050	0.09352	0.18405	0.50813	0.18751
2.25	2.0964	0.08648	0.17404	0.49689	0.18130
2.30	2.1931	0.07997	0.16458	0.48591	0.17539

(*continued on next page*)

TABLE 8.1 continued

M	$\frac{A}{A^*}$	$\frac{p}{p_{t1}}$	$\frac{\rho}{\rho_{t1}}$	$\frac{T}{T_t}$	$\frac{A}{A^*}\frac{p}{p_{t1}}$
2.35	2.2953	0.07396	0.15564	0.47517	0.16975
2.40	2.4031	0.06840	0.14720	0.46468	0.16437
2.45	2.5168	0.06327	0.13922	0.45444	0.15923
2.50	2.6367	0.05853	0.13169	0.44444	0.15432
2.55	2.7630	0.05415	0.12458	0.43469	0.14963
2.60	2.8960	0.05012	0.11787	0.42517	0.14513
2.65	3.0359	0.04639	0.11154	0.41589	0.14083
2.70	3.1830	0.04295	0.10557	0.40684	0.13671
2.75	3.3376	0.03977	0.09994	0.39801	0.13276
2.80	3.5001	0.03685	0.09462	0.38941	0.12897
2.85	3.6707	0.03415	0.08962	0.38102	0.12534
2.90	3.8498	0.03165	0.08489	0.37286	0.12185
2.95	4.0376	0.02935	0.08043	0.36490	0.11850
3.00	4.2346	0.02722	0.07623	0.35714	0.11527
3.50	6.7896	0.01311	0.04523	0.28986	0.08902
4.00	10.719	0.00658	0.02766	0.23810	0.07059
4.50	16.562	0.00346	0.01745	0.19802	0.05723
5.00	25.000	$189(10)^{-5}$	0.01134	0.16667	0.04725
6.00	53.189	$633(10)^{-6}$	0.00519	0.12195	0.03368
7.00	104.143	$242(10)^{-6}$	0.00261	0.09259	0.02516
8.00	190.109	$102(10)^{-6}$	0.00141	0.07246	0.01947
9.00	327.189	$474(10)^{-7}$	0.000815	0.05814	0.01550
10.00	535.938	$236(10)^{-7}$	0.000495	0.04762	0.01263
∞	∞	0	0	0	0

Therefore, the mass-flow rate is proportional to the stagnation pressure and inversely proportional to the square root of the stagnation temperature. To find the condition of maximum flow per unit area, we could compute the derivative of $(\dot{m}/A)$ as given by equation (8.44) with respect to Mach number and set the derivative equal to zero. At this condition, we would find that $M = 1$, so setting $M = 1$ in equation (8.44) yields:

$$\left(\frac{\dot{m}}{A}\right)_{\max} = \frac{\dot{m}}{A^*} = \sqrt{\frac{\gamma}{R}\left(\frac{2}{\gamma+1}\right)^{(\gamma+1)/(\gamma-1)}}\frac{p_{t1}}{\sqrt{T_t}} \tag{8.45}$$

The maximum flow rate per unit area occurs where the cross-sectional area is a minimum (designated A^*), and where the Mach number is one. Therefore, the maximum flow rate per unit area occurs at the sonic throat when the flow is choked. The word *choked* is used to describe this condition because the mass flow rate is maximized—no additional mass can go through the throat per unit time.

Fig. 8.7 shows that for each value of A^*/A, there are two values of M: one subsonic, the other supersonic. Therefore, from Fig. 8.7 we see that, while all static properties of the fluid monotonically decrease with Mach number, the area ratio does not. We conclude that to accelerate a subsonic flow to supersonic speeds, the streamtube must first converge in an isentropic process until sonic conditions are reached (which is called a throat).The flow then accelerates in a diverging streamtube to achieve supersonic

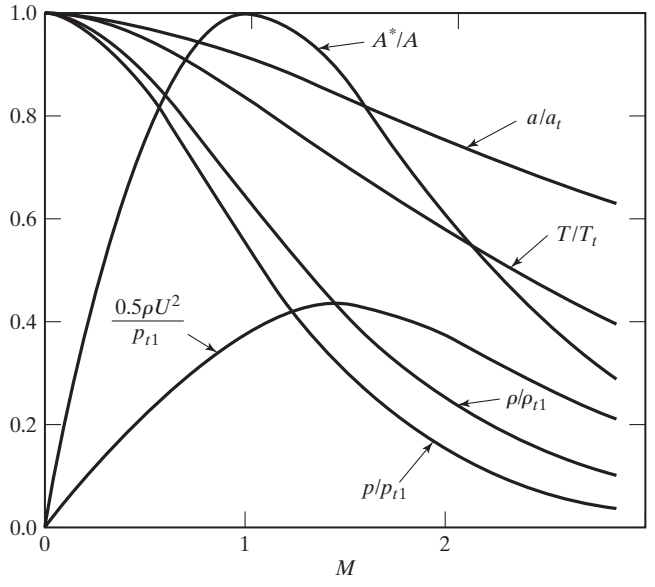

Figure 8.7 Property variations as functions of Mach number for isentropic flow for $\gamma = 1.4$.

Mach numbers. Just because a streamtube is convergent/divergent, it does not necessarily follow that the flow is sonic at the narrowest cross section (or throat). The actual flow depends on the pressure distribution as well as the geometry of the streamtube. However, if the Mach number is to be unity anywhere in the streamtube, it must be unity at the throat.

For certain calculations (e.g., finding the true airspeed from Mach number and stagnation pressure) the ratio $\frac{1}{2}\rho U^2/p_{t1}$ is useful.

$$\frac{\frac{1}{2}\rho U^2}{p_{t1}} = \frac{\frac{1}{2}(p/RT)(\gamma/\gamma)U^2}{p_{t1}} = \frac{1}{2}\frac{\gamma p}{p_{t1}}\frac{U^2}{\gamma RT} = \frac{\gamma M^2}{2}\frac{p}{p_{t1}} \tag{8.46}$$

and,

$$\frac{\frac{1}{2}\rho U^2}{p_{t1}} = \frac{\gamma M^2}{2}\left(1 + \frac{\gamma - 1}{2}M^2\right)^{-\gamma/(\gamma-1)} \tag{8.47}$$

The ratio of the local speed of sound to the speed of sound at the stagnation conditions is

$$\frac{a}{a_t} = \sqrt{\frac{\gamma RT}{\gamma RT_t}} = \left(\frac{T}{T_t}\right)^{0.5} = \left(1 + \frac{\gamma - 1}{2}M^2\right)^{-0.5} \tag{8.48}$$

Note: The nomenclature used here anticipates the discussion of shock waves. Since the stagnation pressure varies across a shock wave, the subscript $t1$ has been used to designate stagnation properties evaluated upstream of a shock wave (which correspond to the free-stream values in a flow with a single shock wave). Since the stagnation temperature is constant across a shock wave (for perfect-gas flows), it is designated by the simple subscript t.

8.4 CONVERGING-DIVERGING NOZZLES

Perhaps the most important application of variable area streamtube results is for a converging-diverging nozzle (also called a Laval nozzle). Finding meaningful relationships for the nozzle requires taking another look at the conservation of mass and momentum for a variable area streamtube. The conservation of mass for a steady, one-dimensional flow between two points in a streamtube, using equation (2.5), is:

$$-\iint \rho_1 U_1 dA_1 + \iint \rho_2 U_2 dA_2 = 0$$

Since the flow properties are constant at each station, we find the well-known result:

$$\rho_1 U_1 A_1 = \rho_2 U_2 A_2 = \rho U A = \text{constant}$$

Differentiating this yields:

$$(d\rho)UA + \rho(dU)A + \rho U(dA) = 0$$

and now dividing by ρUA we have:

$$\frac{d\rho}{\rho} + \frac{dU}{U} + \frac{dA}{A} = 0 \tag{8.49}$$

Now take a look at Euler's equation for an irrotational flow with no body forces, from equation (3.5):

$$d\left(\frac{U^2}{2}\right) + \frac{dp}{\rho} = 0$$

which may be rewritten as:

$$UdU + \frac{dp}{\rho} = 0$$

We can alter Euler's equation using equation (8.26) as:

$$UdU = -\frac{dp}{\rho} = -\frac{dp}{d\rho}\frac{d\rho}{\rho} = -a^2\frac{d\rho}{\rho}$$

and now solving for $d\rho/\rho$:

$$\frac{d\rho}{\rho} = -\frac{UdU}{a^2} = -\frac{U^2 dU}{Ua^2} = -M^2\frac{dU}{U}$$

Now substitute this relationship into equation (8.49) to obtain:

$$-M^2\frac{dU}{U} + \frac{dU}{U} + \frac{dA}{A} = (1 - M^2)\frac{dU}{U} + \frac{dA}{A} = 0$$

After some algebraic manipulation, we obtain:

$$\frac{dU}{U} = \frac{-dA/A}{(1 - M^2)} \tag{8.50}$$

TABLE 8.2 Area-velocity Relationship for Different Mach Number Regimes

M	dA	dU	*Description*
$M = 0$	> 0	< 0	Incompressible $U_1A_1 = U_2A_2$
$0 < M < 1$	> 0	< 0	Subsonic compressible
$M > 1$	< 0	< 0	Supersonic; density decreases faster than velocity increases
$M = 1$	0	Finite	Throat

This is the area-velocity relationship for a streamtube. This relationship shows us how area and velocity relate to each other at different Mach numbers; there are several interesting cases shown in Table 8.2.

In other words, in a converging section with subsonic flow the velocity will increase, and at a throat (assuming the conditions are right) there can be sonic flow, and then in a diverging section the velocity will increase to supersonic speeds. This is a very powerful, and at times confusing, result. Under the proper conditions, it could be possible to accelerate flow to supersonic conditions in a converging-diverging nozzle, assuming the flow reaches $M = 1$ at the throat.

The ability to attain supersonic flow in a converging-diverging nozzle is determined by the pressure ratio, p/p_t, between the pressure at the exit of the nozzle (termed the back pressure) and the total pressure upstream of the nozzle. In Fig. 8.8, the various

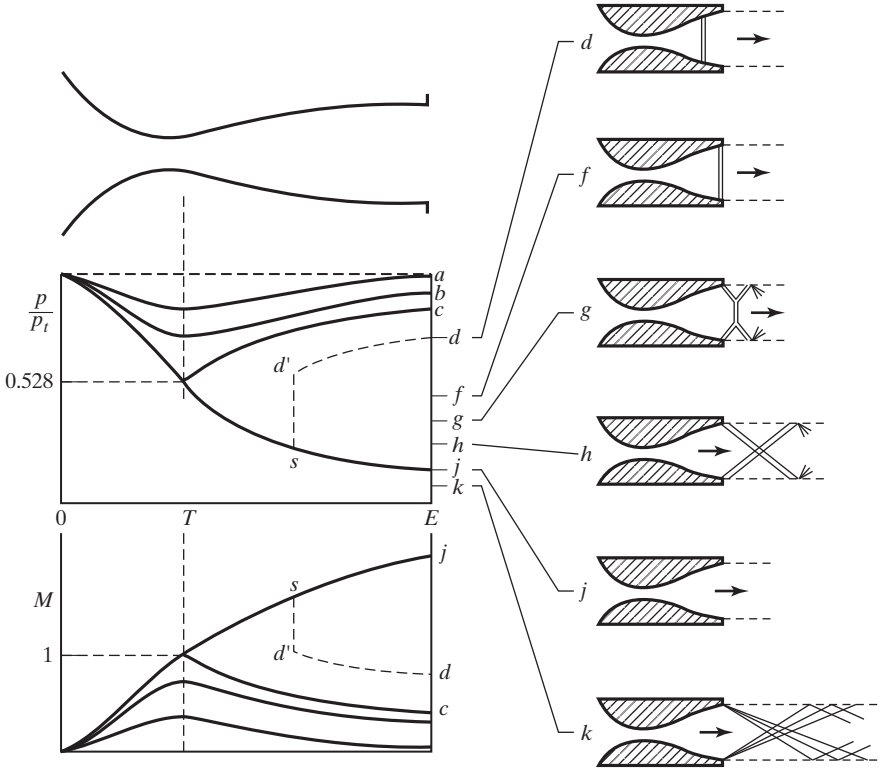

Figure 8.8 Effect of pressure ratio on flow in a converging-diverging nozzle [from Liepmann and Roshko (1957)].

possible flow fields for the nozzle are shown in terms of the pressure ratio. Curves *a* and *b* represent two fully subsonic cases where the nozzle is behaving as a Venturri tube (accelerating the flow in the converging section and decelerating the flow in the diverging section). The back pressure for these two cases determines how much the flow is accelerated at the throat, although the Mach number is always $M < 1$, even at the throat. Curve *c* is also subsonic throughout, with the exception of the throat where the flow just reaches $M = 1$. From Table 8.1 for $M = 1, p/p_t = 0.528$, which is shown on the figure.

Aerodynamics Concept Box: How Jet Engines Can Reach Supersonic Speeds

The thrust of a jet engine is created by increasing the momentum of the air coming into the inlet (according to Newton's second law, if the momentum of a flow increases there must be a net force acting in the opposite direction, such as for a fire hose nozzle). The greater the increase in momentum between the inlet and exhaust planes of the engine, the more thrust is produced. What if you could find a way to increase the velocity of air exiting the jet engine to supersonic speeds? According to the results we just saw for a converging-diverging (C-V) nozzle, if we placed one of these nozzles at the exhaust of the engine, then it will be possible to obtain supersonic exit velocities if the appropriate pressure ratio between the nozzle's inlet and exit is provided. All supersonic fighters have jet engines with C-V nozzles, as seen below for a jet engine being tested in a static test cell at Arnold Engineering Development Center. Once the supersonic exit velocity is obtained, the engine can produce significant amounts of thrust for the cost of including a C-V nozzle in the design of the engine. Of course, the engine is also limited in mass flow rate since the throat is choked, which is why most C-V nozzles on fighters have variable areas both at the throat and nozzle exit plane. When the afterburner is engaged the throat and exit plane areas enlarge to allow increased mass flow. All of this increase in thrust comes with the cost, weight, and complexity of the C-V nozzle. The F100-PW-229 turbojet engine shown below can achieve over 17,000 pounds of thrust, which can be increased to 29,000 pounds with the use of an afterburner.

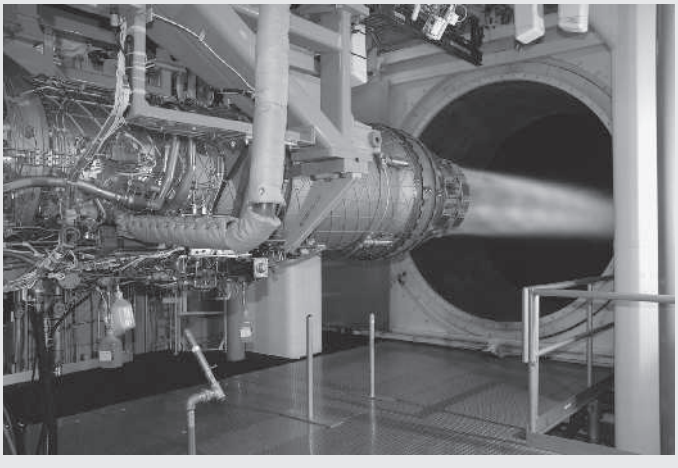

A Pratt & Whitney F100-PW-229 undergoing static testing (courtesy of the Arnold Engineering Development Center, U.S. Air Force)

There is another branch for the flow which reaches $M = 1$ in the throat, which occurs if the back pressure is reduced even further (Curve *j*). In this case, the flow accelerates to $M = 1$ and then continues to accelerate due to the nature of supersonic flow in a diverging section (see Table 8.2). If the back pressure is at a value lower than *c* but higher than *j*, then the flow starts to accelerate through the diverging section, but shocks form and raise the pressure up to the back pressure level. In the case of Curve *d*, a normal shock forms in the nozzle, increasing the pressure and decelerating the flow to subsonic levels (see branch *s* to *d′* to *d*, where *s* to *d′* represents the shock). If the back pressure is further reduced, the normal shock reaches the exit (Curve *f*), and when the back pressure is reduced even more, a shock diamond is formed outside the nozzle in order to obtain the correct back pressure (Curves *g* and *h*). This is known as an underexpanded nozzle since the ideal back pressure for the nozzle is represented by Curve *j*, so flows represented by Curves *d*, *f*, *g*, and *h* have not expanded enough. If the back pressure is lower than the design case (Curve *k*), a series of expansion waves form to reduce the pressure to the actual back pressure; this is known as an over-expanded nozzle. Either over- or under-expanded nozzles are less efficient than the isentropic nozzle (Curve *j*), and will produce less thrust and possibly more drag.

8.5 CHARACTERISTIC EQUATIONS AND PRANDTL-MEYER FLOWS

Consider a two-dimensional flow around a slender airfoil shape. The deflection of the streamlines as flow encounters the airfoil is sufficiently small that shock waves are not generated. Therefore, the flow may be considered as isentropic (excluding the boundary layer, of course). For the development of the equations for a more general flow, refer to Hayes and Probstein (1966). For the present type of flow, the equations of motion in a natural (or streamline) coordinate system, as shown in Fig. 8.9, are:

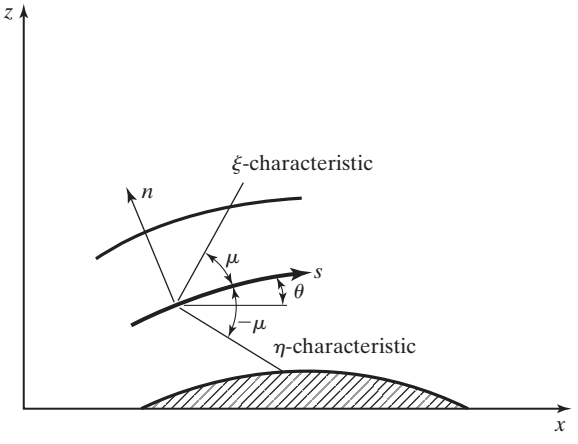

Figure 8.9 Supersonic flow around an airfoil in natural (streamline) coordinates.

continuity equation

$$\frac{\partial(\rho U)}{\partial s} + \rho U \frac{\partial \theta}{\partial n} = 0 \tag{8.51}$$

s-momentum equation

$$\rho U \frac{\partial U}{\partial s} + \frac{\partial p}{\partial s} = 0 \tag{8.52}$$

n-momentum equation

$$\rho U^2 \frac{\partial \theta}{\partial s} + \frac{\partial p}{\partial n} = 0 \tag{8.53}$$

Since the flow is isentropic, the energy equation provides no unique information and is, therefore, not used. However, since the flow is isentropic, the change in pressure with respect to the change in density is equal to the square of the speed of sound, from equation (8.25):

$$\frac{\partial p}{\partial \rho} = a^2 \tag{8.54}$$

and the continuity equation becomes:

$$\frac{\partial p}{\partial s} \frac{M^2 - 1}{\rho U^2} + \frac{\partial \theta}{\partial n} = 0 \tag{8.55}$$

Combining equations (8.53) and (8.55) and introducing the concept of the directional derivative [e.g., Wayland (1957)], we obtain:

$$\frac{\partial p}{\partial \xi} + \frac{\rho U^2}{\sqrt{M^2 - 1}} \frac{\partial \theta}{\partial \xi} = 0 \tag{8.56a}$$

along the line having the direction

$$\frac{dn}{ds} = \tan \mu = \frac{1}{\sqrt{M^2 - 1}}$$

(i.e., the left-running characteristic ξ of Fig. 8.9). A *characteristic* is a line which exists only in supersonic flows. Characteristics should not be confused with finite-strength waves, such as shock waves. The ξ characteristic is inclined to the local streamline by the angle μ, which is the Mach angle,

$$\mu = \sin^{-1}\left(\frac{1}{M}\right)$$

The ξ characteristics correspond to the left-running Mach waves, which are so called because to an observer looking downstream, the Mach wave appears to be going downstream in a leftward direction. Equivalently,

$$\frac{\partial p}{\partial \eta} - \frac{\rho U^2}{\sqrt{M^2 - 1}} \frac{\partial \theta}{\partial \eta} = 0 \tag{8.56b}$$

along the line whose direction is given by:

$$\frac{dn}{ds} = \tan(-\mu)$$

(i.e., the right-running characteristic η of Fig. 8.9). Equations (8.56a) and (8.56b) provide a relation between the local static pressure and the local flow inclination.

Euler's equation for a steady, inviscid flow, which can be derived by neglecting the viscous terms and the body forces in the momentum equation (3.1), states that

$$dp = -\rho U\, d\mathrm{U}$$

For the left-running characteristic, equation (8.56a) becomes:

$$\frac{dU}{U} = \frac{d\theta}{\sqrt{M^2 - 1}} \tag{8.57}$$

But from the adiabatic-flow relations for a perfect gas,

$$\left(\frac{U}{a_t}\right)^2 = M^2\left(1 + \frac{\gamma - 1}{2}M^2\right)^{-1} \tag{8.58}$$

where a_t is the speed of sound at the stagnation conditions. Differentiating equation (8.58) and substituting the result into equation (8.57) yields

$$d\theta = \frac{\sqrt{M^2 - 1}\, dM^2}{2M^2\{1 + [(\gamma - 1)/2]M^2\}} \tag{8.59}$$

Integration of equation (8.59) yields the relation, which is valid for a left-running characteristic:

$$\theta = \nu + \text{constant of integration}$$

where v is a function of the Mach number called the *Prandtl-Meyer function*, which is given by:

$$\nu = \sqrt{\frac{\gamma + 1}{\gamma - 1}}\arctan\sqrt{\frac{\gamma - 1}{\gamma + 1}(M^2 - 1)} - \arctan\sqrt{M^2 - 1} \tag{8.60}$$

Tabulations of the *Prandtl-Meyer function* (ν), the corresponding Mach number, and the corresponding Mach angle (μ) are presented in Table 8.3. You should notice that the Prandtl-Meyer function is an angle with units of degrees in Table 8.3.

So, along a left-running characteristic,

$$\nu - \theta = R \tag{8.61a}$$

which is a constant. Similarly, along a right-running characteristic,

$$\nu + \theta = Q \tag{8.61b}$$

which is another constant. The use of equations (8.61a) and (8.61b) is simplified if the slope of the vehicle surface is such that we only need to consider the waves of a single family (i.e., all the waves are either left-running waves or right-running waves). To make the application clear, we will work through a sample problem.

TABLE 8.3 Mach Number and Mach Angle as a Function of Prandtl-Meyer Angle

ν (deg)	M	μ (deg)	ν (deg)	M	μ (deg)
0.0	1.000	90.000	25.0	1.950	30.847
0.5	1.051	72.099	25.5	1.968	30.536
1.0	1.082	67.574	26.0	1.986	30.229
1.5	1.108	64.451	26.5	2.004	29.928
2.0	1.133	61.997	27.0	2.023	29.632
2.5	1.155	59.950	27.5	2.041	29.340
3.0	1.177	58.180	28.0	2.059	29.052
3.5	1.198	56.614	28.5	2.078	28.769
4.0	1.218	55.205	29.0	2.096	28.491
4.5	1.237	53.920	29.5	2.115	28.216
5.0	1.256	52.738	30.0	2.134	27.945
5.5	1.275	51.642	30.5	2.153	27.678
6.0	1.294	50.619	31.0	2.172	27.415
6.5	1.312	49.658	31.5	2.191	27.155
7.0	1.330	48.753	32.0	2.210	26.899
7.5	1.348	47.896	32.5	2.230	26.646
8.0	1.366	47.082	33.0	2.249	26.397
8.5	1.383	46.306	33.5	2.269	26.151
9.0	1.400	45.566	34.0	2.289	25.908
9.5	1.418	44.857	34.5	2.309	25.668
10.0	1.435	44.177	35.0	2.329	25.430
10.5	1.452	43.523	35.5	2.349	25.196
11.0	1.469	42.894	36.0	2.369	24.965
11.5	1.486	42.287	36.5	2.390	24.736
12.0	1.503	41.701	37.0	2.410	24.510
12.5	1.520	41.134	37.5	2.431	24.287
13.0	1.537	40.585	38.0	2.452	24.066
13.5	1.554	40.053	38.5	2.473	23.847
14.0	1.571	39.537	39.0	2.495	23.631
14.5	1.588	39.035	39.5	2.516	23.418
15.0	1.605	38.547	40.0	2.538	23.206
15.5	1.622	38.073	40.5	2.560	22.997
16.0	1.639	37.611	41.0	2.582	22.790
16.5	1.655	37.160	41.5	2.604	22.585
17.0	1.672	36.721	42.0	2.626	22.382
17.5	1.689	36.293	42.5	2.649	22.182
18.0	1.706	35.874	43.0	2.671	21.983
18.5	1.724	35.465	43.5	2.694	21.786
19.0	1.741	35.065	44.0	2.718	21.591
19.5	1.758	34.673	44.5	2.741	21.398
20.0	1.775	34.290	45.0	2.764	21.207
20.5	1.792	33.915	45.5	2.788	21.017
21.0	1.810	33.548	46.0	2.812	20.830
21.5	1.827	33.188	46.5	2.836	20.644
22.0	1.844	32.834	47.0	2.861	20.459
22.5	1.862	32.488	47.5	2.886	20.277
23.0	1.879	32.148	48.0	2.910	20.096
23.5	1.897	31.814	48.5	2.936	19.916
24.0	1.915	31.486	49.0	2.961	19.738
24.5	1.932	31.164	49.5	2.987	15.561

(*continued on next page*)

TABLE 8.3 continued

ν (deg)	M	μ (deg)	ν (deg)	M	μ (deg)
50.0	3.013	19.386	76.5	4.955	11.642
50.5	3.039	19.213	77.0	5.009	11.517
51.0	3.065	19.041	77.5	5.063	11.392
51.5	3.092	18.870	78.0	5.118	11.268
52.0	3.119	18.701	78.5	5.175	11.145
52.5	3.146	18.532	79.0	5.231	11.022
53.0	3.174	18.366	79.5	5.289	10.899
53.5	3.202	18.200	80.0	5.348	10.777
54.0	3.230	18.036	80.5	5.408	10.656
54.5	3.258	17.873	81.0	5.470	10.535
55.0	3.287	17.711	81.5	5.532	10.414
55.5	3.316	17.551	82.0	5.596	10.294
56.0	3.346	17.391	82.5	5.661	10.175
56.5	3.375	17.233	83.0	5.727	10.056
57.0	3.406	17.076	83.5	5.795	9.937
57.5	3.436	16.920	84.0	5.864	9.819
58.0	3.467	16.765	84.5	5.935	9.701
58.5	3.498	16.611	85.0	6.006	9.584
59.0	3.530	16.458	85.5	6.080	9.467
59.5	3.562	16.306	86.0	6.155	9.350
60.0	3.594	16.155	86.5	6.232	9.234
60.5	3.627	16.006	87.0	6.310	9.119
61.0	3.660	15.856	87.5	6.390	9.003
61.5	3.694	15.708	88.0	6.472	8.888
62.0	3.728	15.561	88.5	6.556	8.774
62.5	3.762	15.415	89.0	6.642	8.660
63.0	3.797	15.270	89.5	6.729	8.546
63.5	3.832	15.126	90.0	6.819	8.433
64.0	3.868	14.983	90.5	6.911	8.320
64.5	3.904	14.840	91.0	7.005	8.207
65.0	3.941	14.698	91.5	7.102	8.095
65.5	3.979	14.557	92.0	7.201	7.983
66.0	4.016	14.417	92.5	7.302	7.871
66.5	4.055	14.278	93.0	7.406	7.760
67.0	4.094	14.140	93.5	7.513	7.649
67.5	4.133	14.002	94.0	7.623	7.538
68.0	4.173	13.865	94.5	7.735	7.428
68.5	4.214	13.729	95.0	7.851	7.318
69.0	4.255	13.593	95.5	7.970	7.208
69.5	4.297	13.459	96.0	8.092	7.099
70.0	4.339	13.325	96.5	8.218	6.989
70.5	4.382	13.191	97.0	8.347	6.881
71.0	4.426	13.059	97.5	8.480	6.772
71.5	4.470	12.927	98.0	8.618	6.664
72.0	4.515	12.795	98.5	8.759	6.556
72.5	4.561	12.665	99.0	8.905	6.448
73.0	4.608	12.535	99.5	9.055	6.340
73.5	4.655	12.406	100.0	9.210	6.233
74.0	4.703	12.277	100.5	9.371	6.126
74.5	4.752	12.149	101.0	9.536	6.019
75.0	4.801	12.021	101.5	9.708	5.913
75.5	4.852	11.894	102.0	9.885	5.806
76.0	4.903	11.768			

EXAMPLE 8.3: Use Prandtl-Meyer relations to calculate the aerodynamic coefficients for a thin airfoil

Consider the infinitesimally thin airfoil which has the shape of a parabola:

$$x^2 = -\frac{c^2}{z_{\max}}(z - z_{\max})$$

where $z_{\max} = 0.10c$, moving through the air at $M_\infty = 2.059$. The leading-edge slope of the airfoil is parallel to the free stream. The thin airfoil will be represented by five linear segments, as shown in Fig. 8.10. For each segment Δx will be $0.2c$. Therefore, the slopes of these segments are as follows:

Segment	*a*	*b*	*c*	*d*	*e*
θ	−1.145°	−3.607°	−5.740°	−8.048°	−10.370°

Solution: For the free-stream flow, using Tables 8.1 and 8.3, we can find:

$$\nu_\infty = 28.000° \qquad \frac{p_\infty}{p_{t1}} = 0.11653 \qquad \theta_\infty = 0°$$

Since the turning angles are small, we will assume that both the acceleration of the flow over the upper surface and the deceleration of the flow over the lower surface are isentropic processes. Notice that the expansion waves on the upper

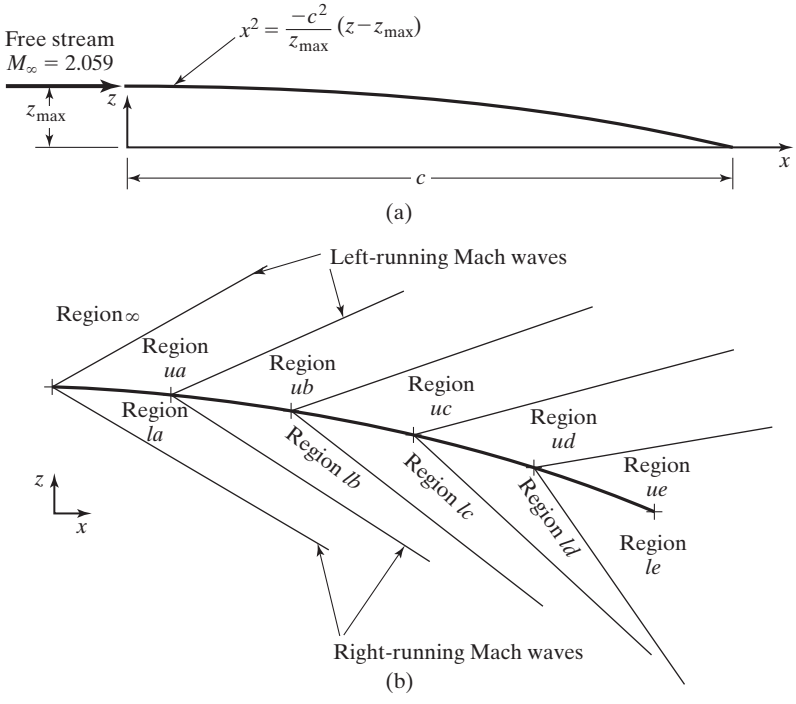

Figure 8.10 Mach waves for supersonic flow past a thin airfoil: (a) airfoil section; (b) wave pattern.

surface diverge as the flow accelerates, but the compression waves of the lower surface coalesce. Since the flow is isentropic, we can use equations (8.61a) and (8.61b). Furthermore, the stagnation pressure is constant throughout the flow field and equal to p_{t1} (which is the value for the free-stream flow).

In going from the free-stream (region ∞ in Fig. 8.10) to the first segment on the upper surface (region *ua*), we move along a right-running characteristic to cross the left-running Mach wave shown in the figure. Therefore,

$$\nu + \theta = Q$$

or

$$d\nu = -d\theta$$

so

$$\begin{aligned} \nu_{ua} &= \nu_\infty - (\theta_{ua} - \theta_\infty) \\ &= 28.000^\circ - (-1.145^\circ) = 29.145^\circ \end{aligned}$$

and using Table 8.3 we can find:

$$M_{ua} = 2.1018$$

Using Table 8.1 for isentropic flow, $p_{ua}/p_{t1} = 0.1091$.

Similarly, in going from the free stream to the first segment on the lower surface (region *la*), we move along a left-running characteristic to cross the right-running Mach wave shown in the figure. Therefore,

$$\nu - \theta = R$$

or

$$d\nu = d\theta$$

so

$$\begin{aligned} \nu_{la} &= \nu_\infty + (\theta_{la} - \theta_\infty) \\ &= 28.000^\circ + (-1.145^\circ) = 26.855^\circ \end{aligned}$$

and using Table 8.3 we can find that:

$$M_{la} = 2.0173$$

and the pressure can be found in Table 8.1 as $p_{la}/p_{t1} = 0.1244$.
A summary of the results for all of the segments follows:

	Upper surface			*Lower surface*		
Segment	ν_u	M_u	$\frac{\rho_u}{\rho_{t1}}$	ν_l	M_l	$\frac{\rho_l}{\rho_{t1}}$
a	29.145°	2.1018	0.1091	26.855°	2.0173	0.1244
b	31.607°	2.1952	0.0942	24.393°	1.9286	0.1428
c	33.740°	2.2784	0.0827	22.260°	1.8534	0.1604
d	36.048°	2.3713	0.0715	19.952°	1.7733	0.1813
e	38.370°	2.4679	0.0615	17.630°	1.6940	0.2045

Notice that the Mach number in Region *ua* is higher than the Mach number in Region *la*, and the pressure in Region *ua* is lower than the pressure in Region *la*. This means there is lift being produced on Segment *a*. The same observation can be applied to all segments to show that a net lift is being produced by the airfoil.

We can now calculate the lift coefficient and the drag coefficient for the airfoil. Note that we have not been given the free-stream pressure (or, equivalently, the altitude at which the airfoil is flying) or the chord length of the airfoil. But that is not critical, since we seek the force coefficients, which are nondimensionalized by the dynamic pressure and the airfoil chord length:

$$C_l = \frac{l}{\frac{1}{2}\rho_\infty U_\infty^2 c}$$

Referring to equation (8.46), we can show that for a perfect gas the dynamic pressure becomes:

$$q_\infty = \frac{1}{2}\rho_\infty U_\infty^2 = \frac{\gamma}{2} p_\infty M_\infty^2 \tag{8.62}$$

So the lift coefficient can be rewritten as:

$$C_l = \frac{l}{(\gamma/2) p_\infty M_\infty^2 c} \tag{8.63}$$

Referring again to Fig. 8.10, the incremental lift force acting on any segment (i.e., the *i*th segment) is:

$$dl_i = (p_{li} - p_{ui})\, ds_i \cos\theta_i = (p_{li} - p_{ui})\, dx_i$$

Similarly, the incremental drag force for any segment is

$$dd_i = (p_{li} - p_{ui})\, ds_i \sin\theta_i = (p_{li} - p_{ui})\, dx_i \tan\theta_i$$

The incremental lift and drag components for each segment are summarized below.

Segment	$\frac{p_{li}}{p_\infty}$	$\frac{p_{ui}}{p_\infty}$	$\frac{dl_i}{p_\infty}$	$\frac{dd_i}{p_\infty}$
a	1.070	0.939	0.0262*c*	0.000524*c*
b	1.226	0.810	0.0832*c*	0.004992*c*
c	1.380	0.710	0.1340*c*	0.01340*c*
d	1.559	0.614	0.1890*c*	0.0264*c*
e	1.759	0.529	0.2460*c*	0.0443*c*
Sum			0.6784*c*	0.0896*c*

Finally, we can sum the incremental components to obtain:

$$C_l = \frac{\sum dl_i}{(\gamma/2) p_\infty M_\infty^2\, c} = \frac{0.6784c}{0.7(4.24)c} = 0.2286$$

$$C_d = \frac{\sum dd_i}{(\gamma/2) p_\infty M_\infty^2 c} = \frac{0.0896c}{0.7(4.24)c} = 0.0302$$

and the lift-to-drag ratio of the airfoil is:

$$\frac{l}{d} = \frac{C_l}{C_d} = 7.57$$

Notice that this is a very low lift-to-drag ratio for a two-dimensional airfoil. For comparison, low-speed airfoils have lift-to-drag ratios of around 100, meaning that supersonic airfoils are much less efficient than subsonic airfoils.

Aerodynamics Concept Box: Re-writing Dynamic Pressure in Terms of Mach Number

It is common in low-speed aerodynamics to write the dynamic pressure as:

$$q = \frac{1}{2}\rho U^2$$

However, when we start working with high-speed aerodynamics, the dynamic pressure would be much easier to work with if it were written in terms of Mach number (since most speeds are given in terms of Mach number instead of velocity). The dynamic pressure can easily be re-written in terms of Mach number by using a few straight-forward relations. Namely, for a perfect gas:

$$p = \rho RT \qquad \text{and} \qquad a^2 = \gamma RT$$

These relations coupled with the definition of the Mach number, $M \equiv U/a$, will give us the appropriate relation:

$$q = \tfrac{1}{2}\rho U^2 = \tfrac{1}{2}\left(\frac{p}{RT}\right)M^2a^2 = \tfrac{1}{2}\left(\frac{p}{RT}\right)M^2\gamma RT$$

With a little algebra, the relation becomes:

$$q = \frac{\gamma}{2}pM^2$$

This relation is also convenient to use for the dynamic pressure in high-speed flow, and leads to a pressure coefficient relation given by:

$$C_p \equiv \frac{p - p_\infty}{q_\infty} = \frac{p - p_\infty}{\frac{\gamma}{2}p_\infty M_\infty^2} = \frac{2}{\gamma M_\infty^2}\left(\frac{p}{p_\infty} - 1\right)$$

This relationship becomes convenient for converting pressure coefficients into pressure ratios, and vice versa.

8.6 SHOCK WAVES

The formation of a shock wave occurs when a supersonic flow decelerates in response to a sharp increase in pressure or when a supersonic flow encounters a sudden, compressive change in direction. For flow conditions where the gas is a continuum, the shock wave is a narrow region (on the order of several molecular mean free paths thick, $\sim 6 \times 10^{-6}$ cm) across which there is an almost instantaneous change in the values of the

flow parameters. Because of the large streamwise variations in velocity, pressure, and temperature, viscous and heat-conduction effects are important within the shock wave. The difference between a shock wave and a Mach wave should be kept in mind. A *Mach wave* represents a surface across which some derivatives of the flow variables (such as the thermodynamic properties of the fluid and the flow velocity) may be discontinuous while the variables themselves are continuous. A *shock wave* represents a surface across which the thermodynamic properties and the flow velocity are essentially discontinuous. Therefore, the characteristic curves, or Mach lines, are patching lines for continuous flows, whereas shock waves are patching lines for discontinuous flows.

Consider the curved shock wave illustrated in Fig. 8.11. The flow upstream of the shock wave, which is stationary in the body-fixed coordinate system, is supersonic. At the plane of symmetry, the shock wave is normal (or perpendicular) to the free-stream flow, and the flow downstream of the shock wave is subsonic. Away from the plane of symmetry, the shock wave is oblique and the downstream flow is often supersonic. The velocity and the thermodynamic properties upstream of the shock wave are designated by the subscript 1. Notice that while the subscript 1 designates the free-stream (∞) properties for flows such as those in Fig. 8.11, it designates the local flow properties just upstream of the shock wave when it occurs in the midchord region of a transonic airfoil (see Chapter 9). The downstream values are designated by the subscript 2. We will analyze oblique shock waves by writing the continuity, the momentum, and the energy equations for the flow through the control volume shown in Fig. 8.12. For a steady flow, the integral equations of motion from Chapter 2 yield the following relations for the flow across an oblique segment of the shock wave:

Continuity:

$$\rho_1 u_1 = \rho_2 u_2 \tag{8.64}$$

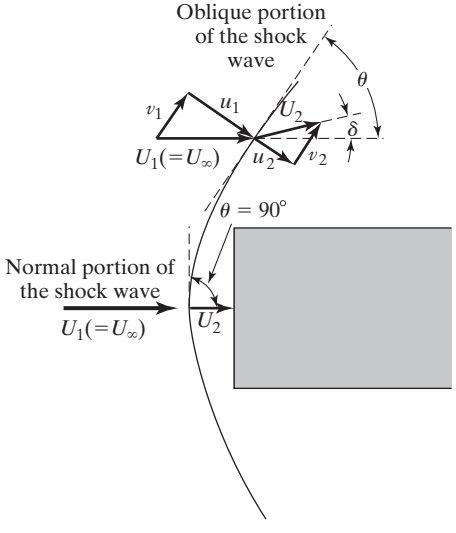

Figure 8.11 Curved shock wave illustrating nomenclature for normal shock wave and for oblique shock wave.

Normal component of momentum:

$$p_1 + \rho_1 u_1^2 = p_2 + \rho_2 u_2^2 \tag{8.65}$$

Tangential component of momentum:

$$\rho_1 u_1 v_1 = \rho_2 u_2 v_2 \tag{8.66}$$

Energy:

$$h_1 + \tfrac{1}{2}(u_1^2 + v_1^2) = h_2 + \tfrac{1}{2}(u_2^2 + v_2^2) \tag{8.67}$$

In addition to describing the flow across an oblique shock wave such as shown in Fig. 8.12, these relations can be used to describe the flow across a normal shock wave, or that portion of a curved shock wave which is perpendicular to the free stream, by letting $v_1 = v_2 = 0$.

Equation (8.65) can be used to calculate the maximum value of the pressure coefficient in the hypersonic limit as $M_1 \to \infty$. In this case, the flow is essentially stagnated ($u_2 \approx 0$) behind a normal shock wave, and equation (8.65) becomes:

$$p_2 - p_1 \approx \rho_1 u_1^2 \tag{8.68}$$

As a result,

$$C_{p_{\max}} = \frac{p_2 - p_1}{\frac{1}{2}\rho_1 U_1^2} \approx 2 \tag{8.69}$$

Notice that at the stagnation point of a vehicle in a hypersonic stream, C_p approaches 2.0. The value of C_p at the stagnation point of a vehicle in a supersonic stream is a function of the free-stream Mach number and is greater than 1.0. Recall that it is 1.0 for a low-speed free stream independent of the velocity, provided that the flow is incompressible.

Comparing equation (8.64) with equation (8.66), we find that for the oblique shock wave,

$$v_1 = v_2 \tag{8.70}$$

That is, the tangential component of the velocity is constant across the shock wave and we need not consider equation (8.66) further. Now the energy equation becomes:

$$h_1 + \tfrac{1}{2}u_1^2 = h_2 + \tfrac{1}{2}u_2^2 \tag{8.71}$$

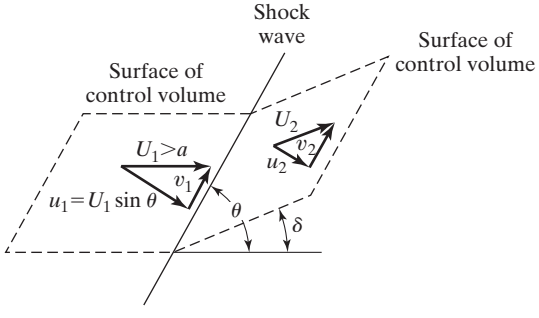

Figure 8.12 Control volume for analysis of flow through an oblique shock wave.

There are four unknowns (p_2, ρ_2, u_2, h_2) in the three equations (8.64), (8.65), and (8.71). We need to introduce an equation of state as the fourth equation. For hypervelocity flows where the shock waves are strong enough to cause dissociation or ionization, we can solve these equations numerically using the equation of state in tabular or in graphical form [e.g., Moeckel and Weston (1958)]. However, for a perfect-gas flow [from equation (1.10)]:

$$p = \rho RT$$

and

$$h = c_p T$$

A comparison of the properties downstream of a normal shock wave using the charts for air in thermodynamic equilibrium with those computed using the perfect-gas model for air is presented in Chapter 12.

Notice that equations (8.64), (8.65), and (8.71) involve only the component of velocity normal to the shock wave:

$$u_1 = U_1 \sin\theta \tag{8.72}$$

So, the property changes across an oblique shock wave are the same as those across a normal shock wave when they are written in terms of the upstream Mach number component perpendicular to the shock; the tangential component of the velocity is unchanged. This is the *sweepback principle*, that the oblique flow is reduced to the normal flow by a uniform translation of the axes (i.e., a Galilean transformation). Note that the tangential component of the Mach number does change, since the temperature (and therefore the speed of sound) changes across the shock wave.

Since the flow through the shock wave is adiabatic, the entropy must increase as the flow passes through the shock wave. Therefore, the flow must decelerate (i.e., the pressure must increase) as it passes through the shock wave. We can now obtain the relation between the shock-wave (θ) and the deflection angle (δ):

$$\cot\delta = \tan\theta\left[\frac{(\gamma + 1)M_1^2}{2(M_1^2 \sin^2\theta - 1)} - 1\right] \tag{8.73}$$

From equation (8.73) we see that the deflection angle is zero for two shock-wave angles: (1) the flow is not deflected when $\theta = \mu$, since the Mach wave results from an infinitesimal disturbance (i.e., a zero-strength shock wave), and (2) the flow is not deflected when it passes through a normal shock wave (i.e., when $\theta = 90°$).

Solutions to equation (8.73) are presented in graphical form in Fig. 8.13a. Notice that for a given deflection angle δ, there are two possible values for the shock-wave angle θ. The larger of the two values of θ is for a *strong* shock wave, while the smaller value is for a *weak* shock wave. In practice, the weak shock wave typically occurs in external aerodynamic flows. However, the strong shock wave occurs if the downstream pressure is sufficiently high. The high downstream pressure associated with the strong shock wave may occur in flows in wind tunnels, engine inlets, or other ducts.

If the deflection angle exceeds the maximum value for an attached weak shock to be generated, a strong, detached shock wave will occur. For instance, a flat-plate airfoil can be inclined 34° to a Mach 3.0 stream and still generate a weak shock wave. This is the maximum deflection angle for a weak shock wave to occur at this Mach number.

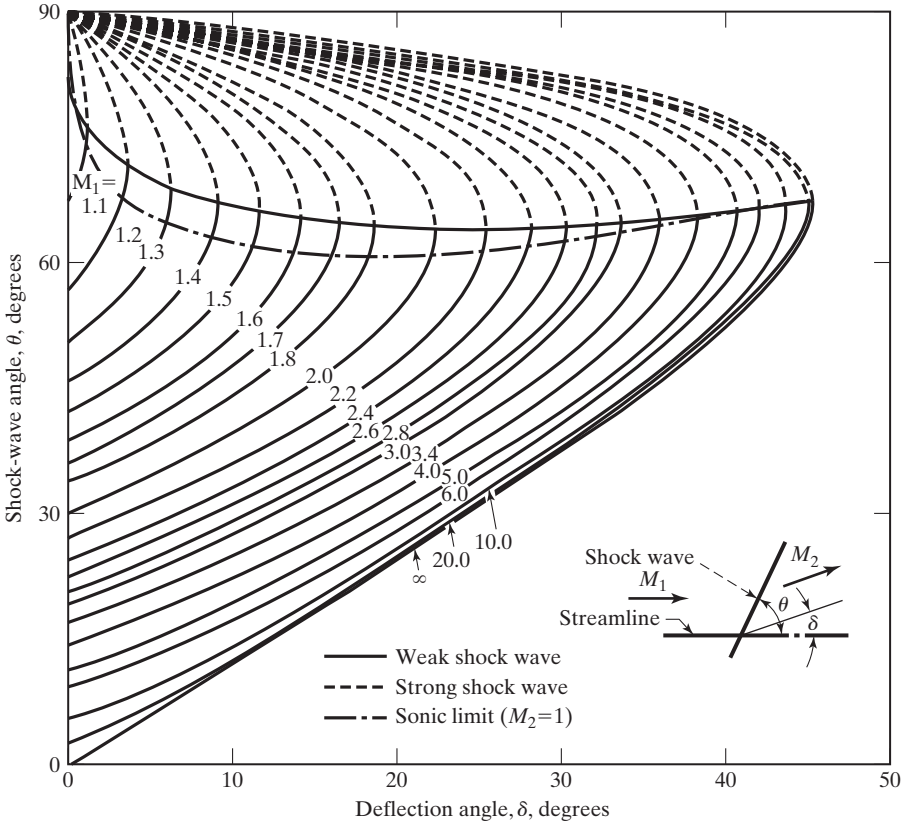

Figure 8.13 Variation of shock-wave parameters with wedge flow-deflection angle for various upstream Mach numbers, $\gamma = 1.4$: (a) shock-wave angle.

If the airfoil were to be inclined at 35° to the Mach 3.0 stream, a strong curved shock wave (known as a *bow shock*) would occur with a complex subsonic/supersonic flow downstream of the shock wave.

Once the shock-wave angle θ has been found for the given values of M_1 and δ, the other downstream properties can be found using the following relations:

$$\frac{p_2}{p_1} = \frac{2\gamma M_1^2 \sin^2\theta - (\gamma - 1)}{\gamma + 1} \tag{8.74}$$

$$\frac{\rho_2}{\rho_1} = \frac{(\gamma + 1)M_1^2 \sin^2\theta}{(\gamma - 1)M_1^2 \sin^2\theta + 2} \tag{8.75}$$

$$\frac{T_2}{T_1} = \frac{[2\gamma M_1^2 \sin^2\theta - (\gamma - 1)][(\gamma - 1)M_1^2 \sin^2\theta + 2]}{(\gamma + 1)^2 M_1^2 \sin^2\theta} \tag{8.76}$$

$$M_2^2 = \frac{(\gamma - 1)M_1^2 \sin^2\theta + 2}{[2\gamma M_1^2 \sin^2\theta - (\gamma - 1)]\sin^2(\theta - \delta)}$$

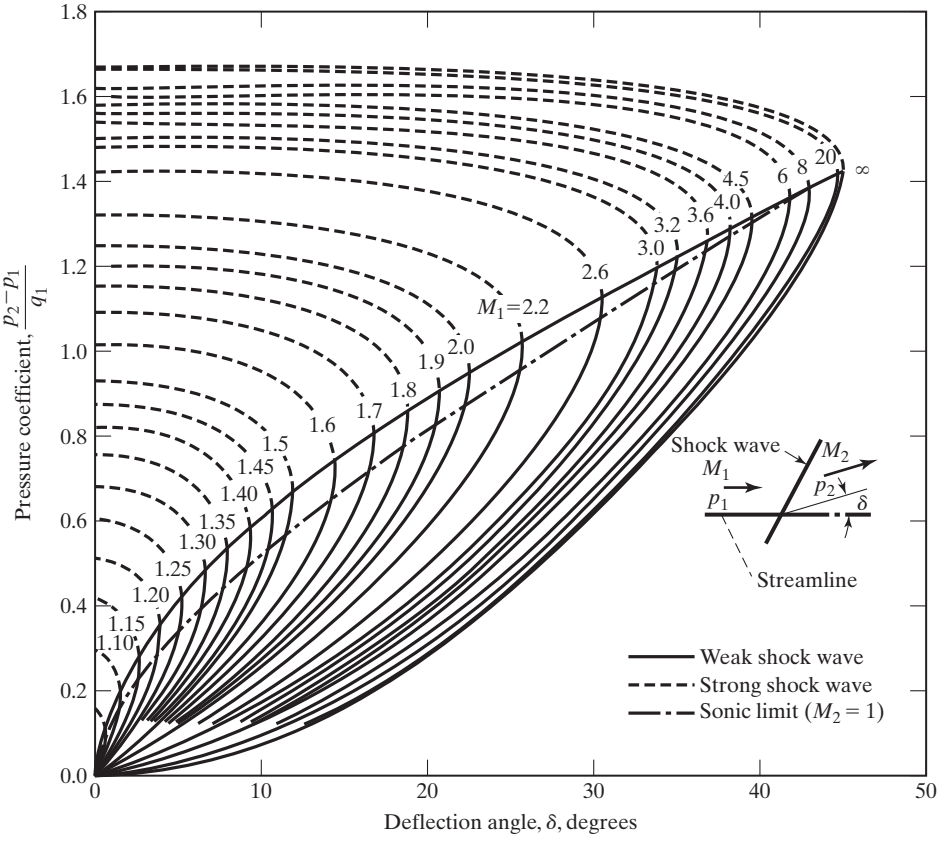

Figure 8.13 continued (b) pressure coefficient.

$$\frac{p_{t2}}{p_{t1}} = e^{-\Delta s/R} \tag{8.77}$$

$$= \left[\frac{(\gamma+1)M_1^2\sin^2\theta}{(\gamma-1)M_1^2\sin^2\theta+2}\right]^{\gamma/(\gamma-1)}\left[\frac{\gamma+1}{2\gamma M_1^2\sin^2\theta-(\gamma-1)}\right]^{1/(\gamma-1)} \tag{8.78}$$

and

$$C_p = \frac{p_2-p_1}{q_1} = \frac{4(M_1^2\sin^2\theta-1)}{(\gamma+1)M_1^2} \tag{8.79}$$

A summary of results for flow across normal and oblique shock waves is presented in Table 8.4. Notice that all of the static properties increase across normal or oblique shocks (the increase in pressure leads to the notion that a shock "compresses" the flow). The Mach number always decreases across a shock, to subsonic values for a normal shock, and to lower supersonic or subsonic values across an oblique shock. Since shocks are not isentropic, the total pressure decreases, but the total temperature is constant since shocks are adiabatic. The major difference between normal and oblique shocks is *how much* the properties change across the shock wave, not *how* the properties change.

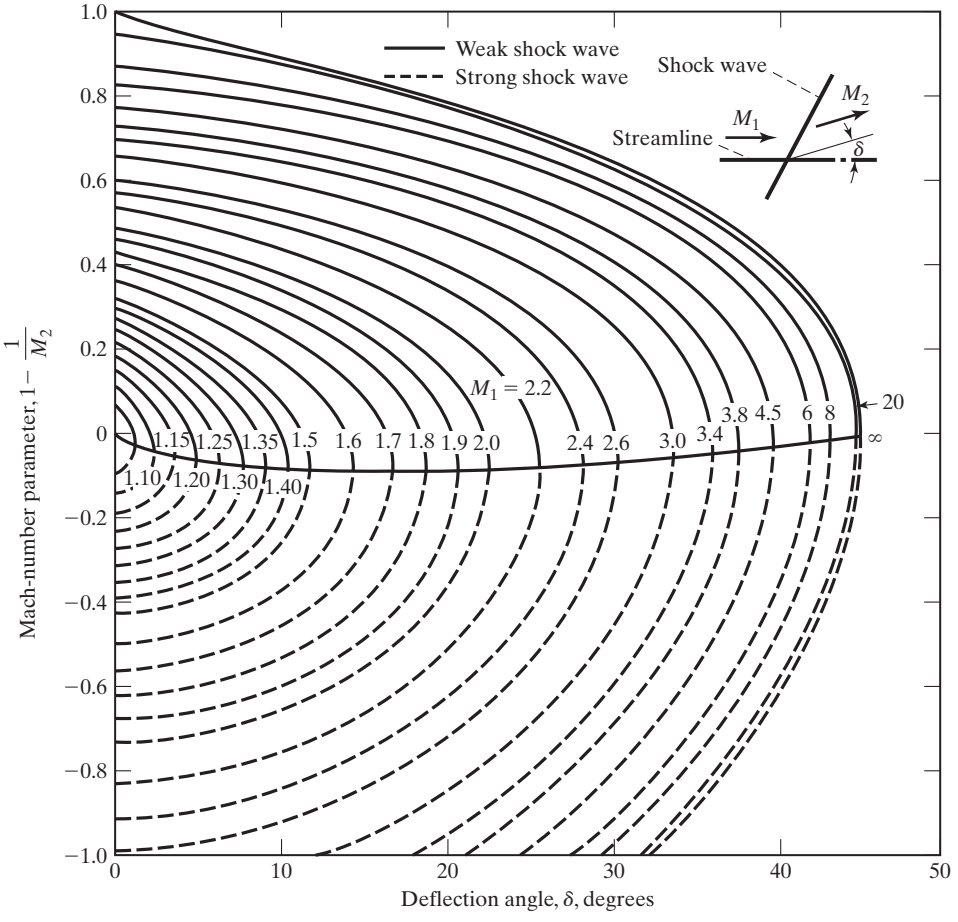

Figure 8.13 continued (c) downstream Mach number.

The pressure coefficient is presented in Fig. 8.13b as a function of δ and M_1. Equation (8.79) is consistent with equation (8.69) for a normal shock since $\gamma \to 1$ as $M_1 \to \infty$ due to the dissociation of molecules in the air at high Mach numbers. The values for many of these ratios are presented for a normal shock wave in Table 8.5 and in Fig. 8.14. The values for the pressure ratios, the density ratios, and the temperature ratios for an

TABLE 8.4 Flow Property Changes across Weak Shock Waves

Normal shock	*Oblique shock*
$p_2 > p_1$	$p_2 > p_1$
$\rho_2 > \rho_1$	$\rho_2 > \rho_1$
$T_2 > T_1$	$T_2 > T_1$
$M_2 < 1$	$M_2 < M_1$
$p_{t,2} < p_{t,1}$	$p_{t,2} < p_{t,1}$
$T_{t,2} = T_{t,1}$	$T_{t,2} = T_{t,1}$

TABLE 8.5 Correlation of Flow Properties across a Normal Shock Wave as a Function of the Upstream Mach Number for Air, $\gamma = 1.4$

M_1	M_2	$\frac{p_2}{p_1}$	$\frac{\rho_2}{\rho_1}$	$\frac{T_2}{T_1}$	$\frac{p_{t2}}{p_{t1}}$
1.00	1.00000	1.00000	1.00000	1.00000	1.00000
1.05	0.95312	1.1196	1.08398	1.03284	0.99987
1.10	0.91177	1.2450	1.1691	1.06494	0.99892
1.15	0.87502	1.3762	1.2550	1.09657	0.99669
1.20	0.84217	1.5133	1.3416	1.1280	0.99280
1.25	0.81264	1.6562	1.4286	1.1594	0.98706
1.30	0.78596	1.8050	1.5157	1.1909	0.97935
1.35	0.76175	1.9596	1.6027	1.2226	0.96972
1.40	0.73971	2.1200	1.6896	1.2547	0.95819
1.45	0.71956	2.2862	1.7761	1.2872	0.94483
1.50	0.70109	2.4583	1.8621	1.3202	0.92978
1.55	0.68410	2.6363	1.9473	1.3538	0.91319
1.60	0.66844	2.8201	2.0317	1.3880	0.89520
1.65	0.65396	3.0096	2.1152	1.4228	0.87598
1.70	0.64055	3.2050	2.1977	1.4583	0.85573
1.75	0.62809	3.4062	2.2781	1.4946	0.83456
1.80	0.61650	3.6133	2.3592	1.5316	0.81268
1.85	0.60570	3.8262	2.4381	1.5694	0.79021
1.90	0.59562	4.0450	2.5157	1.6079	0.76735
1.95	0.58618	4.2696	2.5919	1.6473	0.74418
2.00	0.57735	4.5000	2.6666	1.6875	0.72088
2.05	0.56907	4.7363	2.7400	1.7286	0.69752
2.10	0.56128	4.9784	2.8119	1.7704	0.67422
2.15	0.55395	5.2262	2.8823	1.8132	0.65105
2.20	0.54706	5.4800	2.9512	1.8569	0.62812
2.25	0.54055	5.7396	3.0186	1.9014	0.60554
2.30	0.53441	6.0050	3.0846	1.9468	0.58331
2.35	0.52861	6.2762	3.1490	1.9931	0.56148
2.40	0.52312	6.5533	3.2119	2.0403	0.54015
2.45	0.51792	6.8362	3.2733	2.0885	0.51932
2.50	0.51299	7.1250	3.3333	2.1375	0.49902
2.55	0.50831	7.4196	3.3918	2.1875	0.47927
2.60	0.50387	7.7200	3.4489	2.2383	0.46012
2.65	0.49965	8.0262	3.5047	2.2901	0.44155
2.70	0.49563	8.3383	3.5590	2.3429	0.42359
2.75	0.49181	8.6562	3.6119	2.3966	0.40622
2.80	0.48817	8.9800	3.6635	2.4512	0.38946
2.85	0.48470	9.3096	3.7139	2.5067	0.37330
2.90	0.48138	9.6450	3.7629	2.5632	0.35773
2.95	0.47821	9.986	3.8106	2.6206	0.34275
3.00	0.47519	10.333	3.8571	2.6790	0.32834
3.50	0.45115	14.125	4.2608	3.3150	0.21295
4.00	0.43496	18.500	4.5714	4.0469	0.13876
4.50	0.42355	23.458	4.8119	4.8761	0.09170
5.00	0.41523	29.000	5.0000	5.8000	0.06172
6.00	0.40416	41.833	5.2683	7.941	0.02965
7.00	0.39736	57.000	5.4444	10.469	0.01535
8.00	0.39289	74.500	5.5652	13.387	0.00849
9.00	0.38980	94.333	5.6512	16.693	0.00496
10.00	0.38757	116.50	5.7413	20.388	0.00304
∞	0.37796	∞	6.000	∞	0

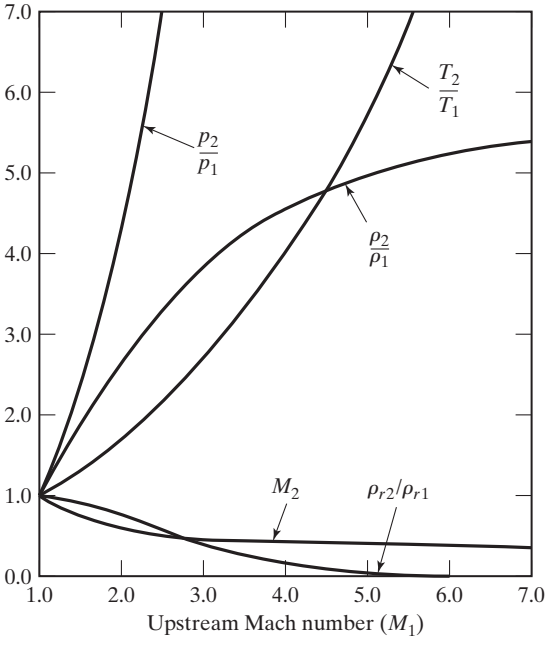

Figure 8.14 Property variations across a normal shock wave.

oblique shock wave can be read from Table 8.5 provided that $M_1 \sin \theta$ is used instead of M_1 in the first column. Note that since it is the tangential component of the velocity which is unchanged and not the tangential component of the Mach number, we cannot use Table 8.5 to calculate the downstream Mach number. The downstream Mach number is presented in Fig. 8.13c as a function of the deflection angle and of the upstream Mach number. An alternative procedure to calculate the Mach number behind the shock wave would be to convert the value of M_2 in Table 8.5 (which is the normal component of the Mach number) to the normal component of velocity, using T_2 to calculate the local speed of sound. Then, we can calculate the total velocity downstream of the shock wave:

$$U_2 = \sqrt{u_2^2 + v_2^2}$$

from which we can calculate the downstream Mach number.

For supersonic flow past a cone at zero angle of attack, the shock-wave angle θ_c depends on the upstream Mach number M_1 and the cone half-angle δ_c. Whereas all properties are constant downstream of the weak, oblique shock wave generated when supersonic flow encounters a wedge, this is not the case for the conical shock wave. In the conical shock wave case, properties are constant along rays (identified by angle ω) emanating from the vertex of the cone, as shown in the sketch of Fig. 8.15. Therefore, the static pressure varies with distance back from the shock along a line parallel to the cone axis. The shock-wave angle, the pressure coefficient:

$$C_p = \frac{p_c - p_1}{q_1}$$

(where p_c is the static pressure along the surface of the cone), and the Mach number of the inviscid flow at the surface of the cone M_c are presented in Fig. 8.16 as a function of the cone semivertex angle δ_c and the free-stream Mach number M_1.

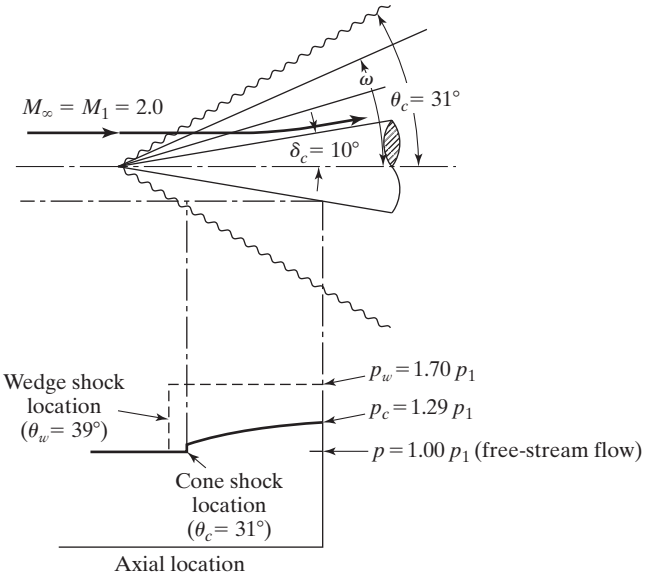

Figure 8.15 Supersonic flow past a sharp cone at zero angle of attack.

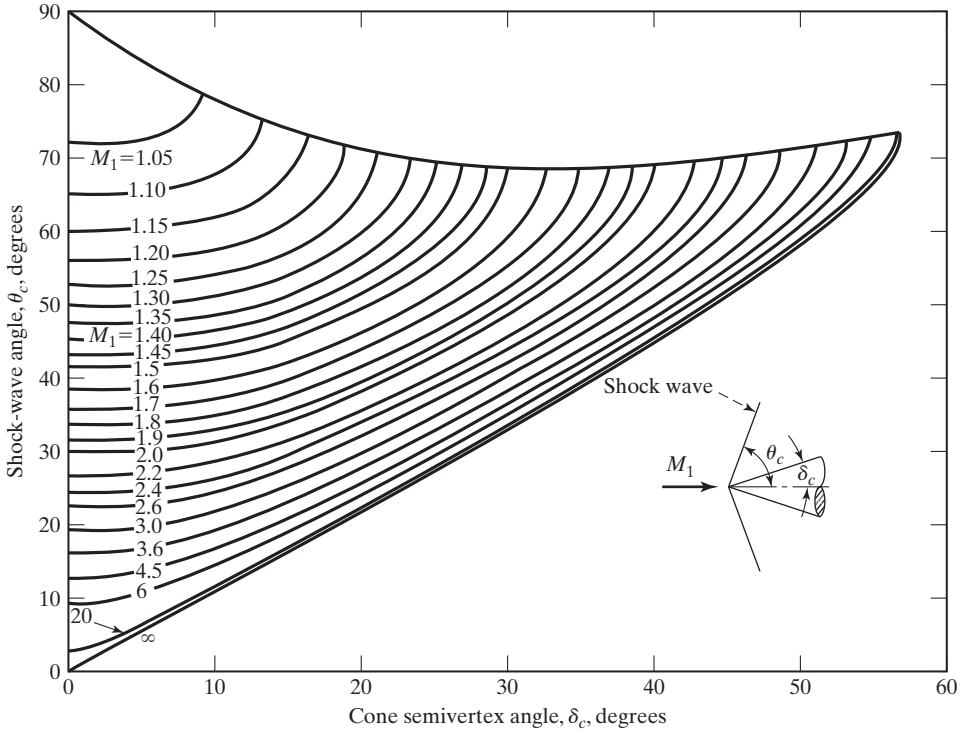

Figure 8.16 Variations of shock-wave parameters with cone semivertex angle for various upstream Mach numbers, $\gamma = 1.4$: (a) shock-wave angle.

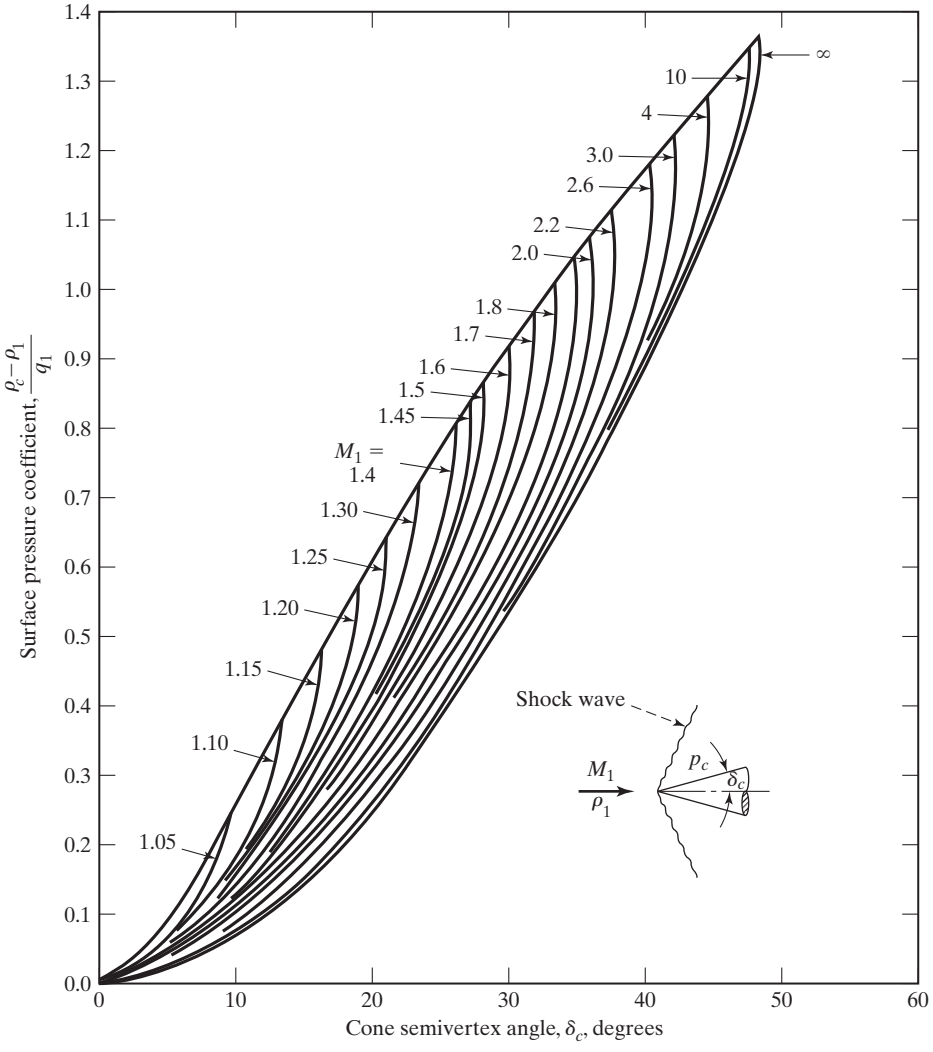

Figure 8.16 continued (b) pressure coefficient.

EXAMPLE 8.4 Supersonic flow past a sharp cone at zero degrees angle-of-attack

Consider the cone whose semivertex angle is 10° exposed to a Mach 2 free stream, as shown in Fig. 8.15. Find the pressure immediately behind the shock and on the surface of the cone.

Solution: Using Fig. 8.16a, the shock-wave angle is 31°. The pressure just downstream of the shock wave is given by equation (8.74) as

$$\frac{p_2}{p_1} = \frac{2(1.4)(4)(0.5150)^2 - 0.4}{2.4} = 1.07$$

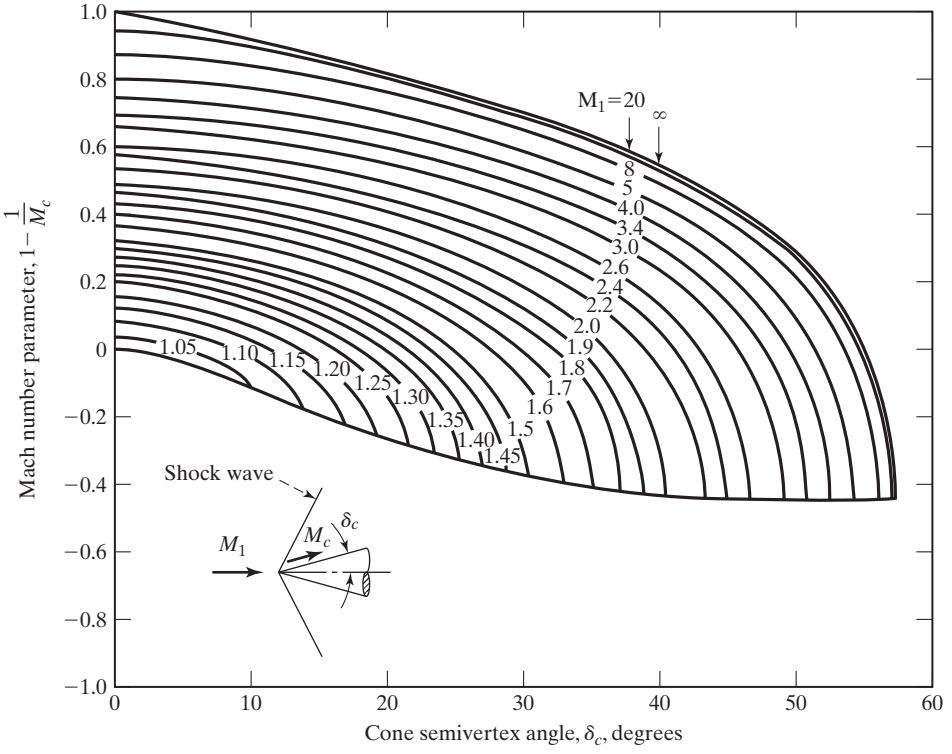

Figure 8.16 continued (c) Mach number on the surface of the cone.

$$p_2 = 1.07p_1 = 1.07p_\infty$$

The pressure increases across the shock layer (i.e., moving parallel to the cone axis), reaching a value of $1.29p_1$ (or $1.29p_\infty$) at the surface of the cone, as can be calculated using Fig. 8.16b. Included for comparison is the pressure downstream of the weak, oblique shock for a wedge with the same turning angle. Notice that the shock-wave angle θ_w and the pressure in the shock layer p_w are greater for the wedge. The difference is due to axisymmetric effects, which allow the flow to spread around the cone (a three-dimensional pressure relief) and which does not occur in the case of the wedge.

8.7 VISCOUS BOUNDARY LAYER

In our analysis of boundary layers in Chapter 4, we considered mostly flows for which the density is constant. The correlations for the skin-friction coefficient which were developed for these low-speed flows were a function of the Reynolds number only. However, as the free-stream Mach number approaches the transonic regime, shock waves occur at various positions on the configuration, as we will discuss in Chapter 9.

The presence of the boundary layer and the resultant shock-wave/boundary-layer interaction can radically alter the flow field. Furthermore, when the free-stream Mach number exceeds two, the work of compression and of viscous energy dissipation produces considerable increases in the static temperature in the boundary layer. Because the temperature-dependent properties, such as the density and the viscosity, are no longer constant, our solution technique must include the energy equation as well as the continuity and momentum equations.

Aerodynamics Concept Box: Schlieren Flow Visualization

A Schlieren photography system "relies on the fact that light rays are bent whenever they encounter changes in density of a fluid. Schlieren systems are used to visualize the flow away from the surface of an object." The Schlieren system shown below uses two optical-quality concave mirrors, one on each side of the test section. A mercury vapor lamp or a spark gap system (or even a high intensity light-emitting diode) is used as a bright source of light. The light is passed through a slit which is placed such that the reflected light from the mirror forms parallel rays that pass through the test section. On the other side of the tunnel, the parallel rays are collected by another mirror and focused to a point at the knife edge. The rays continue on to a recording device like a video camera.

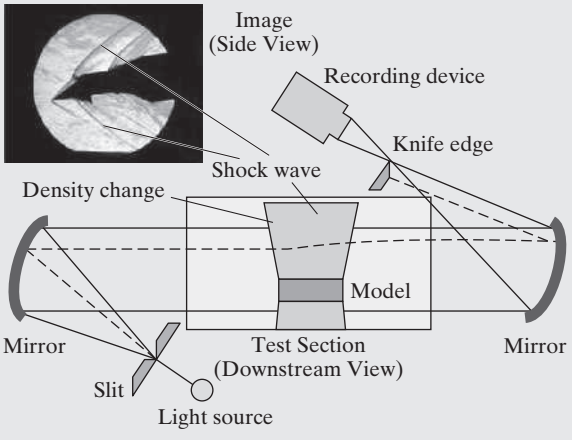

Layout of a Schlieren system
(from NASA Glenn Research Center)

When parallel rays of light encounter a density gradient, the light is refracted (or bent). Since a shock wave is a discontinuous change in density, parallel rays of light passing through the shock wave are bent (see the dashed line in the figure). The bent ray of light misses the focal point, and is blocked by the knife edge. The shock waves are now visible as dark regions on the picture, which allows us to visualize the shock wave patterns. A unique Schlieren photograph of a T-38 flying in the atmosphere is shown below, where the shocks, expansions waves, and wake of the aircraft are clearly visible. More information about Schlieren systems is available in Settles (2001).

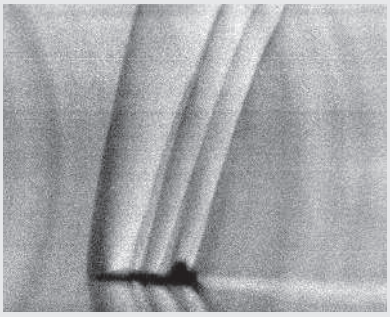

T-38 at Mach 1.1 and 13,700 ft altitude
(courtesy of NASA Dryden Flight Research Center)

Because the density gradients in the compressible boundary layer affect a parallel beam of light passing through a wind-tunnel test section, we can photographically record the boundary layer. A shadowgraph of the flow field for a cone ($\delta_c = 12°$) in a supersonic, Mach 11.5 stream is presented in Fig. 8.17. Boundary-layer transition is in process approximately one-quarter of the way along the portion of the conical generator which

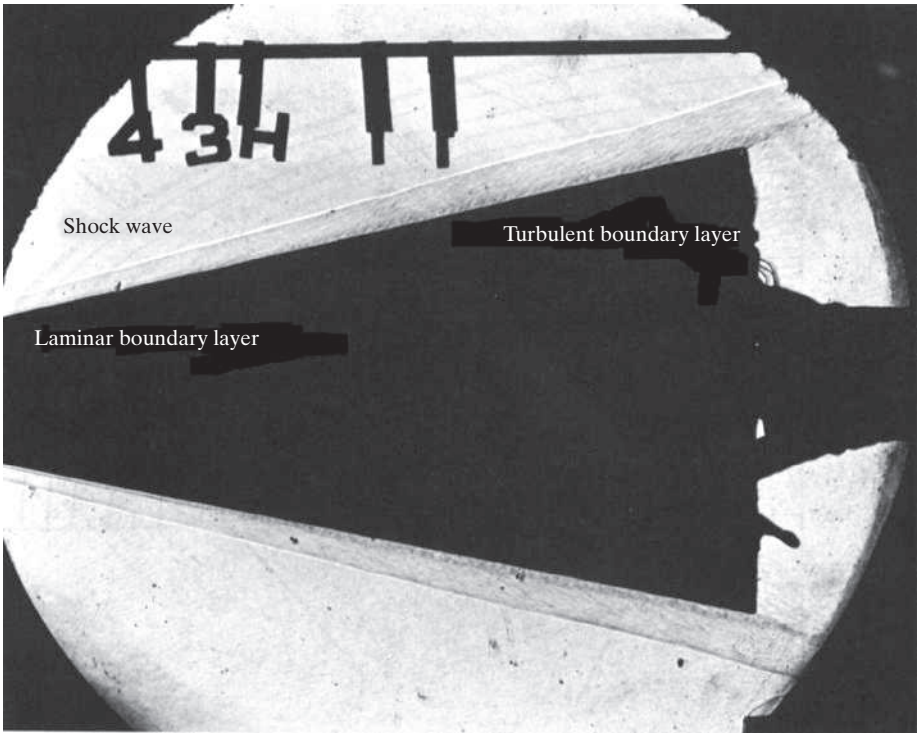

Figure 8.17 Hypersonic flow past a slender cone: $M_\infty = 11.5$; $\mathrm{Re}_{\infty,\mathrm{L}} = 4.28 \times 10^6$; $\delta_c = 12°$ (courtesy of Vought Archives).

appears in the photograph. Upstream (nearer the apex), the laminar boundary layer is thin and "smooth." Downstream (toward the base of the cone), the vortical character of the turbulent boundary layer is evident. Of course, as we discussed in Chapter 4, transition does not take place at a single point, but rather along a finite distance of the cone. You should also notice that the shock-wave angle is approximately 14.6°. The theoretical value, as calculated using Fig. 8.16a, is 14.3°. That a slightly larger angle is observed experimentally is due in part to the displacement effect of the boundary layer.

In addition to the calculations of the aerodynamic forces and moments, the aerodynamicist must address the problem of heat transfer. In the following sections, we will briefly discuss:

- The effects of compressibility
- Shock/wave/boundary-layer interactions (also called viscous/inviscid interactions)
- Shock/shock interactions

8.7.1 Effects of Compressibility

As we previously saw, considerable variations in the static temperature occur in the supersonic flow field around a body. We can calculate the maximum temperature that occurs in the flow of a perfect gas by using the energy equation for an adiabatic flow [i.e., equation (8.34)]. This maximum temperature, which is the *stagnation temperature*, is given by:

$$T_t = T_\infty \left(1 + \frac{\gamma - 1}{2} M_\infty^2 \right)$$

For example, we can calculate the stagnation temperature for a flow past a vehicle flying at a Mach number of 4.84 and at an altitude of 20 km. Referring to Table 1.2, T_∞ is 216.65 K. Also, since a_∞ is 295.069 m/s, U_∞ is 1428 m/s (or 5141 km/h). The total temperature for this flow is:

$$T_t = 216.65[\,1 + 0.2(4.84)^2\,] = 1231.7\ \text{K} = T_{te}$$

which is the stagnation temperature of the air outside of the boundary layer (at locations where the effects of heat transfer are negligible). For this flow we see that the temperature of the air at the stagnation point is sufficiently high that we could not use an aluminum structure. We have calculated the stagnation temperature, which exists only where the flow is at rest relative to the vehicle and where there is no heat transferred from the fluid. However, because heat is transferred from the boundary layer of these flows, the static temperature does not reach this value anywhere else on the surface of the cone (known as the *recovery temperature*). A numerical solution for the static temperature distribution across a laminar boundary layer on a flat-plate wing exposed to this flow is presented in Fig. 8.18. Although the maximum value of the static temperature is well below the stagnation temperature, it is greater than either the temperature at the wall or at the edge of the boundary layer. Therefore, a designer of vehicles that fly at supersonic speeds must consider problems related to convective heat transfer (i.e., the heat transfer due to fluid motion).

The correlation between convective heat transfer and the shear forces acting at the wall, which is known as *Reynolds analogy* and was discussed in Chapter 4, is clearly illustrated in Fig. 8.19. The streaks in the oil-flow pattern obtained in a wind tunnel

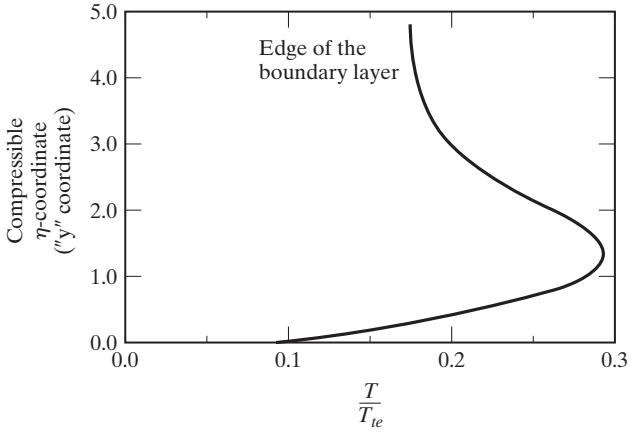

Figure 8.18 Static temperature distribution across a compressible, laminar boundary layer; $M_e = 4.84$; $T_w = 0.095\ T_{te}$.

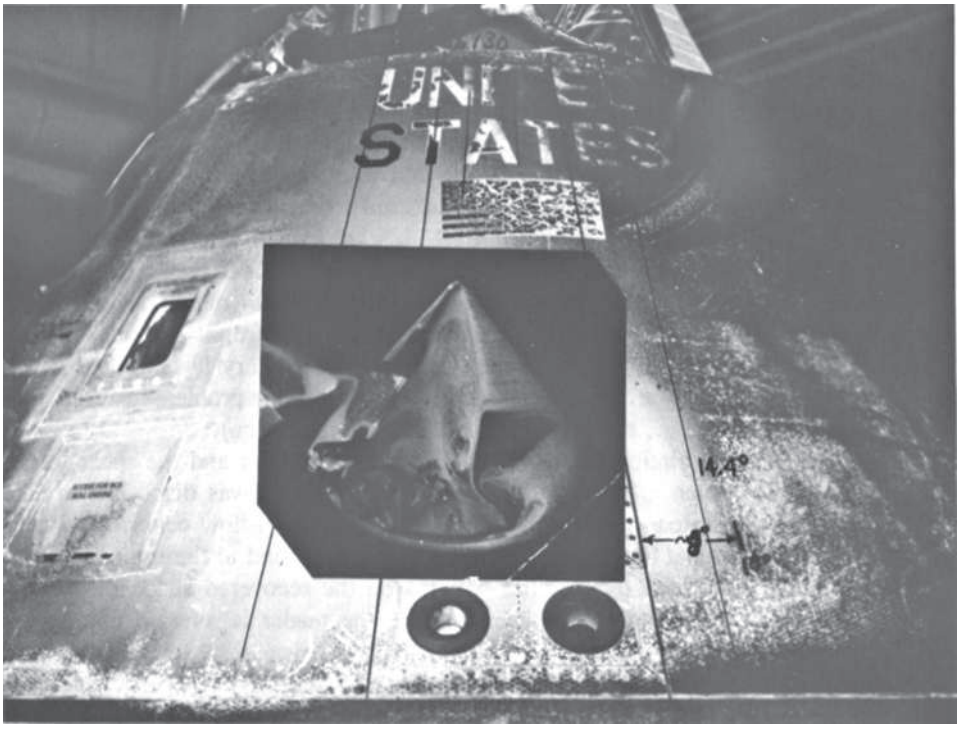

Figure 8.19 Comparison between the oil flow pattern (indicating skin friction) obtained in the wind tunnel and the char patterns on a recovered *Apollo* spacecraft (courtesy of NASA).

show that the regions of high shear correspond to the regions of high heating, which is indicated by the char patterns on the recovered spacecraft. For further information about convective heat transfer, the reader is referred to Chapter 4 and to texts such as Kays (1966) and Chapman (1974).

For high-speed flow past a flat plate, the skin-friction coefficient depends on the local Reynolds number, the Mach number of the inviscid flow, and the temperature ratio, T_w/T_e:

$$C_f = C_f\left(\mathrm{Re}_x, M_e, \frac{T_w}{T_e}\right) \tag{8.80}$$

Spalding and Chi (1964) developed a calculation procedure based on the assumption that there is a unique relation between $F_c C_f$ and $\mathrm{Re}_x F_{\mathrm{Re}}$, where C_f is the skin-friction coefficient, Re_x is the local Reynolds number, $\mathrm{Re}_x F_{\mathrm{Re}}$ is an equivalent incompressible Reynolds number, and F_c and F_{Re} are correlation parameters which depend only on the Mach number and on the temperature ratio. F_c and F_{Re} are presented as functions of M_e and of T_w/T_e in Tables 8.6 and 8.7, respectively. Therefore, given the flow conditions and the surface temperature, we can calculate F_c and F_{Re}. Then we can calculate the product $F_{\mathrm{Re}}\mathrm{Re}_x$ and find the corresponding value of $F_c C_f$ in Table 8.8. Since F_c is known, we can solve for C_f.

The ratio of the experimental skin-friction coefficient to the incompressible value at the same Reynolds number [as taken from Stalmach (1958)] is presented in Fig. 8.20 as a function of the Mach number. The experimental skin-friction coefficients are for adiabatic flows; that is, the surface temperature was such that there was no heat

TABLE 8.6 Values of F_c as a Function of M_e and T_w/T_e

	M_e						
$\frac{T_w}{T_e}$	*0.0*	*1.0*	*2.0*	*3.0*	*4.0*	*5.0*	*6.0*
0.05	0.3743	0.4036	0.4884	0.6222	0.7999	1.0184	1.2759
0.10	0.4331	0.4625	0.5477	0.6829	0.8628	1.0842	1.3451
0.20	0.5236	0.5530	0.6388	0.7756	0.9584	1.1836	1.4491
0.30	0.5989	0.6283	0.7145	0.8523	1.0370	1.2649	1.5337
0.40	0.6662	0.6957	0.7821	0.9208	1.1069	1.3370	1.6083
0.50	0.7286	0.7580	0.8446	0.9839	1.1713	1.4031	1.6767
0.60	0.7873	0.8168	0.9036	1.0434	1.2318	1.4651	1.7405
0.80	0.8972	0.9267	1.0137	1.1544	1.3445	1.5802	1.8589
1.00	1.0000	1.0295	1.1167	1.2581	1.4494	1.6871	1.9684
2.00	1.4571	1.4867	1.5744	1.7176	1.9130	2.1572	2.4472
3.00	1.8660	1.8956	1.9836	2.1278	2.3254	2.5733	2.8687
4.00	2.2500	2.2796	2.3678	2.5126	2.7117	2.9621	3.2611
5.00	2.6180	2.6477	2.7359	2.8812	3.0813	3.3336	3.6355
6.00	2.9747	3.0044	3.0927	3.2384	3.4393	3.6930	3.9971
8.00	3.6642	3.6938	3.7823	3.9284	4.1305	4.3863	4.6937
10.00	4.3311	4.3608	4.4493	4.5958	4.7986	5.0559	5.3657

Source: Spalding and Chi (1964).

TABLE 8.7 Values of F_{Re} as a Function of M_e and T_w/T_e

	M_e						
$\frac{T_w}{T_e}$	*0.0*	*1.0*	*2.0*	*3.0*	*4.0*	*5.0*	*6.0*
0.05	221.0540	232.6437	256.5708	278.2309	292.7413	300.8139	304.3061
0.10	68.9263	73.0824	82.3611	91.2557	97.6992	101.7158	103.9093
0.20	20.4777	22.0029	25.4203	28.9242	31.6618	33.5409	34.7210
0.30	9.8486	10.6532	12.5022	14.4793	16.0970	17.2649	18.0465
0.40	5.7938	6.2960	7.4742	8.7703	9.8686	10.6889	11.2618
0.50	3.8127	4.1588	4.9812	5.9072	6.7120	7.3304	7.7745
0.60	2.6969	2.9499	3.5588	4.2576	4.8783	5.3658	5.7246
0.80	1.5487	1.7015	2.0759	2.5183	2.9247	3.2556	3.5076
1.00	1.0000	1.1023	1.3562	1.6631	1.9526	2.1946	2.3840
2.00	0.2471	0.2748	0.3463	0.4385	0.5326	0.6178	0.6903
3.00	0.1061	0.1185	0.1512	0.1947	0.2410	0.2849	0.3239
4.00	0.0576	0.0645	0.0829	0.1079	0.1352	0.1620	0.1865
5.00	0.0356	0.0400	0.0516	0.0677	0.0856	0.1036	0.1204
6.00	0.0240	0.0269	0.0349	0.0460	0.0586	0.0715	0.0834
8.00	0.0127	0.0143	0.0187	0.0248	0.0320	0.0394	0.0466
10.00	0.0078	0.0087	0.0114	0.0153	0.0198	0.0246	0.0294

TABLE 8.8 Values of F_cC_f as a Function of $F_{\mathrm{Re}}\mathrm{Re}_x$

F_cC_f	$F_{\mathrm{Re}}\mathrm{Re}_x$	F_cC_f	$F_{\mathrm{Re}}\mathrm{Re}_x$
0.0010	5.758×10^{10}	0.0055	8.697×10^{4}
0.0015	4.610×10^{8}	0.0060	5.679×10^{4}
0.0020	4.651×10^{7}	0.0065	3.901×10^{4}
0.0025	9.340×10^{6}	0.0070	2.796×10^{4}
0.0030	2.778×10^{6}	0.0075	2.078×10^{4}
0.0035	1.062×10^{6}	0.0080	1.592×10^{4}
0.0040	4.828×10^{5}	0.0085	1.251×10^{4}
0.0045	2.492×10^{5}	0.0090	1.006×10^{4}
0.0050	1.417×10^{5}		

Source: Spalding and Chi (1964).

transferred from the fluid to the wall. The experimental values are compared with those given by the Spalding-Chi correlation. Another well-used compressible skin-friction relation was developed by Van Driest (1956) which should also be investigated for high-speed estimation purposes.

EXAMPLE 8.5: Skin-friction coefficient for a supersonic, turbulent boundary layer

What is the skin-friction coefficient for a turbulent boundary layer on a flat plate, when $M_e = 2.5$, $\mathrm{Re}_x = 6.142 \times 10^6$, and $T_w = 3.0T_e$?

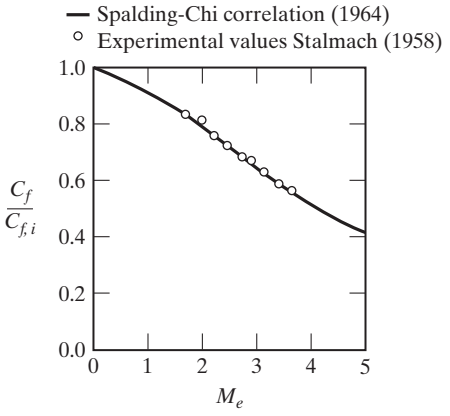

Figure 8.20 Ratio of the compressible, turbulent experimental skin-friction coefficient to the incompressible value at the same Reynolds number as a function of Mach number.

Solution: For these calculations,

$$F_c = 2.056 \text{ (see Table 8.6)}$$

and

$$F_{\text{Re}} = 0.1729 \text{ (see Table 8.7)}$$

Therefore,

$$\text{Re}_x F_{\text{Re}} = 1.062 \times 10^6$$

Using Table 8.8, we obtain

$$F_c C_f = 0.0035$$

so that

$$C_f = 1.70 \times 10^{-3}$$

8.8 SHOCK-WAVE/BOUNDARY-LAYER INTERACTIONS

Severe problems of locally high heating or premature boundary-layer separation may result due to viscous/inviscid interactions (which is another name for shock/boundary layer interactions) which occur during flight at supersonic Mach numbers. The shock wave generated by a deflected flap will interact with the upstream boundary layer, which will generally cause the upstream boundary layer to separate with locally high heating rates occurring when the flow reattaches. The extent of the separation, which can cause a loss of control effectiveness, depends on the character of the upstream boundary-layer. Other viscous interaction problems can occur when the shock waves generated by the forebody and other external components impinge on downstream surfaces of the vehicle. Again, locally severe heating rates or boundary-layer separation may occur.

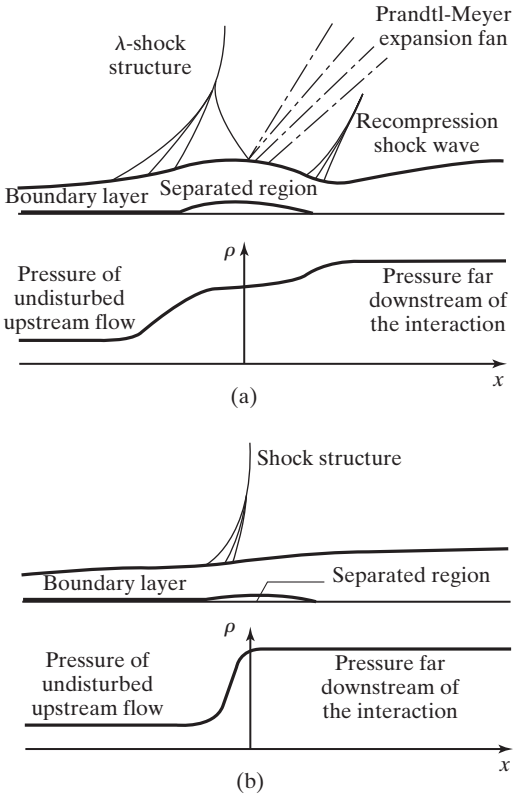

Figure 8.21 Flow field for shock-wave boundary-layer interaction: (a) laminar boundary-layer; (b) turbulent boundary-layer.

The basic features of the interaction between a shock wave and a laminar boundary layer for a two-dimensional flow are shown in Fig. 8.21a. The pressure rise induced by the shock wave is propagated upstream through the subsonic portion of the boundary layer. Recall that pressure disturbances can affect the upstream flow only if the flow is subsonic. As a result, the boundary-layer thickness increases and the momentum decreases. The thickening boundary layer deflects the external stream and creates a series of compression waves to form a λ-like shock structure. If the shock-induced adverse-pressure-gradient is great enough, the skin friction will be reduced to zero and the boundary layer will separate. The subsequent behavior of the flow is a strong function of the geometry. For a flat plate, the flow reattaches at some distance downstream. In the case of a convex body, such as an airfoil, the flow may or may not reattach, depending upon the body geometry, the characteristics of the boundary layer, and the strength of the shock wave.

If the flow reattaches, a Prandtl-Meyer expansion fan results as the flow turns back toward the surface. As the flow reattaches and turns parallel to the plate, a second shock wave (termed the *reattachment shock*) is formed. Immediately downstream of reattachment, the boundary-layer thickness reaches a minimum. It is in this region where the maximum heating rates occur.

In the case of a shock interaction with a turbulent boundary-layer (Fig. 8.21b), the length of the interaction is considerably shorter than the interaction length for a laminar boundary layer. This results because the air particles near the wall of a turbulent boundary-layer have greater momentum than do those near the wall in a laminar boundary-layer and can therefore overcome a greater adverse pressure gradient. Furthermore, since the subsonic portion of a turbulent boundary layer is relatively thin, the region through which the shock-induced pressure rise can propagate upstream is limited. As a result, a much greater pressure rise is required to cause a turbulent boundary layer to separate.

Pressure distributions typical of the shock-wave/boundary-layer interactions are presented in Fig. 8.21 for a laminar boundary layer and for a turbulent one. As we might expect from the preceding description of the shock interaction, the pressure rise is spread over a much longer distance when the boundary layer is laminar.

8.9 SHOCK/SHOCK INTERACTIONS

Perhaps the least understood (historically) area of shock waves is how they interact with each other. There are many situations on aerospace vehicles where shocks coming from different parts of the vehicle can intersect other shocks (such as a nose shock intersecting a wing shock) or can intersect solid surfaces. How we analyze these intersections is a challenging and important area of aerodynamics.

Edney (1968) was the first person to classify different shock interactions. He came up with six basic interactions types, which are shown in Fig. 8.22. Edney's classification types depends on the angle between an impinging shock wave and another shock (shown as a bow shock in front of a hemispherical nose in Fig. 8.22). For larger intersection angles, Edney classified Type I through Type III cases, and for shallower intersection angles there are Type IV through Type VI cases. The location of the

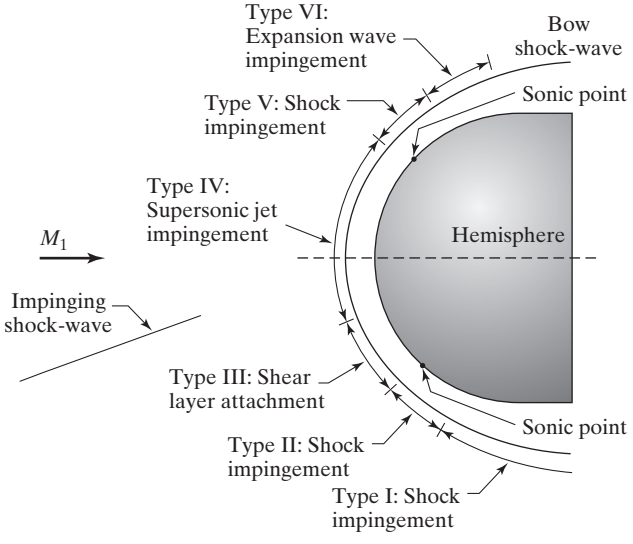

Figure 8.22 Approximate relation of the shock/shock geometry and the type of interference pattern [from Edney (1968)].

impingement point relative to the sonic regions is also important to the results. Each of the cases represents a unique type of shock interaction, with its own features that distinguish it from the other types. Specifically, Edney's classification system includes:

- Type I: shock impingement
- Type II: shock impingement (but at a different angle, creating a different resulting flow field)
- Type III: shear layer attachment
- Type IV: supersonic jet impingement
- Type V: shock impingement
- Type VI: expansion wave impingement

While we will not go into detail about all of the shock/shock interaction types, we will look at two very important cases: Type I and Type IV. Type I shock interactions are perhaps the most common, since they often take place in engine inlets, as represented by the geometry in Fig. 8.23. Two oblique shocks, perhaps created by wedged surfaces at slightly different angles, intersect and alter each other, creating at least six different flow regions (assuming at least one of the shocks reflects off a wall). In order to analyze these six regions, basic concepts from gas dynamics are used, along with some knowledge about the flow field. Region 1 is the free-stream region, whose properties we would know (Mach number, pressure, temperature, flow direction, etc.). We will also assume that the wedge angles are known for the upper and lower wedges, which means oblique shock analysis or tables can be used to find the properties in Regions 2 and 3. Finding the properties in Regions 4 and 5, however, is not as straight forward since we need to know what happened to the two shock waves after they intersected (these shock waves are called the transmitted waves). The resulting shock-wave angles are crucial for our analysis, but they cannot be found without knowing a basic concept: the flows in Regions 4 and 5 have to be parallel and have the same pressure, but do not necessarily have to have the same Mach number.

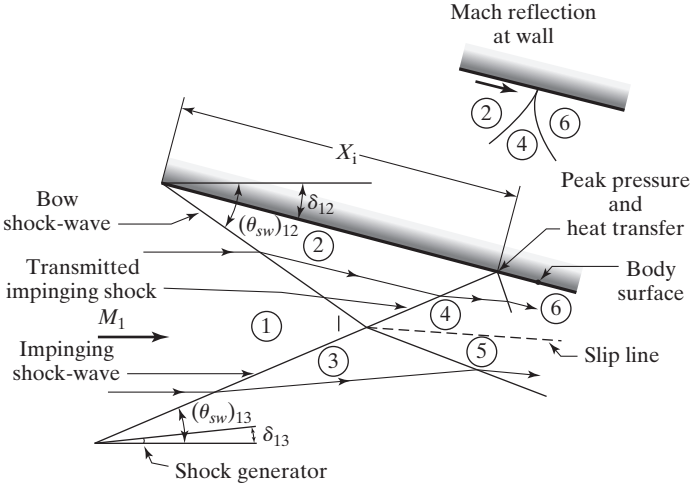

Figure 8.23 Type I shock/shock interaction flow pattern.

This fact is represented in Fig. 8.23 by the slip line, which is a line across which the Mach number can change discontinuously. Of course, in fluid dynamics a slip line is also a line along which a shear layer will form, but for our analysis we will assume that the flows in Regions 3 and 4 do not create a shear layer (based on our inviscid flow assumption). The properties in Regions 4 and 5 must be obtained in a way to make our observation true, which means that a "trial and error" approach is required to find the properties in this region. By assuming the angles of the transmitted shock waves, flow properties in Regions 4 and 5 will be obtained, but in general they will not be parallel or have the same pressure. Once the initial results are obtained, the shock angles can be altered to improve the result, and the process is repeated until the desired results are obtained.

A similar process takes place to determine the result for Region 6, which involves a shock wave reflecting from a solid surface. Once the properties in Region 4 are determined, a reflected shock angle has to be found that will turn the flow parallel to the wall. Once this shock angle is found, then the properties in Region 6 can be determined using oblique shock relations or tables. Of special interest about the wall reflection is what happens very close to the wall, where the shock comes into contact with the boundary layer (our analysis has been inviscid, but we will look at this interaction from a viscous perspective). Instead of cleanly reflecting from the wall, the shock actually interacts with the boundary layer (as discussed in Section 8.8) and forms a normal shock near the surface, and a curved reflected shock away from the surface. Analyzing this viscous flow field is quite difficult, so we will be content with our inviscid analysis.

EXAMPLE 8.6: Estimating properties for a Type I shock/shock interaction

A Type I shock/shock interaction is shown in Fig. 8.23. The free-stream conditions for the flow are $M_1 = 6.0$ and $p_1 = 10^{-3}$ atm. The geometry for the inlet is such that $\delta_{12} = 15°$ and $\delta_{13} = 5°$. Find the pressure and Mach number in Regions 2, 3, 4, and 6.

Solution: The calculations for the impinging shock waves may be accomplished using Fig. 8.13, so the flows in Regions 2 and 3 are relatively straightforward to determine. Since the ramp in front of Region 2 is at 15° and the ramp in front of Region 3 is 5°, we may look up the pressure coefficient and Mach number for Regions 2 and 3 directly:

$$M_2 = 4.00 \qquad C_{p2} = 0.200 \qquad M_3 = 5.32 \qquad C_{p3} = 0.043$$

Using our relationship for pressure coefficient in terms of pressure ratio:

$$C_p = \frac{2}{\gamma M_1^2}\left(\frac{p}{p_1} - 1\right)$$

we can find that:

$$\frac{p_2}{p_1} = 6.04 \qquad p_2 = 6.04 \times 10^{-3}\ \text{atm} \qquad \frac{p_3}{p_1} = 2.08 \qquad p_3 = 2.08 \times 10^{-3}\ \text{atm}$$

Remember that the pressures in Regions 4 and 5 must be equal, which determines the shock strengths for the transmitted shocks. Since the two shocks will

be of different strengths, that means the other properties in Regions 4 and 5 (like velocity and temperature) will be different. The slip line that forms between the two regions will in reality by a shear layer, but our inviscid analysis will allow for a discontinuity of velocity along this line. Finding the properties in Regions 4 and 5 requires an iterative process. Typically the process is done by assuming the flow direction in Regions 4 and 5 (we can call this θ_f, where $\theta_f = 0$ is aligned with the free-stream direction), calculating the change in the flow angles, and using Fig. 8.13 to find the flow in Regions 4 and 5. This process is then repeated until we find the transmitted shock strengths that give $p_4 = p_5$. Therefore, for our previously found Mach numbers in Regions 2 and 3,

$$M_2 = 4.00 \qquad p_2 = 6.04 \times 10^{-3} \text{ atm} \qquad \theta_{f,4} = -15°$$
$$M_3 = 5.32 \qquad p_3 = 2.08 \times 10^{-3} \text{ atm} \qquad \theta_{f,5} = +5°$$

which assumes the flow in both regions has turned back to the free-stream direction. Iterating on θ_f to the nearest tenth of a degree yields:

$$\theta_{f,4} = \theta_{f,5} = -9.7° \qquad \delta_{24} = 5.3° \qquad \delta_{35} = 14.7°$$
$$p_4 = p_5 = 0.0103 \text{ atm} \qquad M_4 = 3.60$$

Since the flow in Region 4 is inclined down at −9.7° and the wedge is inclined at −15°, and since the flow in Region 6 must be parallel to the surface, then the shock wave between Regions 4 and 6 must turn the flow 5.3°. Using Fig. 8.13 we can find:

$$M_6 = 3.33 \qquad C_{p6} = \frac{p_6 - p_4}{\frac{1}{2}\gamma p_4 M_4^2} = 0.062 \qquad \frac{p_6}{p_4} = 1.56 \qquad p_6 = 0.0161 \text{ atm}$$

The Edney Type IV shock interaction is perhaps the most complex, and potentially damaging, interaction (see Fig. 8.24). The Type IV interaction takes place when

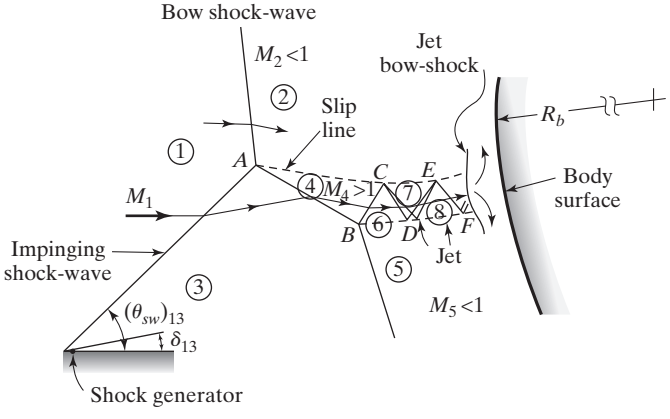

Figure 8.24 Type IV shock/shock interaction flow pattern and resulting supersonic jet.

a shock intersects the bow shock within the sonic region. While some of the initial details about the interaction are similar to other shock interactions, the Type IV interaction has a unique flow pattern. In this case, instead of a simple slip line originating at the intersection point, a supersonic jet is produced. According to Edney (1968), "This is the most important of the various types of interference and the one that leads to the very high peak heatings." Calculating the complete flow field for a Type IV interaction is quite complicated, but a description from Edney (1968) will help to understand the complexity of the flow. "It is simple to calculate the initial velocities U_2 and U_3, Mach numbers M_2 and M_3, and pressures p_2 and p_3 on either side of the shear layer, and the flow deflection angle at the impingement point. . . . we see how the flow is divided into a subsonic and supersonic part at the impingement point, being subsonic above the impingement point and supersonic below. Depending on M_2 and the angle the shear layer makes with the model surface, the shear layer may attach to the surface of the model without being deflected. This occurs when M_2 is sufficiently large, or the attachment angle sufficiently small, for the supersonic part of the flow to be turned downward through an attached oblique shock at the [surface]" [Edney (1968)]. The end result of this flow complexity is that a high temperature supersonic jet impinges on the surface of the vehicle, creating extremely high heating rates, and possibly leading to catastrophic results.

8.10 THE ROLE OF EXPERIMENTS FOR GENERATING INFORMATION DEFINING THE FLOW FIELD

The tools that are available to the designers of high-speed aerospace vehicles include analytical methods, numerical methods, experimental programs using ground-testing facilities, and experimental programs using flight-test programs. Most of the material defining the role of experiments in generating information defining the flow field has been taken from an article in the *Annual Review of Fluid Mechanics* [Bertin and Cummings (2006)].

8.10.1 Ground-Based Tests

Despite the remarkable advances in hardware and software for computational fluid dynamics (CFD) tools, when two critical "return-to-flight" (RTF) concerns were identified in the aerothermodynamic environment of the Space Shuttle, very extensive wind-tunnel programs were conducted. One RTF concern dealt with the heating in the bipod region during launch. The second concern was related to the aerodynamics forces and moments during reentry. Wind-tunnel tests provided the majority of the aerothermal information required by the RTF advisory teams. CFD solutions were used primarily to generate numerical values for use in comparisons with the experimental measurements.

Since there is no single ground-based facility capable of duplicating the entire high-speed flight environment, different facilities are used to address various aspects of the design problems associated with supersonic flight. Most of the measurements that are used during the design process to define the aerothermodynamic environment (i.e., the aerodynamic forces and moments, the surface pressure distribution, and the heat-transfer distribution) are obtained in:

- Conventional wind tunnels
- Shock-heated wind tunnels

- Shock tubes
- Arc-heated test facilities
- Ballistic, free-flight ranges

The parameters that can be simulated in ground-based test facilities include:

- Free-stream Mach number
- Free-stream Reynolds number (and its influence on the character of the boundary layer)
- Free-stream velocity
- Pressure altitude
- Total enthalpy of the flow
- Density ratio across the shock wave
- Test gas
- Wall-to-total temperature ratio
- Thermochemistry of the flow field

Notice that some of the parameters are interrelated (e.g., the free-stream velocity, the total enthalpy of the flow, the free-stream Mach number, and the wall-to-total temperature ratio). However, it is very difficult to match all of these parameters in ground-based facilities. The critical heating to the bipod region of the Shuttle Orbiter occurs in the Mach number range from 3.5 to 4.0—just prior to staging at approximately 30,480 m (100,000 ft). Because the total temperature for Mach 4 flow at 30,480 m (100,000 ft) is approximately 950 K (1710°R), we can simultaneously simulate the free-stream velocity, the total enthalpy of the flow, the free-stream Mach number, and the free-stream Reynolds number in conventional wind-tunnel facilities. Two facilities in which one can match these four parameters are the Supersonic Aerothermal Tunnel C at the Arnold Engineering Development Center (AEDC) [Anderson and Matthews (1993)] and the LENS II facility at the Calspan-University at Buffalo Research Center (CUBRC) [Holden et al. (1995)].

You should also notice that during a specific run of a wind-tunnel test program, the model temperature usually starts out at room temperature. The temperature measurements that are used to determine the heat-transfer rates to the model usually are made early during the test run. Therefore, the temperature of model surfaces remains relatively cool during the data-recording portion of the run. On the other hand, the relatively long exposure to the high-temperature flight environment causes the surface of the vehicle to become very hot. As a result, the wall-to-total-temperature ratio in ground-based tests is usually well below the flight value. To match the flight value of the wall-to-total-temperature ratio, the total temperature of the tunnel flow is reduced below the flight value. Even for this relatively benign flow, we cannot match the flight values of all of the flow-field parameters.

In addition to the nine flow-field related parameters that were identified earlier in this section, several additional factors must be considered when developing a test plan. The additional factors include:

- Model scale
- Test time

- Types of data available
- Flow quality (including uniformity, noise, cleanliness, and steadiness)

Trimmer et al. (1986) noted, "Aerodynamic modeling is the art of partial simulation." The test engineer must decide which parameters are critical to accomplishing the objectives of the test program. In fact, during the development of a particular vehicle, the designers most likely will utilize many different facilities with the run schedule, the model, the instrumentation, and the test conditions for each program tailored to answer specific questions. As stated by Matthews et al. (1985), "A precisely defined test objective coupled with comprehensive pretest planning are essential for a successful test program."

In spite of these shortcomings, however, there are many reasons for conducting ground-based test programs. Some objectives include the following:

Objective 1. Obtain data to define the aerodynamic forces and moments, surface pressures, and/or the heat-transfer distributions for complete configurations whose complex flow fields resist computational modeling.

Objective 2. Use partial configurations to obtain data defining local-flow phenomena, such as the inlet flow field for hypersonic air-breathing engines or the shock/boundary-layer interactions associated with deflected control surfaces (a body flap).

Objective 3. Obtain detailed flow-field data to be used in developing numerical models for use in a computational algorithm (code validation).

Objective 4. Obtain measurements of parameters, such as the heat transfer and the drag, to be used in comparison with computed flow-field solutions over a range of configuration geometries and of flow conditions (code calibration).

Objective 5. Obtain data that can be used to develop empirical correlations for phenomena that resist analytical and/or numerical modeling, such as boundary-layer transition and turbulence modeling.

Objective 6. Certify the performance of air-breathing engines.

Even today, extensive ground-based test programs are conducted during the design process in order to define the aerothermodynamic environment for the entire vehicle. When the access to space study that was conducted by NASA in the early 1990s recommended the development of a fully reusable launch vehicle (RLV) [Bekey et al. (2001)], NASA joined an industry-led technology-development effort for the X-33/RLV. As part of the industry/government partnership, personnel and facilities at the NASA Langley Research Center were assigned the task of providing information regarding the aerodynamic forces and moments, the surface heating, and the criteria for boundary-layer transition to Lockheed Martin in support of X-33 development and design.

A special section in the September–October 2001 issue of the *Journal of Spacecraft and Rockets* presented five archival journal articles, documenting the results from this cooperative effort. Two articles presented information relating to Objective (1), "Obtain data to define the aerodynamic forces and moments, surface pressures, and/or the heat-transfer distributions for complete configurations whose complex flow fields resist

computational modeling." They are the articles by Horvath et al. (2001) and Murphy et al. (2001). Two articles presented information relating to Objective (4), "Obtain measurements of parameters, such as the heat transfer and the drag, to be used in comparison with computed flow-field solutions over a range of configuration geometries and of flow conditions (code calibration)." They are the articles by Hollis et al. (2001a) and Hollis et al. (2001b). One article [Berry et al. (2001a)] related to Objective (5), "Obtain data that can be used to develop empirical correlations for phenomena that resist analytical and/or numerical modeling, such as boundary-layer transition and turbulence modeling."

In 1996 NASA initiated the Hyper-X program as part of an initiative to mature the technologies associated with hypersonic air-breathing propulsion. "The primary goals of the Hyper-X program are to demonstrate and validate the technologies, the experimental techniques, and the computational methods and tools required to design and develop hypersonic aircraft with airframe-integrated, dual-mode scramjet propulsion systems" [Engelund (2001)]. Although hypersonic air-breathing propulsion systems have been studied in the laboratory environment for over 40 years, a complete airframe-integrated vehicle configuration had never been flight tested. Again, personnel and facilities at the NASA Langley Research Center were used to define the aerodynamic and surface heating environments, including information relating to the boundary-layer transition criteria, as part of the design, the development, the construction, and the flight-test program for the X-43.

A special section in the November–December 2001 issue of the *Journal of Spacecraft and Rockets* presented seven archival journal articles summarizing the results from this program. Two articles presented information relating to Objective (1); they are the articles by Engelund et al. (2001) and Holland et al. (2001). One article presented information relating to Objective (4); that was the article by Cockrell et al. (2001). Finally, one article [Berry et al. (2001b)] related to Objective (5).

As described by Woods et al. (2001), the Hyper-X Research Vehicle (also called HXRV or free flyer) required a booster to deliver the vehicle to the engine test points. The test conditions for the first flight included $M_\infty = 7$ and $q_\infty = 47{,}879\ \mathrm{N/m^2}$ (1000 psf) at an altitude of approximately 28,956 m (95,000 ft). The Hyper-X Launch Vehicle (HXLV) stack was initially carried aloft under the wing of a B-52. The HXLV was dropped, the Pegasus vehicle ignited, and the stack accelerated to the desired test Mach number. When the stack reached the desired test conditions and attitude, a stage-separation sequence of events separated the free flyer from the booster. The free-flying research vehicle then followed a preprogrammed trajectory. Although occurring in less than 500 ms, stage separation was critical to reaching the engine test point and was essential to the success of the mission.

Buning et al. (2001) reported that: "Even following the AEDC test, several aerodynamic issues remained in fully understanding the dynamics of the stage separation maneuver. This understanding was complicated by the unsteady nature of the event, the number of degrees of freedom associated with the booster, research vehicle, and control surfaces; and limits in the amount of wind-tunnel data available. These issues were in three basic areas: unsteady effects, aerodynamic database extrapolation, and differences between wind-tunnel and flight conditions." Viscous and inviscid CFD techniques were used to quantify unsteady effects, to examine the cause and the extent of interference between the booster and the research vehicle, and to identify differences between the wind tunnel and the flight environments.

8.10.2 Flight Tests

One of the most important things to know about flight tests is that they are very expensive. Flight tests take a long time to plan and to execute successfully. Furthermore, it is difficult to obtain quality data at well-defined test conditions. Flight tests will never replace ground-based tests or CFD in the design process. Nevertheless, flight tests are critical to our understanding of the hypersonic aerothermodynamic environment, since they provide data which cannot be obtained elsewhere.

There are a variety of reasons for conducting flight tests. Four of these reasons were described by Buck et al. (1963):

- To demonstrate interactive technologies and to identify unanticipated problems.
- To form a catalyst (or a focus) for technology.
- To gain knowledge not only from the flights but also from the process of development.
- To demonstrate technology in flight so that it is credible for larger-scale applications.

Neumann (1988) added three additional reasons:

- To verify ground-test data and/or to understand the bridge between ground-test simulations and actual flight.
- To validate the overall performance of the system.
- To generate information not available on the ground.

Williamson (1992) noted: "Due to the large investment in flight testing, it is then desirable to make as many measurements as possible during the flight to help verify predictions or explain any modeling inaccuracies. The instrumentation should measure as directly as possible the things that have been predicted. This is often not possible and it is often necessary to infer predictions from related but not direct measurements." Neumann (1989) stated: "Heat transfer is a quantity which cannot be directly measured: It is interpreted within the context of a thermal model rather than measured." Therefore, we must be able to develop a numerical model that describes the relation between the measured temperature and the sensor's design, in order to obtain a reasonably accurate value of the experimentally determined heat transfer. However, we must also develop a numerical model depicting how the heat-transfer sensor responds from its location in the vehicle. Serious problems can occur when the heat sensor is not properly integrated into the flight structure such that minimal thermal distortion is produced.

Williamson (1992) notes that, "Measurements fall into three groups. These include atmospheric properties measurements, offboard vehicle related sensor measurements, and onboard vehicle related measurements telemetered to the ground or stored on tape and retrieved post-flight."

There are two types of flight-test programs: (1) Research and Development (R&D) programs and (2) flights of prototype or operational vehicles. R&D programs are focused on technical issues which drive the design of the vehicle and its flight operations. Iliff and Shafer (1992) noted that: "In the 1960's, several programs successfully generated aerothermodynamic flight data to improve the understanding and interpretation of theoretical and ground test results. The ASSET and PRIME programs were flown in the early 1960's and provided aerothermodynamic flight data for ablative and

metallic thermal protection (TPS) concepts." Project Fire provided calorimeter heating measurements on a large-scale blunt body entering the earth's atmosphere at an initial velocity 11.35 km/s (37.24 kft/s). As discussed by Cornette (1966), the forebody of the "Apollo-like" reentry capsule was constructed of three beryllium calorimeter shields, which were alternated with phenolic-asbestos heat shields. This multiple-layer arrangement provided three distinct time periods when measurements defining the aerothermodynamic environment could be obtained. The FIRE program provided flight data that was used to understand radiative heat-transfer that become important for flight through the earth's atmosphere and when returning from lunar and from planetary missions [Ried et al. (1972) and Sutton (1985)].

Flight-test data have been obtained on prototype vehicles [e.g., the flights of the unmanned Apollo Command Modules (017 and 020) as discussed in Lee and Goodrich (1972)] and on operational vehicles [e.g., the Space Shuttle Orbiter, Throckmorton (1995)]. Throckmorton (1993) noted that the concept of using the Shuttle Orbiter as a flight research vehicle as an adjunct to its normal operational mission was a topic of discussion within the research community throughout the 1970s. Aerothermodynamic parameters based on flight-test data obtained from thermocouples embedded in the Space Shuttle Thermal Protection System (TPS) were used to expand the flight envelope for the Orbiter. As noted by Hodge and Audley (1983), "Requirements for the technique include an analytical model for the simulation of the heat transfer to a point on the TPS, flight test maneuvers which cause the thermocouples imbedded near the surface of the TPS to respond sufficiently above the noise levels, and a parameter estimation program to reduce flight thermocouple data. . . . The data reduction program correlates heating with the variables such as angle of attack, sideslip, control surface deflection, and Reynolds number. This technique could also be used for wind tunnel data reduction."

The interactions between impinging shock waves and the bow shock wave can produce locally severe heat-transfer rates. Edney (1968) identified six different shock/shock interactions patterns. The positive deflection of the Orbiter body flap creates a shock wave which interacts with the boundary layer on the Orbiter. The adverse pressure gradient produced by the shock wave causes the boundary layer to thicken and (in many cases) to separate. The upstream extent of the interaction-produced perturbations depends on the size of the subsonic portion of the approach boundary layer and on the strength of the shock wave produced by the turning of the flow. Therefore, as noted by Bertin (1994), the parameters that influence the extent of an interaction are: (1) whether the approach boundary layer is laminar or turbulent, (2) the Mach number of the approach flow, (3) the Reynolds number of the approach flow, (4) the surface temperature, (5) the deflection angle of the ramp, and (6) the chemical state of the gas. Bertin et al. (1996) and Fujii et al. (2001) investigated the perturbed flow fields due to deflected control surfaces using the experimental values of the heat transfer measured during hypersonic flight. The HYFLEX vehicle [Fujii et al. (2001)] was a small-scale R&D vehicle whose length was 4.40 m (14.44 ft). A two-stage launcher provided an initial altitude of 107 km (351 kft) at a velocity of 3.88 km/s (12.73 kft/s).

Despite the oft-mentioned problems with developing boundary-layer transition correlations using flight-test measurements, there are numerous flight-test programs where boundary-layer transition was a major focus of the data gathering efforts. Weston and Fitzkee (1963) noted that observed boundary-layer transition Reynolds numbers on

the Mercury capsule "agree well with Reynolds numbers obtained for wake transition behind spheres flown in a hypervelocity gun facility." Also flown in the 1960s was the Reentry F vehicle which provided hypersonic boundary-layer transition and is still used today. The Reentry F flight provided boundary-layer transition data at Mach numbers up to 20 and altitudes down to 24.38 km (80.00 kft) [Wright and Zoby (1977)].

EXAMPLE 8.7 Wind-tunnel simulation of supersonic missile flow fields

Assume that you are given the task of determining the aerodynamic forces and moments acting on a slender missile which flies at a Mach number of 3.5 at an altitude of 27,432 m (90,000 ft). Aerodynamic coefficients for the missile, which is 20.0 cm (7.874 in) in diameter and 10 diameters long, are required for angles of attack from 0° to 55°. The decision is made to obtain experimental values of the required coefficients in the Vought High-Speed Wind Tunnel (in Dallas, Texas). Upstream of the model shock system, the flow in the wind tunnel is isentropic and air, at these conditions, behaves as a perfect gas. Therefore, the relations developed in this section can be used to calculate the wind-tunnel test conditions.

Solution:

1. ***Flight conditions.*** Using the properties for a standard atmosphere (such as were presented in Chapter 1), the relevant parameters for the flight condition include:

$$U_\infty = 1050 \text{ m/s}$$
$$p_\infty = 1.7379 \times 10^{-2} p_{SL} = 1760.9 \text{ N/m}^2$$
$$T_\infty = 224 \text{ K}$$
$$\text{Re}_{\infty,d} = \frac{\rho_\infty U_\infty d}{\mu_\infty} = 3.936 \times 10^5$$
$$M_\infty = 3.5$$

2. ***Wind-tunnel conditions.*** Information about the operational characteristics of the Vought High-Speed Wind Tunnel is contained in the tunnel handbook [Arnold (1968)]. To ensure that the model is not so large that its presence alters the flow in the tunnel (i.e., the model dimensions are within the allowable blockage area), the diameter of the wind-tunnel model, d_{wt}, will be 4.183 cm (1.6468 in.).

Based on the discussion in Chapter 2, the Mach number and the Reynolds number are two parameters which we should try to simulate in the wind tunnel. The free-stream unit Reynolds number (U_∞/ν_∞) is presented as a function of the free-stream Mach number and of the stagnation pressure for a stagnation temperature of 311 K (100°F) in Fig. 8.25 [which is from Arnold (1968) and has been left in English units]. You can use the equations of this section to verify the value for the unit Reynolds number given the conditions in the stagnation chamber and the free-stream Mach number.

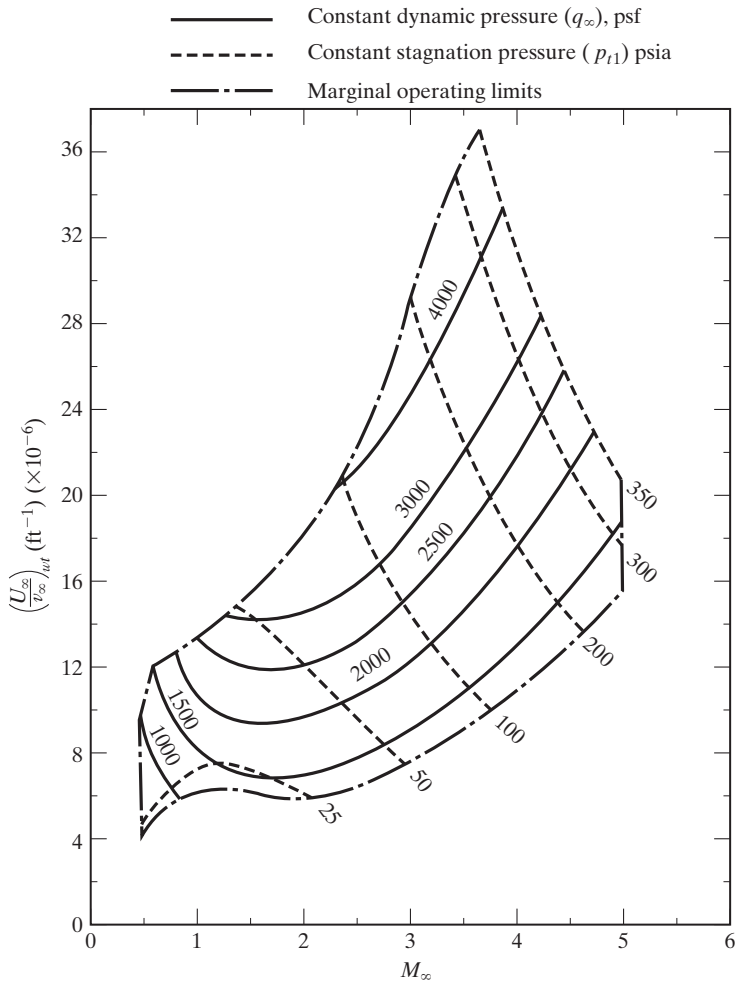

Figure 8.25 Free-stream unit Reynolds number as a function of the free-stream Mach number for $T_t = 100°\text{F}$ in the Vought High-Speed Wind Tunnel [from Arnold (1968)].

In order to match the flight Reynolds number of 3.936×10^5 in the wind tunnel,

$$\left(\frac{U_\infty}{\nu_\infty}\right)_{\text{wt}} = \frac{3.936 \times 10^5}{d_{\text{wt}}} = 2.868 \times 10^6/\text{ft}$$

But as indicated in Fig. 8.20, the lowest unit Reynolds number possible in this tunnel at $M_\infty = 3.5$ is approximately 9.0×10^6/ft. Therefore, if the model is 4.183 cm in diameter, the lowest possible tunnel value of $\text{Re}_{\infty,d}$ is 1.235×10^6, which is greater than the flight value. This is much different than the typical subsonic flow, where (as discussed in Chapter 5) the maximum wind-tunnel Reynolds number is usually much less than the flight value. To obtain the

appropriate Reynolds number for the current supersonic flow, we can choose to use a smaller model. Using a model that is 1.333 cm in diameter would yield a Reynolds number of 3.936×10^5 (as desired). If this model is too small, we cannot establish a tunnel condition which matches both the flight Mach number and the Reynolds number. In this case, you might choose to simulate the Mach number exactly rather than seek a compromise Mach-number/Reynolds-number test condition, since the pressure coefficients and the shock interaction phenomena on the control surfaces are Mach-number-dependent in this range of free-stream Mach number.

The conditions in the stagnation chamber of the tunnel are $T_t = 311$ K (560°R) and $p_{t1} = 5.516 \times 10^5$ N/m^2 (80 psia). So, using either equations (8.34) and (8.36) or the values presented in Table 8.1, we can find that $T_\infty = 90.18$ K (162.32°R) and $p_\infty = 7.231 \times 10^3$ N/m^2 (1.049 psia). The cold free-stream temperature is typical of supersonic tunnels (e.g., most high-speed wind tunnels operate at temperatures near liquefaction of oxygen). Therefore, the free-stream speed of sound is relatively low and, even though the free-stream Mach number is 3.5, the velocity in the test section U_∞ is only 665 m/s (2185 ft/s). In summary, the relevant parameters for the wind-tunnel conditions include:

$$
\begin{aligned}
U_\infty &= 665 \text{ m/s} \\
p_\infty &= 7.231 \times 10^3 \text{ N/m}^2 \\
T_\infty &= 90.18 \text{ K} \\
\text{Re}_{\infty,d} &= 3.936 \times 10^5 \text{ if } d = 1.333 \text{ cm or } 1.235 \times 10^6 \text{ if } d = 4.183 \text{ cm} \\
M_\infty &= 3.5
\end{aligned}
$$

Because of the significant differences in the dimensional values of the flow parameters (such as U_∞, p_∞ and T_∞), we must again nondimensionalize the parameters so that correlations of wind-tunnel measurements can be related to the theoretical solutions or to the design flight conditions.

8.11 COMMENTS ABOUT THE SCALING/CORRECTION PROCESS(ES) FOR RELATIVELY CLEAN CRUISE CONFIGURATIONS

In an article for the *Annual Review of Fluid Mechanics*, Bushnell (2006) noted that, "a survey of 12 commercial transport aircraft, constructed by three major American manufacturers over a 20-year period showed that you are just as likely to estimate too high a drag as too low a drag. Six of the twelve (scaling) 'predictions' were low, four predictions were high, and two were right on. The drag predictions were as much as 22% low and 10% high." Citing the work of other researchers, Bushnell (2006) noted that similar values/discrepancies were obtained for airbreathing missiles. "As the experience from the various applications discussed herein indicates, 'surprise' occurs far too often and flow complexity can seriously degrade the 'scaled predictions'. Typical correction levels . . . include 6% wall interference, −5% Reynolds number, +2% roughness, and −4% sting and aeroelastic distortion effects. Total correction(s) from just these issues/

concerns/effects are the order of +12%. On the other hand, the Viking aeroshell drag observed during Martian entry agreed within some 2% of the scaled ground results, admittedly for a very bluff body with a fairly well characterized flow field."

8.12 SUMMARY

Compressibility adds additional challenges to the aerodynamicist, in some ways leading to concepts and theories that are difficult to learn and understand. Adding the energy equation and first/second laws of thermodynamics to the equation set results in flow behavior that seems counter-intuitive. But those equations yield straightforward theories which apply throughout the Mach number continuum, and which inform the aerodynamicist about how Mach number changes will impact the forces and moments acting on an aircraft. Embracing the challenge of compressible aerodynamics will lead to greater understanding of all Mach regimes, including incompressible aerodynamics, as flow concepts become unified, integrated, and understandable.

PROBLEMS

8.1. The test section of the wind tunnel of Example 8.6 has a square cross section that is $1.5m \times 1.5m$.

(a) What is the mass-flow rate of air through the test section for the flow conditions of the example (i.e., $M_\infty = 3.0$, $p_\infty = 7.0 \times 10^3$ and $T_\infty = 90K$)?

(b) What is the volume flow rate of air through the test section?

8.2. A practical limit for the stagnation temperature of a continuously operating supersonic wind tunnel is 990 K. With this value for the stagnation (or total) temperature, prepare a graph of the static free-stream temperature as a function of the test-section Mach number. The fluid in the free stream undergoes an isentropic expansion. The static temperature should not be allowed to drop below 60 K, since at low pressure oxygen begins to liquefy at this temperature. With this as a lower bound for temperature, what is the maximum Mach number for the facility? Assume that the air behaves as a perfect gas with $\gamma = 1.4$.

8.3. Tunnel B at the Arnold Engineering Development Center (AEDC) in Tennessee is often used for determining the flow field and/or the heating rate distributions. The Mach number in the test section is 8. If the stagnation temperature is 700 K and the stagnation pressure can be varied from 5.90×10^6 to 4.90×10^6 what is the range of Reynolds number that can be obtained in this facility? Assume that the characteristic dimension is 0.75 m, which could be the length of a hypersonic waverider model.

8.4. Given the flow conditions discussed in Problem 8.3,

(a) What is the (range of the) static temperature in the test section? If there is only one value of the static temperature, state why. To what range of altitude (as given in Table 1.2) if any, do these temperatures correspond?

(b) What is the (range of the) velocity in the test section? Does it depend on the pressure?

(c) What is the range of static pressure in the test section? To what range of altitude (as given in Table 1.2) do these pressures correspond?

8.5. A convergent-only nozzle, which exhausts into a large tank, is used as a transonic wind tunnel (Fig. P8.5). Assuming that the air behaves as a perfect gas, answer the following.

(a) If the pressure in the tank is atmospheric (i.e., $1.01325 \times 10^5\ \mathrm{N/m^2}$), what should the stagnation pressure in the nozzle reservoir be so that the Mach number of the exhaust flow is 0.95?

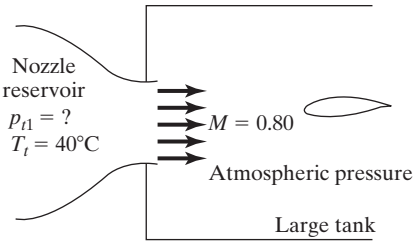

Figure P8.5

(b) If the stagnation temperature is 70°C, what is the static temperature in the test stream?

(c) A transonic airfoil with a 15-cm chord is located in the test stream. What is Re_c for the airfoil?

$$\mathrm{Re}_c = \frac{\rho_\infty U_\infty c}{\mu_\infty}$$

(d) What is the pressure coefficient C_p at the stagnation point of the airfoil?

8.6. A small hole exists in the body of an airplane and serves as a convergent nozzle, as shown in Fig. P8.6. The air in the cabin is at $0.50 \times 10^5\ \mathrm{N/m^2}$. Assume that the cabin volume is sufficiently large that the cabin serves essentially as a stagnation chamber and that the conditions in the cabin remain constant for a period of time, independent of the conditions outside the airplane. Furthermore, assume that the flow in the nozzle is isentropic. Sketch the pressure distribution and calculate the static pressure in the nozzle exit plane when the airplane is at the following altitudes: (a) 7 km, (b) 9 km, (c) 11 km, and (d) 15 km.

Since the air expands isentropically from constant reservoir conditions, the back pressure (i.e., the pressure outside the airplane), p_b, is an important parameter. For the standard atmosphere:

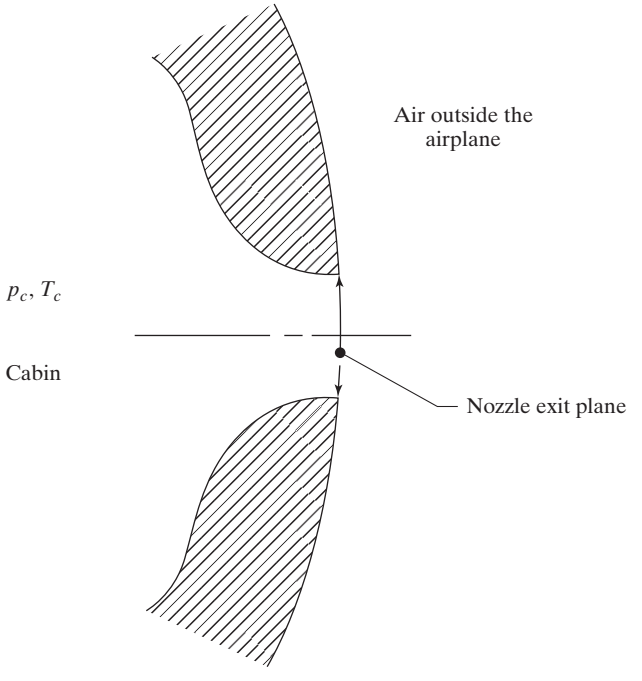

Figure P8.6 Sketch for Problems 8.6 and 8.7

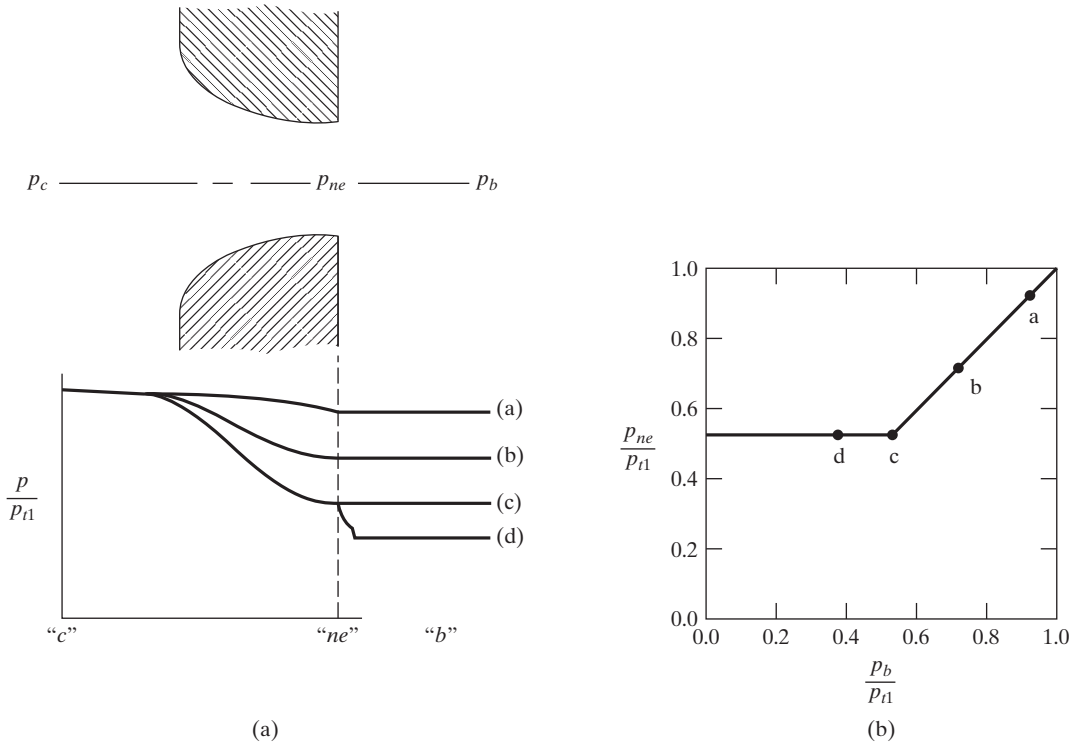

Figure P8.6 (continued) Solution for Problem 8.6 (i) pressure distribution: (ii) pressure ratios.

(a) $p_b = 0.41105 \times 10^5 = 0.82209 p_{t1}$
(b) $p_b = 0.30799 \times 10^5 = 0.61598 p_{t1}$
(c) $p_b = 0.22699 \times 10^5 = 0.45398 p_{t1}$
(d) $p_b = 0.12111 \times 10^5 = 0.24222 p_{t1}$
Where $p_{t1} = p_c = 0.5 \times 10^5\ \mathrm{N/m^2}$.

8.7. If the temperature in the cabin is 37°C and the exit diameter is 0.90 cm, what is the mass flow rate through the hole of Problem 8.6 when the altitude is 9 km? 15 km?

8.8. Consider the flow of air through the convergent-divergent nozzle shown in Fig. P8.8. The conditions in the stagnation chamber are $p_{t1} = 100$ psia and $T_t = 200$°F. The cross-sectional area of the test section is 2.035 times the throat area. The pressure in the test section can be varied by controlling the valve to the vacuum tank. Assuming isentropic flow in the nozzle, calculate the static pressure, static temperature, Mach number, and velocity in the test section for the following back pressures.

(a) $p_b = 100.000$ psia
(b) $p_b = 97.250$ psia
(c) $p_b = 93.947$ psia
(d) $p_b = 9.117$ psia

8.9. Consider the flow of air through the convergent-divergent nozzle shown in Fig. P8.9. The conditions in the stagnation chamber are $p_{t1} = 100$ psia and $T_t = 200$°F. The cross-sectional area of the test section is 2.035 times the throat area. Thus far we have repeated

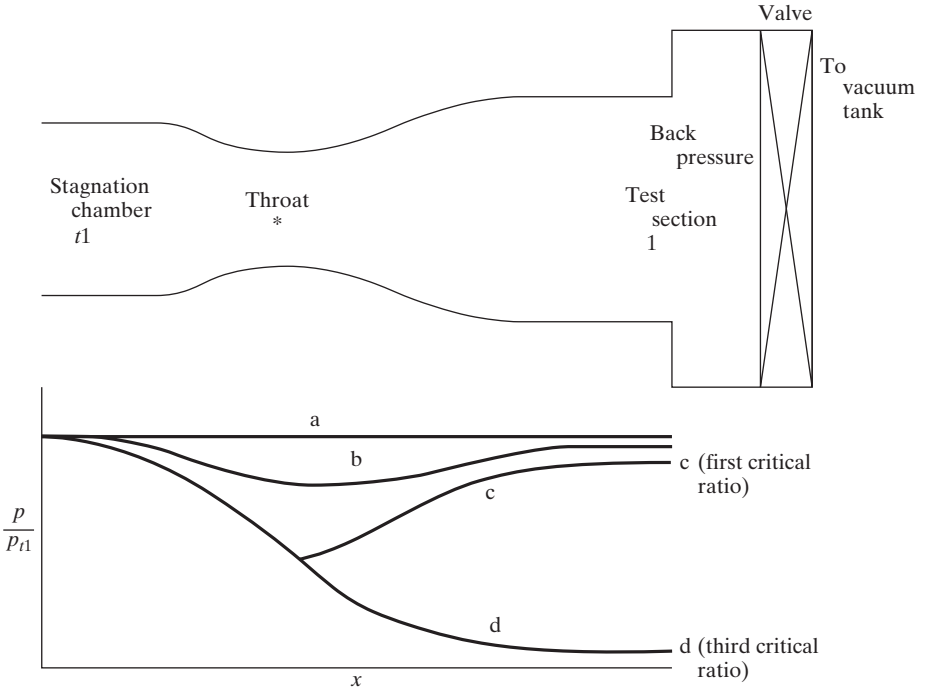

Figure P8.8 Isentropic flow in a convergent-divergent nozzle.

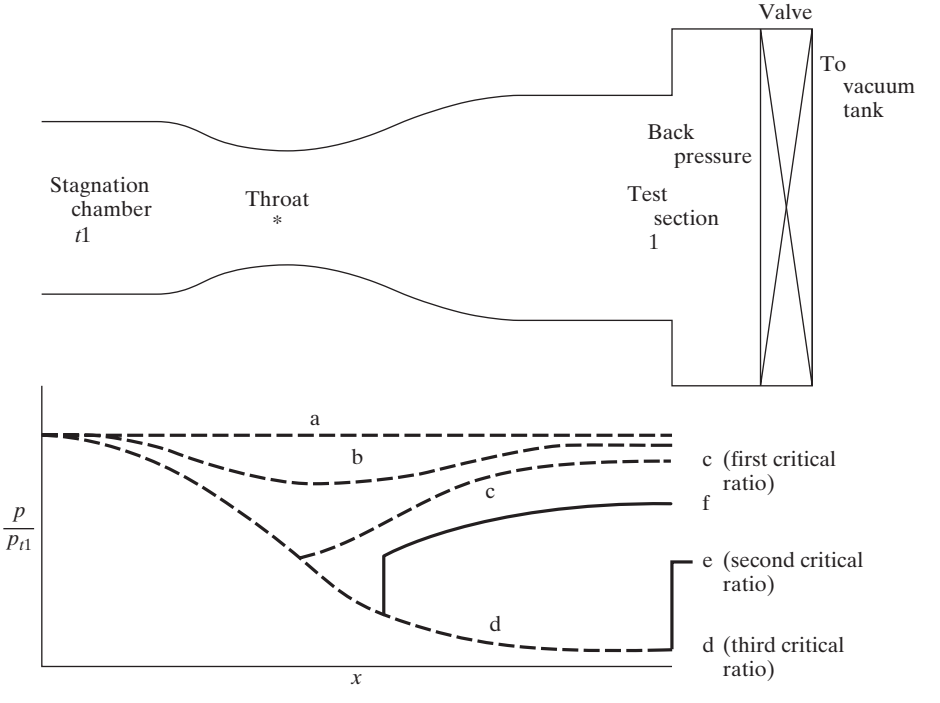

Figure P8.9 Flow in a convergent-divergent nozzle with a shock wave in the divergent section (dashed lines are from Fig. P8.7)

the conditions of Problem 8.8. Calculate the static pressure, static temperature, Mach number, and velocity in the test section for the following back pressures:

(a) $p_b = 51.38$ psia

(b) $p_b = 75.86$ psia

8.10. Air flows through the insulated variable-area stream tube such that it may be considered one dimensional and steady. At one end of the stream tube, and $M_1 = 4.0$ At the other end of the stream tube, $p_{t2} = 2110$ psfa, $A_1 = 6.0$ ft^2, $p_2 = 2100$ psfa, $T_{t2} = 500^\circ$R and $A_2 = 6.0$ ft^2 What is the flow direction; that is, is the flow from (1) to (2) or from (2) to (1)?

8.11. A pitot tube in a supersonic stream produces a curved shock wave standing in front of the nose part, as shown in Fig. P8.11. Assume that the probe is at zero angle of attack and that the shock wave is normal in the vicinity of the nose. The probe is designed to sense the stagnation pressure behind a normal shock (p_{t2}) and the static pressure behind a normal shock (p_2) Derive the relation between p_{t2} and (p_2) in terms of M_∞ by using normal shock relation.

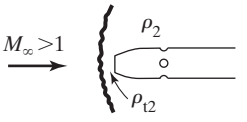

Figure P8.11

8.12. Consider the flow in a streamtube as it crosses a normal shock wave (Fig. P8.12).

(a) Determine the ratio A^*_2/A^*_1.

(b) What are the limits of A^*_2/A^*_1 as $M_1 \rightarrow 1$ and as $M_1 \rightarrow \infty$?

(c) What is the significance of A^*_1? of A^*_2??

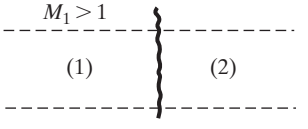

Figure P8.12

8.13. You are to measure the surface pressure on simple models in a supersonic wind tunnel. The air flows from right to left. To evaluate the experimental accuracy, it is necessary to obtain theoretical pressures for comparison with the data. If a 30° wedge is to be placed in a Mach 3.5 stream (Fig. P8.13), calculate

(a) The surface pressure in N/m^2

(b) The pressure difference (in cm Hg) between the columns of mercury in *U*-tube manometer between the pressure experienced by the surface orifice and the wall orifice (which is used to measure the static pressure in the test section)

(c) The dynamic pressure of the free-stream flow

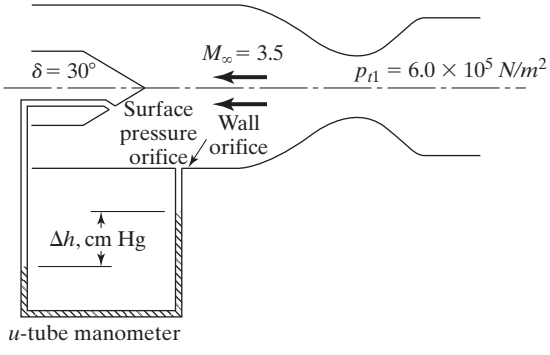

Figure P8.13

Other measurements are that the pressure in the reservoir is 6.0×10^5 N/m^2 and the barometric pressure is 75.2 cm Hg.

8.14. It is desired to turn a uniform stream of air compressively by 10°. The upstream Mach number is 3.

(a) Determine the final Mach number and net change in entropy, if the turning is accomplished by (1) a single 10° sharp turn, (2) two successive 5° sharp turns, or (3) an infinite number of infinitesimal turns.

(b) What do you conclude from the results in part (a)?

(c) In light of the results in part (b), can we make any conclusions as to whether it is better to make *expansive* turns gradually or abruptly, when the flow is supersonic?

8.15. A flat-plate airfoil, whose length is c, is in a Mach 2.0 stream at an angle of attack of 10° (Fig. P8.15).

(a) Use the oblique shock-wave relations to calculate the static pressure in region (2) in terms of the free-stream value p_1.

(b) Use the Prandtl-Meyer relations to calculate the static pressure in region (3) in terms of p_1.

(c) Calculate C_l, C_d, and $C_{m0.5c}$ (the pitching moment about the midchord). Do these coefficients depend on the free-stream pressure (i.e., the altitude)?

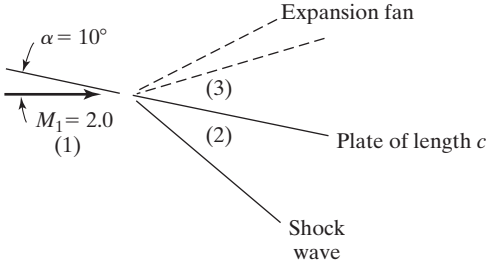

Figure P8.15

8.16. A conical spike whose half-angle (δ_c) is 8° is located in the inlet of a turbojet engine (Fig. P8.16). The engine is operating in a $M_\infty = 2.80$ stream such that the angle of attack of the spike is zero. If the radius of the engine inlet is 1.5 m, determine l, the length of the spike extension, such that the conical shock just grazes the lip of the nacelle.

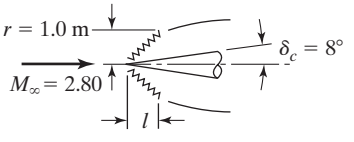

Figure P8.16

8.17. Consider the two-dimensional inlet for a turbojet engine. The upper surface deflects the flow 10°, and the lower surface deflects the flow 5° (Fig. P8.17). The free-stream Mach number is 2.5 (i.e., $M_1 = 2.5$) and the pressure p_1 is 5.0×10^3 N/m^2. Calculate the static

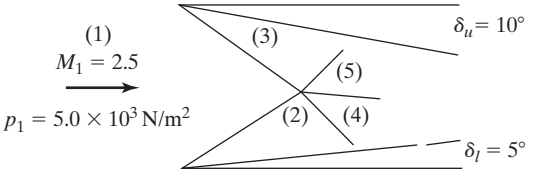

Figure P8.17

pressure, the Mach number, and the flow direction in regions (2), (3), (4), and (5). Note that since regions (4) and (5) are divided by a fluid/fluid interface,

$$p_4 = p_5 \quad \text{and} \quad \theta_4 = \theta_5$$

That is, the static pressure in region (4) is equal to that in region (5), and the flow direction in region (4) is equal to that in region (5).

8.18. A single wedge airfoil is located on the centerline of the test section of a Mach 2.0 wind tunnel (Fig. P8.18). The airfoil, which has a half-angle δ of 5°, is at zero angle of attack. When the weak, oblique shock wave generated at the leading edge of the airfoil encounters the wall, it is reflected so that the flow in region (3) is parallel to the tunnel wall. If the test section is 30.0 cm high, what is the maximum chord length (c) of the airfoil so that it is not struck by the reflected shock wave? Neglect the effects of shock-wave/boundary-layer interactions at the wall.

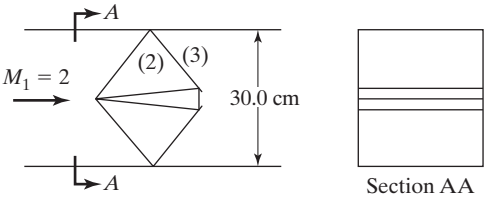

Figure P8.18

8.19. An airplane flies 500 mi/h at an altitude of 30,000 ft where the temperature is -75^0 and the ambient pressure is 470 psfa. What is the temperature and the pressure of the air (outside the boundary layer) at the nose (stagnation point) of the airplane? What is the Mach number for the airplane?

8.20. A three-dimensional bow shock wave is generated by the Shuttle *Orbiter* during entry. However, there is a region where the shock wave is essentially normal to the free-stream flow, as illustrated in Fig. 8.10. The velocity of the Shuttle is 7.50 km/s at an altitude of 70.0 km. The free-stream temperature and the static pressure at this altitude are 300.15 K and 2.00 N/m^2 respectively. Use the normal shock relations to calculate the values of the following parameters downstream of the normal shock wave:

p_2: static pressure
p_{t2}: stagnation pressure
T_2: Static temperature
T_{t2}: stagnation temperature
M_2: Mach number

What is the pressure coefficient at the stagnation point; that is,

$$C_{p,t2} = \frac{p_{t2} - p_\infty}{q_\infty} = ?$$

Use the perfect-gas relations and assume that $\gamma = 1.4$ The perfect-gas assumption is valid for the free-stream flow. However, it is not a good assumption for calculating the flow across the shock wave. Therefore, many of the perfect-gas theoretical values for the shock-flow properties will not even be close to the actual values. See Chapter 12 for further discussions of this problem.

8.21. Consider the hypersonic flow past the cone shown in Fig. 8.17. The cone semivertex angle (δ_c) is 12°. The free-stream flow is defined by

$$M_\infty = 11.5$$
$$T_t = 1970\ \text{K}$$
$$p_\infty = 1070\ \text{N/m}^2$$

Assume that the flow is inviscid, except for the shock wave itself (i.e., neglect the boundary layer on the cone). Assume further that the gas obeys the perfect-gas laws with $\gamma = 1.4$. Using Fig. 8.16b, calculate the static pressure at the surface of the cone (p_c). Using Fig. 8.16c, calculate the Mach number at the surface of the cone (M_c), which is, in practice, the Mach number at the edge of the boundary layer. Calculate the stagnation pressure of the flow downstream of the shock wave. Calculate the Reynolds number at a point 10.0 cm from the apex of the cone.

8.22. Repeat Problem 8.21 for a planar symmetric wedge that deflects the flow 12° (i.e., $\delta = 12°$ in Fig. 8.13).

8.23. An explosion generates a shock wave that moves through the atmosphere at 1000 m/s. The atmospheric conditions ahead of the shock wave are those of the standard sea-level atmosphere. What are the static pressure, static temperature, and velocity of the air behind the shock wave?

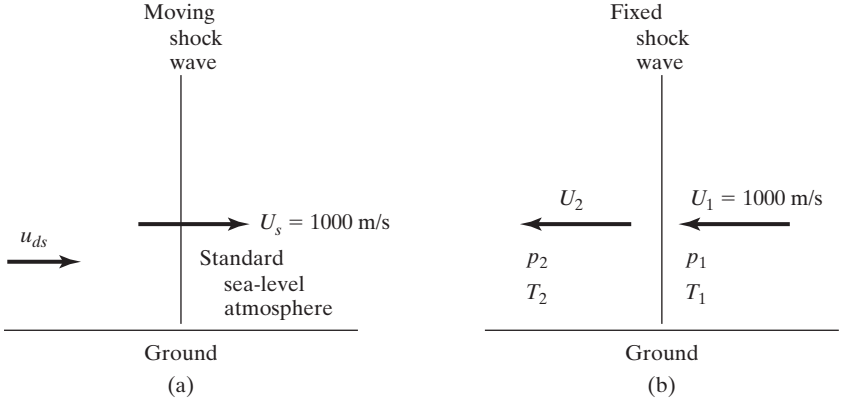

Figure P8.23 Blast wave for Problem 8.23 (a) traveling blast wave; (b) transformed steady flow.

REFERENCES

Ames Research Center Staff. 1953. Equations, tables, and charts for compressible flow. *NACA Report 1135*

Anderson A, Matthews RK. 1993. Aerodynamic and Aerothermal Facilities, I Hypersonic Wind Tunnels. In *Methodology of Hypersonic Testing*, VKI/AEDC Special Course, Rhode-Saint-Genèse, Belgium

Arnold JW. 1968. High Speed Wind Tunnel Handbook. Vought Aeronautics Division AER-EIR-13552-B

Bekey I, Powell R, Austin R. 2001. NASA access to space. *Aerospace America* 32(5):38–43

Berry SA, Horvath TJ, Hollis BR, Thompson RA, Hamilton HH. 2001a. X-33 hypersonic boundary-layer transition. *J. Spacecr. Rockets* 38:646–657

Berry SA, Auslender H, Dilley AD, Calleja JF. 2001b. Hypersonic boundary-layer trip development for Hyper-X. *J. Spacecr. Rockets* 38:853–864

Bertin JJ. 1994. *Hypersonic Aerothermodynamics*. Washington, DC: AIAA

Bertin JJ, Bouslog SA, Wang KC, Campbell CH. 1996. Recent aerothermodynamic flight measurements during Shuttle Orbiter re-entry. *J. Spacecr. Rockets* 33:457–462

Bertin JJ, Cummings RM. 2006. Critical hypersonic aerothermodynamic phenomena. *Annu. Rev. Fluid Mech.* 38:129–157

Buck ML, Benson BR, Sieron TR, Neumann RD. 1963. Aerodynamic and performance analyses of a superorbital re-entry vehicle. In *Dynamics of Manned Lifting Planetary Entry*, Ed. Scala SM, Harrison AC, Rogers M. New York: John Wiley

Buning PG, Wong TC, Dilley AD, Pao JL. 2001. Computational fluid dynamics prediction of Hyper-X stage separation aerodynamics. *J. Spacecr. Rockets* 38:820–827

Bushnell DM. 2006. Scaling: wind tunnel to flight. *Annu. Rev. Fluid Mech*. 38:111–128

Chapman AJ. 1974. *Heat Transfer*. New York: Macmillan

Cockrell CE, Engelund WC, Bittner RD, Jentink TN, Dilley AD, Frendi, A. 2001. Integrated aeropropulsive computational fluid dynamics methodology for the Hyper-X flight experiment. *J. Spacecr. Rockets* 38:836–843

Cornette ES. 1966. Forebody temperatures and calorimeter heating rates measured during project Fire II reentry at 11.35 kilometers per second. *NASA TMX-1035*

Edney BE. 1968. Effects of shock impingement on the heat transfer around blunt bodies. *AIAA J.* 6:15–21.

Engelund WC. 2001. Hyper-X aerodynamics: The X-43A airframe-integrated scramjet propulsion flight-test experiments. *J. Spacecr. Rockets* 38:801–802

Engelund WC, Holland SD, Cockrell CE, Bittner RD. 2001. Aerodynamic database development for the Hyper-X airframe-integrated scramjet propulsion experiments. *J. Spacecr. Rockets* 38:803–810

Fujii K, Watanabe S, Kurotaki T, Shirozu M. 2001. Aerodynamic heating measurements on nose and elevon of hypersonic flight experiment vehicle. *J. Spacecr. Rockets* 38:8–14

Hayes WD, Probstein RF. 1966. *Hypersonic Flow Theory, Vol. I, Inviscid Flows*. New York: Academic Press

Hodge JK, Audley SR. 1983. Aerothermodynamic parameter estimation from shuttle thermocouple data during flight test maneuvers. *J. Spacecr. Rockets* 20:453–460

Holden M, Chadwick K, Kolly J. 1995. *Hypervelocity studies in the LENS facility*. Presented at Intl. Aerosp. Planes Hypers. Tech. Conf., 6th, AIAA Pap. 95–6040, Chattanooga, TN

Holland SD, Woods WC, Engelund WC. 2001. Hyper-X research vehicle experimental aerodynamics test program overview. *J. Spacecr. Rockets* 38:828–835

Hollis BR, Horvath TJ, Berry SA, Hamilton HH, Thompson RA, Alter SJ. 2001a. X-33 computational aeroheating predictions and comparisons with experimental data. *J. Spacecr. Rockets* 38:658–669

Hollis BR, Thompson RA, Murphy KJ, Nowak RJ, Riley CJ, Wood WA, Alter SJ, Prabhu R. 2001b. X-33 aerodynamic computations and comparisons with wind-tunnel data. *J. Spacecr. Rockets* 38:684–691

Horvath TJ, Berry SA, Hollis BR, Liechty DS, Hamilton HH, Merski NR. 2001. X-33 experimental aeroheating at Mach 6 using phosphor thermography. *J. Spacecr. Rockets* 38:634–645

Iliff KW, Shafer MF. 1992. Space Shuttle hypersonic flight research and the comparison to ground test results. Presented at Aerosp. Ground Test. Conf., 17th, AIAA Pap. 92–3988, Nashville, TN

Kays WM. 1966. *Convective Heat and Mass Transfer*. New York: McGraw-Hill

Lee DB, Goodrich WD. 1972. The aerothermodynamic environment of the Apollo Command Module during suborbital entry. *NASA Tech. Note D-6792*

Liepmann HW, Roshko A. 1957. *Elements of Gasdynamics*. New York: John Wiley & Sons, Inc.

Matthews RK, Nutt KW, Wannenwetsch GD, Kidd CT, Boudreau AH. 1985. Developments in aerothermal test techniques at the AEDC supersonic-hypersonic wind tunnels. Presented at Thermophysics Conf., 20th, AIAA Pap. 85–1003, Williamsburg, VA

Moeckel WE, Weston KC. 1958. Composition and thermodynamic properties of air in chemical equilibrium. *NACA Tech. Note 4265*

Murphy KJ, Nowak RJ, Thompson RA, Hollis BR, Prabhu R. 2001. X-33 hypersonic aerodynamic characteristics. *J. Spacecr. Rockets* 38:670–683

Neumann RD. 1988. Missions and requirements. AGARD Report 761, *Special Course on Aerothermodynamics of Hypersonic Vehicles*, Neuilly sur Seine, France

Neumann RD. 1989. Defining the aerothermodynamic methodology. In *Hypersonics, Volume I Defining the Hypersonic Environment*, Ed. Bertin JJ, Glowinski R, Periaux J. Boston: Birkhaeuser Boston

Ried RC, Rochelle WC, Milhoan JD. 1972. Radiative heating to the Apollo Command Module: engineering prediction and flight measurements. *NASA TMX-58091*

Settles GS. 2001. *Schlieren & Shadowgraph Techniques*. Berlin: Springer-Verlag

Spalding DB, Chi SW. 1964. The drag of a compressible turbulent boundary layer on a smooth plate with and without heat transfer. *J. Fluid Mech.* 18:117–143

Stalmach CJ. 1958. Experimental investigation of the surface impact pressure probe method of measuring local skin friction at supersonic speeds. Defense Research Laboratory, The University of Texas at Austin, DRL-410

Sutton K. 1985. Air radiation revisited. In *Progress in Astronautics and Aeronautics Vol. 96: Thermal Design of Aeroassisted Orbital Transfer Vehicles*, Ed. Nelson HF, pp. 419–441

Throckmorton DA. 1993. Shuttle entry aerothermodynamic flight research: the orbiter experiments program. *J. Spacecr. Rockets* 30:449–465

Throckmorton DA, Ed. 1995. Orbiter Experiments (OEX) Aerothermodynamics Symposium. *NASA CP 3248*

Trimmer LL, Cary AM, Voisinet RL. 1986. The optimum hypersonic wind tunnel. Presented at Aerodyn. Test. Conf., 14th, AIAA Pap. 86–0739, West Palm Beach, FL

Van Driest E. 1956. Problem of aerodynamic heating. *Aeronautical Engineering Review* 15:26–41

Wayland H. 1957. *Differential Equations Applied in Science and Engineering.* Princeton, NJ: Van Nostrand

Weston KC, Fitzkee AL. 1963. Afterbody heat transfer measurements obtained during reentry of the spacecraft of the Mercury-Atlas 5 mission. *NASA TM X-564*

Williamson WE. 1992. *Hypersonic flight testing*. Presented at Aerosp. Ground Test. Conf., 17th, AIAA Pap. 92–3989, Nashville, TN

Woods WC, Holland SD, DiFulvio M. 2001. Hyper-X stage separation wind-tunnel test program. *J. Spacecr. Rockets* 38:881–819

Wright RL, Zoby EV. 1977. *Flight boundary layer transition measurements on a slender cone at Mach 20*. Presented at Fluid and Plasmadynamics Conf., 10th, AIAA Pap. 77–0719, Albuquerque, NM

9 COMPRESSIBLE, SUBSONIC FLOWS AND TRANSONIC FLOWS

Chapter Objectives

- Know the impact of compressibility on the derivation of equations that govern subsonic compressible and transonic flows
- Be able to transform incompressible experimental data or geometry to subsonic compressible Mach numbers
- Know the definition of transonic flow and be able to explain the flow characteristics that distinguish this flow regime
- Be able to estimate the critical and drag-divergence Mach numbers
- Understand the impact of wing sweep on airplane aerodynamics
- Have a conceptual understanding how supercritical airfoils work
- Be able to explain how the transonic area rule minimizes wave drag

Flow-field solutions were generated for a variety of configurations using the assumption that the density was constant throughout the flow field in Chapters 3 through 7. As we discussed relative to Fig. 8.6, an error of less than 1% results when the incompressible-flow Bernoulli equation is used to calculate the local pressure provided that the local Mach number is less than or equal to 0.5 in air. Therefore, if the flight speed is small

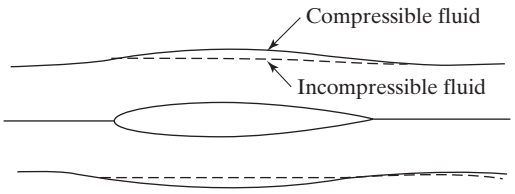

Figure 9.1 Comparison of streamlines for an incompressible flow past an airfoil with those for a subsonic, compressible flow.

compared with the speed of sound, the changes in pressure which are generated by the vehicle motion are small relative to the free-stream static pressure, and the influence of compressibility can be neglected.

Streamlines converge as the incompressible flow accelerates past the midsection of an airfoil, as shown in Fig. 9.1. The widening of the streamtubes near the nose and the contraction of the streamtubes in the regions of increased velocity lead to a progressive reduction in the curvature of the streamlines. As a result, there is a rapid attenuation of the flow disturbance with distance from the airfoil for the compressible flow case.

As the flight speed is increased, the flow may no longer be considered as incompressible. Even though the flow could be subsonic everywhere, the density decreases as the pressure decreases (or, equivalently, as the velocity increases). The variable-density flow requires a relatively high velocity and diverging streamlines in order to get the mass flow past the midsection of the airfoil. The expansion of the minimum cross section of the streamtubes forces the streamlines outward so that they conform more nearly to the curvature of the airfoil surface, as shown in Fig. 9.1. Therefore, the disturbance caused by the airfoil extends vertically to a greater distance.

Increasing the flight speed further, we reach the *critical Mach number*, the name given to the lowest (subsonic) free-stream Mach number for which the maximum value of the local velocity first becomes sonic. Above the critical Mach number, the flow field contains regions of locally subsonic and locally supersonic velocities in juxtaposition. Such mixed subsonic/supersonic flow fields are termed *transonic flows*.

9.1 COMPRESSIBLE, SUBSONIC FLOW

For completely subsonic flows, a compressible flow retains a basic similarity to an incompressible flow, as shown in Fig. 9.1. In particular, the compressible flow can be considered to be an irrotational potential motion in many cases, just like we did for incompressible flow. In addition to the absence of significant viscous forces, the existence of potential motion for a compressible flow depends on the existence of a unique relation between the pressure and the density. In an inviscid flow, the fluid elements are accelerated entirely by the action of the pressure gradient. Therefore, if the density is a function of the pressure only, the direction of the pressure gradient will coincide with that of the density gradient at all points. The force on each element will then be aligned with the center of gravity of the fluid element, and the pressure forces will introduce no rotation; the flow is irrotational.

9.1.1 Linearized Theory for Compressible, Subsonic Flow About a Thin Wing at Relatively Small Angles of Attack

The continuity equation for steady, three-dimensional flow is obtained from equation (2.1):

$$\frac{\partial(\rho u)}{\partial x} + \frac{\partial(\rho v)}{\partial y} + \frac{\partial(\rho w)}{\partial z} = 0 \tag{9.1}$$

In the inviscid region of the flow field (i.e., outside the thin boundary layer), the components of the momentum equation may be written as:

$$u\frac{\partial u}{\partial x} + v\frac{\partial u}{\partial y} + w\frac{\partial u}{\partial z} = -\frac{1}{\rho}\frac{\partial p}{\partial x} \tag{9.2a}$$

$$u\frac{\partial v}{\partial x} + v\frac{\partial v}{\partial y} + w\frac{\partial v}{\partial z} = -\frac{1}{\rho}\frac{\partial p}{\partial y} \tag{9.2b}$$

$$u\frac{\partial w}{\partial x} + v\frac{\partial w}{\partial y} + w\frac{\partial w}{\partial z} = -\frac{1}{\rho}\frac{\partial p}{\partial z} \tag{9.2c}$$

The square of the speed of sound is defined as the change in pressure with respect to the change in density for an isentropic process, from equation (8.26):

$$a^2 = \left(\frac{\partial p}{\partial \rho}\right)_s$$

However, since the flow we are studying actually is isentropic, this may be written in terms of the actual pressure and density changes which result due to the fluid motion:

$$\left(\frac{\partial p}{\partial \rho}\right) = a^2 \tag{9.3}$$

Combining equations (9.1) through (9.3) and noting that the flow is irrotational, we obtain:

$$\left(1 - \frac{u^2}{a^2}\right)\frac{\partial u}{\partial x} + \left(1 - \frac{v^2}{a^2}\right)\frac{\partial v}{\partial y} + \left(1 - \frac{w^2}{a^2}\right)\frac{\partial w}{\partial z} - 2\frac{uv}{a^2}\frac{\partial u}{\partial y} - 2\frac{vw}{a^2}\frac{\partial v}{\partial z} - 2\frac{wu}{a^2}\frac{\partial w}{\partial x} = 0 \tag{9.4a}$$

If we introduce a velocity potential, as we did in Chapter 3, such that $u = \partial\phi/\partial x$, $v = \partial\phi/\partial y$, and $w = \partial\phi/\partial z$, equation (9.4a) becomes:

$$\left(1 - \frac{\phi_x^2}{a^2}\right)\phi_{xx} + \left(1 - \frac{\phi_y^2}{a^2}\right)\phi_{yy} + \left(1 - \frac{\phi_z^2}{a^2}\right)\phi_{zz} - 2\frac{\phi_x\phi_y}{a^2}\phi_{xy} - 2\frac{\phi_y\phi_z}{a^2}\phi_{yz} - 2\frac{\phi_z\phi_x}{a^2}\phi_{zx} = 0 \tag{9.4b}$$

which is the *full potential equation* (also called the *velocity potential equation*). In the form of equation (9.4b), it is easy to see that the full potential equation is highly nonlinear, which makes it very difficult to solve analytically. This equation was also difficult to solve numerically in the early days of computer simulations, which is why further

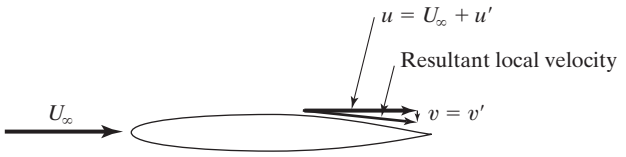

Figure 9.2 Velocity components for subsonic, compressible flow past a thin airfoil at a small angle of attack.

simplifications to the equation were required in order to obtain analytic solutions or to be solvable numerically.

A useful simplification of equation (9.4) can be made for the case of a slender body moving in the x direction at the velocity U_∞. As shown in Fig. 9.2, the magnitude and the direction of the local velocity are changed only slightly from the free-stream velocity. Therefore, the resultant velocity at any point can be represented as the vector sum of the free-stream velocity (a constant) together with the perturbation velocities, u', v', and w':

$$u = U_\infty + u'$$
$$v = v'$$
$$w = w'$$

Since the perturbation velocities are considered to be small in magnitude when compared with the free-stream velocity ($u', v', w' \ll U_\infty$), equation (9.4a) becomes:

$$\left(1 - \frac{u^2}{a^2}\right)\frac{\partial u}{\partial x} + \frac{\partial v}{\partial y} + \frac{\partial w}{\partial z} = 0 \tag{9.5}$$

where u/a is essentially equal to the local Mach number. This simplification, however, is only true if the flow is not transonic ($M \approx 1$) or hypersonic ($M > 5$). Equation (9.5) can be simplified further if we recall that the local speed of sound can be determined using the energy equation for adiabatic flow:

$$\frac{a^2}{a_\infty^2} = 1 - \frac{\gamma - 1}{2}\left(\frac{u^2 + v^2 + w^2}{U_\infty^2} - 1\right)M_\infty^2 \tag{9.6}$$

Since only small perturbations are considered, the binomial theorem can be used to generate the relation:

$$\frac{a_\infty^2}{a^2} = 1 + \frac{\gamma - 1}{2}M_\infty^2\left(2\frac{u'}{U_\infty} + \frac{u'^2 + v'^2 + w'^2}{U_\infty^2}\right) \tag{9.7}$$

To simplify equation (9.5), notice that:

$$1 - \frac{u^2}{a^2} = 1 - \frac{(U_\infty + u')^2}{a^2}\frac{U_\infty^2}{U_\infty^2}\frac{a_\infty^2}{a_\infty^2}$$
$$= 1 - \frac{U_\infty^2 + 2u'U_\infty + u'^2}{U_\infty^2}M_\infty^2\frac{a_\infty^2}{a^2} \tag{9.8}$$

Substituting equation (9.7) into equation (9.8) and neglecting the higher-order terms yields the expression

$$1 - \frac{u^2}{a^2} = 1 - M_\infty^2\left[1 + \frac{2u'}{U_\infty}\left(1 + \frac{\gamma - 1}{2}M_\infty^2\right)\right] \tag{9.9}$$

Using equation (9.9), equation (9.5) can now be rewritten as:

$$(1 - M_\infty^2)\frac{\partial u}{\partial x} + \frac{\partial v}{\partial y} + \frac{\partial w}{\partial z} = M_\infty^2\left(1 + \frac{\gamma - 1}{2}M_\infty^2\right)\frac{2u'}{U_\infty}\frac{\partial u}{\partial x}$$

This equation can be rewritten in terms of the perturbation velocities as:

$$(1 - M_\infty^2)\frac{\partial u'}{\partial x} + \frac{\partial v'}{\partial y} + \frac{\partial w'}{\partial z} = \frac{2}{U_\infty}\left(1 + \frac{\gamma - 1}{2}M_\infty^2\right)M_\infty^2 u'\frac{\partial u'}{\partial x} \qquad \textbf{(9.10)}$$

Furthermore, the term on the right-hand side often can be neglected, as it is of second order in the perturbation velocity components. This is only true if the flow is not transonic, since at Mach numbers close to $M = 1$, the first term in the equation could be of the same order as the term on the right-hand side. As a result, we now obtain the linearized equation:

$$(1 - M_\infty^2)\frac{\partial u'}{\partial x} + \frac{\partial v'}{\partial y} + \frac{\partial w'}{\partial z} = 0 \qquad \textbf{(9.11)}$$

Since the flow is everywhere isentropic, it is also irrotational. The condition of irrotationality allows us to introduce a velocity potential ϕ' which is a point function with continuous derivatives. Let ϕ' be the potential function for the perturbation velocities:

$$u' = \frac{\partial \phi'}{\partial x} \qquad v' = \frac{\partial \phi'}{\partial y} \qquad w' = \frac{\partial \phi'}{\partial z} \qquad \textbf{(9.12)}$$

The resultant expression is obtained by substituting the relations in equation (9.12) into equation (9.11), which applies to a completely subsonic, compressible flow, and is the *linearized velocity potential equation:*

$$(1 - M_\infty^2)\phi'_{xx} + \phi'_{yy} + \phi'_{zz} = 0 \qquad \textbf{(9.13)}$$

which is also known as the *Prandtl-Glauert equation*. Comparing this equation to the full potential equation (velocity potential equation), equation (9.4b), you see that the linearization process has taken a highly non-linear equation and changed it into a linear equation. An equation of this type has a much better chance of being solved analytically. However, from an historical perspective, researchers interested in subsonic compressible flows did not solve this equation directly. Rather, they saw the similarity between this equation and Laplace's equation, equation (3.26). The similarity led them to find a way to transform the linearized velocity potential equation into Laplace's equation, and once the appropriate transformation was found, it would be possible to take incompressible aerodynamics results and transform them into compressible aerodynamics results. This was done in several ways, the two most common being Ackeret's transformation and Göthert's transformation.

9.1.2 The Göthert Transformation

By using a simple coordinate transformation, equation (9.13) can be reduced to Laplace's equation, which we used to describe incompressible, irrotational flows. If the "affine" transformation

$$x' = \frac{x}{\sqrt{1 - M_\infty^2}} \qquad \textbf{(9.14a)}$$

$$y' = y \tag{9.14b}$$

$$z' = z \tag{9.14c}$$

is introduced, equation (9.13) becomes

$$\phi_{x'x'} + \phi_{y'y'} + \phi_{z'z'} = 0 \tag{9.15}$$

Therefore, if the potential field for incompressible flow past a given configuration is known, a corresponding solution for the linearized compressible flow can be readily obtained using this transformation. The potential distribution for an incompressible flow and the corresponding "foreshortened" distribution (which satisfies the compressible flow equation) are compared in Fig. 9.3 at points having the same value of ϕ. Although the calculation of a compressible flow field from a known incompressible flow is relatively straightforward, care must be taken in the determination of the boundary conditions satisfied by the compressible flow field.

Referring to equation (9.14), we see that the transformation in effect changes the ratio of the x dimension to the y and z dimensions. Although the spanwise dimensions are unaltered, the transformed chordwise dimension is changed. Therefore, although the airfoil section of the corresponding wings remains geometrically similar, the aspect ratios for the wings differ. The compressible flow over a wing of aspect ratio AR at the Mach number M_∞ is related to the incompressible flow over a wing of aspect ratio $AR\sqrt{1 - M_\infty^2}$. This is illustrated in the sketch of Fig. 9.4. A study of the changes in a completely subsonic flow field around a given wing as the Mach number is increased corresponds to an investigation of the incompressible flow around a series of wings of progressively reduced aspect ratio.

Using the linearized approximation, the pressure coefficient for the compressible flow is given by

$$C_p = -\frac{2u'}{U_\infty} = -\frac{2}{U_\infty}\frac{\partial \phi'}{\partial x} \tag{9.16a}$$

which is related to the pressure coefficient for the corresponding incompressible flow (C_p') through the correlation

$$C_p = \frac{C_p'}{\sqrt{1 - M_\infty^2}} \tag{9.16b}$$

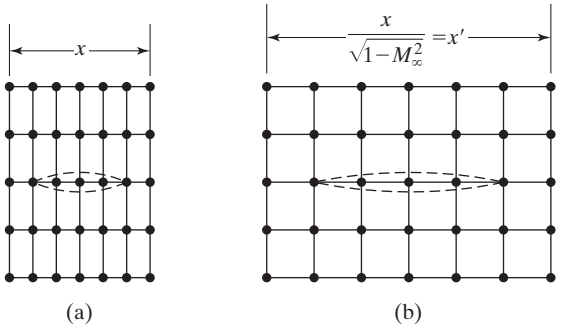

Figure 9.3 Distribution of points having equal values of ϕ in the linearized transformation for subsonic, compressible flow: (a) compressible flow; (b) corresponding incompressible flow.

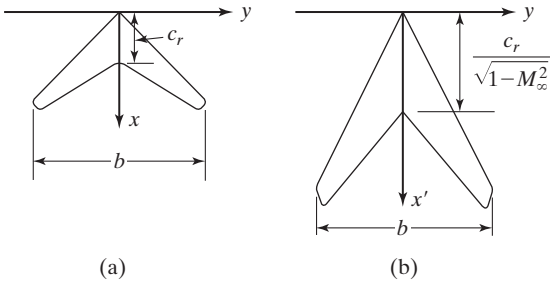

Figure 9.4 Wings for flows related by the linearized transformation: (a) wing for compressible flow; (b) corresponding wing for incompressible flow.

The effect of compressibility on the flow past an airfoil system is to increase the horizontal perturbation velocities over the airfoil surface by the factor $1/\sqrt{1 - M_\infty^2}$. The correlation is known as the *Prandtl-Glauert formula*.

We can calculate the lift by integrating the pressure distribution over the airfoil surface from the leading edge to the trailing edge. Based on equation (9.16b), we find that the section lift and moment coefficients for a compressible subsonic flow also exceed the corresponding value for an incompressible flow by a factor of $1/\sqrt{1 - M_\infty^2}$:

$$C_l = \frac{C_l'}{\sqrt{1 - M_\infty^2}} \qquad C_m = \frac{C_m'}{\sqrt{1 - M_\infty^2}}$$

The resultant variation for the lift-curve slope with Mach number is presented for a two-dimensional unswept airfoil in Fig. 9.5.

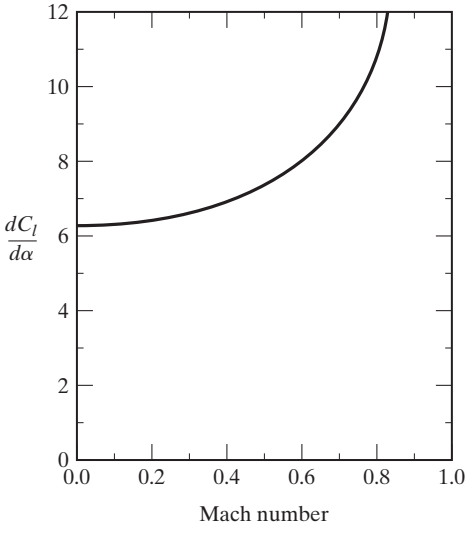

Figure 9.5 Variation of lift-curve slope with Mach number using Prandtl-Glauert formula.

Furthermore, based on the pressure correlation of equation (9.16b), the position of the resultant aerodynamic force for a compressible, subsonic flow is the same as that for an incompressible flow. This, of course, is true provided that there are no shock waves. Thus, in the absence of shock waves, the drag acting on an airfoil in an inviscid, compressible, subsonic flow is the same as the drag acting on an airfoil in an inviscid, incompressible flow. That is, the section drag is zero.

Although the Prandtl-Glauert relation provides a simple method for calculating the flow around an airfoil, Jones and Cohen (1960) warn that the method generally underestimates the effect of compressibility on the magnitude of disturbances for airfoils of finite thickness. As the free-stream Mach number approaches a value of unity, the quantity $1/\sqrt{1 - M_\infty^2}$ approaches infinity, causing various perturbation parameters to approach infinity. Hence, the Prandtl-Glauert formula begins to show increasing departures from reality as the Mach number approaches a value of unity. The relative inaccuracy at a particular Mach number depends on parameters such as the section thickness and the angle of attack.

9.1.3 Additional Compressibility Corrections

When comparing the Prandtl-Glauert correction to compressible experimental data for two-dimensional shapes, the theory typically underpredicts the actual results. Because of this, there are two other commonly used compressibility corrections: the *Karmen-Tsien rule* and *Laitone's rule*. Both of these corrections are based on the Prandtl-Glauert correction, but proceed with different assumptions to derive the improved results. If we rewrite the Prandtl-Glauert correction, which is based on linear theory, with the definition that $\beta = \sqrt{1 - M_\infty^2}$, we obtain:

$$C_p = \frac{C_p'}{\beta}$$

where C_p' is the incompressible pressure coefficient. The first improvement was accomplished by taking into account some aspects of non-linearity and was done by von Karman (1941) and Tsien (1939); it is known as the Karman-Tsien rule:

$$C_p = \frac{C_p'}{\beta + \dfrac{M_\infty^2}{1 + \beta}\dfrac{C_p'}{2}} \tag{9.17}$$

Another improved correction by Laitone (1951) was derived by assuming the free-stream Mach number is replaced by the local Mach number; it is known as Laitone's rule:

$$C_p = \frac{C_p'}{\beta + \dfrac{M_\infty^2}{\beta}\left(1 + \dfrac{\gamma - 1}{2}M_\infty^2\right)\dfrac{C_p'}{2}} \tag{9.18}$$

While these corrections work well for two-dimensional shapes such as airfoils, they do not work as well for three-dimensional slender bodies. Lees (1946) showed that the appropriate compressibility correction for slender bodies is:

$$C_p = \frac{C_p'}{(1 - M_\infty^2)^{3/2}} \tag{9.19}$$

which is a significant departure from the two-dimensional corrections.

9.1.4 The Motivation for Determining the Critical Mach Number

A test flight of the YP-38 took place in September 1940. Major Signa Gilkey peeled off into a steep dive starting at 35,000 ft. "As he headed down and the airspeed built up, the airplane began to shake, mildly at first and then more violently. Even worse, the airplane wanted to nose down further and increase the severity of the dive. The control column was shaking and the control forces had become heavy, and it was impossible to pull the column back to counteract the nose-down tendency. The airplane was out of control" [Foss and Blay (1987)]. Major Gilkey elected to stay with the plane and recovered at 7000 ft. "Major Gilkey had become the first pilot to encounter a new, uncharted high-speed flight regime. He had attained air speeds where new aerodynamic phenomena known as compressibility effects were created" [Foss and Blay (1987)].

In seeking ways to control the aircraft experiencing these compressibility effects, the designers turned to the references of the time. Foss and Blay (1987) note, "In hindsight, it is interesting to note that no one was anticipating the nose down pitching moment tendencies, which were hinted at in the section on pitching moment data. And of course, there were no data to suggest that hinge moments would become unmanageable."

Using a P-38 model in the high-speed wind tunnel of the Ames Research Center, model drag-rise characteristics were measured for the first time. The wind-tunnel correlations, as taken from Foss and Blay (1987), are reproduced in Fig. 9.6. Pressure data and flow visualization clearly revealed the shock-stall conditions and helped confirm the flight-test findings.

9.1.5 Critical Mach Number

The critical Mach number is defined as the Mach number where sonic flow first appears in a flow field. In order to estimate the critical Mach number, we will first need to find the pressure coefficient at this point, which is called the critical pressure coefficient. The pressure coefficient at any point in a flow can be written as:

$$C_p = \frac{2}{\gamma M_\infty^2}\left(\frac{p}{p_\infty} - 1\right) = \frac{2}{\gamma M_\infty^2}\left(\frac{p}{p_t}\frac{p_t}{p_\infty} - 1\right) \tag{9.20}$$

We will assume the flow between the free stream and any point in the flow has constant total pressure (which means the point is not in a boundary layer or behind a shock). Using isentropic relations for the pressure in terms of the total pressure from equation (8.36) we can write this as:

$$C_p = \frac{2}{\gamma M_\infty^2}\left(\left(\frac{1 + \dfrac{\gamma - 1}{2} M_\infty^2}{1 + \dfrac{\gamma - 1}{2} M^2}\right)^{\frac{\gamma}{\gamma - 1}} - 1\right)$$

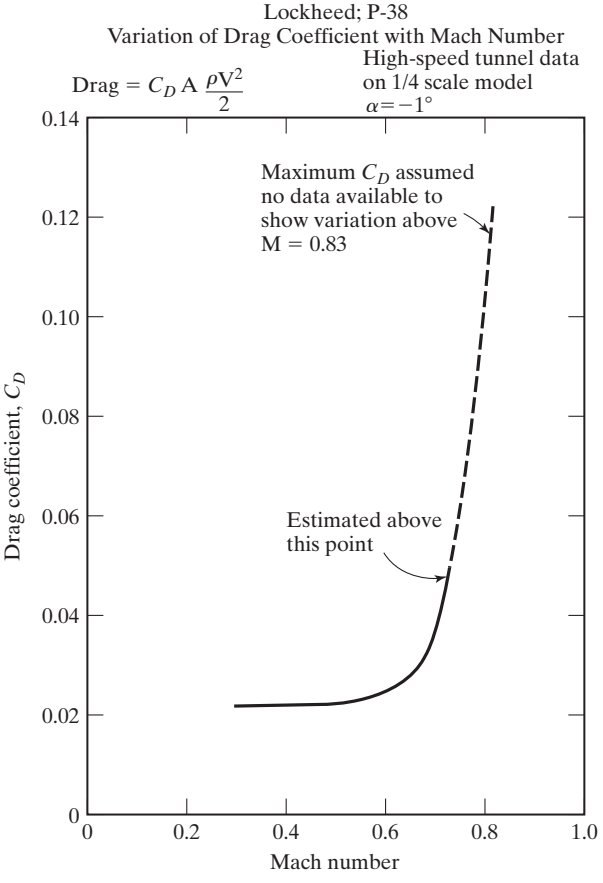

Figure 9.6 High-speed drag variation derived from wind-tunnel tests [from Foss and Blay (1987)].

If the flow at the point in the field has reached a Mach number of $M = 1$, we can write the critical pressure coefficient as:

$$C_{p,crit} = \frac{2}{\gamma M_\infty^2}\left(\left(\frac{1 + \frac{\gamma - 1}{2} M_\infty^2}{1 + \frac{\gamma - 1}{2}}\right)^{\frac{\gamma}{\gamma - 1}} - 1\right) \tag{9.21}$$

This relationship is simply an isentropic relation for the pressure coefficient, and has nothing to do with airfoil or wing geometry: in other words, this equation is always true for any isentropic flow.

We can create a fairly straightforward method for estimating the critical Mach number by using the critical pressure coefficient with our compressibility correction rules. This can be done analytically, but the method is easiest to use graphically, as shown in Fig. 9.7. The critical pressure coefficient variation from equation (9.21) is graphed for Mach numbers between 0.2 and 1. Then the minimum incompressible

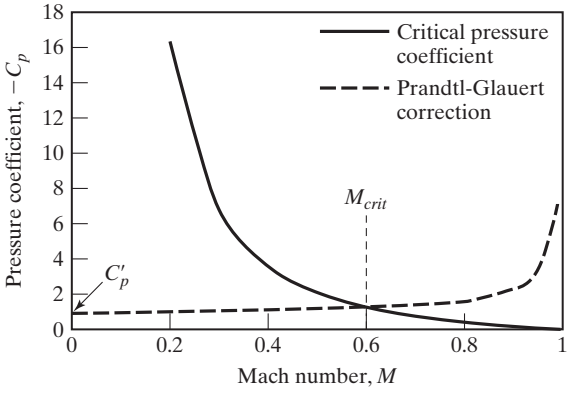

Figure 9.7 Intersection of critical pressure coefficient and Prandtl-Glauert correction curves, signifying the critical Mach number.

pressure coefficient, C'_p is obtained from a prediction or experimental data, and corrected for compressibility using one of the compressibility corrections (the Prandtl-Glauert rule in the case of Fig. 9.7). Where the two curves intersect is the location of the critical Mach number, since this represents the pressure at the minimum pressure location of the airfoil when $M = 1$, which is the definition of the critical Mach number.

The problem with using the various compressibility corrections for thin airfoils with low values of the minimum pressure coefficient is that the spread of critical Mach number estimates can be quite large, as shown in Fig. 9.8. This is why it is important to gain some confidence in using the various correction rules, which typically show that the "correct" answer may be between the Karman-Tsien and Laitone results.

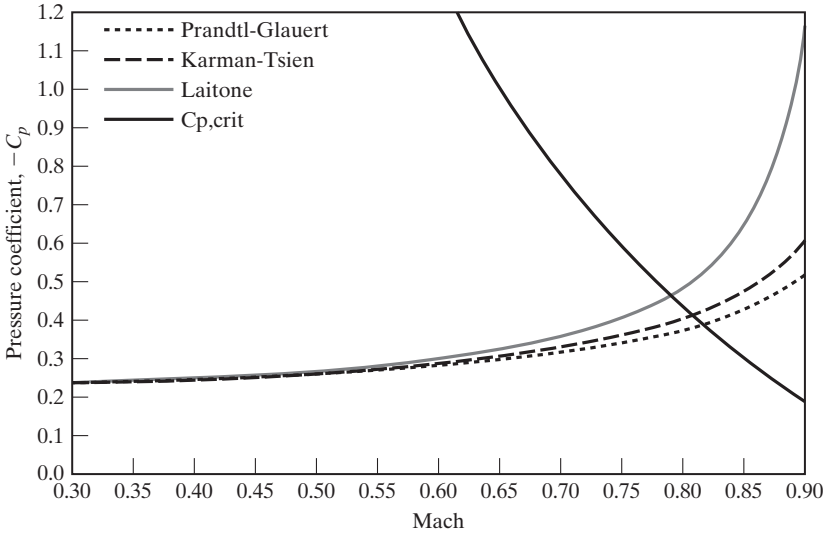

Figure 9.8 Comparison of three compressibility correction rules, showing large variation in critical Mach number estimate.

9.1.6 Drag Divergence Mach Number

While the critical Mach number, M_{crit}, is the gateway to the transonic speed regime, nothing earth shattering actually happens at M_{crit}. Since the flow is only sonic at one point on the airfoil, there are no shocks, no changes in drag coefficient, and no loss of lift taking place. But all of these things will happen at a Mach number just slightly higher than the critical Mach number, which is known as the drag divergence Mach number, M_{dd}. If you look at the zero-lift drag coefficient for the F-4C aircraft in Fig. 9.9 from Heffley and Jewel (1972), you see that the drag coefficient is constant over the subsonic speed regime, with a critical Mach number of approximately $M = 0.90$, but then rises

a) F-4C which was flown at 35,000 ft in level acceleration; W = 38,924 lb with 4 AIM-7 missiles (US Air Force photo)

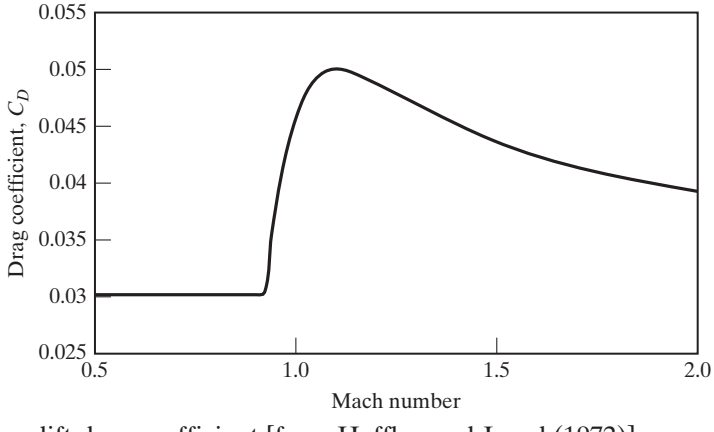

b) Zero-lift drag coefficient [from Heffley and Jewel (1972)]

Figure 9.9 F-4C zero-lift drag coefficient.

steeply above approximately $M = 0.92$. Our method for determining the critical Mach number might accurately predict $M = 0.90$, but would not tell us that the drag would actually start to rise at $M = 0.92$.

Because of the importance of the drag rise to cruising aircraft, the drag divergence Mach number is actually more important than the critical Mach number. There are no reliable analytic methods for predicting the drag divergence Mach number, although practically every aircraft manufacturer has some "rule of thumb" for estimating the value. These methods are typically based on historical trends, but over the years each company developed its own approach, and had its own method. For example, some estimates of the drag divergence Mach number are based on a percentage increase above M_{crit}, perhaps somewhere between 2% and 4% higher. Other methods are based on the slope of the drag coefficient curve with respect to Mach number, dC_D/dM_∞, since the drag divergence Mach number will have a higher slope value than the critical Mach number. But not everyone uses the same value of the slope (some use 0.03, some 0.05, and others 0.10). Of course all of these methods will give slightly different values for M_{dd}, but not as different as it may seem at first. An empirically based formula for estimating M_{dd} is found in Shevell (1988) which is based on a slope of $dC_D/dM_\infty = 0.05$:

$$M_{dd} = M_{crit}[1.02 + 0.08(1 - \cos\Lambda)] \tag{9.22}$$

You can see that the result is approximately 2% above the critical Mach number, with an additional adjustment for the sweep of the wing, Λ (unswept wings having higher values of drag divergence Mach number and swept wings having lower values). When this equation is applied to the F-4C shown in Fig. 9.9, assuming that the critical Mach number is 0.90 and the wing sweep is 40°, the drag divergence Mach number is estimated as $M_{dd} = 0.935$, which compares well with the results in Fig. 9.9.

9.2 TRANSONIC FLOW PAST UNSWEPT AIRFOILS

The section lift coefficient measurements presented in Farren (1956) as a function of Mach number are reproduced in Fig. 9.10. The data indicate that the flow is essentially unchanged up to approximately one-third of the speed of sound. The variations in the section lift coefficient with Mach number indicate complex changes in the flow field through the transonic speed range. You should notice the section lift coefficient at five particular Mach numbers (identified by the letters *a* through *e*). Significant differences exist between the flow fields at these five Mach numbers. To illustrate the essential changes in the flow, line drawings made from Schlieren photographs are reproduced in Fig. 9.11.

(a) When the free-stream Mach number is 0.75, the flow past the upper surface decelerates from local flow velocities which are supersonic without a shock wave. The section lift coefficient is approximately 60% greater than the low-speed values at the same angles of attack.

(b) At $M_\infty = 0.81$, the section lift coefficient reaches its maximum value, which is approximately twice the low-speed value. As indicated in Figs. 9.11b and 9.12a, flow is supersonic over the first 70% of the surface, terminating in a shock wave. The flow on the lower surface is subsonic everywhere. Because the viscous flow separates at the foot of the shock wave, the wake is appreciably wider than for (a).

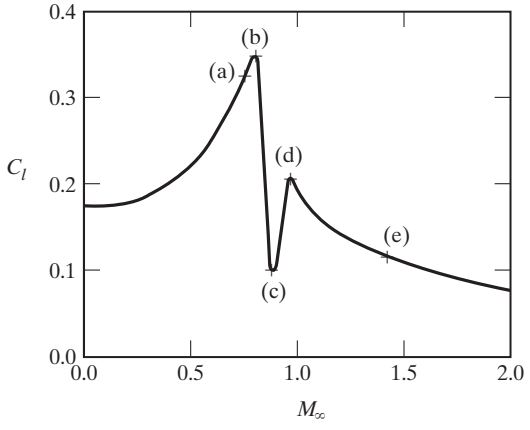

Figure 9.10 Section lift coefficient as a function of Mach number to illustrate the effect of compressibility [from Farren (1956)]. Refer to Fig. 9.11 for the flow fields corresponding to the lettered points on this graph.

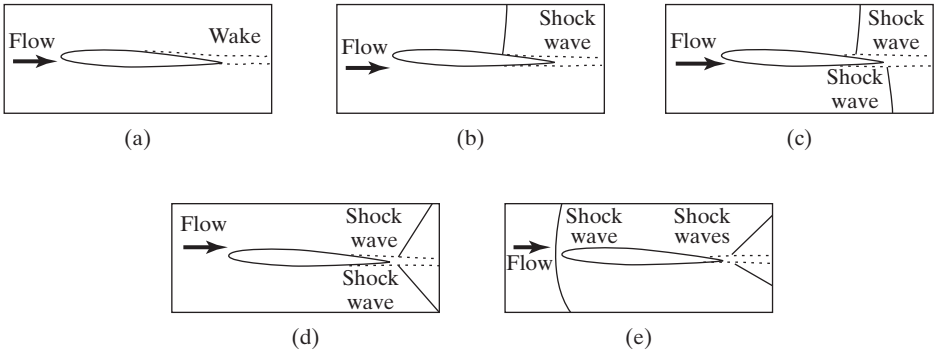

Figure 9.11 Flow field around an airfoil in transonic streams based on schlieren photographs: (a) Mach number $M_\infty = 0.75$; (b) Mach number $M_\infty = 0.81$; (c) Mach number $M_\infty = 0.89$; (d) Mach number $M_\infty = 0.98$; (e) Mach number $M_\infty = 1.4$ [from Farren (1956)].

(c) At $M_\infty = 0.89$, flow is supersonic over nearly the entire lower surface and deceleration to subsonic speed occurs through a shock wave at the trailing edge. As a result, the lower surface pressures are lower at $M_\infty = 0.89$ than at $M_\infty = 0.81$. Flow on the upper surface is not greatly different than that for Fig. 9.11b. As a result, the lift is drastically reduced. Separation at the foot of the upper surface shock wave is more conspicuous and the turbulent wake is wide. The shock wave at the trailing edge of the lower surface effectively isolates the upper surface from the lower surface. As a result, the pressure on the upper surface near the trailing edge is greater than that on the lower surface. The corresponding pressure and local Mach number distributions are presented in Fig. 9.12b.

(d) When the free-stream Mach number is 0.98, the shock waves both for the upper surface and for the lower surface have reached the trailing edge. The local Mach number is supersonic for most of the airfoil (both upper and lower surfaces).

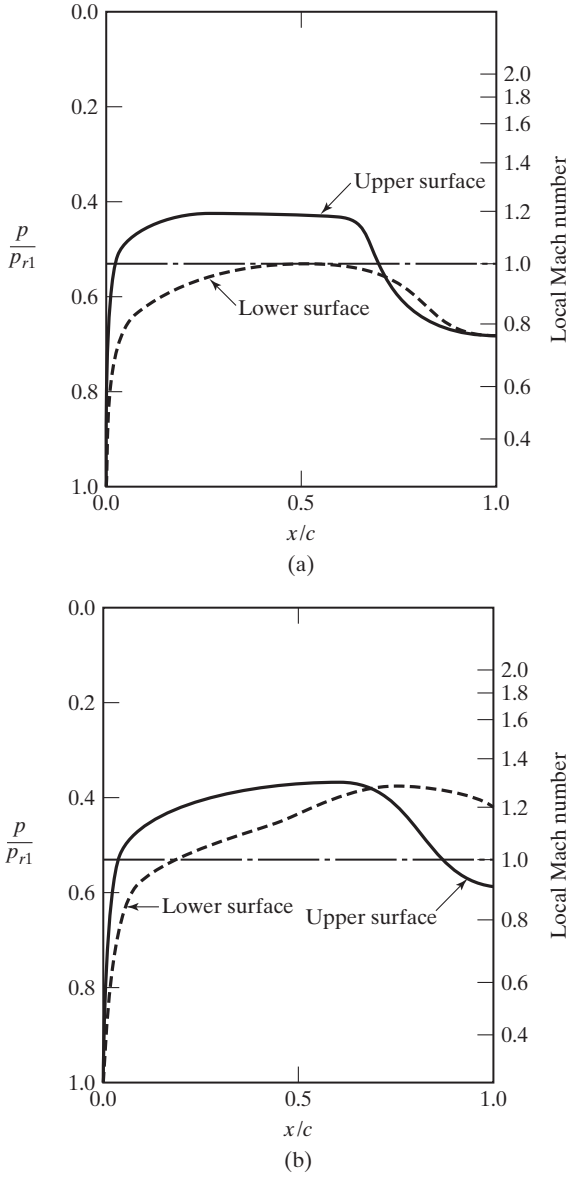

Figure 9.12 Pressure distribution and local Mach number distribution for transonic flows around an airfoil: (a) Flow at the trailing edge is subsonic, $M_\infty = 0.81$; (b) flow at the lower surface trailing edge is supersonic, $M_\infty = 0.89$ [from Farren (1956)].

(e) When the free-stream flow is supersonic, a bow shock wave (i.e., the detached shock wave in front of the leading edge) is generated. The flow around the airfoil is supersonic everywhere except very near the rounded nose. The shock waves at the trailing edge remain, but they have become weaker.

Eventually the shock wave becomes attached and the flow field is entirely supersonic.

The data presented in Figs. 9.10 through 9.12 illustrate the effect of Mach number for a given airfoil section at a particular angle of attack. Parameters such as thickness

ratio, camber, and nose radius also influence the magnitude of the compressibility effects. Transonic flows are very sensitive to the contour of the body surface, since changes in the surface slope affect the location of the shock wave and, therefore, the inviscid flow field as well as the downstream boundary layer.

Furthermore, as was discussed in Chapter 8, the shock-wave/boundary-layer interaction and the possible development of separation downstream of the shock wave are sensitive to the character of the boundary layer, to its thickness, and to its velocity profile at the interaction location. Since a turbulent boundary layer can negotiate higher adverse pressure gradients than a laminar boundary layer, the shock-wave/boundary-layer interaction is smaller for a turbulent boundary layer. Therefore, it is important to consider the Reynolds number when simulating a flow in the wind tunnel. A large Reynolds number difference between the desired flow and its simulation may produce significant differences in shock-wave location and the resultant flow field. The use of artificial trips to force transition to occur at a specified point (as discussed in Chapter 5) may be unsatisfactory for transonic flows, since the shock-wave location as well as the extent of flow separation can become a function of the artificial tripping.

The Cobalt_{60} code [Strang et al. (1999)] has been used to compute the flow field around a NACA 0012 airfoil section at an angle of attack of 3°. The turbulence model of Spalart and Allmaras (1992) was used to represent the viscous boundary layer near the surface of the airfoil. Contours of constant Mach number, as computed by Forsythe and Blake (2000) for a free-stream Mach number of 0.8 at a free-stream Reynolds number (based on the chord length) of 3.0×10^6, are presented in Fig. 9.13. The Mach 1 contours for the upper surface and for the lower surface are highlighted in white. Notice that the relatively large area of supersonic flow on the upper surface is terminated by a shock wave at the downstream (or right-hand) side of the region of supersonic flow. The shock wave is evident in the sudden increase in pressure evident both in the experimental and in the computed pressure distributions for this airfoil, which are taken from Forsythe et al. (2000) and reproduced in Fig. 9.14. The flow conditions for the experimental data, which are taken from Harris (1981), include a free-stream Mach number of 0.799, a Reynolds number of 9.0×10^6, and an angle of attack of 2.86°. The sudden increase in pressure due to the shock wave occurs on the upper surface at mid-chord. The adverse pressure gradient associated with the shock-wave/boundary-layer interaction causes the boundary layer to separate from the aft-end surface of the airfoil. This is evident in the (darkened region) Mach number contours presented in Fig. 9.13.

The section lift coefficient for this two-dimensional flow [Forsythe and Blake (2000)] is presented as a function of the free-stream Mach number in Fig. 9.15. You should notice the similarity between the Mach-number dependence of the computed section lift coefficient, as presented in Fig. 9.15, and that for the measurements presented by Farren (1956), which are reproduced in Fig. 9.10.

The computed flow field for transonic flow over a NACA 0012 airfoil that was presented in Fig. 9.13 depicts regions (both above and below the airfoil) where the flow has accelerated to supersonic values. Since the pressure is decreasing, the acceleration of the flow is often termed an expansion. During the isentropic expansion of the flow, there is a corresponding decrease in the temperature.

If the airplane is flying through an airstream where the relative humidity is high, the local temperature of the expanding flow can decrease below the dew point. Water vapor will condense and become visible. Further downstream, as the flow decelerates

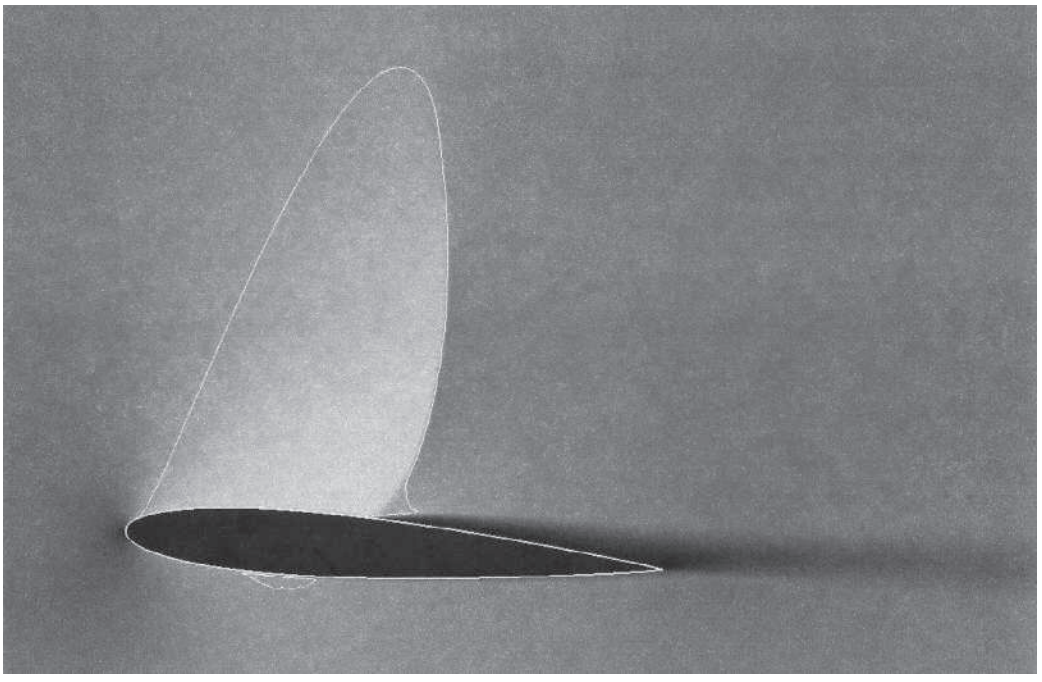

Figure 9.13 Constant-density contours for a NACA 0012 airfoil in a Mach 0.8 stream at $\alpha = 3°$ [provided by Forsythe and Blake (2000)].

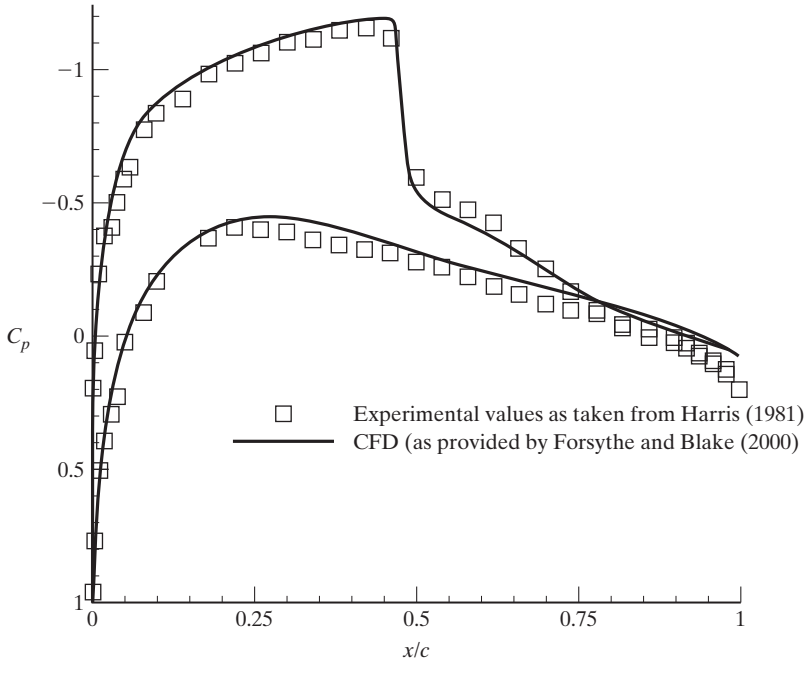

Figure 9.14 Pressure distributions for a NACA 0012 in a Mach 0.8 stream at $\alpha = 3°$.

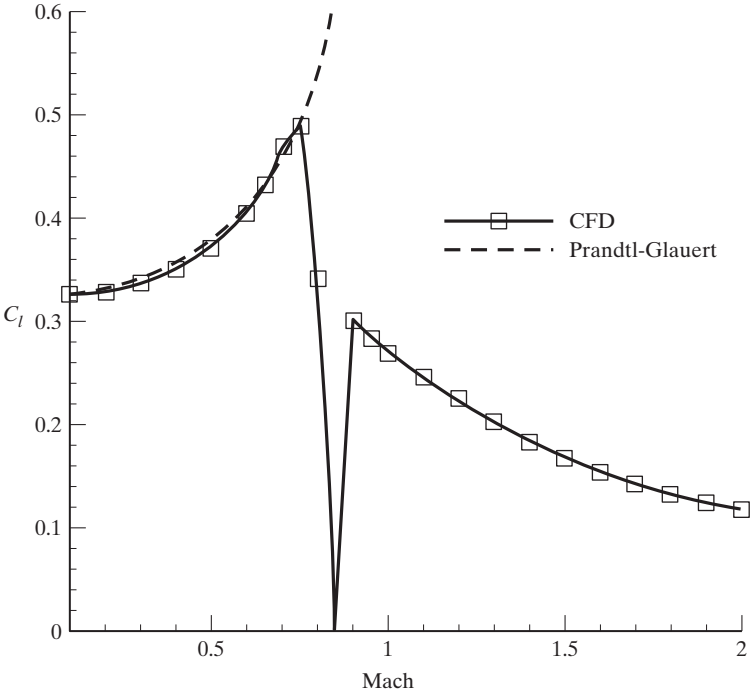

Figure 9.15 Section lift coefficient for a NACA 0012 airfoil as a function of the free-stream Mach number [provided by Forsythe and Blake (2000)].

(perhaps as it passes through a shock wave that terminates the locally supersonic flow), the pressure and the temperature increase. As the local temperature rises above the dew point, the condensed particles evaporate (or vaporize) and are no longer visible. Therefore, when an airplane is flying at transonic speeds in a relatively humid atmosphere, the relatively large accelerations (expansions) and decelerations (compressions) yield a condensation pattern, such as that for the B-1B, which is presented in Fig. 9.16a.

The Schlieren technique, which allows us to see shock waves in a wind-tunnel test, is based on density gradients in the flow field that bend light rays passing through the flow. Under certain circumstances, these density gradients allow us to "see" the shock waves for an airplane in flight, as shown for the transonic flight of an F-111 in Fig. 9.16b.

The experimentally determined lift coefficients for an untwisted rectangular wing whose aspect ratio is 2.75 and whose airfoil section is a NACA 65A005 (a symmetric profile for which $t = 0.05c$) are presented in Fig. 9.17 as a function of angle of attack. The corresponding drag polars are presented in Fig. 9.18. These data from Stahl and Mackrodt (1965) were obtained at Reynolds numbers between 1.0×10^6 and 1.8×10^6. The lift-curve slope is seen to be a function of the free-stream Mach number. Furthermore, the linear relation between the lift coefficient and the angle of attack remains valid to higher angles of attack for supersonic flows.

(a)

(b)

Figure 9.16 (a) Condensation and evaporation of the water vapor delineates regions where the flow has expanded for a B-1B in transonic flight (US Air Force photo). (b) F-111 flying at transonic speeds with shock waves clearly visible (courtesy of R. C. Maydew and S. McAlees of the Sandia National Laboratories).

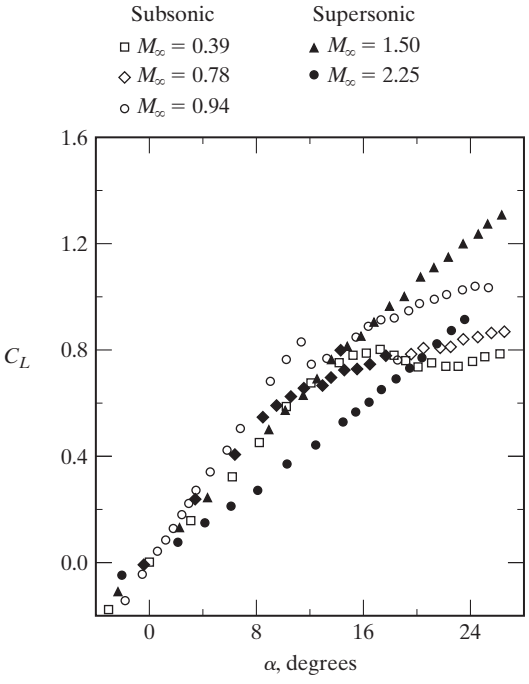

Figure 9.17 Effect of Mach number on the lift-coefficient/angle-of-attack correlation for a rectangular wing, $AR = 2.75$ [data from Stahl and Mackrodt (1965)].

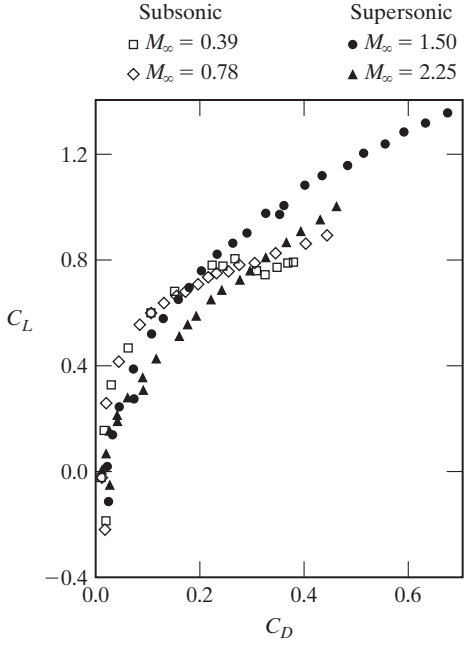

Figure 9.18 Effect of the Mach number on drag polars for a rectangular wing, $AR = 2.75$ [data from Stahl and Mackrodt (1965)].

Bushnell (2004) noted:

> Shock waves are usually detrimental, requiring mitigation. The volume and lift-engendered drag associated with shock waves is additive to the usual friction and vortex drag-due-to-lift, comprising one-third of total aircraft drag in the supersonic cruise case, even for the well-designed configuration. The reason for the decades-long Mach .8ish cruise-speed plateau associated with conventional long-haul transport aircraft (requiring over ten hours of flight time transpacific) is avoidance of the major drag increases due to strong shock formation on the upper wing surfaces at higher speeds. Shock wave drag is also a major reason there are no economically viable supersonic transports yet extant. Due to wave drag, the aerodynamic efficiency of a supersonic transport (SST) is the order of one-half or less of a conventional (subsonic) transport. Usual SST designs require a fuel fraction approaching 60%, including reserves. A 1% overall drag reduction for these designs translates to a 5 to 10% increase in payload.

Aerodynamics Concept Box: What Does "Non-Linear Flow" Mean?

Mathematically, the full potential equation, equation (9.4b), is non-linear. This equation is valid in the transonic speed regime, and when it is linearized it is only valid for subsonic or supersonic speeds. Why? Because the flow is "non linear" in the transonic regime. What does that mean? It means the flow has the following features: shock-boundary layer interactions, mixed subsonic/supersonic flow, and is usually highly unsteady.

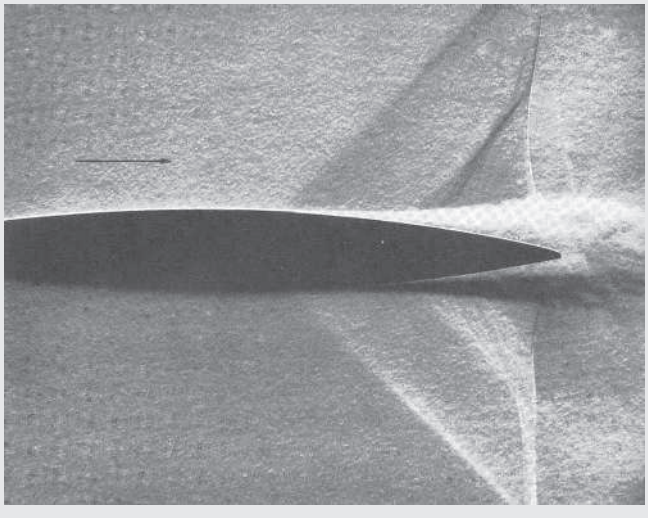

Shock pattern over a transonic airfoil [from Liepmann (1946)]

What is happening here? At a height well above the airfoil, the normal shock bifurcates or separates into two parts. The front leg of the bifurcated system inclines down into the boundary layer at about 50° angle [Sheldon (1967)]. Since an oblique shock increases the pressure, this starts to thicken the boundary layer, eventually leading to flow separation. Flow

separation occurs and turns the flow away from the airfoil, which causes the creation of another oblique shock. As the normal shock interacts with the separated flow region, it is curved (as we discussed in Chapter 8). This flow, with all of the interactions we can see taking place, is also unsteady. This is a picture of non-linear aerodynamics.

9.3 WAVE DRAG REDUCTION BY DESIGN

Since the appearance of shock waves on vehicles typically has such a large negative impact on aircraft performance, it is usually necessary to make design changes in order to reduce the drag rise. There are a variety of ways to accomplish this, and aircraft often take advantage of multiple methods to reduce the increased drag due to shock waves. This is typically accomplished by the use of supercritical airfoils, wing sweep, and the area rule.

9.3.1 Airfoil Contour Wave Drag Approaches

Three features which contribute to the location of the shock wave and, therefore, to the pressure distribution are:

- The flow in the supersonic region ahead of the shock wave
- The pressure rise across the shock wave itself (which involves considerations of the interaction with the boundary layer)
- The subsonic flow downstream of the shock wave (which involves considerations of the boundary-layer development between the shock wave and the trailing edge and of the flow in the near wake) [Holder (1964)]

If the trailing-edge pressure changes as a result of flow separation from the upper surface, the lower surface flow must adjust itself to produce a similar change in pressure (since the pressure near the trailing edge must be approximately equal for the two surfaces, unless the flow is locally supersonic at the trailing edge). The conditions for divergence of the trailing-edge pressure correspond to those for a rapid drop in the lift coefficient and to the onset of certain unsteady flow phenomena, such as buffeting.

9.3.2 Supercritical Airfoil Sections

The Mach-number/lift-coefficient flight envelopes of modern jet aircraft operating at transonic speeds are limited by the compressibility drag rise and by the buffeting phenomenon. Airfoil section designs which alleviate or delay the onset of the drag rise and buffeting can contribute to higher maximum speeds (transport applications) or better lift performance (fighter applications). Using intuitive reasoning and substantiating experiment, Whitcomb and Clark (1965) noted that R. T. Whitcomb and his coworkers have developed a "supercritical" airfoil shape which delays the subsonic drag rise. The principal differences between the transonic flow field for a conventional airfoil and that for a supercritical airfoil are illustrated by the data presented in Fig. 9.19. At supercritical Mach numbers, a broad region of locally supersonic flow extends vertically from both airfoils, as indicated by the pressure coefficients above the sonic value and by the shaded areas of the flow fields in Fig. 9.19. The region of locally supersonic flow usually terminates in a shock wave, which results

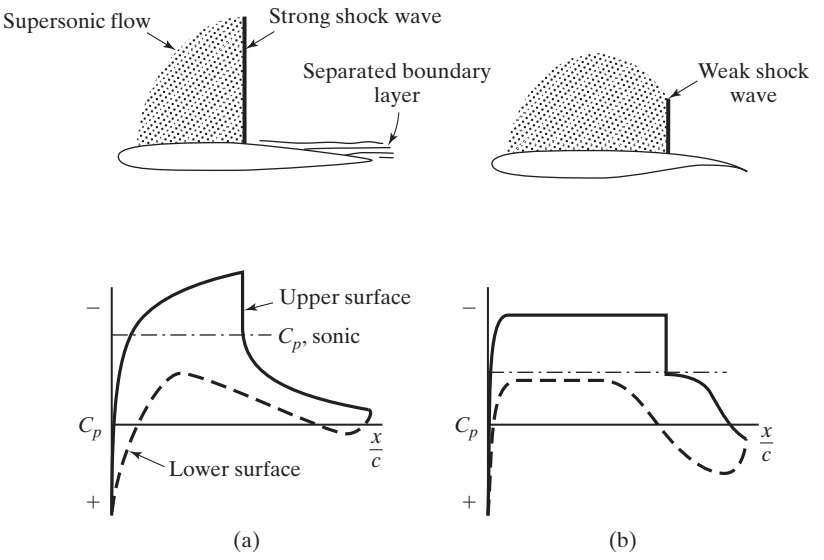

Figure 9.19 Comparison of transonic flow over a NACA 64A series airfoil with that over a "supercritical" airfoil section: (a) NACA 64A series, $M = 0.72$; (b) supercritical airfoil, $M = 0.80$ [from Ayers (1972)].

in increased drag. The much flatter shape of the upper surface of the supercritical airfoil causes the shock wave to occur downstream and therefore reduces its strength. Therefore, the pressure rise across the shock wave is reduced with a corresponding reduction in drag. However, the diminished curvature of the upper surface also results in a reduction of the lift carried by the midchord region of the airfoil section. To compensate for the loss in lift from the midchord region, additional lift must be generated from the region of the airfoil behind the shock wave, particularly on the lower surface. The increase of lift in this area is achieved by substantial positive camber and incidence of the aft region of the airfoil, especially of the lower surface. The increased lift generated by the concave surface near the trailing edge of the lower surface is evident in the experimental pressure distributions presented in Fig. 9.20. The midchord region of the lower surface should be designed to maintain subcritical flow over the range of operating conditions. If not, when the pressure rise associated with a shock wave is superimposed on the pressure rise caused by the cusp, separation of the lower-surface boundary layer would occur. To minimize the surface curvatures (and, therefore, the induced velocities) in the midchord regions of the upper and the lower surfaces, the leading-edge radius is relatively large. Supercritical airfoils are now used on essentially all commercial transports and military aircraft that fly at high subsonic speeds.

9.4 SWEPT WINGS AT TRANSONIC SPEEDS

In the late 1930s, two aerodynamicists who had been taught by Prandtl—Adolf Busemann and Albert Betz—discovered that drag at transonic and supersonic speeds could be reduced by sweeping back the wings; see Miller and Sawers (1970) for more details. At the

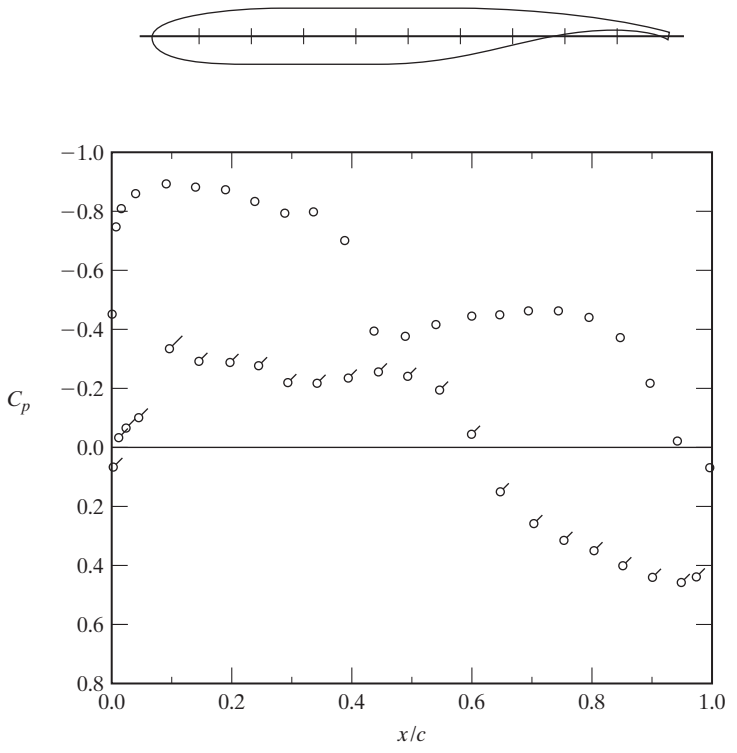

Figure 9.20 Experimentally determined pressure distribution for a supercritical airfoil section, $M_\infty = 0.80$, $C_l = 0.54$, $\mathrm{Re}_c = 3.0 \times 10^6$ (flagged symbols are for the lower surface) [data from Hurley et al. (1975)].

Volta conference in Rome in 1935, in his paper on high-speed flight, Busemann showed that sweepback would reduce drag at supersonic speeds. Betz, in 1939, was the first person to draw attention to the significant reduction in transonic drag which comes when the wing is swept back enough to avoid the formation of shock waves which occurs when the flow over the wing is locally supersonic. The basic principle is that the component of the main flow parallel to the wing leading edge is not perturbed by the wing, so the critical conditions are reached only when the component of the free-stream velocity normal to the leading edge has been locally accelerated at some point on the wing to the local sonic speed. This simple principle is obviously only true (if at all) on an infinite span wing of constant section. Nevertheless, the initial suggestion of Betz led to wind-tunnel tests which substantiated the essence of the theory. The results of the wind-tunnel measurements performed at Göttingen in 1939 by H. Ludwieg [as presented in Schlichting (1960)] are reproduced in Fig. 9.21. These data show that the effects of the shock waves that occur on the wing at high subsonic speeds are delayed to higher Mach numbers by sweepback.

The experimentally determined lift coefficients and drag polars for a delta wing whose aspect ratio is 2.31 and whose airfoil section is NACA 65A005 (a symmetric profile for which $t = 0.05c$) are presented in Fig. 9.22. These data from Stahl and Mackrodt (1965) were obtained at Reynolds numbers between 1.0×10^6 and 1.8×10^6.

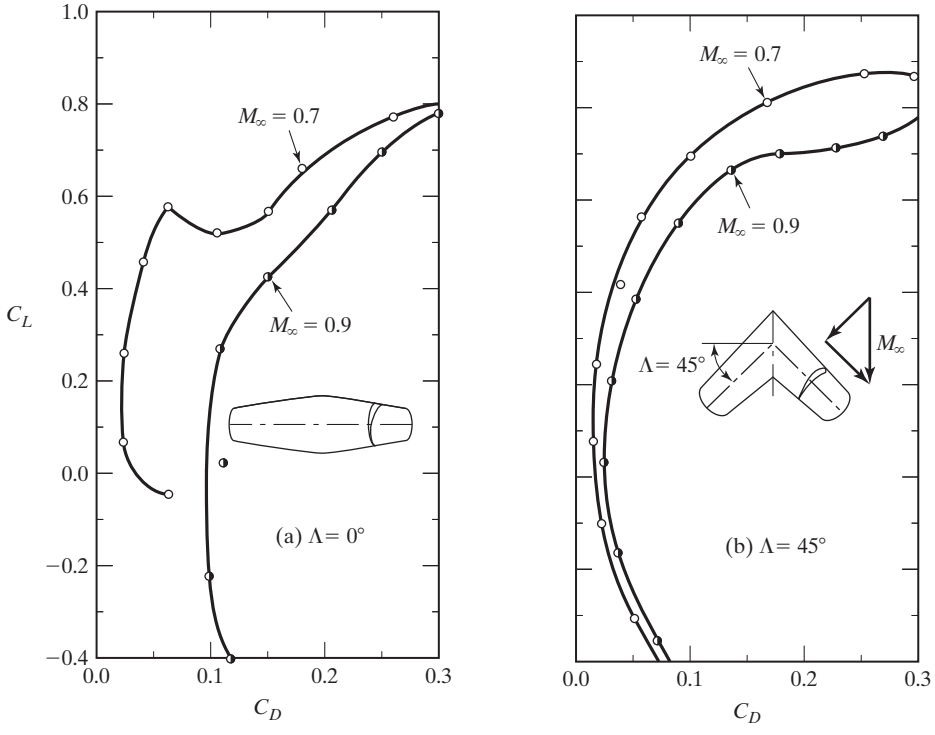

Figure 9.21 Comparison of the transonic drag polar for an unswept wing with that for a swept wing [data from Schlichting (1960)].

At subsonic speeds, the lift-coefficient/angle-of-attack correlation for the delta wing is markedly different than that for a rectangular wing; in addition to the data presented in Figs. 9.17 and 9.22, you should consult Chapter 7 for more details. Even in subsonic free streams, the lift is a linear function of the angle of attack up to relatively high inclination angles. However, over the angle-of-attack range for which the lift coefficient is a linear function of the angle of attack, the lift-curve slope $(dC_L/d\alpha)$ is greater for the rectangular wing for all the free-stream Mach numbers considered.

We could use a variable-geometry (or swing-wing) design to obtain a suitable combination of low-speed and high-speed characteristics. In the highly swept, low-aspect-ratio configuration, the variable-geometry wing provides low wave drag and eliminates the need for wing fold in the case of naval aircraft. At the opposite end of the sweep range, swept wings obtain efficient subsonic cruise and loiter and good maneuverability at lower speeds. Negative factors in a swing-wing design are complexity, a loss of internal fuel capacity, and the considerable weight of the hinge/pivot structure. A variable-geometry design, the Rockwell International B-1, is presented in Fig. 9.23.

9.4.1 Wing–Body Interactions and the "Area Rule"

The chordwise pressure distribution on a plane, finite-span, swept-back wing varies across the span such that the maximum local velocity is reached much farther aft at the root and farther forward at the tip compared to the basic infinite-wing distribution

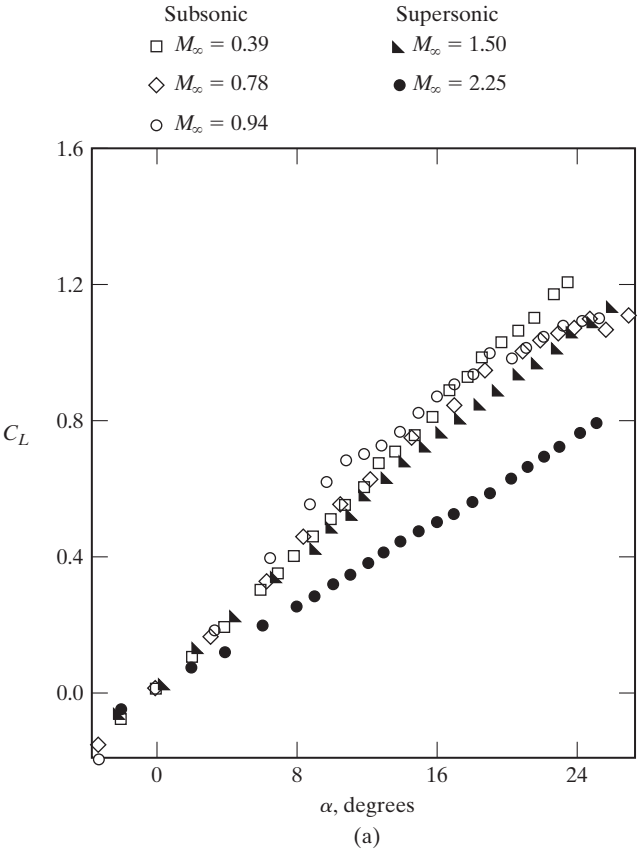

Figure 9.22 Effect of Mach number on the aerodynamic characteristics of a delta wing; $AR = 2.31$, $\Lambda_{LE} = 60°$: (a) lift-coefficient/angle-of-attack correlation [data from Stahl and Mackrodt (1965)].

[Rogers and Hall (1960)]. These distortions at the root and at the tip determine the flow pattern. On a swept wing with a square-cut tip, a shock wave first occurs near the tip, as shown in Fig. 9.24. This "initial tip shock" is relatively short in extent. As the Mach number is increased, a rear shock is developed which dominates the flow. Because of the variation of the component of velocity normal to the wing leading edge, streamlines over the wing surface will tend to be curved. However, the flow at the wing root is constrained to follow the fuselage. Therefore, for a straight fuselage, a set of compression waves originate in the wing-root region to turn the flow parallel to the fuselage. As shown in Fig. 9.24, the compression waves propagate across the wing span and ultimately may coalesce near the tip to form the rear shock.

The interaction between the central fuselage and the swept wing has a significant effect on the transonic flow over the wing. In the early 1950s, Küchemann (1957) recognized that a properly shaped waist-like indentation on the fuselage could be designed to produce a velocity distribution on the wing near the root similar to that on the

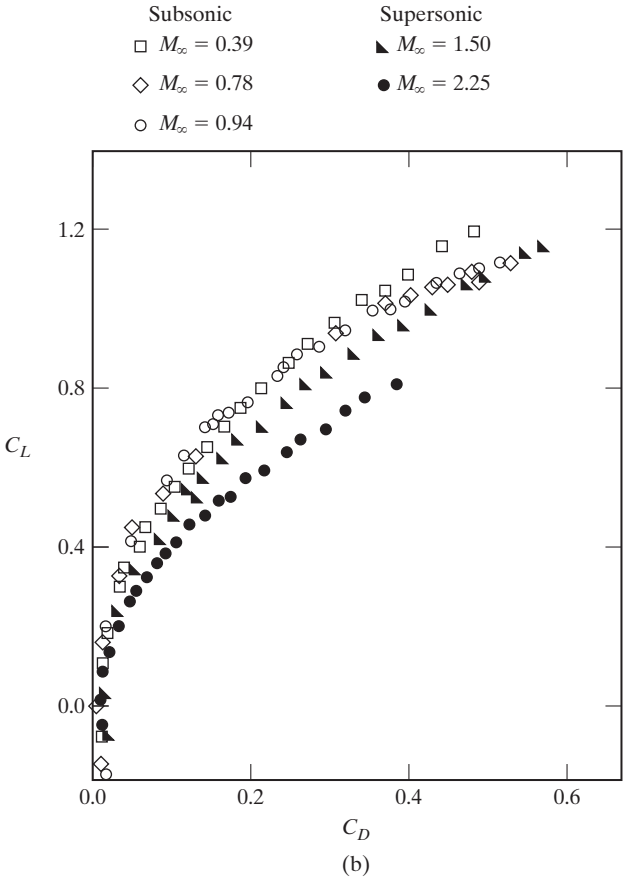

Figure 9.22 (*continued*) (b) drag polar.

corresponding infinite-span wing. Küchemann noted that, "the critical Mach number can be raised and the drag reduced in the transonic and the supersonic type of flow, the wing behaving in some respects like a thinner wing." Whitcomb (1956) found that the zero-lift drag rise is due primarily to shock waves. Furthermore, the shock-wave formations about relatively complex swept-wing/body combinations at zero lift near the speed of sound are similar to those which occur for a body of revolution with the same axial development of cross-sectional area normal to the airstream. Whitcomb concluded that, "near the speed of sound, the zero-lift drag rise of a low-aspect-ratio thin-wing/body combination is primarily dependent on the axial development of the cross-sectional areas normal to the air stream." Therefore, the drag-rise increments near the speed of sound are less for fuselage/wing configurations which have a more gradual change in the cross-sectional area (including the fuselage and the wing) with axial position (as well as a reduction in the relative magnitude of the maximum area). Whitcomb noted that it would be expected that indenting the body of a wing-body combination, so that the combination has nearly the same axial distribution of cross-sectional area as the original body alone, would result in a large reduction in the transonic drag rise. Design

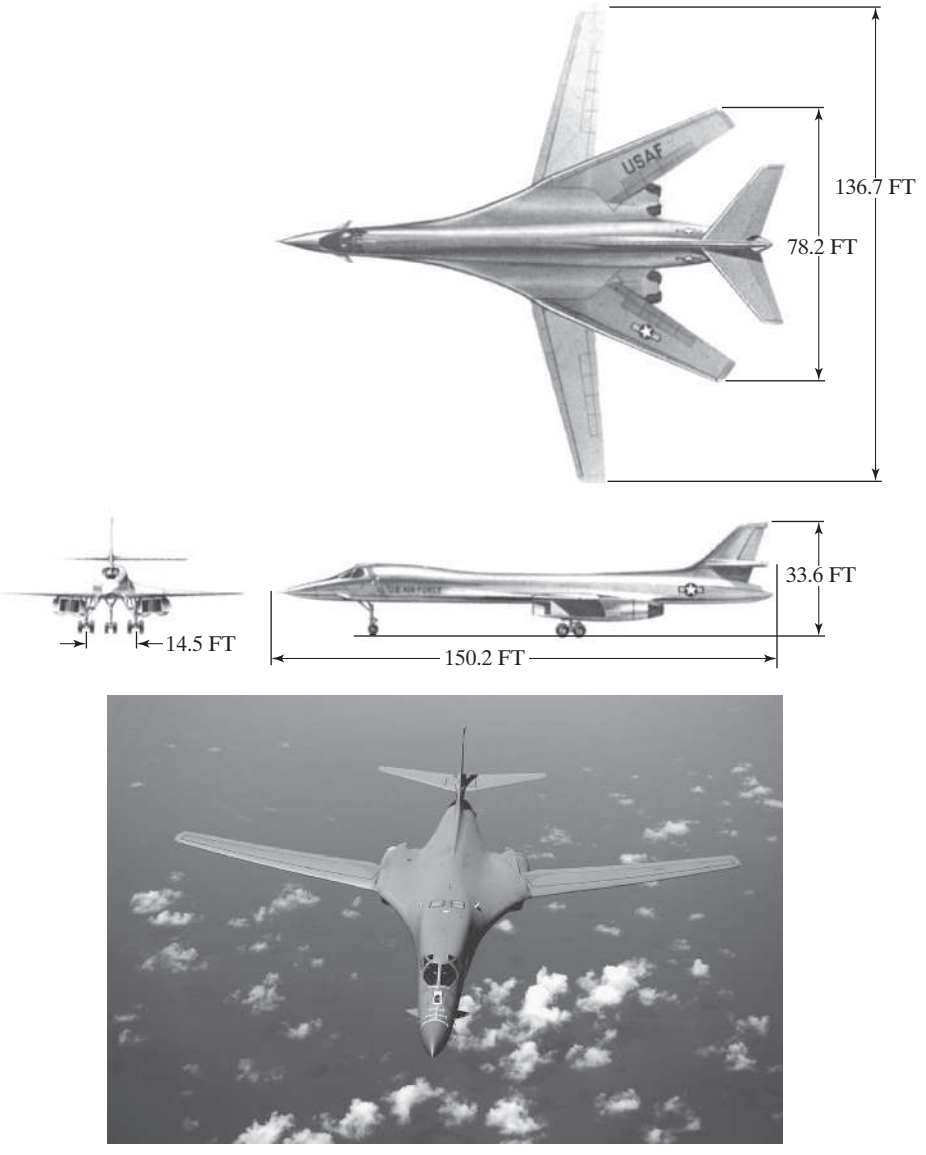

Figure 9.23 Variable geometry (swing-wing) aircraft, the Rockwell International B-1: (a) three-view sketches illustrating the variable-geometry wing; (b) low-speed configuration (US Air Force photo by Staff Sgt. Bennie J. Davis III).

applications of this "theory," which is often known as *Whitcomb's area rule* for transonic configurations, are illustrated in Fig. 9.25.

An example of the application of the area rule is the F-102. Early flight tests revealed that the YF-102, the prototype for the F-102, had serious deficiencies in performance (specifically, it could not reach supersonic speeds, a major deficiency for a

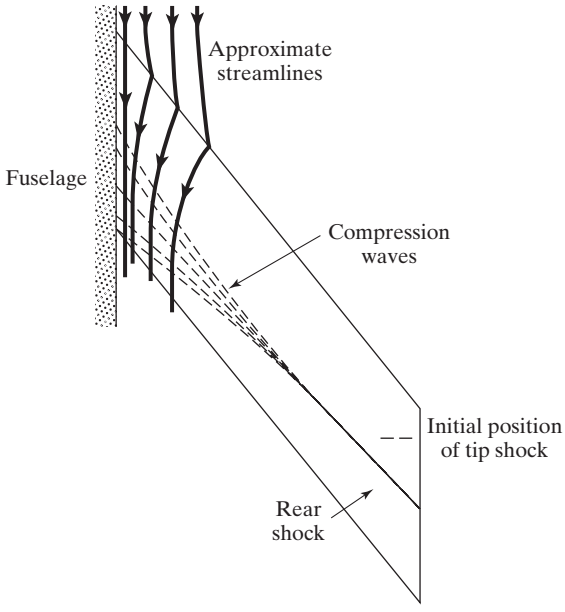

Figure 9.24 Formation of rear shock from compression waves associated with flow near the root [from Rogers and Hall (1960)].

supersonic fighter). A redesign effort included the first application of Whitcomb's area rule to reduce the transonic drag. The modified YF-102A (see Fig. 9.25b) achieved supersonic flight satisfactorily, providing the U.S. Air Force with its first operational delta-wing design [see Taylor (1969)].

The relation between the distribution of the cross-sectional area and the transonic drag rise had a significant effect on the design of the Convair B-58, the Air Force's first supersonic bomber. Free-flight, rocket-powered models of the original Convair design, designated MX-1626, were tested at the Wallops Island Flight Test Range (an NACA facility). The peak drag coefficient at Mach 1.02 was almost twice as high as had been predicted, and the model did not achieve supersonic speeds. An evaluation of the longitudinal cross-sectional area distribution in accordance with the area rule of R. T. Whitcomb, along with data obtained in the Helium Gun Facility at Wallops on a body of revolution having the same longitudinal distribution of the cross-sectional area as the MX-1626, provided an explanation of the unexpectedly high drag. A sketch of the planform of the MX-1626, the longitudinal distribution of the cross-sectional area, and the drag coefficient for the equivalent axisymmetric configuration as a function of the Mach number are shown in Fig. 9.26. Notice how the wing, the wheel fairings, and the nacelles all add area to the fuselage and the weapons/fuel pod, creating a large total cross-sectional area. Furthermore, the placement of these components results in large longitudinal variations in the total cross-sectional area.

To reflect changes in the design requirements due to the unavailability of the originally planned large jet engines, and to changes in the function of the pod, the Air Force changed the Project Number from MX-1626 to MX-1964. R. N. Hopko, R. O. Piland, and J. R. Hall set out to design a vehicle which met the general requirements of the new MX-1964 yet reduced the transonic drag rise. The design, designated PARD Area-Rule

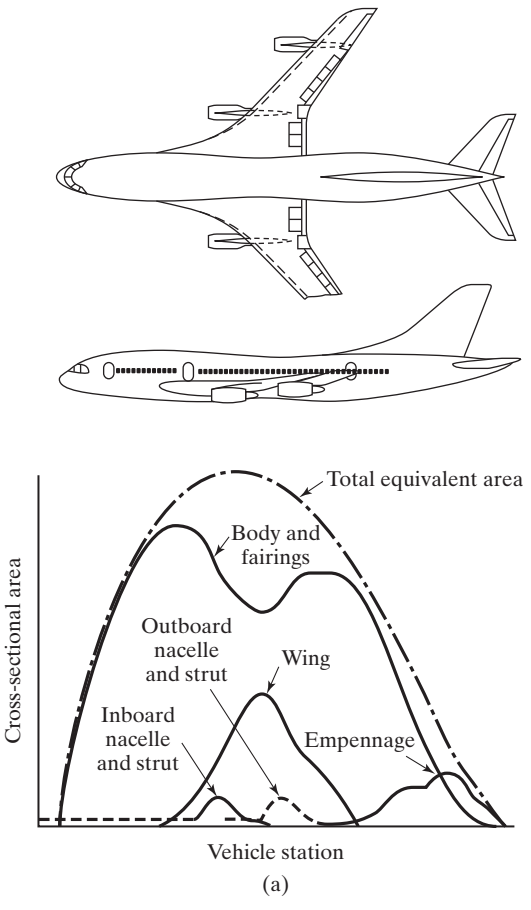

Figure 9.25 Application of the area rule to the axial distribution of the cross-sectional area: (a) area rule applied to the design of a near-sonic transport; (b) sketch of the Convair F-102A [from Goodmanson and Gratzer (1973)].

Design in Fig. 9.26, included a 3% thick, 60° delta wing, modified by a 10° forward swept trailing edge. The diamond-shaped wing provides a more gradual variation in the cross-sectional area distribution. To this wing, they added four separate nacelles, staggered in the chordwise direction, and made the fuselage a body of revolution. The resultant planform for the PARD Area-Rule Design, the longitudinal cross-sectional area distribution, and the measured drag coefficient for the equivalent body of revolution as a function of the Mach number are reproduced in Fig. 9.26b.

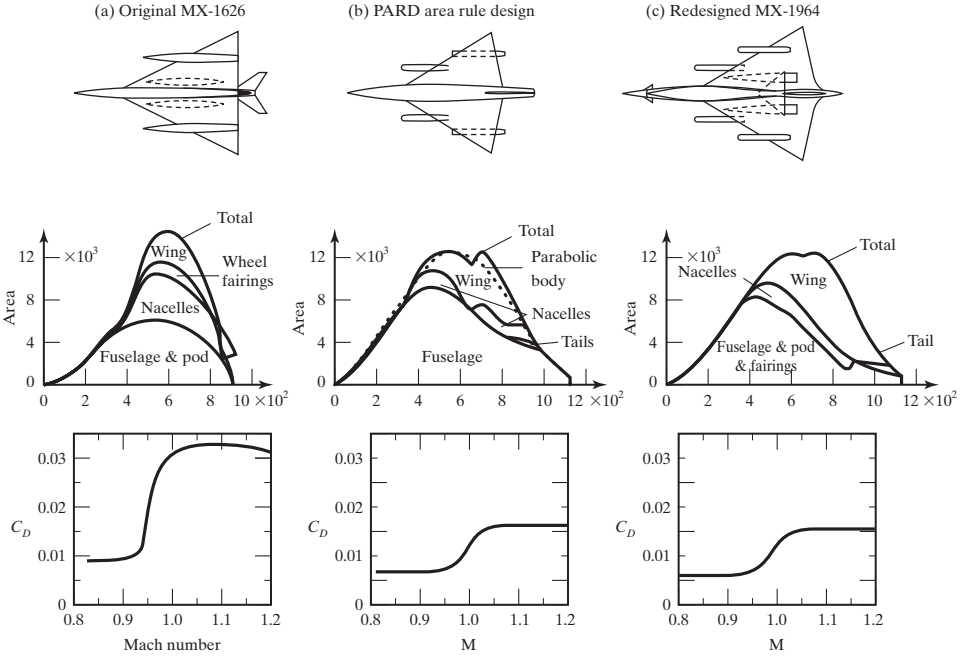

Figure 9.26 Planform sketches, longitudinal distributions of cross-sectional areas, and drag coefficients for equivalent bodies of revolution for supersonic bomber models [from Shortal (1978)].

Based on these data, Convair evaluated four alternative designs. Data for the configuration which had the lowest drag rise of the four Convair configurations are presented in Fig. 9.26c. Notice that the configuration, designated the Redesigned MX-1964, had both a smooth progression of cross-sectional area and the minimum value of the maximum cross-sectional area.

While touring the Air Force Museum at the Wright-Patterson Air Force Base, H. Hillaker (1994) noted, "The area-rule requirements of the B-58 required that the inboard and outboard nacelles be staggered—the inlet face of the outboard nacelle began on the same plane as the exhaust face of the inboard nacelle. We previously had siamese nacelles (engines side-by-side as in a B-52 nacelle) which was lighter in weight but the higher drag more than offset the lower weight." The resulting aircraft configuration is illustrated in the photograph of Fig. 9.27.

Applications of the area rule in the design of the F-5 are illustrated in Figs. 9.28 through 9.30. The benefit due to area ruling, considering a straight-sided fuselage as a base, is a large decrease in drag at transonic speeds. As a result, there is a corresponding increase in transonic acceleration, which is very important to this fighter's design. This is true, according to Stuart (1978) and Bradley (1982), because the major and decisive portions of air-to-air combat take place at altitudes below 30,000 ft and at speeds from Mach 0.5 to 1.0.

Area ruling was also applied to the tip-tank design for the F-5A/B aircraft. Initial prototype flight and wind-tunnel tests indicated that transonic buffet and longitudinal instabilities existed with the originally proposed wingtip tank. Continued development

Figure 9.27 Photograph of B-58 (US Air Force photo).

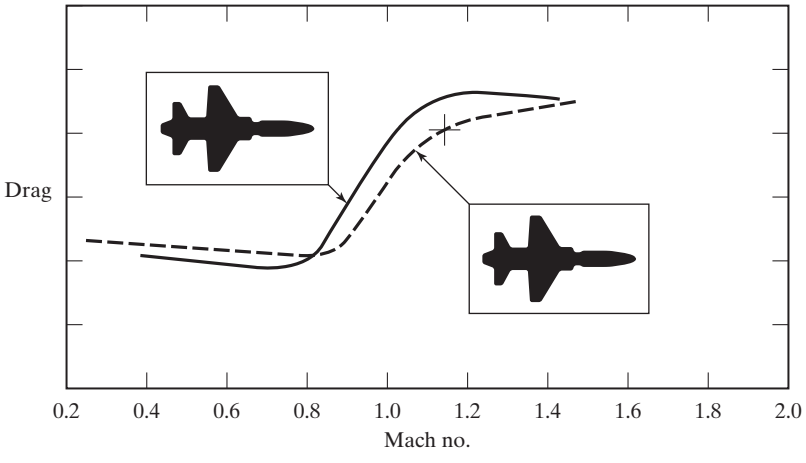

Figure 9.28 Reduction in the transonic drag rise due to the application of area rule to the F-5 fuselage [from Stuart (1978)].

tests in the transonic wind tunnel proved that an area ruling concept (as shown in Fig. 9.29) could be used to essentially eliminate the pitch instabilities in the Mach 0.90 to 0.95 region. A cruise drag benefit also existed because of the improvement in wing-tip airflow characteristics. A slight instability which remained in the wind-tunnel data and was thought to be Reynolds number dependent was never found during the flight tests. The photograph of an F-5 (see Fig. 9.30) illustrates these applications of the area rule.

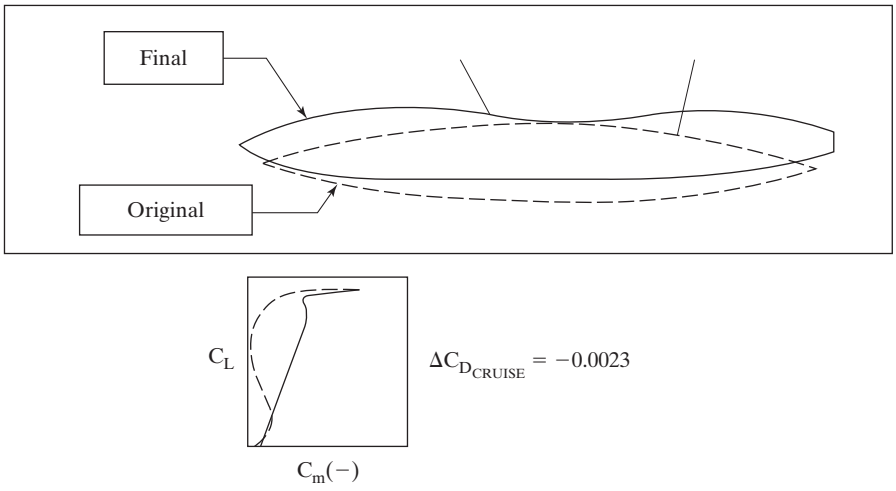

Figure 9.29 Application of area rule to the design of the tip tank for the F-5A/B aircraft [from Stuart (1978)].

By carefully designing the wing and the tail configurations, we can obtain a smooth variation of the cross-sectional area even without adjusting the fuselage cross section. Such is the case for the swept-wing cruise missile which is presented in Fig. 9.31. The cross-sectional area distribution for this configuration is relatively smooth and symmetric about the midbody station, as shown in Fig. 9.32. This result is due, in part, to the high sweep angles for the wing and for the tail. As might be expected, this shape is conducive to low transonic drag and the drag-divergence Mach number is relatively high (i.e., approximately 0.95). Furthermore, the configuration could be trimmed with zero control deflection near the lift coefficient required for the maximum lift-to-drag ratio at a Mach number of 0.95.

Figure 9.30 Illustration of the application of the area rule to the tip tanks of the F-5 (from the collection of John Bertin).

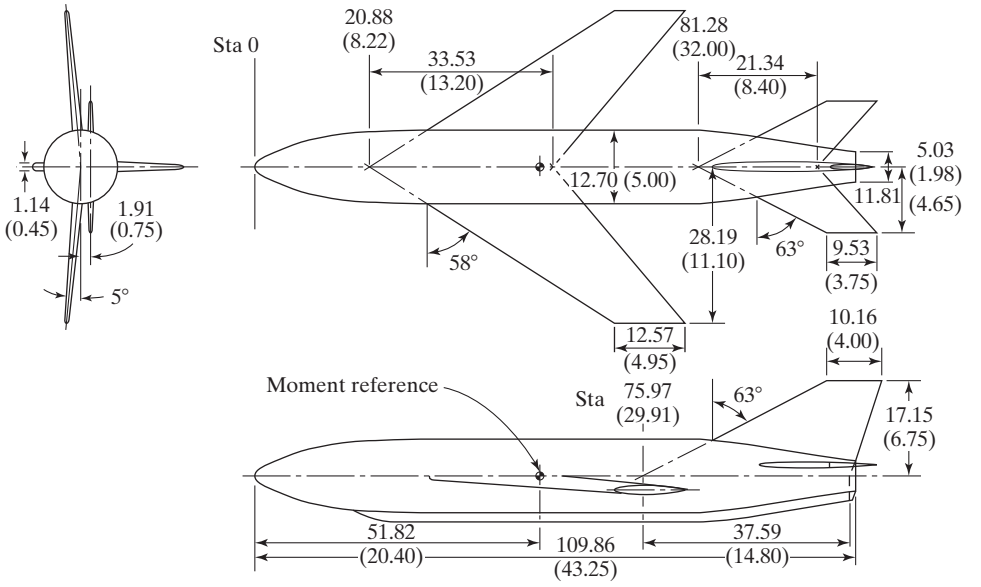

Figure 9.31 Details of a model of a swept-wing cruise missile. Linear dimensions are in centimeters (inches) [from Spearman and Collins (1972)].

9.4.2 Second-Order Area-Rule Considerations

Optimization of the wing/body/nacelle configuration plays a critical role in the design of business jets. Unlike previous business jets developed for cruising speeds near a Mach number of 0.7, new aircraft are designed to cruise at speeds at or above Mach 0.8. Added to the requirement of more speed is the desire for significant increases in range. To meet these requirements, the designs employ wings with more sweep and carefully designed cross sections that minimize the onset of the compressibility drag. Furthermore, these high-speed wings must be compatible with typical business jet configurations that have engines mounted on the fuselage near the wing trailing edge. As noted by Gallman et al. (1996), "These requirements create an aerodynamic design problem that benefits from modern computational fluid dynamics (CFD) and aerodynamic shape optimization. . . . Full potential analysis of the wing-body-nacelle configuration provided an accurate assessment of the influence of the fuselage mounted engines on wing pressures." Gallman et al. (1996) used codes similar to those discussed (briefly) in Chapter 14.

The area rule is essentially a linear-theory concept for zero lift. Whitcomb (1976) noted that, "to achieve the most satisfactory drag characteristics at lifting conditions the fuselage shape had to be modified from that defined by the simple application of the area rule as previously described to account for the nonlinearity of the flow at such conditions. For lifting conditions at near sonic speeds there is a substantial local region of supercritical flow above the wing surface which results in local expansions of the streamtube areas. In the basic considerations of the area rule concept, this expansion is equivalent to an increase in the physical thickness of the wing. To compensate for this

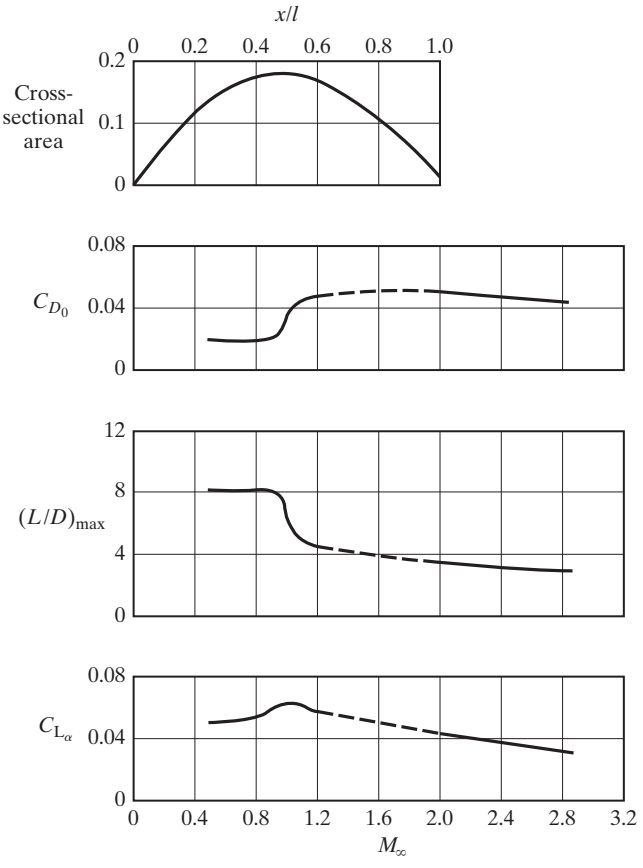

Figure 9.32 Area distribution and various aerodynamic parameters for a swept-wing cruise missile [from Spearman and Collins (1972)].

effect the fuselage indentation required to eliminate the far-field effects of the wing must be increased." The additional correction to the cross-sectional areas required for a transonic transport, as taken from Whitcomb (1976), is illustrated in Fig. 9.33. "The fuselage indentation based on this corrected cross-sectional area distribution resulted in a significant (0.02) delay in the drag rise Mach number compared with that for the indentation based on the zero lift distribution" [Whitcomb (1956)].

However, as noted by Ayers (1972), the fuselage cross-sectional area needed for storing landing gear and aircraft subsystems and for accommodating passenger seating and headroom, conflicts with the area-rule requirements in some cases.

Carlsen (1995) noted: "The sonic area rule is a far field method of predicting and understanding the wave drag due to shock losses. It is based on the idea of perfect pressure disturbance communication between the wing, or other external features, and the fuselage. It proposes that a body of revolution with the same axial development of cross-sectional area will have a wave drag that is similar to the original configuration."

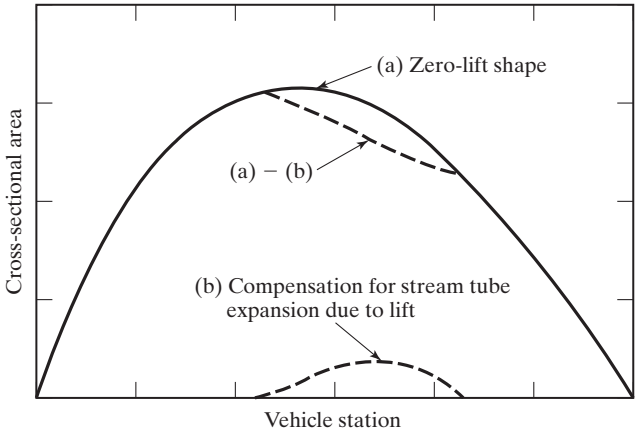

Figure 9.33 Second-order area rule considerations [from Whitcomb (1976)].

Carlsen (1995) noted that the communication between the flow on the wing and the flow on the fuselage changes in the transonic regime because of the mixed supersonic and subsonic flow: "In transonic flow, dissipation of disturbances occurs in the subsonic regions and the stream-tube areas are no longer invariant. As a result of this dissipation, it is erroneous to subtract the total wing volume from the fuselage. Part of the pressure changes created by the indentations in the fuselage is dissipated before it reaches the wing by passing through embedded subsonic regions. To account for the majority of this dissipation, the new transonic method applies a weighting function to the sonic area rule that modifies the volume removed from the fuselage. Only the volume that will relieve the flow on the wing should be removed. This minimizes the volume removed from the fuselage and still maintains the drag rise delay."

Carlsen (1995) recommended the use of weighting functions that would be applied "during the integration of the area of the wing that is intersected by a given Mach 1 plane. Area at the wingtip is given less value than the area near the wing root. The weighted wing area is then subtracted from the fuselage area that is intersected by this same Mach plane. The procedure is repeated at a series of locations along the fuselage axis, resulting in a net volume removal from the fuselage."

Carlsen (1995) concludes that the proposed use of a weighting function adjusts for the effects of mixed flows, that is the communication between the flow over the fuselage and that over its external parts that accounts for the dissipation due to embedded subsonic regions. The dissipating effect of the subsonic regions in the transonic regime significantly influences the approach to area ruling. Drag-rise delays that match the traditional sonic-area-rule can be obtained by modifying the aircraft to only 60% of what traditional sonic-area-rule prescribes.

9.4.3 Forward Swept Wing

The aerodynamic effects (e.g., increased critical Mach number, decreased lift curve slope, etc.) resulting from wing sweepback are also present for forward swept wings

(FSW) as well. However, there are some comparative advantages to a FSW in relation to an aft swept wing (ASW), which will be discussed in this section.

Historically, the use of FSW in aircraft designs was, with minor exceptions, precluded by the relatively low (in comparison with ASW) Mach numbers at which they experience aeroelastic flutter and divergence when they are constructed of conventional aircraft materials such as metals. The reasons for this will be discussed later, but, as an example, Diederich and Budiansky (1948) show that uniform FSWs with sweep angles from -20 to $-60°$ exhibit decreases as high as 78% in aeroelastic divergence dynamic pressures in comparison to straight wings. To eliminate this problem using conventional materials requires a prohibitive structural weight penalty. Until recently the FSW, along with some of its desirable characteristics, has been excluded from the aircraft designer's stable of design options. However, recent advances in the development of composite materials for aircraft structures have permitted the design and fabrication of aeroelastically tailored wings which substantially eliminate the divergence problem.

A swept wing constructed of conventional materials twists under load. An ASW twists down at the tips as the lift increases while the FSW twists up. In the former case, the tips tend to unload, while in the latter case they tend to load the structure further. Therefore, the FSW constructed of conventional materials has a much lower speed for structural divergence which occurs when the elastic restoring forces can no longer overcome the aerodynamic forces causing the deformation. The twisting behavior occurs because the axis of section centers of pressure along the span of an ASW is behind the structural axis of the wing in typical designs, while just the opposite is true for the FSW [Uhuad et al. (1983)]. The structural axis can be thought of as the locus of points along the wing where a load produces only wing bending with no twist.

The solution to this problem for the FSW is to design an aeroelastically tailored wing using composite materials arranged in unidirectional layers or plies which lie at selected angles relative to one another. By careful design and fabrication, the wing can be made to deform under loading so that the divergence problem just described can be delayed to a much higher Mach number. This permits the designer to capitalize on some of the advantages of FSWs compared to ASWs without paying an exorbitant weight penalty. Incidentally, aeroelastic tailoring is not limited to FSWs, but can be applied to straight and aft swept wings as well [Brown et al. (1980)].

The relative advantages of the FSW over the ASW are, of course, a function of the aircraft mission and fall into aerodynamic and other categories. Excellent overall discussions of these FSW characteristics are given in Whitford (1987) and in Krone (1980). We restrict our discussion here to aerodynamic advantages of the FSW. Key aerodynamic advantages of the FSW fall into two categories: reduced drag and enhanced maneuverability at transonic Mach numbers and high angles-of-attack.

Modern aircraft designs rely on wing sweep and supercritical airfoil sections to delay adverse compressibility effects and reduce their severity when they do occur. Good design practices force the shock on the upper surface of the wing to occur as close to the trailing edge as possible and to be as weak as possible (see Section 9.2). Typical shock locations for a supercritical wing occur in the vicinity of the 70% chord line along the span. As noted by Whitford (1987), this results in a more highly swept shock for an FSW compared to an ASW with the same leading-edge sweep angle, wing area, and taper ratio. The more highly swept shock, of course, results in a lower wave drag

penalty. Furthermore, for designs with the same shock sweep angle, the FSW requires less leading-edge sweep, which results in a higher lift-curve slope than the comparable ASW and a reduction in induced drag at subsonic conditions. And although the lower leading-edge sweep will result in higher wave drag at supersonic conditions, drag due to shock-induced separation has been found to be less. So, as we noticed earlier, careful attention to the aircraft mission will determine the design solution to be adopted in each case. Whitford (1987) also points out that an FSW with the same planform area, shock sweep, and span as an ASW has its aerodynamic center closer to the wing root and hence experiences a lower wing root bending moment. Conversely, an FSW can be designed with a higher aspect ratio than a comparable ASW and produce the same bending moment at the wing root. The higher aspect ratio in turn produces lower induced drag.

Flow over an ASW has a component along the span and toward the tips which results in a thicker boundary layer in the tip region than would otherwise exist. This, coupled with the more highly loaded tips of the ASW, can lead to tip stall, with the stall region moving inward toward the root as the stall progresses. This phenomenon can result in loss of aileron control effectiveness at high angles-of-attack with a consequent loss of maneuverability. An additional and undesirable offshoot of this phenomenon is an overall pitch-up tendency since the loss of lift typically occurs aft of the aircraft center of gravity. For the FSW the spanwise flow component is toward the wing root leading to root stall first. Therefore, aileron effectiveness is preserved up to higher angles-of-attack with a consequent improvement in maneuverability. However, the FSW with root stall still suffers the pitch-up tendency since the loss of lift is once again typically aft of the aircraft center of gravity.

To further investigate and validate these and other potential advantages of the FSW relative to the ASW, the Defense Advanced Research Projects Agency (DARPA), NASA, and the U.S. Air Force funded the design and fabrication of the X-29. This aircraft, produced by Grumman, was an experimental flight-test vehicle designed to explore a variety of advanced technologies, including FSW and close-coupled canards. The primary objective of the X-29 program is to give designers confidence in the FSW approach and to validate the advantages of FSW and other technologies for use in future aircraft designs [Putnam (1984)].

The X-29 configuration, illustrated in the three view sketches of Fig. 9.34, has several distinctive design features. These include a three-surface longitudinal control design, consisting of an all-movable close-coupled canard with large deflection capability, symmetric deflection of wing flaperons, and deflectable aft-fuselage strake flaps. Roll control is provided by differential flaperon deflection (or, equivalently, aileron deflection). A conventional rudder provides directional control. The X-29 has a long slender forebody, similar to the F-5 design, which produces strong vortical flow in the stall/poststall region.

Using data obtained in free-flight wind-tunnel tests at NASA Langley Research Center, Croom et al. (1988) studied the low-speed, high-angle-of-attack flight dynamics of the X-29 configuration. As noted by Croom et al. (1988), "The most dominant characteristic of the configuration is the extreme level of inherent static pitch instability (-0.35 static margin). Clearly, the basic airframe is unflyable without stability augmentation. However, the all-movable canard and strake flap control surfaces provide significant

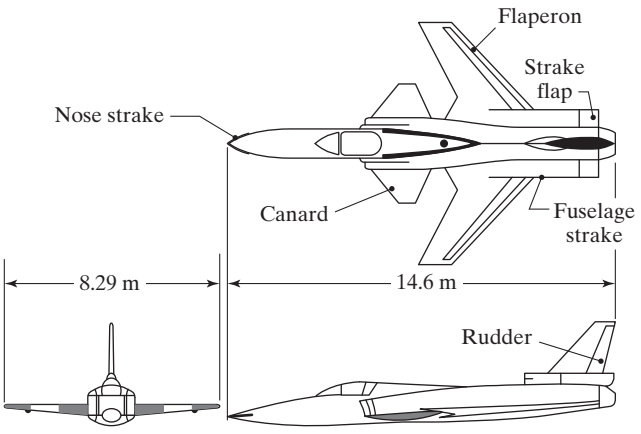

Figure 9.34 Three-view sketch of full-scale X-29 configuration.

control authority throughout the trim angle-of-attack range. . . . Moreover, the large control moments in conjunction with the relatively low pitch inertia, associated with the relatively lightweight design indicate the potential for a high level of pitch agility, which is very desirable for fighter aircraft."

A major benefit arising from the use of forward-swept wings at high angles of attack is the favorable progression of the stall pattern. Flow separation progresses from the wing-root region outboard, resulting in the retention of aileron control power beyond the stall angle of attack. Therefore, significant roll control moments persist to very high angles of attack, and lateral control should be comparatively good throughout the trim angle-of-attack range.

As noted by Croom et al. (1988), "The data show good levels of static directional stability below 20-deg. angle of attack. However, as the angle of attack is increased above 25-deg., the directional stability degrades significantly, resulting in unstable to neutrally stable values for trim canard incidences. The reduction in stability is due to the vertical tail becoming immersed in the low energy wake of the wing. However, at poststall angles of attack, the directional stability is re-established. Past studies have shown that under sideslip conditions, the flat elliptical cross-section forebody generates an asymmetric vortex system that produces a suction force on the windward side of the forebody resulting in yawing moments into the sideslip (i.e., stabilizing)."

9.5 TRANSONIC AIRCRAFT

Transonic aircraft are among the most common aircraft produced worldwide. These include commercial transports of all sizes (from regional jet liners to super-size aircraft like the Boeing 747 and Airbus A380). In addition, cargo aircraft such as the C-17, as well as business jets, fly at transonic speeds. Ayers (1972) notes that "wind-tunnel studies have indicated that combining the supercritical airfoil, the area rule, and wing sweep can push the cruising speed of subsonic aircraft very near Mach 1.0."

The full potential equation, equation (9.4b), is currently the most common starting point for designing transonic wings and full configurations, even though the

Navier-Stokes equations are now solvable for this class of problem. The reason is that the full potential equation can be coupled with multi-disciplinary design optimization (MDO) methods to design the configuration in conjunction with other important design features, such as structures, flight performance, and engine integration.

$$\left(1-\frac{\Phi_x^2}{a^2}\right)\Phi_{xx}+\left(1-\frac{\Phi_y^2}{a^2}\right)\Phi_{yy}+\left(1-\frac{\Phi_z^2}{a^2}\right)\Phi_{zz} - 2\frac{\Phi_x\Phi_y}{a^2}\Phi_{xy}-2\frac{\Phi_y\Phi_z}{a^2}\Phi_{yz}-2\frac{\Phi_z\Phi_x}{a^2}\Phi_{zx}=0 \quad \textbf{(9.4b)}$$

Currently, computer programs such as TranAir, jointly developed by NASA and Boeing, are routinely used to perform such complex designs using MDO methods, resulting in improved performance capabilities for modern aircraft flying at high subsonic Mach numbers.

Aerodynamics Concept Box: Full Aircraft Analysis Using Navier-Stokes Flow Solvers

While still relatively expensive, it is possible to perform full aircraft numerical simulations using Navier-Stokes solvers. Certainly aircraft manufacturers would not use this approach for large numbers of production runs (cruise condition design capability), but for important, specific cases (like the Boeing 777 high-lift geometry shown as a computational grid below) this approach can be quite valuable. The half-body grid below for the 777 from Rogers et al. (2001) shows the leading- and trailing-edge high-lift devices deployed, which occurs during take-off and landing of the aircraft. In spite of the fact that the free-stream velocities are relatively low, the gaps between the flaps and main wing elements can create compressibility effects, which is why Navier-Stokes simulations may be important for this viscous-dominated flow field.

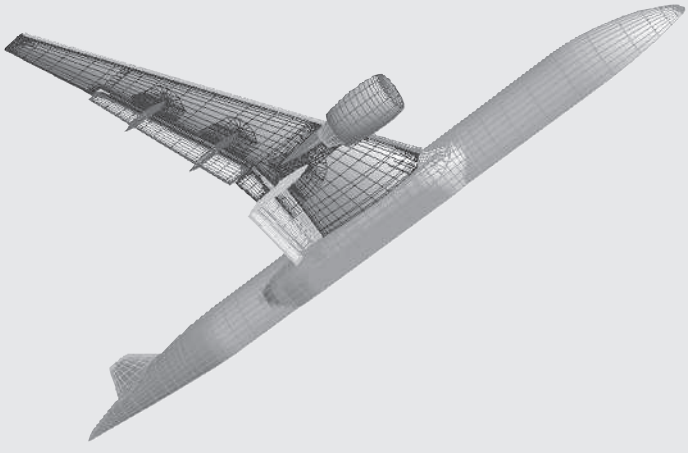

Computational grid for Boeing 777 aircraft from Rogers et al. (2001)

The figure below shows the region between the engine nacelle and fuselage, with the leading-edge flap extended. Notice the region of separated flow in the wing/fuselage junction region. Designing to minimize flow separation is an important job for an aerodynamicist.

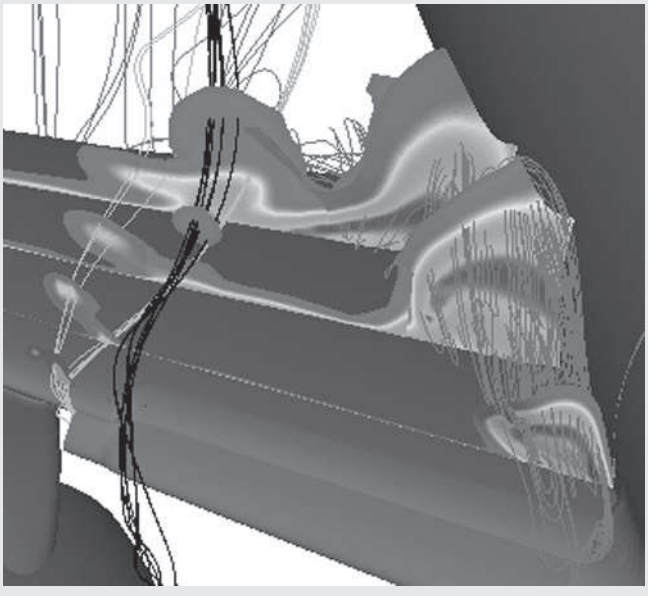

Mach number and particle traces at $\alpha = 16$ in vicinity of Krueger flap with addition of nacelle chine from Rogers et al. (2001)

Prior to using these highly complex MDO methods, however, designers had to use the more restrictive equations using the perturbation velocity potential. These restrictions were due to the computer speed and memory limitations of the time. These original solutions were often performed on a variety of transonic equations using newly developed computer-oriented numerical techniques, such as the transonic equation by Newman and Allison (1971):

$$(1 - M_\infty^2)\phi_{xx} + \phi_{yy} + \phi_{zz} = K\phi_x\,\phi_{xx} \tag{9.23}$$

Comparing equation (9.23) with equation (9.10), we find that, for the particular assumptions made during the development of equation (9.10),

$$K = \frac{2}{U_\infty}\left(1 + \frac{\gamma - 1}{2}M_\infty^2\right)M_\infty^2$$

In the transonic Mach number range, this term cannot be neglected as it was at lower speeds due to the highly non-linear nature of transonic flow.

One of the problems with solving the transonic small disturbance velocity potential equations was the mixed nature of the partial differential equation. Notice that equations like equation (9.10) contain a term $(1 - M_\infty^2)$, which changes sign as the flow changes from subsonic to supersonic. This means that the equation changes type from elliptic to hyperbolic, and different numerical methods are required in order to

solve the equation depending on the local flow conditions, as discussed in Murman and Cole (1971).

Bailey and Ballhaus (1975) used a relaxation procedure to solve the transonic small-disturbance equation:

$$(1 - M_\infty^2)\phi_{xx} + \phi_{yy} + \phi_{zz} = \left(\frac{\gamma + 1}{2} M_\infty^n \phi_x^2\right)_x \tag{9.24}$$

The parameter n reflects the nonuniqueness of the equation and, quoting Bailey and Ballhaus (1975), "can be adjusted to better approximate the exact sonic pressure coefficient." A finite-difference equation is derived by applying the divergence theorem to the integral of equation (9.24) over an elemental, rectangular, computation volume (or cell). The boundary conditions for the wing include the Kutta condition, which requires that the pressure, which is proportional to ϕ_x, be continuous at the trailing edge. This fixes the section circulation, which is equal to the difference in potential at the section trailing edge linearly extrapolated from points above and below. The solution of the difference equation is obtained by a relaxation scheme with the iterations viewed as steps in pseudo-time. The combination of new and old values in the difference operators is chosen so that the related time-dependent equation represents a properly posed problem whose steady-state solution approaches that of the steady-state equation. The calculated and the experimental pressure distributions for a swept-wing/fuselage configuration at $M_\infty = 0.93$ and $\alpha = 0°$ are compared in Fig. 9.35. The wing has an aspect ratio of 4 and a taper ratio of 0.6. The quarter chord of the wing is swept 45° and the streamwise airfoil section is a NACA 65A006. The computed results were obtained using a Cartesian grid (x, y, z) of $91 \times 59 \times 27$ for the wing as well as for the fuselage. The experimental data were obtained at $\mathrm{Re}_c = 2.0 \times 10^6$. As we saw earlier in this chapter, the maximum velocity is reached farther aft for the stations near the root and moves toward the leading edge at stations nearer the tip. The agreement with experiment on the fuselage centerline and the two inboard panels is good. In the computed results, the wing-root shock propagates laterally to $2y/b = 0.60$, but the experimental shock dissipates before reaching that point. Thus, there is a discrepancy between the experimental values and the theoretical predictions. This deficiency results for wings with moderate-to-large sweep angles. Ballhaus et al. (1976) note that a modified small-disturbance equation, containing cross-flow terms which have been previously neglected, would be a suitable approximation to the full potential equation over a wide range of sweep angles. Thus, a small-disturbance differential equation which could be used to describe the resultant three-dimensional flow is

$$\begin{aligned}(1 - M_\infty^2)\phi_{xx} + \phi_{yy} + \phi_{zz} - (\gamma + 1)M_\infty^n \phi_x \phi_{xx} \\ = 2M_\infty^2 \phi_y \phi_{xy} + (\gamma - 1)M_\infty^2 \phi_x \phi_{yy} + \frac{\gamma + 1}{2} M_\infty^2 \phi_x^2 \phi_{xx}\end{aligned} \tag{9.25}$$

Note that the terms on the left-hand side of this equation are those of equation (9.24) and those on the right-hand side are the additional terms of the modified small-disturbance formulation. Boppe (1978) notes that the cross-flow terms, $\phi_y \phi_{xy}$ and $\phi_x \phi_{yy}$, provide the ability to define shock waves which are swept considerably relative to the free-stream flow. Boppe recommends that the higher-order term, $\phi_x^2 \phi_{xx}$, be included to provide an improved approximation to the full potential equation at the

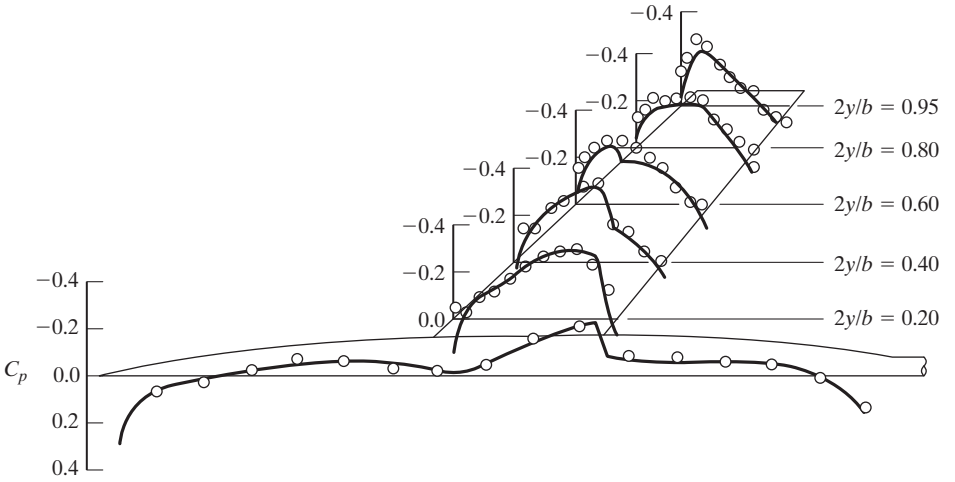

Figure 9.35 Comparison of computed and experimental pressure coefficients C_p for swept-wing/fuselage configuration, $M_\infty = 0.93$; $\alpha = 0°, \Lambda_{c/4} = 45°, \text{AR} = 4, \lambda = 0.6,$ NACA 65A006 streamwise section [from Bailey and Ballhaus (1975)].

critical velocity. Ballhaus et al. (1976) note that the use of an improved form of the governing equation alone does not guarantee that the shock waves will be properly represented. The finite-difference scheme must also adequately describe the physics of the problem.

Flow-field solutions for complex airplane configurations flying at transonic speeds can be computed using numerical programs that solve the Euler or Navier-Stokes equations. The Euler and Navier-Stokes equations for three-dimensional flows are presented in Appendix A. An example of a complex configuration with control surface deflections is shown in Fig. 9.36 [from Morton et al. (2011)]. Notice that both the all-moving

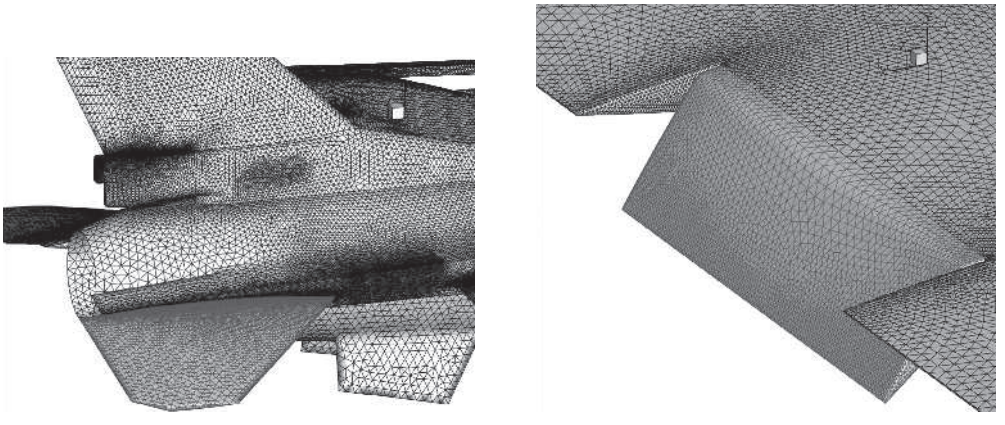

Figure 9.36 Examples of all-moving (left) and continuous-surface (right) control surface deflection meshes for simulation of the F-16 using a Navier-Stokes flow solver [Morton et al. (2011)].

horizontal tail and the flap deflection require specialized grid generation concepts, making the creation of a viscous grid a very challenging part of performing computational simulations. Miranda (1984) notes that the problem of grid generation is a crucial one for the practical application of numerical flow simulation. Both methods of solution, singularity and field, require the construction of complex computational grids: mesh-surface grids for singularity methods and spatial grids for field methods.

9.6 SUMMARY

Transonic flows are inherently nonlinear and highly three dimensional for wing-body combinations. The nonlinear inviscid flow and the resultant shock waves present a considerable challenge to the analyst. Strong shock-wave/boundary-layer interactions cause rapid increases in drag and can lead to buffeting. Shock-induced boundary-layer separation can also limit the lift coefficient. However, experimental investigations have provided considerable insights into desirable design practices for transonic configurations. Furthermore, three-dimensional transonic flow computational techniques have been developed and greatly impact transonic aircraft design.

PROBLEMS

9.1. Derive the expression for stagnation pressure for steady, one-dimensional, Isentropic flow of a perfect gas.

9.2. A rectangular wing having an aspect ratio of 4.0 is flying at $M_\infty = 0.90$ at 12 km. A NACA 0006 airfoil section is used at all spanwise stations. What is the airfoil section and the aspect ratio for the equivalent wing in an incompressible flow?

9.3. When discussing Whitcomb's area rule, it was noted that, for lifting conditions, there is a substantial local region of supercritical flow above the wing surface which results in local expansions of the streamtube areas. Consider flow past a two-dimensional airfoil in a stream where $M_\infty = 0.90$ Calculate the distance between two streamlines, dy_e at a point where the local inviscid Mach number, M_e, is 1.50 in terms of the distance between these two streamlines in the undisturbed flow, dy_∞, Use the integral form of the continuity equation [equation (2.5)],

$$dy_e = \frac{\rho_\infty U_\infty}{\rho_e U_e} dy_\infty$$

Assume an isentropic expansion of a perfect gas.

REFERENCES

Ayers TG. 1972. Supercritical aerodynamics: worthwhile over a range of speeds. *Astronaut. Aeronaut.* 10(8):32–36

Bailey FR, Ballhaus WF. 1975. Comparisons of computed and experimental pressures for transonic flows about isolated wings and wing-fuselage configurations. *NASA Spec. Pub. 347*

Ballhaus WF, Bailey FR, Frick J. 1976. Improved computational treatment of transonic flow about swept wings. *NASA Conf. Proc. 2001*

Boppe CW. 1978. *Computational transonic flow about realistic aircraft configurations*. Presented at AIAA Aerosp. Sci. Meet., 16th, AIAA Pap. 78–104, Huntsville, AL

Bradley RG. 1982. Practical aerodynamic problems—military aircraft. In *Transonic Aerodynamics*. Ed Nixon D, Washington, DC: AIAA

Brown LE, Price MA, Gringrich PB. 1980. *Aeroelastically tailored wing design*. Presented at The Evolution of Wing Design Symp., AIAA Pap. 80–3046, Dayton, OH

Bushnell DM. 2004. Shock wave drag reduction. *Annu. Rev. Fluid Mech*. 36:81–96

Carlsen WD. 1995. Development of transonic area-rule methodology. *J. Aircraft* 32:1056–1061

Croom MA, Whipple RD, Murri DG, Grafton SB, Fratello DJ. 1988. *High-alpha flight dynamics research on the X-29 configuration using dynamic model test techniques*. Proceedings of the Aerosp. Tech. Conf., SAE Pap. 881420, Anaheim, CA

Diederich FW, Budiansky B. 1948. Divergence of swept wings. *NACA Tech. Note 1680*

Farren WS. 1956. The aerodynamic art. *J. Roy. Aero. Soc.* 60:431–449

Forsythe JR, Blake DC. 2000. Private Transmittal

Forsythe JR, Strang WZ, Hoffmann KA. 2000. *Validation of several Reynolds averaged turbulence models in a 3-D unstructured grid code*. Presented at AIAA Fluids 2000 Conf., AIAA Pap. 2000–2552, Denver, CO

Foss RL, Blay R. 1987. From propellers to jets in fighter aircraft design. *Lockheed Horizons* 23:2–17

Gallman JW, Reuther JJ, Pfeiffer NJ, Forrest WC, Bernstorf DJ. 1996. *Business jet wing design using aerodynamic shape optimization*. Presented at AIAA Aerosp. Sci. Meet., 34th, AIAA Pap. 96–0554, Reno, NV

Goodmanson LT, Gratzer LB. 1973. Recent advances in aerodynamics for transport aircraft. *Aeronaut. Astronaut.* 11(12):30–45

Harris CD. 1981. Two-dimensional aerodynamic characteristics of the NACA 0012 airfoil in the Langley 8-foot transonic pressure tunnel. *NASA Tech. Mem. 81927*

Heffley RK, Jewell WF. 1972. Aircraft handling qualities data. *NASA CR-2144*

Hillaker H. 1994. Private Conversation

Holder DW. 1964. The transonic flow past two-dimensional aerofoils. *J. Roy. Aero. Soc.* 68:501–516

Hurley FX, Spaid FW, Roos FW, Stivers LS, Bandettini A. 1975. Detailed transonic flow field measurements about a supercritical airfoil section. *NASA Tech. Mem. X-3244*

Jones RT, Cohen D. 1960. *High Speed Wing Theory*. Princeton, NJ: Princeton University Press

Krone NJ. 1980. *Forward swept wing design*. Presented at The Evolution of Wing Design Symp., AIAA Pap. 80–3047, Dayton, OH

Küchemann D. 1957. Methods of reducing the transonic drag of swept-back wings at zero lift. *J. Roy. Aero. Soc.* 61:37–42

Laitone EV. 1951. New compressibility correction for two-dimensional subsonic flow. *J. Aeronaut. Sci.* 18(5):350

Lees L. 1946. A discussion of the application of the Prandtl-Glauert method to subsonic compressible flow over a slender body of revolution. *NACA TN-1127*

Liepmann HW. 1946. The interaction between boundary layer and shock waves in transonic flow. *J. Aeronaut. Sci*. 13(12):623–637

Miller R, Sawers D. 1970. *The Technical Development of Modern Aviation*. New York: Praeger Publishers

Miranda LR. 1984. Application of computational aerodynamics to airplane design. *J. Aircraft* 21:355–370

Morton SA, Eymann TA, McDaniel DR, Sear DR, Tillman B, Tuckey TR. 2011. Rigid and maneuvering results with control surface and 6DoF motion for Kestrel v2. Presented at AIAA Aersosp. Sci. Meet., 49th, AIAA Paper 2011–1106, Orlando, FL, Jan. 2011.

Murman EM, Cole JD. 1971. Calculation of plane steady transonic flow. *AIAA J*. 9(1): 114–121.

Newman PA, Allison DO. 1971. An annotated bibliography on transonic flow theory. *NASA Tech. Mem. X-2353*

Putnam TW. 1984. The X-29 flight research program. *AIAA Student J.* 22:2–12, 39

Rogers EWE, Hall IM. 1960. An introduction to the flow about plane swept-back wings at transonic speeds. *J. Roy. Aero. Soc.* 64:449–464

Rogers SE, Roth K, Cao HV, Slotnick JP, Whitlock M, Nash SM, Baker MD. 2001. Computation of viscous flow for a Boeing 777 aircraft in landing configuration. *J. Aircraft*. 38(6): 1060–1068

Schlichting H. 1960. Some developments in boundary layer research in the past thirty years. *J. Roy. Aero. Soc.* 64:64–79

Sheldon J. 1967. The flow produced by interaction of a turbulent boundary layer with a normal shock wave of strength sufficient to cause separation. *ARC R&M 3502*

Shevell RS. 1988. *Fundamentals of Flight*. 2nd Ed. Upper Saddle River, NJ: Prentice Hall

Shortal JA. 1978. A new dimension, Wallops Island flight test range: the first fifteen years. *NASA RP-1028*

Spalart PR, Allmaras SR. 1992. *A one-equation turbulence model for aerodynamic flows*. Presented at AIAA Aerosp. Sci, Meet., 30th, AIAA Pap. 92–0439, Reno, NV

Spearman ML, Collins IK. 1972. Aerodynamic characteristics of a swept-wing cruise missile at Mach numbers from 0.50 to 2.86. *NASA Tech. Note D-7069*

Stahl W, Mackrodt PA. 1965. Dreikomponentenmessungen bis zu grossen anstellwinkeln an fuenf tragfluegeln mit verschieden umrissformen in unterschall und ueberschallstroemung. *Z. Flugwissensch.* 13:447–453

Strang WZ, Tomaro RF, Grismer MJ. 1999. *The defining methods of Cobalt$_{60}$: a parallel, implicit, unstructured Euler/Navier-Stokes flow solver*. Presented at AIAA Aerosp. Sci. Meet., 37th, AIAA Pap. 99–0786, Reno, NV, Jan. 1999

Stuart WG. 1978. *Northrop F-5 Case Study in Aircraft Design*. Washington, DC: AIAA

Taylor JWR. (Ed) 1969. *Combat Aircraft of the World*. New York: G. P. Putnam Sons

Tsien HS. 1939. Two-dimensional subsonic flow of compressible fluids. *J. Aeronaut. Sci.* 6(10):399–407

Uhuad GC, Weeks TM, Large R. 1983. Wind tunnel investigation of the transonic aerodynamic characteristics of forward swept wings. *J. Aircraft* 20:195–202

von Karman T. 1941. Compressibility effects in aerodynamics. *J. Aeronaut. Sci.* 8(9): 337–356

Whitcomb RT. 1956. A study of the zero-lift drag-rise characteristics of wing-body combinations near the speed of sound. *NACA Rep. 1273*

Whitcomb RT. 1976. "Advanced Transonic Aerodynamic Technology," Presented in NASA CP 2001*, Adv. Eng. Sci. 4*, Nov. 1976

Whitcomb RT, Clark LR. 1965. An airfoil shape for efficient flight at supercritical Mach numbers. *NASA Tech. Mem. X-1109*

Whitford R. 1987. *Design for Air Combat*. London: Jane's Publishing

10 TWO-DIMENSIONAL, SUPERSONIC FLOWS AROUND THIN AIRFOILS

Chapter Objectives

- Understand why supersonic airfoils have low lift-to-drag ratios compared to subsonic airfoils
- Have a basic understanding of the flow around supersonic airfoils and the shock/expansion wave patterns that develop
- Be able to apply all three theories to the prediction of supersonic airfoils: linear theory, second-order theory, and shock-expansion theory
- Know the limitations and capabilities of all three supersonic airfoil theories

Now that we have discussed subsonic and transonic airfoil concepts, we will turn our attention to supersonic airfoils. We will find that supersonic airfoils behave very differently than subsonic airfoils, which has a significant impact on the design of high-speed aircraft.

The equations that describe inviscid supersonic flows around thin airfoils at low angles of attack will be developed in this chapter. The airfoil is assumed to extend to infinity in both directions from the plane of symmetry (i.e., it is a wing of infinite aspect ratio). Therefore, the flow field is the same for any cross-section perpendicular to the wing and the flow is two dimensional. However, even though the relations developed

in this chapter neglect the effects of viscosity, there will be a significant drag force on a two-dimensional airfoil in a supersonic stream. This drag component is known as *wave drag*, and we will see that wave drag can exist even without shock waves.

In Chapter 8, we derived the Prandtl-Meyer relations to describe the isentropic flow that results when a supersonic flow undergoes an expansive or a compressive change in direction which is sufficiently small that shock waves do not occur. In Example 8.3, the Prandtl-Meyer relations were used to calculate the aerodynamic coefficients for supersonic flow past a thin airfoil. When relatively large compressive changes in the flow direction occur, it is necessary to use the relations describing the non-isentropic flow through an oblique shock wave, as we will see, when the compressive changes in direction are only a few degrees, the pressure increase calculated using the Prandtl-Meyer relations is essentially equal to that calculated using the oblique shock-wave relations. Provided that the assumptions made in the derivations of these techniques are valid, they can be combined to solve for the two-dimensional flow about an airfoil if the shock wave at the leading edge is attached and planar. When the leading-edge shock wave is planar, the flow downstream of the shock wave(s) is isentropic. Therefore, the isentropic relations developed in Chapter 8 can be used to describe the subsequent acceleration of the flow around the airfoil.

Experience has shown that the leading edge and the trailing edge of supersonic airfoils should be sharp (or only slightly rounded) and relatively thin. If the leading edge is not sharp, the leading-edge shock wave will be detached and relatively strong, causing large wave drag. We will consider, therefore, profiles of the general cross section shown in Fig. 10.1. For these thin airfoils at relatively small angles of attack, we can apply the method of small perturbations to obtain theoretical approximations to the aerodynamic characteristics of the two-dimensional airfoils. By "thin" airfoil, we mean that the thickness, camber, and angle of attack of the section are such that the local flow direction at the airfoil surface deviates only slightly from the free-stream direction.

As we proceed through our study of supersonic airfoils, we will first look at the Ackeret, or linearized, theory for thin airfoils and then higher-order theories. The coefficients calculated using the linearized and higher-order theories will be compared with the values calculated using the techniques of Chapter 8.

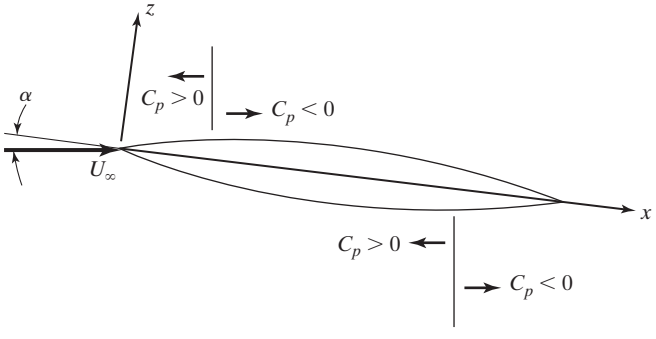

Figure 10.1 General features for linearized supersonic flow past a thin airfoil.

10.1 LINEAR THEORY

The basic assumption of linear theory is that pressure waves generated by thin sections are sufficiently weak that they can be treated as Mach waves. Under this assumption, the flow is isentropic everywhere. The pressure and velocity changes for a small expansive change in flow direction (an acceleration) have already been derived in Chapter 8 [i.e., equation (8.57)]. We will define the free-stream flow direction to be given by $\theta_\infty = 0$. For small changes in θ, we can use Euler's equation and equation (8.55) to calculate the change in pressure:

$$p - p_\infty = -\rho_\infty U_\infty (U - U_\infty) \tag{10.1a}$$

$$\frac{U_\infty - U}{U_\infty} = \frac{\theta}{\sqrt{M_\infty^2 - 1}} \tag{10.1b}$$

We will define the angle θ so that we obtain the correct sign for the pressure coefficient both for left-running characteristics and for right-running characteristics. Combining these relations yields

$$C_p = \frac{p - p_\infty}{\frac{1}{2}\rho_\infty U_\infty^2} = \frac{2\theta}{\sqrt{M_\infty^2 - 1}} \tag{10.1c}$$

which can be used to calculate the pressure on the airfoil surface, since θ is known at every point on the airfoil surface.

A positive pressure coefficient is associated with a compressive change in flow direction relative to the free-stream flow. If the flow is turned toward the upstream Mach waves, the local pressure coefficient is positive (compression) and is greatest where the local inclination is greatest. So, for the double-convex-arc airfoil section shown in Fig. 10.1, the pressure is greatest at the leading edge, being greater on the lower surface when the airfoil is at a positive angle of attack. Flow accelerates continuously from the leading edge to the trailing edge for both the lower surface and the upper surface. The pressure coefficient is zero (i.e., the local static pressure is equal to the free-stream value) at those points where the local surface is parallel to the free stream. Downstream, the pressure coefficient is negative, which corresponds to an expansive change in flow direction.

The pressure coefficients calculated using the linearized approximation and Busemann's second-order approximation (to be discussed in the next section) are compared in Fig. 10.2 with the exact values of Prandtl-Meyer theory for expansive turns and of oblique shock-wave theory for compressive turns. For small deflections, linear theory provides values suitable for engineering calculations.

Since the slope of the surface of the airfoil section measured with respect to the free-stream direction is small, we can set it equal to its tangent. Referring to Fig. 10.3, we can write

$$\theta_u = \frac{dz_u}{dx} - \alpha \tag{10.2a}$$

$$\theta_l = -\frac{dz_l}{dx} + \alpha \tag{10.2b}$$

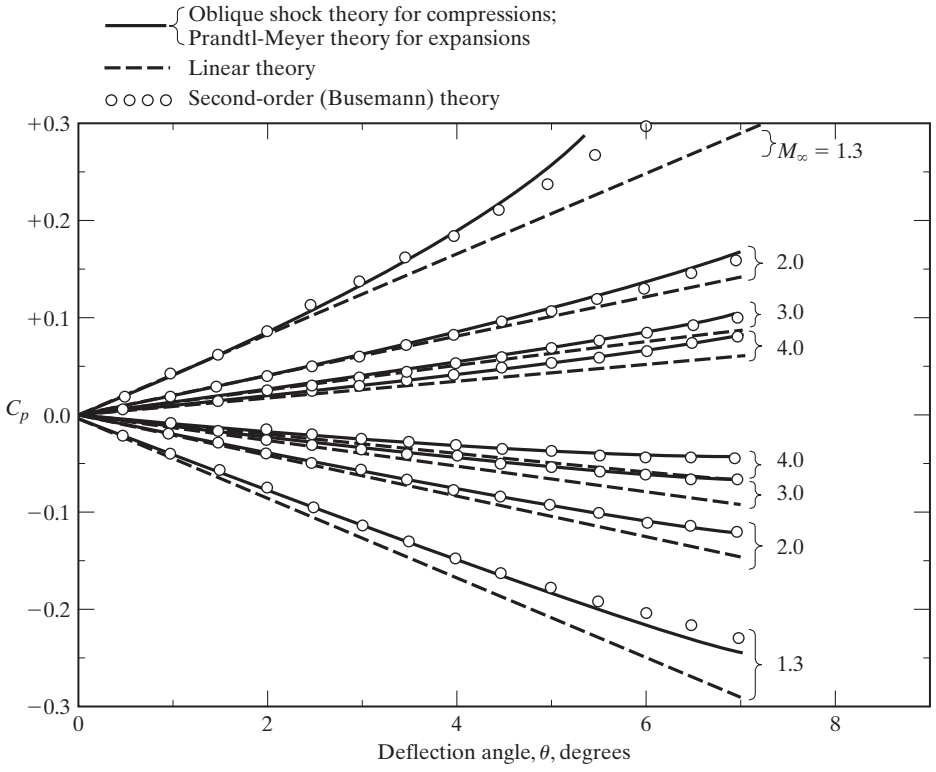

Figure 10.2 Theoretical pressure coefficients as a function of the deflection angle (relative to the stream) for various two-dimensional theories.

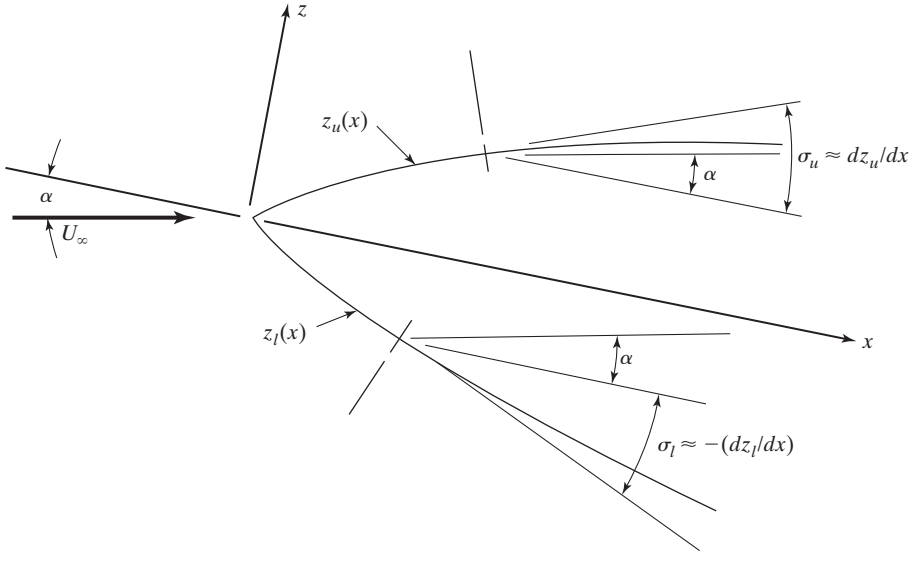

Figure 10.3 Detailed sketch of an airfoil section.

The lift, the drag, and the moment coefficients for the section can now be determined using equations (10.1c) and (10.2).

10.1.1 Lift

Referring to Fig. 10.4, we see that the incremental lift force (per unit span) acting on the chordwise segment $ABCD$ of the airfoil section is

$$dl = p_l\, ds_l \cos\theta_l - p_u\, ds_u \cos\theta_u \tag{10.3}$$

Employing the usual thin-airfoil assumptions (small angles and $ds \approx dx$), equation (10.3) can be written as

$$dl \approx (p_l - p_u)dx \tag{10.4}$$

In coefficient form, we have

$$dC_l \approx (C_{pl} - C_{pu})d\left(\frac{x}{c}\right) \tag{10.5}$$

Using equations (10.1c) and (10.2), equation (10.5) becomes

$$dC_l = \frac{2}{\sqrt{M_\infty^2 - 1}}\left(2\alpha - \frac{dz_l}{dx} - \frac{dz_u}{dx}\right)d\left(\frac{x}{c}\right) \tag{10.6}$$

where, without loss of generality, we have assumed that positive values both for θ_u and θ_l represent compressive changes in the flow direction from the free-stream flow.

We can calculate the total lift of the section by integrating equation (10.6) from $x/c = 0$ to $x/c = 1$. Notice that since $z_u = z_l = 0$ at both the leading edge and the trailing edges, the lower surface integral becomes:

$$\int_0^1 \frac{dz_l}{dx} d\left(\frac{x}{c}\right) = 0 \tag{10.7a}$$

and the upper surface integral is:

$$\int_0^1 \frac{dz_u}{dx} d\left(\frac{x}{c}\right) = 0 \tag{10.7b}$$

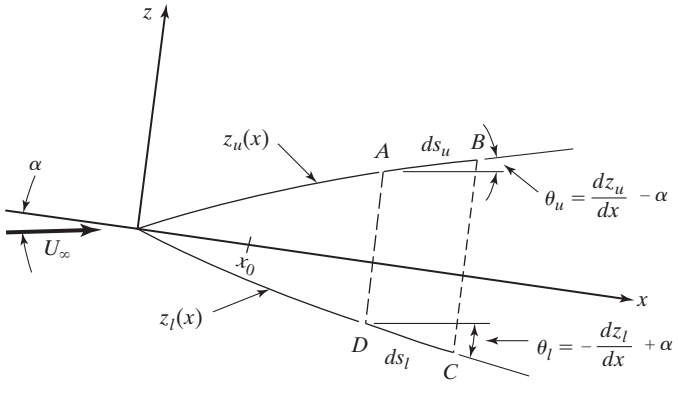

Figure 10.4 Thin-airfoil geometry for determining C_l, C_d, and $C_{m_{x0}}$.

Therefore,

$$C_l = \frac{4\alpha}{\sqrt{M_\infty^2 - 1}} \tag{10.8}$$

We see that, in the linear approximation for supersonic flow past a thin airfoil, the lift coefficient is independent of the camber and of the thickness distribution. Furthermore, the angle of attack for zero lift is zero. The lift-curve slope is seen to be only a function of the free-stream Mach number, since

$$\frac{dC_l}{d\alpha} = \frac{4}{\sqrt{M_\infty^2 - 1}} \tag{10.9}$$

Examining equation (10.9), we see that for $M_\infty \gtrsim 1.185$, the lift-curve slope is less than the theoretical value for incompressible flow past a thin airfoil, which is 2π per radian. These results are in stark contrast to what we learned about subsonic airfoils, where camber and thickness were important for the creation of lift.

10.1.2 Drag

The incremental drag force due to the inviscid flow acting on the arbitrary chordwise element $ABCD$ of Fig. 10.4 is

$$dd = p_l\, ds_l \sin\theta_l + p_u\, ds_u \sin\theta_u \tag{10.10}$$

Again, using the assumptions common to small deflection angles, equation (10.10) becomes

$$dd = p_l\, \theta_l\, dx + p_u\, \theta_u\, dx \tag{10.11}$$

In coefficient form, we obtain:

$$dC_d = (C_{pl}\, \theta_l + C_{pu}\, \theta_u) d\left(\frac{x}{c}\right) + \frac{2}{\gamma M_\infty^2}(\theta_l + \theta_u) d\left(\frac{x}{c}\right) \tag{10.12}$$

Using equation (10.1c) for compressive turns and equation (10.2) to approximate the angles, equation (10.12) yields

$$dC_d = \frac{2}{\sqrt{M_\infty^2 - 1}}\left[2\alpha^2 + \left(\frac{dz_u}{dx}\right)^2 + \left(\frac{dz_l}{dx}\right)^2\right] d\left(\frac{x}{c}\right) + \left[\frac{-4\alpha}{\sqrt{M_\infty^2 - 1}}\left(\frac{dz_l}{dx} + \frac{dz_u}{dx}\right) + \frac{2}{\gamma M_\infty^2}\left(\frac{dz_u}{dx} - \frac{dz_l}{dx}\right)\right] d\left(\frac{x}{c}\right) \tag{10.13}$$

Using equation (10.7), we find that the integration of equation (10.13) yields

$$C_d = \frac{4\alpha^2}{\sqrt{M_\infty^2 - 1}} + \frac{2}{\sqrt{M_\infty^2 - 1}} \int_0^1 \left[\left(\frac{dz_u}{dx}\right)^2 + \left(\frac{dz_l}{dx}\right)^2\right] d\left(\frac{x}{c}\right) \tag{10.14}$$

Note that for the small-angle assumptions commonly used in analyzing flow past a thin airfoil,

$$\frac{dz_u}{dx} = \tan\sigma_u \approx \sigma_u$$

Therefore,

$$\frac{1}{c}\int_0^c \left(\frac{dz_u}{dx}\right)^2 dx = \overline{\sigma_u^2} \tag{10.15a}$$

Similarly, we can write

$$\frac{1}{c}\int_0^c \left(\frac{dz_l}{dx}\right)^2 dx = \overline{\sigma_l^2} \tag{10.15b}$$

We can use these relations to replace the integrals of equation (10.14) by the average values that they represent. So, the section-drag coefficient for this frictionless flow model is

$$C_d = \frac{d}{q_\infty c} = \frac{4\alpha^2}{\sqrt{M_\infty^2 - 1}} + \frac{2}{\sqrt{M_\infty^2 - 1}}\left(\overline{\sigma_u^2} + \overline{\sigma_l^2}\right) \tag{10.16}$$

You should notice that the drag is not zero even though the airfoil has an infinite span and the viscous forces have been neglected. This drag component, which is not present in subsonic flows, is known as *wave drag*. Also notice that, as this small perturbation solution shows, it is not necessary that shock waves be present for wave drag to exist. Such was also the case in Example 8.3, which examined the shock-free flow past an infinitesimally thin, parabolic arc airfoil. Finally, the drag of the airfoil is a function of all angle changes, whether they are due to angle of attack, camber, or thickness. Comparing equation (10.16) with equation (10.8) shows that supersonic airfoils create lift with angle of attack alone, but create drag due to angle of attack, camber, and thickness (within the limitations of linear theory). Therefore, for aerodynamic efficiency to be maximized, camber and thickness should be minimized for supersonic airfoils.

We should now examine the nature of the terms in equation (10.16). Since the lift is directly proportional to the angle of attack and is independent of the section thickness, the first term is called the *wave drag due to lift* or the *induced wave drag* and is independent of the shape of the airfoil section. The second term is often referred to as the *wave drag due to thickness* and depends only on the shape of the section. Equation (10.16) also indicates that, for a given configuration, the wave-drag coefficient decreases with increasing Mach number. If we were to account for the effects of viscosity, we could write:

$$C_d = C_{d,\,\text{due to lift}} + C_{d,\,\text{thickness}} + C_{d,\,\text{friction}} \tag{10.17a}$$

where

$$C_{d,\,\text{due to lift}} = \frac{4\alpha^2}{\sqrt{M_\infty^2 - 1}} = \alpha C_l \tag{10.17b}$$

and

$$C_{d,\,\text{thickness}} = \frac{2}{\sqrt{M_\infty^2 - 1}}\left(\overline{\sigma_u^2} + \overline{\sigma_l^2}\right) \tag{10.17c}$$

You should also notice that $C_{d,\,\text{thickness}}$ is the C_{d_0} of previous chapters.

10.1.3 Pitch Moment

We will now use linear theory to obtain an expression for the pitch moment coefficient. Referring to Fig. 10.4, the incremental moment (taken as positive for nose up relative to the free stream) about the arbitrary point x_0 on the chord is

$$dm_{x0} = (p_u - p_l)(x - x_0)dx \tag{10.18}$$

where we have incorporated the same small-angle assumptions and have neglected the contributions of the chordwise components of p_u and p_l to the pitch moment.

In coefficient form, we have

$$dC_{m_{x0}} = (C_{pu} - C_{pl})\frac{x - x_0}{c}d\left(\frac{x}{c}\right) \tag{10.19}$$

Substituting equation (10.1c) into equation (10.19), we obtain:

$$dC_{m_{x0}} = \frac{2}{\sqrt{M_\infty^2 - 1}}(\theta_u - \theta_l)\frac{x - x_0}{c}d\left(\frac{x}{c}\right) \tag{10.20}$$

Substituting equation (10.2) into equation (10.20) and integrating along the chord gives

$$C_{m_{x0}} = \frac{-4\alpha}{\sqrt{M_\infty^2 - 1}}\left(\frac{1}{2} - \frac{x_0}{c}\right) + \frac{2}{\sqrt{M_\infty^2 - 1}}\int_0^1 \left(\frac{dz_u}{dx} + \frac{dz_l}{dx}\right)\frac{x - x_0}{c}d\left(\frac{x}{c}\right) \tag{10.21}$$

Note that the average of the upper surface coordinate z_u and the lower surface coordinate z_l defines the mean camber coordinate z_c,

$$\tfrac{1}{2}(z_u + z_l) = z_c$$

We can then write equation (10.21) as:

$$C_{m_{x0}} = \frac{-4\alpha}{\sqrt{M_\infty^2 - 1}}\left(\frac{1}{2} - \frac{x_0}{c}\right) + \frac{4}{\sqrt{M_\infty^2 - 1}}\int_0^1 \frac{dz_c}{dx}\frac{x - x_0}{c}d\left(\frac{x}{c}\right) \tag{10.22}$$

where we have assumed that $z_u = z_l$ both at the leading edge and at the trailing edge.

As discussed in Section 5.4.2, the aerodynamic center is that point about which the pitch moment coefficient is independent of the angle of attack. It may also be considered to be that point along the chord at which all changes in lift effectively take place. Therefore, equation (10.22) shows that the aerodynamic center is at the midchord for a thin airfoil in a supersonic flow. This is in contrast to the thin airfoil in an incompressible flow where the aerodynamic center is at the quarter chord. To summarize, camber and thickness may be helpful to tune C_{m_0} of the airfoil, even though earlier we saw that camber and thickness do not contribute to lift, but do increase the drag. The overall result is that camber and thickness should be used minimally for supersonic airfoils.

EXAMPLE 10.1: Use linear theory to calculate the lift coefficient, the wave-drag coefficient, and the pitch moment coefficient

We will now use linear theory to calculate the lift coefficient, wave-drag coefficient, and pitch moment coefficient for the airfoil section whose geometry

is illustrated in Fig 10.5. For purposes of discussion, the flow field has been divided into numbered regions, which correspond to each of the facets of the double-wedge airfoil, as shown. In each region, the flow properties are such that the static pressure and the Mach number are constant, although they differ from region to region. We seek the lift coefficient, the drag coefficient, and the pitch moment coefficient per unit span of the airfoil given the free-stream flow conditions, the angle of attack, and the geometry of the airfoil neglecting the effect of the viscous boundary layer. The only forces acting on the airfoil are the pressure forces. Therefore, once we have determined the static pressure in each region, we can then integrate to find the resultant forces and moments.

Solution: We can now evaluate the various geometric parameters required for the linearized theory:

$$z_u(x) = \begin{cases} x \tan 10^\circ & \text{for } 0 \le x \le \frac{c}{2} \\ (c - x) \tan 10^\circ & \text{for } \frac{c}{2} \le x \le c \end{cases}$$

$$z_l(x) = \begin{cases} -x \tan 10^\circ & \text{for } 0 \le x \le \frac{c}{2} \\ -(c - x) \tan 10^\circ & \text{for } \frac{c}{2} \le x \le c \end{cases}$$

Furthermore,

$$\overline{\sigma_l^2} = \int_0^1 \sigma_l^2 \, d\left(\frac{x}{c}\right) = \delta_w^2$$

and

$$\overline{\sigma_u^2} = \int_0^1 \sigma_u^2 \, d\left(\frac{x}{c}\right) = \delta_w^2$$

We can use equation (10.8) to calculate the section lift coefficient for a 10° angle of attack at $M_\infty = 2.0$:

$$C_l = \frac{4(10\pi/180)}{\sqrt{2^2 - 1}} = 0.4031$$

Similarly, the drag coefficient can be calculated using equation (10.16):

$$C_d = \frac{4(10\pi/180)^2}{\sqrt{2^2 - 1}} + \frac{2}{\sqrt{2^2 - 1}}\left[\left(\frac{10}{57.296}\right)^2 + \left(\frac{10}{57.296}\right)^2\right]$$

Therefore,

$$C_d = 0.1407$$

The lift/drag ratio is

$$\frac{l}{d} = \frac{C_l}{C_d} = \frac{0.4031}{0.1407} = 2.865$$

Notice that in order to clearly illustrate the calculation procedures, this airfoil section is much thicker (i.e., $t = 0.176c$) than typical supersonic airfoil sections for which $t \approx 0.05c$ (see Table 5.1). The result is a relatively low lift/drag ratio.

Similarly, equation (10.22) for the pitch moment coefficient gives

$$C_{m_{x0}} = \frac{-4\alpha}{\sqrt{M_\infty^2 - 1}} \left(\frac{1}{2} - \frac{x_0}{c} \right)$$

since the mean-camber coordinate x_c is everywhere zero. At the midchord, we have

$$C_{m_{c/2}} = 0$$

This is not a surprising result, since equation (10.22) indicates that the moment about the aerodynamic center of a symmetric (zero camber) thin airfoil in supersonic flow vanishes.

Aerodynamics Concept Box: The F-104 Airfoil

The F-104 was a supersonic interceptor designed in the late 1950s and flown beginning in the 1960s by a number of countries. The wing had an aspect ratio of 2.45 and an airfoil which was only 3.34% thick. The airfoil section was a modified bi-convex (bi-convex upper surface and essentially flat lower surface) with sharp leading and trailing edges.

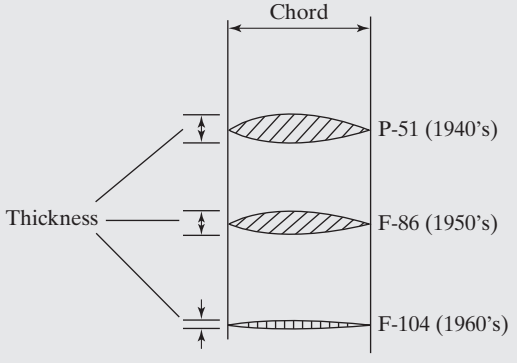

(a) Changes in airfoil sections.

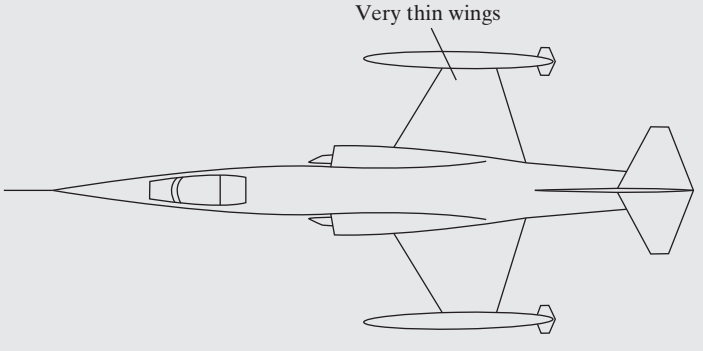

(b) F-104G airplane.

F-104 airfoil and wing geometry from Talay (1975)

Most supersonic airplanes have airfoil sections which are a compromise between subsonic and supersonic characteristics, since the airplanes have to fly in both speed regimes. In the case of the F-104, the designers used an airfoil which had good supersonic capabilities, but rather poor subsonic characteristics (since the design objectives required Mach 2.0 flight). This meant the F-104 required large blown flaps for landing, in addition to a drag chute. In spite of this, the approach speed of the airplane was nearly 200 knots, and the landing distance was quite large. Fighters designed in the 1970s (like the F-16 or F-15) used subsonic airfoil sections (although they were quite thin) to give improved subsonic characteristics, at the cost of supersonic performance.

10.2 SECOND-ORDER THEORY (BUSEMANN'S THEORY)

Equation (10.1c) can actually be viewed as the first term in a Taylor series expansion of Δp in powers of θ. Busemann and Walchner (1933) showed that a more accurate expression for the pressure change resulted if the θ^2 term were retained in the expansion. His result [given in Edmondson et al. (1945)] in terms of the pressure coefficient is

$$C_p = \frac{2\theta}{\sqrt{M_\infty^2 - 1}} + \left[\frac{(\gamma + 1)M_\infty^4 - 4M_\infty^2 + 4}{2(M_\infty^2 - 1)^2}\right]\theta^2 \qquad \textbf{(10.23a)}$$

or

$$C_p = C_1\,\theta + C_2\,\theta^2 \qquad \textbf{(10.23b)}$$

Again, θ is positive for a compression turn and negative for an expansion turn. We note that the θ^2 term in equation (10.23) is always a positive contribution (in other words, the second-order theory will always predict a higher pressure than linear theory). Table 10.1 gives C_1 and C_2 for various Mach numbers in air.

It is important to note that since the pressure waves are treated as Mach waves, the turning angles must be small. These assumptions imply that the flow is isentropic everywhere. Therefore, equations (10.5), (10.12), and (10.19), along with equation (10.23), can still be used to find C_l, C_d, and $C_{m_{x0}}$. Figure 10.2 shows that Busemann's theory agrees even more closely with the results obtained from oblique shock and Prandtl-Meyer expansion theory than does linear theory, for a relatively minor amount of additional effort.

EXAMPLE 10.2: Use Busemann's theory to calculate the lift coefficient, the wave-drag coefficient, and the pitch moment coefficient

We will calculate the pressure coefficient on each panel of the airfoil in Example 10.1 using Busemann's theory, equation (10.23).

Solution: Since panel 1 is parallel to the free stream, $C_{p1} = 0$ as before. For panel 2,

$$\begin{aligned} C_{p2} &= \frac{2(-20\pi/180)}{\sqrt{2^2 - 1}} + \frac{(1.4 + 1)(2)^4 - 4(2)^2 + 4}{2(2^2 - 1)^2}\left(\frac{20\pi}{180}\right)^2 \\ &= -0.4031 + 0.1787 \\ &= -0.2244 \end{aligned}$$

As noted, the airfoil in this sample problem is relatively thick, and therefore the turning angles are quite large. As a result, the differences between linear

TABLE 10.1 Coefficients C_1 and C_2 for the Busemann Theory for Perfect Air, $\gamma = 1.4$

M_∞	C_1	C_2
1.10	4.364	30.316
1.12	3.965	21.313
1.14	3.654	15.904
1.16	3.402	12.404
1.18	3.193	10.013
1.20	3.015	8.307
1.22	2.862	7.050
1.24	2.728	6.096
1.26	2.609	5.356
1.28	2.503	4.771
1.30	2.408	4.300
1.32	2.321	3.916
1.34	2.242	3.599
1.36	2.170	3.333
1.38	2.103	3.109
1.40	2.041	2.919
1.42	1.984	2.755
1.44	1.930	2.614
1.46	1.880	2.491
1.48	1.833	2.383
1.50	1.789	2.288
1.52	1.747	2.204
1.54	1.708	2.129
1.56	1.670	2.063
1.58	1.635	2.003
1.60	1.601	1.949
1.70	1.455	1.748
1.80	1.336	1.618
1.90	1.238	1.529
2.00	1.155	1.467
2.50	0.873	1.320
3.00	0.707	1.269
3.50	0.596	1.248
4.00	0.516	1.232
5.00	0.408	1.219
10.0	0.201	1.204
∞	0	1.200

theory and higher-order approximations are significant but not unexpected. For panel 3,

$$C_{p3} = 0.4031 + 0.1787$$
$$= 0.5818$$

For panel 4,

$$C_{p4} = 0$$

since the flow along surface 4 is parallel to the free stream.

Having determined the pressures acting on the individual facets of the double-wedge airfoil, we can now determine the section lift coefficient:

$$C_l = \frac{\sum p \cos\theta (\frac{c}{2}\cos\delta_w)}{(\gamma/2)p_\infty M_\infty^2 c} \tag{10.24a}$$

where δ_w is the half-angle of the double-wedge configuration. We can use the fact that the net force in any direction due to a constant pressure acting on a closed surface is zero to obtain:

$$C_l = \frac{1}{2\cos\delta_w}\Sigma C_p \cos\theta \tag{10.24b}$$

where the signs assigned to the C_p terms account for the direction of the force. So,

$$\begin{aligned} C_l &= \frac{1}{2\cos 10^\circ}(-C_{p2}\cos 20^\circ + C_{p3}\cos 20^\circ) \\ &= 0.3846 \end{aligned}$$

Similarly, we can calculate the section wave-drag coefficient:

$$C_d = \frac{\Sigma p \sin\theta (0.5c/\cos\delta_w)}{(\gamma/2)p_\infty M_\infty^2 c} \tag{10.25a}$$

or

$$C_d = \frac{1}{2\cos\delta_w}\Sigma C_p \sin\theta \tag{10.25b}$$

Applying this relation to the airfoil section of Fig 10.5, the section wave-drag coefficient for $\alpha = 10^\circ$ is

$$\begin{aligned} C_d &= \frac{1}{2\cos 10^\circ}(C_{p3}\sin 20^\circ - C_{p2}\sin 20^\circ) \\ &= 0.1400 \end{aligned}$$

We can now calculate the moment coefficient with respect to the midchord of the airfoil section (i.e., relative to $x = 0.5c$). As we have seen, the theoretical solutions for linearized flow show that the midchord point is the aerodynamic center for a thin airfoil in a supersonic flow. Since the pressure is constant on each of the facets of the double-wedge airfoil of Fig. 10.5 (i.e., in each numbered region), the force acting on a given facet will be normal to the surface and will act at the midpoint of the panel. So,

$$\begin{aligned} C_{m_{c/2}} = \frac{m_{c/2}}{\frac{1}{2}\rho_\infty U_\infty^2 c^2} &= (-p_1 + p_2 + p_3 - p_4)\frac{c^2/8}{\frac{1}{2}\rho_\infty U_\infty^2 c^2} \\ &\quad + (p_1 - p_2 - p_3 + p_4)\frac{(c^2/8)\tan^2\delta_w}{\frac{1}{2}\rho_\infty U_\infty^2 c^2} \end{aligned} \tag{10.26}$$

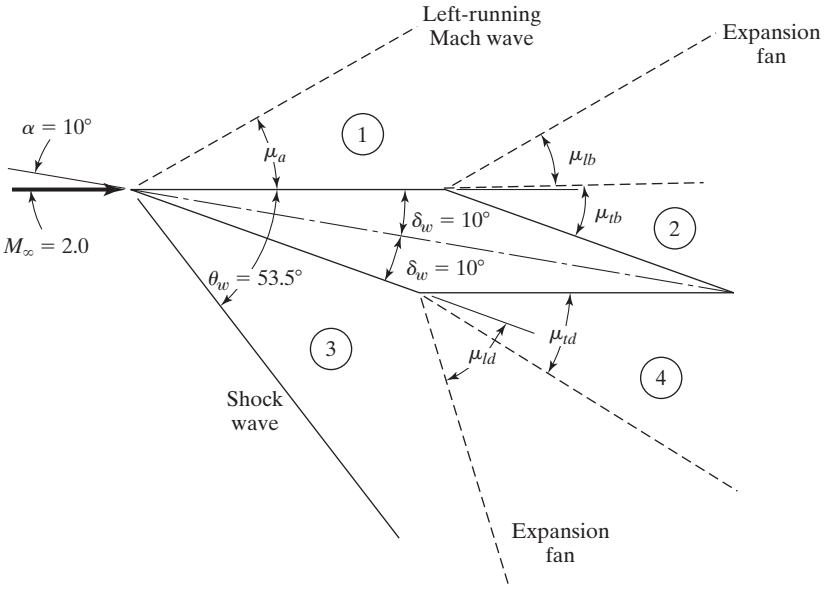

Figure 10.5 Wave pattern for a double-wedge airfoil in a Mach 2 stream.

Recall that a nose-up pitch moment is considered positive. Also notice that we have accounted for terms proportional to $\tan^2 \delta_w$. Since the pitch moment due to a uniform pressure acting on any closed surface is zero, equation (10.26) can be written as

$$C_{m_{c/2}} = (-C_{p1} + C_{p2} + C_{p3} - C_{p4})\frac{1}{8} + (C_{p1} - C_{p2} - C_{p3} + C_{p4})\frac{\tan^2 \delta_w}{8} \qquad \textbf{(10.27)}$$

You are referred to equations (5.11) through (5.15) for a review of the technique. Finally we obtain,

$$C_{m_{c/2}} = 0.04329$$

Notice that in this case the aerodynamic center is not at the midchord, but is only a small distance away.

Aerodynamics Concept Box: Busemann's Supersonic "Biplane" Airfoil System

In the 1930s, Adolf Busemann proposed using two supersonic airfoils adjacent to each other to take advantage of shock wave reflection properties and produce a "biplane" which would

minimize wave drag [Busemann (1935), shown below]. If the airfoil were designed with the proper airfoil and distance between the sections, for a given free stream Mach number, Busemann showed that the wave drag could be eliminated. This unique result is based on the concept of shock wave reflection and cancellation, which we discussed in Chapter 8. Specifically, figure (a) below shows a typical shock wave reflection from a straight wall. Busemann realized that if the wall changed direction at a point of intersection, as shown in figure (b), the shock wave and expansion wave would cancel each other out. Liepmann and Roshko (1957) described it this way: "Part of the expansion wave at the shoulder cancels the compression wave from the leading edge of the opposite plane and produces the symmetrical pressure distribution shown in the figure. The wave drag is zero." However, when the biplane flies at an off-design Mach number, as shown in figure (c), some of the benefits are lost.

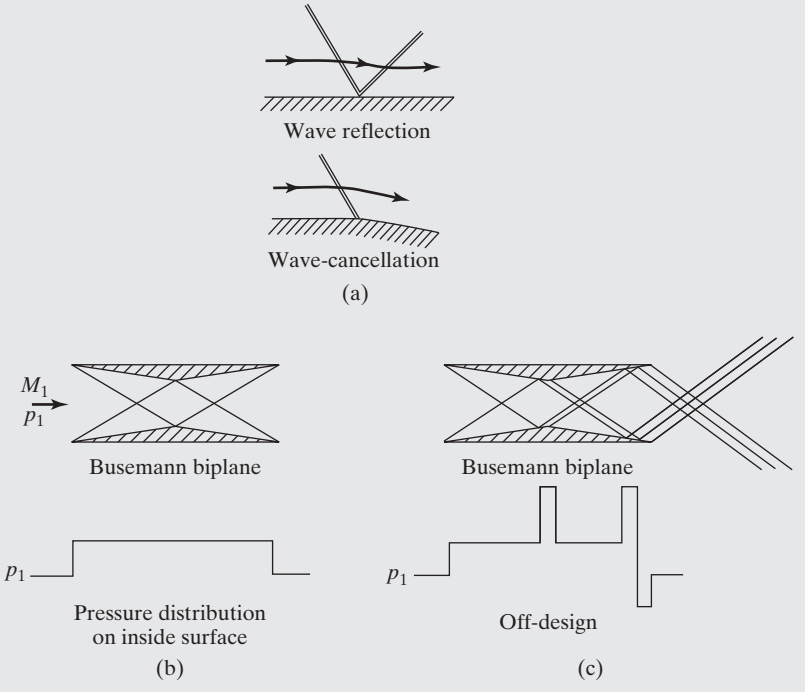

Busemann biplane concept from Liepmann and Roshko (1957).

This concept primarily was only an interesting idea in text books over the years, but has found a renewal of interest recently. With the improved ability of CFD simulations, Kusunose et al. (2011) performed a numerical study of the concept and applied it to a generic supersonic airplane. The predictions showed that the pressure coefficient on the inside of the biplane wing is constant, something that Busemann had noticed. This configuration achieved airplane lift-to-drag ratios of over 20 at very low angles of attack, a very good result for a supersonic aircraft.

10.3 SHOCK-EXPANSION TECHNIQUE

The techniques discussed so far assume that compressive changes in the flow direction are sufficiently small that the inviscid flow is completely isentropic. In reality, a shock wave is formed as the supersonic flow encounters the two-dimensional double-wedge airfoil of the previous example problems. Since the shock wave is attached to the leading edge and is planar, the downstream flow is isentropic (in other words, the flow is isentropic everywhere except across the shock). Therefore, the oblique shock wave and isentropic Prandtl-Meyer relations developed in Chapter 8 can be used to describe the flow around the airfoil. We will use this "shock-expansion" technique, first described by Ackeret (1925), to calculate the flow field around the airfoil shown in Fig. 10.5.

EXAMPLE 10.3 Use the shock-expansion theory to calculate the lift coefficient, the wave-drag coefficient, and the pitch moment coefficient.

For purposes of discussion, the flow field has been divided into numbered regions that correspond to each of the facets of the double-wedge airfoil, as shown in Fig. 10.5. As was true for the approximate theories, the flow properties in each region, such as the static pressure and the Mach number, are constant, although they differ from region to region. We will calculate the section lift coefficient, the section drag coefficient, and the section pitch moment coefficient for the inviscid flow, starting with the free-stream region and working downstream.

Solution: Since the surface of region 1 is parallel to the free stream, the flow does not turn in going from the free-stream conditions (∞) to region 1. Therefore, the properties in region 1 are the same as in the free stream. The pressure coefficient on the airfoil surface bounding region 1 is zero, and:

$$M_1 = 2.0 \quad \nu_1 = 26.380^\circ \quad \theta_1 = 0^\circ \quad C_{p1} = 0.0$$

Furthermore, since the flow is not decelerated in going to region 1, a Mach wave (and not a shock wave) is shown as generated at the leading edge of the upper surface. Since the Mach wave is of infinitesimal strength, it has no effect on the flow. However, for completeness, let us calculate the angle between the Mach wave and the free-stream direction. The Mach angle is:

$$\mu_a = \sin^{-1}\frac{1}{M_\infty} = 30^\circ$$

Since the surface of the airfoil in region 2 "turns away" from the flow in region 1, the flow accelerates isentropically in going from region 1 to region 2. To cross the left-running Mach waves dividing region 1 from region 2, we move along right-running characteristics. Therefore,

$$d\nu = -d\theta$$

Since the flow direction in region 2 is:

$$\theta_2 = -20°$$

the Prantdl-Meyer function in region 2, ν_2, is:

$$\nu_2 = \nu_1 - \Delta\theta = 46.380°$$

Therefore,

$$M_2 = 2.83$$

To calculate the pressure coefficient for region 2, we can use the relationship we developed for the pressure coefficient in Chapter 8:

$$C_{p2} = \frac{p_2 - p_\infty}{\frac{1}{2}\rho_\infty U_\infty^2} = \frac{p_2 - p_\infty}{\frac{\gamma}{2} p_\infty M_\infty^2} = \frac{2}{\gamma M_\infty^2}\left(\frac{p_2}{p_\infty} - 1\right)$$

Since the flow over the upper surface of the airfoil is isentropic,

$$p_{t\infty} = p_{t1} = p_{t2}$$

Therefore,

$$C_{p2} = \frac{2}{\gamma M_\infty^2}\left(\frac{p_2}{p_{t2}}\frac{p_t}{p_\infty} - 1\right)$$

Using Table 8.1, or equation (8.36), to calculate the pressure ratios given the values for M_∞ and for M_2, we find:

$$C_{p2} = \frac{2}{1.4(4)}\left(\frac{0.0352}{0.1278} - 1\right) = -0.2588$$

The fluid particles passing from the free stream to region 3 are turned by the shock wave through an angle of 20°. The shock wave decelerates the flow and the pressure in region 3 is relatively high. To calculate the pressure coefficient for region 3, we must determine the pressure increase across the shock wave. Since we know that $M_\infty = 2.0$ and $\theta = 20°$, we can use Fig. 8.12b to find the value of $C_{p3} = 0.66$. As an alternative procedure, we can use Fig. 8.12 to find the shock-wave angle, θ_w, which is equal to $\theta_w = 53.5°$. Therefore, as discussed in Section 8.5, we can use $M_\infty \sin\theta$ (instead of M_∞), which is 1.608, and the correlations of Table 8.3 to calculate the pressure increase across the oblique shock wave as:

$$\frac{p_3}{p_\infty} = 2.848$$

and the pressure coefficient in region 3 is:

$$C_{p3} = \frac{2}{1.4(4)}(2.848 - 1) = 0.66$$

Using Fig. 8.12c, we now can find that $M_3 = 1.20$.

Having determined the flow in region 3,

$$M_3 = 1.20 \quad \nu_3 = 3.558° \quad \theta_3 = -20°$$

we can determine the flow in region 4 using the Prandtl-Meyer relations. The flow crosses the right-running Mach waves dividing regions 3 and 4 on left-running characteristics, therefore:

$$d\nu = d\theta$$

Since $\theta_4 = 0°$, $d\theta = +20°$ and

$$\nu_4 = 23.558°$$

so

$$M_4 = 1.90$$

Notice that because of the dissipative effect of the shock wave, the Mach number in region 4 (whose surface is parallel to the free stream) is less than the free-stream Mach number.

Whereas the flow from region 3 to region 4 is isentropic, and

$$p_{t3} = p_{t4}$$

the presence of the shock wave causes

$$p_{t3} < p_{t\infty}$$

To calculate the pressure coefficient in region 4, we need to relate the flow properties back to the free-stream values as:

$$C_{p4} = \frac{2}{\gamma M_\infty^2}\left(\frac{p_4}{p_\infty} - 1\right) = \frac{2}{\gamma M_\infty^2}\left(\frac{p_4}{p_3}\frac{p_3}{p_\infty} - 1\right)$$

where the pressure ratio is:

$$\frac{p_4}{p_3} = \frac{p_4}{p_{t4}}\frac{p_{t3}}{p_3}$$

which can be determined since both M_3 and M_4 are known. The ratio p_3/p_∞ has already been found to be 2.848. Therefore,

$$C_{p4} = \frac{2}{1.4(4)}\left[\frac{0.1492}{0.4124}(2.848) - 1\right] = 0.0108$$

We can calculate the section lift coefficient using equation (10.24).

$$C_l = \frac{1}{2\cos 10°}(-C_{p1} - C_{p2}\cos 20° + C_{p3}\cos 20° + C_{p4})$$
$$= 0.4438$$

Similarly, using equation (10.25) to calculate the section wave-drag coefficient,

$$C_d = \frac{1}{2\cos 10^\circ}(C_{p3}\sin 20^\circ - C_{p2}\sin 20^\circ)$$
$$= 0.1595$$

The lift-to-drag ratio for the airfoil in our example is:

$$\frac{l}{d} = 2.782$$

which is quite small for an airfoil lift-to-drag ratio when compared with subsonic airfoils.

In some cases, it is of interest to locate the leading and trailing Mach waves of the Prandtl-Meyer expansion fans at b and d. Using the subscripts l and t to indicate leading and trailing Mach waves, respectively, we have

$$\mu_{lb} = \sin^{-1}\frac{1}{M_1} = 30^\circ$$

$$\mu_{tb} = \sin^{-1}\frac{1}{M_2} = 20.7^\circ$$

$$\mu_{ld} = \sin^{-1}\frac{1}{M_3} = 56.4^\circ$$

$$\mu_{td} = \sin^{-1}\frac{1}{M_4} = 31.8^\circ$$

Each Mach angle is shown in Fig. 10.5.

To calculate the pitch moment about the midchord point, we substitute the values we have found for the pressure coefficients into equation (10.27) and get:

$$C_{m_{c/2}} = 0.04728$$

Aerodynamics Concept Box: How Supersonic Airfoils Produce Lift Compared to Subsonic Airfoils

Look more closely at the results of Example 10.3. If we show the pressures acting on the four surfaces of the airfoil, we see something very interesting (the arrows on the figure below representing the pressure have been drawn to scale to clarify the concept). Lift is produced by having higher pressure on the bottom of an airfoil than the top, so we can see where the lift is

being produced from the figure below. Both surfaces 1 and 4 contribute very little to the lift of the airfoil (since their respective pressures are close to or at the free-stream level). Surface 2 has relatively low pressure, so some lift is being produced on the back half of the airfoil, but very little. The majority of the lift is being produced by the high pressure acting on the bottom surface of the front of the airfoil—the air compressed by the shock wave is pushing the airfoil up!

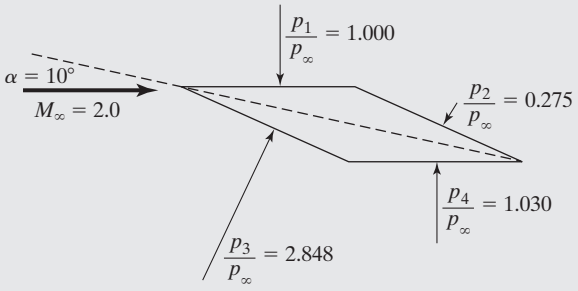

How is this different than how lift is produced on a subsonic airfoil? The pressure variation around a subsonic airfoil (e.g., the Eppler E64 airfoil at 2° angle of attack shown below) shows that lift is primarily generated from the upper surface, with the majority of that lift coming from the leading-edge region. This is because subsonic airfoils create lift by accelerating flow around the leading edge, which increases the velocity and decreases the pressure.

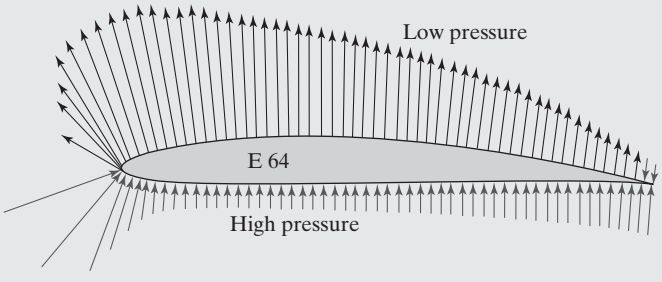

Eppler E64 airfoil pressure distribution (from Martin Hepperle)

This also explains why supersonic airfoils have such low lift-to-drag ratios (less than 10, compared to subsonic airfoils which are around 100). Not only do supersonic airfoils have more drag due to wave drag, they have much less lift due to the lift-producing mechanism we see here.

Example 10.3 illustrates how to calculate the aerodynamic coefficients using the *shock-expansion technique*. This approach is exact provided the relevant assumptions are satisfied. A disadvantage of the technique is that it is essentially a numerical method which does not give a closed-form solution for evaluating airfoil performance parameters, such as the section lift and drag coefficients. However, if the results obtained by the method were applied to a variety of airfoils, we would observe that the most efficient airfoil sections for supersonic flow are thin with little camber and sharp leading edges (you should look at Table 5.1 to see that these features are used on the high-speed aircraft). Otherwise, wave drag becomes prohibitive.

We have used a variety of techniques to calculate the inviscid flow field and the section aerodynamic coefficients for the double-wedge airfoil at an angle of attack of 10° in an airstream where $M_\infty = 2.0$. The various theoretical values are compared in Table 10.2. Although the airfoil section considered in these sample problems is much thicker than those actually used on supersonic airplanes, there is reasonable agreement between the aerodynamic coefficients calculated using the various techniques. Therefore, the errors in the local pressure coefficients tend to compensate for each other when the aerodynamic coefficients are calculated.

The theoretical values of the section aerodynamic coefficients as calculated using these three techniques are compared in Fig. 10.6 along with experimental values taken from Pope (1958). The airfoil is reasonably thin, and the theoretical values for the section lift coefficient and for the section wave-drag coefficient are in reasonable agreement with the data. The experimental values of the section moment coefficient exhibit the angle-of-attack dependence of the shock-expansion theory, but they differ in magnitude. Notice that, for the airfoil shown in Fig. 10.6, C_l is negative at zero angle of attack. This is markedly different from the subsonic result, where the section lift coefficient is positive for a cambered airfoil at zero angle of attack. This is another example illustrating that you should not apply intuitive ideas from subsonic flow to supersonic flows.

TABLE 10.2 Comparison of the Aerodynamic Parameters for the Two-Dimensional Airfoil Section of Fig. 10.5, $M_\infty = 2.0$, $\alpha = 10°$

	Linearized (Ackeret) Theory	*Second-order (Busemann) Theory*	*Shock-expansion Technique*
C_{p1}	0.0000	0.0000	0.0000
C_{p2}	−0.4031	−0.2244	−0.2588
C_{p3}	+0.4031	+0.5818	+0.660
C_{p4}	0.0000	0.0000	+0.0108
C_l	0.4031	0.3846	0.4438
C_d	0.1407	0.1400	0.1595
$C_{m_{0.5c}}$	0.0000	0.04329	0.04728

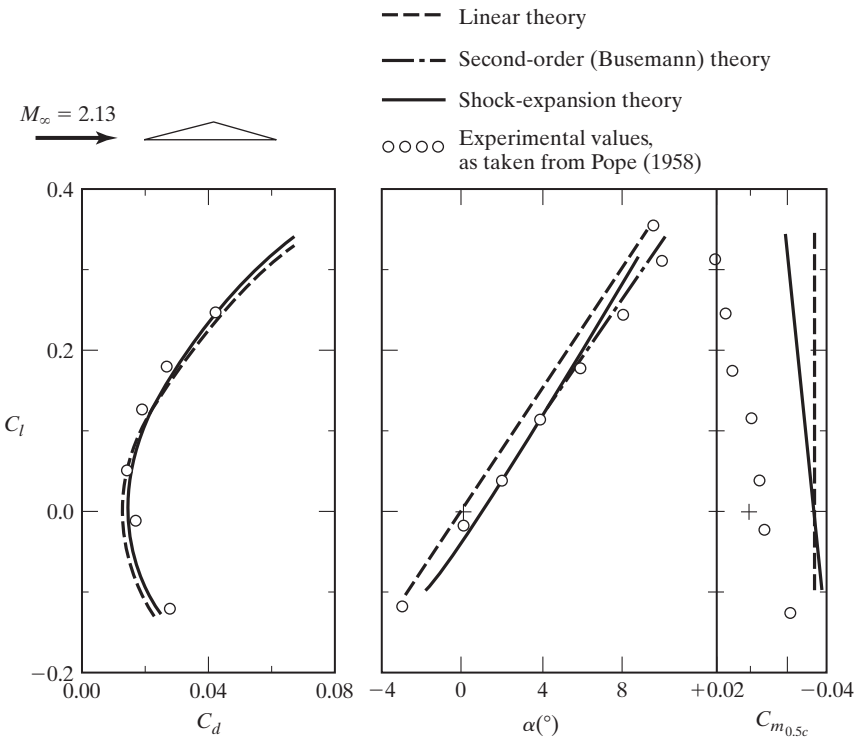

Figure 10.6 Comparison of the experimental and the theoretical values of C_l, C_d, and $C_{m_{0.5c}}$ for supersonic flow past an airfoil.

10.4 SUMMARY

Supersonic airfoils behave very differently than subsonic airfoils. Perhaps that is the most important thing to learn in this chapter. The shock and expansion waves that form around airfoils at supersonic speeds create drag and a pressure distribution that leads to airfoils with very low lift-to-drag ratios when compared with subsonic airfoils. While all of the prediction methods discussed in this chapter assume inviscid flow, the shock-expansion technique leads to the most dependable answers. However, linear theory and Busemann's second-order theory can give quite good answers within the limits of their assumptions, and typically take much less time than the shock-expansion technique. Analyzing supersonic airfoils shows the unusual pressure distribution caused by the shocks and expansion waves, and gives the aerodynamicist a large challenge when designing aircraft that fly at both subsonic and supersonic speeds.

PROBLEMS

10.1. Consider supersonic flow past the thin airfoil shown in Fig. P10.1. The airfoil is symmetric about the chord line. Use linearized theory to develop expressions for the lift coefficient, the drag coefficient, and the pitching-moment coefficient about the midchord. The resultant expressions should include the free-stream Mach number, the constants a_1 and a_2, and

the thickness ratio $t/c(\equiv\tau)$. Show that, for a fixed thickness ratio, the wave drag due to thickness is a minimum when $a_1 = a_2 = 0.4$.

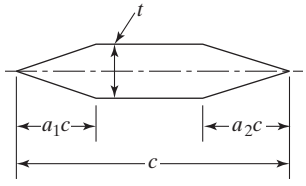

Figure P10.1

10.2. Consider the infinitesimally thin airfoil which has the shape of a parabola:

$$x^2 = -\frac{c^2}{z_{\max}}(z - z_{\max})$$

The leading edge of the profile is tangent to the direction of the oncoming airstream. This is the airfoil of Example 8.3. Use linearized theory for the following:

(a) Find the expressions for the lift coefficient, the drag coefficient, the lift/drag ratio, and the pitching-moment coefficient about the leading edge. The resultant expressions should include the free-stream Mach number and the parameter, $z_{\max}/c$.

(b) Graph the pressure coefficient distribution as a function of x/c for the upper surface and for the lower surface. The calculations are for $M_\infty = 2.059$ and $z_{\max} = 0.1c$. Compare the pressure distributions for linearized theory with those of Example 8.3.

(c) Compare the lift coefficient and the drag coefficient calculated using linearized theory for $M_\infty = 2.059$ and for $z_{\max} = 0.1c$ with those calculated in Example 8.3.

10.3. Consider the double-wedge profile airfoil shown in Fig. P10.3. If the thickness ratio is 0.08 and the free-stream Mach number is 3.0 at an altitude of 22 km, use linearized theory to compute the lift coefficient, the drag coefficient, the lift/drag ratio, and the moment coefficient about the leading edge. Make these calculations for angles of attack of 3.2° and 5.6°.

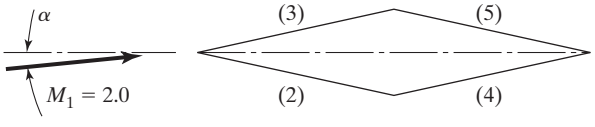

Figure P10.3

10.4. Repeat Problem 10.3 using second-order (Busemann) theory.

10.5. Repeat Problem 10.3 using the shock-expansion technique. What is the maximum angle of attack at which this airfoil can be placed and still generate a weak shock wave?

10.6. Calculate the lift coefficient, the drag coefficient, and the coefficient for the moment about the leading edge for the airfoil of Problem 10.3 and for the same angles of attack, if the flow were incompressible subsonic.

10.7. Verify the theoretical correlations presented in Fig. 10.6. Note that for this airfoil section,

$$\tau = \frac{t}{c} = 0.063$$

Furthermore, the free-stream Mach number is 2.13.

10.8. For linearized theory, it was shown [i.e., equation (10.17c)] that the section drag coefficient due to thickness is

$$C_{d,\,\text{thickness}} = \frac{2}{\sqrt{M_1^2 - 1}}(\overline{\sigma_u^2} + \overline{\sigma_l^2})$$

If τ is the thickness ratio, show that

$$C_{d,\,\text{thickness}} = \frac{4\tau^2}{\sqrt{M_1^2 - 1}}$$

for a symmetric, double-wedge airfoil section and that

$$C_{d,\,\text{thickness}} = \frac{5.33\tau^2}{\sqrt{M_1^2 - 1}}$$

for a biconvex airfoil section. In doing this problem, we are verifying the values for K_1 given in Table 11.1.

10.9. Consider the symmetric, diamond-shaped airfoil section (Fig. P10.9; as shown in the sketch, all four facets have the same value of δ_w) exposed to a Mach 2.20 stream in a wind tunnel. For the wind tunnel, $p_{t1} = 125$ psia and $T_t = 600\,°\text{R}$. The airfoil is such that the maximum thickness t equals to 0.07c. The angle of attack is 6°.

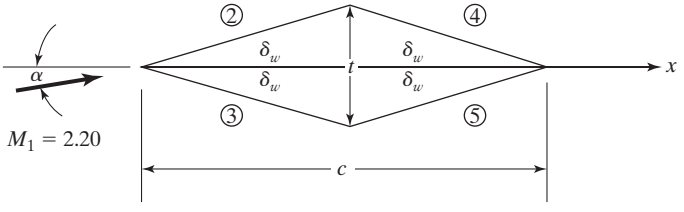

Figure P10.9

(a) Using the shock-wave relations where applicable and the isentropic expansion relations (Prandtl-Meyer) where applicable, calculate the pressures in regions 2 through 5.
(b) Using the linear-theory relations, calculate the pressures in regions 2 through 5.
(c) Calculate C_A, C_N, C_d, and $C_{m_{0.5c}}$ for this configuration. C_A is the axial force coefficient for the force along the axis (i.e., parallel to the chordline of the airfoil) and C_N is normal force coefficient (i.e., normal to the chordline of the airfoil).

10.10. Consider the "cambered," diamond-shaped airfoil exposed to a Mach 2.00 stream in a wind tunnel (Fig. P10.10). For the wind tunnel, $p_{t1} = 125$ psia and $T_t = 650\,°\text{R}$. The airfoil is such that $\delta_2 = 8°$, $\delta_3 = 2°$; the maximum thickness t equals to $0.07c$ and is located at $x = 0.40c$. The angle of attack is 10°.

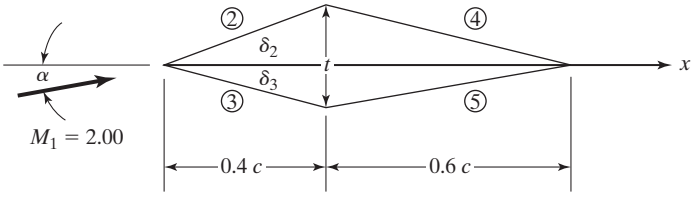

Figure P10.10

(a) Using the shock-wave relations where applicable and the isentropic expansion relations (Prandtl-Meyer) where applicable, calculate the pressures in regions 2 through 5.
(b) Using the linear-theory relations, calculate the pressures in regions 2 through 5.
(c) Calculate C_A, C_N, C_l, C_d, and $C_{m_{0.5c}}$ for this configuration. C_A is the axial force coefficient for the force along the axis (i.e., parallel to the chordline of the airfoil) and C_N is the normal force coefficient (i.e., normal to the chordline of the airfoil).

10.11. Consider the two-dimensional airfoil having a section which is a biconvex profile, that is,

$$R(x) = 2t\frac{x}{L}\left(1 - \frac{x}{L}\right)$$

The model is placed in a supersonic wind tunnel, where the free-stream Mach number in the tunnel test section is 2.2; $p_{t_1} = 125$ lbf/in^2 and $T_t = 600$°R. The airfoil is such that the maximum thickness (t) equals $0.07L$ and it occurs at the mid-chord. The angle of attack is 6°.

Using the shock/Prandtl-Meyer expansion technique to model the flowfield for the biconvex airfoil section, calculate the pressure distributions both for the windward (bottom) and for the leeward (top) sides. Present the results in a single graph that compares the pressure distribution for the windward side with that for the leeward side.

10.12. Consider the two-dimensional airfoil having a section which is a biconvex profile, that is,

$$R(x) = 2t\frac{x}{L}\left(1 - \frac{x}{L}\right)$$

The model is placed in a supersonic wind tunnel, where the free-stream Mach number in the tunnel test section is 2.2; $p_{t_1} = 125$ lbf/in^2 and $T_t = 600$°R. The airfoil is such that the maximum thickness (t) equals $0.07L$ and it occurs at the mid chord. The angle of attack is 6°.

Using the linearized theory relations to model the flowfield for the biconvex airfoil section, calculate the pressure distributions both for the windward (bottom) and for the leeward (top) sides. Present the results in a single graph that compares the pressure distribution for the windward side with that for the leeward side.

10.13. Consider the two-dimensional airfoil having a section which is a biconvex profile, that is,

$$R(x) = 2t\frac{x}{L}\left(1 - \frac{x}{L}\right)$$

The model is placed in a supersonic wind tunnel, where the free-stream Mach number in the tunnel test section is 2.2; $p_{t_1} = 125$ lbf/in^2 and $T_t = 600$°R. The airfoil is such that the maximum thickness (t) equals $0.07L$ and it occurs at the mid chord.

Calculate C_d (the section drag coefficient) for the bi-convex airfoil section over an angle of attack range from 0° to 10°. Use the linearized theory relations to determine the pressure distribution that is required to calculate the form drag. Also, calculate C_d for the symmetric diamond-shaped airfoil section (see Problem 10.9).

Prepare a graph comparing the section drag coefficient (C_d) for the bi-convex airfoil for the angle of attack range from 0° to 10° with that for the symmetric, diamond-shaped airfoil section. The shock/Prandtl-Meyer technique is to be used to calculate the pressure distribution for both airfoil sections. What is the effect of airfoil cross-section on the form drag?

REFERENCES

Ackeret J. 1925. Air forces on airfoils moving faster than the speed of sound. *NACA Tech. Mem. 317*

Busemann A, Walchner O. 1933. Airfoil characteristics at supersonic velocities. *Forschung auf dem gebiete des Ingenieurwesens* 4(2): 87–92

Busemann A. 1935. Aerodynamic lift at supersonic speeds. *Luftfahrtforschung* 12(6): 210–220

Edmondson N, Murnaghan FD, Snow RM. 1945. The theory and practice of two-dimensional supersonic pressure calculations. *Johns Hopkins Univ Appl Physics Lab Bumblebee Report 26*, JHU/APL, December 1945.

Kusunose K, Matsushima K, Maruyama D. 2011. Supersonic biplane—a review. *Prog. Aerosp. Sci.* 47: 53–87

Liepmann HW, Roshko A. 1957. *Elements of Gasdynamics*. New York: John Wiley and Sons

Pope A. 1958. *Aerodynamics of Supersonic Flight*. 2nd Ed. New York: Putnam Publ. Corp.

Talay TA. 1975. Introduction to the aerodynamics of flight. *NASA SP 367*

11 SUPERSONIC FLOWS OVER WINGS AND AIRPLANE CONFIGURATIONS

Chapter Objectives

- Understand the physical concepts that apply to supersonic wing aerodynamics
- Know the difference between a subsonic and supersonic leading edge and how that impacts the airfoils used for the wing
- Know the difference between subsonic and supersonic drag due to lift
- Be able to apply the conical flow method to a wing and analyze the aerodynamics of the wing using airfoil theory
- Understand the basic concepts used in numerically simulating supersonic wings
- Be able to explain how supersonic airplanes make a compromise between subsonic and supersonic aerodynamic performance
- Have a basic understanding of the design considerations for supersonic aircraft
- Be able to apply slender body theory to a fuselage shape, and understand the purpose of a boattail for reducing base drag

The density variations associated with the flow over an aircraft in supersonic flight significantly affect the aerodynamic design considerations relative to those for subsonic flight. As noted in Chapter 10, the inviscid pressure distribution results in a drag component, known as wave drag, even if we assume the flow to be isentropic (i.e., neglects the effects of shock waves). Wave drag represents a significant fraction of the total drag

in supersonic flows and is related to the bluntness of the configuration. As illustrated in Table 5.1, the wing sections for supersonic aircraft tend to have a relatively small thickness ratio, and the wing planform has a relatively small aspect ratio.

Techniques by which the aerodynamic forces and moments can be computed can be classed as either panel (or singularity) methods or field (or computational fluid dynamic) methods. For panel methods, the configuration is modeled by a large number of quadrilateral panels, approximating the aircraft surface. One or more types of singularity distributions (e.g., sources) are assigned to each elementary panel to simulate the effect that panel has on the flow field. A variety of panel methods have been developed, such as, that described in Cenko et al. (1981), which can be used to generate solutions for compressible flow. Panel methods yield good results for slender bodies at small angles of attack. Furthermore, linearized-theory concepts also allow us to separate the drag-due-to-lift into two fundamental components: (1) the vortex drag associated with the spanwise distribution of the lifting force and the resultant downwash behind the wing, and (2) the wave-drag-due-to-lift, which arises only for supersonic flow, associated with the longitudinal distribution of the lift and the resultant disturbance waves propagating into the surrounding air.

However, as the design lift coefficient is increased, methods based on linear-theory approximations no longer provide an adequate simulation of the complex flow fields. At high-lift conditions, the flow becomes extremely nonlinear, requiring the use of higher-order prediction techniques which take into account the various nonlinear flow phenomena in determining the configuration aerodynamics. The high-lift flow regime can be modeled using a fully three-dimensional, inviscid, attached-flow computational approach which employs the full-potential equation [equation (9.4b)].

Field methods include a wide variety of assumptions about the flow models. Walkley and Smith (1987) describe a technique which uses a finite-difference formulation based on the characteristics theory of signal propagation to solve the conservative form of the full potential equation, including flows with embedded shock waves and subsonic flows. Additional rigor is obtained (at the cost of additional computational time and expense) if you solve the Euler equation [e.g., Allen and Townsend (1986)]. Solution techniques employing the Euler equations allow us to incorporate entropy terms that are neglected in the full potential model. For relatively slender vehicles at small angles of attack (so that the flow is attached and the boundary layer is thin), we can expect reasonable accuracy for the pressure distributions and force coefficients if we solve the flow field using the Euler equations. To obtain suitable accuracy when computing the flow fields for higher angles of attack or for configurations where viscous/inviscid interactions are important, it is necessary to model the viscous effects and their interdependence on the inviscid flow. For such applications, Navier-Stokes formulations are needed [e.g., Schiff and Steger (1979) and Forsythe et al. (2002)].

It is beyond the scope of this text to treat all the methods available to calculate the forces and moments acting on supersonic vehicles. Furthermore, even computer codes that are based on the Navier-Stokes equations employ simplifying assumptions in the solution algorithm. Therefore, in reviewing techniques for predicting wing leading-edge vortex flows at supersonic speeds, Wood and Miller (1985) note that, based on their comparisons between computed flows and experimental data, (at least) one Euler code was not well suited for the analysis of wings with separated flow at high lift and low supersonic speeds. Instead, a code based on a linearized-theory method that was modified to account for both nonlinear attached-flow effects (lower surface) and nonlinear separated flow (upper

surface) [Carlson and Mack (1980)] provided the best correlation with the experimentally measured vortex strength, vortex position, and total lifting characteristics. So, it is important to develop an understanding of the general features of supersonic flows and their analysis before blindly using an analytic, semi-empirical, or computational approach.

In this chapter, we will consider steady, supersonic, irrotational flow about wings of finite aspect ratio. The objective is to determine the influence of geometric parameters on the lift, the drag, and the pitch moment for supersonic flows past finite wings. In Chapter 10, we evaluated the effect of the section geometry for flows that could be treated as two dimensional (i.e., wings of infinite aspect ratio). Three-dimensional effects will be included since the wings are of finite span. However, we will continue to concentrate on configurations that can be handled by small disturbance (linear) theories.

After a discussion of the general characteristics of flow about supersonic wings, we will proceed to a development of the governing equation and boundary conditions for the supersonic wing problem. Then we will outline the consequences (particularly as they pertain to determining drag) of linearity on the equation and the boundary conditions, and proceed to discuss two solution methods: the conical-flow and the singularity-distribution methods. Example problems are worked using the latter method. We close the chapter with discussions of aerodynamic interaction effects among aircraft components in supersonic flight and of some design considerations for supersonic aircraft.

11.1 GENERAL REMARKS ABOUT LIFT AND DRAG

A typical lift/drag polar for a supersonic airplane is presented in Fig. 11.1. At supersonic speeds, aircraft drag is composed of:

- Skin-friction drag
- Wave-drag-due-to-thickness (or volume), also known as the zero-lift wave drag
- Drag-due-to-lift

Therefore,

$$C_D = C_{D,\text{friction}} + C_{D,\text{thickness}} + C_{D,\text{due-to-lift}} \tag{11.1}$$

As noted earlier in this chapter, the drag-due-to-lift is itself composed of the vortex drag and of the wave-drag-due-to-lift. Experimental evidence indicates that equation (11.1) can be written using the approximation introduced in Chapter 5 from equation (5.46),

$$C_D = C_{D_0} + kC_L^2 \tag{11.2}$$

where C_{D_0} the zero-lift drag coefficient, is composed of the sum of $C_{D,\text{friction}}$ and $C_{D,\text{thickness}}$. For supersonic flows, k (the drag-due-to-lift factor) is a strong function of the Mach number. For an illustration of the relationship between k and the Mach number, you should look at Example 5.7 and Problems 5.15 and 5.16.

The skin-friction drag results from the presence of the viscous boundary layer near the surface of the vehicle (see Chapters 4 and 8). Reference temperature methods can be used in the calculation of skin-friction coefficients for compressible flows (as we discussed in Chapter 12). As noted in Middleton and Lundry (1980), the zero-lift wave drag can be calculated using either far-field methods (i.e., the supersonic area rule) or near-field methods (i.e., the integration of the surface pressure distribution). The far-field method offers advantages for

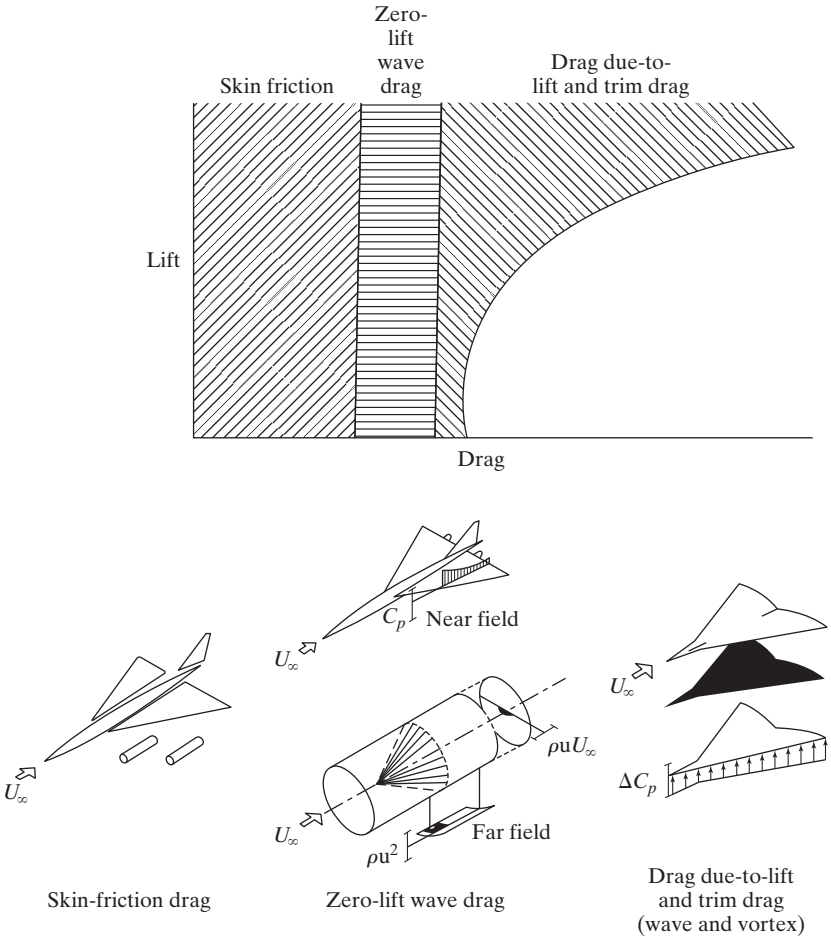

Figure 11.1 Drag buildup using superposition method of drag analysis [from Middleton and Lundry (1980)].

fuselage optimization according to area-rule concepts. The near-field method is used as an analysis tool for applications where the detailed pressure distributions are of interest. The drag-due-to-lift (which includes the trim drag) is computed from lifting-analysis programs. As noted in Middleton et al. (1980), the wing-design and the lift-analysis programs are separate lifting-surface methods which solve the direct or the inverse problem of:

- Design—to define the wing-camber-surface shape required to produce a selected lifting-pressure distribution. The wing-design program includes methods for defining an optimum pressure distribution.
- Lift analysis—to define the lifting pressure distribution acting on a given wing-camber-surface shape and to calculate the associated force coefficients.

For efficient flight at a lift coefficient which maximizes the lift-to-drag ratio, the drag-due-to-lift is about one half of the total drag, as noted in Carlson and Mann (1992).

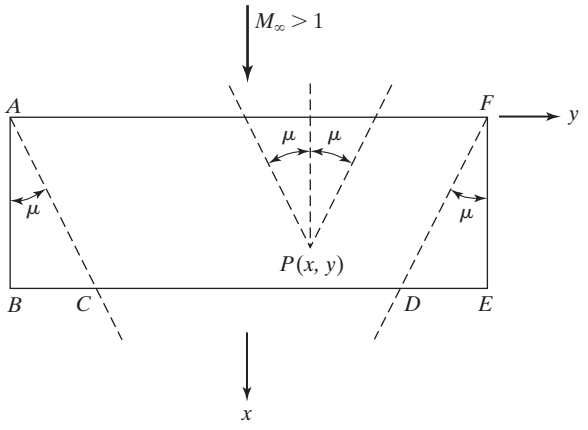

Figure 11.2 Rectangular wing in a supersonic stream.

11.2 GENERAL REMARKS ABOUT SUPERSONIC WINGS

The unique characteristics of supersonic flow lead to some interesting conclusions about wings in a supersonic stream. For example, take a look at the rectangular wing of Fig. 11.2. The pressure at a given point $P(x, y)$ on the wing is influenced only by pressure disturbances generated at points within the upstream Mach cone (determined by $\mu = \sin^{-1} 1/M_\infty$) emanating from P. As a result, the wing tips affect the flow only in the regions BAC and DEF. The remainder of the wing ($ACDF$) is not influenced by the tips and can be treated using the two-dimensional theory developed in Chapter 10.

In the case of an arbitrary planform (as shown in Fig. 11.3), we have the following definitions:

- A supersonic (subsonic) leading edge is that portion of the wing leading edge where the component of the free-stream velocity normal to the edge is supersonic (subsonic).
- A supersonic (subsonic) trailing edge is that portion of the wing trailing edge where the component of the free-stream velocity normal to the edge is supersonic (subsonic).

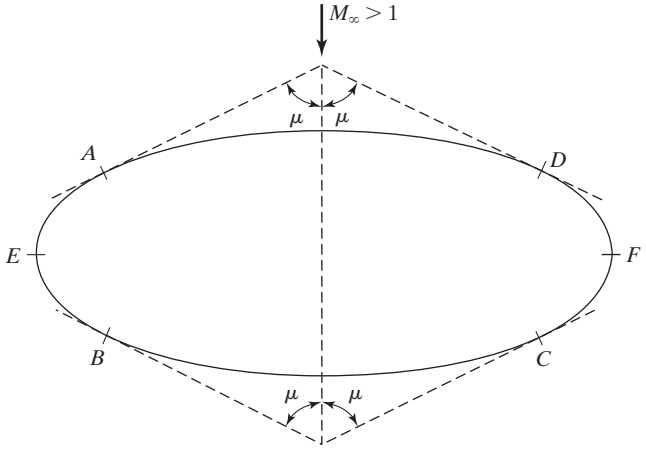

Figure 11.3 Wing of arbitrary planform in a supersonic stream.

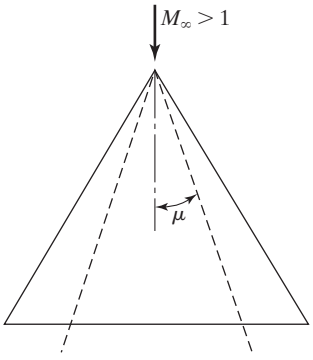

Figure 11.4 Delta wing with supersonic leading and trailing edges.

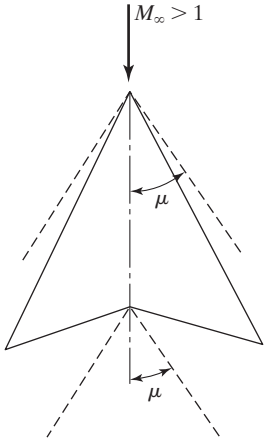

Figure 11.5 Arrow wing with a subsonic leading edge and a supersonic trailing edge.

In Fig. 11.3, *AD* and *BC* are supersonic leading and trailing edges, respectively. *AE* and *DF* are subsonic leading edges, and *EB* and *FC* are subsonic trailing edges. Note that the points, *A*, *D*, *B*, and *C* are the points of tangency of the free-stream Mach cone with the leading and trailing edges. The delta wing of Fig. 11.4 has supersonic leading and trailing edges, while the arrow wing of Fig. 11.5 has a subsonic leading edge and a supersonic trailing edge.

Points on the upper surface within two-dimensional regions that are bounded by supersonic leading edges have flows that are independent of lower surface flow and vice versa, for points on the lower surface. Therefore, in many cases, portions of supersonic wings can be treated by the two-dimensional theory of Chapter 10. From the perspective of wing design, supersonic leading edges lead to using supersonic airfoil profiles which have sharp leading edges and are relatively thin with little or no camber. An example of an airplane designed this way is the F-104.

The conclusion drawn in Chapter 10—that good aerodynamic efficiency in supersonic flight depends on thin-airfoil sections with sharp leading and trailing edges—carries over to finite aspect ratio wings. We also find that the benefits of sweepback (as discussed in Chapter 9) in decreasing wave drag are also present in the supersonic regime.

Points on the upper surface within regions bounded by subsonic leading edges have flows that are not independent of the lower surface flow. In these cases, the wings should be treated with subsonic theories from Chapters 7 and 9. From the perspective of design, subsonic leading edges lead to using subsonic airfoil profiles which have rounded leading edges and are relatively thicker, with some camber for improved low-speed performance. An example of an airplane designed this way is the F-15.

An experimental investigation was conducted to determine the aerodynamic characteristics of a potential high-speed civil transport [Hernandez et al. (1993)]. As noted by Hernandez, "The inboard wing panel has a leading-edge sweep of 79°, which produces a subsonic normal Mach number at the Mach 3.0 cruise condition. Because of the subsonic leading-edge normal Mach number, relatively blunt leading-edges were possible without a substantial zero-lift wave drag penalty."

11.3 GOVERNING EQUATION AND BOUNDARY CONDITIONS

In Chapter 9, we derived the small perturbation (or linear velocity potential) equation (9.13). Although the derivation was for the subsonic case, the assumptions made in that derivation are satisfied by thin wings in supersonic flow as well.

In mathematical form, the assumptions made in deriving equation (9.13) are

$$\begin{aligned} M_\infty^2\left(\frac{u'}{U_\infty}\right)^2 &\ll 1 \quad M_\infty^2\left(\frac{v'}{U_\infty}\right)^2 \ll 1 \quad M_\infty^2\left(\frac{w'}{U_\infty}\right)^2 \ll 1 \\ M_\infty^2\left(\frac{u'v'}{U_\infty^2}\right) &\ll 1 \quad M_\infty^2\left(\frac{u'w'}{U_\infty^2}\right) \ll 1 \quad M_\infty^2\left(\frac{v'w'}{U_\infty^2}\right) \ll 1 \\ \frac{M_\infty^2}{|1-M_\infty^2|}\left(\frac{u'}{U_\infty}\right) &\ll 1 \quad M_\infty^2\left(\frac{v'}{U_\infty}\right) \ll 1 \quad M_\infty^2\left(\frac{w'}{U_\infty}\right) \ll 1 \end{aligned} \tag{11.3}$$

We can observe from equation (11.3) that these assumptions are satisfied for thin wings in supersonic flow provided the free-stream Mach number (M_∞) is not too close to one (transonic regime), nor too great (hypersonic regime). Practically speaking, this restricts supersonic linear theory to the range $1.2 \leq M_\infty \leq 5$.

Rewriting equation (9.13) in standard form (to have a positive factor for the ϕ_{xx} term) yields

$$(M_\infty^2 - 1)\phi_{xx} - \phi_{yy} - \phi_{zz} = 0 \tag{11.4}$$

where ϕ is the perturbation potential. This is a linear, second-order partial differential equation of the hyperbolic type, whereas equation (9.13) is of the elliptic type (when $M_\infty < 1$). This fundamental mathematical difference between the equations governing subsonic and supersonic small perturbation flow has already been discussed in Chapter 8. There, we saw that a small disturbance in a subsonic stream affects the flow upstream and downstream of the disturbance, whereas in a supersonic flow the influence of the disturbance is present only in the "zone of action" defined by the Mach cone emanating in the downstream direction from the disturbance. These behaviors are characteristic of the solutions to elliptic and hyperbolic equations, respectively.

The boundary condition imposed on an inviscid flow is that the flow must be tangent to the surface at all points on the wing. Mathematically, we have:

$$\left(\frac{w'}{U_\infty + u'}\right)_{\text{surface}} = \frac{dz_s}{dx} \tag{11.5}$$

which is the same as the condition imposed on the flow in the subsonic case, as shown in the equation immediately following equation (7.41), where the surface is given by $z_s = z_s(x, y)$.

Consistent with the definition of the perturbation potential, equation (11.5) becomes

$$\left(\frac{\phi_z}{U_\infty + \phi_x}\right)_{\text{surface}} = \frac{dz_s}{dx} \tag{11.6}$$

Applying the assumption that the flow perturbations are small, we have

$$(\phi_z)_{z=0} = U_\infty \frac{dz_s}{dx} \tag{11.7}$$

as the flow tangency boundary condition, since $U_\infty + u' \approx U_\infty$ and the surface corresponds to $z_s \approx 0$. An additional condition that must be applied at a subsonic trailing edge is the *Kutta condition*, which is:

$$C_{pu_{te}} = C_{pl_{te}} \tag{11.8}$$

where the subscripts u_{te} and l_{te} stand for upper and lower wing surface at the trailing edge, respectively. Physically, the condition represented by equation (11.8) means that the local lift at a subsonic trailing edge is zero.

11.4 CONSEQUENCES OF LINEARITY

In Chapter 10 we saw that the effects of angle of attack, camber, and thickness distribution were additive; refer to equations (10.8), (10.14), and (10.22). In general, a wing can also be analyzed using three components (as shown in Fig. 11.6): (a) a flat plate of the same planform at the same angle of attack, (b) a thin plate with the same planform and camber at zero angle of attack, and (c) a wing of the same planform and thickness distribution but with zero camber and zero angle of attack. The perturbation potential for each of these components can be determined separately and added together to get the combined potential describing the flow about the actual wing.

Therefore, the linear nature of the governing equation and the boundary conditions allows us to break the general wing problem into parts, solve each part by some appropriate method, and linearly combine the results to arrive at the final aerodynamic description. The ability to treat thin wings in this manner greatly simplifies what would otherwise be very difficult problems.

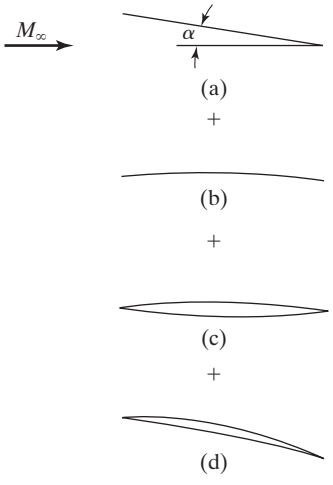

Figure 11.6 Effects of angle of attack, camber, and thickness are additive in linear theory: (a) angle of attack; (b) camber distribution; (c) thickness distribution; (d) resultant wing.

11.5 SOLUTION METHODS

We learned in Chapter 9 that subsonic, compressible flows could be treated by applying an affine transformation [equation (9.14)] to equation (9.13) and the boundary conditions. This resulted in an equivalent incompressible flow problem [equation (9.15)], which could be handled by the methods of Chapters 6 and 7 for two- and three-dimensional flows, respectively. However, no affine transformation exists which can be used to transform [equation (11.4)] into [equation (9.15)].

We will discuss two solution methods for equation (11.4). The first, the conical-flow method, was first proposed by Busemann (1947) and was used extensively before the advent of high-speed digital computers. The second, the singularity-distribution method, has been known for some time [Lomax et al. (1951), Shapiro (1954), and Ferri (1949)] but was not generally exploited until the high-speed digital computer was commonly available. The latter method is particularly suited to solution using computers and is more easily applied to general configurations than the former. Therefore, it is more widely used today. However, the solutions generated using the conical-flow method (where applicable) serve as straightforward comparison checks for solutions using the computerized singularity-distribution method.

11.6 CONICAL-FLOW METHOD

A conical flow exists when flow properties, such as the velocity, the static pressure, and the static temperature, are invariant along rays (e.g., PA in Fig. 11.7) emanating from a point (e.g., point P at the wing tip), as shown by Busemann (1947). If equation (11.4) is transformed from the x, y, z coordinate system to a conical coordinate system [as was done in Snow (1948)], the resulting equation has only two independent variables, since properties are invariant along rays from the apex of the cone. A further transformation [Shapiro (1954)] results in Laplace's equation in two independent variables, which is amenable to solution by well-known methods (complex variable theory, Fourier series, etc.).

Since the conical-flow technique is not generally applicable and is not as adaptable to computers, we will not go through the mathematical details of its development.

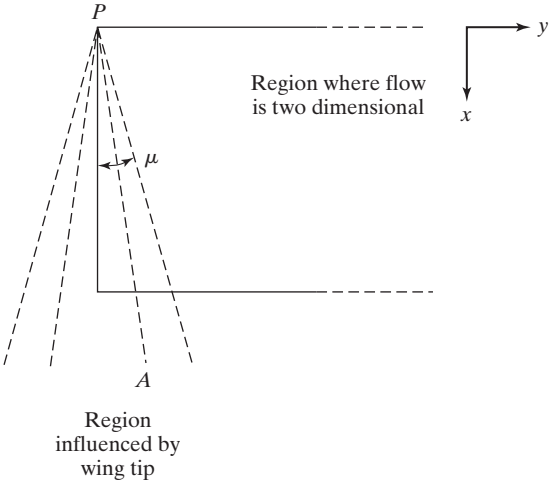

Figure 11.7 In a conical flow, properties are invariant along rays emanating from a point.

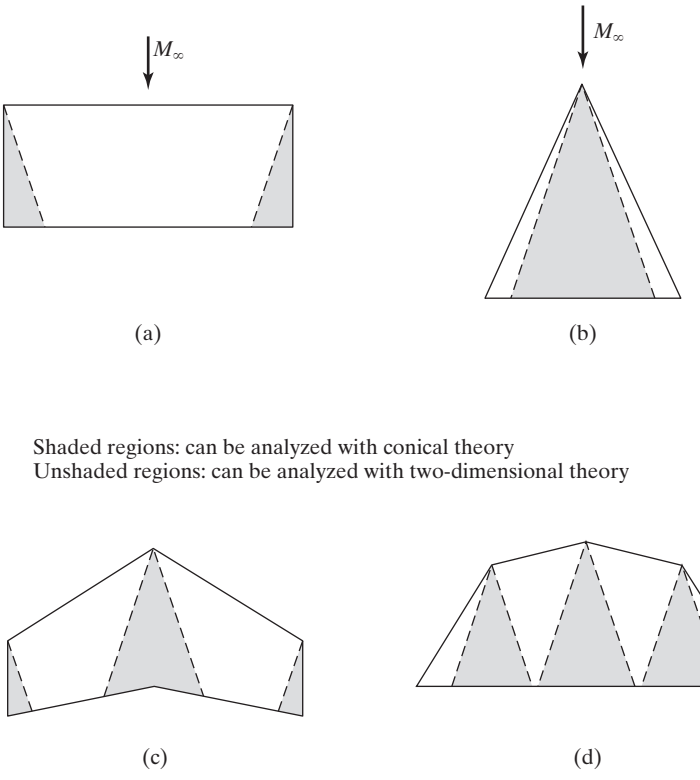

Figure 11.8 Examples of regions that can be treated with conical theory: (a) rectangular wing; (b) delta wing; (c) swept swing; (d) "double" delta wing.

However, we will present some results that are applicable to simple wing shapes. The interested reader is referred to Shapiro (1954), Ferri (1949), Carafoli (1956), and Jones and Cohen (1957), for in-depth presentations of conical flow theory and its applications. Regions of various wings that can be treated using conical-flow theory are illustrated in Fig. 11.8.

11.6.1 Rectangular Wings

Bonney (1947) has shown that the lift inside the Mach cone at the tip of a rectangular wing is one-half the lift of a two-dimensional flow region of equal area. This is illustrated in the pressure distribution for an isolated rectangular wing tip, which is presented in Fig. 11.9. The curve of Fig. 11.9 represents the equation

$$\frac{\Delta p}{\Delta p_{2-d}} = \frac{C_p}{C_{p,2-d}} = \frac{2}{\pi}\sin^{-1}\sqrt{\frac{\tan\mu'}{\tan\mu}}$$

The analysis can be extended to the interaction of the two tip flows when their respective Mach cones intersect (or overlap) on the wing surface. The case where the entire trailing

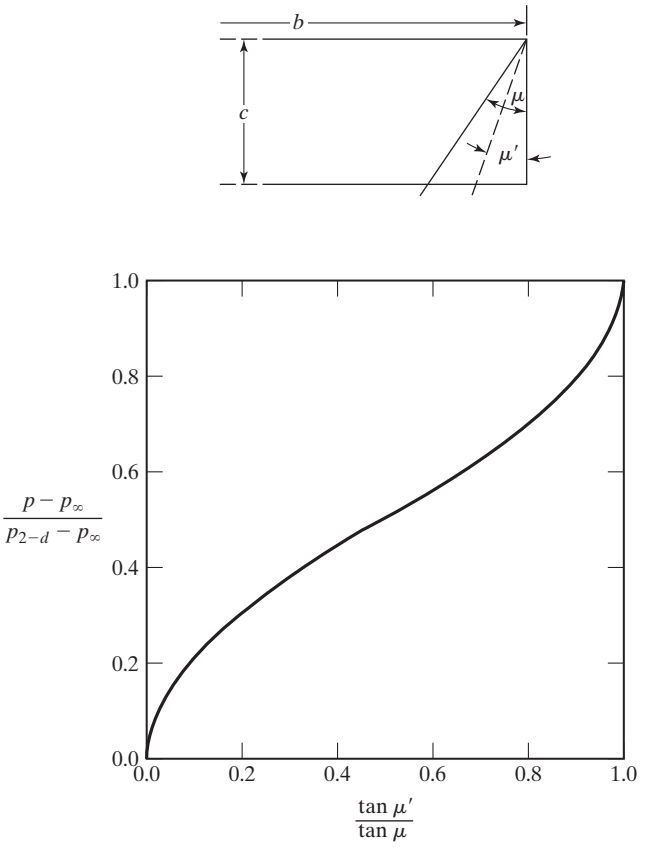

Figure 11.9 Pressure distribution at the tip of a rectangular wing (p = actual pressure due to tip loss, p_{2-d} = corresponding two-dimensional pressure) [from Bonney (1947)].

edge of the wing is in the overlap region of the tip Mach cones is illustrated in Fig. 11.10. The pressure distribution in the region of overlap (when $1 \leq \beta \cdot AR \leq 2$) is determined by adding the pressures due to each tip and subtracting from them the two-dimensional pressure field determined by Busemann's second-order equation (10.23). Note that $\beta^2 = M_\infty^2 - 1$.

The extent of the overlap region is determined by the parameter $\beta \cdot \mathrm{AR}$. Three cases are shown in Fig. 11.11. Conical-flow theory is not applicable in the regions indicated in the figure. Such cases will occur when $\beta \cdot \mathrm{AR} < 1$.

The key assumptions used in this development are as follows:

- Secondary tip effects originating at the point of maximum thickness of a double-wedge airfoil are neglected.
- Tip effects extend to the limits of the Mach cone defined by the free-stream Mach number M_∞ and not to the Mach cone defined by the local Mach number.
- Flow separation does not occur.
- Linear theory applies.

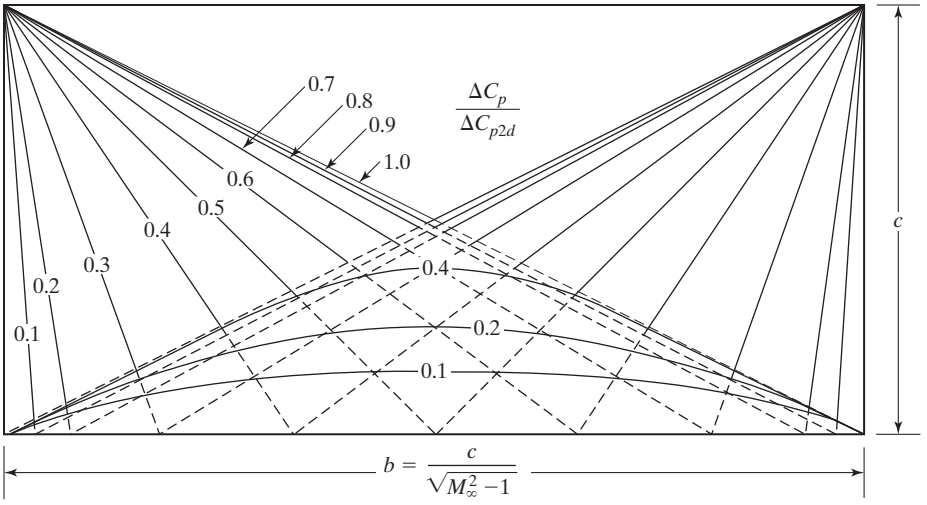

Figure 11.10 Effect of a subsonic wing tip on the pressure distribution for a rectangular wing for which $\beta \cdot \mathrm{AR} = 1$.

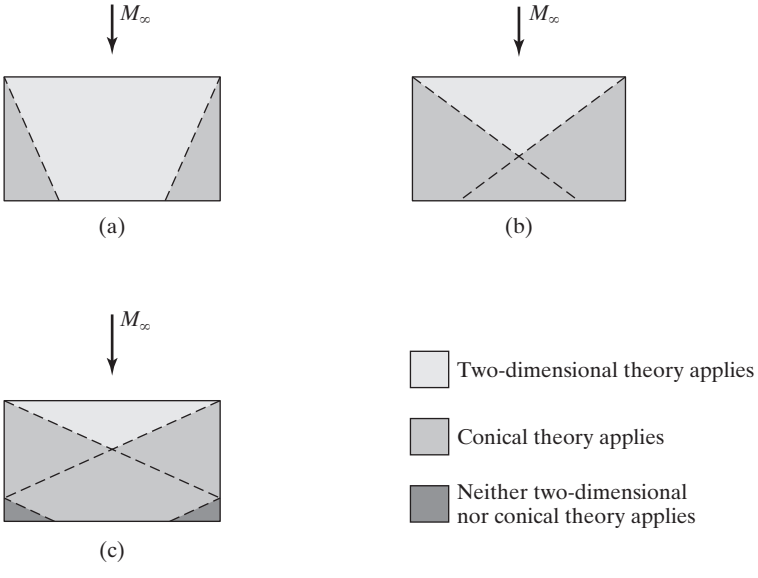

Figure 11.11 Regions where conical flow applies for rectangular wings: (a) $\beta \cdot \mathrm{AR} > 2$: no overlap; (b) $1 \leq \beta \cdot \mathrm{AR} \leq 2$: overlap along the trailing edge; (c) $\beta \cdot \mathrm{AR} < 1$: overlap extends beyond the wing tips.

A summary of the results from Bonney (1947) for the case of nonoverlapping tip effects is given in Table 11.1. Conclusions to be drawn from this analysis are as follows:

- A decrease in the aspect ratio for a given supersonic Mach number and airfoil section results in decreases in the coefficients for the drag-due-to-lift, the lift, and the

TABLE 11.1 Conical-Flow Results for Rectangular Wings Using Busemann Second-Order Approximation Theory

Type	*Flat-Plate Airfoil*	*Flat-Plate Wing*	*Finite-Thickness Airfoil*	*Finite-Thickness Wing*
C_L	$\frac{4\alpha}{\beta}$	$\frac{4\alpha}{\beta}\left(1-\frac{1}{2\mathrm{AR}\cdot\beta}\right)$	$\frac{4\alpha}{\beta}$	$\frac{4\alpha}{\beta}\left[1-\frac{1}{2\mathrm{AR}\cdot\beta}(1-C_3A')\right]$
C_D	$\frac{4\alpha^2}{\beta}+C_{D,\text{friction}}$	$\frac{4\alpha^2}{\beta}\left(1-\frac{1}{2\mathrm{AR}\cdot\beta}\right)+C_{D,\text{friction}}$	$\frac{K_1\tau^2}{\beta}+\frac{4\alpha^2}{\beta}+C_{D,\text{friction}}$	$\frac{K_1\tau^2}{\beta}+C_{D,\text{fraction}}+\frac{4\alpha^2}{\beta}\left[1-\frac{1}{2\mathrm{AR}\cdot\beta}(1-C_3A')\right]$
C_{M_0}	$\frac{2\alpha}{\beta}$	$\frac{2\alpha}{\mathrm{AR}\cdot\beta^2}\left(\mathrm{AR}\cdot\beta-\frac{2}{3}\right)$	$\frac{2\alpha}{\beta}(1-C_3A')$	$\frac{2\alpha}{\mathrm{AR}\cdot\beta^2}\left[\mathrm{AR}\cdot\beta-\frac{2}{3}-C_3A'(\mathrm{AR}\cdot\beta-1)\right]$
x_{cp}	$\frac{c}{2}$	$\left[\frac{\mathrm{AR}\cdot\beta-\frac{2}{3}}{2\mathrm{AR}\cdot\beta-1}\right]c$	$(1-C_3A')\frac{c}{2}$	$\left[\frac{\mathrm{AR}\cdot\beta-\frac{2}{3}-C_3A'(\mathrm{AR}\cdot\beta-1)}{2\mathrm{AR}\cdot\beta-1+C_3A'}\right]c$

$C_3=\dfrac{\gamma M_\infty^4+(M_\infty^2-2)^2}{2(M_\infty^2-1)^{3/2}}$; $A'=\dfrac{\text{airfoil cross-sectional area}}{\text{chord squared}}$; α in radians.

Values of A', K_1:

Type of airfoil	A'	K_1
Double wedge	$\frac{1}{2}\tau$	4
Modified double wedge	$\frac{2}{3}\tau$	6
Biconvex	$\frac{2}{3}\tau$	5.33

Source: Bonney (1947).

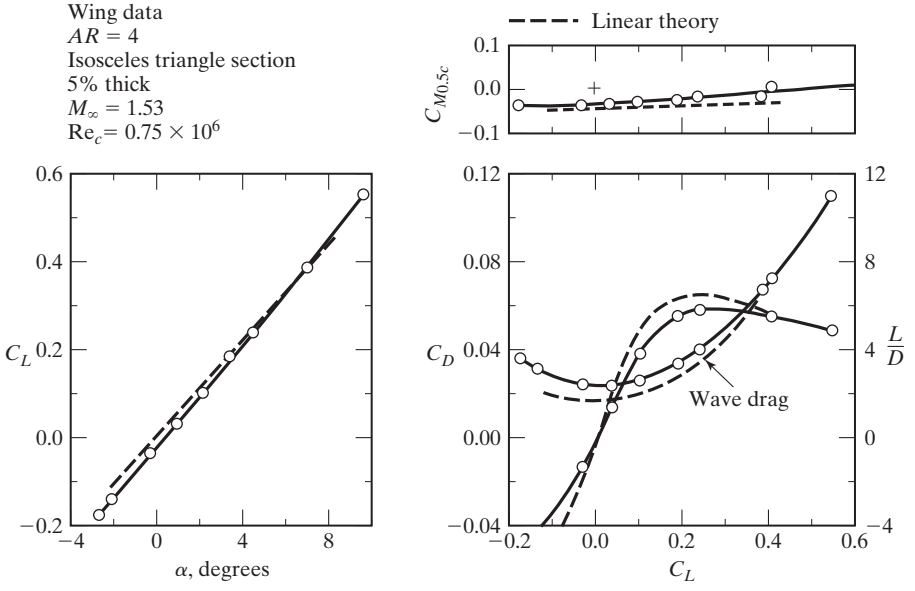

Figure 11.12 Comparison of linear theory results with experimental data for a rectangular wing [data from Nielsen et al. (1948)].

pitching moment. Note that the behavior of the drag-due-to-lift here is in direct contrast to its behavior in subsonic flow. The center of pressure will move forward with a decrease in aspect ratio.

- When the thickness ratio is increased, the coefficients of lift and of drag-due-to-lift for finite-span wings increase slightly, but the moment coefficient about the leading edge decreases. Furthermore, the center of pressure moves forward both for airfoils and for wings as the thickness ratio is increased.
- Airfoils having the same cross-sectional area will have the same center of pressure location.
- The thickness drag will vary with the square of the thickness ratio for a given cross-sectional shape.
- Airfoils of symmetrical cross section with a maximum thickness at the midchord point will have the least drag for a given thickness ratio.

A comparison of conical flow predictions with data obtained from Nielsen et al. (1948) is given in Fig. 11.12 for a double-wedge airfoil for the conditions shown in the figure.

Aerodynamics Concept Box: Example of an Aircraft with True Supersonic Wings and Airfoils

Most aircraft that have to fly at both subsonic and supersonic speeds have wing planforms and airfoil sections which are compromises between the requirements of the two

speed regimes. However, one class of aircraft does not have to make that compromise: supersonic tactical missiles. Shown below is an Advanced Medium-Range Air-to-Air Missile (AMRAAM) being fired from an F-16; AMRAAM flies supersonically almost all of the time.

F-16 firing an AMRAAM missile
(U.S. Air Force photo by Staff Sgt. Eric T. Sheller)

Because of the supersonic nature of the missile, the wings and tails have delta or clipped delta wing planforms with symmetric double wedge and modified double wedge airfoils. These are the airfoils with the lowest wave drag for a given thickness according to linear theory. The airfoil thickness is only compromised by the structural requirements for attachment to the missile fuselage. Seeing a pure supersonic aerodynamic design is unusual, but not unheard of!

11.6.2 Swept Wings

If the wing leading edge is swept aft of the Mach cone originating at the apex of the wing as shown in Fig. 11.13, the disturbances propagate along the Mach lines "warning" the approaching flow of the presence of the wing. As we saw earlier, a leading edge that is swept within the Mach cone is referred to as a subsonic leading edge and the flow approaching the wing is similar to subsonic flow, even though the flight speed is supersonic. When the leading edge is subsonic, the wing can be treated by the methods of Chapters 7 and 9. Furthermore, for sufficiently swept leading edges, the wing leading edge can be rounded similar to those used for subsonic speeds.

There are penalties associated with sweepback (some of which show up at subsonic speeds) including reduction of the lift-curve slope, increased drag-due-to-lift, tip

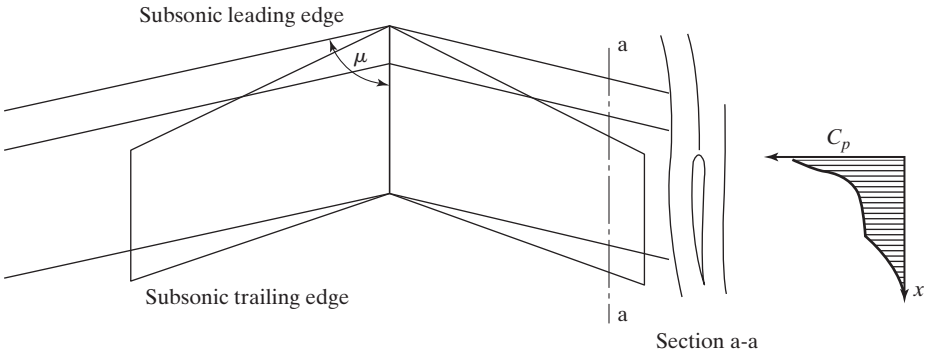

Figure 11.13 Pressure distribution over the wing chord for a section of a swept wing with subsonic leading and trailing edges.

stalling, and reduced effectiveness of high-lift devices. There are structural considerations also. A swept wing has a greater structural span than a straight wing having the same area and aspect ratio. Sweepback introduces additional (possibly severe) torsion because the applied loads on the wing act aft of the wing root.

Consider the flow depicted in Fig. 11.14, where the leading and trailing edges of the wing are supersonic. The tips and center portion of a swept wing can be treated with conical-flow theory while the remaining portion of the wing can be analyzed by the two-dimensional techniques of Chapter 10, if an appropriate coordinate transformation is made. Refer to Fig. 11.15, where a segment of an infinitely long sweptback wing with sweepback angle Λ and angle of attack α are presented. In this case, the free-stream Mach number can be broken into the three components. The component tangent to the leading edge is unaffected by the presence of the wing (if we neglect viscous effects). Therefore, we may consider the equivalent free-stream Mach number M_{∞_e} normal to the leading edge. This will be the flow as seen by an

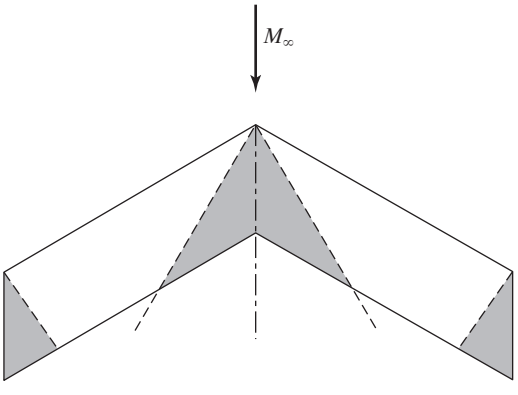

Shaded regions: conical flow theory applies
Unshaded regions: two-dimensional flow theory applies

Figure 11.14 Regions of conical flow and of two-dimensional flow for a swept wing.

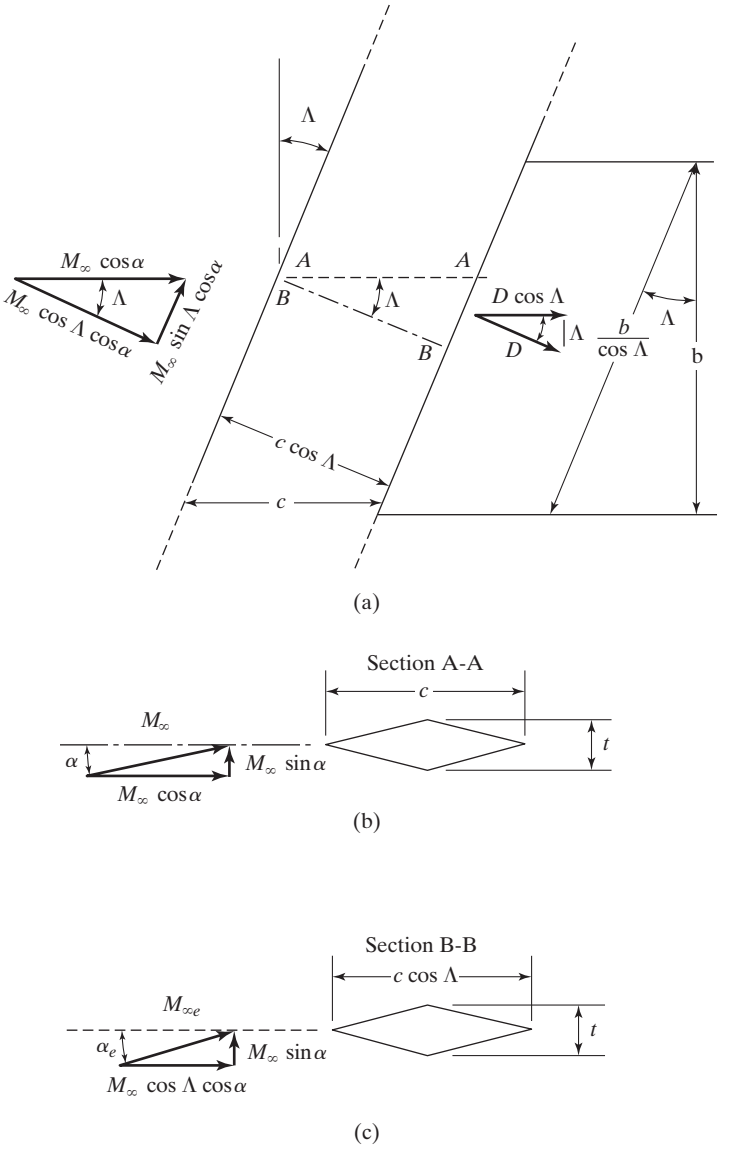

Figure 11.15 Nomenclature for flow around a sweptback wing of infinite aspect ratio: (a) view in plane of wing; (b) view in plane parallel to direction of flight; (c) view in plane normal to the leading edge [from Shapiro (1954)].

observer moving spanwise at the tangential Mach number $M_\infty \sin\Lambda\cos\alpha$. Notice that the airfoil section exposed to M_{∞_e} will be that taken in a plane normal to the leading edge, and the flow at M_{∞_e} about this section can be treated with the two-dimensional theory of Chapter 10.

Referring to the geometry presented in Fig. 11.15, we can see that

$$M_{\infty_e} = [(M_\infty \sin\alpha)^2 + (M_\infty \cos\alpha \cos\Lambda)^2]^{0.5}$$

or

$$M_{\infty_e} = M_\infty(1 - \sin^2\Lambda \cos^2\alpha)^{0.5} \tag{11.9}$$

Also,

$$\alpha_e = \tan^{-1}\frac{M_\infty \sin\alpha}{M_\infty \cos\alpha \cos\Lambda} = \tan^{-1}\frac{\tan\alpha}{\cos\Lambda} \tag{11.10}$$

$$\tau_e = \frac{t}{c\cos\Lambda} = \frac{\tau}{\cos\Lambda} \tag{11.11}$$

where $\tau \equiv t/c$ is the thickness ratio.

Now, the total lift per unit span is not changed by the spanwise motion of the observer; and only M_{∞_e} generates pressure forces necessary to create lift, so the section lift coefficient is:

$$C_l = \frac{l}{(\gamma/2)p_\infty M_\infty^2 c}$$

and

$$C_{le} = \frac{l}{(\gamma/2)p_\infty M_{\infty_e}^2 c\cos\Lambda(1/\cos\Lambda)} \tag{11.12}$$

Similarly, ignoring viscous effects and noting that the wave drag is normal to the leading edge,

$$C_{de} = \frac{l}{(\gamma/2)p_\infty M_{\infty_e}^2 c\cos\Lambda(1/\cos\Lambda)} \tag{11.13}$$

while

$$C_d = \frac{d\cos\Lambda}{(\gamma/2)p_\infty M_{\infty_e}^2 c} \tag{11.14}$$

where $d\cos\Lambda$ is the drag component in the free-stream direction.

Combining equations (11.9) and (11.12), we get

$$C_l = C_{le}\left(\frac{M_{\infty e}}{M_\infty}\right)^2 = C_{le}(1 - \sin^2\Lambda\cos^2\alpha) \tag{11.15}$$

For the drag, we combine equations (11.9), (11.13), and (11.14) to get

$$C_d = C_{de}\cos\Lambda\left(\frac{M_{\infty e}}{M_\infty}\right)^2 = C_{de}\cos\Lambda(1 - \sin^2\Lambda\cos^2\alpha) \tag{11.16}$$

The results just derived are true in general. If we restrict ourselves to the assumptions of the linear (Ackeret) theory, which was discussed in Chapter 10, then

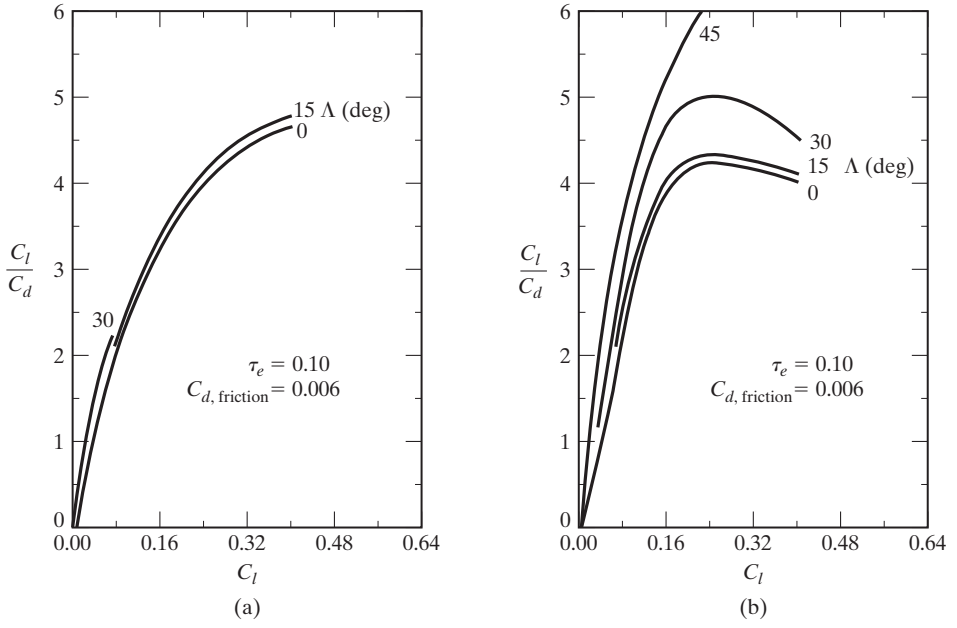

Figure 11.16 Theoretical effect of sweepback for double-wedge section airfoils with supersonic leading edges: (a) lift-to-drag ratio for $M_\infty = 1.5$; (b) lift-to-drag ratio for $M_\infty = 2.0$;

$$C_{le} = \frac{4\alpha_e}{\sqrt{M_{\infty_e}^2 - 1}} \tag{11.17}$$

$$C_{de} = \frac{4}{\sqrt{M_{\infty_e}^2 - 1}} \left(\alpha_e^2 + \frac{\overline{\sigma_{ue}^2} + \overline{\sigma_{le}^2}}{2} \right) \tag{11.18}$$

These results are identical to those obtained in Chapter 10 for infinite aspect ratio wings with leading edges normal to the free-stream flow direction, as shown in equations (10.8) and (10.16).

The results of Ivey and Bowen (1947) for flow about sweptback airfoils with double-wedge profiles are presented in Fig. 11.16. Notice that significant improvement in performance can be realized with sweep. The results in Fig. 11.16 are based on the exact relations [i.e., equations (11.15) and (11.16)], the shock-expansion theory (not linear theory), and the assumption that the skin friction drag coefficient per unit span is 0.006.

11.6.3 Delta and Arrow Wings

Puckett and Stewart (1947) used a combination of a source-distribution and conical-flow theory to investigate the flow about delta- and arrow-shaped planforms, as shown in Fig. 11.17. Cases studied included subsonic and/or supersonic leading and trailing edges with double-wedge airfoil sections. Stewart (1946) and Puckett (1946) used conical-flow theory to investigate the flow about simple delta planforms.

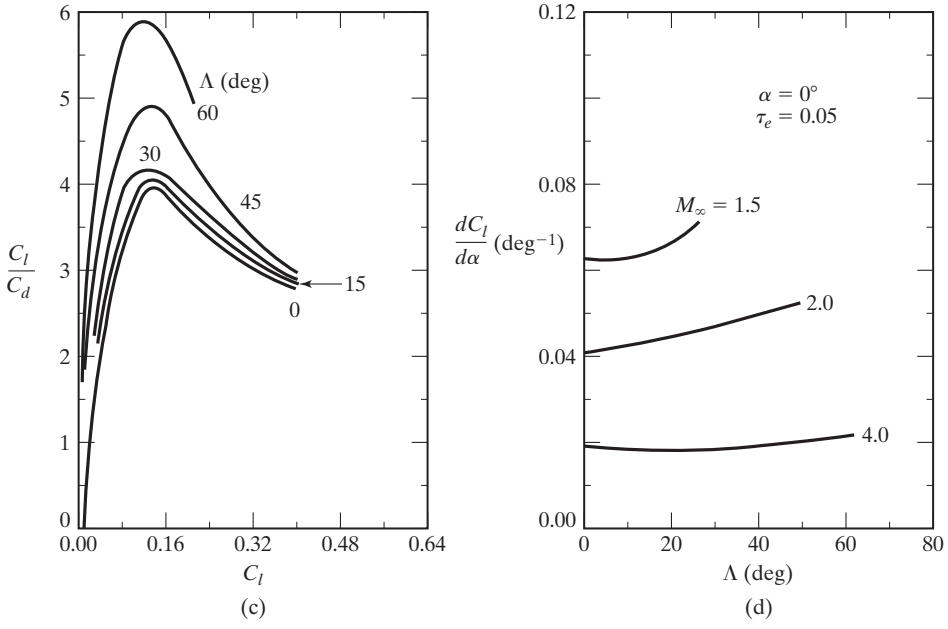

Figure 11.16 (*Continued*) (c) lift-to-drag ratio for $M_\infty = 4.0$; (d) lift-curve slope [from Ivey and Bowen (1947)].

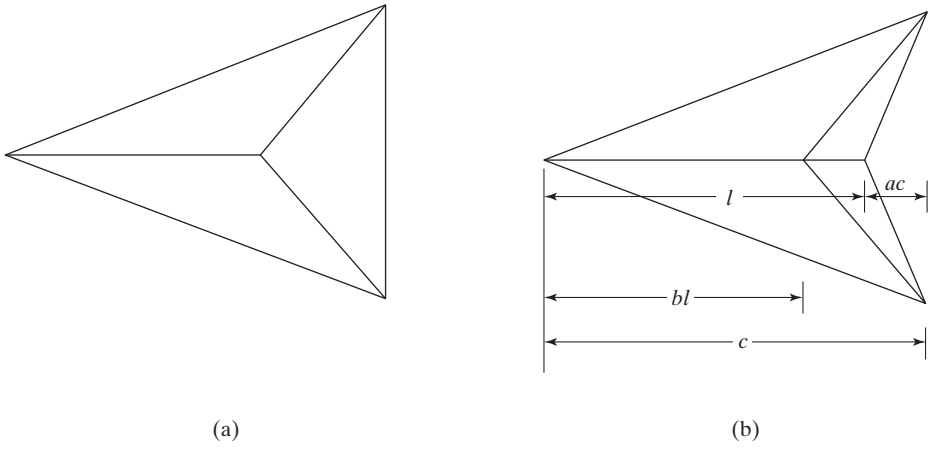

Figure 11.17 Delta- and arrow-wing planforms with double-wedge sections: (a) delta planform; (b) arrow planform.

Two significant conclusions about delta and arrow planforms that can be drawn from these studies are as follows:

- For wings where the sweepback of both leading and trailing edges is relatively small, the strong drag peak at Mach 1 (characteristic of two-dimensional wings) is replaced by a weaker peak at a higher Mach number, corresponding to coincidence of the Mach wave with the leading edge.

TABLE 11.2 Comparison of Aerodynamic Coefficients for Rectangular, Delta, and Arrow Wing Planforms for $M_\infty = 1.50$

Wing Planform	*Rectangular*	*Delta*[a]	*Arrow*[a]
	$\Lambda = 70°$	$\Lambda = 70°$ $b = 0.2$ $\beta \cot \Lambda = 0.4$	$\Lambda = 70°$ $b = 0.2$ $\beta \cot \Lambda = 0.4$
	$AR = 1$	$a = 0$	$a = 0.25$
$\frac{\beta}{4}\frac{dC_L}{d\alpha}$	0.554		0.591
$\frac{dC_L}{d\alpha}$	1.98	1.94	2.11
Relative area, S	1.00	1.018	0.938
Relative root chord, l	1.00	1.69	1.26
Root thickness ratio, τ	0.10	0.059	0.080
$C_{D,\text{thickness}}$	0.0119	0.0048	0.0070
$C_{D,\text{friction}}$	0.0060	0.0060	0.0060
C_{D0}	0.0179	0.0108	0.0130
$\left(\frac{C_L}{C_D}\right)_{\max}$	5.25	8.6	9.3

[a]See Fig. 11.17 for a definition of *a* and *b*.
Source: Puckett and Stewart (1947).

- Delta and arrow wings with subsonic leading edges can have lift curve slopes $(dC_L/d\alpha)$ approaching the two-dimensional value $(4/\beta)$, as shown in equation (10.9), with much lower values of C_D/τ^2 than those characteristic of two-dimensional wings of the same thickness.

A theoretical comparison of a rectangular, delta, and arrow wing is given in Table 11.2. As noted in Wright et al. (1978) and shown in Fig. 11.18, "One of the prominent advantages of the arrow wing is in the area of induced drag . . . where the planform with

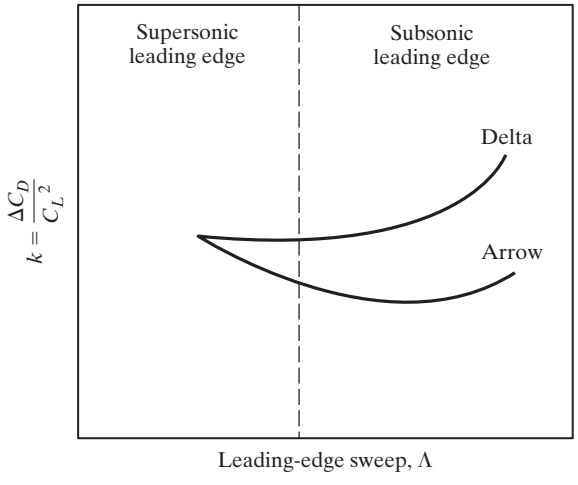

Figure 11.18 Comparison of induced drag for delta- and arrow-wing planforms. *Note:* $\Delta C_D = \Delta C_{D0}$ [from Wright et al. (1978)].

a trailing edge cut out or notch ratio is shown to have lower induced drag. The second advantage of the arrow wing is its ability to retain a subsonic round leading edge at an aspect ratio that is of the same level as that of the lesser swept supersonic leading edge delta. The advantages of the subsonic leading edge are a lower wave drag at cruise and a high L/D for subsonic flight operations due to increased leading edge suction."

11.7 SINGULARITY-DISTRIBUTION METHOD

The second method that can be used to solve equation (11.4) is the singularity-distribution method. Detailed treatment of the mathematical aspects of the theory and applications to various wing planforms are presented in Lomax et al. (1951), Shapiro (1954), Jones and Cohen (1957), and Carlson and Miller (1974). For simple planforms, the singularity-distribution method can provide exact analytical closed-form solutions to three-dimensional wing problems [see Shapiro (1954), Jones and Cohen (1957), and Puckett and Stewart (1947)]. However, the method is quite adaptable for use with computers to solve for flow about complex shapes, and this is where it is most extensively applied.

In Chapter 3 we learned that the governing equation [i.e., equation (3.26)] for incompressible, irrotational flow is linear even without the assumption of small disturbances. This allowed us to combine elementary solutions (i.e., source, sink, doublet, vortex, etc.) of the governing equation to generate solutions for incompressible flows about shapes of aerodynamic interest. In supersonic flow, where the small disturbance assumption is necessary to linearize the governing equation [e.g., equation (11.4)], there are analogs to the simple solutions for the incompressible case. Owing to a mathematical similarity to their incompressible counterparts, the supersonic solutions are quite naturally referred to as supersonic sources, sinks, doublets, and vortices. However, the physical relationship to their subsonic counterparts is not quite so direct and will not be developed fully here.

The supersonic source (recall that a sink is simply a negative source), the doublet, and the horseshoe vortex potentials given by Lomax et al. (1951) are as follows:

$$\text{Source: } \phi_s = -\frac{Q}{r_c} \tag{11.19a}$$

$$\text{Doublet: } \phi_d = +\frac{Qz\beta^2}{r_c^3} \tag{11.19b}$$

where the axis of the doublet is in the positive z direction.

$$\text{Vortex: } \phi_v = -\frac{Qz\nu_c}{r_c} \tag{11.19c}$$

In equation (11.19), Q is the strength of the singularity and

$$r_c = \{(x - x_1)^2 - \beta^2[(y - y_1)^2 + z^2]\}^{0.5}$$

$$\beta^2 = M_\infty^2 - 1$$

$$\nu_c = \frac{x - x_1}{(y - y_1)^2 + z^2}$$

We can verify by direct substitution that equations (11.19a) through (11.19c) satisfy equation (11.4). Notice that the point (x_1, y_1, z_1) is the location of the singularity. Since the wing is in the $z = 0$ plane, $z_1 = 0$ for every singularity for this approximation. This is because the wing is replaced by a distribution of singularities in the plane of the wing. The hyperbolic radius, r_c, is seen to be imaginary outside the Mach cone extending downstream from the location of the singularity in each instance. Therefore, the influence of the singularity is only present in the zone of action downstream of the point $(x_1, y_1, 0)$.

Modern numerical techniques and computers can be used to model a wing or body by replacing it with singularities at discrete points. These singularities are combined linearly to create a flow pattern similar to that about the actual body. The strengths of the singularities are determined so that the boundary condition requiring that the flow be tangent to the body's surface is satisfied at selected points. For configurations with sharp trailing edges, it is also necessary to satisfy the Kutta condition at those sharp trailing edges which are subsonic. Once the singularity distribution is determined, the potential at a given point is obtained by summing the contributions of all the singularities to the potential at that point, and the velocity and pressure distributions can be found using equations (9.12) and (9.16a).

Four types of problems that can be treated by the singularity-distribution method [see Lomax et al. (1951)] are as follows:

Two nonlifting cases:

1. Given the thickness distribution and the planform shape, find the pressure distribution on the wing.
2. Given the pressure distribution on a wing of symmetrical section, find the wing shape (i.e., find the thickness distribution and the planform).

Two lifting cases:

3. Given the pressure distribution on a lifting surface (zero thickness), find the slope at each point of the surface.
4. Given a lifting surface, find the pressure distribution on it. Here, it is necessary to impose the Kutta condition for subsonic trailing edges when they are present.

Cases 1 and 3 are called "direct" problems because they involve integrations with known integrands. Cases 2 and 4 are "indirect" or "inverse" problems, since the unknown to be found appears inside the integral sign. Therefore, the solution of inverse problems involves the inversion of an integral equation.

One might expect that cases 1 and 4 would be the only ones of practical interest, however, this is not the case. Many times, a designer wishes to specify a given loading distribution (e.g., either for structural or for stability analyses) and solve for the wing shape which will give that prescribed loading distribution. Therefore, you may encounter any one of the four cases in aircraft design work. A variation of cases 2 and 3 is to specify the potential on a surface instead of the pressure distribution. Cases 1 and 2 are most conveniently solved using source or doublet distributions, while cases 3 and 4 are most often treated using vortex distributions.

11.7.1 Find the Pressure Distribution Given the Configuration

Consider a distribution of supersonic sources in the xy plane. The contribution to the potential at any point $P(x, y, z)$ due to an infinitesimal source at $P'(x_1, y_1, 0)$ in the plane is, from equation (11.19a),

$$d\phi(x, y, z) = -\frac{C(x_1, y_1)\, dx_1\, dy_1}{\sqrt{(x - x_1)^2 - \beta^2[(y - y_1)^2 + z^2]}} \tag{11.20}$$

where $C(x_1, y_1)$ is the source strength per unit area. Consistent with the linearity assumption, the flow tangency condition [equation (11.7)] gives the vertical (z direction) velocity component in the xy plane as

$$w'(x, y, 0) = \left[\frac{\partial\phi(x, y, z)}{z}\right]_{z=0} = U_\infty \frac{dz_s(x, y)}{dx} \tag{11.21}$$

Taking the derivative with respect to z of equation (11.20) gives

$$\frac{\partial[d\phi(x, y, z)]}{\partial z} = dw'(x, y, z) = -\frac{C(x_1, y_1)\beta^2 z\, dx_1\, dy_1}{\{(x - x_1)^2 - \beta^2[(y - y_1)^2 + z^2]\}^{1.5}} \tag{11.22}$$

Notice that x_1 and y_1 are treated as constants. Taking the limit of equation (11.22) as $z \to 0$, we get $dw'(x, y, 0) = 0$, except very near the point (x_1, y_1) where the limit is indeterminant (i.e., of the form $0/0$). We conclude that the vertical velocity at a point in the xy plane is due only to the source at that point and to no other sources. In other words, a source induces a vertical velocity at its location and nowhere else. A source does, however, contribute to u' and v' (i.e., the x and y components of the perturbation velocity) at other locations. We still must determine the contribution of the source at the point (x_1, y_1) to the vertical velocity at $P'(x_1, y_1, 0)$. Puckett (1946) shows that the latter contribution is

$$dw'(x_1, y_1, 0) = \pi C(x_1, y_1) \tag{11.23a}$$

However, since this is the entire contribution,

$$w'(x_1, y_1, 0) = dw'(x_1, y_1, 0) = \pi C(x_1, y_1) \tag{11.23b}$$

Using equation (11.21), we see that

$$C(x_1, y_1) = \frac{U_\infty}{\pi}\left[\frac{dz_s(x_1, y_1)}{dx_1}\right] \equiv \frac{U_\infty \lambda(x_1, y_1)}{\pi} \tag{11.23c}$$

where λ is the local slope of the wing section. Therefore, we obtain the important result that the source distribution strength at a point is proportional to the local surface slope at the point.

Substituting equation (11.23c) into equation (11.20) and integrating gives

$$\phi(x, y, z) = -\frac{U_\infty}{\pi}\iint_S \frac{\lambda(x_1, y_1)\, dx_1\, dy_1}{[(x - x_1)^2 - \beta^2(y - y_1)^2]^{0.5}} \tag{11.24}$$

where S is the region in the xy plane within the upstream Mach cone with apex at $P(x, y)$. Once the potential is known, the pressure distribution follows from equation (9.16); that is,

$$C_p = -\frac{2(\partial\phi/\partial x)}{U_\infty} \tag{9.16a}$$

Since source distributions are used where the airfoil section is symmetric (see the preceding cases 1 and 2), the pressure distribution determined by equations (11.24) and (9.16) is the same on the upper and lower surfaces. Because linear theory requires that the deflection angles are small, the wave-drag coefficient at zero lift is

$$C_{Dw} = 2 \iint_{S_u} C_{pu}(x, y)\lambda_u(x, y)\, dx\, dy \tag{11.25}$$

where S is the surface of the wing and the subscript u indicates the upper surface. The formula contains the factor 2 to include the contribution of the lower surface since the section is symmetric.

EXAMPLE 11.1: Determine the pressure distribution for the single-wedge delta wing

We will determine the pressure distribution for the simple wing shape shown in Fig. 11.19, which is at zero degrees angle of attack. This is a single-wedge delta with subsonic leading edges. The leading edge is swept by the angle Λ_{LE}, although this wing is not very practical because of its blunt trailing edge.

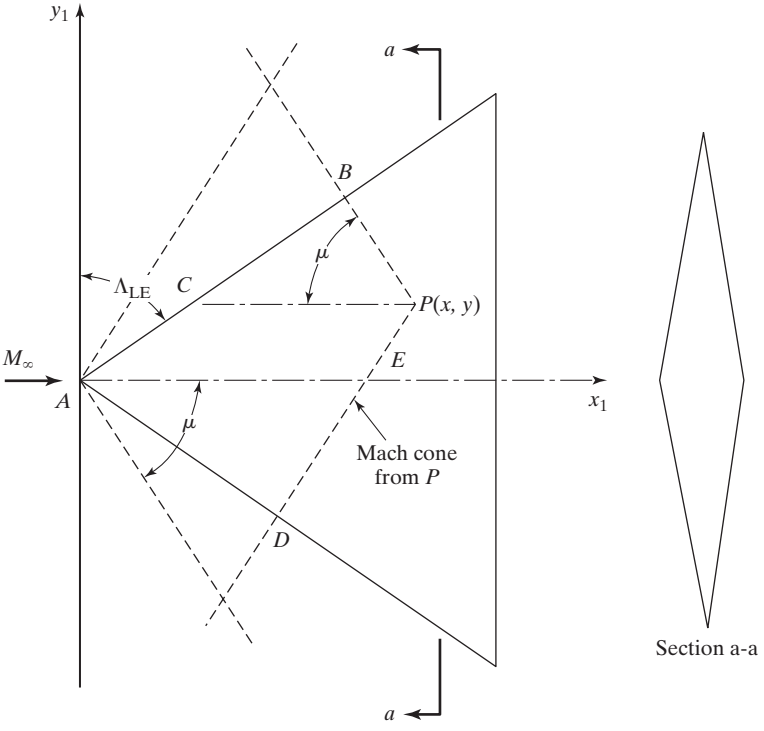

Figure 11.19 Nomenclature and geometry for single-wedge delta wing of Example 11.1.

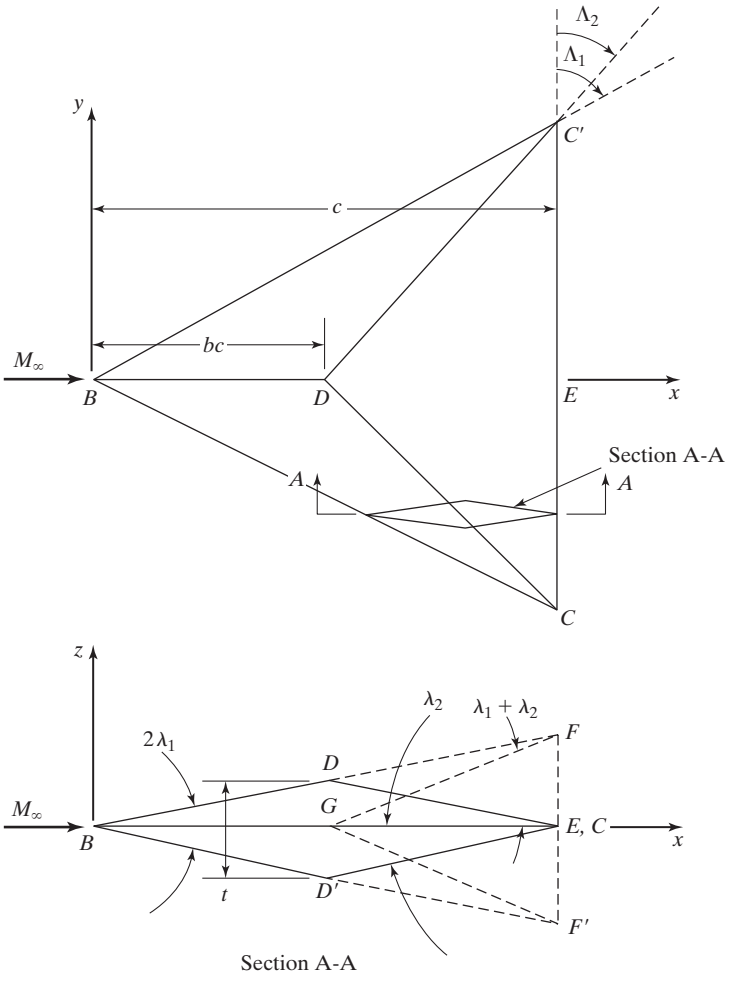

Figure 11.20 Geometry for a delta-wing planform with a double-wedge section [from Shapiro (1954)].

However, neglecting the effects of the presence of the boundary layer, the effects of the trailing edge are not propagated upstream in the supersonic flow. So, to obtain the flow about a wing with a sharp trailing edge, we can add (actually subtract) the solutions for the flow around two delta wings of constant slope such that the desired airfoil section can be obtained. This additive process is illustrated in Fig. 11.20. The simple case considered here can be used as a building block to construct more complex flow fields about wings of more practical shape [see Shapiro (1954) and Stewart (1946)].

Solution: Consider the point $P(x, y)$ in Fig. 11.19. The flow conditions at P are a result of the combined influences of all the sources within the upstream Mach cone from P. From symmetry, the vertical velocity perturbation vanishes ahead

of the wing, and the source distribution simulating the wing extends only to the leading edges. Thus, the source distribution which affects P is contained entirely in the region $ABPD$.

The potential at P is given by equation (11.24):

$$\phi(x, y, 0) = -\frac{\lambda}{\pi} U_\infty \iint_{ABPD} \frac{dx_1\, dy_1}{[(x - x_1)^2 - \beta^2(y - y_1)^2]^{0.5}}$$

where we have moved λ outside the integral sign, since it is a constant in this example.

To carry out the integration, it is convenient to break $ABPD$ into three separate areas, thus:

$$\begin{aligned}\phi(x, y, 0) = -\frac{\lambda}{\pi} U_\infty \Bigg\{ & \iint_{ADE} \frac{dx_1\, dy_1}{[(x - x_1)^2 - \beta^2(y - y_1)^2]^{0.5}} \\ & + \iint_{AEPC} \frac{dx_1\, dy_1}{[(x - x_1)^2 - \beta^2(y - y_1)^2]^{0.5}} \\ & + \iint_{CPB} \frac{dx_1\, dy_1}{[(x - x_1)^2 - \beta^2(y - y_1)^2]^{0.5}} \Bigg\}\end{aligned}$$

To define the limits of integration, we note the following relationships from geometry:

$$\begin{aligned}\text{Along } AD: \quad & x_1 = -y_1 \tan \Lambda_{\text{LE}} \\ \text{Along } ACB: \quad & x_1 = +y_1 \tan \Lambda_{\text{LE}} \\ \text{Along } BP: \quad & x_1 = x - \beta(y_1 - y) \\ \text{Along } DEP: \quad & x_1 = x + \beta(y_1 - y)\end{aligned}$$

Finally, the coordinates of points B and D are

$$B\left[\frac{(x + \beta y)\tan \Lambda_{\text{LE}}}{\tan \Lambda_{\text{LE}} + \beta}, \frac{x + \beta y}{\tan \Lambda_{\text{LE}} + \beta}\right]$$

$$D\left[\frac{(x - \beta y)\tan \Lambda_{\text{LE}}}{\tan \Lambda_{\text{LE}} + \beta}, \frac{-(x - \beta y)}{\tan \Lambda_{\text{LE}} + \beta}\right]$$

Therefore, we have

$$\begin{aligned}\phi(x, y, 0) = \frac{\lambda}{\pi} U_\infty \Bigg[& \int_{\frac{-(x-\beta y)}{\tan \Lambda_{\text{LE}} + \beta}}^{0} dy_1 \int_{-y_1 \tan \Lambda_{\text{LE}}}^{x + \beta(y_1 - y)} \frac{dx_1}{[(x - x_1)^2 - \beta^2(y - y_1)^2]^{0.5}} \\ & + \int_0^y dy_1 \int_{y_1 \tan \Lambda_{\text{LE}}}^{x + \beta(y_1 - y)} \frac{dx_1}{[(x - x_1)^2 - \beta^2(y - y_1)^2]^{0.5}} \\ & + \int_y^{\frac{(x+\beta y)}{\tan \Lambda_{\text{LE}} + \beta}} dy_1 \int_{y_1 \tan \Lambda_{\text{LE}}}^{x - \beta(y_1 - y)} \frac{dx_1}{[(x - x_1)^2 - \beta^2(y - y_1)^2]^{0.5}}\end{aligned}$$

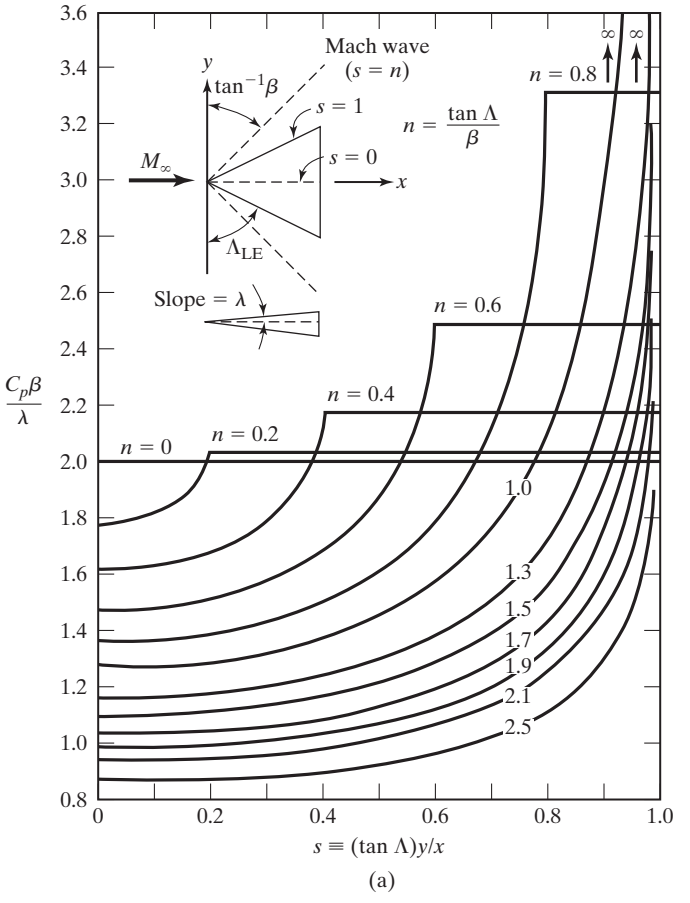

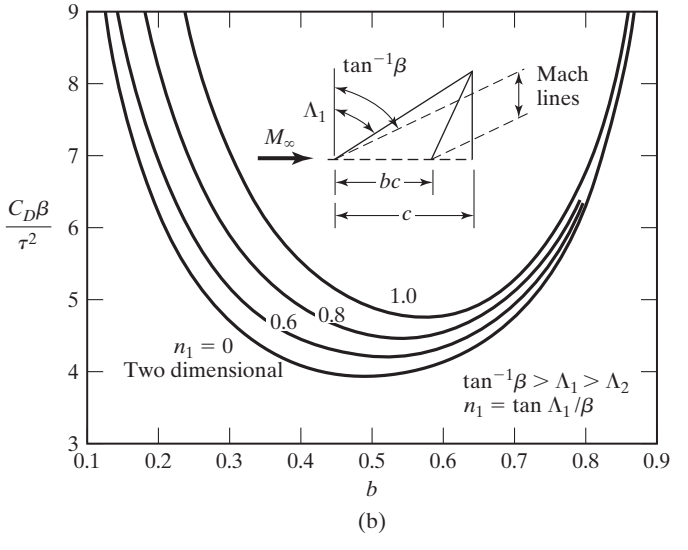

Figure 11.21 Theoretical solutions for a delta wing: (a) pressure distribution for a single-wedge delta wing at $\alpha = 0$; (b) thickness drag of a double-wedge delta wing with a supersonic leading edge and a supersonic line of maximum thickness [from Puckett (1946)].

We can use standard integral tables and relationships involving inverse hyperbolic functions [i.e., see Hodgman (1977)] to show that the result of this integration and subsequent differentiation with respect to x is [see Puckett (1946)]

$$u'(x, y, 0) = +\frac{\partial \phi}{\partial x}$$
$$= -\frac{\lambda}{\pi} U_\infty \frac{2}{\beta[(\tan^2 \Lambda_{LE}/\beta^2) - 1]^{0.5}} \cosh^{-1}\left\{\left(\frac{\tan \Lambda_{LE}}{\beta}\right)\left[\frac{1 - (\beta y/x)^2}{1 - (y^2 \tan^2 \Lambda_{LE})/x^2}\right]^{0.5}\right\}$$

By equation (9.16a), the pressure distribution on the wing is

$$C_p(x, y, 0) = -\frac{2u'}{U_\infty}$$

Notice that C_p is invariant along rays (y/x = constant) from the apex of the wing. Therefore, as we might suspect from the geometry, this is a conical flow.

The wave-drag coefficient can be determined using equation (11.25). Fig. 11.21 presents pressure distributions and wave drag for various configurations of single- and double-wedge delta wings (see Figs. 11.19 and 11.20).

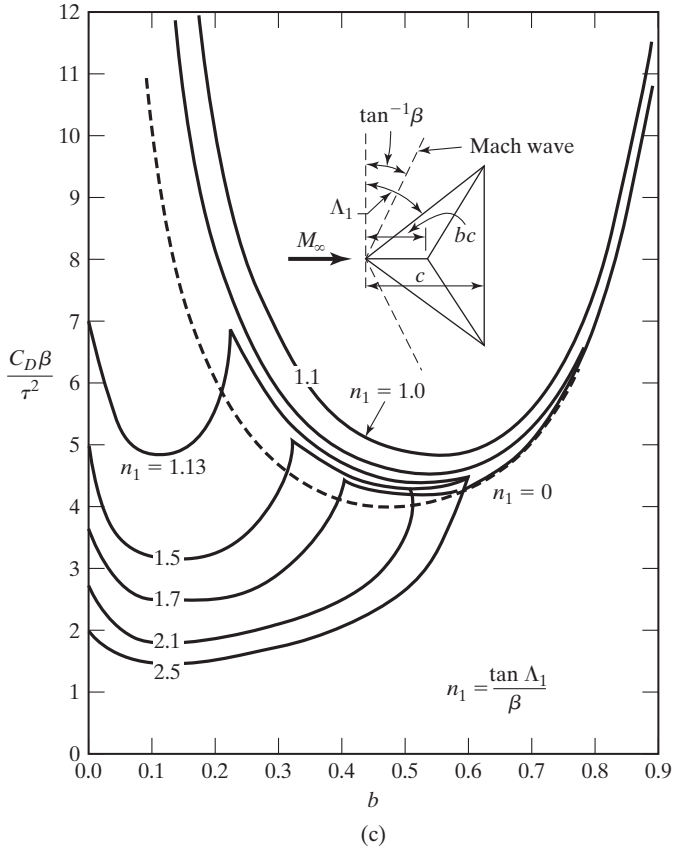

Figure 11.21 (*continued*) (c) thickness drag of a double-wedge delta wing with a subsonic line of maximum thickness.

EXAMPLE 11.2: Prepare graphs of the pressure distribution for a single-wedge delta wing

Consider a single-wedge delta wing with a leading-edge sweep angle of 60°, flying at a Mach number of 2.2. The wing has a thickness-to-chord ratio in the plane of symmetry of 0.04. Thus, referring to Fig. 11.21a, the surface slope λ is 0.02. Prepare graphs of C_p as a function $(x - x_{LE})/c(y)$ for the four planes shown in the sketch of Fig. 11.22 (i.e., at stations $y = 0.125b$; $y = 0.250b$; $y = 0.375b$; and $y = 0.450b$).

Solution: We should first locate the Mach wave originating at the apex of the delta wing:

$$\mu = \sin^{-1}\frac{1}{M_\infty} = \frac{1}{2.2} = 27.04°$$

As shown in the sketch of Fig. 11.23, the Mach wave is downstream of the wing leading edge. Therefore, the wing has a supersonic leading edge. In the shaded region representing that portion of the wing between the leading edge and the Mach wave, the pressure must be constant and the same as that for a two-dimensional oblique airfoil. In this region,

$$C_p = -\frac{2u'}{U_\infty} = \frac{2\lambda}{\beta\sqrt{1 - n^2}} = \frac{2\lambda}{\sqrt{\beta^2 - \tan^2 \Lambda_{LE}}} \qquad \textbf{(11.26)}$$

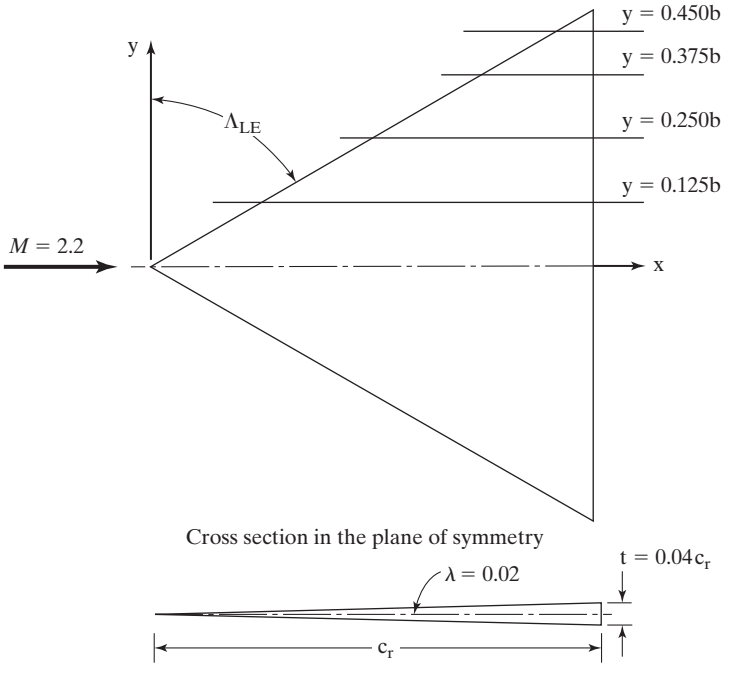

Figure 11.22 Sketch for Example 11.2.

The nomenclature used in equation (11.26) is consistent with that used in Figs. 11.21a and 11.23, so:

$$\beta = \sqrt{M_\infty^2 - 1} = 1.9596$$

and

$$n = \frac{\tan \Lambda_{LE}}{\beta} = 0.88388$$

The expression given in equation (11.26) can be rearranged to the format used in Fig. 11.21a, so that

$$\frac{C_p \beta}{\lambda} = \frac{2}{\sqrt{1 - n^2}} = 4.276$$

You should compare this numerical value with the graphical information presented in Fig. 11.21a. In the region between the wing leading edge and the Mach wave, the pressure coefficient itself is equal to

$$C_p = 0.0436$$

We can use the expression developed by Puckett (1946) to determine the pressure at points on the wing that lie between the Mach wave and the plane of symmetry, when the wing leading edge is supersonic. The points are located in terms of the coordinate s, where

$$s = (\tan \Lambda_{LE}) \frac{y}{x}$$

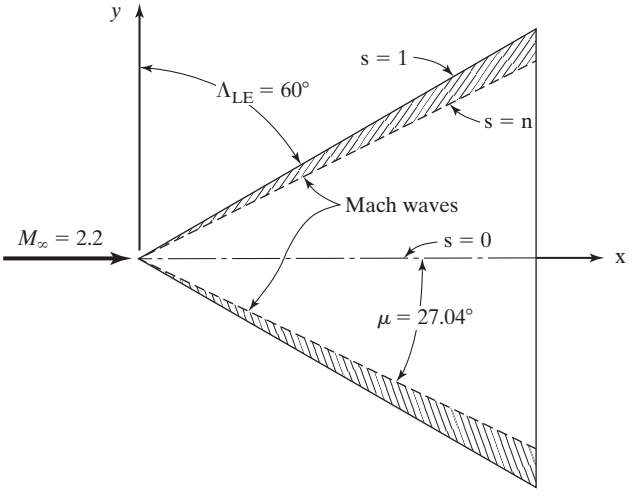

Figure 11.23 Mach waves and lines of constant s for Example 11.2.

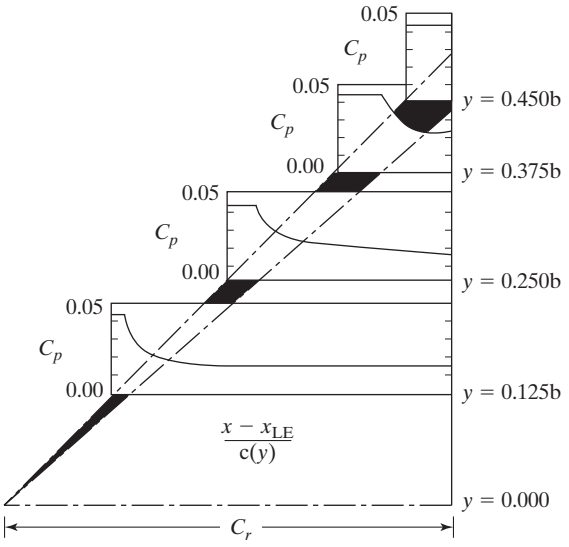

Figure 11.24 Pressure distributions for Example 11.2.

Therefore, $s = 0$ corresponds to the plane of symmetry, $s = 1$ corresponds to the wing leading edge, and $s = n$ corresponds to the Mach wave. The pressure coefficient in this region is given by

$$C_p = \frac{4\lambda}{\beta\pi\sqrt{1-n^2}}\text{Real}\left\{\frac{\pi}{2} - \sin^{-1}\sqrt{\frac{n^2-s^2}{1-s^2}}\right\} \tag{11.27}$$

Graphs of the pressure distributions for the four stations of interest are presented in Fig. 11.24. Note that the Mach wave intersects the wing trailing edge at $y = 0.442b$. As a result, the plane $y = 0.450b$ lies entirely within the shaded region. So, the pressure coefficient in the $y = 0.450b$ plane is independent of x and equal to 0.0436.

11.7.2 Numerical Method for Calculating the Pressure Distribution Given the Configuration

Carlson and Miller (1974) presented a numerical application of the vortex distribution method which is applicable to thin wings of arbitrary profile and of arbitrary planform. In accordance with the concepts of linearized theory, the wing is assumed to have negligible thickness and is assumed to lie approximately in the $z = 0$ plane. We will now discuss the application of their method to determine the lifting pressure coefficient at the field point (x, y).

The equation governing the differential pressure coefficient ($\Delta C_p = C_{pl} - C_{pu}$) is

$$\Delta C_p(x,y) = -\frac{4}{\beta}\frac{\partial z_c(x,y)}{\partial y} + \frac{1}{\pi}\oiint_s R(x-x_1, y-y_1)\Delta C_p(x_1,y_1)d\beta y_1\, dx_1 \tag{11.28}$$

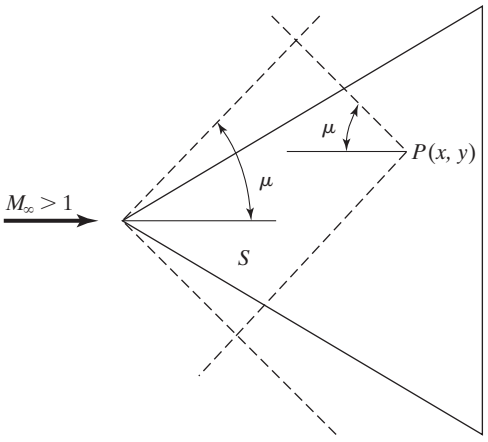

Figure 11.25 S is the region of integration for the supersonic vortex lattice method.

where

$$R(x - x_1, y - y_1) \equiv \frac{x - x_1}{\beta^2(y - y_1)^2[(x - x_1)^2 - \beta^2(y - y_1)^2]^{0.5}}$$

and $z_c(x, y)$ is the z coordinate of the camber line. The function R may be thought of as an influence function relating the local loading at the point (x_1, y_1) to its influence on the flow field.

The integral in equation (11.28) represents the influence of a continuous distribution of horseshoe vortices originating from wing elements with vanishingly small chords and spans. The region of integration, S, originating at the field point (x, y), is shown in Fig. 11.25. The integral gives the appearance of being improper and divergent because of the singularity at $y_1 = y$ within the region of integration. However, the integral can be treated according to the concept of the generalization of the Cauchy principal value [see Lomax et al. (1951)], as indicated by the double-dash marks on the integral signs.

In order to replace the indicated integration in equation (11.28) with an algebraic summation, it is first necessary to replace the Cartesian coordinate system shown in Fig. 11.26a with the grid system shown in Fig. 11.26b. The region of integration, originally bound by the wing leading edge and the Mach lines, now consists of a set of grid elements approximating that region shown by the shaded area of Fig. 11.26b. Inclusion of partial as well as full grid elements provides a better definition of the wing leading edge and tends to reduce any irregularities that may arise in local surface slopes for elements in the vicinity of the leading edge.

Therefore, we will determine the lifting pressure distribution numerically using a system of grid elements similar to those shown in Fig. 11.26b. Notice that, in practice, many more elements would be used. The numbers L and N identify the spaces in the grid which replace the integration element $dx_1\, d\beta y_1$ L^* and N^* identify the element associated with, and immediately in front of, the field point $(x, \beta y)$. Note that $L^* = x$ and $N^* = \beta y$, and x and βy take on only integer values. The region of integration, originally

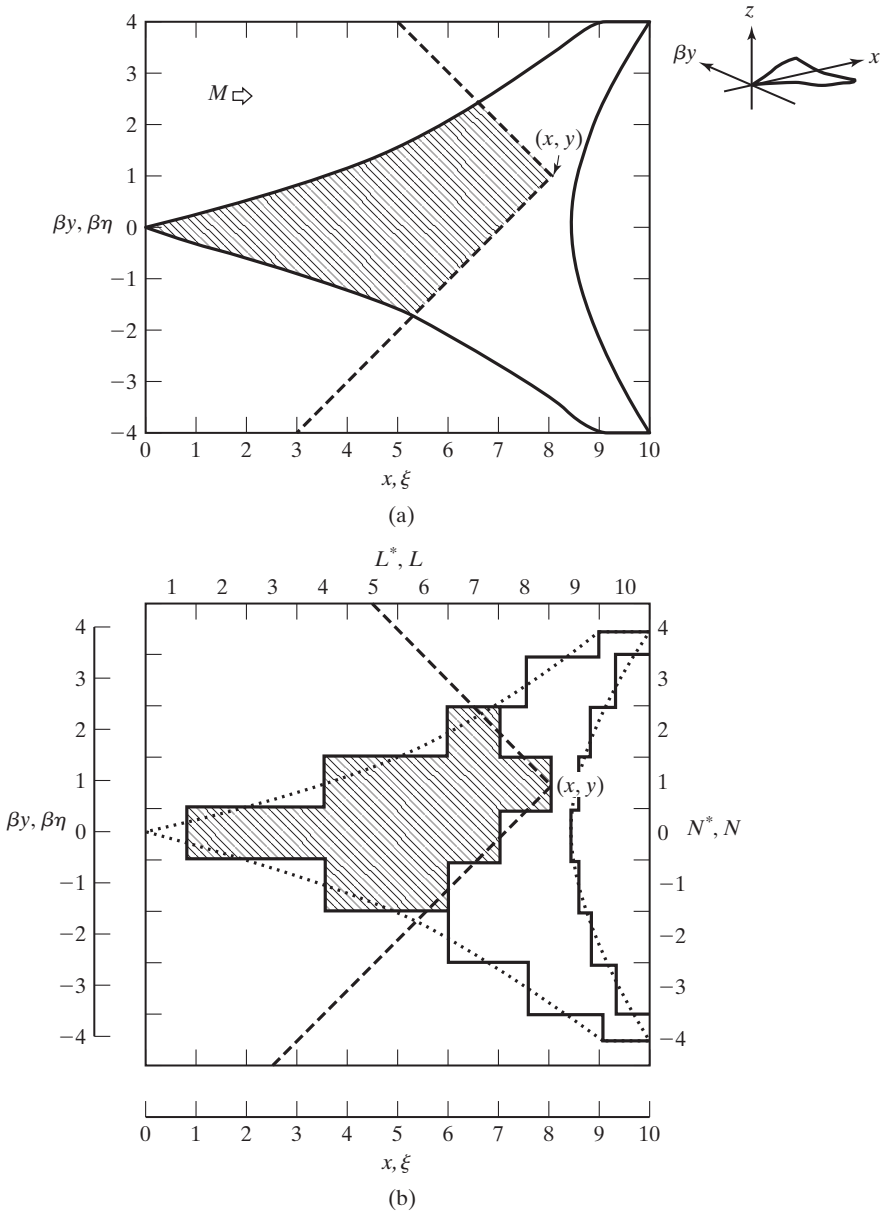

Figure 11.26 Coordinate systems for the linearized, supersonic vortex lattice method: (a) Cartesian coordinate system; (b) grid system used in numerical solution.

bounded by the leading edge and the forecone Mach lines from $(x, \beta y)$, is now approximated by the grid elements within the Mach forecone emanating from $(x, \beta y)$. Note that in the $(x, \beta y)$ coordinate system, the Mach cone half-angle is always 45°.

The summation approximation to equation (11.28) then becomes

$$\Delta C_p(L^*, N^*) = -\frac{4}{\beta}\frac{\partial z_c(L^*, N^*)}{\partial x} + \frac{1}{\pi}\sum_{N_{\min}}^{N_{\max}} \sum_{L_{LE}}^{L^*-|N^*-N|} \overline{R}(L^* - L, N^* - N)A(L, N)B(L, N)C(L, N)\Delta C_p(L, N) \quad \textbf{(11.29)}$$

where $\overline{R}$ is the average value of R within an element and is given by

$$\overline{R}(L^* - L, N^* - N) = \frac{[(L^* - L + 0.5)^2 - (N^* - N - 0.5)^2]^{0.5}}{(L^* - L + 0.5)(N^* - N - 0.5)} - \frac{[(L^* - L + 0.5)^2 - (N^* - N + 0.5)^2]^{0.5}}{(L^* - L + 0.5)(N^* - N + 0.5)} \quad \textbf{(11.30)}$$

A graphical representation of this factor is presented in Fig. 11.27. You should notice the relatively small variations of the factor in the x (or L) direction contrasted with the larger variations in the y (or N) direction. For a given $L^* - L$ set of elements, the spanwise summation of the $\overline{R}$ values is found to be zero, due to the single negative value at $N^* - N = 0$ balancing all the others. At $L^* - L = 0$, where there is only one element in the spanwise summation, the $\overline{R}$ value of that element is zero. This fact ensures that an element will have no influence on itself. Furthermore, the fact that the spanwise summation of the $\overline{R}$ values is found to be zero ensures that the complete wing will produce a flow field which consists of equal amounts of upwash and of downwash and, therefore, introduces no net vertical displacements of the medium through which it is moving.

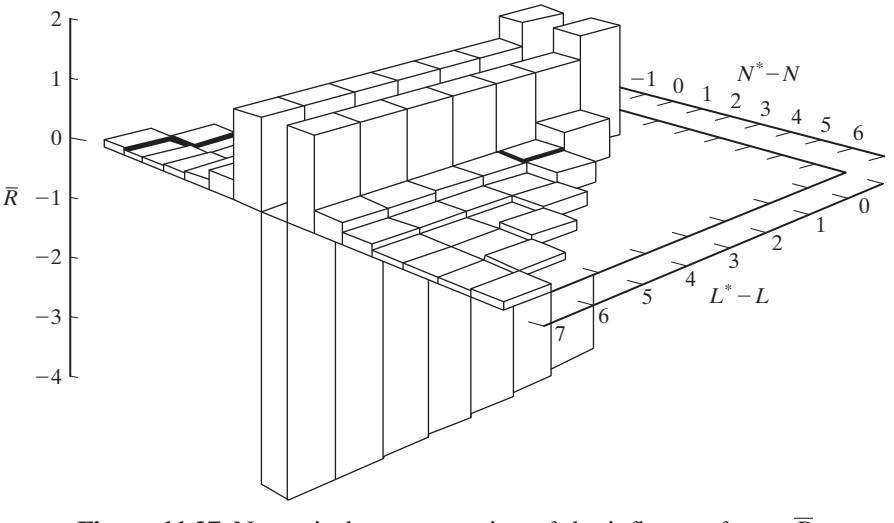

Figure 11.27 Numerical representation of the influence factor $\overline{R}$ (the $\overline{R}$ function).

The limits on L in the summation of equation (11.29) are those of the wing leading edge (i.e., $L_{LE} = 1 + [x_{LE}]$, where $[x_{LE}]$ designates the whole-number part of the quantity) and of the Mach forecone at the selected N value. The vertical lines are used in $|N^* - N|$ to designate the absolute value of the enclosed quantity.

The factor $A(L, N)$ is a weighting factor which allows consideration of partial elements in the summation process and permits a better definition of the wing leading-edge shape. The factor $A(L, N)$ takes on values from 0 to 1, as given by

$$\begin{aligned} A(L,N) &= 0 && L - x_{LE} \le 0 \\ A(L,N) &= L - x_{LE} && 0 < L - x_{LE} < 1 \\ A(L,N) &= 1 && L - x_{LE} \ge 1 \end{aligned}$$

The factor $B(L, N)$ is a weighting factor for the wing trailing-edge shape, which also takes on values from 0 to 1, as given by

$$\begin{aligned} B(L,N) &= 0 && L - x_{TE} \ge 1 \\ B(L,N) &= 1 - (L - x_{TE}) && 0 < L - x_{TE} < 1 \\ B(L,N) &= 1 && L - x_{TE} \le 0 \end{aligned}$$

The factor $C(L, N)$ is a weighting factor for elements at the wing tip, which takes on values either of 0.5 or of 1.0, as given by

$$\begin{aligned} C(L,N) &= 0.5 && N = N_{max} \\ C(L,N) &= 1 && N \ne N_{max} \end{aligned}$$

The differential, or lifting, pressure coefficient at a field point $\Delta C_p(L^*, N^*)$ can be determined for a wing of arbitrary surface shape provided the calculations are carried out in the proper sequence. The order of calculating $\Delta C_p(L^*, N^*)$ is from the apex rearward (i.e., increasing values of L^*). If this sequence is followed, at no time will there be an unknown $\Delta C_p(L, N)$ in the summation in equation (11.29), since the pressure coefficients for all of the points within the Mach fore cone originating at the field point (L^*, N^*) will have been already computed. Note that an element has no influence on itself since $\overline{R}(0, 0) = 0$ from equation (11.30). So, $\Delta C_p(L = L^*, N = N^*)$ is not required in the summation term of equation (11.29). Also, notice that equation (11.29) is the summation to approximate what was originally an integral equation [see Lomax et al. (1951)] and thus already accounts for the flow tangency boundary condition, equation (11.21). This condition is satisfied exactly only at control points located at the midspan of the trailing edge of each grid element (see Fig. 11.28b).

The $\Delta C_p(L^*, N^*)$ given by equation (11.29) is defined at the trailing edge of the (L^*, N^*) element. To eliminate large oscillations in the pressure coefficient which can occur with this numerical technique, a smoothing operation is required. The procedure, taken directly from Carlson and Miller (1974), is as follows:

- Calculate and retain, temporarily, the preliminary ΔC_p values for a given row, with $L^* =$ constant. Designate this as $\Delta C_{p,a}(L^*, N^*)$.
- Calculate and retain, temporarily, ΔC_p values for the following row with $L^* =$ constant + 1, by using the $\Delta C_{p,a}$ values obtained in the previous step for contributions from the row with $L^* =$ constant. Designate this as $\Delta C_{p,b}(L^*, N^*)$.

- Calculate a final ΔC_p value from a fairing of integrated preliminary ΔC_p results.

For leading-edge elements, defined as $L^* - x_{\mathrm{LE}}(N^*) \leq 1$,

$$\Delta C_p(L^*, N^*) = \frac{1}{2}\left[1 + \frac{A(L^*, N^*)}{1 + A(L^*, N^*)}\right] \Delta C_{p,a}(L^*, N^*) + \frac{1}{2}\left[\frac{A(L^*, N^*)}{1 + A(L^*, N^*)}\right] \Delta C_{p,b}(L^*, N^*) \tag{11.31}$$

For all other elements, defined as $L^* - x_{\mathrm{LE}}(N^*) > 1$,

$$\Delta C_p(L^*, N^*) = \tfrac{3}{4}\Delta C_{p,a}(L^*, N^*) + \tfrac{1}{4}\Delta C_{p,b}(L^*, N^*) \tag{11.32}$$

where

$$A(L^*, N^*) = A(L, N)$$

The nomenclature $A(L^*, N^*)$ is used here to be consistent with that of Carlson and Miller (1974). Note: there is an error in Carlson and Miller (1974) for equation (11.31); the formulation given here is correct [see Carlson and Mack (1978)].

EXAMPLE 11.3: Calculate the pressure distribution for a flat-plate delta wing planform

To illustrate the method, let us show how to calculate manually the pressure distribution at $M_\infty = 1.5$ for the flat-plate (zero-camber) delta planform of Fig. 11.28a for the subsonic leading edge case where $\beta \cot \Lambda_{\mathrm{LE}} = 0.6$. We will use the grid element set shown in Fig. 11.28a in order to keep the number of manual calculations within bounds. In an actual application, of course, we would use a much larger number of elements. Note that in Fig. 11.28a we use some partial elements along the leading and the trailing edges. Since ΔC_p is treated as a constant over a given element, partial elements affect only the reference area used when integrating the pressures to calculate the lift coefficient, the drag-due-to-lift coefficient, etc.

Solution: For this case, the wing is assumed to have negligible thickness and is assumed to lie approximately in the $z = 0$ plane. The wing streamwise slope $[\partial z_c(x, y)/\partial x]$ is a constant for the flat plate at incidence and is equal to the negative of the tangent of the wing angle of attack

$$\frac{\partial z_c(x, y)}{x} = \frac{dz_c}{dx} = -\tan \alpha \approx -\alpha$$

since, even here, we are still restricting ourselves to linear theory, which implies that all changes in flow direction about the free-stream direction are small.

For this case, where the free-stream Mach number is 1.5:

$$\beta \equiv \sqrt{M_\infty^2 - 1} = 1.118$$

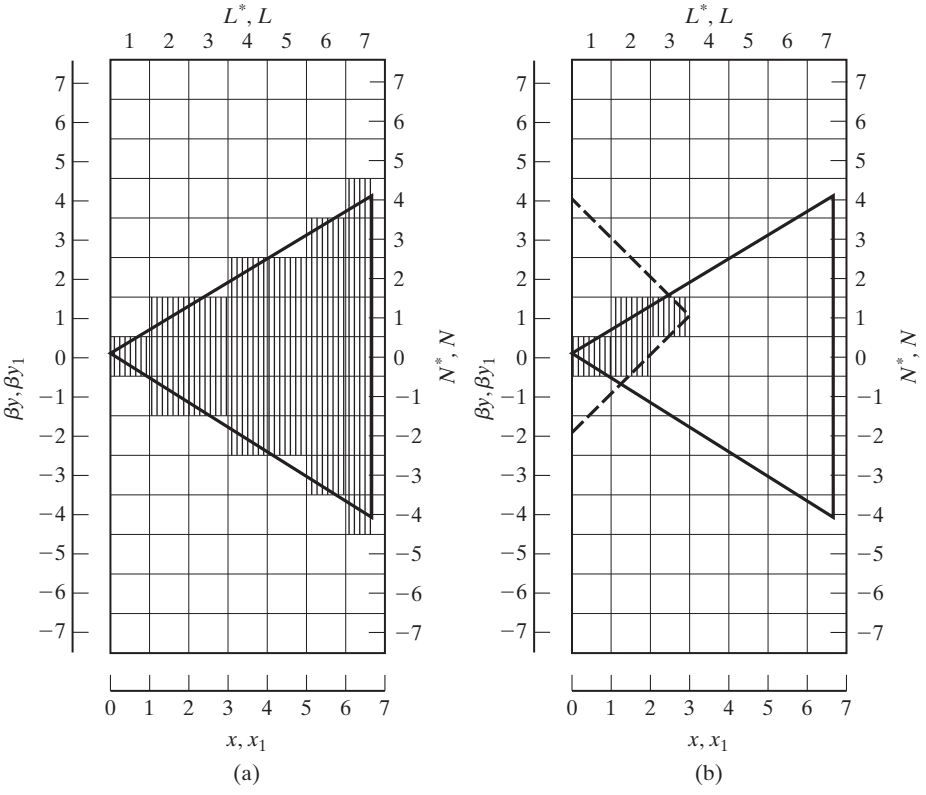

Figure 11.28 Grid element geometry for the supersonic vortex latice method: (a) general pattern; (b) region of integration for element (3, 1) of Example 11.3.

Therefore, the leading-edge sweepback angle corresponding to $\beta \cot \Lambda_{LE} = 0.6$ is 61.78°. Thus, when the transformation is made from the (x, y) to the $(x, \beta y)$ plane, the angle that the leading edge makes with the βy axis is 59.04°. This is shown in Fig. 11.28a along with the grid system.

The equation of the wing leading and trailing edges in the $(x, \beta y)$ system is

$$x_{LE} = \frac{\beta |y|}{0.6} \qquad x_{TE} = \frac{N_{max}}{\beta \cot \Lambda_{LE}} = 6.6667$$

Note that the value of x_{TE} is defined by selection of a maximum N value, N_{max}. For the purposes of this example, we arbitrarily select $N_{max} = 4$. The wing is then scaled to give a semispan of N_{max}. This ensures that the weighting factor $C(L, N) = 0.5$ for $N = N_{max}$ is appropriate. This is important for streamwise tips of nonzero chord. Using this and the relationships defining $A(L, N)$, $B(L, N)$, and $C(L, N)$, we have the following:

$A(L, N)$

N \ L	1	2	3	4	5	6	7
0	1.0000	1.0000	1.0000	1.0000	1.0000	1.0000	1.0000
±1	0.0000	0.3333	1.0000	1.0000	1.0000	1.0000	1.0000
±2	0.0000	0.0000	0.0000	0.6667	1.0000	1.0000	1.0000
±3	0.0000	0.0000	0.0000	0.0000	0.0000	1.0000	1.0000
±4	0.0000	0.0000	0.0000	0.0000	0.0000	0.0000	0.3333

$B(L, N)$:

$$B(7, N) = 0.6667$$

$$B(L, N) = 1 \qquad \text{for all other grid elements}$$

$C(L, N)$:

$$C(7, \pm 4) = 0.5$$

$$C(L, N) = 1 \qquad \text{for all other grid elements}$$

We now proceed to calculate values of ΔC_p for several grid elements to show the technique. We begin at the apex with element (1, 0).

Element (1, 0).

For this element, $L^* = 1, N^* = 0$, and there are no other elements which contribute to the differential pressure coefficient at this element. Therefore,

$$\Delta C_{p,a}(1, 0) = \frac{4\alpha}{\beta}$$

To determine $\Delta C_p(1, 0)$, we must calculate a preliminary value $\Delta C_{p,b}(1, 0)$. This involves consideration of the element at (2, 0). The only element contributing to the pressure differential at (2, 0) is the one at (1, 0). Thus,

$$\Delta C_{p,b}(1, 0) = \frac{4\alpha}{\beta} + \frac{1}{\pi}\left\{\frac{[(2 - 1 + 0.5)^2 - (0 - 0 - 0.5)^2]^{0.5}}{(2 - 1 + 0.5)(0 - 0 - 0.5)} - \frac{[(2 - 1 + 0.5)^2 - (0 - 0 + 0.5)^2]^{0.5}}{(2 - 1 + 0.5)(0 - 0 + 0.5)}\right\}\frac{4\alpha}{\beta}$$

or

$$\Delta C_{p,b}(1, 0) = \frac{4\alpha}{\beta}(1 - 1.2004) = -0.8016\frac{\alpha}{\beta}$$

Therefore,

$$\Delta C_p(1, 0) = \frac{1}{2}\left(1 + \frac{1}{1 + 1}\right)\frac{4\alpha}{\beta} + \frac{1}{2}\left(\frac{1}{1 + 1}\right)(-0.8016)\frac{\alpha}{\beta}$$

or

$$\Delta C_p(1,0) = 2.7996\,\frac{\alpha}{\beta}$$

Element (2, 0).

For this element, $L^* = 2, N^* = 0$, and the only element that contributes to the differential pressure coefficient at this element is the one at (1, 0). Thus,

$$\Delta C_{p,a}(2,0) = 4\frac{\alpha}{\beta} + \frac{1}{\pi}\left\{\frac{[(2-1+0.5)^2 - (0-0-0.5)^2]^{0.5}}{(2-1+0.5)(0-0+0.5)} - \frac{[(2-1+0.5)^2 - (0-0+0.5)^2]^{0.5}}{(2-1+0.5)(0-0+0.5)}\right\}2.7996\,\frac{\alpha}{\beta}$$

or

$$\Delta C_{p,a}(2,0) = 0.6393\,\frac{\alpha}{\beta}$$

To determine $\Delta C_p(2,0)$, we must calculate a preliminary value $\Delta C_{p,b}(2,0)$. This involves consideration of the element at (3, 0). But we note that elements at (1, 0), (2, 0), (2, 1), and (2, −1) contribute to the differential pressure at (3, 0). Thus, we must go ahead and find $\Delta C_{p,a}(2,1)$ and $\Delta C_{p,a}(2,-1)$. These, of course, are equal from symmetry.

The only element influencing the element at (2, 1) is the one at (1, 0). Thus,

$$\Delta C_{p,a}(2,1) = \frac{4\alpha}{\beta} + \frac{1}{\pi}\left\{\frac{[(2-1+0.5)^2 - (1-0-0.5)^2]^{0.5}}{(2-1+0.5)(1-0-0.5)} - \frac{[(2-1+0.5)^2 - (1-0+0.5)^2]^{0.5}}{(2-1+0.5)(1-0+0.5)}\right\}2.7996\,\frac{\alpha}{\beta}$$

or

$$\Delta C_{p,a}(2,1) = 5.6804\,\frac{\alpha}{\beta} = \Delta C_{p,a}(2,-1)$$

Therefore,

$$\Delta C_{p,b}(2,0) = \frac{4\alpha}{\beta} + \frac{1}{\pi}\left\{\frac{[(3-1+0.5)^2 - (0-0-0.5)^2]^{0.5}}{(3-1+0.5)(0-0-0.5)} - \frac{[(3-1+0.5)^2 - (0-0+0.5)^2]^{0.5}}{(3-1+0.5)(0-0+0.5)}\right\}2.7996\,\frac{\alpha}{\beta} + \frac{1}{\pi}\left\{\frac{[(3-2+0.5)^2 - (0-0-0.5)^2]^{0.5}}{(3-2+0.5)(0-0-0.5)} - \frac{[(3-2+0.5)^2 - (0-0+0.5)^2]^{0.5}}{(3-2+0.5)(0-0+0.5)}\right\}0.6393\,\frac{\alpha}{\beta}$$

$$+\frac{2}{\pi}\left\{\frac{[(3-2+0.5)^2-(0-1-0.5)^2]^{0.5}}{(3-2+0.5)(0-1-0.5)}\right.$$

$$\left.-\frac{[(3-2+0.5)^2-(0-1+0.5)^2]^{0.5}}{(3-2+0.5)(0-1+0.5)}\right\}(0.3333)(5.6804)\frac{\alpha}{\beta}$$

where the factor of 2 in front of the last bracketed term accounts for the fact that elements (2, 1) and (2, −1) have an equal influence on element (3, 0).

Thus,

$$\Delta C_{p,b}(2,0) = 2.0128\frac{\alpha}{\beta}$$

Finally,

$$\Delta C_p(2,0) = \frac{3}{4}(0.6393)\frac{\alpha}{\beta}+\frac{1}{4}(2.0128)\frac{\alpha}{\beta}$$

or

$$\Delta C_p(2,0) = 0.9827\frac{\alpha}{\beta}$$

Element (2, 1).

For this element, $L^* = 2, N^* = 1$, and the only element that contributes to the differential pressure coefficient at this element is the one at (1, 0). As shown previously,

$$\Delta C_{p,a}(2,1) = \frac{4\alpha}{\beta}+\frac{1}{\pi}\left\{\frac{[(2-1+0.5)^2-(1-0-0.5)^2]^{0.5}}{(2-1+0.5)(1-0-0.5)}\right.$$

$$\left.-\frac{[(2-1+0.5)^2-(1-0+0.5)^2]^{0.5}}{(2-1+0.5)(1-0+0.5)}\right\}2.7996\frac{\alpha}{\beta}$$

or

$$\Delta C_{p,a}(2,1) = 5.6804\frac{\alpha}{\beta}$$

To determine $\Delta C_p(2,1)$, we must calculate a preliminary value $\Delta C_{p,b}(2,1)$. This involves consideration of the element at (3, 1). We should note, however, that elements at (1, 0), (2, 0), and (2, 1) contribute to the differential pressure at (3, 1), so:

$$\Delta C_{p,b}(2,1) = \frac{4\alpha}{\beta}+\frac{1}{\pi}\left\{\frac{[(3-1+0.5)^2-(1-0-0.5)^2]^{0.5}}{(3-1+0.5)(1-0-0.5)}\right.$$

$$\left.-\frac{[(3-1+0.5)^2-(1-0+0.5)^2]^{0.5}}{(3-1+0.5)(1-0+0.5)}\right\}2.7996\frac{\alpha}{\beta}$$

$$+\frac{1}{\pi}\left\{\frac{[(3-2+0.5)^2-(1-0-0.5)^2]^{0.5}}{(3-2+0.5)(1-0-0.5)}\right.$$

$$- \frac{[(3 - 2 + 0.5)^2 - (1 - 0 + 0.5)^2]^{0.5}}{(3 - 2 + 0.5)(1 - 0 + 0.5)}\Bigg\}0.6393\frac{\alpha}{\beta}$$

$$+ \frac{1}{\pi}\Bigg\{\frac{[(3 - 2 + 0.5)^2 - (1 - 1 - 0.5)^2]^{0.5}}{(3 - 2 + 0.5)(1 - 1 - 0.5)}$$

$$- \frac{[(3 - 2 + 0.5)^2 - (1 - 1 + 0.5)^2]^{0.5}}{(3 - 2 + 0.5)(1 - 1 + 0.5)}\Bigg\}(0.3333)(5.6804)\frac{\alpha}{\beta}$$

or

$$\Delta C_{p,b}(2, 1) = 3.3820\frac{\alpha}{\beta}$$

Notice that we use preliminary (i.e., $\Delta C_{p,a}$) values for the ΔC_p's of influencing elements in the same "L" row as the field-point element under consideration. We have used $\Delta C_{p,a}(2, 0) = 0.6393$ instead of $\Delta C_p(2, 0) = 0.9827$ as the factor of the second major bracketed term in the preceding equation. As an alternative procedure, we could have used ΔC_p instead of $\Delta C_{p,a}$ but we have chosen to be consistent with the method of Carlson and Miller (1974). For influencing elements not in the same "L" row as the field-point element, we use the final (i.e., averaged ΔC_p values) as given by equations (11.31) and (11.32).

Finally,

$$\Delta C_p(2, 1) = \frac{1}{2}\left(1 + \frac{0.3333}{1 + 0.3333}\right)5.6804\frac{\alpha}{\beta} + \frac{1}{2}\left(\frac{0.3333}{1 + 0.3333}\right)3.3820\frac{\alpha}{\beta}$$

or

$$\Delta C_p(2, 1) = 3.9730\frac{\alpha}{\beta} = \Delta C_p(2, -1)$$

from symmetry.

We have now calculated the differential pressure coefficients for elements (1, 0), (2, 0), and (2, ± 1). We can continue in this manner and determine ΔC_p for the remaining elements. Typical numerical results for this case at three chordwise stations are presented in Fig. 11.29. The number of grid elements used in Fig. 11.29 is approximately 2000.

Lifting-pressure distributions for a flat-plate delta wing ($\beta \cot \Lambda_{LE} = 1.20$) as computed by Middleton and Carlson (1965) are reproduced in Fig. 11.30. Agreement between the numerical and analytical solutions is quite good, although the numerical solution does not exhibit the sharp break at the Mach line that is characteristic of the analytical solution. The unevenness of the pressure coefficients observed in the subsonic leading-edge case does not occur because of the reduced effect of the averaging techniques with the less severe variations in the pressure near the leading edge. Fig. 11.31

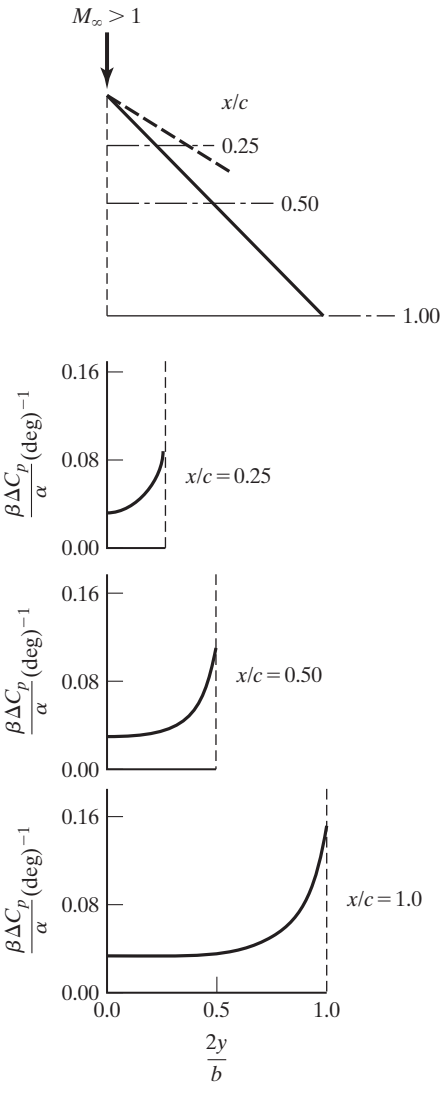

Figure 11.29 Numerical results for a flat-plate delta planform ($\beta \cot \Lambda_{LE} = 0.6$) [from Carlson and Miller (1974)].

shows a comparison of the numerical results with those of exact linear theory for flat delta planforms such as the one used in Example 11.3.

Notice that the numerical method is also applicable to wings of arbitrary camber and planform (e.g., supersonic or subsonic leading and/or trailing edges, etc.). To accommodate non-zero camber, we only need to specify $\partial z_c(x, y)/\partial x$ in equation (11.29). A companion numerical method, also described in Carlson and Miller (1974), provides a means for the design of a camber surface corresponding to a specified loading distribution or to an optimum combination of loading distributions.

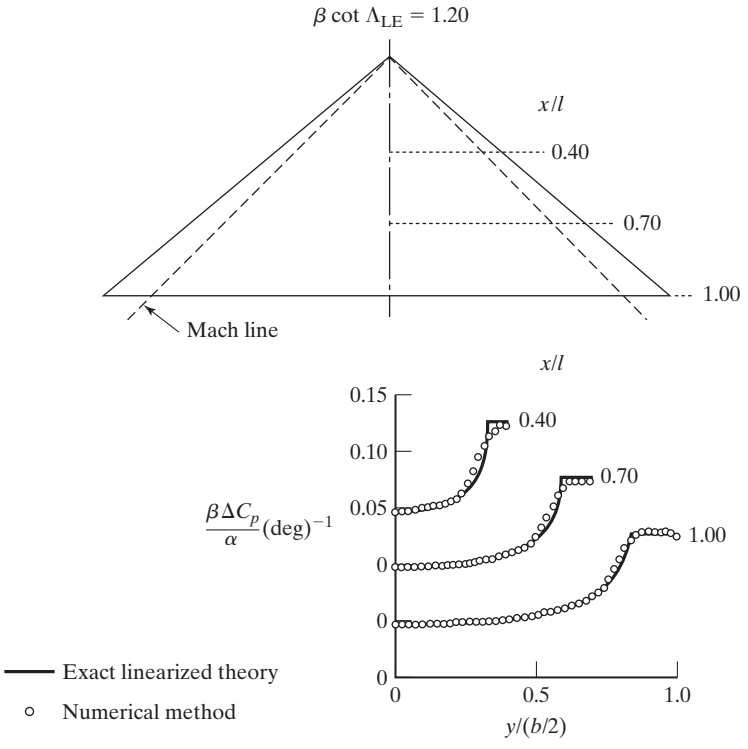

Figure 11.30 Lifting-pressure distributions for a flat-plate delta wing with a supersonic leading edge. $N_{max} = 50$ [from Middleton and Carlson (1965)].

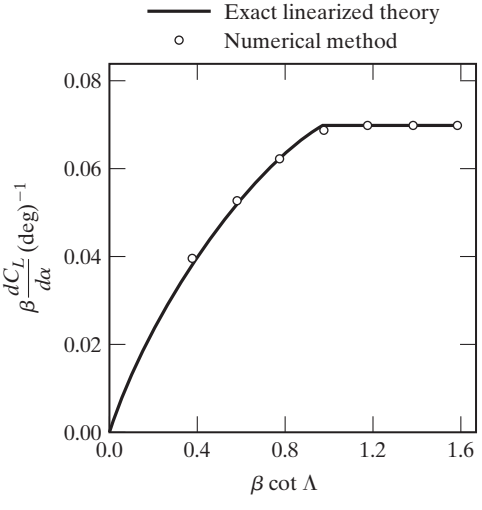

Figure 11.31 Comparison of linear theory with vortex lattice results for a delta wing [from Carlson and Miller (1974)].

Once the lifting pressure coefficients, ΔC_p, have been determined for all the elements, it is possible to compute the aerodynamic coefficients for the wing. The lift coefficient for symmetric loads may be obtained from the following summation over all the elements:

$$C_L = \frac{2}{\beta S} \sum_{N^*=0}^{N^*=N_{\max}} \sum_{L^*=L_{\mathrm{LE}}}^{L^*=L_{\mathrm{TE}}} \left[\frac{3}{4} \Delta C_p(L^*, N^*) + \frac{1}{4} \Delta C_p(L^* + 1, N^*) \right] A(L^*, N^*) B(L^*, N^*) C(L^*, N^*) \tag{11.33}$$

The pitch moment coefficient about $x = 0$ is

$$C_M = \frac{2}{\beta S \bar{c}} \sum_{N^*=0}^{N^*=N_{\max}} \sum_{L^*=L_{\mathrm{LE}}}^{L^*=L_{\mathrm{TE}}} (L^*) \left[\frac{3}{4} \Delta C_p(L^*, N^*) + \frac{1}{4} \Delta C_p(L^* + 1, N^*) \right] A(L^*, N^*) B(L^*, N^*) C(L^*, N^*) \tag{11.34}$$

The drag coefficient may be expressed as

$$C_D = -\frac{2}{\beta S} \sum_{N^*=0}^{N^*=N_{\max}} \sum_{L^*=L_{\mathrm{LE}}}^{L^*=L_{\mathrm{TE}}} \left[\frac{3}{4} \Delta C_p(L^*, N^*) + \frac{1}{4} \Delta C_p(L^* + 1, N^*) \right] \left[\frac{3}{4} \frac{\partial z_c(L^*, N^*)}{x} + \frac{1}{4} \frac{\partial z_c(L^* + 1, N^*)}{x} \right] A(L^*, N^*) B(L^*, N^*) C(L^*, N^*) \tag{11.35}$$

This relationship does not consider any contribution of the theoretical leading-edge-suction force or of any separated flow effects associated with its exclusion and accounts only for the inclination of the normal force to the relative wind.

The leading-edge field-point-element weighting factor takes on values from 0 to 1.5, and are defined as follows:

$$\begin{aligned} A(L^*, N^*) &= 0 && (L^* - x_{\mathrm{LE}} \leq 0) \\ A(L^*, N^*) &= L^* - x_{\mathrm{LE}} + 0.5 && (0 < L^* - x_{\mathrm{LE}} < 1) \\ A(L^*, N^*) &= 1 && (L^* - x_{\mathrm{LE}} \geq 1) \end{aligned}$$

The trailing-edge field-point-element weighting factor also takes on values from 0 to 1.5.

$$\begin{aligned} B(L^*, N^*) &= 0 && (L^* - x_{\mathrm{TE}} \geq 0) \\ B(L^*, N^*) &= 0.5 - (L^* - x_{\mathrm{TE}}) && (0 > L^* - x_{\mathrm{TE}} - 1) \\ B(L^*, N^*) &= 1 && (L^* - x_{\mathrm{TE}} \leq -1) \end{aligned}$$

The centerline or wingtip grid element weighting factor is defined as

$$\begin{aligned} C(L^*, N^*) &= 0.5 && (N^* = 0) \\ C(L^*, N^*) &= 1 && (0 < N^* < N_{\max}) \\ C(L^*, N^*) &= 0.5 && (N^* = N_{\max}) \end{aligned}$$

The wing area used in the expressions for the aerodynamic coefficients may be computed using the summation

$$S = \frac{2}{\beta} \sum_{N^*=0}^{N^*=N_{\max}} \sum_{L^*=1+[x_{LE}]}^{L^*=1+[x_{TE}]} A(L^*, N^*) B(L^*, N^*) C(L^*, N^*) \tag{11.36}$$

11.7.3 Numerical Method for the Determination of Camber Distribution

Equation (11.28) can be rearranged

$$\frac{\partial z_c(x, y)}{\partial x} = -\frac{\beta}{4} \Delta C_p(x, y) + \frac{\beta}{4\pi} \iint \overline{R}(x - x_1, y - y_1) \Delta C_p(x_1, y_1) d\beta y_1 \, dx_1 \tag{11.37}$$

Equation (11.37) can be used to determine the wing surface shape necessary to support a specified lift distribution.

When discussing the numerical representation of the influence factor $\overline{R}$, as presented in Fig. 11.27, Middleton and Lundry (1980) commented, "The physical significance of this $\overline{R}$ variation is that (for positive lift), all elements directly ahead of the field point element contribute only downwash and all other elements contribute upwash. An element at the leading edge near the wing tip of a subsonic leading-edge wing, therefore, sees a concentrated upwash field. It is this upwash field that makes the subsonic leading edge twisted and cambered wing attractive from the standpoint of drag-due-to-lift, since a local element may be inclined forward to produce both lift and thrust."

So, significantly better wing performance can be achieved through the generation of leading-edge thrust. This thrust occurs when the leading edge is subsonic (i.e., when the product $\beta \cot \Lambda_{LE}$ is less than one) and is caused by the flow around the leading edge from a stagnation point on the windward, lower surface. In the case of a cambered wing, the thrust contributes both to the axial force and to the normal force.

Carlson and Mann (1992) recommend a suction parameter for rating the aerodynamic performance of various wing designs. The suction parameter is defined by the parameter S_s:

$$S_s = \frac{C_L \tan(C_L/C_{L\alpha}) - (C_D - C_{D0})}{C_L \tan(C_L/C_{L\alpha}) - C_L^2/\pi AR} \tag{11.38}$$

The term in the numerator $(C_D - C_{D0})$ equals ΔC_D, the drag coefficient due-to-lift. The factor $C_{L\alpha}$ in equation (11.38) represents the theoretical lift-curve slope at $\alpha = 0°$. Limits for the suction parameter can be evaluated using the sketches of the drag polar presented in Fig. 11.32. The lower bound for the suction parameter (i.e., $S_s = 0$) corresponds to the upper drag polar, where $C_D = C_{D0} + C_L \tan(C_L/C_{L\alpha})$. The drag coefficient for this limit is that for a flat wing with no leading-edge thrust and no vortex forces. The upper bound for the suction parameter (i.e., $S_s = 1$) corresponds to the lower drag polar, where $C_D = C_{D0} + C_L^2/(\pi AR)$. The drag coefficient for this limit is the drag for a wing with an elliptical span-load distribution (a uniform downwash)

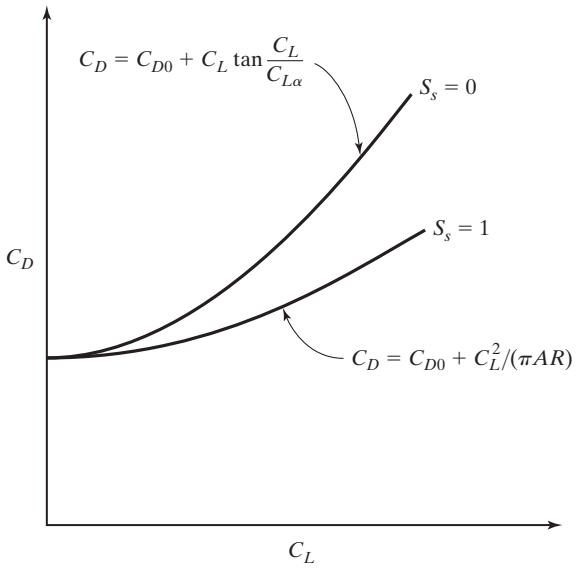

Figure 11.32 The relation between the suction parameter (S_s) and the drag polar [from Carlson and Mann (1992)].

and the full amount of any leading-edge thrust that might be required. This limit is a carryover from subsonic flows, where the limit is reasonably achievable. There is no contribution representing the supersonic wave-drag-due-to-lift. In practice, the presence of wave-drag-due-to-lift at supersonic speeds prevents a close approach to this value. However, the simplicity of the expression and its repeatability make it a logical choice for use in the suction parameter.

Experience has shown that the maximum suction parameters actually achieved were lower than those predicted by linearized theory. Furthermore, the required surface for given design conditions was less severe (smaller departures from a flat surface) than that given by the linearized-theory design methods. Carlson and Mann (1992) suggest a design method which employs two empirical factors: K_D (a design lift-coefficient factor) and K_s (a suction parameter factor). The design factor K_D, which is presented in Fig. 11.33a, provides a design lift coefficient for use in the theoretical wing design to replace the actual operational, or cruise, lift coefficient. Thus, for the selected design Mach number, the design lift-coefficient factor is taken from Fig. 11.33a and used to define the design lift coefficient as:

$$C_{L,\text{des}} = K_D C_{L,\text{cruise}} \tag{11.39}$$

The design lift coefficient is used in the computer code definition of the lifting surface and of the theoretical performance, including $(S_{s,\max})_{\text{th}}$. Next, the appropriate value of K_s is taken from Fig. 11.33b, so that one can estimate the magnitude of the suction parameter that can actually be achieved:

$$S_{s,\text{cruise}} = K_s (S_{s,\max})_{\text{th}} \tag{11.40}$$

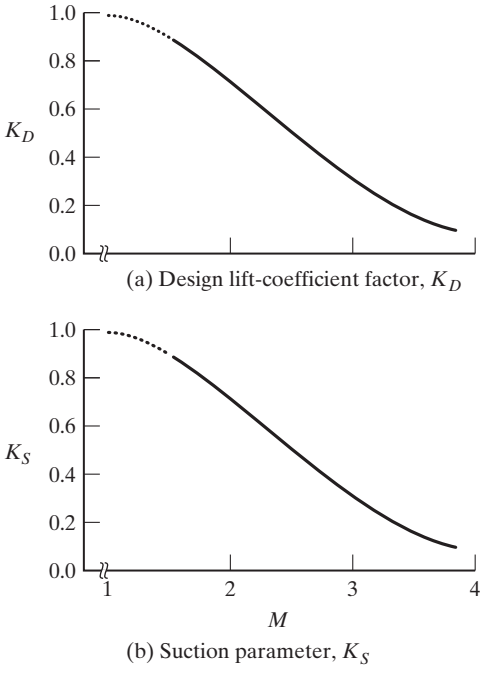

Figure 11.33 Empirical method factors used to select the optimum design lift coefficients and to predict achievable suction parameters [from Carlson and Mann (1992)].

As noted by Carlson and Mann (1992), the code value of $(S_{s,\max})_{\text{th}}$ for $C_{L,\text{des}}$ is used in this expression even though $C_{L,\text{des}}$ differs from $C_{L,\text{cruise}}$. This approximation is acceptable, since for a wing-design family of various $C_{L,\text{des}}$ values, there is very little change in the value of $S_{s,\max}$.

The drag coefficient at the cruise lift coefficient can be estimated using the expression

$$C_{D,\text{cruise}} = C_{D0} + \frac{(C_{L,\text{cruise}})^2}{\pi AR} + (1 - S_{s,\text{cruise}})\left[C_{L,\text{cruise}} \tan\left(\frac{C_{L,\text{cruise}}}{C_{L\alpha}}\right) - \frac{(C_{L,\text{cruise}})^2}{\pi AR} \right] \qquad \textbf{(11.41)}$$

Mann and Carlson (1994) described a process for designing a supersonic wing for given cruise conditions using Fig. 11.33:

- select the cruise lift coefficient and Mach number.
- Use Fig. 11.33a to obtain the K_D factor and equation (11.39) to calculate $C_{L,\text{des}}$.
- Use a linearized theory computer code to compute the optimum performance surface at $C_{L,\text{des}}$ and to obtain the variation of theoretical suction parameter with C_L.
- This is the wing surface that will give maximum performance at the cruise conditions.
- Estimate the wing performance using Fig. 11.33b to obtain a value for the suction parameter factor K_s. [Note that $S_{s,\max,\text{theory}}$ is the maximum suction parameter for a wing designed for a lift coefficient equal to $C_{L,\text{cruise}}$ (not designed for $C_{L,\text{des}}$)].
- Use Equation (11.40) to obtain an estimate of $S_{s,\text{cruise}}$.

The drag coefficient at the cruise lift coefficient can be estimated by use of equation (11.41).

11.8 DESIGN CONSIDERATIONS FOR SUPERSONIC AIRCRAFT

We have seen that theory predicts highly swept wings (such that the leading edge is subsonic) have the potential for very favorable drag characteristics at supersonic flight speeds. However, experiment has shown that many of the theoretical aerodynamic benefits of leading-edge sweepback are not attained in practice because of separation of the flow over the upper surface of the wing. Elimination of separated flow can only be achieved in design by a careful blending of the effects of leading- and trailing-edge sweepback angles, leading-edge nose radius, camber, twist, body shape, wing/body junction aerodynamics, and wing planform shape and thickness distribution. Theory does not give all the answers here, and various empirical design criteria have been developed to aid in accounting for all of these design variables.

Squire and Stanbrook (1964) and Kulfan and Sigalla (1978) have studied the types of flow around highly swept edges. Sketches of the main types of flow on highly swept wings, as taken from their work, are presented in Fig. 11.34. Based on these investigations, we could classify the types of separation as:

- Leading-edge separation due to high suction pressures
- Separation due to spanwise flow
- Inboard shock separation
- Trailing-edge shock separation

In our analysis of swept wings, we found that the effective angle of attack of the wing was given by equation (11.10) as

$$\alpha_e = \tan^{-1}\frac{\tan \alpha}{\cos \Lambda}$$

for small angles. Thus, for highly swept wings with subsonic leading edges, separation can occur quite readily even for small values of wing angle of attack; this is particularly true if the leading edge is sharp. The observed flow from the leading edge is very similar to that for the delta wing in subsonic flow (see Chapter 7). The coiled vortices that form at the leading edges affect the flow below the wing as well, since the leading edge is subsonic, and therefore the top and bottom surfaces can "communicate."

The phenomenon of spanwise flow on a swept wing has also been discussed in Chapter 7. Spanwise flow results in a thickening of the boundary layer near the wing tips, and a thick boundary layer will separate more readily than a thin one exposed to the same adverse pressure gradient.

Inboard shock separation is primarily a function of the geometry of the wing/body junction near the leading edge of the wing. The upper surface flow in this region is toward the body, and therefore a shock is formed to turn the stream tangent to the body. The strength of the shock is, of course, dependent on the turning angle. If the shock is strong enough, the resulting pressure rise will separate the boundary layer.

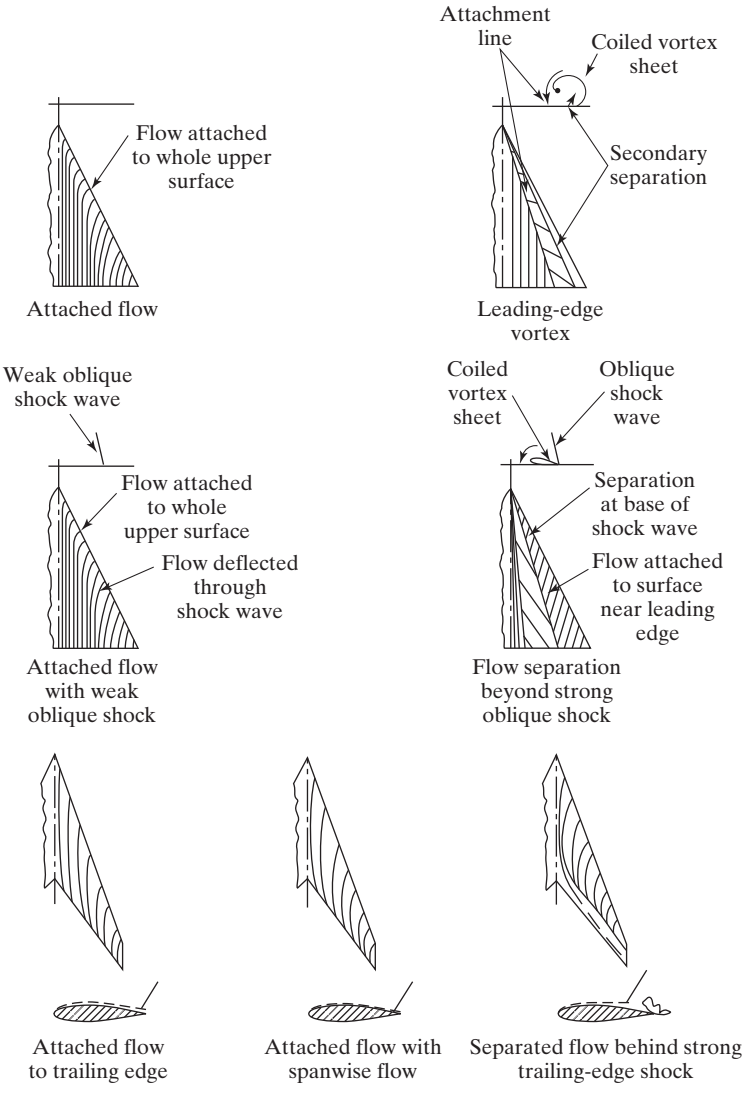

Figure 11.34 Main types of flow on highly swept wings [from Squire and Stanbrook (1964) and Kulfan and Sigalla (1978)].

Trailing-edge shock separation can occur if the wing trailing edge is supersonic (as is the case for delta wings, for example). A shock wave near the trailing edge is required to adjust the upper surface pressure back to the free-stream value. Again, if the required shock strength is too great, it will induce separation of the boundary layer.

The design criteria have been developed to eliminate separation are given in Kulfan and Sigalla (1978) and can be summarized as follows:

- ***Leading-edge separation.*** Reject designs where the theoretical suction pressure exceeds 70% of vacuum pressure.

- ***Separation due to spanwise flow.*** Use thin wing tips. (*Note*: An additional technique is "washout" or a lower section incidence at the wing tips relative to the incidence angles of inboard sections.)
- ***Inboard shock separation.*** Use body contouring to keep the pressure rise across the inboard shock wave to less than 50%.
- ***Trailing-edge shock separation.*** Keep the pressure ratio across the trailing-edge shock below $1 + 0.3M_1^2$, where M_1 is the local Mach number ahead of the shock. For swept trailing edges, use the local normal Mach number ($M_{N1} = M_1 \cos \Lambda_{TE}$) in the preceding equation.

Application of these criteria does not guarantee that the flow will not separate, however, and wind-tunnel tests of proposed designs must be undertaken. This is particularly true for military or sport aircraft designed for maneuvering at high load factors.

Carlson and Mack (1980) note that there are compensatory errors in linearized theory and the failure to account for nonlinearities may introduce little error in prediction of lift and drag. However, significant errors in the prediction of the pitching moment are common, especially for wings that depart from a delta planform. Additionally, for wings with twist and camber, appreciable errors in the prediction of drag due to the surface distortion (camber drag) often occur. In particular, linearized-theory methods do not indicate the proper camber surface for drag minimization (a function of the design lift coefficient). The method of Carlson and Mack (1980), which includes the estimation of nonlinearities associated with leading-edge thrust and the detached leading-edge vortex flow, provides improved prediction over linearized theory, as illustrated by the correlations reproduced in Fig. 11.35. You should refer to Section 13.3 for more information on the design of tactical aircraft.

11.9 SOME COMMENTS ABOUT THE DESIGN OF THE SST AND OF THE HSCT

11.9.1 The Supersonic Transport (SST), the Concorde

In an excellent review of the aerodynamic design of the Supersonic Transport, Wilde and Cormery (1970) reviewed the general design features of the Concorde. "From the beginning, Concorde was conceived to achieve the following overall objectives:

- the required level of performance on the long range North Atlantic mission, which requires the achievement of good lift/drag ratios at subsonic and supersonic conditions,
- good takeoff and landing characteristics, making full use of the very powerful ground effect,
- good flying qualities throughout the speed range by purely aerodynamic means, using artificial stability augmentation only to improve the crew workload, and
- operation without stall or buffet up to lift coefficients above those required for airworthiness demonstration purposes."

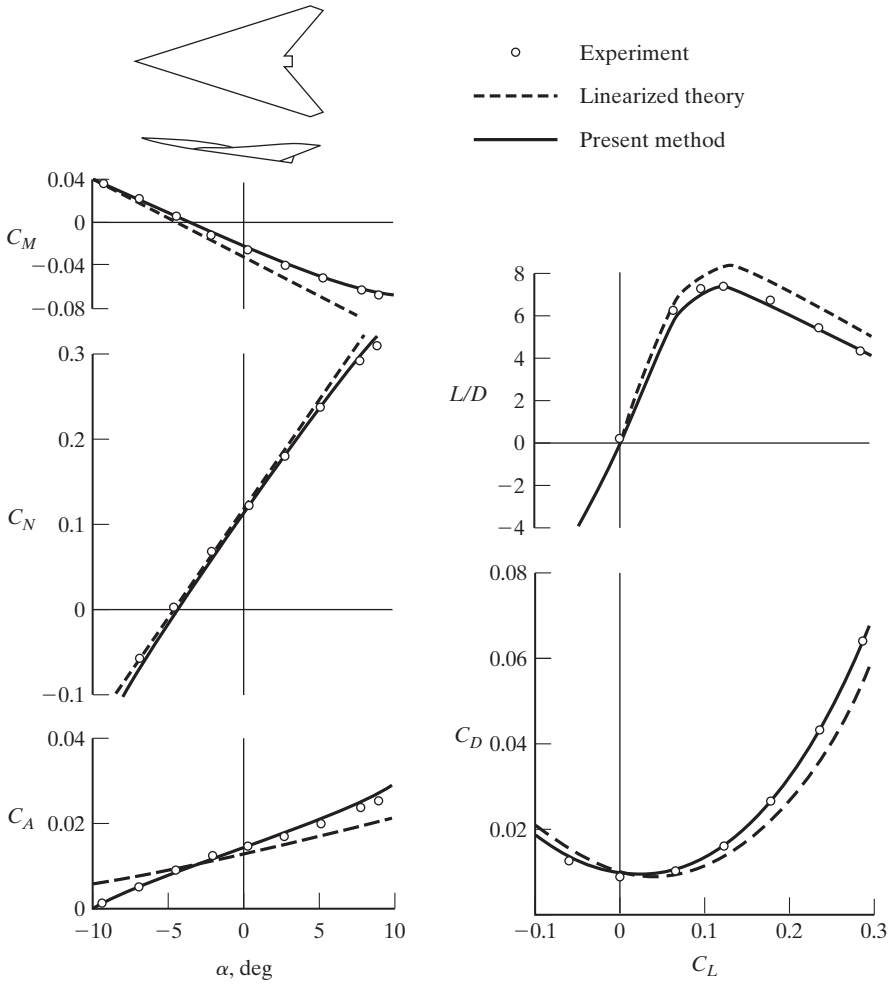

Figure 11.35 Comparison of the predicted and the measured forces and moments for 72.65° swept leading-edge arrow wing; $M_\infty = 2.6$; design value of $C_L = 0.12$ [from Carlson and Mack (1980)].

To achieve these objectives, it was understood "that:

- the wing, fuselage, and nacelles are aerodynamically interdependent,
- the aerodynamic design of the wing must be integrated with the requirements of the structures, systems and production engineers,
- no single speed can be taken as the design speed; supersonic design is very important but subsonic and transonic requirements must also be given proper attention, and
- design for good performance cannot be separated from design for good handling qualities."

Area ruling of the fuselage was seriously considered in the project stages but was rejected on the basis of increased production costs.

Wilde and Cormery (1970) noted that "the performance in supersonic cruise is very important, of course, but about 40% of all fuel uplifted for a trans-Atlantic flight will either be used in subsonic flight conditions or is provisioned in reserves for possible extension of subsonic flight in diversion or holding."

Finally, considerable effort was expended reviewing the consequences of introducing changes to an existing design. For instance, "reducing the leading edge droop over the whole span would improve the supersonic drag, worsen the subsonic and transonic drag and increase the lift curve slope. It is to be noted that increase in lift curve slope is favourable, particularly at low speed since it permits either reduced takeoff and landing speeds at fixed attitude or reduced attitudes at given speeds."

"Inevitably the nacelles have forward facing surfaces which produce supersonic drag but this drag is offset to some extent by the induced interference pressures on the undersurface of the wing which produce lift."

11.9.2 The High-Speed Civil Transport (HSCT)

As noted in a Boeing study [Staff of Boeing Commercial Airplanes (1989)], the aerodynamic tasks in the design of the High-Speed Civil Transport "included:

- Aerodynamic design integration of the study configurations.
- Integration of compatible high-lift system for each concept.
- Evaluation of the aerodynamic characteristics of all concepts to provide necessary resizing data for the airplane performance calculations. These included both flaps-up cruise configuration analyses as well as flaps-down takeoff and landing evaluation.

The aerodynamic design of the study configurations included optimized camber/twist distributions and area-ruled fuselages. The wing spanwise thickness distributions and airfoil shapes were constrained by structural depth requirements."

As the aircraft flight speed increases, careful integration of the propulsion system into the airframe design becomes increasingly important. Therefore, as noted in NASA Contractor Report 4233 and in NASA Contractor Report 4234, "Nacelle shape, size, location, and operating conditions all influence the nacelle interference with other configuration components. The dominant interference effect is between the nacelles and the wing. To arrive at an acceptable nacelle design requires a balance between the isolated drag of the nacelle and the interference drag induced by the nacelle. The nacelles of each of the study configurations were placed below the wing and aft to (1) provide the inlet with a uniform flow field throughout the angle of attack range, (2) take advantage of the precompression caused by the wing shock, and (3) achieve favorable aerodynamic interference."

As noted in the NASA Contractor Reports, "Environmental acceptability is a key element of any HSCT program. If not properly accounted for in the HSCT design, environmental limitations could substantially reduce use of the vehicle and, in the most extreme of circumstance, prohibit vehicle operations altogether. The primary area of

environmental impact identified in the study were engine emissions effects, community noise, and sonic boom. . . . A viable HSCT must be designed so that the engine emissions have no significant impact on the Earth's ozone layer. . . . Operation out of conventional airports was determined to be a requirement for achieving adequate HSCT utilization. Accordingly, a viable HSCT must produce noise levels no higher than its subsonic competition. . . . The airplanes under study have been evaluated with subsonic flight profiles over land, which results in adverse economic and market impact. Thus, there is an impetus to explore low-boom designs that allow some form of overland supersonic operations."

11.9.3 Reducing the Sonic Boom

As noted in the previous section, a viable High Speed Civil Transport (HSCT) must produce noise levels no higher than its subsonic competition. "The problem is not building an aircraft capable of Mach 1+ speeds, but designing one that can fly over land without generating a sonic boom—and then getting the FAA and other international aviation regulatory agencies to certify it for such flights," as noted by Wilson (2007).

Gulfstream Aerospace moved closer to resolving that design issue by testing a design concept that involved attaching a telescoping spike to the nose of an F-15B fighter jet. Note that the ultimate goal is to break up the typical shock-wave that creates a sonic boom into a series of smaller waves that do not.

Quiet Spike was another step in the ability to use technology to make a quiet supersonic business jet. The application of a telescoping spike to reduce the sonic boom would require that we demonstrate the ability to make a quiet supersonic business jet, to show that it could be incorporated into a telescoping structure, to put it on the front of an airplane, and show that the telescoping spike would reduce the noise. Wilson (2007) further notes: "Without a spike you could design an aircraft that is quieter than what is flying today, but not quiet enough to change the regulations [to make] supersonic flight over land unrestricted."

As noted by Croft (2004), "The noise problem with today's supersonic aircraft is caused by an N-wave pressure change that occurs as shock waves move past the observer. When an aircraft like the Concorde flies at supersonic speeds, conical shocks form at the front and rear of the aircraft and at every discontinuity in the flow along the way (for example, at the engine inlets, wing leading edges, and antennas) because the plane is moving faster than the air can move out of the way."

"At a certain distance from the aircraft, the individual shocks coalesce into two stable conical shocks, one at the front of the plane and one at the tail. The effect on the listener is a double boom as each wave passes."

"According to [Peter] Coen [of NASA Langley], shock waves with greater than ambient pressure tend to move faster and collect at the nose, while those with lower than ambient pressure lag to the back. On the ground, the pressure distribution as the waves pass looks like an 'N': As the nose shock passes, the pressure spikes above the ambient pressure, ramps down below ambient, then snaps back to ambient as the tail shock passes."

The Defense Advanced Research Projects Agency (DARPA) funded a Shaped Sonic Boom Demonstration (SSBD) Program to determine if sonic booms could be substantially reduced by incorporating specialized aircraft shaping techniques. Pawlowski et al. (2005) wrote: "Although mitigation of the sonic boom via specialized shaping

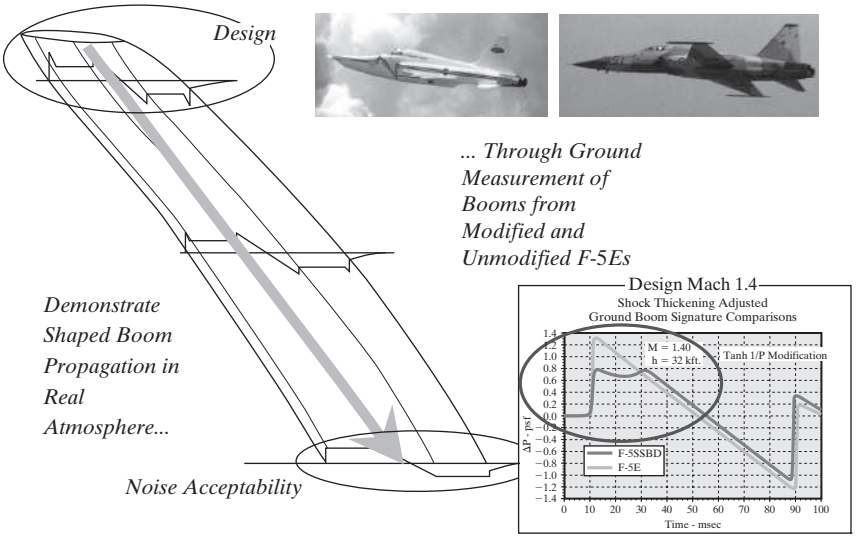

Figure 11.36 Impact of forebody shaping on N-wave production for the F-5E [from Pawlowski et al. (2005), courtesy of Northrop Grumman Corporation].

techniques was theorized decades ago, until now, this theory had never been tested with a flight vehicle subjected to flight conditions in a real atmosphere."

As shown in Fig. 11.36, that was presented by Pawlowski et al. (2005): "Pressure measurements obtained on the ground and in the air confirmed that the specific modifications made to a Northrop Grumman F-5E aircraft not only changed the shape of the shock wave signature emanating from the aircraft, but also produced a 'flat-top' signature whose shape persisted, as predicted, as the pressure waves propagated through the atmosphere to the ground." Kandil et al. (2005) noted: "The modification was made primarily to the nose of the aircraft forward of the cockpit and engine inlets and was designed to propagate a 'flat top' pressure signature (sonic boom) to the ground. This signature, as the name indicates, has a flat pressure distribution downstream of the initial shock (see the sketch in Fig. 11.36). Signatures of this type are desired since they yield weaker initial shocks relative to the N-wave signature normally produced by current supersonic aircraft."

11.9.4 Classifying High-Speed Aircraft Designs

One approach to classifying aircraft designs in relation to their speed regime is using the ratio of semispan $(b/2)$ to length of the aircraft (l) as a measure of *configuration slenderness*. You should look in Küchemann (1978) for more about the reasoning behind the use of this parameter. Harris (1992) presented this parameter for *configuration slenderness* as a function of the maximum cruise Mach number: "Subsonic aircraft, exemplified by the Boeing 747, McDonnell-Douglas MD-11, and Airbus A300, tend to optimize at high values of semispan-to-length ratio because of their high-aspect-ratio wings. The distinction between supersonic and hypersonic designs is taken as the dividing line where the semispan-to-length ratio is equal to the tangent of the Mach angle." From

the definition of the Mach angle in equation (8.22), you can verify that the expression for the tangent of the Mach angle is:

$$\tan \mu = \left[\frac{1}{\sqrt{M_\infty^2 - 1}} \right]$$

Harris (1992) continued (see Fig. 11.36), "Therefore, for the supersonic designs that may have subsonic leading edges, we can maintain relatively weak shock waves. . . . Long-range subsonic aircraft are essentially designed to achieve the highest cruise Mach number that can be attained and still avoid the adverse effects of shock waves."

"Supersonic aircraft, in order to achieve long-range capability, can be designed to minimize shock losses by keeping the configuration slender, that is, a low value of semispan-to-length ratio . . . the short-range supersonic U.S. fighters, which are not designed for efficient cruise performance, fall in the semispan-to-length ratio range of about 0.25–0.35 in contrast to the lower values approaching 0.2 for the Concorde, Tu-144, XB-70, and SR-71 long-range supersonic cruise designs."

Flow-field solutions were generated using the Cobalt_{60} code for an SR-71 configuration at an angle of attack of 5° [Tomaro and Wurtzler (1999)]. Interestingly enough, when the vehicle is at 5° angle of attack, the axis of the cone in each of the engine inlets is aligned with the free-stream velocity vector, so the shock wave generated by the cone is symmetric with the engine flow path. Shock-wave patterns for these computed flow fields are presented in Fig. 11.38 for free-stream Mach numbers of 1.5, 3.2, and 3.8. According to the correlations presented in Fig. 11.37, a Mach number

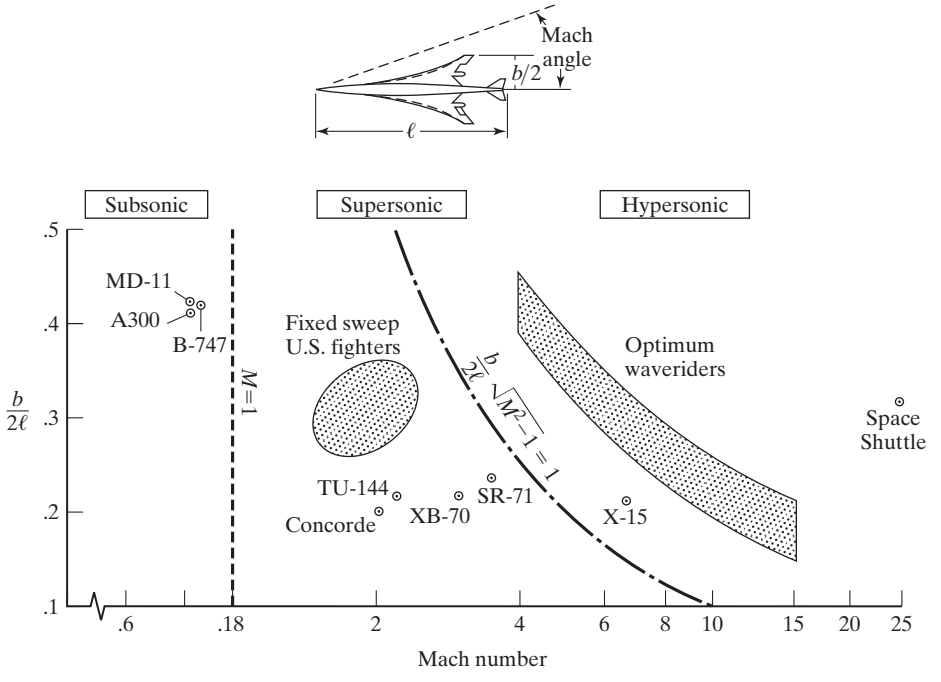

Figure 11.37 Aircraft classification by speed regime [from Harris (1992)].

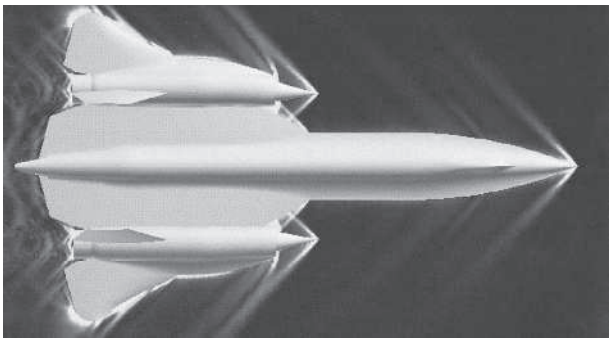

(a)

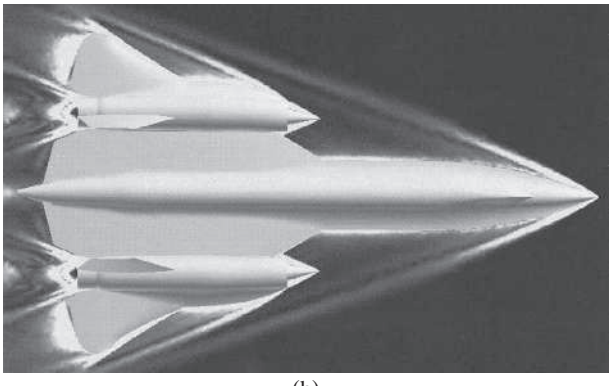

(b)

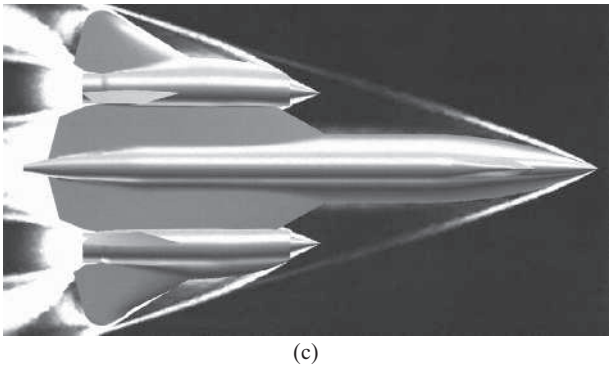

(c)

Figure 11.38 Shock-wave patterns generated by Cobalt_{60} computations for an SR-71 at 5° angle of attack with (a) $M_\infty = 1.5$, (b) $M_\infty = 3.2$, and (c) $M_\infty = 3.8$ [from Tomaro and Wurtzler (1999)].

of 3.8 is approximately the highest cruise Mach number for the SR-71. Referring to Fig. 11.38c, the reader can see that, at this Mach number, the limiting portion of the bow-shock wave as it merges with the shock wave generated by the engine structure is tangent to the wing tips. Therefore, the flow field computed using the full Navier-Stokes equations gives results that are consistent with the correlation presented in

Fig. 11.38. That is, the tangent of the bow-shock wave angle is approximately equal to the semispan-to-length ratio.

11.10 SLENDER BODY THEORY

Significant effort has been made in previous sections of this chapter to describe the aerodynamics of wings in supersonic flow. While wings are certainly the most important supersonic lifting devices, a considerable portion of supersonic lift also can come from the fuselage. Significant work has been done over the years to develop supersonic body theories [see Liepmann and Roshko (1957) for a summary]; and much of the development involves the method of small perturbations [van Dyke (1975)]. A brief review of the assumptions and resulting equations is presented here.

The starting point for slender body theory is the linearized potential equation (9.13):

$$(1 - M_\infty^2)\phi_{xx} + \phi_{yy} + \phi_{zz} = 0$$

or in cylindrical coordinates:

$$(1 - M_\infty^2)\phi_{xx} + \phi_{rr} + \frac{\phi_r}{r} + \frac{1}{r^2}\phi_{\theta\theta} = 0$$

While the formal derivation of the slender body theory concept is quite elaborate [see Ward (1955) for details], the concept is fairly straightforward and follows the concepts for supersonic linear-airfoil theory. For a long, slender body of revolution (see Fig. 11.39), the variation of velocity in the x direction can be assumed to be small compared with the velocity variations in the y or z directions.

$$\phi_{xx} << \phi_{yy}, \phi_{zz} \tag{11.42}$$

This simplification applied to equation (9.13) leads to a rather amazing result

$$\phi_{yy} + \phi_{zz} = 0 \tag{11.43}$$

which is Laplace's equation in the crossflow plane of the slender body (as shown in Fig. 11.40).

So the solution for slender bodies reduces to solving Laplace's equation in the y–z (crossflow) plane successively for each crossflow plane from the front to the rear of the body. This usually is accomplished by placing a distribution of sources or doublets along the axis of revolution to form the body shape and then performing inner and outer expansions of the flow-field to find the velocity and pressure fields around the body [Karamcheti (1980)]. The resulting pressure distribution on the body surface at zero

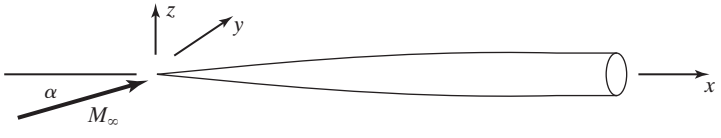

Figure 11.39 Long, slender body of revolution

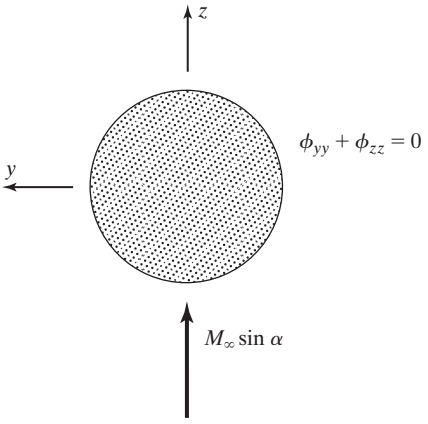

Figure 11.40 Crossflow plane for a slender body of revolution.

angle of attack is presented by Liepmann and Roshko (1957) based on the derivation of van Dyke (1951), using the perturbation methods described in van Dyke (1975), as:

$$C_p(x) = \frac{S''(x)}{\pi}\ln\left(\frac{2}{R(x)\sqrt{M_\infty^2 - 1}}\right) + \frac{1}{\pi}\frac{d}{dx}\int_0^x S''(\xi)\ln(x - \xi)d\xi - \left(\frac{dR(x)}{dx}\right)^2 \quad \textbf{(11.44)}$$

where $R(x)$ is the cross-sectional radius distribution of the body and $S(x)$ is the cross-sectional area distribution of the body. The influence of the source at $x = \xi$ is integrated up to $x = \xi$ so that only upstream affects are included. The pressure distribution can be integrated along the length of the body, L, in order to determine the drag coefficient (excluding the drag on the base of the configuration) as

$$C_D = \frac{1}{S(L)}\int_0^L C_p\frac{dS(x)}{dx}dx \quad \textbf{(11.45)}$$

to obtain the zero-lift wave-drag coefficient [$C_D \equiv D/q_\infty S(L)$]:

$$C_{D_0} = -\frac{1}{2\pi S(L)}\int_0^L\int_0^L S''(\xi)S''(x)\ln|x - \xi|\,d\xi\,dx \quad \textbf{(11.46)}$$

If the original formulation had retained the angle of attack of the slender body, the lift-and-drag-coefficient would have been found to be (for small angles of attack):

$$C_D = C_{D_0} + \alpha^2 \qquad C_N = 2\alpha \qquad C_L \approx 2\alpha \quad \textbf{(11.47)}$$

which are very straightforward relationships that show a linear variation of lift with angle of attack and a squared relationship for the drag variation. As with subsonic flow, drag increases faster than lift with angle of attack, even though the drag is being produced by wave drag in this case. An improved formulation for the normal force coefficient of a slender body has been obtained as [Pitts et al. (1959)]:

$$C_N = \sin(2\alpha)\cos(\alpha/2) + 2L/2R(L)\sin^2\alpha \quad \textbf{(11.48)}$$

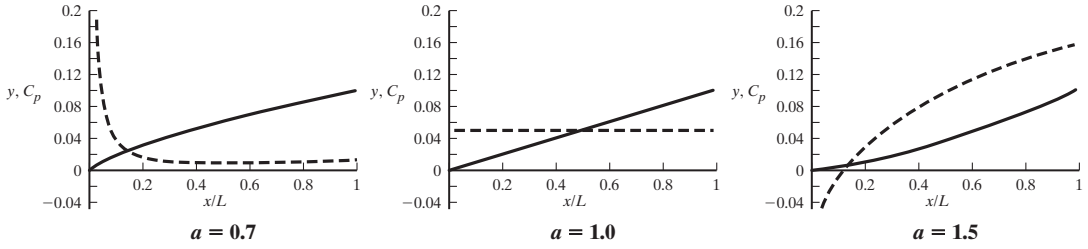

Figure 11.41 Pressure coefficients for various power series body shapes (body shape in solid line, pressure coefficient in dashed line).

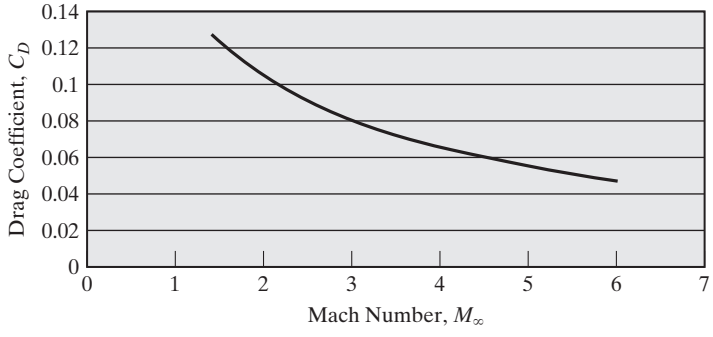

Figure 11.42 Mach variation for power series body ($\varepsilon = 0.1$ and $a = 1.5$).

which gives a nonlinear variation for the normal force as a function of angle-of-attack. For body shapes given by a simple power series, $R(x) = \varepsilon x^a$, a variety of body shapes can be obtained by choosing the factor ε and varying the coefficient a (in this case $\varepsilon = 0.1$ and $a = 0.7, 1.0$, and 1.5) to obtain pressure-coefficient variations (Fig. 11.41) and wave-drag coefficients (Fig. 11.42).

11.11 BASE DRAG

Base flows are commonly encountered in supersonic aerodynamics. This kind of flow is commonly found behind objects, such as missiles, rockets, and projectiles. The low pressure found behind the base causes base drag which can be a sizable portion of the total drag of these vehicles [Forsythe et al. (2002)].

An axisymmetric base flow depicted with pressure contours and streamlines is shown in Fig. 11.43. The large turning angle behind the base causes separation and the formation of a region of reverse flow (known as the recirculation region or the separation bubble). The size of the recirculation region determines the turning angle of the flow coming off the back of the base, and therefore the strength of the expansion waves. A smaller recirculation region causes the flow to turn sharply, leading to a stronger

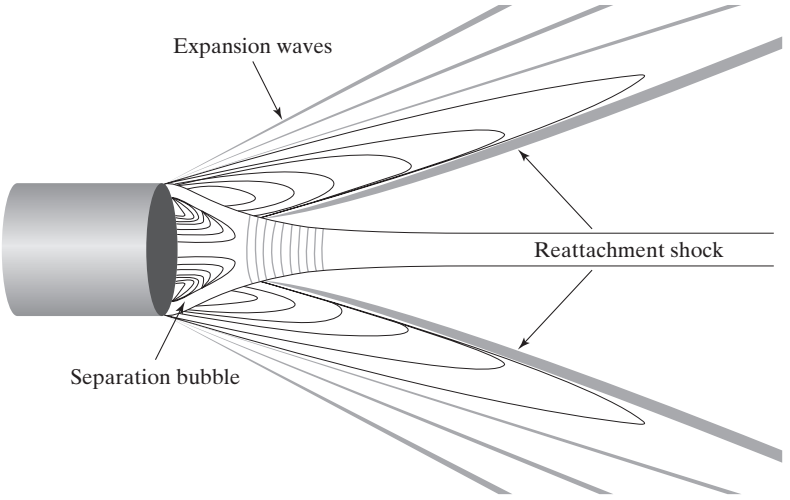

Figure 11.43 Flow field in a supersonic base region [from Forsythe et al. (2002)].

expansion wave, and lower pressures behind the base. Therefore, small separated regions cause larger base drag than large regions.

Directly behind the base, in the recirculation region, the reverse flow can be seen. The point along the axis of symmetry where the streamwise velocity is zero is considered to be the shear layer reattachment point. As the shear layer reattaches, the flow is forced to turn along the axis of symmetry, causing the formation of a reattachment shock. For high Reynolds numbers, the incoming boundary layer and the flow behind the base will be turbulent, leading to highly unsteady flow behind the base.

Murthy and Osborn (1976) provide an excellent overview of the base flow problem, including a collection of semi-empirical approaches to model base pressure and base drag, while Dutton et al. (1995) provide a good overview on the progress in computing high-speed separated base flows. Some of the difficulties and complicating factors in modeling the base flow problem, outlined by Forsythe et al. (2002), are:

- the upstream effects of the presence of a corner in various Mach number flows at different Reynolds numbers
- the effects of separation, compression, expansion, and/or shock formation in the vicinity of the corner
- the influence of the expansion wave at the base corner on the initial turbulence structure of the shear layer, and the impact of that shear layer on the formation of the recirculating flow region
- the shear layer exists under highly compressible conditions (i.e., at high convective Mach numbers), which alters the turbulence structure
- the shear layer encounters a strong adverse pressure gradient at reattachment
- the strong streamline curvature at the reattachment point
- the enclosed recirculating region imposes a highly energetic and nonuniform upstream velocity at the inner edge of the shear layer

- the structure and shape of the recirculating zone
- the effects of the configuration (e.g., diameter, boattail, fins)

Taken in total, these flow features yield a complex flow field that is considerably challenging to model analytically or numerically.

In spite of these challenges, a straightforward relation for base drag has been developed which assumes that the fuselage has a circular cross section and there is no interferance from fins or boattails [from Fleeman (2006)]:

$$C_{D_{base}} = \frac{0.25}{M_\infty}$$

but accurate prediction of base drag should be given a high priority in aerodynamic design.

Aerodynamics Concept Box: What Is a Boattail?

Many supersonic aircraft (airplanes and missiles) have a boattail near their base, as shown below for the AMRAAM missile. Boattails are added to the base region to reduce base drag, especially on aircraft where the jet from the propulsion system exits the vehicle at the base.

AMRAAM being loaded onto an F-15
(U.S. Air Force photo by Senior Airman Laura Turner)

Boattails are geometric devices that reduce the base drag of an aircraft in multiple ways. First, and perhaps most obvious, is a boattail reduces the area of the base, so any pressure acting on the base creates less drag. Second, a boattail starts to turn the flow toward the centerline of the vehicle, decreasing the size of the recirculation bubble and reducing the impact of the base

region on drag. Like all aerodynamic devices, however, boattails come with a cost. By including a boattail a new surface with a rearward projected area is created. When the flow expands around the boattail, the surface of the boattail will create an additional drag. This drag, however, is offset by the reduction in drag due to the previously mentioned positive effects of the boattail. Boattails, therefore, have an optimal angle, above which the boattail may cause an increase in drag, and below which the base area has not been reduced as much as might otherwise be possible.

11.12 AERODYNAMIC INTERACTION

Owing to the complexity of flow fields about most flight vehicles, aerodynamicists often develop theories for the flows about components of such vehicles. However, the designer is faced with the fact that aerodynamic loads on an entire aircraft are not simply the sum of the loads on the individual components; the difference is commonly referred to as *aerodynamic interaction*. Wind-tunnel experiments, flight tests, and physical reasoning have shown that interaction loads can be a significant contribution to the total loading on an aircraft. It was not until advancements in computing became generally available that systematic treatment of the loads on rather arbitrary shapes was even feasible. Theories are still being developed to account for the effects of three-dimensional separated flows about arbitrary shapes. Thus, this is a rapidly changing area of aerodynamic theory. Significant progress has been made, however, and our purpose here is to give a brief account of the physical reasoning associated with the effects of aerodynamic interaction in supersonic flight, and to describe methods of determining these effects.

A simple rectangular wing is mounted on an ogive cylinder with circular cross section, as shown in Fig. 11.44. Two interaction effects are present: the effect of the wing on the body and the effect of the body on the wing. In supersonic flight, the suction pressure on the upper surface of the wing and the relatively higher pressure on the lower surface will be confined to the regions bounded by the Mach waves from the leading

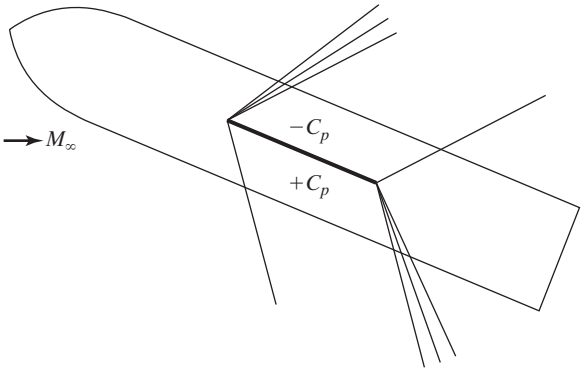

Figure 11.44 Wing-on-body interaction showing regions of positive and negative C_p [adapted from Hilton (1951)].

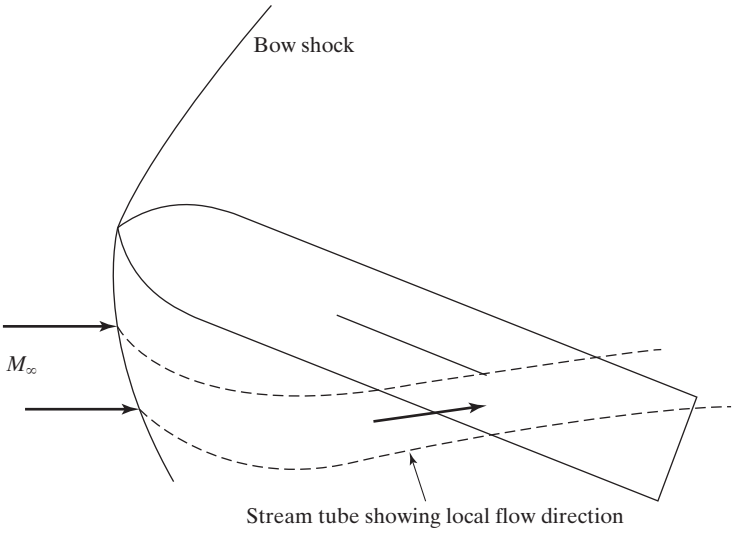

Figure 11.45 Body-on-wing interaction showing upwash-over-wing effect due to the body at angle of attack [adapted from Hilton (1951)].

and trailing edges of the wing, as shown. This pressure differential will carry over onto the body and generate a net lift and wave-drag force on it. Thus, we have an example of the effect of the wing on the body.

Conversely, the effect of the body at angle of attack will be to produce an upwash about the sides of the body (see Fig. 11.45) which will increase the effective angle of attack of the wing. Provided that the resulting angle of attack will not cause the flow to separate on the upper wing surface (i.e., provided that the wing does not stall), the result will be greater wing lift in accordance with equation (10.8).

Hilton (1951) notes that the combined effects of the wing and body for the case shown in Fig. 11.46 are such that the wings produce the full lift to be expected from two-dimensional theory without tip effects. Taking into account tip effects and ignoring interactions, one would expect a wing lift of only three-fourths of this value. Thus, by introducing the body interaction effect, a full 25% increase in wing lift is experienced.

Other interaction effects can also be present (e.g., wing/tail, body/tail, etc.). Some simplifications arise in supersonic flow due to the fact that disturbances cannot propagate upstream. Thus, while one may want to consider the effects of the wings on the tail, the effects of the tail on the wings can usually be neglected unless they are very close to one another.

Many treatments of interacting flows rely on the small disturbance theory governed by equation (11.4). The flow tangency boundary condition at surfaces and the Kutta condition at sharp trailing edges are involved in determining solutions. Problems are solved by distributing a series of singularities (e.g., sources, sinks, doublets, vortices) to simulate the vehicle in a uniform supersonic stream. The strength of these singularities is determined so as to satisfy the boundary conditions at discrete selected locations on the vehicle. In the method of Carmichael and Woodward (1966), wing

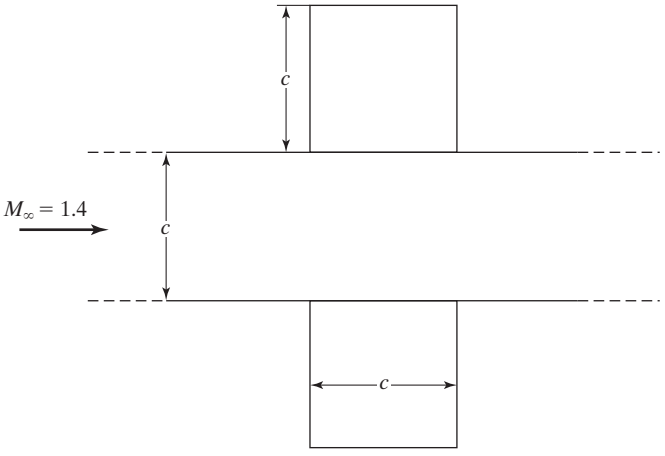

Figure 11.46 Configuration giving increased wing lift [from Hilton (1951)].

camber and incidence are simulated by vortex distributions, while thickness is simulated by source and sink distributions. Thickness, camber, and incidence of the body are represented by line sources and doublets along the axis of the body. The effect of the interaction of the wing on the body is represented by a distribution of vortices on a cylinder whose radius is related to the average radius of the body, while the body-on-wing interaction is represented by a distribution of vortices on the wing camber surface [see Woodward (1968)].

An integrated supersonic design and analysis system is presented by Middleton and Lundry (1980). The analysis program can be used to predict the lifting pressure calculations for a wing camber surface at a selected angle of attack. It can also be used to calculate lifting pressure distributions and force coefficients for complete configurations over a range of angles of attack. The program described by Middleton and Lundry (1980) carries two solutions along: one for the configuration at its input angle of attack and the other an incremental solution per degree angle of attack (called the flat-wing solution). The interference terms associated with the two solutions acting on the other surface shape are also calculated. The summation of these effects into the drag polar and the other force coefficients is performed by superposition. Calculation of the complete configuration lifting pressure solution can involve any or all of the following tasks:

- Determine the isolated fuselage upwash field.
- Determine the nacelle pressure field acting on the wing.
- Compute the pressure field due to asymmetrical fuselage volume.
- Generate a wing/canard solution in the presence of the fuselage upwash field.
- Calculate the effects of the wing pressure field acting on the nacelles.
- Determine the fuselage lift distribution in the presence of the wing downwash field.

- Obtain the horizontal tail solution in the presence of the fuselage and wing flow fields.
- Generate a solution for the complete configuration by superposition of the elemental solutions.

If you are interested in pursuing the subject of aerodynamic interactions, research surveys appear occassionally for the relevant phenomena and solution techniques [e.g., Tomaro and Wurtzler (1999)]; these reviews should be thoroughly read for current information on the topic.

11.13 AERODYNAMIC ANALYSIS FOR COMPLETE CONFIGURATIONS IN A SUPERSONIC FREE STREAM

There is a hierarchy of prediction/computational techniques that can be used to estimate the aerodynamic forces and moments for suitably complex configurations in a supersonic stream. Techniques based on linear theory have been described at length in this chapter. Techniques based on impact methods, on solutions of the Euler equations, and on solutions of the Navier-Stokes equations are discussed in Chapters 12 and 14.

Three-view oil-flow photographs of the Space Shuttle Orbiter are presented in Fig. 11.47 for

$$M_\infty = 1.25$$
$$\alpha = 10^\circ$$

$\delta_{E,L} = -18.8^\circ$ (the left elevon is deflected upward, and the oil-flow pattern indicates a shock wave at the lower right of Fig. 11.47c, just below the OMS pod)

$\delta_{E,R} = +14.4^\circ$ [the right elevon is deflected downward and the surface oil flows through the space between the OMS pod and the right elevon (Fig. 11.47a)]

$\delta_{SB} = -87.2^\circ$ and $\delta_R = -25^\circ$ [the speed brake is open 87.2° and deflected 25° to serve as a rudder, creating a relatively strong shock wave with an attendant viscous/inviscid interaction on one side of the vertical tail (Fig. 11.47a) but not on the other (Fig. 11.47c)]

$\delta_{BF} = 23.7^\circ$ (the body flap is deflected 23.7°)

Also evident in these flow visualization photographs are free-shear layer separations and feather patterns associated with reattaching vortical flows. Because the complex nature of the flow field made it impossible to develop realistic flow models for numerical solutions, a total of 493 wind-tunnel tests using 52,993 hours were used in phase C/D of the Space Shuttle design development program in order to develop an aerodynamic data base [Whitnah and Hillje (1984)]. However, because wind-tunnel flows are also simulations (limited in model scale, high-temperature effects, etc.), wind-tunnel measurements should be correlated with the corresponding computed values based on solution techniques employing adequate flow models before extrapolating to flight.

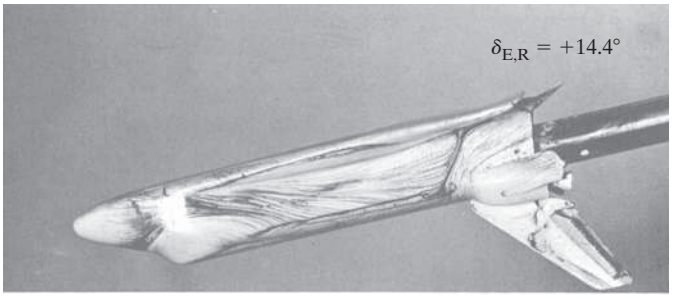

(a)

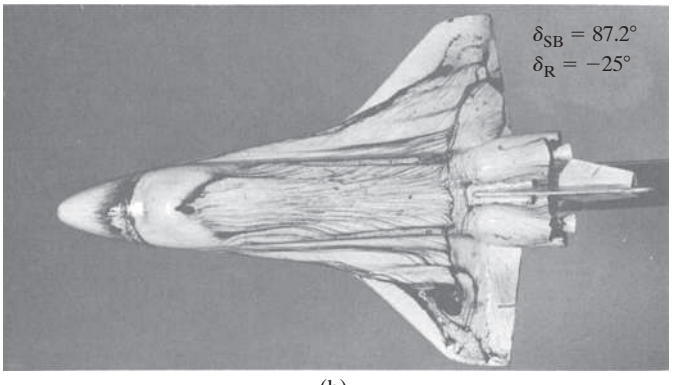

(b)

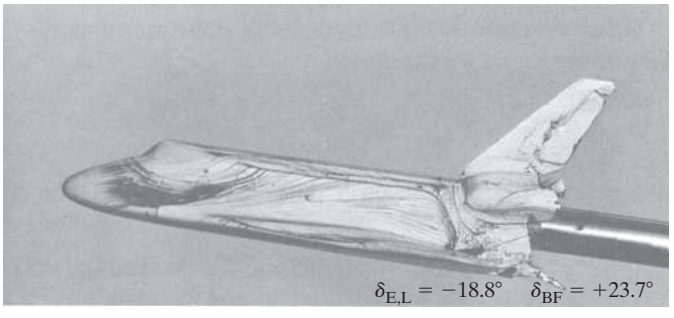

(c)

Figure 11.47 Oil flow patterns for Space Shuttle *Orbiter* at $M_\infty = 1.25$ and $\alpha = 10°$: (a) view of right side; (b) top view; (c) view of left side (courtesy of NASA Johnson Space Center).

11.14 SUMMARY

Three-dimensional supersonic flow is much less complicated to predict than three-dimensional subsonic flow, but three-dimensional affects still take place and must be accounted for. Wing-tip affects, interference affects, and base drag are all challenging aspects of supersonic aerodynamics which must be considered when analyzing

high-speed aircraft. Fairly straightforward methods exist to estimate all aspects of supersonic aerodynamics, but they must be used with an experienced eye toward details, and should be based on knowledge of previous supersonic aircraft which used the same approaches. Supersonic aerodynamics is interesting, yet challenging, and should be approached with a healthy respect for the theories and approaches of those that came before us.

PROBLEMS

11.1. Consider a flat-plate, rectangular wing. Derive the expressions for the lift coefficient, for the drag coefficient, for the coefficient of the moment about the leading edge, and for the location of the center of pressure given in Table 11.1. Assume that $\beta \cdot \mathrm{AR} > 2$ so that the Mach cones emanating from the tip do not overlap.

11.2. Verify the statement given in Table 11.1 that A', which is defined as airfoil cross-sectional area divided by the square of chord, is equal to $\tau/2$ for a double-wedge airfoil section.

11.3. Consider a wing with a rectangular planform, whose aspect ratio is 5.0 and whose section is that shown in Fig. 10.5. Use Bonney's results in Table 11.1 to determine C_L and C_D for this wing for the flow conditions shown in Fig. 10.5.

11.4. **(a)** Using the relations given in Table 11.1, develop expressions for the lift coefficient as a function of α [i.e., $C_L(\alpha)$] and for the drag coefficient [i.e., $C_D(C_L)$] for the wing of Figs. 9.14 and 9.15. The wing has a rectangular planform with an aspect ratio of 2.75. Develop the relations for $M_\infty = 1.50$. Assume that the airfoil section is biconvex with a maximum thickness ratio of 0.05.

(b) Compare the theoretical values with the experimental values presented in Figs. 9.14 and 9.15. What value of $C_{D,\,\text{friction}}$ (at $M_\infty = 1.50$) will cause your theoretical results to agree most closely with the data in the figures?

11.5. Consider the wing of the Northrop F-5E (see Table 5.1). If the airplane is flying at a Mach number of 1.32, will the quarter-chord line of the wing be in a supersonic or a subsonic condition relative to the free-stream flow? What must M_∞ be for the quarter-chord line to be in a sonic condition?

11.6. Derive the equation of the leading-edge sweep angle Λ_{LE} as a function of M_∞ for a sonic leading edge. Prepare a graph of the results. Assume small-angle approximations for α.

11.7. Show that the section lift coefficient for a swept airfoil with a supersonic leading edge is given by

$$C_l = \frac{4 \cos \Lambda}{\sqrt{M_\infty^2 \cos \Lambda - 1}} \alpha$$

The thickness ratio and the angle of attack of the airfoil are sufficiently small that the small-angle approximations may be used.

11.8. Discuss the limits of validity of the result derived in Problem 11.7.

11.9. Using a Taylor's series expansion about $z = 0$, derive equation (11.7) from equation (11.6).

11.10. Consider the flat-plate rectangular wing of Problem 11.1. Assume that there is a plain flap along the entire trailing edge with hinge line at $x_f = fx$, where $0 \le f \le 1$. Derive a formula for C_L as a function of the flap deflection angle δ_f (see Fig. P11.10). Assume that $\beta \cdot \mathrm{AR} > 2$.

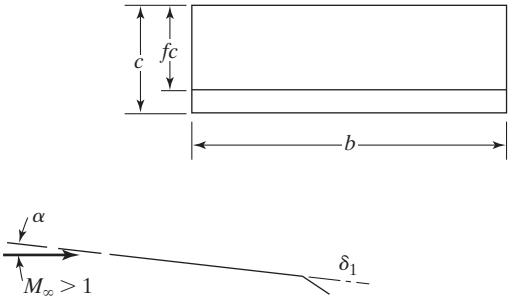

Figure P11.10

11.11. Derive the relation between the aspect ratio of a delta wing and the free-stream Mach number M_∞ if the leading edge is to be sonic.

11.12. Show that equation (11.30) follows from

$$R(x - x_1, y - y_1) \equiv \frac{x - x_1}{\beta^2(y - y_1)^2[(x - x_1)^2 - \beta^2(y - y_1)^2]^{0.5}}$$

The variation of R with x may be assumed to be small.

11.13. Show that subtracting the single wedge FGF' from the single wedge BFF' yields the relations in the double wedge $BDED'$ (see Fig. 11.20). Thus, show that the source strength in region DCD' will be

$$U_\infty = -\frac{C(x,y)}{\lambda_2}$$

where $C = C_1 + C_2$ and C_1 is the source strength due to BFF' and C_2 is the source (sink) strength due to FGF'.

11.14. Determine $\Delta C_p(3, 0)$ for the flow described in Example 11.3.

11.15. Determine $\Delta C_p(3, \pm 1)$ for the flow described in Example 11.3.

11.16. Consider a flat-plate (zero-camber) delta planform in a $M_\infty = 1.2$ stream. The leading-edge sweepback angle (Λ_{LE}) is 40°. Is the leading edge subsonic or supersonic? What is the value of cot Λ_{LE} for this flow?

11.17. For the configuration described in Problem 11.16 and with $N_{max} = 8$, determine $\Delta C_p(3, 0)$.

11.18. For the configuration described in Problem 11.16 and with $N_{max} = 8$, determine $\Delta C_p(3, \pm 1)$.

11.19. Develop the expression for dR/dx as a function of x/L for the slender, axially-symmetric body-of-revolution, which has a profile section of

$$R(x) = 2t\frac{x}{L}\left(1 - \frac{x}{L}\right)$$

Develop the expression for the pressure coefficient as a function of x/L.

11.20. Develop the expression for the pressure coefficient for a two-dimensional airfoil section that has the same bi-convex profile as was specified in Problem 11.19, that is,

$$R(x) = 2t\frac{x}{L}\left(1 - \frac{x}{L}\right)$$

Prepare a graph comparing the pressure distribution for the axially-symmetric body-of-revolution with the pressure distribution for the two-dimensional airfoil section that has the same biconvex profile.

11.21. Test is to be conducted in an indraft wind tunnel. An indraft wind tunnel takes air from the room in which the tunnel is located. The air then accelerates through a convergent-divergent nozzle to the free-stream conditions in the test section. The free-stream Mach number in the test section is 5.0. The "atmospheric" conditions in the room form the stagnation conditions for the tunnel: $p_{t_1} = 15\ \text{lbf/in}^2$ and $T_t = 540°\text{R}$. Calculate the L/D ratio for the two-dimensional airfoil section as a function of the angle of attack from 0° to 10°.

REFERENCES

Allen JM, Townsend JC. 1986. Application of a supersonic Euler code. *J. Aircraft* 23:513–519

Ashley H, Rodden WP. 1972. Wing-body aerodynamic interaction. *Ann. Rev. Fluid Mech.* 4:431–472

Bonney EA. 1947. Characteristics of rectangular wings at supersonic speeds. *J. Aeron. Sci.* 14:110–116

Busemann A. 1947. Infinitesimal conical supersonic flow. *NACA Tech. Mem. 1100*

Carafoli E. 1956. *High Speed Aerodynamics*. Elmsford, NY: Pergamon Press

Carlson HW, Miller DS. 1974. Numerical analysis of wings at supersonic speeds. *NASA Tech. Note D-7713*

Carlson HW, Mack RJ. 1978. Estimation of leading edge thrust for supersonic wings of arbitrary planform. *NASA TP 1270*

Carlson HW, Mack RJ. 1980. Estimation of wing nonlinear aerodynamic characteristics at supersonic speeds. *NASA TP 1718*

Carlson HW, Mann MJ. 1992. Survey and analysis of research on supersonic drag-due-to-lift minimization with recommendations for wing design. *NASA TP 3365*

Carmichael RS, Woodward FA. 1966. Integrated approach to the analysis and design of wings and wing-body combination in supersonic flow. *NASA Tech. Note D-3685*

Cenko A, Tinoco EN, Dyer RD, DeJongh J. 1981. PAN AIR applications to weapons carriage and separation. *J. Aircraft* 18:128–134

Croft J. 2004. Engineering through the sound barrier. *Aerospace Am.* 42(9):24–26, 29–31

Dutton JC, Herrin JL, Molezzi MJ, Mathur T, Smith KM. 1995. Recent progress on high-speed separated base flows. Presented at AIAA Aerosp. Sci. Meet., 33rd, AIAA Pap. 95-0472, Reno, NV

Ferri A. 1949. *Elements of Aerodynamics of Supersonic Flow*. New York: Macmillan Publishing

Fleeman EL. 2006. *Tactical Missile Design*. 2nd Ed. Reston VA: AIAA.

Forsythe JR, Hoffmann KA, Cummings RM, and Squires KD. 2002. Detached-eddy simulation with compressibility corrections applied to a supersonic axisymmetric base flow. *J. Fluids Engr.* 124(4): 911–923

Harris RV. 1992. On the threshold—the outlook for supersonic and hypersonic aircraft. *J. Aircraft* 29:10–19

Hernandez G, Covell PF, McGraw ME. 1993. An experimental investigation of a Mach 2.0 high-speed civil transport at supersonic speeds. *NASA TP 3365*

Hilton WF. 1951. *High Speed Aerodynamics*. New York: Longmans, Green & Co.

Hodgman CD, ed. 1977. *Standard Mathematical Tables*, 12th ed. Cleveland: Chemical Rubber Co.

Ivey HR, Bowen EH. 1947. Theoretical supersonic lift and drag characteristics of symmetrical wedge-shape-airfoil sections as affected by sweepback outside the Mach cone. *NACA Tech. Note 1226*

Jones RT, Cohen D. 1957. Aerodynamics of wings at high speeds. In *Aerodynamic Components of Aircraft at High Speeds*, Princeton: Princeton University Press

Kandil OA, Ozcer IA, Zheng X, Bobbitt PJ. 2005. *Comparison of full-potential propagation-code computations with the F-5E "shaped sonic boom comparison" program*. Presented at Aerosp. Sci. Meet., 43rd, AIAA Pap. 2005–0013, Reno, NV

Karamcheti K. 1980. *Principles of Ideal-Fluid Aerodynamics*. 2nd Ed. Melbourne, FL: Krieger

Küchemann D. 1978. *Aerodynamic Design of Aircraft*. Oxford: Pergamon Press

Kulfan RM, Sigalla A. 1978. *Real flow limitations in supersonic airplane design*. Presented at Aerosp. Sci. Meet., 16th, AIAA Pap. 78–0147, Huntsville, AL

Liepmann HW, Roshko A. 1957. *Elements of Gasdynamics*. New York: John Wiley

Lomax H, Heaslet MA, Fuller FB. 1951. Integrals and integral equations in linearized wing theory. *NACA Report 1054*

Mann MJ, Carlson HW. 1994. Aerodynamic design of supersonic cruise wings with a calibrated linearized theory. *J. Aircraft*. 31:25–41

Middleton WD, Carlson HW. 1965. A numerical method for calculating the flat-plate pressure distribution on supersonic wings of arbitrary planform. *NASA Tech. Note D–2570*

Middleton WD, Lundry JL. 1980. A system for aerodynamic design and analysis of supersonic aircraft. *NASA Contr. Rep. 3351*

Middleton WD, Lundry JL, Coleman RG. 1980. A system for aerodynamic design and analysis of supersonic aircraft. *NASA Contr. Rep. 3352*

Murthy SNB, Osborn JR. 1976. Base flow phenomena with and without injection: experimental results, theories, and bibliography. *Aerodynamics of Base Combustion*, Melkille NY: AIAA, pp. 7–210.

Nielsen JN, Matteson FH, Vincenti WG. 1948. Investigation of wing characteristics at a Mach number of 1.53, III: unswept wings of differing aspect ratio and taper ratio. NACA Res. Mem. A8E06

Pawlowski JW, Graham DH, Boccadoro CH, Coen PG, Maglieri DJ. 2005. *Origins and overview of the shaped sonic boom demonstration program*. Presented at Aerosp. Sci. Meet., 43rd, AIAA Pap. 2005–0005, Reno, NV

Pitts WC, Nielsen JN, Kaatari GE. 1959. Lift and center of pressure of wing-body-tail combinations at subsonic, transonic, and supersonic speeds. *NACA Rep. 1307*

Puckett AE. 1946. Supersonic wave drag of thin airfoils. *J. Aeron. Sci*. 13:475–484

Puckett AE, Stewart HJ. 1947. Aerodynamic performance of delta wings at supersonic speeds. *J. Aeron. Sci*. 14:567–578

Schiff LB, Steger JL. 1979. *Numerical simulation of steady supersonic viscous flow*. Presented at Aerosp. Sci. Meet., 17th, AIAA Pap. 79–0130, New Orleans, LA

Shapiro AH. 1954. *The Dynamics and Thermodynamics of Compressible Fluid Flow*. New York: The Ronald Press

Snow RM. 1948. Aerodynamics of thin quadrilateral wings at supersonic speeds. *Q. Appl. Math*. 5:417–428

Squire LC, Stanbrook A. 1964. Possible types of flow at swept leading edges. *Aeronaut. Quart*. 15:72–82

Staff of Boeing Commercial Airplanes. 1989. High-speed civil transport study. *NASA Contr. Rep. 4233*

Staff of Boeing Commercial Airplanes. 1989. High-speed civil transport study, summary. *NASA Contr. Rep. 4234*

Stewart HJ. 1946. "The lift of a delta wing at supersonic speeds," Quarterly of Applied Math., Vol. 4, No. 3, pp. 246–254

Tomaro RF, Wurtzler KE. 1999. *High speed configuration aerodynamics: SR-71 to SMV*. Presented at Appl. Aerodyn. Conf., 17th, AIAA Pap. 99–3204, Norfolk, VA

Van Dyke MD. 1951. First- and second-order theory of supersonic flow past bodies of revolution. *J. Aero. Sci*. 18(3):161–179

Van Dyke M. 1975. *Perturbation Methods in Fluid Mechanics*. Stanford: Parabolic Press

Walkley KB, Smith GE. 1987. Wave drag analysis of realistic fighter aircraft using a full-potential method. *J. Aircraft*. 24:623–628

Ward GN. 1955. *Linearized Theory of Steady High Speed Flow*. Cambridge: Cambridge University Press

Whitnah AM, Hillje ER. 1984. Space Shuttle wind tunnel testing program summary. *NASA RP 1125*

Wilde MG, Cormery G. 1970. The aerodynamic derivation of the concorde wing. *Can. Aeronaut. Space J*. 16:175–184

Wilson JR. 2007. "Quiet spike, softening the sonic boom," Aerospace America, Oct. 2007, pp. 38–42

Wood RM, Miller DS. 1985. Assessment of preliminary prediction techniques for wing leading-edge vortex flows at supersonic speeds. *J. Aircraft*. 22:473–478

Woodward FA. 1968. Analysis and design of wing-body combinations at subsonic and supersonic speeds. *J. Aircraft*. 5:528–534

Wright BR, Bruckman F, Radovich NA. 1978. *Arrow wings for supersonic cruise aircraft*. Presented at Aerosp. Sci. Meet., 18th, AIAA Pap. 78–0151, Huntsville, AL

12 HYPERSONIC FLOWS

Chapter Objectives

- Be able to describe the five characteristics that distinguish hypersonic flow from supersonic flow
- Understand the use and limitations of the Newtonian and modified Newtonian flow models
- Be able to determine the flow characteristics in the region of the stagnation point of a hypersonic vehicle
- Be able to find the lift, drag, and pitch moment for simple geometries at hypersonic speeds
- Understand the importance of heating at hypersonic speeds and be able to estimate heating rates on blunt bodies
- Have a basic understanding of boundary-layer transition at hypersonic speeds, and know why it is difficult to estimate

The most common question asked about hypersonic flow is "Why is it different than supersonic flow?" That is a good question! If supersonic flow is the regime where the flow is everywhere supersonic, then it would seem like flying at higher Mach numbers would not fundamentally change the nature of the flow. In fact, however, there are at

least five characteristics of hypersonic flow that are different than supersonic flow, or where supersonic flow theories break down. The differentiating characteristics, outlined in Anderson (2006), are:

- thin shock layers
- entropy layers
- viscous-inviscid interactions
- high-temperature effects and extreme heat transfer
- low-density flows

Understanding each of these effects will require learning about additional concepts and devising new ways to simulate these flows. As an example, we will discuss the first distinguishing characteristics, thin shock layers, as an example of why hypersonic flow is a unique flight regime.

A vehicle flying through the atmosphere at hypersonic speeds generates a shock layer (the region between the bow shock wave and the vehicle surface) in which the pressure, the temperature, and/or the density may change by two orders of magnitude, and more. Because the kinetic energy associated with hypersonic flight is converted into high temperatures within the shock layer, the flow-field trade studies conducted during the vehicle design include consideration both of the heat-transfer environment and of the aerodynamic forces and moments. Therefore, aerodynamicists often speak of the aerothermodynamic environment of a hypersonic vehicle.

By definition,

$$M_\infty = \frac{U_\infty}{a_\infty} \gg 1 \tag{12.1}$$

which is the basic assumption for all hypersonic flow theories. Unfortunately, it is not possible to define hypersonic flow in terms of Mach number. The internal thermodynamic energy of the free-stream fluid particles is small compared with the kinetic energy of the free stream for hypersonic flows. In flight applications, this results because the velocity of the fluid particles is relatively large. The limiting case, where M_∞ approaches infinity because the free-stream velocity approaches infinity while the free-stream thermodynamic state remains fixed, produces extremely high temperatures in the shock layer. The high temperatures associated with hypersonic flight cannot be accommodated in most ground test facilities. Therefore, in wind-tunnel applications, hypersonic Mach numbers are achieved through relatively low speeds of sound; that is, for the wind tunnel M_∞ approaches infinity because the speed of sound (the temperature) goes to "zero" while the free-stream velocity is held fixed. As a result, the fluid temperatures remain below the levels that would damage the wind tunnel and the model.

Another assumption common to hypersonic flow is that

$$\varepsilon = \frac{\rho_\infty}{\rho_2} \ll 1 \tag{12.2}$$

which is known as the small-density-ratio assumption. This assumption relates primarily to the properties of the gas downstream of the shock wave. Recall that, for a perfect gas,

$$\varepsilon = \frac{\gamma - 1}{\gamma + 1} \tag{12.3}$$

for a normal shock wave as $M_\infty \to \infty$. So, $\varepsilon = \frac{1}{6}$ for perfect air. Notice that typical hypersonic wind tunnels operate at conditions where the test gas can be approximated by the perfect-gas relations. However, during the reentry of the Apollo Command Module, the density ratio approached $\frac{1}{20}$.

For slender configurations, such as sharp cones and wedges, the strong shock assumption is:

$$M_\infty \sin \theta_b \gg 1 \tag{12.4}$$

which is mixed in nature, since it relates both to the flow and to the configuration. The concept termed the "Mach number independence principle" depends on this assumption.

Typical trajectories of various aircraft/spacecraft and the regions of different physical and chemical processes in the shock layer near such vehicles are shown in Fig. 12.1, which is from Hirschel (1991). Unlike the aerodynamic and heat-transfer characteristics of conventional aircraft, these problems are characterized for reentry (or for ascending) trajectories by a wide range of Reynolds numbers, extremely high Mach numbers, and high temperatures immediately behind the bow shock wave (up to several tens of thousands of degrees before the temperature associated with thermochemical equilibrium is reached). For that portion of the reentry trajectory at altitudes above the continuum flow regime, the stagnation pressure behind the shock wave varies from 10^{-4} to 10^{-3} atmospheres [Tirsky (1993)]. Finding theoretical or semi-empirical models that are appropriate for these trajectories is quite challenging.

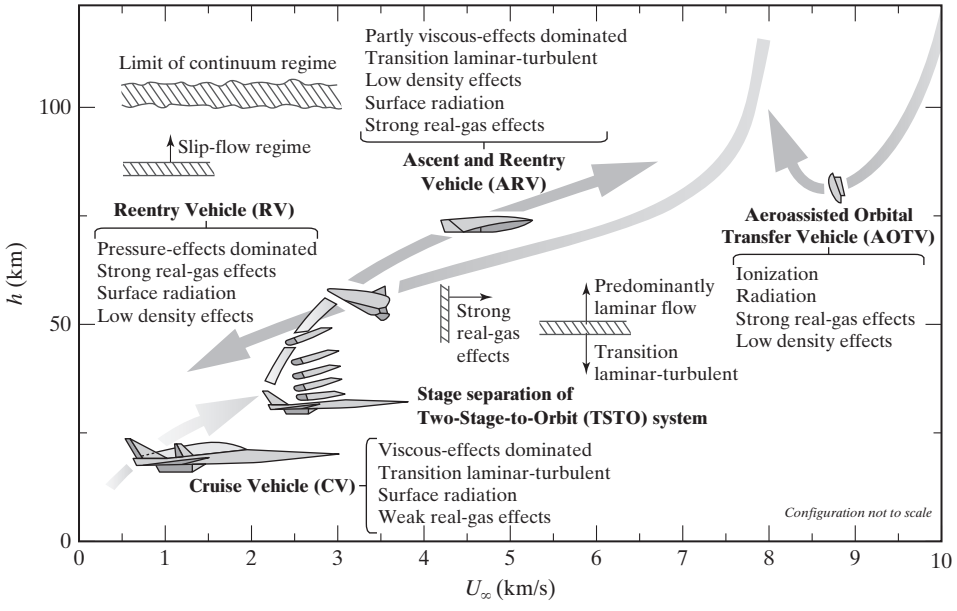

Figure 12.1 Typical trajectories of various spacecraft [from Bertin and Cummings (2006)].

12.1 THE FIVE DISTINGUISHING CHARACTERISTICS

12.1.1 Thin Shock Layers

The shock layer is the region between the shock and the surface of the body. For supersonic Mach numbers the shock layer is quite large, as shown in Fig. 12.2a, where the shock is 33.5° from the wedge surface for a Mach number of 2.0. As the Mach number increases, the shock is swept further aft (the shock angle is smaller), so the shock layer becomes thinner. If we assume that the wedge tables in Chapter 8 correctly predict flow at Mach 20, then Fig. 12.2b shows the position of the shock relative to the surface: the shock is only 5° above the surface. This means that the shock gets closer and closer to a surface as the Mach number increases.

In addition to the shock sweeping further aft, high-speed boundary layers have an interesting relationship between the boundary layer thickness and Mach number:

$$\delta \propto \frac{M_\infty^2}{\sqrt{\mathrm{Re}}}$$

While higher Reynolds numbers yield thinner boundary layers (as we learned in Chapter 4), higher Mach numbers yield thicker boundary layers (and notice that the Mach number is squared in the boundary-layer thickness relation). This means that hypersonic boundary layers, which often occur at high altitudes and Mach numbers, but at low Reynolds numbers, are relatively thick. Couple the fact that the boundary layers are thick with the observation that the shock layers are thin, and you can see why hypersonic flows might be different than supersonic flows. Specifically, thick boundary layers can interact with thin shock layers and increase the skin friction and heating on the surface of the vehicle.

While we were deriving oblique shock theory we assumed that the flow was inviscid. While all flows have some viscous effects, this assumption led to very good results because the viscous effects (skin friction) could be de-coupled from the inviscid effects (the impact of the shock). In hypersonic flow, this de-coupling is not necessarily appropriate, leading to inaccuracies in applying supersonic theory (such as wedge or cone tables or charts) to hypersonic flow. Limitations on the use of supersonic wedge and cone theory for hypersonic applications were determined by Lees (1951 and 1953), which were based on a hypersonic similarity parameter. These limitations primarily related the slenderness of the geometry and the Mach number of application, and found a wide range of applicability for many hypersonic vehicles, even at angle of attack.

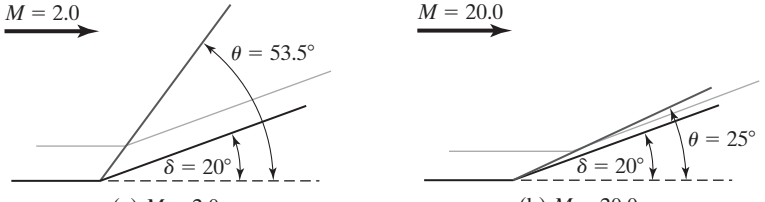

(a) $M = 2.0$ (b) $M = 20.0$

Figure 12.2 Comparison of shock wave angles for a 20° wedge at different Mach numbers.

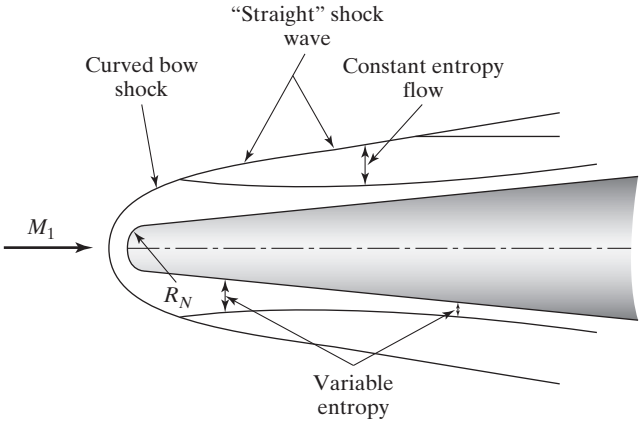

Figure 12.3 Variation of entropy on a blunt body at high speeds [from Bertin (1994)].

12.1.2 Entropy Layers

Supersonic flow theory, as developed in Chapter 8, assumed that the flow was isentropic everywhere except across a shock wave. This was a powerful assumption, since it allowed us to use isentropic relations to calculate flow properties in isentropic regions, and then use normal shock relations to determine the change in properties across the shocks. Implicit to this assumption is the fact that the shock waves had to be straight (or nearly straight). In hypersonic flow, however, bow shocks typically form in front of vehicles which are highly curved, as shown in Fig. 12.3. Along the curved portion of the shock wave, entropy changes vary at each location since the local shock angle is different. This means that there are different levels of entropy behind each location along the shock, so the flow field is not isentropic.

12.1.3 Viscous-Inviscid Interactions

Shock-boundary layer and shock-shock interactions were discussed in Sections 8.8 and 8.9, so you should review those sections for details on viscous-inviscid interactions. However, an example of how those interactions can easily take place on hypersonic vehicles will help in our understanding of why these interactions are so important.

During reentry, the Space Shuttle orbiter travels through a variety of angle of attack and Mach number ranges. At extremely high altitudes, the bow shock from the nose of the Orbiter (see Fig. 12.4) is swept back sharply. When the bow shock reaches the region of the Orbiter wing, it can interact with the shock wave in front of the wing leading edge. This shock-shock interaction may be classified as an Edney Type IV interaction (see Section 8.9), which produces severe heating in the region immediately behind the interaction region. In fact, during the reentry of Space Shuttle Columbia in 2003, a shock-shock interaction took place directly in front of where a piece of foam had impacted Columbia during launch, which led to the destruction of the vehicle. According to Bertin and Cummings (2006), "Post-flight analysis reported

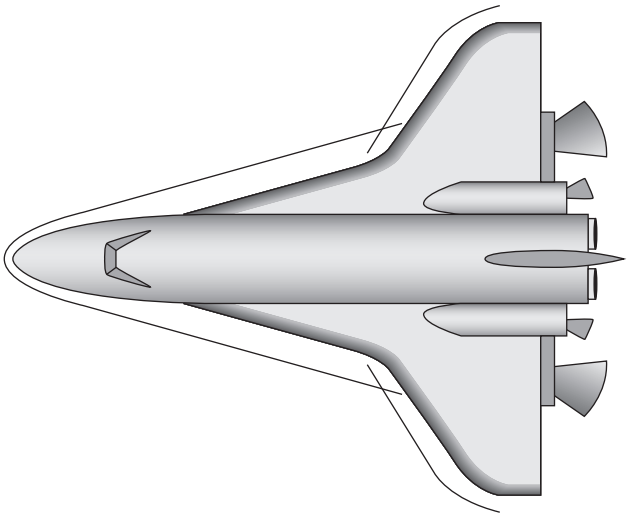

Figure 12.4 Interactions between the bow shock wave and the wing leading-edge shock wave for the Space Shuttle Orbiter [from Bertin (1994)].

by the Columbia Accident Investigation Board (2003) indicated that the impact of the piece of foam produced a breech in the TPS (thermal protection system) . . . a relatively small breech of the TPS provided a path for the hot gases in the entry aerothermodynamics environment to reach the interior of the left wing, creating the ever-expanding damage pattern that ultimately led to the demise of OV-102 (the Columbia) during mission STS-107."

12.1.4 High Temperature Effects

Chemically reacting flows take place when the flow-field temperature reaches levels that cause the molecules in the atmosphere to start reacting and changing their state. For example, at temperatures greater than 800 K molecular vibration occurs. For temperatures above 2000 K diatomic oxygen dissociates (O_2 becomes O), and above 4000 K oxygen dissociation is complete and diatomic nitrogen dissociates and forms nitric oxide (NO), which may ionize. At temperatures above 9000 K nitrogen dissociation is complete and oxygen and nitrogen atoms ionize [Anderson (2006)]. So, what is the impact of these observations? Quite simply, most of our basic assumptions about perfect gasses being in equilibrium with a constant ratio of specific heats are invalid! This means that traditional analysis of heating on hypersonic vehicles can be in error. For example, uncertainties in pre-flight heating estimates for the Shuttle Orbiter based on empirical correlations complemented by analytical solutions are shown in Fig. 12.5. Notice that while the heating estimates for the nose were quite good, the wing leading-edge rates were highly inaccurate, and the predictions at other locations around the vehicle were mediocre at best.

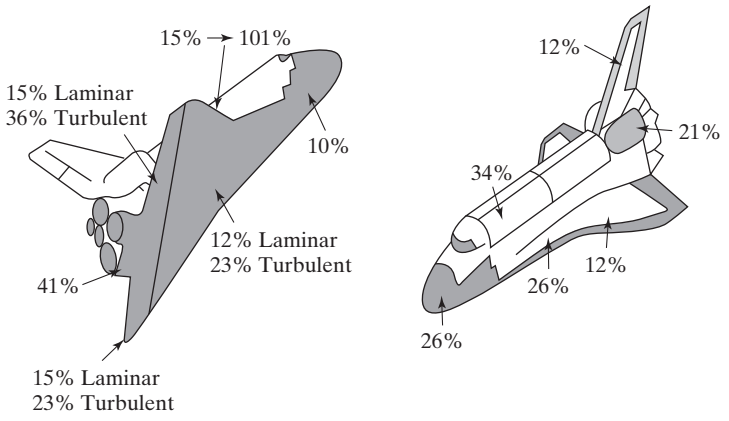

Figure 12.5 Uncertainties in pre-flight heating estimates for the Shuttle Orbiter [from Bertin (1994)].

12.1.5 Low-Density Flows

The peak heat-transfer rates of a vehicle entering the atmosphere typically occur at altitudes where the air behaves as a continuum [Bertin and Cummings (2006)]. Nevertheless, anomalously high temperatures already were being measured on the clevis and the spar during the fatal reentry of Columbia on mission STS-107 at altitudes of approximately 91,441 m (300,000 ft). The density of the air in this altitude range is relatively low and the mean-free path (the distance between collisions of air particles) is relatively high. The ratio of the mean-free path to the characteristic length of the vehicle is known as the Knudsen number, $Kn = \lambda/L$. Since most aerodynamic theories assume that the flow is a continuum (e.g., $\lambda \approx 10^{-7}$ ft at low altitudes and $Kn \approx 0$), at altitudes above 340,000 ft the mean-free path is greater than 1 ft (and $Kn \rightarrow 1$).

Under these conditions, the Navier-Stokes equations are not valid, and flow field solutions should be obtained using the Boltzmann equation. Typically, however, semi-empirical relations are used to simulate low-density flow. An alternative technique known as Direct Simulation Monte Carlo (DSMC) was proposed by Bird in 1973 [see Bird (1978) for more details], which is essentially a numerical technique for approximating the Boltzmann equation.

Aerodynamics Concept Box: A High-Speed "Gotcha" during the X-15 Program

Near the end of the X-15 program in the 1960s, it was decided to test a dummy ramjet engine on the X-15 at hypersonic Mach numbers. In order to alleviate the high heating rates, the X-15 was painted with an ablative coating, which burns away during the flight but protects the aircraft surface material from over-heating. The X-15A-2, with ablative coating, external tanks, and the dummy ramjet engine attached to the lower rear pylon is shown below shortly after launch from a B-52.

X-15A-2 after release from a B-52 (courtesy of NASA Dryden Flight Research Center)

The pilot on October 3, 1967, was Pete Knight, a veteran of the X-15 program. After launch from the B-52, the X-15 accelerated and climbed, eventually recording a Mach number of 6.7. During approach for landing, a NASA chase plane announced that something had fallen from the X-15, and after landing engineers found significant damage to the X-15, but especially to the area around the lower rear pylon . . . and the dummy ramjet was missing! In fact, the lower pylon was severely damaged, with large burned-through regions near the front of the pylon. What had happened? High-speed flight had just given the engineers a "gotcha", where they learned something they had not really known before. At Mach 6.7, the bow shock from the front of the vehicle had intersected the bow shock in front of the dummy ramjet in a Type IV shock-shock interaction, creating a supersonic high-temperature jet which burned away the ramjet and severely damaged the pylon. This would not be the last time such a problem took place, but engineers were now warned about the dangers of shock-shock interactions.

X-15A-2 after landing: notice charring on lower pylon and speed brake on vertical tail (courtesy of NASA Dryden Flight Research Center)

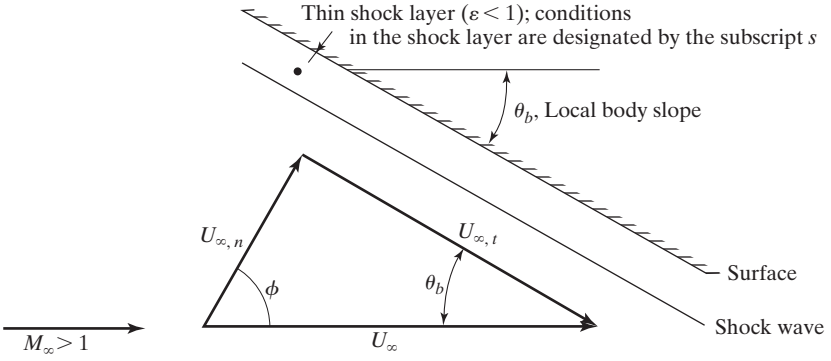

Figure 12.6 Nomenclature for Newtonian flow model.

12.2 NEWTONIAN FLOW MODEL

As the free-stream Mach number approaches infinity and the hypersonic independence principle applies to the flow, the shock layer becomes very thin. As a result, we can assume that the speed and direction of the gas particles in the free stream remain unchanged until they strike the solid surface exposed to the flow. For this flow model (termed *Newtonian flow theory* since it is similar in character to one described by Newton in the seventeenth century), the normal component of momentum of the impinging fluid particle is wiped out, while the tangential component of momentum is conserved. Therefore, using the nomenclature of Fig. 12.6 we can write the integral form of the momentum equation for a constant-area streamtube normal to the surface,

$$p_\infty + \rho_\infty (U_{\infty, n})^2 = p_\infty + \rho_\infty (U_\infty \sin \theta_b)^2 = p_s \tag{12.5}$$

Rearranging so that the local pressure is written in terms of the pressure coefficient gives

$$C_p = \frac{p_s - p_\infty}{\frac{1}{2}\rho_\infty U_\infty^2} = 2 \sin^2 \theta_b = 2 \cos^2 \phi \tag{12.6}$$

The pressure coefficient, as defined in equation (12.6), is known as the Newtonian value, where the 2 represents the pressure coefficient at the stagnation point (which is designated $C_{p, t2}$), since $\theta_b = 90°$ at the Newtonian stagnation point. You should notice that no small angle assumption was made during the derivation of Newtonian flow theory, so it can be applied to a stagnation point on a blunt body. Also, Newtonian flow theory assumes that free-stream pressure, $C_p = 0$, acts on all surfaces that are not directly impacted by the free-stream flow (called "shadow" surfaces).

The Newtonian flow model and the various theories for thin shock layers related to the Newtonian approximation are based on the small-density-ratio assumption. The small-density-ratio requirement for Newtonian theory also places implicit restrictions on the body shape in order that the shock layer be thin. The range of applicability for Newtonian theory, as defined by Marconi et al. (1976), is reproduced in Fig. 12.7. Small perturbation theory yields accurate results only for the flow over slender bodies at small angles of attack in a low supersonic Mach number stream. However, Newtonian theory

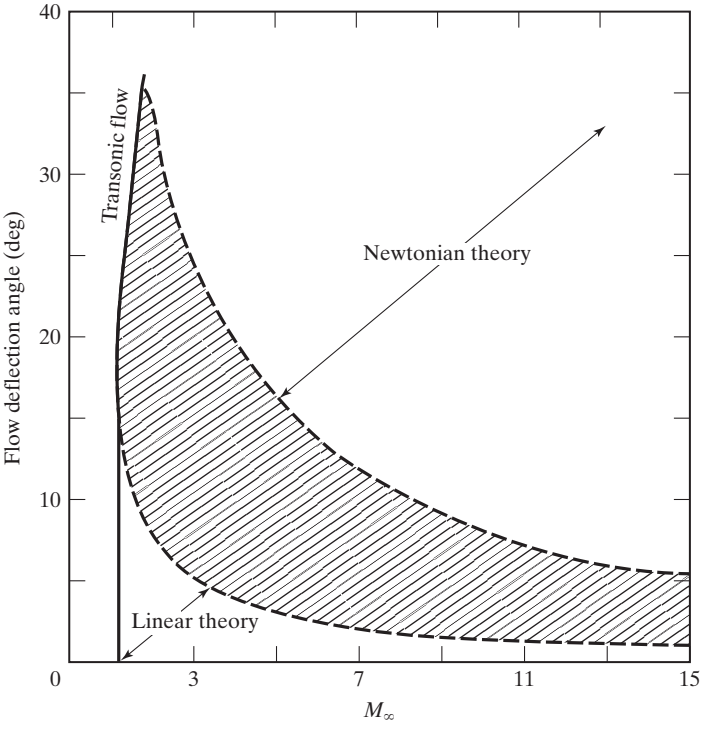

Figure 12.7 Regions of applicability of inviscid flow theories for the surface pressure on a sharp cone [from Marconi et al. (1976)].

provides useful results when the Mach number is large and/or the flow deflection angle is large. This is equivalent to the strong shock assumption

$$M_\infty \sin \theta_b \gg 1$$

Consider the pressure coefficients presented in Fig. 12.8. Theoretical values of C_p (taken from Chapter 8) are presented as a function of M_∞ for a cone whose semivertex angle is 15° and for a 15° wedge. Notice that, as $M_\infty \to \infty$, the pressure coefficients become independent of the Mach number (the Mach number independence principle). The shock layer is thinner for the cone, and the limiting value of C_p is approached at a lower Mach number. Also presented is the Newtonian pressure coefficient (which is independent of the Mach number). As $M_\infty \to \infty$, all three techniques yield roughly the same value for C_p. Therefore, at hypersonic speeds the pressure coefficient for these simple shapes depends primarily on the flow deflection angle.

The Mach number independence principle was derived for inviscid flow, as discussed in Oswatitsch (1956). Since pressure forces are much larger than the viscous forces for blunt bodies or for slender bodies at relatively large angles of attack when the Reynolds number exceeds 10^5, we would expect the Mach number independence principle to hold at these conditions.

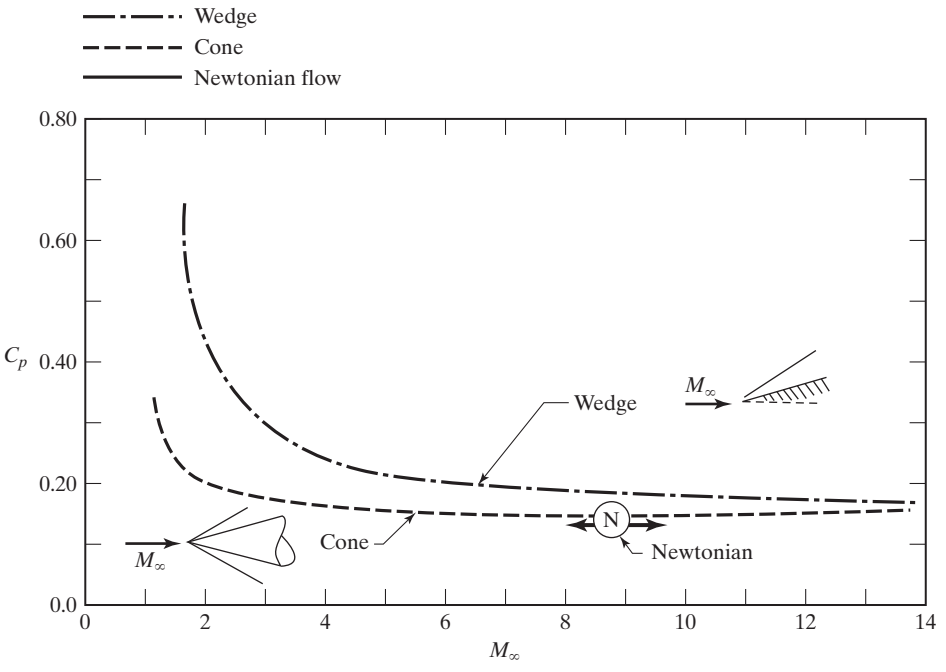

Figure 12.8 Pressure coefficient for the flow of perfect air past a wedge and a cone; deflection angle is 15°.

EXAMPLE 12.1: Comparing predictions using Newtonian flow theory with experimental data

A hemisphere was tested in the U.S. Air Force Academy Trisonic Wind Tunnel at Mach 4.38 at zero degrees angle of attack. The measured pressure coefficient at $\theta_b = 0^\circ, 90^\circ$ was $C_p = 0.0237, 1.818$, respectively. Using Newtonian flow theory, estimate the pressure coefficient at the stagnation point and at the top of the hemisphere and comment on the accuracy of the predictions.

Solution: Newtonian flow theory determines the pressure coefficient solely based on the local slope of the surface. From equation (12.6), the pressure coefficient is:

$$C_p = 2\sin^2\theta_b$$

The local surface slopes, θ_b, for the top of the hemisphere and the stagnation point are 0° and 90°, respectively. Therefore, Newtonian flow theory predicts the pressure coefficient for these two locations to be $C_p = 0.0, 2.0$. These values compare fairly well with the experimental data, although Newtonian flow theory overpredicts the stagnation point pressure coefficient by approximately 10%.

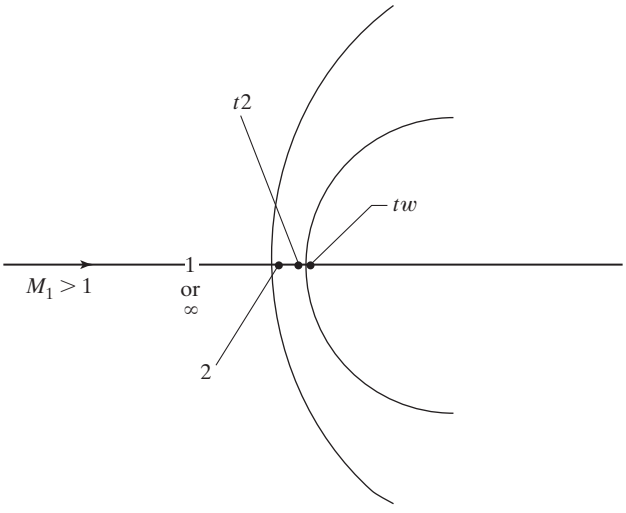

Figure 12.9 Nomenclature for the stagnation region: 1 or ∞, free-stream conditions; 2, conditions immediately downstream of the shock wave; *t*2, conditions at the stagnation point (downstream of the normal portion of the shock wave) but outside the boundary layer; *tw*, conditions at the wall at the downstream stagnation point.

12.3 STAGNATION REGION FLOW-FIELD PROPERTIES

The nomenclature for the flow near the stagnation point of a vehicle in a hypersonic stream is illustrated in Fig. 12.9. The free-stream flow (designated by the subscript ∞ or 1) passes through the normal portion of the shock wave reaching state 2 and then decelerates isentropically to state *t*2, which constitutes the edge condition for the thermal boundary layer at the stagnation point. The streamline from the shock wave to the stagnation point may be curved for nonaxisymmetric flow fields. The pressure and the heating rate at the stagnation point are useful reference values for characterizing hypersonic flows.

The relations for steady, one-dimensional, inviscid, adiabatic flow in a constant-area streamtube were used to compute the conditions across a normal shock wave:

$$\rho_1 U_1 = \rho_2 U_2 \tag{12.7}$$

$$p_1 + \rho_1 U_1^2 = p_2 + \rho_2 U_2^2 \tag{12.8}$$

$$h_1 + \tfrac{1}{2}U_1^2 = h_2 + \tfrac{1}{2}U_2^2 = H_t \tag{12.9}$$

where H_t is the total (or stagnation) enthalpy of the flow.

If we assume that the gas is thermally perfect,

$$p = \rho R T \tag{12.10}$$

and calorically perfect,

$$h = c_p T \tag{12.11}$$

the ratio of the values of flow properties across the shock wave can be written as a unique function of M_1 (or M_∞, the free-stream Mach number) and γ (the ratio of specific heats). Referring to Chapter 8, the relations are:

$$\frac{p_2}{p_1} = \frac{2\gamma M_1^2 - (\gamma - 1)}{\gamma + 1} \tag{12.12}$$

$$\frac{\rho_2}{\rho_1} = \frac{U_1}{U_2} = \frac{(\gamma + 1)M_1^2}{(\gamma - 1)M_1^2 + 2} \tag{12.13}$$

$$\frac{T_2}{T_1} = \frac{[2\gamma M_1^2 - (\gamma - 1)]\,[(\gamma - 1)M_1^2 + 2]}{(\gamma + 1)^2 M_1^2} \tag{12.14}$$

If we also assume that the flow decelerates isentropically from the conditions at point 2 (immediately downstream of the normal portion of the shock wave) to the stagnation point outside of the thermal boundary layer (point $t2$),

$$\frac{p_{t2}}{p_1} = \left[\frac{(\gamma + 1)M_1^2}{2}\right]^{\gamma/(\gamma-1)} \left[\frac{\gamma + 1}{2\gamma M_1^2 - (\gamma - 1)}\right]^{1/(\gamma-1)} \tag{12.15}$$

$$\frac{T_{t2}}{T_1} = \frac{T_{t1}}{T_1} = 1 + \frac{\gamma - 1}{2} M_1^2 \tag{12.16}$$

Notice that, while it is generally true that the stagnation enthalpy is constant across a normal shock wave for an adiabatic flow [see equation (12.9)], the stagnation temperature is constant across a normal shock wave only for the adiabatic flow of a perfect gas [see equation (12.16)]. Also notice that for a perfect gas (i.e., one that is thermally perfect and calorically perfect), the ratio of the downstream value to the free-stream value for the flow properties (across a normal shock wave) can be written as a function of γ and $M_1 (= M_\infty)$ only. Thus, the perfect-gas values for the ratios defined by equations (12.12) through (12.16) do not depend specifically on the altitude.

In reality, for hypersonic flight, the gas molecules that pass through the bow shock wave are excited to higher vibrational and chemical energy modes. This lowers the specific-heat ratio of the gas below the free-stream value if it is assumed that equilibrium exists and that dissociation is not driven to completion. A large amount of the energy that would have gone into increasing the static temperature behind the bow shock wave for a perfect gas is used instead to excite the vibrational energy levels or to dissociate the gas molecules. As additional energy is absorbed by the gas molecules entering the shock layer, the conservation laws and the thermophysics dictate certain changes in the forebody flow. The static temperature, the speed of sound, and the velocity in the shock layer are less for the equilibrium, real-gas flow than for a perfect-gas flow. The real-gas value of the static pressure is slightly larger than the perfect-gas value. The density is increased considerably, and, as a result, the shock layer thickness is reduced.

Equations (12.7) through (12.9) are not restricted to the perfect-gas assumption and can be applied to a high-temperature, hypersonic flow. We will use the U.S. Standard Atmosphere (1976) to define the free-stream properties (i.e., p_1, ρ_1, and h_1, at 150,000 ft). Since there are four unknowns in equations (12.7) through (12.9)

(i.e., p_2, ρ_2, h_2, and U_2), but only three equations, additional relations are needed to obtain a solution. The graphs of Moeckel and Weston (1958) (see Fig. 12.10) were used in tabular form to define:

$$\rho(p, h)$$
$$s(p, h)$$
$$T(h, s)$$

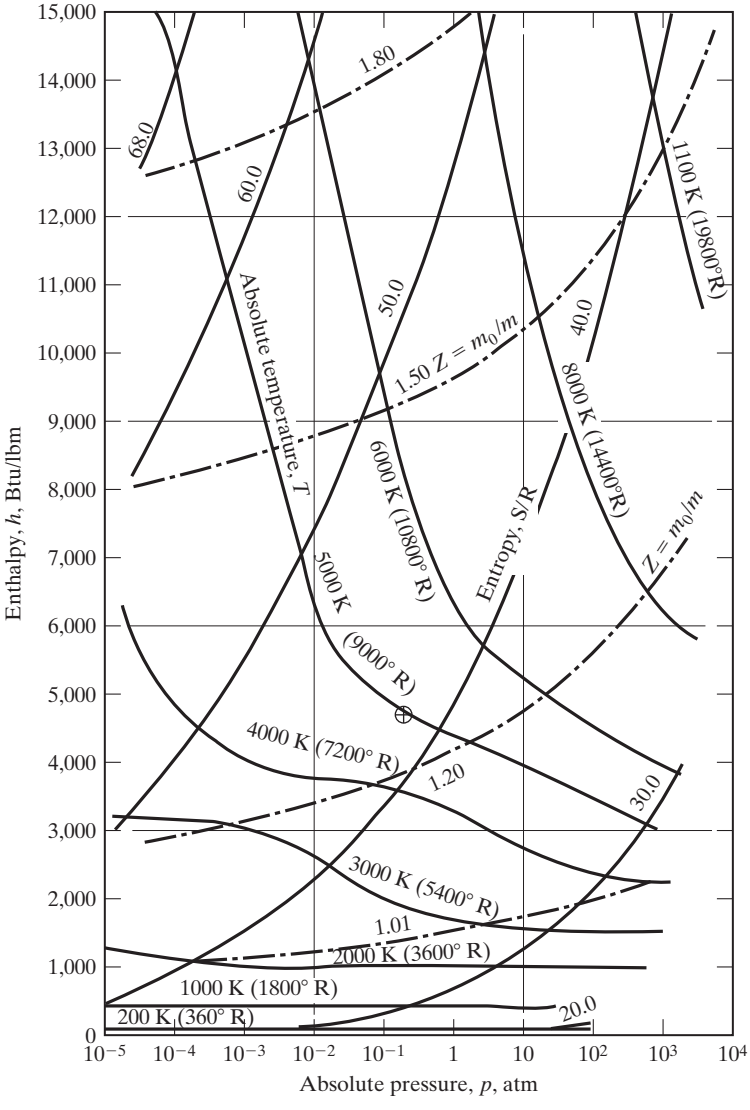

Figure 12.10 Thermodynamic properties of air in chemical equilibrium [from Moeckel and Weston (1958)].

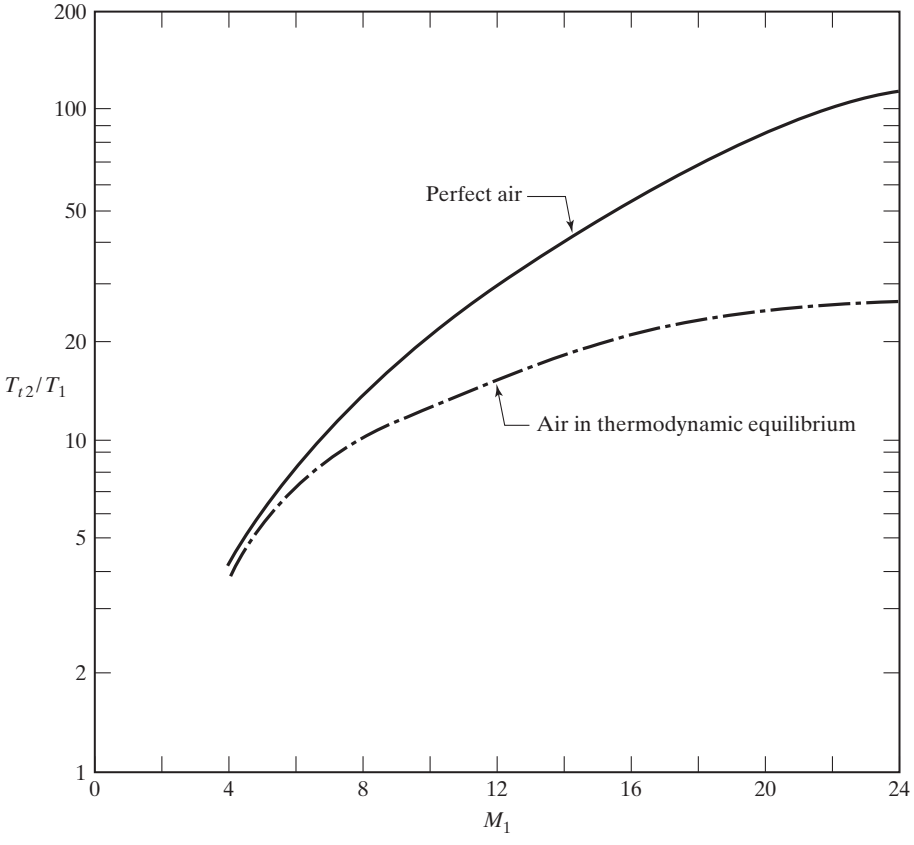

Figure 12.11 Temperature at the stagnation point (at the edge of the boundary layer) of a sphere ($R_N = 0.3048$ m) at an altitude of 45,721 m.

We can now calculate the flow downstream of a normal shock wave when $M_1 = 14$ at an altitude of 150,000 ft. Using the more generally applicable expression equation (12.9),

$$H_{t1} = h_1 + \tfrac{1}{2}U_1^2 = H_{t2} = H_t = 4636.77 \text{ Btu/lbm}$$

Assuming that the air remains in thermodynamic equilibrium as it crosses the shock wave, p_{t2} is 0.3386 atm (716.57 lb/ft^2) and T_{t2} is 8969.6°R, as represented by the $\oplus$ in Fig. 12.10. Using the perfect-gas relations of equations (12.12) through (12.16), p_{t2} is 0.3256 atm (689.12 lb/ft^2) and T_{t2} is 19,325°R.

The perfect-gas values and the equilibrium air values for $T_{t2}/T_1, p_{t2}/p_1$, and $C_{p,t2}$ (the pressure coefficient at the stagnation point) are presented as a function of the free-stream Mach number for an altitude of 150,000 ft in Figs. 12.11, 12.12, and 12.13, respectively. The comments made earlier regarding the qualitative differences between the perfect-gas values and those for equilibrium air (e.g., "The real-gas value of the static pressure is slightly larger than the perfect-gas value") are illustrated in Figs. 12.12 and 12.13.

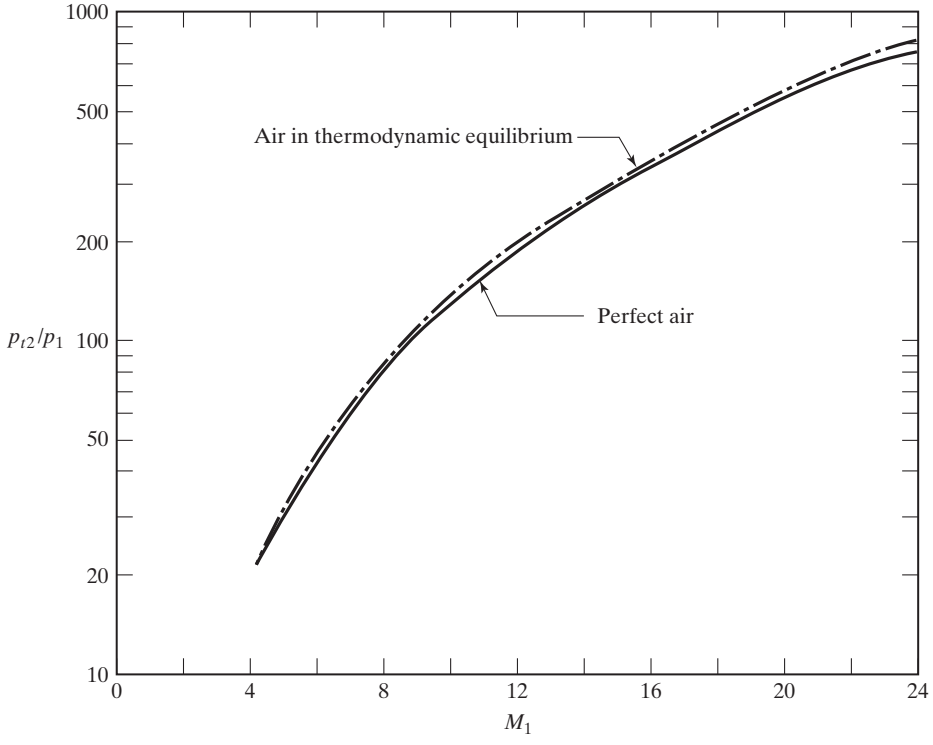

Figure 12.12 Pressure at the stagnation point of a sphere ($R_N = 0.3048$ m) at an altitude of 45,721 m.

The ratio of T_{t2}/T_1 is presented in Fig. 12.11. As noted earlier, the energy absorbed by the dissociation process causes the real-gas equilibrium temperature to be markedly lower than the perfect-gas value. The specific heat correlations that were presented by Hansen (1957) as a function of pressure and of temperature can be used to identify conditions where the dissociation of oxygen and of nitrogen affect the properties. Hansen notes that, at all pressures, the dissociation of oxygen is essentially complete before the dissociation of nitrogen begins. Based on Hansen's correlations, the oxygen dissociation reaction begins near Mach 7 and the nitrogen reaction begins near Mach 18 for the equilibrium air model at 150,000 ft.

The p_{t2}/p_1 ratio and the stagnation-point pressure coefficient are presented in Figs. 12.12 and 12.13, respectively. As noted earlier, the real-gas value of the static pressure is slightly greater than the perfect-gas value. Note that, at $M_1 = 4$, the stagnation pressure coefficient $C_{p,t2}$ is approximately 1.8 for both perfect air and for air in thermodynamic equilibrium. At $M_1 = 24$, $C_{p,t2}$ is 1.932 for the equilibrium air model as compared with 1.838 for perfect air and 2 for Newtonian flow.

From the preceding discussion, it should be clear that the changes in a fluid property across a normal shock wave are a function of M_1 and γ only for a perfect gas [see equation (12.12)], that is,

$$\frac{p_2}{p_1} = f(M_1, \gamma)$$

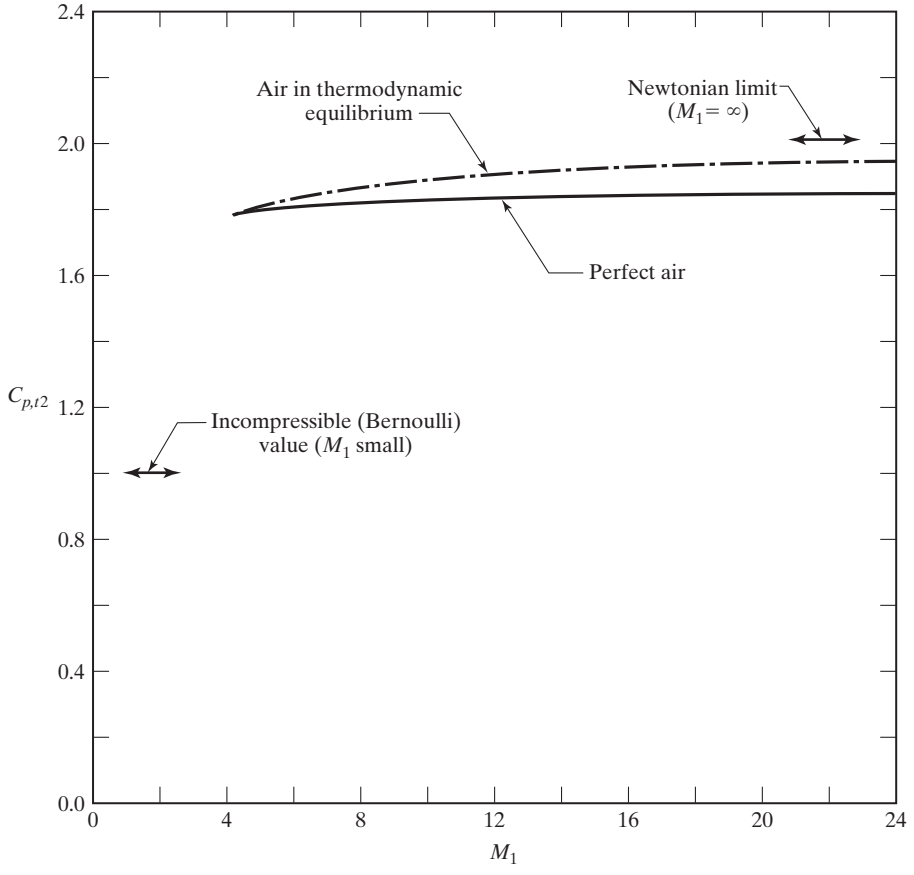

Figure 12.13 Pressure coefficient at the stagnation point of a sphere ($R_N = 0.3048$ m) at an altitude of 45,721 m.

However, for a reacting gas in chemical equilibrium, three free-stream parameters are necessary to obtain the ratios of properties across a normal shock wave (the free-stream velocity and two thermodynamic properties),

$$\frac{p_2}{p_1} = f(U_1, p_1, T_1)$$

12.4 MODIFIED NEWTONIAN FLOW

It is evident in the computed values for the pressure coefficient at the stagnation point presented in Fig. 12.13 that even when $M_1 = 24$, $C_{p,t2}$ is 1.838 for perfect air and is 1.932 for air in thermodynamic equilibrium. Therefore, as noted by Lees (1955), it would be more appropriate to compare the ratio $C_p/C_{p,\max}$ with $\sin^2\theta_b$ (or, equivalently, $\cos^2\phi$). Such a comparison is presented in Fig. 12.14 using data for hemispherically capped cylinders. Even though the data of Fig. 12.14 are for free-stream Mach numbers from 1.97 to 4.76, the $\sin^2\theta_b$ relation represents the data quite adequately

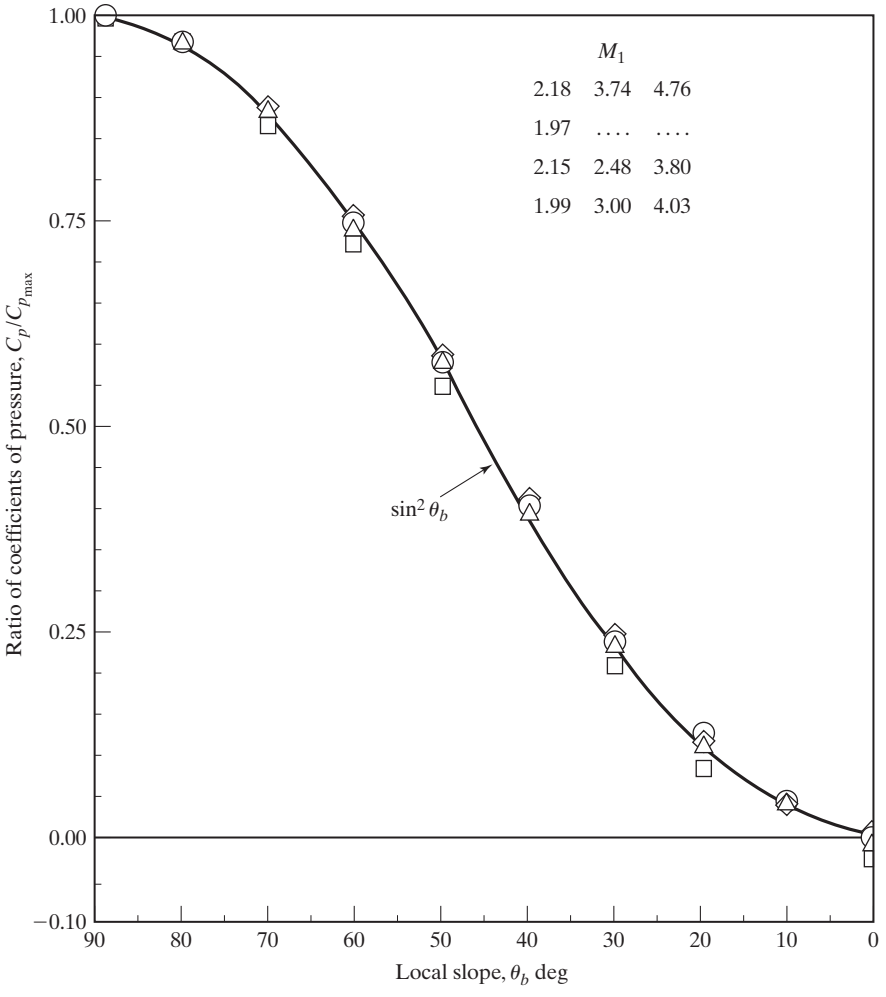

Figure 12.14 Correlation between $C_p/C_{p,\max}$ ratio and local body slope [from Isaacson and Jones (1968)].

for this blunt configuration. Therefore, an alternative representation of the pressure coefficient for hypersonic flow is

$$C_p = C_{p,t2}\sin^2\theta_b = C_{p,t2}\cos^2\phi \tag{12.17}$$

which will be termed *modified Newtonian flow theory*. $C_{p,t2}$ can be obtained from experimental values or by using the Rayleigh pitot formula:

$$\frac{p_{t2}}{p_1} = \underbrace{\frac{p_{t2}}{p_{t1}}}_{\text{Table 8.3}}\underbrace{\frac{p_{t1}}{p_1}}_{\text{Table 8.1}} \qquad C_{p,t2} = \frac{2}{\gamma M_1^2}\left(\frac{p_{t2}}{p_1} - 1\right)$$

Aerodynamics Concept Box: How Well Does Newtonian Flow Theory Really Work?

Newtonian and modified Newtonian flow theories seem so simple, but we often doubt that they can be very accurate. In order to test their applicability, a hemisphere model was instrumented with pressure ports and run in the U.S. Air Force Academy Trisonic Wind Tunnel. The model was run at M = 4.38, and a Schlieren photograph of the model in the tunnel is shown below. Notice the bow shock that has formed in front of the model (dark region) and the expansion region as the flow goes around the hemisphere (light region).

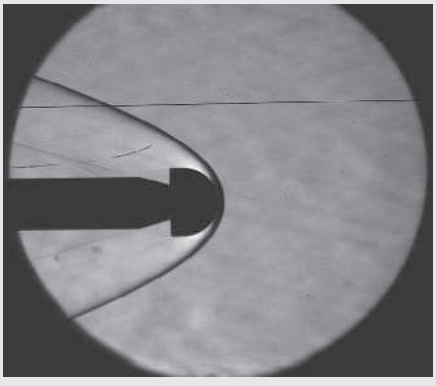

Pressures were measured at 10 tap locations on the hemisphere, ranging from the stagnation point to a position at the top of the model. A comparison of Newtonian and modified Newtonian flow theory predictions with the measured data is shown below. Notice that the Newtonian theory overpredicts the pressures due to the use of the coefficient 2.0, while the modified Newtonian prediction, which uses a coefficient of 1.8, matches the experimental data extremely well.

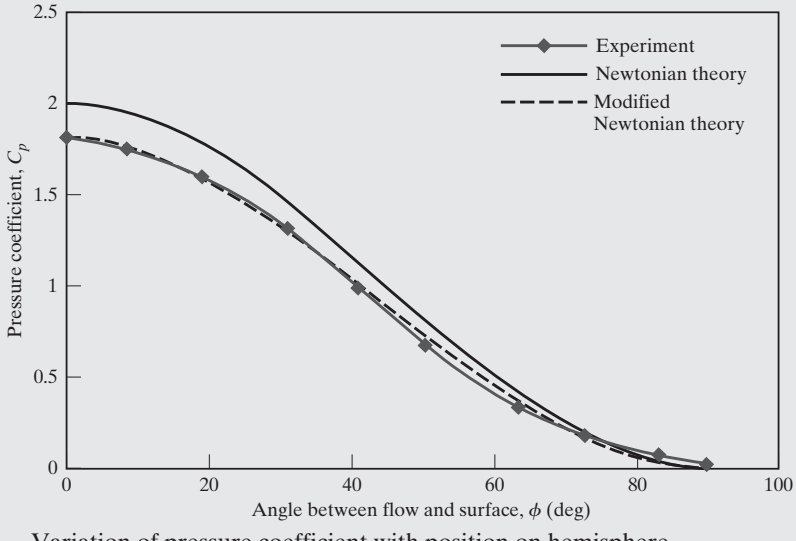

Variation of pressure coefficient with position on hemisphere.

EXAMPLE 12.2: Derive an expression for the drag coefficient of a sphere

Neglecting the effects of skin friction and using the modified Newtonian flow model to describe the pressure distribution, derive an expression for the drag coefficient for a sphere.

Solution: Because the sphere is a blunt configuration, the pressure forces are the principal component of the drag force at high Reynolds numbers. Therefore, using the coordinate system shown in Fig. 12.15, the drag on the sphere due to the pressure is

$$D = \int p[\,2\pi y(ds)\,] \sin\theta_b = \int p2\pi y\, dy$$

where the incremental surface area on which the pressure acts is $[\,2\pi y(ds)\,]$; refer to the shaded region on the forebody in Fig. 12.15. As discussed in Chapter 5, the net resultant force in any direction due to a constant pressure acting over a closed surface is zero. So, the pressure coefficient can be used in our expression for the drag:

$$D = q_\infty \int C_p 2\pi y\, dy \tag{12.18}$$

Using modified Newtonian theory to define the pressure, as given by equation (12.17), with the coordinates shown in Fig. 12.15,

$$C_p = C_{p,t2} \sin^2\theta_b = C_{p,t2}\left(\frac{dy}{ds}\right)^2 = C_{p,t2}\frac{(y')^2}{1 + (y')^2} \tag{12.19}$$

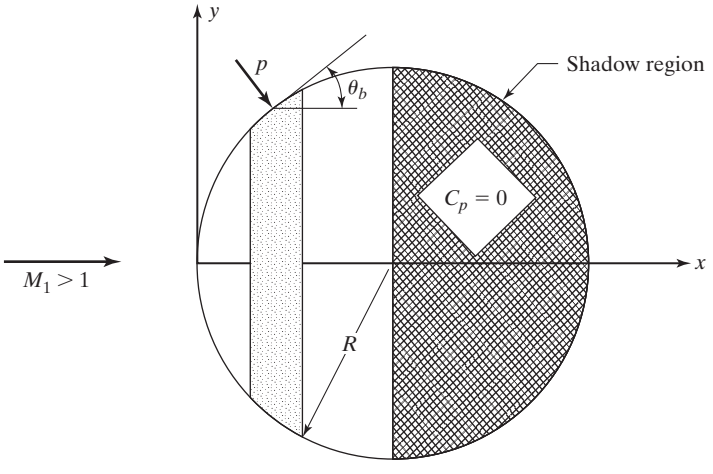

Figure 12.15 Sketch for calculating the modified Newtonian pressure drag on a sphere, Example 12.2.

where $y' = dy/dx$. Combining equations (12.18) and (12.19), the expression for the drag becomes

$$D = q_\infty C_{p,t2} \int_0^R \frac{(y')^2}{1 + (y')^2} 2\pi y\, y'\, dx \tag{12.20}$$

The limits of the integration are $0 \le x \le R$, since, according to the Newtonian flow model, the pressure coefficient on the leeward side (i.e., the crosshatched region of the sphere in Fig. 12.15) is zero.

For the sphere,

$$y = (2xR - x^2)^{0.5}$$

and

$$\frac{dy}{dx} = \frac{R - x}{(2xR - x^2)^{0.5}}$$

Substituting these expressions into equation (12.20),

$$D = 2\pi q_\infty C_{p,t2} \int_0^R \frac{\left[\dfrac{R - x}{(2xR - x^2)^{0.5}}\right]^3}{1 + \dfrac{(R - x)^2}{2xR - x^2}} (2xR - x^2)^{0.5}\, dx$$

Simplifying and integrating yields

$$D = \frac{2\pi q_\infty C_{p,t2}}{R^2}\left[R^3 x - \frac{3}{2}x^2R^2 + x^3R - \frac{x^4}{4}\right]_0^R$$

$$= \frac{C_{p,t2}}{2} q_\infty \pi R^2$$

and the drag coefficient becomes,

$$C_D = \frac{D}{q_\infty \pi R^2} = \frac{C_{p,t2}}{2} \tag{12.21}$$

We will consider the case where the modified Newtonian flow model is applied in a similar manner to calculate the pressure drag on a right circular cylinder whose axis is perpendicular to the free-stream flow. Although the pressure distribution is that given by equation (12.19) and the cross section is a circle, as shown in Fig. 12.15, the flow around the cylinder is two dimensional, whereas the flow around a sphere is axisymmetric. As a result, the section pressure drag coefficient (per unit span) for the cylinder is

$$C_{d,p} = \tfrac{2}{3} C_{p,t2} \tag{12.22}$$

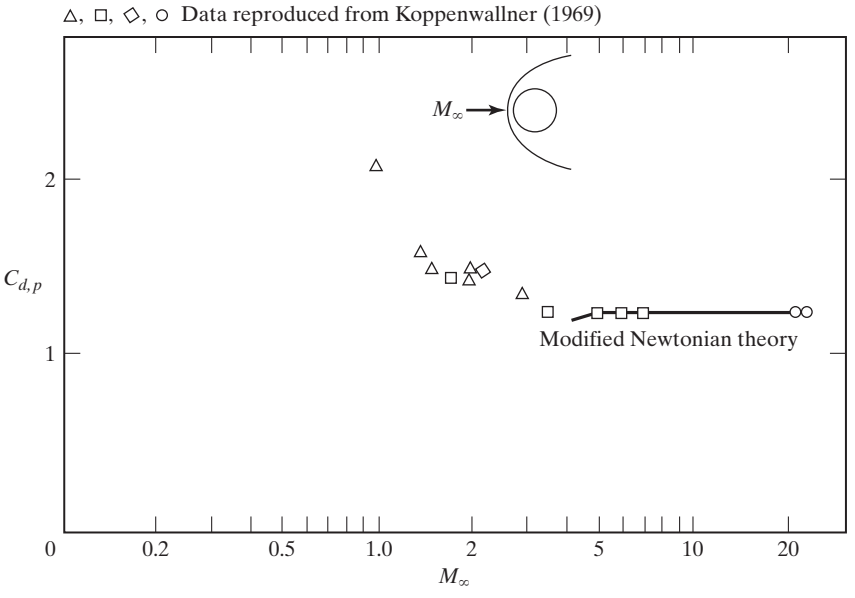

Figure 12.16 Pressure drag of a right circular cylinder as a function of Mach number [from Koppenwallner (1969)].

The values of section pressure drag coefficient calculated using equation (12.22) are compared in Fig. 12.16 with data that were presented in Koppenwallner (1969). Despite the simplifications inherent in this technique to calculate the theoretical drag coefficient, the agreement between the data and the theoretical values is outstanding. Notice also that the pressure drag for the blunt, right circular cylinder reaches its hypersonic limiting value by $M_\infty = 4$.

Data presented by Koppenwallner (1969) indicate a significant increase in the total drag coefficient for a right circular cylinder occurs due to the friction drag when the Knudsen number (which is the ratio of the length of the molecular mean free path to a characteristic dimension of the flow field) is greater than 0.01; the data presented by Koppenwallner are reproduced in Fig. 12.17. Using the Reynolds number based on the flow conditions behind a normal shock wave as the characteristic parameter,

$$\mathrm{Re}_2 = \frac{\rho_2 U_2 d}{\mu_2}$$

the friction drag for $\mathrm{Re}_2 > 10$ is given by

$$C_{d,f} = \frac{5.3}{(\mathrm{Re}_2)^{1.18}} \tag{12.23}$$

The data presented in Figs. 12.16 and 12.17 illustrate the significance of high-altitude effects on the aerodynamic coefficients.

The modified Newtonian flow model can be used to obtain a quick, engineering estimate of the pressure distribution. Consider the axisymmetric configuration shown

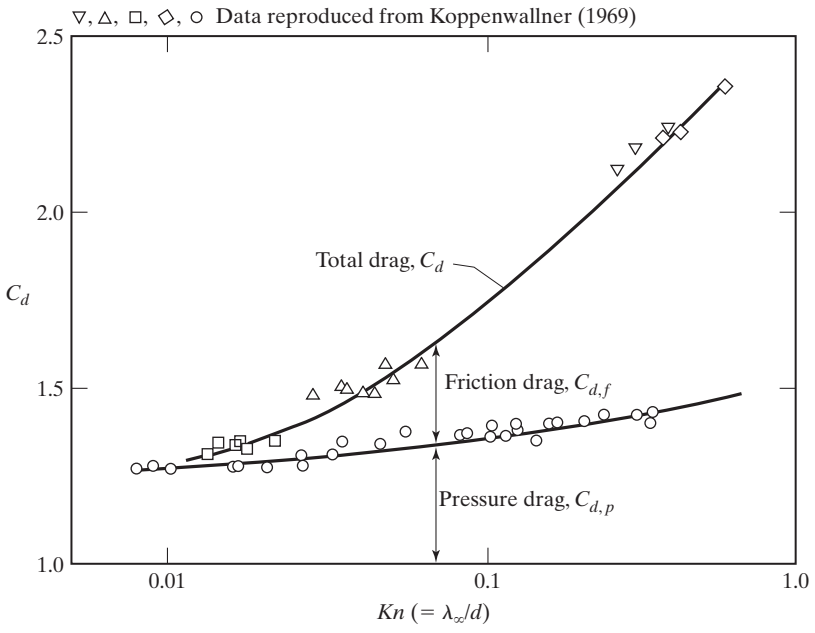

Figure 12.17 Contribution of the total drag due to friction drag and to pressure drag [from Koppenwallner (1969)].

in Fig. 12.18, where $\hat{n}$ is a unit vector that is normal to the surface element dA and is positive in the inward direction, θ is the local surface inclination, and β is the angular position of a point on the surface of the body. The angle η, the angle between the velocity vector $\vec{V}_\infty$ and the inward normal $\hat{n}$, is given by

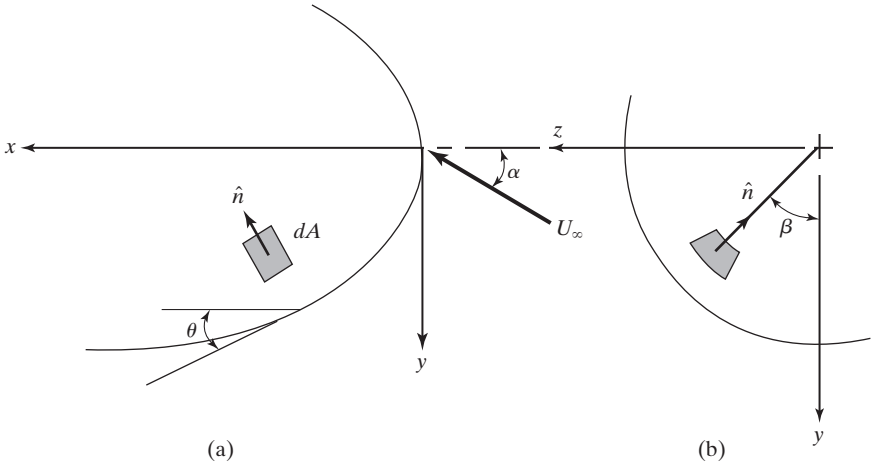

Figure 12.18 Coordinate system nomenclature for axisymmetric configurations: (a) side view; (b) front view.

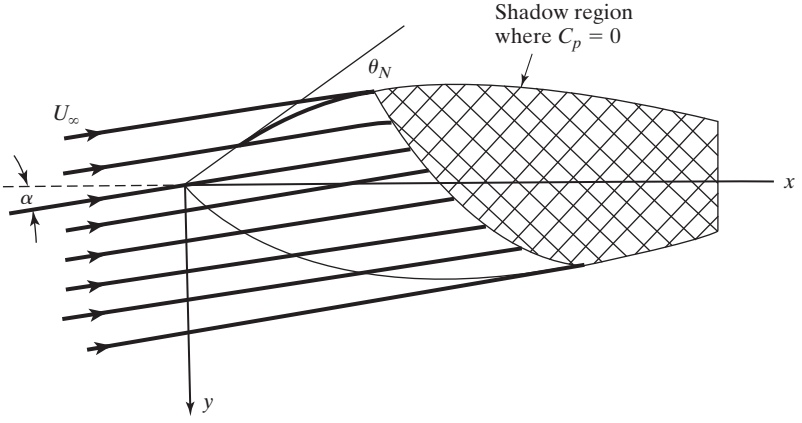

Figure 12.19 Region where $C_p = 0$, that is, that portion of the body which lies in the "shadow of the free stream."

$$\cos \eta = \frac{\vec{V}_\infty \cdot \hat{n}}{|\vec{V}_\infty||\hat{n}|} \tag{12.24}$$

where

$$\vec{V}_\infty = U_\infty \cos \alpha \hat{i} - U_\infty \sin \alpha \hat{j} \tag{12.25}$$

and

$$\hat{n} = \hat{i} \sin \theta - \hat{j} \cos \theta \cos \beta - \hat{k} \cos \theta \sin \beta \tag{12.26}$$

Based on these relations,

$$\cos \eta = \cos \alpha \sin \theta + \sin \alpha \cos \theta \cos \beta \tag{12.27}$$

so that the pressure coefficient is

$$C_p = C_{p,t2} \cos^2 \eta \tag{12.28}$$

In the Newtonian (or the modified Newtonian) model, the free-stream flow does not impinge on those portions of the body surface which are inclined away from the free-stream direction and which may, therefore, be thought of as lying in the "shadow of the free stream." This is illustrated in Fig. 12.19. For the modified Newtonian flow model, $C_p = 0$ in the shaded region of Fig. 12.19.

EXAMPLE 12.3: Determine the aerodynamic coefficients for a sharp cone

Consider hypersonic flow past a sharp cone where $-\theta_c \leq \alpha \leq \theta_c$, as shown in Fig. 12.20. Neglecting the effects of skin friction and using the modified Newtonian flow model to describe the pressure distribution, derive expressions for the lift coefficient, the drag coefficient, and the pitch moment coefficient.

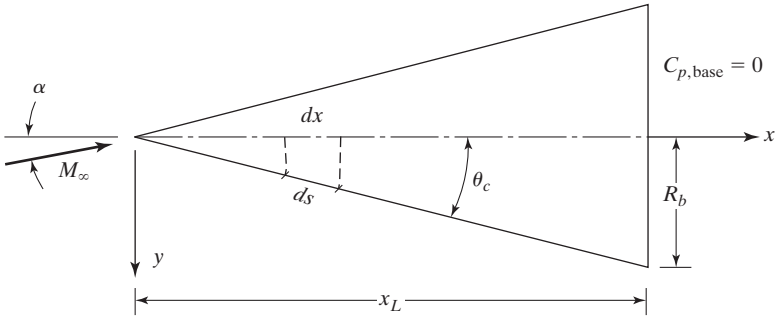

Figure 12.20 Nomenclature for hypersonic flow past a sharp cone.

Solution: For simplicity, let us first calculate the forces in a body-fixed coordinate system. As shown in Fig. 12.21, the forces in the body-fixed coordinate system are A, the force along the axis of the body, and N, the force normal to the body axis. Once A and N have been calculated, the lift and the drag can be calculated since:

$$L = N\cos\alpha - A\sin\alpha \tag{12.29}$$

and

$$D = N\sin\alpha + A\cos\alpha \tag{12.30}$$

Applying equations (12.24) through (12.28) specifically for the sharp cone flow depicted in Fig. 12.20,

$$C_p = C_{p,t2}(\cos\alpha\sin\theta_c + \sin\alpha\cos\theta_c\cos\beta)^2 \tag{12.31}$$

since the deflection angle is the cone semivertex angle, θ_c, which is a constant.

The axial force coefficient is found by integrating the pressure force over the entire (closed) surface of the cone:

$$C_A = \frac{1}{(\frac{1}{2}\rho_\infty U_\infty^2)(\pi R_b^2)} \oiint_S (p - p_\infty)(\hat{n}\, dS)\cdot\hat{i} \tag{12.32}$$

Recall that, since we are integrating over a closed surface, the net force in any direction due to a constant pressure acting on that closed surface is zero, so

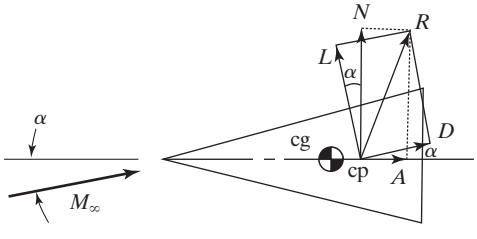

Figure 12.21 Resolving the forces acting on a vehicle.

subtracting p_∞, as is done in equation (12.32), does not affect the value of the axial force. A differential element for the surface of the cone (dS) is:

$$dS = r\,d\beta\,ds = (x\tan\theta_c)\,d\beta\frac{dx}{\cos\theta_c} \tag{12.33}$$

Combining equations (12.31) through (12.33) with equation (12.26) and noting that $C_{p,\text{base}} = 0$, the limits of integration are $0 \le \beta \le \pi$ (if we multiply by 2) and $0 \le x \le x_L$, the axial force coefficient is:

$$C_A = \frac{2C_{p,t2}}{\pi R_b^2}\int_0^{x_L}\left[\int_0^{\pi}(\cos^2\alpha\sin^2\theta_c + 2\sin\alpha\cos\alpha\sin\theta_c\cos\theta_c\cos\beta + \sin^2\alpha\cos^2\theta_c\cos^2\beta)(x\tan\theta_c)\,d\beta\frac{dx}{\cos\theta_c}\sin\theta_c\right]$$

Integrating first over β yields

$$C_A = \frac{2C_{p,t2}}{\pi R_b^2}\int_0^{x_L}\left(\cos^2\alpha\sin^2\theta_c\pi + \sin^2\alpha\cos^2\theta_c\frac{\pi}{2}\right)\tan^2\theta_c\,x\,dx$$

Integrating with respect to x gives us

$$C_A = \frac{2C_{p,t2}}{R_b^2}(\cos^2\alpha\sin^2\theta_c + \frac{1}{2}\sin^2\alpha\cos^2\theta_c)\tan^2\theta_c\frac{x_L^2}{2}$$

Since $R_b = x_L\tan\theta_c$

$$C_A = C_{p,t2}[\sin^2\theta_c + \tfrac{1}{2}\sin^2\alpha(1 - 3\sin^2\theta_c)] \tag{12.34}$$

We will calculate the normal force coefficient due to the pressures acting over the closed surface of the cone. Since the normal force is positive in the negative y direction,

$$C_N = \frac{1}{(\frac{1}{2}\rho_\infty U_\infty^2)(\pi R_b^2)}\oiint_S (p - p_\infty)(\hat{n}\,dS)\cdot(-\hat{j}) \tag{12.35}$$

Combining equations (12.26), (12.31), (12.33), and (12.35) and using the limits of integration, $0 \le \beta \le \pi$ and $0 \le x \le x_L$ (as discussed previously), we have:

$$C_N = \frac{2C_{p,t2}}{\pi R_b^2}\int_0^{x_L}\left[\int_0^{\pi}(\cos^2\alpha\sin^2\theta_c + 2\sin\alpha\cos\alpha\sin\theta_c\cos\theta_c\cos\beta + \sin^2\alpha\cos^2\theta_c\cos^2\beta)(x\tan\theta_c)\,d\beta\frac{dx}{\cos\theta_c}(\cos\theta_c\cos\beta)\right]$$

Integrating first with respect to β gives us:

$$C_N = \frac{2C_{p,t2}}{\pi R_b^2}\int_0^{x_L}\left(2\sin\alpha\cos\alpha\sin\theta_c\cos\theta_c\frac{\pi}{2}\right)\tan\theta_c x\,dx$$

Integrating with respect to x yields:

$$C_N = \frac{2C_{p,t2}}{R_b^2}(\sin\alpha\cos\alpha\sin\theta_c\cos\theta_c)\tan\theta_c\frac{x_L^2}{2}$$

so that

$$C_N = \frac{C_{p,t2}}{2} \sin 2\alpha \cos^2 \theta_c \tag{12.36}$$

Referring to equation (12.29), the lift coefficient is

$$C_L = C_N \cos \alpha - C_A \sin \alpha$$

Using the coefficients presented in equations (12.34) and (12.36), we have

$$C_L = C_{p,t2} \sin \alpha \left[\cos^2 \alpha \cos^2 \theta_c - \sin^2 \theta_c - \tfrac{1}{2} \sin^2 \alpha (1 - 3 \sin^2 \theta_c) \right] \tag{12.37}$$

Correspondingly,

$$C_D = C_{p,t2} \cos \alpha \left[\sin^2 \alpha \cos^2 \theta_c + \sin^2 \theta_c + \tfrac{1}{2} \sin^2 \alpha (1 - 3 \sin^2 \theta_c) \right] \tag{12.38}$$

To calculate the pitch moment, notice that the moment due to the incremental pressure force acting at a radial distance $\vec{r}$ from the origin is

$$\overrightarrow{dM} = \vec{r} \times \overrightarrow{dF} = \vec{r} \times p\hat{n}\, dS$$

Also notice that the incremental moment $\overrightarrow{dM}$ is a vector, which can be written in terms of its components:

$$\overrightarrow{dM} = d\mathcal{L}\, \hat{i} + d\mathcal{N}\, \hat{j} + dM\, \hat{k} \tag{12.39}$$

In equation (12.39), $\mathcal{L}$ is the roll moment (which is positive when causing the right wing to move down), $\mathcal{N}$ is the yaw moment (which is positive when causing the nose to move to the right), and M is the pitch moment (which is positive when causing a nose-up rotation).

If we want to take the moments about the apex of the cone, the moment arm is

$$\vec{r} = x\hat{i} + x \tan \theta_c \cos \beta \hat{j} + x \tan \theta_c \sin \beta \hat{k} \tag{12.40}$$

Now, examine the $\hat{r} \times \hat{n}$ term of the moment expression:

$$\vec{r} \times \hat{n} = \begin{vmatrix} \hat{i} & \hat{j} & \hat{k} \\ x & x \tan \theta_c \cos \beta & x \tan \theta_c \sin \beta \\ \sin \theta_c & -\cos \theta_c \cos \beta & -\cos \theta_c \sin \beta \end{vmatrix}$$

and we can obtain,

$$\begin{aligned} \vec{r} \times \hat{n} = {} & \hat{i}[0] + \hat{j}[x \sin \beta (\tan \theta_c \sin \theta_c + \cos \theta_c)] \\ & - \hat{k}[x \cos \beta (\tan \theta_c \sin \theta_c + \cos \theta_c)] \end{aligned} \tag{12.41}$$

The first term (i.e., the contribution to the roll moment) is always zero, since, in the absence of viscous forces, the only forces are the pressure forces that act normal to the surface and therefore act through the axis of symmetry for a body of revolution. The negative sign for the $\hat{k}$ term (i.e., the pitch moment) results because a pressure force acting in the first and fourth quadrants ($\pi/2 \geq \beta \geq -\pi/2$) produces a nose-down (negative) pitch moment.

For this example we are interested in the pitch moment about the apex, which is considered positive when nose up,

$$M_0 = \iint_S \vec{r} \times (p - p_\infty)\hat{n}\, dS \cdot \hat{k} \tag{12.42}$$

Taking the resultant cross product of the moment arm from the apex ($\vec{r}$) and the inward-directed unit normal to the surface area $\hat{n}$ with the dot product with $\hat{k}$, we obtain:

$$(\vec{r} \times \hat{n}) \cdot \hat{k} = -x \cos\theta_c \cos\beta - x \sin\theta_c \tan\theta_c \cos\beta$$

Therefore, the pitch moment coefficient is:

$$C_{M_0} = \frac{-2}{\pi R_b^2 R_b} \int_0^{x_L} \left[\int_0^{\pi} C_p x \tan\theta_c \, d\beta \frac{dx}{\cos\theta_c} (x \cos\theta_c \cos\beta + x \sin\theta_c \tan\theta_c \cos\beta) \right] \tag{12.43}$$

We can simplify this expression if we focus on the terms containing the cone-half-angle (θ_c), so that

$$\tan\theta_c \frac{1}{\cos\theta_c}(\cos\theta_c + \sin\theta_c \tan\theta_c) = \tan\theta_c(1 + \tan^2\theta_c) = \frac{\tan\theta_c}{\cos^2\theta_c}$$

Substituting the modified-Newtonian-flow expression for the pressure coefficient and integrating with respect to β yields

$$C_{M_0} = -\frac{2C_{p,t2}}{\pi R_b^2 R_b} \frac{\tan\theta_c}{\cos^2\theta_c} \int_0^{x_L} x^2 (\sin\theta \cos\alpha \sin\theta_c \cos\theta_c \pi)\, dx$$

Integrating with respect to x and using the fact that $R_b = x_L \tan\theta_c$, we obtain

$$C_{M_0} = -\frac{C_{p,t2} \sin 2\alpha}{3 \tan\theta_c} \tag{12.44}$$

Although the resultant moment is produced by the integration of the distributed aerodynamic forces over the vehicle surface, it can be represented as composed of two components—one effectively due to the normal-force component and the other due to the axial-force component. Using this concept, we can isolate the two terms of equation (12.43):

$$C_{M_0} = -\frac{2}{\pi R_b^2 R_b} \int_0^{x_L} \left(\int_0^{\pi} C_p x \tan\theta_c \, d\beta \frac{dx}{\cos\theta_c} x \cos\theta_c \cos\beta \right) - \frac{2}{\pi R_{bb}^2} \int_0^{x_L} \left(\int_0^{\pi} C_p x \tan\theta_c \, d\beta \frac{dx}{\cos\theta_c} x \sin\theta_c \tan\theta_c \cos\beta \right)$$

Writing the total pitch moment as the sum of the two components, we have

$$C_{M_0} = C_{M_{0,N}} + C_{M_{0,A}} \tag{12.45}$$

where

$$C_{M_{0,N}} = -\frac{2\tan\theta_c}{\pi R_b^2 R_b}\int_0^{x_L}\left(\int_0^{\pi} C_p \cos\beta\, d\beta\right)x^2\, dx \tag{12.46}$$

and

$$C_{M_{0,A}} = -\frac{2\tan^3\theta_c}{\pi R_b^2 R_b}\int_0^{x_L}\left(\int_0^{\pi} C_p \cos\beta\, d\beta\right)x^2\, dx \tag{12.47}$$

Substituting the modified Newtonian-flow expression for the pressure coefficient yields

$$C_{M_{0,N}} = -\frac{2\tan\theta_c C_{p,t2}}{\pi R_b^2 R_b}\int_0^{x_L}\left[\int_0^{\pi}(\cos^2\alpha\sin^2\theta_c\cos\beta + 2\sin\alpha\cos\alpha\sin\theta_c\cos\theta_c\cos^2\beta + \sin^2\alpha\cos^2\theta_c\cos^3\beta)\right]$$

Integrating gives us

$$C_{M_{0,N}} = -\frac{C_{p,t2}\sin 2\alpha}{R_b^2 R_b}\tan\theta_c\sin\theta_c\cos\theta_c\frac{x_L^3}{3}$$

$$C_{M_{0,N}} = -\frac{C_{p,t2}\sin 2\alpha\cos^2\theta_c}{3}\frac{x_L}{R_b}$$

Using equation (12.36) for the expression for C_N, we can rewrite

$$C_{M_{0,N}} = C_N\left(-\frac{2}{3}\frac{x_L}{R_b}\right) \tag{12.48}$$

Similarly,

$$C_{M_{0,A}} = \frac{-2\tan^3\theta_c C_{p,t2}}{\pi R_b^2 R_b}\int_0^{x_L}\left[\int_0^{\pi}(\cos^2\alpha\sin^2\theta_c\cos\beta + 2\sin\alpha\cos\alpha\sin\theta_c\cos\theta_c\cos^2\beta + \sin^2\alpha\cos^2\theta_c\cos^3\beta\right]x^2\, dx$$

Integrating yields

$$C_{M_{0,A}} = -\frac{C_{p,t2}\sin 2\alpha\sin^2\theta_c}{3}\frac{x_L}{R_b}$$

Using equation (12.34) for the expression for C_A, we can rewrite this as:

$$C_{M_{0,A}} = C_A\frac{-\sin 2\alpha\sin^2\theta_c}{3[\sin^2\theta_c + 0.5\sin^2\alpha(1 - 3\sin^2\theta_c)]}\frac{x_L}{R_b} \tag{12.49}$$

Following this division of the pitch moment into components, we can represent it as an effective net force acting at a "center of pressure," as shown in Fig. 12.22. The pitch moment may be represented by

$$M_0 = M_{0,N} + M_{0,A} = -x_{\text{cp}}N - y_{\text{cp}}A \tag{12.50}$$

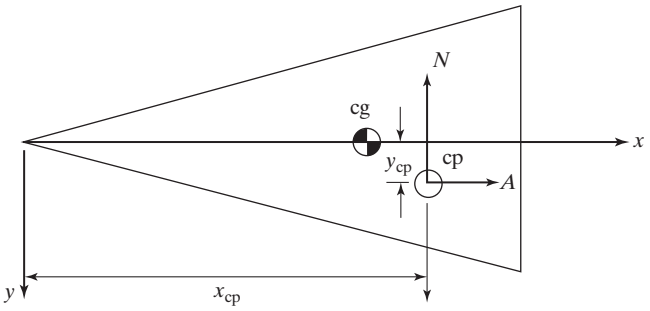

Figure 12.22 Aerodynamic forces acting at the center of pressure as effectively producing the aerodynamic pitching moment.

The two terms represent the effects of the normal force and of the axial force, respectively. In terms of the coefficients, we can write this as:

$$C_{M_0} = \frac{M_0}{q_\infty S R_b} = -C_N \frac{x_{cp}}{R_b} - C_A \frac{y_{cp}}{R_b} \tag{12.51}$$

Comparing the formulations presented in equations (12.48), (12.49), and (12.51), we find that

$$x_{cp} = \frac{2}{3} x_L \tag{12.52}$$

and

$$y_{cp} = \frac{\sin 2\alpha \sin^2 \theta_c x_L}{3[\sin^2 \theta_c + 0.5 \sin^2 \alpha (1 - 3 \sin^2 \theta_c)]} \tag{12.53}$$

If the vehicle is to be statically stable, the center of pressure should be located such that the aerodynamic forces produce a restoring moment when the configuration is perturbed from its "stable orientation." Therefore, if the vehicle pitches up (i.e., α increases), the net pitch moment should be negative (causing a nose-down moment), which decreases α.

The parameter

$$\text{S.M.} = \frac{x_{cp} - x_{cg}}{x_L} \tag{12.54}$$

is the static margin, which must be positive for uncontrolled vehicles. For high-performance, hypersonic vehicles, the static margin is usually 3% to 5% of the length of the vehicle. Note, however, as illustrated in Fig. 12.22, both the axial force and the normal force contribute to the pitch moment. Therefore, it is possible that the vehicle is statically stable when $x_{cp} = x_{cg}$, if y_{cp} is below y_{cg} (as is the case in the sketch of Fig. 12.22). In this case, the axial force will produce the required restoring moment.

EXAMPLE 12.4: What is the total drag acting on a sharp cone?

We neglected the viscous forces and the base pressure in estimating the forces acting on the sharp cone of Example 12.3. Consider a sharp cone ($\theta_c = 10°$) exposed to the Mach 8 flow of Tunnel B at the Arnold Engineering Development

Center (AEDC), as shown in Fig. 12.23. For this problem, the subscript $t1$ designates the flow conditions in the nozzle reservoir, the subscript 1 designates those in the test section, the subscript e designates those at the edge of the boundary layer of the sharp cone (and which are constant along the entire length of the cone), and the subscript w designates conditions at the wall of the cone. If $T_{t1} = 1350°\text{R}$, $p_{t1} = 850$ psia, $T_w = 600°\text{R}$, and $\alpha = 0°$, develop expressions for the forebody pressure coefficient $(C_{p,e})$, the base pressure coefficient $(C_{p,b})$, and the skin friction. What is the total drag acting on the vehicle?

Solution: We can use Figs. 8.15b and c to obtain values for the pressure coefficient and for the Mach number of the inviscid flow at the edge of the boundary layer for a 10°-half-angle cone in a Mach 8 stream. Inherent in this use of these figures is the assumption that the boundary layer is thin and that there are no significant viscous/inviscid interactions which perturb the pressure field. Therefore, $M_e = 6$ and $C_{p,e} = 0.07$. Since $q_1 = \frac{1}{2}\rho_1 U_1^2 = (\gamma/2)p_1 M_1^2$,

$$p_e = p_1\left(1 + \frac{\gamma}{2} M_1^2 C_{p,e}\right)$$

We can use Table 8.1 to calculate the free-stream static pressure (p_1) in the Mach 8 flow of the wind-tunnel test section:

$$p_1 = \frac{p_1}{p_{t1}} p_{t1} = (102 \times 10^{-6})(850) = 0.867 \text{ psia}$$

Therefore,

$$p_e = 0.0867[1.0 + (0.7)(64)(0.07)] = 0.3586 \text{ psia}$$

Since $M_e = 6$, we can use Table 8.1 and the fact that the edge flow is that for an adiabatic flow of a perfect gas, so that $T_{t1} = T_{te}$, and:

$$T_e = \frac{T_e}{T_{te}} T_{te} = (0.12195)(1350) = 164.63°\text{R}$$

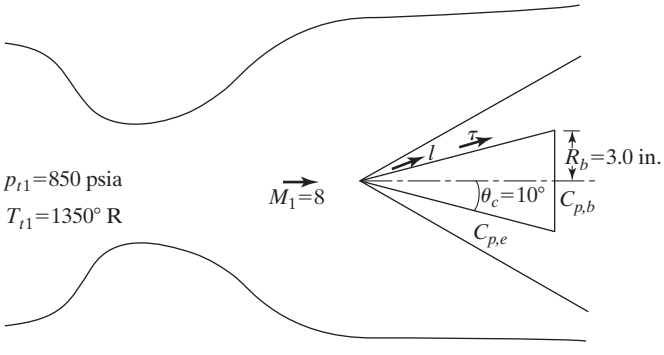

Figure 12.23 Sharp cone mounted in Tunnel B of AEDC.

To aid in our decision as to whether the boundary layer is laminar or turbulent, we will calculate the Reynolds number for the flow at the boundary-layer edge:

$$\mathrm{Re}_l = \frac{\rho_e U_e l}{\mu_e} = \left[\frac{\rho_e}{RT_e}\right]\left[M_e\sqrt{\gamma RT_e}\right]\left[\frac{T_e + 198.6}{2.27 \times 10^{-8} T_e^{1.5}}\right] l$$

where, as shown in Fig. 12.23, l is the wetted distance along a conical generator. Therefore,

$$\mathrm{Re}_l = \left(0.0001828\frac{\mathrm{lbf}\cdot\mathrm{s}^2}{\mathrm{ft}^4}\right)\left(3773.80\frac{\mathrm{ft}}{\mathrm{s}}\right)\left(7.575 \times 10^6 \frac{\mathrm{ft}^2}{\mathrm{lbf}\cdot\mathrm{s}}\right) l$$
$$= 5.226 \times 10^6\, l$$

Based on the wetted length of a conical ray ($l_c = 17.276$ in.),

$$\mathrm{Re}_{lc} = 7.523 \times 10^6$$

You should notice that, although hypersonic boundary layers are very stable, boundary-layer transition could occur for this flow, probably within the first one-half of the cone length. So, we can use the correlation presented in Fig. 12.24 to determine the base pressure as:

$$\frac{p_b}{p_e} = 0.02$$

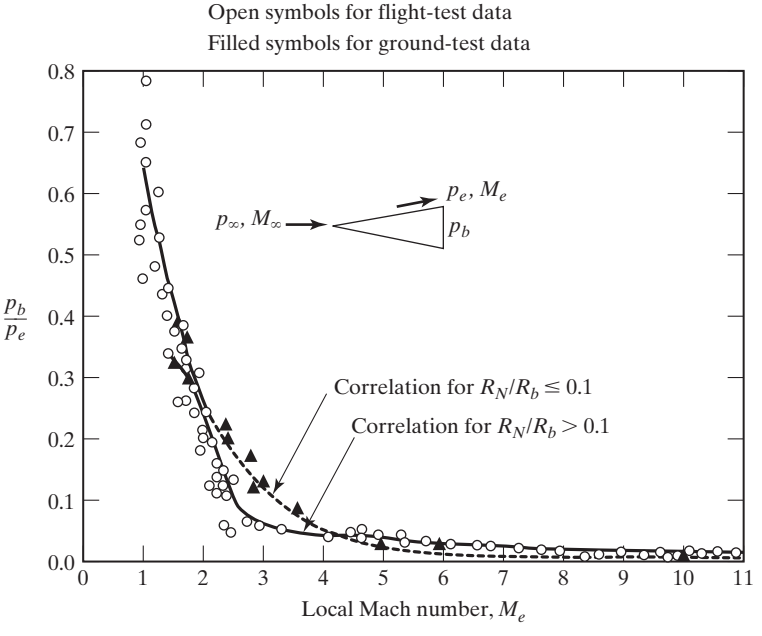

Figure 12.24 Base pressure ratio as a function of the local Mach number for turbulent flow [from Cassanto (1973)].

so that $p_b = 0.00717$ psi.

Notice that since $p_b = 0.02p_e$,

$$C_{p,b} = \frac{p_b - p_1}{q_1} = \left(\frac{p_b}{p_1} - 1\right)\frac{2}{\gamma M_1^2}$$
$$= \left(\frac{p_b}{p_e}\frac{p_e}{p_1} - 1\right)\frac{2}{\gamma M_1^2} = -0.0205$$

Recall that the assumption for Newtonian flow is $C_{p,b} = 0.0$, which is very close to the calculated result.

To calculate the skin-friction contribution, we will use the Reynolds analogy (see Chapter 4). For supersonic flow past a sharp cone, the heat-transfer rate (or, equivalently, the Stanton number) can be calculated using the relatively simple approximation obtained through the Eckert reference temperature approach [Eckert (1955)]. In this approach, the heat-transfer rates are calculated using the incompressible relations [e.g., equation (4.103)] with the temperature-related parameters evaluated at Eckert's reference temperature (T^*). According to Eckert (1955),

$$T^* = 0.5(T_e + T_w) + 0.22r(T_{te} - T_e)$$

where r is the recovery factor. For turbulent flow, the recovery factor is $\sqrt[3]{Pr}$, which is equal to 0.888 for $Pr = 0.70$ and:

$$T^* = 0.5(164.63 + 600) + 0.22(0.888)(1350 - 164.63)$$
$$= 613.89°\text{R}$$

Therefore,

$$\text{Re}_l^* = \left[\frac{p_e}{RT^*}\right][U_e]\left[\frac{T^* + 198.6}{2.27 \times 10^{-8}T^{*1.5}}\right]l$$
$$= \left(0.00004901\frac{\text{lbf}\cdot\text{s}^2}{\text{ft}^4}\right)\left(3773.80\frac{\text{ft}}{\text{s}}\right)\left(2.353 \times 10^6\frac{\text{ft}^2}{\text{lbf}\cdot\text{s}}\right)l$$
$$= 4.353 \times 10^5 l$$

So, using Reynolds' analogy, we have

$$C_f = \frac{0.0583}{(\text{Re}_l^*)^{0.2}} = \frac{0.004344}{l^{0.2}}$$

and

$$\tau = C_f\left(\frac{\gamma}{2}p_e M_e^2\right) = \frac{0.03926}{l^{0.2}}\frac{\text{lbf}}{\text{in.}^2}$$

To calculate the total drag, we add the surface pressure and shear stress components, and also add in the base pressure:

$$D = \int p_e 2\pi r\, dl \sin\theta_c + \int \tau_w 2\pi r\, dl \cos\theta_c - p_b \pi R_b^2$$

Noting that p_e is constant along the length of the conical generator, $dl \sin \theta_c = dr$, and

$$r = l \sin \theta_c$$

Noting that p_e is constant along the length of the conical generator, $dl \sin \theta_c = dr$, and $r = l \sin \theta_c$,

$$\begin{aligned} D &= p_e \pi R_b^2 + 0.03926(2\pi)(\cos \theta_c \sin \theta_c) \int_0^{l_c} l^{0.8} dl - p_b \pi R_b^2 \\ &= (0.3586)(9\pi) + (0.04218)\frac{l_c^{1.8}}{1.8} - (0.00717)(9\pi) \\ &= 10.139 + 3.956 - 0.203 = 13.892 \text{ lbf} \end{aligned}$$

Various researchers have developed numerical techniques using the two-layer approach, that is, one in which an inviscid solution is first computed providing the flow conditions (e.g., the static pressure and the entropy) at the edge of the boundary layer. Having defined the pressure and the entropy distribution, the remaining flow properties can be calculated and the inviscid streamlines generated. Brandon and DeJarnette (1977) and Riley et al. (1990) have generated numerical solutions of Euler's equation complemented by streamline tracing techniques to define the inviscid properties and the inviscid streamlines for various blunt configurations. Once the boundary conditions are known, solutions of the boundary layer will provide the temperature, the velocity, and the gas-component distributions adjacent to the surface from which we can determine the convective heat-transfer rate and the skin friction. Techniques of various rigor can be used to generate distributions for the convective heat-transfer rate and the skin friction. Zoby et al. (1981) have computed the laminar heat-transfer distributions for the Shuttle *Orbiter* using an incompressible Blasius relation (a similarity transformation) with compressibility effects accounted for by Eckert's reference-enthalpy method. Bertin and Cline (1980) developed a nonsimilarity boundary-layer code to generate solutions for laminar, transitional, and turbulent boundary layers. Although these two techniques are very different, they produced very similar computations of the Shuttle's reentry environment.

12.5 HIGH *L/D* HYPERSONIC CONFIGURATIONS—WAVERIDERS

Atmospheric reentry, as shown in Fig. 12.1, requires significant deceleration, but using ballistic trajectories creates negative g's which are extreme. Nonweiler (1959) concluded that "The most effective method of alleviating the deceleration is by the introduction of lift, which also serves to decrease the peak heating rate, though the total heat absorbed is usually greater." To achieve high *L/D* (lift/drag), Nonweiler proposed all-wing designs of a delta planform, such that the shock wave is attached to the leading edges at the design Mach number and at the design angle of attack. Therefore, the wing appears to ride on its shock wave, and the vehicle is known as a "waverider." Shapes of the wing undersurface of a delta amenable to treatment by exact shock-wave theory, as proposed by Nonweiler are reproduced in Fig. 12.25.

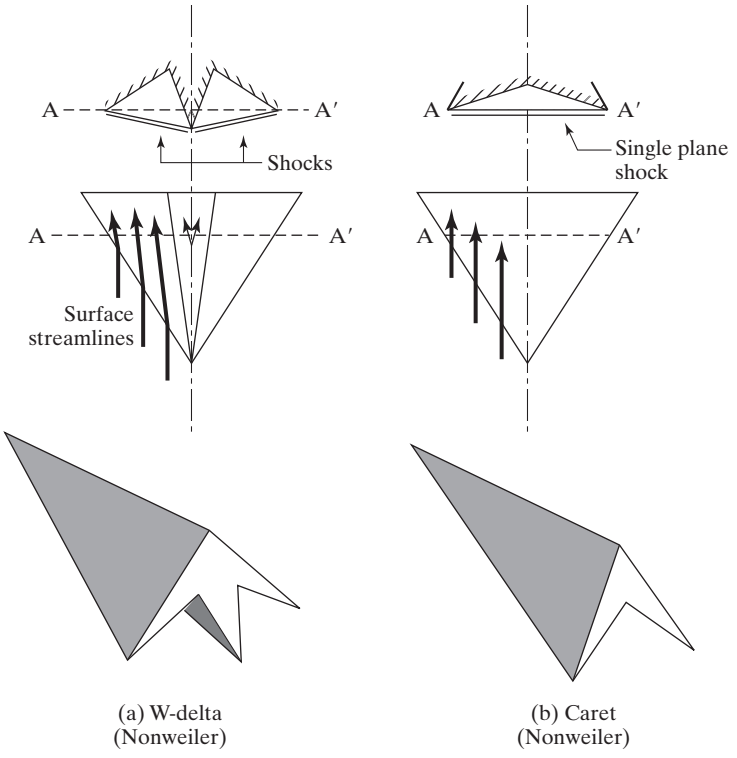

(a) W-delta (Nonweiler) (b) Caret (Nonweiler)

Figure 12.25 Shapes of all-wing delta planforms amenable to treatment by exact shock-wave theory, as proposed by Nonweiler (1959).

Experimental studies of Nonweiler's waverider configurations indicated lower aerodynamic performance (i.e., lower lift-to-drag ratio) than was predicted. The experimentally observed deficiencies in the aerodynamic performance of the caret waveriders have been attributed to their large wetted area and the corresponding relatively high skin-friction drag.

Squire (1976b) studied the conditions for which the flow on the upper surface of a wing was independent of that on the lower surface of the wing. If the Mach number normal to the leading edge, which is defined in equation (11.9), is sufficiently high, and the incidence normal to the leading edge, which is defined in equation (11.10), is not too great, the flow near the leading edge is similar to that over an infinitely swept wing. That is, the shock wave below the wing is attached to the wing leading edges and there is a Prandtl-Meyer expansion around the edges, producing a region of uniform suction on the upper surface. This is designated as region C in Fig. 12.26, which is taken from Squire (1976a). As the Mach number normal to the leading edge decreases or as the angle of attack normal to the leading edge increases, the shock wave detaches from the windward surface. This is designated region B in Fig. 12.26. Once the shock wave detaches from the compression surface of a thin wing, flows on the two surfaces are no longer independent. For these conditions, the pressure near the leading edge of the compression surface is relatively high, so that there is a strong outflow around the leading edge on to the upper surface. However, since

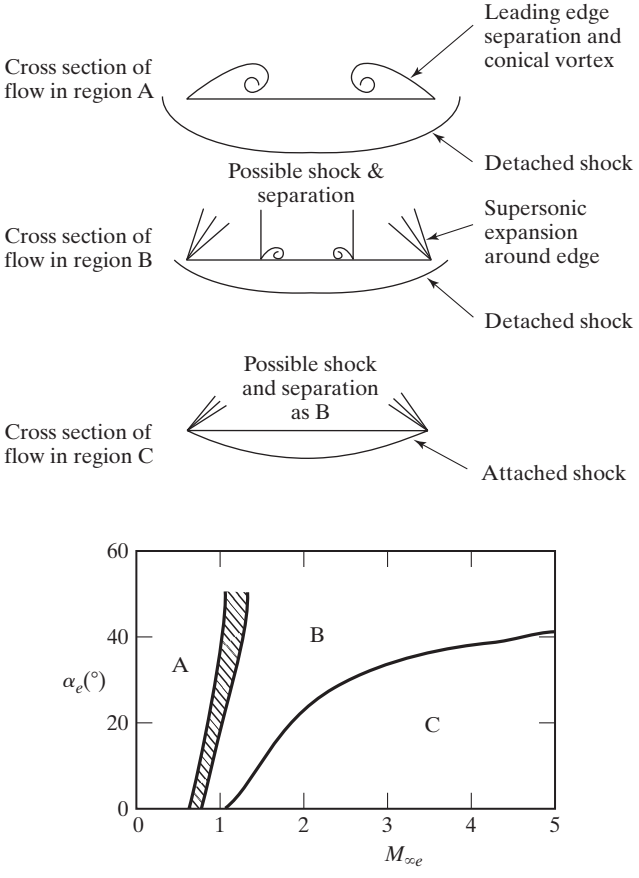

Figure 12.26 Types of flow on thin delta wings at supersonic speeds [from Squire (1976a)].

the detached shock wave (of region B) is close to the leading edge, the crossflow reaches sonic speed as it accelerates around the leading edge. So, the shape of the upper surface does not influence the flow on the lower surface. For region A, the conditions are such that the shock wave is well detached from the windward surface. For such conditions, the flows on the upper and on the lower surfaces are no longer independent. The flow on the suction surface is sensitive to changes in the shape of the windward (lower) surface.

Anderson et al. (1990) describe the way a waverider configuration works, as shown in Fig. 12.27:

- a waverider is a high-speed vehicle designed to have an *attached* shock wavealong the leading edge of the configuration, as shown in Fig. 12.27a
- "the vehicle appears to be riding on top of its shock wave, hence the term waverider. This is in contrast to a more conventional hypersonic vehicle, where the shock wave is usually detached from the leading edge." (as sketched in Fig. 12.27b) [Anderson et al. (1990)]

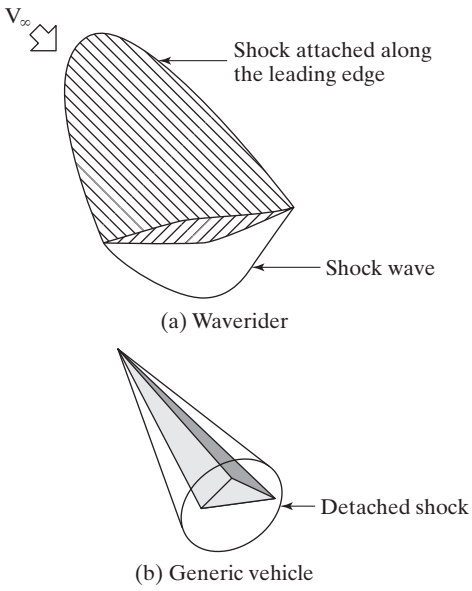

Figure 12.27 Comparison of a waverider with a generic hypersonic configuration [from Anderson et al. (1990)].

- the advantage of a waverider configuration, as shown in Fig. 12.27a, where "the high pressure behind the shock wave under the vehicle does not 'leak' around the leading edge to the top surface; the flowfield over the bottom surface is contained, and the high pressure is preserved" [Anderson et al. (1990)]
- for the vehicle shown in Fig. 12.27b, pressure information can be passed between the lower and upper surfaces, so pressure leaks around the leading edges and reduce the pressure acting on the lower surface, which also reduced the lift. This is shown in Fig. 12.28, where the lift curves (L versus α) are sketched for the two vehicles shown in Fig. 12.27.

Anderson et al. (1990) note further that "when waveriders are optimized for maximum L/D, the previous studies have demonstrated that the driving parameter that alters the L/D ratio is the skin friction drag."

The design of a hypersonic waverider configuration employs a variety of computational methods. One basic design methodology, which was first developed for conical flow fields, is illustrated in Fig. 12.29. A capture flow tube (whose streamlines are parallel to the axis of the shock-generating cone) intersects the conical shock wave. The leading edge of the waverider is the intersection of the capture flow tube and the conical shock wave. The shape of the waverider leading edge is dependent on the shape of the capture flow tube, the shock angle, and the distance from the capture flow tube to the conical shock-wave centerline. The lower surface is defined by tracing streamlines from the leading edge to the desired base location of the waverider. Eggers and Radespiel (1993) state, "An obvious choice for the upper surface of hypersonic waveriders is the undisturbed Flow Capture Tube used to define the leading edge of the configuration.

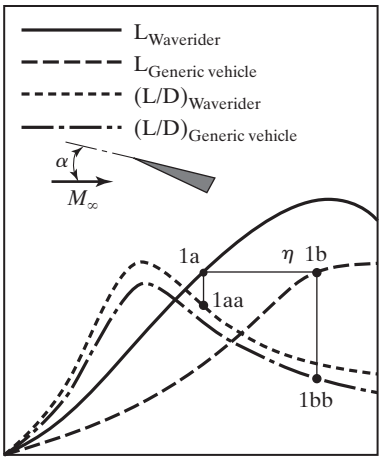

Figure 12.28 Curves of lift and (L/D) versus angle of attack: comparison between a waverider and a generic vehicle [from Anderson et al. (1990)].

This results in zero pressure coefficient along the upper surface and the aerodynamic behavior is completely governed by the lower surface. However, with a more careful consideration of typical waverider missions, a designer would like to have more options at his disposal for several reasons. Firstly, variations of the flow state along the upper surface will result in a redistribution of the vehicle's volume which is useful to assist integration of fuels, systems, and payload. A careful use of flow expansion along the upper surface may also enhance L/D at the design point. Finally, flow expansion in the rear part of a waverider will decrease the base drag of vehicles in the subsonic, transonic, and supersonic part of the vehicle's trajectory." The process described in this paragraph can be used to derive a waverider from any axisymmetric flow field.

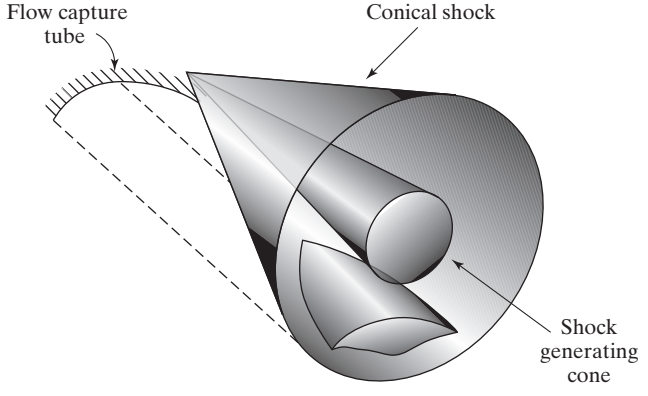

Figure 12.29 Derivation of waverider configurations from a conical flow field.

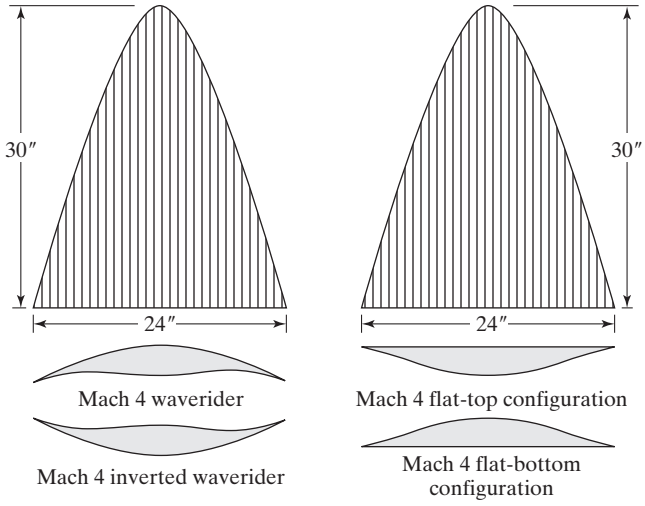

Figure 12.30 Waverider configurations tested in the Langley Unitary Plan Wind Tunnel (UPWT) [from Bowcutt et al. (1987)].

To achieve realistic estimates of the *L/D* ratio, the effect of skin-friction drag, which represents a relatively large fraction of the total drag, must be included in deriving the waverider configuration. Bowcutt et al. (1987) have developed a numerical procedure for optimizing cone-derived waveriders, which includes the effect of skin friction.

The results of an experimental investigation which was conducted to determine the aerodynamic characteristics of waverider configurations are reported in Bauer et al. (1990). The Mach 4 waverider configuration, which was determined using the conical flow field process described previously (including both the pressure drag and the friction drag in the optimization procedure), is depicted in Fig. 12.30. A second wind-tunnel model was built with a flat top, but having the same planform and cross-sectional area distribution. Data were also obtained with the two configurations inverted in the Unitary Plan Wind Tunnel (UPWT) at NASA Langley Research Center at a Mach number of 4 and at a unit Reynolds number of 2×10^6 per foot. To ensure that the boundary layer on the model was fully turbulent, grit particles (with a particle diameter of 0.0215 in.) were applied 4.0 in. aft of the leading edge to promote the onset of transition at the desired location on the model.

Bauer et al. (1990) note, "The Mach 4 waverider is seen to have the most lifting potential followed by the flat-bottom configurations, which exhibit a 7% reduction in $C_{L\alpha}$. The Mach 4 waverider has 15% higher $C_{L\alpha}$ than when inverted."

The experimentally determined drag coefficients, as determined for $(L/D)_{\max}$ and presented in Bauer et al. (1990), are reproduced in Fig. 12.31. The grit drag was found to be only a very small part of the total drag. Since the base drag was found to be 25% to 30% of the total drag, a significant effort was made to measure the base drag accurately. The estimates of the skin friction drag, $C_{D,f}$, were made using the reference temperature method. The skin-friction drag, which is roughly 25% of the total forebody drag, was found to be slightly lower for the flat-top/flat-bottom configurations than for

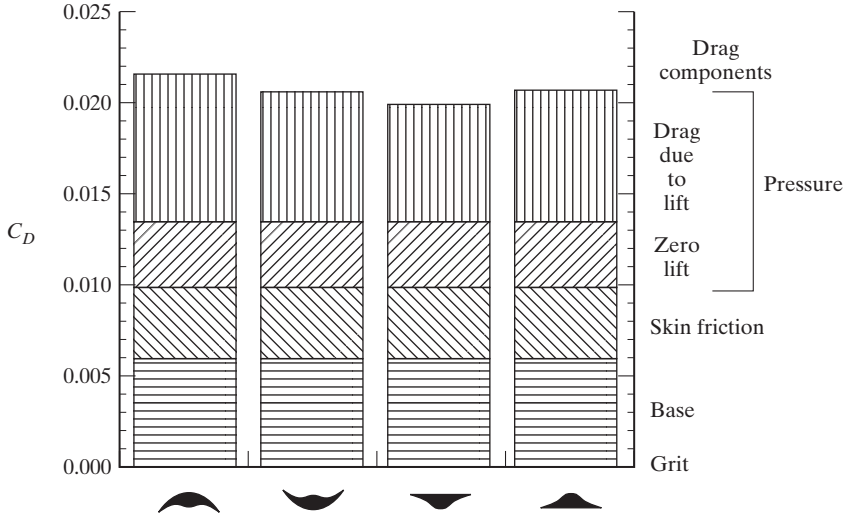

Figure 12.31 Breakdown of drag components at maximum L/D conditions, $M_\infty = 4$, $\mathrm{Re}_\infty/\mathrm{ft} = 2 \times 10^6$. [from Bauer et al. (1990)].

the waverider, because the flat-top configuration has a smaller wetted area. The wetted surface area for the flat-top configuration was 897.6 in.^{2}, while that for the waverider was 915.2 in.^{2} The zero-lift pressure drag $(C_{D0})_p$ was determined by subtracting the estimated value of $C_{D,f}$ from the measured value of C_{D0}. The value of $(C_{D0})_p$, thus determined for the flat-top/flat-bottomed configurations, was 13% lower than that for the waverider. This is the main reason why $(L/D)_{\max}$ is higher for the flat-top/flat-bottom configurations than for the waverider, as will be discussed for Fig. 12.32.

The aerodynamic characteristics at $(L/D)_{\max}$, as experimentally determined for the four configurations and as computed using the design code, are reproduced in

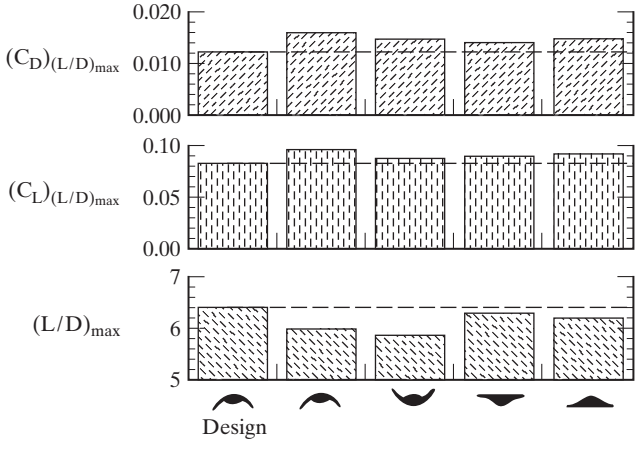

Figure 12.32 Aerodynamic characteristics at maximum L/D conditions, $M_\infty = 4$, $\mathrm{Re}_\infty/\mathrm{ft} = 2 \times 10^6$ [from Bauer et al. (1990)].

Fig. 12.32. Base drag and grit drag have been removed from the values presented in Fig. 12.32. The values both of C_L and of C_D when (L/D) is a maximum were found to be higher than the design values for all four configurations. However, none of the four configurations achieved a value of $(L/D)_{\max}$ equal to that predicted using the design code. The experimental value of $(L/D)_{\max}$ for the Mach 4 waverider was 13% lower than that predicted using the design code. $(L/D)_{\max}$ was 5% higher for the flat-top configuration than for the waverider. However, Bauer et al. (1990) noted that "the waverider has higher L/D values than the flat-top configuration for $C_L > 0.16$." Furthermore, Bauer et al. conclude, "These measured performance deficiencies may be attributed to the slight shock detachment that was observed at the design Mach number and angle of attack."

Not only is the aerodynamic performance of a waverider sensitive to viscous effects, but so is the heat transfer. Waveriders, by design, have sharp leading edges so that the bow shock wave is attached. However, for flight Mach numbers above 5, heat transfer to the leading edge can result in surface temperatures exceeding the limits of most structural materials. As will be discussed in the next section, "Aerodynamic Heating," the heat flux to the leading edge can be reduced by increasing the radius of the leading edge. However, while increasing the leading-edge radius can alleviate heating concerns, there is a corresponding increase in drag and, hence, a reduction in L/D. Eggers and Radespiel (1993) note, "Defining the thickness of the leading edge to be about 10/5000 [of the vehicle's length] due to model manufacture requirements one obtains significant detachment of the bow shock and corresponding wave drag. Moreover, the shock is no longer confined to the lower surface which reduces the overall lift. Consequently, the inviscid L/D reduces by about 25% for this large amount of bluntness." Therefore, the specification of the leading-edge radius for an aerodynamically efficient waverider that is to operate at Mach numbers in excess of 5 leads to the need for compromise. The leading-edge radius should be sufficiently large to limit the heat flux, yet be as small as possible to minimize the leading-edge drag.

As noted by Haney and Beaulieu (1994), "However, a waverider by itself doesn't necessarily make a good hypersonic aircraft. To do that attention needs to be paid to volumetric efficiency, stability and control, and airframe-engine integration." Cervisi and Grantz (1994) note, "The forebody compression surface sets up the flow environment for the remainder of the vehicle. It constitutes a large fraction of the vehicle drag and provides airflow to the engine inlet. However, once a particular forebody is selected, the available design space for the rest of the vehicle becomes very constrained due to the highly integrated nature of hypersonic flight." Thus, the designer must consider the relation between the forebody compression surface and the boundary-layer transition front, fuselage lift and drag, the inlet capture area, etc.

The sketch presented in Fig. 12.33 illustrates how the inlet capture area can be quickly estimated from a conically derived forebody. For two-dimensional or axisymmetric inlets, the bow-shock-wave location defines the mass flow as a function of inlet width. For shock-on-lip designs (i.e., designs for which the bow shock wave intersects the cowl lip), this condition corresponds to the design point. Since increasing the capture area also increases the engine size and weight, finding the proper balance between the capture area and the nonflowpath drag is a goal for the forebody configuration.

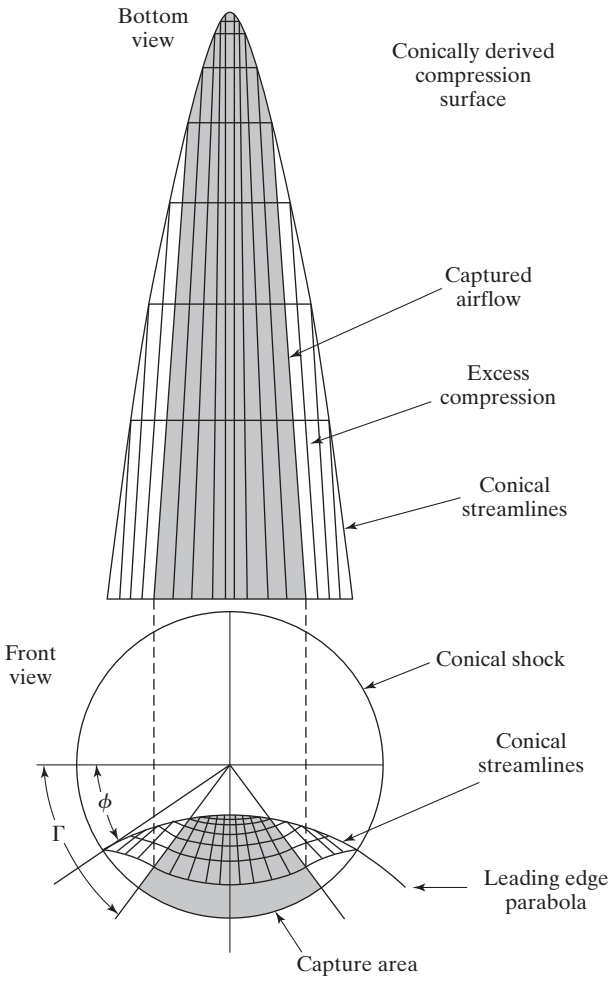

Figure 12.33 Compression surface derived from a conical flow field [from Cervisi and Grantz (1994)].

Aerodynamics Concept Box: Hypersonic Scramjet Success

Scramjets are typically viewed as a necessary propulsion system for hypersonic cruise vehicles. The problem is the difficulty in designing a system that can start and sustain combustion at hypersonic speeds. This has been described by some as lighting a match in a hurricane and keeping it lit! Until recently there was very limited experimental data for working scramjets.

That changed when the X-51A Waverider made the longest supersonic combustion ramjet-powered hypersonic flight in 2010. The X-51's scramjet engine burned for more than 200 seconds and accelerated the vehicle to Mach 5. "We are ecstatic to have accomplished most of our test points on the X-51A's very first hypersonic mission," said Charlie Brink, a X-51A program manager with the Air Force Research Laboratory. "We equate this leap in

engine technology as equivalent to the post-World War II jump from propeller-driven aircraft to jet engines."

The X-51 was launched from a B-52 at 50,000 ft over Point Mugu Naval Air Warfare Center. Four seconds later, a solid rocket booster accelerated the X-51 to about Mach 4.8 before it was jettisoned. "This first flight was the culmination of a six-year effort by a small, but very talented AFRL, DARPA and industry development team," Mr. Brink said. "Now we will go back and really scrutinize our data. No test is perfect, and I'm sure we will find anomalies that we will need to address before the next flight. But anyone will tell you that we learn just as much, if not more, when we encounter a glitch." Mr. Brink said he believes the X-51A program will provide knowledge required to develop the game changing technologies needed for future access to space and hypersonic weapon applications.

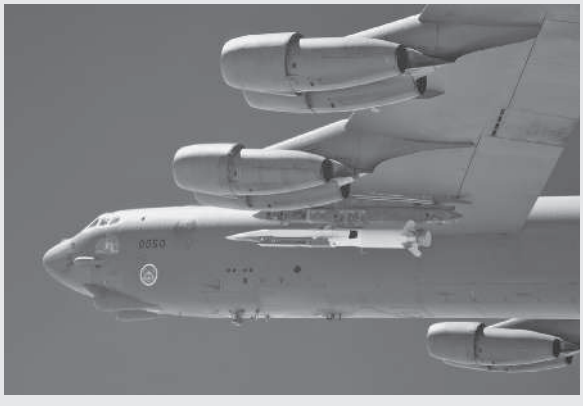

A B-52 carries an X-51A Waverider prior to the scramjet's first hypersonic flight test (U.S. Air Force photo)

Quotes are from USAF press release, "X-51 Waverider makes historic hypersonic flight," May 26, 2010.

12.6 AERODYNAMIC HEATING

As noted in the introduction to this chapter, the kinetic energy associated with hypersonic flight is converted to high temperatures within the shock layer. As a result, heat transfer is a very important factor in the design of hypersonic vehicles. Sharp leading edges would experience such extremely large heating rates in hypersonic flight that they would quickly melt or ablate (depending on the material used). Therefore, if a low-drag configuration is desired, the design would probably involve a slender cone with a spherically blunted nose. For a manned reentry craft, where the time of flight can be long and the dissipation of kinetic energy at relatively high altitude is desirable, the resultant high-drag configurations may be an airplane-like Space Shuttle that flies at high angles of attack or a blunt, spherical segment such as the Apollo Command Module.

The expression for the modified-Newtonian-flow pressure coefficient [equation (12.17)] can be rearranged to give

$$\frac{p_s}{p_{t2}} = \sin^2\theta_b + \frac{p_\infty}{p_{t2}}\cos^2\theta_b = \cos^2\phi + \frac{p_\infty}{p_{t2}}\sin^2\phi \qquad \textbf{(12.55)}$$

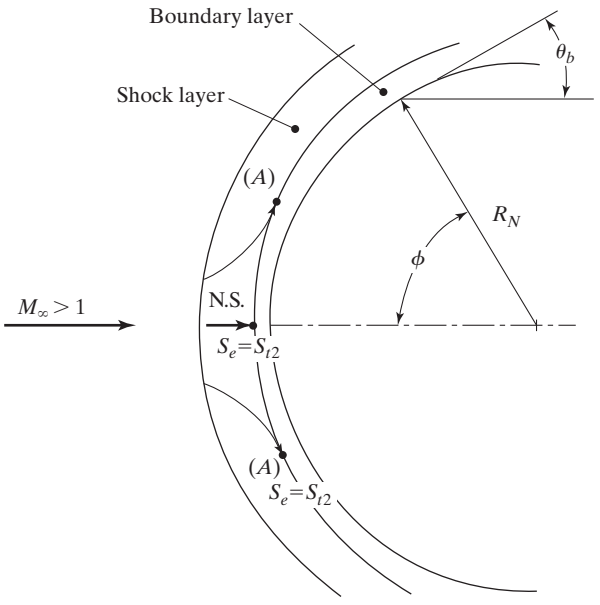

Figure 12.34 Sketch of the normal shock/isentropic expansion flow model for hypersonic flow over a blunt body. The air at the edge of the boundary layer at point A has passed through the (nearly) normal part of the shock wave. Thus, the entropy of the air particles at the edge of the boundary layer (S_e) is essentially equal to S_{t2} at all stations. In essence, the air has passed through the normal part of the shock wave (NS) and has undergone an isentropic expansion (IE) to the local pressures.

We will apply equation (12.55) to the relatively simple flow depicted in Fig. 12.34. As the boundary layer grows in the streamwise direction, air is entrained from the inviscid portion of the shock layer. Therefore, when determining the fluid properties at the edge of the boundary layer, we must determine the entropy of the streamline at the boundary-layer edge. Notice that the streamlines near the axis of symmetry of a blunt-body flow, such as those depicted in Fig. 12.34, have passed through that portion of the bow shock wave which is nearly perpendicular to the free-stream flow. As a result, we can assume that all the air particles at the edge of the boundary layer have essentially the same entropy. Therefore, the entropy at the edge of the boundary layer and, as a result, p_{t2} are the same at all streamwise stations. The local flow properties are the same as if the air had passed through a normal shock (NS) wave and had undergone an isentropic expansion (IE) to the local pressure (designated an NS/IE process). For such an isentropic expansion, the ratio of p_s/p_{t2} can then be used to define the remaining flow conditions (for an equilibrium flow). Note that, if the flow expands isentropically to a point where the local static pressure (p_s) is approximately $0.5p_{t2}$, the flow is essentially sonic for all values of γ. Solving equation (12.55), we find that $p_s \approx 0.5p_{t2}$ when $\theta_b = 45°$ (i.e., the sonic points occur when the local body slope is 45°).

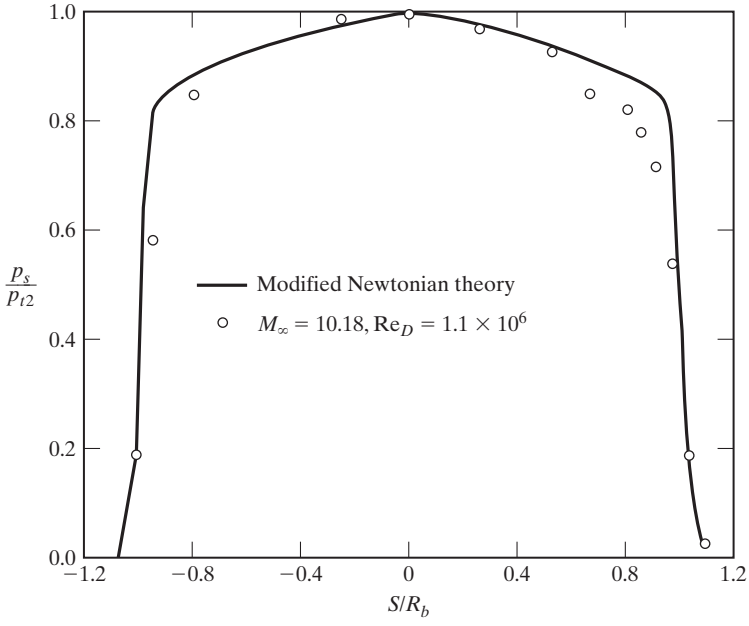

Figure 12.35 Comparison of the modified Newtonian pressures and the experimental pressures for the Apollo Command Module at $\alpha = 0°$ [from Bertin (1966)].

The modified Newtonian pressures for the zero-angle-of-attack Apollo Command Module are compared in Fig. 12.35 with data obtained in Tunnel C at AEDC that were presented by Bertin (1966). The experimental pressures measured in Tunnel C at a nominal free-stream Mach number of 10 and at a Reynolds number of $\mathrm{Re}_{\infty, D} = 1.1 \times 10^6$ have been divided by the calculated value of the stagnation pressure behind a normal shock wave (p_{t2}). For reference, a sketch of the Apollo Command Module is presented in Fig. 12.36. Notice that an S/R_b ratio of 0.965 defines the tangency point of the spherical heat shield and the toroidal surface, while an S/R_b ratio of 1.082 corresponds to the maximum body radius. Because the windward heat shield of the Apollo Command Module is a truncated spherical cap, the actual sonic points, which occur near the tangency point of the spherical heat shield and the toroidal surface, are inboard of the locations that they would occupy for a full spherical cap. As a result, the entire flow field in the subsonic portion of the shock layer is modified, and the streamwise velocity gradients are relatively large in order to produce sonic flow at the "corners" of the Command Module. Therefore, significant differences exist between the modified Newtonian pressures and the measured values as the flow approaches the edge of the spherical heat shield. Because the velocity gradient at the stagnation point of a hemispherical segment is increased above the value for a full hemisphere, the stagnation point heating rate will also be increased. Investigations of the stagnation region velocity gradients as a function of R_b/R_N have been reported by Stoney (1958) and by Inouye et al. (1968).

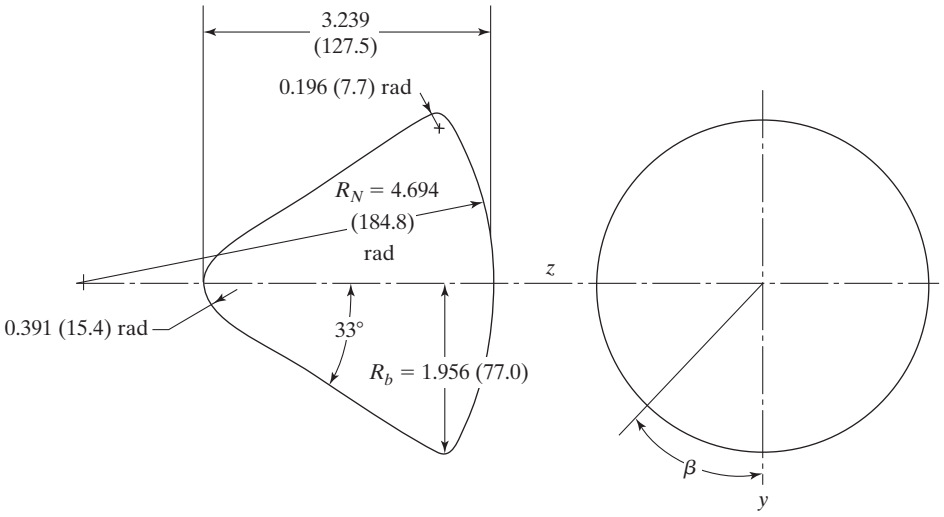

Figure 12.36 Clean (no protuberances) Apollo Command Module. Dimensions in meters (inches).

12.6.1 Similarity Solutions for Heat Transfer

The magnitude of the heat transfer from a compressible boundary layer composed of dissociating gases can be approximated by

$$|\dot{q}_w| = \left(k\frac{\partial T}{\partial y}\right)_w + \left(\rho \sum D_i h_i \frac{\partial C_i}{\partial y}\right)_w \tag{12.56}$$

where the heat is transported by conduction and by diffusion [see Dorrance (1962)]. We will assume that the flow has a Lewis number approximately equal to unity, the hot gas layer is in chemical equilibrium, and the surface temperature is much less than the external stream temperature. The Lewis number is the non-dimensional ratio of the thermal diffusivity to the mass diffusivity. For these assumptions, the magnitude of the heat transferred to the wall is

$$|\dot{q}_w| = \left(\frac{k}{c_p}\frac{\partial h}{\partial y}\right)_w \tag{12.57}$$

There are many situations where a coordinate transformation can be used to reduce the governing partial differential equations for a laminar boundary layer to ordinary differential equations [see Dorrance (1962)]. Fay and Riddell (1958) note, "As is usual in boundary-layer problems, one first seeks solutions of restricted form which permit reducing exactly the partial differential equations to ordinary differential form. An easily recognizable case is that of the stagnation point flow, where, because of symmetry, all the dependent variables are chosen to be functions of y alone, except u which must be taken proportional to x times a function of y. This also appears to be the *only case* for which the exact ordinary differential equations may be obtained regardless of the recombination rate."

Using the similarity transformations suggested by Fay and Riddell (1958), we obtain

$$\eta(x_1, y_1) = \frac{\rho_w u_e r^k}{\sqrt{2S}} \int_0^{y_1} \frac{\rho}{\rho_w} dy \tag{12.58}$$

and

$$S(x_1) = \int_0^{x_1} \rho_w \mu_w u_e r^{2k} dx \tag{12.59}$$

where r is the cross-section radius of the body of revolution and k denotes whether the flow is axisymmetric ($k = 1$) (e.g., a sphere) or two dimensional ($k = 0$) (e.g., a cylinder whose axis is perpendicular to the free stream). Limiting approximations are used to describe the flow in the vicinity of the stagnation point, for example,

$$u_e \approx \left(\frac{du_e}{dx}\right)_{t2} x; \quad r \approx x; \quad \text{and } \rho_w = \text{constant}$$

Therefore, at the stagnation point,

$$S \approx \rho_w \mu_w \left(\frac{du_e}{dx}\right)_{t2} \int x x^{2k}\, dx = \rho_w \mu_w \left(\frac{du_e}{dx}\right)_{t2} \frac{x^{2(k+1)}}{2(k+1)} \tag{12.60}$$

and

$$\eta \approx \frac{(du_e/dx)_{t2} x x^k}{\sqrt{2S}} \int \rho\, dy = \left[\frac{(du_e dx)_{t2}(k+1)}{\rho_w \mu_w}\right]^{0.5} \int \rho\, dy \tag{12.61}$$

Notice that using equation (12.61) as the expression for the transformed y coordinate, together with the definition for the heat transfer as given by equation (12.57), we find that (given the same flow condition),

$$(\dot{q}_{t,\text{ref}})_{\text{axisym}} = \sqrt{2}(\dot{q}_{t,\text{ref}})_{\text{2-dim}} \tag{12.62}$$

(i.e., the stagnation-point heat-transfer rate for a sphere is the $\sqrt{2}$ times that for a cylinder).

The stagnation-point heat-transfer rate for a laminar boundary layer of a spherical cap may be written as

$$\dot{q}_{t,\text{ref}} = \frac{\text{Nu}_x}{\sqrt{\text{Re}_x}} \sqrt{\rho_{w,t} \mu_{w,t} \left(\frac{du_e}{dx}\right)_{t2} \frac{H_{t2} - h_{w,t}}{Pr}} \tag{12.63}$$

For a Lewis number of 1, Fay and Riddell (1958) found that

$$\frac{\text{Nu}_x}{\sqrt{\text{Re}_x}} = 0.67 \left(\frac{\rho_{t2}\mu_{t2}}{\rho_{w,t}\mu_{w,t}}\right)^{0.4} \tag{12.64}$$

for velocities between 5800 ft/s (1768 m/s) and 22,800 ft/s (6959 m/s) and at altitudes between 25,000 ft (7620 m) and 120,000 ft (36,576 m).

We now can use Euler's equation to evaluate the velocity gradient at the stagnation point:

$$\left(\frac{dp_e}{dx}\right)_{t2} = -\rho_e u_e \left(\frac{du_e}{dx}\right)_{t2} \approx -\rho_{t2} \left(\frac{du_e}{dx}\right)_{t2}^2 x \tag{12.65}$$

Using the modified Newtonian flow pressure distribution [i.e., equation (12.55)] to evaluate the pressure gradient at the stagnation point, we obtain:

$$\left(\frac{dp_e}{dx}\right)_{t2} = -2p_{t2}\cos\phi\sin\phi\frac{d\phi}{dx} + 2p_\infty\cos\phi\sin\phi\frac{d\phi}{dx} \tag{12.66}$$

Since $\sin\phi \approx \phi = x/R_N$, $\cos\phi \approx 1$, and $d\phi/dx = 1/R_N$, we find that

$$\left(\frac{du_e}{dx}\right)_{t2} = \frac{1}{R_N}\sqrt{\frac{2(p_{t2} - p_\infty)}{\rho_{t2}}} \tag{12.67}$$

Combining the expressions given by equations (12.63) through (12.67), we obtain the equilibrium correlation of Fay and Riddell (1958):

$$\dot{q}_{t,\text{ref}} = \frac{0.67}{Pr_{t2}}(\rho_{t2}\mu_{t2})^{0.4}(\rho_{w,t}\mu_{w,t})^{0.1}(H_{t2} - h_{w,t})\left[\frac{1}{R_N}\left(\frac{2(p_{t2} - p_\infty)}{\rho_{t2}}\right)^{0.5}\right]^{0.5} \tag{12.68}$$

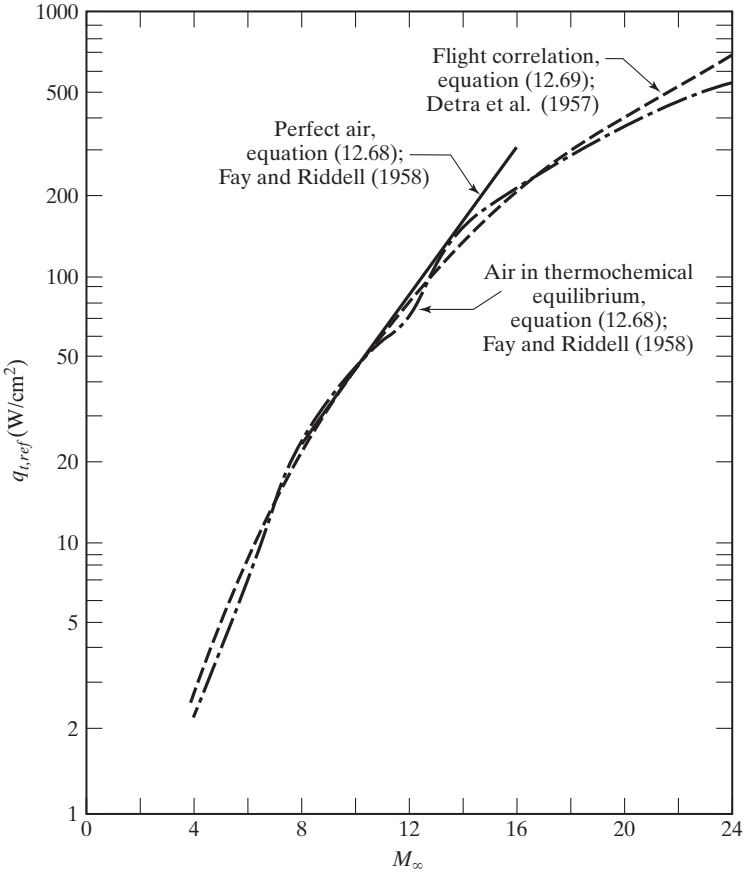

Figure 12.37 Heat-transfer rate at the stagnation point of a sphere ($R_N = 0.3048$ m) at an attitude of 45,721 m.

This relation can be used either for wind-tunnel flows or for flight conditions. Detra et al. (1957) have also developed a correlation:

$$\dot{q}_{t,\,\mathrm{ref}} = \frac{17{,}600}{(R_N)^{0.5}}\left(\frac{\rho_\infty}{\rho_{S.L.}}\right)^{0.5}\left(\frac{U_\infty}{U_{c.o.}}\right)^{3.15} \tag{12.69}$$

In equation (12.69), R_N is the nose radius in feet, $\rho_{\mathrm{S.L.}}$ is the sea-level density, $U_{\mathrm{c.o.}}$ is the velocity for a circular orbit, and $\dot{q}_{t,\,\mathrm{ref}}$ is the stagnation point heat-transfer rate in $\mathrm{Btu/ft^2 \cdot s}$.

The heat-transfer rate at the stagnation point of a 1-ft (0.3048-m) sphere flying at 150,000 ft (45,721 m) has been calculated using equation (12.68) for both the perfect-air model and the equilibrium-air model and using equation (12.69). The computed values are presented in Fig. 12.37 as a function of M_∞. Above $M_\infty = 14$, the perfect-gas model no longer provides realistic values of $\dot{q}_{t,\,\mathrm{ref}}$.

12.7 A HYPERSONIC CRUISER FOR THE TWENTY-FIRST CENTURY?

Harris (1992) considered the flight-block time for global-range fraction for several cruise Mach numbers. A vehicle cruising at Mach 10 would have global range in three hours flight-block time. Therefore, he concluded that Mach numbers greater than about 10 to 15 provide an insignificant improvement in flight-block time both for civil and for military aircraft.

Hunt and Rausch (1998) noted that, for hypersonic airplanes carrying a given payload at a given cruise Mach number, range is a good figure of merit. This figure of merit is impacted by the fuel selection. Calculations indicate that Mach 8 is approximately the cruise speed limit for which a dual mode ramjet/scramjet engine can be cooled with state-of-the-art cooling techniques, when endothermic hydrocarbon fuels are used. On the other hand, liquid hydrogen has a much greater cooling capacity. Furthermore, hydrogen-fueled vehicles have considerably more range than hydrocarbon-fueled vehicles flying at the same Mach number. In addition, the range of hydrogen-fueled vehicles maximizes at about a Mach number of 10, which is beyond the maximum flight Mach number associated with the cooling limits for endothermic hydrocarbon fuels.

Therefore, for hypersonic airplanes the constraints on cooling the engine limit endothermic-hydrocarbon-fueled vehicles to Mach numbers of approximately 8 or less. Airplanes that cruise at Mach numbers of 8 or greater will be hydrogen fueled. However, hydrogen-fueled systems can be designed for vehicles that cruise at Mach numbers below 8. The shape of the vehicle and the systems that constitute it will be very different for endothermic-hydrocarbon-fueled vehicles than for the hydrogen-fueled vehicles. Because of the dramatic differences in the fuel density and in the planform required to generate the required loading, the fuel type will greatly impact the design of the vehicle.

Other than fuel, the greatest impact on the system architectures will come from issues relating to airframe/propulsion-system integration. The entire lower surface of the vehicle is considered to be a boundary for the flowpath for airbreathing-propulsion system. The forebody serves as an external precompression surface for the engine inlet and the aftbody serves as a high expansion-ratio nozzle. Since the propulsion system

must take the vehicle from takeoff roll to cruise Mach number and back, the engine flowpath may contain a single duct, two ducts, or other concepts. The propulsion system may include auxiliary rocket components.

Configuration development studies for a global-reach, Mach 10 dual-fuel design have considered a variety of concepts. Bogar et al. (1996a) considered two classes of vehicles: a waverider and a lifting body. "When pressure forces alone are considered, the waverider enjoys a considerable advantage. However, as addition effects are added, this advantage erodes. Due to its larger wetted area, the waverider has higher viscous drag. And while the lifting body derives a benefit from trim effects, the waverider suffers a penalty because of the much larger forebody pitching moments which need to be balanced by the control surfaces." Bogar et al. (1996a) conclude, "At Mach 10 cruise conditions, lifting bodies and waveriders provide comparable performance. Reshaping the vehicle to improve volumetric efficiency and provide moderate increases in fineness improves mission performance."

Bogar et al. (1996b) explored concepts for a Mach 10 vehicle capable of global-reach missions, which could reach a target 8500 nautical miles (nmi) away in less than 90 minutes after takeoff. A sketch of the concept, which is approximately 200 ft in length and has a reference area of approximately 10,000 sq ft, is presented in Fig. 12.38. The vehicle has a takeoff gross weight of approximately 500,000 pounds. A dual-fuel concept (i.e., one that uses both hydrogen and endothermic hydrocarbons) was preferred for the return mission due to its capability for in-flight refueling on the return leg. The all-hydrogen vehicle was superior on the one-way mission due to its higher specific impulse (I_{sp}). The buildup of the components for the minimum drag for the baseline lifting body is presented in Fig. 12.39. The major components are pressure/wave drag, viscous drag,

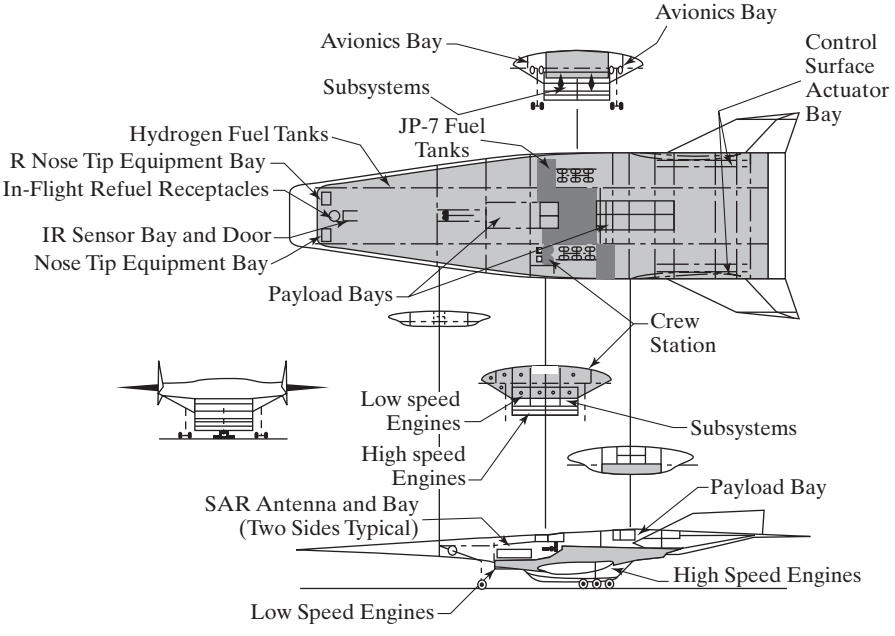

Figure 12.38 Mach 10 dual-fuel lifting-body cruise configuration [from Bogar et al. (1996b)].

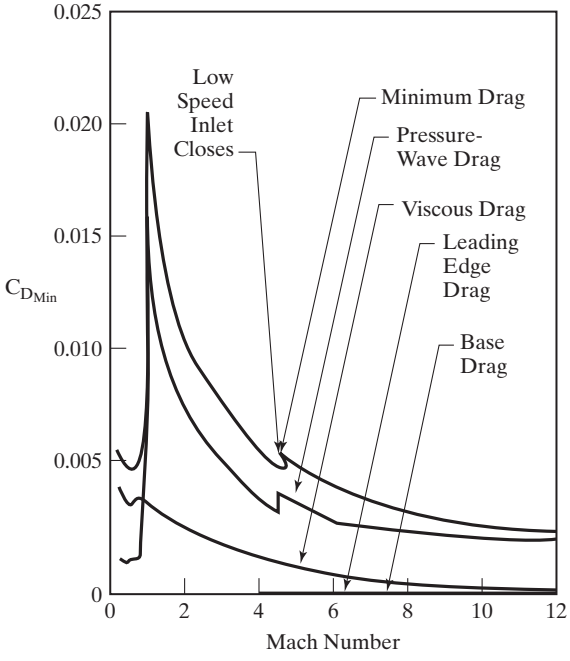

Figure 12.39 Minimum drag buildup for baseline vehicle [from Bogar et al. (1996b)].

leading-edge drag, and base drag. At cruise speed, the pressure drag is responsible for 78% of the total drag, while the viscous drag accounts for 15% of the total drag (notice the relatively high transonic-drag rise). Therefore, although the vehicle is designed to cruise at Mach 10, its shape is significantly affected by the transonic portion of the flight.

To help develop the technology base for the airbreathing-propulsion systems for hypersonic vehicles, NASA has initiated the Hyper-X Program. As discussed by McClinton et al. (1998), "The goal of the Hyper-X Program is to demonstrate and validate the technology, the experimental techniques, and computational methods and tools for design and performance prediction of hypersonic aircraft with airframe-integrated hydrogen-fueled, dual-mode combustion scramjet propulsion systems. Accomplishing this goal requires flight demonstration of and data from a hydrogen-fueled scramjet powered hypersonic aircraft."

McClinton et al. (1998) further state, "The Hyper-X Program concentrates on three main objectives required to significantly advance the Mach 5 to 10 scramjet technology leading to practical hypersonic flight:

1. vehicle design and flight test risk reduction—i.e., preflight analytical and experimental verification of the predicted aerodynamic, propulsive, structural, and integrated air-vehicle system performance and operability of the Hyper-X Research Vehicle (HXRV),
2. flight validation of design methods, and
3. methods enhancements—i.e., continued development of the advanced tools required to refine scramjet-powered vehicle designs.

"These objectives include experimental, analytical and numerical (CFD) activities applied to design the research vehicle and scramjet engine; wind tunnel verification of the vehicle aerodynamic, propulsion, and propulsion-airframe integration, performance and operability, vehicle aerodynamic database and thermal loads development; thermal-structural design; boundary layer transition analysis and control; flight control law development; and flight simulation model development. Included in the above is HXLV boost, stage separation and all other critical flight phases."

12.8 IMPORTANCE OF INTERRELATING CFD, GROUND-TEST DATA, AND FLIGHT-TEST DATA

Woods et al. (1983) note that preflight predictions based on the aerodynamics in the Aerodynamics Design Data Book (ADDB) indicated that a 7.5° deflection of the body flap would be required to trim the Space Shuttle *Orbiter* for the center of gravity and for the vehicle configuration of STS-1. In reality, the body flap had to deflect to much larger values ($\delta_{BF} \approx 16°$) to maintain trim at the proper angle of attack ($\alpha = 40°$). Comparisons of equilibrium-air calculations and perfect-gas calculations indicate that at least part of this so-called "hypersonic anomaly" is due to real-gas effects at very high Mach numbers. At Mach 8, the flight data and the ADDB values agreed, as reported by Woods et al. (1983).

Consider the flow depicted in the sketch of Fig. 12.40. For perfect air ($\gamma = 1.4$), $\rho_2 = 6\rho_1$ across the normal portion of the shock wave, whereas $\rho_2 = 15\rho_1$ for air in thermodynamic equilibrium ($\gamma = 1.14$). Therefore, for the equilibrium-air model the shock layer is thinner and the inclination of the bow shock wave relative to the free

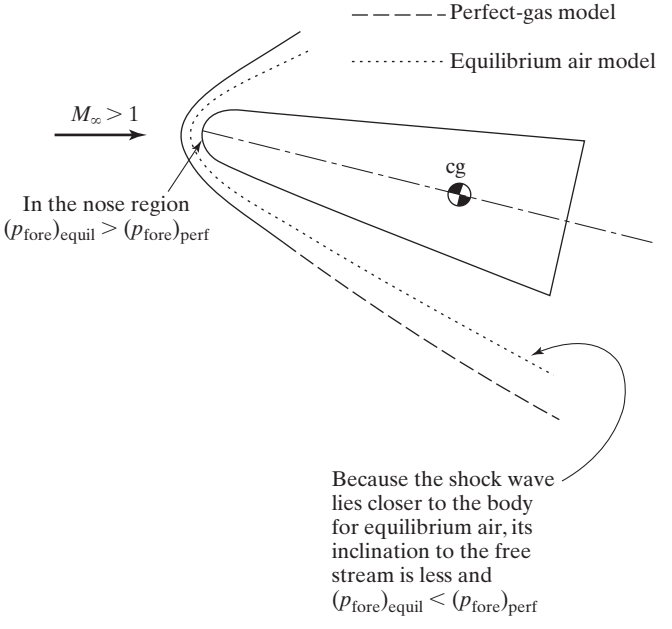

Figure 12.40 Hypersonic flow past an inclined spherically blunted cone comparing perfect-gas and equilibrium-air pressures.

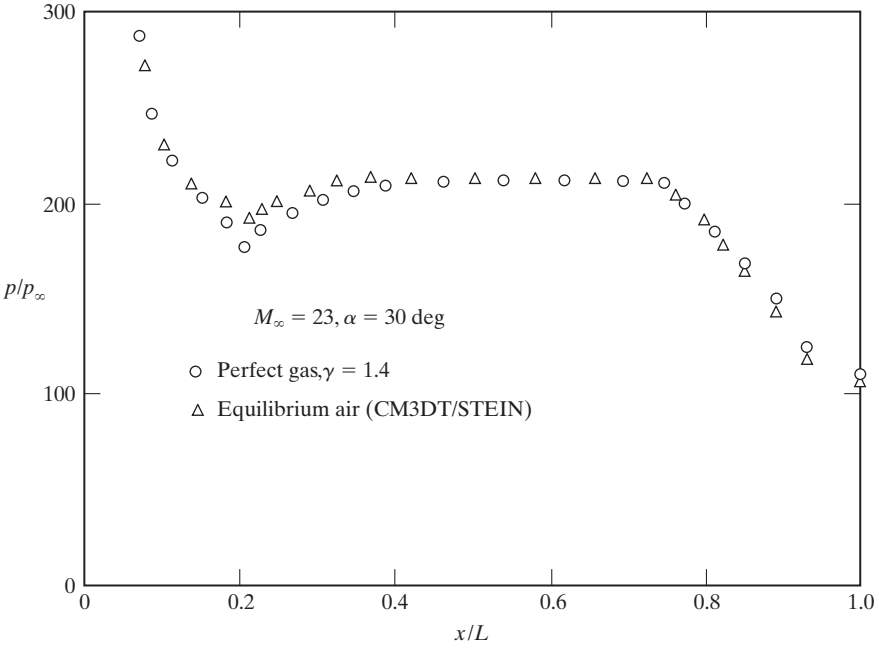

Figure 12.41 Comparison of perfect-gas and equilibrium-air calculations of the windward pitch-plane pressure distribution for the Space Shuttle *Orbiter* at $\alpha = 30°$ [from Maus et al. (1984)].

stream is less than that for the perfect-air model. Tangent-cone theory (which assumes the local pressure is given by the pressure on a cone with the same local slope; see Fig. 8.15) applied to the afterbody region shows a decrease in pressure with decreasing gamma. Using this simplistic flow model, we would expect the equilibrium-air pressures on the aft end of the vehicle to be less than those for perfect air. Computations of the flow field over simplified Orbiter geometries as reported by Woods et al. (1983) and by Maus et al. (1984) indicate that this is the case. The calculations of Maus et al. are reproduced in Fig. 12.41.

Maus et al. (1984) further note that the stagnation pressure increases with decreasing gamma. Therefore, as presented in Fig. 12.12, the equilibrium-air value for the stagnation pressure is greater than that for perfect air. This, too, is reflected in the nose region pressures presented in the more rigorous solutions of Woods et al. (1983) and Maus et al. (1984).

The differences between the equilibrium-air pressure distribution and the perfect-air pressure distribution may appear to be relatively small. Indeed, there is little difference in the normal force coefficients for the equilibrium-air model and for the perfect-air model. However, because the equilibrium-air (real-gas) values are higher at the nose and lower at the tail, the real-gas effects tend to drive C_M more positive. The pitching moments for the Space Shuttle *Orbiter* at $M_\infty = 23$ presented by Maus et al. (1984) are reproduced in Fig. 12.42. Therefore, detailed studies incorporating wind-tunnel data, flight-test data, and CFD solutions, as reported by Woods et al. (1983) and by Maus et al. (1984), provide insight into understanding a sophisticated aerodynamic problem.

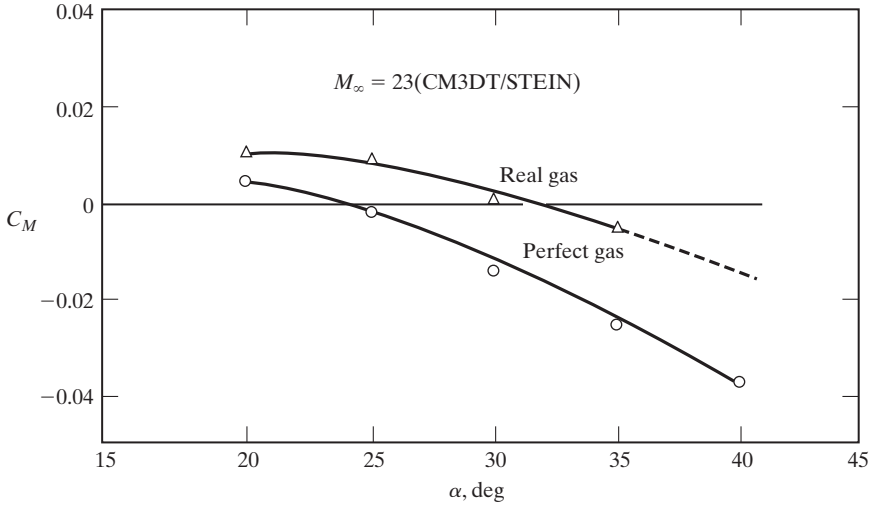

Figure 12.42 Comparison of perfect-gas and equilibrium-air calculations of the pitching moment for Space Shuttle *Orbiter* at $M_\infty = 23$ [from Maus et al. (1984)].

Interest in hypersonic technology regularly waxes and wanes. Two books have been written to preserve this technology, one for the aerothermodynamic environment by Bertin (1994) and one for airbreathing propulsion systems [Heiser and Pratt (1994)] of vehicles which fly at hypersonic speeds.

12.9 BOUNDARY-LAYER-TRANSITION METHODOLOGY

Laminar-to-turbulent boundary-layer transition in high-speed boundary layers is critical to the prediction and control of heat transfer, skin friction, and other boundary-layer properties. Bertin (1994) noted that the mechanisms leading to transition are still poorly understood. The Defense Science Board (1992) found that boundary-layer transition was one of the two technical areas which needed further development before a demonstrator version of the National Aerospace Plane (NASP) could be justified.

Schneider (2004) notes that there are: "two major ways in which transition appears to be relevant for capsule flows. The first is transition on the blunt face, which can have a significant effect on heating, depending on ballistic coefficient, angle of attack, geometry, roughness, and so on. The second is the effect of transition on the shear layer that separates from the rim of the blunt face. This shear layer may be important, if it may reattach to the afterbody, or otherwise affect the aerodynamic stability or the aerothermodynamic heating. Sinha et al. (2004) shows that transition in the wake can have a significant effect on base heating. Transition may or may not occur in the shear layer in a significant way, again depending on the configuration and trajectory."

Schneider (2004) continued: "For the designer, one issue is whether transition has a significant effect on the thermal-protection system mass via increased heating. The

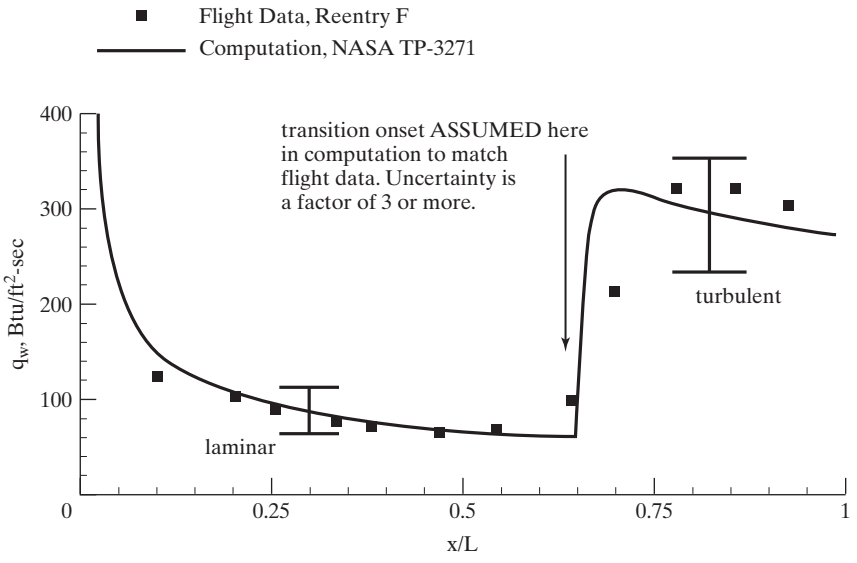

Figure 12.43 Heating-rate distribution along cone for reentry F.

other issue is the effect on lift-to-drag ratio through changes in the afterbody flow that affect moments and the trim angle of attack."

The high-heating rates of a turbulent boundary layer are illustrated in Fig. 12.43, which presents computations and measurements of the surface heat transfer during the Reentry F flight test. Reda (1979) noted that the ballistic RV of the Reentry F was a 3.96-m (13-ft) beryllium cone that reentered at a peak Mach number of about 20 and a total enthalpy of about 18 MJ/kg (7753 Btu/lbm). Schneider (1999) summarized that the cone half-angle was 5°; the angle-of-attack was near zero; and the graphite nosetip had an initial radius of 0.25 cm (0.1 in.). The individual measurements, which are represented by the symbols, are compared with the heat-transfer rates that were computed using a variable-entropy boundary-layer code that included equilibrium chemistry. To provide the best agreement between the experimental heat-transfer rates and the numerical values, the computed boundary layer was assumed to transition instantaneously at an x/L 0.625, where x is the axial distance from the apex of the cone and L is the length of the cone. With the transition location for the computed boundary layer positioned to match the location based on the experimentally determined heat-transfer distribution, agreement was good both for the laminar and for the turbulent regions. Hamilton, who performed the computations, said that typical accuracies are 20% to 25% for the turbulent boundary layer and 15% to 20% for the laminar boundary layer. Schneider (2004) noted: "Present empirical correlations for the onset and the extent of transition are uncertain by a factor of three or more. Thus, our computational capabilities for laminar and turbulent heating in attached flows are fairly good, the uncertainty in prediction of the overall heating is now often dominated by the uncertainty in predicting the location of transition."

Schneider (2004) reported, "A 1988 review by the Defense Science Board [Defense Science Board (1988)] found that . . . estimates [of the point of transition] range from 20 to 80% along the body . . . The assumption made for the point of

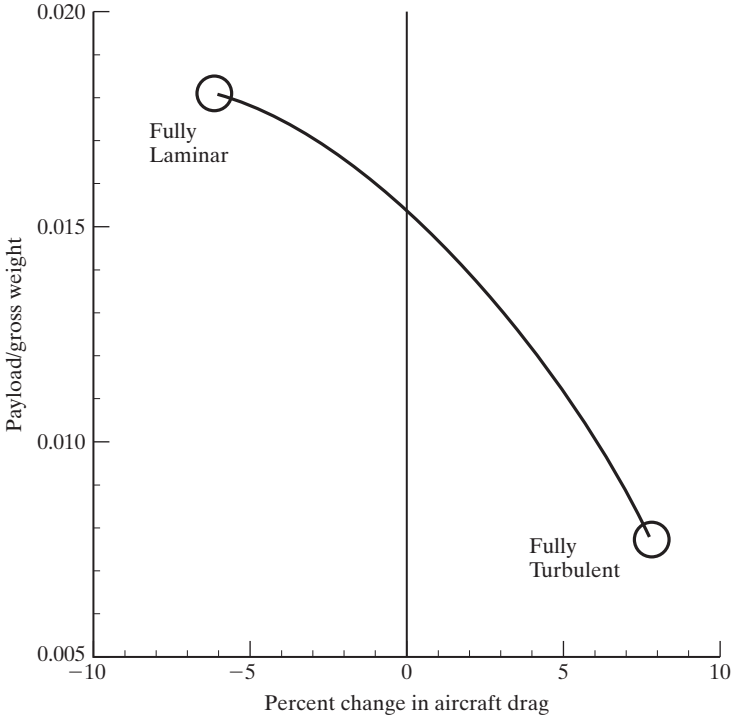

Figure 12.44 Effect of transition on NASP design.

transition can affect the vehicle gross takeoff weight by a factor of two or more." This point is illustrated in Fig. 12.44, which is taken from Whitehead (1989). A fully laminar boundary layer reduces the drag by approximately 6% for the baseline design of a single-stage-to-orbit National Aerospace Plane (NASP), while a fully turbulent boundary layer increases the drag by about 8%. For the baseline configuration, with substantial laminar flow on the forebody, the reduced drag and lower heating can result in a 60% to 70% increase in payload over the all-turbulent boundary-layer condition, as noted by Whitehead (1989).

Consider transition of the boundary layer of a sharp cone at zero angle-of-attack (AOA) in a supersonic/hypersonic stream. Despite the relative simplicity of the flow field, Schneider (2004) notes that the experimentally determined transition locations "in air at perfect-gas conditions are affected by cone half-angle, Mach number, tunnel size and noise, stagnation temperature, surface temperature distribution, surface roughness, and any blowing or ablation, as well as measurement technique. Sharp-cone, smooth-wall instability growth does not scale with Mach number, Reynolds number, and T_w/T_t, even under perfect-gas conditions [Kimmel and Poggie (2000)]. The mean boundary-layer profiles and their instability and transition depend on the absolute temperature; this is because the viscosity and heat-transfer coefficients depend on absolute temperature and do not scale. AOA effects are difficult to rule out, except by systematic azimuthal comparisons that are all too rare."

Bertin and Cummings (2003) note,

> The difficulty in developing criteria for predicting boundary-layer transition is complicated by the fact that the location of the onset of boundary-layer transition is very sensitive to the measurement technique used. The experimentally-determined heat-transfer rates increase above the laminar values at the upstream end of the boundary-layer transition process, i.e., at the onset of transitional flow. A schlieren photograph of the hypersonic flow field reveals vortices in the boundary layer associated with the various steps in the breakdown, i.e., in the transition of the boundary layer. However, for a flow as simple as a hypersonic flow over a slender, sharp cone, the boundary-layer transition location determined using the heat-transfer distribution along a conical generator is very different than that determined using a schlieren photograph.

Even if every researcher were to define and to measure transition in the same way, the scatter of transition data as a function of the Mach number still would be considerable. However, researchers employ a wide range of techniques in a wide variety of test simulations, which results in considerable scatter in transition correlations. This is illustrated in Fig. 12.45, which was originally presented by Beckwith and Bertram (1972).

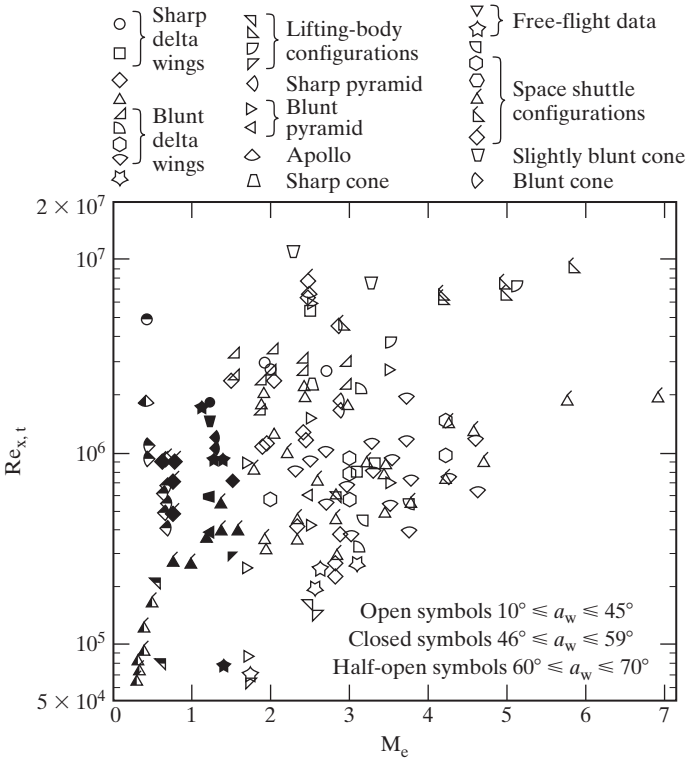

Figure 12.45 Transition Reynolds number as a function of local Mach number.

This presentation of data makes it difficult to imagine a single relationship that could correlate all of the data. Making matters worse is the fact that transition rarely occurs along a line. Turbulent zones spread and merge in the longitudinal direction, which further complicates the development of correlations for boundary-layer transition.

12.10 SUMMARY

Hypersonic flow is distinguished from supersonic flow by five characteristics: thin shock layers, entropy layers, viscous-inviscid interactions, high-temperature effects, and low density flows. These characteristics make this flow regime significantly different from supersonic aerodynamics, leading to theories and approaches which are unique from supersonic theories. Understanding how hypersonic vehicles differ from supersonic vehicles, such as the importance and impact of boundary layer transition, is crucial for the successful design and analysis of hypersonic flight.

PROBLEMS

12.1. Consider a hypersonic vehicle flying through the earth's atmosphere at 10,000 ft/s at an altitude of 200,000 ft. At 200,000 ft, $p_\infty = 0.4715$ lbf/ft^2, $\rho_\infty = 6.119 \times 10^{-7}$ slug/ft^3, $T_\infty = 449°$R, and $h_\infty = 2.703 \times 10^6$ ft · lbf/slug. Using the thermodynamic properties of equilibrium air presented in Fig. 12.10, what are the static pressure (p_2), the static temperature (T_2), the enthalpy (h_2), and the static density (ρ_2) downstream of a normal shock wave? For comparison, use the normal-shock relations for perfect air, as given in Chapter 8, to calculate p_2, T_2, h_2, and ρ_2.

12.2. Consider a hypersonic vehicle reentering the earth's atmosphere at 20,000 ft/s at an altitude of 200,000 ft. Repeat Problem 12.1, that is, calculate p_2, ρ_2, T_2, and h_2 assuming that the air **(a)** is in thermodynamic equilibrium and **(b)** behaves as a perfect gas.

12.3. Consider a hypersonic vehicle reentering the earth's atmosphere at 26,400 ft/s at an altitude of 200,000 ft. Repeat Problem 12.1, that is, calculate p_2, ρ_2, T_2, and h_2 assuming that the air **(a)** is in thermodynamic equilibrium and **(b)** behaves as a perfect gas.

12.4. If the free-stream Mach number is 5, calculate the pressure coefficient on the surface of a wedge, whose deflection angle is 40°, using the correlations of Fig. 8.12b and using Newtonian theory. How does the altitude influence the resultant values of C_p?

12.5. If the free-stream Mach number is 9, calculate the pressure coefficient on the surface of a sharp cone, whose deflection angle is 40°, using the correlations of Fig. 8.16b and using Newtonian theory.

12.6. In equation (12.22), it was stated without proof that the section drag coefficient (per unit span) for modified Newtonian pressures acting on a right circular cylinder is: $C_{d,p} = \frac{2}{3}C_{p,t2}$ Prove that $C_{d,p} = \frac{10}{3}C_{p,t2}$ is correct for 5 spans.

12.7. Consider the sharp cone in a hypersonic stream, which was the subject of Example 12.3. If $M_\infty = 10$ and $\theta_c = 10°$, prepare a graph of C_D as a function of α for $-10° \leq \alpha \leq 10°$.

12.8. Consider the sharp cone in a hypersonic stream, which was the subject of Example 12.3. If $M_\infty = 10$ and $\theta_c = 10°$, prepare a graph of C_L as a function of α for $-10° \leq \alpha \leq 10°$.

12.9. Consider the sharp cone in a hypersonic stream, which was the subject of Example 12.3. If $M_\infty = 10$ and $\theta_c = 10°$, prepare a graph of L/D as a function of α for $-10° \leq \alpha \leq 10°$.

12.10. Consider the sharp cone in a hypersonic stream, which was the subject of Example 12.3. If $M_\infty = 10$ and $\theta_c = 10°$, prepare a graph of C_M as a function of α for $-10° \leq \alpha \leq 10°$. Is the configuration statically stable if $x_{cg} = 0.6x_L$?

12.11. A configuration that would generate lift at low angles of attack is a half-cone model, such as shown in Fig. P12.11. Neglecting the effects of skin friction and assuming the pressure is that of the Newtonian flow model, develop an expression for the lift-to-drag ratio as a function of θ_c for $0 \leq \alpha \leq \theta_c$.

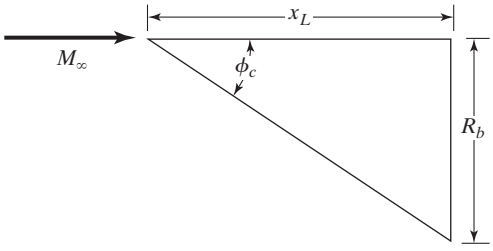

Figure P12.11

12.12. Develop expressions for y_{cp} and x_{cp} for the flow described in Problem 12.11.

12.13. Using the Newtonian flow model to describe the pressure field and neglecting the effects of viscosity, what is the drag coefficient on the $\theta_c = 10°$ sharp cone of Example 12.4? What would the drag coefficient be if you used the modified Newtonian flow model?

12.14. Following the procedure developed in Example 12.4, develop expressions for the forebody pressure coefficient $(C_{p,e})$, the base pressure coefficient $(C_{p,b})$, and the skin friction, if $\theta_c = 20°$ for the sharp cone exposed to the Mach 8 flow of Tunnel B.

12.15. We will model the flow on the windward surface of a reentry vehicle and its body flap by the double wedge configuration shown in Fig. P12.15. The lower surface of the fuselage is inclined $10°(\alpha = 10°)$ to the free-stream flow, producing the supersonic flow in region 2. A body flap is deflected $10°$(so that $\alpha + \delta_{BF} = 20°$).

(a) Calculate the pressure coefficient for regions 2 and 3 using the Newtonian flow model for $M_1 = 2, 4, 6, 8, 10$, and 20.

(b) Using the correlations of Fig. 8.13, calculate the pressure coefficients for regions 2 and 3 for $M_1 = 2{,}4, 6, 8, 10$, and 20. The flow remains supersonic throughout the flow field for these deflection angles. Note that to go from region 2 to 3 using the charts of Fig. 8.13, treat region 2 as an equivalent free-stream flow ("1"); then region 3 corresponds to region 2. Note, however, that $C_{p3} = (p_3 - p_1)/q_1$, that is, the reference conditions are those of the free stream.

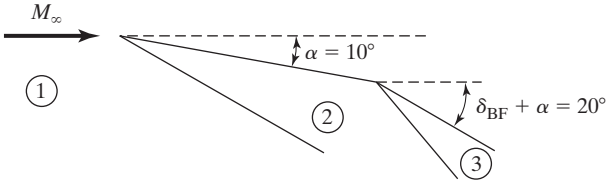

Figure P12.15

REFERENCES

Anderson JD, Lewis MJ, Corda S. 1990. *Several families of viscous optimized waveriders—a review of waverider research at the University of Maryland*. Presented at International Hypersonic Waverider Symposium, 1st, College Park, MD

Anderson JD. 2006. Hypersonic and High-Temperature Gas Dynamics. 2nd Ed. Reston VA: AIAA

Bauer SXS, Covell PF, Forrest DK, McGrath BE. 1990. *Preliminary assessment of a Mach 4 and a Mach 6 waverider*. Presented at International Hypersonic Waverider Symposium, 1st, College Park, MD

Beckwith IE, Bertram MH. 1972. A survey of NASA Langley studies on high-speed transition and the Quiet Tunnel. *NASA Tech. Mem. X-2566*

Bertin JJ. 1966. The effect of protuberances, cavities, and angle of attack on the wind-tunnel pressure and heat-transfer distributions for the Apollo Command Module. *NASA TMX*-11243

Bertin JJ. 1994. *Hypersonic Aerothermodynamics*. Washington, DC: AIAA

Bertin JJ, Cline DD. 1980. Variable-grid-size transformation for solving nonsimilar laminar and turbulent boundary-layers. Ed. M. Gersten and P. R. Choudhury. *Proceedings of the 1980 Heat Transfer and Fluid Mechanics Institute*, Stanford, CA: Stanford University Press

Bertin JJ, Cummings RM. 2003. Fifty years of hypersonic, where we've been, where we're going. *Progr. Aerosp. Sci.* 39:511–536

Bertin JJ, Cummings RM. 2006. Critical hypersonic aerothermodynamic phenomena. *Annu. Rev. Fluid Mech.* 38: 129–157

Bird GA. 1978. Monte Carlo simulation of gas flows. *Annu. Rev. Fluid Mech*. 10:11–31

Bogar TJ, Eiswirth EA, Couch LM, Hunt JL, McClinton CR. 1996a. *Conceptual design of a Mach 10 global reach reconnaisance aircraft*. Presented at Joint Propulsion Conference, 32nd, AIAA Pap. 96–2894, Lake Buena Vista, FL

Bogar TJ, Alberico JF, Johnson DB, Espinosa AM, Lockwood MK. 1996b. *Dual-fuel lifting body configuration development*. Presented at Intern. Space Planes and Hypersonic Systems and Techn. Conf., AIAA Pap. 96–4592, Norfolk, VA

Bowcutt KG, Anderson JD, Capriotti D. 1987. *Viscous optimized hypersonic waveriders*. Presented at Aerosp. Sci. Meet., 25th, AIAA Pap. 87–0272, Reno, NV

Brandon HJ, DeJarnette FR. 1977. *Three-dimensional turbulent heating on an ogive at angle of attack including effects of entropy-layer swallowing*. Presented at Thermophysics Conf., 12th, AIAA Pap. 77–754, Albuquerque, NM

Cassanto JM. 1973. A base pressure experiment for determining the atmospheric profile of the planets. *J. Spacecr. Rockets* 10:253–261

Cervisi RT, Grantz AC. 1994. *Efficient hypersonic accelerators derived from analytically defined flowfields*. Presented at Aerosp. Sci. Meet., 32nd, AIAA Pap. 94–0726, Reno, NV

Columbia Accident Investigation Board. 2003. *Accident Analysis*. US Govt. Printing Office. 1(3):49–84

Defense Science Board. 1988. *Report of the Defense Science Board Task Force on the National Aerospace Plane (NASP)*. Washington, DC: Dept. of Defense

Defense Science Board. 1992. *Report of the Defense Science Board Task Force on the National Aerospace Plane*. Washington, DC: Dept. of Defense

Detra RW, Kemp NH, Riddell FR. 1957. Addendum to heat transfer to satellite vehicles reentering the atmosphere. *Jet Propulsion* 27:1256–1257

Dorrance WH. 1962. *Viscous Hypersonic Flow*. New York: McGraw-Hill Book Co.

Eckert ERG. 1955. Engineering relations for friction and heat transfer to surfaces in high velocity flow. *J. Aeronaut. Sci.* 22:585–587.

Eggers T, Radespiel R. 1993. *Design of waveriders*. Presented at Space Course on Low Earth Orbit Transportation, 2nd, Munich, Germany

Fay JA, Riddell FR. 1958. Theory of stagnation point heat transfer in dissociated air. *J. Aeronaut. Sci.* 25:73–85, 121

Haney JW, Beaulieu WD. 1994. *Waverider inlet integration issues*. Presented at Aerosp. Sci. Meet., 32nd, AIAA Pap. 94–0383, Reno, NV

Hansen CF. 1957. Approximations for the thermodynamic and transport properties of high-temperature air. *NACA Tech. Rep. R-50*

Harris RV. 1992. On the threshold—the outlook for supersonic and hypersonic aircraft. *J. Aircraft* 29:10–19

Heiser WH, Pratt D. 1994. *Hypersonic Airbreathing Propulsion*. Washington, DC: AIAA

Hirschel EH. 1991. *Viscous effects*. Proc. Space Course, pp. 12:1–35. MBBFE202/S/PUB/441. Aachen, Germany

Hunt JL, Rausch VL. 1998. *Airbreathing hypersonic systems focus at NASA Langley Research Center*. Presented at International Spaceplanes and Hypersonic Systems and Tech. Conf., 8th, AIAA Pap. 98–1641, Norfolk, VA

Inouye M, Marvin JG, Sinclair AR. 1968. Comparison of experimental and theoretical shock shapes and pressure distributions on flat-faced cylinders at Mach 10.5. *NASA Tech. Note D-4397*

Isaacson LK, Jones JW. 1968. Prediction techniques for pressure and heat-transfer distributions over bodies of revolution in high subsonic to low-supersonic flight. *Naval Weapons Center TP 4570*

Kimmel RL, Poggie J. 2000. Effect of total temperature on boundary-layer stability at Mach 6. *AIAA J.* 38:1754–1755

Koppenwallner G. 1969. Experimentelle untersuchung der druckverteilung und des widerstands von querangestroemten kreiszylindern bei hypersonischen Machzahlen in bereich von Kkontinuums-bis freier Mmolekularstroemung. *Z. Flugwissenschaften* 17:321–332.

Lees L. 1951. Note on the hypersonic similarity law for an unyawed cone. *J. Aeronaut. Sci.* 18(10):700–702

Lees L. 1953. Hypersonic viscous flow over an inclined wedge. *J. Aeronaut. Sci.* 20(11): 794, 795

Lees L. 1955. Hypersonic flow. *Proceedings of the 5*th *International Aeronautical Conference*, Los Angeles, CA, pp. 241–275

Marconi F, Salas M, Yeager L. 1976. Development of a computer code for calculating the steady supersonic/hypersonic inviscid flow around real configurations. *NASA Contr. Rep. 675*

Maus JR, Griiffith BJ, Szema KY, Best JT. 1984. Hypersonic Mach number and real gas effects on Space Shuttle Orbiter aerodynamics. *J. Spacecr. Rockets* 21:136–131

McClinton CR, Voland RT, Holland SC, Engelund WC, White JT, Pahle JW. 1998. *Wind tunnel testing, flight scaling, and flight validation with Hyper-X*. Presented at Advanced Measurement and Ground Test. Conf., 20th, AIAA Pap. 98–2866, Albuquerque, NM

Moeckel WE, Weston KC. 1958. Composition and thermodynamic properties of air in chemical equilibrium. *NACA Tech. Note 4265*

Nonweiler TRF. 1959. Aerodynamic problems of manned space vehicles. *J. Roy. Aeronaut. Soc.* 63:521–528

Oswatitsch K. 1956. *Gas Dynamics*. New York: Academic Press

Reda WC. 1979. Boundary-layer-transition experiments on sharp, slender cones in supersonic free flight. *AIAA J.* 17:803–810

Riley CJ, DeJarnette FR, Zoby EV. 1990. Surface pressure and streamline effects on laminar calculations. *J. Spacecr. Rockets* 27:9–14

Schneider SP. 1999. Flight data for boundary-layer transition at hypersonic and supersonic speeds. *J. Spacecr. Rockets* 36:8–20

Schneider SP. 2004. Hypersonic laminar-turbulent transition on circular cones and scramjet forebodies. *Progr. Aerosp. Sci.* 40:1–50

Sinha K, Barnhardt M, Candler GV. 2004. Detached eddy simulation of hypersonic base flows with application to Fire II experiments. Presented at Fluid Dynamics Conf., 34th, AIAA Pap. 2004–2633, Portland, OR

Squire LC. 1976a. Flow regimes over delta wings at supersonic and hypersonic speeds. *Aeronaut. Quart.* 27:1–14

Squire LC. 1976b. The independence of upper and lower wing flows at supersonic speeds. *Aeronaut. J.* 80:452–456

Stoney WE. 1958. Aerodynamic heating of blunt-nose shapes at Mach numbers up to 14. *NACA 58E05a*

Tirsky GA. 1993. Up-to-date gasdynamic models of hypersonic aerodynamics and heat transfer with real gas properties. *Annu. Rev. Fluid Mech*. 25:151–81

U. S. Standard Atmosphere 1976. Washington, DC: U.S. Government Printing Office

Whitehead A. 1989. *NASP aerodynamics*. Presented at National Aerosp. Plane Conf., AIAA Pap. 89–5013, Dayton, OH

Woods WC, Arrington JP, Hamilton HH. 1983. A review of preflight estimates of real-gas effects on Space Shuttle aerodynamic characteristics. In *Shuttle Performance: Lessons Learned*, NASA 2283, Part I

Zoby EV, Moss JN, Sutton K. 1981. Approximate convective-heating equations for hypersonic flows. *J. Spacecr. Rockets* 18:64–70.

13 AERODYNAMIC DESIGN CONSIDERATIONS

Chapter Objectives

- Understand that aerodynamic design decisions are rarely made without considering multidisciplinary design factors
- Have a good idea of how to increase lift on an airplane, and how to modify an airplane in order to achieve aerodynamic improvements
- Learn about drag reduction and how important reducing drag is to aircraft development programs
- Study aircraft from the past and see how aerodynamic considerations were included in the design

In the previous chapters we have discussed techniques for obtaining flow-field solutions when the free-stream Mach number is either low subsonic, high subsonic, transonic, supersonic, or hypersonic. Many airplanes must perform satisfactorily over a wide speed range, which may include more than one speed regime (e.g., subsonic and transonic). Therefore, the thin, low-aspect ratio wings designed to minimize drag during supersonic cruise must deliver sufficient lift at low speeds to avoid unacceptably high landing speeds and/or landing field length. When these moderate aspect ratio, thin, swept wings operate at high angles of attack during high subsonic Mach number maneuvers, their performance is significantly degraded because of shock-induced boundary-layer

separation and, at high angles of attack, because of leading-edge separation and wing stall. Furthermore, because of possible fuel shortages and sharp fuel price increases, the wings of a high-speed transport may be optimized for minimum fuel consumption instead of for maximum productivity. In this chapter, we consider design parameters that improve the aircraft's performance over a wide range of speed.

13.1 HIGH-LIFT CONFIGURATIONS

Consider the case where the aerodynamic lifting forces acting on an airplane are equal to its weight (steady, level, unaccelerated flight, which is typically called SLUF):

$$W = L = \tfrac{1}{2}\rho_\infty U_\infty^2 S C_L \tag{13.1}$$

To support the weight of the airplane at relatively low speeds, we could either increase the surface area over which the lift forces act or increase the lift coefficient of the lifting surface. Airplanes accomplish this in different ways, most commonly by increasing the lift coefficient, but in many civil transports also by increasing the wing area. We will look at each approach individually.

13.1.1 Increasing the Area

During the early years of aviation, the relatively crude state of the art in structural analysis limited the surface area that could be obtained with a single wing. Thus, as discussed in Cowley and Levy (1918), "In the attempt to increase the wing area in order to obtain the greatest lift out of an airfoil it was found that there was a point beyond which it was not advantageous to proceed. This stage was reached when the extra weight of construction involved in an increase in wing area was just sufficient to counterbalance the increase in lift. The method of using aerofoils in biplanes is desirable in the first place from the fact that, with a smaller loss in the necessary weight of construction, extra wing area may thus be obtained." Therefore, although some of the combatants used monoplanes at the start of World War I [e.g., the Morane-Saulnier type N (France) and the Fokker series of E-type fighters (E for Eindecker; Germany)], most of the planes in service at the end of the war were biplanes [e.g., the SE5a (United Kingdom), the Fokker D-VII (Germany), and the SPAD XIII (France)] to carry the increased weight of the engine and of the payload.

Although the serious design of biplanes continued until the late 1930s, with the Fiat C.R. 42 (Italy) making its maiden flight in 1939, the improved performance of monoplane designs brought them to the front, primarily due to significant improvements in light weight materials and structures. Various methods of changing the wing geometry in flight were proposed in the 1920s and 1930s. Based on a concept proposed by test pilot V. V. Shevchenko, Soviet designer V. V. Nikitin developed a fighter that could translate from a biplane to a monoplane, or vice versa, at the will of the pilot [Air International (1975)]. In the design of Nikitin (known as the *IS*-2), the inboard sections of the lower wing were hinged at their roots, folding upward into recesses in the fuselage sides. The sections outboard of the main undercarriage attachment points also were articulated and, rising vertically and inward, occupied recesses in the upper wing. Therefore, a single airplane combined the desirable short-field and low-speed characteristics of a lightly-loaded biplane with the higher performance offered by a highly loaded monoplane.

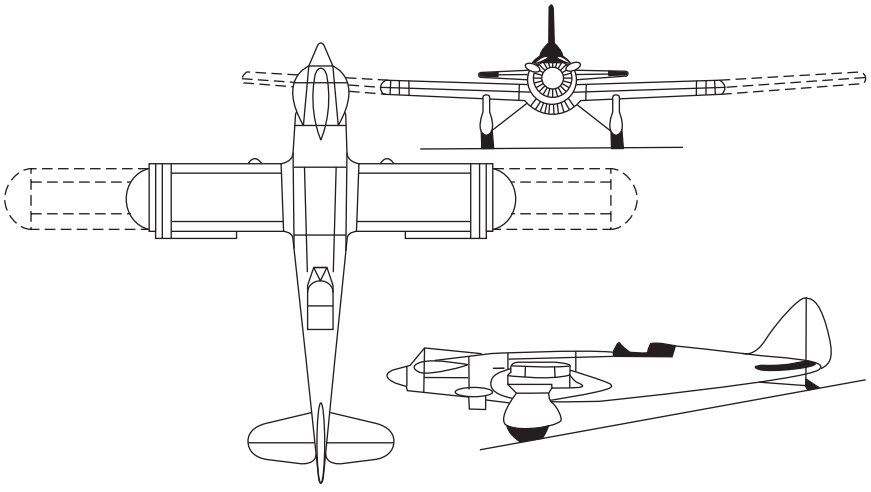

Figure 13.1 Makhonine MAK-10 variable-geometry (telescoping wing) aircraft [from Air International (1975)].

The variable-area concepts included the telescoping wing, an example of which is illustrated in Fig. 13.1, which shows the MAK-10, built in France to the design of an expatriate Russian, Ivan Makhonine. The wing outer panel telescoped into the inner panel to reduce span and wing area for high-speed flight and could be extended for economic cruise and landing.

Trailing-edge flaps, such as the Fowler flap, which extend beyond the normal wing-surface area when deployed, are modern examples of design features that increase the wing area for landing (aerodynamic data for these flaps are discussed in the section on multielement airfoils in Chapter 6 and later in this chapter). The increase in the effective wing area offered by typical multielement, high-lift configurations is illustrated in Fig. 13.2. The area increases available from using a plain (or aileron) type flap, a circular motion flap similar to that used on the Boeing 707, and the extended Fowler flap used on the Boeing 737 are compared in Fig. 13.3. The large increase in area for the 737-type flap is the sum of: (1) the aft motion of the entire flap, (2) the aft motion of the main flap from the fore flap, (3) the motion of the auxiliary (aft) flap, and (4) the movement of the leading-edge devices. Notice that the wing can increase in area by over 30% when all of the high-lift devices are fully deployed.

13.1.2 Increasing the Lift Coefficient

The progress in developing equivalent straight-wing, nonpropulsive high-lift systems is illustrated in Fig. 13.4. Note the relatively high values obtained by experimental aircraft such as the L-19 of Mississippi State University and the MA4 of Cambridge University. Both of these aircraft use distributed suction on the wing so that the flow stays attached and approximates that for inviscid flow.

A companion figure from the work of Cleveland (1970) has been included for the interested reader. The parasite drag coefficient, which includes interference drag but

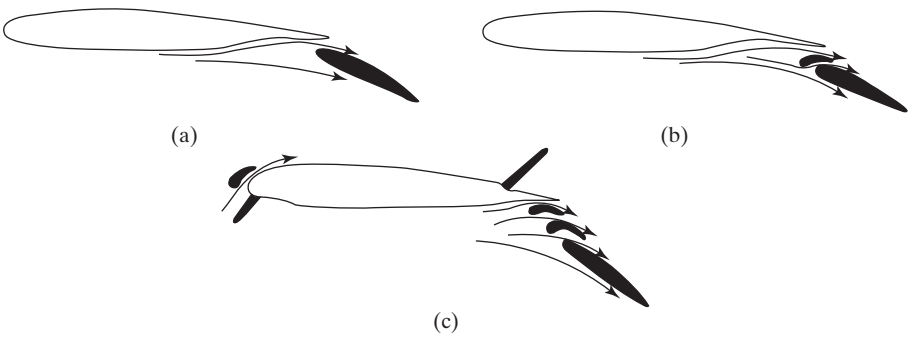

Figure 13.2 Multielement, high-lift configurations: (a) Fowler flap; (b) double-slotted flap; (c) leading-edge slat, Krueger leading-edge flap, spoiler, and triple-slotted flaps (representative of Boeing 727 wing section); (d) Fowler flaps on the HS 748 (courtesy of BAE Systems).

does not include induced or compressibility drag, is presented for several airplanes in Fig. 13.5.

The Chance-Vought F-8H Crusader offers an interesting design approach for obtaining a sufficiently high lift coefficient for low-speed flight while maintaining good visibility for the pilot during landing on the restricted space of an aircraft carrier deck. As shown in Fig. 13.6, the entire wing could be pivoted about its rear spar to increase its incidence by 7° during takeoff and landing. Therefore, while the wing is at a relatively high incidence angle, the fuselage is nearly horizontal and the pilot has excellent visibility over the nose of the aircraft. Furthermore, when the wing is raised, the protruding center section also serves as a large speed brake.

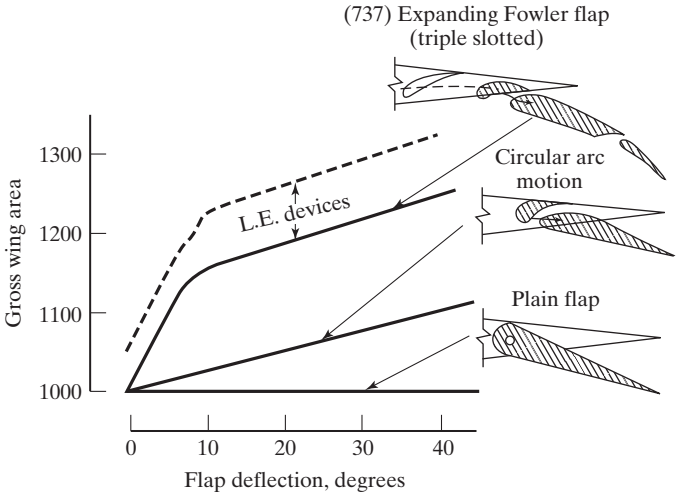

Figure 13.3 Use of flaps to increase the wing area [from Olason and Norton (1966)].

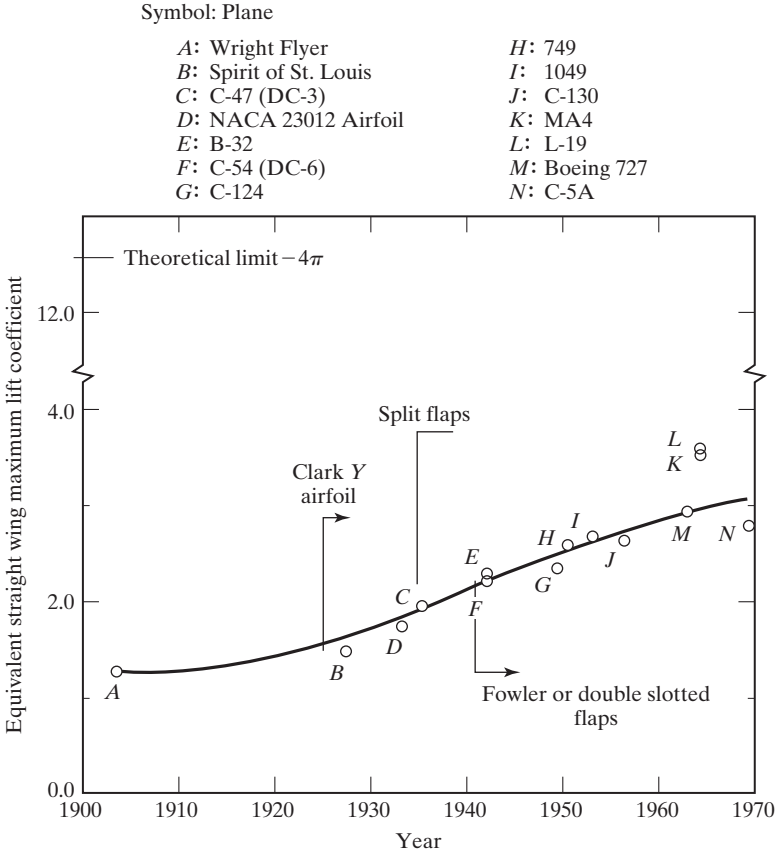

Figure 13.4 History of nonaugmented maximum lift coefficient [from Cleveland (1970)].

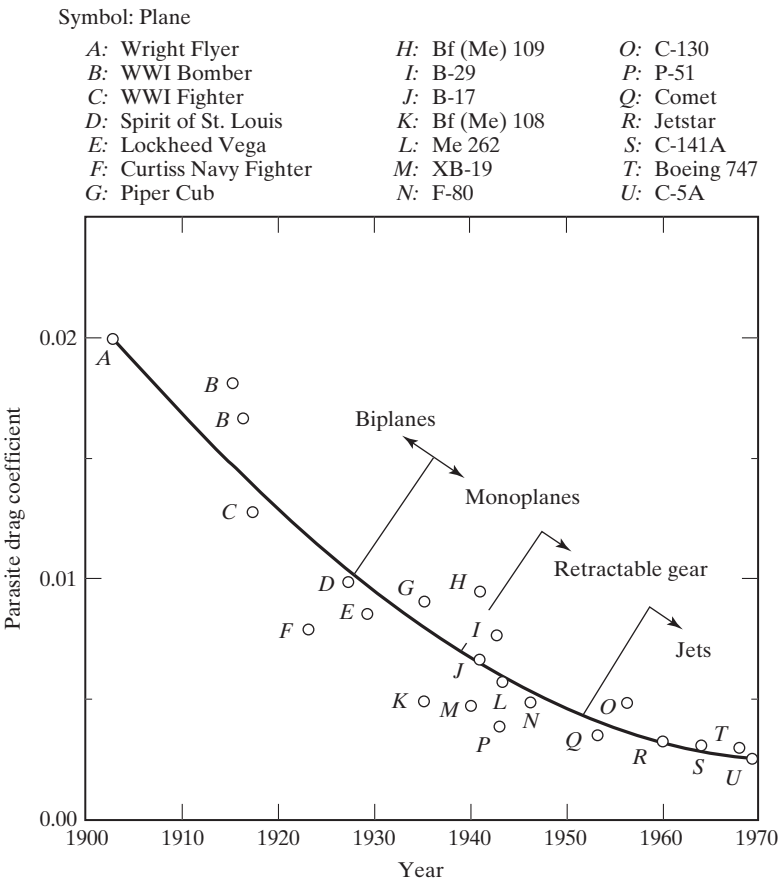

Figure 13.5 History of parasite drag coefficient, where the drag coefficient is based on total surface area [from Cleveland (1970)].

13.1.3 Flap Systems

Olason and Norton (1966) note that "if a clean flaps-up wing did not stall, a flap system would not be needed, except perhaps to reduce nose-up attitude (more correctly, angle of attack) in low-speed flight." So, a basic goal of the flap system design is to attain the highest possible L/D ratio at the highest possible lift coefficient, as illustrated in Fig. 13.7. A flap system can do this by: (1) increasing the effective wing area, (2) increasing the camber of the airfoil section (thereby increasing the lift produced at a given angle of attack), (3) providing leading-edge camber to help prevent leading-edge stall, and (4) including slots which affect the boundary layer and its separation characteristics.

Significant increases in the lift coefficient (and in the drag coefficient) can be obtained by increasing the camber of the airfoil section. The effect of deploying a split flap, which is essentially a plate deflected from the lower surface of the airfoil, is illustrated

Figure 13.6 Chance-Vought F-8H Crusader showing incidence for the wing during landing (U.S. Navy photo by PH2. P. Staley)

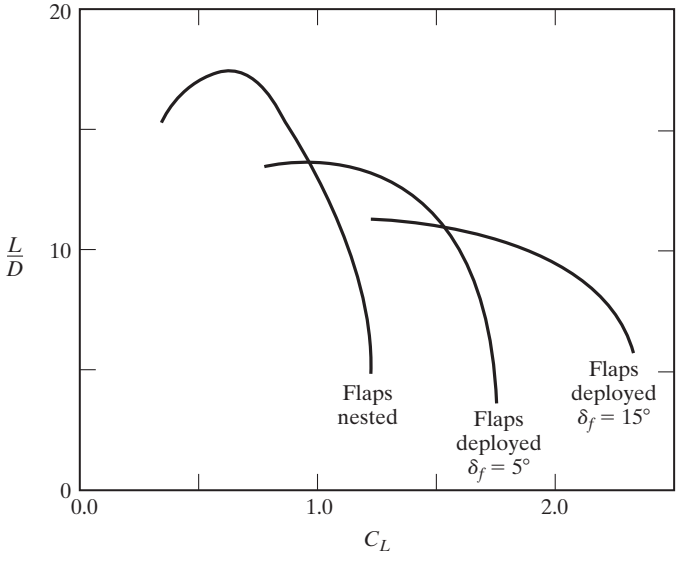

Figure 13.7 Effect of flap deployment on the aerodynamic forces.

in the pressure distributions of Fig. 13.8. Deployment of the split flap not only causes an increase in the pressure acting on the lower surface upstream of the flap but also causes a pressure reduction on the upper surface of the airfoil. Therefore, the deployment of the split flap produces a marked increase in the circulation around the section and, therefore, increases the lift. The relatively low pressure in the separated region

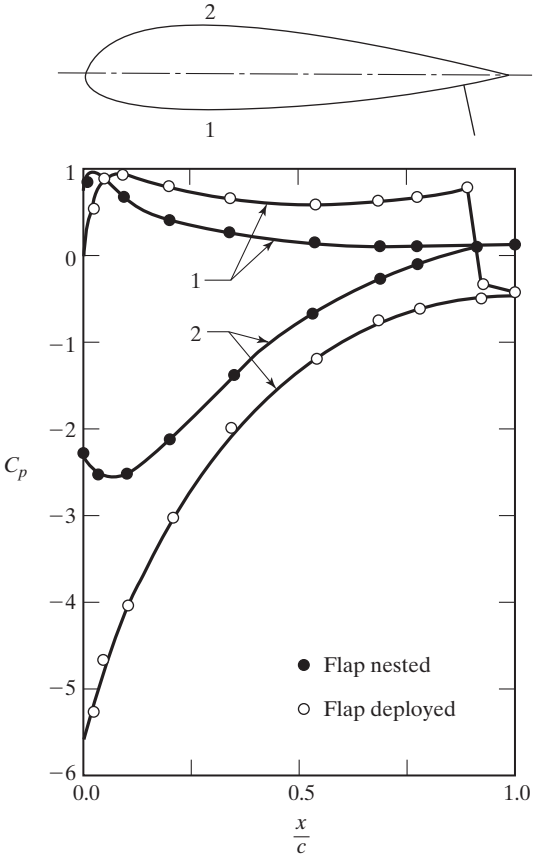

Figure 13.8 Pressure distribution for an airfoil with a split flap [data from Schlichting and Truckenbrodt (1969)].

in the wake downstream of the deployed plate causes the drag to be relatively high. The effect is so pronounced that it affects the pressure at the trailing edge of the upper surface (as shown in Fig. 13.8). The relatively high drag may not be a disadvantage if the application requires relatively steep landing approaches over obstacles or higher power from the engine during approach in order to minimize engine acceleration time in the event of a wave-off. The effect of the flap deflection angle on the lift coefficient for a split flap is presented in Fig. 13.9. Data are presented both for a plain flap and for a split flap; both flaps were $0.2c$ in length. The split flap produces a slightly greater increase in $C_{l,\max}$ than does the plain flap.

Simple hinge systems such as on a plain flap, even though sealed, can have significant adverse effects on the separation point and the lift and drag of the wing. The adverse effect of the break at the hinge line is indicated in data presented in Stevens et al. (1971). Pressure distributions are compared in this reference for a plain flap, which is $0.25c$ in length and is deflected 25°, and for a variable camber flap whose centerline is a circular arc having a final slope of 25°. Although separation occurs for both flaps, it occurs nearer

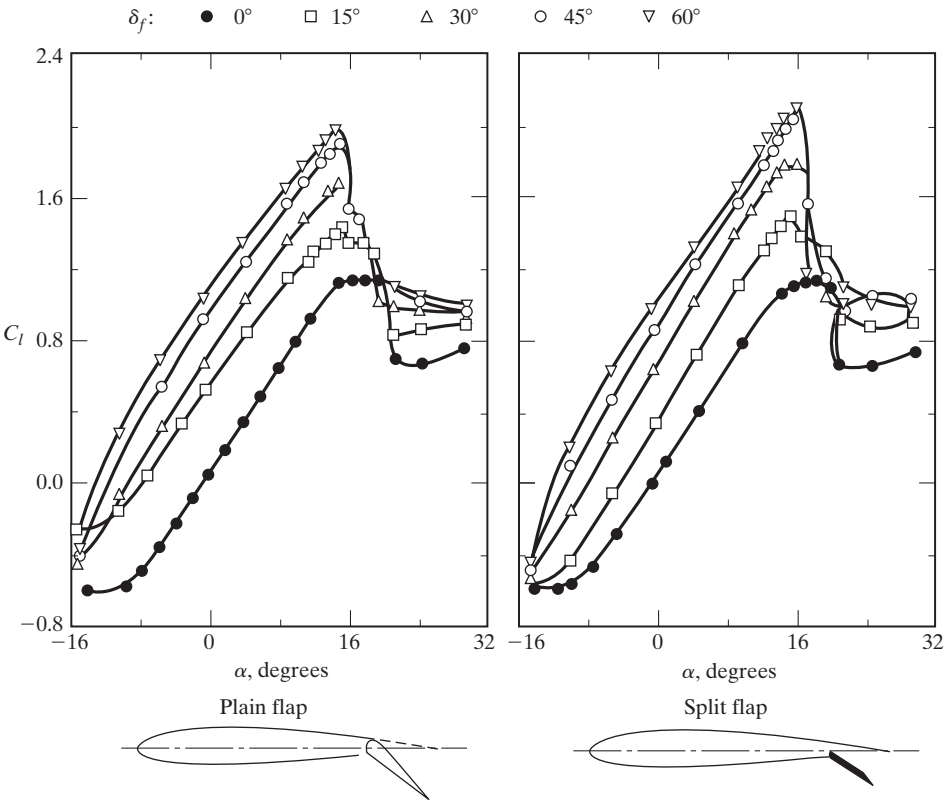

Figure 13.9 Effect of flap angle on the sectional lift coefficient for a NACA 23012 airfoil section, $\mathrm{Re}_c = 6 \times 10^5$ [data from Schlichting and Truckenbrodt (1969)].

the trailing edge for the variable camber shape, which, "turns out to be better only because of its drastic reduction in the suction peak" [the quotes are from Stevens et al. (1971)].

13.1.4 Multi-element Airfoils

As we discussed in Chapter 6, the location of separation has a significant effect on the lift, drag, and moment acting on an airfoil section. It has long been recognized that gaps between the main section and the leading edge of the flap (called slotted flaps) can cause a significant increase in $C_{l_{\max}}$ over that for a split flap or a plain flap. Furthermore, the drag for the slotted flap configurations is reduced. Sketches of airfoil sections with leading-edge slats or with slotted flaps are presented in Fig. 13.2.

Smith (1975) notes that the air through the slot cannot really be called high-energy air, since all the air outside the boundary layer has the same total pressure. Smith states, "There appear to be five primary effects of gaps, and here we speak of properly designed aerodynamic slots.

- ***Slat effect.*** In the vicinity of the leading edge of a downstream element, the velocities due to circulation on a forward element (e.g., a slat) run counter to the velocities on the downstream element and so reduce pressure peaks on the downstream element.
- ***Circulation effect.*** In turn, the downstream element causes the trailing edge of the adjacent upstream element to be in a region of high velocity that is inclined to the mean line at the rear of the forward element. Such flow inclination induces considerably greater circulation on the forward element.
- ***Dumping effect.*** Because the trailing edge of a forward element is in a region of velocity appreciably higher than free stream, the boundary layer 'dumps' at a high velocity. The higher discharge velocity relieves the pressure rise impressed on the boundary layer, thus alleviating separation problems or permitting increased lift.
- ***Off-the-surface pressure recovery.*** The boundary layer from forward elements is dumped at velocities appreciably higher than free stream. The final deceleration to free-stream velocity is done in an efficient manner. The deceleration of the wake occurs out of contact with a wall. Such a method is more effective than the best possible deceleration in contact with a wall.
- ***Fresh-boundary-layer effect.*** Each new element starts out with a fresh boundary layer at its leading edge. Thin boundary layers can withstand stronger adverse gradients than thick ones."

Since the viscous boundary layer is a dominant factor in determining the aerodynamic performance of a high-lift multi-element airfoil, inviscid theory is not sufficient for overall design requirements. Typical theoretical methods iteratively couple potential-flow solutions with boundary-layer solutions, and eventually the use of Navier-Stokes solutions. The potential-flow methods used to determine the velocity at specified locations on the surface of the airfoil usually employ singularity-distribution methods. As discussed in Chapters 3 and 6, singularity-distribution methods, which have been widely used since the advent of computers large enough to solve the large systems of simultaneous equations, can handle arbitrarily shaped airfoils at "any" orientation relative to the free stream (the word "any" is in quotes since there are limits to the validity of the numerical simulation of the actual flow). For singularity-distribution methods, either source, sink, or vortex singularities are distributed on the surface of the airfoil and integral equations formulated to determine the resultant velocity induced at a point by the singularities. The airfoil surface is divided into N segments with the boundary condition that the inviscid flow is tangent to the surface at the control point of each and every segment. The integral equations can be approximated by a corresponding system of $N - 1$ simultaneous equations. By satisfying the Kutta condition at the trailing edge of the airfoil, the Nth equation can be formulated and then the singularity strengths determined with a matrix-inversion technique. As noted previously, the Kutta condition which is usually employed is that the velocities at the upper and lower surface trailing edge be tangent to the surface and equal in magnitude. The various investigators use diverse combinations of integral and finite-difference techniques to generate solutions to the laminar, the transitional, and the turbulent boundary layers. You should read the discussion in Chapter 6 for more details, or to one of the numerous analyses of

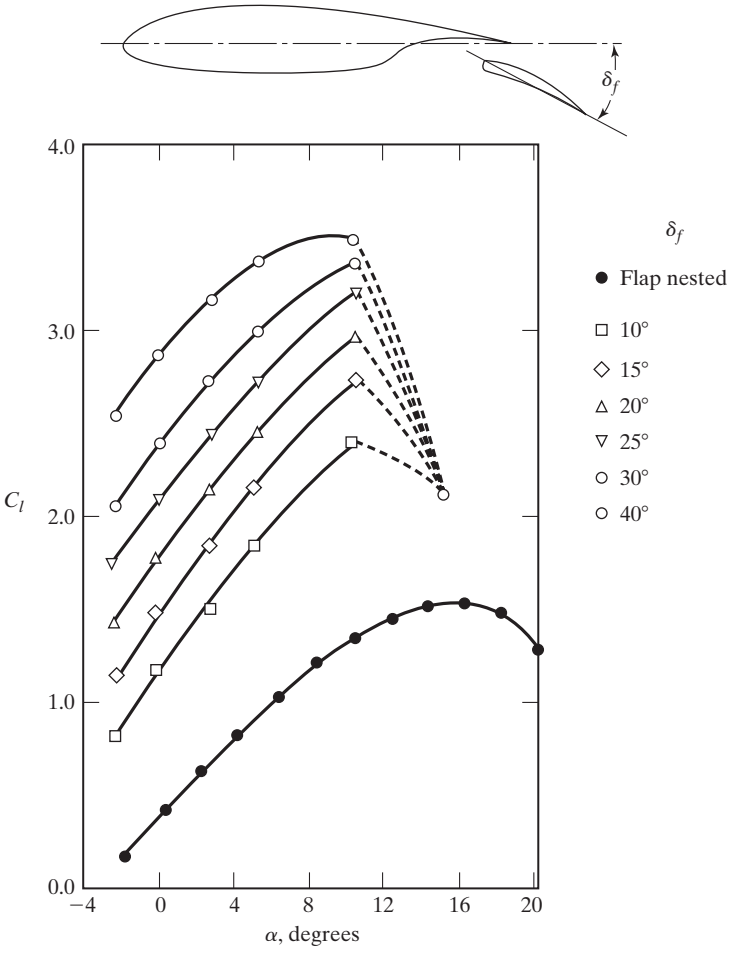

Figure 13.10 Experimental lift coefficient for a GA(W)-1 airfoil with a slotted Fowler flap [from Wentz and Seetharam (1974)].

multi-element airfoil problems [e.g., Stevens et al. (1971), Morgan (1975), Olsen and Dvorak (1976), and Air International (1993)].

The lift coefficients for a GA(W)-1 airfoil with a Fowler-type, single-slotted flap which are taken from Wentz and Seetharam (1974) are presented as a function of angle of attack in Fig. 13.10. Notice the large increases in $C_{l,\max}$ which are obtained with the slotted Fowler flap. As shown in the sketch of the airfoil section, the deflected flap segment is moved aft along a set of tracks that increases the chord and the effective wing area. Therefore, the Fowler flap is characterized by large increases in $C_{l,\max}$ with minimum changes in drag. The ability of numerical techniques to predict the pressure distribution is illustrated in Fig. 13.11. Data are presented for the GA(W)-1 airfoil at an angle of attack of 5°, with a flap deflection of 30°.

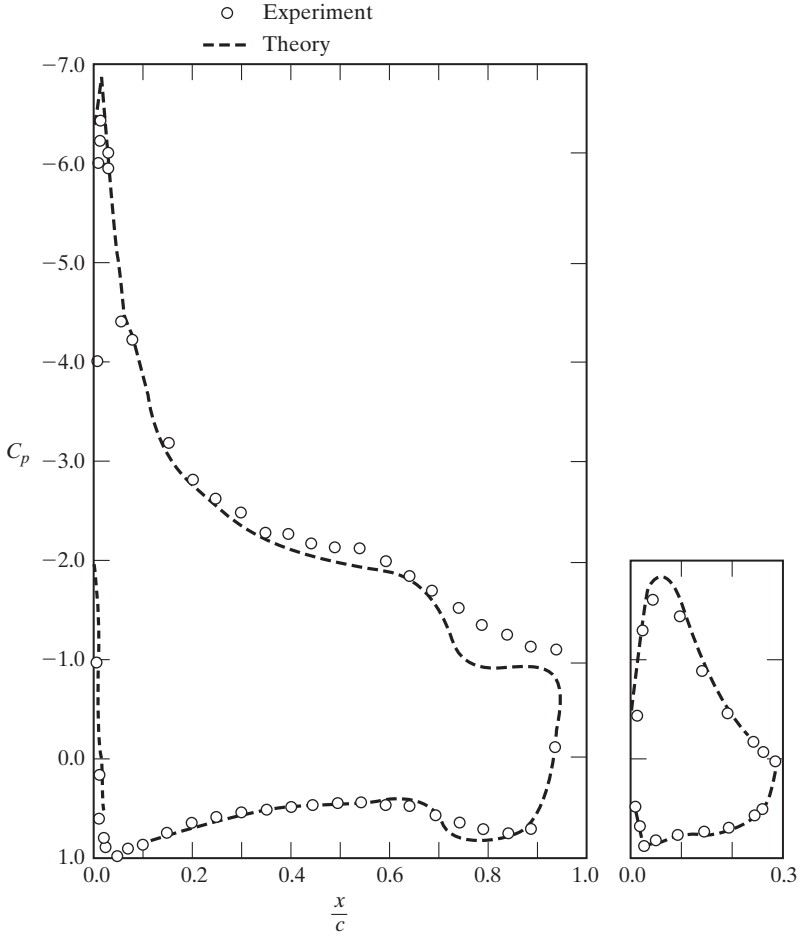

Figure 13.11 Comparison of the theoretical and the experimental pressure distribution for a GA(W)-1 airfoil with a slotted flap, $\alpha = 5°, \delta_f = 30°$ [from Wentz and Seetharam (1974)].

In this section, we have seen how the use of mechanical changes in camber can be used to increase the lift generated by airfoils and wings, independent of the change in angle of attack. Typically, you could expect maximum values of C_L of 2.5 to 3.5 using mechanical systems on wings of commercial and military transports. In addition to the obvious mechanical complexity (e.g., tracks, brackets, and actuators) and weight, mechanical systems are limited aerodynamically in the maximum lift they can generate. One limitation, the Kutta condition, essentially fixes airfoil circulation (and the lift) to the value where the free-system flow leaves the airfoil at the trailing edge. A second limitation, viscous effects, usually reduces the attainable lift to less than that value, because the flow separates from the highly curved flap upper surface before the trailing edge is reached. Slotted flaps, of course, reduce the effects of separation. Nevertheless,

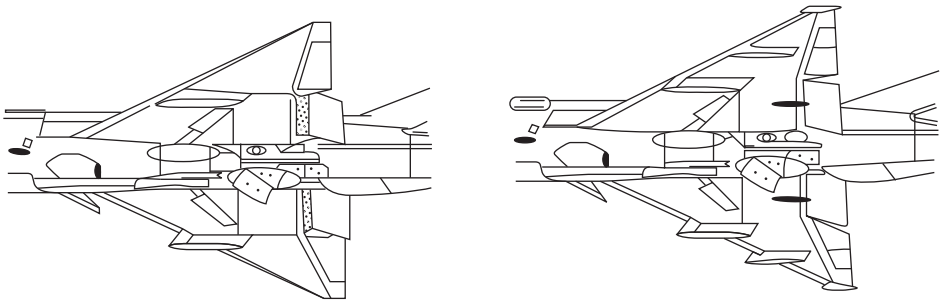

(a) (b)

Figure 13.12 Fowler-type flaps used on early series MiG 21s and the blown flaps used on later series: (a) Fowler-type flaps employed on the MiG-21 PF; (b) blown flaps employed on the MiG-21 MF [from Air International (1974)].

concepts employing jet-engine bleed gases are often used to generate increased lift, as we saw for the C-17 in Chapter 5.

13.1.5 Power-Augmented Lift

An additional factor to consider in the comparison of flap types is the aerodynamic moment created by deployment of the flap. Positive camber produces a nose-down pitch moment, which is especially large when applied well aft on the chord, and produces twisting loads on the structure. The pitch moments must be controlled with the horizontal tail, which produced trim drag. Unfortunately, the flap types which produce the greatest increase in $C_{l,\max}$ usually produce the largest moments. Therefore, as shown in the sketches of the MiG 21s presented in Fig. 13.12, the Fowler flap with its extended guides and fairing plates is replaced by blown flaps for some applications. Separation from the surface of the flap is delayed by discharging fluid from the interior of the main airfoil section. The fluid injected tangentially to the surface imparts additional energy to the fluid particles in the boundary layer so that the boundary layer remains attached due to the Coanda effect (the tendency of a fluid to remain attached to a solid surface).

The internally blown flap is compared with two other techniques which use engine power to achieve very high lift in Fig. 13.13. The corresponding drag polars [as taken from Goodmanson and Gratzer (1973)] are included. The externally blown flap (EBF) spreads and turns the jet exhaust directed at the trailing-edge flap. A portion of the flow emerging through the flap slots maintains attachment of the boundary layer over the flap's upper surface. The upper-surface-blowing (USB) concept resembles the externally blown flaps. However, the data indicate "better performance than the externally blown flap if the air-turning process is executed properly. Also, the path of the engine exhaust permits a certain amount of acoustic shielding by the wing, and consequently a significant reduction in noise." The quote is from Goodmanson and Gratzer (1973) from The Boeing Company, which designed the YC-14 AMST (Advanced Medium STOL Transport) which is an aircraft that employed USB.

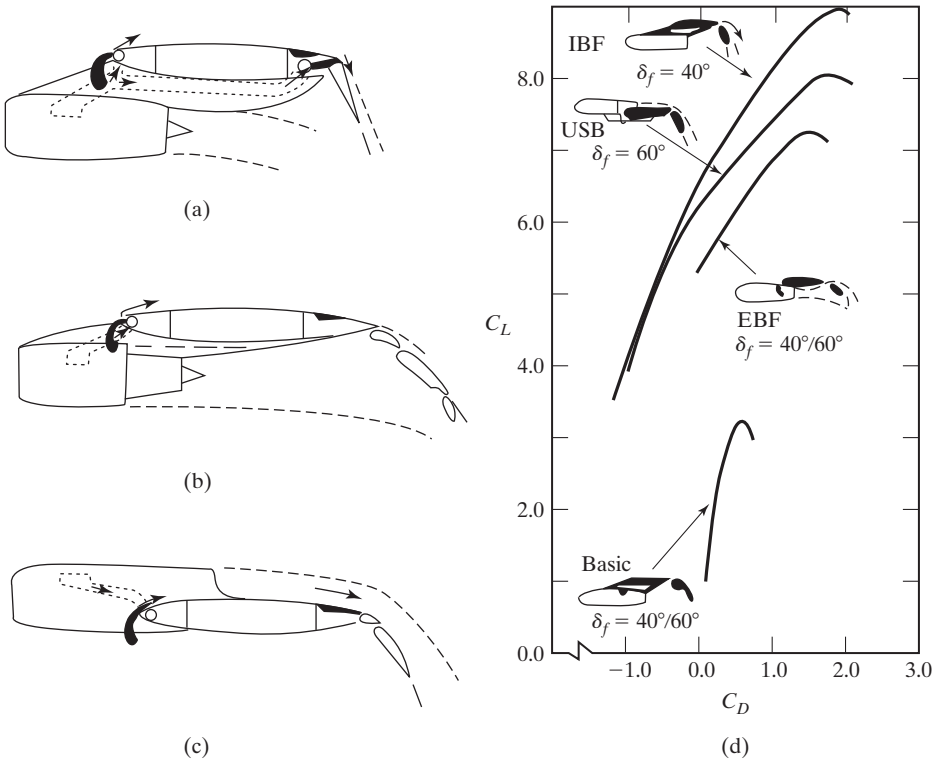

Figure 13.13 Power-augmented high-lift configurations: (a) internally blown flap (IBF); (b) externally blown flap (EBF); (c) upper-surface blowing (USB); (d) drag polars for four-engine configuration. $cj = 2.0$ for blown configuration [from Goodmanson and Gratzer (1973)].

Using suction to remove the decelerated fluid particles from the boundary layer before they separate from the surface in the presence of the adverse pressure gradient is another means of increasing the maximum lift. The "new" boundary layer which is formed downstream of the suction slot can overcome a relatively large adverse pressure gradient without separating. Flight data obtained in the late 1930s at the Aerodynamische Versuchsanstalt at Göttingen are reproduced in Fig. 13.14. The data demonstrate that the application of suction through a slit between the wing and the flap can prevent separation. Since the flaps can operate at relatively large deflection angles, and the airfoil can operate at relatively high angles of attack without separation, large increases in lift can be obtained. The maximum lift coefficients for the airplanes equipped with suction are almost twice that for the Fieseler Storch (Fi 156), a famous short takeoff and landing (STOL) airplane of the World War II period, which is shown in Fig. 13.15. The entire trailing edge of the Storch wing was hinged; the outer portions acting as statically balanced and slotted ailerons, and the inner portions as slotted camber-changing flaps. A fixed slot occupied the entire leading edge. Initial flight tests showed the speed range of the Fieseler Storch

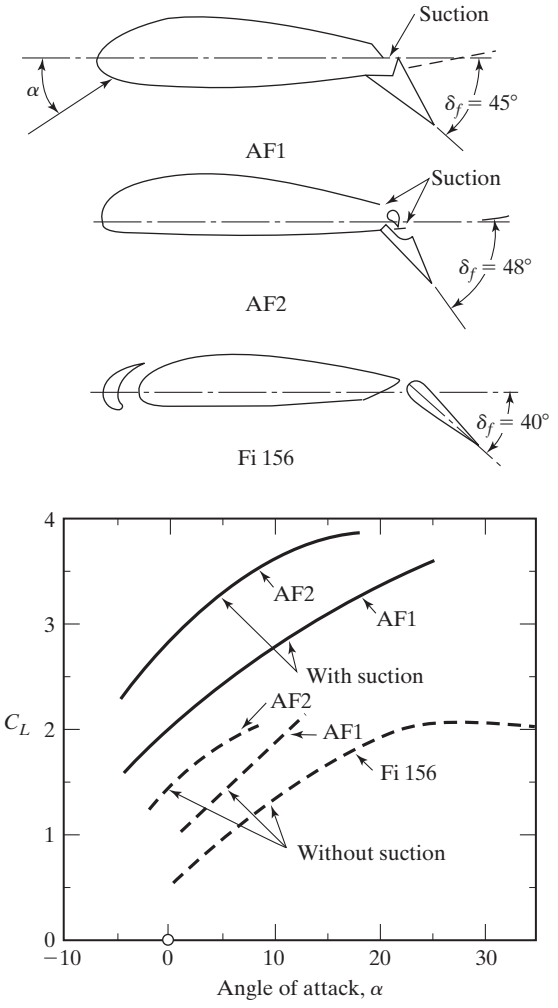

Figure 13.14 Lift of three STOL airplanes for full landing flap deflection (power off). AF1 and AF2 are boundary layer control airplanes of the Aerodynamische Versuchsanstalt. Fi 156 is the Fieseler Storch [data from Schlichting (1960)].

to be 51 to 174 km/h (32 to 108 mi/h) and that the landing run in a 13 km/h (8 mi/h) wind using brakes is 16 m. You should refer to Green (1970) for more details.

13.2 CIRCULATION CONTROL WING

As discussed by Englar (1987), the circulation control wing (CCW) concept avoids the problems of mechanical and blown flaps by replacing the sharp trailing edge with a fixed nondeflecting, round or near-round surface, such as shown in Fig. 13.16. The tangential blowing jet remains attached to the curved surface by creating a balance between the

Figure 13.15 Fieseler Storch, Fi 156, showing fixed leading-edge slots and hinged trailing edge (courtesy of David Schultz Photography).

subambient pressure and the centrifugal force, known as the Coanda effect. Therefore, as shown in Fig. 13.16, at low values for the blowing momentum coefficient, it serves as a boundary-layer control (BLC) device to entrain the flow field and prevent it from separating. Once the flow is returned to the inviscid condition, the jet continues to turn around the trailing edge. The jet entrains and deflects the flow field, providing

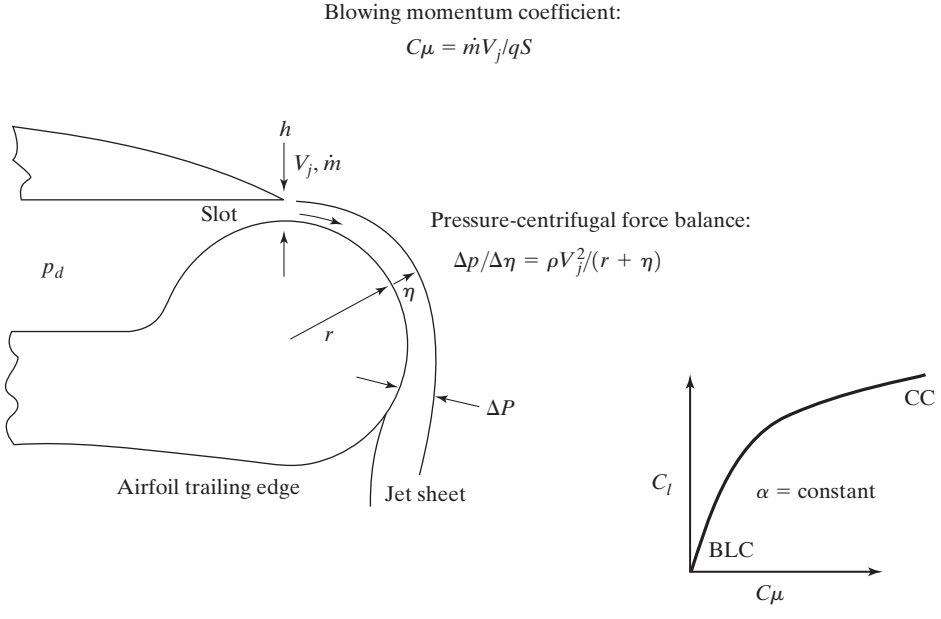

Figure 13.16 Basic principles of circulation control aerodynamics [from Englar (1987)].

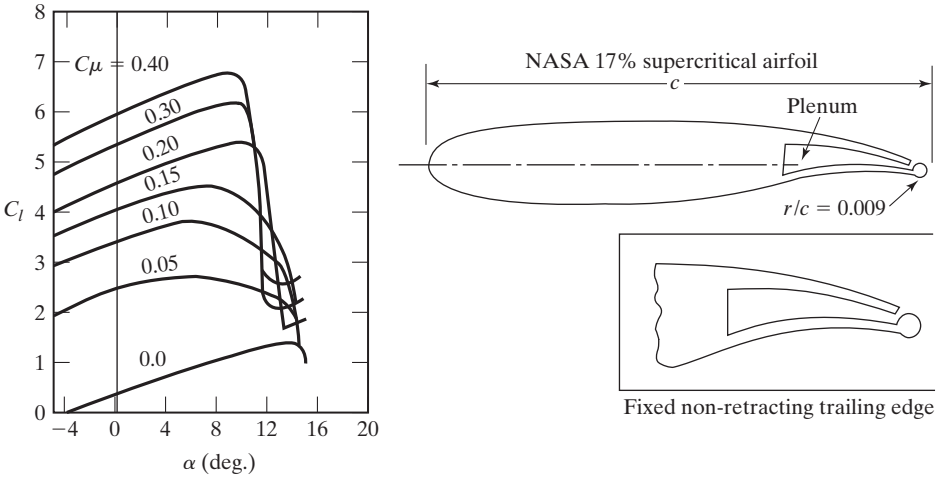

Figure 13.17 Sectional lift characteristics for a 17% thick CCW/supercritical airfoil [from Englar (1987)].

pneumatic deflection of the streamlines (equivalent to camber) and resulting in supercirculation lift. In the circulation control region (CC), very high lift can be generated since the jet turning is not limited by a sharp trailing edge. As shown in Fig. 13.17, relatively high lift coefficients can be generated for two-dimensional CCW airfoils with much less blowing than that typical of mechanical blown flaps.

13.3 DESIGN CONSIDERATIONS FOR TACTICAL MILITARY AIRCRAFT*

As noted by Bradley (1981), the designer of a tactical military aircraft is faced with a multitude of design points throughout the subsonic/supersonic flow regimes plus many off-design constraints. The design goals for a tactical weapons system may include efficient cruise at both subsonic and supersonic Mach numbers, superior maneuverability at both subsonic and supersonic Mach numbers, and rapid acceleration.

Bradley (1981), referring to the results shown in Figs. 13.18 and 13.19, states, "The multiple design point requirement turns out to be the major driver for the designer of fighter aircraft. The aerodynamic requirements for each of the design points often present conflicting requirements. For example, the need for rapid acceleration to supersonic flight and efficient supersonic cruise calls for thin wing sections with relatively high sweep and with camber that is designed to trim out the moments resulting from aft ac movement at supersonic flight. However, these requirements are contrary to those requirements for efficient transonic maneuver, where the designer would prefer to have thicker wing sections designed with camber for high C_L operation and a high-aspect-ratio planform to provide a good transonic drag polar. Designers are thus faced with a situation of compromise. These conflicting requirements suggest

*Quotations and data presented in this section are reproduced by permission from General Dynamics Corporation.

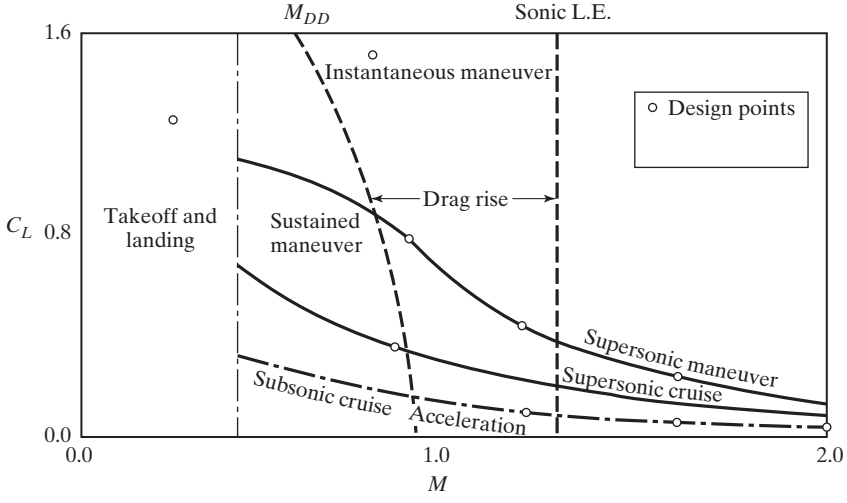

Figure 13.18 Typical performance map for fighters [from Bradley (1981)].

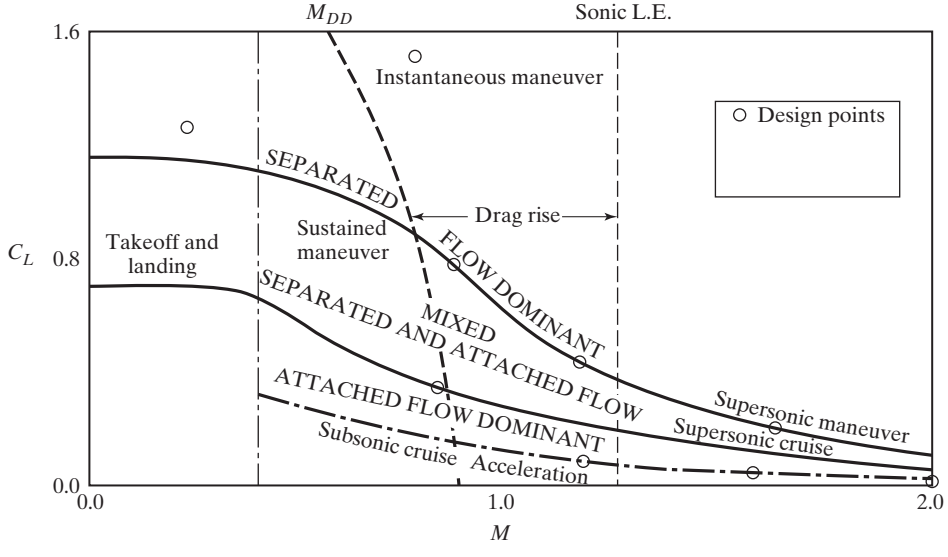

Figure 13.19 General flow regimes encountered for fighters [from Bradley (1981)].

the obvious solution of variable geometry, that is, variable sweep wing and/or variable camber. Although this is a satisfactory aerodynamic solution, in many cases the resultant weight increases to a configuration can be prohibitive."

Bradley (1981) shows typical performance results corresponding to requirements for a specific mission in Fig. 13.18: "The low Mach end of the spectrum throughout the C_L range is typical of takeoff and landing for the configuration. The subsonic cruise and supersonic cruise portions are noted in the moderate lift range. Acceleration to high

supersonic speeds occurs at the low lift coefficients. Sustained maneuver takes place in the C_L range of less than one for most fighter configurations. Above this lift coefficient, the aircraft is in the instantaneous maneuver regime. Drag rise occurs, depending on the wing geometry, in the range of 0.8 to 1.2 Mach."

Referring to Fig. 13.19, Bradley (1981) states, "At the cruise and acceleration points, the aircraft designer is dealing primarily with attached flow, and his design objective is to maintain attached flow for maximum efficiency. At the higher C_L's, corresponding to instantaneous maneuver, separated flow becomes the dominant feature. Current designs take advantage of the separated flow by forming vortex flows in this range. Intermediate C_L's, corresponding to sustained maneuver are usually a mixture of separated and attached flow. Consequently, if the aircraft is designed with camber to minimize separation in the maneuver regime, the configuration will have camber drag and may have lower surface separation, which increases drag at the low C_L's, needed for acceleration."

"Thus, the aircraft design is a compromise to achieve an optimal flow efficiency considering the numerous design points associated with the mission objectives. It is easily seen that the transonic flow problems that must be addressed in fighter design are driven to a very large extent by the constraints imposed at the other design points—supersonic and subsonic."

Bradley (1981) notes that "supersonic design enjoys relatively precise computation and optimization thanks to wide applicability of linearized theory." Furthermore, Bradley states that "the design of efficient transonic configurations may proceed from two conceptual schools of logic. One acknowledges that the optimum low-drag flow must accelerate rapidly over the airfoil to supercritical flow and decelerate in a nearly isentropic manner, avoiding strong shocks and/or steep gradients that can lead to significant regions of separation. This approach sets attached flow or near fully attached flow as an intuitive design goal and is typically used for aircraft that permit strong emphasis to be placed on transonic cruise or sustained maneuver design points." The design of airfoils for transonic cruise applications was discussed extensively in Chapter 9.

Bradley (1981) continues, "The second school of thought recognizes the inevitability of significant flow separations at design conditions and adopts a philosophy of controlling certain regions of separation through vortex flows to complement other regions of attached supercritical flow. This approach is appropriate for configurations constrained by multiple design points that emphasize added supersonic requirements. Current tactical fighters that rely on high wing loadings for transonic performance are good examples. The F-16 and F-18 employ a combination of controlled vortex flow and variable camber to achieve maneuverability."

Even though a designer has worked carefully to design a wing for attached flow, the flow fields associated with sustained and instantaneous maneuvers involve predominantly separated flows. The manner in which the flow separates and how the separation develops over the configuration will strongly affect the vehicle's drag and its controllability at the higher C_L's. Aircraft, such as the F-16 and the F-18, employ strakes or leading-edge extension devices to provide a controlled separated flow. Controlled vortex flow can then be integrated with variable camber devices on the wing surface to provide satisfactory high-lift, stability and control, and buffet characteristics. The resulting flow field is a complex one, combining attached flows over portions of the wing with the vortex flow from the strake.

Figure 13.20 Strake vortex system on an F-16 (U.S. Air Force photo by Josh Plueger).

The F-16 forebody strake vortex system is clearly visible as it interacts with the wing flow field in Fig. 13.20. Forebody strakes and canards have similar aerodynamic effects—both good and bad. For example, the F-16 forebody strake design required extensive integration with the wing variable leading edge flap system and empennage to achieve significant aerodynamic improvements. The aerodynamic improvements achieved with the forebody strake/variable leading edge flap combination are illustrated in Fig. 13.21 for the YF-16 aircraft. The dashed curve depicts the lift curve and

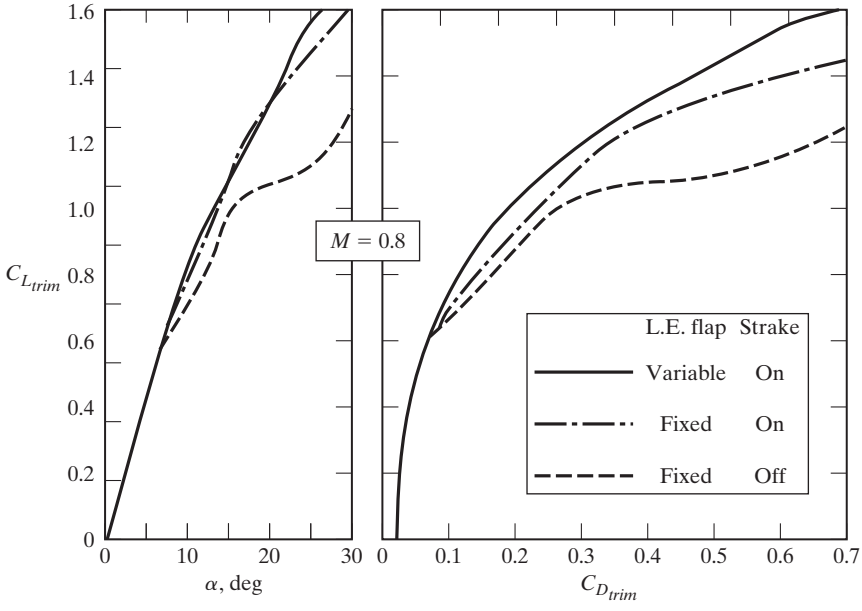

Figure 13.21 Aerodynamic benefits of combined forebody-strake/variable-camber system [from Bradley (1981)].

drag polar for the wing without the strake and variable leading edge flaps. The strake with no leading-edge flap significantly improves the static aerodynamic characteristics. Further improvement is seen with the variable leading-edge flap in combination with the strake configuration.

Bradley (1981) states: "We should not pass from the separated flow wing design discussion without mentioning a new concept of controlled vortex flow for designing military aircraft having emphasis on supersonic configurations. Wing planforms for supersonic cruise have higher leading edge sweep and generally lower aspect ratios; these planforms develop vortex flows at relatively low angle of attack. As a result, the transonic drag characteristics are lacking in the maneuver regime since drag polars generally reflect very little leading edge suction recovery. Recently, wings of this type have been designed to take advantage of the separated vortex flows rather than to try to maintain attached flow to higher C_L values."

13.4 DRAG REDUCTION

Possible fuel shortages combined with sharp price increases and the requirements of high performance over a wide-speed range emphasize the need for reducing the drag on a vehicle and, therefore, improving the aerodynamic efficiency. In fact, almost all aircraft development programs require drag reduction efforts at some point during the life of the program. Of the various possible drag reduction concepts, we will discuss:

- Variable-twist, variable-camber wings
- Laminar-flow control (LFC)
- Wingtip devices
- Wing planform

13.4.1 Variable-Twist, Variable-Camber Wings

Survivability and mission effectiveness of a supersonic-cruise military aircraft requires relatively high lift/drag ratios while retaining adequate maneuverability. The performance of a moderate-aspect-ratio, thin swept wing is significantly degraded at high lift coefficients at high subsonic Mach numbers because of shock-induced boundary-layer separation and, at higher angles of attack, because of leading-edge separation and wing stall. The resulting degradation in handling qualities significantly reduces the combat effectiveness of such airplanes. There are several techniques to counter leading-edge stall, including leading-edge flaps, slats, and boundary-layer control by suction or by blowing. These techniques, along with trailing-edge flaps, have been used effectively to increase the maximum usable lift coefficient for low-speed landing and for higher subsonic speeds.

Low-thickness-ratio wings incorporating variable camber and twist appear to offer higher performance for fighters with a fixed-wing planform [Meyer and Fields (1978)], since the camber can be reduced or reflexed for the supersonic mission and increased to provide the high lift coefficients required for transonic and subsonic maneuverability.

A test program was conducted to determine the effect of variable-twist, variable-camber on the aerodynamic characteristics of a low-thickness-ratio wing [Ferris (1977)].

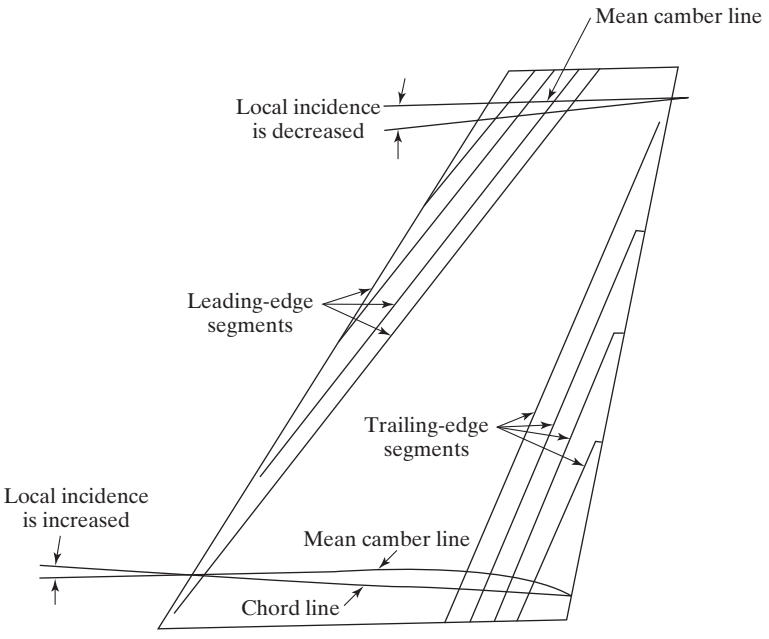

Figure 13.22 Use of leading-edge segments and trailing-edge segments to produce camber and twist on a basic planar wing.

The basic wing was planar with a NACA 65A005 airfoil at the root and a NACA 65A004 airfoil at the tip (i.e., there was no camber and no twist). Section camber was varied using four leading-edge segments and four trailing-edge segments, all with spanwise hinge lines. Variable twist was achieved since the leading-edge (or trailing-edge) segments were parallel and were swept more than the leading edge (or trailing edge). Camber and twist could be applied to the wing as shown in Fig. 13.22. Deploying the trailing-edge segments near the root creates a cambered section whose effective chord is at an increased incidence. Similarly, deploying the leading-edge segments near the wing tip creates a cambered section whose local incidence is decreased. Therefore, the modified wing could have an effective twist of approximately 8° washout. As noted in Ferris (1977), use of leading-edge camber lowers the drag substantially for lift coefficients up to 0.4. Furthermore, use of leading-edge camber significantly increases the maximum lift/drag ratio over a Mach number range of 0.6 to 0.9. At the higher lift coefficients (≥ 0.5), the combination of twist and camber achieved using both leading-edge segments and trailing-edge segments was effective in reducing the drag. Trailing-edge camber causes very large increments in C_L with substantial negative shifts in the pitch moment coefficients.

Aerodynamics Concept Box: Active Aeroelastic Wing

The Active Aeroelastic Wing project at NASA Dryden Flight Research Center was a two-phase flight research program that investigated the potential of aerodynamically twisting flexible wings to improve roll maneuverability of high-performance aircraft at transonic and

supersonic speeds. Traditional control surfaces such as ailerons and leading-edge flaps are used as active trim tabs to aerodynamically induce the twist. From flight test and simulation data, the program developed structural modeling techniques and tools to help design lighter, more flexible high aspect-ratio wings for future high-performance aircraft, which could translate to more economical operation or greater payload capability.

The program used a modified F/A-18A Hornet as its testbed aircraft, with wings that had similar flexibility compared with the original pre-production F-18 wing. Other aircraft modifications included a new actuator to operate the outboard portion of a divided leading edge flap over a greater range and rate, and a research flight control system to host the aeroelastic wing control laws.

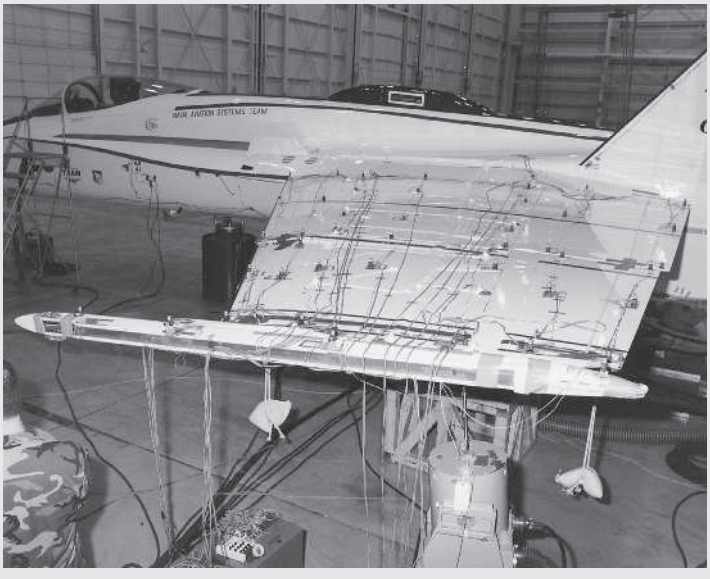

NASA F-18 Active Aeroelastic Wing ground testing
(photo courtesy of NASA Dryden Flight Research Center)

The upper wing surfaces of the Active Aeroelastic Wing F/A-18 test aircraft were covered with accelerometers and other sensors during ground vibration tests. An electro-mechanical shaker device (cylinder at the lower right of the picture) generated vibrations into the airframe during the tests, which helped engineers determine if aerodynamically induced vibrations were controlled or suppressed during flight. The tests were the last major ground tests prior to the initiation of research flights.

Information from NASA Dryden Flight Research Center fact sheet for the AAW program.

The effectiveness of leading-edge segments and trailing-edge segments in increasing the lift coefficient and in reducing the drag coefficient at these relatively high lift coefficients is illustrated in the data presented in Fig. 13.23. As a result, the maximum lift/drag ratio for this particular configuration at $M_\infty = 0.80$ is 18, and it occurs when $C_L = 0.4$.

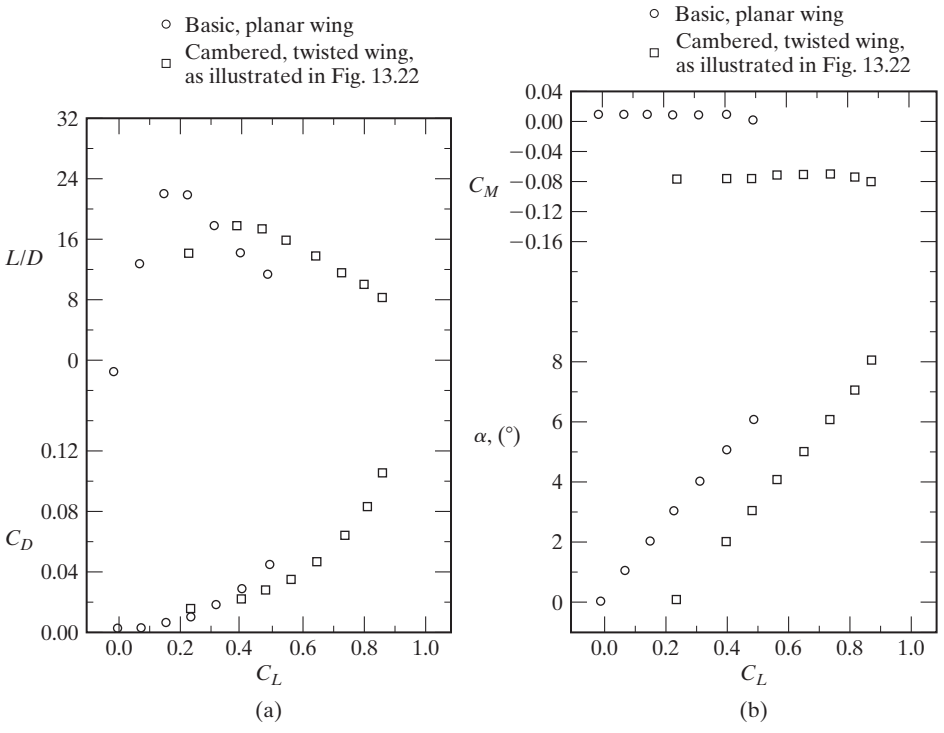

Figure 13.23 Effect of twist and camber on the longitudinal aerodynamic characteristics $M_\infty = 0.80, \mathrm{Re}_c = 7.4 \times 10^6$: (a) lift-to-drag ratio and the drag polar; (b) pitch moment and lift coefficients [from Ferris (1977)].

13.4.2 Laminar-Flow Control

In previous chapters, we have seen that the skin-friction component of the drag is markedly higher when the boundary layer is turbulent. Therefore, in an effort to reduce skin friction, which is a major part of the airplane's "parasitic" drag, attempts have been made to maintain laminar flow over substantial portions of the aircraft's surface. Attempts at delaying transition by appropriately shaping the airfoil section geometry were discussed in Chapter 5. However, a natural boundary layer cannot withstand even very small disturbances at the higher Reynolds numbers, making transition difficult to avoid. Theoretical solutions reveal that removing the innermost part of the boundary layer using even very small amounts of suction substantially increases the stability of a laminar boundary layer. Maintaining a laminar profile by suction is termed *laminar-flow control* (LFC).

The aerodynamic analysis of a LFC surface is typically divided into three parts: (1) the prediction of the inviscid flow field, (2) the calculation of the natural development of the boundary layer, and (3) the suction system analysis. In this approach (which may in reality require an iterative procedure), the first step is to determine the pressure and the velocity distribution of the inviscid flow at the edge of the boundary layer. The second step is to calculate the three-dimensional boundary layer, including

both the velocity profiles and the integral thicknesses. It might be noted that because of cross flow, the boundary layer on a swept wing may be more unstable than that on an unswept wing. Finally, the suction required to stabilize the boundary layer must be calculated and the suction system designed.

In 1960, two WB-66 aircraft were adapted to a 30° swept wing with an aspect ratio of 7 and a thickness ratio of approximately 10%. The modified aircraft were designated X-21A. A suction system consisting of turbocompressor units removed boundary-layer air from the wing through many narrowly spaced LFC suction slots. With suction-inflow velocities varying from $0.0001U_\infty$ in regions of negligible pressure gradient to $0.0010U_\infty$ near the wing leading edge, full-chord laminar flows were obtained up to a maximum Reynolds number of 45.7×10^6 [Kosin (1965)]. It was concluded that laminar-flow control significantly reduced the wake drag on the wing.

Using the propulsion, structural, flight controls and system technologies predicted for 1985, Jobe et al. (1978) predicted fuel savings from 27% to 30% by applying LFC to the design of large subsonic military transports. Jobe et al. assumed that the LFC system used in their design would maintain a laminar boundary layer to $0.70c$, even though full-chord laminarization of a wing with trailing-edge controls is technically feasible. The optimum wing planform for the minimum-fuel airplane has the highest aspect ratio, the lowest thickness-chord ratio, and a quarter-chord sweep of about 12°. The cruise Mach number for this aircraft design is 0.78. As noted in Table 13.1, their sensitivity analysis showed that a high aspect ratio is the most important parameter for minimizing fuel consumption, wing thickness is of secondary importance, and sweep is relatively unimportant. However, since productivity varies linearly with the cruise speed, a maximum productivity airplane requires a relatively high sweep, a maximum aspect ratio, and a low thickness ratio for the section. The resultant aircraft cruises at a Mach number of 0.85. The sensitivity analysis of Jobe et al. (1978) indicates that a low thickness ratio is most important to the design of the wing for a maximum productivity airplane, followed by aspect ratio and sweep.

TABLE 13.1 Desirable Laminar-Flow Control Wing Planform Characteristics

	Wing Design Parameter		
Figure of Merit	*Aspect Ratio*	*Thickness Ratio*	*Sweep*
Performance			
Minimum fuel	High	Low	NMC[a]
Minimum takeoff gross weight	High	NMC	Low
Maximum $\frac{\text{maximum payload}}{\text{takeoff gross weight}}$	High	Low	NMC
Ease of laminarization			
Low chord Reynolds number	High	NMC	NMC
Low unit Reynolds number	NMC	NMC	NMC
Minimize cross flow	NMC	Low	Low
Minimize leading-edge contamination	High	Low	Low

[a]NMC, not a major consideration.
Source: Jobe et al. (1978).

Aerodynamics Concept Box: The F-16XL and Supersonic Laminar Flow Control

Two advanced fighter aircraft, designated the F-16XL, were designed by General Dynamics and flight tested at NASA Dryden Flight Research Center in the 1990s. The second aircraft was designed to test laminar flow control at supersonic speeds, and is shown below with the laminar flow "glove" on the port wing.

F-16XL with laminar flow glove on port wing
(photo courtesy of NASA Dryden Flight Research Center)

The research conducted involved a delta-winged F-16XL modified with a "glove" made of titanium. The glove contained more than 10 million holes and had a suction system attached to the lower surface which was composed of tubes, valves, and a compressor. During research flights, the suction systems pulled a small part of the boundary layer of air through the glove's porous surface to create laminar (or smooth) air flow. Researchers believe that laminar flow conditions can reduce aerodynamic drag (friction) and contribute to reduced operating costs by improving fuel consumption and lowering aircraft weight. The project flew the F-16XL-2 45 times between October 1995 and November 1996, obtaining significant amounts of valuable flight research data.

Information from NASA Dryden Flight Research Center fact sheet on the F-16XL program.

13.4.3 Wingtip Devices

As discussed in Chapter 7, one of the ways of decreasing the induced drag is by increasing the aspect ratio. Although increased wing span provides improved lift/drag ratios, the higher bending moments at the wing root create the need for a stronger wing structure. Furthermore, there are problems in maneuvering and parking once on the ground. As noted by Thomas (1985), using large-aspect-ratio wings will reduce the induced drag because the tip vortices will be further separated, reducing the strength of the average induced flow between them. However, as Thomas points out, as the aspect ratio is increased for the same chord, there is a weight penalty that may offset the drag reduction. So, as noted in Thomas (1985), "optimal wing aspect ratio for a transport aircraft varies from 7.5 for minimum acquisition cost, to 9.8 for minimum gross weight, to 12.0 for minimum direct operating cost, and to 15.2 for minimum fuel. At present aspect ratios as large as 15.2 are not structurally feasible but the importance of aspect ratio is clear."

A possible means of reducing the drag is by the use of fixed winglets. As illustrated in Fig. 13.24, winglets were used on the Gates Learjet Model 28/29, the Longhorn. The drag polars at $M_\infty = 0.7$ and at $M_\infty = 0.8$ for the M28/29 are compared with those for the M25D/F in Fig. 13.25. As can be seen in these data, the greatest improvement is at the lower Mach number. However, this is of no concern for this design application, since the normal cruise speed and long-range cruise speed of this airplane are always less than $M_\infty = 0.8$.

To generate an optimum winglet for a particular flight condition, we must calculate the flow field for the complex wing. The subsonic aerodynamic load distributions for a lifting surface with winglets can be calculated using the vortex lattice method discussed in Chapter 7. The theoretical lift-curve slopes for a swept wing with end plates which were calculated using a distribution of vortices, such as illustrated in Fig. 13.26, were in good agreement with experimentally determined data [see Blackwell (1969)].

Figure 13.24 Gates Learjet Model 28/29, the Longhorn, illustrating use of winglets (Image provided courtesy of Bombardier Inc.).

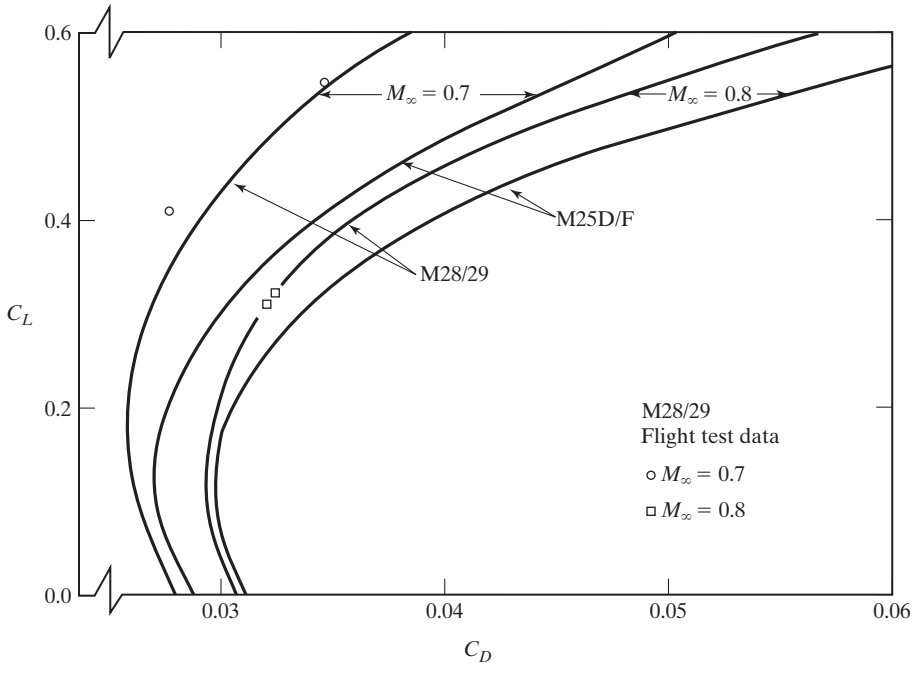

Figure 13.25 Comparison of the drag polars for the Gates Learjet M28/29 with those for the M25D/F (unpublished data provided by Gates Learjet Corp).

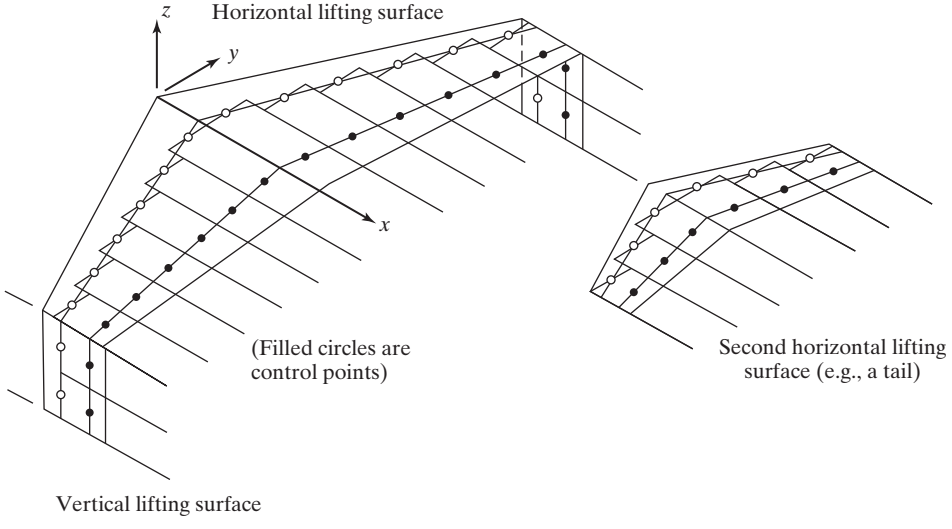

Figure 13.26 Distribution of vortices which can be used to calculate the aerodynamic load distribution for a combination of lifting surfaces [from Blackwell (1969)].

The lifting-surface geometry shown in the sketch indicates that the technique can be used to calculate the aerodynamic load distribution for lifting surfaces involving a nonplanar wing, a wing with end plates, and/or a wing and empennage.

For best performance, the proper design of winglets includes the following [Thomas (1985)]:

- For supercritical performance, the winglet should be tapered and swept aft. It should be mounted behind the region of lowest pressure of the main wing to minimize interference effects.
- Smooth fillets should be used between the wing tip and the winglet or smaller drag reduction benefits might result.
- Some toe-out of the winglet is needed due to the inflow angles at the wing tip. This is also desirable, since it reduces the likelihood of winglet stall during sideslip.
- Although the drag reduction increases with winglet span, the decrease is less than linear. Therefore, the optimal winglet height involves a trade-off between improved aerodynamics and the increased moments due to longer moment arms.

Various additional wing-tip devices, as shown in Fig. 13.27, have been used in recent years in an attempt to reduce drag, especially on aircraft that fly long distances in cruise configuration where the drag reduction would have an appreciable impact on the range and fuel efficiency of the aircraft. Some of the wing-tip concepts that have been used include winglets, blended winglets, split winglets, raked wing-tips, and spiroids [McLean (2005)]. Greater insight into winglet design can be found from the

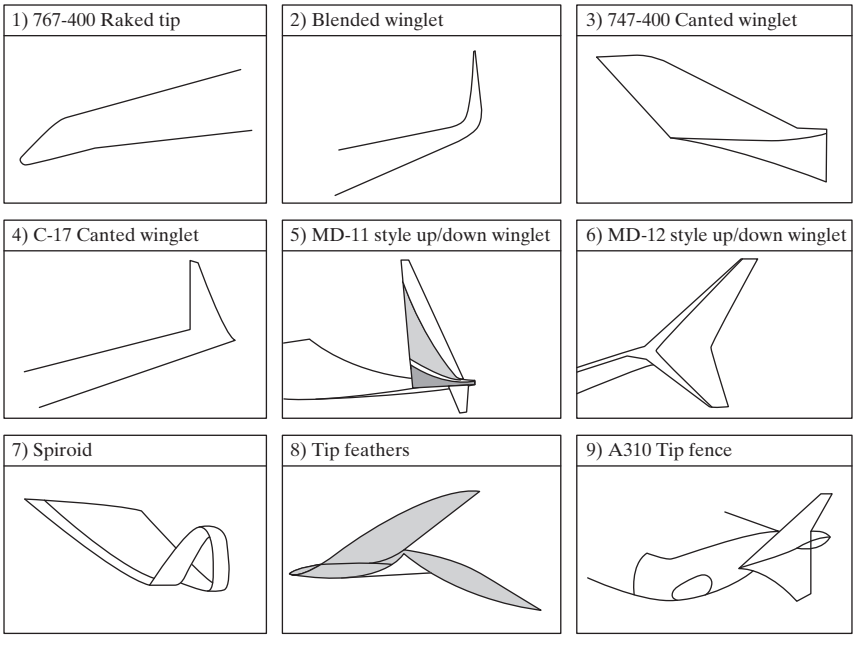

Figure 13.27 An assortment of wing-tip device configurations [adapted from McLean (2005)].

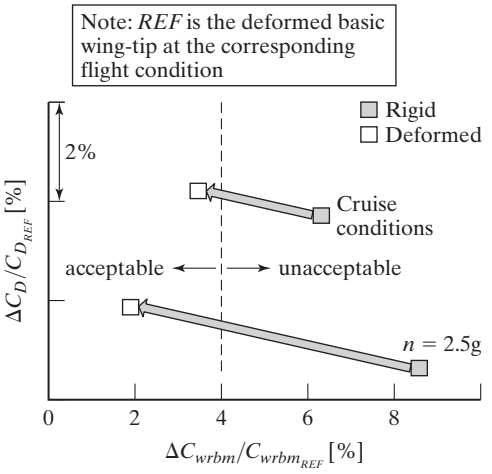

Figure 13.28 Winglet drag reduction as a function of wing root bending moment increase for rigid and deformed shapes; wrbm = wing root bending moment [adapted from Streit et al. (2008)].

results obtained by a European Union Project M-DAW (The Modeling and Design of Modern Winglets) [see Streit et al. (2004) and Mann (2006)]. In this project, which was headed by Airbus, numerical analysis, design, and wind tunnel evaluation of winglets with different shapes was considered at low and transonic speed conditions.

Whitcomb (1976) was one of the first to fully realize the benefit of wing-tip devices (such as winglets) and to realize that while the goal of using a winglet was to reduce induced drag, there were several offsetting impacts that needed to be optimized in order to make any given wing-tip device worthwhile. Specifically, wing-tip devices have the positive impact of reducing induced drag at takeoff and during cruise, but they also add to profile drag of the wing by increasing the planform area and adding junctions to the wing-tip [McLean (2005)]. In addition, the weight and structural requirements of the wing also are changed by the addition of a wing-tip device. As with any aerodynamic concept, there are positive and negative aspects to the design feature.

Another important consideration is the flexibility of the wing. Since transport aircraft wings are highly flexible, large structural deformations can occur depending on the flight condition. Therefore, to have a realistic assessment of winglet designs, designs should not be restricted to cruise conditions with a rigid wing shape. A fluid-structure coupling should be performed in order to compute the performance and structural loading (fatigue of a metal wing) at cruise conditions, as well as at ultimate structure loadings for deformed shapes (i.e. gusts, pull out of a dive, etc.). Winglet designs considering a flexible wing at different flight conditions have been conducted by Streit et al. (2008), as represented in Fig. 13.28. Trends are shown for both cruise conditions and for a load factor of n = 2.5g, where wrbm is the wing root bending moment, an important structural parameter. According to Streit et al. (2008), "The deformed shapes lead to a decrease in wrbm and an increase in drag in comparison to the rigid shapes. This means that for each device the deformed shapes show a displaced aerodynamic benefit optimum at the 4% wrbm constraint." The 4% wrbm constraint was chosen as a reasonable limitation in structural load capability for the study, and the results showed that including structural deformation actually was crucial for determining the overall benefits of the wing tip devices.

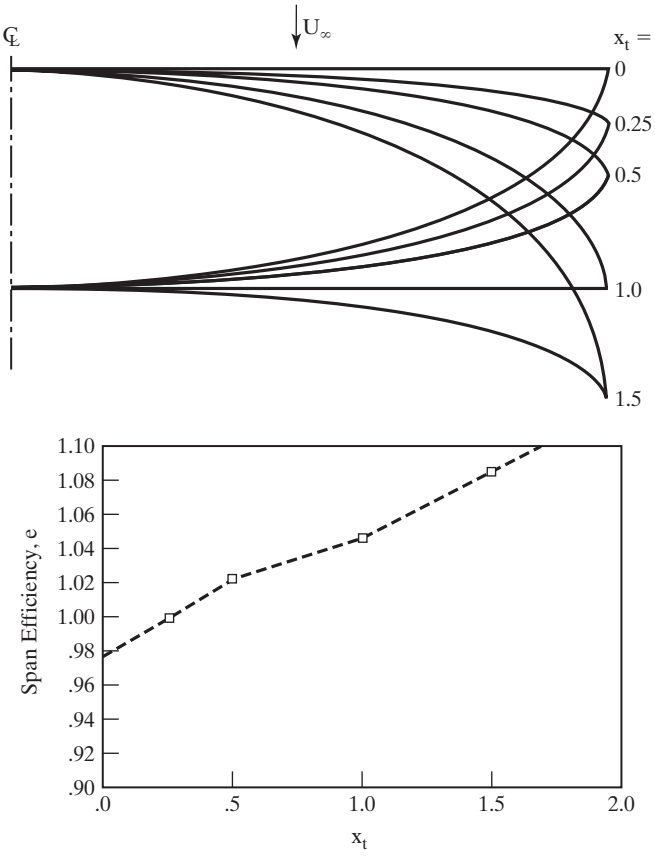

Figure 13.29 Crescent shaped wings and their corresponding span efficiency factors [from van Dam (1987)].

13.4.4 Wing Planform

Since the induced drag of an airplane is determined by the total shed vorticity from the wing (not just the wing-tip shape), some researchers have chosen to modify the wing-planform shape as another method for reducing induced drag. One of the more interesting approaches along these lines is the lunate or crescent wing, which mimics wing shapes often found in nature (see Fig. 13.29). Some of these shapes were found to reduce induced drag (or increase the span-efficiency factor) by as much as 8% in wind tunnel tests [van Dam et al. (1991)] and computational simulations [van Dam (1987)]. Other numerical simulations did not find the drag savings to be quite that high, showing drag reduction closer to 1% in some cases [Smith and Kroo (1993)]. Van Dam (1987) hypothesized that the decrease in drag was due to favorable interactions of the rolled-up wake of the wing.

Results such as these have led to an evolution of wing design in recent years, although the extreme crescent shapes have not been used on commercial aircraft (probably due to manufacturing limitations and costs). Wing-tip devices, such as the raked wing-tip used on the Boeing 767–400, originally were done as a wing-tip extension rather

Figure 13.30 The Boeing 787 with a blended raked wing-tip.

than as a planform modification. However, the geometric impact of araked or blended winglet is to make the planform more "crescent-like," and when that is coupled with wing sweep, the use of trailing-edge extensions (referred to as "Yehudis"), and highly flexible structures, the advanced wing design for aircraft like the Boeing 787 or the Airbus A350 (see Fig. 13.30) are certainly similar to earlier "lunate" shapes.

13.5 DEVELOPMENT OF AN AIRFRAME MODIFICATION TO IMPROVE THE MISSION EFFECTIVENESS OF AN EXISTING AIRPLANE

13.5.1 The EA-6B

The EA-6B is a four-place, subsonic, twin-jet, electronic countermeasures airplane designed for land and carrier-based operations. As noted in Hanley (1987), the EA-6B airplane was difficult to handle when the pilot attempted to maneuver the aircraft at low airspeeds (approximately 250 KIAS). These problems relate to the fact that, through the evolution of the design, the airplane had grown to a gross weight above 54,000 lb. To compound the problem further, both the lateral and directional moments become unstable near the stall angle of attack (approximately 16°). These characteristics contribute to the sharp roll-off and directional nose slice that is inherent in the EA-6B at stall.

As noted by Gato and Masiello (1987), the EA-6B Prowler is 10,000 lb heavier than the A-6 Intruder. In addition to additional ECM equipment and structural weight, the EA-6B was provided with more powerful engines. However, in the cruise configuration, there were no aerodynamic changes to account for the extra weight. Since the two aircraft have the same maximum lift capability (when maneuvering at low speeds and/or high altitude), the heavier EA-6B flies much closer to the stall angle of attack than its predecessor, the A-6. This is illustrated in Fig. 13.31, "where the lift coefficient required

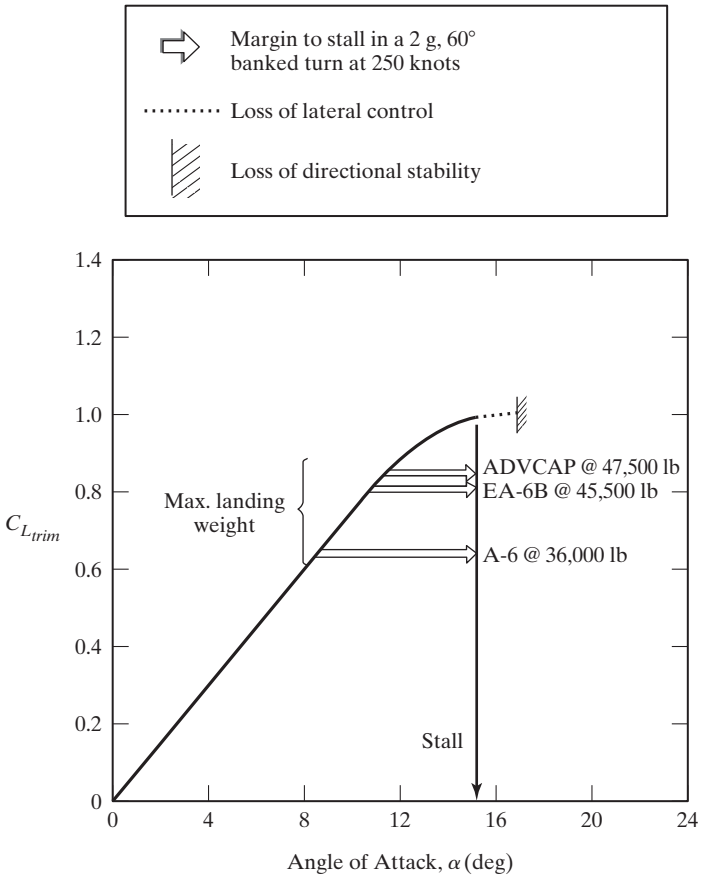

Figure 13.31 EA-6B/A-6 cruise configuration lift [from Gato and Masiello (1987)].

to execute a banked 2*g*, 60 degree banked turn at 250 knots and the angle of attack margin to stall are indicated for an A-6, a current production EA-6B, and a future ADVCAP EA-6B at representative landing weights. This is a typical maneuver for these aircraft, always performed while decelerating prior to entering the landing pattern and initiating landing gear, slat, and flap extension. Incidentally, the stall for these aircraft is defined by loss of lateral control and subsequent roll-off. Further penetration of the stall results in a directional departure which may develop into a spin" [Gato and Masiello (1987)].

In order to diagnose the flow mechanism contributing to the directional instability near stall, flow visualization studies were conducted [Jordan et al. (1987)]. Results from these studies showed that a pair of vortices are generated at the fuselage-wing junctures. These vortices trail behind the wing, close to the fuselage and below the tail at low angles of attack (Fig. 13.32a). As angle of attack is increased, wing downwash maintains the vortex system at the same relative location—that is, low with respect to the vertical tail. At stall angles of attack, flow separation on the wing and consequent downwash breakdown cause the vortices to rise to the level of the vertical tail (Fig. 13.32b). In sideslip, the vortex

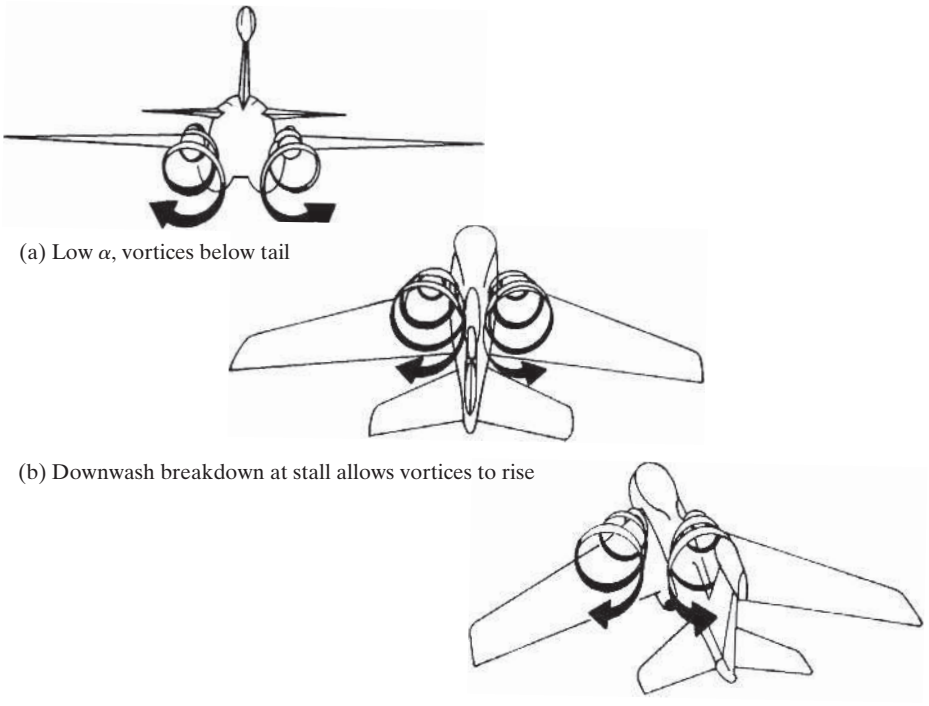

(a) Low α, vortices below tail

(b) Downwash breakdown at stall allows vortices to rise

(c) In sideslip, windward wing vortex creates adverse/destabilizing flow field

Figure 13.32 Directional destabilizing vortex system [from Jordan et al. (1987)].

generated on the windward side of the airplane drifts leeward such that, as angle of attack is increased through stall, the vertical tail becomes immersed in the windward vortex flow field (Fig. 13.32c). Because of the rotational sense of the vortex system, the bottom portion of the vertical tail first becomes immersed in a region of proverse (stabilizing) sidewash—the top portion of the windward vortex. As angle of attack is increased and the vortex system rises further, the vertical tail becomes immersed in the lower portion of the windward vortex where a condition of adverse (destabilizing) sidewash exists. Clearly, the abrupt changes in sidewash that occur as the windward vortex traverses the span of the vertical tail have a direct impact on directional stability. In fact, it is this phenomenon that causes the directional instability the airplane configuration experiences near stall.

To eliminate these dangers and to provide the EA-6B with electronics growth capability, the Navy undertook a comprehensive Maneuvering Improvement Program. The ground rules imposed by the Navy were that no major changes were allowed to the main wing or airframe structure. The project involved personnel from the Navy, Grumman Aircraft Systems Division, and NASA Langley Research Center. The results of the various tasks are described in Gato and Masiello (1987), Hanley (1987), Jordan et al. (1987), Sewall et al. (1987), and Waggener and Allison (1987).

Based on these re-design efforts, including an integrated mix of computational and experimental investigations, an aerodynamic upgrade package was proposed for

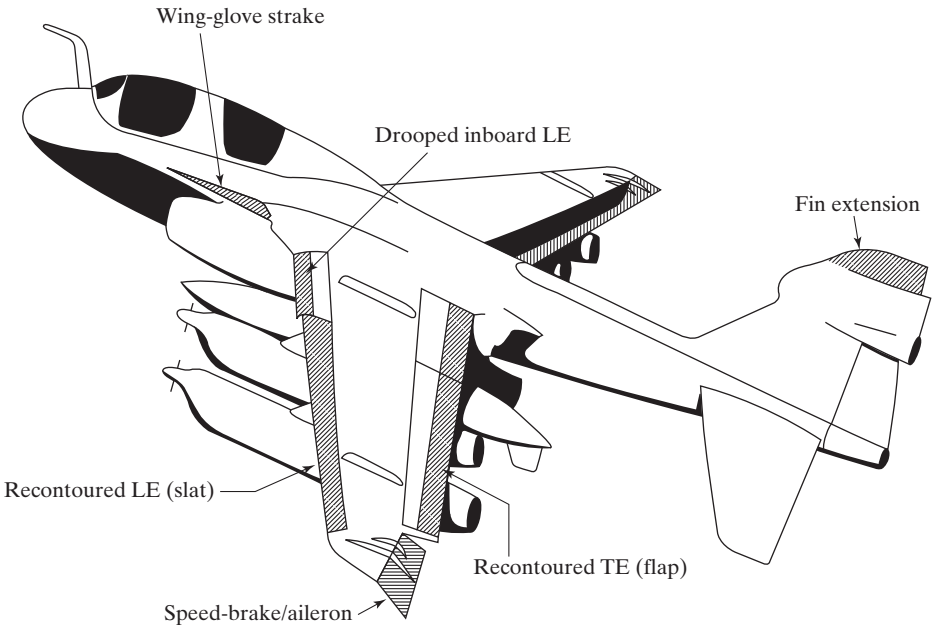

Figure 13.33 Proposed aerodynamics upgrade package for the EA-6B Prowler [from Gato and Masiello (1987)].

the EA-6B Prowler, as shown in Fig. 13.33. The upgrade package includes the following features:

- Drooped inboard leading edges (add-on to inboard slat elements)
- Wing-glove strakes
- A fin extension
- Wing-tip speed-brake/ailerons

The combined effect of fin extension, strakes, and drooped inboard leading edges on directional stability is illustrated in Fig. 13.34. The unstable directional characteristic was shifted to higher angles of attack, by a total of 6°. The level of directional stability at low angles of attack was also significantly increased as a result of the additional vertical tail area. In fact, the fin extension was sized to provide the EA-6B with the same low angle of attack directional stability as the A-6, thereby compensating for the destabilizing effect of the longer fuselage.

Besides improving the lateral-directional stability, the strakes and the drooped inboard leading edges increased the maximum lift and the stall angle of attack, as shown in Figs. 13.35 and 13.36. This combination of aerodynamic modifications/devices provides significant improvements in the maximum lift coefficient. As shown in Fig. 13.35, the increase in cruise configuration maximum usable lift is 22% at low Mach numbers and 30% at higher Mach numbers. Consequently, the aerodynamically upgraded EA-6B has essentially the same stall/maneuver margins of the lighter A-6. Improved lateral-directional stability and positive lateral control beyond stall allow full use of this increment in maximum lift.

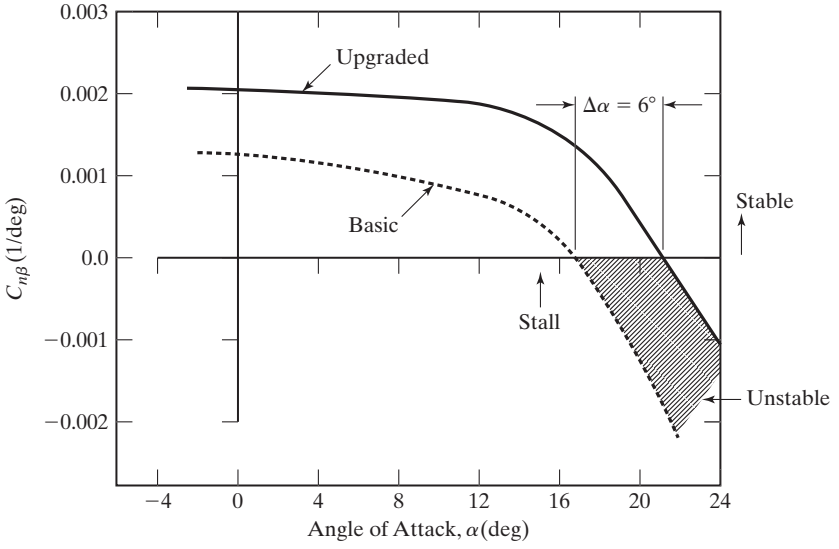

Figure 13.34 Combined effect of fin extension, strakes, and drooped inboard leading edges on lateral-directional stability [from Gato and Masiello (1987)].

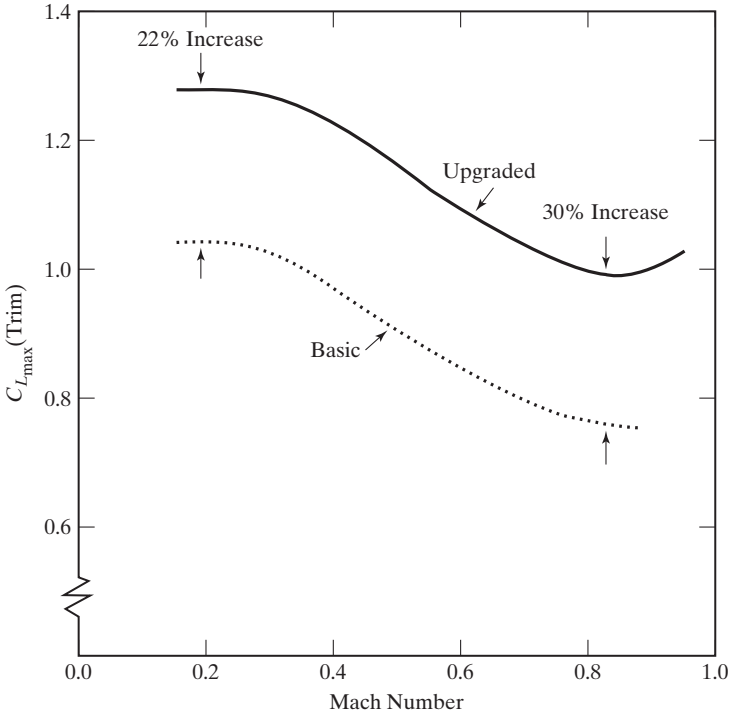

Figure 13.35 Increase in maximum usable lift [from Gato and Masiello (1987)].

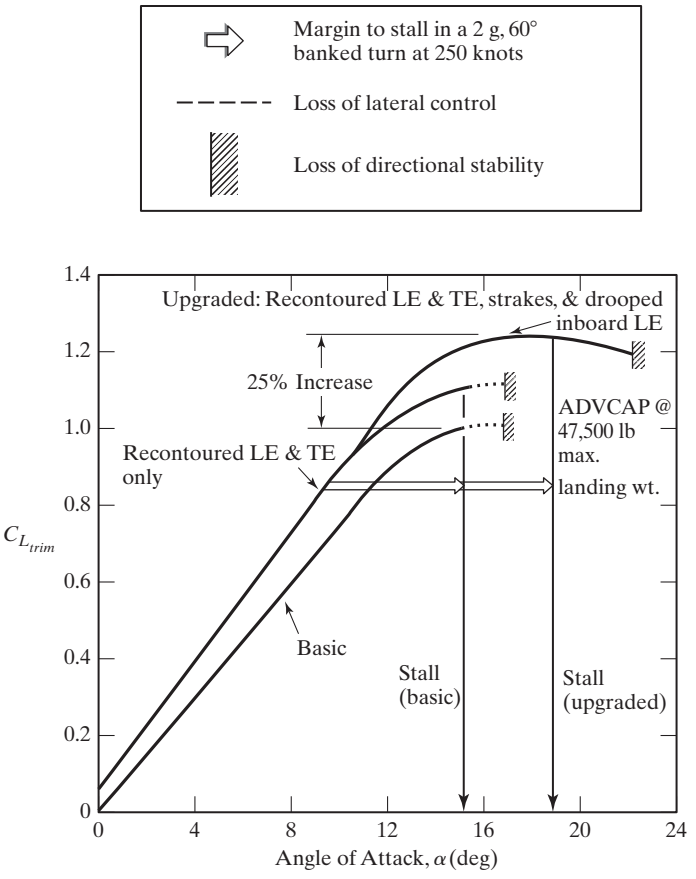

Figure 13.36 Combined effect of recontoured leading and trailing edges, strakes, and drooped inboard leading edges on cruise configuration lift [from Gato and Masiello (1987)].

13.5.2 The Evolution of the F-16

As stated by Bradley (1981), "The design of tactical military aircraft presents quite a challenge to the aerodynamicist because of the vast spectrum of operational requirements encompassed by today's military scenario. The designer is faced with a multitude of design points throughout the subsonic-supersonic flow regimes plus many off-design constraints that call for imaginative approaches and compromises. Transonic design objectives are often made more difficult by restraints imposed on by subsonic and supersonic requirements. For example, wings designed for efficient transonic cruise and maneuver must also have the capability to accelerate rapidly to supersonic speeds and exhibit efficient performance in that regime."

Bradley continues, "The design problem is further complicated by the fact that the weapon systems of today are required to fill multiple roles. For example, an aircraft designed to fill the basic air superiority role is often used for air-to-ground support, strike penetration, or intercept missions. Thus, carriage and delivery of ordnance and carriage

of external fuel present additional key considerations for the aerodynamicist. The resulting aircraft flowfield environment encompasses a complex mixture of interacting flows."

"For example, the need for rapid acceleration to supersonic flight and efficient supersonic cruise calls for thin wing sections with relatively high sweep and with camber that is designed to trim out the aft ac movement at supersonic flight. However, these requirements are contrary to those requirements for efficient transonic maneuver, where the designer would prefer to have thicker wing sections designed with camber for high C_L operation and a high-aspect-ratio planform to provide a good transonic drag polar."

Harry Hillaker (1997), who was the Chief Project Engineer on the YF-16 and Vice President and Deputy Program Director of the F-16XL Program, discussed early studies that provided the technology base from which the YF-16 design was developed (see the discussion on Hillaker in Chapter 1). Examination of results from air-to-air combat over Southeast Asia/Vietnam revealed that aircraft in the U.S. inventory had only marginal success over their opponents. From 1965 to 1968, engineers at General Dynamics in Fort Worth examined the data from the Southeast Asian conflict to determine what parameters provided an edge in air-to-air combat. Wing loadings, thrust loadings, control issues, g-tolerances for the pilot, and empty-weight fraction were identified as key parameters in air-to-air combat. Since these studies were focused on technology, there were no associated configuration designs done at the time.

In 1997 Hillaker continued, "From 1969–1971, an extensive wind-tunnel program was conducted in which data were obtained on a wide variety of configurations over a range of free-stream test conditions and angles of attack." As shown in the sketches of Fig. 13.37,

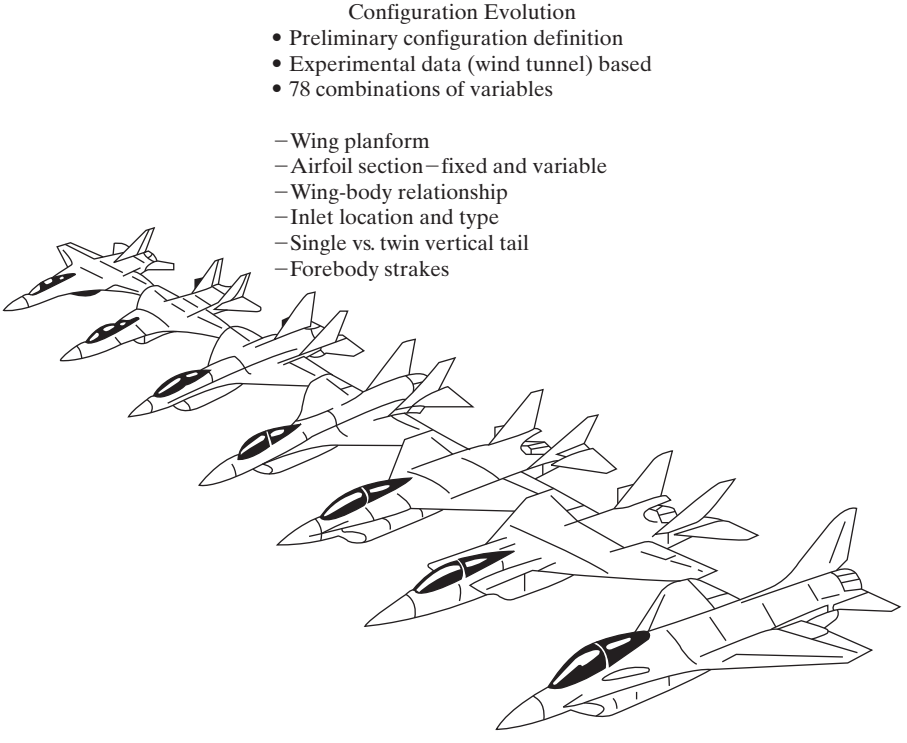

Figure 13.37 Configuration evolution for the F-16.

configuration variables included wing planforms, airfoil sections, wing-body relationships, inlet locations, horizontal and vertical tail configurations, and forebody strakes. Buckner et al. (1974) reported, "The 1969–1970 period produced technology studies in four areas very important to air combat maneuvering fighter design:

- Project Tailormate (1969, 1970)—an experimental study of a wide variety of inlet types and locations on typical fighter designs with the goal of maintaining low distortion and high-pressure recovery over wide ranges of angle of attack and sideslip. The YF-16 inlet location is largely a result of the experience gained in this work.
- Wing mounted Roll Control Devices for Transonic, High-Light (sic) Conditions (1969)—a study of a variety of leading- and trailing-edge devices for roll control in the combat Mach number and high-angle-of-attack range.
- Aerodynamic Contouring of a Wing-Body Design for an Advanced Air-Superiority Fighter (1970)—an add-on to the roll-control study, which produced analytical information on a blended wing-body design. This experience was helpful in the later development of the YF-16 overall planform and blended cross-section concept.
- Buffet Studies (1969–1970)—a series of efforts producing new knowledge and methodology on the phenomenon of increased buffet with increasing angle of attack. The methodology, in turn, allowed the YF-16 to be designed for buffet intensity to be mild enough to permit tracking at essentially any angle of attack the pilot can command in the combat arena.

The above studies produced knowledge that was brought to bear on the configuration studies, specifically for the development of a lightweight low-cost fighter, accomplished in 1970 and 1971."

The lightweight, low-cost fighter configuration studies intensified when a new set of guidelines were defined for application to combat scenarios in Europe. Hillaker (1997) noted, "These mission rules included a 525 nautical mile (nm) radius, four turns at 0.9M at 30,000 feet, accelerate from 0.8M to 1.6M, three turns at 1.2M at 30,000 feet, and pull a four-*g*-sustained turn at 0.8M at 40,000 feet. Furthermore, the aircraft had to demonstrate operability both for the U.S. Air Force and its NATO allies."

As noted by Buckner et al. (1974): "The YF-16 really got its start, then, as a result of the 'in-house' studies initiated in late 1970 in response to the new mission rules . . . Major emphasis was placed on achieving flight and configuration characteristics that would contribute directly to the air-to-air kill potential in the combat arena—specifically maximizing maneuver/energy potential and eliminating aerodynamic anomalies up to the maneuver angle-of-attack limits." Buckner and Webb (1974) reported, "Examples of the 'design to cost' in the case of the YF-16 aerodynamic features are (1) a single engine, eliminating the complex question of what to do between the nozzles, (2) an empennage/nozzle integrated design, devoid of adverse interference, (3) a single vertical tail tucked in safely between the forebody vortices, (4) a simple underslung, open-nosed inlet with no complex moving parts, (5) a thin-wing airfoil with only slight camber, minimizing the question of Reynolds number effects on transonic shock locations, and (6) simple trailing-edge ailerons. All of these features reduced the cost through virtual elimination of design changes in the refinement stage after contract go-ahead and through simplification of the task required to fully define the vehicle aerodynamics." In

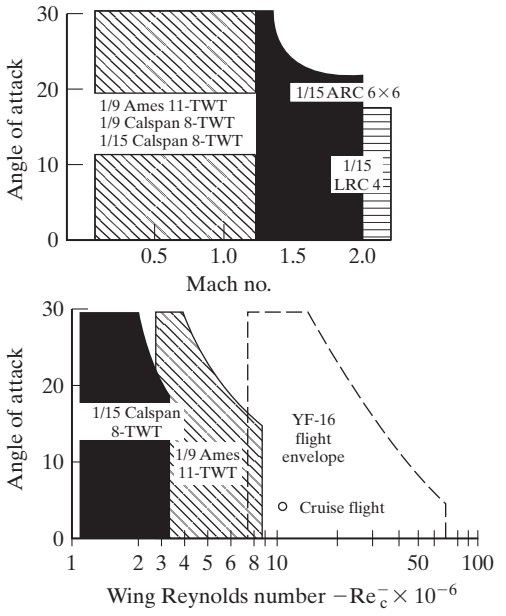

Figure 13.38 Angle of attack, Mach number, Reynolds number coverage for YF-16 design tests [from Buckner et al. (1974)].

1972, aerodynamic data were obtained over a wide range of Mach number, Reynolds number, and angle of attack. The ranges of these variables, as taken from Buckner and Webb (1974), are reproduced in Fig. 13.38.

Buckner et al. (1974) reported that "from these data it is obvious that the taper ratio (λ) should be as low as practical, consistent with reasonable tip-chord structural thickness and early tip-stall configurations. The final selection was a taper ratio of 0.227. The start combat weight is lowest at a wing aspect ratio of 3.0, the final selected value, and is relatively independent of wing sweep in the range of 35 to 40 degrees. The greater wing sweep is beneficial to the supersonic performance, giving reduced acceleration time and increased turn rate. Some penalty in aircraft size is noted as the wing sweep is increased to 45 degrees, and the higher-sweep wings are more prone to have a aileron reversal because of aeroelastic effects. As a result, wind tunnel tests were limited to sweep angles between 35 and 45 degrees. Perturbation of wing thickness ratio t/c indicates a lighter weight airplane results with a thicker wing, but supersonic maneuverability improves with thinner wings. The desire to achieve a balance in subsonic and supersonic maneuver capability dictated selection of the thinnest practical wing as thin a wing as practical ($t/c = 0.04$), consistent with flutter and aileron reversal considerations."

Bradley (1981) notes: "The tactical military aircraft design problem is made more difficult by the supersonic acceleration requirement. The wings must be as thin as structurally feasible to reduce drag, but fixed camber suitable for optimum transonic maneuver is not practical because of supersonic camber drag. An obvious solution is a smoothly varying wing camber design. However, structural and actuation system weights prove to be prohibitive for thin wings. Simple leading edge and trailing edge

flaps often prove to be the most practical compromise for high-performance, multiple design point configurations."

"The extreme possibilities are apparent. One may design a wing with optimized transonic maneuver camber and twist and attempt to decamber the wing with simple flaps for supersonic flight. On the other hand, one may design the wing with no camber or with a mild supersonic camber and attempt to obtain transonic maneuver with simple flaps."

Even though the designer has worked carefully to design a wing for attached flow and to optimize its performance, there are points in the sustained and instantaneous maneuver regimes where the flow field contains extensive regions of separated flow. The manner in which the flow separates will strongly affect the vehicle's drag and its controllability at the higher values of the lift coefficient. For many designs, strakes or leading-edge extension devices are used to provide a controlled separated flow. Controlled vortex flow can then be integrated with the variable camber devices on the wing surface to provide satisfactory high-lift, stability and control, and buffet characteristics. The resulting flowfield is a complex one, combining attached flows over portions of the wing with the vortex flow from the strake, as shown in Fig. 13.20.

One of the questions addressed by the designers of the Lightweight Fighter was single vertical tail versus twin-tailed configurations (see Fig. 13.37). NASA data available at the time indicated advantages of the twin-tailed configurations. However, as noted by Hillaker (1997), the NASA data were limited to angles of attack of 15° or less. Buckner et al. (1974) noted, "To the dismay of the design team, however, the directional stability characteristics of the twin-vertical-tailed 401F-0 configuration were not as expected. In fact, a severe loss of directional stability occurred at moderate-to-high angles of attack. . . . Analysis of oil flow visualization photographs led to the belief that forebody flow separations and the interaction of the resulting vortices with the wing and vertical tail flow fields were major causes of the stability problem."

Modifications were made to delay forebody separation to higher angles of attack. Buckner et al. (1974) reported, "It was more difficult to make the twin-tail configurations satisfactory compared to the single vertical tail configurations (in addition, some combinations of angle of attack and sideslip produced visible buffeting of the twin tails). Beneficial effects on the directionally stability derivatives were noted when relatively small highly swept 'vortex generators' (strakes) were located on the maximum half-breadth of the forebody."

"At this point, NASA Langley Research Center aerodynamicists were consulted and they suggested that the lift of the wide forebody could be increased by sharpening the leading edge to strengthen the vortices rather than weaken them as our earlier attempts had done. The point was that forebody separation is inevitable at very high angle of attack; therefore, the lift advantages offered by sharp leading edges should be exploited. This also would allow the forebody vortices to dominate and stabilize the high-angle-of-attack flow field over the entire aircraft, improving, even, the flow over the outboard wing panels."

Once the YF-16 was in the flight-test program with the YF-17, it was no longer called the Lightweight Fighter. It was called the Air Combat Fighter (ACF). Orders for the ACF, the F-16, came in 1975. The first operational units were formed in 1978. In the late 1970s, production versions of the F-16 were quickly modified to add a full

radar capability, to add hard points to accommodate the ability to handle air-to-ground capability, and to increase the combat radius to 725 nautical miles; the aircraft had become the Multi-Role Fighter (MRF).

13.5.3 External Carriage of Stores

Starting in the 1950s, the air-to-ground role was often performed by military aircraft carrying the ordnance externally. In a photo provided by Bracken (2000), an F-105D is shown on a mission during the Vietnam War. The F-105D (Fig. 13.39) carries externally two 500-pound bombs (one outboard on each wing), two 450-gallon fuel tanks (one on each wing), and six 750-pound bombs (clustered near the centerline of the aircraft).

Whitford (1991) reported large improvements in the load-carrying ability from the designs of the 1950s to more recent designs. As shown in Fig. 13.40, the Hawk 200 is able to lift an external load equal to 85% of its empty weight.

Bradley (1981) notes, "Perhaps the greatest irony for the tactical aircraft designer results from the fact that an aircraft designed to be the ultimate in aerodynamic efficiency throughout a performance spectrum is often used as a 'truck' to deliver armaments. Aircraft that are designed in a clean configuration are often used operationally to carry an assortment of pylons, racks, missiles, fuel tanks, bombs, designator seeker pods, launchers, dispensers, and antennaes that are attached to the configuration at any conceivable location."

Although the F-16 was originally conceived as a lightweight fighter (see Fig. 7.41), it has assumed a multirole capability to meet the demands of widely differing operational requirements, including air superiority, air intercept, battlefield support, precision-strike/interdiction, defense suppression, maritime interdiction, (airborne) forward air controller, and reconnaissance. Weapons that could be carried by the F-16 in the 1990s are presented in Fig. 13.41, which was described by M. J. Nipper (1996). The figure, which illustrates the certified stores capability, clearly exhibits the F-16's versatility of weapons carriage. New weapons are being constantly developed that will be certified on the F-16 over the years.

According to Bradley (1981), who is referring to the results in Fig. 13.42, "The carriage drag of the stores is often of the same order of magnitude as the total minimum drag of the aircraft itself. For example, the minimum drag of the F-16 aircraft is compared . . . with and without the air-to-ground weapons load. It is readily seen that the store drags themselves present as large a problem to the aircraft designer as the drag of the clean configuration. Store carriage on modern technical aircraft is extremely important, particularly as one approaches the transonic regime, where the interference effect of the stores and pylons are highest and most detrimental to performance."

Bradley (1981) continues, "Not only must external stores be carried efficiently by tactical aircraft, but they must release cleanly and follow a predictable trajectory through the vehicle's flowfield. The store trajectory is governed by the highly unsteady forces and moments acting on the store produced by the nonuniform flowfield about the configuration and the aerodynamic characteristics and motions of the store itself. The problem is complicated by realistic combat requirements for jettison or launch at maneuver conditions and multiple release conditions where the weapons must not 'fly' into one another."

Figure 13.39 An F-105D piloted by Major E. R. Bracken on a mission during Vietnam War carrying ten stores externally (photo provided by M. Gen. E. R. Bracken, USAF Ret.).

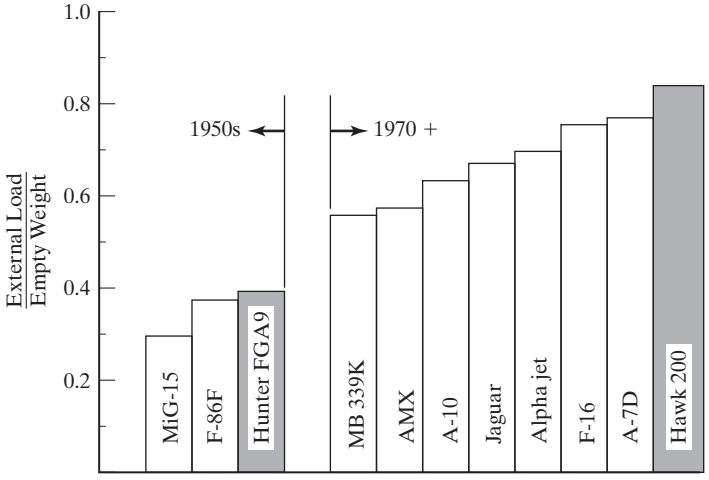

Figure 13.40 Capability of aircraft to carry stores externally [taken from Whitford (1991)].

Military aircraft of the future will have added emphasis on store carriage and release early in the design process. Some possible concepts for weapons carriage are contrasted in Table 13.2.

Bradley (1981) presented wind-tunnel measurements that compared the drag for conformal carriage versus conventional installations of MK-82 bombs. As shown in Fig. 13.43, conformal carriage permits 14MK-82 bombs to be carried at substantially less drag than a 12 MK-82 pylon/multiple bomb rack mounting. Bradley (1981) notes, "Significant benefits for the conformal carriage approach, in addition to increased range, are realized: increased number of weapons and carriage flexibility; increased penetration speed; higher maneuver limits; and improved supersonic persistence. Lateral directional stability is actually improved with the weapons on."

Hillaker (1997) noted that in 1974 General Dynamics embarked on a Supersonic Cruise and Maneuver Program (SCAMP) to develop a supersonic cruise derivative of the F-16. The "supercruiser" concept envisioned optimization at supersonic cruise lift conditions so that sustained cruise speeds on dry power (non-afterburner power) could be achieved in the Mach 1.2 to 1.3 speed range. Trade-offs to the aerodynamics required for supersonic cruise, subsonic cruise, and maneuvering flight were explored. The goal was to arrive at a design that would offer at least a 50% increase in the supersonic lift-to-drag ratio (L/D) that would retain a high subsonic L/D ratio and that would provide the level of maneuverability of a fighter.

Hillaker (1997) noted that, by 1977 to 1978, it was clear that the F-16 was to serve both the air-to-air mission and the air-to-ground mission (with the air-to-ground mission dominating). Therefore, engineers sought to develop a design that was a straightforward modification of the F-16. The approach was to build on the technology developed for the original SCAMP configuration adding a maneuver requirement to the supersonic cruise capability. From 1974 to 1982, the SCAMP/F-16XL configurations underwent significant refinements. The configuration evolution, as taken from a paper by Hillaker

Figure 13.41 Weapons that can be carried by the F-16 (US Air Force photo).

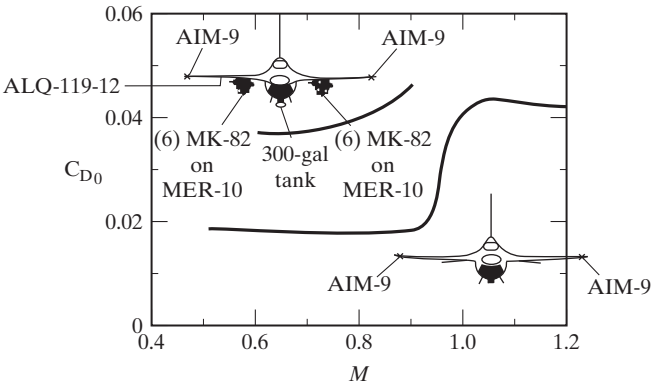

Figure 13.42 Stores drag effect [from Bradley (1981)].

TABLE 13.2 Weapon Carriage Concepts

Store Carriage Concepts	*Advantages*	*Disadvantages*
1. Wing pylon carriage	Most flexible carriage mode—large payloads, inefficient store shapes	High drag High radar cross section
2. Internal carriage	Low drag	Limited weapon flexibility
	Low radar cross section	Increased fuselage volume
3. Semisub-merged carriage	Low drag	"Holes" must be covered up after weapons drop
	Low radar cross section	
		Severely restricted payload flexibility
4. Conformal carriage	Most flexible of low drag carriage concepts	Size restrained

Source: Bradley (1981).

(1982), is reproduced in Fig. 13.44. Hillaker (1982) reported, "The planform requirements included a forebody blend (strake area) for high angle-of-attack stability, an inboard trailing-edge extension for pitching moment improvement, and fixed wing tips with ailerons and leading-edge device to enhance the flow over the aileron at high angles of attack. The combination of ailerons and a leading-edge device (flaps for flow control, not lift) was developed to resolve the mechanical and structural complexities of the all-movable wing tip on the previous configuration. All-movable wing tips provided high roll rates and adverse yaw for resistance to yaw divergence at high angles of attack. The aileron-leading-edge device combination provided the same aerodynamic advantages

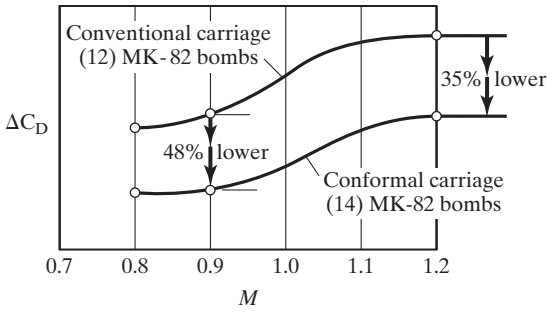

Figure 13.43 Drag comparison—conformal vs. conventional carriage [from Bradley (1981)].

and simplified wing structure, reduced weight, increased fuel volume, and allowed tip missile carriage."

The benefits of the F-16XL configuration include 40% to 85% lower drag with the integrated weapons carriage, 50% better supersonic lift-to-drag ratio with no subsonic penalty, 17% lower wave drag with drag with 83% more internal fuel, and increased lift with expanded maneuver angle of attack.

The first two demonstrator aircraft (modified from two F-16A aircraft) took to the air at Carswell Air Force Base in Fort Worth, Texas, on July 3, 1982, and were used by NASA for flight research.

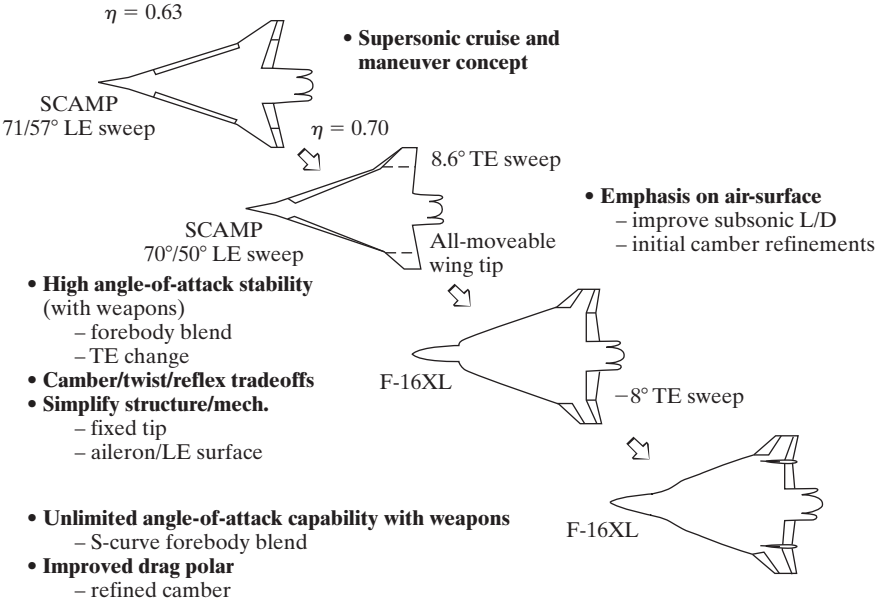

Figure 13.44 F-16XL configuration evolution [from Hillaker (1982)].

TABLE 13.3 Summary of Main Design Features Required to Achieve a Variety of Operational Requirements

Operational Requirements	*Primary Design Features*
Short take-off	High afterburning (A/B) thrust/weight (T/W) ratio, high flap lift, low wing loading (W/S), thrust vectoring
Economical transit/loiter	Low throttled specific fuel consumption (sfc), high cruise lift-to-drag (L/D) ratio
High penetration speed	High dry thrust/weight (T/W) ratio, low store drag, good ride quality
High combat agility	High dry thrust/weight (T/W) ratio, high control power, good lift-to-drag (L/D) ratio at high g, high usable lift, thrust vectoring
High combat persistence	Low combat specific fuel consumption (sfc), good lift-to-drag (L/D) ratio at high g, versatility of weapon carriage
High combat mobility	High afterburning (A/B) thrust/weight (T/W) ratio, low drag at all Mach numbers
High survivability	Stealth (to give first shoot/first kill), threat awareness and countermeasures, robustness/redundancy
Short landing	High flap lift, low wing loading (W/S), flareless, good retardation

Source: Whitford (1991).

13.5.4 Additional Comments

The ability to modify a design to accommodate the increased weights allows an aircraft to satisfy added missions, handle more ordnance, be fitted with more powerful engines, and so on. The Supermarine Spitfire, a single-engine pursuit aircraft of World War II, grew by the weight of 32 airline passengers and their luggage during its evolution from 1936 through 1946.

The examples discussed in this section illustrate the philosophy represented by the comment made by Montulli (1986): "When establishing airplane performance requirements, allow for potential changes in operational requirements. Do not allow a point design." Table 13.3, which is taken from Whitford (1991), identifies the main design features that allow a military aircraft to achieve a variety of operational requirements.

13.6 CONSIDERATIONS FOR WING/CANARD, WING/TAIL, AND TAILLESS CONFIGURATIONS

The relative merits of wing/canard, wing/tail, and tailless configurations for high-performance aircraft have been the subject of numerous investigations over the years. The use of canards usually allows for a shorter fuselage, which results in less skin-friction drag, and a more optimum cross-sectional area distribution, which results in less wave drag. However, although aft-tail configurations need a longer fuselage, they usually have smaller wing area, which also results in lower skin-friction drag and in lower wave drag.

The stall progression for a forward swept wing (FSW) is compared with that for an aft swept wing (ASW) in Fig. 13.45, which is taken from Weeks (1986). As depicted in Fig. 13.45a, the stall pattern for a forward swept wing proceeds from the root to the tip, as

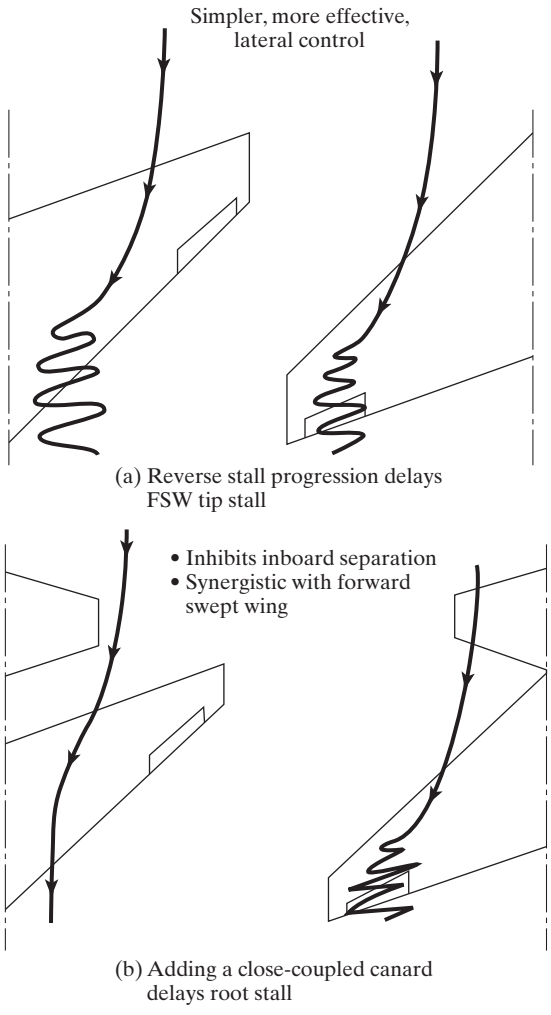

Figure 13.45 Stall-progression patterns for a forward swept wing (FSW) as compared with those for an aft swept wing [from Weeks (1986)].

opposed to the normal behavior for aft swept wings, in which the stall pattern starts at the tip and proceeds inboard toward the root. See the discussion in Section 7.3.5. Both cases would result in pitch-up tendencies. Weeks continued by referring to the results shown in Fig. 13.45b by placing a full authority canard ahead of the wing root region, the FSW configuration avoids pitch-up and achieves delayed stall providing full utilization of the inboard, large lift contributing portions of the wing to high angles-of-attack. Lateral control can then be maintained with simple (light weight) tip region located ailerons. By further integrating negative subsonic stall margin and nearly neutral supersonic margin, positive lift to trim can be maintained over the entire envelope. Then, by further introduction of variable camber and three-surface control, airframe drag can be minimized.

In 1982 and 1983, General Dynamics and NASA Langley Research Center conducted a wind-tunnel test program to generate a data base needed for a more general understanding of the aerodynamic performance comparisons between a wing/canard configuration, a wing/tail configuration, and a tailless configuration. Data were obtained for two sets of configurations: one employed a 60° leading-edge-sweep delta wing and the other employed a 44° leading-edge-sweep trapezoidal wing. Data for the 44° leading-edge-sweep trapezoidal wing, as presented in Nicholas et al. (1984), will be reproduced here. A description of the models is presented in Fig. 13.46. The leading and trailing-edge flaps were optimally scheduled to minimize the drag for the wing/canard configuration and for the wing/tail configuration. For the tailless configuration, the subsonic data were insufficient to define the trimmed polars. At supersonic speeds, trailing-edge flap deflections were governed by the trim requirements rather than by drag optimization.

Referring to the data presented in Fig. 13.47, Nicholas et al. (1984) noted, "At subsonic speeds, large negative static margins are required to achieve small polar benefits for the wing-canard as compared to the wing-tail. The wing-tail drag is optimized with subsonic static margins in the range of -10 to $-15\%\bar{c}$. This nominal level of instability is considered achievable because of satisfactory high-angle-of-attack stability and control characteristics observed on the transonic fighter model. Furthermore, the drag penalties for slightly increased stability on the wing-tail are not severe. The wing-canard subsonic

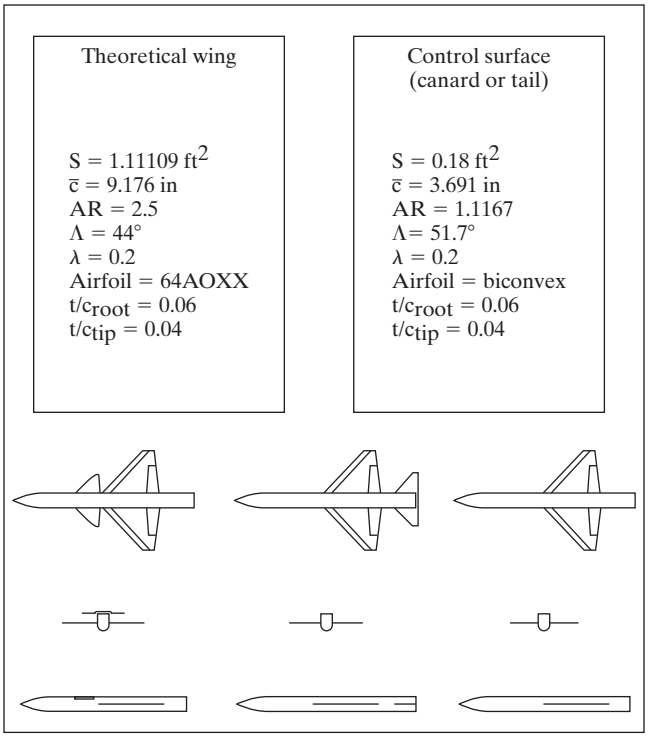

Figure 13.46 Description of models for wing/canard, wing/tail, and tailless configurations comparisons [from Nicholas et al. (1984)].

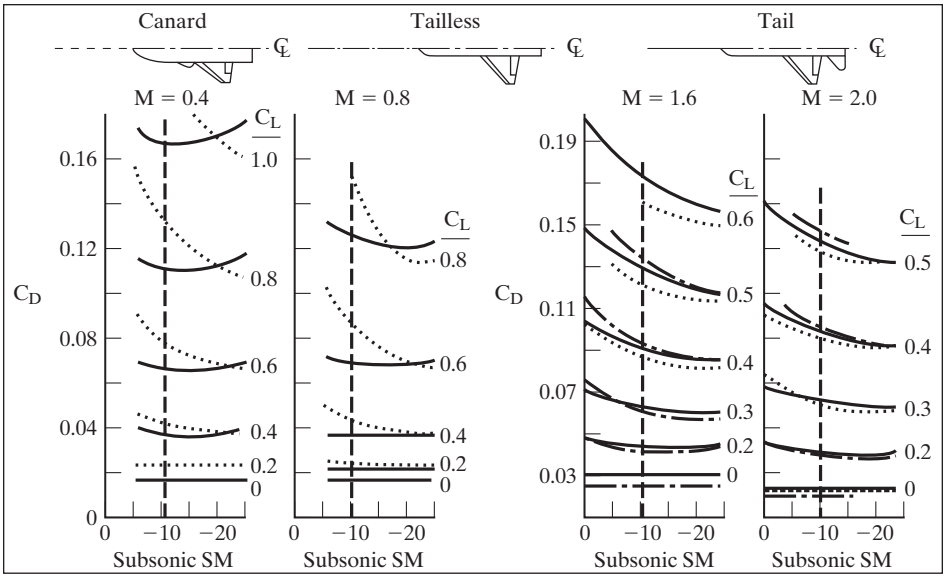

Figure 13.47 Summary of trimmed drag comparison of canard, tail, and tailless arrangements with the 44° sweep trapezoidal wing [from Nicholas et al. (1984)].

drag polar appears to be approaching optimum with a subsonic static margin of $-25\%\bar{c}$, and increased stability is accompanied by severe drag penalties. The risk associated with an aircraft designed for this level of instability is significant, and the potential drag benefits appear to be small. It is also apparent that the subsonic polar shapes of both the canard and tailless arrangements are far more sensitive to subsonic static margin variations than those of the wing-tail."

Nicholas et al. (1984), referring to the data in Fig. 13.48, continued, "At supersonic speeds, static margin sensitivity is roughly similar for the canard, tail, and tailless arrangements. Here, the optimization comparison between canard and tail is somewhat reversed, with the subsonic static margin being optimum at $-15\%\bar{c}$ to $-20\%\bar{c}$ for the wing-canard versus approaching optimum at $-25\%\bar{c}$ for the wing-tail. The reason for this reversal is associated with aerodynamic center (defined with all surfaces fixed at zero deflection) travel from subsonic to supersonic speeds, which is greater for the wing-tail than for the wing-canard. . . . This happens because the fraction of the total lift carried by the tail increases significantly as the wing downwash field decreases from subsonic to supersonic speeds. However, because of its forward location, the canard experiences relatively little variation in the fraction of total lift that it carries between subsonic and supersonic speeds. Therefore, for a fixed level of subsonic stability, the wing-body is more stable at supersonic speeds for the wing-tail than it is for the wing-canard. It is this supersonic wing-body stability that determines canard or tail trim requirements. Both the wing-canard and the wing-tail optimize with approximately 12% of the total lift carried in the control surface, as shown for Mach 1.6 in Fig. 13.49. This optimum control-surface/wing lift ratio is achieved with

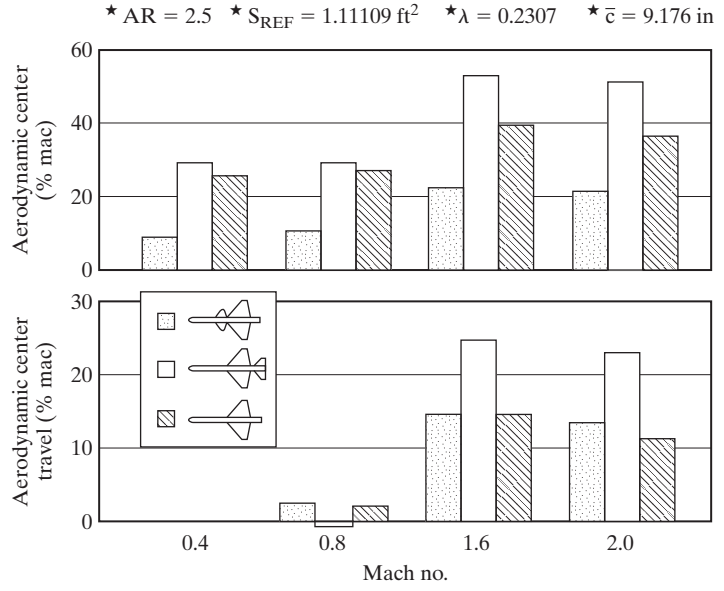

Figure 13.48 Variation of aerodynamic center with Mach number for canard, tail, and tailless arrangements with the 44° sweep trapezoidal wing [from Nicholas et al. (1984)].

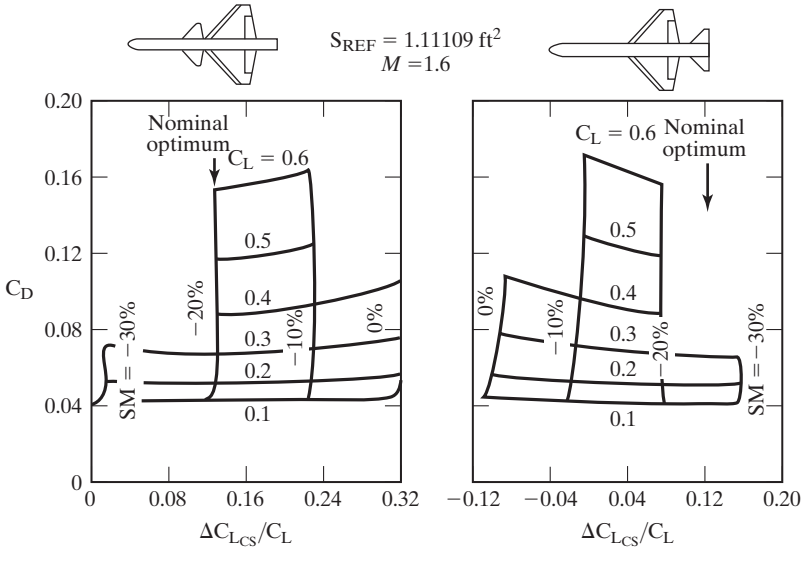

Figure 13.49 Effect of control surface lift on trimmed supersonic drag for canard and tail arrangements with the 44° sweep trapezoidal wing [from Nicholas et al. (1984)].

a subsonic static margin of nominally $-21\%\bar{c}$ for the wing-canard versus $-27\%\bar{c}$ for the wing-tail. The net result is that, at supersonic speeds, the wing-canard provides a small drag advantage over the wing-tail with a reasonable level of subsonic static margin (i.e., -10 to $-15\%\bar{c}$)."

Both for wing-canard and wing-tail configurations, the optimum polars are achieved by carrying a very small fraction of the total lift in the control surface.

From the results of their studies, Nicholas et al. (1984) reached the following conclusions:

- For highly efficient, variable-camber wings, large negative stability levels are required to achieve small subsonic polar shape benefits for wing-canard arrangements, as compared to wing-tail arrangements. However, these large negative stability levels are accompanied by reduced maximum lift for canard arrangements along with potential stability and control problems at high angles of attack. The need for large negative stability levels with a wing-canard diminishes as the main wing efficiency is decreased.
- Subsonic polars for canard and tailless arrangements are more sensitive to subsonic static margin than those of wing-tail arrangements.
- At supersonic speeds, the canard arrangements show some advantage because their polar shapes optimize at higher subsonic stability levels than wing-tail or tailless arrangements.
- The minimum drag and weight advantages of tailless delta arrangements can overcome polar shape deficiency to provide a TOGW advantage for typical advanced fighter mission/performance requirements.
- Static margin limit is a critical issue in control surface (canard, tail, tailless) selection.

13.7 COMMENTS ON THE F-15 DESIGN

A planform view of an F-15 in flight is presented in the photograph of Fig. 13.50. We will discuss two features evident in the photograph: (1) the notch or "snag" in the leading edge of the stabilator and (2) the clipped tip of the wing. The following information on these two features was provided by Peters et al. (2001):

"The notch, or snag, in the leading edge of the F-15 stabilator solved a flutter-margin issue. Moving the inboard leading-edge aft moved the center of pressure aft and also removed mass from the leading edge. This allowed the F-15 stabilator to meet an 800 KCAS (Knot Calibrated Air Speed) +15% margin requirement. The snag design was one of several options that were investigated for improving the flutter margin of the empennage. The other options (structural beef-up, mass balance, tip pods, etc.) introduced more weight and/or had aero performance penalties."

"During the 80% flight-loads testing of the F-15, it was discovered that the maximum bending moment was 3% to 4% higher than the estimates based on the wind-tunnel results. To reduce the bending moments, the wing tips were cut off on the spot and were replaced with raked tips made out of mahogany. The mahogany wing tips flew until ship number 4 was retired many years later. With the modified wing tips in place, the flight-loads testing was completed successfully."

Figure 13.50 Plan view of F-15 (U.S. Air Force photo by Josh Plueger).

13.8 THE DESIGN OF THE F-22

The F-22 design is the result of more than 20 years of work to build an Advanced Tactical Fighter (ATF). As noted by Hehs (1998a) "the term *advanced tactical fighter* and its abbreviation ATF, however, appeared in a general operational requirements document issued to contractors . . . in 1972." However, 1981 is usually cited as the beginning of the ATF program. The basic challenge of the ATF design was to pack stealth, supercruise, highly integrated avionics, and agility into an airplane with an operating range that bettered the F-15, the aircraft it was to replace.

Skow (1992) noted, "Whereas there is universal agreement that agility in air combat is valuable, many other aircraft attributes such as acceleration, speed, maneuverability, and payload/range performance have a value also. Each of these attributes has a value and a cost."

Mullin (1992) reported, "The configuration design evolution was primarily driven by the requirement to obtain excellent subsonic and supersonic aerodynamics and low observability. With the requirement for internal weapons carriage and all mission fuel internal (except for the ferry mission), the design challenge was formidable." All configurations were premised on the availability of the following technologies:

- External aircraft geometry
  - Low observable
  - Low supersonic drag
  - Unrestricted maneuverability
- Propulsion
  - Low observable supersonic inlet
  - Low observable augmenter/thrust vectoring nozzle

- Avionics
  - Common modules
  - Liquid cooling for reliability
  - Low observable apertures (radar, infrared, communications/navigation, electronics warfare)
- Other subsystems and equipment
  - Low observable air data systems
  - Low observable canopy

Unlike stealth and supercruise, high maneuverability is more often used as a defensive tactic rather than an offensive one. As reported by Hehs (1998a), "Maneuverability was quantified in the 1960s by John R. Boyd in his energy-maneuverability theory. Boyd's ideas were used on the F-15, but the F-16 was the first airplane to be designed specifically to emphasize the principles established by his theory. The most common measures of merit for energy maneuverability are sustained g capability (the ability to turn hard without losing airspeed and altitude); instantaneous g (the ability to turn the nose without regard to the effect on speed); and specific excess power (a measure of an aircraft's potential to climb, accelerate, or turn at any flight condition). Another parameter of interest is transonic acceleration time (for example, the time needed to go from Mach 0.8 to Mach 1.2). Comparing these characteristics for two fighters shows which one should have the tactical advantage in a maneuvering engagement."

Skow (1992) noted, "In an aggressive engagement against a highly maneuverable adversary, maximum load factor or maximum lift maneuvering may be required for survivability. The high values of turn rate that are achieved at these maximum conditions come at the expense of energy. Since maximum rate maneuvering bleeds energy rapidly, it can only be continued for short durations. When the pilot decides to terminate a maximum rate maneuver that has caused his airspeed to be bled to a low value, he needs to accelerate quickly. . . . Two factors influence the ability of the aircraft to accelerate rapidly: thrust minus drag and gravity. . . . For a high thrust/weight fighter, the rate at which thrust increases after a movement of the throttle can have an important effect on the energy addition achieved during a short acceleration. However, the rate at which drag is reduced can have a substantially greater effect."

Hehs (1998b) wrote that Dick Hardy (the ATF Program Director for Boeing) said, "One problem we typically face when trying to stuff everything inside an airplane is that everything wants to be at the center of gravity. . . . The weapons want to be at the center of gravity so that when they drop, the airplane doesn't change its stability modes. . . . The fuel volume wants to be at the center of gravity, so the center of gravity doesn't shift as the fuel tanks empty. Having the center of gravity move as fuel burns reduces stability and control."

Mullin (1992) wrote, "Although they are really inseparable, we faced two major areas of issues during the ATF Dem/Val program:

1. System engineering issues, based on performance requirements versus flyaway cost and weight. Many initial 'requirements' which seemed to be no problem turned out to be major drivers of weight and/or cost, and, as a result, were substantially changed by the Air Force, based on our trade study data.

2. Design engineering issues, based on conflicting requirements, such as supersonic drag versus internal fuel and weapons load, supersonic and subsonic maneuverability, installed propulsion performance versus low observability, and many others."

Lockheed, Boeing, and General Dynamics teamed to develop a demonstration/validation (dem/val) design phase for the ATF. From 1986 to 1989 the team accumulated 20,000 hours in the wind tunnel. The resultant external configuration of the F-22 is shown in Fig. 13.51. Notice that the modified diamond wing has a reference area of 840 sq ft with

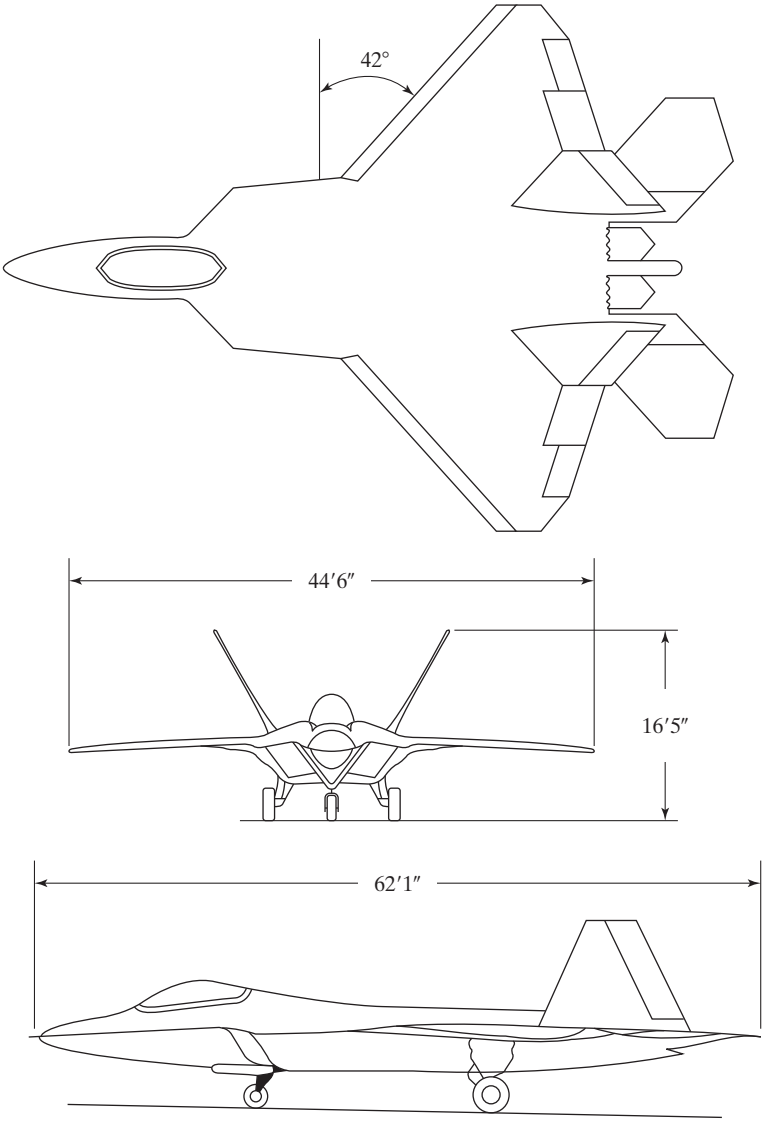

Figure 13.51 External configuration of the F-22 [taken from Mullin (1992)].

a wing span of 44.6 ft (compatible with existing aircraft shelters), and an aspect ratio of 2.37. The F-22 has constant chord full leading-edge flaps, ailerons, and flaperons.

13.9 THE DESIGN OF THE F-35

The F-35 design is the product of the Joint Strike Fighter (JSF) program and represents one of the most ambitious military aircraft designs pursued in many years. The program is also the largest aerospace defense program in history. The resulting aircraft (now named the Lightning II) has to accomplish diverse missions, while at the same time being affordable. In fact, in spite of numerous difficult design requirements, the primary goal of the program is affordability. The F-35 was designed to fulfill the following roles:

- A strike fighter to complement the F/A-18E/F for the U.S. Navy (designated CV for Carrier Variant).
- A multirole aircraft to replace the F-16 and A-10 and to complement the F-22 for the U.S. Air Force (designated CTOL for Conventional Take-Off and Landing).
- A strike fighter with short-takeoff and vertical landing capability to replace the AV-8B and F/A-18 for the U.S. Marines and the Harriers of the U.K. Royal Navy (designated STOVL for Short Take-Off and Vertical Landing).

Designing a single airframe that can accomplish all of these missions while also being affordable is a necessarily difficult task. The approach taken by Lockheed Martin is to manufacture a single airframe with differing systems for the CTOL, STOVL, and CV versions (the CV version also has a larger wing). This has proven to be a cost-effective approach.

In addition to the multirole and low-cost nature of the aircraft, there were numerous other technical requirements that have to be fulfilled by the F-35, including [Hehs (1998a, b)]:

- Overall performance similar to the F-16 and F-18
- Low observable
- Electronic countermeasures
- Advanced avionics, including adverse-weather precision targeting
- Increased range with internal fuel and weapons storage
- State-of-the-art “health” management for maintainability

The design of the F-35 involved significant use of computational fluid dynamics (CFD) for developing the overall configuration and for the addition of unique features to the aircraft. The CFD analysis was used to design and improve the outer shape of the fuselage to maximize internal fuel-storage volume, design the vertical-tail cant and rotation, and incorporate the diverterless supersonic inlet [Wooden and Azevedo (2006)]. Of special interest, the diverterless supersonic inlet [Hehs (2000)] replaces the boundary-layer diverter present for most inlets and also provides the compression necessary for operating the engine at supersonic speeds (see Fig. 13.52). This feature reduces drag and also is favorable for low observability.

Figure 13.52 The JSF diverterless supersonic inlet (photo courtesy of Lockheed Martin).

Extensive wind-tunnel testing of all variants of the F-35 has been performed at a number of wind tunnels in both the U.S. and U.K., especially the U.S. Air Force wind tunnels at the Arnold Engineering Development Center (AEDC). The AEDC tests were performed using an integrated test and evaluation approach that takes advantage of the rapid growth in CFD capabilities over the past 20 years. "As computational power has increased, so has the capability of computational analysis to contribute to aircraft design" [Skelley et al. (2007)]. Specifically, a typical full-aircraft CFD simulation from 1988 could be represented by simulating the F-15E with an Euler equation calculation on a grid with approximately 1 million grid points and requiring a turnaround time of four weeks (grid generation, solution, and post-processing time). Skelley stated in 2007 that their current CFD capability has given them a nearly four order of magnitude improvement over the 1988 capability. They could now simulate the JSF with the Navier-Stokes equations on a grid with 25 million grid points and a turnaround time of two weeks. This rapid increase in CFD capability led to full integration of the ground testing and computational analysis throughout the design phase of the F-35, including the analysis of inlet performance, carriage loads of stores, store separation, and free-flight data.

The STOVL variant of the F-35 (shown in Fig. 13.53) uses a unique lift system during take-offs and landings. The Harrier aircraft uses direct lift by rotating the jet exhaust downward and creating vertical thrust, while the F-35 uses a combination of direct lift and a unique lift fan system. The Pratt & Whitney 119-611 engine is used to create three very different lift and control devices: (a) the core nozzle with a swivel duct at the end of the aircraft provides direct lift, (b) a drive shaft and gearbox from the engine rotates a lift fan located directly behind the cockpit, and (c) bleed air from the engine is used for roll control with roll posts and ducts on the wing of the aircraft [Hehs (2001)].

Specifically, the lift system operates in the following way: "The conversion from CTOL to STOVL begins when the pilot pulls back on the thrust vector lever. Doors open above and below the lift fan. Doors behind the lift fan intake open for an auxiliary engine intake. The engine nozzle twists and vectors downward. The clutch engages and transfers energy from the spinning shaft via the gearbox to the lift fan. Control valves open to divert bypass air from the engine to the roll posts. All of these various changes occur in seconds in precise, computer-controlled order" [Hehs (2001)]. While this approach may seem unnecessarily complex, the goal of this lifting approach is multifold,

Figure 13.53 The Lockheed Martin X-35B approaching landing in STOVL configuration [from Buccholz (2002); photo courtesy of Lockheed Martin].

including the avoidance of ingesting hot gasses into the engine intake (which can cause the engine damage or failure), avoiding hot-exhaust damage to runway surfaces, and aiding the aircraft in accomplishing the difficult task of landing vertically. Hehs (2001) notes: "The lift fan approach was chosen for its many attributes. It extracts power from the engine, thus reducing exhaust temperatures from the engine by about 200 degrees compared to exhaust temperatures of direct-lift systems. It significantly reduces exhaust velocity as well. Engine exhaust air combines with low-temperature and low-velocity air from the lift fan to produce a more benign ground environment. Cool exhaust air from the fan prevents hotter [engine] exhaust from being reingested into the intakes. Hot gas reingestion, a common problem on legacy Harrier-type approaches, causes compressor stalls, and other severe engine performance degradations. Most importantly, the lift fan system was chosen because it does not detract from the up-and-away performance of the JSF 119-611 engine." This approach was verified with significant wind-tunnel testing and flight testing, including defining the transition capabilities of the F-35 as it changes from horizontal to vertical flight [Buchholz (2002)].

Lockheed Martin, Northrop Grumman, and BAE Systems teamed to develop the F-35 during the concept development phase (CDP) from 1997 through 2001 and the system development and demonstration (SDD) period starting in 2001. Wind-tunnel testing during CDP included 3500 hours at AEDC, as well as significant wind-tunnel testing of the STOVL variant at BAE Systems, NASA Ames, NASA Langley, and DNW, the German-Dutch wind tunnels [Buchholz (2002)]. The first flight of the F-35 took place in 2006, and flight testing is ongoing, with the first delivery scheduled for 2009. Approximately 23 aircraft will be built and tested during SDD [Hehs (2007)] as the flight envelope is expanded, including testing of the STOVL capabilities of the aircraft.

13.10 SUMMARY

Aerodynamic design is a challenging and exciting field, made even more interesting by the systems-based requirements that every airplane has. One of my favorite things to tell would-be aircraft designers (whether they are students or practicing engineers) is that "everything affects everything else." Whether you are trying to increase the maximum lift coefficient, or reduce drag, there are impacts of the aerodynamic choices on all other areas of the design, including the aircraft performance, structures, propulsion system, and controls (to name only a few) [McMasters and Kroo (1998)]. Always remember that your design choices will impact other groups within the design process, and seek to find solutions that maximize not just aerodynamic efficiencies, but the overall performance of the aircraft.

PROBLEMS

13.1. Discuss the variation of C_L as a low-speed aircraft consumes fuel during a constant altitude, constant airspeed cruise. What is the variation of α?

13.2. Based on the results of Problem 5.3, discuss ways to increase $(L/D)_{\max}$.

13.3. Discuss the desirability of using laminar flow airfoils on

(a) an acrobatic aircraft

(b) a commercial transport

13.4. Discuss the desirability of adding winglets to

(a) a transport aircraft that operates for long periods in cruise flight

(b) a stunt or aerobatic-type airplane

13.5. You are a "spy" who has taken a position near one of the runways of an important military air base of your opponent. You plan to observe the enemy aircraft as they fly over and use the projected view of the aircraft and the trailing vortices to determine the capabilities of the aircraft.

Consider the planform views of the airplanes presented in Figs. P13.4(a) through P13.4(b). For each of the six planforms, predict the corresponding value of the "design" Mach number. Also, what is the aspect ratio of the wing and the approximate value of $(L/D)_{\max}$? You get extra credit if you can identify the aircraft by its name and the company that originally built it.

M_∞ _____

AR _____

$(L/D)_{\max}$ _____

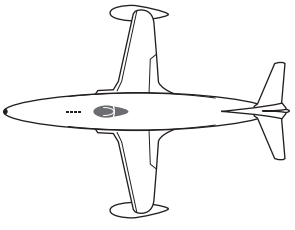

Figure P13.4(a)

M_∞ _____

AR _____

$(L/D)_{\max}$ _____

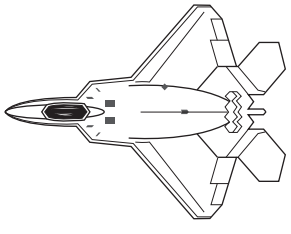

Figure P13.4(b)

M_∞ _____
AR _____
$(L/D)_{max}$ _____

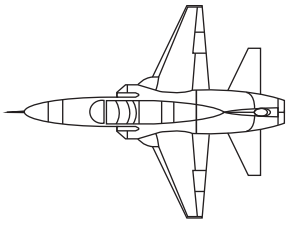

Figure P13.4(c)

M_∞ _____
AR _____
$(L/D)_{max}$ _____

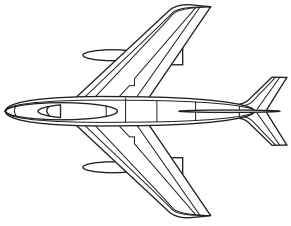

Figure P13.4(d)

M_∞ _____
AR _____
$(L/D)_{max}$ _____

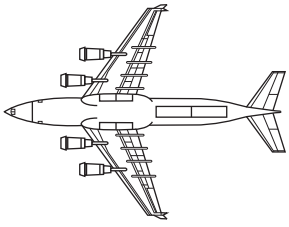

Figure P13.4(e)

M_∞ _____
AR _____
$(L/D)_{max}$ _____

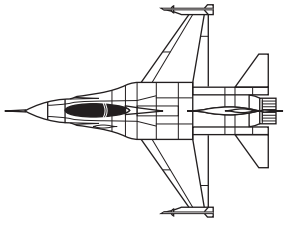

Figure P13.4(f)

13.6. A T-41 (Cessna 172) is cruising at an airspeed of 75 knots at an altitude of 16,000 *ft*. Let us treat the airfoil cross-section as a flat-plat at zero angle-of-attack. The wing plan form is essentially unswept and rectangular with a span of 35 *ft* and a chord of 6 *ft*.

In order to obtain "very approximate" estimates of the location of boundary-layer transition, we need a transition criteria and a method for calculating the values of the required parameters. We will assume that the local Reynolds number is obtained by using the free-stream values in place of the parameters at the edge of the boundary layer (which is true for an x-coordinate):

$$Re_x = \frac{\rho_\infty U_\infty x}{\mu_\infty}$$

If the boundary-layer transition Reynolds number is 500,000,

$$x_{tr} = \frac{Re_{x_{tr}} \mu_\infty}{\rho_\infty U_\infty} = \frac{500{,}000\ \mu_\infty}{\rho_\infty U_\infty}$$

Does the boundary layer for the T-41 remain laminar for the entire airfoil section. If it does not remain laminar, where does boundary-layer transition occur?

REFERENCES

Air International. 1993. High-lift system aerodynamics. *AGARD CP-515*

Air International. 1974. Two decades of the "Twenty-One." *Air Enthusiast International* 6(5):226–232

Air International. 1975. The annals of the polymorph, a short history of V-G. *Air International* 8(3):134–140

Blackwell JA. 1969. A finite-step method for calculation of theoretical load distributions for arbitrary lifting surface arrangements at subsonic speeds. *NASA Tech. Note D-5335*

Bracken ER. 2000. Private Communication

Bradley RG. 1981. *Practical aerodynamic problems—military aircraft*. Presented at Transonic Perspective, NASA Ames Research Center, CA

Buchholz MD. 2002. *Highlights of the JSF X-35 STOVL jet effects test effort*. Presented at Biennial International Powered Lift Conf. AIAA Pap. 2002–5962, Williamsburg, VA

Buckner JK, Hill PW, Benepe D. 1974. *Aerodynamic design evolution of the YF-16*. Presented at Aircraft Design, Flight Test, and Operations Meet., 6th, AIAA Pap. 74–935, Los Angeles, CA

Buckner JK, Webb JB. 1974. *Selected results from the YF-16 wind-tunnel test program*. Presented at Aerodynamic Testing Conference, 8th, AIAA Pap. 74–619, Bethesda, MD

Cleveland FA. 1970. Size effects in conventional aircraft design. *J. Aircraft* 7:483–512

Cowley WL, Levy H. 1918. *Aeronautics in Theory and Experiment*. London: Edward Arnold, Publisher

Englar RJ. 1987. Circulation control technology for powered-lift STOL aircraft. *Lockheed Horizons* 24:44–55

Ferris JC. 1977. Wind-tunnel investigation of a variable camber and twist wing. *NASA Tech. Note D-8457*

Gato W, Masiello MF. 1987. *Innovative aerodynamics: the sensible way of restoring the growth capability of the EA-6B Prowler*. Presented at Appl. Aerodynamics Conf., 5th, AIAA Pap. 87–2362, Monterey, CA

Goodmanson LT, Gratzer LB. 1973. Recent advances in aerodynamics for transport aircraft. *Aeronaut. Astronaut.* 11(12):30–45

Green W. 1970. *The Warplanes of the Third Reich*. Garden City, NJ: Doubleday & Company

Hanley RJ. 1987. Development of an airplane modification to improve the mission effectiveness of the EA-6B airplane. Presented at Appl. Aerodynamics Conf., 5th, AIAA Pap. 87–2358, Monterey, CA

Hehs E. 1998a. F-22 design evolution. *Code One Magazine* 13(2)

Hehs E. 1998b. F-22 design evolution, part II. *Code One Magazine* 13(4)

Hehs E. 2000. JSF diverterless supersonic inlet. *Code One Magazine* 15(3)

Hehs E. 2001. Going vertical—X-35B flight testing. *Code One Magazine* 16(3)

Hehs E. 2007. F-35 Lightning II flight tests. *Code One Magazine* 22(2)

Hillaker HJ. 1982. A supersonic cruise fighter evolution. Paper 14

Hillaker HJ. 1997. Private Communication

Jobe CE, Kulfan RM, Vachal JC. 1978. *Application of laminar flow control to large subsonic military transport airplanes*. Presented at Aerosp. Sci. Meet., 16th, AIAA Pap. 78–0095, Huntsville, AL

Jordan FL, Hahne DE, Masiello MF, Gato W. 1987. *High-angle-of-attack stability and control improvements for the EA-6B Prowler*. Presented at Appl. Aerodynamcis Conf., 5th, AIAA Pap. 87–2361, Monterey, CA

Kosin RE. 1965. Laminar flow control by suction as applied to the X-21A aircraft. *J. Aircraft*. 2:384–390

Mann A. 2006. The Modelling and Design of Modern Winglets, M-DAW, Aeronautics Days, Vienna Austria

McLean D. 2005. Wingtip devices: what they do and how they do it. Presented at Boeing Performance and Flight Operations Engineering Conf., Article 4, St. Louis, MO

McMasters JH, Kroo IM. 1998. Advanced configurations for very large transport airplanes. *Aircraft Design* 1:217–242

Meyer RC, Fields WD. 1978. *Configuration development of a supersonic cruise strike-fighter*. Presented at Aerosp. Sci. Meet., 16th, AIAA Pap. 78–0148, Huntsville, AL

Montulli LT. 1986. *Lessons learned from the B-52 program evolution: past, present, and future*. Presented at Aircraft Systems, Design, and Tech. Meet., AIAA Pap. 86–2639, Dayton, OH

Morgan HL. 1975. A computer program for the analysis of multielement airfoils in two-dimensional subsonic, viscous flow. *NASA Spec. Pub. 347*

Mullin SN. 1992. *The evolution of the F-22 Advanced Tactical Fighter*. Presented at Aircraft Design Systems Meet., AIAA Pap. 92–4188, Hilton Head Island, SC

Nicholas WU, Naville GL, Hoffschwelle JE, Huffman JK, Covell PF. 1984. *An evaluation of wing-canard, tail-canard, and tailless arrangements for advanced fighter applications*. Presented at Congress of the Intern. Council of the Aeronaut. Sci., ICAS Pap. 84–2.7.3, Tolouse, France

Nipper MJ. 1996. Private Communication

Olason ML, Norton DA. 1966. Aerodynamic design philosophy of the Boeing 737. *J. Aircraft* 3:524–528

Olsen LE, Dvorak FA. 1976. *Viscous/potential flow about multi-element two-dimensional and infinite-span swept wings: theory and experiment*. Presented at the Aerosp. Sci. Meet., 14th, AIAA Pap. 76–18, Washington, DC

Peters CE, Roos HN, Graber GL. 2001. Private Communication

Schlichting H. 1960. Some developments in boundary layer research in the past thirty years. *J. Roy. Aeronaut. Soc.* 64(590):4–79

Schlichting H, Truckenbrodt E. 1969. *Aerodynamik des Flugzeuges*. Berlin: Springer Verlag

Sewall WG, McGhee RJ, Ferris JC. 1987. *Wind-tunnel test results of airfoil modifications for the EA-6B*. Presented at the Appl. Aerodynamics Conf., 5th, AIAA Pap. 87–2359, Monterey, CA

Skelley ML, Langham TF, Peters WL, Frantz BG. 2007. *Lessons learned during the Joint Strike Fighter ground testing and evaluation at AEDC*. Presented at USAF T&E Days. AIAA Pap. 2007–1635, Destin, FL

Skow AM. 1992. Agility as a contributor to design balance. *J. Aircraft* 29:34–46

Smith AMO. 1975. High-lift aerodynamics. *J. Aircraft* 12:501–530

Smith SC, Kroo IM. 1993. Computation of induced drag for elliptical and crescent-shaped wings. *J. Aircraft* 30: 446–452

Stevens WA, Goradia SH, Braden JA. 1971. Mathematical model for two-dimensional multi-component airfoils in viscous flow. *NASA Cont. Rep. 1843*

Streit T, Himisch J, Heinrich R, Nagel B, Horstmann KH, Liersch C. 2008. Design of a retrofit winglet for a transport aircraft with assessment of cruise and ultimate structural loads. *Notes on Numerical Fluid Mechanics and Multidisciplinary Design*. 96: 62–70

Streit T, Ronzheimer A, Büscher A. 2006. Numerical analysis of transport aircraft using different wing tip devices. *Notes on Numerical Fluid Mechanics and Multidisciplinary Design.* 92:59–68

Thomas ASW. 1985. Aircraft drag reduction technology. *AGARD Report 723* (Quotations from this reference are reproduced by permission of AGARD and ASW Thomas, Lockheed Aeronautical Systems Company, Georgia Division)

van Dam CP. 1987. Induced-drag characteristics of crescent-moon-shaped wings. *J. Aircraft* 24: 115–119

van Dam CP, Vijgen PMHW, Holmes BJ. 1991. Experimental investigation on the effect of crescent planform on lift and drag. *J. Aircraft* 28: 713–730

Waggoner EG, Allison DO. 1987. *EA-6B high-lift wing modifications*. Presented at the Appl. Aerodynamics Conf., 5th, AIAA Pap. 87–2360, Monterey, CA

Weeks TM. 1986. *Advanced technology integration for tomorrow's fighter aircraft*. Presented at the Aircraft Systems, Design, and Tech. Meet., AIAA Pap. 86–2613, Dayton, OH

Wentz WH, Seetharam FC. 1974. Development of a Fowler flap system for a high performance general aviation airfoil. *NASA Cont. Rep. 2443*

Whitcomb RT. 1976. A design approach and selected wind tunnel results at high subsonic speeds for wing-tip mounted winglets. NASA TN-D-8260

Whitford R. 1991. Four decades of transonic fighter design. *J. Aircraft* 28:805–811

Whitford R. 1996. Fundamentals of fighter design, part I – requirements. *Air International* 52(1):37–43

Wooden PA, Azevedo JJ. 2006. *Use of CFD in developing the JSF F-35 outer mold lines*. Presented at Appl. Aerodyn. Conf., 24th, AIAA Pap. 2006–3663, San Francisco, CA

14 TOOLS FOR DEFINING THE AERODYNAMIC ENVIRONMENT

Chapter Objectives

- Learn about the primary ways to determine the aerodynamics of a vehicle
- Understand the value and limitations of semi-empirical methods
- Be able to determine which levels of computational aerodynamic tools are appropriate for determining various aerodynamic characteristics (e.g., stall, cruise drag, cruise lift)
- Know the advantages of ground-based experimental testing, as well as the limitations and inaccuracies
- Learn about the positive and negative aspects of flight testing

Aircraft designers have a wide variety of tools available to them for understanding the aerodynamics of a vehicle. We will divide the tools into two categories:

- Analytical tools, which include exact analytical solutions, empirical-based conceptual design codes, and computational fluid dynamics (CFD) codes
- Experimental programs, which employ either ground-based test facilities (e.g., wind tunnels) or flight tests

Most aircraft designers use both analytical tools and experimental programs to define the configurations that could meet their mission requirements (range, payload, costs, maintainability, etc.). The division between the usage of analytical tools and experimental programs depends on the organization's history of design practices (i.e., experience), on the facilities (computational and experimental) available to the designers, and on the personnel resources of the organization.

Kafyeke and Mavriplis (1997) noted: "The approach to aircraft design has traditionally been based on wind tunnel testing with flight testing being used for final validation. CFD emerged in the late 1960s. Its role in aircraft design increased steadily as speed and memory of computers increased. Today CFD is a principal aerodynamic technology along with wind tunnel testing and flight testing. State-of-the-art capabilities in each of these technologies are needed to achieve superior performance with reduced risk and low cost." This last sentence recommending that state-of-the-art capabilities are needed in each of these three areas to achieve superior performance (with reduced risk and low cost) is a key to the designers' success.

The assumptions that we can make for a steady, low-speed flow of a viscous fluid in an infinitely long, two-dimensional channel of height h, or in an infinitely long circular pipe, allow us to obtain exact solutions to the simplified governing equations. Examples of these flows, which are called Poiseuille flow, Couette flow, etc., appear in Chapter 2. Such applications provide us with important practice in developing the governing equations, in specifying the boundary conditions, and in solving viscous flow problems. However, they have limited practical use for aircraft design applications.

Rapid advances in computer hardware and in computer software have enabled designers to use relatively sophisticated CFD codes to generate flow-field solutions for realistic aerodynamic configurations. However, CFD is not purely theoretical analysis. CFD changes the fundamental nature of the analysis from calculus to arithmetic and from the continuum domain to the discrete domain so that the problem of interest can be solved using a computer. The existing mathematical theory for numerical solutions of nonlinear partial differential equations is continually being improved. The computational fluid dynamicist often relies on the mathematical analysis of simpler, linearized formulations, and on heuristic reasoning, physical intuition, data from experimental programs, and trial-and-error procedures. Furthermore, the numerical algorithms that are chosen depend heavily on the dominant physics of the specific application.

Therefore, even the most rigorous CFD codes employ models and approximations both for physical properties and for fluid dynamic processes (such as turbulence). The approximations range from the model used to generate numerical values for the absolute viscosity as a function of pressure and temperature to the numerical algorithm used to model the turbulent boundary layer. It is important to keep in mind that turbulence models are not universal. One turbulence model may provide reasonable values for the engineering parameters for a particular class of flows, but not work well for another type of flow. See Chapter 4 for a brief discussion of turbulence models.

As noted by Shang (1995): "As an analog, the ground testing facilities can easily measure the global aerodynamic force and moment exerted by the flow field on the tested model. Once a scaled model is installed in the test section, the data-generating process is the most efficient among all simulation techniques. Therefore, for a large class of design problems, the ground testing method is preferred over others. However, like

CFD, experimental simulation does not necessarily reproduce accurate results in flight. The inherent limitation is derived from the principle of dynamic similarity—the scaling rule. Even if a perfect match to flight conditions is reached in dimensionless similarity parameters of Mach, Reynolds, and Eckert numbers, the small-scale model still may not describe the fine-scale surface features. If the flow fields under study are strongly influenced by fine-scale turbulence and laminar-turbulent transition, the accuracy of simulations to flow physics is uncertain."

Although testing in ground-based facilities can deliver prodigious amounts of quality data, the ability to extrapolate the information obtained to the flight environment may be affected by shortcomings in the simulation of the flow. Data obtained in ground-based test facilities may be affected by model scale. As a result, we may fail to match critical simulation parameters (e.g., the Reynolds number). Only a full-scale vehicle flying at the desired velocity, the desired altitude, and the desired attitude (i.e., its orientation with respect to the free-stream velocity vector) provides information about the aerodynamic parameters in the true environment. However, flight-test experiments present considerable challenges to define the free-stream conditions with suitable accuracy (especially for high-altitude flights at hypersonic speeds). Furthermore, because of their size, their weight, and their fragile nature, many of the types of instrumentation available to the wind-tunnel-test engineer are not available to the flight-test engineer.

14.1 COMPUTATIONAL TOOLS

There are a wide variety of analytical/computational tools that incorporate flow models of varying degrees of rigor available to the aircraft designer. Some readers of this text will participate in the development of their organization's CFD codes; a large fraction of the readers will have had no role in the development of the CFD codes that they use. Often multiple organizations participate for several years in the development of a single code. Whether you are developing your own code or using a code that was developed elsewhere, it is important that you understand (1) the grid scheme that is used to represent the body and the grid scheme that is used in the solution of the flow field; (2) the numerical algorithms used to obtain the flow-field solution; and (3) the models used to represent fluid mechanic phenomena, thermochemical phenomena, and flow properties. In this section, we will discuss these analytical/computational tools in their increasing order of sophistication.

14.1.1 Semiempirical Methods

There are a large number of codes that employ semiempirical, data-based methods that are used for preliminary design purposes. An example of a semiempirical code, which uses a combination of theoretical methods with nonlinear corrections for the body and an extensive experimental database for wing and tail fin loads, is the MISL3 code, developed by Lesieutre et al. (1989). As Mendenhall et al. (1990) discuss, "The data base inherently includes viscous and compressibility effects as well as fin-body gap effects. . . . Mutual interference between control surfaces is also considered in the data base." The MISL3 code is limited to applications of Mach 5 or less.

There is a variety of conceptual design codes for predicting the aerothermodynamic environment for configurations in hypersonic flows (i.e., Mach numbers of approximately 5 or greater). One such code is the Supersonic/Hypersonic Arbitrary Body Program (S/HABP) [Gentry et al. (1973)]. In the first step, the vehicle geometry is divided into flat elemental panels. Frequently used techniques for computing the inviscid pressure acting on a panel employ one of the many simple techniques based on impact or on expansion methods. Once the pressure distribution has been determined, boundary-layer correlations are used to estimate the skin friction and the heat transfer acting at the vehicle surface. The local pressures and the local skin-friction forces can be integrated to compute estimates of the resultant forces and moments acting on the vehicle. These types of methods have been widely used over the years on a variety of aircraft programs.

14.1.2 Surface Panel Methods for Inviscid Flows

As the level of complexity of the flow increases, more detailed information is needed. Therefore, numerical codes using panel surface methods, or surface singularity methods, have been under development since the 1960s. These panel surface methods use the linearized/potential flow equations we discussed in Chapter 3. Panel surface method codes for subsonic flows are discussed in Chapter 7 and for supersonic flows are discussed in Chapter 11.

For subsonic flows, vortex lattice methods (VLMs) combine the basic building blocks of the constant source panel and the vortex lattice methods, representing thickness effects with source panels and lift effects with vortex panels (see Chapter 7). Every panel has some form of source singularity imposed upon it, whether it is a lifting or nonlifting component. Lifting components have vortex singularities imposed upon them or interior to them. There are an infinite number of combinations of vortex singularity variations that will provide lift and satisfy the boundary conditions. Therefore, a numerical technique must be developed to generate a unique solution. This is done by prescribing an assumed chordwise variation and spanwise variation of vortex strength, then solving both for the source strengths and for the vortex strengths, subject to the Kutta condition. The particular variation of the vortex singularity chosen impacts the resulting magnitudes of the source strengths. An improper choice can lead to large source gradients and inaccuracies in the solution.

For each of the control points in the lattice, the velocities induced at that control point by each of the panels of the configuration are summed, resulting in a set of linear algebraic equations which express the exact boundary condition of flow tangency on the surface. The local velocities are then used to compute the static pressure acting on each of the panels. These pressures are then integrated to obtain the forces and the moments.

The PAN AIR code was developed to model both subsonic and supersonic linear potential flows about arbitrary configurations [Towne et al. (1983)]. The Prandtl-Glauert equations [the reader should refer to equation (9.13)] represent inviscid, compressible, subsonic/supersonic, irrotational, isentropic, small perturbation flows. PAN AIR uses a linear source distribution and a quadratic doublet distribution on each panel to reduce the number of panels needed to attain a given accuracy. The flexibility of the PAN AIR code provides the user with a great deal of freedom and capability in modeling linear potential flow problems.

Everson et al. (1987) noted that "panel methods have long been able to handle complex configurations and boundary conditions, but they are limited to linear flows." Thus, TRANAIR was developed to solve the full potential equation about arbitrary configurations. The key to the ability to handle complex configurations is the use of a rectangular grid rather than a surface fitted grid. Therefore, the grid is defined by a hybrid method employing both *surface panels* and a grid containing points away from the surface where solutions to the flow field parameters are generated.

Since the VLM, the PAN AIR code, and the TRANAIR code all are inviscid codes, they do not model the boundary layer. So, these codes do not provide estimates for the skin-friction component of the drag coefficient. Furthermore, they do not model the shock-wave/boundary-layer interactions that produce the separation-induced-drag component of the drag coefficient at transonic speeds. However, these codes provide reasonable estimates of the wave drag for supersonic flows. The lift and pitch moment coefficients generated using these codes are best for low angles of attack (i.e., cruise applications). Furthermore, because only a surface discretization scheme is required, very complex configurations can be modeled in which the panel density is adjustable to the desired accuracy. Therefore, since the computational intensity for panel methods is very low, the cost of computing the lift and pitch moment is relatively inexpensive for those conditions where these methods are applicable.

14.1.3 Euler Codes for Inviscid Flow Fields

Neglecting the viscous terms in the Navier-Stokes equations (see Appendix A) provides the analyst with the Euler equations to model the flow field. Since the Euler equations neglect all viscous terms, the solutions cannot be used to compute either the shear forces or the heat transfer to the surface of the vehicle. However, they can provide solutions for the unsteady, inviscid flow field over the configuration in either subsonic, transonic, or supersonic streams. Therefore, Euler codes can be used to compute engineering estimates of the lift and pitch moment. In comparison with panel methods, one of the difficulties of numerically solving the Euler equations involves generating a body-fitted, discrete grid about the configuration geometry (i.e., a grid that is curved to follow the contours of the body). The job of creating a surface definition for a complicated three-dimensional geometry that is needed for panel methods is much easier than the generation of a body-fitted grid that is needed for an Euler-based code.

Rapid developments of grid-generation tools support the growing use of Euler codes. Therefore, Euler codes are available to even the smallest design groups due to the ever-improving capabilities of computational hardware and software. Since the costs for use continue to decrease, more and more organizations are using Euler codes to generate the lift and pitch moment for those applications where these aerodynamic coefficients were formerly computed using the surface panel methods described in the previous paragraphs.

14.1.4 Two-Layer Flow Models

If we want to estimate the shear forces and the heat transfer to the surface of the vehicle, we can use computations based on a two-layer flow model. As noted in the prologue for Chapter 4, for many high Reynolds number flows, the flow field may be divided into

two regions: (1) a viscous boundary layer adjacent to the surface and (2) the essentially inviscid flow outside of the boundary layer. Therefore, in the two-layer flow model, the Euler technique or a panel method can be used to generate the inviscid portion of the flow field and, therefore, the boundary conditions at the outer edge of the boundary layer. The two velocity boundary conditions at the wall are defined by the no-slip condition ($u = 0$) and by the assumption that either there is no flow through the wall ($v = 0$) or a transpiration boundary condition. The temperature boundary condition at the wall that is required for high-speed flows is either that the wall temperature (T_W) is given (isothermal) or that there is no heat transfer to the wall [i.e., the adiabatic-wall assumption ($\partial T/\partial y = 0$)]. A solution for the boundary layer is computed subject to these boundary conditions and the transition/turbulence models. An iterative procedure is used to compute the flow field using the two-layer model. To start the second iteration, the inviscid flow field is recalculated, replacing the actual configuration by the *effective configuration*. The effective configuration is determined by adding the displacement thickness of the boundary layer as computed during the first iteration to the surface coordinate of the actual configuration. The boundary layer is recalculated using the second-iterate inviscid flow field as the boundary condition.

Two-layer flow models can be used for applications where the viscous boundary layer near the surface is thin and does not significantly alter the inviscid-region flow field. Therefore, this procedure would not apply to flow fields for which there are shock-wave/boundary-layer interactions or significant regions of separated flow. So, the two-layer method would not be the proper tool to generate solutions for a transonic flow, where shock-wave/boundary-layer interactions cause the boundary layer to separate or for flows where the vehicle is at large angles of attack, so that there are extensive regions of separated flow.

14.1.5 Computational Techniques That Treat the Entire Flow Field in a Unified Fashion

Because of the limitations described in the previous paragraphs, the ultimate computational tool treats the entire flow field (both the viscous regions and the inviscid regions) in a unified fashion. Starting with the Navier-Stokes equations (see Appendix A), we can develop a code that treats the entire flow field in a unified fashion. Li (1989) stated, "The CFD code development and application may follow seven steps:

1. Select the physical processes to be considered.
2. Decide upon the mathematical and topographical models.
3. Build body geometry and space grid.
4. Develop a numerical solution method.
5. Incorporate the above into a computer code.
6. Calibrate and validate the code against benchmark data.
7. Predict aerodynamic coefficients, flow properties, and aeroheatings."

Every code that is used to compute the flow field requires a definition of the geometric characteristics of the vehicle and a grid scheme to identify points or volumes within the flow field. There are a number of techniques that have been developed for

generating the computational grids that are required in the finite-difference, the finite-volume, and the finite-element solutions of the equations for arbitrary regions.

Grids may be structured or unstructured, and there are no a priori requirements on how grids are to be oriented. However, in some cases, the manner in which the flow-modeling information is formulated may influence the grid structure. For instance, since turbulence models are often formulated in terms of the distance normal to the surface, the grid schemes utilized for these turbulent boundary-layer models employ surface-oriented coordinates, where one of the coordinate axes is locally perpendicular to the body surface.

The use of adaptive grid techniques is a grid-generation strategy that can be used both with structured and unstructured grids. Adaptive grid techniques might be applied to portions of the flow field where accurate numerical solutions require the resolution of events within extremely small distances. Often such resolution requirements lead to the use of very fine grids and lengthy computations. Aftosmis and Baron (1989) state, "Adaptive grid embedding provides a promising alternative to more traditional clustering techniques. This method locally refines the computational mesh by sub-dividing existing computational cells based on information from developing solutions. By responding to the resolution demands of chemical relaxation, viscous transport, or other features, adaptation provides additional mesh refinement only where actually required by the developing solution." Grid-clustering strategies also provide a valuable tool, when shock-capturing formulations are employed.

A variety of assumptions and simplifications may be introduced into the computational models that are used to treat the flow field in a unified fashion. For instance, as noted by Deiwert et al. (1988), when there is no flow reversal and when the inviscid portion of the flow field is supersonic in the streamwise direction, the Navier-Stokes equations can be simplified by neglecting the streamwise viscous terms. By neglecting the unsteady terms and the streamwise viscous derivative terms in the full Navier-Stokes equations, we can obtain the *parabolized* Navier-Stokes (PNS) equations. These are reasonable assumptions for large Reynolds number flows over bodies which do not experience severe geometric variations in the streamwise direction. Therefore, a practical limitation for the PNS method is that there is no streamwise separation, but crossflow separation is allowed. These PNS equations are used to compute the shock-layer flow field for certain high-Mach-number flows. If we assume that the viscous, streamwise derivatives are small compared with the viscous, normal, and circumferential derivatives, a tremendous reduction in computing time and in storage requirements is possible over that required for the time-dependent approaches. Since the equations are parabolic in the streamwise direction, a spatial marching-type numerical-solution technique can be used. A PNS code requires a starting solution to generate the initial conditions on a surface where the inviscid portion of the flow is supersonic. Mendenhall et al. (1990) used an Euler code to generate the starting conditions for the region of the flow field modeled by the PNS formulation.

14.1.6 Integrating the Diverse Computational Tools

The aerodynamic design of the Pegasus^{TM} launch vehicle was based on proven techniques developed during the design of existing vehicles. No wind-tunnel tests were included in the program. However, readily available computational codes were used for all

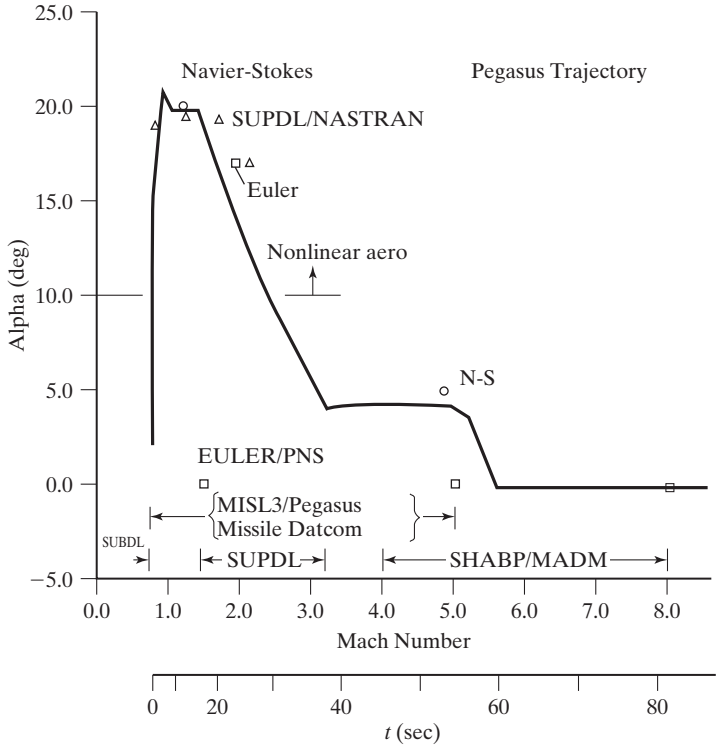

Figure 14.1 Aerodynamic analysis flight envelope; CFD tools used for α/M_∞ space for the Pegasus™ [from Mendenhall et al. (1990)].

aerodynamic analyses. As shown in Fig. 14.1, all levels of codes, ranging in complexity from empirical data-based methods to three-dimensional Navier-Stokes codes, were used in the program to develop the aerodynamic design of the Pegasus™ [Mendenhall et al. (1990)]. A PNS code was used to predict fuselage pressure distributions; an axisymmetric Navier-Stokes code was used to explore the possibility of rocket-plume-induced separation near the tail control surfaces; and a three-dimensional code was used to compute the complete flow field for critical conditions to check details of the flow, which may have been missed by the simpler methods. The CFD results were used to compute the aerodynamic heating environment in the design of the thermal protection system.

However, this approach did not prove to be completely adequate. The initial launches were successful, and it appeared that the accuracy of the aerodynamic analysis was acceptable for this unmanned vehicle. However, after a subsequent launch failure, a dispute arose over whether the aerodynamics had been adequately predicted, or whether the control system was too sensitive to imperfections in the aerodynamic model (the problem was determined to be in the lateral-directional aerodynamic characteristic of the vehicle, something which the methods of the day predicted to be slightly stable, while the actual vehicle turned out to be slightly unstable). Understanding the uncertainties in the analysis required careful evaluation since no prediction is exact.

14.2 ESTABLISHING THE CREDIBILITY OF CFD SIMULATIONS

Neumann (1988) notes, "The codes are NOT an end in themselves. . . . They represent engineering tools; tools that require engineering to use and critical appraisal to understand. Hypersonics must be dominated by an increased understanding of fluid mechanic reality and an appreciation between reality and the modeling of that reality. CFD represents the framework for that modeling study and experiments represent the technique for introducing physical reality into the modeling process. Finally, classical analytical theory and the trend information produced by theory gives us the direction with which to assemble the point data from these numerical solutions in an efficient and meaningful way."

Shang (1995) notes: "Poor numerical approximations to physical phenomena can result from solving over-simplified governing equations. Common mistakes have been made in using Euler equations to investigate viscous dominated flows, and employing the thin-layer approximation to Navier-Stokes equations for flowfield containing catastrophic separation. Under these circumstances, no meaningful quantification of errors for the numerical procedure can be achieved. The physically correct value and the implementation of initial and/or boundary conditions are another major source of error in numerical procedures in which the appropriate placement and type of boundary/initial conditions have a determining effect on numerical accuracy."

As suggested by Barber (1996), we will "focus on the issues of accuracy and achieving reduced variability (robustness), wherein a range of physical processes and a variety of desired outcomes can occur. Most organizations seek to achieve this goal by performing validation or certification studies. When the end-user is a research group, the metrics for evaluating the accuracy of the code (the desired outcomes) are typically fundamental flow variables (streamlines, velocity profiles, etc.). However, when the end-user is a member of a design team, the metrics are more performance oriented, e.g. lift and drag coefficients, system efficiency, etc. The central basis of the validation process is benchmarking, whereby a limited number of numerical predictions are made and compared to experimental data. Even though one successfully performs such calculations, the choice of cases frequently is not appropriate for minimizing the risk of faulty data for a given design process. Significant risks can be introduced by, for example, poorly defined design requirements. This can occur from a failure to choose the test cases (validation/calibration) from an operational or end-user perspective, but instead choosing them from a research perspective."

Bradley (1988) defined the concepts of *code validation* and *code calibration* as follows.

> "CFD code validation implies detailed surface and flow field comparisons with experimental data to verify the code's ability to accurately model the critical physics of the flow. Validation can occur only when the accuracy and limitations of the experimental data are known and thoroughly understood and when the accuracy and limitations of the code's numerical algorithms, grid-density effects, and physical basis are equally known and understood over a range of specified parameters.
>
> CFD code calibration implies the comparison of CFD code results with experimental data for realistic geometries that are similar to the ones of design interest,

made in order to provide a measure of the code's ability to predict specific parameters that are of importance to the design objectives without necessarily verifying that all the features of the flow are correctly modeled."

To the two definitions for *validation* and *calibration*, Barber (1996) and Rizzi and Vos (1996) add the terms *verification* and *certification*. Verification establishes the ability of a computer code to generate numerical solutions for the specific set of governing equations and boundary conditions. Through the verification process, the accuracy of the solution and the sensitivity of the results to parameters appearing in the numerical formulation are established through purely numerical experiments. These numerical experiments include both grid-refinement studies and comparison with solutions to problems that have exact analytical solutions.

Certification relates to programming issues (e.g., logic checks, programming style, documentation, and quality assurance issues). Therefore, certification test cases are run before a new version of the code is released in order to be certain that no new errors have been introduced into the previously certified version.

Rizzi and Vos (1996) note that the code developers are responsible for building a credible code and verifying and certifying that code. Experts with a strong background in developing numerical models to represent physical processes carry out the tasks of validating and of calibrating the code. The code is then passed on to the users, who are experts neither in code development nor in numerical modeling.

Cosner (1995) suggests that "a range of test cases is analyzed which illustrates the various outcomes which can be expected across the design range of interest. Also, a set of standard practices usually are defined, to be used throughout the validation study. The skill level of the user should be representative of the engineering (user) environment. Therefore, it is preferable that this validation should be performed by representative engineers from the user community, not by the experts in the code or technology which is being tested."

Cosner (1995) also notes, "Computational Fluid Dynamics technology, as a basis for design decisions, is rapidly gaining acceptance in the aerospace industry. The pace of acceptance is set by the advancing confidence of design team leaders that reliance on CFD can improve the quality of their end product, and reduce the schedule, costs and risks in developing that product." Barber (1996) concluded, "Risk reduction to an engineering design team is rooted in (sic) a determination to deliver *reliable* engineering data having a specified level of *accuracy*, in a specified *time*, and for a specified *cost*."

Bradley (1995) has said, "Engineers have always been able to use less than perfect tools coupled with experiences and calibration to known physical quantities to provide design guidance. Calibration and validation should not be confused. Calibration provides an error band or correction factor to enhance the ability of a particular code to predict specific parameters that are important to the design objectives for a particular design without verifying that all other features of the flow are modeled accurately. For example, one might calibrate a code's ability to predict shock location and lift and moment on a wing without any assurance that the flowfield off the surface and the wake behind the wing are properly modeled. Or one may calibrate a code's ability to compute the gross pressure loss through a supersonic inlet-duct combination without concern for the distortion distribution at the compressor face. Although the use of calibrated CFD

solutions is dangerous because of the subtle viscous interactions that are extremely sensitive to geometry and flowfield, skilled engineers can often obtain useful design information and guidance from relatively immature codes."

14.3 GROUND-BASED TEST PROGRAMS

A large fraction of the relevant experimental information about flow fields of interest to the aerodynamicist is obtained in ground-based test facilities. Since complete simulations of the flow field are seldom obtained in a ground-based facility, the first and most important step in planning a ground-based test program is establishing the test objectives. As stated by Matthews et al. (1985), "A precisely defined test objective coupled with comprehensive pretest planning are essential for a successful test program."

There are many reasons for conducting ground-based test programs. The test objectives include the following:

- Obtain data defining the aerodynamic forces and moments and/or heat-transfer distributions (especially for complete configurations whose complex flow fields resist computational modeling).
- Use partial configurations to obtain data defining local flow phenomena, such as shock-wave/boundary-layer interactions, using a fin or a wing mounted on a plane surface.
- Determine the effects of specific design features on the overall aerodynamic coefficients of the vehicle (e.g., the drag increment due to protuberances of the full-scale aircraft).
- Certify airbreathing engines in ground-based test programs.
- Obtain detailed flow-field data to be used in developing flow models for use in a computational algorithm (i.e., tests to obtain code-validation data).
- Obtain measurements of parameters, such as the heat transfer or the total drag, to be used in comparison with computed flow field solutions over a range of configuration geometries and of flow conditions (i.e., tests to obtain code-calibration data).

As noted in Chapter 13, Lockheed, Boeing, and General Dynamics used 20,000 hours in the wind tunnel during the demonstration/validation design phase for the Advanced Technology Fighter. Therefore, even for a relatively recent design activity, considerable resources were spent on wind-tunnel programs to achieve the first objective in the preceding list.

Niewald and Parker (2000) noted that the drag increment due to the protuberances on the full-scale aircraft is significant and must be included during the database development phase. "An extensive effort was made to identify and estimate the drag of all protuberance items. The design process included continuous tracking of all outer moldline protuberances to facilitate trade studies. There were 94 types of protuberances, resulting in a total of 386 individual protuberance items. The items included external fasteners of various types, which numbered 88,340, and skin panel gaps totaling 2,180 ft in length. Outer moldline surveys of production F/A-18C aircraft were used to determine the percentage of gaps that would be forward or aft facing. The large model scale permitted testing of the most significant protuberance items (see Fig. 14.2). Seventy-one percent of the

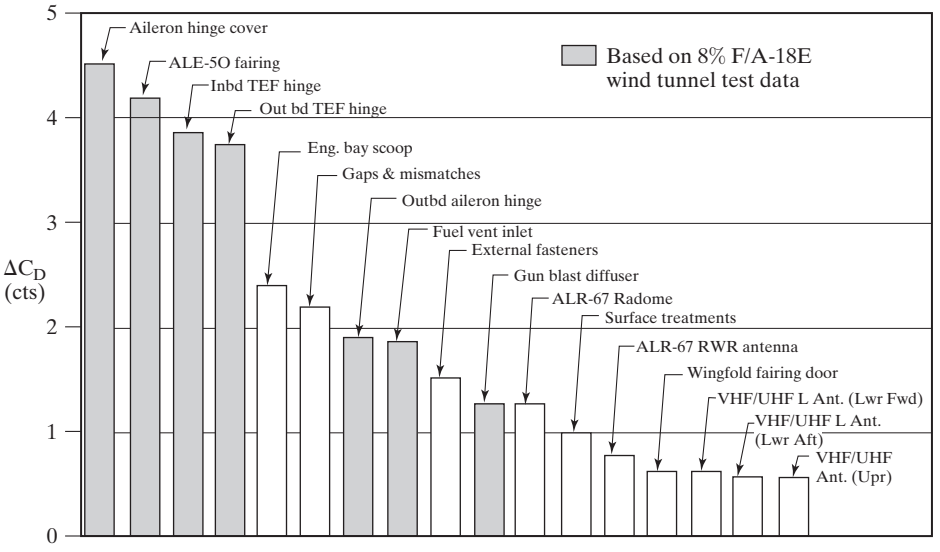

Figure 14.2 Protuberance drag for the F/A-18E [from Niewald and Parker (2000)].

F/A-18E protuberance drag was based on wind-tunnel test data." When using Fig. 14.2, the reader should note that *one drag count* corresponds to a drag coefficient of 0.0001.

Niewald and Parker (2000) concluded, "Development of a credible preflight database for accurate aircraft predictions requires commitment and resources. The success of the F/A-18E/F wind-tunnel program was a direct result of both of these. The commitment was made at the outset to develop and implement test techniques that would properly account for each item impacting aircraft performance either by wind-tunnel testing or by estimation. Adequate resources allowed the development of high-fidelity models, use of large, interference-free wind-tunnels, comprehensive test programs, and integration of CFD methods to ensure first-time quality test results. Front loading the project resources to the wind-tunnel program were beneficial to the subsequent performance flight test program. The excellent agreement between wind-tunnel and flight results allowed the performance flight evaluation plan to be reduced by 60 flights and eliminated aircraft development flight testing for drag reduction as a result of optimistic predictions."

The planner of a ground-based test program should consider the following parameters:

- the free-stream Mach number,
- the free-stream Reynolds number (and its influence on the character of the boundary layer),
- the free-stream velocity,
- the pressure altitude,
- the wall-to-total temperature ratio,
- the total enthalpy of the flow,

- the density ratio across the shock wave,
- the test gas, and
- the thermochemistry of the flow field.

You should realize that some of these nine parameters are important only for hypersonic flows (e.g., the density ratio across the shock wave, the test gas, and the thermochemistry of the flow field).

Notice that some parameters are interrelated (e.g., the free-stream velocity, the free-stream Mach number, and the free-stream Reynolds number). For example, you should review the discussion relating to skin friction in Chapter 5. Most often, the boundary layer is turbulent over the majority of the aircraft in flight. However, wind-tunnel models are usually of relatively small scale. In such cases, the Reynolds number is relatively low for conventional wind tunnels and the boundary layer may be laminar or transitional. This may not be critical if the objective of the test is to generate lift and/or pitch moment data at low angles of attack. However, for determining the onset of stall or for estimating drag, simulation of the Reynolds number is much more important.

Laster et al. (1998) note: "Experience has shown that lift and pitching moments are usually not too sensitive to Reynolds number up to the onset of buffet; but, buffet boundary, maximum lift, drag, and drag rise are usually very sensitive to Reynolds number. Therefore, the aircraft developer is faced with accounting for Reynolds number effects with these parameters as best he/she can. The usual practice is to use a combination of test techniques and empirical corrections. Because of little sensitivity of lift and pitching moment to Reynolds number below buffet onset, in most cases, the engineer has been able to directly use low Reynolds number wind tunnel measurements of lift and pitching moment in his/her design without having to resort to Reynolds number corrections. However, this is not necessarily true for wings with high aft loading. Test technique plays an important role in the determination of drag from wind tunnel data. Because the boundary layer is mostly turbulent in flight, experience has shown that forcing the model boundary layer to be turbulent in the wind tunnel makes the task easier in accounting for Reynolds number effects."

Laster et al. (1998) continue, "For accurate calculation of the forces (especially drag), the location of transition of the model boundary layer from laminar to turbulent must be accurately predicted, measured, or fixed. Otherwise, in the case of transonic flow, the shock/boundary-layer interaction cannot be properly modeled. For transition fixing, the prediction of the untripped transition location is important to assure that the boundary-layer trips are placed ahead of the location where transition occurs 'naturally' in the test facility. The transition location is dependent on the pressure gradient, surface roughness, turbulence and/or noise, and instabilities associated with the three-dimensionality of the flow. Therefore, the location of transition is both model- and flow-field dependent."

Complete simulations of the flow field are rarely obtained in any one ground-based facility. In a statement attributed to Potter, Trimmer et al. (1986) noted: "Aerodynamic modeling is the art of partial simulation." Thus, one must decide which parameters are critical to accomplishing the objectives of the test program. In fact, during the development of a particular vehicle, the designers will most likely utilize many different facilities with the run schedule, the model, the instrumentation, and the test conditions for each program tailored to answer specific questions.

Aerodynamics Concept Box: High-speed Testing on a Train Track

The U.S. Air Force 846th Test Squadron operates the Holloman High Speed Test Track (HHSTT) which simulates selected portions of the flight environment under accurately programmed and instrumented conditions. This is accomplished by using a 50,788 ft test track, coupled with high-speed sleds containing various rocket propulsion systems to accelerate the sleds. This capability fills the gap between laboratory investigations and full-scale flight tests.

The 846th Test Suadron upgraded its capability under the "Hypersonic Upgrade Program" and set a world record in 2003, as shown below. The program provides increased velocity capabilities as well as a four-fold improvement in the dynamic environment of sled tests. This improvement not only allows faster test velocities, but also provides a higher fidelity payload capability.

Shocks visible on high-speed test article at Holloman High-Speed Test Track (U.S. Air Force photo)

The world record rocket sled test on the HHSTT obtained a velocity of 9465 ft per second or 6453 mph … over Mach 9! The test validated the program that significantly increased the capabilities at the HHSTT to meet a variety of hypersonic test needs. The test included improvements in rocket sled design, rail alignment, rocket propulsion, and modeling and simulation. The HHSTT is the only ground test facility capable of achieving the speed/payload combinations necessary to simulate full-scale vehicles in flight. A Super Roadrunner (SRR) rocket motor, developed specifically for the program, powered each of the last two stages. The SRR motor produces 228,000-pounds of thrust for 1.4 seconds and only weighs 1100 pounds. The maximum acceleration of the sled was 157-g's or 157 times the force exerted by gravity. When the payload impacted the target, it had 363 megajoules of energy or the energy of a car impacting a brick wall at 2020 mph.

From USAF 846th Test Squadrom fact sheet.

14.4 FLIGHT-TEST PROGRAMS

Neumann (1986) suggests a variety of reasons for conducting flight tests. To the four reasons suggested by Draper et al. (1983), which are:

- to demonstrate interactive technologies and to identify unanticipated problems,
- to form a catalyst (or a focus) for technology,
- to gain knowledge not only from the flights but also from the process of development, and
- to demonstrate technology in flight so that it is credible for larger-scale applications.

Neumann added three reasons of his own:

- to verify ground-test data and/or to understand the bridge between ground-test simulations and actual flight,

- to validate the overall performance of the system, and
- to generate information not available on the ground.

Saltzman and Ayers (1982) wrote, "Although aircraft designers must depend heavily upon model data and theory, their confidence in each should occasionally be bolstered by a flight demonstration to evaluate whether ground-based tools can indeed simulate real-world aerodynamic phenomena. Over the years as the increments of improvement in performance have become smaller and aircraft development costs have risen, casual model-to-flight drag comparisons have sometimes given way to very comprehensive correlation efforts involving even more precise sensors, the careful control of variables, and great attention to detail on behalf of both tunnel experimenters and their flight counterparts."

Lift and drag characteristics for the F/A-18E have been determined throughout the flight envelope via in-flight thrust determination techniques, as reported by Niewald and Parker (1999). Three maneuver types were employed during the flight-test program to establish the aerodynamic database: steady-state maneuvers, quasi-steady-state maneuvers, and dynamic maneuvers. Steady-state maneuvers (e.g., cruise at constant Mach number and constant altitude) yield the most accurate data but require a large amount of flight time and airspace. It takes one minute of stabilization and three minutes of data-acquisition time to define one point on the drag polar using cruise. Quasi-steady maneuvers, such as constant-Mach-number climbs, provide more points for the drag polar definition. However, uncertainty is increased relative to steady-state maneuvers. Dynamic maneuvers, such as the pitch up/pitch down maneuvers, also known as the roller coaster, allow the estimation of aerodynamic characteristics covering a range of angle of attack that cannot be achieved through steady-state maneuvers or quasi-steady-state maneuvers. However, highly accurate instrumentation and data synchronization are required to reduce the potentially large data scatter that may result. As a result of the difficulties with dynamic maneuvers, they were not used in the F/A-18E flight-test program.

14.5 INTEGRATION OF EXPERIMENTAL AND COMPUTATIONAL TOOLS: THE AERODYNAMIC DESIGN PHILOSOPHY

The vehicle design integration process should integrate experimental data obtained from ground-based facilities with computed flow-field solutions and with data from flight tests to define the aerodynamic parameters and the heating environments (the combination of aerodynamic parameters and the heating environments is termed the *aerothermodynamic environments*) to which the vehicle is subjected during its mission.

At the time of this writing, flight tests are relatively expensive. One test point in a store separation flight-test program might cost \$1M. Therefore, an extensive flight-test program of store separation and deployment might cost \$50M. One Research and Development flight test to develop the technology base for a Mach 10 vehicle might cost \$50M itself. Sophisticated wind-tunnel programs for a high-performance vehicle may cost \$250K to \$900K for the model and for the tunnel occupancy costs. To run a code is relatively cheap, say \$50K to generate solutions for a number of flow conditions. And this is the cost once the code has been developed. Furthermore, as has been noted, it might take several years to develop the code to the point where it will deliver the desired computations. In addition, generating grids for the vehicle surface and for the flow field may take months. The grid generation process is a key element in generating

suitable numerical solutions, when using Euler codes or Navier-Stokes codes. Thus, a very crude order of magnitude estimate for the costs might be as follows:

- a flight-test program is two orders-of-magnitude more expensive than a wind-tunnel program, while
- a wind-tunnel-test program is an order-of-magnitude more expensive than a CFD program.

You should be cautioned that these numbers are very approximate and highly dependent on the types of testing being used.

Mullin (1992) noted, "The aeronautical technology changes over 87-years have been enormous; almost beyond description, but the most important factor in successful aeronautical engineering has not changed: making technical decisions based on analysis, test data, and good engineering judgement. Then and now, the paramount obligation of aeronautical engineers is to make critical technical decisions. The increasingly dominant role of digital computers in aircraft design and analysis has tended to confuse some of our engineering colleagues, but the truth of the matter is inescapable."

All of the tools available to the aircraft designer, whether analytical/computational or experimental, require that he or she bring judgment born of experience to the application of these tools in the design process. *Good judgment comes from experience; experience comes from bad judgment.*

14.6 SUMMARY

Aerodynamicists have many "tools" available for predicting and understanding how airplanes will fly. In addition to the analytical approaches discussed throughout this book, there are also computational tools and experimental methods. The advent of high speed computers has made CFD of ever-increasing importance in aerodynamics, and the various ground and flight test capabilities continue to be essential for aerodynamic design. Understanding and being able to use the various "tools" is essential to being a good aerodynamicist.

REFERENCES

Aftosmis MJ, Baron JR. 1989. *Adaptive grid embedding in nonequilibrium hypersonic flow*. Presented at Thermophysics Conference, 24th, AIAA Pap. 89–1652, Buffalo, NY

Barber TJ. 1996. *The role of code validation and certification in the design environment*. Presented at Fluid Dynamics Conference, 27th, AIAA Pap. 96–2033, New Orleans, LA

Bradley RG. 1988. *CFD validation philosophy*. Presented at Validation of Computational Fluid Dynamics Conf., AGARD Conf. Proc. 437, Pap. 1, Lisbon, Portugal

Bradley RG. 1995. Private Transmission

Cosner RR. 1995. *Validation requirements for technology transition*. Presented at Fluid Dynamics Conf., 26th, AIAA Pap. 95–2227, San Diego, CA

Deiwert GS, Strawa AW, Sharma SP, Park C. 1988. *Experimental program for real gas flow code validation at NASA Ames Research Center*. Presented at Validation of Computational Fluid Dynamics Conf., AGARD Conf. Proc. 437, Pap. 20, Lisbon, Portugal

Draper AC, Buck ML, Selegan DR. 1983. *Aerospace technology demonstrators/research and operational options*. Presented at Aircraft Prototype and Technology Demonstrator Symp., AIAA Pap. 83–1054, Dayton, OH

Everson BL, Bussoletti JE, Johnson FT, Samant SS. 1987. *TRANAIR and its NAS implementation*. Presented at the NASA Conf. on Supercomputing in Aerosp., Moffett Field, CA

Gentry AE, Smyth DN, Oliver WR. 1973. The Mark IV supersonic-hypersonic arbitrary-body program. *AFFDL-TR-73–159*

Kafyeke F, Mavriplis F. 1997. *CFD for the design of Bombardier's Global Express*^{R} *high performance jet*. Presented at the Appl. Aerodynamics Conf., 15th, AIAA Pap. 97–2269, Atlanta, GA

Laster M, Stanewsky E, Sinclair FW, Sickles WL. 1998. *Reynolds number scaling at transonic speeds*. Presented at Advanced Measurement and Ground Testing Tech. Conf., 20th, AIAA Pap. 98–2878, Albuquerque, NM

Lesieutre DJ, Dillenius MFE, Mendenhall MR, Torres TO. 1989. Aerodynamic analysis program MISL3 for conventional missiles with cruciform fin sections. *Nielsen Engineering and Research TR 404*

Li CP. 1989. Computations of Hypersonic Flow Fields. In *Hypersonics, Volume II: Computation and Measurement of Hypersonic Flows*, Eds. Bertin JJ, Glowinski R, Periaux J. Boston: Birkhauser Boston

Matthews RK, Nutt KW, Wannenwetsch GD, Kidd CT, Boudreau AH. 1985. *Developments in aerothermal test techniques at the AEDC supersonic-hypersonic wind tunnels*. Presented at Thermophysics Conf., 20th, AIAA Pap. 85–1003, Snowmass, CO

Mendenhall MR, Lesieutre DJ, Caruso SC, Dillenius MFE, Kuhn GD. 1990. Aerodynamic design of Pegasus^{TM}, concept to flight with CFD. In *Missile Aerodynamics*, AGARD Conf. Proc. No. 493, Symposium of the Fluid Dynamics Panel, Friedrichshafen, Germany

Mullin SN. 1992. *The evolution of the F-22 Advanced Tactical Fighter*. Presented at Aircraft Design Systems Meet., AIAA Pap. 92–4188, Hilton Head Island, SC

Neumann RD. 1986. *Designing a flight test program*. Presented at University of Texas Short Course on Hypersonics, Austin, TX

Neumann RD. 1988. *Missions and requirements*. Presented at Special Course on Aerothermodynamics of Hypersonic Vehicles, AGARD Report 761, Neuilly sur Seine, France

Niewald PW, Parker SL. 1999. *Flight test techniques employed successfully to verify F/A-18E in-flight lift and drag*. Presented at Aerosp. Sci. Meet., 37th, AIAA Pap. 99–0768, Reno, NV

Niewald PW, Parker SL. 2000. Wind-tunnel techniques to successfully predict F/A-18E in-flight lift and drag. *J. Aircraft* 37:9–14

Rizzi A, Vos J. 1996. *Towards establishing credibility in CFD simulations*. Presented at Fluid Dyn. Conf., 27th, AIAA Pap. 96–2029, New Orleans, LA

Saltzman EJ, Ayers TG. 1982. Review of flight-to-wind-tunnel drag correlations. *J. Aircraft* 19:801–811

Shang JS. 1995. Assessment of technology for aircraft development. *J. Aircraft* 32:611–617

Towne MC, Strande SM, Erickson LL, Kroo IM, Enomoto FY, Carmichael RL, McPherson KF. 1983. *PAN AIR modeling studies*. Presented at Appl. Aerodyn. Conf., AIAA Pap. 83–1830, Danvers, MA

Trimmer LL, Cary A, Voisinet RL. 1986. *The optimum hypersonic wind tunnel*. Presented at Aerodyn. Test. Conf., AIAA Pap. 86–0739, West Palm Beach, FL

A THE EQUATIONS OF MOTION WRITTEN IN CONSERVATION FORM

In the main text the basic equations of motion were developed and were used in the nonconservative form, e.g., the momentum equation (equation (2.12)] and the energy equation (equation (2.32)]. However, the reader who pursues advanced applications of fluid mechanics often encounters the basic equations in conservation form for use in computational fluid dynamics. The conservation form of the basic equations is used for the following reasons (among others). First, it is easier to derive a noniterative, second-order, implicit algorithm if the nonlinear equations are in conservation form. Second, when shock waves and shear layers are expected in the flow field, it is essential that conservative difference approximations be used if one uses a "shock-capturing" method (Ref. A.1). *Shock capturing* is defined as ignoring the presence of embedded discontinuities in the sense that they are not treated as internal boundaries in the difference algorithm.

Let us establish the following nomenclature for the general form of the equations of motion in conservation form:

$$\frac{\partial U}{\partial t} + \frac{\partial (E_i - E_v)}{\partial x} + \frac{\partial (F_i - F_v)}{\partial y} + \frac{\partial (G_i - G_v)}{\partial z} = 0 \qquad \textbf{(A.1)}$$

where the subscript i denotes the terms that are included in the equations of motion for an inviscid flow and the subscript v denotes the terms that are unique to the equations of motion when the viscous and heat-transfer effects are included.

Recall that the continuity equation (2.1) is

$$\frac{\partial \rho}{\partial t} + \frac{\partial (\rho u)}{\partial x} + \frac{\partial (\rho v)}{\partial y} + \frac{\partial (\rho w)}{\partial z} = 0 \qquad \textbf{(A.2)}$$

Note that this equation is already in conservation form. It is valid for an inviscid flow as well as a viscous flow. Therefore, comparing equations (A.1) and (A.2), we obtain

$$U = \rho \qquad E_i = \rho u \qquad F_i = \rho v \qquad G_i = \rho w \qquad \textbf{(A.3a)–(A.3d)}$$

$$E_v = F_v = G_v = 0 \qquad \textbf{(A.3e)–(A.3g)}$$

Consider the x component of the momentum equation, as given by equation (2.11a). Assuming that the body forces are negligible, as is commonly done for gas flows,

$$\rho \frac{\partial u}{\partial t} + \rho u \frac{\partial u}{\partial x} + \rho v \frac{\partial u}{\partial y} + \rho w \frac{\partial u}{\partial z} = -\frac{\partial p}{\partial x} + \frac{\partial (\tau'_{xx})}{\partial x} + \frac{\partial (\tau_{yx})}{\partial y} + \frac{\partial (\tau_{zx})}{\partial z} \qquad \textbf{(A.4)}$$

To obtain equation (A.4), we have divided the expression for the normal shear stress τ_{xx}, as defined in Chapter 2, into the sum of the pressure p which is present in the equations for an inviscid flow and a term relating to the viscous flow τ'_{xx}. This is done to satisfy more easily the format of equation (A.1). Thus,

$$\tau'_{xx} = -\frac{2}{3}\mu \nabla \cdot \vec{V} + 2\mu \frac{\partial u}{\partial x}$$

The definitions for τ_{yx} and τ_{zx} remain as defined in Chapter 2. If we multiply the continuity equation (A.2) by u, we obtain

$$u \frac{\partial \rho}{\partial t} + u \frac{\partial (\rho u)}{\partial x} + u \frac{\partial (\rho v)}{\partial y} + u \frac{\partial (\rho w)}{\partial z} = 0 \qquad \textbf{(A.5)}$$

Adding equations (A.4) and (A.5) and rearranging, we obtain

$$\frac{\partial (\rho u)}{\partial t} + \frac{\partial}{\partial x}[(p + \rho u^2) - (\tau'_{xx})] + \frac{\partial}{\partial y}[(\rho u v) - (\tau_{yx})] + \frac{\partial}{\partial z}[(\rho u w) - (\tau_{zx})] = 0 \qquad \textbf{(A.6)}$$

Comparing equation (A.6) to the general form of the equations of motion in conservation form, equation (A.1), it is clear that

$$U = \rho u \qquad E_i = p + \rho u^2 \qquad F_i = \rho u v \qquad G_i = \rho u w \qquad \textbf{(A.7a)–(A.7d)}$$

$$E_v = \tau'_{xx} \qquad F_v = \tau_{yx} \qquad G_v = \tau_{zx} \qquad \textbf{(A.7e)–(A.7g)}$$

Similar manipulations of the y momentum will yield

$$U = \rho v \qquad E_i = \rho v u \qquad F_i = p + \rho v^2 \qquad G_i = \rho v w \qquad \textbf{(A.8a)–(A.8d)}$$

$$E_v = \tau_{xy} \qquad F_v = \tau'_{yy} \qquad G_v = \tau_{zy} \qquad \textbf{(A.8e)–(A.8g)}$$

where

$$\tau'_{yy} = -\frac{2}{3}\mu \nabla \cdot \vec{V} + 2\mu \frac{\partial v}{\partial y}$$

Similarly, the z-momentum equation can be written in conservation form, if

$$U = \rho w \qquad E_i = \rho wu \qquad F_i = \rho wv \qquad G_i = p + \rho w^2 \qquad \textbf{(A.9a)–(A.9d)}$$

$$E_v = \tau_{xz} \qquad F_v = \tau_{yz} \qquad G_v = \tau'_{zz} \qquad \textbf{(A.9e)–(A.9g)}$$

where

$$\tau'_{zz} = -\frac{2}{3}\mu \nabla \cdot \vec{V} + 2\mu \frac{\partial w}{\partial z}$$

The energy equation (2.25) is

$$\rho \dot{q} - \rho \dot{w} = \rho \frac{d}{dt}(ke) + \rho \frac{d}{dt}(pe) + \rho \frac{d}{dt}(u_e) \qquad \textbf{(2.25)}$$

Neglecting the changes in potential energy and using the definitions for $\rho \dot{q}$ and $\rho \dot{w}$, we obtain

$$\begin{aligned} &\frac{\partial}{\partial x}\left(k\frac{\partial T}{\partial x}\right) + \frac{\partial}{\partial y}\left(k\frac{\partial T}{\partial y}\right) + \frac{\partial}{\partial z}\left(k\frac{\partial T}{\partial z}\right) \\ &\qquad - \frac{\partial}{\partial x}(up) + \frac{\partial}{\partial x}(u\tau'_{xx}) + \frac{\partial}{\partial x}(v\tau_{xy}) + \frac{\partial}{\partial x}(w\tau_{xz}) \\ &\qquad + \frac{\partial}{\partial y}(u\tau_{yx}) - \frac{\partial}{\partial y}(vp) + \frac{\partial}{\partial y}(v\tau'_{yy}) + \frac{\partial}{\partial y}(w\tau_{yz}) \\ &\qquad + \frac{\partial}{\partial z}(u\tau_{zx}) + \frac{\partial}{\partial z}(v\tau_{zy}) - \frac{\partial}{\partial z}(wp) + \frac{\partial}{\partial z}(w\tau'_{zz}) \\ &\qquad = \rho \frac{de_t}{dt} = \rho \frac{\partial e_t}{\partial t} + \rho u \frac{\partial e_t}{\partial x} + \rho v \frac{\partial e_t}{\partial y} + \rho w \frac{\partial e_t}{\partial z} \end{aligned} \qquad \textbf{(A.10)}$$

where e_t, the specific total energy of the flow (neglecting the potential energy), is given by

$$e_t = u_e + \tfrac{1}{2}(u^2 + v^2 + w^2) \qquad \textbf{(A.11)}$$

The continuity equation multiplied by e_t is

$$e_t \frac{\partial \rho}{\partial t} + e_t \frac{\partial(\rho u)}{\partial x} + e_t \frac{\partial(\rho v)}{\partial y} + e_t \frac{\partial(\rho w)}{\partial z} = 0 \qquad \textbf{(A.12)}$$

Adding equations (A.10) and (A.12) and rearranging, we obtain

$$\begin{aligned} &\frac{\partial}{\partial t}(\rho e_t) + \frac{\partial}{\partial x}[\,(\rho e_t + p)u - (u\tau'_{xx} + v\tau_{xy} + w\tau_{xz} + \dot{q}_x)\,] \\ &\qquad + \frac{\partial}{\partial y}[\,(\rho e_t + p)v - (u\tau_{yx} + v\tau'_{yy} + w\tau_{yz} + \dot{q}_y)\,] \\ &\qquad + \frac{\partial}{\partial z}[\,(\rho e_t + p)w - (u\tau_{zx} + v\tau_{zy} + w\tau'_{zz} + \dot{q}_z)\,] \end{aligned} \qquad \textbf{(A.13)}$$

Equation (A.13) is the energy equation in the conservation form. Comparing equation (A.13) to the general form, equation (A.1), it is clear that

$$U = \rho e_t \qquad E_i = (\rho e_t + p)u \qquad F_i = (\rho e_t + p)v$$

$$G_i = (\rho e_t + p)w \qquad \textbf{(A.14a)–(A.14d)}$$

$$E_v = u\tau'_{xx} + v\tau_{xy} + w\tau_{xz} + \dot{q}_x \qquad \textbf{(A.14e)}$$

$$F_v = u\tau_{yx} + v\tau'_{yy} + w\tau_{yz} + \dot{q}_y \qquad \textbf{(A.14f)}$$

$$G_v = u\tau_{zx} + v\tau_{zy} + w\tau'_{zz} + \dot{q}_z \qquad \textbf{(A.14g)}$$

When the fundamental equations governing the unsteady flow of gas, without body forces or external heat addition, are written in conservation form [i.e., equation (A.1)], the terms $U, E_i, E_v, F_i, F_v, G_i$, and G_v can be represented by the following vectors.

$$U = \begin{bmatrix} \rho \\ \rho u \\ \rho v \\ \rho w \\ \rho e_t \end{bmatrix}$$

$$E_i = \begin{bmatrix} \rho u \\ p + \rho u^2 \\ \rho uv \\ \rho uw \\ (\rho e_t + p)u \end{bmatrix} \qquad E_v = \begin{bmatrix} 0 \\ \tau'_{xx} \\ \tau_{xy} \\ \tau_{xz} \\ (u\tau'_{xx} + v\tau_{xy} + w\tau_{xz} + \dot{q}_x) \end{bmatrix}$$

$$F_i = \begin{bmatrix} \rho v \\ \rho vu \\ p + \rho v^2 \\ \rho vw \\ (\rho e_t + p)v \end{bmatrix} \qquad F_v = \begin{bmatrix} 0 \\ \tau_{yx} \\ \tau'_{yy} \\ \tau_{yz} \\ (u\tau_{yx} + v\tau'_{yy} + w\tau_{yz} + \dot{q}_y) \end{bmatrix}$$

$$G_i = \begin{bmatrix} \rho w \\ \rho wu \\ \rho wv \\ p + \rho w^2 \\ (\rho e_t + p)w \end{bmatrix} \qquad G_v = \begin{bmatrix} 0 \\ \tau_{zx} \\ \tau_{zy} \\ \tau'_{zz} \\ (u\tau_{zx} + v\tau_{zy} + w\tau'_{zz} + \dot{q}_z) \end{bmatrix}$$

The successive lines of these vectors are the continuity equation, the x-momentum equation, the y-momentum equation, the z-momentum equation, and the energy equation. Note that considering only U and the inviscid terms (E_i, F_i, and G_i) of lines 2 through 4 yields Euler's equations in conservation form.

Repeating the information of Chapter 2 (with the modifications noted previously),

$$\tau'_{xx} = 2\mu\frac{\partial u}{\partial x} - \frac{2}{3}\mu\nabla\cdot\vec{V}$$

$$\tau'_{yy} = 2\mu\frac{\partial v}{\partial y} - \frac{2}{3}\mu\nabla\cdot\vec{V}$$

$$\tau'_{zz} = 2\mu\frac{\partial w}{\partial z} - \frac{2}{3}\mu\nabla\cdot\vec{V}$$

$$\tau_{xy} = \tau_{yx} = \mu\left(\frac{\partial u}{\partial y} + \frac{\partial v}{\partial x}\right)$$

$$\tau_{xz} = \tau_{zx} = \mu\left(\frac{\partial u}{\partial z} + \frac{\partial w}{\partial x}\right)$$

$$\tau_{yz} = \tau_{zy} = \mu\left(\frac{\partial v}{\partial z} + \frac{\partial w}{\partial y}\right)$$

$$\dot{q}_x = k\frac{\partial T}{\partial x} \qquad \dot{q}_y = k\frac{\partial T}{\partial y} \qquad \dot{q}_z = k\frac{\partial T}{\partial z}$$

Similar procedures can be followed to develop the conservative form of the governing equations for flow in cylindrical coordinates.

$$\frac{\partial U}{\partial t} + \frac{\partial(F_i - F_v)}{\partial z} + \frac{\partial(G_i - G_v)}{\partial r} + \frac{\partial(H_i - H_v)}{\partial\theta} + (R_i - R_v) = 0$$

$$U = \begin{bmatrix} \rho \\ \rho v_z \\ \rho v_r \\ \rho v_\theta \\ \rho e_t \end{bmatrix}$$

$$F_i = \begin{bmatrix} \rho v_z \\ p + \rho v_z^2 \\ \rho v_z v_r \\ \rho v_z v_\theta \\ (\rho e_t + p)v_z \end{bmatrix} \qquad F_v = \begin{bmatrix} 0 \\ \tau_{zz} \\ \tau_{zr} \\ \tau_{z\theta} \\ (v_z\tau_{zz} + v_r\tau_{zr} + v_\theta\tau_{z\theta} + \dot{q}_z) \end{bmatrix}$$

$$G_i = \begin{bmatrix} \rho v_r \\ \rho v_r v_z \\ p + \rho v_r^2 \\ \rho v_r v_\theta \\ (\rho e_t + p)v_r \end{bmatrix} \qquad G_v = \begin{bmatrix} 0 \\ \tau_{rz} \\ \tau_{rr} \\ \tau_{r\theta} \\ (v_z\tau_{rz} + v_r\tau_{rr} + v_\theta\tau_{r\theta} + \dot{q}_r) \end{bmatrix}$$

$$H_i = \frac{1}{r}\begin{bmatrix} \rho v_\theta \\ \rho v_\theta v_z \\ \rho v_\theta v_r \\ p + \rho v_\theta^2 \\ (\rho e_t + p) v_\theta \end{bmatrix} \qquad H_v = \frac{1}{r}\begin{bmatrix} 0 \\ \tau_{\theta z} \\ \tau_{\theta r} \\ \tau_{\theta\theta} \\ (v_z \tau_{z\theta} + v_r \tau_{r\theta} + v_\theta \tau_{\theta\theta} + \dot{q}_\theta) \end{bmatrix}$$

$$R_i = \frac{1}{r}\begin{bmatrix} \rho v_r \\ \rho v_r v_z \\ \rho v_r^2 - \rho v_\theta^2 \\ 2\rho v_r v_\theta \\ (\rho e_t + p) v_r \end{bmatrix} \qquad R_v = \frac{1}{r}\begin{bmatrix} 0 \\ \tau_{rz} \\ \tau_{rr} - \tau_{\theta\theta} \\ 2\tau_{r\theta} \\ (v_z \tau_{zr} + v_r \tau_{rr} + v_\theta \tau_{\theta r} + \dot{q}_r) \end{bmatrix} \tag{A.15}$$

where

$$\tau_{rr} = 2\mu \frac{\partial v_r}{\partial r} - \frac{2}{3}\mu \nabla \cdot \vec{V}$$

$$\tau_{\theta\theta} = 2\mu\left(\frac{1}{r}\frac{\partial v_\theta}{\partial \theta} + \frac{v_r}{r}\right) - \frac{2}{3}\mu \nabla \cdot \vec{V}$$

$$\tau_{zz} = 2\mu \frac{\partial v_z}{\partial z} - \frac{2}{3}\mu \nabla \cdot \vec{V}$$

$$\tau_{\theta z} = \tau_{z\theta} = \mu\left(\frac{1}{r}\frac{\partial v_z}{\partial \theta} + \frac{\partial v_\theta}{\partial z}\right)$$

$$\tau_{\theta r} = \tau_{r\theta} = \mu\left(\frac{\partial v_\theta}{\partial r} - \frac{v_\theta}{r} + \frac{1}{r}\frac{\partial v_r}{\partial \theta}\right)$$

$$\tau_{zr} = \tau_{rz} = \mu\left(\frac{\partial v_r}{\partial z} + \frac{\partial v_z}{\partial r}\right)$$

$$q_z = k\frac{\partial T}{\partial z} \qquad q_r = k\frac{\partial T}{\partial r} \qquad q_\theta = \frac{k}{r}\frac{\partial T}{\partial \theta}$$

REFERENCES

Warming RF, Beam RM. 1978. On the construction and application of implicit factored schemes for conservation laws. *SIAM-AMS Proceedings* 11:85–129

B A COLLECTION OF OFTEN USED TABLES

TABLE 1.2A U.S. Standard Atmosphere, 1976 SI Units

Geometric Altitude (*km*)	*Pressure* (N/m^2)	*Temperature* (*K*)	*Density* (kg/m^3)	*Viscosity* ($kg/m \cdot s$)	*Speed of Sound* (m/s)
0	1.0133 *E* + 05	288.150	1.2250 *E* + 00	1.7894 *E* − 05	340.29
1	8.9875 *E* + 04	281.651	1.1117 *E* + 00	1.7579 *E* − 05	336.43
2	7.9501 *E* + 04	275.154	1.0066 *E* + 00	1.7260 *E* − 05	332.53
3	7.0121 *E* + 04	268.659	9.0926 *E* − 01	1.6938 *E* − 05	328.58
4	6.1669 *E* + 04	262.166	8.1934 *E* − 01	1.6612 *E* − 05	324.59
5	5.4048 *E* + 04	255.676	7.3643 *E* − 01	1.7885 *E* − 05	320.55
6	4.7217 *E* + 04	249.187	6.6012 *E* − 01	1.5949 *E* − 05	316.45
7	4.1105 *E* + 04	242.700	5.9002 *E* − 01	1.5612 *E* − 05	312.31
8	3.5651 *E* + 04	236.215	5.2578 *E* − 01	1.5271 *E* − 05	308.11
9	3.0800 *E* + 04	229.733	4.6707 *E* − 01	1.4926 *E* − 05	303.85
10	2.6500 *E* + 04	223.252	4.1351 *E* − 01	1.4577 *E* − 05	299.53
11	2.2700 *E* + 04	216.774	3.6481 *E* − 01	1.4223 *E* − 05	295.15
12	1.9399 *E* + 04	216.650	3.1193 *E* − 01	1.4216 *E* − 05	295.07

(*continued on next page*)

TABLE 1.2A (*Continued*)

Geometric Altitude (*km*)	*Pressure* (N/m^2)	*Temperature* (*K*)	*Density* (kg/m^3)	*Viscosity* ($kg/m \cdot s$)	*Speed of Sound* (m/s)
13	1.6579 *E* + 04	216.650	2.6660 *E* − 01	1.4216 *E* − 05	295.07
14	1.4170 *E* + 04	216.650	2.2786 *E* − 01	1.4216 *E* − 05	295.07
15	1.2111 *E* + 04	216.650	1.9475 *E* − 01	1.4216 *E* − 05	295.07
16	1.0352 *E* + 04	216.650	1.6647 *E* − 01	1.4216 *E* − 05	295.07
17	8.8497 *E* + 03	216.650	1.4230 *E* − 01	1.4216 *E* − 05	295.07
18	7.5652 *E* + 03	216.650	1.2165 *E* − 01	1.4216 *E* − 05	295.07
19	6.4675 *E* + 03	216.650	1.0400 *E* − 01	1.4216 *E* − 05	295.07
20	5.5293 *E* + 03	216.650	8.8911 *E* − 02	1.4216 *E* − 05	295.07
21	4.7289 *E* + 03	217.581	7.5715 *E* − 02	1.4267 *E* − 05	295.70
22	4.0474 *E* + 03	218.574	6.4510 *E* − 02	1.4322 *E* − 05	296.38
23	3.4668 *E* + 03	219.567	5.5006 *E* − 02	1.4376 *E* − 05	297.05
24	2.9717 *E* + 03	220.560	4.6938 *E* − 02	1.4430 *E* − 05	297.72
25	2.5491 *E* + 03	221.552	4.0084 *E* − 02	1.4484 *E* − 05	298.39
26	2.1883 *E* + 03	222.544	3.4257 *E* − 02	1.4538 *E* − 05	299.06
27	1.8799 *E* + 03	223.536	2.9298 *E* − 02	1.4592 *E* − 05	299.72
28	1.6161 *E* + 03	224.527	2.5076 *E* − 02	1.4646 *E* − 05	300.39
29	1.3904 *E* + 03	225.518	2.1478 *E* − 02	1.4699 *E* − 05	301.05
30	1.1970 *E* + 03	226.509	1.8411 *E* − 02	1.4753 *E* − 05	301.71

TABLE 1.2B U.S. Standard Atmosphere, 1976 English Units

Geometric Altitude (*kft*)	*Pressure* (lbf/ft^2)	*Temperature* (°*R*)	*Density* ($slug/ft^3$)	*Viscosity* ($slug/ft \cdot s$)	*Speed of Sound* (ft/s)
0	2.1162 *E* + 03	518.67	2.3769 *E* − 03	3.7383 *E* − 07	1116.44
2	1.9677 *E* + 03	511.54	2.2409 *E* − 03	3.6982 *E* − 07	1108.76
4	1.8277 *E* + 03	504.41	2.1109 *E* − 03	3.6579 *E* − 07	1100.98
6	1.6960 *E* + 03	497.28	1.9869 *E* − 03	3.6173 *E* − 07	1093.18
8	1.5721 *E* + 03	490.15	1.8685 *E* − 03	3.4764 *E* − 07	1085.33
10	1.4556 *E* + 03	483.02	1.7556 *E* − 03	3.5353 *E* − 07	1077.40
12	1.3462 *E* + 03	475.90	1.6479 *E* − 03	3.4939 *E* − 07	1069.42
14	1.2436 *E* + 03	468.78	1.5455 *E* − 03	3.4522 *E* − 07	1061.38
16	1.1473 *E* + 03	461.66	1.4480 *E* − 03	3.4102 *E* − 07	1053.31
18	1.0575 *E* + 03	454.53	1.3553 *E* − 03	3.3679 *E* − 07	1045.14
20	9.7733 *E* + 02	447.42	1.2673 *E* − 03	3.3253 *E* − 07	1036.94

(*continued on next page*)

TABLE 1.2B (*Continued*)

Geometric Altitude (*kft*)	*Pressure* (lbf/ft^2)	*Temperature* (°*R*)	*Density* ($slug/ft^3$)	*Viscosity* ($slug/ft \cdot s$)	*Speed of Sound* (ft/s)
22	8.9459 *E* + 02	440.30	1.1836 *E* − 03	3.2825 *E* − 07	1028.64
24	8.2116 *E* + 02	433.18	1.1044 *E* − 03	3.2392 *E* − 07	1020.31
26	7.5270 *E* + 02	426.07	1.0292 *E* − 03	3.1958 *E* − 07	1011.88
28	6.8896 *E* + 02	418.95	9.5801 *E* − 04	3.1519 *E* − 07	1003.41
30	6.2966 *E* + 02	411.84	8.9070 *E* − 04	3.1078 *E* − 07	994.85
32	5.7457 *E* + 02	404.73	8.2704 *E* − 04	3.0633 *E* − 07	986.22
34	5.2347 *E* + 02	397.62	7.6695 *E* − 04	3.0185 *E* − 07	977.53
36	4.7611 *E* + 02	390.51	7.1029 *E* − 04	2.9734 *E* − 07	968.73
38	4.3262 *E* + 02	389.97	6.4640 *E* − 04	2.9700 *E* − 07	968.08
40	3.9311 *E* + 02	389.97	5.8728 *E* − 04	2.9700 *E* − 07	968.08
42	3.5722 *E* + 02	389.97	5.3366 *E* − 04	2.9700 *E* − 07	968.08
44	3.2477 *E* + 02	389.97	4.8494 *E* − 04	2.9700 *E* − 07	968.08
46	2.9477 *E* + 02	389.97	4.4068 *E* − 04	2.9700 *E* − 07	968.08
48	2.6806 *E* + 02	389.97	4.0046 *E* − 04	2.9700 *E* − 07	968.08
50	2.4360 *E* + 02	389.97	3.6393 *E* − 04	2.9700 *E* − 07	968.08
52	2.2138 *E* + 02	389.97	3.3072 *E* − 04	2.9700 *E* − 07	968.08
54	2.0119 *E* + 02	389.97	3.0056 *E* − 04	2.9700 *E* − 07	968.08
56	1.8288 *E* + 02	389.97	2.7315 *E* − 04	2.9700 *E* − 07	968.08
58	1.6618 *E* + 02	389.97	2.4824 *E* − 04	2.9700 *E* − 07	968.08
60	1.5103 *E* + 02	389.97	2.2561 *E* − 04	2.9700 *E* − 07	968.08
62	1.3726 *E* + 02	389.97	2.0505 *E* − 04	2.9700 *E* − 07	968.08
64	1.2475 *E* + 02	389.97	1.8637 *E* − 04	2.9700 *E* − 07	968.08
66	1.1339 *E* + 02	390.07	1.6934 *E* − 04	2.9706 *E* − 07	968.21
68	1.0307 *E* + 02	391.16	1.5351 *E* − 04	2.9775 *E* − 07	969.55
70	9.3725 *E* + 01	392.25	1.3920 *E* − 04	2.9845 *E* − 07	970.90
72	8.5250 *E* + 01	393.34	1.2626 *E* − 04	2.9914 *E* − 07	972.24
74	7.7572 *E* + 01	394.43	1.1456 *E* − 04	2.9983 *E* − 07	973.59
76	7.0587 *E* + 01	395.52	1.0397 *E* − 04	3.0052 *E* − 07	974.93
78	6.4257 *E* + 01	396.60	9.4387 *E* − 05	3.0121 *E* − 07	976.28
80	5.8511 *E* + 01	397.69	8.5711 *E* − 05	3.0190 *E* − 07	977.62
82	5.3293 *E* + 01	398.78	7.7855 *E* − 05	3.0259 *E* − 07	978.94
84	4.8552 *E* + 01	399.87	7.0739 *E* − 05	3.0328 *E* − 07	980.28
86	4.4248 *E* + 01	400.96	6.4290 *E* − 05	3.0396 *E* − 07	981.63
88	4.0335 *E* + 01	402.05	5.8446 *E* − 05	3.0465 *E* − 07	982.94
90	3.6778 *E* + 01	403.14	5.3147 *E* − 05	3.0533 *E* − 07	984.28
92	3.3542 *E* + 01	404.22	4.8344 *E* − 05	3.0602 *E* − 07	985.60
94	3.0601 *E* + 01	405.31	4.3985 *E* − 05	3.0670 *E* − 07	986.94
96	2.7924 *E* + 01	406.40	4.0029 *E* − 05	3.0738 *E* − 07	988.25
98	2.5488 *E* + 01	407.49	3.6440 *E* − 05	3.0806 *E* − 07	989.57
100	2.3272 *E* + 01	408.57	3.3182 *E* − 05	3.0874 *E* − 07	990.91

TABLE 8.1 Correlations for a One-Dimensional, Isentropic Flow of Perfect Air ($\gamma = 1.4$)

M	$\frac{A}{A^*}$	$\frac{p}{p_{t1}}$	$\frac{\rho}{\rho_{t1}}$	$\frac{T}{T_t}$	$\frac{A}{A^*}\frac{p}{p_{t1}}$
0	/	1.00000	1.00000	1.00000	/
0.05	11.592	0.99825	0.99875	0.99950	11.571
0.10	5.8218	0.99303	0.99502	0.99800	5.7812
0.15	3.9103	0.98441	0.98884	0.99552	3.8493
0.20	2.9635	0.97250	0.98027	0.99206	2.8820
0.25	2.4027	0.95745	0.96942	0.98765	2.3005
0.30	2.0351	0.93947	0.95638	0.98232	1.9119
0.35	1.7780	0.91877	0.94128	0.97608	1.6336
0.40	1.5901	0.89562	0.92428	0.96899	1.4241
0.45	1.4487	0.87027	0.90552	0.96108	1.2607
0.50	1.3398	0.84302	0.88517	0.95238	1.12951
0.55	1.2550	0.81416	0.86342	0.94295	1.02174
0.60	1.1882	0.78400	0.84045	0.93284	0.93155
0.65	1.1356	0.75283	0.81644	0.92208	0.85493
0.70	1.09437	0.72092	0.79158	0.91075	0.78896
0.75	1.06242	0.68857	0.76603	0.89888	0.73155
0.80	1.03823	0.65602	0.74000	0.88652	0.68110
0.85	1.02067	0.62351	0.71361	0.87374	0.63640
0.90	1.00886	0.59126	0.68704	0.86058	0.59650
0.95	1.00214	0.55946	0.66044	0.84710	0.56066
1.00	1.00000	0.52828	0.63394	0.83333	0.52828
1.05	1.00202	0.49787	0.60765	0.81933	0.49888
1.10	1.00793	0.46835	0.58169	0.80515	0.47206
1.15	1.01746	0.43983	0.55616	0.79083	0.44751
1.20	1.03044	0.41238	0.53114	0.77640	0.42493
1.25	1.04676	0.38606	0.50670	0.76190	0.40411
1.30	1.06631	0.36092	0.48291	0.74738	0.38484
1.35	1.08904	0.33697	0.45980	0.73287	0.36697
1.40	1.1149	0.31424	0.43742	0.71839	0.35036
1.45	1.1440	0.29272	0.41581	0.70397	0.33486
1.50	1.1762	0.27240	0.39498	0.68965	0.32039
1.55	1.2115	0.25326	0.37496	0.67545	0.30685
1.60	1.2502	0.23527	0.35573	0.66138	0.29414
1.65	1.2922	0.21839	0.33731	0.64746	0.28221
1.70	1.3376	0.20259	0.31969	0.63372	0.27099
1.75	1.3865	0.18782	0.30287	0.62016	0.26042
1.80	1.4390	0.17404	0.28682	0.60680	0.25044
1.85	1.4952	0.16120	0.27153	0.59365	0.24102
1.90	1.5555	0.14924	0.25699	0.58072	0.23211
1.95	1.6193	0.13813	0.24317	0.56802	0.22367
2.00	1.6875	0.12780	0.23005	0.55556	0.21567
2.05	1.7600	0.11823	0.21760	0.54333	0.20808
2.10	1.8369	0.10935	0.20580	0.53135	0.20087
2.15	1.9185	0.10113	0.19463	0.51962	0.19403
2.20	2.0050	0.09352	0.18405	0.50813	0.18751

(*continued on next page*)

TABLE 8.1 (*Continued*)

M	$\frac{A}{A^*}$	$\frac{p}{p_{t1}}$	$\frac{\rho}{\rho_{t1}}$	$\frac{T}{T_t}$	$\frac{A}{A^*}\frac{p}{p_{t1}}$
2.25	2.0964	0.08648	0.17404	0.49689	0.18130
2.30	2.1931	0.07997	0.16458	0.48591	0.17539
2.35	2.2953	0.07396	0.15564	0.47517	0.16975
2.40	2.4031	0.06840	0.14720	0.46468	0.16437
2.45	2.5168	0.06327	0.13922	0.45444	0.15923
2.50	2.6367	0.05853	0.13169	0.44444	0.15432
2.55	2.7630	0.05415	0.12458	0.43469	0.14963
2.60	2.8960	0.05012	0.11787	0.42517	0.14513
2.65	3.0359	0.04639	0.11154	0.41589	0.14083
2.70	3.1830	0.04295	0.10557	0.40684	0.13671
2.75	3.3376	0.03977	0.09994	0.39801	0.13276
2.80	3.5001	0.03685	0.09462	0.38941	0.12897
2.85	3.6707	0.03415	0.08962	0.38102	0.12534
2.90	3.8498	0.03165	0.08489	0.37286	0.12185
2.95	4.0376	0.02935	0.08043	0.36490	0.11850
3.00	4.2346	0.02722	0.07623	0.35714	0.11527
3.50	6.7896	0.01311	0.04523	0.28986	0.08902
4.00	10.719	0.00658	0.02766	0.23810	0.07059
4.50	16.562	0.00346	0.01745	0.19802	0.05723
5.00	25.000	$189(10)^{-5}$	0.01134	0.16667	0.04725
6.00	53.189	$633(10)^{-6}$	0.00519	0.12195	0.03368
7.00	104.143	$242(10)^{-6}$	0.00261	0.09259	0.02516
8.00	190.109	$102(10)^{-6}$	0.00141	0.07246	0.01947
9.00	327.189	$474(10)^{-7}$	0.000815	0.05814	0.01550
10.00	535.938	$236(10)^{-7}$	0.000495	0.04762	0.01263
∞	∞	0	0	0	0

TABLE 8.2 Mach Number and Mach Angle as a Function of Prandt-Meyer Angle

ν (deg)	M	μ (deg)	ν (deg)	M	μ (deg)
0.0	1.000	90.000	7.5	1.348	47.896
0.5	1.051	72.099	8.0	1.366	47.082
1.0	1.082	67.574	8.5	1.383	46.306
1.5	1.108	64.451	9.0	1.400	45.566
2.0	1.133	61.997	9.5	1.418	44.857
2.5	1.155	59.950	10.0	1.435	44.177
3.0	1.177	58.180	10.5	1.452	43.523
3.5	1.198	56.614	11.0	1.469	42.894
4.0	1.218	55.205	11.5	1.486	42.287
4.5	1.237	53.920	12.0	1.503	41.701
5.0	1.256	52.738	12.5	1.520	41.134
5.5	1.275	51.642	13.0	1.537	40.585
6.0	1.294	50.619	13.5	1.554	40.053
6.5	1.312	49.658	14.0	1.571	39.537
7.0	1.330	48.753	14.5	1.588	39.035

(*continued on next page*)

TABLE 8.2 (*Continued*)

ν (deg)	M	μ (deg)	ν (deg)	M	μ (deg)
15.0	1.605	38.547	40.0	2.538	23.206
15.5	1.622	38.073	40.5	2.560	22.997
16.0	1.639	37.611	41.0	2.582	22.790
16.5	1.655	37.160	41.5	2.604	22.585
17.0	1.672	36.721	42.0	2.626	22.382
17.5	1.689	36.293	42.5	2.649	22.182
18.0	1.706	35.874	43.0	2.671	21.983
18.5	1.724	35.465	43.5	2.694	21.786
19.0	1.741	35.065	44.0	2.718	21.591
19.5	1.758	34.673	44.5	2.741	21.398
20.0	1.775	34.290	45.0	2.764	21.207
20.5	1.792	33.915	45.5	2.788	21.017
21.0	1.810	33.548	46.0	2.812	20.830
21.5	1.827	33.188	46.5	2.836	20.644
22.0	1.844	32.834	47.0	2.861	20.459
22.5	1.862	32.488	47.5	2.886	20.277
23.0	1.879	32.148	48.0	2.910	20.096
23.5	1.897	31.814	48.5	2.936	19.916
24.0	1.915	31.486	49.0	2.961	19.738
24.5	1.932	31.164	49.5	2.987	15.561
25.0	1.950	30.847	50.0	3.013	19.386
25.5	1.968	30.536	50.5	3.039	19.213
26.0	1.986	30.229	51.0	3.065	19.041
26.5	2.004	29.928	51.5	3.092	18.870
27.0	2.023	29.632	52.0	3.119	18.701
27.5	2.041	29.340	52.5	3.146	18.532
28.0	2.059	29.052	53.0	3.174	18.366
28.5	2.078	28.769	53.5	3.202	18.200
29.0	2.096	28.491	54.0	3.230	18.036
29.5	2.115	28.216	54.5	3.258	17.873
30.0	2.134	27.945	55.0	3.287	17.711
30.5	2.153	27.678	55.5	3.316	17.551
31.0	2.172	27.415	56.0	3.346	17.391
31.5	2.191	27.155	56.5	3.375	17.233
32.0	2.210	26.899	57.0	3.406	17.076
32.5	2.230	26.646	57.5	3.436	16.920
33.0	2.249	26.397	58.0	3.467	16.765
33.5	2.269	26.151	58.5	3.498	16.611
34.0	2.289	25.908	59.0	3.530	16.458
34.5	2.309	25.668	59.5	3.562	16.306
35.0	2.329	25.430	60.0	3.594	16.155
35.5	2.349	25.196	60.5	3.627	16.006
36.0	2.369	24.965	61.0	3.660	15.856
36.5	2.390	24.736	61.5	3.694	15.708
37.0	2.410	24.510	62.0	3.728	15.561
37.5	2.431	24.287	62.5	3.762	15.415
38.0	2.452	24.066	63.0	3.797	15.270
38.5	2.473	23.847	63.5	3.832	15.126
39.0	2.495	23.631	64.0	3.868	14.983
39.5	2.516	23.418	64.5	3.904	14.840

(*continued on next page*)

TABLE 8.2 (*Continued*)

ν (deg)	M	μ (deg)	ν (deg)	M	μ (deg)
65.0	3.941	14.698	85.5	6.080	9.467
65.5	3.979	14.557	86.0	6.155	9.350
66.0	4.016	14.417	86.5	6.232	9.234
66.5	4.055	14.278	87.0	6.310	9.119
67.0	4.094	14.140	87.5	6.390	9.003
67.5	4.133	14.002	88.0	6.472	8.888
68.0	4.173	13.865	88.5	6.556	8.774
68.5	4.214	13.729	89.0	6.642	8.660
69.0	4.255	13.593	89.5	6.729	8.546
69.5	4.297	13.459	90.0	6.819	8.433
70.0	4.339	13.325	90.5	6.911	8.320
70.5	4.382	13.191	91.0	7.005	8.207
71.0	4.426	13.059	91.5	7.102	8.095
71.5	4.470	12.927	92.0	7.201	7.983
72.0	4.515	12.795	92.5	7.302	7.871
72.5	4.561	12.665	93.0	7.406	7.760
73.0	4.608	12.535	93.5	7.513	7.649
73.5	4.655	12.406	94.0	7.623	7.538
74.0	4.703	12.277	94.5	7.735	7.428
74.5	4.752	12.149	94.5	5.935	9.701
75.0	4.801	12.021	95.0	7.851	7.318
75.5	4.852	11.894	95.5	7.970	7.208
76.0	4.903	11.768	96.0	8.092	7.099
76.5	4.955	11.642	96.5	8.218	6.989
77.0	5.009	11.517	97.0	8.347	6.881
77.5	5.063	11.392	97.5	8.480	6.772
78.0	5.118	11.268	98.0	8.618	6.664
78.5	5.175	11.145	98.5	8.759	6.556
79.0	5.231	11.022	99.0	8.905	6.448
79.5	5.289	10.899	99.5	9.055	6.340
80.0	5.348	10.777	100.0	9.210	6.233
80.5	5.408	10.656	100.5	9.371	6.126
81.0	5.470	10.535	101.0	9.536	6.019
81.5	5.532	10.414	101.5	9.708	5.913
82.0	5.596	10.294	102.0	9.885	5.806
82.5	5.661	10.175			
83.0	5.727	10.056			
83.5	5.795	9.937			
84.0	5.864	9.819			
84.5	5.935	9.701			
85.0	6.006	9.584			

TABLE 8.3 Correlation of Flow Properties Across a Normal Shock Wave as a Function of the Upstream Mach Number for Air, $\gamma = 1.4$

M_1	M_2	$\frac{p_2}{p_2}$	$\frac{\rho_2}{\rho_1}$	$\frac{T_2}{T_1}$	$\frac{p_{t2}}{p_{t1}}$
1.00	1.00000	1.00000	1.00000	1.00000	1.00000
1.05	0.95312	1.1196	1.08398	1.03284	0.99987
1.10	0.91177	1.2450	1.1691	1.06494	0.99892

(*continued on next page*)

TABLE 8.3 (*Continued*)

M_1	M_2	$\frac{p_2}{p_2}$	$\frac{\rho_2}{\rho_1}$	$\frac{T_2}{T_1}$	$\frac{p_{t2}}{p_{t1}}$
1.15	0.87502	1.3762	1.2550	1.09657	0.99669
1.20	0.84217	1.5133	1.3416	1.1280	0.99280
1.25	0.81264	1.6562	1.4286	1.1594	0.98706
1.30	0.78596	1.8050	1.5157	1.1909	0.97935
1.35	0.76175	1.9596	1.6027	1.2226	0.96972
1.40	0.73971	2.1200	1.6896	1.2547	0.95819
1.45	0.71956	2.2862	1.7761	1.2872	0.94483
1.50	0.70109	2.4583	1.8621	1.3202	0.92978
1.55	0.68410	2.6363	1.9473	1.3538	0.91319
1.60	0.66844	2.8201	2.0317	1.3880	0.89520
1.65	0.65396	3.0096	2.1152	1.4228	0.87598
1.70	0.64055	3.2050	2.1977	1.4583	0.85573
1.75	0.62809	3.4062	2.2781	1.4946	0.83456
1.80	0.61650	3.6133	2.3592	1.5316	0.81268
1.85	0.60570	3.8262	2.4381	1.5694	0.79021
1.90	0.59562	4.0450	2.5157	1.6079	0.76735
1.95	0.58618	4.2696	2.5919	1.6473	0.74418
2.00	0.57735	4.5000	2.6666	1.6875	0.72088
2.05	0.56907	4.7363	2.7400	1.7286	0.69752
2.10	0.56128	4.9784	2.8119	1.7704	0.67422
2.15	0.55395	5.2262	2.8823	1.8132	0.65105
2.20	0.54706	5.4800	2.9512	1.8569	0.62812
2.25	0.54055	5.7396	3.0186	1.9014	0.60554
2.30	0.53441	6.0050	3.0846	1.9468	0.58331
2.35	0.52861	6.2762	3.1490	1.9931	0.56148
2.40	0.52312	6.5533	3.2119	2.0403	0.54015
2.45	0.51792	6.8362	3.2733	2.0885	0.51932
2.50	0.51299	7.1250	3.3333	2.1375	0.49902
2.55	0.50831	7.4196	3.3918	2.1875	0.47927
2.60	0.50387	7.7200	3.4489	2.2383	0.46012
2.65	0.49965	8.0262	3.5047	2.2901	0.44155
2.70	0.49563	8.3383	3.5590	2.3429	0.42359
2.75	0.49181	8.6562	3.6119	2.3966	0.40622
2.80	0.48817	8.9800	3.6635	2.4512	0.38946
2.85	0.48470	9.3096	3.7139	2.5067	0.37330
2.90	0.48138	9.6450	3.7629	2.5632	0.35773
2.95	0.47821	9.986	3.8106	2.6206	0.34275
3.00	0.47519	10.333	3.8571	2.6790	0.32834
3.50	0.45115	14.125	4.2608	3.3150	0.21295
4.00	0.43496	18.500	4.5714	4.0469	0.13876
4.50	0.42355	23.458	4.8119	4.8761	0.09170
5.00	0.41523	29.000	5.0000	5.8000	0.06172
6.00	0.40416	41.833	5.2683	7.941	0.02965
7.00	0.39736	57.000	5.4444	10.469	0.01535
8.00	0.39289	74.500	5.5652	13.387	0.00849
9.00	0.38980	94.333	5.6512	16.693	0.00496
10.00	0.38757	116.50	5.1743	20.388	0.00304
∞	0.37796	∞	6.000	∞	0

ANSWERS TO SELECTED PROBLEMS

CHAPTER 1

1.1 $V = 1087.771\,ft/s$, $(L/D)_{\max} = 5.88$
1.2 $E = 270.60 \times 10^6\,ft - lbf$, $H_e = 27{,}060\,ft$, $P_s = 101.1\,ft/s$
1.3 $a_{\max} = 4.26\,ft^2/s$, $(dh/dt)_{\max} = 6{,}066\,ft/\text{min}$
1.6 $\nu_{N_2} = 3.33563 \times 10^{-5} ft^2/s$, $\nu_{air} = 3.33995 \times 10^{-5} ft^2/s$
1.8 $\rho_2 = 3.528\,kg/m^3$
1.9 $\rho_2 = 0.536\,kg/m^3$
1.10 $\rho = 0.195\,kg/m^3$, $\mu = 1.4216 \times 10^{-5} kg/m - s$
1.11 $\vartheta = 7.29 \times 10^{-5} m^2/s$, $a = 295.07\ m/s$
1.12 $u = 898.59\,m/s$
1.13 $\rho_\infty = 0.03760\,kg/m^3$, $\mu_\infty = 3.542 \times 10^{-6} kg/s \cdot m$, $U_\infty = 1034\,m/s$
1.14 $\rho = 0.6415\,kg/m^3$, $\mu = 3.9567 \times 10^{-5}\,kg/m - s$
1.16 $u = 239.53\,m/s = 786.06\,ft/s = 465.42\,knots$
1.17 $P = 0.30397\,P_{SL}$
1.19 $p = 0.07397\,p_{SL}$, $\rho = 0.1205\,kg/m^3$, $\mu = 1.422 \times 10^{-5} kg/s \cdot m$, $a = 295.1\,m/s$
1.21 $p_\infty = 973.27\,lbf/ft^2$, $\rho_\infty = 0.001267\,slug/ft^3$, $\mu_\infty = 3.3268 \times 10^{-7}\,lbf - s/ft^2$, $T_\infty = 447.42°R$, $a_\infty = 1036.94\,ft/s$
1.22 $h_p = 15\,kft$, $h_T = 12\,kft$, $h_\rho = 15.5\,kft$
1.23 $p_A = 165.747 \times 10^3 N/m^2$
1.24 $p = 3999.7 N/m^2$, gage
1.26 $\Delta p = 53329\,N/m^2$, $F = 42{,}663\,N$.

CHAPTER 2

2.2 continuity is satisfied
2.4 $v_r = 0, v_\theta = K/r$
2.5 continuity is satisfied
2.6 $v = \dfrac{a_1 y^2}{4x^{1.5}} - \dfrac{3a_2 y^4}{8x^{2.5}}$
2.8 $V_1 = 3.979\,m/s, V_2 = 15.915\,m/s, V_3 = 1.768\,m/s$
2.9 $U_0 = 299.586\,cm/s$
2.10 $Q = U_\infty H$
2.11 $H_U = H_D/2$
2.12 $Q = 2U_\infty H/\pi$
2.13 $H_U = 0.6817\,H_D$
2.14 $V_{out_{end}} = 0.087\,m/s$
2.17 $\vec{a} = \dfrac{3x}{4t^2}\hat{i}$
2.21 $t = 1.55\,hours$
2.23 $t = 31\,days$
2.26 $\left(\dfrac{dp}{dx}\right)_2 = \dfrac{1}{16}\left(\dfrac{dp}{dx}\right)_1$
2.27 $C_d = 0.0167$
2.30 $C_d = 0.01933$
2.32 **a:** $\mathrm{Re} = 1.848 \times 10^5, M = 0.176$; **b:** $\mathrm{Re} = 5 \times 10^8, M = 0.834$
2.38 $T_t = 270.45\,K$
2.39 $T_t = 398.8\,K$

CHAPTER 3

3.1 $h = 2.388m$
3.6 **a:** $M = 0.254, \mathrm{Re} = 6.71 \times 10^6$;
b: $p_2 = 7.328 \times 10^4 N/m^2 = 10.63psi, p_3 = p_4 = 6.065 \times 10^4 N/m^2 = 8.797psi$,
$p_5 = p_6 = 7.063 \times 10^4 N/m^2 = 10.24psi$;
c: $dp/dy = 0$ in boundary layer;
d: $U_2 = 0.00, U_2 = 166.66\,m/s, U_2 = 76.38\,m/s$
3.7 If the airplane were flying at sea level where the density (ρ) is $1.2250\,kg/m^3$; Airspeed $= 205.74\,km/h$
3.10 $U_\infty = 76.78\,m/s, q_\infty = 1500\,N/m^2, U_e = 143.65\,m/s, U_{rel} = 66.87\,m/s, C_p = -2.5$
3.11 The volumetric flow rate $Q = U_2 A_2 = 7.3386\,ft^3/s$
3.12 $\mathrm{P_{ts}} = 77{,}689.12\,N/m_2, \mathrm{P_t} = \mathrm{P_{atm}} = 79{,}501\,N/m_2$
3.14 $p_1 = 2121.6\,lbf/ft^2, U_2 = 67.1\,ft/s, Q_2 = 3.294\,ft^3/s$
3.17 $Circulation = -\Gamma$
3.18 The flow is rotational because of the effect of viscosity.
3.19 **a:** 17/3, **b:** 83/15, **c:** 17/3
3.20 rotational, $\Gamma = 0, \Gamma = 0$
3.22 **a:** $\vec{V} = \dfrac{Kx}{x^2 + y^2}\hat{i} + \dfrac{Ky}{x^2 + y^2}\hat{j}$, irrotational, at (2,0) $|\vec{V}| = K/2, \theta = 0°$; at $(\sqrt{2}, \sqrt{2})|\vec{V}| = K/2$, $\theta = 45°$; at (0,2) $|\vec{V}| = K/2, \theta = 90°$.
b: $\psi = K\theta$.
c: streamlines are perpendicular to lines of constant velocity potential.
3.24 $u = y + x, v = -y$

3.25 -4

3.26 **a:** continuity is satisfied, $\psi = \dfrac{x^2y^2}{2} - \dfrac{xy^3}{3} + C$;

b: flow is irrotational so no velocity potential exists; **c:** $-1/12$

3.28 $l = \rho_\infty U_\infty \Gamma - \dfrac{\rho_\infty \Gamma^2}{4\pi h}$, as $h \to \infty l = \rho_\infty U_\infty \Gamma$

3.30 $P - P_\infty = -1.654 \times 10^3\, N/m^2$

3.32 $\psi = U_\infty \sin\theta\left(r - \dfrac{R^2}{r}\right) + \dfrac{\Gamma}{2\pi}\ln r$

3.33 $\pm 30°$ from stagnation point, $\dfrac{dp}{d\theta} = -3.464 q_\infty$

3.34 $p_u = 1.23 \times 10^5 N/m^2$, $p_l = 9.98 \times 10^4 N/m^2$, cylinder will move down

3.35 $D = 436.9\,N$, $M = 1.092 \times 10^4 N - m$, $\mathrm{Re} = 7.34 \times 10^5$

3.37 $P = 83290\,N/m^2$, $V_{\theta=90°} = -36\,m/s$, $V_{\theta=270°} = 180\,m/s$

3.39 $C_l = 0$, $C_d = 8/3$

3.41 $B = 2.25 \times 10^4 ft^3/s$, $l = 952\,lbf$, $d = 0$

3.43 $C_l = \dfrac{\Gamma}{RU_\infty}$

3.44 $L = 110.64\,N$

3.46 $C_D = 1.15$

3.47 $C_L = 0$, $C_D = 1.6875$

3.48 $D = 251.92$

3.49 $\omega = 60°$

3.51 $\psi = K\theta/2\pi$

CHAPTER 4

4.1 $\delta = 3.0215 \times 10^{-3} m, \delta^* = 1.0394 \times 10^{-3} m, C_f = 1.605 \times 10^{-3}, \tau = 0.0983\,N/m^2, D = 0.4915\,N$

4.2 $\beta = 1.32, f'' = 1.3781, \dfrac{\tau_{\beta=1.32}}{\tau_{\beta=0}} = \dfrac{5.11\,A^{1.5}x^3}{u_\infty^{1.5}}$

4.3 $\beta = 1.0, 0.992, 0.667, 0.162$ for $\theta = 0°, 10°, 65°, 85°$ respectively.

4.5 $f(x=0) = 1.320\sqrt{x}$

4.6 $v_w = \dfrac{2.22 \times 10^{-2}}{\sqrt{x}} ft/s$

4.8 $\dfrac{\delta}{x}\sqrt{\mathrm{Re}_x} = 4.6409, \dfrac{\delta^*}{x}\sqrt{\mathrm{Re}_x} = 1.7403, \dfrac{v_e}{u_e}\sqrt{\mathrm{Re}_x} = 0.8702, C_f\sqrt{\mathrm{Re}_x} = 0.64643, C_f\sqrt{\mathrm{Re}_x} = 1.2929$

4.10 $D = 46.608\,lbf$, $C_d = 0.01216$

4.13 $C_d = 0.00696$

4.14 Blasius/Prandtl-Schlichting: $C_D = 0.003872$, $D = 1.334\,N$; equation (4.87): $C_D = 0.003536$, $D = 1.218\,N$

4.15 $D/b = 19.48\,N/m$ using the Prandtl $-$ Schlichting relation, $D/b = 18.014\,N/m$ using the approximate formula

4.17 $K = 1.7154 \times 10^{-4}\, cal/cm \cdot s \cdot k$, $\mathrm{Pr} = 0.7349$

4.19 $Q = 11.83\,Btu/s$

4.20 $\theta = 0.08971°$

CHAPTER 5

5.1 $AR = 4, b = 14.14\,m$

5.2 $AR = 1/\tan_{c/4}$

5.4 $C_L = 0.70798$
5.7 $C_d = 0.006173$, 15% over-prediction
5.9 $C_D = 0.001058$
5.13 $\alpha = -4$, $C_{m0.25c} = 0.3387$; $\alpha = +2$, $C_{m0.25c} = 0.0864$; $\alpha = +16$, $C_{m0.25c} = 0.0538$. Only the AVD measurement at $\alpha = -4°$ is close
5.17 $D = 29.58\,lbf$
5.18 $C_f = 0.00288$, $C_{D_0} = 0.00674$, $C_{Di} = 0.2715$, $C_D = 0.2782$

CHAPTER 6

6.1 Kutta condition is satisfied, $\alpha = 4.56°$, $m_{3c/4} = \pi\rho_\infty U_\infty^2 \alpha c^2/2$
6.2 $A_0 = \alpha_{eff} + 0.4381$, $A_1 = 0.22591$, $A_2 = -0.13974$, $C_l = 6.18831\,\alpha + 1.50184$, $C_{m_{c/4}} = -0.27857$
6.3 $C_l = 2\pi\alpha + 4\pi k$, $C_{m_{ac}} = -\pi k$
6.4 $A_0 = \alpha - 0.02866$, $A_1 = 0.09550$, $A_2 = 0.07915$, $C_l = 2\pi\alpha + 10.11992$, $C_{m_{c/4}} = -0.01285$

CHAPTER 7

7.1 $\Gamma_0 = 2.06\,m^2/s$, $w_{y1} = -1.412\,m/s$, $C_{Dv} = 0.00242$, $\propto_e = 9.877°$, $\propto = 11.027°$
7.2 $(w_{y1})_p/(w_{y1})_e = 1$
7.3 $\propto_2 = 6.4°, 6.82°$ for $AR_2 = 6.5, 5.0$, respectively
7.8 $w_{1,1s} = -71.5187\,\Gamma_1/4\pi b$
7.9 $C_L = 1.1576\pi\alpha$
7.10 $C_L = 1.1385\pi\alpha$
7.11 $C_L = 0.97401\pi(\alpha + 0.0164)$
7.12 $C_L = 0.57111\pi\alpha$
7.13

α	0°	5°	10°	15°
C_L	0.000	0.154	0.377	0.601

7.14 $\Delta C_D = 0.0, 0.0135, 0.066, 0.161$ for $\alpha = 0°, 5°, 10°, 15°$, respectively

CHAPTER 8

8.1 $\dot{m} = 342.75.0\,kg/s$, $Q = 1226.17\,m^3/s$
8.2 $M_\infty = 8.803$
8.3 $\mathrm{Re}_\infty = 1.0454 \times 10^6$ to 0.864×10^6
8.4 $T_\infty = 50.722\,K$, $U_\infty = 1142.17\,m/s$ and is independent of pressure, $p_\infty = 499.8\,N/m^2$
8.5 $p_t = 1.81112 \times 10^5\,N/m^2$, $T_\infty = 290.55\,K$, $\mathrm{Re} = 3.002178 \times 10^6$, $C_p = 1.24643$
8.7 $\dot{m}_9 = 6.54174 \times 10^{-3}\,kg/s$, $\dot{m}_{15} = 8.84558 \times 10^{-3}\,kg/s$
8.8 For 97.250 *psia*: $p = 93.947\,psia$, $T = 647.94°R$, $M = 0.30$, $U = 374.3\,ft/s$, for 93.947 *psia*: $p = 9.117\,psia$, $T = 332.69°R$, $M = 2.23$, $U = 1993.88\,ft/s$, for 9.117 *psia*: $p = 97.250\,psia$, $T = 654.36°R$, $M = 0.20$, $U = 250.79\,ft/s$
8.9 For 51.38 *psia*: $p = 51.38\,psia$, $T = 626.65°R$, $M = 0.5432$, $U = 666.52\,ft/s$
8.10 The flow must be from 2 to 1
8.11 $\left(\dfrac{p_{t2}}{p_2}\right) = \sqrt[a]{\dfrac{7.2\,M_\infty^2}{(7\,M_\infty^2 - 1)}}$
8.13 $p = 5.2274 \times 10^4\,N/m^2$, $\Delta h = 33.30\,cm$ Hg, $q = 6.745 \times 10^4\,N/m^2$
8.14 For a single ramp: $M_2 = 2.5$, $\Delta s/R = 0.0388$; for two 5 degree ramps: $M_2 = 2.519$, $\Delta s/R = 0.0104$; for infinite: $M_2 = 2.527$, $\Delta s/R = 0.0$
8.15 $p_2 = 1.70p_1$, $p_3 = 0.5479p_1$, $C_l = 0.4052$, $C_d = 0.0715$, $C_{m_{c/2}} = 0.0$
8.16 $L = 3.712\,m$
8.17 Region 2: $p = 6.395 \times 10^3\,N/m^2$, $M = 2.272$, $\theta = 5°$; Region 3: $p = 9.345 \times 10^3\,N/m^2$, $M = 2.075$, $\theta = -10°$; Regions 4 and 5: $p = 2.50p_1$, $M = 1.886$, $\theta = -5.2°$

8.18 $c_{\max} = 39.7\,cm$
8.19 $p_t = 698\,lbf/ft^2$, $T_t = 429.24°R$, $M = 0.762$
8.20 $P_2 = 1122.84\,N/m^2$, $1142.14\,N/m^2$, $28,376.15\,k$, $T_t = 28521\,K$, $M = .14437$

CHAPTER 9

9.1 $p_{t1} = p_\infty + \dfrac{\rho_\infty U_\infty^2}{2}$
9.2 NACA 0003 airfoil section, $AR' = 1.744$
9.3 $dy_e = 1.1657\,dy_\infty$

CHAPTER 10

10.2 $C_l = \dfrac{4}{\sqrt{M_\infty^2 - 1}}\dfrac{z_{\max}}{c}$, $C_d = \dfrac{1}{\sqrt{M_\infty^2 - 1}}\left(4\alpha^2 + \dfrac{2}{3}\left(\dfrac{z_{\max}}{c}\right)^2\right)$, $C_m = \dfrac{1}{\sqrt{M_\infty^2 - 1}}\left(-2\alpha - \dfrac{2}{3}\dfrac{z_{\max}}{c}\right)$
10.3 For $\alpha = 3.2°$: $C_l = 0.0789$, $C_d = 0.0138$ $C_l/C_d = 5.717$, $C_m = -0.039$
10.4 For $\alpha = 5°$: $C_l = 0.20041$, $C_d = 0.02124$ $C_l/C_d = 9.44$, $C_m = -0.09565$
10.5 For $\alpha = 5°$: $C_l = 0.20026$, $C_d = 0.02129$ $C_l/C_d = 9.41$, $C_m = -0.09566$
10.6 For $\alpha = 10°$: $C_l = 1.095$, $C_d = 0.0$, $C_m = -0.274$
10.9 $C_A = 0.0096$, $C_N = 0.192$, $C_l = 0.19$, $C_d = 0.03$, $C_{m_{c/2}} = 0.008$
10.12 $C_{p_u} = 1.021[\,0.14(1 - 2x) - 0.1047\,]$, $C_{p_l} = 1.021[\,0.14(1 - 2x) + 0.1047\,]$

CHAPTER 11

11.3 $C_L = 0.2438$, $C_D = 0.6242 + C_{D,\,friction}$
11.4 $C_L = 0.05315\alpha$, $C_D = C_L\alpha + 0.0270$
11.5 $M = 1.179$
11.16 $\cot \Delta_{LE} = 2.68$
11.20 $C_p = 4\left(\dfrac{t}{L}\right)\dfrac{1 - 2(x/L)}{\sqrt{M_\infty^2 - 1}}$

CHAPTER 12

12.4 $C_p = 0.6427$
12.11 $L/D = 2/(\pi \tan\theta_c)$ for $\alpha = 0°$
12.12 $x_{cp} = 2x_L/3$

CHAPTER 13

13.1 $\alpha = \alpha_{0l} + \dfrac{W}{q_\infty S C_{L_\alpha}}$
13.5 $x_{tr} = 0.93\,ft$

Index

Credits

p. 15, Werner, Johannes, Knight of Germany: Oswald Boelcke – German Ace; **p. 17,** Tribute to John R. Boyd. Code One Magazine12(3), 1997. Lockheed Martin; **p. 18,** The Viper revolution. Reprinted by permission from Air Force Magazine, published by the Air Force Association; **p. 139, Fig. 3.17,** Boundary Layer Theory, 1968. McGraw-Hill; **p. 144, Fig. 3.21,** Boundary Layer Theory. 6th Ed.; **p. 161, Fig. 3.31,** Boundary Layer Theory. 6th Ed.; **p. 201, Fig. 4.12,** Source: Data from Viscous Fluid Flow. 3rd Ed; **p. 242,** Based on Theory of Wing Sections; **p. 245, Unnumbered,** Source: Data from Theory of Wing Sections; **pp. 250–251, Table 5.1,** Source: Data from Jane's All the World's Aircraft, 1973–1974, 1966–1967, 1984–1985, and 2011–2012; **p. 257, Fig. 5.13,** Source: Data from Theory of Wing Sections; **p. 261, Fig. 5.14,** Source: Data from Theory of Wing Sections; **p. 269, Fig. 5.17,** Source: Data from Theory of Wing Sections; **p. 270,** Based on Theory of Wing Sections; **p. 271, Fig. 5.18,** Source: Data from Theory of Wing Sections; **p. 273,** Source: Data from Aerodynamics, Aeronautics and Flight Mechanics; **p. 277, Fig. 5.21,** Shevell, Richard S., Fundamentals of Flight, 2nd Ed., © 1989, pp. 182, 183. Reprinted and Electronically reproduced by permission of Pearson Education, Inc., Upper Saddle River, New Jersey; **p. 278, Fig. 5.23,** Shevell, Richard S., Fundamentals of Flight, 2nd Ed., © 1989, pp. 182, 183. Reprinted and Electronically reproduced by permission of Pearson Education, Inc., Upper Saddle River, New Jersey; **p. 287, Fig. 5.27,** F-16 Air Combat Fighter. General Dynamics Report F-16-060, 1979; **p. 290, Fig. 5.29,** Analysis and comparison of Air Force flight test performance data with predicted and generalized flight test performance data for the F-106A and B airplanes, 1961; **pp. 299–300, Table 5.6,** Pinkerton, Robert M. Calculated and measured pressure distributions over the midspan section of the NACA 4412 airfoil; **p. 315, Fig. 6.6,** Source: Data from Theory of Wing Sections; **p. 323, Fig. 6.8,** Source: Data from Theory of Wing Sections; **p. 324, Fig. 6.9,** Source: Data from Theory of Wing Sections; **p. 325, Fig. 6.10,** Source: Data from Theory of Wing Sections; **p. 330, Fig. 6.17,** Based on Low Reynolds number airfoil design. In Low Reynolds Number Aerodynamics of Aircraft, VKI Lecture Series; **p. 331,** High-lift aerodynamics. J. Aircraft, VOL. 12, NO. 6. A. M. O. Smith. McDonnell Douglas Corporation, Long Beach, Calif; **pp. 331, 333,** Data from A class of airfoils designed for high lift in incompressible flows. J. Aircraft 10; **p. 332, Fig. 6.18,** Data from A class of airfoils designed for high lift in incompressible flows. J. Aircraft 10; **p. 332, Fig. 6.19,** Data from A class of airfoils designed for high lift in incompressible flows. J. Aircraft 10; **p. 333, Fig. 6.20,** Data from A class of airfoils designed for high lift in incompressible flows. J. Aircraft 10; **p. 334, Fig. 6.21,** Data from A class of airfoils designed for high lift in incompressible flows. J. Aircraft 10; **p. 335, Fig. 6.22,** Data from A class of airfoils designed for high lift in incompressible flows. J. Aircraft 10; **pp. 337–338, Fig. 6.23,** Source: Data from Low-speed aerodynamic characteristics of a 7-percent thick section designed for general aviation applications. NASA Tech. Note D-7428; **p. 339, Fig. 6.24,** Based on Navier-Stokes calculations on multi-element airfoils using a chimera-based solver. In High-Lift System Aerodynamics, AGARD CP 515; **pp. 339–340,** Data from High-lift design for large civil aircraft. In High-Lift System Aerodynamics, AGARD CP 515; **p. 340, Fig. 6.25,** Data from Flaig A, Hilbig R. 1993. High-lift design for large civil aircraft. In High-Lift System Aerodynamics, AGARD CP 515; **p. 341, Fig. 6.26,** Data from High-lift design for large civil aircraft. In High-Lift System Aerodynamics, AGARD CP 515; **p. 342, Fig. 6.27,** Based on Theoretical and experimental study of the drag of multielement airfoils. Presented at Fluid and Plasma Dyn. Conf., 11th, AIAA; **p. 342, Fig. 6.28,** Based on Theoretical and experimental study of the drag of multielement airfoils. Presented at Fluid and Plasma Dyn. Conf., 11th, AIAA; **p. 343, Fig. 6.29,** Based on A solution to the 2-D separated wake modeling problem and its use to predict of arbitrary airfoil sections. Presented at AIAA Aerospace Science Meeting; **p. 344, Fig. 6.30,** Based on Rechkzeh, D. 2003, Aerodynamic design of the high-lift wing for a megaliner aircraft. Aerosp. Sci. Tech, 7:107–119; **p. 346, Fig. 6.32,** Source: Data from Evaluation of turbulence models for high lift military airfoil flowfields and High lift research program for a fighter-type, multielement airfoil at high Reynolds numbers, both papers presented at AIAA Aerosp. Sci. Meet, 34th, AIAA Pap. 96–0057; **p. 346, Fig. 6.33,** Data from High lift research program for a fighter-type, multi-element airfoil at high Reynolds numbers. Presented at AIAA Aerosp. Sci. Meet., 34th, AIAA Paper 96–0057; **p. 383, Fig. 7.20,** Data from Lifting-line theory for arbitrarily shaped wings. J. Aircraft 36; **pp. 383–384,** Data from Numerical lifting line theory applied to drooped leading-edge wings below and above stall. J. Aircraft 17; **p. 384, Fig. 7.21,** Data from Numerical lifting line theory applied to drooped leading-edge wings below and above stall. J. Aircraft 17; **p. 385, Fig. 7.22,** Data from Numerical lifting line theory applied to drooped leading-edge wings below and above stall. J. Aircraft 17; **p. 388, Fig. 7.24,** Based on Subsonic panel methods—a comparison of several production codes. Presented at AIAA Aerosp. Sci. Meet., 23rd, AIAA Pap. 85-0280; **p. 406, Fig. 7.34,** Source: Data from Low-speed tests on 45-deg swept-back wings, part I: pressure measurements on wings of aspect ratio 5. ARC R&M 2882; **p. 407, Fig. 7.35,** Data from Some developments in boundary layer research in the past thirty years. J. Roy. Aeron. Soc. 64; **p. 415, Fig. 7.41c, d,** Data from Computational and physical aspects of vortex breakdown on delta wings. Presented at AIAA Aerosp. Sci. Meet., 33rd, AIAA

Pap. 95 -0585; **p. 416, Fig. 7.43,** Data from Predictions of vortex-lift characteristics by a leading-edge suction analogy. J. Aircraft 8; **p. 417, Fig. 7.44,** Data from Predictions of vortex-lift characteristics by a leading-edge suction analogy. J. Aircraft 8; **p. 419, Fig. 7.46,** Source: Data from Experimental investigations of influence of edge shape on the aerodynamic characteristics of low aspect ratio wings at low speeds. J.Aeron. Sci. 22; **p. 420, Fig. 7.47,** Source: Data from Aerodynamik des Flugzeuges; **p. 420, Fig. 7.48,** Source: Data from Experimental investigations of influence of edge shape on the aerodynamic characteristics of low aspect ratio wings at low speeds. J. Aeron. Sci. 22; **p. 421, Fig. 7.49,** Source: Data from Experimental investigations of influence of edge shape on the aerodynamic characteristics of low aspect ratio wings at low speeds. J.Aeron. Sci. 22; **p. 423,** Computational and physical aspects of vortex breakdown on delta wings. Presented at AIAA Aerosp. Sci. Meet., 33rd, AIAA Pap. 95-0585; **pp. 424–425,** Aerodynamic features of designed strake-wing configurations. J. Aircraft 19. American Institute of Aeronautics and Astronautics; **p. 425, Fig. 7.51,** Data from Aerodynamic features of designed strake-wing configurations. J. Aircraft 19; **p. 426, Fig. 7.52,** Data from Aerodynamic features of designed strake-wing configurations. J. Aircraft 19; **p. 426, Fig. 7.53,** Erickson GE. 1982. Vortex flow correlation. Presented at Congr. Intl. Coun. Aeron. Sci., 13th, ICAS Pap. 82–6.61, Seattle, WA; **p. 427, Fig. 7.54,** Wurtzler KE, Tomaro RF. 1999; **p. 428, Fig. 7.55,** Data from Northrop F-5 Case Study in Aircraft Design Washington, DC: AIAA; **p. 429, Fig. 7.56,** Data from Asymmetric vortex shedding from bodies of revolution. AIAA; **p. 430, Fig. 7.57,** Data from High-angle-of-attack yawing moment asymmetry of the X-31 aircraft from flight test. Presented at Appl. Aerodyn. Conf., 12th, AIAA Pap. 94-1803; **pp. 430–431,** High-angle-of-attack yawing moment asymmetry of the X-31 aircraft from flight test. Presented at Appl. Aerodyn. Conf., 12th, AIAA Pap. 94-1803; **p. 431, Fig. 7.58,** Data from High-angle-of-attack yawing moment asymmetry of the X-31 aircraft from flight test. Presented at Appl. Aerodyn. Conf., 12th, AIAA Pap. 94-1803; **p. 431,** Cobleigh BR. 1994. High-angle-of-attack yawing moment asymmetry of the X-31 aircraft from flight test. Presented at Appl. Aerodyn. Conf., 12th, AIAA Pap. 94–1803, Colorado Springs, CO; **p. 432,** Data from Asymmetric vortex shedding from bodies of revolution. AIAA; **p. 432,** Data from Predicted aerodynamic characteristics of maneuvering aircraft. Presented at Appl. Aerodyn. Conf., 14th, AIAA Pap. 96-2433; **p. 433, Fig. 7.59,** Data from Predicted aerodynamic characteristics of maneuvering aircraft. Presented at Appl. Aerodyn. Conf., 14th, AIAA Pap. 96-2433; **pp. 433–434,** X-31 Project Description; **p. 434, Fig. 7.60,** Data from In-flight flow field analysis on the NASA F-18 high alpha research vehicle with comparison to the ground facility data. Presented at AIAA Aerosp. Sci. Meet., 28th, AIAA Pap. 90-0231; **pp. 433–434,** In-flight flow field analysis on the NASA F-18 high alpha research vehicle with comparison to the ground facility data. Presented at AIAA Aerosp. Sci. Meet., 28th, AIAA Pap. 90-0231; **p. 434, Table 7.3,** Data from A discussion of aerodynamic control effectors for unmanned air vehicles. Presented at Tech. Conf.Workshop Unmanned Aerosp. Veh., 1st, AIAA Pap. 2002-3494; **p. 435, Fig. 7.61,** Data from A discussion of aerodynamic control effectors for unmanned air vehicles. Presented at Tech. Conf.Workshop Unmanned Aerosp. Veh., 1st, AIAA Pap. 2002 -3494; **p. 435, Fig. 7.62,** Data from The role of size in the future of aeronautics. Presented at Intl. Air Space Symp., AIAA Pap. 2003-2902; **p. 436, Fig. 7.63,** Data from A numerical investigation of novel planforms for micro UAVs. Presented at AIAA Aerosp. Sci. Meet., 44th, AIAA Pap. 2006-1265; **p. 488, Table 8.6,** Data from The drag of a compressible turbulent boundary layer on a smooth plate with and without heat transfer. J. Fluid Mech. 18; **p. 489, Table 8.8,** Data from The drag of a compressible turbulent boundary layer on a smooth plate with and without heat transfer. J. Fluid Mech. 18; **p. 496,** Source: Data from Bertin and Cummings, Annual Review of Fluid Mechanics; **p. 498,** American Institute of Aeronautics and Astronautics; **p. 498,** Special section in the September–October 2001 issue of the Journal of Spacecraft and Rockets; **p. 500,** Source: Data from Aerodynamic and performance analyses of a superorbital re-entry vehicle. In Dynamics of Manned Lifting Planetary Entry, New York: John Wiley; **p. 500,** Source: Data from Missions and requirements.AGARD Report 761, Special Course on Aerothermodynamics of Hypersonic Vehicles, Neuilly sur Seine, France; **p. 503, Fig. 8.25,** Data from High Speed Wind Tunnel Handbook. Vought Aeronautics Division AER-EIR-13552-B; **p. 523,** Data from propellers to jets in fighter aircraft design. Lockheed Horizons 23; **p. 524, Fig. 9.6,** Data from propellers to jets in fighter aircraft design. Lockheed Horizons 23; **p. 528, Fig. 9.10,** Data from The aerodynamic art. J. Roy. Aero. Soc. 60; **p. 528, Fig. 9.11,** Data from The aerodynamic art. J. Roy. Aero. Soc. 60; **p. 529, Fig. 9.12,** Data from The aerodynamic art. J. Roy. Aero. Soc. 60; **p. 531, Fig. 9.13,** Forsythe, J R; Blake DC. 2000. Private Transmittal; **p. 531, Fig. 9.14,** Dreikomponentenmessungen bis zu grossen anstellwinkeln an fuenf tragfluegeln mit verschieden umrissformen in unterschall und ueberschallstroemung. Z.Flugwissensch. 13:447-453; **p. 532, Fig. 9.15,** Dreikomponentenmessungen bis zu grossen anstellwinkeln an fuenf tragfluegeln mit verschieden umrissformen in unterschall und ueberschallstroemung. Z.Flugwissensch. 13:447-453; **p. 535,** Shock wave drag reduction. Annual Review of Fluid Mechanics 36:814-96; **p. 536,** Source: Data from The transonic flow past two-dimensional aerofoils. J. Roy. Aero. Soc. 68; **p. 537, Fig. 9.19,** Data from Supercritical aerodynamics: worthwhile over a range of speeds. Astronaut. Aeronaut. 10(8); **p. 539, Fig. 9.21,** Source: Data from Some developments in boundary layer research in the past thirty years. J. Roy. Aero. Soc. 64; **p. 543, Fig. 9.24,** Data from An introduction to the flow about plane swept-back wings at transonic speeds. J. Roy. Aero. Soc. 64; **p. 544, Fig. 9.25,** Data from Recent advances in aerodynamics for transport aircraft. Aeronaut. Astronaut; **pp. 546–547, Fig. 9.28 and 9.29,** Data from Northrop F-5 Case Study in Aircraft Design. Washington, DC:AIAA; **p. 548, Fig. 9.31,** Source: Courtesy of NASA; **p. 557, Fig. 9.36,** Morton SA, Eymann TA, McDaniel DR, Sear DR, Tillman B, Tuckey TR. 2011. Rigid and maneuvering results with control surface and 6DoF

motion for Kestrel v2. Presented at AIAA Aersosp. Sci. Meet., 49th, AIAA Paper 2011-1106, Orlando, FL, Jan. 2011; **p. 597, Fig. 11.9,** Data from Characteristics of rectangular wings at supersonic speeds. J. Aeron. Sci. 14; **p. 599, Table 11.1,** Source: Data from Characteristics of rectangular wings at supersonic speeds. J. Aeron. Sci. 14; **p. 600, Fig. 11.12,** Source: Data from Investigation of wing characteristics at a Mach number of 1.53, III: unswept wings of differing aspect ratio and taper ratio. NACA Res. Mem. A8E06; **p. 603, Fig. 11.15,** Source: The Dynamics and Thermodynamics of Compressible Fluid Flow. New York: The Ronald Press; **pp. 607–608,** Data from Arrow wings for supersonic cruise aircraft. Presented at Aerosp. Sci. Meet., 18th, AIAA Pap. 78–0151, Huntsville, AL; **p. 607, Table 11.2,** Aerodynamic performance of delta wings at supersonic speeds. J. Aeron. Sci. 14. Journal of the Aeronautical Society, AIAA; **p. 607, Fig. 11.18,** Data from Arrow wings for supersonic cruise aircraft. Presented at Aerosp. Sci. Meet., 18th, AIAA Pap. 78–0151, Huntsville, AL; **p. 612, Fig. 11.20,** Source: The Dynamics and Thermodynamics of Compressible Fluid Flow. New York: The Ronald Press; **pp. 614–615, Fig. 11.21,** Data from Aerodynamic performance of delta wings at supersonic speeds. J. Aeron. Sci. 14; **p. 636, Fig. 11.34,** Source: Data from Possible types of flow at swept leading edges. Aeronaut.Quart. 15:72–82 and Real flow limitations in supersonic airplane design. Presented at Aerosp. Sci. Meet., 16th, AIAA Pap. 78–0147, Huntsville, AL; **pp. 637–639,** Used with the permission of the Canadian Aeronautics and Space Institute; **p. 641, Fig. 11.36,** Origins and overview of the shaped sonic boom demonstration program. Presented at Aerosp. Sci. Meet., 43rd, AIAA Pap. 2005–0005, Reno, NV; **pp. 641, 642,** Data from Harris RV. 1992. On the threshold—the outlook for supersonic and hypersonic aircraft. J. Aircraft 29; **p. 642, Fig. 11.37,** Data from Harris RV. 1992. On the threshold—the outlook for supersonic and hypersonic aircraft. J. Aircraft 29; **p. 643, Fig. 11.38,** Tomaro RF, Wurtzler KE. 1999. High speed configuration aerodynamics: SR-71 to SMV. Presented at Appl. Aerodyn. Conf., 17th, AIAA Pap. 99–3204, Norfolk, VA; **p. 661, Fig. 12.1,** Annual Review of Fluid Mechanics by Bertin article, William Rees. Reproduced with permission of Annual Reviews in the format Republish in a book via Copyright Clearance Center; **pp. 663–664,** Annual Review of Fluid Mechanics by Bertin article, William Rees. Reproduced with permission of Annual Reviews in the format Republish in a book via Copyright Clearance Center; **p. 664, Fig. 12.4,** Bertin JJ. 1994. Hypersonic Aerothermodynamics. Washington, DC: AIAA; **p. 665, Fig. 12.5,** Bertin JJ. 1994. Hypersonic Aerothermodynamics. Washington, DC: AIAA; **p. 672, Fig. 12.10,** Data from Composition and thermodynamic properties of air in chemical equilibrium. NACA Tech. Note 4265; **p. 690, Fig. 12.24,** Data from A base pressure experiment for determining the atmospheric profile of the planets. J. Spacecr. Rockets 10; **p. 693, Fig. 12.25,** Based on Aerodynamic problems of manned space vehicles. J. Roy. Aeronaut. Soc. 63; **p. 694, Fig. 12.26 ,** Based on Squire LC. 1976a. Flow regimes over delta wings at supersonic and hypersonic speeds. Aeronaut. Quart. 27; **p. 695,** Several families of viscous optimized waveriders – a review of waverider research at the University of Maryland. Presented at International Hypersonic Waverider Symposium, 1st, College Park, MD; **p. 695–696, Fig. 12.27, and Fig. 12.28,** Based on Several families of viscous optimized waveriders – a review of waverider research at the University of Maryland. Presented at International Hypersonic Waverider Symposium, 1st, College Park, MD; **pp. 695–696,** Design of waveriders. Presented at Space Course on Low Earth Orbit Transportation, 2nd, Munich, Germany; **p. 697, Fig. 12.30,** Based on Viscous optimized hypersonic waveriders. Presented at Aerosp. Sci. Meet., 25th, AIAA Pap. 87–0272, Reno, NV; **p. 698, Fig. 12.31 and Fig. 12.32,** Source: Data from Preliminary assessment of a Mach 4 and a Mach 6 waverider. Presented at International Hypersonic Waverider Symposium, 1st, College Park, MD; **p. 700, Fig. 12.33,** Based on Efficient hypersonic accelerators derived from analytically defined flowfields. Presented at Aerosp. Sci; **pp. 709–710,** Wind tunnel testing, flight scaling, and flight validation with Hyper-X. Presented at Advanced Measurement and Ground Test. Conf., 20th, AIAA Pap. 98–2866, Albuquerque, NM; **pp. 708–709, Fig. 12.38 and Fig. 12.39,** Based on Dual-fuel lifting body configuration development. Presented at Intern. Space Planes and Hypersonic Systems and Techn. Conf., AIAA Pap. 96–4592, Norfolk, VA; **pp. 710–711, Fig. 12.40 and Fig. 12.41,** Data from Hypersonic Mach number and real gas effects on Space Shuttle Orbiter aerodynamics. J. Space. Rockets 21; **pp. 712, 713, 714,** Flight data for boundary-layer transition at hypersonic and supersonic speeds. J. Spacecr. Rockets 36. American Institute of Aeronautics and Astronautics; **p. 715,** Fifty years of hypersonic, where we've been, where we're going. Progr. Aerosp. Sci. 39; **p. 723, Fig. 13.1,** Based on The annals of the polymorph, a short history of V-G. Air International 8(3); **p. 725, Fig. 13.3,** Data from Aerodynamic design philosophy of the Boeing 737. J. Aircraft 3; **pp. 725–726, Fig. 13.4, 13.5,** Data from Size effects in conventional aircraft design. J. Aircraft 7; **pp. 728–729, Fig. 13.8 and Fig. 13.9,** Source: Data from Aerodynamik des Flugzeuges. Berlin: Springer Verlag; **pp. 729–730,** Smith A.M.O. 1975. High-lift aerodynamics. J. Aircraft 12:501–530. **p. 733, Fig. 13.12,** Based on Two decades of the 'Twenty-One'. Air Enthusiast International 6(5); **p. 733,** Recent advances in aerodynamics for transport aircraft. Aeronaut. Astronaut. 11(12); **p. 734, Fig. 13.13,** Based on Recent advances in aerodynamics for transport aircraft. Aeronaut. Astronaut. 11(12); **p. 735, Fig. 13.14,** Source: Data from Some developments in boundary layer research in the past thirty years. J. Roy. Aeronaut. Soc. 64(590); **pp. 736–737, Fig. 13.16 and Fig. 13.17,** Based on Circulation control technology for powered-lift STOL aircraft. Lockheed Horizons 24; **pp. 738, 740, 766, 767, Figs. 13.18,13.19,13.21, 13.42 and 13.43,** Source: Practical aerodynamic problems—military aircraft. Transonic Aerodynamics, by D. Nixon. Essay by R.G. Bradley. Transonic Perspective Symposium, Moffett Field, CA, Feb. 18-20, 1981. American Institute of Aeronautics and Astronautics; **p. 745, Table 13.1,** Application of laminar flow control to large subsonic military transport airplanes. Presented at Aerosp. Sci. Meet., 16th, AIAA Pap. 78–0095, Huntsville, AL; **p. 748, Fig. 13.25,** Source: Data

from Gates Learjet, unpublished data; **p. 749,** Aircraft drag reduction technology. AGARD Report 723; **p. 751, Fig. 13.29,** Data from Induced-drag characteristics of crescent-moon-shaped wings. J. Aircraft 24; **pp. 752–753,** Data from Innovative aerodynamics: the sensible way of restoring the growth capability of the EA-6B Prowler. Presented at Appl. Aerodynamics Conf., 5th, AIAA Pap. 87–2362, Monterey, CA; **pp. 753, 755–757, Figs. 13.31, 13.33–13.36,** Data from Innovative aerodynamics: the sensible way of restoring the growth capability of the EA-6B Prowler. Presented at Appl. Aerodynamics Conf., 5th, AIAA Pap. 87–2362, Monterey, CA; **pp. 753–754,** High-angle-of-attack stability and control improvements for the EA-6B Prowler. Presented at Appl. Aerodynamcis Conf. American Institute of Aeronautics and Astronautics; **p. 754, Fig. 13.32,** Based on High-angle-of-attack stability and control improvements for the EA-6B Prowler. Presented at Appl. Aerodynamcis Conf., 5th; **pp. 759–761,** Aerodynamic design evolution of the YF-16. Presented at Aircraft Design, Flight Test, and Operations Meet., 6th, AIAA Pap. 74–935, Los Angeles, CA; **p. 760, Fig. 13.38,** Based on Aerodynamic design evolution of the YF-16. Presented at Aircraft Design, Flight Test, and Operations Meet., 6th, AIAA Pap. 74–935, Los Angeles, CA; **p. 764, Fig. 13.40,** Based on Four decades of transonic fighter design. J. Aircraft 28; **p. 766, Table 13.2,** Source: Practical aerodynamic problems—military aircraft. Transonic Aerodynamics, by D. Nixon. Essay by R.G. Bradley. Transonic Perspective Symposium, Moffett Field, CA, Feb. 18-20, 1981. American Institute of Aeronautics and Astronautics; **p. 767, Fig. 13.44,** A supersonic cruise fighter evolution. Paper 14, H.L. Hillaker F-16XL Flight Test Program Overview, AIAA-83-2730; **p. 768, Table 13.3,** Based on Four decades of transonic fighter design. J. Aircraft 28; **p. 769,** Data from Advanced technology integration for tomorrow's fighter aircraft. Presented at the Aircraft Systems, Design, and Tech. Meet., AIAA Pap. 86–2613, Dayton, OH; **p. 769, Fig. 13.45,** Data from Advanced technology integration for tomorrow's fighter aircraft. Presented at the Aircraft Systems, Design, and Tech. Meet., AIAA Pap. 86–2613, Dayton, OH; **pp. 770–771, Figs. 13.46–13.49,** Data from An evaluation of wing-canard, tail-canard, and tailless arrangements for advanced fighter applications. Presented at Congress of the Intern. Council of the Aeronaut. Sci., ICAS Pap. 84–2.7.3, Tolouse, France; **pp. 770–773,** An evaluation of wing-canard, tail-canard, and tailless arrangements for advanced fighter applications. Presented at Congress of the Intern. Council of the Aeronaut. Sci., ICAS Pap. 84–2.7.3, Tolouse, France; **p. 774,** F-22 design evolution. Code One Magazine 13(2); F-22 design evolution, part II. Code One Magazine 13(4), 1998. Lockheed Martin; **pp. 774, 775, 776,** The evolution of the F-22 Advanced Tactical Fighter. Presented at Aircraft Design Systems Meet., AIAA Pap. 92–4188, Hilton Head Island, SC; **pp. 775, 777,** F-22 design evolution. Code One Magazine 13(2); F-22 design evolution, part II. Code One Magazine 13(4), 1998. Lockheed Martin; **p. 776, Fig. 13.51,** Based on The evolution of the F-22 Advanced Tactical Fighter. Presented at Aircraft Design Systems Meet., AIAA Pap. 92–4188, Hilton Head Island, SC; **pp. 778, 779,** Going vertical—X-35B flight testing. Code One Magazine 16(3), 2001. Lockheed Martin; **p. 792, Fig. 14.1,** Data from Aerodynamic design of Pegasus TM, concept to flight with CFD. In Missile Aerodynamics, AGARD Conf. Proc. No. 493, Symposium of the Fluid Dynamics Panel, Friedrichshafen, Germany; **pp. 795–796,** Wind-tunnel techniques to successfully predict F/A-18E in-flight lift and drag. J. Aircraft 37. American Institute of Aeronautics and Astronautics; **p. 796, Fig. 14.2,** Data from Wind-tunnel techniques to successfully predict F/A-18E in-flight lift and drag. J. Aircraft 37; **p. 797,** Reynolds number scaling at transonic speeds. Presented at Advanced Measurement and Ground Testing Tech. Conf., 20th, AIAA Pap. 98–2878, Albuquerque, NM; **p. 800,** The evolution of the F-22 Advanced Tactical Fighter. Presented at Aircraft Design Systems Meet., AIAA Pap. 92–4188, Hilton Head Island, SC.